Complexity

Filtering, Control, and Optimization of Distributed Networked Systems

Lead Guest Editor: Rui Wang
Guest Editors: Youmin Zhang, Jing Na, and Xue-bo Jin

Filtering, Control, and Optimization of Distributed Networked Systems

Complexity

Filtering, Control, and Optimization of Distributed Networked Systems

Lead Guest Editor: Rui Wang
Guest Editors: Youmin Zhang, Jing Na, and Xue-bo Jin

Contents

Contents

Research on the Multiobjective Optimization of Microwave Wireless Power Receiving in an Unmanned Aerial Vehicle Network

Yuanming Song, Yajie Liu, Wanli Xu, Xu Yang, and Rui Wang

Research Article (8 pages), Article ID 8882528, Volume 2020 (2020)

Hindawi
Complexity
Volume 2022, Article ID 9924163, 11 pages
https://doi.org/10.1155/2022/9924163

Research Article

Differential Evolution Algorithm Combined with Uncertainty Handling Techniques for Stochastic Reentrant Job Shop Scheduling Problem

Rong Hu,[1,2] **Xing Wu**,[1,3] **Bin Qian**,[2] **Jianlin Mao**,[2] **and Huaiping Jin**[2]

[1]*Faculty of Mechanical & Electrical Engineering, Kunming University of Science and Technology, Kunming 650500, China*
[2]*Faculty of Information Engineering and Automation, Kunming University of Science and Technology, Kunming 650500, China*
[3]*Yunnan Vocational College of Mechanical and Electrical Technology, Kunming 650500, China*

Correspondence should be addressed to Xing Wu; xwu@kust.edu.cn

Received 5 March 2021; Revised 11 November 2021; Accepted 18 December 2021; Published 31 January 2022

Academic Editor: Xue-bo Jin

This paper considers two kinds of stochastic reentrant job shop scheduling problems (SRJSSP), i.e., the SRJSSP with the maximum tardiness criterion and the SRJSSP with the makespan criterion. Owing to the NP-complete complexity of the considered RJSSPs, an effective differential evolutionary algorithm (DEA) combined with two uncertainty handling techniques, namely, DEA_UHT, is proposed to address these problems. Firstly, to reasonably control the computation cost, the optimal computing budget allocation technique (OCBAT) is applied for allocating limited computation budgets to assure reliable evaluation and identification for excellent solutions or individuals, and the hypothesis test technique (HTT) is added to execute a statistical comparison to reduce some unnecessary repeated evaluation. Secondly, a reentrant-largest-order-value rule is designed to convert the DEA's individual (i.e., a continuous vector) to the SRJSSP's solution (i.e., an operation permutation). Thirdly, a conventional active decoding scheme for the job shop scheduling problem is extended to decode the solution for obtaining the criterion value. Fourthly, an *Insert*-based exploitation strategy and an *Interchange*-based exploration strategy are devised to enhance DEA's exploitation ability and exploration ability, respectively. Finally, the test results and comparisons manifest the effectiveness and robustness of the proposed DEA_UHT.

1. Introduction

The job shop scheduling problem (JSSP) is one of the most well-known combinatorial optimization problems. As a variant of the JSSP, the reentrant JSSP (RJSSP) can be found in many real-life production and manufacturing environments, such as in semiconductor manufacturing enterprises [1, 2] and textile factories [3]. The main characteristic of the RJSSP is that one job may visit a set of machines more than once during the production process. Since the JSSP has NP-complete property [4] and it can be reduced to the RJSSP, the latter is also NP-complete. The studies on the RJSSP are still limited. Pan and Chen [5] presented two extended binary integer programming formulations for the RJSSP. Topaloglu and Kilincli [6] proposed a modified shifting bottleneck heuristic for the RJSSP with makespan criterion. Chen et al. [7] presented a hybrid estimation of distribution algorithm for the RJSSP with sequence-dependent setup times to minimize makespan.

As we all know, uncertainties are very common in many real-world manufacturing scenarios. At present, some uncertain JSSPs have been studied. Most of them are the JSSP with stochastic processing times [8–22], and the rest are the JSSP with probabilistic machine availability [23], the JSSP with fuzzy processing times [24], and the JSSP with fuzzy machine availability [25]. In these studies, evolutionary algorithms are the main methodology, and makespan or tardiness/earliness is the main optimization criterion. In terms of the JSSP with stochastic processing times, how to evaluate the solution's expected objective value

(i.e., criterion value) reasonably is one of the key links in the design of the algorithm. The direct method is to sample the corresponding stochastic model multiple times to obtain multiple objective values, and then use the average of these sampling values as an approximate estimation of the expected objective value. Obviously, the more the sampling times, the more stable and reliable the estimated value is. This method is the most used method in existing research. However, such a method usually has a high computation cost. Thus, several researchers have adopted three types of techniques to control and reduce the computation cost. The first is the optimal computing budget allocation technique (OCBAT) [26]. Zhang et al. [13] and Yang et al. [16] utilized it to allocate limited computation budgets to assure more reliable evaluation for better solutions. The second is the problem conversion technique. Shen and Zhu [19] used it to convert the stochastic models of the JSSPs to the deterministic ones, in which the confidence or robustness level is considered. Then, the objective value of each solution was calculated via these deterministic models. The third is the objective value prediction technique, which is mainly driven by the simulation metamodel. Ghasemi et al. [22] constructed a metamodel by using genetic programming (GP) to directly predict the solution's objective value. However, as for the uncertain RJSSPs, only Mohammadi [27] designed a simulated annealing algorithm and a genetic algorithm for the RJSSP with fuzzy processing times to minimize makespan, and the stochastic RJSSP has not been studied until now.

From the above literature review, it can be known that it is very necessary to carry out a study on the stochastic RJSSP. Hence, the RJSSP with stochastic processing time is considered here. Recently, many effective evolutionary algorithms have been successfully designed to deal with different complex optimization problems [28–37]. For example, Duan et al. [28] developed a hybrid estimation of distribution algorithm for the distributed permutation flow shop scheduling problem (FSSP) with flowline eligibility. Guo et al. [31] proposed a particle swarm optimization algorithm for the dynamic multi-objective vehicle routing problem. Sang et al. [33] presented three invasive weed optimization algorithms for the distributed assembly permutation FSSP. Guo et al. [36] devised a novel interactive preference-based multiobjective evolutionary algorithm for the optimization problem of the bolt supporting network. Zhang et al. [37] designed a matrix-cube-based estimation of distribution algorithm for the distributed assembly permutation FSSP. Computational comparisons demonstrated that these evolutionary algorithms can obtain very satisfactory solutions with a reasonable computational time. Due to the NP-completeness of the stochastic RJSSP, an effective population-based evolutionary algorithm, i.e., differential evolution algorithm (DEA), is also selected to deal with this complex problem. DEA was firstly presented for addressing optimization problems in continuous domain [38, 39]. Because of its simple concept and quick convergence, DEA has gained many applications in a variety of fields. Nevertheless, owing to its continuous nature, the studies on DEA for the JSSPs is still very limited. Thus, in this paper, an enhanced DEA integrated with uncertainty handling techniques (DEA_UHT) is designed for solving the stochastic RJSSP under the maximum tardiness $T_{\max}$ and the stochastic RJSSP under the makespan $C_{\max}$.

The main features of DEA_UHT lie in two aspects: the reasonable uncertainty handling techniques and the effective DEA-based search. As for the uncertainty handling techniques, not only is the aforementioned OCBAT used to identify better solutions (i.e., individuals) with high confidence under limited computation cost but also the hypothesis test technique (HTT) is added to avoid the unnecessary repetitive evaluation for the poor solutions. That is, the solutions with high quality can be selected during the DEA's search process, which is helpful to guide the algorithm search faster to the truly promising regions in the stochastic solution space. As for the DEA-based search, an *Insert*-based exploitation strategy and an *Interchange*-based exploration strategy are devised to enhance DEA's exploitation ability and exploration ability, respectively. The test results and comparisons verify the effectiveness and robustness of the proposed DEA_UHT.

The remainder of the paper is organized as follows. Two kinds of stochastic RJSSPs are introduced in the next section. The basic DEA, OCBAT, and HTT are briefly described in Section 3. After presenting the solution representation, the extended decoding scheme, the revised OCBAT, and two special crossover strategies, DEA_UHT is proposed via combining DEA with OCBAT and HTT in Section 4. The test results and comparisons are given and analyzed in Section 5. Finally, concluding remarks and further study directions are summarized in Section 6.

2. Stochastic RJSSP

Consider the stochastic RJSSP that consists of n jobs and m machines. Each job should be processed on each machine L ($L > 1$) times. The processing time of each job on each machine is a random value under a certain distribution. Let $\pi = [\pi_1, \pi_2, \ldots, \pi_{n\times m\times L}]$ denote the operation-based solution or sequence to be processed, π_j ($j \in \{1, \ldots, n \times m \times L\}$ and $\pi_j \in \{1, \ldots, n\}$) the jth job in π, $l(\pi_j)$ the repeat or reentrant times of job π_j in $[\pi_1, \pi_2, \ldots, \pi_j]$, ξ the noise or uncertain factors, $p(\pi_j, k, l(\pi_j), \xi)$ the $l(\pi_j)th$ stochastic processing time of job π_j on machine k, $E(C(\pi_j, l(\pi_j), \xi))$ the $l(\pi_j)th$ expected completion time of job π_j, $d(\pi_j)$ the due date of job π_j, $E(L(\pi_j, \xi)) = E(C(\pi_j, L, \xi)) - d(\pi_j)$ the excepted lateness of job π_j, $E(T(\pi_j, \xi)) = \max\{E(L(\pi_j, \xi)), 0\}$ the excepted tardiness of job π_j. Here $p(\pi_j, k, l(\pi_j), \xi)$ is supposed to be subjected to a uniform distribution $U[((1-\xi)E(P_{\pi_j,k,l(\pi_j)}), \ (1+\xi)E(P_{\pi_j,k,l(\pi_j)}))]$, where $P_{\pi_j,k,l(\pi_j)}$ is the expected processing time and ξ denotes noise magnitude.

Then, the expected maximum tardiness $E(T_{\max}(\pi, \xi))$ can be given as

$$E(T_{\max}(\boldsymbol{\pi}, \xi)) = \max\{E(T(1, \xi)), \ldots, E(T(n, \xi))\}. \quad (1)$$

The stochastic RJSSP under the maximum tardiness (SRJSSP-$T_{\max}$) can be formulated as

$$\min_{\pi\in\Pi} E\left(T_{\max}(\pi,\xi)\right), \tag{2}$$

where Π denotes the set of all possible permutations.

Similarly, the expected makespan $E(C_{\max}(\pi,\xi))$ can be given as

$$E\left(C_{\max}(\boldsymbol{\pi},\xi)\right) = \max\{E\left(C(\pi_1,L,\xi)\right),\ldots,E\left(C(\pi_n,L,\xi)\right)\}. \tag{3}$$

The stochastic RJSSP under the makespan (SRJSSP-$C_{\max}$) can be formulated as

$$\min_{\pi\in\Pi} E\left(C_{\max}(\boldsymbol{\pi},\xi)\right), \tag{4}$$

where Π denotes the set of all possible permutations.

Obviously, infinite sampling of the above problem model can make the objective values of equations (1) and (3) stable, but in fact it is practically impossible. In the actual calculation, the value of equations (1) or (3) is usually approximated by the average of finite sampling values (e.g., Monte Carlo simulation) [8–18]. Thus, $E(T_{\max}(\pi,\xi))$ can be estimated with

$$\overline{T_{\max}(\boldsymbol{\pi},\xi)} = \sum_{ll=1}^{LL} T_{\max}\frac{(\boldsymbol{\pi},\xi)}{LL}. \tag{5}$$

and $E(C_{\max}(\pi,\xi))$ can be estimated with

$$\overline{C_{\max}(\boldsymbol{\pi},\xi)} = \sum_{ll=1}^{LL} C_{\max}\frac{(\boldsymbol{\pi},\xi)}{LL}. \tag{6}$$

3. Introduction to DEA, OCBAT, and HTT

3.1. DEA. Differential evolution algorithm (DEA) [38, 39] is a kind of evolutionary algorithms for solving continuous optimization problems. The basic DEA aims at finding the global optimal solutions by using the differentiations among current individuals. Specifically, each individual's search behavior is dynamically controlled via changing the differentiation's direction and step length. At each generation, the *mutation* and *crossover* operators are applied to current individuals to generate a candidate population, and then the *selection* operator is utilized to determine a new population of the next generation. Nowadays, there are several variants/schemes of DEA.

3.2. OCBAT. OCBAT is a dynamic allocation technique of computing budget [26, 40]. Specifically, it can optimize the sampling times for each candidate solution so that the truly better solutions can be identified under a given computation cost. Denote S the total number of potential solutions, n_i^k (resp. n_b^k) the computation cost or sampling times allocated to solution i (resp. the current best solution) after the kth allocation, s_i^k (resp. s_b^k) the standard deviation among the sampling objective values of solution i (resp. the current best solution) after the kth allocation, $\overline{f_i^k}$ (resp. $\overline{f_b^k}$) the average sampling objective value of solution i (resp. the current best solution) after the kth allocation, $\delta_{b,i}^k = \overline{f_b^k} - \overline{f_i^k}$ the difference between $\overline{f_b^k}$ and $\overline{f_i^k}$ after the kth allocation, T^k the total sampling times after the kth allocation, and T the given total sampling times.

According to the above definitions, the standard OCBAT's algorithm is provided as follows:

Step 0. Set $k=0$, $n_i^k = n_0$ $(i=1,2,\ldots,S)$ and $T^k = \sum_{i=1}^{S} n_i^k$.

Step 1. If $\sum_{i=1}^{S} n_i^k \geq T$, the algorithm should be stopped.

Step 2. Execute n_i^k samples (i.e., simulation replications) for each solution i, and then set $T^{k+1} = T^k + \Delta$.

Step 3. Calculate each n_i^{k+1} via using $n_b^{k+1} = s_b^k \left(\sum_{i=1, i\neq b}^{S} (n_i^k)^2/(s_i^k)^2\right)^{1/2}$ and $n_i^{k+1}/n_j^{k+1} = ((s_i^k/\delta_{b,i}^k)/(s_j^k/\delta_{b,j}^k))^2$ $(i\neq j\neq b)$.

Step 4. Execute $\max\{n_i^{k+1} - n_i^k, 0\}$ samples for each solution i.

Step 5. Set $k = k+1$, and return to Step 1.

Based on Reference [26], the recommended value ranges of n_0 and Δ are [5, 20] and [S/5, S/10], respectively.

3.3. HTT. HTT is a statistical inference method that can be used to judge whether the difference between two solutions i and j is caused by sampling error or essential difference [41]. Let the null hypothesis H_0 be "$f_i = f_j$," and then the alternative hypothesis H_1 is "$f_i \neq f_j$." Based on the statistical theory, the critical region of H_0 is defined as follows:

$$\left|\overline{f_i} - \overline{f_j}\right| \geq T_{\alpha/2} = t_{\alpha/2}\left(n_i + n_j - 2\right) \times \sqrt{\left[\frac{(n_i-1)s_i^2 + \left(n_j-1\right)s_j^2}{\left(n_i+n_j-2\right)}\right]} \times \sqrt{\left[\frac{\left(n_i+n_j\right)}{\left(n_i n_j\right)}\right]}, \tag{7}$$

where t is the t distribution and α is the evidence level. When $\overline{f_i} - \overline{f_j} > T_{\alpha/2}$, it can be judged that solution j is better than solutions i.

4. DEA_UHT for Stochastic RJSSP

4.1. Encoding Scheme. Since DEA's individual is a real vector, a conventional DEA cannot be directly used to deal with the discrete optimization problem. Thus, we utilize a reentrant-largest-order-value (RLOV) rule derived from the existing largest-order-value (LOV) rule [42] to transform DEA's ith individual $X_i = [x_{i,1}, x_{i,2}, \ldots, x_{i,n\times m\times L}]$ to the job sequence $\pi_i = [\pi_{i,1}, \pi_{i,2}, \ldots, \pi_{i,n\times m\times L}]$. Based on the RLOV rule, the elements in X_i are firstly ranked by descending order to obtain a temporary discrete sequence $\varphi_i = [\varphi_{i,1}, \varphi_{i,2}, \ldots, \varphi_{i,n\times m\times L}]$. Then, the operation-based solution π_i can be generated via

$$\pi_{i,k} = \left[\frac{\varphi_{i,k} - 1}{m\times L}\right] + 1, \tag{8}$$

where $[x]$ is an operator to get the integral part of (e.g., $[2.78] = 2$). Table 1 illustrates the encoding of vector X_i in DEA for a small RJSSP $(L=3, n=2, m=1)$.

Table 1: Solution's encoding scheme.

Dimension k	1	2	3	4	5	6
$x_{i,k}$	2.16	0.33	1.51	3.67	0.86	2.79
$\varphi_{i,k}$	3	6	4	1	5	2
$\pi_{i,k}$	1	2	2	1	2	1

4.2. Decoding Scheme. Based on the characteristics of RJSSP, an optimal solution must be an active schedule under regular criteria (e.g., the maximum tardiness $T_{\max}$ and the makespan $C_{\max}$) [43]. This means that the solution's quality can be improved via transforming the semi-active schedule into the active one. Therefore, when decoding a solution to a feasible schedule, each operation should be filled in the first idle time interval in the current Gantt chart instead of the last idle time interval. This active decoding scheme is utilized in our proposed algorithm.

Let $M_{i,j,l}$ be the machine number of the jth operation that processes the lth reentrant job I, $T_{i,j,l}$ the processing time of the lth reentrant job j on machine i, and $S(\pi_{i,j})$ the possible earliest starting time of job $\pi_{i,j}$. Notice that the value of $S(\pi_{i,j})$ should meet the following inequality:

$$\max\left\{S\left(\pi_{i,j}\right), t_1\right\} + T_{M\left(\pi_{i,j}\right),\pi_{i,j},l\left(\pi_{i,j}\right)} \leq t_2, \tag{9}$$

where $M(\pi_{i,j}) = M_{\pi_{i,j},h(\pi_{i,j}),l(\pi_{i,j})}$, and $[t_1, t_2]$ represents any idle time interval on the machine.

Based on the above definitions, the decoding scheme that generates an active schedule for a RJSSP's solution π_i is provided as follows:

Step 1. Set $k(w) = 1$ and $l(w) = 1$, $w = 1, \ldots, n$ and $j = 1$.

Step 2. If $k(\pi_{i,j}) > 1$ and $(k(\pi_{i,j}) \bmod m = 1)$, then set $l(\pi_{i,j}) = l(\pi_{i,j}) + 1$.

Step 3. Set $h(\pi_{i,j}) = k(\pi_{i,j}) - (l(\pi_{i,j}) - 1) \times m$.

Step 4. Calculate $S(\pi_{i,j})$, and set $k(\pi_{i,j}) = k(\pi_{i,j}) + 1$.

Step 5. Set $j = j + 1$. If $j \leq n \times m \times L$, then return to Step 2.

4.3. Application of Roulette Wheel Rule in OCBAT. For stochastic RJSSPs, the difference between $\delta_{b,i}^k$ and $\delta_{b,j}^k$ $(i \neq j)$ is usually much larger than that between s_i and s_j. This can cause $\sum_{i=1}^{S} \max\{n_i^{k+1} - n_i^k, 0\} \gg \Delta$. Based on Step 4 of the standard OCBAT (see Section 3.2), the repeated times of Steps 1–5 of this standard algorithm may be much less than $(T - n_0)/\Delta$. That is, the number of times that OCBAT can be used to dynamically allocate computing budget is very limited. As a result, the reliable evaluation ability of OCBAT cannot be well utilized.

Under this situation, the so-called "most starving" rule [40] is usually used to handle this obstacle. However, this rule sets Δ to 1 and needs to execute the OCBAT's Steps 1–5 T times. This may increase the running time of the OCBAT's algorithm. Since the OCBAT decides the budget fractions instead of the number, here we utilize the "roulette wheel" rule to allocate Δ. That is, Step 4 of the standard OCBAT should be changed to the following two substeps:

Step 4.1. Calculate the allocation probability P_i^{k+1} $(P_i^{k+1} = n_i^{k+1} / \sum_{i=1}^{S} n_i^{k+1})$ for each solution i at $(k+1)$th allocation.

Step 4.2. Apply the "roulette wheel" rule to allocate Δ to each solution i according to P_i^{k+1}, and update each n_i^{k+1}.

4.4. Special Exploitation and Exploration Strategies. Based on References [44, 45], the solution space of the RJSSP can be regarded as a "big valley," where the local optima are often close to each other, and close to the global optima at the bottom of the "big valley," and either the *Insert*-based operator or the *Interchange*-based operator can execute a more compact search. Meanwhile, DEA has been proved to be an effective algorithm to find the promising solutions or regions in the whole valley [42, 44]. As for the stochastic RJSSP, the shape and the bottom regions of the big valley are always changing. Thus, to improve our DEA_UHT's search ability, we devise an *Insert*-based exploitation strategy and an *Interchange*-based exploration strategy to replace DEA's original *mutation* and *crossover*, which cannot obtain enough promising solutions. The former strategy selects some reliable good individuals identified by OCBAT and HTT to replace some poor individuals, and executes an *Insert*-based operator on these selected individuals. The latter strategy performs an *Interchange*-based operator guided by DEA's basic scheme on all individuals except those replaced poor individuals. The detailed procedures of these strategies are provided in Step 5 in the next section.

4.5. DEA_UHT. In DEA_UHT, DEA-based search is devised according to the DE/rand-to-best/1/exp strategy to perform global search or exploration, where the base vector is the current best individual. Therefore, the information of the best individual can be shared by other individuals. By incorporating OCBAT, HTT, and two special exploitation and exploration strategies into DEA, a hybrid approach, namely, DEA_UHT, is proposed for the stochastic RJSSP.

Denote G a generation, $\mathrm{Pop}(t)$ a population with size PS at generation t, $W\_\mathrm{Pop}(t)$ an archive set to save the individuals which need to adopt the *special Insert*-based *crossover*, $X_i(t)$ the ith individual with dimension N $(N = n)$ in $\mathrm{Pop}(t)$, $\mathrm{Tmp\_Pop}(t)$ a temporary population with size PS in generation t, $\mathrm{Tmp\_}X_i(t)$ the ith individual in $\mathrm{Tmp\_Pop}(t)$, $x_{i,k}(t)$ the kth variable/component of individual $X_i(t)$, tmp_k the kth variable of tmp, $\mathrm{tmp01}_k$ the kth variable of tmp01, CR the crossover probability, F the scaling factor, $O\_d(x_{i,k}(t)) = \varphi_{i,k}(t)$ the ordinal number of $x_{i,k}(t)$ in $X_i(t)$ in descending order (see Section 4.1), $RO\_d(x_{i,k}(t)) = \pi_{i,k}(t)$ the $x_{i,k}(t)$'s corresponding job number in the job permutation $\pi_i(t)$ (see Section 4.1), and $\mathrm{random}(0,1)$ the random value in the interval [0, 1]. Based on these definitions, the framework of DEA_UHT is given as follows:

Step 1. Input N, $PS \geq 3$, $CR \in [0,1]$, and let bounds be $\mathrm{lower}(x_{i,k}) = 0$ and $\mathrm{upper}(x_{i,k}) = 4$, $k = 1, \ldots, N$.

Step 2. Population initialization

Step 2.1. Generate $x_{i,k}(0) = \text{lower}(x_{i,k}) + \text{random}(0,1) * (\text{upper}(x_{i,k}) - \text{lower}(x_{i,k}), k = 1), \ldots, N$ for $i = 1, \ldots, PS$

Step 2.2. Use the algorithm of OCBAT in Sections 3.2 and 4.3 to allocate T sampling budgets (i.e., evaluation times) for all individuals while estimating the objective values of all individuals and set $W\_\text{Pop}(0) =$ null set.

Step 3. Set $t = 1$ and select an individual $X_{\text{best}}(0)$ from $\text{Pop}(0)$ as *bestit* with the minimum objective value.

Step 4. Evolution phase (between Steps 4 and 9). Set $i = 1$.

Step 5. Mutation and *crossover* phase.

Step 5.1. If $X_i(t-1)$ belongs to $W\_\text{Pop}(t-1)$, then execute the *Insert*-based exploitation (see Section 4.4).

Step 5.1.1. Randomly select one individual from the best five percent of $\text{Pop}(t-1)$ and set it as tmp.

Step 5.1.2. Randomly generate u and v $(u < v)$, and randomly set r_i to 1 or 2.

Step 5.1.3. If $r\_i = 1$, then insert tmp_u after tmp_v.

Step 5.1.4. If $r\_i = 2$, then insert tmp_v before tmp_u.

Step 5.1.5. Set $\text{tmp}\_X_i(t) = \text{tmp}$ and go to Step 6.

Step 5.2. Perform the *Interchange*-based exploration (see Section 4.4). Set *the trial vector* $\text{tmp} = X_i(t-1)$, $\text{tmp01} = X_i(t-1)$ and $L' = 0$. Randomly select $r1, r2 \in (1, \ldots, PS)$, where $r1 \neq r2 \neq i$, and randomly select $k \in (1, \ldots, N)$.

Step 5.2.1. Set $\text{tmp}_k = \text{tmp}_k + F * (\text{bestit}_k - \text{tmp}_k) + F * (x_{r1,k}(t-1) - x_{r2,k}(t-1))$, and $v1 = O\_d(\text{tmp}_k)$.

Step 5.2.2. If $(RO\_d(\text{tmp}_k) < > RO\_d(\text{tmp01}_k))$, then find $u1$ satisfying $O\_d(\text{tmp01}_{u1}) = v1$ and interchange tmp01_k with tmp01_{u1}; else randomly generate $v1$ $((RO\_d(\text{tmp01}_k) < > RO\_d(\text{tmp01}_{v1})))$ and interchange tmp01_k with tmp01_{v1}.

Step 5.2.3. Set tmp = tmp01.

Step 5.2.4. Set $k = (k+1) \bmod N$ and $L' = L' + 1$.

Step 5.2.5. If $\text{random}(0,1) < CR$ and $(L' < 2)$, then return to Step 5.2.1.

Step 5.2.6. Set $\text{Tmp}\_X_i(t) = \text{tmp}$.

Step 6. Set $i = i+1$. If $i \leq PS$, then return to Step 5.

Step 7. Use the algorithm of OCBAT in Sections 3.2 and 4.3 to estimate the objective values of all individuals of $\text{Tmp}\_\text{pop}(t)$.

Step 8. Selection phase. Perform HHT in Section 3.3 on $\text{Tmp}\_X_i(t)$ with $X_i(t-1)$, $i = 1, \ldots, PS$.

Step 8.1. If the null hypothesis holds and $\bar{J}(X_i(t-1) - \bar{J}(\text{Tmp}\_X_i(t)) > \tau$, then set a Boolean variable *b_replace* = true; else set *b_replace* = false

Step 8.2. If *b_replace* = true then set $X_i(t) = \text{Tmp}\_X_i(t)$; else set $X_i(t) = X_i(t-1)$.

Step 8.3. If *b_replace* = true and $\bar{J}(\text{Tmp}\_X_i(t)) < \bar{J}(bestit)$, then set $bestit = \text{Tmp}\_X_i(t)$.

Step 8.4. If *b_replace* = false and $X_i(t-1)$ is in the worst 20 percent of $\text{Pop}(t-1)$, then add $X_i(t-1)$ to $W\_\text{Pop}(t)$.

Step 9. Set $t = t+1$. If $t \leq t\_\max$ (the maximum generation), then return to Step 4.

Step 10. Output π_{output} $(\pi_{\text{output}} = bestit)$ and its objective value.

From the above procedure, it can be known that DEA_UHT not only utilizes OCBAT to ensure reliable evaluation for good solutions but also adopts HTT to reduce repetitive search. Furthermore, the DEA-based search combined with two special strategies is devised to effectively execute exploration and exploitation in solution space. Meanwhile, "$(L' < 2)$" in Step 5.2.5 is used to control the search range of the *Interchange*-based exploration. In addition, it is worth noting that although Step 5.1 (resp. Step 5.2) directly performs the *Insert* (resp. *Interchange*) operation on the individual, it is equivalent to performing the same *Insert* (resp. *Interchange*) operation on the corresponding permutation of this individual (see the RLOV rule in Section 4.1).

5. Simulation Results and Comparisons

5.1. Experimental Setup. To verify DEA_UHT's performance, ten instances of the deterministic RJSSP are created via the following steps:

Step 1. Select one out of ten JSSP's classic benchmarks [46] in turn as *PP*

(i.e., FT06, FT10, FT20, LA01, LA06, LA11, LA16, LA21, LA26, and LA31 [46]).

Step 2. Set the reentrant times $L = 2$.

Step 3. Set each $M_{i,j,1}$ and each $T_{i,j,1}$ to the corresponding data in *PP*.

Step 4. Set $M_{i,j,2} = M_{i+1,j,1}$ for $i = 1, \ldots, n-1$ and $j = 1, \ldots, m$.

Step 5. Set $M_{n,j,2} = M_{1,j,1}$ for $j = 1, \ldots, m$.

Step 6. Set $T_{i,j,2} = T_{i,j+1,1}$ for $j = 1, \ldots, n-1$ and $i = 1, \ldots, m$.

Step 7. Set $T_{i,n,2} = T_{i,1,1}$ for $i = 1, \ldots, m$.

Using the above steps, ten RJSSP's instances can be created. These instances are named FT06_R2, FT10_R2, FT20_R2, LA01_R2, LA06_R2, LA11_R2, LA16_R2, LA21_R2, LA26_R2, and LA31_R2, respectively. Each of these names is formed by adding "_R2" after the name of the corresponding JSSP's benchmark. Obviously, these RJSSP's instances are obtained by simply extending the classical JSSP's instances. Since each $M_{i,j,1}$ and $T_{i,j,1}$ are randomly generated between [1, n] and [1, 100], respectively, the internal correlation within each RJSSP's instance can be ignored. Using the above steps to obtain the RJSSP's instances is just for the convenience of other researchers to generate the same instances.

Table 2: Comparisons of PDEA, DEA_UHT_O, and DEA_UHT.

Problem	n, m, L	ξ	PDEA		DEA_UHT_O		DEA_UHT	
			BRE	ARE	BRE	ARE	BRE	ARE
S1_FT06_R2_$T_{\max}$	6, 6, 2	0.3	17.00	22.53	*16.00*	*21.37*	11.00	**15.13**
S1_LA01_R2_$T_{\max}$	10, 5, 2	0.3	*409.00*	479.07	429.00	*469.87*	**282.00**	**369.27**
S1_LA06_R2_$T_{\max}$	15, 5, 2	0.3	848.00	924.57	*777.00*	*902.17*	**614.00**	**760.17**
S1_LA11_R2_$T_{\max}$	20, 5, 2	0.3	1299.00	1374.03	*1244.00*	*1341.90*	**1071.00**	**1179.30**
S1_FT10_R2_$T_{\max}$	10, 10, 2	0.3	579.00	721.17	*537.00*	*694.57*	**199.00**	**363.57**
S1_FT20_R2_$T_{\max}$	20, 5, 2	0.3	1429.00	1518.73	*1371.00*	*1489.83*	**955.00**	**1090.87**
S1_LA16_R2_$T_{\max}$	10, 10, 2	0.3	558.00	621.13	*485.00*	*585.07*	**221.00**	**315.97**
S1_LA21_R2_$T_{\max}$	15, 10, 2	0.3	*964.00*	1128.67	1011.00	*1075.13*	**407.00**	**538.00**
S1_LA26_R2_$T_{\max}$	20, 10, 2	0.3	*1436.00*	1604.73	1449.00	*1559.93*	**847.00**	**949.57**
S1_LA31_R2_$T_{\max}$	30, 10, 2	0.3	2469.00	2611.97	*2300.00*	*2546.90*	**1573.00**	**1848.00**
S1_FT06_R2_$T_{\max}$	6, 6, 2	0.6	19.00	25.80	*17.00*	*22.47*	**10.00**	**16.37**
S1_LA01_R2_$T_{\max}$	10, 5, 2	0.6	464.00	539.60	*414.00*	*487.43*	**307.00**	**379.43**
S1_LA06_R2_$T_{\max}$	15, 5, 2	0.6	872.00	947.50	*810.00*	*915.33*	**626.00**	**780.53**
S1_LA11_R2_$T_{\max}$	20, 5, 2	0.6	1304.00	1418.83	*1289.00*	*1366.57*	**1170.00**	**1252.27**
S1_FT10_R2_$T_{\max}$	10, 10, 2	0.6	625.00	765.93	*534.00*	*698.93*	**176.00**	**375.43**
S1_FT20_R2_$T_{\max}$	20, 5, 2	0.6	1477.00	1586.27	*1403.00*	*1517.70*	**1043.00**	**1199.67**
S1_LA16_R2_$T_{\max}$	10, 10, 2	0.6	503.00	675.83	*499.00*	*617.30*	**244.00**	**370.60**
S1_LA21_R2_$T_{\max}$	15, 10, 2	0.6	1035.00	1172.10	*1002.00*	*1100.77*	**557.00**	**685.80**
S1_LA26_R2_$T_{\max}$	20, 10, 2	0.6	1465.00	1663.93	*1407.00*	*1559.27*	**928.00**	**1033.50**
S1_LA31_R2_$T_{\max}$	30, 10, 2	0.6	2560.00	2689.83	*2405.00*	*2579.50*	**1761.00**	**1993.90**
Average			1016.60	1124.61	*969.95*	*1077.60*	**650.10**	**775.87**

For any created instance, each job's due date can be obtained via the following steps:

Step 1. Randomly created a permutation $\pi = [\pi_1, \pi_2, \ldots, \pi_{n\times m\times L}]$ for each RJSSP's instance z.

Step 2. Calculate each $C_z(\pi_j, L)$ $(\pi_j \in \pi)$ via the decoding scheme in Section 4.2.

Step 3. Specify each job's due date via

$$d_z(\pi_j) = C_z(\pi_j, L) + \text{random}\left[\frac{-C_z(\pi_j, L)}{10}, \frac{C_z(\pi_j, L)}{10}\right], \tag{10}$$

where random$[-C_z(\pi_j, L)/10, C_z(\pi_j, L)/10]$ is a random value between $[-C_z(\pi_j, L)/10, C_z(\pi_j, L)/10]$. Because the ability to address tight due dates affects an enterprise's competence and the problem under tight due dates is more difficult to solve than under loose due dates, (10) is designed to obtain a tight due date.

Next, the instances of the stochastic RJSSP can be obtained by changing each original processing time $p(\pi_j, k, l(\pi_j))$ of the above RJSSP's instances to a uniform distribution $U[((1-\xi)E(P_{\pi_j,k,l(\pi_j)}), (1+\xi)E(P_{\pi_j,k,l(\pi_j)}))]$, where $E(P_{\pi_j,k,l(\pi_j)})$ is the expected processing time that equals to the original $p(\pi_j, k, l(\pi_j))$ and ξ denotes noise magnitude. To test the performance of the algorithm more comprehensively, two kinds of stochastic RJSSPs are considered. The first kind is the stochastic RJSSP under $T_{\max}$. Ten instances with $\xi = 0.3$ and them with $\xi = 0.6$ are generated. These instances are denoted by S1_Iname_R2_$T_{\max}$, where Iname indicates that S1_Iname_R2_$T_{\max}$ is derived from the deterministic instance Iname. The second kind is the stochastic RJSSP under $C_{\max}$, whose ten instances with $\xi = 0.6$ are generated. Similarly, these instances are donated by S1_Iname_R2_$C_{\max}$. Moreover, since it is a common scenario that only a part of the machines are unstable, a variant of the first kind of problem is also considered. This variant, namely, S2_Iname_R2_$T_{\max}$, only sets the processing time of each job on machine one and machine three to a uniform distribution $U[((1-\xi)E(P_{\pi_j,k,l(\pi_j)}), (1+\xi)E(P_{\pi_j,k,l(\pi_j)}))]$ $(k = 1, 3$ and $\xi = 0.6)$

The proposed DEA_UHT and the other compared algorithms were implemented in Delphi 2010 and the experiments were executed on an Intel 3.0 GHz PC with 8 GB memory. The main parameters of DEA_UHT are set as follows: the population size $PS = 100$, $F = 0.7$, $CR = 0.1$, $T = 1000$, $n_0 = 5$, and $\Delta = 10$. The maximum generation of each compared algorithm is set to 300. Each compared algorithm is executed thirty times independently on each instance.

To show the effectiveness of DEA_UHT, two variants of it are compared. The abbreviations of these variants are given as follows:

(i) PDEA: DEA_UHT without OCBAT, HTT, the *Insert*-based exploitation strategy and the *Interchange*-based exploration strategy. The details can be described as follows:

(1) *DEA_UHT without OCBAT.* At Steps 2.2 and 7 of DEA_UHT, the algorithm of OCBAT is replaced with twenty evaluation times for each solution's performance estimation.

(2) *DEA_UHT without HTT.* At Step 8 of DEA_UHT, the HTT-based selection is replaced with the normal DE's *selection*.

(3) DEA_UHT without the *Insert*-based exploitation strategy: Step 5.1 is deleted.

Table 3: Comparisons of PDEA, DEA_UHT_O, and DEA_UHT on two other kinds of stochastic RJSSP.

Problem	n, m, L	ξ	PDEA		DEA_UHT_O		DEA_UHT	
			BRE	ARE	BRE	ARE	BRE	ARE
S2_FT06_R2_$T_{\max}$	6, 6, 2	0.6	19.00	23.77	*17.00*	*21.60*	**10.00**	**15.13**
S2_LA01_R2_$T_{\max}$	10, 5, 2	0.6	*414.00*	485.80	423.00	*470.63*	**282.00**	**371.93**
S2_LA06_R2_$T_{\max}$	15, 5, 2	0.6	862.00	937.60	*811.00*	*907.67*	**650.00**	**781.43**
S2_LA11_R2_$T_{\max}$	20, 5, 2	0.6	1319.00	1387.10	*1299.00*	*1339.53*	**1136.00**	**1243.43**
S2_FT10_R2_$T_{\max}$	10, 10, 2	0.6	525.00	718.60	*512.00*	*681.37*	**210.00**	**316.20**
S2_FT20_R2_$T_{\max}$	20, 5, 2	0.6	*1381.00*	1528.30	1441.00	*1512.57*	**1022.00**	**1192.00**
S2_LA16_R2_$T_{\max}$	10, 10, 2	0.6	521.00	629.07	*475.00*	*596.47*	**262.00**	**362.90**
S2_LA21_R2_$T_{\max}$	15, 10, 2	0.6	989.00	1133.57	*963.00*	*1101.43*	**411.00**	**569.77**
S2_LA26_R2_$T_{\max}$	20, 10, 2	0.6	1421.00	1589.57	*1418.00*	*1532.90*	**855.00**	**981.10**
S2_LA31_R2_$T_{\max}$	30, 10, 2	0.6	2371.00	2588.87	*2288.00*	*2542.00*	**1758.00**	**1910.33**
S1_FT06_R2_$C_{\max}$	6, 6, 2	0.6	108.00	115.87	*107.00*	*112.50*	**102.00**	**108.70**
S1_LA01_R2_$C_{\max}$	10, 5, 2	0.6	*1407.00*	1499.43	*1406.00*	*1452.53*	**1332.00**	**1375.33**
S1_LA06_R2_$C_{\max}$	15, 5, 2	0.6	1913.00	2031.70	*1908.00*	*1959.97*	**1852.00**	**1877.40**
S1_LA11_R2_$C_{\max}$	20, 5, 2	0.6	2555.00	2652.23	*2525.00*	*2610.67*	**2444.00**	**2476.73**
S1_FT10_R2_$C_{\max}$	10, 10, 2	0.6	*2186.00*	2355.87	2196.00	*2299.10*	**1961.00**	**2045.67**
S1_FT20_R2_$C_{\max}$	20, 5, 2	0.6	*2678.00*	2829.07	2692.00	*2782.90*	**2490.00**	**2572.93**
S1_LA16_R2_$C_{\max}$	10, 10, 2	0.6	*2136.00*	2271.33	2142.00	*2241.23*	**1864.00**	**2004.90**
S1_LA21_R2_$C_{\max}$	15, 10, 2	0.6	2871.00	2963.77	*2769.00*	*2863.10*	**2284.00**	**2485.43**
S1_LA26_R2_$C_{\max}$	20, 10, 2	0.6	3440.00	3592.53	*3380.00*	*3485.20*	**2843.00**	**2982.27**
S1_LA31_R2_$C_{\max}$	30, 10, 2	0.6	*4408.00*	4694.07	4465.00	*4585.60*	**3871.00**	**4071.83**
Average			1676.20	1801.41	*1661.85*	*1754.95*	**1381.95**	**1487.27**

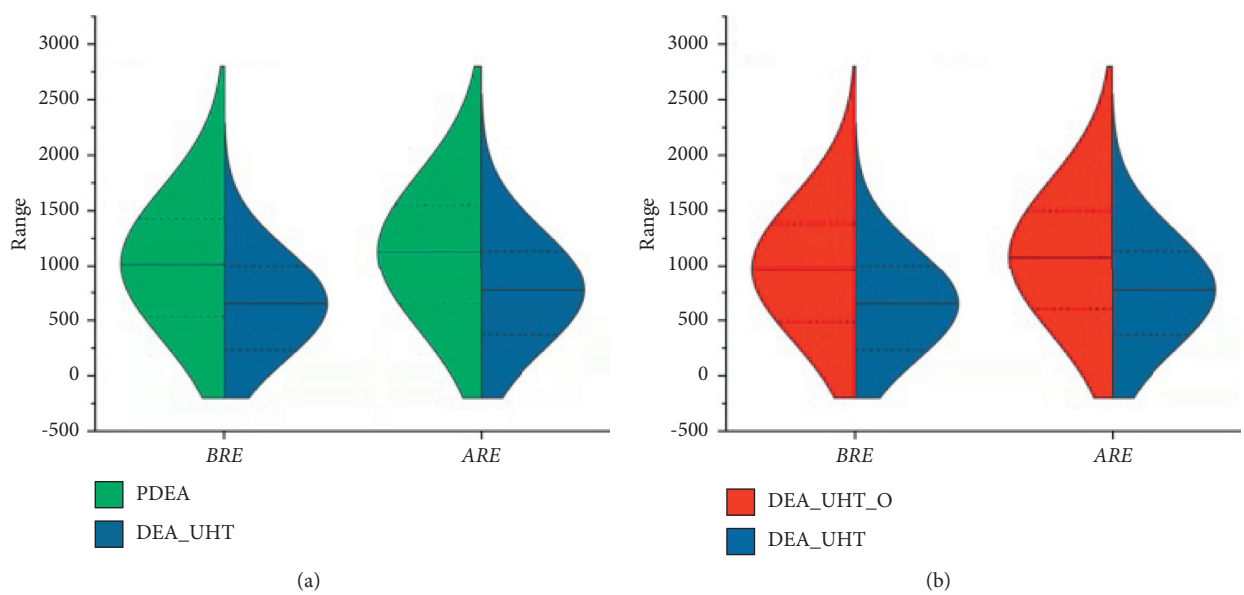

Figure 1: Violin plots for comparison results in Table 1. (a) PDEA vs DEA_UHT. (b) DEA_UHT_O vs DEA_UHT.

(4) DEA_UHT without the *Interchange*-based exploitation strategy: Steps 5.2.2 and 5.2.3 are deleted, and "$(L' < 2)$" in Step 5.2.5 is replaced with "$(L' < N)$."

(2) *DEA_UHT_O*. DEA_UHT without HTT, the *Insert*-based exploitation strategy and the *Interchange*-based exploration strategy.

5.2. Simulation Results and Comparisons. The statistical results are summarized in Tables 2 and 3, where ξ is the noise magnitude, *BRE* is the best expected maximum tardiness or makespan, and *ARE* is the average expected maximum tardiness or makespan. To make the statistical results clearer, in Tables 2 and 3, the best and the second-best values in each row are represented by using the bold and the italic fonts, respectively. For the final output solution π_{output} obtained by each compared algorithm at each run, its expected objective value $E(T_{\max}(\pi_{\text{output}}, \xi))$ or $E(C_{\max}(\pi_{\text{output}}, \xi))$ is calculated with the expected processing time (i.e., the processing time without noise). Obviously, *BRE* and *ARE* can reflect the performance of these compared algorithms in a statistical

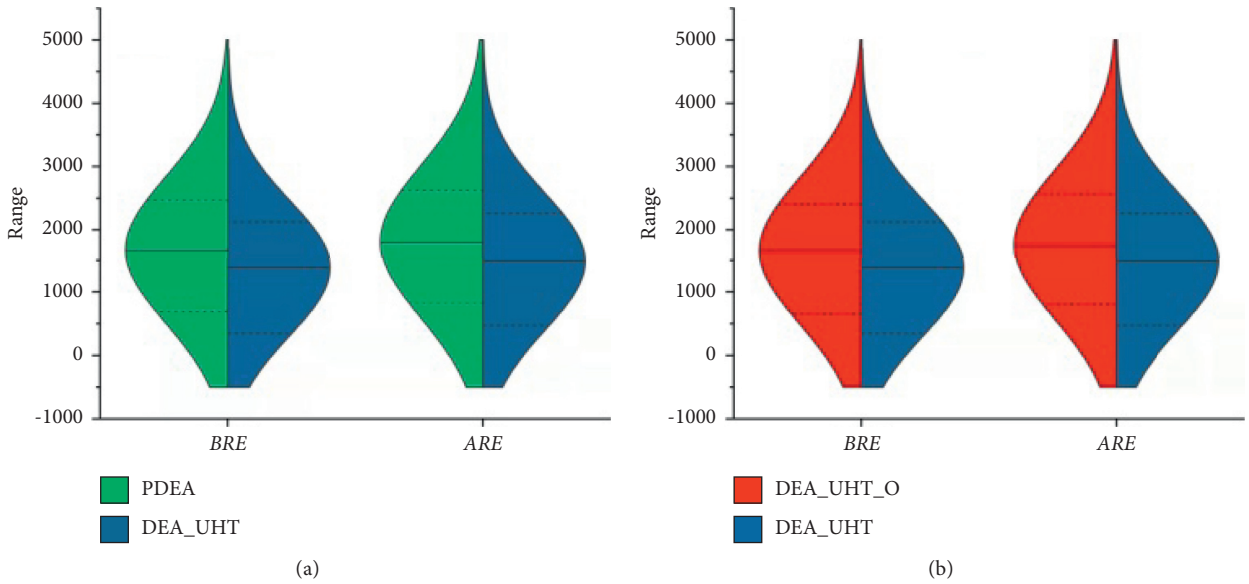

Figure 2: Violin plots for comparison results in Table 2. (a) PDEA vs DEA_UHT. (b) DEA_UHT_O vs DEA_UHT.

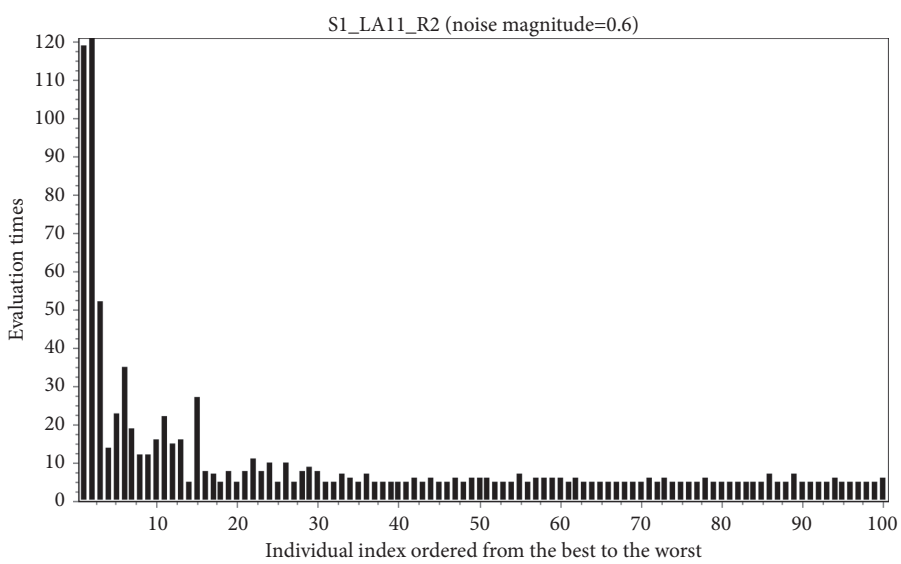

Figure 3: Computing budget allocation of OCBAT in DEA_UHT for S1_LA11_R2_$T_{\max}$ (generation $t = 20$).

sense. Moreover, to further show the statistical distributions of the results in Tables 1 and 2, the violin plots for the algorithm pairs "PDEA vs. DEA_UHT" and "DEA_UHT_O vs. DEA_UHT" are given in Figures 1 and 2.

From Tables 2 and 3, it is clear that both the *BRE* values and the *ARE* values obtained by DEA_UHT are better than those obtained by PDEA, which validates the effectiveness via incorporating OCBAT, HTT, the *Insert*-based exploitation strategy, and the *Interchange*-based exploration strategy into PDEA. This also means that DEA_UHT can achieve a better balance between exploration and exploitation than PDEA and DEA_UHT_O. Meanwhile, most of the *BRE* values and all of the *ARE* values obtained by DEA_UHT_O are better than those obtained by PDEA, from which it can be concluded that OCBAT is necessary to improve the optimization performance. It is worth noting that the above conclusions can still be drawn when considering the instances in Tables 1 and 2, where $\xi = 0.1$ or 0.3. In addition, from Figures 1 and 2, it can be seen that DEA_UHT has better statistical distributions and better median lines compared with PDEA and DEA_UHT_O. These violin plots confirm the competitiveness of DEA_UHT.

To show the role of OCBAT, the computing budget allocation of OCBAT in DEA_UHT for the middle-size instance S1_LA11_R2_ is provided in Figure 3. In addition, to illustrate the effectiveness of DEA_UHT, the convergence curves of the compared algorithms on the same instance are

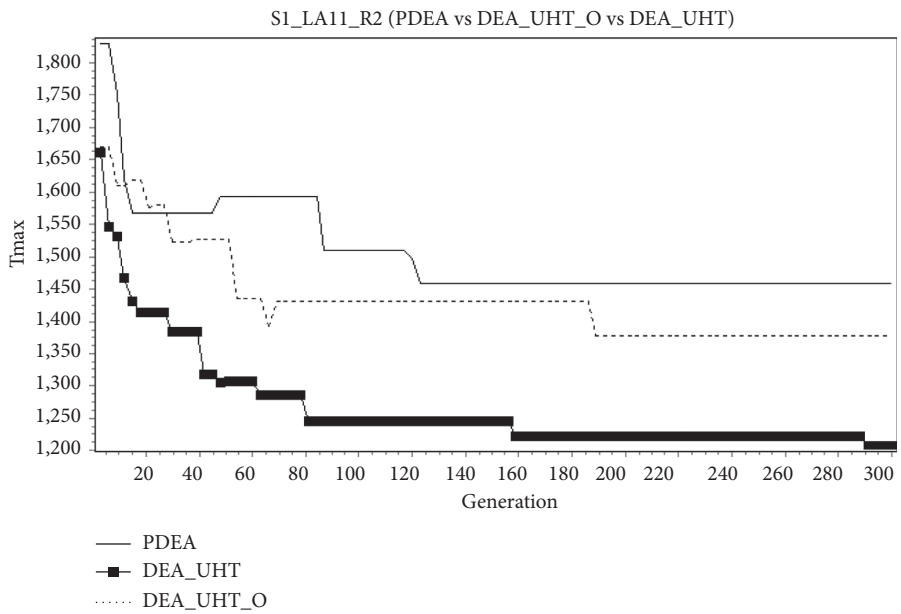

Figure 4: Convergence curves of the compared algorithms on S1_LA11_R2_$T_{\max}$ (noise magnitude = 0.6).

given in Figure 4, where the curves are formed by connecting the $E(T_{\max}(\pi, \xi))$'s value of the best individual *bestit* at each generation of the corresponding algorithm. $E(T_{\max}(\pi, \xi))$ here is calculated by setting $\xi = 0$ (i.e., $E(T_{\max}(bestit, \xi)) = T_{\max}(bestit)$). The computing budget allocation and the convergence curves for other instances are similar as those in Figures 3 and 4.

From Figure 3, it is shown that OCBAT can intelligently assign more evaluation times to better individuals. That is to say, OCBAT can enhance the algorithm's ability to find more reliable high-quality solutions or regions at each generation under the same computing budget. From Figure 4, it can be seen that the convergence speed of DEA_UHT is obviously faster than those of the other compared algorithms. This manifests that DEA_UHT can guide the whole population to move to the bottom of the expected "big valley" (i.e., the bottom of the "big valley" without noise) in solution space faster, and thus has better search performance. Moreover, the $E(T_{\max}(\pi, \xi))$'s values of DEA_UHT_O are less than those of PEDA in most cases, which verifies that OCBAT helps to guide the search to really promising regions in noisy environment.

6. Conclusion and Future Research

This paper proposed a novel DEA_UHT by combining DEA with OCBAT and HTT to address the stochastic RJSSP. This kind of problem has many real-world applications in modern enterprises. To the best of the authors' knowledge, this is the first time that DEA has been applied to such an important problem. With the help of OCBAT to intelligently allocate limited sampling budgets to perform reliable identification on excellent or good individuals, and with the help of HTT to reserve good individuals with high confidence, as well as with the *Insert*-based and *Interchange*-based strategies to effectively execute enhanced exploitation and exploration, DEA_UHT is of good performance for different kinds of stochastic RJSSP. In the future, our work is to extend DEA_UHT to other kinds of stochastic scheduling problems.

Data Availability

Data were curated by the authors and are available upon request.

Conflicts of Interest

The authors declare that they have no conflicts of interest.

Acknowledgments

This research was partially supported by the National Natural Science Foundation of China (61963022 and 62173169) and the Basic Research Key Project of Yunnan Province (202101AS070097).

References

[1] E. Levner, V. Kats, D. Alcaide López de Pablo, and T. C. E. Cheng, "Complexity of cyclic scheduling problems: a state-of-the-art survey," *Computers & Industrial Engineering*, vol. 59, no. 2, pp. 352–361, 2010.

[2] A. K. Gupta and A. I. Sivakumar, "Job shop scheduling techniques in semiconductor manufacturing," *International Journal of Advanced Manufacturing Technology*, vol. 27, no. 11, pp. 1163–1169, 2006.

[3] S. Topaloglu and G. Kilincli, "A new bottleneck-based heuristic for reentrant job shops: a case study in a textile factory," *in Operations Research Proceedings 2008*, Springer, Berlin, Germany, pp. 159–164, 2009.

[4] M. R. Garey, D. S. Johnson, and R. Sethi, "The complexity of flowshop and jobshop scheduling," *Mathematics of Operations Research*, vol. 1, no. 2, pp. 117–129, 1976.

[5] J. C.-H. Pan and J.-S. Chen, "Mixed binary integer programming formulations for the reentrant job shop scheduling problem," *Computers & Operations Research*, vol. 32, no. 5, pp. 1197–1212, 2005.

[6] S. Topaloglu and G. Kilincli, "A modified shifting bottleneck heuristic for the reentrant job shop scheduling problem with makespan minimization," *International Journal of Advanced Manufacturing Technology*, vol. 44, no. 7, pp. 781–794, 2009.

[7] S.-F. Chen, B. Qian, B. Liu, R. Hu, and C.-S. Zhang, "Bayesian statistical inference-based estimation of distribution algorithm for the re-entrant job-shop scheduling problem with sequence-dependent setup times," *Intelligent Computing Methodologies*, vol. 8589, pp. 686–696, 2014.

[8] D. Golenko-Ginzburg, S. Kesler, and Z. Landsman, "Industrial job-shop scheduling with random operations and different priorities," *International Journal of Production Economics*, vol. 40, no. 2, pp. 185–195, 1995.

[9] J. Gu, X. Gu, and M. Gu, "A novel parallel quantum genetic algorithm for stochastic job shop scheduling," *Journal of Mathematical Analysis and Applications*, vol. 355, no. 1, pp. 63–81, 2009.

[10] J. Gu, M. Gu, C. Cao, and X. Gu, "A novel competitive coevolutionary quantum genetic algorithm for stochastic job shop scheduling problem," *Computers & Operations Research*, vol. 37, no. 5, pp. 927–937, 2010.

[11] D. Lei, "Simplified multi-objective genetic algorithms for stochastic job shop scheduling," *Applied Soft Computing*, vol. 11, no. 8, pp. 4991–4996, 2011.

[12] S.-C. Horng, S.-S. Lin, and F.-Y. Yang, "Evolutionary algorithm for stochastic job shop scheduling with random processing time," *Expert Systems with Applications*, vol. 39, no. 3, pp. 3603–3610, 2012.

[13] R. Zhang, S. Song, and C. Wu, "A two-stage hybrid particle swarm optimization algorithm for the stochastic job shop scheduling problem," *Knowledge-Based Systems*, vol. 27, pp. 393–406, 2012.

[14] M. van den Akker, K. van Blokland, and H. Hoogeveen, "Finding robust solutions for the stochastic job shop scheduling problem by including simulation in local search," in *Experimental Algorithms*, vol. 7933, pp. 402–413, Springer, Berlin, Germany, 2013.

[15] X. Hao, L. Lin, M. Gen, and K. Ohno, "Effective estimation of distribution algorithm for stochastic job shop scheduling problem," *Procedia Computer Science*, vol. 20, pp. 102–107, 2013.

[16] H.-A Yang, Y. Lv, C. Xia, S. Sun, and H. Wang, "Optimal computing budget allocation for ordinal optimization in solving stochastic job shop scheduling problems," *Mathematical Problems in Engineering*, vol. 2014, Article ID 619254, 10 pages, 2014.

[17] P. Sharma and A. Jain, "Performance analysis of dispatching rules in a stochastic dynamic job shop manufacturing system with sequence-dependent setup times: simulation approach," *CIRP Journal of Manufacturing Science and Technology*, vol. 10, pp. 110–119, 2015.

[18] S. Kemmoe-Tchomte, D. Lamy, and N. Tchernev, "A metaheuristic based on simulation for stochastic Job-shop optimization," *in*:, IEEE, in *Proceedings of the 2015 International Conference on Industrial Engineering and Systems Management (IESM)*, pp. 108–116, October 2015.

[19] J. Shen and Y. Zhu, "Chance-constrained model for uncertain job shop scheduling problem," *Soft Computing*, vol. 20, no. 6, pp. 2383–2391, 2016.

[20] X. Hao, M. Gen, L. Lin, and G. A. Suer, "Effective multi-objective EDA for bi-criteria stochastic job-shop scheduling problem," *Journal of Intelligent Manufacturing*, vol. 28, no. 3, pp. 833–845, 2017.

[21] S. Shoval and M. Efatmaneshnik, "A probabilistic approach to the stochastic job-shop scheduling problem," *Procedia Manufacturing*, vol. 21, pp. 533–540, 2018.

[22] A. Ghasemi, A. Ashoori, and C. Heavey, "Evolutionary learning based simulation optimization for stochastic job shop scheduling problems," *Applied Soft Computing*, vol. 106, pp. 1–18, Article ID 107309, 2021.

[23] Y.-K. Lin, P.-C. Chang, L. C.-L. Yeng, and S.-F. Huang, "Bi-objective optimization for a multistate job-shop production network using NSGA-II and TOPSIS," *Journal of Manufacturing Systems*, vol. 52, pp. 43–54, 2019.

[24] D. Lei, "Pareto archive particle swarm optimization for multi-objective fuzzy job shop scheduling problems," *International Journal of Advanced Manufacturing Technology*, vol. 37, no. 1–2, pp. 157–165, 2008.

[25] S. M. K. Hasan, R. Sarker, and D. Essam, "Genetic algorithm for job-shop scheduling with machine unavailability and breakdowns," *International Journal of Production Research*, vol. 49, no. 16, pp. 4999–5015, 2011.

[26] C.-H. Chen, J. Lin, E. Yücesan, and S. E. Chick, "Simulation budget allocation for further enhancing the efficiency of ordinal optimization," *Discrete Event Dynamic Systems*, vol. 10, no. 3, pp. 251–270, 2000.

[27] G. Mohammadi, "Scheduling parallel machines with sequence dependent set-up times in job shop industries using GA and SA," *International Journal of Systems Science: Operations & Logistics*, vol. 5, no. 3, pp. 282–294, 2018.

[28] W. Z. Duan, Z. Y. Li, M. C. Ji, Y. X. Yang, S. Y. Wang, and B. Liu, "A hybrid estimation of distribution algorithm for distributed permutation flowshop scheduling with flowline eligibility," in *Proceedings of the IEEE Congress on Evolutionary Computation (CEC)*, pp. 2581–2587, Vancouver, Canada, July 2016.

[29] W. Z. Duan, Z. Y. Li, Y. X. Yang, B. Liu, and K. Y. Wang, "EDA based probabilistic memetic algorithm for distributed blocking permutation flowshop scheduling with sequence dependent setup time," in *Proceedings of the IEEE Congress on Evolutionary Computation (CEC)*, pp. 992–999, Donostia, Spain, June 2017.

[30] B. Qian, Z.-c. Li, and R. Hu, "A copula-based hybrid estimation of distribution algorithm for m-machine reentrant permutation flow-shop scheduling problem," *Applied Soft Computing*, vol. 61, pp. 921–934, 2017.

[31] Y.-N. Guo, J. Cheng, S. Luo, D. Gong, and Y. Xue, "Robust dynamic multi-objective vehicle routing optimization method," *IEEE/ACM Transactions on Computational Biology and Bioinformatics*, vol. 15, no. 6, pp. 1891–1903, 2018.

[32] Y. Guo, H. Yang, M. Chen, J. Cheng, and D. Gong, "Ensemble prediction-based dynamic robust multi-objective optimization methods," *Swarm and evolutionary computation*, vol. 48, pp. 156–171, 2019.

[33] H.-Y. Sang, Q.-K. Pan, J.-Q. Li et al., "Effective invasive weed optimization algorithms for distributed assembly permutation flowshop problem with total flowtime criterion," *Swarm and evolutionary computation*, vol. 44, pp. 64–73, 2019.

[34] Z. C. Li, B. Qian, R. Hu, L. L. Chang, and J. B. Yang, "An elitist nondominated sorting hybrid algorithm for multi-objective flexible job-shop scheduling problem with sequence-dependent setups," *Knowledge-Based Systems*, vol. 173, pp. 83–112, 2019.

[35] Y. Han, J. Li, H. Sang, Y. Liu, K. Gao, and Q. Pan, "Discrete evolutionary multi-objective optimization for energy-efficient blocking flow shop scheduling with setup time," *Applied Soft Computing*, vol. 93, Article ID 106343, 2020.

[36] Y.-N. Guo, X. Zhang, D.-W. Gong, Z. Zhang, and J.-J. Yang, "Novel interactive preference-based multiobjective evolutionary optimization for bolt supporting networks," *IEEE Transactions on Evolutionary Computation*, vol. 24, no. 4, pp. 750–764, 2020.

[37] Z. Q. Zhang, B. Qian, R. Hu, H. P. Jin, L. Wang, and J. B. Yang, "A matrix-cube-based estimation of distribution algorithm for the distributed assembly permutation flow-shop scheduling problem," *Swarm and Evolutionary Computation*, vol. 60, pp. 1–22, Article ID 100785, 2021.

[38] R. Storn and K. Price, "Differential evolution-A simple and efficient heuristic for global optimization over continuous spaces," *Journal of Global Optimization*, vol. 11, no. 4, pp. 341–359, 1997.

[39] V. Feoktistov, *Differential Evolution: In Search of Solutions*, Springer, Berlin, Germnay, 2006.

[40] C.-H. Chen, S. E. Chick, L. H. Lee, N. A. Pujowidianto, and A. Pujowidianto, "Ranking and Selection: Efficient Simulation Budget Allocation," *Handbook Of Simulation Optimization*, Springer, Berlin, Germnay, pp. 45–80, 2015.

[41] X. Liu, *Introduction to Statistics*, Tsinghua university Press, Beijing, China, 1998.

[42] B. Qian, L. Wang, R. Hu, W. L. Wang, D. X. Huang, and X. Wang, "A hybrid differential evolution for permutation flow-shop scheduling," *International Journal of Advanced Manufacturing Technology*, vol. 38, no. 7-8, pp. 757–777, 2008.

[43] L. Wang, *Shop Scheduling with Genetic Algorithms*, Tsinghua University & Springer Press, Beijing,China, 2003.

[44] B. Qian, L. Wang, D. X. Huang, and X. Wang, "Scheduling multi-objective job shops using a memetic algorithm based on differential evolution," *International Journal of Advanced Manufacturing Technology*, vol. 35, no. 9-10, pp. 1014–1027, 2008.

[45] T. Schiavinotto and T. Stützle, "A review of metrics on permutations for search landscape analysis," *Computers & Operations Research*, vol. 34, no. 10, pp. 3143–3153, 2007.

[46] S. Lawrence, *Resource Constrained Project Scheduling: An Experimental Investigation of Heuristic Scheduling Techniques*, Graduate school of industrial administration, Carnegie Mellon University, Pittsburgh, PA, USA, 1984.

Hindawi
Complexity
Volume 2021, Article ID 5576782, 10 pages
https://doi.org/10.1155/2021/5576782

Research Article

Compressed Sensing for THz FMCW Radar 3D Imaging

Shanshan Gu,[1] **Guangrong Xi**,[2] **Lingyu Ge**,[3] **Zhong Yang**,[1] **Yizhi Wang**,[1] **Weina Chen**,[1] **and Zhenzhong Yu**[1]

[1]*College of Intelligent Science and Control Engineering, Jinling Institute of Technology, Nanjing 211169, China*
[2]*Shanghai Geometrical Perception and Learning Co., Ltd., Shanghai 201206, China*
[3]*Nanjing Metro Group Co., Ltd., Nanjing 210018, China*

Correspondence should be addressed to Zhong Yang; yz@jit.edu.cn

Received 1 March 2021; Accepted 17 August 2021; Published 27 August 2021

Academic Editor: Jing Na

A terahertz (THz) frequency-modulated continuous wave (FMCW) imaging radar system is developed for high-resolution 3D imaging recently. Aiming at the problems of long data acquisition periods and large sample sizes for the developed imaging system, an algorithm based on compressed sensing is proposed for THz FMCW radar 3D imaging in this paper. Firstly, the FMCW radar signal model is built, and the conventional range migration algorithm is introduced for THz FMCW radar imaging. Then, compressed sensing is extended for THz FMCW radar 3D imaging, and the Newton smooth L0-norm (NSL0) algorithm is presented for sparse measurement data reconstruction. Both simulation and measurement experiments demonstrate the feasibility of reconstructing THz images from measurements even at the sparsity rate of 20%.

1. Introduction

Terahertz (THz) wave lies between infrared wave and millimeter wave, which is an electromagnetic wave that has not been fully recognized and utilized by human beings. Due to its ability of material penetration and harmless nonionizing radiation to human body, THz technology can be employed to effectively identify stealth and deceptive measures that cannot be distinguished by conventional means in the military fields and to identify concealed objects made of metal or inorganic materials for security check. As THz has a smaller wavelength and a wider bandwidth which will result in a higher resolution, THz imaging has been widely used in nondestructive inspections and medical diagnosis [1, 2]. With the rapid development of information countermeasures, antistealth, target search, and tracking, and materials science, THz imaging technology has made a great progress during the past decades.

Motivated by the huge application potential of high-resolution THz imaging technology, there has been growing interest in developing 3D imaging radar working at THz range. In 2007, a 220 GHz experimental frequency-modulated continuous wave (FMCW) inverse synthetic aperture radar (SAR) with a bandwidth of 8 GHz is designed to determine high-resolution scattering center distributions of targets [3]. A 240 GHz 3D FMCW imaging radar with a maximum bandwidth of 42 GHz is discussed in [4]. An imaging radar with the operation frequency of 580 GHz which is implemented in an all-solid-state design is developed at Jet Propulsion Laboratory (JPL) [5]. The first THz radar for fast standoff personnel screening with the operation frequency of 675 GHz is also built by JPL. A fast scanning device is designed to enable imaging at a frame rate of 1 Hz [6, 7]. An active FMCW imaging system ranging from 514 to 565 GHz (frequency centered at 540 GHz) is studied to image objects with a resolution of millimeter [8].

It can be found that THz 3D imaging is commonly realized with SAR technique, rather than building antenna arrays. This is due to that expensive devices in THz regime will lead to a high-cost imaging system having multiple transceivers. For a THz imaging system with SAR technique, the single transceiver is moved in a grid-like manner to produce an image with the processing approaches. Several SAR imaging algorithms in time domain, frequency domain,

and wavenumber domain have been proposed for THz FMCW SAR, respectively. A typical time domain back-projection algorithm is studied to obtain the image with 2D aperture synthesis for the SynView THz 3D imaging system [9]. A back-projection imaging approach has been presented in [10] for data processing of a 300 GHz imaging system. However, imaging algorithms in the time domain have a heavy calculation burden though they are able to process SAR data under a great variety of imaging geometries. A revised range-Doppler algorithm is presented for FMCW SAR imaging by compensating radar migration [11]. A nonlinear frequency-scaling algorithm is proposed by Meta et al. to achieve FMCW SAR focusing by applying Doppler-range correction [12]. However, the range-Doppler algorithm and the nonlinear frequency-scaling algorithm in frequency domain will result in deviations due to the high-order phase error. So, the range migration algorithm (RMA) in wavenumber domain is preferable for THz FMCW SAR imaging [8, 13].

As mentioned above, a single transceiver is moved in a grid-like manner to acquire data for THz FMCW SAR imaging in most cases. And the mechanical scanning parameters should obey the Nyquist–Shannon sampling theorem for the RMA imaging algorithm. However, a smaller wavelength in THz regime requires a smaller scanning step, and it will lead to a larger collection points and a longer data acquirement time. The THz imaging efficiency is low for the conventional imaging algorithms. To reduce imaging data acquirement time and to improve imaging efficiency, an algorithm based on compressed sensing is proposed for 3D imaging of THz FMCW SAR in this paper. The proposed algorithm relies on the advantages of compressed sensing that it can reconstruct signal from the sparse data samples.

The paper is organized as follows. The developed 220 GHz FMCW SAR imaging system is introduced in Section 2. And the RMA for THz FMCW radar imaging is given in Section 3. Section 4 describes the proposed 3D imaging algorithm based on compressed sensing. The experimental results are given and analyzed in Section 5 to verify the proposed imaging algorithm. The last section is Conclusion.

2. THz FMCW Imaging System

2.1. System Briefs. As shown in Figure 1, the FMCW THz imaging system developed in this paper consists of radio frequency transceiver subsystem, signal acquisition and processing subsystem, and planar scanning subsystem.

When the THz FMCW imaging system works, an X-band FMCW signal generated through the direct digital synthesizer serves as the driving source of the transmission link which will output a THz FMCW signal. Then, the transmitted signal will be reflected by target and then received by the antenna. The received echoed signal is mixed with the reference signal to get the intermediate frequency (IF) signal which will be processed with the IF processing unit. Lastly, the processed IF signal is acquired with the data acquisition unit. The planar scanner controlled by the data acquisition and processing subsystem moves with a "stop-go-stop" manner. The echoed signals at certain points are acquired and stored by the processing software and are processed to generate 3D images after finalization of scanning. The picture of the developed THz FMCW imaging system is presented in Figure 2. And the specification parameters are illustrated in Table 1.

2.2. THz FMCW Signal Modeling. The transmitted signal of the THz FMCW imaging system can be expressed as

$$s_t(t) = \exp\left(j\pi k_r t^2\right)\exp\left(j2\pi f_c t\right), \tag{1}$$

where f_c denotes the central frequency, T means the sweep duration, and k_r is the chirp frequency rate. Assumed that the distance between the target and the radar is R, the echoed signal can be expressed as

$$s_r(t-\tau_R) = g\cdot\ \exp\left[j\pi k_r (t-\tau_R)^2\right]\exp\left[j2\pi f_c (t-\tau_R)\right], \tag{2}$$

where $\tau_R = 2R/c$ is the echoed signal delay and g represents the target reflection coefficient. Dechirp signal processing technique is adopted in the developed imaging system to obtain IF signal. That is, IF signal is output by mixing the transmitted signal and the echoed signal, and it can be written as

$$s(t) = g\cdot\ \exp\left[-j\pi k_r\left(2\tau_R t - \tau_R^2\right)\right]\exp\left(-j2\pi f_c \tau_R\right), \tag{3}$$

where $\pi k_r \tau_R^2$ is the residual phase error (RVP) after dechirp. In general, this item can be ignored for imaging. Then, equation (3) can be simplified as

$$\begin{aligned} s(t) &= g\cdot\ \exp\left[-j2\pi\left(k_r t + f_c\right)\tau_R\right], \\ &= g\cdot\ \exp\left(-j2\pi f \tau_R\right), \end{aligned} \tag{4}$$

where $f = k_r t + f_c$, so the above expression can be rewritten as

$$s(t) = g\cdot\ \exp\left(-\frac{j4\pi f R}{c}\right). \tag{5}$$

3. Range Migration Algorithm for THz FMCW Radar Imaging

Though several algorithms have been developed for THz FMCW radar imaging, RMA in the wave number domain is widely used due to a higher efficiency. The imaging geometry and RMA for THz FMCW radar will be introduced in this section.

The imaging geometry of the developed imaging system is presented in Figure 3. The transceiver mounted on the planar scanner is controlled to move with a grid-like manner, which will lead to a 2D rectangular synthetic aperture formation e on the $X'O'Y'$ plane which is parallel to the XOY plane.

For the convenience of expression, equation (5) is rewritten as

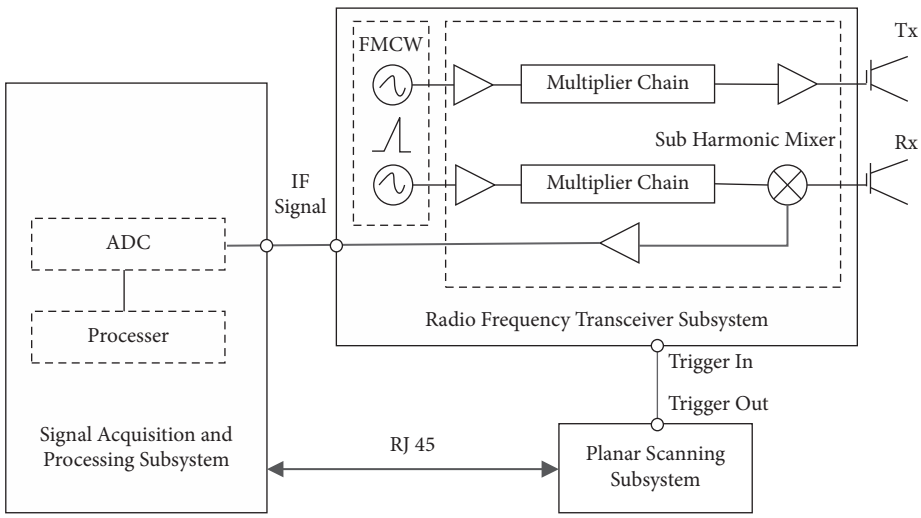

Figure 1: Schematic diagram of the developed THz FMCW imaging system.

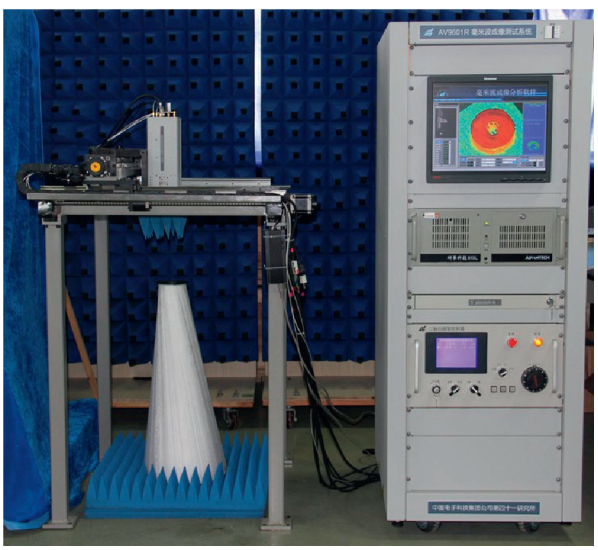

Figure 2: Picture of the developed THz FMCW imaging system.

$$s(t) = g \cdot e^{-j2kR}, \tag{6}$$

where $k = 2\pi f/c$ and $R = \sqrt{(x'-x)^2 + (y'-y)^2 + (z_0 - z)^2}$ is the range between the measurement point (x', y', z_0) and the scattering center (x, y, z). Then, the sum of all received echoed signals at a measurement point (x', y', z_0) within the imaging area is

$$s(x', y', k) = \iiint_P g(x, y, z) e^{-j2kR} \mathrm{d}x\mathrm{d}y\mathrm{d}z, \tag{7}$$

where P denotes the imaging area and $g(x, y, z)$ represents the reflection coefficient matrix of target.

Applying two-dimensional Fourier transform of the received echoed signals along the scanning direction,

Table 1: The developed THz FMCW imaging system parameters.

Parameters	Value
Center frequency	195 GHz
Bandwidth	50 GHz
Output power	>−2 dBm
Receiver sensitivity	−100 dBm
Sweep duration	0.1–1 ms
Maxim scanning area	500 mm* 500 mm

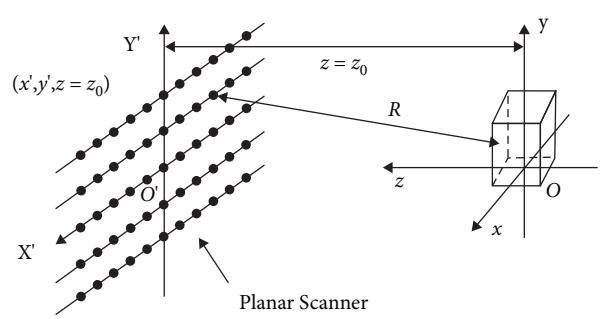

Figure 3: Imaging geometry of the developed THz FMCW imaging radar system.

$$\begin{aligned} S(k_x, k_y, k) &= \iint \iiint_P g(x, y, z) e^{-j2kR} \mathrm{d}x\mathrm{d}y\mathrm{d}z \\ &\quad \cdot e^{-jk_x x'} e^{-jk_y y'} \mathrm{d}x'\mathrm{d}y', \\ &= \iiint_P g(x, y, z) S_0(k_x, k_y, k) \mathrm{d}x\mathrm{d}y\mathrm{d}z, \end{aligned} \tag{8}$$

where k_x and k_y represent the spatial frequencies in the X- and Y-directions and $S_0(k_x, k_y, k) = \iint e^{-j2kR} e^{-jk_x x'} e^{-jk_y y'} \mathrm{d}x'\mathrm{d}y'$. And $S_0(k_x, k_y, k)$ can be solved as

$$S_0\left(k_x, k_y, k\right) = e^{j\sqrt{4k^2-k_x^2-k_y^2}\left(z_0-z\right)}e^{-jk_x x}e^{-jk_y y}. \quad (9)$$

Considering that $k_x^2 + k_y^2 + k_z^2 = 4k^2$, equation (8) can be rewritten as

$$S\left(k_x, k_y, k\right) = \iiint_P g(x, y, z)e^{j\sqrt{4k^2-k_x^2-k_y^2}z_0}e^{-jk_x x}e^{-jk_y y}e^{-jk_z z}\mathrm{d}x\mathrm{d}y\mathrm{d}z. \quad (10)$$

After multiplying the reference function $e^{-j\sqrt{4k^2-k_x^2-k_y^2}z_0}$, we can obtain the following expression:

$$S_1\left(k_x, k_y, k\right) = \iiint_P g(x, y, z)e^{-jk_x x}e^{-jk_y y}e^{-jk_z z}\mathrm{d}x\mathrm{d}y\mathrm{d}z. \quad (11)$$

It can be found from equation (11) that $S_1(k_x, k_y, k)$ is the Fourier transform of $g(x, y, z)$, so the reflection coefficient matrix $g(x, y, z)$ which corresponds to the image of target can be derived by applying inverse Fourier transform. However, the measured data are not uniformly distributed in the k_z domain due to a nonlinear conversion from k to k_z. Generally, the Stolt interpolation method is used to obtain a uniformly distributed data in the k_z domain. Finally, the reflection coefficient matrix $g(x, y, z)$ can be obtained with

$$g(x, y, z) = \mathrm{IFFT}_{\left(k_x,k_y,k_z\right)} \cdot \left\{\mathrm{stolt}_{k\longrightarrow k_z}\left[S\left(k_x, k_y, k\right)e^{j\sqrt{4k^2-k_x^2-k_y^2}z_0}\right]\right\}. \quad (12)$$

The THz FMCW SAR imaging algorithm based on RMA can be summarized as follows:

(1) 2D Fourier transform is applied on the data collected by planar scanning to obtain wavenumber domain formulation $S(k_x, k_y, k)$

(2) The reference function $e^{-j\sqrt{4k^2-k_x^2-k_y^2}z_0}$ is multiplied at the reference range z_0

(3) Stolt interpolation is performed to generate data which are uniformly distributed in the k_z domain

(4) Finally, 3D inverse Fourier transform is performed to produce the image of target.

4. Imaging Algorithm Based on Compressed Sensing

4.1. Compressed Sensing Principle. Compressed sensing is a signal processing technique which is able to realize the recovery of a sparse signal with fewer samplers required by the Nyquist sampling theorem. In view of the advantages of compressed sensing, this technique is investigated for THz FMCW SAR imaging to reduce the requirement for data sampling and to increase the imaging speed.

Suppose g is a discrete signal with a length of N in the time domain, and it can be represented linearly by a set of orthonormal basis as

$$g = \mathbf{\Psi}x = \sum_{i=1}^{N}\mathbf{\Psi}_i x_i, \quad (13)$$

where $\Psi = \{\Psi_1, \ldots, \Psi_N\}$ is the sparse transformation basis and $x = \{x_1, \ldots, x_N\}$ is the weighting coefficients of g satisfying that $x_i = \Psi_i^T g$.

It can be seen from equation (13) that x is the equivalent representation of g. If there are only K nonzero elements in x, then x is the K-sparse representation of signal g, and the signal sparsity is K.

Generally, the received THz FMCW radar signal is nonsparse in the time domain. So, it is necessary to transform the nonsparse time domain signal to the sparse transform domain. Fourier transform is employed here for signal transform operations in this paper. Compressed sampling is realized with a measurement matrix ϕ which projects high-dimensional signal on the low-dimensional space:

$$y = \phi g = \phi\mathbf{\Psi}x = Ax, \quad (14)$$

where y is the vector of measurements of the original high-dimensional signal g under a random matrix ϕ, Ψ is the sparse basis matrix, and $A = \phi\Psi$ is the sensing matrix with a dimension of $M \times N\,(M \ll N)$.

The N-dimensional signal x can be recovered from the M-dimensional measurement data through signal reconstruction. And the signal reconstruction is realized by solving the L_0-norm minimization problem expressed as

$$\begin{aligned} \hat{x} &= \arg\min \|x\|_0, \\ \text{s.t. } y &= Ax. \end{aligned} \quad (15)$$

Though the above minimum L_0-norm is an NP-hard problem which cannot be solved directly, an optimal solution can be realized with greedy search or convex optimization algorithms.

4.2. THz FMCW Radar Imaging Algorithm Based on Compressed Sensing. Because the recovery accuracy of greedy search reconstruction algorithms like orthogonal matching pursuit (OMP) [14, 15], stage-wise orthogonal matching pursuit (StOMP) [16], regularized orthogonal matching pursuit (ROMP) [17], and compressive sampling matching pursuit (CoSaMP) [18] is poor with lower signal noise ratio (SNR), an improved smoothed L_0-norm minimization (SL0) algorithm based on the convex optimization is presented in this paper.

For the SL0 algorithm, the objective function is defined as follows [19, 20]:

$$\begin{aligned} &\arg\min F_\sigma(x), \\ &\text{s.t.}\, y = Ax, \\ &\|x\|_0 = \lim_{\sigma\longrightarrow 0} F_\sigma(x) = \lim_{\sigma\longrightarrow 0}\sum_{i=1}^{N} F_\sigma(x_i), \end{aligned} \quad (16)$$

where $F_\sigma(x)$ is a smoothed function, which can be regarded as $\|x\|_0$ when σ is close to 0. It is obvious that the smoothed function $F_\sigma(x)$ will approximate to the optimal solution by choosing a suitable σ. And $F_\sigma(x_i)$ is defined as

$$F_\sigma(x_i) = \frac{\exp\left(x_i^2/2\sigma^2\right) - \exp\left(-x_i^2/2\sigma^2\right)}{\exp\left(x_i^2/2\sigma^2\right) + \exp\left(-x_i^2/2\sigma^2\right)}. \quad (17)$$

Compared with the Gauss smoothed function, the presented smoothed function will get a better performance in signal reconstruction as this leads to a closer approximation to $\|x\|_0$.

The steepest descent algorithm is commonly applied to solve equation (16). However, it is difficult to estimate the optimal searching step in the algorithm, and this will lead to a slower convergence speed. A revised Newton method in [21] is utilized in this paper to solve the optimization problem more efficiently. The Newton directions is revised as

$$d = -G^{-1}\nabla F_\sigma(x), \quad (18)$$

where $\nabla F_\sigma(x) = [(\partial f_\sigma(x_1)/\partial x_1), \ldots, (\partial f_\sigma(x_N)/\partial x_N)]^T$, $G = \nabla^2(F_\sigma(x)) + \varepsilon_k \mathbf{I}$, $\mathbf{I}$ is identity matrix, and ε_k is positive to make sure that diagonal values of G are also positive. Here, ε_k is set as

$$\varepsilon_k = \frac{4/\sigma^2\left[\left(3x_i^2/\sigma^2\right)\exp\left(-x_i^2/2\sigma^2\right) - \left(x_i^2/\sigma^2\right)\exp\left(x_i^2/2\sigma^2\right)\right]}{\left[\exp\left(-x_i^2/2\sigma^2\right) + \exp\left(-x_i^2/2\sigma^2\right)\right]^3}. \quad (19)$$

So, the revised Newton directions can be written as

$$d = \left(-\frac{\sigma^2 x_1}{\sigma^2 + x_1^2}, \ldots, -\frac{\sigma^2 x_i}{\sigma^2 + x_i^2}, \ldots, -\frac{\sigma^2 x_n}{\sigma^2 + x_n^2}\right)^T. \quad (20)$$

The realization steps of the presented sparse signal reconstruction algorithm based on the Newton smooth L_0-norm (NSL0) are summarized in Table 2.

Initialization:

(1) $x_0 = A^T(AA^T)^{-1}y$.

(2) Choose a suitable decreasing sequence for σ, $\{\sigma_1, \sigma_2, \ldots, \sigma_j\}$, $\sigma_j = \beta\sigma_{j-1}$, $\beta(0 < \beta < 1)$ is the decreasing factor.

Realization:

(1) For $j = 1, 2, 3, \ldots, J$

A, $\sigma = \sigma_j$;

B, $x_j = x_{j-1}$;

C, $r_0 = 0$;

D, For $n = 1, 2, 3, \ldots, N$

(a) Calculate the Newton direction $d = (-(\sigma^2 x_1/\sigma^2 + x_1^2), \ldots, -(\sigma^2 x_n/\sigma^2 + x_n^2))$

(b) Update $x_{j_n} \leftarrow x_{j_n} + d$

(c) Project x back onto the feasible set $x_{j_n} \leftarrow x_{j_n} - A^T(AA^T)^{-1}(Ax_{j_n} - y)$

(d) Let $r = y - Ax_{j_n}$;

(e) If $\|r - r_0\| < e$, break; Else, $r_0 = r$;

E, $x_j = x_{j_n}$;

(2) Final answer is $\hat{x} = x_j$.

Table 2: NSL0 algorithm.

	Algorithm	
Sparsity rate (%)	SL0	NSL0
10	7.8157	6.8796
20	11.6065	10.6881
30	17.2381	16.3765
40	24.3518	23.1646
50	32.8382	31.9270

Based on the above sparse signal reconstruction algorithm, the 3D imaging algorithm of THz FMCW SAR based on compressed sensing proposed in this paper can be summarized as follows:

(1) Design a measurement matrix ϕ which is able to meet the requirement for data acquisition

(2) Collect THz FMCW SAR echoed signal at the corresponding position given by the designed measurement matrix to obtain measurement signal y

(3) Reconstruct original signal $\hat{g}$ from the sparse measurement data using the presented NSL0 algorithm

(4) Apply 2D Fourier transform with respect to the reconstructed signal $\hat{g}$

(5) Perform reference function multiplying (RFM)

(6) Perform Stolt interpolation

(7) Perform 3D inverse Fourier transform to generate the image

The proposed THz FMCW SAR imaging algorithm based on compressed sensing is shown in Figure 4.

5. Experimental Result

Simulation and measurement experiments are performed to verify the presented THz FMCW SAR imaging algorithm in this paper.

5.1. Point Targets Simulation. The THz FMCW SAR imaging model is built with MATLAB, and six-point targets are simulated for imaging. The coordinates of targets are (0.2m, 0m, 0m), (−0.2m, 0m, 0m), (0m, 0.2m, 0m), (0m, −0.2m, 0m), (0m, 0m, 0.2m), and (0m, 0m, −0.2m). The imaging radar system parameters used in the simulation are listed in Table 3. The measurement matrix used in the simulation is a sparse random matrix, and the sparse sampling rate is 50%.

The sparse simulated data are firstly recovered with compressed sensing. Then, the recovered signal is processed with RMA to produce a 3D image as shown in Figure 5(a). Also, the imaging results with the full data using RMA are presented in Figure 5(b) for comparison.

It can be seen from the figures that the produced 3D images are almost the same. And, it shows that the presented THz FMCW SAR imaging algorithm works well with the sparse measurement.

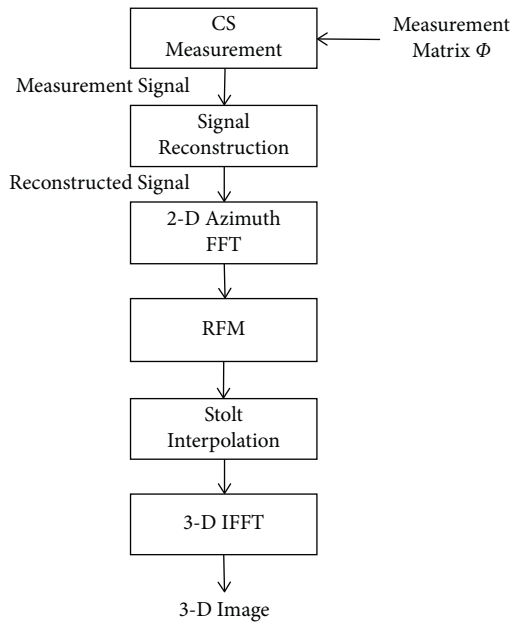

Figure 4: THz FMCW SAR imaging algorithm based on compressed sensing.

Table 3: Simulation parameters.

Frequency range	170 GHz–220 GHz
Bandwidth	50 GHz
Distance z_0	0.5 m
Scanning step along $X\prime$-axis	0.001 m
Scanning step along $Y\prime$-axis	0.001 m
Scanning points along $X\prime$-axis	1000
Scanning points along $Y\prime$-axis	1000

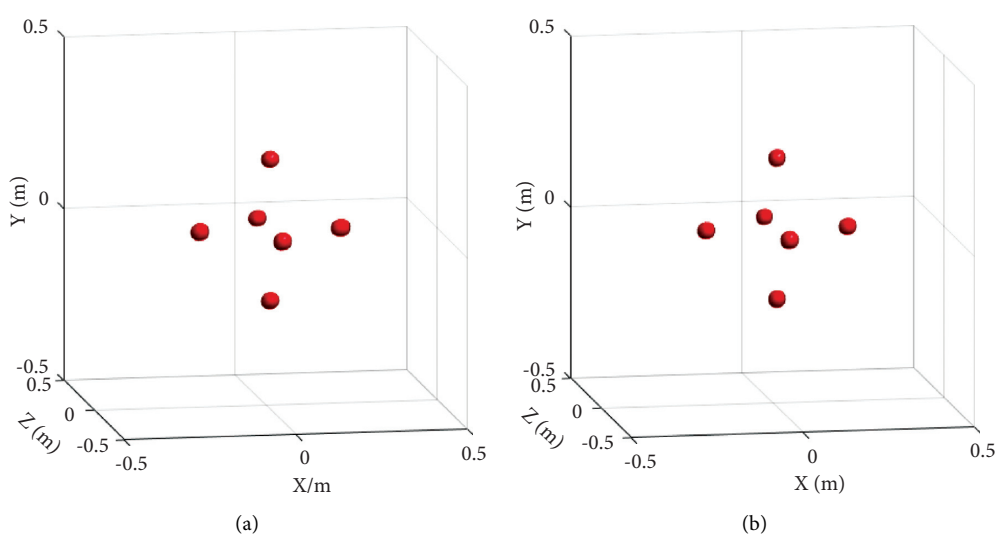

Figure 5: Reconstructed 3D images of point targets: (a) presented algorithm in this paper; (b) RMA.

(a) (b)

Figure 6: Targets for imaging experiments: (a) disc; (b) scissors.

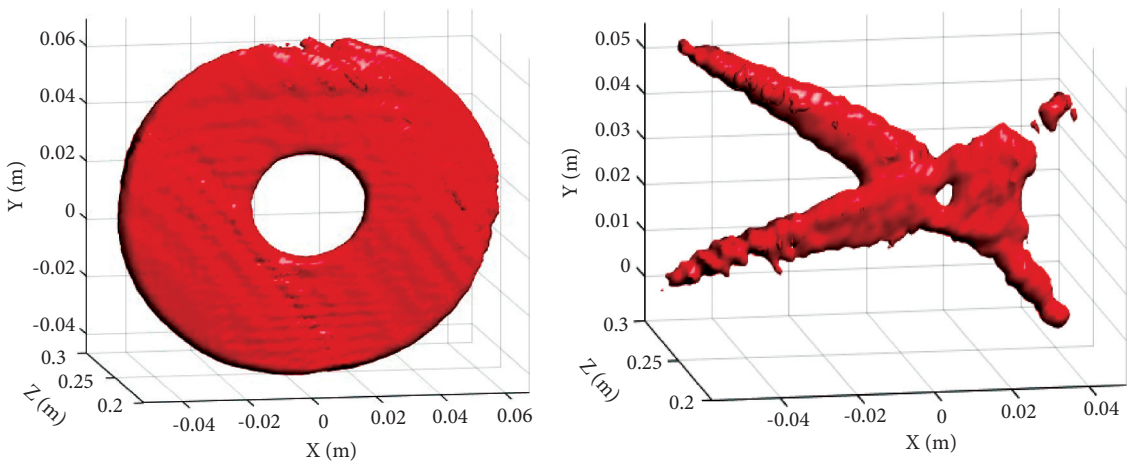

(a) (b)

Figure 7: Reconstructed 3D images of targets with RMA: (a) disc; (b) scissors.

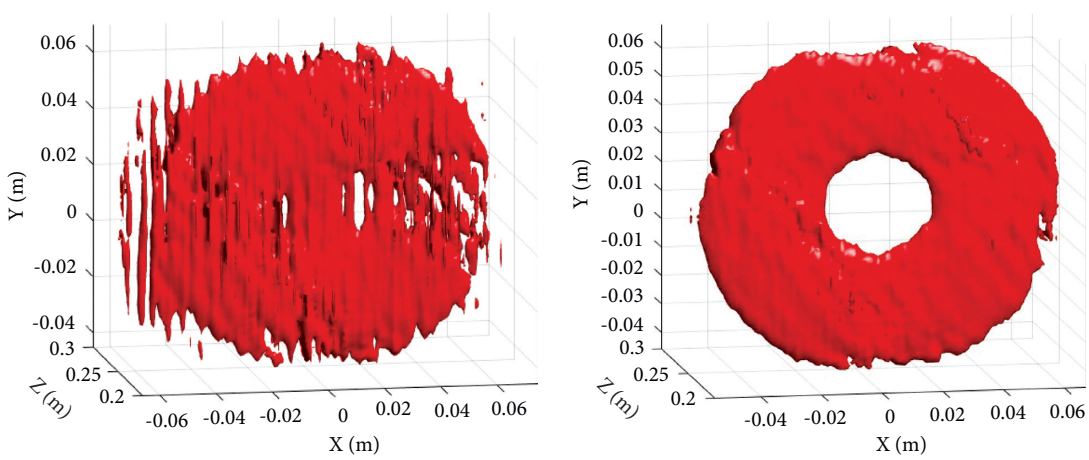

(a) (b)

Figure 8: Continued.

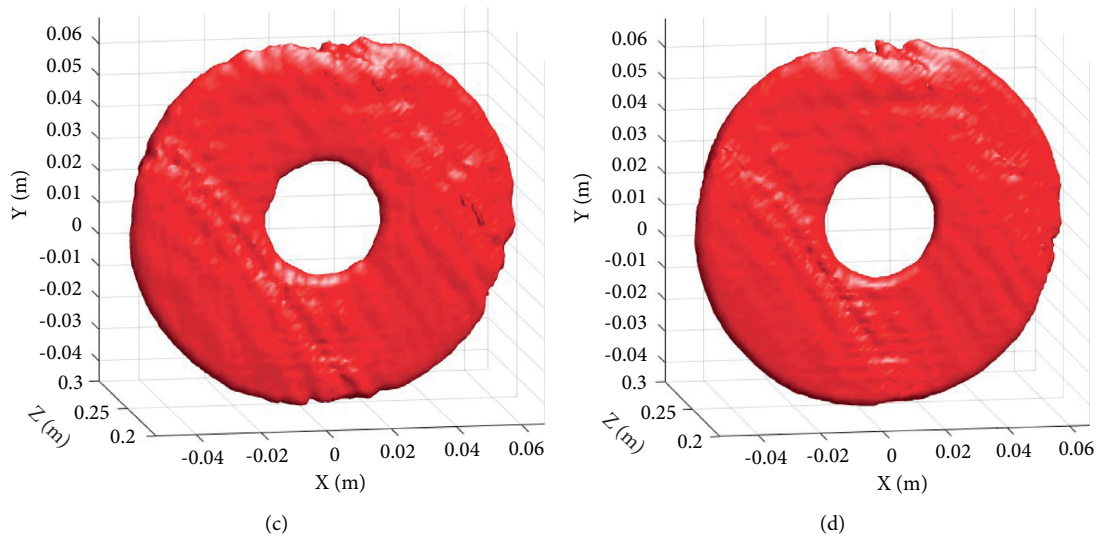

Figure 8: Reconstructed 3D images of disc with the presented algorithm under different data sparsity rates: (a) 10%; (b) 20%; (c) 30%; (d) 50%.

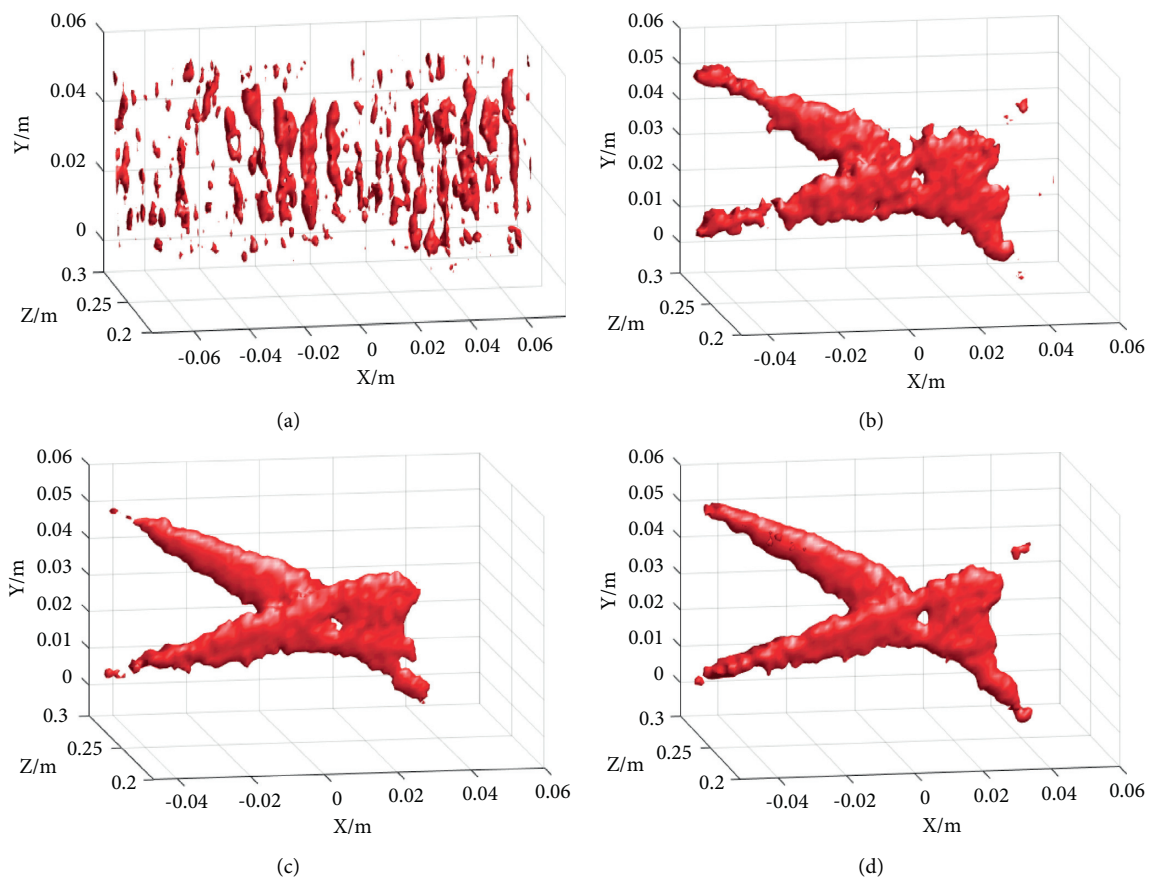

Figure 9: Reconstructed 3D images of scissors with the presented algorithm under different data sparsity rates: (a) 10%; (b) 20%; (c) 30%; (d) 50%.

5.2. Measurement Experiment. In order to further verify the proposed 3D imaging algorithm for THz FMCW SAR, experiments are conducted with the developed THz FMCW imaging radar system. The operation frequency range of the system is 170–220 GHz. The targets to be imaged are placed on a foam column which is 0.5 m away from the planar

Table 4: Reconstruction error comparisons between SL0 and NSL0.

	Algorithm	
Sparsity rate (%)	SL0	NSL0
10	0.8627	0.8354
20	0.6447	0.6265
30	0.4835	0.4693
40	0.3545	0.3423
50	0.2757	0.2641

Table 5: Calculation time comparisons between SL0 and NSL0 (s).

	Algorithm	
Sparsity rate (%)	SL0	NSL0
10	7.8157	6.8796
20	11.6065	10.6881
30	17.2381	16.3765
40	24.3518	23.1646
50	32.8382	31.9270

scanning plane, and the scanning area is 151 mm × 151 mm. The planar scanner moves with a "stop-go-stop" manner with a scanning step of 1 mm. The collected full data are processed to reconstruct the image of target with RMA first. The reconstructed images of a disc and a pair of scissors as shown in Figure 6 are presented in Figure 7. Then, 10%, 20%, 30%, and 50% of the collected data are extracted according to the measurement matrix ϕ. The extracted sparse data are then processed with the proposed compressed sensing imaging algorithm. The reconstructed images under different sparsity rates are shown in Figures 8 and 9.

It can be seen from the experimental results that the reconstructed 3D image quality is poor with the 10% data sparsity rate, and it is difficult to identify the specific targets. However, the images can be reconstructed well even at 20% data sparsity rate. And a larger data will result in a better image. Also, a reconstruction error ε is introduced to evaluate the quality of the images reconstructed with different reconstruction algorithms:

$$\varepsilon = \frac{\sqrt{\left(\sum_{i=1}^{n} \left|g'(x,y,z) - g(x,y,z)\right|^2\right)/n^2}}{\sqrt{\left(\sum_{i=1}^{n} \left|g(x,y,z)\right|^2\right)/n^2}}, \tag{21}$$

where $g'(x,y,z)$ is the reconstructed signal and $g(x,y,z)$ denotes the original signal. A larger ε denotes a significant deviation of the reconstructed signal from the original signal and thus means a poorer performance of the reconstruction algorithm. The reconstruction error comparisons between SL0 and NSL0 under different sparsity rates are listed in Table 4.

Also, the calculation time of the algorithms is presented in Table 5. The CPU is Intel Core i5-4210 M @ 2.6 GHz, and the memory is 8 GB.

The above results show that the presented NSL0 reconstruction algorithm has a smaller error and a fast calculation speed compared with the SL0 reconstruction algorithm. This is contributed by Newton's method in the NSL0 algorithm.

6. Conclusions

An algorithm for THz FMCW SAR imaging based on compressed sensing is investigated in this paper. The developed 220 GHz FMCW imaging radar system is introduced, and the signal model is built firstly. RMA for the developed THz FMCW SAR is then derived. Compressed sensing is described, and the NSL0 reconstruction algorithm is presented to reconstruct signal with sparse samples. And the algorithm based on compressed sensing for the developed THz FMCW SAR is summarized. Experiments are performed to verify the presented imaging algorithms. The experimental results show that it is able to reconstruct the image well even at the sparsity rate of 20%. The presented 3D imaging algorithm for the THz FMCW imaging radar system can improve the imaging efficiency by reducing the requirements for spatial data acquisition.

The developed 220 GHz FMCW SAR imaging system has been used for nondestructive testing of composite materials in aerospace and critical structural applications. As only a single transceiver is integrated in the system, it must employ a grid-like mechanical scanning to cover an area and results in a high time cost. The imaging system can be upgraded to multiple transceivers which will have a faster imaging speed. The proposed compressed sensing image reconstruction algorithm can be also applied for sparse transceiver array configuration which is able to achieve a lower imaging system cost by reducing THz transceivers.

Data Availability

The data used to support this study are included within this articles as tables. If there is a need for any other information, the corresponding author may be contacted by e-mail.

Conflicts of Interest

The authors declare that there are no conflicts of interest regarding the publication of this paper.

Acknowledgments

This work was partially supported by the Science Foundation of the Jiangsu Higher Education Institutions of China (No. 18KJB413003), the High-Level Talent Foundation of Jinling Institute of Technology (Nos. Jit-b-201713, Jit-b-202029, Jit-b-201816, and Jit-b-201628), the Research Fund Incubation Project of Jinling Institute of Technology (No. jit-fhxm-201705), the Shanghai Science and Technology Innovation Action Plan (No. 19511108400), and the Jiangsu Province Fifth "333 High-Level Talent Training Project" Second-Level Funding Research Project (No. 2019).

References

[1] R. I. Stantchev, X. Yu, T. Blu, and E. Pickwell-MacPherson, "Real-time terahertz imaging with a single-pixel detector," *Nature Communications*, vol. 11, no. 1, pp. 2535–2538, 2020.

[2] D. M. Mittleman, "Twenty years of terahertz imaging [Invited]," *Optics Express*, vol. 26, no. 8, pp. 9417–9431, 2018.

[3] H. Essen, A. Wahlen, R. Sommer et al., "High-bandwidth 220 GHz experimental radar," *Electronics Letters*, vol. 43, no. 20, pp. 1114–1116, 2007.

[4] T. Jaeschke, C. Bredendiek, and N. Pohl, "3D FMCW SAR imaging based on a 240 GHz SiGe transceiver chip with integrated antenna," in *Proceedings of German Microwave Conference*, pp. 1–4, Aachen, Germany, March 2014.

[5] K. B. Cooper, R. J. Dengler, G. Chattopadhyay et al., "A high-resolution imaging radar at 580 GHz," *IEEE Microwave and Wireless Components Letters*, vol. 18, no. 1, pp. 64–66, 2008.

[6] K. B. Cooper, R. J. Dengler, N. Llombart et al., *Fast High-Resolution Terahertz Radar Imaging at 25 Meters, Terahertz Physics, Devices, and Systems IV: Advanced Applications in Industry and Defense*Proceeding of SPIE, Orlando, FL, USA, 2010.

[7] K. B. Cooper, R. J. Dengler, and N. Llombart, "An approach for sub-second imaging of concealed objects using terahertz (THz) radar," *Journal of Infrared, Millimeter and Terahertz Waves*, vol. 30, no. 12, pp. 1297–1307, 2009.

[8] J. Jinshan Ding, M. Kahl, O. Loffeld, and P. H. Bolivar, "THz 3-D image formation using SAR techniques: simulation, processing and experimental results," *IEEE Transactions on Terahertz Science and Technology*, vol. 3, no. 5, pp. 606–616, 2013.

[9] A. Keil, T. Hoyer, J. Peuser, H. Quast, and T. Löffler, "All-electronic 3D THz synthetic reconstruction imaging system," in *Proceeding of 2011 36th Int. Conf. On Infrared, Millim. THz Waves (IRMMW-THz)*, pp. 1-2, Houston, TX, USA, October 2011.

[10] J. Moll, P. Schops, and V. Krozer, "Towards three-dimensional millimeter-wave radar with the bistatic fast-factorized back-projection algorithm-Potential and limitations," *IEEE Transactions on Terahertz Science and Technology*, vol. 2, no. 4, pp. 432–440, 2012.

[11] J. J. M. De Wit, A. Meta, and P. Hoogeboom, "Modified range-Doppler processing for FM-CW synthetic aperture radar," *IEEE Geoscience and Remote Sensing Letters*, vol. 3, no. 1, pp. 83–87, 2006.

[12] A. Meta, P. Hoogeboom, and L. P. Ligthart, "Non-linear frequency scaling algorithm for FMCW SAR data," in *Proceedings of the Eur. Radar Conf.*, pp. 9–12, Manchester, UK, September 2006.

[13] H. Gao, C. Li, S. Wu et al., "Study of the extended phase shift migration for three-dimensional MIMO-SAR imaging in terahertz band," *IEEE Access*, vol. 8, pp. 24773–24783, 2020.

[14] J. A. Tropp and A. C. Gilbert, "Signal recovery from random measurements via orthogonal matching pursuit," *IEEE Transactions on Information Theory*, vol. 53, no. 12, pp. 4655–4666, 2007.

[15] J. F. Determe, J. Louveaux, L. Jacques, and F. Horlin, "On the noise robustness of simultaneous orthogonal matching pursuit," *IEEE Transactions on Signal Processing*, vol. 65, pp. 864–875, 2016.

[16] D. L. Donoho, Y. Tsaig, I. Drori, and J.-L. Starck, "Sparse solution of underdetermined systems of linear equations by stagewise orthogonal matching pursuit," *IEEE Transactions on Information Theory*, vol. 58, no. 2, pp. 1094–1121, 2012.

[17] D. Needell and R. Vershynin, "Signal recovery from incomplete and inaccurate measurements via regularized orthogonal matching pursuit," *IEEE Journal of Selected Topics in Signal Processing*, vol. 4, no. 2, pp. 310–316, 2010.

[18] D. Needell and J. A. Tropp, "CoSaMP," *Communications of the ACM*, vol. 53, no. 12, pp. 93–100, 2010.

[19] H. Mohimani, M. Babaie-Zadeh, and C. Jutten, "A fast approach for overcomplete sparse decomposition based on smoothed $\ell ^{0}$ norm," *IEEE Transactions on Signal Processing*, vol. 57, no. 1, pp. 289–301, 2009.

[20] L. Wang, X. Yin, H. Yue, and J. Xiang, "A regularized weighted smoothed L₀ norm minimization method for underdetermined blind source separation," *Sensors*, vol. 18, no. 12, 2018.

[21] R. Zhao, W. Lin, H. Li, and S. Hu, "Reconstruction algorithm for compressive sensing based on smoothed L0 norm and revised Newton method," *Journal of Computer Aided Design and Computer Graphics*, vol. 24, pp. 478–484, 2012.

Hindawi
Complexity
Volume 2021, Article ID 6646843, 8 pages
https://doi.org/10.1155/2021/6646843

Research Article

Averaging Principle for Caputo Fractional Stochastic Differential Equations Driven by Fractional Brownian Motion with Delays

Pengju Duan, Hao Li, Jie Li, and Pei Zhang

School of Mathematics and Statistics, Suzhou University, Suzhou 234000, Anhui, China

Correspondence should be addressed to Pengju Duan; pjduan1981@hotmail.com

Received 26 November 2020; Revised 5 April 2021; Accepted 17 July 2021; Published 3 August 2021

Academic Editor: Xue-bo Jin

In this article, we investigate a class of Caputo fractional stochastic differential equations driven by fractional Brownian motion with delays. Under some novel assumptions, the averaging principle of the system is obtained. Finally, we give an example to show that the solution of Caputo fractional stochastic differential equations driven by fractional Brownian motion with delays converges to the corresponding averaged stochastic differential equation.

1. Introduction

Fractional differential equations have been developing as an active area on medicine, electrical engineering, biochemistry, and mechanical systems [1–5]. Because the systems are often subjected to noisy fluctuations, it is important to consider randomness into models. Since the fractional Brownian motion (fBm for short) owns many excellent properties, for example, long-range dependence and self-similar, it is usually used to describe the uncertainty. Since then, stochastic calculus with respect to fBm has been paid much attention in the stochastic analysis field, and many interesting works have obtained both qualitative and quantitative properties of stochastic differential equations (SDEs for short) driven by fBm [6–8]. Furthermore, the applications of fractional stochastic differential equations (FSDEs for short) driven by fBm have been widely applied in mathematical quantum, physics, and biology [9–11].

For the deterministic systems, many varieties of methods are proposed for average systems, such as gradient-based and least squares-based iterative algorithms for Hammerstein systems using the hierarchical identification principle, two-stage least squares-based iterative estimation algorithm for CARARMA system modeling, decomposition-based fast least squares algorithm for output error systems, and gradient-based and least squares-based iterative estimation algorithms for multi-input multi-output systems [12–14]. Compared to the deterministic systems, due to influence of stochastic factors, the exact solution of FSDEs driven by fBm is difficult to realize, and the above-mentioned methods do not work. Because the averaging principle shows that the complex original systems can be ignored and one can only concentrate on the average systems instead, it is usually taken as an effective tool to reduce the amount of calculation of the original systems. Khasminskii [15] first started with the averaging method to approximate the complex system with a simpler system. In recent years, the averaging method has been developed in many ways [16–18]. For example, Pei et al. [19] investigated stochastic averaging for stochastic differential equations driven by fBm and Brownian motion. Recently, Luo et al. [20] discussed the averaging principle for FSDEs of Itô-Doob with delays driven by Brownian motion. Xu et al. [21] presented the averaging principle for stochastic differential equations with Caputo fractional derivative.

Inspired by the above works, we will discuss averaging principle of a new kind of SDEs with Caputo derivative driven by fBm and Brownian motion, which is a general case of [19, 20]. On the other hand, because Lipschitz conditions restrict the application, we will adopt weakened Lipschitz conditions to obtain the result. Moreover, in order to overcome the influence of Caputo derivative and fBm, we introduce a new averaging method to realize the stochastic averaging principle.

In this article, we will deal with averaging principle of the following Caputo FSDEs driven by fBm and Brownian motion with delays:

$$\begin{cases} D_t^{\alpha} X(t) = f(t, X(t), X_t) + g(t, X(t), X_t)\dfrac{\mathrm{d}W_t}{\mathrm{d}t} + \sigma(t, X(t), X_t)\dfrac{\mathrm{d}B_t^H}{\mathrm{d}t}, & t \in [0, T], \\ X(t) = \varphi(t), & -\tau \le t \le 0, \end{cases} \tag{1}$$

where D_t^{α} is the Caputo fractional derivative, $\alpha \in (1/2, 1)$. f: $[0, T] \times U \times \mathrm{B} \longrightarrow U$, g: $[0, T] \times U \times \mathrm{B} \longrightarrow \mathscr{L}_2^0(V, U)$, σ: $[0, T] \times U \times \mathrm{B} \longrightarrow \mathscr{L}_2^0(V, U)$. B_t^H is a V-valued Q-cylindrical fBm with the Hurst parameter $H \in (1/2, 1)$, W_t is a standard Wiener process on a real and separable Hilbert space V independent of B_t^H, and $X_t = \{X(t+\theta), \theta \in [-\tau, 0]\}$ is the B value stochastic process. The initial value $\varphi = \{\varphi(\theta)\colon -\tau \le \theta \le 0\}$ is an $\mathscr{F}_0$-measurable B-valued random variable independent of fBm B_t^H and Wiener process W_t with finite second moment.

The rest part is arranged as follows. Section 2 is devoted to some preliminary results and assumptions. In Section 3, the averaging principle is presented. An example is provided to show the result in Section 4.

2. Preliminary

Let $(\Omega, \mathscr{F}, \mathbb{P})$ be a completed probability space. For any $t \in [0, T]$, $\mathscr{F}_t$ denotes the σ field generated by $B_s^H, W_s, s \in [0, t]$, and all $\mathbb{P}$ null sets. A one-dimensional fractional Brownian motion with Hurst parameter $H \in (0, 1)$ is a centered Gaussian process $\beta^H = \beta^H(t)$ with the covariance function:

$$R(t, s) = E\left[\beta^H(t)\beta^H(s)\right] = \frac{1}{2}\left(|t|^{2H} + |s|^{2H} - |t-s|^{2H}\right). \tag{2}$$

When $H > 1/2$, $\beta^H(t)$ has the following representation:

$$\beta^H(t) = \int_0^t K(t, s)\mathrm{d}\beta(s), \tag{3}$$

where $\beta(s)$ is a standard Brownian motion, and the kernel $K(t, s)$ is given by

$$K(t, s) = c_H s^{(1/2)-H} \int_s^t (u-s)^{H-3/2} u^{H-1/2} \mathrm{d}u, \quad t \ge s, \tag{4}$$

where c_H is a nonnegative constant with respect to H.

For function $\varphi \in L^2([0, T])$, the fractional Wiener integral of φ with respect to β^H is defined by

$$\int_0^T \varphi(s)\mathrm{d}\beta^H(s) = \int_0^T K_H^* \varphi(s)\mathrm{d}\beta(s), \tag{5}$$

where $K_H^*\varphi(s) = \int_s^T \varphi(t)(\partial K(t, s)/\partial t)\mathrm{d}t$.

$(V, \|\cdot\|_V)$ and $(U, \|\cdot\|_U)$ are the two real separable Hilbert spaces with their vectors norms. Let $\mathscr{L}(V, U)$ denote the collection of all linear-bounded operators from V to U equipped with the norm $\|\cdot\|$. For the sake of convenience, we shall use the same notation $\|\cdot\|$ to denote the norms in $V, U, \mathscr{L}(V, U)$. $Q \in \mathscr{L}(V, U)$ is an operator defined by $Qe_n = \lambda_n e_n$ with finite trace $\mathrm{tr}Q = \sum_{n=1}^{+\infty}\lambda_n < +\infty$, where $\lambda_n (n = 1, 2, \ldots)$ are nonnegative real numbers, and $e_n (n = 1, 2, \ldots)$ denotes a complete orthonormal basis in V. We define the infinite dimensional fBm on V with covariance Q as

$$B_t^H = \sum_{n=1}^{\infty} \beta_n^H(t) Q^{1/2} e_n = \sum_{n=1}^{\infty} \sqrt{\lambda_n} e_n \beta_n^H(t), \tag{6}$$

where $\beta_n^H(t)$ are the real, independent fBms. The process B_t^H called V-valued Q-fBm, starts from 0, has zero mean and covariance:

$$E\langle B_t^H, x\rangle\langle B_s^H, y\rangle = R(t, s)\langle Q(x), y\rangle, \quad \text{for all } x, y \in V \text{ and } t, s \in [0, T]. \tag{7}$$

In the following parts, we shall introduce Wiener integral with respect to the Q-fBm B_t^H. Let $\mathscr{L}_2^0 = \mathscr{L}_2^0(V, U)$ denote the space of all Q-Hilbert–Schmidt operators ψ: $V \longrightarrow U$ equipped with the norm

$$\|\psi\|_{\mathscr{L}_2^0} = \sum_{n=1}^{\infty} \left\| \sqrt{\lambda_n}\, \psi e_n \right\|^2 < \infty, \tag{8}$$

and the inner product $\langle \varphi, \psi\rangle_{\mathscr{L}_2^0} = \sum_{n=1}^{\infty}\langle \varphi e_n, \psi e_n\rangle$ for $\varphi, \psi \in \mathscr{L}_2^0$.

Now, we give the definition of the fractional Wiener integral of the function ψ: $[0, T] \longrightarrow \mathscr{L}_2^0$ with respect to Q-fBm as follows:

$$\begin{aligned} \int_0^t \psi(s)\mathrm{d}B_s^H &= \sum_{n=1}^{\infty} \int_0^t \psi(s) Q^{1/2} e_n \mathrm{d}\beta_n^H(s) \\ &= \sum_{n=1}^{\infty} \int_0^t \left(K_H^*\left(\psi Q^{1/2} e_n\right)\right)(s)\mathrm{d}\beta_n(s), \end{aligned} \tag{9}$$

where β_n is the standard Brownian motion with respect to β_n^H.

We introduce $B([-\tau,0],L^2(\Omega,U))$ (B for simply) denotes the family of all $\mathscr{F}_0$-measurable bounded continuous functions ξ: $[-\tau,0]\longrightarrow L^2(\Omega,U)$ endowed with the norm $\|\xi(t)\|^2=\sup_{-\tau\le\theta\le t}E\|\xi(\theta)\|^2$. It is important of the following lemma to prove our main results, which is appeared in [22].

Lemma 1. *If ψ: $[0,T]\longrightarrow\mathscr{L}_2^0(V,U)$ satisfies*

$$\int_0^T\|\psi(t)\|_{\mathscr{L}_2^0}^2\mathrm{d}t<\infty, \tag{10}$$

then, for any $0\le s\le t\le T$,

$$E\left(\left\|\int_s^t\sigma(r)\mathrm{d}B_r^H\right\|^2\right)\le C_H(t-s)^{2H-1}\int_s^t\|\sigma(r)\|_{\mathscr{L}_2^0}^2\mathrm{d}r. \tag{11}$$

Now, we recall some notations and preliminary results about fractional calculus and some special functions.

Definition 1. For any $\alpha\in(0,1)$ and function f: $[0,T]\longrightarrow U$, the Riemann–Liouville fractional integral operator of order α is defined

$$I^\alpha f(t)=\frac{1}{\Gamma(\alpha)}\int_0^t(t-s)^{\alpha-1}f(s)\mathrm{d}s,\quad 0\le t\le T, \tag{12}$$

where $\Gamma(\alpha)=\int_0^\infty r^{\alpha-1}e^{-r}\mathrm{d}r$.

Definition 2. The Caputo fractional derivative with order α of function $f(t)\in\mathscr{C}^n([0,T];U)$ is defined as

$$D_t^\alpha f(t)=\begin{cases}\dfrac{1}{\Gamma(n-\alpha)}\displaystyle\int_0^t\frac{f^{(n)}(s)}{(t-s)^{\alpha+1-n}}\mathrm{d}s, & n-1<\alpha<n,\\[2ex] \dfrac{\mathrm{d}^n}{\mathrm{d}t^n}f(t), & \alpha=n.\end{cases} \tag{13}$$

In order to study the averaging principle of the system (1), we impose the following assumptions on the coefficient functions.

Assumption 1. For each $x_i\in U$, $y_i\in B$, $i=1,2$, there exists a nonnegative function $\lambda(t)$, such that

$$\begin{aligned}&\|f(t,x_1,y_1)-f(t,x_2,y_2)\|^2\vee\|g(t,x_1,y_1)-g(t,x_2,y_2)\|_{\mathscr{L}_2^0}^2\\&\quad\vee\|\sigma(t,x_1,y_1)-\sigma(t,x_2,y_2)\|_{\mathscr{L}_2^0}^2\\&\le\lambda(t)\left(\|x_1-x_2\|^2+\|y_1-y_2\|^2\right),\end{aligned} \tag{14}$$

where $\sup_{0\le t\le T}\lambda(t)<+\infty$.

Assumption 2. For each $T_1\in[0,T]$, $x\in U$ and $y\in$ B, there exist positive bounded functions $\lambda_i(t)$, $i=1,2$ and measurable functions $\overline{f}$: $U\times\mathscr{R}\longrightarrow U$, $\overline{g}\,\overline{\sigma}$: $U\times\mathscr{R}\longrightarrow\mathscr{L}_2^0(V,U)$, such that

$$\begin{aligned}&\frac{1}{T_1}\int_0^{T_1}(t-s)^{2\alpha-2}\|f(s,x,y)-\overline{f}(x,y)\|^2\mathrm{d}s\le\lambda_1(T_1)\left(\|x\|^2+\|y\|^2\right),\\&\frac{1}{T_1}\int_0^{T_1}(t-s)^{2\alpha-2}\|g(s,x,y)-\overline{g}(x,y)\|_{\mathscr{L}_2^0}^2\mathrm{d}s\le\lambda_2(T_1)\left(\|x\|^2+\|y\|^2\right),\\&\frac{1}{T_1}\int_0^{T_1}(t-s)^{2\alpha-2}\|\sigma(s,x,y)-\overline{\sigma}(x,y)\|_{\mathscr{L}_2^0}^2\mathrm{d}s\le\lambda_3(T_1)\left(\|x\|^2+\|y\|^2\right).\end{aligned} \tag{15}$$

Remark 1. In Assumption 1, if we let $\lambda(t)=C$, then it becomes the Lipschitz condition.

Remark 2. If we let $\alpha=1$, then (16) is the common stochastic delay differential equation driven by fBm, and the Assumption 2 turns to classical averaging principle.

Definition 3. A U value stochastic process $\{X(t)\}_{-\tau\le t\le T}$ is called a mild solution of (16) if $X(t)$ satisfies the following:

(1) $X(t)$ is continuous and $\mathscr{F}_t$-measurable, X_t is a B value stochastic process;

(2) For $t\in[-\tau,0]$, $X(t)=\varphi(t)$

(3) For each $0 \le t \le T$, $X(t)$ satisfies the following integral equation:

$$X(t) = \begin{cases} X(0) + \dfrac{1}{\Gamma(\alpha)} \displaystyle\int_0^t (t-s)^{\alpha-1} f(s, X(s), X_s) \mathrm{d}s + \dfrac{1}{\Gamma(\alpha)} \displaystyle\int_0^t (t-s)^{\alpha-1} g(s, X(s), X_s) \mathrm{d}W_s \\ + \dfrac{1}{\Gamma(\alpha)} \displaystyle\int_0^t (t-s)^{\alpha-1} \sigma(s, X(s), X_s) \mathrm{d}B_s^H, \\ X(t) = \xi, \quad -\tau \le t \le 0. \end{cases} \tag{16}$$

Remark 3. If we let $\sigma(t, \cdot, \cdot) = 0$, then (16) becomes stochastic differential equations with Caputo fractional derivative in [21]. Moreover, the averaging principle in [21] is the special case of this study.

3. Main Results

In this section, combining the existence and uniqueness results in the second part, we investigate the averaging principle for the Caputo FSDEs. Let us consider the standard form of (16):

$$\begin{aligned} X^\varepsilon(t) = X(0) &+ \frac{\varepsilon}{\Gamma(\alpha)} \int_0^t (t-s)^{\alpha-1} f(s, X^\varepsilon(s), X_s^\varepsilon) \mathrm{d}s \\ &+ \frac{\sqrt{\varepsilon}}{\Gamma(\alpha)} \int_0^t (t-s)^{\alpha-1} g(s, X^\varepsilon(s), X_s^\varepsilon) \mathrm{d}W_s \\ &+ \frac{\varepsilon^H}{\Gamma(\alpha)} \int_0^t (t-s)^{\alpha-1} \sigma(s, X^\varepsilon(s), X_s^\varepsilon) \mathrm{d}B_s^H, \end{aligned} \tag{17}$$

where $\varepsilon \in (0, \varepsilon_0]$ is a positive small parameter with ε_0 being a fixed number.

The following step is to introduce the original solution $X^\varepsilon(t)$ converges, as ε tends to zero, to the solution $Y^\varepsilon(t)$ of the averaged system:

$$\begin{aligned} Y^\varepsilon(t) = X(0) &+ \frac{\varepsilon}{\Gamma(\alpha)} \int_0^t (t-s)^{\alpha-1} \overline{f}(Y^\varepsilon(s), Y_s^\varepsilon) \mathrm{d}s \\ &+ \frac{\sqrt{\varepsilon}}{\Gamma(\alpha)} \int_0^t (t-s)^{\alpha-1} \overline{g}(Y^\varepsilon(s), Y_s^\varepsilon) \mathrm{d}W_s \\ &+ \frac{\varepsilon^H}{\Gamma(\alpha)} \int_0^t (t-s)^{\alpha-1} \overline{\sigma}(Y^\varepsilon(s), Y_s^\varepsilon) \mathrm{d}B_s^H. \end{aligned} \tag{18}$$

Theorem 1. *Suppose that Assumptions 1 and 2 hold. Then, for a given arbitrary small $\delta > 0$, there exist constants $L > 0, \varepsilon_1 \in (0, \varepsilon_0]$ and $\beta \in (0, 1]$, such that for all $\varepsilon \in (0, \varepsilon_1]$,*

$$\sup_{t \in [-\tau, L\varepsilon^{-\beta}]} E\left(\left\| X^\varepsilon(t) - Y^\varepsilon(t) \right\|^2 \right) \le \delta. \tag{19}$$

Proof. Based on the standard forms of (17) and (18), it deduces

$$\begin{aligned} X^\varepsilon(t) - Y^\varepsilon(t) = &\frac{\varepsilon}{\Gamma(\alpha)} \int_0^t (t-s)^{\alpha-1} \left(f(s, X^\varepsilon(s), X_s^\varepsilon) - \overline{f}(Y^\varepsilon(s), Y_s^\varepsilon) \right) \mathrm{d}s \\ &+ \frac{\sqrt{\varepsilon}}{\Gamma(\alpha)} \int_0^t (t-s)^{\alpha-1} \left(g(s, X^\varepsilon(s), X_s^\varepsilon) - \overline{g}(Y^\varepsilon(s), Y_s^\varepsilon) \right) \mathrm{d}W_s \\ &+ \frac{\varepsilon^H}{\Gamma(\alpha)} \int_0^t (t-s)^{\alpha-1} \left(\sigma(s, X^\varepsilon(s), X_s^\varepsilon) - \overline{\sigma}(Y^\varepsilon(s), Y_s^\varepsilon) \right) \mathrm{d}B_s^H. \end{aligned} \tag{20}$$

For $t \in [0, T]$, by the elementary inequality, we have

$$
\begin{aligned}
E\left(\left\|X^{\varepsilon}(t)-Y^{\varepsilon}(t)\right\|^{2}\right) \leq & \frac{3\varepsilon^{2}}{\Gamma(\alpha)^{2}} E\left(\left\|\int_{0}^{t}(t-s)^{\alpha-1}\left(f\left(s, X^{\varepsilon}(s), X_{s}^{\varepsilon}\right)-\overline{f}\left(Y^{\varepsilon}(s), Y_{s}^{\varepsilon}\right)\right) \mathrm{d} s\right\|^{2}\right) \\
& +\frac{3\epsilon}{\Gamma(\alpha)^{2}} \varepsilon E\left(\left\|\int_{0}^{t}(t-s)^{\alpha-1}\left(g\left(s, X^{\varepsilon}(s), X_{s}^{\varepsilon}\right)-\overline{g}\left(Y^{\varepsilon}(s), Y_{s}^{\varepsilon}\right)\right) \mathrm{d} W_{s}\right\|^{2}\right) \\
& +\frac{3\varepsilon^{2H}}{\Gamma(\alpha)^{2}} E\left(\left\|\int_{0}^{t}(t-s)^{\alpha-1}\left(\sigma\left(s, X^{\varepsilon}(s), X_{s}^{\varepsilon}\right)-\overline{\sigma}\left(Y^{\varepsilon}(s), Y_{s}^{\varepsilon}\right)\right) \mathrm{d} B_{s}^{H}\right\|^{2}\right) =: I_{1}+I_{2}+I_{3}.
\end{aligned} \tag{21}
$$

By the elementary inequality, Cauchy–Schwarz inequality, the Assumptions 1 and 2, we get

$$
\begin{aligned}
I_{1} \leq & \frac{6\varepsilon^{2}}{\Gamma(\alpha)^{2}} E\left(\left\|\int_{0}^{t}(t-s)^{\alpha-1}\left(f\left(s, X^{\varepsilon}(s), X_{s}^{\varepsilon}\right)-f\left(s, Y^{\varepsilon}(s), Y_{s}^{\varepsilon}\right)\right) \mathrm{d} s\right\|^{2}\right) \\
& +\frac{6\varepsilon^{2}}{\Gamma(\alpha)^{2}} E\left(\left\|\int_{0}^{t}(t-s)^{\alpha-1}\left(f\left(s, Y^{\varepsilon}(s), Y_{s}^{\varepsilon}\right)-\overline{f}\left(Y^{\varepsilon}(s), Y_{s}^{\varepsilon}\right)\right) \mathrm{d} s\right\|^{2}\right) \\
\leq & \frac{6\varepsilon^{2} t}{\Gamma(\alpha)^{2}} E\left(\int_{0}^{t}(t-s)^{2\alpha-2}\left\|f\left(s, X^{\varepsilon}(s), X_{s}^{\varepsilon}\right)-f\left(s, Y^{\varepsilon}(s), Y_{s}^{\varepsilon}\right)\right\|^{2} \mathrm{d} s\right) \\
& +\frac{6\varepsilon^{2} t}{\Gamma(\alpha)^{2}} E\left(\int_{0}^{t}(t-s)^{2\alpha-2}\left\|f\left(s, Y^{\varepsilon}(s), Y_{s}^{\varepsilon}\right)-\overline{f}\left(Y^{\varepsilon}(s), Y_{s}^{\varepsilon}\right)\right\|^{2} \mathrm{d} s\right) \\
\leq & \frac{6\varepsilon^{2} t \sup_{0 \leq t \leq T} \lambda(t)}{\Gamma(\alpha)^{2}} \int_{0}^{t}(t-s)^{2\alpha-2}\left(E\left\|X^{\varepsilon}(r)-Y^{\varepsilon}(r)\right\|^{2}+E\left\|X_{s}^{\varepsilon}-Y_{s}^{\varepsilon}\right\|^{2}\right) \mathrm{d} s \\
& +\frac{6\varepsilon^{2} t^{2}}{\Gamma(\alpha)^{2}} \sup_{0 \leq s \leq t} \lambda_{1}(t)\left(\sup_{0 \leq s \leq t} E\left\|Y^{\varepsilon}(s)\right\|^{2}+\sup_{0 \leq s \leq t} E\left\|Y_{s}^{\varepsilon}\right\|^{2}\right).
\end{aligned} \tag{22}
$$

By the Itô isometry, the elementary inequality, Cauchy–Schwarz inequality, the Assumptions 1 and 2, we get

$$
\begin{aligned}
I_{2} \leq & 3\varepsilon \Gamma(\alpha)^{2} E \int_{0}^{t}(t-s)^{2\alpha-2}\left\|g\left(s, X^{\varepsilon}(s), X_{s}^{\varepsilon}\right)-\overline{g}\left(Y^{\varepsilon}(s), Y_{s}^{\varepsilon}\right)\right\|_{\mathscr{L}_{2}^{0}}^{2} \mathrm{d} s \\
\leq & \frac{6\varepsilon}{\Gamma(\alpha)^{2}} E \int_{0}^{t}(t-s)^{2\alpha-2}\left\|g\left(s, X^{\varepsilon}(s), X_{s}^{\varepsilon}\right)-g\left(s, Y^{\varepsilon}(s), Y_{s}^{\varepsilon}\right)\right\|_{\mathscr{L}_{2}^{0}}^{2} \mathrm{d} s \\
& +\frac{6\varepsilon}{\Gamma(\alpha)^{2}} E \int_{0}^{t}(t-s)^{2\alpha-2}\left\|g\left(s, Y^{\varepsilon}(s), Y_{s}^{\varepsilon}\right)-\overline{g}\left(Y^{\varepsilon}(s), Y_{s}^{\varepsilon}\right)\right\|_{\mathscr{L}_{2}^{0}}^{2} \mathrm{d} s \\
\leq & \frac{6\varepsilon \sup_{0 \leq t \leq T \lambda(t)}}{\Gamma(\alpha)^{2}} \int_{0}^{t}(t-s)^{2\alpha-2}\left(E\left\|X^{\varepsilon}(s)-Y^{\varepsilon}(s)\right\|^{2}+E\left\|X_{s}^{\varepsilon}-Y_{s}^{\varepsilon}\right\|^{2}\right) \mathrm{d} s \\
& +\frac{6\varepsilon t}{\Gamma(\alpha)^{2}} \sup_{0 \leq s \leq t} \lambda_{2}(s)\left(\sup_{0 \leq s \leq t} E\left\|Y^{\varepsilon}(s)\right\|^{2}+\sup_{0 \leq s \leq t} E\left\|Y_{s}^{\varepsilon}\right\|^{2}\right).
\end{aligned} \tag{23}
$$

By Lemma 1, elementary inequality, we have

$$
\begin{aligned}
I_3 &\le \frac{3\varepsilon^{2H}}{\Gamma(\alpha)^2} E\left(\left\|\int_0^t (t-s)^{\alpha-1}\left(\sigma\left(s, X^\varepsilon(s), X_s^\varepsilon\right) - \overline{\sigma}\left(Y^\varepsilon(s), Y_s^\varepsilon\right)\right)\mathrm{d}B_s^H\right\|^2\right) \\
&\le \frac{3C_H\varepsilon^{2H}t^{2H-1}}{\Gamma(\alpha)^2} E\int_0^t (t-s)^{2\alpha-2}\left\|\sigma\left(s, X^\varepsilon(s), X_s^\varepsilon\right) - \overline{\sigma}\left(Y^\varepsilon(s), Y_s^\varepsilon\right)\right\|_{\mathscr{L}_2^0}^2 \mathrm{d}s \\
&\le \frac{6C_H\varepsilon^{2H}t^{2H-1}}{\Gamma(\alpha)^2} E\int_0^t (t-s)^{2\alpha-2}\left\|\sigma\left(s, X^\varepsilon(s), X_s^\varepsilon\right) - \sigma\left(s, Y^\varepsilon(s), Y_s^\varepsilon\right)\right\|_{\mathscr{L}_2^0}^2 \mathrm{d}s \\
&\quad + \frac{6C_H\varepsilon^{2H}t^{2H-1}}{\Gamma(\alpha)^2} E\int_0^t (t-s)^{2\alpha-2}\left\|\sigma\left(s, Y^\varepsilon(s), Y_s^\varepsilon\right) - \overline{\sigma}\left(Y^\varepsilon(s), Y_s^\varepsilon\right)\right\|_{\mathscr{L}_2^0}^2 \mathrm{d}s \\
&\le \frac{6C_H\varepsilon^{2H}t^{2H-1}\sup_{0\le t\le T}\lambda(t)}{\Gamma(\alpha)^2}\int_0^t (t-s)^{2\alpha-2}\left(E\left\|X^\varepsilon(s) - Y^\varepsilon(s)\right\|^2 + E\left\|X_s^\varepsilon - Y_s^\varepsilon\right\|^2\right)\mathrm{d}s \\
&\quad + \frac{6C_H\varepsilon^{2H}t^{2H}}{\Gamma(\alpha)^2}\sup_{0\le s\le t}\lambda_3(s)\left(\sup_{0\le s\le t} E\left\|Y^\varepsilon(s)\right\|^2 + \sup_{0\le s\le t} E\left\|Y_s^\varepsilon\right\|^2\right).
\end{aligned}
\tag{24}
$$

Submitting (22), (23), (24) to (21), we get

$$
\begin{aligned}
&E\left(\left\|X^\varepsilon(t) - Y^\varepsilon(t)\right\|^2\right) \\
&\le \frac{6\varepsilon^2 t + 6\varepsilon + 6C_H\varepsilon^{2H}t^{2H-1}}{\Gamma(\alpha)^2}\sup_{0\le t\le T}\lambda(t)\int_0^t (t-s)^{2\alpha-2}\left(E\left\|X^\varepsilon(s) - Y^\varepsilon(s)\right\|^2 + E\left\|X_s^\varepsilon - Y_s^\varepsilon\right\|^2\right)\mathrm{d}s \\
&\quad + \frac{6\varepsilon^2 t^2 + 6\varepsilon t + 6C_H\varepsilon^{2H}t^{2H}}{\Gamma(\alpha)^2}\sum_{i=1}^{3}\sup_{0\le s\le t}\lambda_i(s)\left(\sup_{0\le s\le t} E\left\|Y^\varepsilon(s)\right\|^2 + \sup_{0\le s\le t} E\left\|Y_s^\varepsilon\right\|^2\right).
\end{aligned}
\tag{25}
$$

Noting that $E(\|X^\varepsilon(t) - Y^\varepsilon(t)\|^2) = 0$ when $-\tau \le t \le 0$, it reduces

$$
\begin{aligned}
&E\left(\left\|X^\varepsilon(t) - Y^\varepsilon(t)\right\|^2\right) \\
&\le \frac{12\varepsilon^2 t + 12\varepsilon + 12C_H\varepsilon^{2H}t^{2H-1}}{\Gamma(\alpha)^2}\sup_{0\le t\le T}\lambda(t)\int_0^t (t-s)^{2\alpha-2}\left(E\left\|X^\varepsilon(s) - Y^\varepsilon(s)\right\|^2\right)\mathrm{d}s \\
&\quad + \frac{6\varepsilon^2 t^2 + 6\varepsilon t + 6C_H\varepsilon^{2H}t^{2H}}{\Gamma(\alpha)^2}\sum_{i=1}^{3}\sup_{0\le s\le t}\lambda_i(s)\left(\sup_{0\le s\le t} E\left\|Y^\varepsilon(s)\right\|^2 + \sup_{0\le s\le t} E\left\|Y_s^\varepsilon\right\|^2\right).
\end{aligned}
\tag{26}
$$

By the Gronwall–Bellman inequality ([23]), we have

$$E\left(\left\|X^{\varepsilon}(t)-Y^{\varepsilon}(t)\right\|^{2}\right)$$
$$\leq \frac{6\varepsilon^{2}t^{2}+6\varepsilon t+6C_{H}\varepsilon^{2H}t^{2H}}{\Gamma(\alpha)^{2}}\sum_{i=1}^{3}\sup_{0\leq s\leq t}\lambda_{i}(s)\left(\sup_{0\leq s\leq t}E\left\|Y^{\varepsilon}(s)\right\|^{2}+\sup_{0\leq s\leq t}E\left\|Y_{s}^{\varepsilon}\right\|^{2}\right)$$
$$\times\sum_{k=0}^{\infty}\frac{\left(12\varepsilon^{2}t^{\alpha+1}+12\varepsilon t^{\alpha}+12C_{H}\varepsilon^{2H}t^{2H+\alpha-1}\right)^{k}\sup_{0\leq t\leq T}\lambda(t)}{\Gamma(\alpha)^{k}\Gamma(k\alpha+1)}. \tag{27}$$

So,

$$\sup_{-\tau\leq s\leq t}E\left\|X^{\varepsilon}(t)-Y^{\varepsilon}(t)\right\|^{2}$$
$$\leq \frac{6\varepsilon^{2}t^{2}+6\varepsilon t+6C_{H}\varepsilon^{2H}t^{2H}}{\Gamma(\alpha)^{2}}\sum_{i=1}^{3}\sup_{0\leq s\leq t}\lambda_{i}(s)\left(\sup_{0\leq s\leq t}E\left\|Y^{\varepsilon}(s)\right\|^{2}+\sup_{0\leq s\leq t}E\left\|Y_{s}^{\varepsilon}\right\|^{2}\right)$$
$$\times\sum_{k=0}^{\infty}\frac{\left(12\varepsilon^{2}t^{\alpha+1}+12\varepsilon t^{\alpha}+12C_{H}\varepsilon^{2H}t^{2H+\alpha-1}\right)^{k}\left(\sup_{0\leq t\leq T}\lambda(t)\right)^{k}}{\Gamma(\alpha)^{k}\Gamma(k\alpha+1)}. \tag{28}$$

So, we can select $\beta\in(0,1)$ and $L>0$, such that for every $t\in[0,L\varepsilon^{-\beta}]\subseteq[0,T]$,

$$\sup_{-\tau\leq t\leq L\varepsilon^{-\beta}}E\left\|X^{\varepsilon}(t)-Y^{\varepsilon}(t)\right\|^{2}\leq C\varepsilon^{1-\beta}, \tag{29}$$

where

$$C=6L^{2}\varepsilon^{1-\beta}+6L+6L^{2H}C_{H}\varepsilon^{(2H-1)(1-\beta)}\Gamma(\alpha)^{2}$$
$$\times\sum_{i=1}^{3}\sup_{0\leq s\leq L\varepsilon^{-\beta}}\lambda_{i}(s)\left(\sup_{0\leq s\leq L\varepsilon^{-\beta}}E\left\|Y^{\varepsilon}(s)\right\|^{2}+\sup_{0\leq s\leq L\varepsilon^{-\beta}}E\left\|Y_{s}^{\varepsilon}\right\|^{2}\right)$$
$$\times\sum_{k=0}^{\infty}\frac{\left(12L^{\alpha+1}\varepsilon^{2-\alpha\beta-\beta}+12L^{\alpha}\varepsilon^{1-\alpha\beta}+12L^{2H+\alpha-1}C_{H}\varepsilon^{2H-\beta(2H+\alpha-1)}\right)^{k}\left(\sup_{0\leq t\leq T}\lambda(t)\right)^{k}}{\Gamma(\alpha)^{k}\Gamma(k\alpha+1)}. \tag{30}$$

Therefore, for any $\delta>0$, there exists $\varepsilon_{1}\in(0,\varepsilon_{0}]$, such that for any $\varepsilon\in(0,\varepsilon_{1}]$ and $t\in[0,L\varepsilon^{-\beta}]$,

$$\sup_{-\tau\leq t\leq L\varepsilon^{-\beta}}E\left\|X^{\varepsilon}(t)-Y^{\varepsilon}(t)\right\|^{2}\leq\delta. \tag{31}$$

The proof is completed. □

4. Example

Let us consider the following FSDEs with delays:

$$D_{t}^{\alpha}x(t)=\left[x(t)+x(t)(t-1)^{2}\right]+1\frac{\mathrm{d}W_{t}}{\mathrm{d}t}+1\frac{\mathrm{d}B_{t}^{H}}{\mathrm{d}t}, \tag{32}$$

where $t\in[0,1]$, $f(t,x(t),x_{t})=x(t)+x(t)(t-1)^{2}$, $g(t,x(t),x_{t})=1$, $\sigma(t,x(t),x_{t})=1$, $1/2<\alpha<1$.

It is easy to verify that f,g,σ satisfy the Assumptions 1 and 2. Define $\overline{f}(x,y)$ as follows:

$$\int_{0}^{1}\overline{f}(x,y)(1-t)^{2\alpha-2}\mathrm{d}t=\int_{0}^{1}f(t,x,y)(1-t)^{2\alpha-2}\mathrm{d}t. \tag{33}$$

We can derive that $\overline{f}(x,y)=x(1+((2\alpha-1)/(2\alpha+1)))$. Similarly, $\overline{g}(x,y)=1,\overline{\sigma}(x,y)=1$. The averaging form of (32) can be defined as

$$D_{t}^{\alpha}y(t)=y(t)\left(1+\frac{2\alpha-1}{2\alpha+1}\right)+1\frac{\mathrm{d}W_{t}}{\mathrm{d}t}+1\frac{\mathrm{d}B_{t}^{H}}{\mathrm{d}t}. \tag{34}$$

According to Theorem 1, as ε goes to zero, the solutions $x(t)$ and $y(t)$ are equivalent in the sense of mean square. So, the results can be checked.

Data Availability

The data used to support the findings of this study are freely available.

Conflicts of Interest

The authors declare that they have no conflicts of interest.

Acknowledgments

This research was funded by the Foundation for Excellent Young Talents Fund Program of Higher Education Institutions of Anhui Province (gxyq2018102), Natural Science Foundation of Anhui Colleges (KJ2020A0731), Research Projects of Humanities and Social Science of Anhui Province (SK2020A0527), Ministry of Education Cooperative Education Project (202002165040), Consulting Projects Entrusted by Enterprises (2020xhx119), and Key Scientific Research Projects of Suzhou University (2019yzd08).

References

[1] B. Bandyopadhyay and S. Kamal, "Stabilization and control of fractional order systems: A sliding mode approach," *Lecture Notes in Electrical Engineering*, Springer International Publishing, Berlin, Germany, 2015.

[2] A. Kilbas, H. Srivastava, and J. Trujillo, "Theory and applications of fractional differential equations," *North-Holland Mathematics Studies*, Elsevier Science B. V., Amsterdam, Netherlands, 2006.

[3] T. Doan, P. Huong, P. Kloeden, and H. Tuan, "Asymptotic separation between solutions of Caputo fractional stochastic differential equations," *Stochastic Analysis and Applications*, vol. 36, no. 4, pp. 654–664, 2018.

[4] B. Shiri and D. Baleanu, "System of fractional differential algebraic equations with applications," *Chaos, Solitons & Fractals*, vol. 120, pp. 203–212, 2019.

[5] B. Shiri, G.-C. Wu, and D. Baleanu, "Collocation methods for terminal value problems of tempered fractional differential equations," *Applied Numerical Mathematics*, vol. 156, pp. 385–395, 2020.

[6] Z. Li, Y. Y. Jing, and L. Xu, "Controllability of neutral stochastic evolution equations driven by fBm with Hurst parameter less than 1/2," *International Journal of Systems Science*, vol. 50, no. 9, pp. 1835–1846, 2019.

[7] Z. Li and L. Yan, "Ergodicity and stationary solution for stochastic neutral retarded partial differential equations driven by fractional Brownian motion," *Journal of Theoretical Probability*, vol. 32, no. 3, pp. 1399–1419, 2019.

[8] H. M. Ahmed, M. M. El-Borai, A. S. O. El Bab, and M. E. Ramadan, "Approximate controllability of non-instantaneous impulsive Hilfer fractional integrodifferential equations with fractional Brownian motion," *Boundary Value Problems*, vol. 2020, no. 1, p. 120, 2020.

[9] L. Xu and Z. Li, "Stochastic fractional evolution equations with fractional brownian motion and infinite delay," *Applied Mathematics and Computation*, vol. 336, pp. 36–46, 2018.

[10] P. Tamilalagan and P. Balasubramaniam, "Moment stability via resolvent operators of fractional stochastic differential inclusions driven by fractional Brownian motion," *Applied Mathematics and Computation*, vol. 305, pp. 299–307, 2017.

[11] H. M. Ahmed and M. M. El-Borai, "Hilfer fractional stochastic integro-differential equations," *Applied Mathematics and Computation*, vol. 331, pp. 182–189, 2018.

[12] J. Pan, H. Ma, X. Jiang, W. Ding, and F. Ding, "Adaptive gradient-Based iterative algorithm for multi-variable controlled autoregressive moving average systems using the data filtering technique," *Complexity*, vol. 2018, Article ID 9598307, 11 pages, 2018.

[13] X. B. Jin, "Deep-learning prediction model with serial two-Level decomposition based on Bayesian optimization," *Complexity*, vol. 2020, Article ID 4346803, 14 pages, 2020.

[14] J. Ding, "The hierarchical iterative identification algorithm for multi-input-output-error systems with autoregressive noise," *Complexity*, vol. 2017, Article ID 5292894, 11 pages, 2017.

[15] R. Khasminskii, "On the principle of averaging the Itô stochastic differential equations," *Kibernetika*, vol. 4, pp. 260–279, 1968.

[16] B. Pei, Y. Xu, G. Yin, and X. Zhang, "Averaging principles for functional stochastic partial differential equations driven by a fractional Brownian motion modulated by two-time-scale Markovian switching processes," *Nonlinear Analysis: Hybrid Systems*, vol. 27, pp. 107–124, 2018.

[17] H. Ahmeda and Q. Zhu, "The averaging principle of Hilfer fractional stochastic delay differential equations with Poisson jumps," *Applied Mathematics Letters*, vol. 112, Article ID 106755, 2021.

[18] Z. Li and L. Yan, "Stochastic averaging for two-time-scale stochastic partial differential equations with fractional Brownian motion," *Nonlinear Analysis: Hybrid Systems*, vol. 31, pp. 317–333, 2019.

[19] B. Pei, Y. Xu, and J. Wu, "Stochastic averaging for stochastic differential equations driven by fractional Brownian motion and standard Brownian motion," *Applied Mathematics Letters*, vol. 100, Article ID 106006, 2020.

[20] D. Luo, Q. Zhu, and Z. Luo, "An averaging principle for stochastic fractional differential equations with time-delays," *Applied Mathematics Letters*, vol. 105, Article ID 106290, 2020.

[21] W. Xu, W. Xu, and S. Zhang, "The averaging principle for stochastic differential equations with Caputo fractional derivative," *Applied Mathematics Letters*, vol. 93, pp. 79–84, 2019.

[22] T. Caraballo, M. Garrido-Atienza, and T. Taniguchi, "The existence and exponential behavior of solutins to stochastic delay evolution equations with a fractional Brownian motion," *Nonlinear Analysis: Theory, Methods and Applications*, vol. 74, no. 211, pp. 3671–3684, 2011.

[23] H. Ye, J. Gao, and Y. Ding, "A generalized Gronwall inequality and its application to a fractional differential equation," *Journal of Mathematical Analysis and Applications*, vol. 328, no. 2, pp. 1075–1081, 2017.

Hindawi
Complexity
Volume 2021, Article ID 6690761, 14 pages
https://doi.org/10.1155/2021/6690761

Research Article

Analysis of Distributed Wireless Sensor Systems with a Switched Quantizer

Hui Sun,[1] **Xianyu Wang**,[2] **Kaixin Yang**,[2] **and Tongrui Peng**[3]

[1]*College of Electronic Information and Automation, Civil Aviation University of China, South Campus, Tianjin 300300, China*
[2]*Tianjin College, University of Science and Technology Beijing, Tianjin 301830, China*
[3]*College of Science, Shanghai Institute of Technology, Shanghai 200235, China*

Correspondence should be addressed to Tongrui Peng; tongrui2.peng@sit.edu.cn

Received 17 November 2020; Accepted 17 July 2021; Published 29 July 2021

Academic Editor: Jing Na

In this article, a switched quantizer is proposed to solve the bandwidth limitation application problem for distributed wireless sensor networks (WSNs). The proposed estimator based on switched quantitative event-triggered Kalman consensus filtering (KCF) algorithm is used to monitor the aircraft cabin environmental parameters when suffering packet loss and path loss issues during the communication process for WSN. The quantization error of the novel switched quantizer structure is bounded, and the corresponding stability theory for the quantitative estimation approach is proved. Compared with other methods, the simulation results for the introduced method verify that the environmental parameters can be estimated accurately and timely and reduce the burden of network communication bandwidth.

1. Introduction

Due to the rapid development of the civil aviation industry, the safe and comfortable cabin environment has become one of the most important foci for aircraft designers and operators. Passengers and crew members have also imposed higher requirements on the cabin environment. Once mechanical failures, pipe ruptures, or seal failures occur in the narrow and closed cabins and cargos, the cabin environment probably is contaminated, which can cause passengers and crew members dizziness, headaches, ear disease, dry eye syndrome, throat pains, and other adverse events, even severe neurological disorders [1, 2]. This will seriously threaten flight safety. The higher air recirculation rate is a trend for the design of future aircraft for guaranteeing air quality in the cabin [3]. Currently, aircraft cabins install fire monitoring systems. However, false alarms often occur in reality. Therefore, it is necessary to develop a method to estimate environmental parameters and monitor sudden environmental issues accurately in cabins. With the rapid development of wireless sensing technology, the design of aircraft will move from the current fly-by-wire system to the fly-by-wireless direction [4]. Wireless sensor network (WSN) combines sensor technology, wireless communication, information fusion, and other technologies, a multidisciplinary technology. At present, WSN has shown great application value and broad business vision in applications such as environmental testings, military, health, agriculture, and other areas. As an emerging application of information technology, WSN realizes the function of collaborative sensing and processing the physical information of the detected objects through wireless transmission and information interaction and provides direct, effective, and real information support for real-time monitoring and fast processing detection time [5, 6]. Also, it becomes possible that some specific WSNs such as short-range WSN can be employed in monitoring narrow and complex spaces, such as cabin and cargo environments which are the trend for the future aircraft industry. Then, estimating environment parameters accurately and quickly is the first prior issue for the correct alarm decision to monitor inside environments.

Simultaneously, many researchers focus on distributed state estimation algorithms over distributed WSNs. Furthermore, it is well known that the Kalman filter can help

filter noises applied to systems. Therefore, the above researches are always combined with Kalman filters. For example, Yang et al. apply the sensor network for distributed estimation as the research background, review the Kalman consensus filtering problem, systematically introduce various Kalman uniform filtering related algorithms, and summarize the research status in this field in detail [7]. Olfati-Saber proposes a scalable distributed Kalman consensus algorithm [8]. The work in [9] further studies the optimality of the discrete form of the algorithm and also establishes stability analysis. The study in [10] proposes independent consensus matrices with each neighbor's information. Most of the above research works are carried out under ideal communication preconditions. For example, the network bandwidth is infinite and the communication information is the ideal value.

However, these assumptions are difficult to implement in practical applications. In the real world, bandwidth is limited. A feasible way to solve the above problem is to insert quantizers in the systems, such as from sensor to controller or from the controller to the actuator. The quantizer here can be summarized as a class of quantizers that satisfy regional bounded conditions, such as logarithmic quantizers, and uniform quantizers [11]. The introduction of quantizers will inevitably introduce quantization errors, which may degrade system performance and even cause system instability. Therefore, it is an important direction in the current research of WSNs to study the statistical characteristics and error types introduced by quantization and minimize the quantization errors. In 1956, Kalman et al. proposed to add a quantizer to the control system. Later, in the study of some related quantization algorithms, the quantization error was generally treated as an augmented noise. Ribeiro et al. propose a quantized Kalman filter considering the communication constraints in the network, which made only one sensor activated in each sampling period of the distributed filtering [12, 13]. In [14, 15], an adaptive quantization-based input quantization control scheme is proposed for a class of linear systems. The work in [16] studies the input quantization control problem for a class of nonlinear systems. In [17], the Lyapunov method is used to study the quantization control problem of a class of nonlinear systems with time delays. The study in [18] describes the latest developments in quantitative control of linear systems. In [19], the quantization control problem for input and output quantization is considered. The work in [20] proposes a Kalman filtering algorithm based on event-triggered consensus for cabin pollutants monitoring. However, it does not consider the network bandwidth pressure of the system. The study in [21] introduces a hybrid trigger scheme and quantization and studies the quantization state estimation problem of neural networks with network attacks and hybrid trigger communication schemes to reduce the pressure of network transmission and save network resources. In [22], several operational modes are designed for quantizers and estimators and a nonfragile H_∞ estimation problem for a class of complex networks with switched topologies and quantization effects is studied. The work in [23] focuses on the linear least mean square estimation of network discrete time-varying linear systems affected by data quantization and communication constraints. The study in [24] proposes a new descriptor sliding mode observer method to solve the problem that signal quantization will reduce the estimation performance. In [25], the quantization state estimation suitable for general vector measurement is derived based on Bayesian theory. The work in [26] studies a recursive filtering algorithm to deal with state estimation problems in power systems with quantized nonlinear measurements. In [27], a linear distributed Luenberger observer is proposed to ensure that the estimation error of distributed state estimation is bounded for quantized multiagent data in the case of a limited communication data rate. In [28], quantization of data with the Laplacian distribution is considered in networks. The work in [29] deals with the event-triggered fuzzy filtering issue by considering data quantization in-vehicle sideslip angle estimation.

Therefore, inspired by the above literature, this paper designs a switched quantizer for the WSN-based pollutant concentration estimation algorithm to solve the communication bandwidth limitation. This is consecutive to [20]. The proposed event-trigger based algorithm with quantizers can not only help accurately estimate the cabin environment parameters in time but can also save communication bandwidth.

According to the motivation mentioned above, an analysis method is addressed via a switched quantizer. In summary, two contributions of this paper are given as follows:

(1) An estimation algorithm with consideration of event-trigger of distributed wireless sensor networks is proposed. A switched quantizer is used to reduce the occupancy of bandwidth for transmitting information by quantizing the data from the observers. The proposed approach can save the communication bandwidth for path loss and random packet loss events.

(2) A series of stability theorems are deduced and provided for the proposed switched quantizer-based estimation algorithm.

The following contents of this paper are arranged as follows. Section 2 introduces the preliminary knowledge and system model including the monitoring network and the integrated sensing error model. Section 3 proposes the event-triggered switched quantizer-based Kalman consensus filtering algorithm in the event of interferences. Furthermore, stability analyses of the algorithm and the sufficient conditions for bounded mean square exponential estimation error of the algorithm are given. Section 4 demonstrates simulation results that verify the effectiveness of the algorithm proposed in this paper. Conclusions are summarized in the last section.

2. Preliminaries

2.1. Integrated Sensor Structure. In aircraft cabins, there are various kinds of pollutants generated by sudden environmental events. The measurement results are always sensitive

to interferences by using one single sensor. Therefore, it is necessary to construct WSN with integrated nodes to estimate concentrations in cabins. The most mature field for the application of integrated sensing structures is the integrated navigation system of aircraft. The relevant introduction can be found in [30].

This paper will select an output correction structure as the node structure and use KCF. The comparison among several integrated measurement structures is proposed in [31]. Based on this integrated sensor measurement structure, the study in [20] proposes integrated sensor nodes to construct a distributed integrated sensor monitoring network and presents an event-triggered Kalman consensus filter algorithm (ET-KCF). A monitoring network is shown in Figure 1 where the dotted line is the neighbor node of node i. The measurement result of the primary sensor is Z_{Pi}, and Z_{Si} is that of the secondary sensor. Z_i is the difference between Z_{Pi} and Z_{Si}. It is fused with estimated information of the neighbors based on the ET-KCF method. Then the measured value coming from the primary sensor is corrected by using the error estimate to get the optimal estimate value of concentration, Z_{Oi}.

The topology diagram of the wireless sensor network is defined as $G = (V, E, A)$, where $V = \{v_1, v_2, \ldots, v_n\}$ is the set of sensor nodes and $E = V \times V$ is the set of edges between nodes. The set of neighbors of the sensor i is denoted by $N_i = \{v_j \in V | (v_i, v_j) \in E\}$, while the number of its neighbors is called the degree of the sensor node and denoted by $d_i = |N_i|$. The degree matrix D of the topological graph G is defined as a diagonal matrix of diagonal elements of each sensor node degree, and denoted by $D = \mathrm{diag}\{d_1, \ldots, d_N\}$, $A = [a_{ij}]$ is an adjacency matrix representing the communication relationship among sensors. When sensor i and the sensor j communicate with each other, a_{ij} takes a value of 1, otherwise 0. The Laplacian matrix of graph G is represented as $L = D - A$. If the matrix L has a nonzero eigenvalue, then the undirected topological graph G is connected [32].

Referring to [31], this paper discusses a general environment parameter monitoring algorithm model without considering the specific concentration parameter monitoring dynamic model.

As shown in Figure 1, the ET-KCF is performed on the measuring errors between the primary sensor and the secondary sensor. Suppose the primary and secondary sensor dynamic equations of the integrated sensors are shown in equations (1) and (2).

The primary sensor dynamic equation is shown in the following equation:

$$\begin{cases} x_p^+ = A_p x_p + B_p w_p, \\ z_{pi} = H_{pi} x_p + F_{pi} v_{pi}, \end{cases} \tag{1}$$

and the secondary sensor dynamic equation is shown in the following equation:

$$\begin{cases} x_s^+ = A_s x_s + B_s w_s, \\ z_{si} = H_{si} x_s + F_{si} v_{si}, \end{cases} \tag{2}$$

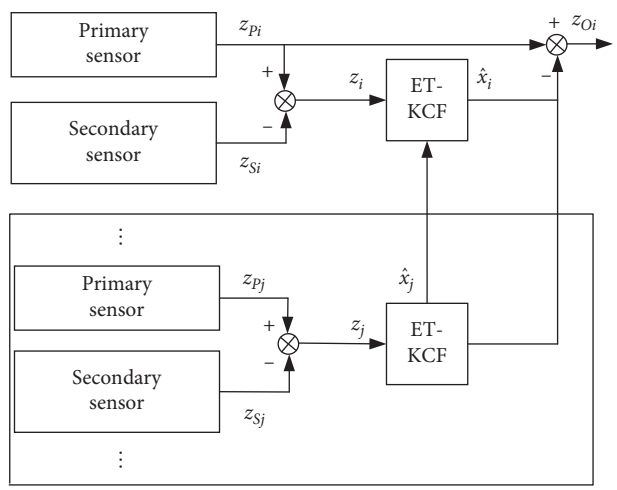

Figure 1: Schematic diagram of a distributed integrated sensing monitoring network [19].

where superscript + means the updated value of variables. $x_p \in R^{mp}$ and $x_s \in R^{ms}$ are state vectors of the primary and secondary sensors. $z_{pi} \in R^p$ and $z_{si} \in R^s$ are output vectors of the primary and secondary sensors. $(A_p, B_p, H_{pi}, F_{pi})$ and $(A_s, B_s, H_{si}, F_{si})$ are system matrices with appropriate dimensions. w_p, v_{pi}, w_s, and v_{si} are independent white Gaussian noises and their covariance matrices satisfy

$$\begin{aligned} E\left[w(k)w(l)^T\right] &= Q(k)\delta_{kl}, \\ E\left[v_i(k)v_j(l)^T\right] &= R_{ij}(k)\delta_{kl}, \end{aligned} \tag{3}$$

where δ_{kl} is an impulse response function. When $k = l$, δ_{kl} equals 1, otherwise 0. Q and R_{ij} are the corresponding noise covariance matrices. When $i = j$, R_{ii} is represented as R_i.

Then, the corresponding error dynamics equation of the integrated sensor can be obtained as shown in equation (4). The following analyses in this paper will ignore the measurement noise for the secondary sensor for simplification because of the difficulty of sampling times consistency between the primary sensor and the secondary sensor. The error equation of the integrated sensor is shown as follows:

$$\begin{aligned} x^+ &= \begin{bmatrix} x_p^+ \\ x_s^+ \end{bmatrix} = \begin{bmatrix} A_p & 0 \\ 0 & A_s \end{bmatrix} \begin{bmatrix} x_p \\ x_s \end{bmatrix} + \begin{bmatrix} B_p & 0 \\ 0 & B_s \end{bmatrix} \begin{bmatrix} w_p \\ w_s \end{bmatrix}, \\ z_i &= z_{pi} - z_{si}. \end{aligned} \tag{4}$$

To facilitate the following analysis, equation (5) can be derived by equation (4).

$$\begin{cases} x_{k+1} = A_k x_k + B_k w_k, \\ z_{i,k+1} = H_{i,k} x_k + F_{i,k} v_{i,k}, \end{cases} \tag{5}$$

where $x_k = \mathrm{col}(x_p, x_s)$ is the error state vector and $w_k = \mathrm{col}(w_p, w_s)$ represents the system noise vector in the integrated error system. v_i is the measurement noise of the primary sensor, that is, $v_i = v_{pi}$. $A_k = \mathrm{diag}(A_p, A_S)$ and $B_k = \mathrm{diag}(B_p, B_S)$ are system matrices with proper dimensions. H_i is measuring matrices. F_i is the fault matrices.

2.2. Event-Triggered Consensus Kalman Filter (ET-KCF). In practical applications, the sensor nodes are constrained by sensing abilities and perceived environments, etc. Uncertainties and errors exist in the same type of sensor nodes located in different positions when the sensor node acquires the local information. The packet loss has two different types. The loss of communication values happens in nodes of the wireless sensor network. Furthermore, loss of the measurement data for each node occurs in networks. The packet loss can impact the accuracy of the algorithm estimates and may even diverge estimates. From a network perspective, one of the most important indexes reflecting communication state in wireless sensor networks is the packet loss rate. The packet loss rate of the data receiving terminal in the general network environment is as high as 5%–10% [33]. At the same time, because the different materials and sizes of the obstacles will inevitably lead to path loss in the transmission process, it will affect the accuracy of the algorithm estimation [34]. Path loss is the magnitude of the attenuation of the signal caused by the incoming electromagnetic environment between the transmitting and receiving nodes. Undoubtedly, the existence of path loss will impact the estimation accuracy of WSN. Therefore, the estimation algorithm of the wireless sensor network must have corresponding fault tolerance characteristics when considering the impacts of packet losses and path losses.

In [20], considering the influence of packet losses and path losses on the algorithm, an event-triggered-based KCF algorithm is proposed. Due to the complexity of computation and scalability of the algorithm, the suboptimal filter of each node is designed as follows [20]:

$$\begin{cases} \hat{x}_{i,k+1} = A_k \cdot \hat{x}_{i,k} + \alpha_k A_k \cdot K_{i,k}\left(Z_{i,k} - H_{i,k} \cdot \hat{x}_{i,k}\right) + \beta_k A_k \cdot C_{i,k} \sum_{j \in \mathcal{N}_i} \left[\left(1 - \gamma_{ij}\right)\hat{x}^o_{j,k} - \hat{x}_{i,k}\right], \\ K_{i,k} = P_{i,k} H^T_{i,k}\left(H_{i,k} P_{i,k} H^T_{i,k} + R_{i,k}\right)^{-1}, \\ P_{i,k+1} = \left(A_k - A_k K_{i,k} H_{i,k}\right) P_{i,k}\left(A_k - A_k K_{i,k} H_{i,k}\right)^T + A_k K_{i,k} R_{i,k} K^T_{i,k} A^T_k + B_k Q_{i,k} B^T_k. \end{cases} \tag{6}$$

The algorithm will be collectively referred to as ET-KCF, and its specific content can be found in [20]. ET-KCF can effectively decrease the computational complexity of the algorithm and improve the real-time performance over WSN. At the same time, the existence of the trigger mechanism reduces the energy consumption among sensor transmissions. The consensus term of the state estimation can make all sensor nodes converge to the same estimated value. That is, each sensor node combines its measured value with information from neighbor nodes to achieve global consistent estimation, which can well help solve the problem of sensor false alarm in the cabin.

3. Event-Triggered Kalman Consensus Filtering Algorithm under Switched Quantitative Communication

The quantification of signals can be regarded as converting the input threshold-known signal into a finite number of discrete signals within the boundary value according to the protocol. When the signal is transmitted, only the discrete values need to be encoded and transmitted, and then transmission loads can be greatly reduced. Normally, the quantizer sets relevant initial parameters in advance, such as quantitative bits. The more bits, the more accurate. However, the quantizer becomes more complex. Therefore, the complexity and data accuracy for using a quantizer are contradictory. It is necessary to select the suitable relevant parameters of the quantizer.

3.1. Uniform Quantizer. The uniform quantizer is a linear quantizer that uniformly divides the input signal into quantized intervals according to the set quantization level. Suppose that the range of the observed signal of a node is between $[-U, U]$, where U is a known parameter. The quantization level is divided according to the interval of the range of the observation signal of the sensor node. In general, the quantization level is generally divided according to the integer order of 2, where the order is the number of quantization bits. x is the state variable to be estimated. The measured value z is quantized into a new value with l' bits, quantization interval length $\Delta = (2U/(2^{l'} - 1))$, quantification level $2^{l'}$, output value $u_i = -U + \Delta i, i = (1, 2, \ldots)$. Then, a uniform quantitative mathematical model can be expressed as follows:

$$Q(z) = u_i, \quad z \in \left(u_i, u_{i+1}\right). \tag{7}$$

Lemma 1 (see [35]). *Define Q(z) as a quantized observation value in $z_{i,k+1} = H_{i,k} x_k + F_{i,k} v_{i,k}$ with quantized bits l', $Q(z) \in [-U, U]$. Then, Q(z) is an unbiased estimate of state, x, and*

$$E\left(|Q(z) - x|^2\right) \le \frac{U^2}{\left(2^{l'} - 1\right)^2} + R, \quad l' \ge 1, \tag{8}$$

where R is the observed noise covariance. The schematic diagram of the uniform quantization with even quantization intervals is shown in Figure 2.

It can be seen that since the uniform quantizer divides the original signal evenly, the quantization error caused by the uniform quantizer has an upper bound, and the boundary value is related to the quantization level.

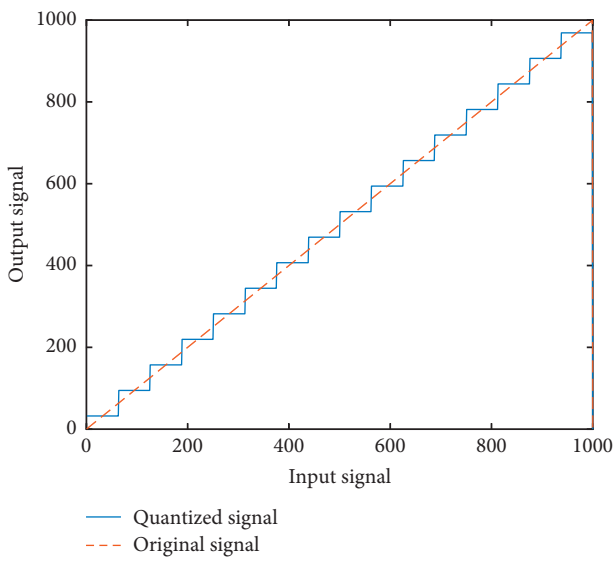

Figure 2: Schematic diagram of a uniform quantizer with even quantization intervals.

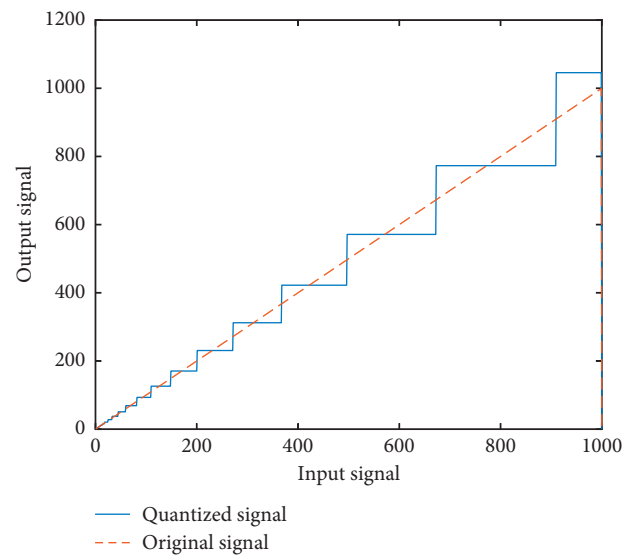

Figure 3: The schematics of a logarithmic quantizer with uneven intervals.

3.2. Logarithmic Quantizer. Logarithmic quantization is a nonuniform quantization strategy that divides the quantization interval into logarithmic levels. The corresponding mathematical model can be depicted as follows:

$$Q(u) = \begin{cases} u_i, & \dfrac{u_i}{1+\delta} < u < \dfrac{u_i}{1-\delta}, \\ 0, & 0 \le u < \dfrac{d}{1+\delta}, \\ -q(-u), & u < 0, \end{cases} \tag{9}$$

where $u_i = \rho^{(1-i)}d$, $(i = 1, 2, \ldots)$, $\rho = ((1+\delta)/(1-\delta))$ is the quantizer parameter $d > 0, 0 < \rho < 1$, and δ determines the quantization density. A schematic diagram of a logarithmic quantizer with uneven intervals is illustrated as shown in Figure 3.

If the quantization density selects logarithmic distribution and the quantized signal is large, the quantization error will be large and will impact the system performance, even causing the system to be unstable. If the quantized signal is a small signal, such as a small estimated error that fluctuates near the origin, the output signal of the logarithm quantizer is more accurate.

The uniform quantizer can directly quantize the original information, and the quantization error has good statistical characteristics. Therefore, it is suitable for the quantization of the original measurement signal. The logarithmic quantizer uses a nonlinear quantization interval division method, which can ensure that the quantized information has good precision. So it is more suitable for quantifying error signals instead of the original signals. According to the comparison between the uniform quantizer and the logarithm quantizer, these two algorithm structures are easy to implement because they are both static quantizers and only need to determine the boundary value of the input signal and the division of the quantization interval. Therefore, both quantizers can be combined and used in practical engineering, such as state estimations of cabin pollutant concentrations.

3.3. Event-Triggered Kalman Consensus Filtering Algorithm under Switched Quantitative Communication. To reduce the burden of signal transmission bandwidth, it is necessary to quantify the observation values transmitted from the observer to the estimator and the estimated values among nodes. The state estimation algorithm used in this paper employs the distributed ET-KCF integrated sensor structure when considering the inevitable packet loss phenomena in the actual environment. The observed value is the error of the observation values between the primary and secondary sensors, respectively. If packet loss of any sensor for each node happens, the error amount becomes close to the observation value from another sensor. Furthermore, the quantized error will correspondingly be large, affecting estimation accuracy. Therefore, this article proposes a novel switched quantizer that includes the properties of logarithmic quantization and uniform quantization. The expression is shown as follows:

$$q(u) = \begin{cases} \rho^i d, & 0 < u \le u_{\text{th}}, \\ u_{th} + \Delta_q\left(i + 1 - 2^{l'}\right), & u > u_{\text{th}}, \\ -q(-u), & u < 0, \end{cases} \tag{10}$$

where parameters ρ, d satisfy $((\rho^{l'-2}d)/(1-\delta)) - ((\rho^{l'-2}d)/(1+\delta)) < \Delta_q$ and $u_{\text{th}} \in (((\rho^{l'-1}d)/(1+\delta)), ((\rho^{l'-1}d)/(1+\delta)) + \Delta_q)$.

It can be seen that the selection of parameters ρ, d ensures that the quantization error of the designed switched quantizer does not exceed the quantization error, Δ_q of the uniform quantizer, and the selection of the threshold u_{th} is

related to Δ_q. When there is no packet loss, the first half of the logarithm quantizer can ensure that it has a high quantization precision since the error is the amount that fluctuates around the origin. However, when the packet loss occurs, the input amount becomes biased. The uniform quantization in the latter half can ensure that the quantization error of the entire quantizer is less than Δ_q. The schematic diagram between input and output signals for the switched quantizer proposed in this paper is shown in Figure 4.

Therefore, this paper studies a switched quantizer-based event-triggered Kalman consensus filter (QEF-KCF). Figure 5 shows a schematic diagram of a node over the distributed integrated network with switched quantizers. As Figure 5 shows, the quantizer is used between the observer and estimator. That is, the estimator receives the quantized signals. Another quantizer is also applied behind the estimator. Then, the quantized output of the estimator was simultaneously transmitted to the neighbor nodes. Each quantizer is a switched quantizer. ET-KCF algorithm is employed to estimate the state values.

The specific steps of the QET-KCF estimation algorithm are listed as follows, i denotes the i-th sensor:

Step 1. Initialize the state and error covariance matrices.

$$\begin{aligned} P_i &= P_0, \\ \hat{x}_i &= x_o. \end{aligned} \tag{11}$$

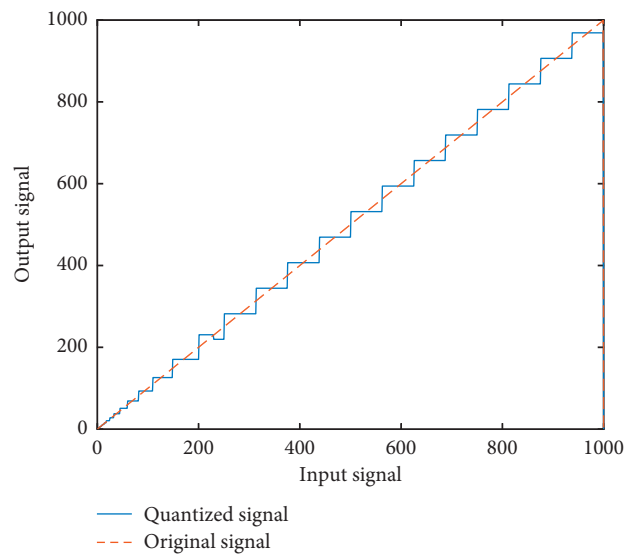

Figure 4: The schematics of a switched quantizer.

Step 2. Quantize the measured values from neighbor sensors.

$$z = Q(z). \tag{12}$$

Step 3. Calculate the estimated values by the estimator.

$$\hat{x}_{i,k+1} = A_k \cdot \hat{x}_{i,k} + \alpha_k A_k \cdot K_{i,k}\left[Q\left(Z_{i,k}\right) - H_{i,k} \cdot \hat{x}_{i,k}\right] + \beta_k A_k \cdot C_{i,k} \sum_{j \in \mathcal{N}_i} \left[\left(1 - \gamma_{ij}\right) Q\left(\hat{x}^o_{j,k}\right) - \hat{x}_{i,k}\right], \tag{13}$$

where γ_{ij} indicates the path loss rate between node i and node j, $\hat{x}^o_j$ is the broadcast estimate at the current time, α_k is a Bernoulli distributed sequence with a value 0, or 1 and satisfies $P\{\alpha_k = 1\} = \mu$, $C_{i,k}$ is the consensus gain matrices.

Step 4. Determine whether triggered conditions are energized or not by the following function:

$$\hat{x}_{i,k+1} = \begin{cases} \hat{x}_{i,k+1}, & \varphi_i > 0, \\ \hat{x}^o_{i,k}, & \varphi_i \le 0, \end{cases} \tag{14}$$

where $\varphi_i = (\hat{x}^o_{i,k} - \hat{x}_{i,k})^T (\hat{x}^o_{i,k} - \hat{x}_{i,k}) - g_i$, $\hat{x}^o_{i,k}$ is the broadcasted estimate at the previous time instant, and g_i is the triggered threshold and positive. If $\varphi_i > 0$, trigger the event, then transmit current estimated values. Otherwise, use previous values. In this case, no transmissions occur and energy is saved.

Step 5. Quantize the estimated values and transmit them to neighbors.

$$\hat{x}_{i,k+1} = Q\left(\hat{x}_{i,k+1}\right). \tag{15}$$

Step 6. Update the gain matrices and error covariance matrices.

$$\begin{aligned} K_{i,k} &= P_{i,k} H^T_{i,k}\left[H_{i,k} P_{i,k} H^T_{i,k} + \left(R_{i,k} + \Delta_q^2\right)\right]^{-1}, \\ P_{i,k+1} &= \left(A_k - A_k K_{i,k} H_{i,k}\right) P_{i,k} \left(A_k - A_k K_{i,k} H_{i,k}\right)^T + A_k K_{i,k}\left(R_{i,k} + \Delta_q^2\right) K^T_{i,k} A^T_k \\ &\quad + B_k\left(Q_{i,k} + \Delta_q^2\right) B^T_k. \end{aligned} \tag{16}$$

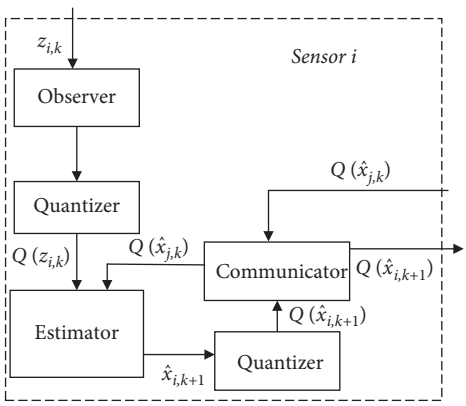

Figure 5: Schematic diagram of a node over a distributed integrated network.

Step 7. Calculate real-time assessment for different environment parameters.

$$Z_{Oi} = Z_{Pi} - \hat{x}_i. \tag{17}$$

If any environment parameter is greater than the corresponding safe threshold, $Z_{Oi} \geq Z_{bl}$, then alarm. Otherwise, output air quality index AQI,

$$\mathrm{AQI} = \sum_l \frac{\alpha_l (Z_{bl} - Z_{Oi})}{\|Z_{bl}\|}, \tag{18}$$

where Z_{bl} is the safe threshold for a certain pollutant, l, and α_l is weighted value for the corresponding pollutant.

Step 8. Return to Step 2 and cycle through.

After inserting quantizers in sensor networks, as long as the number of bits of quantizers and the range of the quantization interval are specified in advance, the binary digits can be used instead of the analogical value for state estimation to communicate among nodes. Therefore, the bandwidth requirement of communication is effectively reduced. The performance of the quantized algorithm will be demonstrated by simulation verifications in Section 4 by comparing it to the ET-KCF algorithm proposed in [20].

3.4. Stability Analysis for Switched Quantitative ET-KCT Algorithm. As illustrated in Figure 5, one quantizer is located between observer and estimator, and the other one is placed behind the estimator. It is known that the quantization error is smaller than Δ_q. Therefore, the observation noise should also consider the quantization error. That is, the observation noise covariance matrix becomes $R' = R + \Delta_q^2$.

Furthermore, to analyze the stability of the switched QET-KCF, some assumptions are set as follows.

Assumption 1. Matrix A_k is the nonsingular for each $k > 0$.

Assumption 2. $(A_k, H_{i,k})$ is uniformly observable.

Assumption 3. The system and parameter matrices are bounded by the positive scalars $\overline{a}, \overline{b}, \overline{h}, \underline{q}, \underline{r}, \overline{d}, \underline{p}, \overline{p}$:

$$\begin{aligned} \|A_k\| &\leq \overline{a}, \\ \|B_k\| &\leq \overline{b}, \\ \|H_{i,k}\| &\leq \overline{h}, \\ Q_k &\geq \underline{q} I, \\ R'_{i,k} &\geq \underline{r} I, \\ \|F_{i,k}\| &\leq \overline{d}, \\ \underline{p}_i I \leq P_{i,k} &\leq \overline{p}_i I, \end{aligned} \tag{19}$$

where I is the identity matrix.

According to [36], if the matrix $(A_k, H_{i,k})$ meets the uniform observable condition for each time constant k in the system (5), $P_{i,k}$ has upper and lower bounds.

Lemma 2 ([36], Lemma 2.1). *Assume there is a stochastic process $V_k(\xi_k)$ and real numbers $\underline{v}, \overline{v}, l > 0$ and $0 \leq \alpha \leq 1$ such that*

$$\begin{aligned} \underline{v}\|\xi_k\|^2 \leq V_k(\xi_k) \leq \overline{v}\|\xi_k\|^2, \\ E\{V_k(\xi_k)|\xi_{k-1}\} \leq (1-\alpha)V_{k-1}(\xi_{k-1}) + l. \end{aligned} \tag{20}$$

Then, the stochastic process is exponentially bounded in the mean square, such that

$$E\left\{\|\xi_k\|^2\right\} \leq \frac{\overline{v}}{\underline{v}} E\left\{\|\xi_0\|^2\right\}(1-\alpha)^k + \frac{l}{\underline{v}} \sum_{i=1}^{k} (1-\alpha)^i, \tag{21}$$

and the stochastic process is bounded with probability 1.

In the following analyses, Lemma 1 will be used as the boundary condition for the estimation process of QET-KCF. The boundaries of these parameters for each sensor node are obtained as described by Lemmas 3 and 4.

Lemma 3 (see [36], Lemma 3.1). *Based on Assumption 3, there exists a real number, $0 < \kappa_i < 1$ ($i = 1, 2, \ldots, N$), making the following equation works:*

$$\left(A_k - \mu A_k \cdot K_{i,k} \cdot H_{i,k}\right)^T \cdot P_{i,k+1}^{-1}\left(A_k - \mu A_k \cdot K_{i,k} \cdot H_{i,k}\right) \leq (1-\kappa_i)P_{i,k}^{-1}, \tag{22}$$

where

$$\kappa_i = 1 - \frac{1}{1 + \left(\underline{q}/\overline{p}\left(\left(\overline{a} + \mu \cdot \overline{a} \cdot \overline{p} \cdot \overline{h}^2\right)/\underline{r}\right)^2\right)}. \tag{23}$$

Lemma 4 (see [36], Lemma 3.3). *Under Assumption 3, there is a real number $\epsilon_i > 0 (i = 1, 2, \ldots, N)$ such that*

$$E\left\{\begin{array}{c} \mu^2 v_{i,k}^T \cdot F_{i,k}^T \cdot K_{i,k}^T \cdot A_k^T \cdot P_{i,k+1}^{-1} \cdot A_k \cdot K_{i,k} F_{i,k} \cdot v_{i,k} + \\ w^T \cdot B^T \cdot P_{i,k+1}^{-1} \cdot B \cdot w \end{array}\right\} \le \varepsilon_i. \tag{24}$$

In the following part, the analysis results of stability are discussed.

Theorem 1. *According to Assumptions 1–3, an estimation error of a discrete linear time-varying system (5) with QET-KCF is exponentially bounded in the mean square with probability 1 when the initial prediction error is bounded.*

The proving process of Theorem 1 is represented in the appendix.

The upper bound of σ for the consensus gain, σ^*, is

$$\begin{aligned} \sigma^* &= \frac{-\overline{p}(\beta_1 + \beta_2) + \theta}{2\mu_2\left(\overline{p}\beta_1^2 + \overline{p}\beta_1^2(1 - m')/\left(\underline{p} + \overline{p}\beta_1\beta_2\right)\right)\lambda_{\max}\left(\mathscr{L}^T\mathscr{L}\right)}, \\ \theta &= \left[\overline{p}^2(\beta_1 + \beta_2)^2 + 4\left(\frac{\overline{p}\beta_1^2 + \overline{p}\beta_1^2(1 - m')}{\underline{p} + \overline{p}\beta_1\beta_2}\right)\lambda_{\max}\left(\mathscr{L}^T\mathscr{L}\right)m'\right]^{1/2}. \end{aligned} \tag{25}$$

Remark 1. It is noticed that compared to the upper bound value presented in [19], the upper limit σ^* becomes smaller in this paper. It is known that the observation error covariance matrix becomes $R' = R + \Delta_q^2$ due to the introduction of quantization error. This leads m in [20] to m' in this paper, where $m' = \min\{\kappa_1, \ldots, \kappa_N\}$; therefore, the upper bound limit decreases.

4. Performance Simulations for the Switched ET-KCF Algorithm

The mean estimation error (MEE) and mean consensus error (MCE) defined in [31] are used as the performance indexes. The simulation is performed with the Monte Carlo method on the Matlab platform. The statistical averages are used to analyze the error responses of the wireless sensor monitoring system.

Mean estimation error (MEE) is

$$\mathrm{MEE}_k = \sqrt{\frac{\sum_{i=1}^N \left(e_{i,k}^T e_{i,k}\right)}{N}}, \tag{26}$$

where $e_{i,k} = x_{i,k} - \widehat{x}_{i,k}$.

Mean consensus error (MCE) is

$$\mathrm{MCE}_k = \sqrt{\frac{\sum_{i=1}^N \left(\delta_{i,k}^T \delta_{i,k}\right)}{N}}, \tag{27}$$

where $\delta_{i,k} = \widehat{x}_{i,k} - (\sum_{i=1}^N \widehat{x}_{i,k}/N)$, k is defined as the time instant, and N is the node number.

This article does not provide the approach to get the dynamic equations of integrated sensors in detail. As illustrated in [20], there are several ways to derive the models such as the theoretical analysis of the measurement error and identification of practical measurement values. In order to be convenient to compare the proposed method to the previous works in [20], this paper selects the same dynamic models for the 10 nodes over the distributed monitoring integrated sensor network illustrated in Figure 6 and conducts simulation validations.

Suppose that the measurement error dynamics of an integrated sensor is as follows:

$$\begin{aligned} x_{i,k+1} &= \begin{bmatrix} 1 + 0.005 \cdot \sin(j) & -0.002 \cdot \cos(j) + 0.0001 \cdot \mathrm{rand} \\ 0.002 \cdot \cos(j) + 0.0001 \cdot \mathrm{rand} & 1 + 0.005 \cdot \sin(j) \end{bmatrix} x_{i,k} + \begin{bmatrix} 0.5 & 0 \\ 0 & 0.5 \end{bmatrix} w_k, \\ z_{i,k+1} &= \begin{bmatrix} 1 + 0.005 \cdot \cos(j) & -0.002 \cdot \sin(j) + 0.0001 \cdot \mathrm{rand} \\ 0.002 \cdot \sin(j) + 0.0001 \cdot \mathrm{rand} & 1 + 0.005 \cdot \cos(j) \end{bmatrix} x_{i,k} \\ &\quad + \begin{bmatrix} 1 + 0.5 \cdot \cos(j) & -0.02 \cdot \sin(j) + 0.001 \cdot \mathrm{rand} \\ 0.02 \cdot \sin(j) + 0.001 \cdot \mathrm{rand} & 1 + 0.5 \cdot \cos(j) \end{bmatrix} v_{pi}. \end{aligned} \tag{28}$$

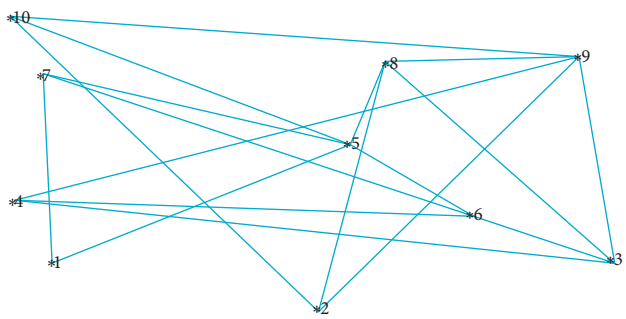

Figure 6: The topological graph of a distributed monitoring sensor network.

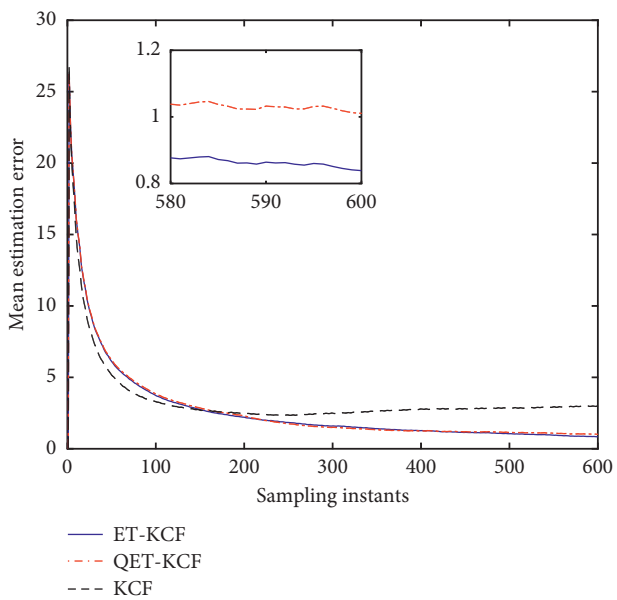

Figure 7: Comparison of mean estimation errors among different filters in the event of packet and path losses.

In this example, also assume the initial measurement error $x_0 = (8, 12)^T$, the initial prediction error matrix $P_0 = 10I_2$. The network and the measurement noises are described by independent Gaussian white noises with covariance 10 and $100i$, respectively. Let the path loss rate γ_{ij} between nodes i and j be 0.05. The sampling duration is 5 ms. And the observed packet loss and the communication packet loss rates are 0.2 and $\mu_1 = \mu_2 = 0.8$ respectively. The quantizer parameters, δ and d are set to be 0.05 and 1. The number of quantization bits is $l' = 4$.

As seen from Figure 7, when packet losses and path losses exist, KCF diverges. However, ET-KCF and switched QET-KCF can still converge stably. However, the accuracy of the switched QET-KCF is slightly reduced. This is because the quantization error is introduced by inserting the quantizers. The unquantized algorithm is developed based on the ideal condition without the transmission bandwidth limitation in each state estimation. Therefore, the accuracy is better. However, the quantized algorithm can effectively reduce the demand for communication bandwidth while

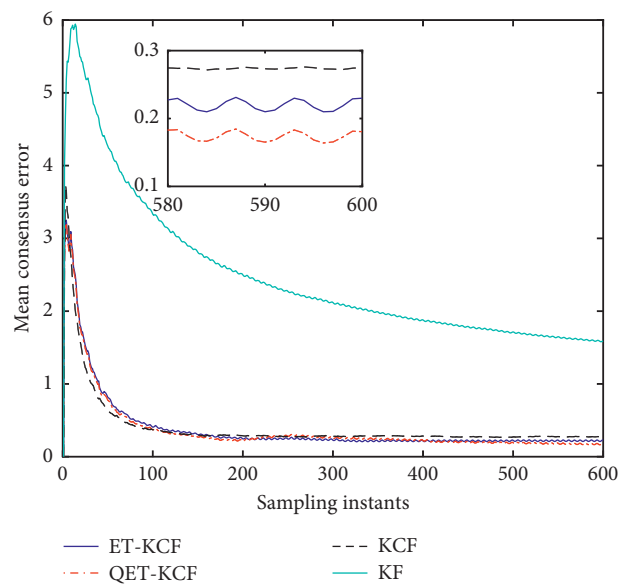

Figure 8: Comparison of mean consensus errors among different filters in the event of packet and path losses.

only sacrificing the accuracy slightly. Therefore, the advantages of the introduction of quantizers can overwhelm the disadvantages.

As seen from Figure 8, the mean consensus error of the switched quantized QET-KCF has the same order as ET-KCF and KCF and is closed to them. Furthermore, it is much less than that of the local Kalman filter algorithm in the event of packet and path losses.

It can be concluded that the performance of the algorithm by adding the quantizers is not greatly affected. The estimation error still converges to the finite value very quickly, and the consensus error still maintains a low level which means the estimated values among nodes tend to be consistent. Simultaneously, the burdens of communications have been improved greatly.

5. Conclusion

This paper designs a new switched quantizer and applies the new quantizers in ET-KCF to form a switched QET-KCF algorithm that is employed in cabin environment parameter estimations. The proposed quantizer can ensure that the quantization error is bounded. The corresponding stability analysis is theoretically proved. The simulation results show that the proposed algorithm in this paper can accurately and timely estimate parameters and effectively reduce the burdens of network communication bandwidths. This is a promising method to solve the communication burden issue in cabin WSN in the future.

Appendix

Proof. The prediction error is defined as $e_k = [e_1^T, \ldots, e_N^T]^T$. $P = \mathrm{diag}\{P_1, \ldots, P_N\}$ is the corresponding block diagonal matrix. The following Lyapunov function is constructed:

$$V_k(e_k) = e_k^T P^{-1} e_k = \sum_{i=1}^{N} e_{i,k}^T P_{i,k}^{-1} e_{i,k}. \tag{A.1}$$

As mentioned in Assumption 2, $\underline{p}_i I \le P_{i,k} \le \overline{p}_i I$; then,

$$\frac{1}{\overline{p}}\|e_k\|^2 \le V_k(e_k) \le \frac{1}{\underline{p}}\|e_k\|^2, \tag{A.2}$$

where $\overline{p} = \max\{\overline{p}_1, \ldots, \overline{p}_N\}$ and $\underline{p} = \max\{\underline{p}_1, \ldots, \underline{p}_N\}$.

Inequality (A.2) satisfies Lemma 1. And we have to discuss the expectation value of the Lyapunov function $E\{V_{k+1}(e_{k+1})\}$ of next time instant to prove that exponential boundedness of the process e. Based on the definition of $e_{i,k}$, the prediction error dynamics of $e_{i,k+1}$ are defined as follows:

$$\begin{aligned} e_{i,k+1} = &\left(A_k - \alpha_k A_k \cdot K_{i,k} \cdot H_{i,k}\right) \cdot e_{i,k} + \alpha_k A_k \cdot K_{i,k} F_{i,k} \cdot v_{i,k} \\ &+ \beta_k A_k \cdot C_{i,k} \sum_{j \in \mathcal{N}_i} \left(1 - \gamma_{ij}\right) \tilde{e}_{j,k} + \beta_k A_k \cdot C_{i,k} \sum_{j \in \mathcal{N}_i} \left(1 - \gamma_{ij}\right)\left(e_{j,k} - e_{i,k}\right) \\ &- \beta_k A_k \cdot C_{i,k} \sum_{j \in \mathcal{N}_i} \gamma_{ij} \hat{x}_{i,k} + \beta_k A_k \cdot C_{i,k} \sum_{j \in \mathcal{N}_i} \left(1 - \gamma_{ij}\right) \Delta q - B_k w_k. \end{aligned} \tag{A.3}$$

According to the definition of the Lyapunov function, we have the following:

$$\begin{aligned} E\{V_{k+1}(e_{k+1})\} = &\sum_{i=1}^{N} e_{i,k}^T \left(A_k - \mu_1 A_k \cdot K_{i,k} \cdot H_{i,k}\right)^T \cdot P_{i,k+1}^{-1} \cdot \left(A_k - \mu_1 A_k \cdot K_{i,k} \cdot H_{i,k}\right) e_{i,k} \\ &+ 2\mu_2 \sum_{i=1}^{N} \sum_{j \in \mathcal{N}_i} \left(1 - \gamma_{ij}\right) e_{i,k}^T \left(A_k - \mu_1 A_k \cdot K_{i,k} \cdot H_{i,k}\right)^T \cdot P_{i,k+1}^{-1} \cdot A_k \cdot C_{i,k} \tilde{e}_{j,k} \\ &+ 2\mu_2 \sum_{i=1}^{N} \sum_{j \in \mathcal{N}_i} \left(1 - \gamma_{ij}\right) e_{i,k}^T \left(A_k - \mu_1 A_k \cdot K_{i,k} \cdot H_{i,k}\right)^T \cdot P_{i,k+1}^{-1} \cdot A_k \cdot C_{i,k} \left(e_{j,k} - e_{i,k}\right) \\ &- 2\mu_2 \sum_{i=1}^{N} \sum_{j \in \mathcal{N}_i} \gamma_{ij} e_{i,k}^T \left(A_k - \mu_1 A_k \cdot K_{i,k} \cdot H_{i,k}\right)^T \cdot P_{i,k+1}^{-1} \cdot A_k \cdot C_{i,k} \hat{x}_{i,k} \\ &+ \sum_{i=1}^{N} \mu_1^2 v_{i,k}^T \cdot F_{i,k}^T \cdot K_{i,k}^T \cdot A_k^T \cdot P_{i,k+1}^{-1} \cdot A_k \cdot K_{i,k} \cdot F_{i,k} \cdot v_{i,k} \\ &+ \mu_2^2 \sum_{i=1}^{N} \sum_{j \in \mathcal{N}_i} \left(1 - \gamma_{ij}\right)^2 \tilde{e}_{j,k}^T C_{i,k}^T \cdot A_k^T \cdot P_{i,k+1}^{-1} \cdot A_k \cdot C_{i,k} \tilde{e}_{j,k} \\ &+ 2\mu_2^2 \sum_{i=1}^{N} \sum_{j \in \mathcal{N}_i} \left(1 - \gamma_{ij}\right)^2 \tilde{e}_{j,k}^T C_{i,k}^T \cdot A_k^T \cdot P_{i,k+1}^{-1} \cdot A_k \cdot C_{i,k} \left(e_{j,k} - e_{i,k}\right) \\ &- 2\mu_2^2 \sum_{i=1}^{N} \sum_{j \in \mathcal{N}_i} \left(1 - \gamma_{ij}\right) \gamma_{ij} \tilde{e}_{j,k}^T C_{i,k}^T \cdot A_k^T \cdot P_{i,k+1}^{-1} \cdot A_k \cdot C_{i,k} \hat{x}_{i,k} \\ &+ \mu_2^2 \sum_{i=1}^{N} \sum_{j \in \mathcal{N}_i} \left(1 - \gamma_{ij}\right)^2 \left(e_{j,k} - e_{i,k}\right)^T C_{i,k}^T \cdot A_k^T \cdot P_{i,k+1}^{-1} \cdot A_k \cdot C_{i,k} \left(e_{j,k} - e_{i,k}\right) \\ &- 2\mu_2^2 \sum_{i=1}^{N} \sum_{j \in \mathcal{N}_i} \left(1 - \gamma_{ij}\right) \gamma_{ij} \left(e_{j,k} - e_{i,k}\right)^T C_{i,k}^T \cdot A_k^T \cdot P_{i,k+1}^{-1} \cdot A_k \cdot C_{i,k} \hat{x}_{i,k} \\ &+ \mu_2^2 \sum_{i=1}^{N} \sum_{j \in \mathcal{N}_i} \gamma_{ij}^2 \hat{x}_{i,k}^T C_{i,k}^T \cdot A_k^T \cdot P_{i,k+1}^{-1} \cdot A_k \cdot C_{i,k} \hat{x}_{i,k} \\ &+ \mu_2^2 \sum_{i=1}^{N} \sum_{j \in \mathcal{N}_i} \left(1 - \gamma_{ij}\right)^2 \hat{x}_{i,k}^T \Delta_q^T \cdot C_{i,k}^T \cdot A_k^T \cdot P_{i,k+1}^{-1} \cdot A_k \cdot C_{i,k} \Delta_q \\ &+ \sum_{i=1}^{N} w_k^T \cdot B_k^T \cdot P_{i,k+1}^{-1} \cdot B_k \cdot w_k. \end{aligned} \tag{A.4}$$

Define $\begin{cases} \eta_{i,k} = \sum_{j\in N_i} \tilde{e}_{j,k} \\ q_{i,k} = \sum_{j\in N_i} (e_{j,k} - e_{i,k}) \end{cases}, \begin{cases} \sum_{i=1}^{N} \cdot \sum_{r\in \mathcal{N}_i} (1-\gamma_{ri}) = \beta_1 \\ \sum_{i=1}^{N} \cdot \sum_{r\in \mathcal{N}_i} \gamma_{ri} = \beta_2 \end{cases}.$

To reduce the complexity of analysis, let the consensus gain be as follows:

$$\begin{aligned} C_{i,k} &= \sigma\left[\left(A_k - \mu A_k \cdot K_{i,k} \cdot H_{i,k}\right)^T \cdot P_{i,k+1}^{-1} \cdot A_k\right]^{-1} \Lambda_{i,k}, \\ \Lambda_{i,k} &= \left(A_k - \mu A_k \cdot K_{i,k} \cdot H_{i,k}\right)^T \cdot P_{i,k+1}^{-1} \cdot \left(A_k - \mu A_k \cdot K_{i,k} \cdot H_{i,k}\right). \end{aligned} \tag{A.5}$$

Then,

$$\begin{aligned} C_{i,k}^T \cdot A_k^T \cdot P_{i,k+1}^{-1} \cdot \left(A_k - \mu A_k \cdot K_{i,k} \cdot H_{i,k}\right) &= \sigma \cdot \Lambda_{i,k}, \\ C_{i,k}^T \cdot A_k^T \cdot P_{i,k+1}^{-1} \cdot A_k \cdot C_{i,k} &= \sigma^2 \cdot \Lambda_{i,k}. \end{aligned} \tag{A.6}$$

Therefore,

$$\begin{aligned} E\{V_{k+1}(e_{k+1})\} \le & \sum_{i=1}^{N} \varepsilon_i + \sum_{i=1}^{N} (1-\kappa_i) e_{i,k}^T \cdot P_{i,k}^{-1} \cdot e_{i,k} \\ & + 2\mu_2\left(\beta_1 \sigma e_k^T \Lambda_k \eta_k + 2\beta_1 \sigma e_k^T \Lambda_k q_k - 2\beta_2 \sigma e_k^T \Lambda_k \hat{x}_k\right) \\ & + \mu_2^2\left(\beta_1^2 \sigma^2 q_k^T \Lambda_k q_k - 2\beta_1\beta_2\sigma^2 q_k^T \Lambda_k \hat{x}_k + \beta_2^2 \sigma^2 \hat{x}_k^T \Lambda_k \hat{x}_k + \beta_1^2 \sigma^2 \Delta_q^T \Lambda_k \Delta_q\right), \end{aligned} \tag{A.7}$$

where

$$\begin{aligned} \eta_k &= \mathscr{A} \cdot \tilde{e}_k, \\ \mathscr{A} &= E \otimes I, \\ q_k &= -\mathscr{L} \cdot e_k, \\ \mathscr{L} &= [(1-\gamma_r)D - E] \otimes I, \\ \eta_k^T \eta_k &= \tilde{e}_k^T \mathscr{A}^T \mathscr{A} \tilde{e}_k \le \lambda_{\max}\left(\mathscr{A}^T \mathscr{A}\right)\Delta, \end{aligned} \tag{A.8}$$

and $\Delta = \sum_{i=1}^{N} \delta_i$.

E and D are the adjacency matrix and degree matrix of graph G, respectively.

And,

$$\begin{aligned} +2\beta_1 \sigma e_k^T \Lambda_k \eta_k &\le \beta_1 \sigma\left(\eta_k^T \Lambda_k^T \Lambda_k \eta_k + e_k^T e_k\right) \\ &\le \beta_1 \sigma\left(\lambda_{\max}\left(\Lambda_k^T \Lambda_k\right)\lambda_{\max}\left(\mathscr{A}^T \mathscr{A}\right)\Delta\right) + \beta_1 \sigma e_k^T e_k. \end{aligned} \tag{A.9}$$

For the fourth term,

$$2\beta_1 \sigma e_k^T \Lambda_k q_k \le -2\sigma \lambda_{\min}(\Lambda_k) e_k^T \mathscr{L} e_k \le 0. \tag{A.10}$$

For the fifth term,

$$\begin{aligned} -2\beta_2 \sigma e_k^T \Lambda_k \hat{x}_k &\le \beta_2 \sigma\left(e_k^T e_k + \hat{x}_k^T \Lambda_k^T \Lambda_k \hat{x}_k\right) \\ &\le \beta_2 \sigma e_k^T e_k + \beta_2 \sigma \lambda_{\max}\left(\Lambda_k^T \Lambda_k\right)\hat{x}_k^T \hat{x}_k. \end{aligned} \tag{A.11}$$

For the sixth term,

$$\beta_1^2 \sigma^2 \eta_k^T \Lambda_k \eta_k \le \beta_1^2 \sigma^2 \lambda_{\max}\left(\mathscr{A}^T \mathscr{A}\right)\lambda_{\max}(\Lambda_k)\Delta. \tag{A.12}$$

For the seventh term,

$$2\beta_1^2 \sigma^2 \eta_k^T \Lambda_k q_k \le \beta_1^2 \sigma^2\left(\eta_k^T \Lambda_k^T \Lambda_k \eta_k + e_k^T \mathscr{L}^T \mathscr{L} e_k\right). \tag{A.13}$$

For the eighth term,

$$\begin{aligned} -2\beta_1\beta_2\sigma^2 \eta_k^T \Lambda_k \hat{x}_k &\le \beta_1\beta_2\sigma^2\left(\eta_k^T \eta_k + \hat{x}_k^T \Lambda_k^T \Lambda_k \hat{x}_k\right) \\ &\le \beta_1\beta_2\sigma^2 \lambda_{\max}\left(\mathscr{A}^T \mathscr{A}\right)\Delta + \beta_1\beta_2\sigma^2 \lambda_{\max}\left(\Lambda_k^T \Lambda_k\right)\hat{x}_k^T \hat{x}_k. \end{aligned} \tag{A.14}$$

For the ninth term,

$$\beta_1^2 \sigma^2 q_k^T \Lambda_k q_k \le \beta_1^2 \sigma^2 \lambda_{\max}(\Lambda_k)\lambda_{\max}\left(\mathscr{L}^T \mathscr{L}\right) e_k^T e_k. \tag{A.15}$$

For the tenth term,

$$\begin{aligned} -2\beta_1\beta_2\sigma^2 q_k^T \Lambda_k \hat{x}_k &\le \beta_1\beta_2\sigma^2\left(q_k^T q_k + \hat{x}_k^T \Lambda_k^T \Lambda_k \hat{x}_k\right) \\ &\le \beta_1\beta_2\sigma^2 \lambda_{\max}\left(\mathscr{L}^T \mathscr{L}\right) e_k^T e_k \\ &\quad + \beta_1\beta_2\sigma^2 \lambda_{\max}\left(\Lambda_k^T \Lambda_k\right)\hat{x}_k^T \hat{x}_k. \end{aligned} \tag{A.16}$$

For the eleventh term,

$$\beta_2^2 \sigma^2 \hat{x}_k^T \Lambda_k \hat{x}_k \le \beta_2^2 \sigma^2 \lambda_{\max}(\Lambda_k)\hat{x}_k^T \hat{x}_k. \tag{A.17}$$

For the twelfth item

$$\beta_1^2 \sigma^2 \Delta_q^T \Lambda_k \Delta_q \le \beta_1^2 \sigma^2 \lambda_{\max}(\Lambda_k)\Delta_q^T \Delta_q. \tag{A.18}$$

Therefore,

$$
\begin{aligned}
E\{V_{k+1}(e_{k+1})\} \le & \sum_{i=1}^{N} \varepsilon_i + \sum_{i=1}^{N} (1-\kappa_i) e_{i,k}^T \cdot P_{i,k}^{-1} \cdot e_{i,k} + \Big[\big(\mu_2^2\beta_1^2\sigma^2 + \mu_2\beta_1\sigma\big)\lambda_{\max}\big(\Lambda_k^T\Lambda_k\big) \\
& + \mu_2^2\beta_1^2\sigma^2\lambda_{\max}(\Lambda_k) + \mu_2^2\beta_1\beta_2\sigma^2\Big]\lambda_{\max}\big(\mathscr{A}^T\mathscr{A}\big)\Delta \\
& + \Big[\mu_2\beta_1\sigma + \mu_2^2\big(\beta_1^2\sigma^2 + \beta_1^2\sigma^2\lambda_{\max}(\Lambda_k) + \beta_1\beta_2\sigma^2\big)\lambda_{\max}\big(\mathscr{L}^T\mathscr{L}\big) + \mu_2\beta_2\sigma\Big] e_k^T e_k \\
& + \Big[\big(\mu_2\beta_2\sigma + 2\mu_2^2\beta_1\beta_2\sigma^2\big)\lambda_{\max}\big(\Lambda_k^T\Lambda_k\big) + \mu_2^2\beta_2^2\sigma^2\lambda_{\max}(\Lambda_k)\Big]\hat{x}_k^T\hat{x}_k \\
& + \mu_2^2\beta_1^2\sigma^2\lambda_{\max}(\Lambda_k)\Delta_q^T\Delta_q \\
\le & \Big[1 - m' + \mu_2\overline{p}(\beta_1+\beta_2)\sigma + \mu_2^2\overline{p}\big(\beta_1^2\sigma^2 + \beta_1^2\sigma^2\lambda_{\max}(\Lambda_k) + \beta_1\beta_2\sigma^2\big)\lambda_{\max}\big(\mathscr{L}^T\mathscr{L}\big)\Big] e_k^T P^{-1} e_k \\
& + \Big[\big(\mu_2^2\beta_1^2\sigma^2 + \mu_2\beta_1\sigma\big)\lambda_{\max}\big(\Lambda_k^T\Lambda_k\big) + \mu_2^2\beta_1^2\sigma^2\lambda_{\max}(\Lambda_k) + \mu_2^2\beta_1\beta_2\sigma^2\Big]\lambda_{\max}\big(\mathscr{A}^T\mathscr{A}\big)\Delta \\
& + \Big[\big(\mu_2\beta_2\sigma + 2\mu_2^2\beta_1\beta_2\sigma^2\big)\lambda_{\max}\big(\Lambda_k^T\Lambda_k\big) + \mu_2^2\beta_2^2\sigma^2\lambda_{\max}(\Lambda_k)\Big]\Delta_1 \\
& + \mu_2^2\beta_1^2\sigma^2\lambda_{\max}(\Lambda_k)\Delta_2 + \sum_{i=1}^{N}\varepsilon_i,
\end{aligned}
\tag{A.19}
$$

where

$$
\begin{aligned}
\Delta_1 &= x_k^T x_k, \\
\Delta_2 &= \Delta_q^T \Delta_q, \\
m' &= \min\{\kappa_1, \ldots, \kappa_N\}.
\end{aligned}
\tag{A.20}
$$

As shown in Lemma 3, we can obtain $\lambda_{\max}(\Lambda_k) \le ((1-m')/\underline{p})$.

$$
\lambda_{\max}\big(\Lambda_k^T\Lambda_k\big) = \lambda_{\max}\big(\Lambda_k^2\big) = \lambda_{\max}^2(\Lambda_k) \le \left(\frac{1-m'}{\underline{p}}\right)^2.
\tag{A.21}
$$

Therefore,

$$
E\{V_{k+1}(e_{k+1})\} \le \left[1 - m' + \mu_2\overline{p}(\beta_1+\beta_2)\sigma + \mu_2^2\overline{p}\left(\beta_1^2\sigma^2 + \beta_1^2\sigma^2\frac{1-m'}{\underline{p}} + \beta_1\beta_2\sigma^2\right)\lambda_{\max}\big(\mathscr{L}^T\mathscr{L}\big)\right] V_k(e_k) + l'',
\tag{A.22}
$$

where

$$
\begin{aligned}
l'' = & \Big[\big(\mu_2^2\beta_1^2\sigma^2 + \mu_2\beta_1\sigma\big)\lambda_{\max}\big(\Lambda_k^T\Lambda_k\big) + \mu_2^2\beta_1^2\sigma^2\lambda_{\max}(\Lambda_k) + \mu_2^2\beta_1\beta_2\sigma^2\Big] \\
& \cdot \lambda_{\max}\big(\mathscr{A}^T\mathscr{A}\big)\Delta + \Big[\big(\mu_2\beta_2\sigma + 2\mu_2^2\beta_1\beta_2\sigma^2\big)\lambda_{\max}\big(\Lambda_k^T\Lambda_k\big) + \mu_2^2\beta_2^2\sigma^2\lambda_{\max}(\Lambda_k)\Big]\Delta_1 \\
& + \mu_2^2\beta_1^2\sigma^2\lambda_{\max}(\Lambda_k)\Delta_2 + \sum_{i=1}^{N}\varepsilon_i.
\end{aligned}
\tag{A.23}
$$

Substituting (A.23) into Lemma 1,

$$
\alpha = m' - \mu_2\overline{p}(\beta_1+\beta_2)\sigma - \mu_2^2\overline{p}\left(\frac{\beta_1^2\sigma^2 + \beta_1^2\sigma^2(1-m')}{\underline{p}} + \beta_1\beta_2\sigma^2\right)\lambda_{\max}\big(\mathscr{L}^T\mathscr{L}\big).
\tag{A.24}
$$

Due to the conditions of Lemma 1, we know that

$$0 < \alpha < 1,$$
$$\sum_{i=1}^{N} \varepsilon_i > 0. \tag{A.25}$$

Then,

$$0 < m' - \mu_2 \overline{p}(\beta_1 + \beta_2)\sigma - \mu_2^2 \overline{p}\left(\frac{\beta_1^2\sigma^2 + \beta_1^2\sigma^2(1-m')}{\underline{p}} + \beta_1\beta_2\sigma^2\right)\lambda_{\max}\left(\mathscr{L}^T\mathscr{L}\right) < 1. \tag{A.26}$$

The condition $\sigma < \sigma^*$ makes the above quadratic inequality hold, where

$$\sigma^* = \frac{-\overline{p}(\beta_1 + \beta_2) + \left[\overline{p}^2(\beta_1 + \beta_2)^2 + \tau\right]}{2\mu_2\left(\overline{p}\beta_1^2 + \overline{p}\beta_1^2(1-m')/\underline{p} + \overline{p}\beta_1\beta_2\right)\lambda_{\max}\left(\mathscr{L}^T\mathscr{L}\right)}, \tag{A.27}$$

where $\tau = 4((\overline{p}\beta_1^2 + \overline{p}\beta_1^2(1-m')/\underline{p}) + \overline{p}\beta_1\beta_2)\lambda_{\max}(\mathscr{L}^T\mathscr{L})m']^{1/2}$. □

Data Availability

The figures .zip data used to support the findings of this study are available from the corresponding author upon request.

Conflicts of Interest

The authors declare that there are no conflicts of interest regarding the publication of this paper.

Acknowledgments

This work was supported by the Tianjin Natural Science Foundation (18JCYBJC42300) and Scientific Research Project of Tianjin Education Commission (2019KJ143).

References

[1] National Research Council, *The Airliner Cabin Environment and the Health of Passengers and Crew*, The National Academies Press, Washington, DC, USA, 2001.

[2] F. Li, J. Liu, J. Ren, X. Cao, and Y. Zhu, "Numerical investigation of airborne contaminant transport under different vortex structures in the aircraft cabin," *International Journal of Heat and Mass Transfer*, vol. 96, no. IV, pp. 287–295, 2016.

[3] S. C. Lee, C. S. Poon, X. D. Li, and F. Luk, "Indoor air quality investigation on commercial aircraft," *Indoor Air*, vol. 9, no. 3, pp. 180–187, 2010.

[4] G. Studor, "Fly-by-Wireless: a revolution in aerospace vehicle architecture for instrumentation and control," NASA technical report, Johnson Space Center, Houston, TX, USA, 2007.

[5] R. Priyanka, D. S. Kamal, C. Hankima, and M. B. Jean, "Wireless sensor networks: a survey on recent developments and developments and potential synergies," *Journal Supercomputer*, vol. 68, pp. 1–48, 2014.

[6] K. Sohraby, D. Minoli, and T. Znati, *Wireless Sensor Networks: Technology, Protocols, and Applications*, Wiley-Interscience, Hoboken. NJ, USA, 2007.

[7] W. Yang, X. Wang, and H. Shi, *Optimal Consensus-Based Distributed Estimation with Intermittent communication*, Taylor & Francis, Inc., Milton Park, UK, 2011.

[8] R. Olfati-Saber, "Distributed Kalman filtering for sensor networks," in *Proceedings of the IEEE Conference on Decision and Control*, pp. 5492–5498, New Orleans, LA, USA, December 2007.

[9] R. Olfati-Saber, "Kalman-consensus filter: optimality, stability, and performance," in *Proceedings of the IEEE Conference on Decision and Control*, pp. 7036–7042, Shanghai, China, December 2009.

[10] D. H. Matthew and Z. H. Qu, "An optimal kalman-consensus filter for distributed implementation over a dynamic communication network," *IEEE Access*, pp. 66696–66706, 2021, inpress.

[11] M. Minyue Fu and L. Lihua Xie, "The sector bound approach to quantized feedback control," *IEEE Transactions on Automatic Control*, vol. 50, no. 11, pp. 1698–1711, 2005.

[12] A. Ribeiro and G. B. Giannakis, "Bandwidth-constrained distributed estimation for wireless sensor networks-part I: Gaussian case," *IEEE Transactions on Signal Processing*, vol. 54, no. 3, pp. 1131–1143, 2006.

[13] A. Ribeiro and G. B. Giannakis, "Bandwidth-constrained distributed estimation for wireless sensor networks-part II: unknown probability density function," *IEEE Transactions on Signal Processing*, IEEE Press, vol. 54, no. 7, , pp. 2784–2796, 2006.

[14] T. Hayakawa, H. Ishii, and K. Tsumura, "Adaptive quantized control for linear uncertain discrete-time systems," *Automatica*, vol. 45, no. 3, pp. 692–700, 2009.

[15] H. Sun, N. Hovakimyan, and T. Basar, "L1 adaptive controller for systems with input quantization," in *Proceedings of American Control Conference*, IEEE, Baltimore, MD, USA, June 2010.

[16] T. Hayakawa, H. Ishii, and K. Tsumura, "Adaptive quantized control for nonlinear uncertain systems," in *Proceedings of American Control Conference*, June 2006.

[17] C. De Persis and F. Mazenc, "Stability of quantized time-delay nonlinear systems: a Lyapunov-Krasowskii-functional approach," *Mathematics of Control, Signals, and Systems*, vol. 21, no. 4, pp. 337–370, 2010.

[18] G. N. Nair, F. Fagnani, S. Zampieri et al., "Feedback control under data rate constraints: an overview," *Proceedings of the IEEE*, vol. 95, no. 1, pp. 108–137, 2007.

[19] D. F. Coutinho, M. Minyue Fu, and C. E. De Souza, "Input and output quantized feedback linear systems," *IEEE Transactions on Automatic Control*, vol. 55, no. 3, pp. 761–766, 2010.

[20] R. Wang, X. Wang, H. Sun, Y. Huang, and Z. Chen, "Analysis of estimator and energy consumption with multiple faults over the distributed integrated WSN," *International Journal of Modelling Identification and Control*, vol. 32, no. 2, 2019.

[21] J. Liu, J. Xia, J. Cao et al., "Quantized state estimation for neural networks with cyber attacks and hybrid triggered communication scheme," *Neurocomputing*, vol. 291, pp. 35–49, 2018.

[22] Z. G. Wu, Z. Xu, P. Shi et al., "Nonfragile state estimation of quantized complex networks with switching topologies," *IEEE Transactions on Neural Networks and Learning Systems*, vol. 29, no. 10, pp. 5111–5121, 2018.

[23] H. Ren, R. Lu, J. Xiong, and Y. Xu, "Optimal estimation for discrete-time linear system with communication constraints and measurement quantization," *IEEE Transactions on Systems, Man, and Cybernetics: Systems*, vol. 50, no. 5, pp. 1932–1942, 2020.

[24] M. Liu, L. Zhang, P. Shi, and Y. Zhao, "Fault estimation sliding-mode observer with digital communication constraints," *IEEE Transactions on Automatic Control*, vol. 63, no. 10, pp. 3434–3441, 2018.

[25] Z. Zhang, J. Li, and L. Liu, "Distributed state estimation and data fusion in wireless sensor networks using multi-level quantized innovation," *Science China Information Sciences*, vol. 59, no. 2, pp. 1–15, 2016.

[26] L. Hu, Z. Wang, and X. Liu, "Dynamic state estimation of power systems with quantization effects: a recursive filter approach," *IEEE Transactions on Neural Networks and Learning Systems*, vol. 27, no. 8, pp. 1604–1614, 2017.

[27] F. F. C. Rego, Y. Pu, A. Alessandretti et al., "Design of a distributed quantized luenberger filter for bounded noise," in *Proceedings of American Control Conference*, July 2016.

[28] P. Zoran, S. Milan, D. Milan, V. Nikola, D. Danijel, and M. Srdjan, "Floating point and fixed point 32-bits quantizers for quantization of weights of neural networks," in *Proceedings of 12th International Symposium on Advanced Topics in Electrical Engineering (ATEE)*, Bucharest, Romania, March 2021.

[29] W. Li, Z. Xie, P. K. Wong, Y. Hu, G. Ge, and J. Zhao, "Event-triggered asynchronous fuzzy filtering for vehicle sideslip angle estimation with data quantization and dropouts," *IEEE Transactions on Fuzzy Systems*, p. 1, 2021 inpress.

[30] H. Bian, *Application of Modern Information Fusion Technology in Integrated Navigation System*, National Defence Industrial Press, Beijing, China, 2010.

[31] R. Wang, Y. Li, H. Sun, and Z. Chen, "Analyses of integrated aircraft cabin contaminant monitoring network based on Kalman consensus filter," *ISA Transactions*, vol. 71, pp. 112–120, 2017.

[32] K. Ranganathan, *A Textbook of Graph Theory*, Springer, Berlin, Germany, 2012.

[33] E. S. Biagioni and G. Sasaki, "Wireless sensor placement for reliable and efficient data collection," in *Proceedings of IEEE 36th Annual Hawaii International Conference on System Sciences, 2003*, p. 10, Big Island, HI, USA, January 2003.

[34] C. P. Njebla, "Topology and capacity planning for wireless heterogeneous networks in aircraft cabins," in *Proceedings of IEEE International Symposium on Personal Indoor and Mobile Radio Communications*, Helsinki, Finland, September 2006.

[35] J. Jin-Jun Xiao, S. Shuguang Cui, S. Zhi-Quan Luo, and A. J. Goldsmith, "Power scheduling of universal decentralized estimation in sensor networks," *IEEE Transactions on Signal Processing*, vol. 54, no. 2, pp. 413–422, 2006.

[36] K. Reif, S. Gunther, E. Yaz, and R. Unbehauen, "Stochastic stability of the discrete-time extended kalman filter," *IEEE Transactions on Automatic Control*, vol. 44, no. 4, pp. 714–728, 1999.

Hindawi
Complexity
Volume 2021, Article ID 9927850, 12 pages
https://doi.org/10.1155/2021/9927850

Research Article

Discrete-Time Sliding Mode Control Coupled with Asynchronous Sensor Fusion for Rigid-Link Flexible-Joint Manipulators

Guangyue Xue,[1] **Xuemei Ren**,[2] **Kexin Xing**,[3] **and Qiang Chen**[3]

[1]*China Transport Telecommunications & Information Center, Chaoyang District, Beijing 100011, China*
[2]*School of Automation, Beijing Institute of Technology, Beijing 100081, China*
[3]*College of Information Engineering, Zhejiang University of Technology, Hangzhou 310023, China*

Correspondence should be addressed to Guangyue Xue; iviiivi@163.com

Received 4 March 2021; Revised 11 May 2021; Accepted 15 July 2021; Published 27 July 2021

Academic Editor: Xue-bo Jin

This paper proposes a novel discrete-time terminal sliding mode controller (DTSMC) coupled with an asynchronous multirate sensor fusion estimator for rigid-link flexible-joint (RLFJ) manipulator tracking control. A camera is employed as external sensors to observe the RLFJ manipulator's state which cannot be directly obtained from the encoders since gear mechanisms or flexible joints exist. The extended Kalman filter- (EKF-) based asynchronous multirate sensor fusion method deals with the slow sampling rate and the latency of camera by using motor encoders to cover the missing information between two visual samples. In the proposed control scheme, a novel sliding mode surface is presented by taking advantage of both the estimation error and tracking error. It is proved that the proposed controller achieves convergence results for tracking control in the theoretical derivation. Simulation and experimental studies are included to validate the effectiveness of the proposed approach.

1. Introduction

In many high-performance robotic manipulator applications, positioning of the end effector (or/and links) is critical as the ultimate goal is to track the desired trajectory. However, the challenge of achieving high accuracy and dynamic performance is increased due to the nonlinear flexibilities found in rigid-link flexible-joint (RLFJ) manipulators. Some researchers have designed observers to estimate states in the robot model, since link positions/velocities are typically not measured in the industrial robot system. Nicosia and Tomei [1, 2] designed a controller combined with the observer which estimates motor positions or/and motor velocities for RLFJ manipulators. Dixon et al. [3] developed a globally adaptive output-feedback tracking controller for the RLFJ dynamics, which is based on the link velocity filter. Globally, output-feedback methods are not easily implemented in the real system because of the requirement of link position measurements which are not frequently measured in real systems. A controller was designed in [4, 5] by using a neural network (NN) observer to estimate link and motor positions/velocities and dynamic parameters. But NN observer-based controllers do not take advantage of motor positions. Kalman filter (KF) and extended Kalman filter (EKF) are utilized to estimate positions of joints or/and end effectors, driving torque, and dynamic parameters for manipulators [6]. Lightcap and Banks [7] designed an EKF-RLFJ controller by using EKF to estimate link and motor positions/velocities. Garcła et al. [8] proposed compliant robot motion controllers by using EKF to fuse wrist force sensors, accelerometers, and joint position sensors. EKF-based sensor fusion was presented by Jassemi-Zargani and Necsulescu [9] to estimate the acceleration for operational space control of a robotic manipulator. However, these reported EKF-based control methods do not discuss the case of asynchronous measurements from multirate sensors for RLFJ manipulators.

Observer-based sliding mode control (SMC) is one of the most important approaches to handle systems with uncertainties and nonlinearities [10]. For the RLFJ manipulator system, observer-based SMC of robot manipulators has been widely studied since the state of manipulators (e.g.,

acceleration velocity of joints) need not always be measured directly [11]. The terminal SMC (TSMC) is used in rigid manipulator control (e.g., robust TSMC and finite-time control) since it has some superior properties compared with SMC such as better tracking precision and fast error convergence [12–14]. In particular, the singularity problem of the TSMC was addressed in [15, 16]. However, most of these papers use the continuous-time dynamic model of the manipulator. Indeed, discrete-time models exist widely in the real digital control system. It has been proved that the discrete-time SMC has technological advances in digital electronics, computer control, and robotic system. Corradinia and Orlando [17] presented a robust DSMC coupled with an uncertainty estimator designed for planar robotic manipulators. However, the flexibilities of joints are not involved in those controller designs.

To remedy such limitations, the paper proposes a novel controller, AMSFE-DTSMC, which is implemented based on DTSMC coupled with an asynchronous multirate sensor fusion estimator. The robotic multirate sensor unit contains vision and non-vision-based sensors whose sampling rate and processing time are different. In the proposed scheme, the delayed slow sampling vision measurement is treated as a kind of periodic "out-of-sequence" measurement (OOSM) [18] which is used to update the non-vision-based state estimation in an EKF-based asynchronous multirate sensor fusion algorithm. Using the position and velocity estimation from sensor fusion estimator, the DTSMC is designed by using a novel sliding surface which is implemented by considering estimation error and tracking error. The main contributions of this work are summarized as follows.

(i) We propose a novel tracking control scheme, AMSFE-DTSMC, which is based on the DTSMC coupled with the sensor fusion estimator for a RLFJ manipulator. The sliding surface of AMSFE-DTSMC is designed by utilzing estimation error and tracking control error.

(ii) We construct an asynchronous multirate measurement model for robotic sensors and design a sensor fusion to fuse such asynchronous multirate data for robotic state estimation.

This paper is organized as follows. Section 2 gives the problem formulation. In Section 3, the multirate sensor data fusion algorithm is presented. Section 4 designs a novel DTSMC for tracking control. The simulation and experimental studies are implemented in Section 5. The paper ends with conclusion about the proposed approach.

2. Problem Formulation

In this paper, a robotic manipulator system is given with the sensor unit including joint motor encoders and cameras fixed in the workspace. The tracking control scheme for RLFJ manipulators can be developed by using the robotic state estimate via multisensor fusion. The state of the robot is estimated by these sensors directly and indirectly; however, there are some limitations for a single sensor to obtain precise information. To fuse asynchronous multirate data from different sensors, the dynamic and sensor models are formulated in this section.

2.1. Discrete Rigid-Link Flexible-Joint Robot Model. The discrete dynamic model of an n–link RLFJ manipulator can be obtained by the minimization of the action functional suggested by Nicosia [2] as follows:

$$q(k+1) = q(k) + T\dot{q}(k), \tag{1a}$$

$$\dot{q}(k+1) - \dot{q}(k) = M^{-1}(\overline{q},\theta)TK_s\delta(k) - F_L(\overline{q},q,\dot{q},\theta)T, \tag{1b}$$

$$M_m\left[\dot{q}_m(k+1) - \dot{q}_m(k)\right] + F_m\dot{q}_m(k)T = Tu(k) - K_s\delta(k)T, \tag{1c}$$

$$\delta(k) = q_m(k) - q(k), \tag{1d}$$

where $q(k), \dot{q}(k)$ and $q_m(k), \dot{q}_m(k)$ denote the position, velocity of the link and motor angles at k time, respectively, $\overline{q}(k) \cong q(k) + T\dot{q}(k)$, T is the sampling interval, $M(\cdot)$ is the invertible inertia matrix which satisfies $\xi_{\min} \le \|M\| \le \xi_{\max}$, $F_L(\overline{q},q,\dot{q},\theta) = -M^{-1}(\overline{q},\theta)[M(\overline{q},\theta)\dot{q} - M(q,\theta)\dot{q} - Tf(q,\dot{q}),\theta]$, $f(\cdot)$ represents centrifugal, Coriolis and gravitational forces; K_s, M_m and F_m are constant, diagonal, positive-definite matrices representing joint stiffness, motor inertia, motor viscous friction, respectively; the joint deflection $\delta(k)$ is defined as the difference between the motor and link position and $u(k)$ denotes the motor torque; the unknown or varying dynamic parameter in the robotic model is defined as $\theta(k)$ which satisfy $\theta(k+1) - \theta(k) = Tw_\theta(k)$, the dynamics uncertainties of the links and motors are modeled with random variables $w_l(k)$ and $w_m(k)$.

Define a state vector

$$x(k) = \left[\, q(k)^T \;\; \dot{q}(k)^T \;\; q_m(k)^T \;\; \dot{q}_m(k)^T \;\; \theta(k)^T \,\right]^T. \tag{2}$$

The dynamics in equations (1a)–(1d) can be transformed to a state space representation:

$$x(k+1) = F_{k+1,k}(x(k),u(k)) + \Gamma_k\omega(k+1,k), \tag{3}$$

where

$$F_{k+1,k}(x(k),u(k)) = \begin{bmatrix} q(k) + T\dot{q}(k) \\ \dot{q}(k) - F_L(k)T + M^{-1}(\overline{q})\left(K_s\delta(k)T\right) \\ q_m(k) + T\dot{q}_m(k) \\ M_m^{-1}\left[\dot{q}_m(k) - F_m\dot{q}_m(k)T - K_s\delta(k)T + Tu(k)\right] \\ \theta(k) \end{bmatrix},$$

$$\Gamma_k = \begin{bmatrix} 0 & 0 & 0 \\ M(\overline{q},\theta)^{-1} & 0 & 0 \\ 0 & 0 & 0 \\ 0 & M_m^{-1} & 0 \\ 0 & 0 & IT \end{bmatrix}, \tag{4}$$

$$\omega(k+1,k) = \left[w_l(k)^T, w_m(k)^T, w_\theta(k)^T\right]^T.$$

2.2. Measurement Model. The observation vector is given by

$$h(x(k)) = \left(q_m(k)^T\ \dot{q}_m(k)^T\ y(k)^T\right)^T, \tag{5}$$

where $q_m(k), \dot{q}_m(k)^T$ are the position and velocity of motor angles and $y(k)$ represents the position of the end effector in image space observed by a fixed camera.

By using the standard pinhole camera model, the mapping from the Cartesian space to image space is given by

$$y(k) = I_m(r(k)), \tag{6}$$

where $r(k)$ denotes the position of the end effector in the Cartesian space and $I_m(\cdot)$ is a transformation function from task space to image space. From the forward kinematics, the position relationship between robotic joints and end effector is described by a transform relationship as follows:

$$r(k) = F_k(q(k)), \tag{7}$$

where $r(k)$ is the position of the end effector at kth time and $F_k(\cdot)$ is a transformation function from the joint space to task space.

From the equations (6) and (7), The joint position can be observed by a fixed camera:

$$y(k) = I_k(q(k)), \tag{8}$$

where $I_k(\cdot) = I_m(F_k(\cdot))$ is the mapping from the joint space to image space. With the random noise $\nu(k) = \left[\nu_1^T\ \nu_2^T(k)\nu_3^T(k)(k)\right]$, the measurement equation is given by

$$z^i(k) = h_k^i(x(k)) + \nu^i(k), \quad i = c, m, \tag{9}$$

where $z^i(k)$ is the measurement of the state from different sensor, $i = c$ denotes the camera measurement, and $i = m$ represents the measurement from motors. We assume that the process noise $\omega(k)$ and measurement noise $\nu(k)$ are sampled from the independent and identically distributed white Gaussian noise which satisfies following equations at time t_k:

$$\begin{cases} E\{\omega(k+1,k)\} = 0, \\ E\{\nu(k)\} = 0, \\ E\left\{\nu(j)\omega^T(k+1,k)\right\} = 0, \\ E\left\{\omega(j+1,j)\omega_N^T(k+1,k)\right\} = Q(k)\delta_{jk}, \\ E\left\{\nu(j)\nu^T(k)\right\} = R(k)\delta_{jk}. \end{cases} \tag{10}$$

Since the measurement of the vision sensor at time t_k is obtained from the visual image taken at time step $t_\kappa = t_k - t_d$, t_d denotes the delay time. The relation of different sensors' sampling rates is given by

$$s_m = ls_c, \tag{11}$$

where s_m and s_c denote the sampling rate of motor encoders and visual sensors, respectively, and l is a positive integer.

We show the sampling rate difference between vision and non-vision measurements in Figure 1, where l step lags of vision measurements are described. According to the characteristics of visual sensor, we treat the vision measurements as the periodic l-step lag out-of-sequence measurements.

Remark 1. The velocity of joints (or/and end effector) also can be observed by vision sensors, $\dot{y}(k) = J_{ik}(q(k))\dot{q}(k)$, with the Jacobian matrix $J_{ik}(q) = J_i(r)J_k(q)$ mapping from the joint space to the image space. $J_i(r)$ is the image Jacobian matrix, and $J_k(q)$ denotes the Jacobian matrix from joint space to task space. However, the measurement of velocity is always impaired by the noisy image data with slow sampling rate and the dynamic uncertainties in the RLFJ manipulator system. Therefore, the velocity measurement in the image space is not utilized in the measurement model.

Remark 2. Assume that the camera can cover the entire workspace of the robot. With the prior knowledge of motion planning of the robot, it is basically assumed that there is an one-to-one mapping from the image space to joint space in the real robotic system.

3. Asynchronous Multirate Sensor Fusion Estimation

According to the system model described in Section 2, the robotic link position can be estimated by using the multi-sensor system. For asynchronous multirate sensors, the sensor fusion method is designed to use the late measurements for updating the current estimated state to get a more accurate estimation in two steps:

Step 1: when the vision measurement is unavailable, the robotic state is estimated using the non-vision-based sensors which keep the real-time estimate by recovering the missing information between two vision samples.

Step 2: as the delayed vision measurement arrives at every vision sample at time $t = t_{lk}, l = 1, 2, \ldots$, the state should be re-estimated to cope with the limitations of other sensors in the absolute position measurement.

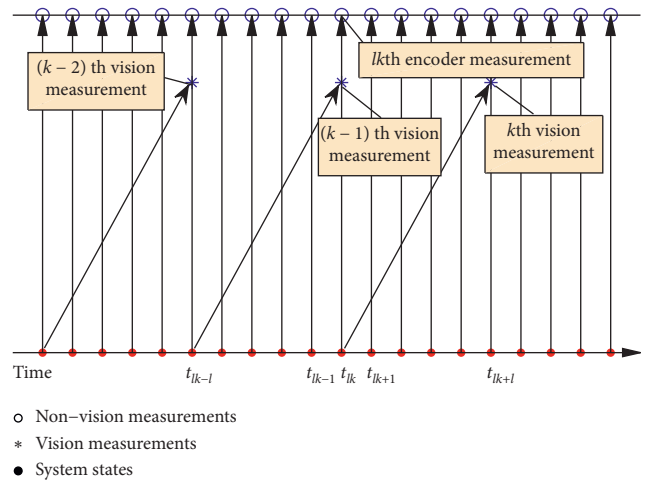

Figure 1: The schematic diagram of the relation between vision and non-vision measurements.

3.1. Estimation by Using Non-Vision Sensor Measurements. From Figure 1, before the $(k-1)$th vision frame is available, we have the estimation of the state at time t_{lk} using the non-vision sensor measurements:

$$\begin{aligned} \hat{x}(lk|lk) &= E\left\{x(lk)|Z_m^{lk}\right\}, \\ P(lk|lk) &= \operatorname{cov}\left\{x(lk)|Z_m^{lk}\right\}, \end{aligned} \tag{12}$$

where $Z_{lk}^m = \{z^m(1), z^m(2), \ldots, z^m(lk)\}$ represents all encoder motor measurements up to time t_{lk}. Using the extended Kalman filter (EKF), the estimation at time t_{lk} via the motor encoder measurement is given as follows:

$$\hat{x}^-(lk|lk) = F_{lk,lk-1}(\hat{x}(lk-1|lk-1), u(lk)), \tag{13}$$

$$P(lk|lk-1) = A_{lk}P(lk-1|lk-1)A_{lk}^T + W_{lk}Q(lk-1)W_{lk}^T, \tag{14}$$

$$K_{lk} = P(lk|lk-1)H_{lk}^T\left[H_{lk} \times P(lk|lk-1)H_{lk}^T + R(lk)\right]^{-1}, \tag{15}$$

$$\hat{x}(lk|lk) = \hat{x}^-(lk|lk) + K_{lk}\left(z^m(lk) - h_{lk}^m(\hat{x}^-(lk|lk), 0)\right), \tag{16}$$

$$P(lk|lk) = (I - K_{lk}H_{lk})P(lk|lk-1), \tag{17}$$

where A_{lk}, W_{lk}, H_{lk}, and V_{lk} are Jacobian matrices and K_{lk} is the correction gain vector. According to above equations, the state and covariance estimates are updated with the measurement with a fast sampling rate.

3.2. Re-Estimation via Vision Sensor Measurements. Suppose that at the time t_{lk} the vision measurement at time $t_\kappa = t_{kl-l}$ is obtained. A new estimation $\hat{x}(lk|\kappa^+)$ is calculated using the information about the delayed $(k-1)$th vision measurement $z^c(\kappa)$. $\hat{x}(lk|\kappa^+)$ is defined with $\mathbb{Z}_{lk} = \{Z_{lk}^m, z^c(\kappa)\}$:

$$\begin{aligned} \hat{x}(lk|\kappa^+) &= E\{x(lk)|\mathbb{Z}_{lk}\}, \\ P(lk|\kappa^+) &= \operatorname{cov}\{x(lk)|\mathbb{Z}_{lk}\}. \end{aligned} \tag{18}$$

The delayed measurement $z^c(\kappa)$ observed by vision measurement will be used to correct the accumulated estimation errors which are caused by sensors with fast sampling rate. The equations for updating the estimation $\hat{x}(lk|lk)$ with the delayed vision measurement $z^c(\kappa)$ are given by

$$\hat{x}(lk|\kappa^+) = \hat{x}(lk|lk) + P_{xz}(lk,\kappa|lk) \times P_{zz}(\kappa|lk)^{-1}[z(\kappa) - \hat{z}(\kappa|lk)], \tag{19}$$

$$P(lk|\kappa^+) = P(lk|lk) - P_{xz}(lk,\kappa|lk) \times P_{zz}(\kappa|lk)^{-1}P_{xz}(lk,\kappa|lk)^T, \tag{20}$$

where $P_{xz}(lk,\kappa|lk)$ represents cross covariance between $\hat{x}(lk|lk)$ and $\hat{z}(\kappa|lk)$, $P_{zz}(\kappa|lk)$ is the covariance of $\hat{z}(\kappa|lk)$ which denotes the estimation of measurement at time t_κ, and

$$\begin{aligned} P_{xz}(lk,\kappa|lk) &= E\left\{\tilde{x}(lk)\tilde{z}^c(\kappa)^T\right\}, \\ P_{xz}(lk,\kappa|lk) &= E\left\{\tilde{z}^c(\kappa)\tilde{z}^c(\kappa)^T\right\}, \\ \hat{z}(\kappa|lk) &= E\{z(\kappa)|Z_{lk}\}, \end{aligned} \tag{21}$$

with $\tilde{x}(lk) = x(lk) - \hat{x}(lk|lk), \tilde{z}^c(\kappa) = z^c(\kappa) - \hat{z}(\kappa|lk)]^T$.

Using the EKF, $P_{xz}(lk,\kappa|lk), P_{xz}(lk,\kappa|lk)$, and $\hat{z}(\kappa|lk)$ are obtained by assuming that the function $F_{k,\kappa}(\cdot)$ is invertible. Define $F_{lk,\kappa}^{-1}(\cdot) = F_{\kappa,lk}(\cdot)$ which denotes the backward transition function to estimate the state back from t_{lk} to t_κ. Since the previous state $x(\kappa)$ is not affected by present input signal $u(lk)$, we give the state relationship between t_κ and t_{lk} by

$$x(\kappa) = F_{\kappa,lk}(x(lk) - \omega(lk,\kappa)), \tag{22}$$

where the process noise $\omega(lk,\kappa)$ and covariance $Q(kl,\kappa)$ are calculated by

$$\begin{aligned}\omega(lk,\kappa) &\approx \Gamma_{lk}\omega(lk,lk-1)+A_{lk,lk-1}\Gamma_{lk-1}\omega(lk-1,lk-2)\\ &\quad+\cdots+A_{lk,lk-1}A_{lk-1,lk-2}\times\cdots\times A_{lk-l+2,lk-l+1}\Gamma_{lk-l+1}\omega(lk-l+1,lk-l),\\ Q(kl,\kappa) &= E\left\{\tilde{\omega}(lk,\kappa)\tilde{\omega}(lk,\kappa)^T\right\},\\ \tilde{\omega}(lk,\kappa) &= \omega(lk,\kappa)-\hat{\omega}(lk,\kappa).\end{aligned} \tag{23}$$

The estimation in equation (19) can be determined by

$$\begin{aligned}\hat{z}(\kappa|lk) &= H_{lk}^m(\kappa)\hat{x}(\kappa|lk),\\ \hat{x}(\kappa|lk) &= F_{\kappa,lk}(\hat{x}(lk|lk)-\hat{\omega}(lk,\kappa|lk)).\end{aligned} \tag{24}$$

To estimate the process noise as in equations (13)–(17), we have

$$\hat{\omega}(lk,\kappa|lk) = Q(lk,\kappa)H_{lk}^T P_{zz}(lk|lk-1)^{-1}\times(z(lk)-z(lk-1)). \tag{25}$$

Then, $P_{xz}(lk,\kappa|lk)$ and $P_{zz}(\kappa|lk)$ are obtained as follows:

$$\begin{aligned}P_{xz}(lk,\kappa|lk) &= \left(P(lk,\kappa|lk)-P_{x\omega}(lk,\kappa|lk)\right)A_{\kappa,lk}^T H(\kappa)^T,\\ P_{zz}(\kappa|lk) &= H(\kappa)P(\kappa|lk)H(\kappa)^T+R(\kappa),\end{aligned} \tag{26}$$

where the covariances $P(\kappa|lk)$ and $P_{x\omega}(lk,\kappa|lk)$ are derived as follows:

$$\begin{aligned}P(\kappa|lk) &= A_{\kappa,lk}\left(P(lk|lk)+P_{\omega\omega}(\kappa|lk)-P_{x\omega}(lk,\kappa|lk)^T\right)A_{\kappa,lk}^T-P_{x\omega}(lk,\kappa|lk),\\ P_{\omega\omega}(\kappa|lk) &= Q(lk,\kappa)-Q(lk,\kappa)H_{lk}^T\times P_{zz}(lk|lk-1)^{-1}H_{lk}Q(lk,\kappa)^T,\\ P_{x\omega}(lk,\kappa|lk) &= Q(lk,\kappa)-P(lk|lk-1)H_{lk}^T\times P_{zz}(lk|lk-1)^{-1}H_{lk}Q(lk,\kappa)^T.\end{aligned} \tag{27}$$

3.3. Summary of the Fusion Estimate Method. The state of a RLFJ manipulator is estimated using the indirect measurements from asynchronous multirate sensors. The sensor fusion estimate can be implemented in the practical application using a switching mechanism in accordance with sampling time. As shown in Figure 1, the update equations are chosen at the different sampling times. The state estimation can be given by

$$\hat{x}_F(k|k) = \begin{cases} F_{k,k-1}(\hat{x}^-(k|k)+K_k[z^m(k)-h_k^m(\hat{x}^-(k|k),0)], & t\neq t_{lk},\\ \hat{x}(k|k)+P_{xz}(k,k-l|k)P_{zz}^{-1}(k-l|k)(z^c(k-l)-\hat{z}(k-l|k)), & t=t_{lk}.\end{cases} \tag{28}$$

Remark 3. The exponential convergence of the sensor fusion estimate can be proved in the similar way which is presented in [19], which has more detailed conclusion on the stability.

4. Rigid-Link Flexible-Joint Tracking Control

In this section, the discrete-time terminal sliding mode tracking control-based fusion estimation (AMSFE-DTSMC) is presented for rigid-link flexible manipulators whose state is estimated by the sensor fusion method described in the previous section. The controller is designed by using both position and velocity of the link from the sensor fusion estimate. To design the novel controller, the model in (1a)–(1d) can written as

$$q(k+1) = q(k)+T\dot{q}(k), \tag{29a}$$

$$\dot{q}(k+1) = \dot{q}(k)+M^{-1}(\overline{q},\theta)Tu(k)-\mathbb{F}\left(\overline{q},q,\dot{\overline{q}}_m,\dot{q}_m,T,\theta\right), \tag{29b}$$

where $\mathbb{F}(\overline{q},q,\dot{\overline{q}}_m,\dot{q}_m,T,\theta) = F_L(\overline{q},q,\dot{q},\theta)T+M^{-1}(\overline{q},\theta)[M_m(\dot{q}_m(k+1)-\dot{q}_m(k))+F_m\dot{q}_m(k)]$ denotes the variable which includes dynamic parameters of links and motors.

In order to formulate the tracking control, define the tracking error $\tilde{q}_t(k)$ and estimation error $\tilde{q}_e(k)$ at time t_k as

$$\begin{aligned}\tilde{q}_t(k) &= q(k)-q_d(k),\\ \tilde{q}_e(k) &= q(k)-\hat{q}(k),\end{aligned} \tag{30}$$

where $q_d(k)$ is the desired position and $\hat{q}(k)$ denotes the estimation position.

Define the reference velocity for tracking and estimation:

$$\begin{aligned}\dot{q}_t(k) &= \dot{q}_d(k)+\Lambda_t(q_d(k)-\hat{q}(k))\\ &= \dot{q}_d(k)-\Lambda_t(\tilde{q}_t(k)-\tilde{q}_e(k)),\\ \dot{q}_e(k) &= \dot{\hat{q}}(k)-\Lambda_e(q(k)-\hat{q}(k))\\ &= \dot{\hat{q}}(k)-\Lambda_e\tilde{q}_e(k),\end{aligned} \tag{31}$$

where $\dot{\hat{q}}(k)$ denotes the estimation of $\dot{q}(k)$ and Λ_t,Λ_e are constants and diagonal matrices.

Define the filtered variables including the estimation error:

$$\dot{\tilde{q}}_t(k) = \dot{q}(k) - \dot{q}_t(k) = \dot{\tilde{q}}_t(k) + \Lambda_t\left(\tilde{q}_t(k) - \tilde{q}_e(k)\right). \quad (32)$$

Consider the discrete terminal sliding surface as follows:

$$s(k) = \dot{\tilde{q}}_t(k) + \lambda\tilde{q}_t(k)^p, \quad (33)$$

where λ is a positive constant diagonal parameter matrix and $p = p_1/p_2$, in which p_1 and p_2 are positive odd integers satisfying $p_2 > p_1$. Motivated by the reaching law presented by Weibing Gao et al. in [20], we use the reaching law for exponential discrete sliding mode control as follows:

$$s(k+1) = (I - Th)s(k) - T\varepsilon\operatorname{sgn}(s(k)), \quad (34)$$

where $\operatorname{sgn}(\cdot)$ is the signum function, $\varepsilon > 0$, and $h > 0$.

Since system states cannot be measured directly, parameters which contain variables $q(k), \dot{q}(k)$, and θ need to be estimated in the controller design. Assume that the estimate error and uncertainties are bounded, and we have

$$\begin{aligned} M(\overline{q},\theta) &= \widehat{M}(\overline{q},\theta) + \Delta M(\overline{q},\theta), \\ \mathbb{F}\left(\overline{q}, q, \dot{\overline{q}}_m, \dot{q}_m, T, \theta\right) &= \widehat{M}\mathbb{F}\left(\overline{q}, q, \dot{\overline{q}}_m, \dot{q}_m, T, \theta\right) + \Delta\mathbb{F}\left(\overline{q}, q, \dot{\overline{q}}_m, \dot{q}_m, T, \theta\right), \end{aligned} \quad (35)$$

where $\dot{\overline{q}}_m$ denotes $\dot{q}_m(k+1)$; $\widehat{M}(\overline{q},\theta) = M(\widehat{\overline{q}},\widehat{\theta})$ and $\widehat{\mathbb{F}}(\overline{q}, q, \dot{\overline{q}}_m, \dot{q}_m, T, \theta) = \mathbb{F}(\widehat{\overline{q}}, \widehat{q}, \dot{\widehat{\overline{q}}}_m, \widehat{\dot{q}}_m, T, \widehat{\theta})$ represent the estimation of dynamic parameters; and $\Delta M(\overline{q},\theta)$ and $\Delta\mathbb{F}(\overline{q}, q, \dot{\overline{q}}_m, \dot{q}_m, T, \theta)$ are bounded variables including the estimation error and system uncertainties, which satisfy

$$\begin{aligned} \|\Delta M(\overline{q},\theta)\| &\le \delta_M, \\ \left\|\Delta\mathbb{F}\left(\overline{q}, q, \dot{\overline{q}}_m, \dot{q}_m, T, \theta\right)\right\| &\le \delta_{\mathbb{F}}, \end{aligned} \quad (36)$$

where δ_M and δ_F are constants.

Theorem 1. *Consider the rigid-link flexible-joint manipulator system described by equations (29a) and (29b) and the discrete sliding manifold described by equation (33); by using the reaching law in equation (34), stable control law is designed as*

$$\begin{aligned} u(k) = \frac{\widehat{M}(\overline{q},\theta)}{T}\Big[&\widehat{\mathbb{F}}\left(\overline{q}, q, \dot{\overline{q}}_m, \dot{q}_m, T, \theta\right) + \dot{q}_t(k) - \dot{q}_t(k-1) + \lambda\tilde{q}_t^p(k) \\ &- \lambda\left[T\left(\dot{\tilde{q}}_t(k) - \Lambda_t\tilde{q}_t(k) + \Lambda_t\tilde{q}_e(k)\right) + \tilde{q}_t(k)\right]^p \\ &- T\left(hs(k) + \varepsilon(k)\operatorname{sgn}(s(k))\right)\Big], \end{aligned} \quad (37)$$

where ε and h are positive diagonal matrices which satisfy the following inequations:

$$\begin{aligned} \varepsilon(k) > \frac{1}{T}\xi_{\mathbb{M}}&\left\|\Delta\dot{q}_t(k) - \lambda\left[T\left(\dot{\tilde{q}}_t(k) - \Lambda_t\tilde{q}_t(k) + \Lambda_t\tilde{q}_e(k)\right) + \tilde{q}_t(k)\right]^p - \lambda\tilde{q}_t^p(k)\right\| \\ &+ \frac{1}{T}\xi_{\mathbb{F}} + h\|s(k)\|, \end{aligned} \quad (38)$$

$$T < \frac{2\|s(k) - \Delta\mathbb{F}\|}{h\|s(k)\| + \|\varepsilon(k)\|}. \quad (39)$$

Proof. Substituting control law (37) in the rigid-link flexible-joint system equations (29a) and (29b), the error dynamics are obtained:

$$\tilde{q}_t(k+1) = \tilde{q}_t(k) + T\left(\dot{\tilde{q}}_t(k) - \Lambda_t\tilde{q}_t(k) + \Lambda_t\tilde{q}_e(k)\right), \quad (40)$$

$$\begin{aligned} \dot{\tilde{q}}_t(k+1) = \dot{\tilde{q}}_t(k) &+ \lambda\tilde{q}_t(k)^p \\ &- \lambda\left[T\left(\dot{\tilde{q}}_t(k) - \Lambda_t\tilde{q}_t(k) + \Lambda_t\tilde{q}_e(k)\right) + \tilde{q}_t(k)\right]^p \\ &+ \left(M^{-1}\widehat{M} - I\right)\Big[\widehat{\mathbb{F}} + \Delta\dot{q}_t(k) - \lambda\Big[T\Big(\dot{\tilde{q}}_t(k) \\ &- \Lambda_t\tilde{q}_t(k) + \Lambda_t\tilde{q}_e(k)\Big) + \tilde{q}_t(k)\Big]^p - \lambda\tilde{q}_t^p(k)\Big] \\ &+ M^{-1}\widehat{M}\left[\Delta\mathbb{F} - T\left(hs(k) + \varepsilon(k)\operatorname{sgn}(s(k))\right)\right]. \end{aligned} \quad (41)$$

For simplicity, define $\mathbb{M} = M^{-1}\widehat{M}$ which is invertible and $\mathbb{M}^{-1} = \widehat{M}^{-1}M$. Substituting (40) and (41) into (34) yields

$$\begin{aligned} s(k+1) = s(k) &+ \mathbb{M}[-T(hs(k) - \varepsilon(k)\operatorname{sgn}(s(k)))] \\ &+ \mathbb{M}\widehat{\mathbb{F}} - \mathbb{F} + (\mathbb{M} - I)\left[\Delta\dot{q}_t(k) - \lambda\tilde{q}_t^p(k)\right. \\ &\left. - \lambda\left[T\left(\tilde{\dot{q}}_t(k) - \Lambda_t\tilde{q}_t(k) + \Lambda_t\tilde{q}_e(k)\right) + \tilde{q}_t(k)\right]^p\right]. \end{aligned} \tag{42}$$

Stability conditions for the discrete sliding mode control are given by Sarpturk [21]:

$$s^T(k)(s(k+1) - s(k)) < 0, \tag{43a}$$

$$s^T(k)(s(k+1) + s(k)) > 0. \tag{43b}$$

Combining (42) and (43a), we have

$$\begin{aligned} s^T[-\mathbb{M}T[hs(k) + \varepsilon(k)\operatorname{sgn}(s(k))] + \mathbb{M}\widehat{\mathbb{F}} - \mathbb{F} \\ + (\mathbb{M} - I)\left[\Delta\dot{q}_t(k) - \lambda\left(T\tilde{\dot{q}}_t(k) - T\Lambda_t\tilde{q}_t(k)\right.\right. \\ \left.\left. + T\Lambda_t\tilde{q}_e(k) + \tilde{q}_t(k)\right)^p - \lambda\tilde{q}_t^p(k)\right]\Big] < 0. \end{aligned} \tag{44}$$

If $s(k) > 0$, $\operatorname{sgn}(s(k)) = 1$, and $s(k+1) - s(k) < 0$, the sliding gain lower bound can be given as

$$\begin{aligned} \varepsilon(k) > \frac{1}{T}\left(I - \mathbb{M}^{-1}\right)\Big[-\lambda\Big[T\Big(\tilde{\dot{q}}_t(k) - \Lambda_t\tilde{q}_t(k) \\ + \Lambda_t\tilde{q}_e(k)\Big) + \tilde{q}_t(k)\Big]^p - \lambda\tilde{q}_t^p(k)\Big] + \frac{1}{T}\left(I - \mathbb{M}^{-1}\right)\Delta\dot{q}_t(k) + \frac{1}{T}\left(\widehat{\mathbb{F}} - \mathbb{M}^{-1}\mathbb{F}\right) - hs(k), \end{aligned} \tag{45}$$

Employ $\xi_{\mathbb{M}}$ and $\xi_{\mathbb{F}}$ which satisfy $\|I - \mathbb{M}^{-1}\| < \xi_{\mathbb{M}}$, $\|\widehat{\mathbb{F}} - \mathbb{M}^{-1}\mathbb{F}\| < \xi_{\mathbb{F}}$, we can obtain $\varepsilon(k)$ as follows:

$$\begin{aligned} \varepsilon(k) > \frac{1}{T}\xi_{\mathbb{M}}\Big\|\Delta\dot{q}_t(k) - \lambda\Big[T\Big(\tilde{\dot{q}}_t(k) - \Lambda_t\tilde{q}_t(k) + \Lambda_t\tilde{q}_e(k)\Big) \\ + \tilde{q}_t(k)\Big]^p - \lambda\tilde{q}_t^p(k)\Big\| + \frac{1}{T}\xi_{\mathbb{F}} + h\|s(k)\|. \end{aligned} \tag{46}$$

If $s(k) < 0$, then $\operatorname{sgn}(s(k)) = -1$, and $s(k+1) - s(k)$ can be calculated by

$$\begin{aligned} s(k+1) = s(k) + \mathbb{M}T[\varepsilon(k) - hs(k)] + \mathbb{M}\widehat{\mathbb{F}} - \mathbb{F} \\ + (\mathbb{M} - I)\left[\Delta\dot{q}_t(k) - \lambda\tilde{q}_t^p(k) - \lambda\left[T\left(\tilde{\dot{q}}_t(k) - \Lambda_t\tilde{q}_t(k) + \Lambda_t\tilde{q}_e(k)\right) + \tilde{q}_t(k)\right]^p\right]. \end{aligned} \tag{47}$$

Employ $\varepsilon(k)$ given by equation (46), and we have

$$\begin{aligned} s(k+1) - s(k) > \mathbb{M}Th[\|s(k)\| - s(k)] \\ + \left[\mathbb{M}\xi_{\mathbb{F}} - \mathbb{M}\widehat{\mathbb{F}} + \mathbb{F}\right] \\ + \mathbb{M}\xi_{\mathbb{M}}\Big\|\Delta\dot{q}_t(k) - \lambda\left[T\tilde{\dot{q}}_t(k) - T\Lambda_t\tilde{q}_t(k)\right. \\ \left. + T\Lambda_t\tilde{q}_e(k) + \tilde{q}_t(k)\right]^p - \lambda\tilde{q}_t^p(k)\Big\| \\ - (\mathbb{M} - I)\Big[\Delta\dot{q}_t(k) - \lambda\Big(T\tilde{\dot{q}}_t(k) - T\Lambda_t\tilde{q}_t(k) \\ + T\Lambda_t\tilde{q}_e(k) + \tilde{q}_t(k)\Big)^p - \lambda\tilde{q}_t^p(k)\Big], \end{aligned} \tag{48}$$

where $s(k+1)-s(k)>0$ is obtained by adopting $\varepsilon(k)$ according to equation (46). Therefore, equation (46) satisfied the Sarpturk stability (43a).

Assuming $\mathbb{M}=I$, Sarpturk condition (3) is formulated by combining equations (42) and (43b):

$$s(k+1)+s(k)=2s(k)-\Delta\mathbb{F} - T[hs(k)+\varepsilon(k)\mathrm{sgn}(s(k))]. \tag{49}$$

If $s(k)<0$, $s(k+1)+s(k)<0$, we have

$$2s(k)-T(hs(k)-\varepsilon(k))-\Delta\mathbb{F}<0. \tag{50}$$

Else if $s(k)>0$, $s(k+1)+s(k)>0$, we have

$$2s(k)-T(hs(k)+\varepsilon(k))-\Delta\mathbb{F}>0. \tag{51}$$

The sampling time T which satisfies the following equation can guarantee the condition in (43b):

$$0<T<\frac{2\|s(k)-\Delta\mathbb{F}\|}{h\|s(k)\|+\|\varepsilon(k)\|}. \tag{52}$$

From (52), we know that the stability conditions of DTSMC given by (43a) and (43b) are guaranteed by chosen parameters ε and h defined in (38) and (39). Theorem 1 is proved. □

5. Simulation and Experimental Studies

5.1. Simulation Study. The results obtained from the simulation of proposed control scheme on a two-link RLFJ manipulators shown in Figure 2 are presented in this section. In the simulation, the aim is make the RLFJ manipulator track desired trajectories $q_{1,d}=\sin(\pi t)$ and $q_{2,d}=\cos(\pi t)$ from the initial position $[q_{1i}\,q_{2i}]=[0.5,0.5]$. The robotic dynamic parameters are given by

$$\begin{aligned}
M(q)&=\begin{bmatrix} M_{11} & M_{12}\\ M_{21} & m_2l_2^2\end{bmatrix},\\
g(q)&=\begin{bmatrix} g_1\\ -m_2gl_2\sin(q_1+q_2))\end{bmatrix},\\
C&=\begin{bmatrix} -m_2l_1l_2\sin(q_2)\left(2\dot{q}_1\dot{q}_2+\dot{q}_2^2\right)\\ -m_2l_1l_2\sin(q_2)\dot{q}_1\dot{q}_2,\end{bmatrix},\\
M_{11}&=m_1+m_2)l_1^2+m_2l_2^2+2m_2l_1l_2\cos(q_2),\\
M_{12}&=M_{21}=m_2l_2^2+m_2l_1l_2\cos(q_2),\\
g_1&=-(m_1+m_2)gl_1\sin(q_1)-m_2gl_2\sin(q_1+q_2),
\end{aligned} \tag{53}$$

where m_i and l_i are given in Table 1. For $i=1,2$, m_i and l_i denote mass and length of the ith link. $k_m=\mathrm{diag}\{10,10\}$Num/rad, $M_m=\mathrm{diag}\{0.5,0.5\}\,\mathrm{kg}\cdot\mathrm{m}^2$, $F_m=\mathrm{diag}\{4,0.5\}\,\mathrm{Nm}\cdot\mathrm{sec/rad}$.

In order to demonstrate the influence of estimation for tracking performance, a DTSMC controller without estimation is also simulated. The DTSMC control law is given by

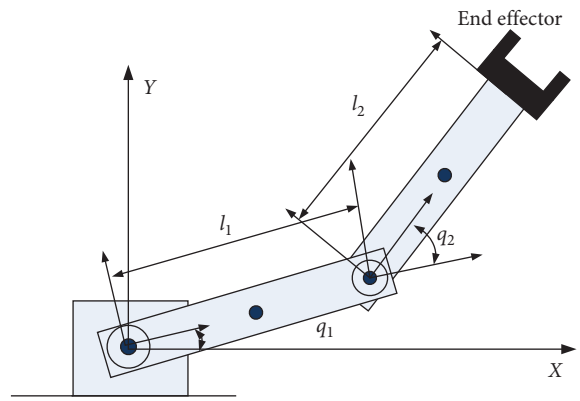

Figure 2: The schematic diagram of robotic manipulator with kinematics parameters.

Table 1: The manipulator parameters.

Link$_i$	m_i (kg)	l_i (cm)	q_i
1	2.5	35	q_1 (0° ~ 180°)
2	3	20	q_2 (−160° ~ 160°)

$$\begin{aligned}
u(k)=\frac{\widehat{M}}{T}\Big[&\widehat{\mathbb{F}}+\left(\dot{q}_d(k)-\dot{q}_d(k-1)+\lambda\tilde{q}_t^p(k)\right.\\
&\left.-\lambda\left[T\dot{\tilde{q}}_t(k)+\tilde{q}_t(k)\right]^p\right]-hs(k)-\varepsilon(k)\mathrm{sgn}(s(k)),
\end{aligned} \tag{54}$$

with a sliding surface $s(k)=\dot{\tilde{q}}_t(k)+\lambda\tilde{q}_t(k)^p$ which is different from proposal sliding mode surface.

Parameters of the proposed controller and DTSMC are selected as $T=0.001$ s, $h=\mathrm{diag}\{2,2\}$, $\lambda=\mathrm{diag}\{1.5,1.5\}$, $\Lambda_t=\mathrm{diag}\{5,5\}$, and $\varepsilon=\mathrm{diag}\{25,25\}$. $\theta(k)=0.15$ is chosen as a constant model parameter whose initial value is $\theta(k)=0$, $p=3$, $q=5$, $\xi_{\mathbb{M}}=\mathrm{diag}\{3,3\}$, and $\xi_{\mathbb{F}}=\mathrm{diag}\{1,1\}$. In the simulation, as shown in Figure 3, we assume that the end effector is observed by a fixed camera whose delayed measurements are used directly to calculate the joint position. The delayed time of slow measurement is 0.125 s. The process and measurement noise are chosen as $Q=0.01I$ and $R=0.1I$. The initial position value of joints (joint1, joint2) for tracking control is given by $(0.5\,\mathrm{rad}, 0.5\,\mathrm{rad})$, and for fusion estimator, it is given by $(0.9\,\mathrm{rad}, 0.9\,\mathrm{rad})$. The initial velocity value for tracking control is given by $(0,0)$, and for estimation, it is given by $(0.25\,\mathrm{rad/s}, 0)$.

The estimate errors of position and velocity are plotted in Figure 4. The estimate errors of parameter θ are shown in Figure 5. The position tracking of the proposed method for two links is shown in Figures 6 and 7 where the comparative result of SMC without fusion estimator is also plotted. In conclusion, the simulation results clearly indicate that the proposed approach guarantees the convergence of tracking errors and has better tracking accuracy.

5.2. Experimental Study. To validate the applicability of the proposed control schemes, a single-link flexible-joint

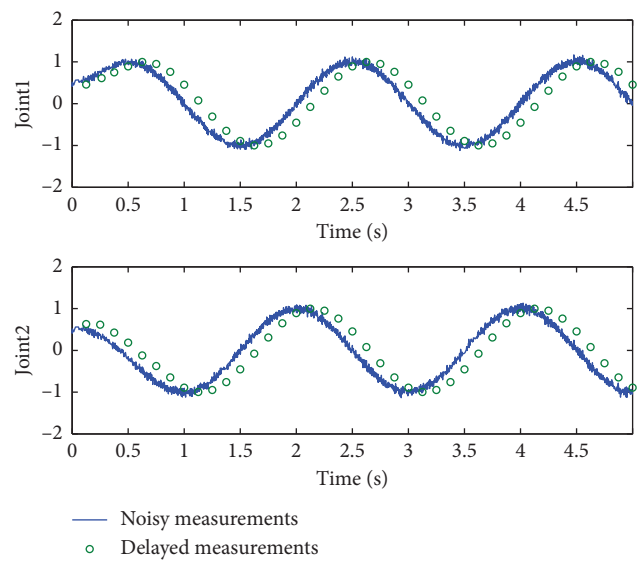

Figure 3: Asynchronous multirate sensor measurements.

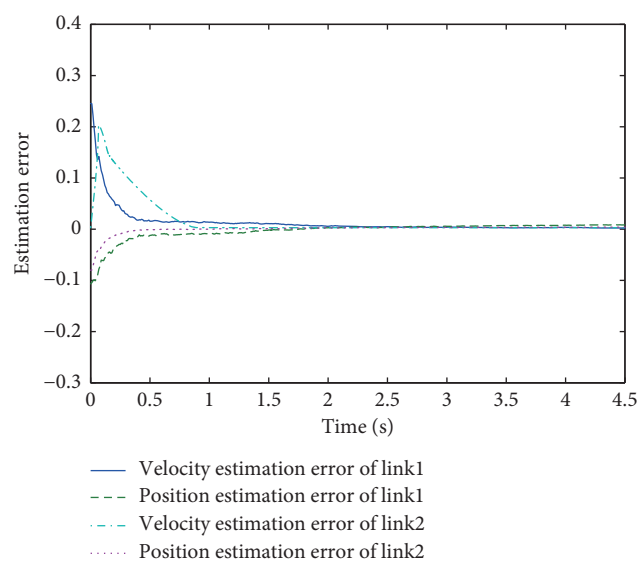

Figure 4: The estimation errors of $q_1, \dot{q}_1, q_2, \dot{q}_2$.

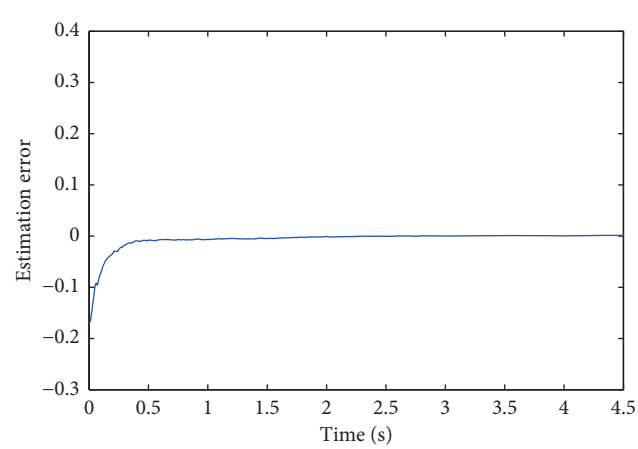

Figure 5: The estimation error of θ.

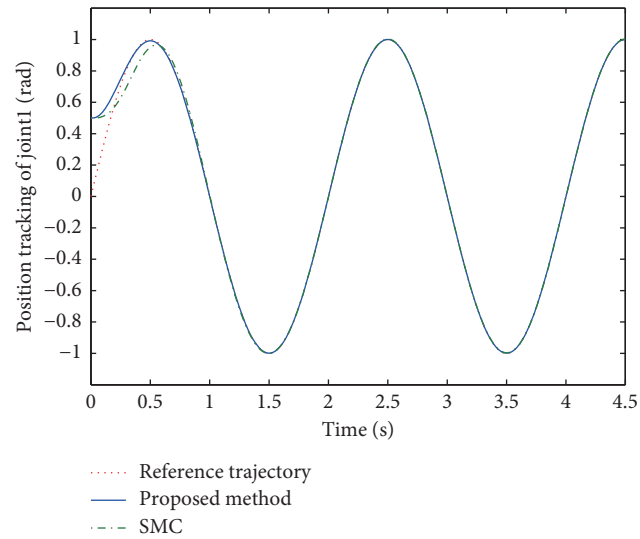

Figure 6: Comparative control performances of joint1 between the proposed method and SMC.

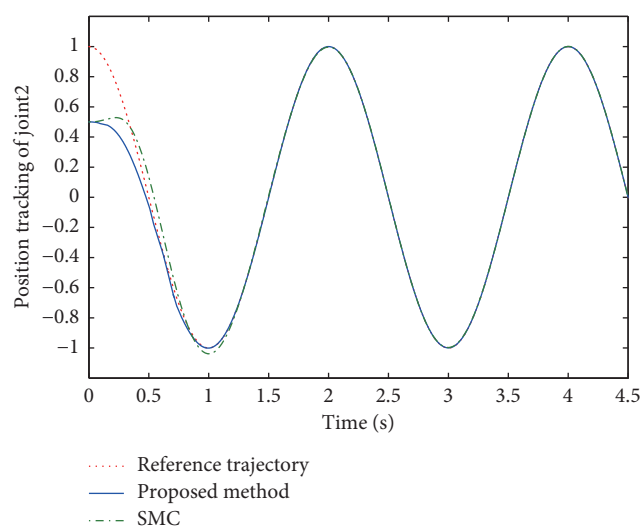

Figure 7: Comparative control performances of joint2 between the proposed method and SMC.

manipulator with a fixed camera is employed as the experimental plant which is shown in Figure 8. The aim is to make the end effector move along the desired trajectory $x_d = l_1 \cos(q_d)$, $y_d = l_1 \sin(q_d)$ with $q_d = (0.4 - t)/75$, and the initial position of joint is $q_i = 0.35$ rad. Parameters of the single-link robot are measured offline: $l_1 = 0.6$ m and $m_1 = 10$ kg; the measurement errors are $\Delta l_1 = 0.05$ m and $\Delta m_1 = 0.1$ kg.

To observe the state of end effector, the calibrated camera is fixed perpendicular to the robot notion plane. The coordinate relation of Cartesian space and image space is shown in Figure 9. Camera measurements are obtained from the image sequences shown in Figure 10. We define the position in the image coordinate $y(k) = [x_m(k), y_m(k)]$ given in Figure 11, and the position in Cartesian coordinate

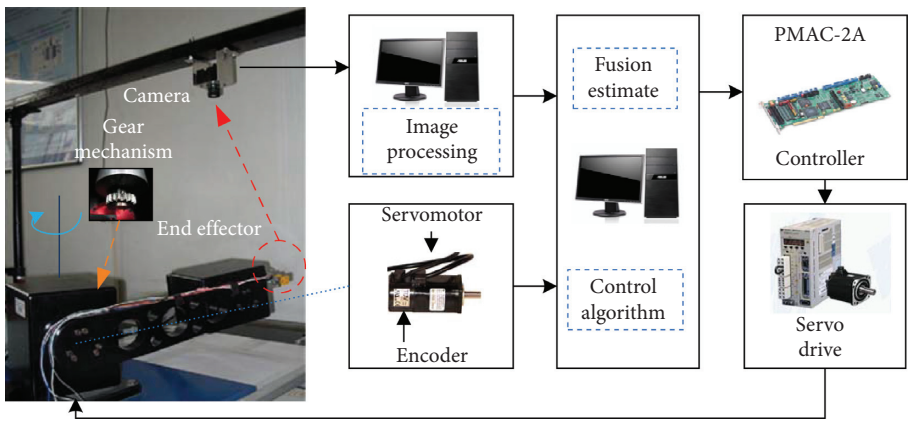

Figure 8: The experiment setup.

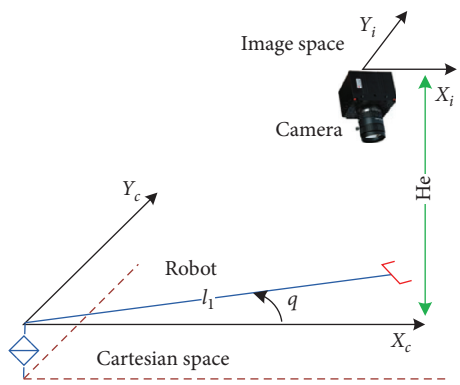

Figure 9: The coordinate relation of Cartesian space and image space.

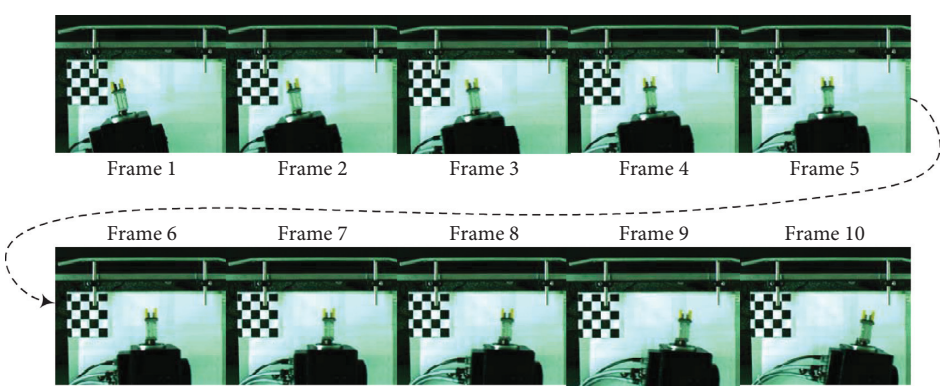

Figure 10: The image sequences of 10 frames.

is $r(k) = [x_c(k), y_c(k)]$. By using the pinhole camera model, we calculate the mapping from the joint space to image space $I_k(\cdot)$ in equation (14) as follows:

$$\frac{f}{H_c - f}\begin{bmatrix} x_m(k) \\ y_m(k) \end{bmatrix} = \begin{bmatrix} x_c(k) \\ y_c(k) \end{bmatrix} = \begin{bmatrix} l_1 \cos q(k) \\ l_2 \sin q(k) \end{bmatrix}, \tag{55}$$

where H_c is the perpendicular distance between the camera and the robot motion plane and f denotes the focal length of the camera. In the experiment, camera parameters are $f = 0.035$ m, 640×512 pixels, and $H_c = 0.8$ m. According to the mapping $I_k(\cdot)$, the joint position can be obtained by calculating the inverse circular trigonometric functions $\arccos[x_m(k) f/(l_1(H_c - f))]$ or $\arcsin[y_m(k) f/(l_1(H_c - f))]$. The delayed vision measurements $[x_m(k), y_m(k)]$ are converted to joint measurements $\arccos[x_m(k) f/(l_1(H_c - f))]$ which are shown in Figure 12, where the encoder measurements are also plotted. The position estimation of

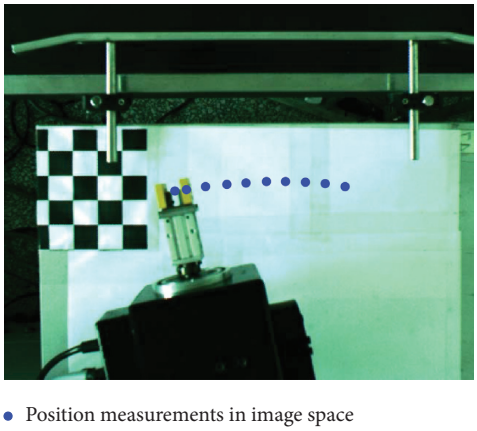

Figure 11: The trajectories of end effector in image space.

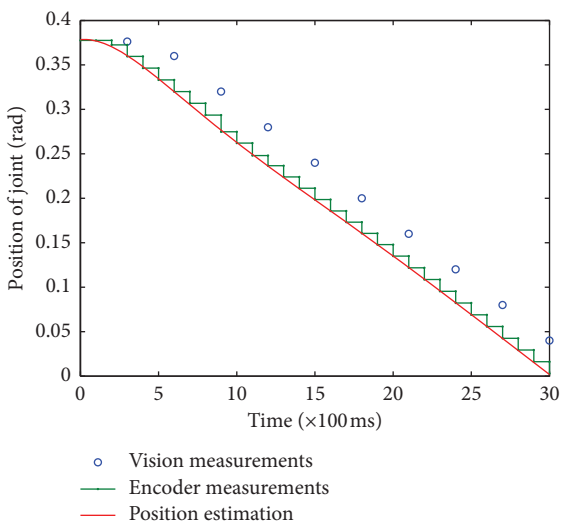

Figure 12: The encoder and visual measurements.

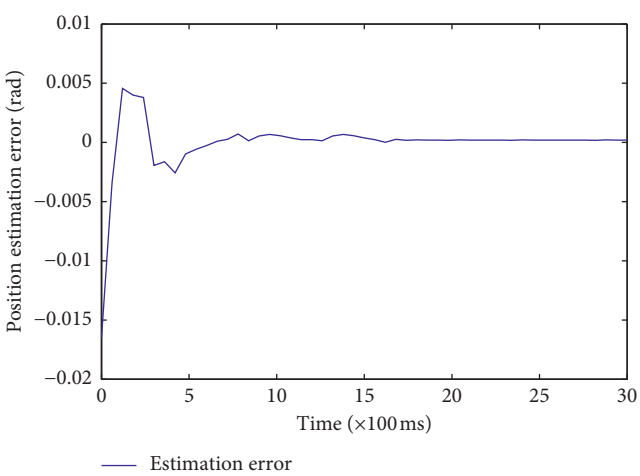

Figure 13: The position estimation error of the joint.

the joint is calculated by using the proposed fusion estimate method shown as red solid line in Figure 12. To show the

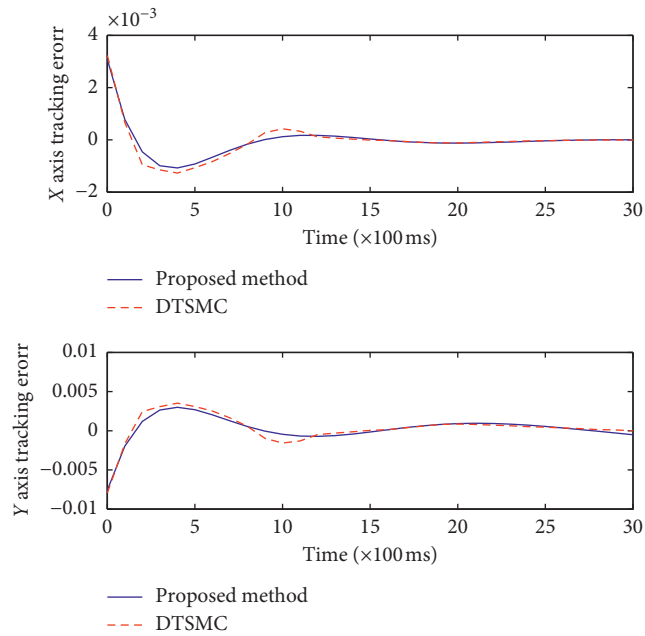

Figure 14: Comparative position tracking errors of the end effector.

performance detail of the fusion estimate method, Figure 13 shows the error of joint position estimation.

To validate the performance of the fusion estimate-based DTSMC, comparative experiments are implemented in this paper. The proposed controller and a DTSMC without estimator are employed in this test. Parameters are selected as $T = 0.01\,\mathrm{s}$, $h = 3$, $\lambda = 2$, $\Lambda_t = 4$ and $\varepsilon = 20$, $\theta(k) = 0.05$; $p = 3$, $q = 5$, $\xi_{\mathbb{M}} = 0.2$ and $\xi_{\mathbb{F}} = 2$. According to the comparative position tracking performances given in Figure 14, it is obvious that the proposed controller provides a superior behavior.

6. Conclusion

A novel RLFJ manipulator tracking controller, AMSFE-DTSMC, is proposed in this paper based on DTSMC coupled with asynchronous multirate sensor fusion. States of the manipulator are estimated by EKF-based sensor fusion algorithm which combines asynchronous multirate measurements from visual and non-vision-based sensors. Compared with the non-vision measurements, visual measurements are considered as periodic out-of-sequence measurements, which are used to re-estimate the state. With the state estimation, DTSMC is designed by using a novel sliding surface that includes tracking error and estimation error. By using the Sarpturk inequalities, boundedness of the controlled variables is proved. The effectiveness of the proposed approach is shown in simulation and experimental studies.

Data Availability

No data were used to support this study.

Disclosure

An earlier version of multirate sensor fusion-based DTSMC has been presented in the 10th International Conference on Control and Automation (ICCA) [12]; however, a totally new controller is designed by using a new sliding surface including both tracking error and estimation error in this paper, and the effectiveness of the proposed approach is proved both in the simulation and experimental studies.

Conflicts of Interest

The authors declare that they have no conflicts of interest.

References

[1] S. Nicosia and P. Tomei, "A tracking controller for flexible joint robots using only link position feedback," *IEEE Transactions on Automatic Control*, vol. 40, no. 5, pp. 885–890, 1995.

[2] S. Nicosia, P. Tomei, and A. Tornambe, "A nonlinear observer for elastic robots," *IEEE Journal on Robotics and Automation*, vol. 4, no. 1, pp. 45–52, 1988.

[3] W. E. Dixon, E. Zergeroglu, D. M. Dawson, and M. W. Hannan, "Global adaptive partial state feedback tracking control of rigid-link flexible-joint robots," *Robotica*, vol. 18, no. 3, pp. 325–336, 2000.

[4] F. Abdollahi, H. A. Talebi, and R. V. Patel, "A stable neural network-based observer with application to flexible-joint manipulators," *IEEE Transactions on Neural Networks*, vol. 17, no. 1, pp. 118–129, 2006.

[5] J. Na, B. Jing, Y. Huang, G. Gao, and C. Zhang, "Unknown system dynamics estimator for motion control of nonlinear robotic systems," *IEEE Transactions on Industrial Electronics*, vol. 67, no. 5, pp. 3850–3859, 2020.

[6] S. Jean, M. Tomizuka, and T. Katou, "Kinematic kalman filter (KKF) for robot end-effector sensing," *Journal of Dynamic Systems, Measurement, and Control*, vol. 131, no. 2, pp. 1–8, 2009.

[7] C. A. Lightcap and S. A. Banks, "An extended kalman filter for real-time estimation and control of a rigid-link flexible-joint manipulator," *IEEE Transactions on Control Systems Technology*, vol. 18, no. 1, pp. 91–103, 2010.

[8] J. G. Garcła, A. Robertsson, J. G. Ortega, and R. Johansson, "Sensor fusion for compliant robot motion control," *IEEE Transactions on Robotics*, vol. 24, no. 2, pp. 430–441, 2008.

[9] R. Jassemi-Zargani and D. Necsulescu, "Extended kalman filter-based sensor fusion for operational space control of a robot arm," *IEEE Transactions on Instrumentation and Measurement*, vol. 51, no. 6, pp. 1279–1282, 2002.

[10] S. Wang, L. Tao, Q. Chen, J. Na, and X. Ren, "USDE-based sliding mode control for servo mechanisms with unknown system dynamics," *IEEE/ASME Transactions on Mechatronics*, vol. 25, no. 2, pp. 1056–1066, 2020.

[11] K. Jezernik, B. Curk, and J. Harnik, "Observer-based sliding mode control of a robotic manipulator," *Robotica*, vol. 12, no. 5, pp. 443–448, 1994.

[12] G. Xue, X. Ren, K. Xing, and Q. Chen, "Discrete-time sliding mode control coupled with asynchronous sensor fusion for rigid-link flexible-joint manipulators," in *Proceedings of the 2013 10th IEEE International Conference on Control and Automation (ICCA)*, pp. 238–243, Hangzhou, China, June 2013.

[13] Y. Gao, S. S. Majidabad, and H. T. Shandiz, "Discrete-time based sliding-mode control of robot manipulators," *International Journal of Intelligent Computing and Cybernetics*, vol. 5, no. 3, pp. 340–358, 2012.

[14] M. L. Corradini, V. Fossi, A. Giantomassi, G. Ippoliti, S. Orlando, and G. Orlandob, "Discrete time sliding mode control of robotic manipulators: development and experimental validation," *Control Engineering Practice*, vol. 20, no. 8, pp. 816–822, 2012.

[15] L. Wang, T. Chai, and L. Zhai, "Neural-network-based terminal sliding-mode control of robotic manipulators including actuator dynamics," *IEEE Transactions on Industrial Electronics*, vol. 56, no. 9, pp. 3296–3304, 2009.

[16] Y. Feng, X. Yu, and Z. Man, "Non-singular terminal sliding mode control of rigid manipulators," *Automatica*, vol. 38, no. 12, pp. 2159–2167, 2002.

[17] M. L. Corradini and G. Orlando, "Linear unstable plants with saturating actuators: robust stabilization by a time varying sliding surface," *Automatica*, vol. 43, no. 1, pp. 88–94, 2007.

[18] Y. Bar-Shalom, H. Huimin Chen, and M. Mallick, "One-step solution for the multistep out-of-sequence-measurement problem in tracking," *IEEE Transactions on Aerospace and Electronic Systems*, vol. 40, no. 1, pp. 27–37, 2004.

[19] K. Reif, F. Sonnemann, and R. Unbehauen, "An EKF-based nonlinear observer with a prescribed degree of stability," *Automatica*, vol. 34, no. 9, pp. 1119–1123, 1998.

[20] W. Gao, Y. Wang, and A. Homaifa, "Discrete-time variable structure control systems," *IEEE Transactions on Industrial Electronics*, vol. 42, no. 2, pp. 117–122, 1995.

[21] S. Sarpturk, S. Y. Istefanopulos, Y. Istefanopulos, and O. Kaynak, "On the stability of discrete-time sliding mode control systems," *IEEE Transactions on Automatic Control*, vol. 32, no. 10, pp. 930–932, 1987.

Hindawi
Complexity
Volume 2021, Article ID 9962115, 15 pages
https://doi.org/10.1155/2021/9962115

Research Article

An Enhanced Half-Quasi-Z-Source Inverter for Wind Energy Conversion System with D-PMSG

Yang Zhang,[1] Zhun Cheng,[2] Qing Chen,[2] and Qingmei Li[2]

[1]*College of Electrical and Information Engineering, Hunan University of Technology, Zhuzhou 412007, China*
[2]*College of Rail Transit Equipment Intelligent Manufacturing, Hunan Railway Professional Technology College, Zhuzhou 412001, China*

Correspondence should be addressed to Zhun Cheng; hrptc_cz@163.com

Received 4 March 2021; Revised 28 April 2021; Accepted 23 June 2021; Published 2 July 2021

Academic Editor: Jing Na

To solve the problem of the traditional quasi-Z-source inverters with low voltage gain, an enhanced half-quasi-Z-source inverter (E-HQZSI) is proposed and applied to direct-drive permanent-magnet wind power generation systems in this paper. The expression of the boosting factor is deduced, which shows that E-HQZSI has higher voltage gain compared with the QZSI and HQZSI. However, the higher voltage gain of the E-HQZSI will lead to the large distortion of the generator stator current necessarily. In this paper, a periodic shoot-through duty ratio control scheme is proposed to reduce the stator current harmonics for E-HQZSI. According to the change rule of the single-phase stator current, the shoot-through duty ratio is compromised to make that the three-phase stator currents are as close as possible to the sine wave. Finally, the correctness of the theoretical analysis is verified by simulation and experiment.

1. Introduction

In recent years, wind power generation has developed rapidly due to the advantages of green, clean, and pollution-free [1–5]. According to the statistics of the Global Wind Energy Council [6], by the end of 2017, the cumulative installed capacity of wind power generation has reached 539.58 GW around the world, and the added installed capacity has reached 52.57 GW.

At present, domestic wind power generation system (WPGS) is mainly developing towards large-scale, while the small- and medium-sized WPGS have been highly regarded in European and American countries at the same time [7, 8]. In the United States and Germany, the added installed capacity of small- and medium-sized WPGS in 2017 increased by 25% and 33%, respectively, compared with the previous year. Compared with MW-class WPGS, small- and medium-sized WPGS have the following advantages:

(1) Three-phase diode rectifier is utilized in small- and medium-sized WPGS generally, and the cost of converter is lower

(2) The cutting in and out of a single small- and medium-sized wind turbine has less impact on the large power grid

(3) The adjustment of small- and medium-sized WPGS is more flexible, which is helpful for peak load shifting of the power grid

The types of generators used in WPGS mainly include doubly fed induction generator (DFIG) and permanent-magnet synchronous generator (PMSG) [9–12]. Compared with the DFIG, the PMSG has the advantages of light weight, small volume, high power factor, and good reliability and thus has become the mainstream choice of current WPGS gradually.

The topology with three-phase diode rectifier, boost converter, and three-phase six-switch PWM inverter is often

used in the small- and medium-sized WPGS with PMSG. This topology has the advantages of simple structure and controllable generator speed, but the topology needs to be controlled by two stages, and the control is complicated [13–16].

With the continuous development of power electronics topology, a power conversion topology with the three-phase diode rectifier and three-phase impedance source inverter (ISI) has emerged. This topology has the advantages of single-stage control and no need to insert dead time, which reduces the complexity of the control system and further improves the reliability of the inverter. In addition, the shoot-through of the three-phase impedance source inverter can derive a degree of freedom, thereby realizing the controllable generator speed. However, the three-phase diode rectifier is still utilized between PMSG and ISI; it is bound to produce a large stator current harmonics of the generator [17–21].

To solve the problems shown above, a half-quasi-Z-source inverter (HQZSI) is proposed in [22] and applied to the WPGS with PMSG. When the inverter is in the shoot-through state, the rate of change of the generator stator current is only related to the stator voltage of the generator, which provides a possibility for the output power factor correction of the PMSG. However, HQZSI has lower boosting capability, which is due to the high switching voltage stress. It will increase the probability of device damage.

In this paper, an enhanced half-quasi-Z-source inverter (E-HQZSI) is proposed for direct-drive permanent-magnet wind power generation systems in Section 2, which have higher voltage gain compared with the QZSI and HQZSI. Then, the input current change rate of the E-HQZS wind power conversion system (WPCS) is deduced in Section 3. In addition, the input power factor is analyzed in Section 4. Furthermore, a periodic shoot-through duty ratio control scheme is proposed to reduce the stator current harmonics of the generator in Section 5. Finally, experiment verification is presented in Section 6.

2. Proposed E-HQZSI

The topology of E-HQZSI is shown in Figure 1, which includes DC power supply, impedance source network, and three-phase inverter bridge. The impedance source network is composed of four diodes, two capacitors, and three inductors.

To simplify the analysis, it is assumed that all switching devices, capacitors, and inductors are ideal components. And, inductors L_1, L_2, and L_3 have an inductance of L. When the E-HQZSI is in the shoot-through state, the three-phase inverter bridge can be equivalent to the short circuit; the diodes D_1 and D_3 are turned off, and diodes D_2 and D_4 are turned on, as shown in Figure 2. In the shoot-through state, the inductor L_1 is charged by DC power supply through the diodes D_2 and D_4 and the shoot-through loop; the inductor L_2 is charged by the capacitor C_1 through the diode D_4 and the shoot-through loop, and the inductor L_3 is charged by the capacitor C_2 through the shoot-through loop.

From Figure 2, the following equations are obtained:

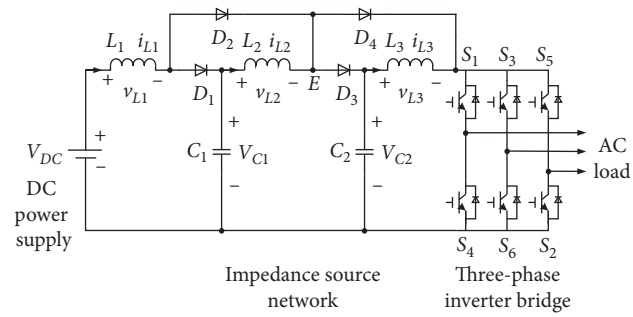

Figure 1: Enhanced half-quasi-Z-source inverter.

$$\begin{cases} -V_{\mathrm{DC}} + L\dfrac{\mathrm{d}i_{L1}}{\mathrm{d}t} = 0, \\ -V_{\mathrm{DC}} + L\dfrac{\mathrm{d}i_{L2}}{\mathrm{d}t} = 0, \\ -V_{\mathrm{DC}} + L\dfrac{\mathrm{d}i_{L3}}{\mathrm{d}t} = 0, \end{cases} \tag{1}$$

where V_{DC} is the voltage of the DC power supply and i_{L1}, i_{L2}, and i_{L3} are the currents of the impedance source inductors L_1, L_2, and L_3, respectively.

When the E-HQZSI is in the nonshoot-through state, the three-phase inverter bridge can be equivalent to a current source; the diodes D_1 and D_3 are turned off, and diodes D_2 and D_4 are turned on, as shown in Figure 3. In the nonshoot-through state, the inductor L_1, L_2, and L_3 and the DC power supply are discharged for the load and the capacitors C_1 and C_2.

From Figure 3, the following equations are obtained:

$$\begin{cases} -V_{\mathrm{DC}} + L\dfrac{\mathrm{d}i_{L1}}{\mathrm{d}t} + V_{C1} = 0, \\ -V_{C1} + L\dfrac{\mathrm{d}i_{L2}}{\mathrm{d}t} + V_{C2} = 0, \\ -V_{C2} + L\dfrac{\mathrm{d}i_{L3}}{\mathrm{d}t} + v_i = 0, \end{cases} \tag{2}$$

where V_{C1} and V_{C2} are the voltages of the impedance source capacitors C_1 and C_2, respectively, and v_i is the output voltage of the impedance source network.

It is noticed that the average voltage of the inductors L_1, L_2, and L_3 is zero in one switching cycle. According to equations (1) and (2), it can be obtained as

$$\begin{cases} \dfrac{T_0}{T}V_{\mathrm{DC}} + \dfrac{T_1}{T}\left(V_{\mathrm{DC}} - V_{C1}\right) = 0, \\ \dfrac{T_0}{T}V_{C1} + \dfrac{T_1}{T}\left(V_{C1} - V_{C2}\right) = 0, \\ \dfrac{T_0}{T}V_{C2} + \dfrac{T_1}{T}\left(V_{C2} - v_i\right) = 0, \end{cases} \tag{3}$$

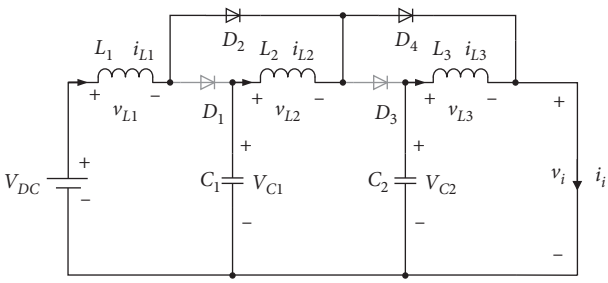

Figure 2: Equivalent circuit of the E-HQZSI in the shoot-through state.

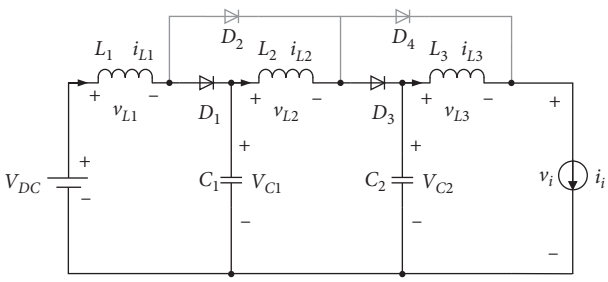

Figure 3: Equivalent circuit of the E-HQZSI in the nonshoot-through state.

where T_0 and T_1 are the times of the shoot-through state and nonshoot-through state in one switching cycle.

It can be derived from equation (3) that

$$\begin{cases} V_{C1} = \dfrac{1}{1-d_0}V_{\mathrm{DC}}, \\ V_{C2} = \dfrac{1}{1-d_0}V_{C1} = \dfrac{1}{(1-d_0)^2}V_{\mathrm{DC}}, \\ v_i = \dfrac{1}{1-d_0}V_{C2} = \dfrac{1}{(1-d_0)^3}V_{\mathrm{DC}}, \end{cases} \tag{4}$$

where d_0 is the shoot-through duty ratio of the E-HQZSI.

Thus, the average output voltage of the impedance source network can be expressed as follows:

$$\begin{aligned} V_{iav} &= \frac{(0T_0 + v_i T_1)}{T} \\ &= \frac{1}{(1-d_0)^2}V_{\mathrm{DC}} = V_{C2}. \end{aligned} \tag{5}$$

It can be seen from [17] that the relationship between the boost factor and the shoot-through duty ratio of the quasi-Z-source inverter (QZSI) can be expressed as

$$B_0 = \frac{1}{1-2d_0}, \tag{6}$$

where B_0 is the boost factor of the impedance source inverter.

It can be obtained from [22] that the relationship between the boost factor and the shoot-through duty ratio of the half-quasi-Z-source inverter (HQZSI) can be expressed as

$$B_0 = \frac{1}{(1-d_0)^2}. \tag{7}$$

According to equation (4), the relationship between the boost factor and the shoot-through duty ratio of the E-HQZSI can be written as

$$B_0 = \frac{1}{(1-d_0)^3}. \tag{8}$$

The voltage gain of E-HQZSI can be expressed as

$$G = \frac{M}{(1-d_0)^3}, \tag{9}$$

where M is the modulation index of the E-HQZSI.

The comparison of boost factor B_0 between the QZSI and the HQZSI is shown in Figure 4. It can be seen that the QZSI has the greater boost capacity compared to the HQZSI.

The comparison of boost factor B_0 between the QZSI and the E-HQZSI is shown in Figure 5. It can be obtained that the E-HQZSI has the greater boost capacity compared to the QZSI.

It can be seen from Figures 6–8 that, under the same voltage gain, the HQZSI requires the largest shoot-through duty ratio, the QZSI is the second, and the E-HQZSI requires the smallest shoot-through duty ratio. In addition, the maximum modulation degree can be achieved under the same boosting factor; the E-HQZSI is the largest, the QZSI is the second, and the HQZSI is the smallest.

However, under the same system parameters, the input current waveform sinusoid of the rectifier is inversely proportional to the boost factor of the impedance source inverter, when the input voltage of the impedance source inverter is provided by a three-phase diode rectifier. So the input current harmonic of the E-HQZSI is larger compared to the HQZSI.

3. Input Current Change Rate of E-HQZS WPCS

Because E-HQZSI has higher voltage gain, it is suitable for the wind power conversion system. The input current change rate of the E-HQZS WPCS will be analyzed in this section.

The voltage waveform of the three-phase AC power supply is shown in Figure 9. According to its polarity, the half AC period of the three-phase power supply can be divided into six sectors. The following research of E-HQZSI is analyzed in the case of the sector II. Since the AC period of the three-phase power supply is much longer than the switching cycle, the voltage of three-phase AC power supply can be approximated as a constant value in one switching cycle. When the E-HQZSI is in the shoot-through state, the equivalent function $V_Z = 1$; when the E-HQZSI is in the nonshoot-through state, the equivalent function $V_Z = 0$. Figure 10 is the waveform of three-phase input current during one switching cycle in sector III.

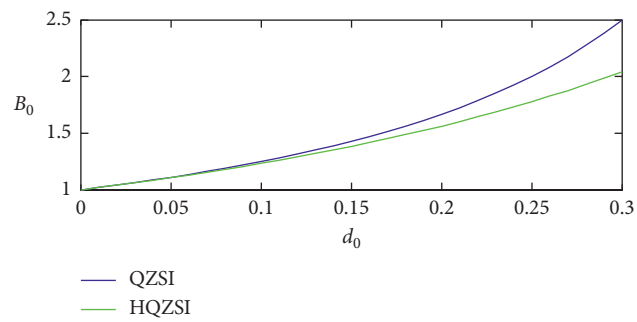

Figure 4: Comparison of boost factor B_0 via shoot-through duty ratio d_0 between the QZSI and the HQZSI.

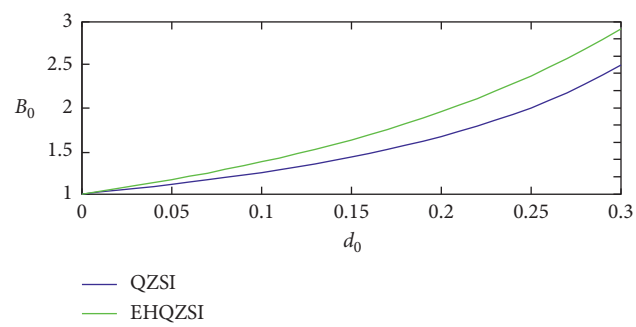

Figure 5: Comparison of boost factor B_0 via shoot-through duty ratio d_0 between the QZSI and the E-HQZSI.

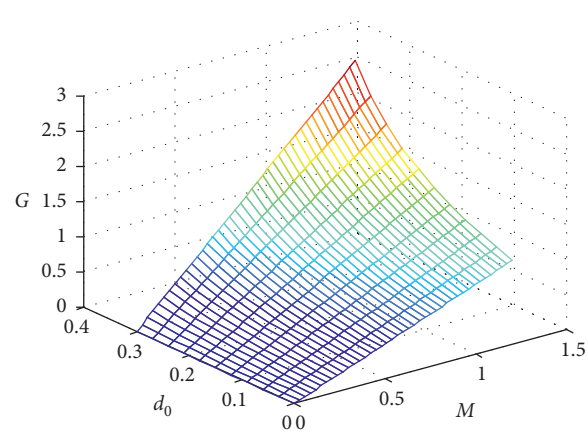

Figure 6: Relationship voltage gain of the QZSI G with modulation index M and shoot-through duty ratio d_0.

A switching cycle is divided into three operation modes during sector III, as shown in Figures 9 and 10. E-HQZSI operates in the Mode 1 from t_0 to t_1. In this case, the diodes D_2, D_4, D_6, D_8, and D_{10} are in the ON state, while the diodes D_1, D_3, D_5, D_7, and D_9 are in the OFF state. Inductor L_1 is charged by three-phase AC power supply, and inductor L_2 is charged by capacitor C_1. At the same time, the inductor L_3 is charged by capacitor C_2.

From Figure 11(a), it can be obtained that

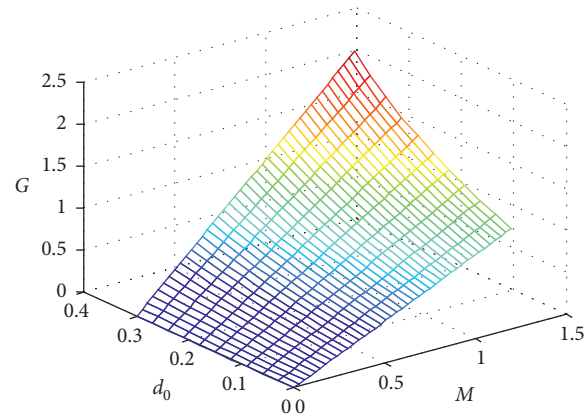

Figure 7: Relationship voltage gain of the HQZSI G with modulation index M and shoot-through duty ratio d_0.

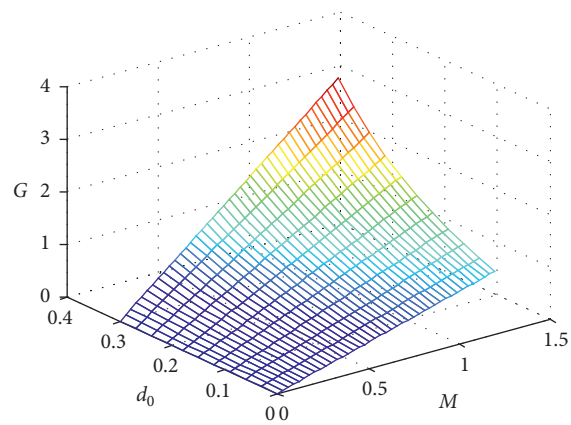

Figure 8: Relationship voltage gain of the E-HQZSI G with modulation index M and shoot-through duty ratio d_0.

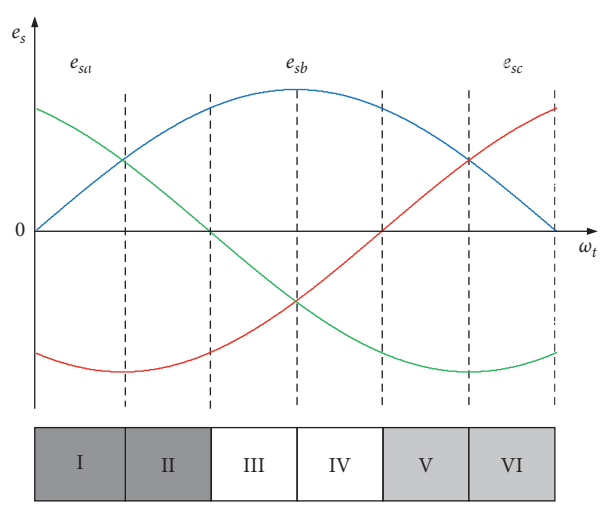

Figure 9: Six sectors in the half AC period.

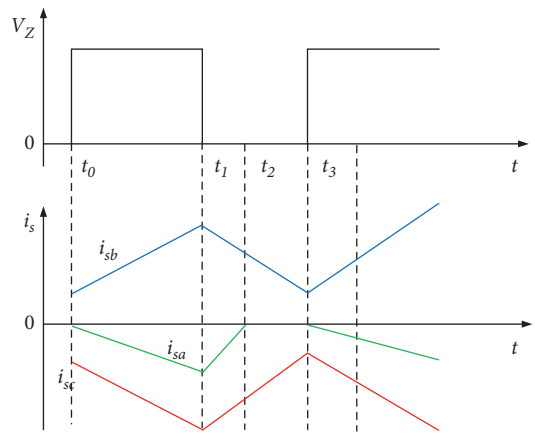

FIGURE 10: The three-phase input current during one switching cycle in sector III.

$$\begin{cases} e_{sa} - L_a \dfrac{di_{sa}}{dt} = v_{NO}, \\ e_{sb} - L_b \dfrac{di_{sb}}{dt} - L_1 \dfrac{di_{sb}}{dt} = v_{NO}, \\ e_{sc} - L_c \dfrac{di_{sc}}{dt} = v_{NO}, \end{cases} \tag{10}$$

where e_{sa}, e_{sb}, and e_{sc} are the three-phase stator electromotive force (EMF) of the permanent-magnet synchronous generator (PMSG), i_{sa}, i_{sb}, and i_{sc} are the three-phase stator current of PMSG, and v_{NO} is the voltage between the reference point N and the input power midpoint O.

The three-phase equivalent inductance of PMSG can be equal to L. The three equations in equation (10) can be added to obtain that

$$v_{NO} = \frac{1}{3}\left(e_{sa} + e_{sb} + e_{sc}\right) - \frac{L}{3}\left(\frac{di_{sa}}{dt} + \frac{di_{sb}}{dt} + \frac{di_{sc}}{dt}\right) - \frac{L_1}{3}\frac{di_{sb}}{dt}. \tag{11}$$

Equation (12) can be obtained because of Kirchhoff's law and symmetry of e_{sa}, e_{sb}, and e_{sc}:

$$v_{NO} = -\frac{L_1}{3}\frac{di_{sb}}{dt}. \tag{12}$$

Bringing equation (12) into equation (10), the change rate of i_{sa}, i_{sb}, and i_{sc} can be expressed as

$$\begin{cases} \dfrac{di_{sa}}{dt} = \dfrac{L_1 e_{sb}}{3L^2 + 2LL_1} + \dfrac{e_{sa}}{L}, \\ \dfrac{di_{sb}}{dt} = \dfrac{3e_{sb}}{3L + 2L_1}, \\ \dfrac{di_{sc}}{dt} = \dfrac{e_{sb}}{3L^2 + 2LL_1} + \dfrac{e_{sc}}{L}. \end{cases} \tag{13}$$

It can be seen from equation (13) that the derivative of i_{sa}, i_{sb}, and i_{sc} is only related to the three-phase stator electromotive force of PMSG in Mode 1.

E-HQZSI operates in the Mode 2 from t_1 to t_2. In this case, the diodes D_1, D_3, D_6, D_8, and D_{10} are in the ON state, while the diodes D_2, D_4, D_5, D_7, and D_9 are in the OFF state. The load and capacitors C_1 and C_2 are charged by three-phase AC power supply and inductors L_1, L_2, and L_3.

From Figure 11(b), it can be obtained that

$$\begin{cases} e_{sa} - L\dfrac{di_{sa}}{dt} = v_{NO}, \\ e_{sb} - L\dfrac{di_{sb}}{dt} - L_1\dfrac{di_{sb}}{dt} - V_{C1} = v_{NO}, \\ e_{sc} - L\dfrac{di_{sc}}{dt} = v_{NO}. \end{cases} \tag{14}$$

The three equations in equation (14) can be added to obtain that

$$v_{NO} = \frac{1}{3}\left(e_{sa} + e_{sb} + e_{sc}\right) - \frac{L}{3}\left(\frac{di_{sa}}{dt} + \frac{di_{sb}}{dt} + \frac{di_{sc}}{dt}\right)\Bigg) - \frac{L_1}{3}\frac{di_{sb}}{dt} - \frac{V_{C1}}{3}. \tag{15}$$

Equation (16) can be obtained because of Kirchhoff's law and symmetry of e_{sa}, e_{sb}, and e_{sc}:

$$v_{NO} = -\frac{L_1}{3}\frac{di_{sb}}{dt} - \frac{V_{C1}}{3}. \tag{16}$$

Bringing equation (16) into (14), the change rate of i_{sa}, i_{sb}, and i_{sc} can be expressed as

$$\begin{cases} \dfrac{di_{sa}}{dt} = \dfrac{3Le_{sa} + 2L_1 e_{sa} + L_1 e_{sb} + LV_{C1}}{3L^2 + 2LL_1}, \\ \dfrac{di_{sb}}{dt} = \dfrac{3e_{sb} - 2V_{C1}}{3L + 2L_1}, \\ \dfrac{di_{sc}}{dt} = \dfrac{3Le_{sc} + 2L_1 e_{sc} + L_1 e_{sb} + LV_{C1}}{3L^2 + 2LL_1}. \end{cases} \tag{17}$$

It can be seen from equation (17) that the derivative of i_{sa}, i_{sb}, and i_{sc} is related to the three-phase stator electromotive force of PMSG and the voltage of capacitor C_1 in Mode 2.

E-HQZSI operates in the Mode 3 from t_2 to t_3. In this case, the diodes D_1, D_3, D_6, and D_{10} are in the ON state, while the diodes D_2, D_4, D_5, D_7, D_8, and D_9 are in the OFF state.

From Figure 11(c), it can be obtained that

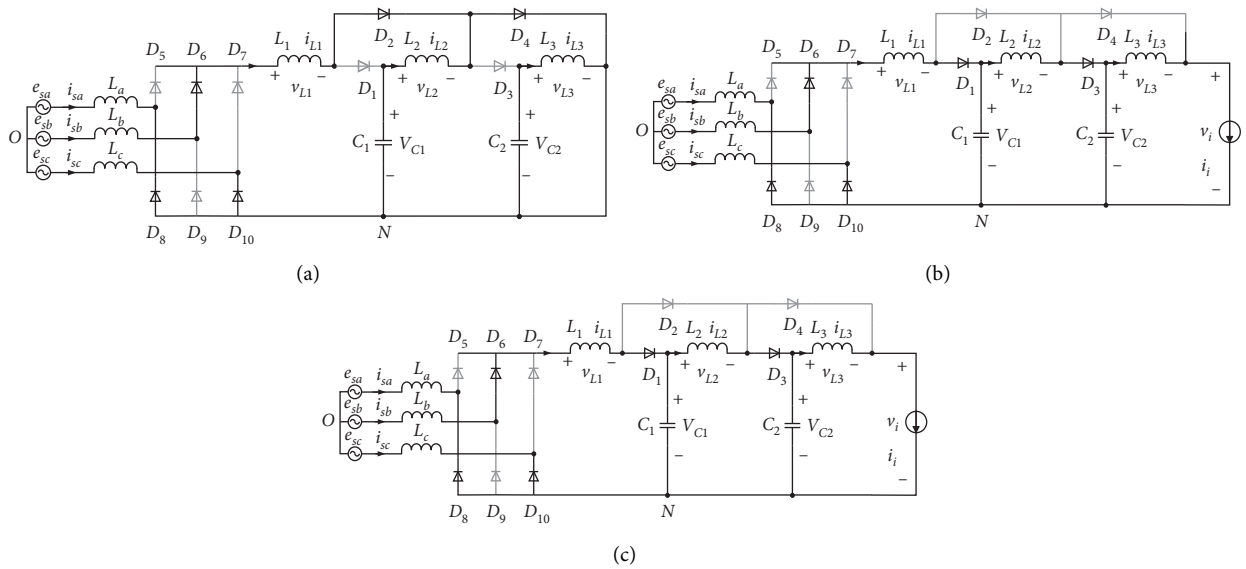

Figure 11: The equivalent circuit of E-HQZS WPGS in each modes. (a) Mode 1. (b) Mode 2. (c) Mode 3.

$$\begin{cases} i_{\mathrm{sa}} = 0, \\ e_{\mathrm{sb}} - e_{\mathrm{sc}} - L\left(\dfrac{\mathrm{d}i_{\mathrm{sb}}}{\mathrm{d}t} - \dfrac{\mathrm{d}i_{\mathrm{sc}}}{\mathrm{d}t}\right) - L_1\dfrac{\mathrm{d}i_{\mathrm{sb}}}{\mathrm{d}t} - V_{C1} = 0, \\ i_{\mathrm{sc}} = -i_{\mathrm{sb}}. \end{cases} \tag{18}$$

The change rate of i_{sa}, i_{sb}, and i_{sc} can be expressed as

$$\begin{cases} \dfrac{\mathrm{d}i_{\mathrm{sa}}}{\mathrm{d}t} = 0, \\ \dfrac{\mathrm{d}i_{\mathrm{sb}}}{\mathrm{d}t} = \dfrac{e_{\mathrm{sb}} - e_{\mathrm{sc}} - V_{C1}}{2L + L_1}, \\ \dfrac{\mathrm{d}i_{\mathrm{sc}}}{\mathrm{d}t} = -\dfrac{e_{\mathrm{sb}} - e_{\mathrm{sc}} - V_{C1}}{2L + L_1}. \end{cases} \tag{19}$$

It can be seen from equation (19) that the derivative of i_{sa}, i_{sb}, and i_{sc} is related to the three-phase stator electromotive force of PMSG and the voltage of capacitor C_1 in Mode 3.

4. Analysis of Input Power Factor

Considering that the phase current of the three-phase AC power supply is 1/4 cycle symmetry, the average expression of the current of phase b in the interval $[0, \pi/2]$ is derived.

The b-phase current of the three-phase AC power supply in the interval $[\pi/3, \pi/2]$ can be expressed as

$$i_{\mathrm{sbav}} = \frac{1}{T}\left(\int_{t_0}^{t_1} i_{\mathrm{sb}}(\xi)\mathrm{d}\xi + \int_{t_1}^{t_2} i_{\mathrm{sb}}(\xi)\mathrm{d}\xi + \int_{t_2}^{t_3} i_{\mathrm{sb}}(\xi)\mathrm{d}\xi\right). \tag{20}$$

From equation (13), it can be seen that

$$\int_{t_0}^{t_1} i_{\mathrm{sb}}(\xi)\mathrm{d}\xi = \int_{t_0}^{t_1} \frac{3e_{\mathrm{sb}}}{3L + 2L_1}\mathrm{d}\xi. \tag{21}$$

Since the switching period is much smaller than the period of AC power supply, it can be considered that e_{sa}, e_{sb}, and e_{sc} are constant from t_0 to t_1; then, equation (21) can be expressed as

$$\int_{t_0}^{t_1} i_{\mathrm{sb}}(\xi)\mathrm{d}\xi = \frac{3e_{\mathrm{sb}}}{3L + 2L_1}d_0T. \tag{22}$$

From equation (17), it can be seen that

$$\begin{aligned} \int_{t_1}^{t_2} i_{\mathrm{sb}}(\xi)\mathrm{d}\xi &= \int_{t_1}^{t_2} \frac{3e_{\mathrm{sb}} - 2V_{C1}}{3L + 2L_1}\mathrm{d}\xi \\ &= \frac{3e_{\mathrm{sb}} - 2V_{C1}}{3L + 2L_1}(t_2 - t_1). \end{aligned} \tag{23}$$

It can be seen from Figure 10 that t_2–t_1 is the time for the a-phase current to drop from t_1 to t_2, so t_2–t_1 can be expressed as

$$t_2 - t_1 = \frac{L_1e_{\mathrm{sb}} + 3e_{\mathrm{sa}}L + 2e_{\mathrm{sa}}L_1}{3Le_{\mathrm{sa}} + 2e_{\mathrm{sa}}L_1 + L_1e_{\mathrm{sb}} + LV_{C1}}d_0T. \tag{24}$$

Bringing equation (24) into equation (23), it can be obtained that

$$\int_{t_1}^{t_2} i_{\mathrm{sb}}(\xi)\mathrm{d}\xi = \frac{(3e_{\mathrm{sb}} - 2V_{C1})(L_1e_{\mathrm{sb}} + 3e_{\mathrm{sa}}L + 2e_{\mathrm{sa}}L_1)}{(3L + 2L_1)(3Le_{\mathrm{sa}} + 2e_{\mathrm{sa}}L_1 + L_1e_{\mathrm{sb}} + LV_{C1})}d_0T. \tag{25}$$

From equation (19), it can be seen that

$$\begin{aligned} \int_{t_2}^{t_3} i_{\mathrm{sb}}(\xi)\mathrm{d}\xi &= \int_{t_2}^{t_3} \frac{e_{\mathrm{sb}} - e_{\mathrm{sc}} - V_{C1}}{2L + L_1}\mathrm{d}\xi \\ &= \frac{e_{\mathrm{sb}} - e_{\mathrm{sc}} - V_{C1}}{2L + L_1}(t_3 - t_2). \end{aligned} \tag{26}$$

It can be seen from Figure 10 that t_3-t_2 can be expressed as

$$\begin{aligned} t_3 - t_2 &= T - (t_1 - t_0) - (t_2 - t_1) \\ &= T - \mathrm{d}_0 T - \frac{L_1 e_{\mathrm{sb}} + 3e_{\mathrm{sa}} L + 2e_{\mathrm{sa}} L_1}{3Le_{\mathrm{sa}} + 2e_{\mathrm{sa}} L_1 + L_1 e_{\mathrm{sb}} + LV_{C1}} d_0 T \\ &= \left(1 - \frac{6Le_{\mathrm{sa}} + 4e_{\mathrm{sa}} L_1 + 2L_1 e_{\mathrm{sb}} + LV_{C1}}{3Le_{\mathrm{sa}} + 2e_{\mathrm{sa}} L_1 + L_1 e_{\mathrm{sb}} + LV_{C1}} \mathrm{d}_0\right) T. \end{aligned} \tag{27}$$

Bringing equation (27) into equation (26), it can be obtained that

$$\int_{t_2}^{t_3} i_{\mathrm{sb}}(\xi)\mathrm{d}\xi = \left[\frac{e_{\mathrm{sb}} - e_{\mathrm{sc}} - V_{C1}}{2L + L_1} - \frac{(e_{\mathrm{sb}} - e_{\mathrm{sc}} - V_{C1})(6Le_{\mathrm{sa}} + 4e_{\mathrm{sa}} L_1 + 2L_1 e_{\mathrm{sb}} + LV_{C1})}{(2L + L_1)(3Le_{\mathrm{sa}} + 2e_{\mathrm{sa}} L_1 + L_1 e_{\mathrm{sb}} + LV_{C1})} d_0\right] T. \tag{28}$$

Bringing equations (22), (25), and (28) into equation (20), the b-phase current of the three-phase AC power supply in the interval $[\pi/3, \pi/2]$ can be expressed as

$$\begin{aligned} i_{\mathrm{sbav}} &= \frac{3e_{\mathrm{sb}} d_0 + 3L + 2L_1}{3L + 2L_1} \\ &+ \frac{(3e_{\mathrm{sb}} - 2V_{C1})(L_1 e_{\mathrm{sb}} + 3e_{\mathrm{sa}} L + 2e_{\mathrm{sa}} L_1)}{(3L + 2L_1)(3Le_{\mathrm{sa}} + 2e_{\mathrm{sa}} L_1 + L_1 e_{\mathrm{sb}} + LV_{C1})} d_0 \\ &- \frac{6Le_{\mathrm{sa}} + 4e_{\mathrm{sa}} L_1 + 2L_1 e_{\mathrm{sb}} + LV_{C1}}{3Le_{\mathrm{sa}} + 2e_{\mathrm{sa}} L_1 + L_1 e_{\mathrm{sb}} + LV_{C1}} d_0. \end{aligned} \tag{29}$$

In a similar way, the b-phase current of the three-phase AC power supply in the interval $[0, \pi/6]$ can be expressed as

$$\begin{aligned} i_{\mathrm{sbav}} &= \frac{e_{\mathrm{sa}}(6L + L_1) - e_{\mathrm{sb}}(3L + L_1)}{3L^2 + 2LL_1} d_0 \\ &+ \frac{[e_{\mathrm{sb}}(3L + L_1) - L_1 e_{\mathrm{sa}} - LV_{C1}][e_{\mathrm{sa}}(6L + L_1) - e_{\mathrm{sb}}(3L + L_1)]}{[3L^2 + 2LL_1][e_{\mathrm{sb}}(3L + L_1) - L_1 e_{\mathrm{sa}} - LV_{C1}]} d_0. \end{aligned} \tag{30}$$

The b-phase current of the three-phase AC power supply in the interval $[\pi/6, \pi/3]$ can be expressed as

$$\begin{aligned} i_{\mathrm{sbav}} &= \frac{e_{\mathrm{sb}}(6L + L_1) - e_{\mathrm{sc}}(3L + L_1)}{3L^2 + 2LL_1} d_0 \\ &+ \frac{[e_{\mathrm{sc}}(3L + L_1) - L_1 e_{\mathrm{sa}} - LV_{C1}][e_{\mathrm{sb}}(3L - L_1) + e_{\mathrm{sc}} L_1]}{[e_{\mathrm{sb}}(3L + L_1) - e_{\mathrm{sc}} L_1 - LV_{C1}][3L^2 + 2LL_1]} d_0. \end{aligned} \tag{31}$$

From equations (29)–(31), the b-phase current of the three-phase AC power supply in the interval $[0, \pi/2]$ can be expressed as

$$i_{\mathrm{sbav}} = k_1 d_0 + k_2, \tag{32}$$

where k_1 and k_2 can be calculated as

$$k_1 = \begin{cases} \dfrac{e_{sa}(6L+L_1) - e_{sb}(3L+L_1)}{3L^2+2LL_1} + \dfrac{[e_{sb}(3L+L_1) - L_1 e_{sa} - LV_{C1}][e_{sa}(6L+L_1) - e_{sb}(3L+L_1)]}{[3L^2+2LL_1][e_{sb}(3L+L_1) - L_1 e_{sa} - LV_{C1}]}, & \left[0, \dfrac{\pi}{6}\right], \\ \dfrac{e_{sb}(6L+L_1) - e_{sc}(3L+L_1)}{3L^2+2LL_1} + \dfrac{[e_{sc}(3L+L_1) - L_1 e_{sa} - LV_{C1}][e_{sb}(3L-L_1) + e_{sc}L_1]}{[e_{sb}(3L+L_1) - e_{sc}L_1 - LV_{C1}][3L^2+2LL_1]}, & \left[\dfrac{\pi}{6}, \dfrac{\pi}{3}\right], \\ \dfrac{3e_{sb}}{3L+2L_1} - \dfrac{6Le_{sa} + 4e_{sa}L_1 + 2L_1 e_{sb} + LV_{C1}}{3Le_{sa} + 2e_{sa}L_1 + L_1 e_{sb} + LV_{C1}} + \dfrac{(3e_{sb} - 2V_{C1})(L_1 e_{sb} + 3e_{sa}L + 2e_{sa}L_1)}{(3L+2L_1)(3Le_{sa} + 2e_{sa}L_1 + L_1 e_{sb} + LV_{C1})}, & \left[\dfrac{\pi}{3}, \dfrac{\pi}{2}\right], \end{cases}$$

$$k_2 = \begin{cases} 0, & \left[0, \dfrac{\pi}{6}\right], \\ 0, & \left[\dfrac{\pi}{6}, \dfrac{\pi}{3}\right], \\ 1, & \left[\dfrac{\pi}{3}, \dfrac{\pi}{2}\right]. \end{cases} \tag{33}$$

So the input power factor of E-HQZS WPCS can be obtained as

$$\begin{aligned} \mathrm{PF}_{\mathrm{DHQZS}} &= \frac{P_{\mathrm{sbav}}}{E_S I_{\mathrm{sbrms}}} = \frac{(4/T)\int_0^{T/4} e_{\mathrm{sb}} i_{\mathrm{sbav}} \mathrm{d}t}{E_S \sqrt{(4/T)\int_0^{T/4} i_{\mathrm{sbav}}^2 \mathrm{d}t}} \\ &= \frac{(2/\sqrt{\pi})\int_0^{\pi/2} \cos(\omega t - (2\pi/3))(k_1 d_0 + k_2)\mathrm{d}t}{\sqrt{\int_0^{\pi/2} (k_1 d_0 + k_2)^2 \mathrm{d}t}}, \end{aligned} \tag{34}$$

where P_{sbav} is the average input power of phase b, I_{sbrms} is the root mean square (RMS) of b-phase input current, and E_S is the RMS of e_{sb}.

5. Periodic Shoot-Through Duty Ratio Control Method

Since the impedance source inverter including the E-HQZSI is equivalent to only one additional degree of freedom in the shoot-through state, the converter system cannot realize input power factor correction with the constant shoot-through duty ratio. Consider d_0 in equation (35) as the periodic shoot-through duty ratio as follows:

$$d_{0b} = D_0 \frac{\cos(\omega t - (2\pi/3))}{k_1}, \tag{35}$$

where D_0 is a constant.

Bringing equation (35) into equation (32), the b-phase current of the three-phase AC power supply can be expressed as

$$i_{\mathrm{sbav}} = D_0 \cos\left(\omega t - \left(\frac{2\pi}{3}\right)\right) + k_2. \tag{36}$$

It can be seen from equation (36) that the b-phase current is closer to the ideal sine wave when the shoot-through duty ratio of E-HQZSI is changed in accordance with equation (35).

In a similar way, the equivalent periodic shoot-through duty ratio of a-phase current can be expressed as

$$d_{0a} = D_0 \frac{\cos \omega t}{k_3}, \tag{37}$$

where k_3 can be calculated as

$$k_3 = \begin{cases} \dfrac{e_{sa}(3L - L_1) + e_{sb}L_1}{3L^2 + 2LL_1} - \dfrac{[e_{sa} - e_{sc} - V_{C1}][e_{sa}(6L + L_1) - L_1 e_{sa} - LV_{C1}]}{[2L + L_1][3Le_{sa} + 2e_{sa}L_1 + L_1 e_{sb} + LV_{C1}]} \\ + \dfrac{[e_{sa}(3L + L_1) - e_{sb}L_1 - LV_{C1}][e_{sa}(6L + L_1) - e_{sb}(3L + L_1)]}{[3L^2 + 2LL_1][3Le_{sa} + 2e_{sa}L_1 + L_1 e_{sb} + LV_{C1}]}, & \left[0, \dfrac{\pi}{6}\right], \\ \dfrac{e_{sa}(6L + L_1) - e_{sb}(3L + L_1)}{3L^2 + 2LL_1} \\ + \dfrac{[e_{sb}(3L + L_1) - L_1 e_{sa} - LV_{C1}][e_{sa}(3L - L_1) + e_{sb}L_1]}{[3Le_{sa} + 2e_{sa}L_1 + L_1 e_{sb} + LV_{C1}][3L^2 + 2LL_1]}, & \left[\dfrac{\pi}{6}, \dfrac{\pi}{3}\right], \\ \dfrac{3e_{sc}}{2L_1 + 3L} + \dfrac{[e_{sa}(3L - L_1) + e_{sb}L_1][3e_{sc} + 2V_{C1}]}{[3L + 2L_1][3Le_{sa} + 2e_{sa}L_1 + L_1 e_{sb} + LV_{C1}]} \\ + \dfrac{[6Le_{sa} - LV_{C1}][e_{sa} - e_{sc} - V_{C1}]}{[2L + L_1][3Le_{sa} + 2e_{sa}L_1 + L_1 e_{sb} + LV_{C1}]}, & \left[\dfrac{\pi}{3}, \dfrac{\pi}{2}\right]. \end{cases} \tag{38}$$

The equivalent periodic shoot-through duty ratio of a-phase current can be expressed as

$$d_{0c} = D_0 \frac{\cos(\omega t + (2\pi/3))}{k_4}, \tag{39}$$

where k_4 can be calculated as

$$k_4 = \begin{cases} \dfrac{e_{sc}(3L - L_1) + e_{sa}L_1}{3L^2 + 2LL_1} - \dfrac{[e_{sc} - e_{sb} - V_{C1}][e_{sc}(6L + L_1) - L_1 e_{sc} - LV_{C1}]}{[2L + L_1][3Le_{sa} + 2e_{sa}L_1 + L_1 e_{sb} + LV_{C1}]} \\ + \dfrac{[e_{sc}(3L + L_1) - e_{sa}L_1 - LV_{C1}][e_{sc}(6L + L_1) - e_{sa}(3L + L_1)]}{[3L^2 + 2LL_1][3Le_{sa} + 2e_{sa}L_1 + L_1 e_{sb} + LV_{C1}]}, & \left[0, \dfrac{\pi}{6}\right], \\ \dfrac{e_{sc}(6L + L_1) - e_{sa}(3L + L_1)}{3L^2 + 2LL_1} \\ + \dfrac{[e_{sa}(3L + L_1) - L_1 e_{sc} - LV_{C1}][e_{sc}(3L - L_1) + e_{sa}L_1]}{[3Le_{sa} + 2e_{sa}L_1 + L_1 e_{sb} + LV_{C1}][3L^2 + 2LL_1]}, & \left[\dfrac{\pi}{6}, \dfrac{\pi}{3}\right], \\ \dfrac{3e_{sb}}{2L_1 + 3L} + \dfrac{[e_{sc}(3L - L_1) + e_{sa}L_1][3e_{sb} + 2V_{C1}]}{[3L + 2L_1][3Le_{sa} + 2e_{sa}L_1 + L_1 e_{sb} + LV_{C1}]} \\ + \dfrac{[6Le_{sc} - LV_{C1}][e_{sc} - e_{sb} - V_{C1}]}{[2L + L_1][3Le_{sa} + 2e_{sa}L_1 + L_1 e_{sb} + LV_{C1}]}, & \left[\dfrac{\pi}{3}, \dfrac{\pi}{2}\right]. \end{cases} \tag{40}$$

Figure 12 is the three-phase equivalent periodic shoot-through duty ratio curve, which can be obtained according to equations (35), (37), and (39). Due to the lack of degrees of freedom, a constant shoot-through duty ratio cannot be

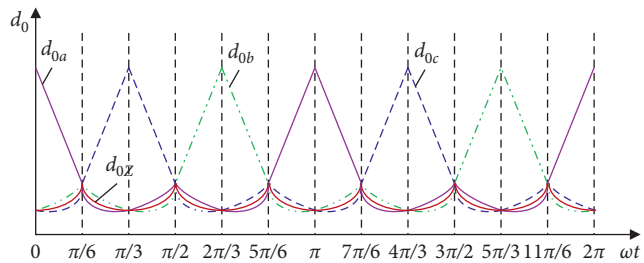

Figure 12: Three-phase equivalent periodic shoot-through duty ratio.

Table 1: Main parameters of PMSG.

Parameters	Value
Stator phase resistance	1.162 Ω
Number of pole pairs	2
Rated speed of PMSG	1500 RPM
d-axis inductances	0.00196 H
q-axis inductances	0.00196 H
Flux linkage of permanent magnets	0.205 Wb

found to realize the PFC of the input current of the E-HQZS WPCS. Therefore, in order to make the three-phase input current of the E-HQZS WPCS as close as possible to the sine wave, it is necessary to compromise the shoot-through duty ratio of the E-HQZSI. Then, the weighted equivalent periodic shoot-through duty ratio of E-HQZSI can be obtained as

$$d_{0Z} = y_1 d_{0a} + y_2 d_{0b} + y_3 d_{0c}, \tag{41}$$

where y_1, y_2, and y_3 are the weighting coefficient of d_{0a}, d_{02}, and d_{03}, respectively.

6. Experiment Verification

The RT-Lab OP5600 is adopted to simulate the converter and PMSG. TMS320F2812 is selected as the DSP controller for E-HQZSI. The hardware-in-the-loop simulation (HILS) of WPCS can be realized by downloading the compiled code from PMSG and converter model in OP5600 and by downloading the C-code generated from the designed controller model in DSP. The average output voltage of the impedance source network is 560 V, and the rated power of the system is 2.2 kW. The inductance of impedance source inductors L_1, L_2, and L_3 is 1.5 mH, and the capacitance of impedance source capacitors C_1 and C_2 is 900 μF. The main parameters of PMSG used in the experiment are shown in Table 1, and the experimental results are shown in Figures 13–18.

In Figure 13, the voltage stress of the E-HQZSI is compared with that of the QZSI and the HQZSI when the PMSG rotates at 1500 RPM. Figure 13(a) shows that the output voltage peck of the impedance source network is 610 V, when the voltage of the QZS capacitor C_1 is set to 560 V. Figure 13(b) shows that the output voltage peck of the impedance source network is 616 V, when the voltage of the HQZS capacitor C_1 is set to 560 V. Figure 13(c) shows that the output voltage peck of the impedance source network is 586 V, when the voltage of the E-HQZS capacitor C_2 is set to 560 V. It can be seen that compared to the QZSI and the HQZSI, the voltage stress of the E-HQZSI is minimum.

In Figure 14, the voltage stress of the E-HQZSI is compared with that of the QZSI and the HQZSI when the PMSG rotates at 1200 RPM. Figure 14(a) shows that the output voltage peck of the impedance source network is 710 V, when the voltage of the QZS capacitor C_1 is set to 560 V. Figure 14(b) shows that the output voltage peck of the impedance source network is 769 V, when the voltage of the HQZS capacitor C_1 is set to 560 V. Figure 14(c) shows that the output voltage peck of the impedance source network is 656 V, when the voltage of the E-HQZS capacitor C_2 is set to 560 V. It can be seen that compared to the QZSI and the HQZSI, the voltage stress of the E-HQZSI is decreased by 7.6% and 14.7%, respectively. The results reflect that the E-HQZSI has higher boost capacity compared to the QZSI and the HQZSI.

In Figures 15 and 16, the stator current and spectrum of the PMSG with the E-HQZSI are compared to that with the QZSI and the HQZSI at the 1500 RPM. It can be seen that compared to the HQZSI and the E-HQZSI, the THD of the stator current with the E-HQZSI and the periodic shoot-through duty ratio control scheme is decreased by 27.7% and 34.1%, respectively.

In Figures 17 and 18, the stator current and spectrum of the PMSG with the E-HQZSI are compared to that with the QZSI and the HQZSI at the 1200 RPM. It can be seen that the THD of the stator current is only 11.43% with the E-HQZSI and the periodic shoot-through duty ratio control method, which is much smaller than that with the HQZSI and the E-HQZSI.

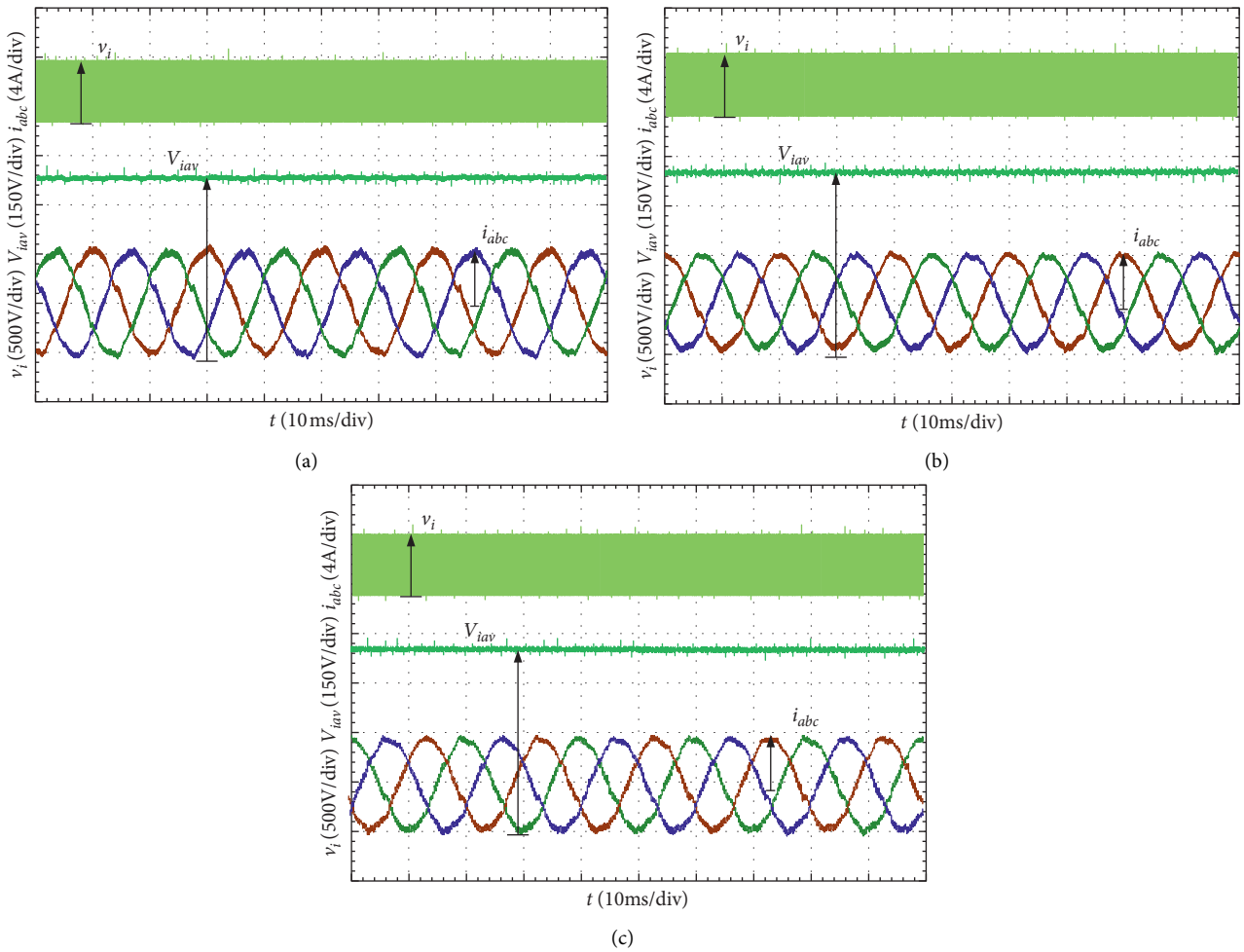

Figure 13: Experimental comparison of the three topologies when the PMSG rotates at 1500 RPM. (a) Quasi-Z-source WPCS. (b) Half-quasi-Z-source WPCS. (c) Enhanced half-quasi-Z-source WPCS.

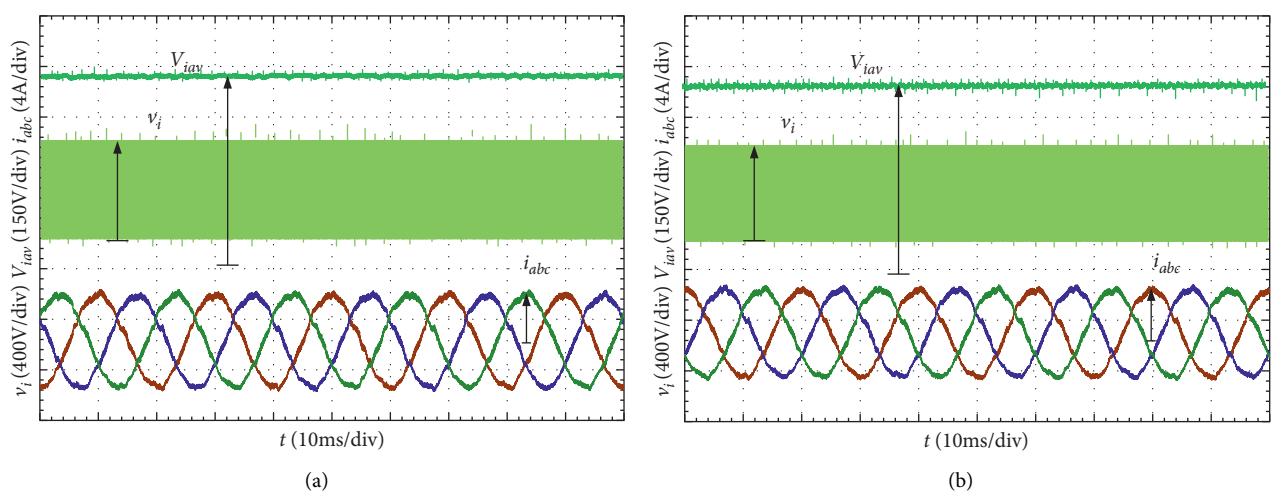

Figure 14: Continued.

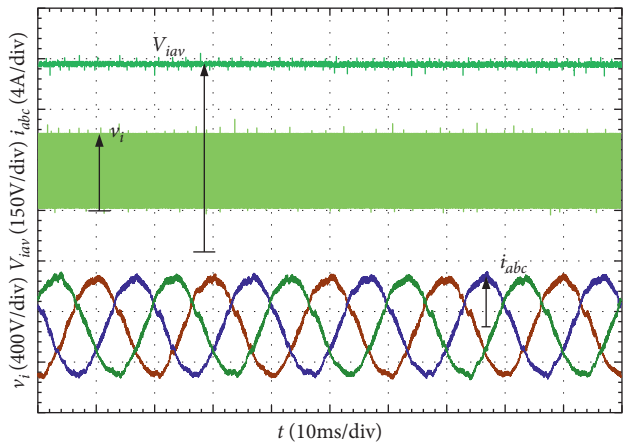

(c)

Figure 14: Experimental comparison of the three topologies when the PMSG rotates at 1200 RPM. (a) Quasi-Z-source WPCS. (b) Half-quasi-Z-source WPCS. (c) Enhanced half-quasi-Z-source WPCS.

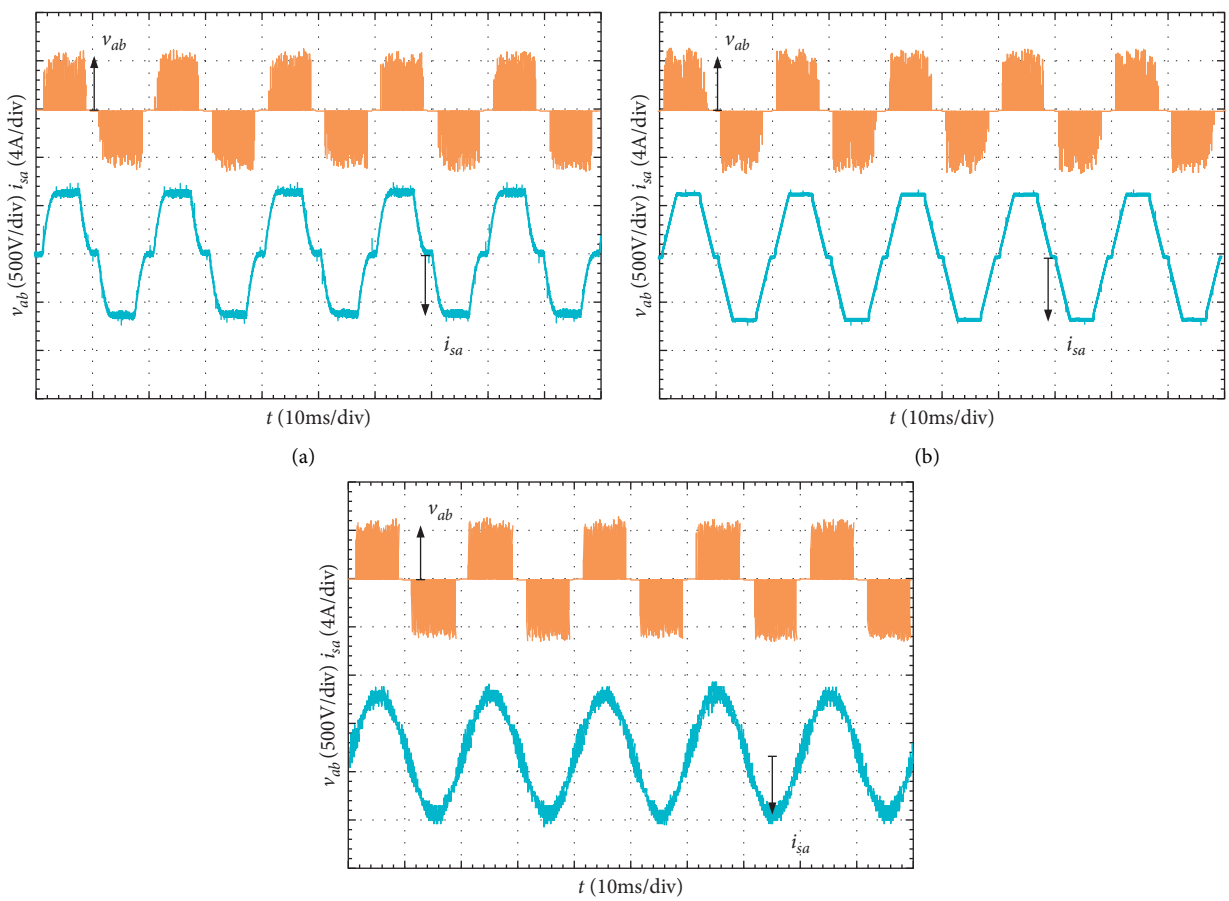

Figure 15: Experimental results of the stator voltage and stator current when the PMSG rotates at 1500 RPM. (a) With half-quasi-Z-source inverter. (b) With enhanced half-quasi-Z-source inverter. (c) With enhanced half-quasi-Z-source inverter and the periodic shoot-through duty ratio control scheme.

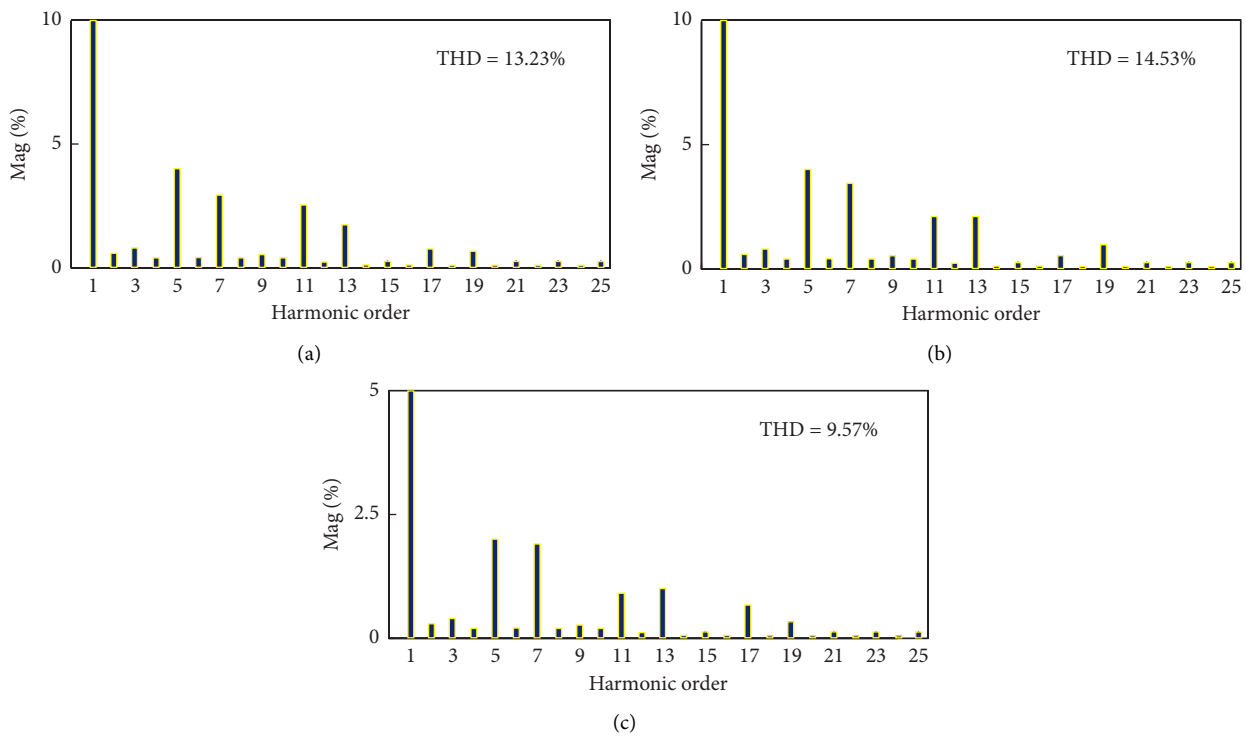

Figure 16: Experimental results of the stator current frequency spectrum when the PMSG rotates at 1500 RPM. (a) With half-quasi-Z-source inverter. (b) With enhanced half-quasi-Z-source inverter. (c) With enhanced half-quasi-Z-source inverter and the periodic shoot-through duty ratio control method.

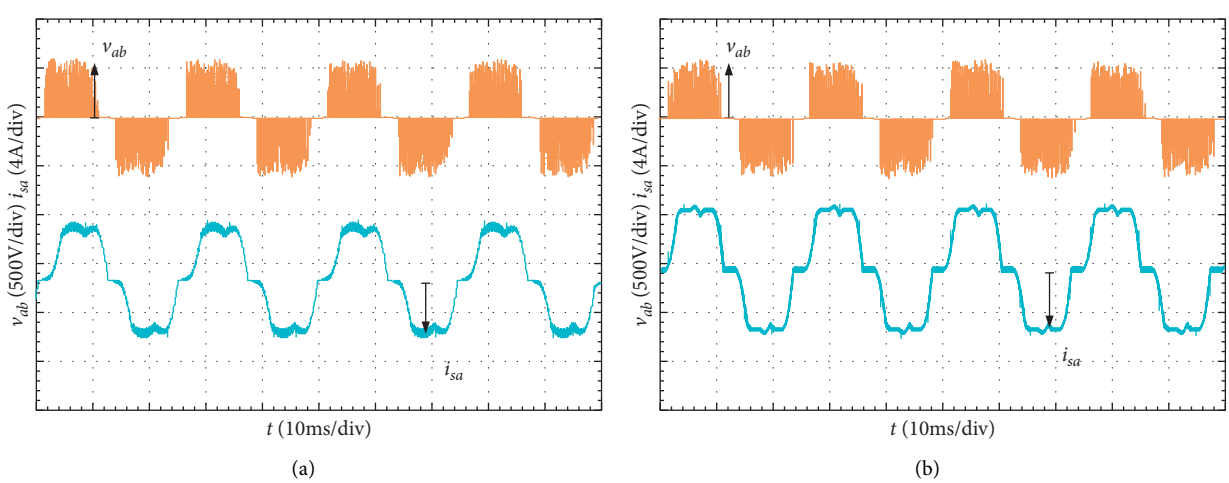

Figure 17: Continued.

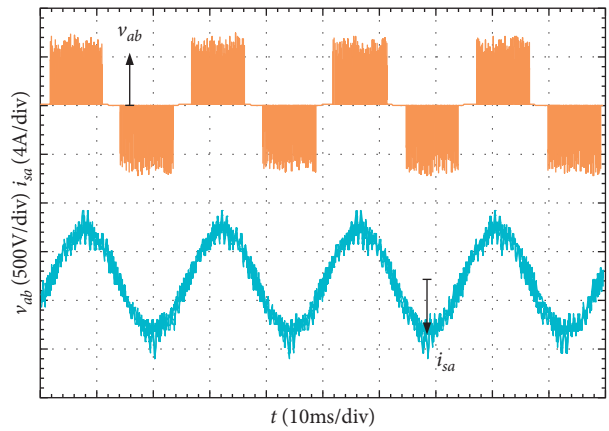

(c)

Figure 17: Experimental results of the stator voltage and stator current when the PMSG rotates at 1200 RPM. (a) With half-quasi-Z-source inverter. (b) With enhanced half-quasi-Z-source inverter. (c) With enhanced half-quasi-Z-source inverter and the periodic shoot-through duty ratio control method.

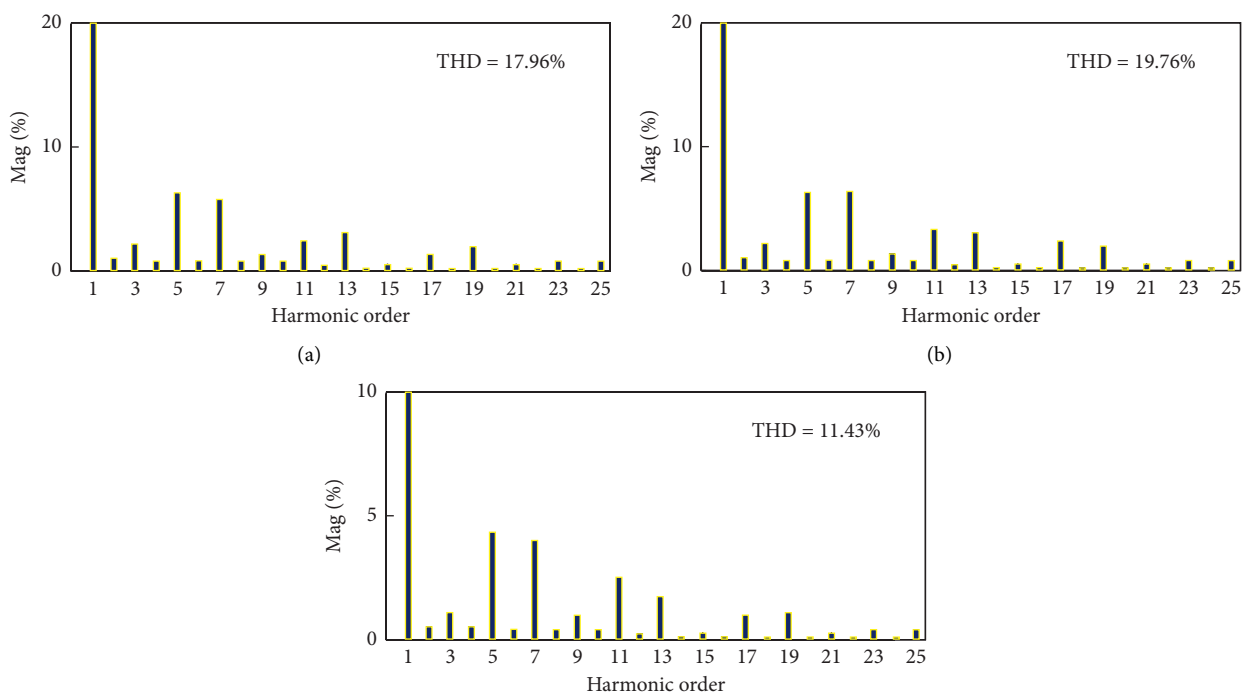

(c)

Figure 18: Experimental results of the stator current frequency spectrum when the PMSG rotates at 1200 RPM. (a) With half-quasi-Z-source inverter. (b) With enhanced half-quasi-Z-source inverter. (c) With enhanced half-quasi-Z-source inverter and the periodic shoot-through duty ratio control method.

7. Conclusion

In this paper, an enhanced half-quasi-Z-source inverter has been proposed, which has higher boost capacity due to the lower voltage stress of the inverter bridge. In this paper, the system configuration, operating principle, and voltage gain of the proposed E-HQZSI were analyzed in detail. However, the THD of stator current is increased along with the higher boost capacity of E-HQZSI. So a periodic shoot-through duty ratio control scheme is proposed to reduce the THD of the stator current in this paper. In this part of the paper, input current change rate, input power factor, and periodic shoot-through duty ratio of the proposed E-HQZSI were analyzed in detail. It can be seen that the THD of stator current with the proposed scheme was significantly reduced compared to the traditional scheme according to the experimental results.

Data Availability

The data used to support the findings of the study are included within the article.

Conflicts of Interest

The authors declare that there are no conflicts of interest regarding the publication of this paper.

Acknowledgments

This research was funded by National Natural Science Foundation of China, Grant no. 51907061, Natural Science Foundation of Hunan Province, Grant no. 2019JJ50119, and National Engineering Laboratory of UHV Engineering Technology, Kunming, Guangzhou, Grant no. NEL202008.

References

[1] T. Ding, S. Liu, W. Yuan, Z. Bie, and B. Zeng, "A two-stage robust reactive power optimization considering uncertain wind power integration in active distribution networks," *IEEE Transactions on Sustainable Energy*, vol. 7, no. 1, pp. 301–311, 2016.

[2] J. Ouyang, M. Li, Y. Diao, T. Tang, and Q. Xie, "Active control method of large-scale wind integrated power system with enhanced reactive power support for wind speed fluctuation," *IET Generation, Transmission & Distribution*, vol. 12, no. 21, pp. 5664–5671, 2018.

[3] M. Hassan Zamani, G. Hossein Riahy, and M. Abedi, "Rotor-speed stability improvement of dual stator-winding induction generator-based wind farms by control-windings voltage oriented control," *IEEE Transactions on Power Electronics*, vol. 31, no. 8, pp. 5538–5546, 2016.

[4] Y. Zhao, L. Ye, W. Wang, H. Sun, Y. Ju, and Y. Tang, "Data-driven correction approach to refine power curve of wind farm under wind curtailment," *IEEE Transactions on Sustainable Energy*, vol. 9, no. 1, pp. 95–105, 2018.

[5] Ł. H. Kocewiak, B. L. Ø. Kramer, O. Holmstrøm, K. H. Jensen, and L. Shuai, "Resonance damping in array cable systems by wind turbine active filtering in large offshore wind power plants," *IET Renewable Power Generation*, vol. 11, no. 7, pp. 1069–1077, 2017.

[6] Global Wind Energy Council (GWEC). Global wind energy Council (GWEC), 2005, [Online]. Available:.

[7] American wind energy association (AWEA). American wind energy association (AWEA), 1974, [Online]. Available:.

[8] European Wind Energy Association (EWEA). European wind energy association (EWEA), 1982 [Online]. Available.

[9] R. Zhu, Z. Chen, Y. Tang, F. Deng, and X. Wu, "Dual-loop control strategy for DFIG-based wind turbines under grid voltage disturbances," *IEEE Transactions on Power Electronics*, vol. 31, no. 3, pp. 2239–2253, 2016.

[10] Y. Song and F. Blaabjerg, "Analysis of middle frequency resonance in DFIG system considering phase-locked loop," *IEEE Transactions on Power Electronics*, vol. 33, no. 1, pp. 343–356, 2018.

[11] C. Wei, Z. Zhang, W. Qiao, and L. Qu, "An adaptive network-based reinforcement learning method for MPPT control of PMSG wind energy conversion systems," *IEEE Transactions on Power Electronics*, vol. 31, no. 11, pp. 7837–7848, 2016.

[12] M. Ashourianjozdani, L. A. C. Lopes, and P. Pillay, "Power electronic converter based PMSG emulator: a testbed for renewable energy experiments," *IEEE Transactions on Industry Applications*, vol. 54, no. 4, pp. 3626–3636, 2018.

[13] H. Polinder, F. F. A. De Vilder, and P. J. Tavner, "Comparison of direct-drive and geared generator concepts for wind turbines," *IEEE Transactions on Energy Conversion*, vol. 21, no. 3, pp. 725–733, 2006.

[14] M. F. Iacchetti, G. M. Foglia, A. Di Gerlando, and A. J. Forsyth, "Analytical evaluation of surface-mounted PMSG performances connected to a diode rectifier," *IEEE Transactions on Energy Conversion*, vol. 30, no. 4, pp. 1367–1375, 2015.

[15] M. S. U. Khan, A. I. Maswood, M. Tariq, H. D. Tafti, and A. Tripathi, "Parallel operation of unity power factor rectifier for PMSG wind turbine system," *IEEE Transactions on Industry Applications*, vol. 55, no. 1, pp. 721–731, 2019.

[16] F. Blaabjerg and M. Liserre, "Power electronics converters for wind turbine systems," *IEEE Trans. on Industry Applications*, vol. 48, no. 2, pp. 708–719, 2007.

[17] Y. S. Liu, B. M. Ge, F. Z. Peng, A. R. Haitham, A. T. de Almeida, and F. J. T. E. Ferreira, "Quasi-Z-source inverter based PMSG wind power generation system," in *Proceedings of IEEE Energy Conversion Congress and Exposition Conference*, pp. 291–297, Phoenix, AZ, USA, September 2011.

[18] A. Hussien, M. Taha, and O. A. Mahgoub, "Design and control of a quasi-Z-source inverter based for wind power generation using PMSG," in *Proceedings of 2015 IEEE 15th International Conference on Environment and Electrical Engineering (EEEIC)*, pp. 2050–2055, Rome, Italy, June 2015.

[19] T. Maity, H. Prasad, and V. R. Babu, "Study of the suitability of recently proposed Quasi Z-source Inverter for wind power conversion," in *Proceedings of 2014 International Conference on Renewable Energy Research and Application (ICRERA)*, pp. 837–841, Milwaukee, WI, USA, October 2014.

[20] B. K. Ramasamy, A. Palaniappan, and S. Mohamed Yakoh, "Direct-drive low-speed wind energy conversion system incorporating axial-type permanent magnet generator and Z -source inverter with sensorless maximum power point tracking controller," *IET Renewable Power Generation*, vol. 7, no. 3, pp. 284–295, 2013.

[21] S. M. Dehghan, M. Mohamadian, and A. Y. Varjani, "A new variable-speed wind energy conversion system using permanent-magnet synchronous generator and Z-Source inverter," *IEEE Transactions on Energy Conversion*, vol. 24, no. 3, pp. 714–724, 2009.

[22] S. D. Huang, Y. Zhang, and S. J. Hu, "Stator current harmonic reduction in a novel half quasi-Z-source wind power generation system," *Energies*, vol. 9, no. 10, pp. 7701–77015, 2016.

Hindawi
Complexity
Volume 2021, Article ID 5558949, 18 pages
https://doi.org/10.1155/2021/5558949

Research Article

Hybrid Estimation of Distribution Algorithm for Solving Three-Stage Multiobjective Integrated Scheduling Problem

Chao Deng,[1] Rong Hu,[1,2] Bin Qian,[1,2] and Huai P. Jin[2]

[1]*Faculty of Mechanical and Electrical Engineering, Kunming University of Science and Technology, Kunming 650500, China*
[2]*Faculty of Information Engineering and Automation, Kunming University of Science and Technology, Kunming 650500, China*

Correspondence should be addressed to Rong Hu; ronghu@vip.163.com

Received 8 February 2021; Accepted 26 April 2021; Published 1 June 2021

Academic Editor: Xue-bo Jin

Aiming at reducing the total energy consumption of three stages processing-transportation-assembly in the assembly manufacturing industry, a three-stage multiobjective integrated scheduling problem with job batch transportation considering the energy consumption (3sMISP_JBTEC) is proposed, and a comprehensive energy consumption model of multistage of 3sMISP_JBTEC with an improved turn off/on strategy in the processing stage and considering speed in the transportation stage is formulated. Then, a hybrid estimation of distribution algorithm with variable neighborhood search (HEDA_VNS) is developed to solve the scheduling problem. In the HEDA_VNS, the reasonable coding/decoding rules and speed scheduling scheme (SSS) are designed. Moreover, two local search strategies are designed to further enhance the performance of HEDA_VNS. Among them, three types of neighborhood search strategies are devised in Local Search I to improve the search efficiency while retaining the structure of the original high-quality solution. A variable neighborhood hybrid operation based on the speed scheduling set is designed in Local Search II to further improve the quality of the solution while balancing the optimization goals. Finally, simulations and comparisons show the efficiency of the proposed HEDA_VNS.

1. Introduction

As environmental pollution becomes a serious challenge for the world, the development of the manufacturing industry is gradually changing towards the green manufacturing. According to relevant surveys, the energy efficiency of the manufacturing industry is low and pollution emissions are high at moment. For instance, in China, the proportion of industrial GDP, 34.3%, is obtained by consuming 68% of the national energy in 2015 [1]. The production process plays an important role in the manufacturing industry. In recent years, in order to reduce energy consumption in the production process, many studies have been conducted on improving the energy efficiency [2–6]. However, among the methods, production scheduling is the most effective and prioritized way to improve the energy efficiency of the manufacturing industry [7].

The assembly manufacturing industry is an important sector of manufacturing enterprises. The production process includes multiple stages of processing, transportation, and assembly. Energy consumption should not be ignored in the whole production process. The existing researches of assembly manufacturing industry have focused on the two-stage scheduling problem (2sSP) containing the processing-assembly and the three-stage scheduling problem (3sSP) containing the processing-transport-assembly. Compared with 2sSP, the transportation between the processing and assembly stages has a nonnegligible process in 3sSP. However, a large number of studies assumed that the transportation time of each job is constant in the transportation stage [8–11]; i.e., the number or load of transportation vehicles is unlimited, which is far from the actual problem. Therefore, Deng et al. [12] have integrated production and transportation, and the three-stage integration scheduling problem with job batch transportation (3sISP_JBT) of processing-transportation-assembly has been studied, which makes the problem model of the assembly manufacturing industry more realistic. However, the

study only considers minimizing the makespan as the optimization goal. Although a close connection among the three stages has been established through the optimization, it leads to production process not compact enough in the single stage. Especially in the processing stage, a large idleness may be generated between two adjacent jobs on the same machine in the process of processing, which causes energy waste seriously. Furthermore, in the transportation stage, the energy consumption is affected by the load and speed of the vehicle closely. In terms of computational complexity, 2sSP has been proven to be NP-hard [13]. It is reduced to 3sSP. Also, 3sSP can be reduced to 3sISP_JBT. Therefore, the considered problem is also NP-hard. To sum up, the comprehensive energy consumption optimization for 3sISP_JBT needs to be further studied.

For the energy-optimized multiobjective green scheduling problem of the production process, the existing research has largely focused on optimizing the machining process with methods of machine speed control, turn off/on machine strategy, etc. [14–18]. However, the transport of workpieces is ignored in the production process. Then, Lu et al. [19] investigated a permutation flow shop scheduling problem with sequence-dependent setup and controllable transportation time in the processing stage from a real-world manufacturing enterprise, where the objects include the makespan and energy consumption, and a hybrid multiobjective backtracking search algorithm (HMOBSA) has proposed to solve the problem. Dai et al. [20] studied a flexible job shop scheduling problem considering the transportation time in the processing stage, where the objects include makespan and the total energy consumption, and an improved genetic algorithm (GA) has been proposed to solve it. However, in the above literature, many scholars considered transportation in the energy optimization problem of workshop scheduling, but they mainly consider the impact of the transportation time on the entire makespan and do not study the energy consumption of transportation in the energy consumption index. After that, Tanimizu and Amano [21] studied the integrated scheduling problem of the processing-transportation stage, a processing-transportation comprehensive energy consumption model has been constructed to minimize the total delay time and the energy consumption, and a genetic algorithm (GA) based on heuristic rules has been adopted to solve this problem. Guo et al. [22] also studied the integrated scheduling problem of the processing-transportation stage, and a hybrid memetic algorithm has been proposed to minimize the total cost and energy consumption. Liu et al. [23] studied a novel integrated green scheduling problem of flexible job shop and crane transportation in the processing stage, a comprehensive energy consumption model has been built to optimize the comprehensive energy consumption and makespan, and an integrated algorithm of a genetic algorithm (GA) and glowworm swarm optimization (GSO) with green transport heuristic strategy has been proposed. It is noted that the above results have considered the transportation time and transportation process in the workshop scheduling optimization and have conducted energy consumption optimization research on this issue, while mainly considering the impact of load factors (constraints) of vehicles on the transportation stage and ignoring the impact of transportation speed on energy consumption. However, the impact of speed on energy consumption cannot be ignored in practice in the actual transportation process. A large number of existing studies have verified the impact of transportation speed on the energy consumption and scheduling schemes on the green transportation scheduling problems considering speed [24–26]. Hence, for 3sISP_JBT of the assembly manufacturing industry, in addition to designing effective energy-saving strategies for the two production stages of processing and assembly, it is necessary to further consider the impact of transportation speed on the energy consumption in the transportation stage to improve the entire production process energy optimization.

At present, a large number of intelligent algorithms have emerged to solve scheduling problems [27–29]. The estimation of distribution algorithm (EDA) is an emerging evolutionary algorithm based on statistics. It learns high-quality individuals in the population in a statistical manner and constructs the probability model, and then the probability model is sampled to generate a new population. It guides the search direction of the algorithm and has a good global search capability. In recent years, EDA has been successfully applied to solve a variety of scheduling problems, including parallel machine scheduling problem [30], flow shop scheduling problem [31], job shop scheduling problem [32, 33], energy-saving job shop scheduling problem [34], vehicle transportation scheduling problem [35], and integrated scheduling problem [12]. Judging from the research status of EDA in scheduling optimization problems, EDA itself has the advantage of probabilistic model global search. In addition, it can be reasonably mixed with other effective algorithms and operations, which can greatly enrich the search ability and improve the algorithm performance.

This paper aims to optimize the three-stage multiobjective integration scheduling problem with job batch transportation considering the energy consumption (3sMISP_JBTEC) in the assembly manufacturing industry. In the processing stage, the machining environment is a heterogeneous parallel machine of multiprocessing with release time. In the transportation stage, the transportation facilities are the same type vehicles. In the assembly stage, only one machine is used for assembly. The focus of this paper is to explore the interrelationship between the three stages processing-transportation-assembly and the key factors affecting energy consumption at each stage to further optimize the comprehensive energy consumption of the assembly manufacturing industry. The contributions of this paper are as follows:

(1) A mathematic model is formulated for the 3sMISP_JBTEC, in which the objective is to minimize the comprehensive energy consumption and makespan of the production task.

(2) In the proposed model, a comprehensive energy consumption model with an improved turn off/on strategy in the processing stage and speed factor in

the transportation stage is built to optimize the comprehensive energy efficiency of the three stages, processing-transportation-assembly.

(3) A hybrid estimation of distribution algorithm with variable neighborhood search (HEDA_VNS) is presented to solve the proposed model.

(4) In HEDA_VNS, the reasonable coding/decoding rules and speed scheduling scheme are designed based on the specific characteristics. Then, two local search strategies are designed to further enhance the HEDA_VNS's performance. Among them, three types of neighborhood search strategies are devised in Local Search I to improve the search efficiency while retaining the structure of the original high-quality solution. A variable neighborhood hybrid operation based on the speed set is designed in Local Search II to further improve the quality of the solution while balancing the optimization goals.

The remainder of this paper is organized as follows. A mathematic model of the proposed 3sMISP_JBTEC is developed in Section 2. HEDA_VNS algorithm is designed for solving 3sMISP_JBTEC in Section 3. Section 4 details the HEDA_VNS. Simulation experiment results and analysis is conducted in Section 5. Section 6 presents the conclusions.

2. Mathematical Formulation

In this section, the introduced 3sMISP_JBTEC is described in detail based on the assembly manufacturing environment. Then, a mathematical model is proposed to formulate the 3sMISP_JBTEC with the consideration of comprehensive energy consumption and makespan.

2.1. Problem Description and Assumptions. The 3sMISP_JBTEC problem is described as follows. According to the customer order (demand), we set the number of processed products as H_P, the number of processing machines in the processing stage as m_1, the number of transport vehicles in the transportation stage as H_{TR}, and the number of assembled machines in the assembly stage as one. Each product is composed of multiple jobs, and each job needs to be processed in different procedures. The procedures of the jobs need to be processed in sequence on the machine that meets the processing constraints at the processing stage. After the jobs are processed, they are loaded by the same type vehicle in the transportation stage. Transport at a certain speed v to the assembly stage to wait for assembly. The jobs of each product are processed in three stages in the order of processing. Then, the model diagram is shown in Figure 1.

Without loss of generality, the 3sMISP_JBTEC is investigated based on the following reasonable assumptions:

(1) Any processing machine in the processing stage can only process one job at the same time, and different jobs have release time; a process of job is immediately transferred to the next process after being processed, and the transfer time of job between the required machine is ignored; the preparation time of all processes of job is not related to the processing sequence and is included in the processing time of the process. Different processes of the same job cannot be processed at the same time; each process of each job cannot be interrupted once it starts processing.

(2) The assembly machine in the assembly stage can only assemble the same product at the same time, and the setup time between different products is set to zero; the initial state of the assembly machine is idle, and at zero time, any task is feasible.

(3) If the same raw material is processed through the same process in the processing stage, it is the same job, and one or more jobs that make up different products are not the same.

2.2. Notation. The main notations used in formulating the mathematical model of the 3sMISP_JBTEC problem are listed as follows:

P: product set. $z \in P$, $P = \{1, 2, \ldots, H_P\}$.

Q: jobs set. $j \in Q$, $Q = \{1, 2, \ldots, q\}$.

O: process set. $i \in O$, $O = \{1, 2, \ldots, H_O\}$.

T: vehicle set. $t \in T$, $T = \{1, 2, \ldots, H_{\mathrm{TR}}\}$.

M: machine set in processing stage. $k \in M$, $M = \{1, 2, \ldots, m_1\}$.

H_k: the number of processes on the processing machine k.

w_t: the number of round trips of vehicle t. $w_t \geq 1$.

H_T: the total number of transport vehicles. $H_T \not\subset \infty$.

V_T: the vehicle rated load (fixed value).

Dis_{P-A}: the distance from the processing stage to the transportation stage.

S: the vehicle speed set.

W^T_{idle}: the unload weight of the vehicle.

$\mathrm{SV}_{\mathrm{use}}$: the speed use set. $\mathrm{SV}_{\mathrm{use}} = \{v_1, \ldots, v_t, \ldots, v_{H_T}\}$.

$\pi^K = [\pi^K_{[1]}, \pi^K_{[2]}, \ldots, \pi^K_{[H_o]}]$: the permutation of the processes of all jobs in the processing stage. The jobs in the permutation are allocated to the corresponding machines for processing from left to right according to rules and parallel processing constraints.

$\pi^k = [\pi^k_{[1]}, \pi^k_{[2]}, \ldots, \pi^k_{[i]}, \ldots, \pi^k_{[H_k]}]$: the permutation of the process of the job on the processing machine k in the processing stage, where $\pi^k_{[i]}$ is the process of the job at the position i of π^k.

$\pi^{\mathrm{TR}} = [\pi^{\mathrm{TR}}_{[1]}, \pi^{\mathrm{TR}}_{[2]}, \ldots, \pi^{\mathrm{TR}}_{[j]}, \ldots, \pi^{\mathrm{TR}}_{[q1]}]$: the permutation of all the jobs in the transportation stage, where $\pi^{\mathrm{TR}}_{[j]}$is the job at the position j of π^{TR}.

$\pi^{\mathrm{TR}-V} = [\pi^{\mathrm{TR}-V}_{[1]}, \pi^{\mathrm{TR}-V}_{[2]}, \ldots, \pi^{\mathrm{TR}-V}_{[t]}, \ldots, \pi^{\mathrm{TR}-V}_{[H_T]}]$: the speed permutation of all vehicles in the transportation phase, where $\pi^{\mathrm{TR}-V}_{[t]}$ is the vehicle at the position t of $\pi^{\mathrm{TR}-V}$.

$\pi^P = [\pi^P_{[1]}, \pi^P_{[2]}, \ldots, \pi^P_{[z]}, \ldots, \pi^P_{[H_P]}]$: the permutation of the products to be processed on the assembly machine

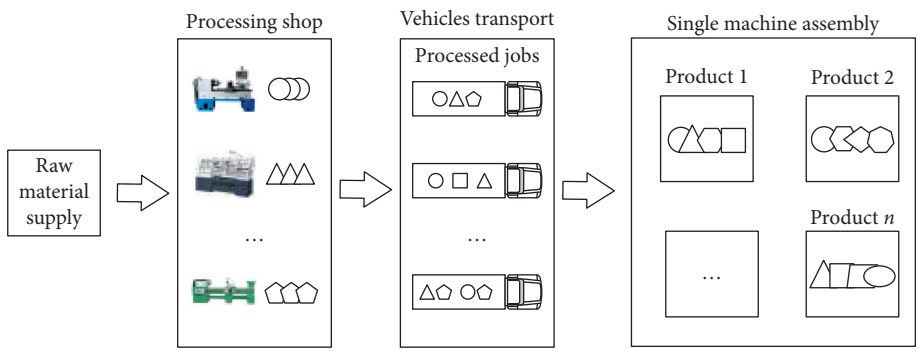

Figure 1: The problem model of 3sMISP_JBTEC.

in the assembly stage, where $\pi^P_{[z]}$ is the product at the position z of π^P.

$P(\pi^k_{[i]})$: the processing time of $\pi^k_{[i]}$.

$R(\pi^k_{[i]})$: the release time when the job at the position i of π^k first arrived at the processing machine k.

$P(\pi^P_{[z]})$: the assembly time of π^P_z.

$V(\pi^{\mathrm{TR}}_{[j]})$: the weight of the job at position j of π^{TR}.

$v(\pi^{\mathrm{TR}-V}_{[t]})$: the speed at of the vehicle at position t of $\pi^{\mathrm{TR}-V}$.

T_{on}: the time required to turn on a machine.

T_{off}: the time required to turn off a machine.

$T^{\mathrm{Num-off}}_k$: the number of turning off the machine k.

$\mathrm{e}^{\mathrm{idle}}_k$: the energy consumption of idle time of machine k.

e^R_k: the energy consumption of release time of machine k.

e^P_k: the average energy consumption of processing time of machine k.

e^T_{tv}: the energy consumption of vehicle t at a speed v.

$E_{\mathrm{off-on}}$: the energy consumption requirement for turn off, then turn on the machine.

E^{idle}_T: the energy consumption of vehicle t return one time without load.

$\mathrm{pre\_}m(\pi^k_{[i]})$: the machine number of the previous processing operation of $\pi^k_{[i]}$; the permutation of the previous process of $\pi^k_{[i]}$ with the machine number $\mathrm{pre\_}m(\pi^k_{[i]})$ expressed as $\pi^{\mathrm{pre\_}m(\pi^k_{[i]})}_{[i]}$. If the job $\pi^k_{[i]}$ is processed for the first time, then $\mathrm{pre\_}m(\pi^k_{[i]}) = 0$.

$\mathrm{pre\_}k(\pi^k_{[i]})$: the process number of the previous processed job when $\pi^k_{[i]}$ processing on the machine k. The position of the process in the permutation is recorded as $\pi^k_{\mathrm{pre\_}k(\pi^k_{[i]})}$. If the machine k is processing the job for the first time, then $\mathrm{pre\_}k(\pi^k_{[i]}) = 0$.

$C(\pi^k_{[i]})$: the processing complete time of $\pi^k_{[i]}$.

$C_{\mathrm{st1}}(\pi^{\mathrm{TR}}_{[j]})$: the processing completion time of the job j of π^{TR}.

$S(\pi^{\mathrm{TR}}_{[j]})$: the transportation starting time of the job j of π^{TR} in vehicle t.

$C(\pi^{\mathrm{TR}}_{[j]})_{w_t}$: the transportation completion time of the job j of π^{TR} in w_t trips of vehicle t.

$C_{\mathrm{st2}}(\pi^{\mathrm{TR}}_{[j]})$: the transportation completion time of the job j of π^{TR}.

$S(\pi^P_{[z]})$: the assembly start time of π^P_z.

$C_{\mathrm{st3}}(\pi^P_{[z]})$: the assembly completion time of π^P_z.

2.3. Comprehensive Energy Consumption Model. In the section, a comprehensive energy consumption model of 3sMISP_JBTEC is given in the three stages, respectively. In the processing stage, the energy consumption includes the release process, the processing process, and the idle process. Besides, an improved turn off/on strategy is proposed to better save energy and extend the life of the machine. In the transportation stage, the impact factor of speed and load is both considered to calculate energy consumption during transportation.

2.3.1. Energy Consumption of the Processing Stage (EC_{st1}). The processing stage is a multiprocess heterogeneous parallel machine scheduling problem with release time. The processing workshop is a flexible workshop, and multiple processes of the jobs can be processed on different machines. It is flexible and versatile, but it is also one of the industrial workshops with the highest energy consumption [36]. Figure 2 is the energy consumption of the flexible machine k in the processing stage of the problem. It can be seen from Figure 2 that the energy consumption of this processing stage ($\mathrm{EC}_{\mathrm{st1}}$) is composed of the energy consumption of the release process ($\mathrm{EC}^{\mathrm{st1}}_R$) when the jobs arrives at the machine for the first time, the energy consumption of the processing process ($\mathrm{EC}^{\mathrm{st1}}_P$) of the different jobs in machines, and the energy consumption of the idle process ($\mathrm{EC}^{\mathrm{st1}}_{\mathrm{idle}}$). If the energy consumption caused by job transfermation between different machines is ignored, then the total energy consumption of the processing stage ($\mathrm{EC}_{\mathrm{st1}}$) is calculated by using equation (1). In order to simplify the calculation, this paper simplified the unit energy consumption of each part to the average value:

$$\mathrm{EC}_{\mathrm{st1}} = \mathrm{EC}^{\mathrm{st1}}_R + \mathrm{EC}^{\mathrm{st1}}_P + \mathrm{EC}^{\mathrm{st1}}_{\mathrm{idle}}. \quad (1)$$

(1) *Energy Consumption of Release Process* ($\mathrm{EC}^{\mathrm{st1}}_R$). The energy consumption of the release process depends on the release time of jobs. Because there are differences between the jobs (i.e., size, shape, material, and weight) and

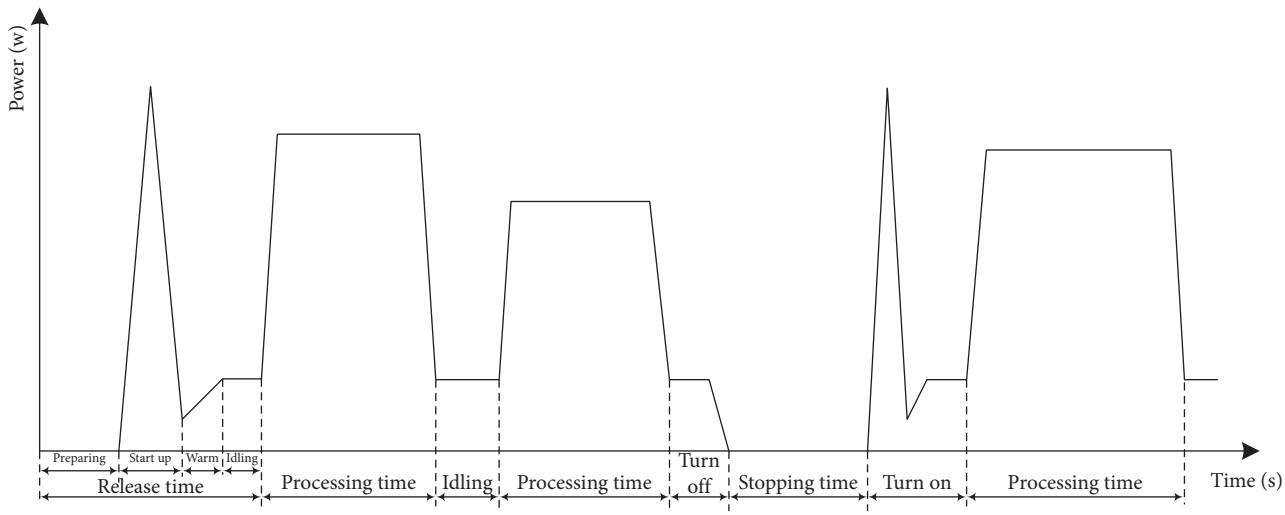

Figure 2: Example of energy consumption of a processing machine.

machines, it directly affects $\mathrm{EC}_R^{\mathrm{st1}}$. Thus, the energy consumption of the machine's release process is calculated by the following equation:

$$\mathrm{EC}_R^{\mathrm{st1}} = \sum_k e_k^R \cdot R\left(\pi_{[i]}^k\right), \quad i = 1, \ldots, H_k; k = 1, \ldots, m_1. \tag{2}$$

(2) *Energy Consumption of the Processing Process* ($\mathrm{EC}_P^{\mathrm{st1}}$). The energy consumption of the process depends on the processing time of the corresponding process of the job on the machine. The energy consumption of all machines in the processing process is calculated as

$$\mathrm{EC}_P^{\mathrm{st1}} = \sum_i \sum_k e_k^P \cdot P\left(\pi_{[i]}^k\right), \quad i = 1, \ldots, H_k; k = 1, \ldots, m_1. \tag{3}$$

(3) *Energy Consumption of the Idle Process* ($\mathrm{EC}_{\mathrm{idle}}^{\mathrm{st1}}$) *and an Improved Turn Off/On Strategy*. The energy consumption of the process depends on the idle time of the machine. The idle time i on the machine k can be expressed as $P_{k,i}^{\mathrm{idle}} = S(\pi_{[i+1]}^k) - C(\pi_{[i]}^k)$, where $P_{k,i}^{\mathrm{idle}} > 0$. If the machine's idle time is too long, it will cause a waste of energy. Therefore, the machine needs to be turned off to save energy at the appropriate time. The work in [37] gives the decision time period T_B for whether or not to shut down the machine, where $T_B = \max\{E_{\mathrm{off-on}}/e_k^{\mathrm{idle}}, T_{\mathrm{on}} + T_{\mathrm{off}}\}$. If $P_k^{\mathrm{idle}} \geq T_B$, the machine should be turned off. Although the power-off method can reduce energy consumption, it frequently may shorten the service life of the machine. Therefore, the work in [38] gives the maximum allowable number of machine turn off, where $T_{\mathrm{Num-off}}$. Then, in order to further save energy and prolong the life of the machine, an energy-saving strategy for turn on/off of machine was proposed in [19]. However, the closeness of adjacent idle in the same machine is not considered. If the adjacent idles are too close and $P_k^{\mathrm{idle}} \geq T_B$, turning the machine on and off frequently would still affect the life of the machine in the actual production process. Therefore, this paper designs an improved energy-saving strategy based on the above studies. The steps are as follows:

Step 1: calculate P_k^{idle} of the machine k, then record the time $T_{k,i}^{\mathrm{dis}}$ between two adjacent idles, $T_{k,n}^{\mathrm{dis}} = SP_{k,i+1}^{\mathrm{idle}} - CP_{k,i}^{\mathrm{idle}}$, where $T_{k,i}^{\mathrm{dis}} > 0$.

Step 2: compare with $P_{k,i}^{\mathrm{idle}}$ and T_B in turn. If $P_{k,i}^{\mathrm{idle}} \geq T_B$ and $T_{k,i}^{\mathrm{dis}} \leq \varepsilon$ (where ε is a certain value), then put $\max\left\{P_{k,i}^{\mathrm{idle}}, P_{k,i+1}^{\mathrm{idle}}\right\}$ into set Ω and put $\min\left\{P_{k,i}^{\mathrm{idle}}, P_{k,i+1}^{\mathrm{idle}}\right\}$ in the taboo table to avoid repeated comparisons, else put $P_{k,i}^{\mathrm{idle}}$ (where $P_{k,i}^{\mathrm{idle}} \geq T_B$) into the set Ω directly.

Step 3: sort P_k^{idle} which in the set Ω in nonascending order. Then, select the first number $T_{\mathrm{Num-off}}$ of P_k^{idle} in the sequence and put them in the set Ω' which is recorded as $P_k^{\mathrm{Stop\_idle}}$.

From the above, the energy consumption of the idle process is calculated as

$$\begin{aligned}
\mathrm{EC}_{\mathrm{idle}}^{\mathrm{st1}} &= \sum_i \sum_k e_k^{\mathrm{idle}} \cdot P_{k,i}^{\mathrm{idle}} - \sum_i \sum_k e_k^{\mathrm{idle}} \cdot P_{k,i}^{\mathrm{Stop_idle}} + \sum_i \sum_k E_{\mathrm{off-on}} \cdot T_{\mathrm{Num-off}} \\
&= \sum_i \sum_k e_k^{\mathrm{idle}} \cdot \left(S\left(\pi_{[i+1]}^k\right) - C\left(\pi_{[i]}^k\right)\right) - \sum_i \sum_k e_k^{\mathrm{idle}} \cdot P_{k,i}^{\mathrm{Stop_idle}} \\
&\quad + \sum_i \sum_k E_{\mathrm{off-on}} \cdot T_{\mathrm{Num-off}}, \quad i = 1, \ldots, H_k - 1; k = 1, \ldots m_1; P_k^{\mathrm{Stop_idle}} \in \Omega'.
\end{aligned} \tag{4}$$

2.3.2. Energy Consumption of Transportation Stage (EC_{st2}). In the transportation stage, the jobs completed in the processing stage will be transported to the assembly place for assembly by multiple vehicles of the same type under certain constraints of load and speed. The constant Dis_{P-A} is the distance from the processing stage to the assembly stage. The vehicle can go back and forth multiple times, and thus, the vehicle is empty during the return process. The speed of each vehicle without load is a constant value v_c, and the energy consumption is a constant value E_T^{idle}. It should be emphasized that once all vehicles begin to transport, the constant speed of vehicles should be maintained throughout the transportation process.

In this line, some studies have been conducted on the energy consumption of vehicle transportation. Palmer [39] incorporated the energy consumption indicators into the vehicle transportation problem and proposed an energy consumption model that considers the total length or distance of the path. Kara et al. [40] proposed an energy consumption model considering the load of vehicle and distance. Kuo [24] further considered the vehicle speed and proposed a time-dependent speed and vehicle load energy consumption model. Demir et al. [25] developed a mathematical model of energy consumption of multiple parameters with speed, distance, and load. In the equation, P_{tract} (kilowatts) is the unit traction power of the vehicle, τ is the acceleration, $M = w + f$ (w is the mass of the vehicle and f is the mass of the cargo carried by the vehicle), and the rest is the vehicle-related parameter. In this paper, the uniform speed of the vehicles is considered, where $\tau = 0$, but the influence of the gradient of the vehicle is not considered. Then, the per unit time of the vehicle t is shown in equation (6). Therefore, the energy consumption of the transportation stage can be given as shown in equation (7), where the unit of speed is m/s:

$$P^{\mathrm{tract}} = \frac{\left(M\tau + Mg\sin\theta + 0.5C_d\rho A v^2 + MgC_r\cos\theta\right)v}{1000}, \tag{5}$$

$$P_t^{\mathrm{tract}} = \frac{\left(0.5C_d\rho A v^2 + MgC_r\right)v}{1000}, \tag{6}$$

$$\begin{aligned} EC_{\mathrm{st2}} &= \sum_t \frac{P_t^{\mathrm{tract}} \cdot \mathrm{Dis}_{P-A}}{v\left(\pi_{[t]}^{\mathrm{TR}-V}\right)} + \sum_t \sum_w E_T^{\mathrm{idle}} \cdot w_t \\ &= \sum_t \frac{\left(0.5C_d\rho A \cdot v\left(\pi_{[t]}^{\mathrm{TR}-V}\right)^2\right) + \left(W_{i\,dl\,e}^T + \sum_j V\left(\left(\pi_{[j]}^{TR}\right)gC_r\right) \cdot \mathrm{Dis}_{P-A}\right.}{1000} \\ &\quad + \sum_t \sum_w \frac{\left(0.5C_d\rho A v_c^2 + W_{\mathrm{idle}}^T gC_r\right) \cdot \mathrm{Dis}_{P-A} \cdot w_t}{1000}, \quad j = 1, \ldots, q; t = 1, \ldots, H_T; v \in S; w = 1, 2, \ldots. \end{aligned} \tag{7}$$

2.3.3. Energy Consumption of Assembly Stage (EC_{st3}). The assembly stage is a single machine scheduling problem. Since the assembly time of each product on the machine is unchanged, it will not affect the processing energy consumption so that the energy consumption is only related to the machine's idle time. Therefore, energy consumption of the assembly process is calculated as

$$\mathrm{EC}_{\mathrm{st3}} = \sum_z e_{m_2}^{\mathrm{idle}} \cdot \left(S\left(\pi_{[z+1]}^P\right) - C\left(\pi_{[z]}^P\right)\right), \quad z = 1, 2, \ldots, H_P. \tag{8}$$

In summary, the total energy consumption of 3sMISP_JBTEC is calculated as

$$\mathrm{EC}_{\mathrm{total}} = \mathrm{EC}_{\mathrm{st1}} + \mathrm{EC}_{\mathrm{st2}} + \mathrm{EC}_{\mathrm{st3}}. \tag{9}$$

2.4. Formulation of Multiobjective Model of 3sMISP_JBTEC. The 3sMISP_JBTEC is formulated as the following mathematical model, in which two objectives of makespan and total energy consumption are considered:

(1) The processing stage: it is a multiprocess heterogeneous parallel machine scheduling problem with release time in the processing stage. If the job $\pi_{[i]}^k$ is processed for the first time, then $\mathrm{pre}\_m(\pi_{[i]}^k) = 0$; If the machine that processed job $\pi_{[i]}^k$ is the first time to process the job, then $\mathrm{pre}\_k(\pi_{[i]}^k) = 0$. The completion time $C(\pi_{[i]}^k)$ of $\pi_{[i]}^k$ is calculated as follows:

$$
\begin{aligned}
&C\left(\pi_{[i]}^{k}\right)=\min\left\{P\left(\pi_{[i]}^{k}\right)+R\left(\pi_{[i]}^{k}\right)\right\}, \mathrm{pre\_}m\left(\pi_{[i]}^{k}\right)=0; \mathrm{pre\_}k\left(\pi_{[i]}^{k}\right)=0,\\
&C\left(\pi_{[i]}^{k}\right)=\min\left\{\max\left\{C\left(\pi_{\left[\mathrm{pre\_}k\left(\pi_{[i]}^{k}\right)\right]}^{k}\right), R\left(\pi_{[i]}^{k}\right)\right\}+P\left(\pi_{[i]}^{k}\right)\right\}, \mathrm{pre\_}m\left(\pi_{[i]}^{k}\right)=0; \mathrm{pre\_}k\left(\pi_{[i]}^{k}\right)\neq 0,\\
&C\left(\pi_{[i]}^{k}\right)=\min\left\{C\left(\pi_{[i]}^{\mathrm{pre\_}m\left(\pi_{[i]}^{k}\right)}\right)+P\left(\pi_{[i]}^{k}\right)\right\}, \mathrm{pre\_}m\left(\pi_{[i]}^{k}\right)\neq 0; \mathrm{pre\_}k\left(\pi_{[i]}^{k}\right)=0,\\
&C\left(\pi_{[i]}^{k}\right)=\min\left\{\max\left\{C\left(\pi_{[i]}^{\mathrm{pre\_}m\left(\pi_{[i]}^{k}\right)}\right), C\left(\pi_{\mathrm{pre\_}k\left(\pi_{[i]}^{k}\right)}^{k}\right)\right\}+P\left(\pi_{[i]}^{k}\right)\right\}, \mathrm{pre\_}m\left(\pi_{[i]}^{k}\right)\neq 0; \mathrm{pre\_}k\left(\pi_{[i]}^{k}\right)\neq 0,\\
&C_{\mathrm{st1}}\left(\pi_{[j]}^{t}\right)=C\left(\pi_{[i]}^{k}\right), \quad k=1,2,\ldots,m_1; j=1,2,\ldots,q; i=1,2,\ldots,H_k.
\end{aligned}
\tag{10}
$$

(2) The transportation stage: it is a multivehicle single-point delivery problem with the constraints of load and speed in the transportation stage. The total load of all jobs loaded in the vehicle t cannot exceed the vehicle rated load (V_T). The transportation time of the vehicle t is determined by the speed $v(\pi_{[t]}^{\mathrm{TR}-V})$. The transportation completion time of the job j of π^{TR} is calculated as follows

:

$$
\begin{aligned}
&S\left(\pi_{[j]}^{\mathrm{TR}}\right)_{w_t}=\max\left\{C_{\mathrm{st1}}\left(\pi_{[j]}^{\mathrm{TR}}\right)_{w_t}\right\}, \quad w_t=1,\\
&S\left(\pi_{[j]}^{\mathrm{TR}}\right)_{w_t}=\max\left\{C_{\mathrm{st1}}\left(\pi_{[j]}^{\mathrm{TR}}\right)_{w_t}^{t}, S\left(\pi_{[j]}^{\mathrm{TR}}\right)_{w_t-1}+\left(\frac{\mathrm{Dis}_{p-t}}{v\left(\pi_{[t]}^{\mathrm{TR}-V}\right)}+\frac{\mathrm{Dis}_{p-t}}{v_c}\right)\right\}, \quad w_t\neq 1,\\
&C_{\mathrm{st2}}\left(\pi_{[j]}^{\mathrm{TR}}\right)_{w_t}=S\left(\pi_{[j]}^{\mathrm{TR}}\right)_{w_t}+\frac{\mathrm{Dis}_{p-t}}{v\left(\pi_{[t]}^{\mathrm{TR}-V}\right)}, \quad j=1,2,\ldots,q; w_t=1,2,\ldots,l; t=1,2,\ldots,H_T.
\end{aligned}
\tag{11}
$$

(3) The assembly stage: it is a single-machine scheduling problem with arrival time or release time. The calculation formula for the assembly completion time $C_{\mathrm{st3}}(\pi_{[z]}^{P})$ of the product π_z^P is shown as follows:

$$
\begin{aligned}
&S\left(\pi_{[z]}^{P}\right)=\max\left\{C_{\mathrm{st2}}\left(\pi_{[j]}^{\mathrm{TR}}\right)\right\},\\
&C_{\mathrm{st3}}\left(\pi_{[z]}^{P}\right)=\max\left\{C_{\mathrm{st3}}\left(\pi_{[z-1]}^{P}\right), S\left(\pi_{[z]}^{P}\right)\right\}+P\left(\pi_{[z]}^{P}\right), \quad z=1,2,\ldots,H_P, j=1,2,\ldots,q.
\end{aligned}
\tag{12}
$$

(4) The optimization goal: the optimization goal is to find an optimal sequence $\pi^*=(\pi^K,\pi^{TR},\pi^{\mathrm{TR}-V},\pi^P)$ in the set Π of the three-stage sequence from processing and transportation to assembly of the job which composed products so that the makespan $C_{\max}$ and the total energy consumption E_{total} of the three stages are minimized:

$$
\begin{aligned}
&C_{\max}\left(\boldsymbol{\pi}^*\right)=\min_{\left(\boldsymbol{\pi}^K,\boldsymbol{\pi}^{TR},\boldsymbol{\pi}^{\mathrm{TR}-V},\boldsymbol{\pi}^P\right)\in\Pi}\left\{C_{\max}\left(\boldsymbol{\pi}^K,\boldsymbol{\pi}^{TR},\boldsymbol{\pi}^{\mathrm{TR}-V},\boldsymbol{\pi}^P\right)\right\},\\
&E_{\mathrm{total}}\left(\boldsymbol{\pi}^*\right)=\min_{\left(\boldsymbol{\pi}^K,\boldsymbol{\pi}^{TR},\boldsymbol{\pi}^{\mathrm{TR}-V},\boldsymbol{\pi}^P\right)\in\Pi}\left\{E_{total}\left(\boldsymbol{\pi}^K,\boldsymbol{\pi}^{TR},\boldsymbol{\pi}^{\mathrm{TR}-V},\boldsymbol{\pi}^P\right)\right\},\\
&\pi^*=\arg\left\{\begin{array}{l} C_{\max}\left(\boldsymbol{\pi}^K,\boldsymbol{\pi}^{TR},\boldsymbol{\pi}^{\mathrm{TR}-V},\boldsymbol{\pi}^P\right),\\ E_{\mathrm{total}}\left(\boldsymbol{\pi}^K,\boldsymbol{\pi}^{TR},\boldsymbol{\pi}^{\mathrm{TR}-V},\boldsymbol{\pi}^P\right)\end{array}\right\}\longrightarrow\min, \quad \forall\left(\boldsymbol{\pi}^K,\boldsymbol{\pi}^{TR},\boldsymbol{\pi}^{\mathrm{TR}-V},\boldsymbol{\pi}^P\right)\in\Pi.
\end{aligned}
\tag{13}
$$

3. HEDA_VNS for 3sMISP_JBTEC

3.1. Characteristics of 3sMISP_JBTEC. The characteristic of 3sMISP_JBTEC have the following three aspects:

(1) The problem is holistic and systematic. 3sMISP_JBTEC is a multistage integration problem. The scheduling result of the previous stage directly affects the latter stage. Therefore, the overall optimization should be considered when designing the solution algorithm.

(2) The connection between stages is close. Each stage of 3sMISP_JBTEC is not independent, and there are constraints between the process set, the job set, and the product set. Moreover, all the processes belonging to the same job must be processed before the job is transported, and the jobs belonging to the same product must be transported to the assembly place before assembly. Therefore, there is strong coupling between stages.

(3) The solution space of the problem is complicated. 3sMISP_JBTEC is a multistage and multiobjective scheduling problem, and its solution space is very complicated. In addition to the processing sequence π^K, the transportation job sequence π^{TR}, and the product sequence π^P, the problem also involves the speed-based vehicles sequence $\pi^{\mathrm{TR}-V}$. Therefore, it is necessary to analyze and use the characteristics of the problem to reasonably narrow the search space. Meanwhile, $\pi^{\mathrm{TR}-V}$ in the transportation stage needs to be designed with reasonable operation in order to solve the problem better.

Based on the above analysis, the following rules are proposed:

Rule 1. Jobs belonging to the same product are assigned the same priority in the processing stage.

Rule 2. Jobs belonging to the same product should be put into the same vehicle as far as possible under the vehicle loading constraints.

Rule 3. Transport vehicles are filled first and transported first.

Rule 4. All jobs belonging to the same product are assembled first when they arrive at the assembly place first in the assembly stage.

3.2. Design of HEDA_VNS Algorithm. In this section, the HEDA_VNS is designed to improve the efficiency for solving 3sMISP_JBTEC. Because the problem solution space is very complicated, HEDA_VNS only searches the solution space of the subproblems in the processing stage (π^K). Then, π^{TR} and π^P are generated according to the characteristics of the problem and rules proposed in Section 3.1. Meanwhile, a reasonable speed scheduling scheme (SSS) is proposed for $\pi^{\mathrm{TR}-V}$ in the transportation stage to further improve the quality of the nondominated solution of the problem.

3.2.1. Encoding and Decoding

(i) Encoding and decoding of the processing stage. The encoding of the processing stage is the process-based permutation. Its length is determined by the product-job-process layer. Obviously, the job set P_z is determined by the product z, and the process set Q_{zj} is determined by the job j, which is in the setP_z, $z \in P$, $j \in Q$. The decoding adopts the method of earliest completion time (ECT) combined with insertion rule to determine the starting time of each process, while the machine allocation is completed. Then, the completion time of the job j in the processing stage and the energy consumption of the machine can be determined.

(ii) Encoding and decoding of the transportation stage. In the transportation stage, the encoding and decoding of the job and the vehicle are involved. The job encoding of the transportation phase is based on the sorting of the jobs in the nondescending order of the completion time in the processing stage. The job decoding of the transport phase is based on Rule 2 in Section 3.1. $V_{[t]}$ is the current load of the vehicle t, and set $V_{[t]} = 0$ as the initial situation. The specific steps of decoding are given as follows:

Step 1: select the jobs $\pi^{\mathrm{TR}}_{[j]}$ belonging to the product $\pi^{\mathrm{P}}_{[z]}$ from left to right in π^{TR}.

Step 2: put the selected $\pi^{\mathrm{TR}}_{[j]}$ into the vehicle t in turn under the conditions $V(\pi^{\mathrm{TR}}_{[j]}) + V_{[t]} \le V_T$. If $V(\pi^{\mathrm{TR}}_{[j]}) + V_{[t]} > V_T$, put the job j into the vehicle $t+1$ and then update $V_{[t]}$ and the set of jobs to be transported ($\pi^{\mathrm{TR}'}$).

Step 3: check whether there is a job $\pi^{\mathrm{TR}}_{[k]}$ in the set $\pi^{\mathrm{TR}'}$ that satisfies $V(\pi^{\mathrm{TR}}_{[k]}) + V_{[t]} \le V_T$. If $V(\pi^{\mathrm{TR}}_{[k]}) + V_{[t]} \le V_T$, put the job $\pi^{\mathrm{TR}}_{[j]}$ into the vehicle t until $V(\pi^{\mathrm{TR}}_{[k]}) + V_{[t]} > V_T$, update $V_{[t]}$ and $\pi^{\mathrm{TR}'}$, $t = t+1$, $z = z+1$.

Step 4: turn to step 1, until $\pi^{\mathrm{TR}'}$ is empty.

Following the above steps, the start transportation time of the job is determined by the job decoding in the transportation stage.

The vehicle encoding is based on the sorting of vehicle speed $\pi^{\mathrm{TR}-V}$. The decoding of vehicle is based on Rule 3, and the vehicle speed can be obtained by the speed scheduling set. Then, the transportation completion time of the job and transportation energy consumption are determined.

(iii) Encoding and decoding of the assembly stage. The assembly encoding is the product-based sorting in the assembly stage, and the product encoding π^P is arrangement of nondescending order which is determined by the time when all the jobs belonging to the product arrive at the assembly workshop. The assembly decoding is based on Rule 4, and then, the product completion time and energy consumption are determined. Thus, the three-stage encoding of 3sMISP_JBTEC is shown in Figure 3.

3.2.2. The Speed Scheduling Scheme. The speed interval set in the transportation stage of 3sMISP_JBTEC is $v \in [v_{\min}, v_{\max}]$. If the speed of vehicle is generated

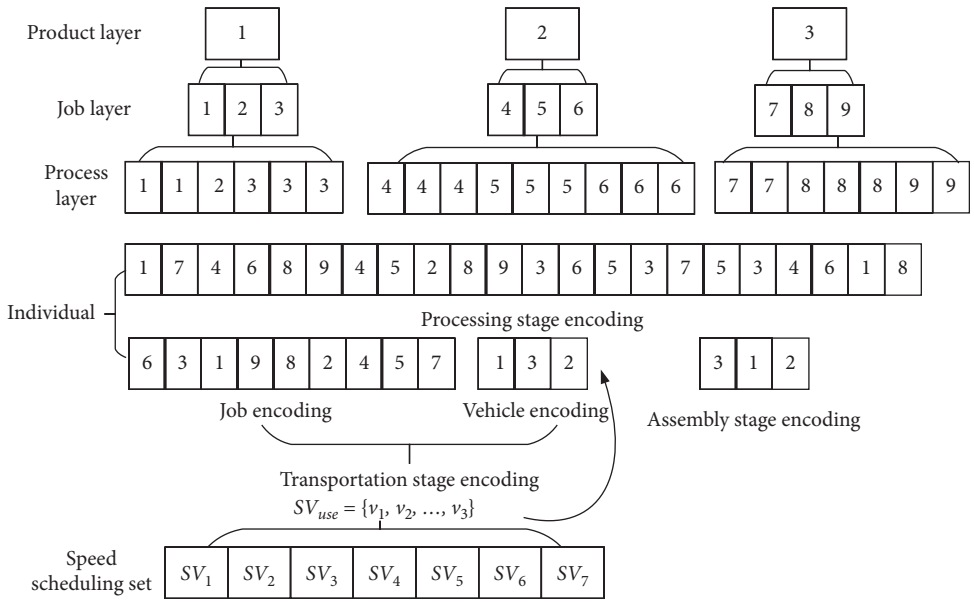

Figure 3: The coding method of scheduling solution.

randomly, there is a large span in this interval. Then, it is not easy to find a more accurate nondominated solution to the problem in a short time. Therefore, in the section, a speed scheduling scheme (SSS) is designed to further refine the speed range, which can better solve the problem. The specific operations are as follows:

(1) The speed interval is divided into three speed subintervals: low, medium, and high speed. The low-speed interval is $\mathrm{SV}_{\mathrm{low}} = [v_{\min}, v_a]$, the medium is $\mathrm{SV}_{\mathrm{mid}} = [v_a, v_b]$, and the high is $\mathrm{SV}_{\mathrm{high}} = [v_b, v_{\max}]$, where $v_{\min} < v_a < v_b < v_{\max}$.

(2) The speed scheduling set $\mathrm{SV}_{\mathrm{use}}$ can be randomly generated from the following seven intervals. $\mathrm{SV}_{\mathrm{use}}$ obtained by different modes can be traversed to the interval of different speeds while continuously updating the speed set to improve the quality of the solution:

① $\mathrm{SV}_{\mathrm{use}} \subset \mathrm{SV}_{\mathrm{low}}$, marked as SV_1.
② $\mathrm{SV}_{\mathrm{use}} \subset \mathrm{SV}_{\mathrm{mid}}$, marked as SV_2.
③ $\mathrm{SV}_{\mathrm{use}} \subset \mathrm{SV}_{\mathrm{high}}$, marked as SV_3.
④ $\mathrm{SV}_{\mathrm{use}} \subset (\mathrm{SV}_{\mathrm{low}} \cup \mathrm{SV}_{\mathrm{mid}})$, marked as SV_4.
⑤ $\mathrm{SV}_{\mathrm{use}} \subset (\mathrm{SV}_{\mathrm{low}} \cup \mathrm{SV}_{\mathrm{high}})$, marked as SV_5.
⑥ $\mathrm{SV}_{\mathrm{use}} \subset (\mathrm{SV}_{\mathrm{mid}} \cup \mathrm{SV}_{\mathrm{high}})$, marked as SV_6.
⑦ $\mathrm{SV}_{\mathrm{use}} \subset (\mathrm{SV}_{\mathrm{low}} \cup \mathrm{SV}_{\mathrm{mid}} \cup \mathrm{SV}_{\mathrm{high}})$, marked as SV_7.

4. Methodology of HEDA_VNS

4.1. HEDA_VNS Global Search

4.1.1. Initialization of Population, Probability Model, and Speed Scheduling Set. According to Rule 1, the product aggregation (PA) method is designed to generate the number of $\eta \times$ popsize individuals in the processing stage, and the remaining individuals are generated randomly to initialize the population. The PA is a rule to generate an individual. The specific steps about PA are as follows (shown in Figure 4): first, a product sequence is randomly generated. Then, a job sequence that belongs to the same product is randomly generated. At last, a process sequence that is based on the same job is randomly generated. According to PA, the jobs that make up the same product can be more concentrated. After the jobs have been processed in the processing stage, they can be transported to the assembly stage faster and more concentrated.

According to the encoding method in Section 3.2.1, the process arrangement matrix ρ is used as the probability model. In order to ensure that the algorithm searches the solution space uniformly as much as possible, the probability model $\rho_{i,j}$ adopts a uniform distribution, and $\rho_{i,j}(0) = (1/A)$. The initial speed scheduling set is $\mathrm{SV}_{\mathrm{use}} \subset \mathrm{SV}_7$ so that the transportation speed is generated randomly in $[v_{\min}, v_{\max}]$.

4.1.2. Update Probability Matrix. For multiobjective optimization, the nondominated solution is selected in iteration to update the probability model. $I_{i,j}$ is the number of times that the job j appeared at or before the position i of the process sequence vector. $E_{i,j}(g)$ is the probability obtained through the nondominated solution statistics in the iteration g. This can be updated by $\rho_{i,j}(g)$, where $\gamma \in (0,1)$ is the learning rate:

$$I_{i,j} = \begin{cases} 1, & \text{job } j \text{ appears at or before position } i, \\ 0, & \text{else}, \end{cases}$$

$$E_{i,j}(g) = \frac{I_{i,j}}{\sum_{i=1}^{n} I_{i,j}}, \quad \forall i, j,$$

$$\rho_{i,j}(g+1) = (1-\gamma)\rho_{i,j}(g) + \gamma E_{i,j}. \tag{14}$$

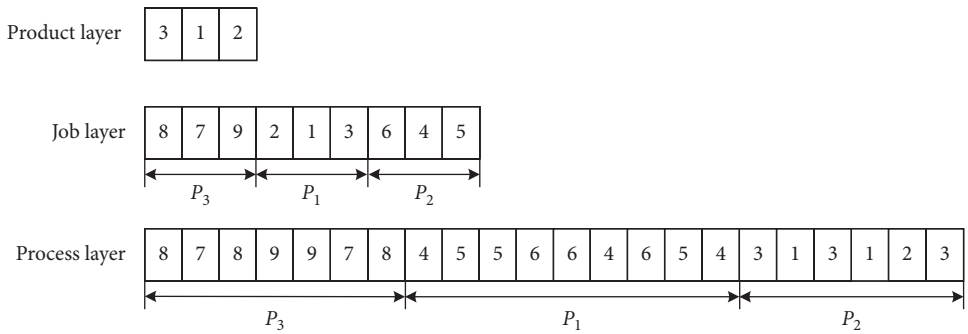

Figure 4: An example of the PA rule.

4.1.3. Sampling Method. In subsequent iteration of the algorithm, a new population is generated by sampling the probability matrix. The sampling method in this paper is designed for the problem model. The purpose is to make the jobs belong to the same product more likely to be aggregated together to produce higher-quality individuals, but each sampling uses roulette operation which guarantees the diversity of the population to a certain extent. Once a new individual is generated, it constitutes a new population for the next iteration. Specific steps are as follows:

Step 1: when $i = 1$, the roulette method is used to sample the matrix to select the workpiece directly and judge whether $j \in P_z$. The probability that the job j appears in position i is $\rho_{i,j}(g)$. If the number of job j occurrences in the matrix ρ is equal to the total number of processes of job j, set the column j of the matrix ρ to zero and normalize each row.

Step 2: when $i \neq 1$, add the probabilities of the job j belonging to P_z of the row i to get $\sum_{j=m}^{k} \rho_{i,j}$, where $j \in P_z$:

Step 2.1: if $\sum_{j=m}^{k} \rho_{i,j} = 0$, the roulette method is used to sample directly.

Step 2.2: if $\sum_{j=m}^{k} \rho_{i,j} \neq 0$, a random number $\varepsilon, \varepsilon \in (0.5, 0.8)$ is generated and compared with $\sum_{j=m}^{k} \rho_{i,j}$. If $\sum_{j=m}^{k} \rho_{i,j} \geq \varepsilon$, the roulette method is used to sample directly; if $\sum_{j=m}^{k} \rho_{i,j} < \varepsilon$, then readjust the probability of job j on the current row i to obtain a new probability. Among them, the probability of job j belonging to the product P_z is calculated using formula (16) or otherwise using formula (17). Use roulette to sample after adjustment. If the number of job j in the matrix ρ is equal to the total number of processes of job j, set the column of the matrix to zero and normalize each row:

$$\rho_{i,j}^{*} = \frac{\rho_{i,j}^{z}}{\sum_{j_z=m}^{k} \rho_{i,j}^{z}} \times \varepsilon, \quad j \in P_z, \tag{15}$$

$$\rho_{i,j}^{*} = \frac{\rho_{i,j}^{z}}{1 - \sum_{j_z=m}^{k} \rho_{i,j}^{z}} \times (1 - \varepsilon), \quad j \notin P_z. \tag{16}$$

Step 3: judge whether the job j in the row i of sampling by Step 2 belongs to P_z; if job $j \in P_z$, then $j = j + 1$ directly. If $j \in P_z^{*}$, then order $P_z^{*} = P_z$ and $j = j + 1$, until all the processes of the job j belonging to P_z are selected completely.

4.2. Local Search Strategy

4.2.1. Local Search I. After new individuals of the population are sampled through the probability matrix, the probability matrix is updated with the individuals who have obtained nondominated solutions. A local search strategy is designed with Rule 1 in three situations to better guide the global search direction and beneficial to avoid some invalid search. Meanwhile, the original solution structure can be better retained.

For the nondominant solution π_r obtained in the population (where $r = 1, 2, \ldots, m$), two positions u, v $(u \neq v)$ in π_r are selected randomly, and $\pi_r(u)$ is the job encoding of the position u of π_r.

Situation 1. If $\pi_r(u) = \pi_r(v)$, it means that the two positions are the same job; the Swap operation will be invalid, then the Insert operation is performed at this time. If $u < v$, insert forward. Otherwise, insert back and to generate a new individual π_r'. If $f_1(\pi_r) > f_1(\pi_r')$ and $f_2(\pi_r) > f_2(\pi_r')$, let $\pi_r = \pi_r'$, then update the nondominated solution set.

Situation 2. If $\pi_r(u) \neq \pi_r(v)$and it does not belong to the same product, let $x = \max(u, v) - \min(u, v)$ and $k = (H_O/H_P - 1)$ (where H_O is the total number of processes of all products, i.e., the length of the individual π_r in the processing stage and H_P is the total number of products); if $x \leq k$, the Swap operation is performed to generate a new individual. If $f_1(\pi_r) > f_1(\pi_r')$ and $f_2(\pi_r) > f_2(\pi_r')$, let $\pi_r = \pi_r'$, update the nondominated solution set.

Situation 3. If $\pi_r(u) \neq \pi_r(v)$, it means that the two positions belong to different jobs. If they belong to the same product, then a hybrid operation based on the variable neighborhood local search of Insert and Swap is performed. Specific steps are given as follows (Algorithm 1).

4.2.2. Local Search II. In the transportation stage, the faster the vehicle transportation speed and the shorter the transportation time, and the jobs will be faster, reaching the assembly stage for assembly. Meanwhile, the makespan decreases, but the energy consumption increases. Hence, the two target values conflict. In order to balance the two goals and improve the quality of nondominated solutions, it is also necessary to search for the transportation speed and vehicle order. Combining the speed scheduling scheme given in Section 3.2.2, a variable neighborhood search hybrid operation based on the speed set is designed in this section.

For the nondominant solution set $\kappa = \{\pi_1, \pi_2, \pi_3, \ldots, \pi_m\}$, $\pi_a^{\mathrm{TR}-V}$ is the vehicle sequence corresponding to individual π_a in the transportation stage. Two positions u, v $(u \neq v)$ are selected randomly in $\pi_a^{\mathrm{TR}-V}$, and $\pi_o^{\mathrm{TR}-V}(u)$ is the vehicle encoding of the position u of the individual $\pi_o^{\mathrm{TR}-V}$. $\mathrm{SV}_{\mathrm{use}} = \{v_1, \ldots, v_{H_T}\}$ is the current speed scheduling set, and SV_x is the speed scheduling set x, where $x = 1, \ldots, 7$. The specific operations are as follows (Algorithm 2).

4.3. Species Diversity Determination and Control Mechanism. With the continuous iteration of the algorithm, the diversity of the population will decrease, and the individuals in the population will become very similar, which will cause the algorithm to fall into a local optimum. In order to solve the problem, a population control mechanism of literature [41] is used in this paper to calculate the diversity value θ_{div} of contemporary populations. A diversity threshold δ is given; when $\theta_{\mathrm{div}} \leq \delta$, the current population is adjusted to retain noninferior individuals in the contemporary population, and $\varphi \times$ popsize/3 individuals are randomly generated by the PA rule, and the rest are randomly generated.

4.4. The Framework of HEDA_VNS. In HEDA_VNS, firstly, a probability model is adopted to learn high-quality solution information and guides the algorithm to search globally. Secondly, a Local Search I is designed by using the rules obtained from the analysis of the problem in Section 3.1. Then, in order to improve the quality of the solution, the Local Search II is combined with the speed scheduling set to realize an effective search in the velocity space. Finally, a population control mechanism is designed to maintain the diversity of the population. The framework of HEDA_VNS is shown in Figure 5.

5. Simulation Results and Discussion

5.1. Experimental Settings and Evaluation Index

5.1.1. Experimental Settings. All test questions of 3sMISP_JBTEC are based on the structural of the three-stage integrated system. For test data, the number of jobs composed of each product and the number of procedures corresponding to the jobs are randomly generated in the interval of [2, 5] and [1, 3], respectively. The processing time of each job and the assembly time of each product are randomly generated in the interval of [20, 80] and [100, 200], respectively. The load of each job is randomly generated in the interval of [20, 50], and the unit energy consumption of the processing machine is randomly generated in the interval of [3, 5]. According to the literature [24], the parameters of vehicle-related are as follows: $C_d = 0.7$, $C_r = 0.01$, $\rho = 1.2041$, $A = 3.912$, and $g = 9.81$. The distance of vehicle transportation is $\mathrm{Dis}_{P-A} = 8000$.

In addition to the number of products and machines, the results of the test problems are also affected by the number of transport vehicles. Therefore, the test problems listed in this paper are expressed as P_M_T. All algorithms and test procedures are implemented by Delphi 2010 programming, and the operating system is WinXP.

5.1.2. Evaluation Index. In the comparison, two indexes are used to evaluate the algorithm [42]. There are $R\_N(S_j)$ and $N\_N(S_j)$. $R\_N(S_j)$ is used to evaluate the quality of the nondominated solutions (shown in equation (17)). When $R\_N(S_j) = 0$, the solutions in S_j are all dominated by other solutions. Also, when $R\_N(S_j) = 1$, the solutions in S_j are all nondominated solutions in S. $N\_N(S_j)$ is the number of solutions in S_j which are not dominated by other solutions (shown in equation (18)). The larger the value of $N\_N(S_j)$, the greater the number of nondominated solutions. Obviously, $R\_N(S_j)$ is the dominant ratio, which evaluates the overall quality of the algorithm to obtain nondominated solutions, and $N\_N(S_j)$ is the number of dominants, which evaluates the ability of the algorithm to obtain nondominated solutions. There is a positive correlation between these two indicators, and the correlation coefficient is $1/S_j$:

$$R\_N(S_j) = \left| \frac{S_j - x \in S_j | \exists y \in S\colon\ y \prec x|}{|S_j} \right|, \tag{17}$$

$$N\_N(S_j) = |S_j - x \in S_j | \exists y \in S\colon\ y \prec x|. \tag{18}$$

5.2. Key Parameter Setting and Influence of HEDA_VNS. In the section, the three key parameters of HEDA_VNS which are population size (popsize), iterative probability sampling parameters (η), and learning rate (γ) are analyzed by the Design of Experiment (DOE) method of medium-scale problems. On the basis of combining existing research, four levels of each parameter are determined (shown in Table 1); thereby, an orthogonal experimental table is established with a scale of $L_{16}(4^3)$. The algorithm runs independently for each set of parameters for 10 medium-scale questions of 20 times, with $2 \times P \times M \times T$ seconds as the termination condition for each scale and the average value AVG of each scale under different parameter combinations of the algorithm as the evaluation index to determine the appropriate parameters combination. The results are shown in Table 2.

From the experimental results (shown in Table 3 and Figure 6), it can be found that different parameter combinations have a greater impact on the performance of the algorithm. Based on the experimental analysis results, the best parameters popsize = 50, $\eta = 0.4$, and $\gamma = 0.3$ are

```
Set loop = 1;
  Repeat
    Set count = 0; max_count = 2;
      Repeat
        If count = 0, then the Insert operation is performed on π_r to get π'_r;
        If count = 1, then the Swap operation is performed on π_r to get π'_r;
          If f_1(π_r) > f_1(π'_r) and f_2(π_r) > f_2(π'_r), then count = 0, π_r = π'_r, update nondominated solution set;
          Else, let count = count + 1;
      Until count = max_count;
  Until loop = max_loop;
End.
```

Algorithm 1: Local search insertSwap method.

```
For a = 1 to m
  For x = 1 to 7
    SV_use = SV_x;
      Set loop = 1;
        Repeat
          Set count = 0; max_count = 2;
            Repeat
            If count = 0, then the Insert operation is performed on π_a^{TR-V} to get (π_a^{TR-V})';
            If count = 1, then the Swap operation is performed on π_a^{TR-V} to get (π_a^{TR-V})';
              If f_1(π_a, π_a^{TR-V}, SV_use) > f_1(π_a, (π_a^{TR-V})', SV_use) and f_2(π_a, π_a^{TR-V}, SV_use) > f_2(π_a, (π_a^{TR-V})', SV_use) then set
count = 0, π_a^{TR-V} = (π_a^{TR-V})', update nondominated solution set;
            Else, set count = count + 1;
          Until count = max_count;
        Until loop = max_loop;
      End;
    End.
```

Algorithm 2: Local search speed mechanism.

set in this paper, and further performance testing and comparison will be carried out based on this parameter setting.

5.3. Analysis of the Results of Energy Consumption and Makespan under a Certain Problem Scale. In this section, HEDA_VNS is used to solve the 3sMISP_JBTEC with a problem scale of (3_3_2). The scale of the problem can be described as follows: 3 heterogeneous parallel machines in the processing stage, 2 vehicles with the same load in the transportation stage, and one machine in the assembly stage. 3 products are required to be processed and assembled during the three stages. The product composition is shown in Figure 7. The 3 products are assembled from multiple jobs. Each job has multiple processes, and each process can be processed on multiple machines. The vehicle's return to no-load speed is $v_c = 40$. The data of each stage of the product are shown in Table 4.

Figure 8 shows the noninferior solution set of the problem, and other scales are similar. It can be seen from Figure 8 that all the solutions are independent of each other due to conflicts and constraints between the makespan and total energy consumption (TEC). The conflicts and containments are embodied in both machine processing stage and vehicle transportation stage. The solution at point A in Figure 8 shows that it has a large span in the machine processing stage, but it has close connection between the stages, and all vehicles are transported at high speed. Meanwhile, the makespan is relatively smallest, but energy consumption is relatively highest. On the one hand, high-speed transportation can reduce the transportation time and the accumulation of intermediate inventory and effectively prevent delays in the manufacturing process. On the other hand, high-speed transportation may cause that jobs arrive early for assembly, which is prone to bottlenecks and a backlog of finished products. Therefore, it is not a blind pursuit of makespan, and it is necessary to limit the maximum speed level of transportation vehicles. The solution at point B in Figure 8 represents that the machining span is small, but the connection between the stages is not tight enough, and all vehicles are transported at low speed. Meanwhile, the makespan is relatively largest, but energy consumption is relatively lowest. In this case, although the processing stage is compact, the delivery delay time and the intermediate inventory level will be at the highest level, and the delivery of the finished product may be delayed. It can be

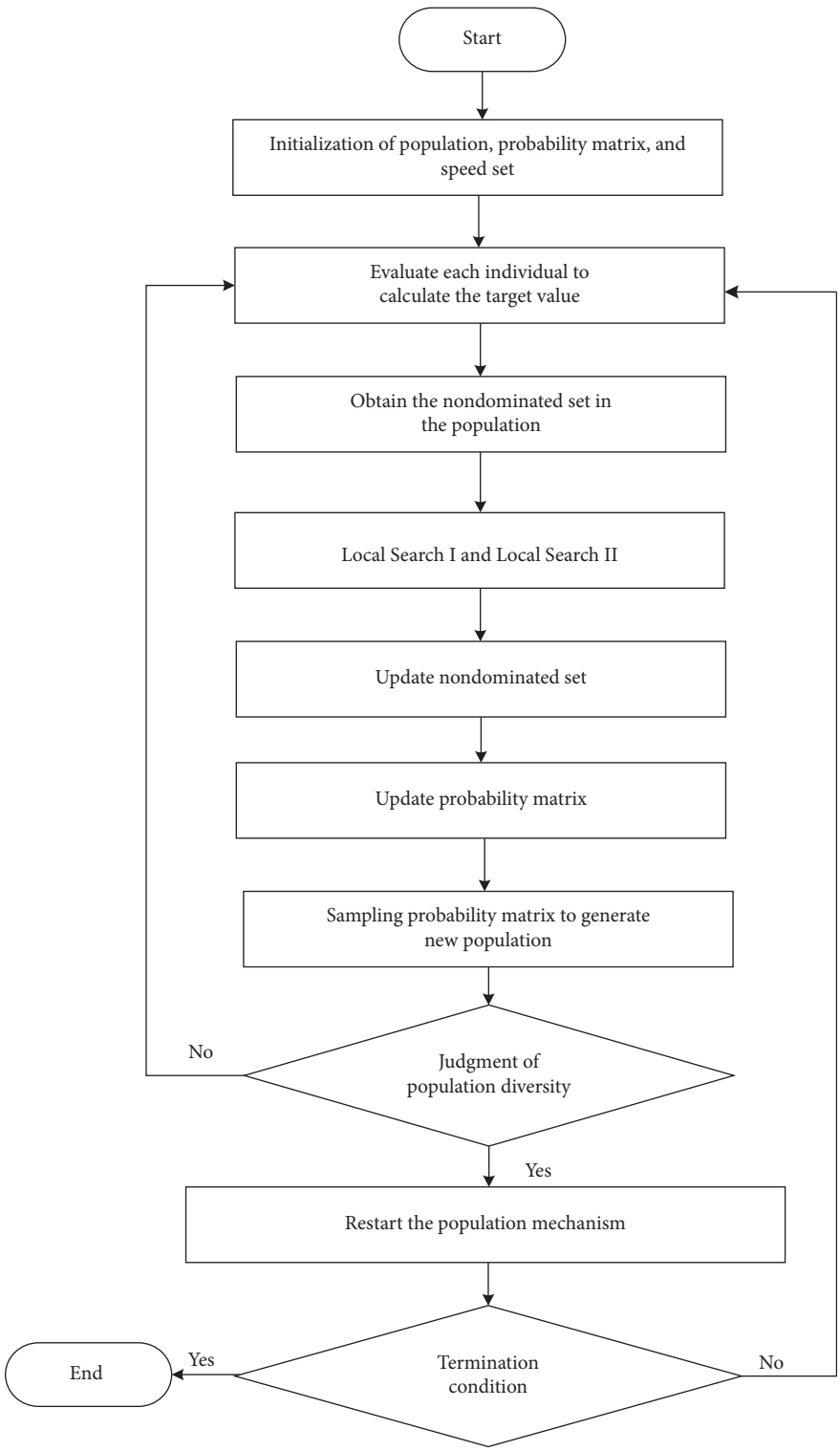

Figure 5: The framework of HEDA_VNS.

seen that although it is the same problem, the noninferior solution will be affected due to different vehicle transportation speeds. Hence, enterprise managers need to make decisions based on the company itself and related policies, taking into account factors such as order time and demand; for example, the selected solution will be different if the same order is completed in a shorter planning period and the selected solution is completed in a longer planning period, but under normal circumstances, decision makers generally choose point C because the makespan and energy consumption are at a normal and acceptable level.

Table 1: Parameter level.

Parameter	Level			
	1	2	3	4
Popsize	30	40	50	60
η	0.3	0.4	0.5	0.6
γ	0.1	0.2	0.3	0.4

Table 2: Orthogonal table and average statistics.

Parameter combination	Level			AVG × 10
	Popsize	η	γ	
1	1	1	1	0.501
2	1	2	2	0.447
3	1	3	3	0.393
4	1	4	4	0.299
5	2	1	2	0.375
6	2	2	3	0.491
7	2	3	4	0.386
8	2	4	1	0.293
9	3	1	3	0.607
10	3	2	4	0.583
11	3	3	1	0.412
12	3	4	2	0.286
13	4	1	4	0.456
14	4	2	1	0.486
15	4	3	2	0.363
16	4	4	3	0.368

Table 3: The response value of parameters.

Level	Popsize	η	γ
1	0.410	0.485	0.423
2	0.386	**0.502**	0.368
3	**0.472**	0.389	**0.465**
4	0.419	0.312	0.431

5.4. Comparison of Experimental Results of HEDA_VNS with Other Intelligent Algorithms. In order to further verify the effectiveness of HEDA_VNS compared with HMOBSA [19] and GA-GSO-GTHS [23], a large number of experiments can be carried out by means of the generated different types of problems. HMOBSA is an effective multiobjective backtracking algorithm. The performance of HMOBSA is superior to the well-known multiobjective algorithm (nondominated sorting genetic algorithm, NSGAII) and MOEA/D in solving energy consumption problems. The turn off/on strategy is also used when calculating energy consumption in the processing stage. GA-GSO-GTHS is a multiobjective hybrid optimization algorithm with strategy. The performance of GA-GSO-GTHS is better than most of the latest multiobjective optimization algorithms that are widely used in scheduling problems. It is effective in solving production energy consumption problems that consider transportation. In addition, the parameters of HMOBSA are set as follows: popsize = 50, crossover probability $p_c = 0.9$, and mutation probability $p_m = 0.1$. The parameters of GA-GSO-GTHS are set as follows: popsize = 100, $p_c = 0.6$, $p_m = 0.05$, step size $s = 5$, maximum perceptual radius $r_s = 20$, volatility coefficient $\rho = 0.4$, enhancement factor $\gamma = 0.6$, perceptual radius scaling factor $\beta = 0.08$, $n_t = 5$, and $l(0) = 5$. The parameters selected by the three algorithms are all good parameters. Besides, HEDA_VNS runs for 200 generations, and other algorithms run the same time as HEDA_VNS. The comparative results of the three algorithms to solve 3sMISP_JBTEC under the randomly generated speed in $[v_{\min}, v_{\max}]$ are listed in Table 5. Among them, R_N and N_N, respectively, represent the index values of the evaluation solutions corresponding to the three algorithms. The data in Table 5 are the average values of the algorithm after 20 runs.

It can be seen from Table 5, for the 25 examples to be tested in this paper, the proposed HEDA_VNS finds more and better nondominated solutions for 23 instances of the 25 problem instances in terms of R_N and N_N. Moreover, as the problem size increases, HEDA_VNS is more effective. This is because HEDA_VNS is designed based on the characteristic of the problem, and the advantages of HEDA_VNS are mainly reflected in the following three aspects:

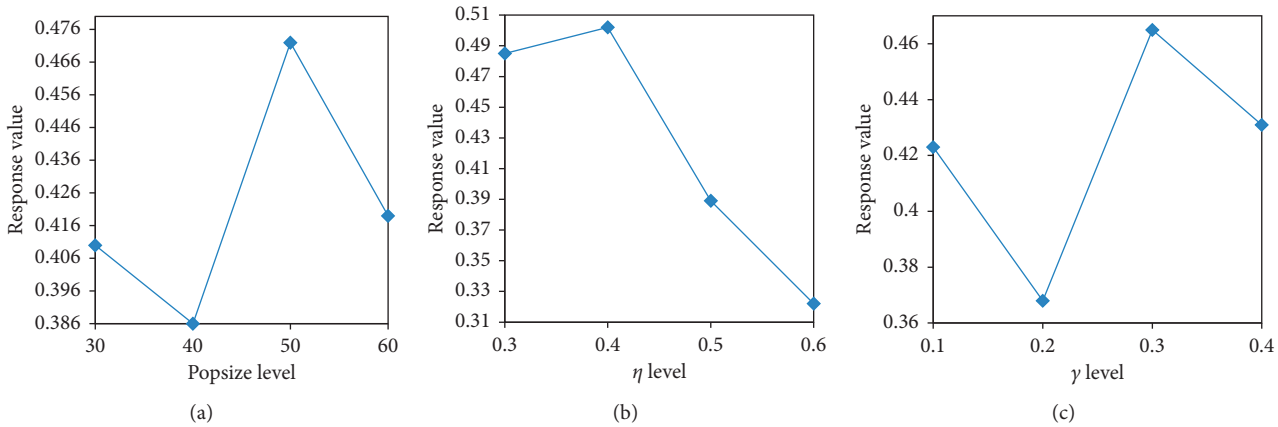

Figure 6: The level trend of the influence of each parameter on the algorithm performance.

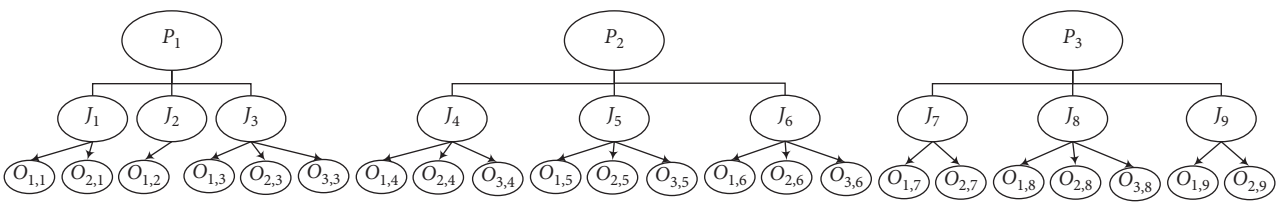

Figure 7: The product composition of the problem scale of (3_3_2).

Table 4: Data at each stage of the problem scale of (3_3_2).

		P_1						P_2									P_3						
		J_1		J_2		J_3		J_4			J_5			J_6			J_7			J_8		J_9	
P_{ijk}	m_1	27	—	99	—	—	—	116	91	—	113	75	54	—	—	87	—	—	—	—	80	98	—
	m_2	25	—	—	39	—	75	101	110	62	—	—	—	31	112	—	59	—	—	—	—	—	80
	m_3	77	107	—	59	28	57	56	—	33	26	101	—	50	60	—	—	97	97	83	—	—	—
R_{jk}	m_1	55		93		62		41			101			66			39			84		59	
	m_2	88		75		87		70			101			47			80			37		49	
	m_3	25		55		69		60			64			88			114			72		30	
V_j		33		48		25		52			6			36			31			25		33	
A_z				161							128									99			

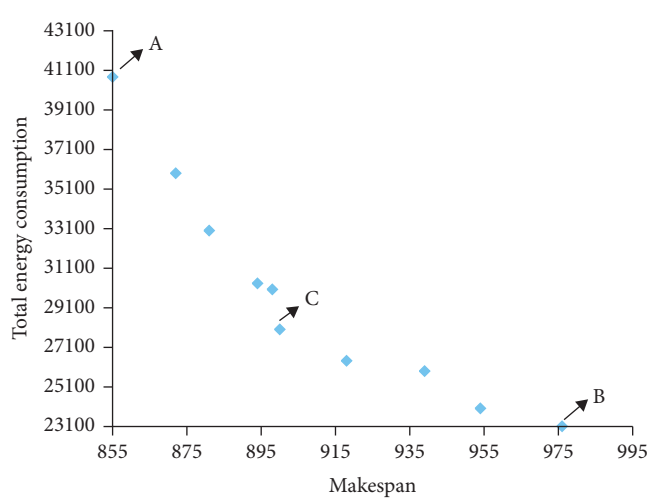

Figure 8: The noninferior solution set of the problem scale of (3_3_2).

Table 5: Comparison of HEDA_VNS with HMOBSA and GA-GSO-GTHS.

No.	*P_M_T*	HMOBSA		GA-GSO-GTHS		HEDA_VNS	
		R_N	*N_N*	*R_N*	*N_N*	*R_N*	*N_N*
01	2_3_2	0.20	0.50	**0.55**	**1.30**	0.47	1.25
02	3_2_2	0.05	0.10	0.50	0.97	**0.52**	**1.30**
03	3_3_2	0.02	0.05	0.35	1.35	**0.80**	**2.15**
04	4_4_2	0.05	0.30	**0.75**	**1.55**	0.60	1.50
05	4_5_3	0.07	0.02	0.35	1.15	**0.68**	**1.80**
06	5_3_3	0.03	0.01	0.27	0.45	**0.81**	**1.60**
07	5_4_3	0.05	0.15	0.52	0.85	**0.75**	**1.55**
08	5_5_3	0.15	0.35	0.13	0.65	**0.80**	**1.95**
09	5_6_3	0.02	0.05	0.15	0.35	**0.92**	**2.05**
10	6_4_3	0.00	0.00	0.13	0.35	**0.95**	**2.20**
11	6_5_3	0.05	0.10	0.27	0.50	**0.86**	**2.05**
12	6_6_3	0.02	0.05	0.22	0.65	**0.90**	**2.20**
13	6_4_4	0.03	0.10	0.28	0.50	**0.83**	**1.95**
14	6_5_4	0.02	0.05	0.32	0.85	**0.78**	**1.90**
15	6_6_4	0.00	0.00	0.11	0.35	**0.92**	**2.65**
16	7_5_4	0.00	0.00	0.16	0.30	**0.95**	**2.80**
17	7_6_4	0.02	0.05	0.24	0.45	**0.93**	**2.25**
18	7_7_4	0.03	0.05	0.12	0.35	**0.93**	**2.05**
19	8_8_4	0.00	0.00	0.25	0.95	**0.95**	**2.60**
20	9_9_4	0.00	0.00	0.10	0.25	**0.95**	**1.85**
21	9_9_5	0.05	0.15	0.15	0.20	**0.93**	**1.70**
22	10_10_5	0.02	0.05	0.08	0.15	**0.92**	**2.05**
23	10_10_8	0.00	0.00	0.03	0.10	**0.96**	**1.60**
24	15_15_5	0.00	0.00	0.02	0.05	**0.95**	**1.95**
25	15_15_10	0.00	0.00	0.01	0.05	**0.96**	**1.55**

(1) The solution generated by the PA rule in the initialization phase can better improve the quality of the initial solution.

(2) A sampling mechanism based on the nature of the problem is designed so that the jobs belonging to the same product can be selected with a higher probability, which can more clearly guide the algorithm to search in the high-quality solution area.

(3) Two local search strategies are designed to improve the performance of the algorithm. Among them, three different search methods are designed in the Local Search I to perform a detailed search on the noninferior solution high-quality regions to improve the efficiency of the solution, which can effectively avoid some invalid searches and better retain the original high-quality solution structure. Then, a variable neighborhood hybrid operation based on the speed set is designed in Local Search II to search for transportation speed and vehicle order, which can balance the two optimization goals while further improving the quality of the solution.

6. Conclusion

This paper aims at solving the three-stage multiobjective integrated scheduling problem considering the energy consumption (3sMISP_JBTEC) of processing-transport-assembly and studying the multiobjective problem modeling and solution algorithm with makespan and energy consumption. In terms of modeling, a mathematical model of multiobjective optimization problems is established. Then, the improved energy-saving strategy is adopted to save energy and extend the life of the machine in the processing and assembly stages. Meanwhile, the impact of speed on energy consumption is considered in the transportation stage. For solving the problem, the HEDA_VNS is designed to solve 3sMISP_JBTEC based on the characteristics of the problem. There is a conflict between the makespan and the energy consumption through the results of testing same-scale problems, and decision-makers need to make decisions based on different actual conditions. Moreover, HEDA_VNS is compared with other algorithms on large-scale problems, and comparative simulations show the efficiency of the proposed HEDA_VNS. This obtained result can provide a reference for the implementation of intelligent production in the assembly manufacturing industry.

Data Availability

Data were curated by the authors, the link for the test data is (https://dx.doi.org/10.13140/RG.2.2.29751.44969).

Conflicts of Interest

The authors declare that there are no conflicts of interest regarding the publication of this paper.

Acknowledgments

This work was supported by the National Natural Science Foundation of China (Grant nos. 61963022 and 51665025)

and Scientific Research Foundation of Yunnan Provincial Department of Education (Grant no. 2021J0052).

References

[1] N. Salahi and M. A. Jafari, "Energy-performance as a driver for optimal production planning," *Applied Energy*, vol. 174, no. 15, pp. 88–100, 2016.

[2] J. M. Bloemhof, P. Beek, L. Hordijka et al., "Interactions between operational research and environmental management," *European Journal of Operation Research*, vol. 85, no. 2, pp. 229–243, 1995.

[3] G. May, M. Taisch, B. Stahl et al., "Toward energy efficient manufacturing: a study on practices and viewpoint of the industry," *Competitive Manufacturing for Innovative Products and Services*, vol. 8, 2012.

[4] Y. Liu and A. Tiwari, "An investigation into minimising total energy consumption and total completion time in a flexible job shop for recycling carbon fiber reinforced Polymer," *Procedia CIRP*, vol. 29, no. 3, pp. 722–727, 2015.

[5] Q. Zhu, J. F. Lu, A. Mayyas et al., "Production energy optimization using low dynamic programming, a decision support tool for sustainable manufacturing," *Journal of Cleaner Production*, vol. 15, no. 2, pp. 135–147, 2014.

[6] K. Geng, C. Ye, Z. h. Dai, and L. Liu, "Bi-objective re-Entrant hybrid flow shop scheduling considering energy consumption cost under time-of-use electricity tariffs," *Complexity*, vol. 2020, no. 1, pp. 1–17, 2020.

[7] B.-H. Zhou and C.-Y. Shen, "Multi-objective optimization of material delivery for mixed model assembly lines with energy consideration," *Journal of Cleaner Production*, vol. 192, no. 1, pp. 293–305, 2018.

[8] C. Koulamas and G. J. Kyparisis, "The three-stage assembly flowshop scheduling problem," *Computers & Operations Research*, vol. 28, no. 7, pp. 689–704, 2001.

[9] S. Hatami, S. Ebrahimnejad, M. R. Tavakkoli et al., "Two meta-heuristics for three-stage assembly flowshop scheduling with sequence-dependent setup times," *International Journal of Advanced Manufacturing Technology*, vol. 50, no. 12, pp. 1153–1164, 2010.

[10] A. Maleki and I. Seyedi, "A three-stage assembly flow shop scheduling problem with blocking and sequence-dependent setup times," *Journal of Industrial Engineering International*, vol. 8, no. 1, pp. 1–7, 2012.

[11] S. C. Campos and J. E. C. Arroyo, "NSGA-II with iterated greedy for a bi-objective three-stage assembly flowshop scheduling problem, Conference on Genetic & Evolutionary Computation," *ACM*, vol. 12, no. 1, pp. 429–436, 2014.

[12] C. Deng, B. Qian, R. Hu et al., "Rule-based hybrid EDA for three-stage assembly integrated scheduling problem with job batches transportation problem," *Control and Decision*, vol. 35, no. 10, pp. 2507–2513, 2020.

[13] J. N. D. Gupta, "Two-stage, hybrid flowshop scheduling problem," *Journal of the Operational Research Society*, vol. 39, no. 4, pp. 359–364, 1988.

[14] J. Y. Ding, S. Song, and C. Wu, "Carbon-efficient scheduling of flow shops by multi–objective optimization," *European Journal of Operational Research*, vol. 248, no. 3, pp. 758–771, 2015.

[15] J. Yan, L. Li, F. Zhao, F. Zhang, and Q. Zhao, "A multi-level optimization approach for energy-efficient flexible flow shop scheduling," *Journal of Cleaner Production*, vol. 137, no. 1, pp. 1543–1552, 2016.

[16] D. Tang, M. Dai, M. A. Salido, and A. Giret, "Energy-efficient dynamic scheduling for a flexible flow shop using an improved particle swarm optimization," *Computers in Industry*, vol. 81, no. 1, pp. 82–95, 2016.

[17] R. Zhang and R. Chiong, "Solving the energy-efficient job shop scheduling problem: a multi-objective genetic algorithm with enhanced local search for minimizing the total weighted tardiness and total energy consumption," *Journal of Cleaner Production*, vol. 112, no. 7, pp. 3361–3375, 2015.

[18] X. Zheng, S. Zhou, R. Xu et al., "Energy-efficient scheduling for multi-objective two-stage flow shop using a hybrid ant colony optimisation algorithm," *International Journal of Production Research*, vol. 58, no. 13, pp. 1–18, 2020.

[19] C. Lu, L. Gao, X. Li, Q. Pan, and Q. Wang, "Energy-efficient permutation flow shop scheduling problem using a hybrid multi-objective backtracking search algorithm," *Journal of Cleaner Production*, vol. 144, no. 6, pp. 228–238, 2017.

[20] M. Dai, D. Tang, A. Giret, and M. A. Salido, "Multi-objective optimization for energy-efficient flexible job shop scheduling problem with transportation constraints," *Robotics and Computer-Integrated Manufacturing*, vol. 59, no. 1, pp. 143–157, 2019.

[21] Y. Tanimizu and K. Amano, "Integrated production and transportation scheduling for multi-objective green supply chain network design," *Procedia CIRP*, vol. 57, no. 12, pp. 152–157, 2016.

[22] Z. Guo, L. Shi, L. Chen, and Y. Liang, "A harmony search-based memetic optimization model for integrated production and transportation scheduling in MTO manufacturing," *Omega*, vol. 66, no. 2, pp. 327–343, 2017.

[23] Z. Liu, S. Guo, and L. Wang, "Integrated green scheduling optimization of flexible job shop and crane transportation considering comprehensive energy consumption," *Journal of Cleaner Production*, vol. 211, no. 20, pp. 765–786, 2019.

[24] Y. Kuo, "Using simulated annealing to minimize fuel consumption for the time-dependent vehicle routing problem," *Computers & Industrial Engineering*, vol. 59, no. 1, pp. 157–165, 2010.

[25] E. Demir, T. Bektaş, and G. Laporte, "An adaptive large neighborhood search heuristic for the pollution-routing problem," *European Journal of Operational Research*, vol. 223, no. 2, pp. 346–359, 2012.

[26] M. Salehi, M. Jalalian, and M. M. Vali Siar, "Green transportation scheduling with speed control: trade-off between total transportation cost and carbon emission," *Computers & Industrial Engineering*, vol. 113, no. 3, pp. 392–404, 2017.

[27] J.-Q. Li, Y. Du, K.-Z. Gao et al., "A hybrid iterated greedy algorithm for a crane transportation flexible job shop problem," *IEEE Transactions on Automation Science and Engineering*, vol. 99, no. 1, pp. 1–18, 2021.

[28] J. Q. Li, Y. Q. Han, P. Y. Duan et al., "Meta-heuristic algorithm for solving vehicle routing problems with time windows and synchronized visit constraints in prefabricated systems," *Journal of Cleaner Production*, vol. 250, no. 2, pp. 223–356, 2019.

[29] J. Li, Z.-M. Liu, C. Li, and Z. Zheng, "Improved artificial immune system algorithm for type-2 fuzzy flexible job shop scheduling problem," *IEEE Transactions on Fuzzy Systems*, vol. 99, no. 1, pp. 1–191, 2020.

[30] Z.-w. Sun and X.-s. Gu, "A novel hybrid estimation of distribution algorithm for solving hybrid flowshop scheduling problem with unrelated parallel machine," *Journal of Central South University*, vol. 24, no. 8, pp. 1779–1788, 2017.

[31] B. Qian, Z.-c. Li, and R. Hu, "A copula-based hybrid estimation of distribution algorithm for m-machine reentrant permutation flow-shop scheduling problem," *Applied Soft Computing*, vol. 61, no. 3, pp. 921–934, 2017.

[32] X. Wang, K. Xing, X. Li, and J. Luo, "An estimation of distribution algorithm for scheduling problem of flexible manufacturing systems using Petri nets," *Applied Mathematical Modelling*, vol. 55, no. 6, pp. 776–788, 2018.

[33] Z. C. Li, B. Qian, R. Hu, L. L. Chang, and J. B. Yang, "An elitist nondominated sorting hybrid algorithm for multi-objective flexible job-shop scheduling problem with sequence-dependent setups," *Knowledge-Based Systems*, vol. 173, no. 6, pp. 83–112, 2019.

[34] M. Dai, Z. Zhang, A. Giret, and M. A. Salido, "An enhanced estimation of distribution algorithm for energy-efficient job-shop scheduling problems with transportation constraints," *Sustainability*, vol. 11, no. 11, pp. 3085–3098, 2019.

[35] Z. J. Yang, Z. Wang, Y. Wang et al., "Two-stage estimation of distribution algorithm to solve multi-vehicle carpooling problem," *Journal of Transportation Systems Engineering and Information Technology*, vol. 16, no. 2, pp. 164–168, 2016.

[36] H. Mokhtari and A. Hasani, "An energy-efficient multi-objective optimization for flexible job-shop scheduling problem," *Computers & Chemical Engineering*, vol. 104, no. 4, pp. 339–352, 2017.

[37] M. B. Yildirim and G. Mouzon, "Single-machine sustainable production planning to minimize total energy consumption and total completion time using a multiple objective genetic algorithm," *IEEE Transactions on Engineering Management*, vol. 59, no. 4, pp. 585–597, 2012.

[38] M. Dal, D. Tang, A. Giret et al., "Energy-efficient scheduling for a flexible flow shop using an improved genetic-simulated annealing algorithm," *Robotics and Computer Integrated Manufacturing*, vol. 29, no. 9, pp. 418–429, 2016.

[39] A. Palmer, *The Development to Fan Integrated Routing and Carbon Dioxide Emissions Model for Goods Vehicles*, Cranfield University, School of Management, Cranfield, UK, 2007.

[40] L. Kara, B. Y. Kara, and M. K. Yetis, "Energy minimizing vehicle routing problem," *International Conference on Combinatorial Optimization and Applications*, vol. 105, no. 5, pp. 916–1024, 2007.

[41] Q.-K. Pan and R. Ruiz, "An estimation of distribution algorithm for lot-streaming flow shop problems with setup times," *Omega*, vol. 40, no. 2, pp. 166–180, 2012.

[42] H. Ishibuchi, T. Yoshida, and T. Murata, "Balance between genetic search and local search in memetic algorithms for multiobjective permutation flowshop scheduling," *IEEE Transactions on Evolutionary Computation*, vol. 7, no. 2, pp. 204–223, 2003.

Hindawi
Complexity
Volume 2021, Article ID 5563888, 21 pages
https://doi.org/10.1155/2021/5563888

Research Article

Sampling-Based Event-Triggered Control for Neutral-Type Complex-Valued Neural Networks with Partly Unknown Markov Jump and Time-Varying Delay

Zhen Wang, Lianglin Xiong, Haiyang Zhang, and Yingying Liu

School of Mathematics and Computer Science, Yunnan Minzu University, Kunming 650500, China

Correspondence should be addressed to Lianglin Xiong; lianglin_5318@126.com

Received 6 January 2021; Accepted 10 May 2021; Published 24 May 2021

Academic Editor: Rui Wang

This work is devoted to studying the stochastic stabilization of a class of neutral-type complex-valued neural networks (CVNNs) with partly unknown Markov jump. Firstly, in order to reduce the conservation of our stability conditions, two integral inequalities are generalized to the complex-valued domain. Secondly, a state-feedback controller is designed to investigate the stability of the neutral-type CVNNs with $H\infty$ performance, making the stability problem a further extension, and then, the stabilization of the CVNNs with $H\infty$ performance is investigated through a sampling-based event-triggered (SBET) control for the first time that the transmission event is not triggered except when it violates the event-triggered condition. Finally, two examples are given to illustrate the validity and correctness of our obtained theorems.

1. Introduction

In terms of the wide application in electromagnetic processing, light wave and sound wave, the neural networks have attracted much attention in recent decades [1–3]. In the meantime, complex-valued signals occur inevitably in practice, and more and more scholars began to make investigations on CVNNs [4–12]. There are two methods usually used in the study of CVNNs: one is to divide the neural networks into the real part and imaginary part, then, the original CVNNs will be changed into real-valued neural networks [8–10]. The other method is when the activation function in CVNNs cannot be separated, the stability condition of the system will be sure by the complex-valued LKFs under the condition that the activation function satisfies the complex-valued Lipschitz continuity [11, 12], and it would increase the difficulty of the analysis. Considering the network works which are transformed in the first method are real-valued systems, it is easier to understand. Unfortunately, the dimensions of the obtained real-valued neural networks are twice the dimension of the original CVNNs. Also, the partial derivatives of the real and imaginary parts of state variables of the activation function are required not only to exist but also to be continuous and bounded, resulting in problems in our analysis and the application of the obtained conclusions would be limited. According to the state of the art, the LKFs method is often used to deal with neural networks problems because of its simplicity and effectiveness [10, 13–15], so it is necessary to construct LKFs with conjugate transpose of state vector to study the CVNNs by the method which do not separate the original system.

Due to the complexity of the reality, certain systems are sometimes difficult to apply to the reality, making the research of uncertain systems more valuable and practical [16]. $H\infty$ control provides a good method of dealing with unstructured uncertain systems, and research related has grown over the past two decades. Besides, it was increasingly used to analyse problems in the field of robotics, aerospace, and power systems [13, 16–20]. Reference [16] was concerned with the stabilization problem for uncertain T-S fuzzy systems with time-varying delays via a robust $H\infty$ state-feedback controller. And more general LKFs method with relaxed conditions was constructed through an improved time-delay interval segmentation method. The

state-feedback $H\infty$ control problem of time-delay systems is studied in [13], and the reciprocal convex inequality was used to obtain stability conditions of the system. However, the research we mentioned is all committed to the real systems; there is little related research on the $H\infty$ performance of CVNNs, and it is one of the main tasks in this paper. Furthermore, many scholars have specialized in the dynamic system with Markov jumping on account of the universal of Markov phenomenon, and abundant achievements have been made [14, 21–27]. In the applications of practical engineering, the analysis and control synthesis of Markov jumping systems are troubled by many dicey factors, such as the partial unknown transmission probability and the uncertainty of transmission rates. Some preliminary results have been obtained in the study of Markov jumping systems with partially unknown transmission probability [21, 23, 24, 27]. To our knowledge, less effort has been made on CVNNs with Markov phenomenon. To sum up, it is necessary to analyze the stability and $H\infty$ performance of Markov jumping CVNNs in the case of partially unknown transmission probability.

In the past few years, the sampled-data control and event-triggered control as a discrete control have attracted much attention from scholars [15, 28–40]. The so-called event-triggered control refers to a control of the tasks; whether to be executed is determined by the given event-triggered conditions in advance rather than according to the time. The control tasks would execute d immediately when the event-triggered mechanism is broken out. Comparing to the controller with time mechanism [32], events-triggered control can save the computing resources, battery energy, and communication resources obviously. Note that the event-triggered was continuous in the inchoate phase and that special hardware is needed to monitor the status continuously. Yue dong et al. proposed the (SBET) control, which is a discrete one [34]. And the monitor only needs to observe the state of the system at discrete instants with a SBET scheme that can effectively reduce the number of control tasks and save the communication resources significantly. In literature [37], the global asymptotic stability of the CVNNs under the framework of event-triggered control was studied by dividing the system into real and imaginary parts. There is an output-feedback $H\infty$ control under the event-triggered framework with nonuniform sampling used to explain the stability of networked control systems by Peng and Zheng [33]. Unfortunately, there is almost no research on CVNNs with a SBET control. So, how to stabilize the CVNNs by designing a sampling-based event-triggered controller is of our interest.

To date, this paper focuses on the stabilization of CVNNs with partly unknown Markov jump and time-varying delay. Firstly, a $H\infty$ state-feedback control is proposed to explain the stability of neutral-type CVNNs; to our knowledge, there is little research about the stabilization of neural networks in the complex field. Secondly, the stabilization of Markov jumping neutral-type CVNNs with $H\infty$ performance is considered under the framework of a SBET controller. And it is the first time to study CVNNs with a sampling-based event-triggered mechanism while avoid splitting the system into two parts, which reduces the computational complexity greatly.

Notations: throughout this work, $\mathscr{C}$ denotes the complex field and $\mathscr{C}^n$ is the n dimensional complex space. $\mathscr{A} > 0$ (or $\mathscr{A} < 0$) means that $\mathscr{A}$ is a positive Hermitian matrix (or negative Hermitian matrix), $\mathrm{sym}\{\mathscr{A}\} = \mathscr{A}^H + \mathscr{A}$, where $\mathscr{A}^H$ and $\mathscr{A}^T$, respectively, mean the conjugate transpose matrix and transpose matrix of $\mathscr{A}$, $*$ in a matrix denotes the self-conjugate part of the Hermitian matrix.

2. Problem Description and Preliminaries

2.1. Problem Description. Consider a class of neutral-type CVNNs with partly unknown Markov jump as follows:

$$\begin{cases} \dot{\vartheta}(t) - \mathscr{B}_1(r_t)\dot{\vartheta}(t-\sigma(t)) = -\mathscr{A}_1(r_t)\vartheta(t) + \mathscr{C}_1(r_t)\varphi(\vartheta(t)) + \mathscr{D}_1(r_t)\varphi(\vartheta(t-\sigma(t))) + \mathscr{E}_1(r_t)\omega(t) + \mathscr{E}_2(r_t)u(t), \\ v(t) = -\mathscr{A}_2(r_t)\vartheta(t) + \mathscr{C}_2(r_t)\varphi(\vartheta(t)) + \mathscr{D}_2(r_t)\varphi(\vartheta(t-\sigma(t))) + \mathscr{H}_1(r_t)\omega(t), \\ \vartheta(t_0+\theta) = \psi(\theta), \quad \forall\theta \in [-\sigma, 0], \end{cases} \tag{1}$$

where $\vartheta(t) \in \mathscr{C}^n$ is the state vector, which is described as $(\vartheta_1(t), \vartheta_2(t), \ldots, \vartheta_j(t))$ and $\vartheta_j(t)$ expresses the state of the jth neuron. $\omega(t) \in \mathscr{C}^n$ is the external disturbance, $u(t) \in \mathscr{C}^n$ is a control input, $v(t) \in \mathscr{C}^m$ is the control output, $0 \le \sigma(t) \le \sigma, \dot{\sigma}(t) \le \sigma_d$ is the time-varying delay, and $\varphi(\theta) \in \mathscr{C}^n$ is the initial value condition. $\varphi(\vartheta(t)) = col\{\varphi_1(\vartheta(t)), \varphi_2(\vartheta(t)), \ldots, \varphi_n(\vartheta(t))\} \in \mathscr{C}^n$, $\{r_t\}$ denotes a Markov process with on the probability space $t \ge 0$, which is right-continuous, and it takes values in set $\wp = \{1, 2, \ldots, n\}$ with the transition rate matrix $\Pi = (\pi_{pq})$, $p, q \in \wp$ given by

$$\Pr\{r_{t+\Delta} = q \mid r_t = p\} = \begin{cases} \pi_{pq}\Delta + o(\Delta), & q \ne p, \\ 1 + \pi_{pq}\Delta + o(\Delta), & q = p. \end{cases} \tag{2}$$

However, not all the information of our transition rates can be obtained; then, the transition rate matrix Π with $\mathbb{N}$ modes can be expressed as

$$\Pi = \begin{pmatrix} \pi_{11} & ? & \pi_{13} & \cdots & ? \\ ? & ? & ? & \cdots & \pi_{2n} \\ \vdots & \vdots & \vdots & \ddots & \vdots \\ ? & \pi_{n2} & \pi_{n3} & \cdots & \pi_{nn} \end{pmatrix}, \tag{3}$$

where ? expresses the transition rates which are unknown and, for $\forall p \in \wp$, the set $\mathscr{P}^p$ is expressed as $\mathscr{P}^p = \mathscr{P}_k^p \bigcup \mathscr{P}_{uk}^p$ with

$$\begin{aligned} \aleph_k^p &\triangleq \left\{q\colon \pi_{pq} \text{ is known for } q \in \wp\right\}, \\ \aleph_{uk}^p &\triangleq \left\{q\colon \pi_{pq} \text{ is uknown for } q \in \wp\right\}. \end{aligned} \tag{4}$$

With $r_t = p$ and the controllers being considered as $u(t) = \mathscr{K}_p \vartheta(t)$, then system (1) would be reexpressed as

$$\begin{cases} \dot{\vartheta}(t) = \left(-\mathscr{A}_{1p} + \mathscr{E}_{2p}\mathscr{K}_p\right)\vartheta(t) + \mathscr{B}_{1p}\dot{\vartheta}(t-\sigma(t)) + \mathscr{C}_{1p}\varphi(\vartheta(t)) + \mathscr{D}_{1p}\varphi(\vartheta(t-\sigma(t))) + \mathscr{E}_{1p}\omega(t), \\ \nu(t) = -\mathscr{A}_{2p}\vartheta(t) + \mathscr{C}_{2p}\varphi(\vartheta(t)) + \mathscr{D}_{2p}\varphi(\vartheta(t-\sigma(t))) + \mathscr{H}_{1p}\omega(t). \end{cases} \tag{5}$$

2.2. The SBET Scheme. To economize resource, we study the stabilization of the CVNNs (1) under the SBET control in this section. Assuming that the sampling device performs periodically sampling on the system state, $\mathsf{F}_1 = \{0, h, 2h, \ldots, kh, \ldots\}$ is the sampling sequence with $k \in Z^+$, and h is the constant sampling period, set $\mathsf{F}_2 = \{0, \iota_1 h, \iota_2 h, \ldots, \iota_k h, \ldots\}$, $\iota_k \in Z^+$, describe the event-triggered sequence, it is clear that $\mathsf{F}_2 \subseteq \mathsf{F}_1$, and the sampling-based event-triggered scheme is given as

$$\iota_{k+1}h = \iota_k h + \inf\left\{lh \mid e^H(\iota_k h + lh)\mathscr{G}e(\iota_k h + lh) \geq \varpi\vartheta^H(\iota_k h)\mathscr{G}\vartheta(\iota_k h)\right\} = (\iota_k + l_m)h, \tag{6}$$

where $l_m = (1/h)\inf\{lh | e^H(\iota_k h + lh)\mathscr{G}e(\iota_k h + lh) \geq \varpi\vartheta^H(\iota_k h)\mathscr{G}\vartheta(\iota_k h)\}$ and $\mathscr{G}$ is a positive Hermitian matrix, $e(\iota_k h + lh) = \vartheta(\iota_k h + lh) - \vartheta(\iota_k h)$, with $l \in Z^+$, $0 \leq \varpi < 1$. As a matter of fact, the network-induced time delay is inevitable when signals are transmitted between the event generator and the actuator at time t, which can be expressed as $\varsigma(\iota_k h)$, and $\varsigma(\iota_k h) \in [0, \varsigma]$. In $[t_k, t_{k+1})$, the control signal is hold by a zero-order-hold (ZOH) function. For $j = 0, 1, \ldots, l_{m-1}$, set $\mathscr{T}_k = [(\iota_k + j)h + \varsigma((\iota_k + j)h), (\iota_k + j + 1)h + \varsigma((\iota_k + j + 1)h)]$, and define $\eta(t) = t - (\iota_k + j)h - \varsigma((\iota_k + j)h)$, $\eta^*(t) = \eta(t) + \varsigma((\iota_k + j)h)$, $0 < \eta(t) \leq \eta^*(t) \leq \eta = h + \varsigma$, with $t_k = \iota_k h + \varsigma(\iota_k h)$, and the SBET controllers are represented as

$$u(t) = \tilde{\mathscr{K}}_p\vartheta(\iota_k h) = \tilde{\mathscr{K}}_p\vartheta(t - \eta^*(t)) - \tilde{\mathscr{K}}_p e(t - \eta^*(t)), \tag{7}$$

with $t \in \mathscr{T}_k$; system (1) would be transformed to

$$\begin{cases} \dot{\vartheta}(t) = -\mathscr{A}_{1p}\vartheta(t) + \mathscr{B}_{1p}\dot{\vartheta}(t-\sigma(t)) + \mathscr{C}_{1p}\varphi(\vartheta(t)) + \mathscr{D}_{1p}\varphi(\vartheta(t-\sigma(t))) + \mathscr{E}_{1p}\omega(t) + \mathscr{E}_{2p}\tilde{\mathscr{K}}_p\vartheta(t-\eta^*(t)) - \mathscr{E}_{2p}\tilde{\mathscr{K}}_p e(t - \eta*(t)), \\ \nu(t) = -\mathscr{A}_{2p}\vartheta(t) + \mathscr{C}_{2p}\varphi(\vartheta(t)) + \mathscr{D}_{2p}\varphi(\vartheta(t-\sigma(t))) + \mathscr{H}_{1p}\omega(t). \end{cases} \tag{8}$$

Remark 1. The parameter ϖ can make a significant difference in whether the data would be released or not. As ϖ gets smaller, conditions (6) are more likely to be violated.

Case 1: if $\varpi = 0$, the SBET scheme would be degenerated into

$$\iota_{k+1}h = \iota_k h + \inf\left\{lh \mid e^H(\iota_k + lh)\mathscr{G}e(\iota_k + lh) \geq 0\right\}, \tag{9}$$

that all the sampled data would be transmitted, and the SBET scheme (6) reduces to a periodic time-triggered one.

Case 2: if the right-hand side of the inequality is a constant $\flat > 0$, the SBET scheme would be changed into

$$\iota_{k+1}h = \iota_k h + \inf\left\{lh \mid e^H(\iota_k + lh)\mathscr{G}e(\iota_k + lh) \geq \flat\right\}, \tag{10}$$

and then, the SBET scheme (6) is converted from a relative threshold event-trigger condition to a fixed threshold event-trigger condition. However, an event-triggered control with the condition in case 2 may cause the system to be unstable and fail to achieve the control intention.

The following assumptions are put forward to draw the main results.

Assumption 1. Each activation function $\varphi_p(\cdot)$ in (5) satisfies the following condition:

$$\left|\varphi_p(\vartheta_1) - \varphi_p(\vartheta_2)\right| \leq l_p\left|\vartheta_1 - \vartheta_2\right|, \tag{11}$$

where $\vartheta_1 \neq \vartheta_2$ and $L = \mathrm{diag}\{l_1, l_2, \ldots, l_n\}$ with $l_i > 0, i = 1, 2, \ldots, n$.

Definition 1 (see [28]). System (5) is said to be stochastically stable if the following inequality holds:

$$\mathbb{E}\left\{\int_0^\infty \|\vartheta(s)\|^2 \mathrm{d}s\right\} < \infty. \tag{12}$$

Definition 2. If the CVNNs satisfy Definition 1 under the initial condition, and $\|G\|_\infty < \gamma$, that is,

$$\int_0^\infty v^H(s)v(s)\mathrm{d}s \le \gamma^2 \int_0^\infty \omega^H(s)\omega(s)\mathrm{d}s, \tag{13}$$

then we say system (5) possesses $H\infty$ performance with attenuation index γ.

Several essential lemmas are given before the proof of our theorems.

Lemma 1 (see [12]). *For any vector $\zeta \in \mathscr{C}^m$, there is a scalar $\gamma \in (0,1)$, and $\mathscr{H} \in \mathscr{C}^{n\times n}$ is a positive defined matrix, matrices $F_1, F_2 \in \mathscr{C}^{n\times m}$, and $\Phi(\gamma, \mathscr{H})$ is considered as*

$$\Phi(\gamma, \mathscr{H}) = \frac{1}{\gamma}\zeta^H F_1^H \mathscr{H} F_1 \zeta + \frac{1}{1-\gamma}\zeta^H F_2^H S F_2 \zeta. \tag{14}$$

If the matrix $U \in \mathscr{C}^{n\times n}$ satisfies $\begin{bmatrix} \mathscr{H} & U \\ * & \mathscr{H} \end{bmatrix} > 0$, then

$$\min_{\beta\in(0,1)} \Phi(\gamma, \mathscr{H}) \ge \begin{bmatrix} F_1\zeta \\ F_2\zeta \end{bmatrix}^H \begin{bmatrix} \mathscr{H} & U \\ * & \mathscr{H} \end{bmatrix} \begin{bmatrix} F_1\zeta \\ F_2\zeta \end{bmatrix}. \tag{15}$$

Lemma 2 (see [41, 42]). *$\mathfrak{R} > 0$ is a Hermitian matrix, for any continuous and differentiable function ϑ: $[c,d] \longrightarrow \mathscr{C}^n$; the following inequality holds*

$$\int_c^d \vartheta^H(s)\mathfrak{R}\vartheta(s)\mathrm{d}s \ge \frac{\Theta_1^H \mathfrak{R}\Theta_1 + 3\Theta_2^H \mathfrak{R}\Theta_2}{d-c}, \tag{16}$$

where

$$\begin{aligned} \Theta_1 &= \vartheta(d) - \vartheta(c), \\ \Theta_2 &= \vartheta(d) + \vartheta(c) - \frac{2}{d-c}\int_c^d \vartheta(s)\mathrm{d}s. \end{aligned} \tag{17}$$

By combining Lemma 1 with Lemma 2, we have the following lemma.

Lemma 3. *For Hermitian matrix $\mathfrak{S}$ and arbitrary matrices $\mathcal{S}_{11}, \mathcal{S}_{22}, \mathcal{S}_{12}$, which belong to $\mathscr{C}^{n\times n}$, setting $0 < \sigma(t) \le \sigma$, we have*

$$-\sigma\int_{t-\sigma}^t \dot{\vartheta}^H(s)\mathfrak{S}\dot{\vartheta}(s)\mathrm{d}s \le -\Gamma^H\Omega\Gamma, \tag{18}$$

where

$$\Omega = \begin{bmatrix} \mathfrak{S} & 0 & \mathcal{S}_{11} & \mathcal{S}_{12} \\ * & 3\mathfrak{S} & \mathcal{S}_{12}^H & \mathcal{S}_{22} \\ * & * & \mathfrak{S} & 0 \\ * & * & * & 3\mathfrak{S} \end{bmatrix} \ge 0,$$

$$\Gamma = \begin{bmatrix} \vartheta(t) - \vartheta(t-\sigma(t)) \\ \vartheta(t) + \vartheta(t-\sigma(t)) - \dfrac{2}{\sigma(t)}\displaystyle\int_{t-\sigma(t)}^t \vartheta(s)\mathrm{d}s \\ \vartheta(t-\sigma(t)) - \vartheta(t-\sigma) \\ \vartheta(t-\sigma(t)) + \vartheta(t-\sigma) - \dfrac{2}{\sigma-\sigma(t)}\displaystyle\int_{t-\sigma}^{t-\sigma(t)} \vartheta(s)\mathrm{d}s \end{bmatrix}. \tag{19}$$

Proof. By dividing the left-hand side of inequality (18) into two parts, the following formula is obtained:

$$\begin{aligned} -\sigma\int_{t-\sigma}^t \dot{\vartheta}^H(s)\mathfrak{S}\dot{\vartheta}(s)\mathrm{d}s = -\sigma\int_{t-\sigma(t)}^t \dot{\vartheta}^H(s) \\ \cdot \mathfrak{S}\dot{\vartheta}(s)\mathrm{d}s - \sigma\int_{t-\sigma}^{t-\sigma(t)} \dot{\vartheta}^H(s)\mathfrak{S}\dot{\vartheta}(s)\mathrm{d}s, \end{aligned} \tag{20}$$

estimating the two parts of the right-hand side of the above inequality, respectively, by Lemma 2, and then, combining the obtained parts via Lemma 1, we have

$$\begin{aligned} -\sigma\int_{t-\sigma}^t \dot{\vartheta}^H(s)\mathfrak{S}\dot{\vartheta}(s)\mathrm{d}s &\le -\frac{\sigma\left(\eta_1^H\mathfrak{S}\eta_1 + 3\eta_2^H\mathfrak{S}\eta_2\right)}{\sigma(t)} - \frac{\sigma\left(\eta_3^H\mathfrak{S}\eta_3 + 3\eta_4^H\mathfrak{S}\eta_4\right)}{\sigma-\sigma(t)} \\ &\le -\begin{bmatrix} \eta_1 \\ \eta_2 \\ \eta_3 \\ \eta_4 \end{bmatrix}^H \begin{bmatrix} \mathfrak{S} & 0 & \mathcal{S}_{11} & \mathcal{S}_{12} \\ * & 3\mathfrak{S} & \mathcal{S}_{12}^H & \mathcal{S}_{22} \\ * & * & \mathfrak{S} & 0 \\ * & * & * & 3\mathfrak{S} \end{bmatrix} \begin{bmatrix} \eta_1 \\ \eta_2 \\ \eta_3 \\ \eta_4 \end{bmatrix}, \end{aligned} \tag{21}$$

with

$$\eta_1^H = \vartheta^H(t) - \vartheta^H(t-\sigma(t)),$$
$$\eta_2^H = \vartheta^H(t) + \vartheta^H(t-\sigma(t)) - \frac{2}{\sigma(t)}\int_{t-\sigma(t)}^{t}\vartheta^H(s)\mathrm{d}s,$$
$$\eta_3^H = \vartheta^H(t-\sigma(t)) - \vartheta^H(t-\sigma),$$
$$\eta_4^H = \vartheta^H(t-\sigma(t)) + \vartheta^H(t-\sigma) - \frac{2}{\sigma-\sigma(t)}\int_{t-\sigma}^{t-\sigma(t)}\vartheta^H(s)\mathrm{d}s, \tag{22}$$

and this ends the proof. □

Remark 2. A similar conclusion has been obtained in real domain. Lemma 3 is an extension which can apply to the complex domain with complex-valued matrices and vectors $\vartheta(t), \vartheta(t-\sigma(t))$. It is worth noting that the quadratic form $\dot{\vartheta}^H(s)\mathfrak{S}\dot{\vartheta}(s)$ is in the real number field because $\mathfrak{S}$ is a Hermitian matrix.

Lemma 4 (see [35]). *Set $U > 0$ as an arbitrary matrix in R^n, and $v(t)$ is a vector with appropriate dimensional. Thus, the following inequality is obtained:*

$$-\int_{t_1}^{t_2} v^T(s)Uv(s)\mathrm{d}s \le (t_2-t_1)\lambda^T(t)V^TU^{-1}V\lambda(t) + 2\lambda^T(t)V^T\int_{t_1}^{t_2} v(s)\mathrm{d}s, \tag{23}$$

for any V and vector $\lambda(t)$ with appropriate dimensional are not dependent on integral variables.

This lemma is currently only used in the real number field; the following corollary will extend it to the domain of complex numbers.

Corollary 1. U *is a positive defined Hermitian matrix, and $\xi(t)$ is a complex vector with appropriate dimensional. Thus, the following inequality is obtained:*

$$\begin{aligned}-\int_{t_1}^{t_2}\xi^H(s)\mathrm{U}\xi(s)\mathrm{d}s &\le (t_2-t_1)\lambda^H(t)V^H\mathrm{U}^{-1}V\lambda(t)\\ &+\lambda^H(t)V^H\int_{t_1}^{t_2}\xi(s)\mathrm{d}s + \int_{t_1}^{t_2}\xi(s)\mathrm{d}sV\lambda(t),\end{aligned} \tag{24}$$

for any V and vector $\lambda(t)$ with appropriate dimensional are not dependent on integral variables.

Proof. $\mathrm{U} > 0$ is a Hermitian matrix; for complex vectors a, b with appropriate dimension, we have

$$(a+Yb)^HY^{-1}(a+Yb) \ge 0, \tag{25}$$

that is to say,

$$a^HY^{-1}a + a^Hb + b^Ha + b^HYb \ge 0, \tag{26}$$

and, then, the following conclusion is obtained:

$$\begin{aligned}&-\lambda^H(t)V^H\int_{t_1}^{t_2}\xi(s)\mathrm{d}s - \int_{t_1}^{t_2}\xi^H(s)\mathrm{d}sV\lambda(t)\\ &= \int_{t_1}^{t_2}\left[-\lambda^H(t)V^H\xi(s) - \xi^H(s)V\lambda t\right]\mathrm{d}s\\ &\le \int_{t_1}^{t_2}\lambda^H(t)V^H\mathrm{U}^{-1}V\lambda(t)\mathrm{d}s + \int_{t_1}^{t_2}\xi^H(s)\mathrm{U}\xi(s)\mathrm{d}s\\ &= (t_2-t_1)\lambda^H(t)V^H\mathrm{U}^{-1}V\lambda(t) + \int_{t_1}^{t_2}\xi^H(s)\mathrm{U}\xi(s)\mathrm{d}s.\end{aligned} \tag{27}$$

This ends the proof. □

Remark 3. In the proof of Corollary 1, we can clearly see that $-\lambda^H(t)V^H\int_{t_1}^{t_2}\xi(s)\mathrm{d}s$ and $-\int_{t_1}^{t_2}\xi(s)\mathrm{d}sV\lambda(t)$ cannot be merged into $-2\lambda^H(t)V^H\int_{t_1}^{t_2}\xi(s)\mathrm{d}s$ because it may be an imaginary number. Also, the condition $U > 0$ in Lemma 4 is changed into U, which is a positive defined Hermitian matrix, which can ensure that both sides of the inequality are real numbers so that the magnitudes can be compared. Therefore, the above inequality can be used in the complex domain in the form of Corollary 1.

3. Main Result

Two main theorems will be presented in this section. In the first place, we study the stabilization of system (5) with $H\infty$ performance without a SBET scheme; and then, by

employing the SBET scheme (6), we derive a sufficient condition for the stability of system (8). Now we define the following vectors and matrices for clarity:

$$
\begin{aligned}
v_1 &= \frac{1}{\sigma(t)}\int_{t-\sigma(t)}^{t}\vartheta(s)\mathrm{d}s,\\
v_2 &= \frac{1}{\sigma-\sigma(t)}\int_{t-\sigma}^{t-\sigma(t)}\vartheta(s)\mathrm{d}s,\\
v_3 &= \frac{1}{\eta(t)}\int_{t-\eta(t)}^{t}\vartheta(s)\mathrm{d}s,\\
v_4 &= \frac{1}{\eta-\eta(t)}\int_{t-\eta}^{t-\eta(t)}\vartheta(s)\mathrm{d}s,\\
v_5 &= \frac{1}{\eta*(t)}\int_{t-\eta^*(t)}^{t}\vartheta(s)\mathrm{d}s,\\
v_6 &= \frac{1}{\eta-\eta*(t)}\int_{t-\eta}^{t-\eta^*(t)}\vartheta(s)\mathrm{d}s,\\
\overline{\mathcal{Q}_1} &= \begin{bmatrix} \widehat{\mathcal{Q}}_3 & 0 & \widehat{\mathcal{S}}_{11} & \widehat{\mathcal{S}}_{12}\\ * & 3\widehat{\mathcal{Q}}_3 & \widehat{\mathcal{S}}_{12}^H & \widehat{\mathcal{S}}_{22}\\ * & * & \widehat{\mathcal{Q}}_3 & 0\\ * & * & * & 3\widehat{\mathcal{Q}}_3 \end{bmatrix}\geq 0,\\
\overline{\mathcal{Q}_2} &= \begin{bmatrix} \widehat{\mathcal{Q}}_4 & 0 & \widehat{\mathcal{S}}_{33} & \widehat{\mathcal{S}}_{34}\\ * & 3\widehat{\mathcal{Q}}_4 & \widehat{\mathcal{S}}_{34}^H & \widehat{\mathcal{S}}_{44}\\ * & * & \widehat{\mathcal{Q}}_4 & 0\\ * & * & * & 3\widehat{\mathcal{Q}}_4 \end{bmatrix}\geq 0,\\
\overline{\mathcal{Q}_3} &= \begin{bmatrix} \widehat{\mathcal{Q}}_6 & 0 & \widehat{\mathcal{S}}_{55} & \widehat{\mathcal{S}}_{56}\\ * & 3\widehat{\mathcal{Q}}_6 & \widehat{\mathcal{S}}_{56}^H & \widehat{\mathcal{S}}_{66}\\ * & * & \widehat{\mathcal{Q}}_6 & 0\\ * & * & * & 3\widehat{\mathcal{Q}}_6 \end{bmatrix}\geq 0,\\
\mathcal{Q}_1 &= \begin{bmatrix} \mathcal{Q}_3 & 0 & \mathcal{S}_{11} & \mathcal{S}_{12}\\ * & 3\mathcal{Q}_3 & \mathcal{S}_{12}^H & \mathcal{S}_{22}\\ * & * & \mathcal{Q}_3 & 0\\ * & * & * & 3\mathcal{Q}_3 \end{bmatrix}\geq 0,\\
\mathcal{Q}_2 &= \begin{bmatrix} \mathcal{Q}_4 & 0 & \mathcal{S}_{33} & \mathcal{S}_{34}\\ * & 3\mathcal{Q}_4 & \mathcal{S}_{34}^H & \mathcal{S}_{44}\\ * & * & \mathcal{Q}_4 & 0\\ * & * & * & 3\mathcal{Q}_4 \end{bmatrix}\geq 0,\\
\mathcal{Q}_3 &= \begin{bmatrix} \mathcal{Q}_6 & 0 & \mathcal{S}_{55} & \mathcal{S}_{56}\\ * & 3\mathcal{Q}_6 & \mathcal{S}_{56}^H & \mathcal{S}_{66}\\ * & * & \mathcal{Q}_6 & 0\\ * & * & * & 3\mathcal{Q}_6 \end{bmatrix}\geq 0.
\end{aligned}
\tag{28}
$$

Theorem 1. *Under the condition of Assumption 1, for given scalar σ, σ_d and m, if there exist positive defined Hermitian matrices $\widehat{\mathcal{P}}_p, \widehat{\mathcal{Q}}_p, \widehat{\mathcal{Q}}_3, \widehat{\mathcal{W}}_p$ in $\mathcal{C}^{n\times n}$, $\widehat{\mathcal{R}}_p, \widehat{\mathcal{R}}, \widehat{\mathcal{M}}_p \in \mathcal{C}^{2n\times 2n}$, $\widehat{E}_1, \widehat{E}_2$ are positive diagonal matrices, and any matrices $Y_{1p}, \widehat{\mathcal{S}}_{11}, \widehat{\mathcal{S}}_{12}, \widehat{\mathcal{S}}_{22}, \mathcal{K}_p$, nonsingular matrix $\mathcal{X}$ with proper dimension such that the following LMIs, are established with $p \in \{1, 2, 3\}$:*

$$
\Omega_1 = \begin{bmatrix} \Xi_1 + \Xi_2 & \Lambda\\ * & -I \end{bmatrix} < 0, \tag{29}
$$

$$
\begin{aligned}
&\sum_{q\in\aleph_k^p}\pi_{pq}\left(\widehat{\mathcal{R}}_q - \widehat{\mathcal{M}}_p\right)\leq \widehat{\mathcal{R}},\\
&\widehat{\mathcal{P}}_q - \widehat{\mathcal{W}}_p \leq 0, q\in\aleph_{uk}^p, p\neq q, \widehat{\mathcal{R}}_q - \widehat{\mathcal{M}}_p \leq 0,\\
&\qquad q\in\aleph_{uk}^p, p\neq q,\\
&\widehat{\mathcal{P}}_q - \widehat{\mathcal{W}}_p \geq 0, q\in\aleph_{uk}^p, p = q, \widehat{\mathcal{R}}_q - \widehat{\mathcal{M}}_p \geq 0,\\
&\qquad q\in\aleph_{uk}^p, p = q,
\end{aligned}
\tag{30}
$$

where

$$
\begin{aligned}
\Xi_1 &= e_{10}^H\widehat{\mathcal{Q}}_1 e_{10} - (1-\sigma_d)e_8^H\widehat{\mathcal{Q}}_1 e_8 + e_1^H\widehat{\mathcal{Q}}_2 e_1 - (1-\sigma_d)\\
&\quad\cdot e_3^H\widehat{\mathcal{Q}}_2 e_3 + \sigma^2 e_{10}^H\widehat{\mathcal{Q}}_3 e_{10} - \Gamma_1^H\widehat{\mathcal{Q}}_1\Gamma_1 + \sigma\Gamma_2^H\widehat{\mathcal{R}}\Gamma_2\\
&\quad + \mathrm{sym}\left\{e_1^H\widehat{\mathcal{P}}_p e_{10}\right\} + \Gamma_2^H\widehat{\mathcal{R}}_p\Gamma_2 + \Gamma_3^H\widehat{\mathcal{R}}_p\Gamma_3\\
&\quad + e_1^H\sum_{q\in\aleph_k^p}\pi_{pq}\left(\widehat{\mathcal{P}}_q - \widehat{\mathcal{W}}_p\right)e_1 + e_1^H L^H\widehat{E}_1 L e_1 - e_4^H\widehat{E}_1 e_4\\
&\quad + e_3^H L^H\widehat{E}_2 L e_3 - e_5^H\widehat{E}_2 e_5 - \gamma^2 e_{11}^H\widehat{I}e_{11} - e_{12}^H\widehat{I}e_{12},\\
\Xi_2 &= \mathrm{sym}\Big\{\left(me_1^H + e_{10}^H\right)\Big(-\mathcal{X}e_{10} - \left(\mathcal{A}_{1p}\mathcal{X} - \mathrm{E}_{2p}Y_p\right)e_1\\
&\quad + \mathcal{B}_{1p}\mathcal{X}e_8 + \mathcal{C}_{1p}\mathcal{X}e_4 + \mathcal{D}_{1p}\mathcal{X}e_5 + \mathcal{E}_{1p}\mathcal{X}e_{11}\Big)\Big\},\\
\Lambda &= \left[-\mathcal{X}\mathcal{A}_{2p}, 0, 0, \mathcal{X}\mathcal{C}_{2p}, \mathcal{X}\mathcal{D}_{2p}, 0, 0, 0, \mathcal{X}\mathcal{H}_{1p}\right],\\
\xi_1^H(t) &= \Big[\vartheta^H(t), \vartheta^H(t-\sigma), \vartheta^H(t-\sigma(t)), \varphi^H(\vartheta(t)),\\
&\quad \varphi^H(\vartheta(t-\sigma(t))), v_1^H, v_2^H, \dot{\vartheta}^H(t-\sigma(t)),\\
&\quad \varphi^H(\vartheta(t-\sigma), \dot{\vartheta}(t), \omega(t)\Big]^H,\\
\xi_2^H(t) &= \left[\vartheta^H(t), \varphi^H(\vartheta(t))\right]^H,\\
e_p &= \left[0_{n\times(p-1)n}\ \ I_n\ \ 0_{n\times(11-p)n}\right],\\
\Gamma_1 &= \begin{bmatrix} e_1 - e_3\\ e_1 + e_3 - 2e_6\\ e_3 - e_2\\ e_3 + e_2 - 2e_7 \end{bmatrix},\\
\Gamma_2 &= \left[e_1, e_4\right],\\
\Gamma_3 &= \left[e_2, e_9\right].
\end{aligned}
\tag{31}
$$

Then, system (5) is asymptotically stable via $u(t) = \mathscr{K}_p \vartheta(t)$ with $H\infty$ disturbance attenuation γ and the controller gain matrices are designed as $\mathscr{K}_p = Y_{1p}\mathscr{X}^{-1}$.

Proof. Consider the following LKF:

$$V(\vartheta(t), t, p) = \sum_{m=1}^{5} V_m(\vartheta(t), t, p), \tag{32}$$

where

$$\begin{aligned}
V_1(\vartheta(t), p) &= \vartheta^H(t)\mathscr{P}_p\vartheta(t),\\
V_2(\vartheta(t), p) &= \int_{t-\sigma}^{t} \xi_2^H(s)\mathscr{R}_p\xi_2(s)\mathrm{d}s,\\
V_3(\vartheta(t), p) &= \int_{t-\sigma(t)}^{t} \dot{\vartheta}^H(s)\mathscr{Q}_1\dot{\vartheta}(s)\mathrm{d}s + \int_{t-\sigma(t)}^{t} \vartheta^H(s)\mathscr{Q}_2\vartheta(s)\mathrm{d}s,\\
V_4(\vartheta(t), p) &= \sigma\int_{\sigma}^{0}\int_{t-\theta}^{t} \dot{\vartheta}^H(s)\mathscr{Q}_3\dot{\vartheta}(s)\mathrm{d}s\mathrm{d}\theta,\\
V_5(\vartheta(t), p) &= \int_{t-\sigma}^{t}\int_{\theta}^{0} \xi_2^H(s)\mathscr{R}\xi_2(s)\mathrm{d}s\mathrm{d}\theta,
\end{aligned} \tag{33}$$

with

$$\mathscr{P}_p = \left(\mathscr{X}^H\right)^{-1}\widehat{\mathscr{P}}_p\mathscr{X}^{-1}, \mathscr{Q}_p = \left(\mathscr{X}^H\right)^{-1}\widehat{\mathscr{Q}}_p\mathscr{X}^{-1}, \mathscr{R}_p = \left(\mathscr{X}^H\right)^{-1}\widehat{\mathscr{R}}_p\mathscr{X}^{-1}, \mathscr{R} = \left(\mathscr{X}^H\right)^{-1}\widehat{\mathscr{R}}\mathscr{X}^{-1}, \quad p \in \{1, 2, 3\}. \tag{34}$$

Adopting the weak infinitesimal operator L in [21], which acts on $V_m(\vartheta(t), t, i)$ as

$$LV(\vartheta(t), p) = \lim_{\Delta\longrightarrow\infty} \frac{1}{\Delta}\left[\mathbb{E}\{V(\vartheta(t+\Delta), t, r_{t+\Delta})|\vartheta(t), r_t = p\} - V(\vartheta(t), t, p)\right], \tag{35}$$

then, similar to the computation in [26, 27], we have

$$LV_1(\vartheta(t), p) = \vartheta^H(t)\mathscr{P}_p\dot{\vartheta}(t) + \dot{\vartheta}^H(t)\mathscr{P}_p\vartheta(t) + \vartheta^H(t)\sum_{q=1}^{n}\pi_{pq}\mathscr{P}_q\vartheta(t), \tag{36}$$

$$LV_2(\vartheta(t), p) = \xi_2^H(t)\mathscr{R}_p\xi_2(t) - \xi_2^H(t-\sigma)\mathscr{R}_p\xi_2(t-\sigma) + \int_{t-\sigma}^{t}\xi_2^H(s)\sum_{q=1}^{n}\pi_{pq}\mathscr{R}_q\xi_2(s)\mathrm{d}s, \tag{37}$$

and considering the transition rate matrix includes not only the known part but also the unknown part, the following equations would hold for matrices $\mathscr{W}_p = (\mathscr{X}^H)^{-1}\widehat{\mathscr{W}}_p\mathscr{X}^{-1}, \mathscr{M}_p = (\mathscr{X}^H)^{-1}\widehat{\mathscr{M}}_p\mathscr{X}^{-1}$:

$$\begin{aligned}
0 &= -\vartheta^H(t)\left(\sum_{q=1}^{n}\pi_{pq}\mathscr{W}_p\right)\vartheta(t), \quad \forall p \in \wp,\\
0 &= -\int_{t-\sigma}^{t}\vartheta^H(s)\left(\sum_{q=1}^{n}\pi_{pq}\mathscr{M}_p\right)\vartheta(s)\mathrm{d}s, \quad \forall p \in \wp.
\end{aligned} \tag{38}$$

Then, (36) and (37) are equal to the following equations:

$$LV_1(\vartheta(t),p) = \vartheta^H(t)\mathscr{P}_p\dot{\vartheta}(t) + \dot{\vartheta}^H(t)\mathscr{P}_p\vartheta(t) + \vartheta^H(t)\sum_{q\in\aleph_k^p}\pi_{pq}\left(\mathscr{P}_q - \mathscr{W}_p\right)\vartheta(t) + \vartheta^H(t) \cdot \sum_{q\in\aleph_{uk}^p}\pi_{pq}\left(\mathscr{P}_q - \mathscr{W}_p\right)\vartheta(t), \tag{39}$$

$$LV_2(\vartheta(t),p) = \xi_2^H(t)\mathscr{R}_p\xi_2(t) - \xi_2^H(t-\sigma)\mathscr{R}_p\xi_2(t-\sigma) + \int_{t-\sigma}^{t}\xi_2^H(s)\sum_{q\in\aleph_k^p}\pi_{pq}\left(\mathscr{R}_q - \mathscr{M}_p\right)\xi(s)_2\mathrm{d}s + \int_{t-\sigma}^{t}\xi_2^H(s)\sum_{q\in\aleph_{uk}^p}\pi_{pq}\left(R_q - \mathscr{M}_p\right)\xi_2(s)\mathrm{d}s. \tag{40}$$

Via easy calculations, the following equations are given:

$$LV_3(\vartheta(t),p) \le \dot{\vartheta}^H(t)\mathscr{Q}_1\dot{\vartheta}(t) - \left(1-\sigma_d\right)\dot{\vartheta}^H(t-\sigma(t))\mathscr{Q}_1\dot{\vartheta}(t-\sigma(t)) + \vartheta^H(t)\mathscr{Q}_2\vartheta(t) - \left(1-\sigma_d\right)\vartheta^H(t-\sigma(t))\mathscr{Q}_2\vartheta(t-\sigma(t)), \tag{41}$$

$$LV_4(\vartheta(t),p) = \sigma^2\dot{\vartheta}^H(t)\mathscr{Q}_3\dot{\vartheta}(t) - \sigma\int_{t-\sigma}^{t}\dot{\vartheta}^H(s)\mathscr{Q}_3\dot{\vartheta}(s)\mathrm{d}s, \tag{42}$$

$$LV_5(\vartheta(t),p) = \sigma\xi_2^H(t)\mathscr{R}\xi_2(t) - \int_{t-\sigma}^{t}\xi_2^H(s)\mathscr{R}\xi_2(s)\mathrm{d}s. \tag{43}$$

Dealing with the integral term containing the Markov jump, by pre- and postmultiplying $(\mathscr{X}^H)^{-1}$ and $\mathscr{X}^{-1}$ with (30), we have and then, the following inequalities are obtained:

$$\begin{aligned}
&\sum_{q\in\aleph_k^p}^{n}\pi_{pq}\left(\mathscr{R}_q - \mathscr{M}_p\right) \le \mathscr{R},\\
&\mathscr{P}_q - \mathscr{W}_p \le 0, q\in\aleph_{uk}^p, p\ne q, \mathscr{R}_q - \mathscr{M}_p \le 0, q\in\aleph_{uk}^p, p\ne q,\\
&\mathscr{P}_q - \mathscr{W}_p \ge 0, q\in\aleph_{uk}^p, p = q, \mathscr{R}_q - \mathscr{M}_p \ge 0, q\in\aleph_{uk}^p, p = q,
\end{aligned} \tag{44}$$

$$\begin{aligned}
&\int_{t-\sigma}^{t}\xi_2^H(s)\sum_{q\in\aleph_k^p}\pi_{pq}\left(\mathscr{R}_q - \mathscr{M}_p\right)\xi_2(s)\mathrm{d}s - \int_{t-\sigma}^{t}\xi_2^H(s)\mathscr{R}\xi_2(s)\mathrm{d}s \le 0,\\
&\vartheta^H(t)\sum_{q\in\aleph_{uk}^p}\pi_{pq}\left(\mathscr{P}_q - \mathscr{W}_p\right)\vartheta(t) + \int_{t-\sigma}^{t}\xi_2^H(s)\sum_{q\in\aleph_{uk}^p}\pi_{pq}\left(\mathscr{R}_q - \mathscr{M}_p\right)\xi_2(s)\mathrm{d}s \le 0.
\end{aligned} \tag{45}$$

For arbitrary matrices $\mathcal{S}_{11}, \mathcal{S}_{22}, \mathcal{S}_{12} \in \mathcal{C}^{n\times n}$, because of Lemma 3, $-\sigma\int_{t-\sigma}^{t}\dot{\vartheta}^{H}(s)\mathcal{Q}_3\dot{\vartheta}(s)\mathrm{d}s$ in (42) will be processed as follows: by dividing it into two parts, we have

$$-\sigma\int_{t-\sigma}^{t}\dot{\vartheta}^{H}(s)\mathcal{Q}_3\dot{\vartheta}(s)\mathrm{d}s = -\sigma\int_{t-\sigma(t)}^{t}\dot{\vartheta}^{H}(s)\mathcal{Q}_3\dot{\vartheta}(s)\mathrm{d}s - \sigma\int_{t-\sigma}^{t-\sigma(t)}\dot{\vartheta}^{H}(s)\mathcal{Q}_3\dot{\vartheta}(s)\mathrm{d}s, \tag{46}$$

estimating the two parts of the right-hand side of the above inequality, respectively, by Lemma 2, and then, combining the obtained parts via Lemma 1, we have

$$\begin{aligned}
-\sigma\int_{t-\sigma}^{t}\dot{\vartheta}^{H}(s)\mathcal{Q}_3\dot{\vartheta}(s)\mathrm{d}s &\le -\frac{\sigma\left(\eta_1^H\mathcal{Q}_3\eta_1 + 3\eta_2^H\mathcal{Q}_3\eta_2\right)}{\sigma(t)} - \frac{\sigma\left(\eta_3^H\mathcal{Q}_3\eta_3 + 3\eta_4^H\mathcal{Q}_3\eta_4\right)}{\sigma-\sigma(t)}\\
&\le -\begin{bmatrix}\eta_1\\ \eta_2\\ \eta_3\\ \eta_4\end{bmatrix}^H\begin{bmatrix}\mathcal{Q}_3 & 0 & \mathcal{S}_{11} & \mathcal{S}_{12}\\ * & 3\mathcal{Q}_3 & \mathcal{S}_{12}^H & \mathcal{S}_{22}\\ * & * & \mathcal{Q}_3 & 0\\ * & * & * & 3\mathcal{Q}_3\end{bmatrix}\begin{bmatrix}\eta_1\\ \eta_2\\ \eta_3\\ \eta_4\end{bmatrix}\\
&= -\xi_1^H(t)\Gamma_1^H\mathcal{Q}_1\Gamma_1\xi_1(t).
\end{aligned} \tag{47}$$

Thus,

$$LV_4(\vartheta(t),p) \le \sigma^2\dot{\vartheta}^{H}(t)\mathcal{Q}_3\dot{\vartheta}(t) - \xi_1^H(t)\Gamma_1^H\mathcal{Q}_1\Gamma_1\xi_1(t). \tag{48}$$

On the other hand, for diagonal matrices $E_1 = (\mathcal{X}^H)^{-1}\widehat{E}_1\mathcal{X}^{-1}, E_2 = (\mathcal{X}^H)^{-1}\widehat{E}_2\mathcal{X}^{-1}$, Assumption 1 implies that

$$\begin{aligned}
&\vartheta^H(t)LE_1L\vartheta(t) - \varphi^H(\vartheta(t))E_1\varphi(\vartheta(t)) \ge 0,\\
&\vartheta^H(t-\sigma(t))LE_2L\vartheta(t-\sigma(t)) - \varphi^H(\vartheta(t-\sigma(t)))E_2\varphi(\vartheta(t-\sigma(t))) \ge 0.
\end{aligned} \tag{49}$$

One can also obtain the following equation from (5) for any nonsingular matrix $\mathcal{X}_2$ with the appropriate dimension, we defined $\mathcal{X}_1 = m\mathcal{X}_2$, and it is clearly that $\mathcal{X}_2$ is also nonsingular, such that

$$\begin{aligned}
0 = &\left(\vartheta^H(t)\mathcal{X}_1^H + \dot{\vartheta}^H(t)\mathcal{X}_2^H\right)\left(-\dot{\vartheta}(t) + \left(-\mathcal{A}_{1p} + \mathrm{E}_{2p}\mathcal{K}_p\right)\vartheta(t) + \mathcal{B}_{1p}\dot{\vartheta}(t-\sigma(t)) + \mathcal{C}_{1p}\varphi(\vartheta(t)) + \mathcal{D}_{1p}\varphi(\vartheta(t-\sigma(t)))\right.\\
&\left.+\mathcal{E}_{1p}\omega(t)\right) + \left(-\dot{\vartheta}(t) + \left(-\mathcal{A}_{1p} + \mathcal{E}_{2p}\mathcal{K}_p\right)\vartheta(t) + \mathcal{B}_{1p}\dot{\vartheta}(t-\sigma(t)) + \mathcal{C}_{1p}\varphi(\vartheta(t)) + \mathcal{D}_{1p}\varphi(\vartheta(t-\sigma(t)))\right.\\
&\left.+\mathcal{E}_{1p}\omega(t)\right)^H\left(\mathcal{X}_1\vartheta(t) + \mathcal{X}_2\dot{\vartheta}(t)\right).
\end{aligned} \tag{50}$$

Through the analysis in (39)–(50), we have

$$
\begin{aligned}
LV(\vartheta(t),p)+v^H(t)v(t)-\gamma^2\omega^H(t)\omega(t)\le{}&\vartheta^H(t)\mathscr{P}_p\dot{\vartheta}(t)+\dot{\vartheta}^H(t)\mathscr{P}_p\vartheta(t)+\vartheta^H(t)\sum_{q\in\aleph_k^p}\pi_{pq}\left(\mathscr{P}_q-\mathscr{W}_p\right)\vartheta(t)\\
&+\xi_2^H(t)\mathscr{R}_p\xi_2(t)-\xi_2^H(t-\sigma)\mathscr{R}_p\xi_2(t-\sigma)+\dot{\vartheta}^H(t)\left(\mathscr{Q}_1+\sigma^2\mathscr{Q}_3\right)\dot{\vartheta}(t)\\
&-(1-\sigma_d)\dot{\vartheta}^H(t-\sigma(t))\mathscr{Q}_1\dot{\vartheta}(t-\sigma(t))\\
&+\vartheta^H(t)\mathscr{Q}_2\vartheta(t)-(1-\sigma_d)\vartheta^H(t-\sigma(t))\mathscr{Q}_2\vartheta(t-\sigma(t))-\xi_1^H(t)\Gamma_1^H\mathscr{Q}_1\Gamma_1\xi_1(t)+\sigma\xi_2^H(t)\mathscr{R}\xi_2(t)\\
&+\vartheta^H(t)LE_1L\vartheta(t)\\
&-\varphi^H(\vartheta(t))E_1\varphi(\vartheta(t))+\vartheta^H(t-\sigma(t))LE_2L\vartheta(t-\sigma(t))-\varphi^H(\vartheta(t-\sigma(t)))E_2\varphi(\vartheta(t-\sigma(t)))\\
&+\operatorname{sym}\Big\{\left(\vartheta^H(t)\mathscr{X}_1^H+\dot{\vartheta}^H(t)\mathscr{X}_2^H\right)\left(-\dot{\vartheta}(t)+\left(-\mathscr{A}_{1p}+\mathscr{E}_{2p}\mathscr{K}_p\right)\vartheta(t)+\mathscr{B}_{1p}\dot{\vartheta}(t-\sigma(t))+\mathscr{C}_{1p}\varphi(\vartheta(t))\right.\\
&\left.+\mathscr{D}_{1p}\varphi(\vartheta(t-\sigma(t)))+\mathscr{E}_{1p}\omega(t)\right)\Big\}+v^H(t)v(t)-\gamma^2\omega^H(t)\omega(t)=\xi_1^H\Omega\xi_1,
\end{aligned}
\tag{51}
$$

where

$$
\begin{aligned}
\Omega={}&\operatorname{sym}\left\{e_1^H\mathscr{P}_pe_{10}\right\}+e_1^H\sum_{q\in\aleph_k^p}\pi_{pq}\left(\mathscr{P}_q-\mathscr{W}_p\right)e_1+\Gamma_2^H\mathscr{R}_p\Gamma_2+\Gamma_3^H\mathscr{R}_p\Gamma_3+e_{10}^H\mathscr{Q}_1e_{10}+\sigma^2e_{10}^H\mathscr{Q}_3e_{10}\\
&-(1-\sigma_d)e_8^H\mathscr{Q}_1e_8+e_1^H\mathscr{Q}_2e_1-(1-\sigma_d)e_3^H\mathscr{Q}_2e_3-\Gamma_1^H\mathscr{Q}_1\Gamma_1+\sigma\Gamma_2^H\mathscr{R}\Gamma_2+e_1^HL^HE_1Le_1-e_4^HE_1e_4\\
&+\operatorname{sym}\left\{\left(e_1^H\mathscr{X}_1^H+e_{10}^H\mathscr{X}_2^H\right)\left(-e_{10}-\left(\mathscr{A}_{1p}-\mathscr{E}_{2p}\mathscr{K}_p\right)e_1+\mathscr{B}_{1p}e_8+\mathscr{C}_{1p}e_4+\mathscr{D}_{1p}e_5+\mathscr{E}_{1p}e_{11}\right)\right\}\\
&+e_3^HL^HE_2Le_3-e_5^HE_2e_5-\gamma^2e_{11}^HIe_{11}+\chi^H\chi,\\
\chi={}&-\mathscr{A}_{2p}e_1+\mathscr{E}_{2p}e_4+\mathscr{D}_{2p}e_5+\mathscr{H}_{1p}e_{11}.
\end{aligned}
\tag{52}
$$

Defining

$$
\begin{aligned}
&\mathscr{X}=\mathscr{X}_2^{-1},Y_{1p}=\mathscr{K}_p\mathscr{X},\mathfrak{X}_\hbar=\operatorname{diag}\left\{\underbrace{\mathscr{X},\mathscr{X},\ldots,\mathscr{X}}_{\hbar}\right\},\widehat{\mathscr{P}}_p=\mathscr{X}^H\mathscr{P}_p\mathscr{X},\widehat{\mathscr{W}}_p=\mathscr{X}^H\mathscr{W}_p\mathscr{X},\\
&\widehat{\mathscr{M}}_p=\mathscr{X}^H\mathscr{M}_p\mathscr{X},\widehat{\mathscr{P}}_q=\mathscr{X}^H\mathscr{P}_q\mathscr{X},\widehat{\mathscr{R}}_q=\mathscr{X}^H\mathscr{R}_q\mathscr{X},\widehat{\mathscr{R}}_p=\mathscr{X}^H\mathscr{R}_p\mathscr{X},\widehat{\mathscr{Q}}_p=\mathscr{X}^H\mathscr{Q}_p\mathscr{X},\widehat{\mathscr{Q}}_4=\mathscr{X}^H\mathscr{Q}_4\mathscr{X},\\
&\widehat{\mathscr{R}}=\mathscr{X}^H\mathrm{RX},\widehat{\mathscr{E}}_1=\mathscr{X}^H\mathscr{E}_1\mathscr{X},\widehat{\mathscr{E}}_2=\mathscr{X}^H\mathscr{E}_2\mathscr{X},\widehat{I}=\mathscr{X}^HI\mathscr{X},\widehat{\mathscr{S}}_{11}=\mathscr{X}^H\mathscr{S}_{11}\mathscr{X},\widehat{\mathscr{S}}_{12}=\mathscr{X}^H\mathscr{S}_{12}\mathscr{X},\widehat{\mathscr{S}}_{22}=\mathscr{X}^H\mathscr{S}_{22}\mathscr{X},
\end{aligned}
\tag{53}
$$

and then, by pre- and postmultiplying $\mathfrak{X}_\hbar^H$ and $\mathfrak{X}_\hbar\,(\hbar=11)$ with Ω, (29) is obtained. Combining (29) with (51) and using the Schur complement, we have

$$
LV(\vartheta(t),p)+v^H(t)v(t)-\gamma^2\omega^H(t)\omega(t)<0,
\tag{54}
$$

and integrating the formula above from 0 to ∞, we have

$$
V(\vartheta(\infty))-V(\varphi(\theta))\le-\int_0^\infty v^H(t)v(t)\mathrm{d}t+\gamma^2\int_0^\infty\omega^H(t)\omega(t)\mathrm{d}t,
\tag{55}
$$

and, with the zero initial condition $\phi=0$, we have $V(\varphi(\theta))=0$, $V(\vartheta(\infty))\ge0$; thus,

$$
-\int_0^\infty v^H(t)v(t)\mathrm{d}t+\gamma^2\int_0^\infty\omega^H(t)\omega(t)\mathrm{d}t>V(\vartheta(\infty))\ge0.
\tag{56}
$$

This completes the proof.

Next, based on Theorem 1 and Lemma 3 and Corollary 1, a sampling-based event-triggered controller will be used to study the stabilization and $H\infty$ performance of CVNNs with uncertain Markov jump. □

Theorem 2. *For the given positive scalars $\sigma,\sigma_d,\rho,\eta$ and $0\le\varpi<1$, if there exist Hermitian matrices $\widehat{\mathscr{P}}_p,\widehat{\mathscr{Q}}_p,\widehat{\mathscr{Q}}_4,\widehat{\mathscr{Q}}_5,\widehat{\mathscr{Q}}_6,\widehat{\mathscr{R}},\widehat{\mathscr{G}},\widehat{\mathscr{W}}_p$ in $\mathscr{C}^{n\times n}$, $\widehat{\mathscr{R}}_p,\widehat{\mathscr{R}},\widehat{\mathscr{M}}_p\in\mathscr{C}^{2n\times2n}$, and $E_1,E_2,\widehat{E}_1,\widehat{E}_2$ are positive diagonal matrices, matrices $\widetilde{\mathscr{K}}_p$, and nonsingular matrix $\widetilde{\mathscr{X}}\in\mathscr{C}^{n*n}$ are proper dimension matrices with $p\in\{1,2,3\}$, such that the following conditions hold:*

$$\tilde{\Omega}_2(0) = \begin{bmatrix} \hat{\Xi} & \hat{\Lambda} \\ * & -I \end{bmatrix} < 0, \tag{57}$$

$$\tilde{\Omega}_2(\eta) = \begin{bmatrix} \hat{\Xi} + \eta\hat{\Xi}_1 & \hat{\Lambda} \\ * & -I \end{bmatrix} < 0, \tag{58}$$

$$\tilde{\Omega}_3(\eta) = \begin{bmatrix} \hat{\Xi} - \eta\hat{e}_{17}^H\hat{U}_{22}\hat{e}_{17} & \hat{\Lambda} & \begin{bmatrix} \hat{e}_1^H & \hat{e}_{10}^H & \hat{e}_{17}^H \end{bmatrix}\tilde{V} \\ * & -I & 0 \\ * & * & -\frac{1}{\eta}U_{11} \end{bmatrix} < 0, \tag{59}$$

where

$$\begin{aligned} &\sum_{q \in \aleph_k^p} \pi_{pq}\left(\hat{\mathscr{R}}_q - \widehat{\mathscr{M}}_p\right) \le \hat{\mathscr{R}}, \\ &\hat{\mathscr{P}}_q - \widehat{\mathscr{W}}_p \le 0, \quad q \in \aleph_{uk}^p,\ p \ne q, \\ &\hat{\mathscr{R}}_q - \widehat{\mathscr{M}}_p \le 0, \quad q \in \aleph_{uk}^p,\ p \ne q, \\ &\hat{\mathscr{P}}_q - \widehat{\mathscr{W}}_p \ge 0, \quad q \in \aleph_{uk}^p,\ p = q, \\ &\hat{\mathscr{R}}_q - \widehat{\mathscr{M}}_p \ge 0, \quad q \in \aleph_{uk}^p,\ p = q, \end{aligned} \tag{60}$$

$$\begin{aligned} \hat{\Xi} = {} & \mathrm{sym}\left\{\left(\rho\hat{e}_1^H + \hat{e}_{10}^H\right)\left(-\hat{\mathscr{X}}\hat{e}_{10} - \mathscr{A}_{1p}\hat{\mathscr{X}}\hat{e}_1 + \mathscr{B}_{1p}\hat{\mathscr{X}}\hat{e}_8 + \mathscr{C}_{1p}\hat{\mathscr{X}}\hat{e}_4 + \mathscr{D}_{1p}\hat{\mathscr{X}}\hat{e}_5 + \mathscr{E}_{1p}\hat{\mathscr{X}}\hat{e}_9 + \mathscr{E}_{2p}Y_{2p}\left(\hat{e}_{12} - \hat{e}_{14}\right)\right)\right\} \\ & + \hat{e}_{10}^H\hat{\mathscr{Q}}_1\hat{e}_{10} - (1-\sigma_d)\hat{e}_8^H\hat{\mathscr{Q}}_1\hat{e}_8 + \hat{e}_1^H\hat{\mathscr{Q}}_2\hat{e}_1 - (1-\sigma_d)\hat{e}_3^H\hat{\mathscr{Q}}_2\hat{e}_3 + \sigma^2\hat{e}_{10}^H\hat{\mathscr{Q}}_3\hat{e}_{10} - \Gamma_1^H\overline{\mathscr{Q}}_1\Gamma_1 + \sigma\Gamma_2^H\hat{\mathscr{R}}\Gamma_2 \\ & + \mathrm{sym}\left\{\hat{e}_1^H\hat{\mathscr{P}}_p\hat{e}_{10}\right\} + \Gamma_2^H\hat{\mathscr{R}}_p\Gamma_2 + \Gamma_3^H\hat{\mathscr{R}}_p\Gamma_3 + \hat{e}_1^H\sum_{q \in \aleph_k^p}\pi_{pq}\left(\hat{\mathscr{P}}_q - \widehat{\mathscr{W}}_p\right)\hat{e}_1 + \hat{e}_1^H L^H\hat{E}_1 L\hat{e}_1 - \hat{e}_4^H\hat{E}_1\hat{e}_4 \\ & + \hat{e}_3^H L^H\hat{E}_2 L\hat{e}_3 - \hat{e}_5^H\hat{E}_2\hat{e}_5 + \eta^2\hat{e}_{10}^H\left(\hat{\mathscr{Q}}_4 + \hat{\mathscr{Q}}_6\right)\hat{e}_{10} - \Gamma_4^H\overline{\mathscr{Q}}_2\Gamma_4 - \Gamma_5^H\overline{\mathscr{Q}}_3\Gamma_5 - \left(\hat{e}_1 - \hat{e}_{17}\right)^H\hat{\mathscr{Q}}_5\left(\hat{e}_1 - \hat{e}_{17}\right) \\ & - \Gamma_7^H\hat{\mathscr{V}}\Gamma_7 - \mathrm{sym}\left\{\left(\hat{e}_1 - \hat{e}_{17}\right)^H\hat{U}_{12}\hat{e}_{17}\right\} + \mathrm{sym}\left\{\begin{bmatrix} \hat{e}_1^H & \hat{e}_{10}^H & \hat{e}_{17}^H \end{bmatrix}\hat{V}\left(\hat{e}_1 - \hat{e}_{17}\right)\right\} \\ & - \gamma^2\hat{e}_{11}^H I\hat{e}_{11} - \hat{e}_{20}^H I\hat{e}_{20} - \hat{e}_{14}^H\hat{\mathscr{G}}\hat{e}_{14} + \omega\left(\hat{e}_{12} - \hat{e}_{14}\right)^H\hat{\mathscr{G}}\left(\hat{e}_{12} - \hat{e}_{14}\right) \\ \hat{\Xi}_1 = {} & \mathrm{sym}\left\{\left(\hat{e}_1 - \hat{e}_{17}\right)^H\hat{\mathscr{Q}}_5\hat{e}_{10}\right\} + \hat{e}_{10}\left[\mathrm{sym}\left(\hat{\mathscr{V}}_1\right)\hat{e}_1 + \mathrm{sym}\left(\hat{\mathscr{V}}_2 - \hat{\mathscr{V}}_1\right)\hat{e}_{17}\right] + \Gamma_8^H\hat{U}\Gamma_8, \end{aligned} \tag{61}$$

$$\begin{aligned} \xi_4^H(t) &= \left[\dot{\vartheta}^H(t), \vartheta^H(t - \eta(t))\right], \\ \xi_5^H(t) &= \Big[\vartheta^H(t), \vartheta^H(t-\sigma), \vartheta^H(t - \sigma(t)), \varphi^H(\vartheta(t)), \varphi^H(\vartheta(t - \sigma(t))), v_1^H, v_2^H, \dot{\vartheta}^H(t - \sigma(t)), \varphi^H(\vartheta(t-\sigma)), \dot{\vartheta}^H(t), \\ &\quad \omega^H(t), \vartheta^H(t - \eta^*(t)), \vartheta^H(t-\eta), e^H(t - \eta^*(t))v_3^H, v_4^H, \vartheta^H(t - \eta(t)), v_5^H, v_6^H\Big], \\ \xi_6^H(t) &= \left[\vartheta(t)^H, \dot{\vartheta}^H(t), \vartheta(t - \eta(t))^H\right], \\ \xi_7^H(t) &= \left[\vartheta^H(t), \vartheta^H(t - \eta(t))\right], \\ \hat{\Lambda} &= \left[-\hat{\mathscr{X}}\mathscr{A}_{2p}, 0, 0, \hat{\mathscr{X}}\mathscr{C}_{2p}, \hat{\mathscr{X}}\mathscr{D}_{2p}, 0, 0, 0, 0, 0, \hat{\mathscr{X}}\mathscr{H}_{1p}, 0, 0, 0, 0, 0, 0, 0, 0\right], \end{aligned} \tag{62}$$

$$\begin{aligned} \Gamma_4 &= \begin{bmatrix} \hat{e}_1 - \hat{e}_{17} \\ \hat{e}_1 + \hat{e}_{17} - 2\hat{e}_{15} \\ \hat{e}_{17} - \hat{e}_{13} \\ \hat{e}_{17} + \hat{e}_{13} - 2\hat{e}_{16} \end{bmatrix}, \\ \Gamma_5 &= \begin{bmatrix} \hat{e}_1 - \hat{e}_{12} \\ \hat{e}_1 + \hat{e}_{12} - 2\hat{e}_{18} \\ \hat{e}_{12} - \hat{e}_{13} \\ \hat{e}_{12} + \hat{e}_{13} - 2\hat{e}_{19} \end{bmatrix}, \\ \Gamma_6 &= \begin{bmatrix} \hat{e}_1 \\ \hat{e}_{10} \\ \hat{e}_{17} \end{bmatrix}, \\ \Gamma_7 &= \begin{bmatrix} \hat{e}_1 \\ \hat{e}_{17} \end{bmatrix}, \\ \Gamma_8 &= \begin{bmatrix} \hat{e}_{10} \\ \hat{e}_{17} \end{bmatrix}, \\ \hat{e}_p &= \begin{bmatrix} 0_{n\times(p-1)n} & I_n & 0_{n\times(19-p)n} \end{bmatrix}. \end{aligned} \tag{63}$$

System (8) possessing $H\infty$ performance is asymptotically stable under the SBET scheme (6), and the controller gain matrices in (7) are designed as $\widetilde{\mathscr{K}}_p = Y_{2p}\widehat{\mathscr{X}}^{-1}$.

Proof. Choose the following LKF:

$$\begin{aligned}
V(\vartheta(t),t,p) &= \sum_{m=1}^{5} V_m(\vartheta(t),t,p),\\
V_1(\vartheta(t),t,p) &= \vartheta^H(t)\mathscr{P}_p\vartheta(t) + \int_{t-\sigma}^{t}\xi_2^H(s)\mathscr{R}_p\xi_2(s)\mathrm{d}s + \int_{t-\sigma(t)}^{t}\dot{\vartheta}^H(s)\mathscr{Q}_1\dot{\vartheta}(s)\mathrm{d}s + \int_{t-\sigma(t)}^{t}\vartheta^H(s)\mathscr{Q}_2\vartheta(s)\mathrm{d}s\\
&\quad + \sigma\int_{\sigma}^{0}\int_{t-\theta}^{t}\dot{\vartheta}^H(s)\mathscr{Q}_3\dot{\vartheta}(s)\mathrm{d}s\mathrm{d}\theta + \int_{t-\sigma}^{t}\int_{\theta}^{0}\xi_2^H(s)\mathscr{R}\xi_2(s)\mathrm{d}s\mathrm{d}\theta\\
V_2(\vartheta(t),t,p) &= \eta\int_{\eta}^{0}\int_{t-\theta}^{t}\dot{\vartheta}^H(s)\mathscr{Q}_4\dot{\vartheta}(s)\mathrm{d}s\mathrm{d}\theta\\
V_3(\vartheta(t),t,p) &= \eta\int_{\eta}^{0}\int_{t-\theta}^{t}\dot{\vartheta}^H(s)\mathscr{Q}_6\dot{\vartheta}(s)\mathrm{d}s\mathrm{d}\theta,\\
V_4(\vartheta(t),t,p) &= (h_k-\eta(t))\int_{t-\eta(t)}^{t}\xi_4^H(s)U\xi_4(s)\mathrm{d}s,\\
V_5(\vartheta(t),t,p) &= (h_k-\eta(t))[\vartheta(t)-\vartheta(t-\eta(t))]^H\mathscr{Q}_5[\vartheta(t)-\vartheta(t-\eta(t))]\\
&\quad + (h_k-\eta(t))\xi_7^H(t)\mathscr{V}\xi_7(t),
\end{aligned} \tag{64}$$

with

$$\begin{aligned}
h_k &= h + \varsigma((\iota_k+j+1)h) - \varsigma((\iota_k+j)h),\\
\mathscr{P}_p &= \left(\widehat{\mathscr{X}}^H\right)^{-1}\widehat{\mathscr{P}}_p\widehat{\mathscr{X}}^{-1},\\
\mathscr{Q}_p &= \left(\widehat{\mathscr{X}}^H\right)^{-1}\widehat{\mathscr{Q}}_p\widehat{\mathscr{X}}^{-1},\\
\mathscr{Q}_4 &= \left(\widehat{\mathscr{X}}^H\right)^{-1}\widehat{\mathscr{Q}}_4\widehat{\mathscr{X}}^{-1},\\
\mathscr{Q}_5 &= \left(\widehat{\mathscr{X}}^H\right)^{-1}\widehat{\mathscr{Q}}_5\widehat{\mathscr{X}}^{-1},\\
\mathscr{R}_p &= \left(\widehat{\mathscr{X}}^H\right)^{-1}\widehat{\mathscr{R}}_p\widehat{\mathscr{X}}^{-1},\\
\mathscr{R} &= \left(\widehat{\mathscr{X}}^H\right)^{-1}\widehat{\mathscr{R}}\widehat{\mathscr{X}}^{-1},\\
p &\in \{1,2,3\},
\end{aligned} \tag{65}$$

being positive defined Hermitian matrices with proper dimension, and

$$\begin{aligned}
U &= \begin{bmatrix} U_{11} & U_{12}\\ * & U_{22}\end{bmatrix},\\
\mathscr{V} &= \begin{bmatrix} \mathrm{sym}\left(\dfrac{\mathscr{V}_1}{2}\right) & -\mathscr{V}_1+\mathscr{V}_2\\ * & \mathrm{sym}\left(\dfrac{\mathscr{V}_1}{2}-\mathscr{V}_2\right)\end{bmatrix}.
\end{aligned} \tag{66}$$

From the definition of $V(\vartheta(t),p)$, noting $V_{\mathscr{J}}(\vartheta(t),p)$, $\mathscr{J}=1,2,3$, is a continuous function; it is easy to see that

$$\lim_{t\longrightarrow((\iota_k+j)h+\varsigma((\iota_k+j)h))^-} V_{\mathscr{J}}(\vartheta(t),p) = V_{\mathscr{J}}(\vartheta((\iota_k+j)h+\varsigma((\iota_k+j)h)),p). \tag{67}$$

Also, we can derive that

$$\begin{aligned}
\lim_{t\longrightarrow((\iota_k+j)h+\varsigma((\iota_k+j)h))^-} V_4(\vartheta(t),p) &= \lim_{t\longrightarrow((\iota_k+j)h+\varsigma((\iota_k+j)h))^+} V_4(\vartheta(t),p) = V_4(\vartheta((\iota_k+j)h+\varsigma((\iota_k+j)h)),p) = 0,\\
\lim_{t\longrightarrow((\iota_k+j)h+\varsigma((\iota_k+j)h))^-} V_5(\vartheta(t),p) &= \lim_{t\longrightarrow((\iota_k+j)h+\varsigma((\iota_k+j)h))^+} V_5(\vartheta(t),p) = V_5(\vartheta((\iota_k+j)h+\varsigma((\iota_k+j)h)),p) = 0.
\end{aligned} \tag{68}$$

Therefore, $V(\vartheta(t), p)$ is continuous at $t = (\iota_k + j)h + \varsigma((\iota_k + j)h)$. Moreover, $V_{\mathcal{J}}(\vartheta(t), p) \geq 0$, that $V(\vartheta(t), p) = V_{\mathcal{J}}(\vartheta(t), p) + V_4(\vartheta(t), p) + V_5(\vartheta(t), p) \geq 0$ for any k. By pre- and postmultiplying $(\widehat{\mathcal{X}}^H)^{-1}$ and $\widehat{\mathcal{X}}^{-1}$ with (60), we have

$$\begin{aligned}
&\sum_{q \in \aleph_k^p} \pi_{pq}\left(\mathcal{R}_q - \mathcal{M}_p\right) \leq \mathcal{R},\\
&\mathcal{P}_q - \mathcal{W}_p \leq 0, q \in \aleph_{uk}^p, p \neq q, \mathcal{R}_q - \mathcal{M}_p \leq 0, q \in \aleph_{uk}^p, p \neq q,\\
&\mathcal{P}_q - \mathcal{W}_p \geq 0, q \in \aleph_{uk}^p, p = q, \mathcal{R}_q - \mathcal{M}_p \geq 0, q \in \aleph_{uk}^p, p = q,
\end{aligned} \tag{69}$$

and following the same procedure to Theorem 1, we have

$$\begin{aligned}
LV_1(\vartheta(t), p) \leq{}& \vartheta^H(t)\mathcal{P}_p\dot{\vartheta}(t) + \dot{\vartheta}^H(t)\mathcal{P}_p\vartheta(t) + \vartheta^H(t)\sum_{q\in\aleph_k^p}\pi_{pq}\left(\mathcal{P}_q - \mathcal{W}_p\right)\vartheta(t) + \xi_2^H(t)\mathcal{R}_p\xi_2(t)\\
&- \xi_2^H(t-\sigma)\mathcal{R}_p\xi_2(t-\sigma) + \dot{\vartheta}^H(t)\left(\mathcal{Q}_1 + \sigma^2\mathcal{Q}_3\right)\dot{\vartheta}(t) - (1-\sigma_d)\dot{\vartheta}^H(t-\sigma(t))\mathcal{Q}_1\dot{\vartheta}(t-\sigma(t)) + \vartheta^H(t)\mathcal{Q}_2\vartheta(t)\\
&- (1-\sigma_d)\vartheta^H(t-\sigma(t))\mathcal{Q}_2\vartheta(t-\sigma(t)) - \xi_5^H(t)\Gamma_1^H\overline{\mathcal{Q}}_1\Gamma_1\xi_5(t) + \sigma\xi_2^H(t)\mathcal{R}\xi_2(t) + \vartheta^H(t)LE_1L\vartheta(t)\\
&- \varphi^H(\vartheta(t))E_1\varphi(\vartheta(t)) + \vartheta^H(t-\sigma(t))LE_2L\vartheta(t-\sigma(t)) - \varphi^H(\vartheta(t-\sigma(t)))E_2\varphi(\vartheta(t-\sigma(t))).
\end{aligned} \tag{70}$$

The following inequalities can be obtained because of Lemma 3 with arbitrary matrices $\mathcal{S}_{33}, \mathcal{S}_{44}, \mathcal{S}_{34}, \mathcal{S}_{55}, \mathcal{S}_{66}, \mathcal{S}_{56} \in \mathcal{C}^{n\times n}$:

$$\begin{aligned}
LV_2(\vartheta(t), p) ={}& \eta^2\dot{\vartheta}^H(t)\mathcal{Q}_4\dot{\vartheta}(t) - \eta\int_{t-\eta}^{t}\dot{\vartheta}^H(s)\mathcal{Q}_4\dot{\vartheta}(s)\mathrm{d}s = \eta^2\dot{\vartheta}^H(t)\mathcal{Q}_4\dot{\vartheta}(t) - \eta\int_{t-\eta(t)}^{t}\dot{\vartheta}^H(s)\mathcal{Q}_4\dot{\vartheta}(s)\mathrm{d}s\\
&- \eta\int_{t-\eta}^{t-\eta(t)}\dot{\vartheta}^H(s)\mathcal{Q}_4\dot{\vartheta}(s)\mathrm{d}s \leq \eta^2\dot{\vartheta}^H(t)\mathcal{Q}_4\dot{\vartheta}(t) - \xi_5^H(t)\Gamma_4^H\mathcal{Q}_2\Gamma_4\xi_5(t),\\
LV_3(\vartheta(t), p) ={}& \eta^2\dot{\vartheta}^H(t)\mathcal{Q}_6\dot{\vartheta}(t) - \eta\int_{t-\eta}^{t}\dot{\vartheta}^H(s)\mathcal{Q}_6\dot{\vartheta}(s)\mathrm{d}s = \eta^2\dot{\vartheta}^H(t)\mathcal{Q}_6\dot{\vartheta}(t) - \eta\int_{t-\eta^*(t)}^{t}\dot{\vartheta}^H(s)\mathcal{Q}_6\dot{\vartheta}(s)\mathrm{d}s\\
&- \eta\int_{t-\eta}^{t-\eta^*(t)}\dot{\vartheta}^H(s)\mathcal{Q}_6\dot{\vartheta}(s)\mathrm{d}s \leq \eta^2\dot{\vartheta}^H(t)\mathcal{Q}_6\dot{\vartheta}(t) - \xi_5^H(t)\Gamma_5^H\mathcal{Q}_3\Gamma_5\xi_5(t),\\
LV_4(\vartheta(t), p) ={}& (h_k - \eta(t))\xi_4^HU\xi_4 - \int_{t-\eta(t)}^{t}\xi_4^HU\xi_4\mathrm{d}s = (h_k - \eta(t))\xi_4^HU\xi_4 - \int_{t-\eta(t)}^{t}\dot{\vartheta}^H(s)U_{11}\dot{\vartheta}(s)\mathrm{d}s\\
&- \int_{t-\eta(t)}^{t}\dot{\vartheta}^H(s)\mathrm{d}sU_{12}\vartheta(t-\eta(t)) - \vartheta^H(t-\eta(t))U_{12}\int_{t-\eta(t)}^{t}\dot{\vartheta}(s)\mathrm{d}s - \eta(t)\vartheta^H(t-\eta(t))U_{22}\vartheta(t-\eta(t)).
\end{aligned} \tag{71}$$

From the corollary of Lemma 4, the following formula is established with V of appropriate dimensions:

$$-\int_{t-\eta(t)}^{t}\dot{\vartheta}^H(s)U_{11}\dot{\vartheta}(s)\mathrm{d}s \leq \eta(t)\xi_6^H(t)V^HU_{11}^{-1}V\xi_6(t) + \xi_6^H(t)V^H\int_{t-\eta(t)}^{t}\dot{\vartheta}(s)\mathrm{d}s + \int_{t-\eta(t)}^{t}\dot{\vartheta}(s)\mathrm{d}sV\xi_6(t). \tag{72}$$

Then, we have

$$\begin{aligned} LV_4(\vartheta(t),p) &= (h_k-\eta(t))\xi_4^H U\xi_4 - \int_{t-\eta(t)}^{t} \xi_4^H U\xi_4 \mathrm{d}s \le (h_k-\eta(t))\xi_4^H U\xi_4 + \eta(t)\xi_6^H(t)V^H U_{11}^{-1}V\xi_6(t) \\ &+ \xi_6^H(t)V^H \int_{t-\eta(t)}^{t} \dot{\vartheta}(s)\mathrm{d}s + \int_{t-\eta(t)}^{t} \dot{\vartheta}(s)\mathrm{d}sV\xi_6(t) - \eta(t)\vartheta^H(t-\eta(t))U_{22}\vartheta(t-\eta(t)) \\ &- \int_{t-\eta(t)}^{t} \dot{\vartheta}^H(s)\mathrm{d}sU_{12}\vartheta(t-\eta(t)) - \vartheta^H(t-\eta(t))U_{12}\int_{t-\eta(t)}^{t} \dot{\vartheta}(s)\mathrm{d}s. \end{aligned} \tag{73}$$

Noticing that $\eta(t) = t - (\iota_k + j)h - \varsigma((\iota_k + j)h)$, the following inequality is obtained:

$$\begin{aligned} LV_5(\vartheta(t),p) \le & -[\vartheta(t)-\vartheta(t-\eta(t))]^H \mathcal{Q}_5[\vartheta(t)-\vartheta(t-\eta(t))] - \xi_7^H(s)\mathcal{V}\xi_7(s) \\ & + (h_k-\eta(t))[\vartheta(t)-\vartheta(t-\eta(t))]^H \mathcal{Q}_5\dot{\vartheta}(t) + (h_k-\eta(t))\dot{\vartheta}^H(t)\mathcal{Q}_5[\vartheta(t)-\vartheta(t-\eta(t))] \\ & + (h_k-\eta(t))\left[\dot{\vartheta}^H(t)\left(\mathcal{V}_1+\mathcal{V}_1^H\right)\vartheta(t) + (h_k-\eta(t))\dot{\vartheta}^H(t)(\mathcal{V}_2-\mathcal{V}_1)\vartheta(t-\eta(t))\right] \\ & + (h_k-\eta(t))\vartheta^H(t-\eta(t))(\mathcal{V}_2-\mathcal{V}_1)\dot{\vartheta}(t). \end{aligned} \tag{74}$$

From the event-triggered mechanism (6), when $t \in \mathcal{T}_k$, it is clear that

$$e^H(\iota_k h + lh)\mathcal{G}e(\iota_k h + lh) < \varpi[\vartheta(\iota_k h + lh) - e(\iota_k h + lh)]^H \mathcal{G}[\vartheta(\iota_k h + lh) - e(\iota_k h + lh)]. \tag{75}$$

It means that the data of the current sampling moment is not transmitted. Moreover, one can obtain the following zero equality based on system (8) with any nonsingular matrix $\mathcal{X}_4$ with appropriate dimension, defining $\mathcal{X}_3 = \rho\mathcal{X}_4$, that $\mathcal{X}_4$ is nonsingular:

$$\begin{aligned} 0 = & \left(\vartheta^H(t)\mathcal{X}_3^H + \dot{\vartheta}^H(t)\mathcal{X}_4^H\right)\left(-\dot{\vartheta}(t) - \mathcal{A}_{1p}\vartheta(t) + \mathcal{B}_{1p}\dot{\vartheta}(t-\sigma(t)) + \mathcal{C}_{1p}\varphi(\vartheta(t)) + \mathcal{D}_{1p}\varphi(\vartheta(t-\sigma(t))) + \mathrm{E}_{1p}\omega(t)\right. \\ & \left. + \mathcal{E}_{2p}\tilde{\mathcal{K}}_p\vartheta(t-\eta*(t)) - \mathcal{E}_{2p}\tilde{\mathcal{K}}_p e(t-\eta*(t))\right) + \left(-\dot{\vartheta}(t) - \mathcal{A}_{1p}\vartheta(t) + \mathcal{B}_{1p}\dot{\vartheta}(t-\sigma(t)) + \mathcal{C}_{1p}\varphi(\vartheta(t))\right. \\ & \left. + \mathcal{D}_{1p}\varphi(\vartheta(t-\sigma(t))) + \mathcal{E}_{1p}\omega(t) + \mathcal{E}_{2p}\tilde{\mathcal{K}}_p\vartheta(t-\eta^*(t)) - \mathcal{E}_{2p}\tilde{\mathcal{K}}_p e(t-\eta^*(t))\right)^H\left(\mathcal{X}_3\vartheta(t) + \mathcal{X}_4\dot{\vartheta}(t)\right). \end{aligned} \tag{76}$$

Combining with (69)–(76), we have the following equation:

$$\begin{aligned} LV(\vartheta(t),p) + v^H(t)v(t) - \gamma^2\omega^H(t)\omega(t) \le & LV(\vartheta(t),p) + v^H(t)v(t) - \gamma^2\omega^H(t)\omega(t) - e^H(t_k h + lh)\mathcal{G}e(t_k h + lh) \\ & + \varpi[\vartheta(\iota_k h + lh) - e(\iota_k h + lh)]^H\mathcal{G}[\vartheta(\iota_k h + lh) - e(\iota_k h + lh)] + \mathrm{sym}\left\{\left(\vartheta^H(t)\mathcal{X}_3^H + \dot{\vartheta}^H(t)\mathcal{X}_4^H\right)\left(-\dot{\vartheta}(t) - \mathcal{A}_{1p}\vartheta(t)\right.\right. \\ & \left.\left. + \mathcal{B}_{1p}\dot{\vartheta}(t-\sigma(t)) + \mathcal{C}_{1p}\varphi(\vartheta(t)) + \mathcal{D}_{1p}\varphi(\vartheta(t-\sigma(t))) + \mathcal{E}_{1p}\omega(t) + \mathcal{E}_{2p}\tilde{\mathcal{K}}_p\vartheta(t-\eta(t)) - \mathcal{E}_{2p}\tilde{\mathcal{K}}_p e(t-\eta(t))\right)\right\}. \end{aligned} \tag{77}$$

By dividing the right-hand side of the above inequality into three parts, we have

$$\begin{aligned} &LV(\vartheta(t),p)+v^H(t)v(t)-\gamma^2\omega^H(t)\omega(t)\le\xi_5^H(t)\big(\tilde{\Xi}+(h_k-\eta(t))\tilde{\Xi}_1+\eta(t)\tilde{\Xi}_2+\varrho^H\varrho\big)\xi_5(t)\\ &=\xi_5^H(t)\left[\frac{h_k-\eta(t)}{h_k}\Omega_2(h_k)+\frac{\eta(t)}{h_k}\Omega_3(h_k)\right]\xi_5(t), \end{aligned} \tag{78}$$

with

$$\begin{aligned} \Omega_2(h_k)&=\tilde{\Xi}+h_k\tilde{\Xi}_1+\varrho^H\varrho,\\ \Omega_3(h_k)&=\tilde{\Xi}+h_k\tilde{\Xi}_2+\varrho^H\varrho,\\ \tilde{\Xi}&=\mathrm{sym}\big\{\big(\hat{e}_1^H\mathcal{X}_3^H+\hat{e}_{10}^H\mathcal{X}_4^H\big)\big(-\hat{e}_{10}-\mathcal{A}_{1p}\hat{e}_1+\mathcal{B}_{1p}\hat{e}_8+\mathcal{C}_{1p}\hat{e}_4+\mathcal{D}_{1p}\hat{e}_5+\mathcal{E}_{1p}\hat{e}_9+\mathcal{E}_{2p}\tilde{\mathcal{K}}_p(\hat{e}_{12}-\hat{e}_{14})\big)\big\}\\ &\quad+\mathrm{sym}\big\{\hat{e}_1^H\mathcal{P}_p\hat{e}_{10}\big\}+\hat{e}_1^H\sum_{q\in\aleph_k^p}\pi_{pq}\big(\mathcal{P}_q-\mathcal{W}_p\big)\hat{e}_1+\Gamma_2^H\mathcal{R}_p\Gamma_2+\Gamma_3^H\mathcal{R}_p\Gamma_3+\hat{e}_{10}^H\mathcal{Q}_1\hat{e}_{10}-(1-\sigma_d)\hat{e}_8^H\mathcal{Q}_1\hat{e}_8\\ &\quad+\hat{e}_1^H\mathcal{Q}_2\hat{e}_1-(1-\sigma_d)\hat{e}_3^H\mathcal{Q}_2\hat{e}_3+\sigma^2\hat{e}_{10}^H\mathcal{Q}_3\hat{e}_{10}-\Gamma_1^H\mathcal{Q}_1\Gamma_1+\sigma\Gamma_2^H\mathcal{R}\Gamma_2+\hat{e}_1^HL^HE_1L\hat{e}_1-\hat{e}_4^HE_1\hat{e}_4\\ &\quad+\hat{e}_3^HL^HE_2L\hat{e}_3-\hat{e}_5^HE_2\hat{e}_5+\eta^2\hat{e}_{10}^H(\mathcal{Q}_4+\mathcal{Q}_6)\hat{e}_{10}-\Gamma_4^H\mathcal{Q}_2\Gamma_4-\Gamma_5^H\mathcal{Q}_3\Gamma_5-(\hat{e}_1-\hat{e}_{17})^H\mathcal{Q}_5(\hat{e}_1-\hat{e}_{17})\\ &\quad-\Gamma_7^H\mathcal{V}\Gamma_7-\mathrm{sym}\big\{(\hat{e}_1-\hat{e}_{17})^HU_{12}\hat{e}_{17}\big\}+\mathrm{sym}\big\{\big[\hat{e}_1^H\ \ \hat{e}_{10}^H\ \ \hat{e}_{17}^H\big]V(\hat{e}_1-\hat{e}_{17})\big\}-\gamma^2\hat{e}_{11}^HI\hat{e}_{11}\\ &\quad-\hat{e}_{14}^H\mathcal{G}\hat{e}_{14}+\varpi(\hat{e}_{12}-\hat{e}_{14})^H\mathcal{G}(\hat{e}_{12}-\hat{e}_{14}),\\ \tilde{\Xi}_1&=\mathrm{sym}\big\{(\hat{e}_1-\hat{e}_{17})^H\mathcal{Q}_5\hat{e}_{10}\big\}+\hat{e}_{10}\big[\mathrm{sym}(\mathcal{V}_1)\hat{e}_1+\mathrm{sym}(\mathcal{V}_2-\mathcal{V}_1)\hat{e}_{17}\big]+\Gamma_8^HU\Gamma_8,\\ \tilde{\Xi}_2&=-\hat{e}_{17}^HU_{22}\hat{e}_{17}+\Gamma_6^HVU_{11}^{-1}V^H\Gamma_6,\\ \varrho&=-\mathcal{A}_{2p}\hat{e}_1+\mathcal{C}_{2p}\hat{e}_4+\mathcal{D}_{2p}\hat{e}_5+\mathcal{H}_{1p}\hat{e}_{11}. \end{aligned} \tag{79}$$

Define

$$\begin{aligned} &\hat{\mathcal{X}}=\mathcal{X}_4^{-1},Y_{2p}=\tilde{\mathcal{K}}_p\hat{\mathcal{X}},\tilde{V}=\hat{\mathcal{X}}^HV^H,\hat{\mathfrak{X}}_\hbar=\mathrm{diag}\Big\{\underbrace{\hat{\mathcal{X}},\hat{\mathcal{X}},\ldots,\hat{\mathcal{X}}}_{\hbar}\Big\},\hat{\mathcal{P}}_p=\hat{\mathcal{X}}^H\mathcal{P}_p\hat{\mathcal{X}},\hat{\mathcal{W}}_p=\hat{\mathcal{X}}^H\mathcal{W}_p\hat{\mathcal{X}},\\ &\hat{\mathcal{M}}_p=\hat{\mathcal{X}}^H\mathcal{M}_p\hat{\mathcal{X}},\hat{\mathcal{P}}_q=\hat{\mathcal{X}}^H\mathcal{P}_q\hat{\mathcal{X}},\hat{\mathcal{R}}_q=\hat{\mathcal{X}}^H\mathcal{R}_q\hat{\mathcal{X}},\hat{\mathcal{R}}_p=\hat{\mathcal{X}}^H\mathcal{R}_p\hat{\mathcal{X}},\hat{\mathcal{Q}}_p=\hat{\mathcal{X}}^H\mathcal{Q}_p\hat{\mathcal{X}},\hat{\mathcal{Q}}_4=\hat{\mathcal{X}}^H\mathcal{Q}_4\hat{\mathcal{X}},\\ &\hat{\mathcal{Q}}_5=\hat{\mathcal{X}}^H\mathcal{Q}_5\hat{\mathcal{X}},\hat{\mathcal{Q}}_6=\hat{\mathcal{X}}^H\mathcal{Q}_6\hat{\mathcal{X}},\hat{\mathcal{R}}_p=\hat{\mathcal{X}}^H\mathcal{R}_p\hat{\mathcal{X}},\hat{\mathcal{E}}_1=\hat{\mathcal{X}}^H\mathcal{E}_1\hat{\mathcal{X}},\hat{\mathcal{E}}_2=\hat{\mathcal{X}}^H\mathcal{E}_2\hat{\mathcal{X}},\hat{\mathcal{S}}_{11}=\hat{\mathcal{X}}^H\mathcal{S}_{11}\hat{\mathcal{X}},\hat{\mathcal{S}}_{12}=\hat{\mathcal{X}}^H\mathcal{S}_{12}\hat{\mathcal{X}},\\ &\hat{\mathcal{S}}_{22}=\hat{\mathcal{X}}^H\mathcal{S}_{22}\hat{\mathcal{X}},\hat{\mathcal{S}}_{33}=\hat{\mathcal{X}}^H\mathcal{S}_{33}\hat{\mathcal{X}},\hat{\mathcal{S}}_{34}=\hat{\mathcal{X}}^H\mathcal{S}_{34}\hat{\mathcal{X}},\hat{\mathcal{S}}_{44}=\hat{\mathcal{X}}^H\mathcal{S}_{44}\hat{\mathcal{X}},\hat{\mathcal{S}}_{55}=\hat{\mathcal{X}}^H\mathcal{S}_{55}\hat{\mathcal{X}},\\ &\hat{\mathcal{S}}_{56}=\hat{\mathcal{X}}^H\mathcal{S}_{56}\hat{\mathcal{X}},\hat{\mathcal{S}}_{66}=\hat{\mathcal{X}}^H\mathcal{S}_{66}\hat{\mathcal{X}},\hat{U}_{11}=\hat{\mathcal{X}}^HU_{11}\hat{\mathcal{X}},\hat{U}_{12}=\hat{\mathcal{X}}^HU_{12}\hat{\mathcal{X}},\hat{U}_{22}=\hat{\mathcal{X}}^HU_{22}\hat{\mathcal{X}},\hat{I}=\hat{\mathcal{X}}^HI\hat{\mathcal{X}},\\ &\hat{\mathcal{G}}=\hat{\mathcal{X}}^H\hat{\mathrm{GX}},\hat{\mathcal{V}}=\hat{\mathcal{X}}^H\hat{\mathcal{X}},\hat{\mathcal{V}}_1=\hat{\mathcal{X}}^H\mathcal{V}_1\hat{\mathcal{X}},\hat{\mathcal{V}}_2=\hat{\mathcal{X}}^H\mathcal{V}_2\hat{\mathcal{X}},\hat{U}=\hat{\mathcal{X}}^HU\hat{\mathcal{X}},\hat{V}=\hat{\mathcal{X}}^HV\hat{\mathcal{X}}, \end{aligned} \tag{80}$$

and then, by pre- and postmultiplying $\hat{\mathfrak{X}}_\hbar^H$ and $\hat{\mathfrak{X}}_\hbar$ $(\hbar=19)$ with $\Omega_2(h_k)$ and $\Omega_3(h_k)$, combining (57)–(61) and (78), then applying Schur complement, we have $\tilde{\Xi}+h_k\tilde{\Xi}_1+\varrho^H\varrho<0$, $\tilde{\Xi}+h_k\tilde{\Xi}_2+\varrho^H\varrho<0$, that $LV(\vartheta(t),p)+v^H(t)v(t)-\gamma^2\omega^H(t)\omega(t)<0$ for $t\in\mathcal{T}_k$. Therefore, if the LMIs in Theorem 2 hold, according to the similar proof line as Theorem 1, the CVNNs (8) with Markovian jump are asymptotically stable and possess $H\infty$ performance based on a SBET controller; this completes the proof. □

Remark 4. As far as we know, a discrete sampling-based event-triggered controller which is designed for the neutral-type CVNNs with partly unknown Markov jump in this work has not received much attention, which reduces the data transmission rate greatly for it only needs to monitor the state of our system at the discrete moment. Also, the partial unknown Markov phenomenon is taken into account which makes the results more general and practical.

Remark 5. The segmented sawtooth structure caused by sampling hold is fully considered by $V_4(\vartheta(t), p)$ and $V_5(\vartheta(t), p)$ that the conservatism of our results would be reduced. Furthermore, we analyze the CVNNs under the sampling-based event-driven framework while not dividing it into the real part and the imaginary part; it is able to reduce computational complexity greatly while the desired effect is achieved.

Remark 6. $V_2(\vartheta(t), p)$ and $V_3(\vartheta(t), p)$ in Theorem 2 have a very similar presentation, but in fact, they are different, and different interval segmentations are adopted for the processing of the two LKFs, which can also be merged together as $V_6(\vartheta(t), t, p) = \eta \int_{\eta}^{0} \int_{t-\theta}^{t} \dot{\vartheta}^H(s) \mathcal{Q}_7 \dot{\vartheta}(s) \mathrm{d}s \mathrm{d}\theta$:

$$\begin{aligned} LV_6(\vartheta(t), t, p) &= \eta^2 \dot{\vartheta}^H(t) \mathcal{Q}_7 \dot{\vartheta}(t) - \eta \int_{t-\eta}^{t} \dot{\vartheta}^H(s) \mathcal{Q}_7 \dot{\vartheta}(s) \mathrm{d}s \\ &= \eta^2 \dot{\vartheta}^H(t) \mathcal{Q}_7 \dot{\vartheta}(t) - \eta \int_{t-\eta(t)}^{t} \dot{\vartheta}^H(s) \mathcal{Q}_7 \dot{\vartheta}(s) \mathrm{d}s \\ &\quad - \eta \int_{t-\eta^*(t)}^{t-\eta(t)} \dot{\vartheta}^H(s) \mathcal{Q}_7 \dot{\vartheta}(s) \mathrm{d}s - \eta \int_{t-\eta}^{t-\eta^*(t)} \dot{\vartheta}^H(s) \mathcal{Q}_7 \dot{\vartheta}(s) \mathrm{d}s. \end{aligned} \tag{81}$$

According to Lemma 1,

$$\begin{aligned} LV_6(\vartheta(t), t, p) &\le \eta^2 \dot{\vartheta}^H(t) \mathcal{Q}_7 \dot{\vartheta}(t) - \frac{\eta}{\eta(t)} \alpha_1^H \mathcal{Q}_7 \alpha_1 \\ &\quad - \frac{\eta}{\eta^*(t) - \eta(t)} \alpha_2^H \mathcal{Q}_7 \alpha_2 - \frac{\eta}{\eta - \eta^*(t)} \alpha_3^H \mathcal{Q}_7 \alpha_3 \\ &\le \eta^2 \dot{\vartheta}^H(t) \mathcal{Q}_7 \dot{\vartheta}(t) - \begin{bmatrix} \alpha_1 \\ \alpha_2 \\ \alpha_3 \end{bmatrix}^H \begin{bmatrix} \mathcal{Q}_7 & S_1 & S_2 \\ * & \mathcal{Q}_7 & S_3 \\ * & * & \mathcal{Q}_7 \end{bmatrix} \begin{bmatrix} \alpha_1 \\ \alpha_2 \\ \alpha_3 \end{bmatrix}, \end{aligned} \tag{82}$$

with

$$\begin{aligned} \alpha_1 &= \vartheta(t) - \vartheta(t - \eta(t)), \\ \alpha_2 &= \vartheta(t - \eta(t)) - \vartheta(t - \eta^*(t)), \\ \alpha_3 &= \vartheta(t - \eta^*(t)) - \vartheta(t), \\ S_1, S_2, S_3 &\in \mathcal{C}^{n \times n}. \end{aligned} \tag{83}$$

However, the vectors that are contained in $LV_6(\vartheta(t), t, p)$ are not as comprehensive as those in $LV_2(\vartheta(t), t, p)$ and $LV_3(\vartheta(t), t, p)$.

4. Numerical Examples

Through numerical simulations, two examples are given to demonstrate the superiority and effectiveness of our conclusions derived from previous chapters.

Example 1. Consider the CVNNs (5) with the following parameters:

$$\begin{aligned}
\mathscr{A}_{11} &= \begin{pmatrix} 0.8 & 0 \\ 0 & 0.7 \end{pmatrix}, \\
\mathscr{A}_{12} &= \begin{pmatrix} 0.6 & 0 \\ 0 & 0.5 \end{pmatrix}, \\
\mathscr{A}_{13} &= \begin{pmatrix} 0.5 & 0 \\ 0 & 0.4 \end{pmatrix}, \\
\mathscr{A}_{21} &= \begin{pmatrix} 0.6 & 0 \\ 0 & 0.5 \end{pmatrix}, \\
\mathscr{A}_{22} &= \begin{pmatrix} 0.7 & 0 \\ 0 & 0.6 \end{pmatrix}, \\
\mathscr{A}_{23} &= \begin{pmatrix} 0.7 & 0 \\ 0 & 0.6 \end{pmatrix}, \\
\mathscr{B}_{11} &= \begin{pmatrix} -0.03 + 0.08i & -0.05 + 0.02i \\ -0.03 - 0.02i & 0.08 + 0.02i \end{pmatrix}, \\
\mathscr{B}_{12} &= \begin{pmatrix} -0.04 - 0.02i & -0.04 + 0.02i \\ -0.04 - 0.03i & 0.06 + 0.04i \end{pmatrix}, \\
\mathscr{B}_{13} &= \begin{pmatrix} -0.05 + 0.07i & -0.02 + 0.05i \\ -0.05 - 0.08i & -0.05 + 0.02i \end{pmatrix}, \\
\mathscr{C}_{11} &= \begin{pmatrix} 0.5 - 0.4i & -0.3 + 0.3i \\ 0.4 + 0.3i & -0.7 - 0.9i \end{pmatrix}, \\
\mathscr{C}_{12} &= \begin{pmatrix} 0.6 - 0.5i & -0.4 + 0.4i \\ 0.5 + 0.4i & -0.8 - 0.8i \end{pmatrix}, \\
\mathscr{C}_{13} &= \begin{pmatrix} 0.7 - 0.6i & -0.5 + 0.5i \\ 0.6 + 0.5i & -0.9 - 0.7i \end{pmatrix}, \\
\mathscr{D}_{11} &= \begin{pmatrix} 0.4 - 0.4i & 0.2 - 0.2i \\ -0.4 + 0.3i & 0.3 + 0.2i \end{pmatrix}, \\
\mathscr{D}_{12} &= \begin{pmatrix} 0.5 - 0.5i & -0.4 - 0.5i \\ -0.5 + 0.4i & 0.4 + 0.3i \end{pmatrix}, \\
\mathscr{D}_{13} &= \begin{pmatrix} -0.5 - 0.6i & 0.4 - 0.4i \\ -0.6 + 0.5i & 0.5 + 0.4i \end{pmatrix}, \\
\mathscr{E}_{11} &= \begin{pmatrix} -0.4 - 0.6i & 0.3 - 0.5i \\ -0.6 + 0.5i & 0.5 - 0.6i \end{pmatrix}, \\
\mathscr{E}_{12} &= \begin{pmatrix} -0.3 - 0.6i & 0.6 - 0.3i \\ -0.7 + 0.5i & 0.3 - 0.5i \end{pmatrix}, \\
\mathscr{E}_{13} &= \begin{pmatrix} -0.5 - 0.4i & 0.5 - 0.5i \\ -0.4 + 0.5i & 0.4 - 0.5i \end{pmatrix}, \\
\mathscr{E}_{21} &= \begin{pmatrix} -0.5 - 0.6i & 0.4 - 0.2i \\ -0.6 + 0.5i & 0.5 - 0.7i \end{pmatrix}, \\
\mathscr{E}_{22} &= \begin{pmatrix} 0.7 - 0.8i & -0.4 - 0.3i \\ -0.6 + 0.5i & 0.1 - 0.4i \end{pmatrix}, \\
\mathscr{E}_{23} &= \begin{pmatrix} -0.2 - 0.5i & 0.4 - 0.1i \\ -0.5 + 0.5i & 0.6 + 0.2i \end{pmatrix}, \\
\mathscr{C}_{21} &= \begin{pmatrix} 1.2 - 1.5i & -1.6 + 0.3i \\ 1.5 + 0.4i & 1.6 - 0.4i \end{pmatrix}, \\
\mathscr{C}_{22} &= \begin{pmatrix} 1.3 - 0.4i & -1.4 + 0.6i \\ 1.8 + 0.5i & 1.3 - 0.7i \end{pmatrix}, \\
\mathscr{C}_{23} &= \begin{pmatrix} 1.4 - 1.3i & -1.3 + 0.2i \\ 1.4 + 0.6i & 1.4 - 0.6i \end{pmatrix}, \\
\mathscr{D}_{21} &= \begin{pmatrix} 0.5 - 0.4i & -0.3 + 0.3i \\ -0.4 - 0.3i & 0.3 - 0.3i \end{pmatrix}, \\
\mathscr{D}_{22} &= \begin{pmatrix} 0.6 - 0.5i & -0.4 + 0.4i \\ -0.5 - 0.4i & 0.4 - 0.4i \end{pmatrix}, \\
\mathscr{D}_{23} &= \begin{pmatrix} 0.7 - 0.6i & -0.5 + 0.5i \\ -0.6 - 0.5i & 0.5 - 0.5i \end{pmatrix}, \\
\mathscr{H}_{11} &= \begin{pmatrix} -0.4 - 0.6i & 0.4 - 0.4i \\ -0.6 + 0.5i & 0.8 - 0.9i \end{pmatrix}, \\
\mathscr{H}_{12} &= \begin{pmatrix} 0.5 - 0.2i & 0.3 + 0.4i \\ -0.4 + 0.5i & 0.3 - 0.4i \end{pmatrix}, \\
\mathscr{H}_{13} &= \begin{pmatrix} -0.5 - 0.6i & 0.4 - 0.2i \\ -0.1 + 0.5i & 0.3 - 0.2i \end{pmatrix}.
\end{aligned} \tag{84}$$

Π represents the partly unknown transition rate matrix, which is considered as

$$\Pi = \begin{bmatrix} -6 & ? & ? \\ 5 & ? & ? \\ ? & ? & -4 \end{bmatrix}. \tag{85}$$

In the following, a $H\infty$ controller will be designed based on Theorem 1, where the activation function is set as $\varphi(\vartheta(t)) = \tanh(\vartheta(t)) + i\tanh(\vartheta(t))$, $\sigma = 0.4, \sigma_d = 0.1$, $L = [1\ \ 0\,;\ 0\ \ 1]$, and $\sigma(t) = t - (0.3 + 0.1 * \sin(t))$ expresses the time-varying delay. If the initial value is set as $\psi(t) = [-0.3 + 0.5i; 0.5 - 0.3i]$, the solution could be obtained by the LMI toolbox, and $\gamma = 7.6623$ is obtained, the corresponding controller gain matrices are computed as

$$\begin{aligned}
\mathscr{K}_1 &= \begin{pmatrix} 9.4442 - 38.5585i & -10.3759 + 26.9077i \\ 21.1045 - 23.0361i & -31.4861 - 1.6866i \end{pmatrix}, \\
\mathscr{K}_2 &= \begin{pmatrix} -7.6922 - 13.4025i & 16.2192 + 6.3072i \\ 4.0202 - 11.3110i & 5.6539 - 22.0753i \end{pmatrix}, \\
\mathscr{K}_3 &= \begin{pmatrix} -4.3350 - 31.0012i & 4.9612 + 25.3198i \\ -10.1567 - 23.3295i & -13.8700 + 12.1124i \end{pmatrix},
\end{aligned} \tag{86}$$

and then system (5) is stochastically stable under the controllers $u(t) = \mathscr{K}_p\vartheta(t)$, $p \in \{1, 2, 3\}$, and the states are shown as in Figures 1 and 2 .

Figures 3 and 4 depict the imaginary part and real part of the states of $u(t)$, respectively, Figures 1 and 2 depict the states of the imaginary and the real part, respectively, via

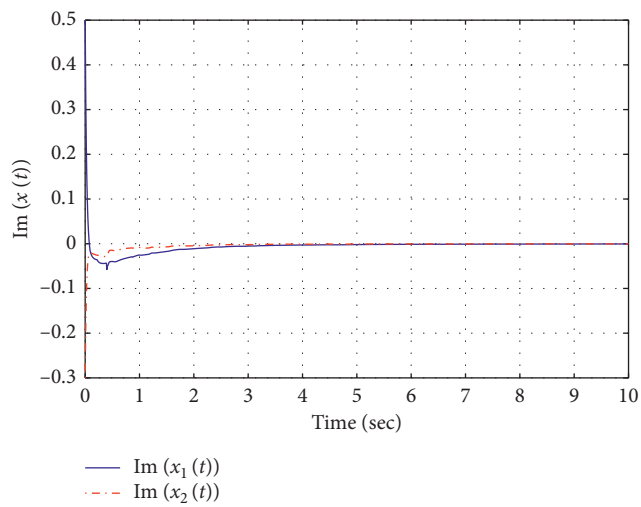

Figure 1: Responses the state of the imaginary part.

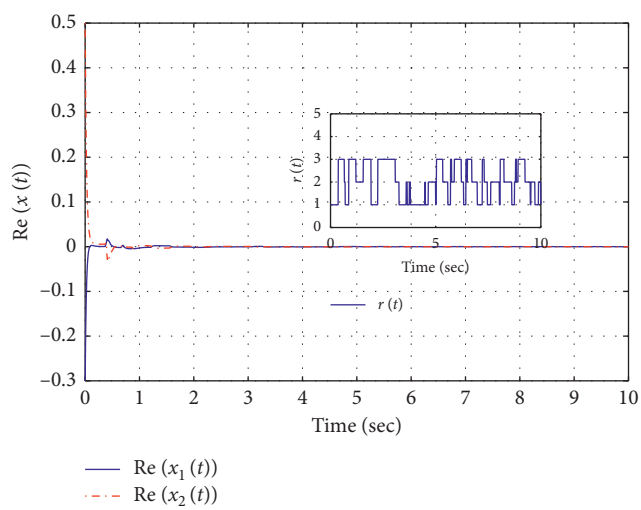

Figure 2: Responses the state of the real part.

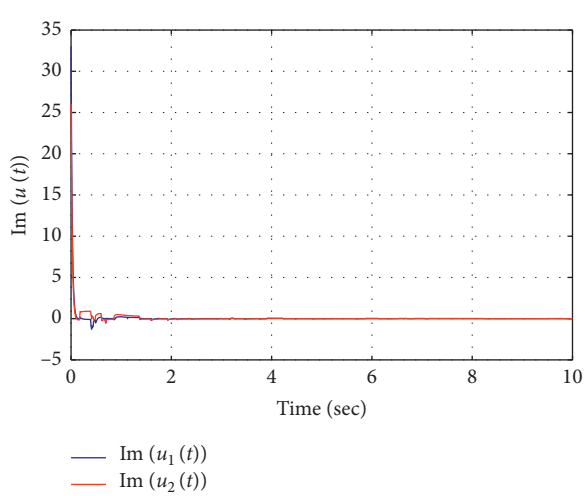

Figure 3: Responses input $u(t)$ of the imaginary part.

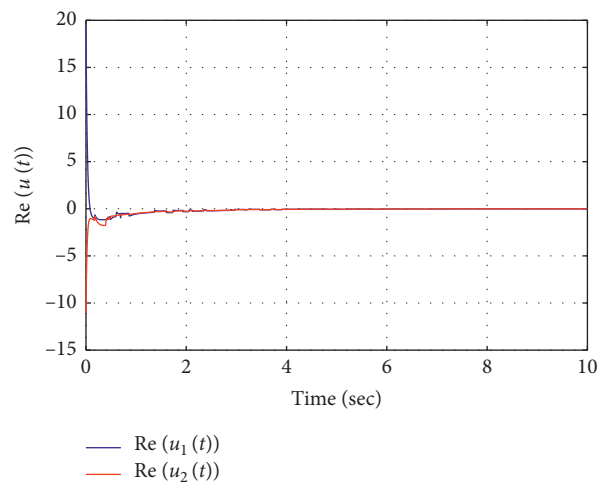

Figure 4: Responses control input $u(t)$ of the real part.

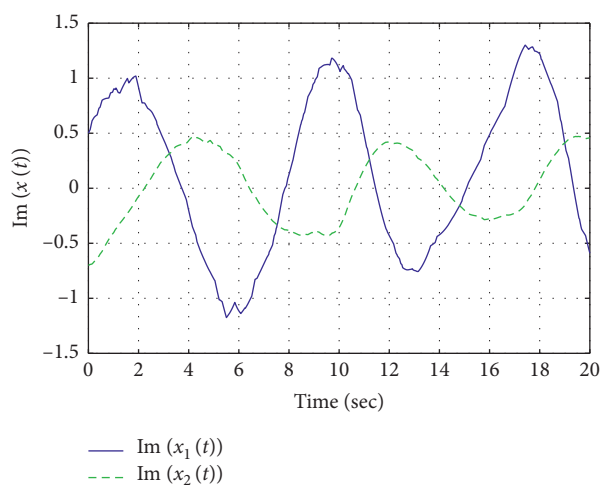

Figure 5: The imaginary part of the state without $u(t)$.

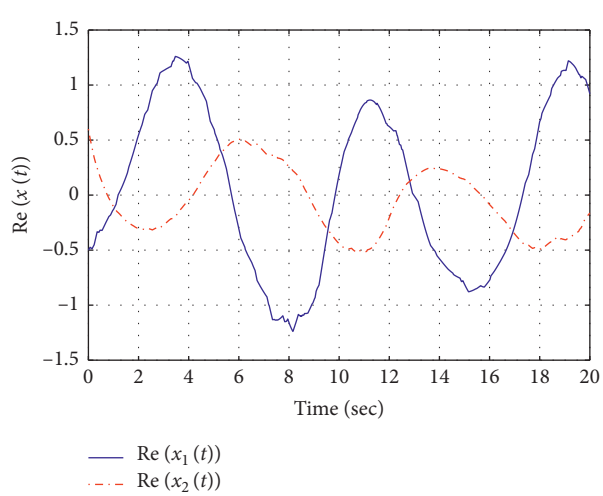

Figure 6: The real part of the state without $u(t)$.

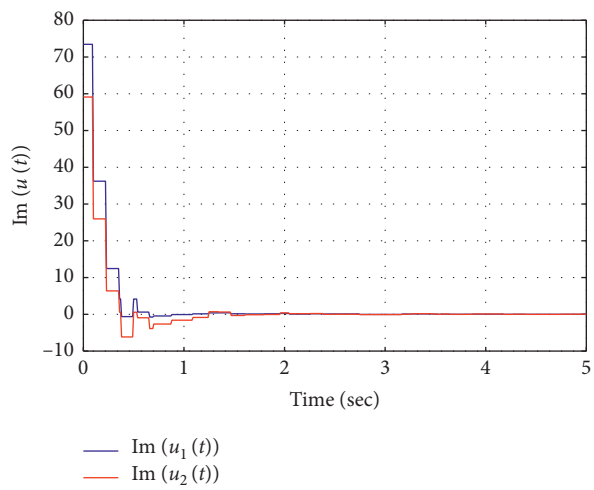

Figure 7: Responses input $u(t)$ of the imaginary part.

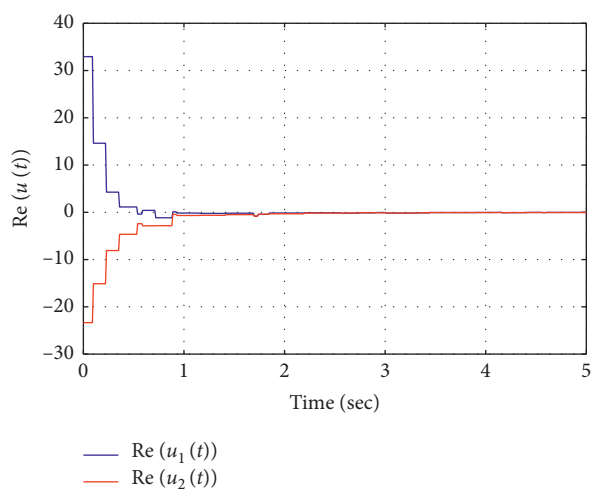

Figure 8: Responses control input $u(t)$ of the real part.

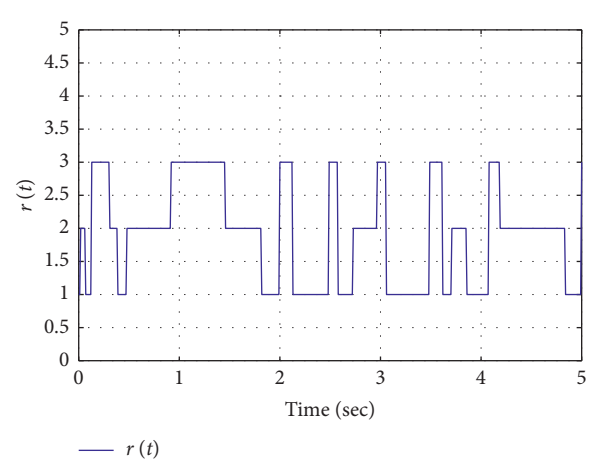

Figure 9: Markov signal.

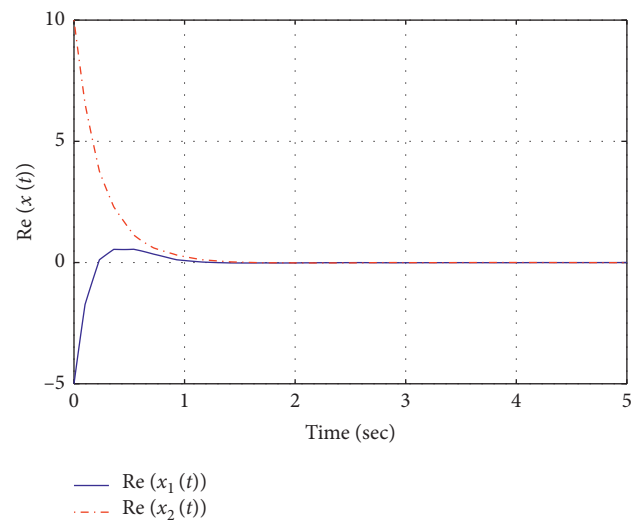

Figure 10: Responses the state of the real part.

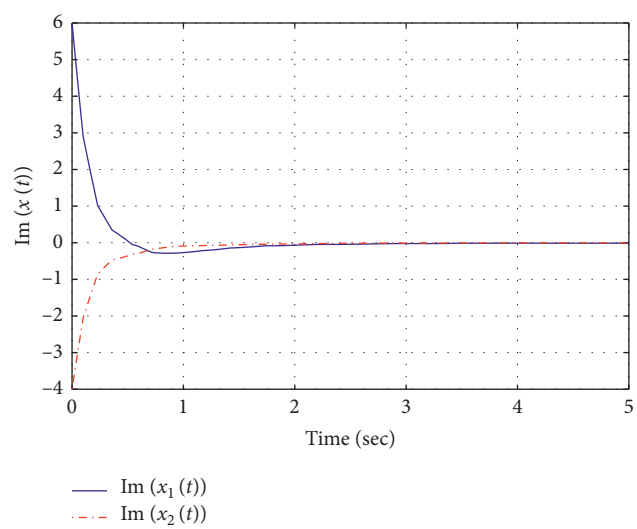

Figure 11: Responses the state of the imaginary part.

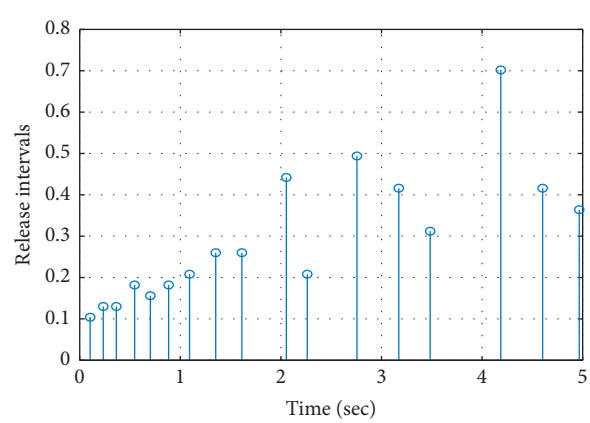

Figure 12: The interval of the event-triggered.

applying the controller, and also, the signal of Markov jump is represented in (7). Compared with Figures 5 and 6 which are the state of Example 1 without controller, it is clear that the controller we designed can stabilize an unstable system effectively.

Example 2. For the same system parameters with Example 1, $\sigma(t) = t - (0.3 - 0.1\sin(t))$ expresses the time-varying delay, and $\sigma_d = 0.1$, set $\varpi = 0.2, h = 0.036, \varsigma = 0.01$, and $\rho = 20$, with the external disturbance $\omega = (1/1 - t^2)$. When the initial value is set as $\psi(t) = [-5 + 6i; 10 - 4i]$ that the SBET weighted matrix and control gain matrices are obtained,

$$\begin{aligned}
\widehat{\mathscr{G}} &= 10^3 \times \begin{pmatrix} 4.1883 + 0.0000i & -0.6747 - 0.2273i \\ -0.6747 + 0.2273i & 3.1574 + 0.0000i \end{pmatrix}, \\
\widetilde{\mathscr{K}}_1 &= \begin{pmatrix} 0.9748 - 6.5659i & -1.3351 + 2.9435i \\ 3.3333 - 4.7188i & -3.5523 + 0.1313i \end{pmatrix}, \\
\widetilde{\mathscr{K}}_2 &= \begin{pmatrix} -1.2784 - 2.0467i & 1.6042 + 0.7371i \\ 1.5378 - 2.2989i & 0.1075 - 2.3443i \end{pmatrix}, \\
\widetilde{\mathscr{K}}_3 &= \begin{pmatrix} -1.2773 - 5.5737i & 0.3576 + 3.1295i \\ -2.5166 - 4.9823i & -1.6298 + 1.9885i \end{pmatrix}.
\end{aligned} \tag{87}$$

Under the conditions which are given in this example, the imaginary part and real part of control inputs $u(t)$ are portrayed in Figures 7 and 8 and Figure 9 is the Markov signals. Figures 10 and 11 are given to show the states of the real part and imaginary part, respectively. It is easy to see system (8) is tending towards stability soon under the controllers which are designed in Theorem 2. Figure 12 shows the release instants of the controller clearly. With the sample interval $h = 0.036$, it is not difficult to find that the number of data transfers is reduced dramatically by comparing to the time-driven one.

5. Conclusions

In this work, the stability and stabilization of a class of neutral-type CVNNs with time-varying delay and partly unknown Markov jump have been addressed. After designing a $H\infty$ state-feedback control to investigate the stabilization of our system, we have studied the stabilization of CVNNs with time-varying delay and partly unknown Markov jump by a sampling-based event-triggered controller for the first time. Moreover, the feasibility and validity of our results have been proved through two examples. However, there are also some issues that need further consideration, for instance, to design a new event-triggered to reduce the number of data-sampling transmission and to develop novel LKFs to reduce the conservatism of the stabilization conditions, and the derivation of less conservative integral inequalities can also help us to get better results; they will put into practice in our work in the near future.

Data Availability

No data were used to support this study.

Conflicts of Interest

The authors declare that they have no conflicts of interest.

Acknowledgments

This work was supported by the National Nature Science Foundation of China under grant/award no. 12061088.

References

[1] Y. Kao, Y. Li, J. H. Park et al., "Mittag-leffler synchronization of delayed fractional memristor neural networks via adaptive control," *IEEE Transactions on Neural Networks and Learning Systems*, vol. 99, pp. 1–6, 2020.

[2] X. Ji, J. Lu, J. Lou et al., "A unified criterion for global exponential stability of quaternion-valued neural networks with hybrid impulses," *International Journal of Robust and Nonlinear Control*, vol. 30, pp. 8098–8116, 2020.

[3] L. Hua, S. Zhong, K. Shi, and X. Zhang, "Further results on finite-time synchronization of delayed inertial memristive neural networks via a novel analysis method," *Neural Networks*, vol. 127, pp. 47–57, 2020.

[4] J. Guo, Z. Meng, and Z. Xiang, "Passivity analysis of stochastic memristor-based complex-valued recurrent neural networks with mixed time-varying delays," *Neural Processing Letters*, vol. 47, no. 3, pp. 1097–1113, 2018.

[5] R. Samidurai, R. Sriraman, J. Cao, and Z. Tu, "Eects of leakage delay on global asymptotic stability of complex-valued neural networks with interval time-varying delays via new complex-valued Jensens inequality," *International Journal of Adaptive Control and Signal Processing*, vol. 32, no. 9, pp. 1294–1312, 2018.

[6] L. Li, Z. Wang, Y. Li, H. Shen, and J. Lu, "Hopf bifurcation analysis of a complex-valued neural network model with discrete and distributed delays," *Applied Mathematics and Computation*, vol. 330, pp. 152–169, 2018.

[7] D. Liu, S. Zhu, and W. Chang, "Input-to-state stability of memristor-based complex-valued neural networks with time delays," *Neurocomputing*, vol. 221, pp. 159–167, 2017.

[8] J. Hu and J. Wang, "Global stability of complex-valued recurrent neural networks with time-delays," *IEEE Transactions on Neural Networks and Learning Systems*, vol. 23, no. 6, pp. 853–865, 2012.

[9] Z. Zhang and S. Yu, "Global asymptotic stability for a class of complex-valued Cohen Grossberg neural networks with time delays," *Neurocomputing*, vol. 171, pp. 1158–1166, 2015.

[10] X. Xu, J. Zhang, and J. Shi, "Exponential stability of complex-valued neural networks with mixed delays," *Neurocomputing*, vol. 128, pp. 483–490, 2014.

[11] Y. Yuan, Q. Song, Y. Liu, and F. E. Alsaadi, "Synchronization of complex-valued neural networks with mixed two additive time-varying delays," *Neurocomputing*, vol. 332, pp. 149–158, 2019.

[12] J. Liang, K. Li, Q. Song, Z. Zhao, Y. Liu, and F. E. Alsaadi, "State estimation of complex-valued neural networks with two additive time-varying delays," *Neurocomputing*, vol. 309, pp. 54–61, 2018.

[13] V. Vembarasan, P. Balasubramaniam, and E. M. Joo, "$H\infty$ state-feedback control of time-delay systems using

reciprocally convex approach," *Journal of Process Control*, vol. 24, no. 6, pp. 892–904, 2014.

[14] J. Xiong, J. Lam, H. Gao, and D. W. C. Ho, "On robust stabilization of Markovian jump systems with uncertain switching probabilities," *Automatica*, vol. 41, no. 5, pp. 897–903, 2005.

[15] K. Shi, J. Wang, S. Zhong, Y. Tang, and J. Cheng, "Non-fragile memory filtering of T-S fuzzy delayed neural networks based on switched fuzzy sampled-data control," *Fuzzy Sets and Systems*, vol. 394, pp. 40–64, 2020.

[16] X. Cai, S. Zhong, J. Wang, and K. Shi, "Robust $H\infty$ control for uncertain delayed T-S fuzzy systems with stochastic packet dropouts," *Applied Mathematics and Computation*, vol. 385, Article ID 125432, 2020.

[17] H. Shen, F. Li, H. Yan, H. R. Karimi, and H.-K. Lam, "Finite-time event-triggered $\mathcal{H}_{\infty }$ control for T-S fuzzy markov jump systems," *IEEE Transactions on Fuzzy Systems*, vol. 26, no. 5, pp. 3122–3135, 2018.

[18] X. H. Chang, *Robust Output Feedback $H\infty$ Control and Filtering for Uncertain Linear Systems*, Springer Science Business, Berlin, Germany, 2014.

[19] C. Huang, Y. Bai, and X. Liu, "H1state feedback control for a class of networked cascade control systems with uncertain delay," *IEEE Transactions on Industrial Informatics*, vol. 6, no. 1, pp. 62–72, 2010.

[20] X. H. Chang, "$H\infty$ controller design for linear systems with time-invariant uncertainties," *International Journal of Control, Automation and Systems*, vol. 9, no. 2, pp. 1–5, 2011.

[21] L. Xiong, H. Zhang, Y. Li et al., "Improved stability and $H\infty$ performance for neutral systems with uncertain markovian jump," *Nonlinear Analysis, Hybrid Systems*, vol. 19, pp. 13–25, 2016.

[22] Y. Kang, Y. B. Zhao, and P. Zhao, *Stability Analysis of Markovian Jump Systems*, Science Press, Beijing, Germany, 2018.

[23] X. Liu and H. Xi, "Stability analysis for neutral delay markovian jump systems with nonlinear perturbations and partially unknown transition rates," *Advances in Mathematical Physics*, vol. 2013, Article ID 592483, 20 pages, 2013.

[24] Y. Zhang, Y. He, M. Wu, and J. Zhang, "Stabilization for Markovian jump systems with partial information on transition probability based on free-connection weighting matrices," *Automatica*, vol. 47, no. 1, pp. 79–84, 2011.

[25] A. C. Sowmiya, B. R. Raja, C. Q. Zhu et al., "Further mean-square asymptotic stability of impulsive discrete-time stochastic BAM neural networks with markovian jumping and multiple time-varying delays," *Journal of the Franklin Institute*, vol. 356, no. 1, pp. 561–591, 2019.

[26] X. Mao, "Stability of stochastic differential equations with markovian switching," *Stochastic Processes and Their Applications*, vol. 79, no. 1, pp. 45–67, 1999.

[27] L. Xiong, J. Tian, and X. Liu, "Stability analysis for neutral markovian jump systems with partially unknown transition probabilities," *Journal of the Franklin Institute*, vol. 349, no. 6, pp. 2193–2214, 2012.

[28] Z. Wu, P. Shi, H. Su, and J. Chu, "Stochastic synchronization of markovian jump neural networks with time-varying delay using sampled data," *IEEE Transactions on Cybernetics*, vol. 46, no. 3, pp. 1796–1806, 2013.

[29] H. Zhang, J. Wang, Z. Wang, and H. Liang, "Sampled-data synchronization analysis of markovian neural networks with generally incomplete transition rates," *IEEE Transactions on Neural Networks and Learning Systems*, vol. 28, no. 3, pp. 740–752, 2017.

[30] C. Zhao, S. Zhong, X. Zhang et al., "Novel results on non-fragile sampled-data exponential synchronization for delayed complex dynamical networks," *International Journal of Robust and Nonlinear Control*, vol. 30, no. 10, pp. 4022–4042, 2020.

[31] P. Tabuada, "Event-triggered real-time scheduling of stabilizing control tasks," *IEEE Transactions on Automatic Control*, vol. 52, no. 9, pp. 1680–1685, 2007.

[32] W. P. M. H. Heemels, J. H. Sandee, and P. P. J. Van Den Bosch, "Analysis of event-driven controllers for linear systems," *International Journal of Control*, vol. 81, no. 4, pp. 571–590, 2008.

[33] C. Peng and J. Zhang, "Event-triggered output-feedback $H\infty$ control for networked control systems with time-varying sampling," *IET Control Theory & Applications*, vol. 9, no. 9, pp. 1384–1391, 2015.

[34] D. Yue, E. Tian, and Q.-L. Han, "A delay system method for designing event-triggered controllers of networked control systems," *IEEE Transactions on Automatic Control*, vol. 58, no. 2, pp. 475–481, 2013.

[35] R. Zhang, D. Zeng, S. Zhong, and Y. Yu, "Event-triggered sampling control for stability and stabilization of memristive neural networks with communication delays," *Applied Mathematics and Computation*, vol. 310, pp. 57–74, 2017.

[36] K. J. Astrom and B. Bo, "Comparison of periodic and event based sampling for first order stochastic systems," in *Proceedings of IFAC World Congress*, pp. 301–306, Elsevier, Beijing, China, September 1999.

[37] X. Wang, Z. Wang, Q. Song, H. Shen, and X. Huang, "A waiting-time-based event-triggered scheme for stabilization of complex-valued neural networks," *Neural Networks*, vol. 121, pp. 329–338, 2020.

[38] Z. Wang, L. Shen, J. Xia, H. Shen, and J. Wang, "Finite-time non-fragilel2–l∞control for jumping stochastic systems subject to input constraints via an event-triggered mechanism," *Journal of the Franklin Institute*, vol. 355, no. 14, pp. 6371–6389, 2018.

[39] C. Peng and T. C. Yang, "Event-triggered communication and $H\infty$ control co-design for networked control systems," *Automatica*, vol. 49, no. 5, pp. 1326–1332, 2013.

[40] C. Hu, H. Yan, H. Zhang, and S. Chen, "Event-triggered output feedback $H\infty$ control for networked control systems with time-varying sampling and packet losses," in *Proceedings of the Chinese Control Conference*, pp. 8002–8007, Dalian, China, July 2017.

[41] A. Seuret and F. Gouaisbaut, "Wirtinger-based integral inequality: application to time-delay systems," *Automatica*, vol. 49, no. 9, pp. 2860–2866, 2013.

[42] C.-A. Popa, "Global μ-stability of neutral-type impulsive complex-valued BAM neural networks with leakage delay and unbounded time-varying delays," *Neurocomputing*, vol. 376, no. 1, pp. 73–94, 2020.

Hindawi
Complexity
Volume 2021, Article ID 9974803, 16 pages
https://doi.org/10.1155/2021/9974803

Research Article

Optimization and Performance Analysis of Rail-Train Coupling System with Inerters

Shichang Han,[1] **Xian Wang**,[1] **Chunxi Yang**,[1] **Guowei Xie**,[2] **Zhongcheng Qiu**,[1] **and Chen Wang**[1]

[1]*Faculty of Mechanical and Electrical Engineering, Kunming University of Science and Technology, Kunming 650500, China*
[2]*Shanghai Headquarters, QST Corporation, Shanghai 201210, China*

Correspondence should be addressed to Xian Wang; 375835425@qq.com

Received 5 March 2021; Accepted 22 April 2021; Published 8 May 2021

Academic Editor: Youmin Zhang

Optimization for vertical vibration performance of a rail-train coupling system is investigated in this paper with the introduction of inerters for both primary and secondary suspensions. A model of a typical Chinese passenger train that travels on a traditional rail with track, sleepers, and ballast is simulated. The goal is to improve the ride quality for the train and vibration attenuation for the rail system in response to track irregularities. Optimizations for only inertance and all suspension parameters are carried out by the particle swarm algorithm (PSO). Performance benefits for both the train and the rail system are demonstrated and suspension layouts with inerters connected in parallel and series are compared with the traditional one in both time domain and frequency domain.

1. Introduction

Vertical performance of a train when it travels on a track is an important index for the running quality, such as the riding comfort for a passenger train. Improvement of the performance has been explored for years. And, the parameters optimization of the train or rail system has been proven useful by using many methods. Optimization of a light rail vehicle was done by Pombo et al. [1] using the direct multisearch (DMS) method with consideration of a curve and slope rail to get better running safety and ride quality. In the study by [2], the suspension parameters of high-speed rail vehicles are obtained via the Taguchi robust optimization method leading to an obvious improvement in the vertical running stability of the vehicle under different running conditions. And, Liu et al. [3] dealt with multiobjective optimization for the suspension parameters of railcars and proposed an optimization strategy combining the collaborative optimization method and the metamodel method. The results show that the dynamic performance of railcars is improved remarkably with the robust collaborative optimization of the suspension parameters. In paper [4], using a combination of multibody dynamics and a genetic algorithm (GA), the curving performance of a transit rail vehicle model with 21 degrees of freedom was optimized, where the optimal design variables were searched for minimizing the noise or wear arising from misalignment of the wheelsets with the track. Wang et al. [5] used the improved sequential quadratic programming (SQP) method to generate a sequence of improving profiles to improve vehicle running stability in the switch panel of high-speed railway turnouts, which would decrease the rolling radii difference. Furthermore, in study [6], Dullinger took both GA and SQP for multiobjective optimization of the traction system configuration of trains' decision variables. And, the particle swarm optimization (PSO) algorithm was used by Sun [7] to optimize the parameters of suspensions. The advantages of PSO, which are simple programming and fast searching speed, have been proven efficient in the suspension optimization.

Some modelling and control strategies can also benefit the performance of a system [8–10], even when there are some uncertainties [11, 12]. However, on comparing the cost

of the system modelling and control, structure improvement can be more practical. A mechanical network element called inerter is reported these days since it was brought out by Smith [13] and successfully used to benefit a car suspension [14]. Great interest has been put in inerters from different fields such as car suspensions, energy sink [15], isolation system [16], and civil engineering [17]. Rail vehicles with inerters are also explored. Wang [18, 19] investigated the performance benefits of train suspension systems employing an inerter in both vertical performance and lateral stability. Passenger comfort, dynamic wheel load, and critical speed were evaluated with different inerter combinations. Wang et al. [20] also constructed a 28 degree-of-freedom train model with inerters to investigate the critical speed, settling time, and passenger comfort for a full train system. Jiang [21, 22] focused on the improvement of rail vehicle performance with inerters in both lateral and vertical suspension systems. In [21], a two-axle single-stage railway vehicle was investigated under track irregularities. And, in [22], the lateral body movement of the vehicle when entering a curved track was considered in the lateral direction.

Research studies have proven that either parameters optimization or inerters are of great benefits to the performance of rail vehicles, which will be a novel way to optimize the train problems. However, few reported the effect on the rail when the inerter-equipped train travels over. This paper firstly considers a typical Chinese passenger train on active duty and uses PSO to optimize its first and second suspension parameters for better ride comfort and suspension displacements, while inerters are introduced in both suspensions. Then, a rail-train coupling system is introduced to evaluate the effect of the optimization parameters to the rail system which consists of rail, sleepers, and ballast.

This paper is organized as follows: in Section 2, a 10-degree of freedom and a 16-degree of freedom train models with contact force are described. Different suspension layouts with inerters, which are parallel and series connected, are considered. Section 3 shows optimization of the suspension parameters to minimize the ride comfort and suspension displacements. Section 4 describes the performance of the rail-train coupling system. The acceleration of rail, sleepers, and ballast is discussed in different suspension layouts. Lastly, some conclusions are made in Section 5.

2. System Description

Although nowadays the high-speed railway develops rapidly, our national rail net is mostly served by the traditional railway, which consists of rail, sleepers, and ballast. So, analysis of a traditional railway is still of important worth. And, a commonly seen passenger train is also considered in this paper. The rail-train coupling system is established the same as in the research of Zhai [23]. Figure 1 shows the rail-train system, in which the train model consists of one car body, two bogies and four wheelsets, and the rail model consists of rail, uniformly distributed sleepers and ballast underneath. Only vertical direction is focused in the following sections.

2.1. Model of the Rail System. As shown in Figure 1, rail, sleepers, and ballast are all considered in the rail system in this paper. The rail is modelled as a continuous Euler beam with discrete sleeper supports which can be expressed as follows [23]:

$$EI\frac{\partial^4 Z_r(x,t)}{\partial x^4}+m_r\frac{\partial^2 Z_r(x,t)}{\partial t^2}=-\sum_{i=1}^{N}F_{rsi}(t)\delta(x-x_i)+\sum_{j=1}^{4}p_j\delta\left(x-x_{wj}\right), \quad (1)$$

where EI is the rail beam bending stiffness (N·m^2), Z_r is the vertical displacement of the rail (m), x is the location of the rail (m), x_i is the location of the ith rail pad (m), which supports the rail, x_{wj} is the location of the jth wheel (m), where contact force between the wheel and rail exists, F_{rsi} is i^{th} rail pad supporting force (N), and p_j is the jth wheel-rail contact force (N). δ denotes the Dirac function. And, the other parameters can be found in Table 1.

the sleepers are modelled as uniformly distributed. It can be expressed easily by the Newton–Euler approach. On the contrary, the ballast is modelled as a discrete ballast mass according to [23]. The expression of the discrete ballast mass M_b is as follows:

$$M_b=\rho_b V_b=\rho_b h_b\left[l_e l_b+(l_e+l_b)h_b\tan\alpha+\frac{4}{3}h_b^2\tan^2\alpha\right], \quad (2)$$

where all the meaning of parameters can be found in Table 1. And, it is worth to mention, in this paper, the ballast mass is discrete and has no overlapping since standard sleeper spacing is taken.

The three layers of springs and dampers represent the elasticity and damping of the rail pad, the ballast, and the subgrade, respectively. By using the Ritz method [24], equation (1) of the rail can be converted into the second-order ordinary differential equation. The system dynamics equations of the rail, sleeper, and ballast can be established by the Newton–Euler approach and are shown in the appendix. Table 1 shows the parameters of the rail in the equations.

2.2. Train Model and Suspensions with the Inerter. As shown in Figure 1, one car body, two bogies, and four wheelsets are modelled. 10 degrees of freedom are considered, as shown in Table 2.

Springs and dampers between wheels and bogies represent the elasticity and damping of the primary suspension,

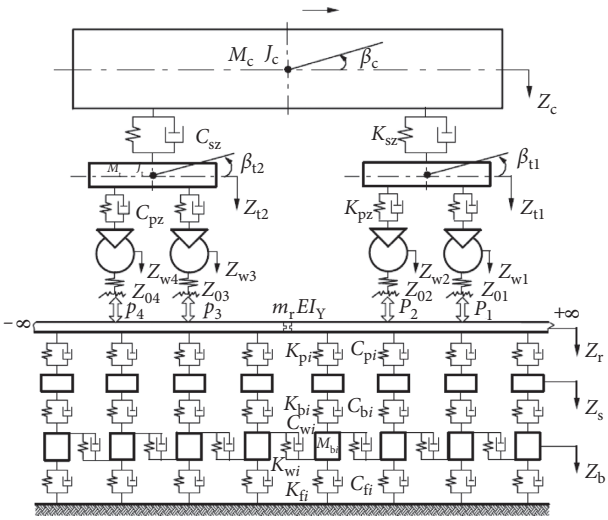

Figure 1: A rail-train coupling model [23].

Table 1: Parameters of the rail system.

Symbol	Parameter	Unit	Nominal value
E	Elastic modulus of rail	N/m^2	2.059×10^{11}
I	Rail cross-sectional inertia	m^4	3.217×10^{-5}
m_r	Rail mass per unit length	kg/m	60.64
m_s	Sleeper mass (half)	kg	125.5
K_p	Rail pad stiffness	N/m	1.0×10^8
C_p	Rail pad damping	N·s/m	7.5×10^4
l_s	Sleeper spacing	m	0.545
l_e	Effective support length of half sleeper	m	0.95
l_b	Sleeper bottom width	m	0.273
ρ_b	Ballast density	kg/m^3	1.8×10^3
E_b	Elastic modulus of ballast	N/m^2	1.1×10^8
C_b	Ballast damping	N·s/m	5.88×10^4
K_w	Ballast shear stiffness	N/m	7.84×10^7
C_w	Ballast shear damping	N·s/m	8×10^4
α	Ballast stress distribution angle	(°)	35
h_b	Ballast thickness	m	0.35
E_f	Subgrade K30 modulus	MPa/m	1.9×10^8
C_f	Subgrade damping	N·s/m	1.0×10^5

Table 2: 10 degrees of freedom of the train.

Component	Translational motion	Pitch motion
Car body	Z_c	β_c
Bogie	$Z_{ti}\,(i = 1 \sim 2)$	$\beta_{ti}\,(i = 1 \sim 2)$
Wheelsets	$Z_{wi}\,(i = 1 \sim 4)$	—

and those between car body and bogies represent the secondary suspension of the train. The traditional suspension consists of a parallel combination of a spring and a damper. To make the basic understanding of the effect by the inerter, only one inerter is added in each suspension. It is arranged in parallel or series with the damper, as shown in Figure 2.

In this paper, the parallel or series layout will be investigated separately, which means the same type of layout will be added in all suspensions at the same time. So, the dynamic equations can be obtained as in the appendix. The equations of the traditional suspension are omitted since it will be same as the parallel equations when $b = 0$ kg. On the contrary, an extra freedom between the inerter and damper should be considered when they are series connected. The train model with the series-connected inerter has 16 degrees of freedom with 6 suspension's extra freedom. All the parameters of the train are given in Table 3.

2.3. Contact Force between the Wheel and Rail. There are mainly normal force and creep force in the wheel-rail interaction. However, analysis of vertical performance can neglect the creep force with only normal force in consideration. In this case, the normal force, which is the contact force between the wheel and rail, can use the nonlinear Hertzian elastic contact theory to model. The nonlinear Hertzian elastic contact theory has been applied for the wheel-rail contact for years because of its easy calculation and high accuracy [25].

To calculate the normal force, the wheel-rail normal elastic compressing deformation at each contact point at every moment must be obtained. The equation of the theory is

$$p(t) = \left[\frac{1}{G}\delta Z(t)\right]^{(3/2)}, \tag{3}$$

where G is the wheel-rail contact coefficient ($m/N^{2/3}$) and $\delta Z(t)$ is the elastic compressing deformation (m). In this paper, the wheel with cone tread is selected, so the wheel-rail contact coefficient is $G = 4.57R^{-0.149}e^{-8}$, in which R is wheel radius.

When only vertical direction is considered, the compressing deformation equals to the vertical relative displacement of the wheel and rail. The expression is as follows:

$$\delta Z(t) = Z_w(t) - Z_r(x_w, t) - Z_0(t), \tag{4}$$

where $Z_w(t)$ is the vertical displacement of the wheel (m), $Z_r(x_w, t)$ is the vertical displacement of the rail under the wheel (m), and $Z_0(t)$ is the rail irregularity in the vertical direction. When the compressing deformation is analysed, it can be applied for 4 wheels using a time delay. The time delay is simply calculated by distances between each wheel divided by the traveling speed of the train. If the time for the first wheel is $t_{w1} = t_0$, then, $t_{w2} = t_0 + (2l_t/v)$, $t_{w3} = t_0 + (2l_c/v)$, and $t_{w4} = t_0 + (2(l_c + l_t)/v)$, where v is the speed of the train.

2.4. System Input and Equation-Solving Method

2.4.1. System Input. Since the different directions of motion are weakly coupled in the rail-train system, the height irregularity, which mainly affects the vertical motion of the system, is only considered as the system input. A height irregularity power spectral density (PSD) obtained by Federal Railway Administration of America is introduced in this paper. The expression is

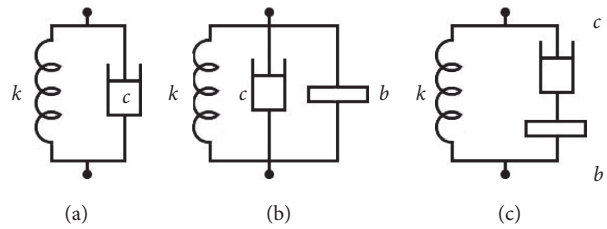

Figure 2: Suspension candidates with the inerter. (a) Traditional one. (b) Parallel one. (c) Series one.

Table 3: Parameters of the train model.

Symbol	Parameter	Unit	Nominal value
m_c	Vehicle body mass	kg	38500
m_t	Bogie frame mass	kg	2980
m_w	Wheelset mass	kg	1350
J_c	Vehicle pitch inertia	kg·m^2	2.446×10^6
J_t	Bogie pitch inertia	kg·m^2	3605
K_{pz}	Primary suspension stiffness per axle box	N/m	2.14×10^6
K_{sz}	Secondary suspension stiffness	N/m	2.535×10^6
C_{pz}	Primary suspension damping per axle box	N·s/m	4.9×10^4
C_{sz}	Secondary suspension damping	N·s/m	1.96×10^5
l_c	Semilongitudinal spacing of vehicle	m	8.4
l_t	Semilongitudinal spacing of bogie	m	1.2
R	Wheel radius	m	0.4575

$$S_v(\Omega) = \frac{kA_v\Omega_c^2}{\Omega^2\left(\Omega^2+\Omega_c^2\right)}. \tag{5}$$

In which, Ω is the spatial frequency of track irregularity (1/m), k is the safety number, A_v is the roughness constant (cm^2·rad/m), and Ω_c is the cut-off frequencies (rad/m).

According to the rail PSD parameters, a class 6 rail is selected with allowed max speed of 176 km/h. The roughness constant is $A_v = 0.0339\,\text{cm}^2\cdot\text{rad/m}$, and the cut-off frequencies is $\Omega_c = 0.8245$ rad/m. And, we use a safety number $k = 2.5$. In this paper, the speed takes a middle value of the speed range as 90 km/h, which is also a normal speed used in reality. The time-domain irregularity can be transformed from PSD by using the trigonometric series method [26], as shown in Figure 3.

2.4.2. Numerical Method for Equation Solving. From Section 2.1 to 2.3, the equations of the rail-train coupling system can be expressed as a unified matrix form as follows:

$$M\ddot{X} + C\dot{X} + KX = F, \tag{6}$$

where M, C, and K are the mass (including inerters), damping, and stiffness matrices and F is the forces of the system.

However, the size of the matrix depends on the number of the system's degrees of freedom. Take the mass matrix for example, it will consist of the train body, bogies, wheelsets, modes of rail, sleepers, and discrete ballasts. The size will equal the total number of them. Such a large matrix transformation and calculation is hard to be solved in the theoretical way. So, the step-by-step time integration method will be used to solve the equations of the system. In this paper, the method in [27] is used, which is successfully applied in the field of analysis of vehicle-track coupled dynamics. The basic scheme is constructed as follows:

$$\begin{cases} \{X\}_{n+1} = \{X\}_n + \{v\}_n\Delta t + \left(\dfrac{1}{2}+\psi\right)\{A\}_n\Delta t^2 - \psi\{A\}_{n-1}\Delta t^2, \\ \{v\}_{n+1} = \{v\}_n + (1+\varphi)\{A\}_n\Delta t - \varphi\{A\}_{n-1}\Delta t, \end{cases} \tag{7}$$

where n indicates the steps and ψ and φ are parameters that control the stability and numerical dissipation of the algorithm; we take $\psi = 0.25$ and $\varphi = 0.5$ in this paper. In addition, to keep the stability of the integration, time steps are used in 10^{-5} s for train analysis and optimization, and 10^{-6} s for rail-train coupling system analysis. The error to control the integration uses 0.1.

3. Optimization of Suspension Performance

3.1. Optimization of Suspension Parameters. Once an inerter is arranged in the suspension layout, the parameters should be identified. The PSO is taken to do the optimization of the suspension parameters. A simplification is made here that, due to the complexity the rail system brings to the matrix and all the optimizing parameters are of the suspension of the train, only the train model is used to do the optimization. The objective of this procedure is to minimize the train body acceleration for better riding comfort and less primary suspension displacement.

For the riding comfort, the RMS value of the train body acceleration a_{tb} is used as an index with the comparison of the traditional suspension a_{tb0}. On the contrary, the less the primary suspension displacement is, the less the force

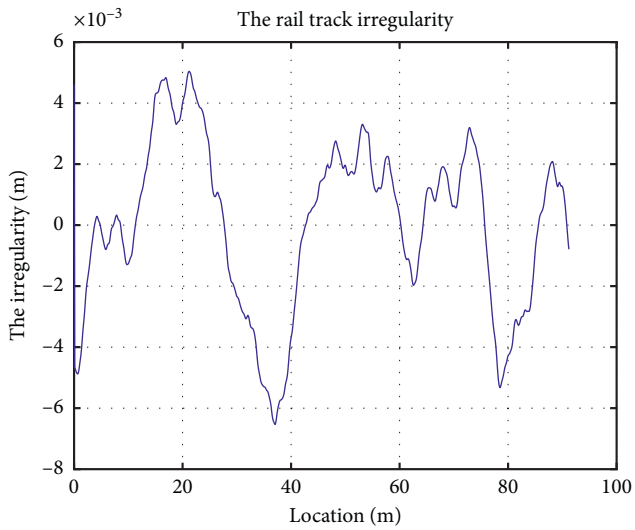

Figure 3: Track irregularity of class 6.

applied on the wheelsets will be, which are contacted with the rail. So, the RMS value of primary suspension displacements x_p will be mainly focused. For the optimizing procedure, the train body acceleration and primary suspension displacements are equally considered. So, their weight in the optimization will be 0.5 for each value. Furthermore, all primary suspension displacements of four wheels are taking an equal weight, which is 0.125 out of 0.5. The optimized objective function can be written as follows:

$$\min Y = 0.5 \times \frac{a_{tb}}{a_{tb0}} + \sum_{i=1}^{4} 0.125 \times \frac{x_{pi}}{x_{pi0}}. \quad (8)$$

In which, i stands for the number of the wheelset, x_{pi} is the primary suspension displacement on the ith wheel, and x_{pi0} is that of the traditional one. For all the parameter range of stiffness K and damping C, the upper and lower limits are roughly 30% up and down the parameters of the traditional suspension, as shown in Table 4. For the inerter's value B, a range of 0–60000 kg is used during the optimization.

Optimization is carried out by two steps. First, keep the K and C their traditional value and optimize inertance B only; Table 5 shows the optimal values of the inerters in parallel and series layouts. And, the second step optimizes all the values of K, C, and B. The optimized parameters are shown in Table 6. It is also worth to mention that the primary suspensions are considered the same in the front and rear bogies.

3.2. Performance Verification. From Section 3.1, optimization is carried out in two cases. Both two cases are studied in this section to verify the performance and find a better parameter setting for the next coupling system analysis. The train model with different suspension layouts is simulated at the speed of 90 km/h. Acceleration of the train body and displacements of both the body and the primary suspension are discussed.

Table 4: The optimal parameter ranges.

Parameter	K (kN/m)	C (kN/m/s)	B (kg)
Lower limits	1500	35	0
Upper limits	3300	250	60000

Table 5: The optimal parameter of the suspension (only B).

Inerter	Suspension	B (kg)
In parallel	Primary	208
	Secondary	7861
In series	Primary	49844
	Secondary	33168

Table 6: The optimal parameter of the suspension (K, C, and B).

Inerter	Suspension	K (kN/m)	C (kN/m/s)	B (kg)
In parallel	Primary	2554.6	147.4	200
	Secondary	2415.3	131.1	34200
In series	Primary	3276.3	243.3	58900
	Secondary	2519.9	170.5	32200

In the following figures, the legend needs to explain in advance that, the "tradition" black solid curve represents the traditional layout, the "parallel" red dash curve represents the layout with the optimized inerter in parallel, and the "series" blue dot-dash curve represents the layout with the optimized inerter in series. Furthermore, the "parallel for all" pink dot curve represents the parallel layout with all optimized K, C, and B values. And, the last, the "series for all" green thin line with star marks' curve represents the series layout with all optimized K, C, and B values.

The accelerations of the train body in all layouts are shown in Figure 4, and all the curves have a good agreement in tendency. Compared with the traditional layout, all four inerter ones contribute an improvement of 8.12% for "parallel," 8.74% for "series," 23.26% for "parallel for all," and 45.68% for "series for all," respectively, as shown in Table 7 and 8. From Figure 5, PSD of accelerations of the train body shows that all the inerter layouts lower the natural frequency of the train body from 1.6 Hz to 1.2 Hz. All of them but "series" have lowered the amplitude at the natural frequency as well. We can also see that "parallel for all" introduces more noise in a frequency range around 10–40 Hz.

The displacements of the train body are discussed as well. From Figure 6, the displacements can be seen that, except the curve of "series for all," the other curves are basically the same in the time domain, which can be proven in Tables 7 and 8 that there is almost no improvement, while the curve of "series for all" contributes 13.63% improvement. In the frequency domain in Figure 7, all curves with the inerter lower the natural frequency but the series curve has its amplitude increased.

For the primary suspension displacement, in Figures 8 and 9, no improvement occurs in both parallel and series curves in the time and frequency domain. On the contrary, cases of "parallel for all" and "series for all" improve the

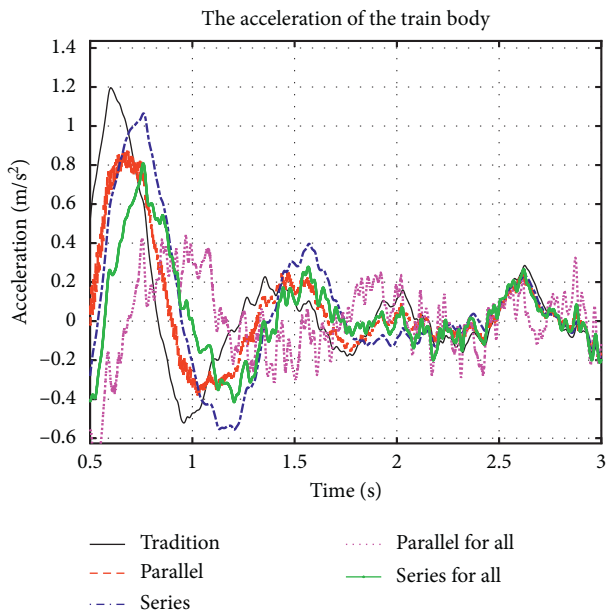

Figure 4: Acceleration of the train body.

Table 7: The performance with B optimized.

	Vehicle body accelerations (m/s^2)	Vehicle body displacement (m)	Primary suspension displacement (m)
Tradition	0.6878	0.1265	0.0514
Parallel	0.632	0.1264	0.0514
Improvement	8.12%	0	0
Series	0.6277	0.1276	0.0515
Improvement	8.74%	−0.1%	−0.3%

Table 8: The performance with K, C, and B optimized.

	Vehicle body accelerations (m/s^2)	Vehicle body displacement (m)	Primary suspension displacement (m)
Tradition	0.6878	0.1265	0.0514
Parallel for all	0.5278	0.1216	0.0429
Improvement	23.26%	3.85%	16.58%
Series for all	0.3737	0.1092	0.0337
Improvement	45.68%	13.63%	34.39%

displacements of the primary suspension by 16.58% and 34.39%, respectively. The natural frequency is the same as train body displacements that lowered from 1.6 Hz to 1.2 Hz.

From all the analysis above, we can see that, after the optimization, the inerter layouts do have the benefit for the performance of the train. And, with the optimizing values of all parameters, the layouts show a better improvement than the ones with only inertance optimized. We will investigate the performance of the rail-train coupling system in the next section with these parameters in Table 6.

4. Performance of the Rail-Train Coupling System

Performance of the rail-train coupling system is analysed in this section. The rail uses a distance of 175 m, which consists 320 sleepers in total. And, the maximum mode number of the rail selects 160. The ballast is modelled as the discrete ballast mass as mentioned in section 2 with the shear stiffness and damping counted. And, no overlapping of adjacent ballast masses occurs in this paper. Both the displacement of wheels and rails are considered in this part as equation (4), so the contacting force will be calculated by equation (3). The traveling speed is 90 km/h as well. Comparison of the performance between the layouts with the inerter and the traditional layout is analysed as follows.

4.1. Performance of the Train. Performance of the train body is discussed first to check if the benefit with the inerter still holds. In the simulation, a balance procedure is arranged in the beginning, which means to lay the train on the track and make the forces on wheels balance to the weight of the train. So, the performance we are looking through will neglect the balance period and start from 0.5 s. A 2.5 s period of the curve is analysed in this section.

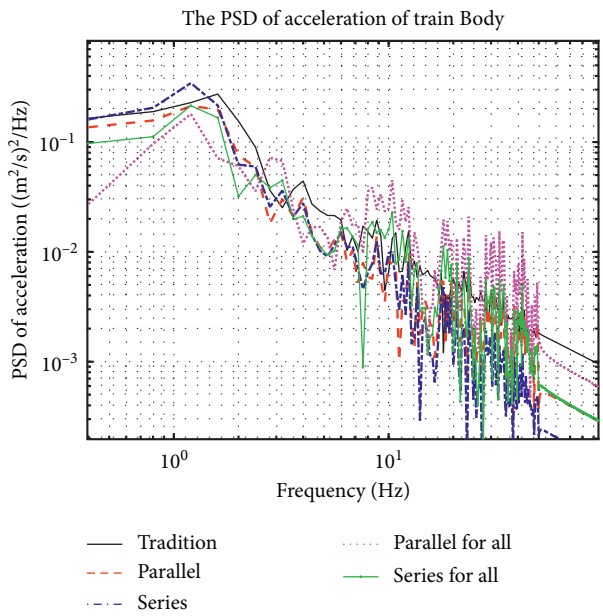

Figure 5: PSD of vehicle body acceleration.

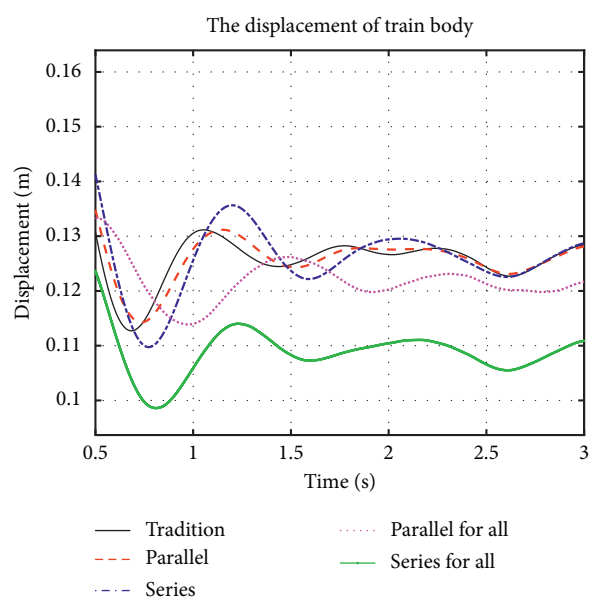

Figure 6: Displacement of the vehicle body.

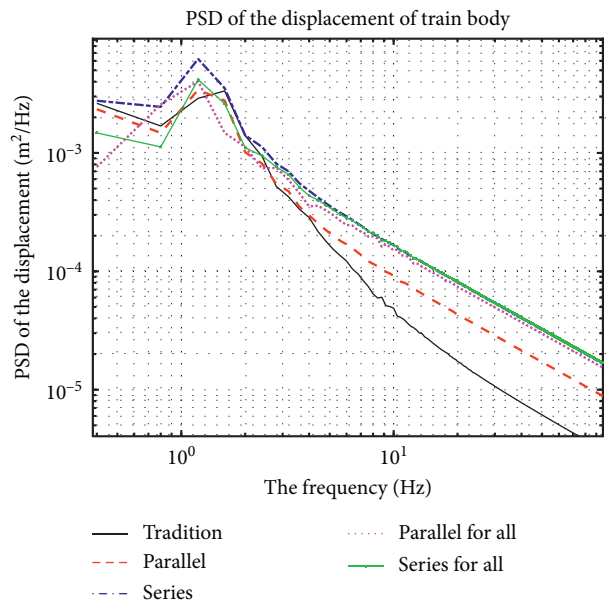

Figure 7: PSD of vehicle body displacement.

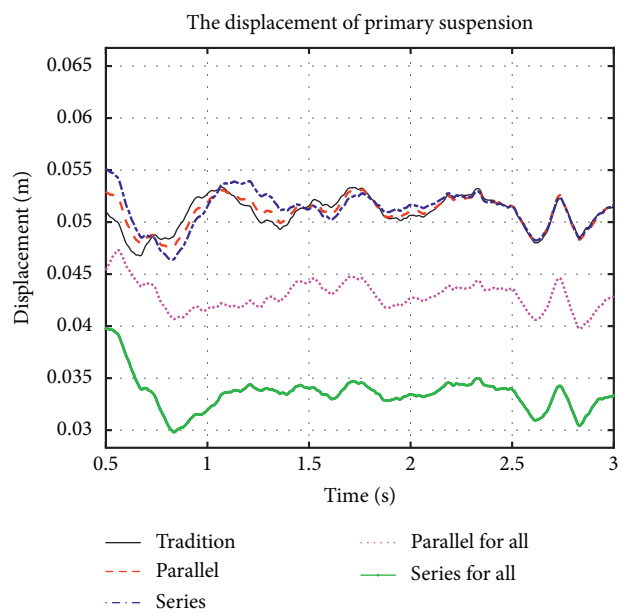

Figure 8: Primary suspension displacement.

The acceleration of the train body and its PSD are firstly analysed. Figure 10 shows the accelerations of the train body in the time domain. And, from the curves, improvement is still unclear except the max peak location. However, as calculated in Table 9, the RMS value of the acceleration gives a 43.64% and 30.29% improvement, respectively. Furthermore, lots of noise can be found in the curve of parallel compared with the others in Figure 10. It can be explained by Figure 11, which shows PSD of train body acceleration. In Figure 11, the inerters in both parallel and series layouts show an influence that the natural frequency of the acceleration has been lowered both in amplitude and frequency. The natural frequency changes from 1.6 Hz to 1.2 Hz, which is the same as Section 3.2, and the amplitude lowered from 0.3448 to 0.1967 and 0.2795 $(m/s^2)^2/Hz$. However, the isolation for higher frequencies, which is in the range of 10–40 Hz, is weakened by using the inerter, especially in the parallel layout.

The pitch of the train body is also considered in Figures 12 and 13. Compared to the traditional layout, the natural frequency of pitch is lowered form 2.4 Hz to 0.8 Hz. However, pitch accelerations of the layouts with the inerter suffer influence of the high frequencies as well. The RMS value of the parallel layout worsens 9.73% because of the introduction of the high frequencies, while the RMS value of the series layout improves to 15.84%.

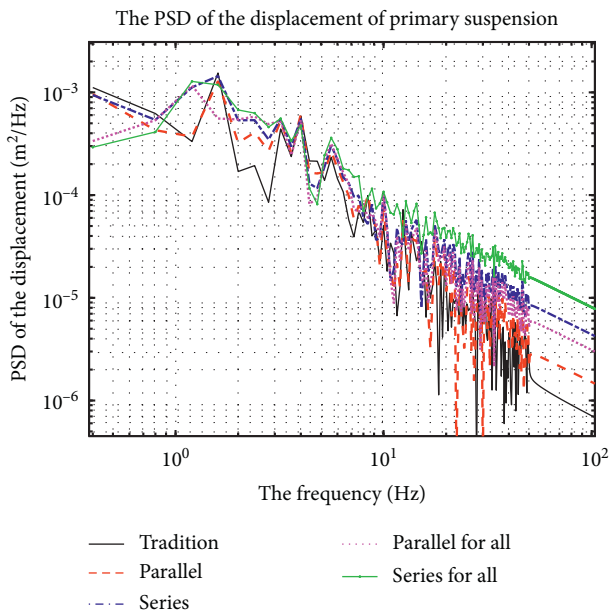

Figure 9: PSD of suspension displacement.

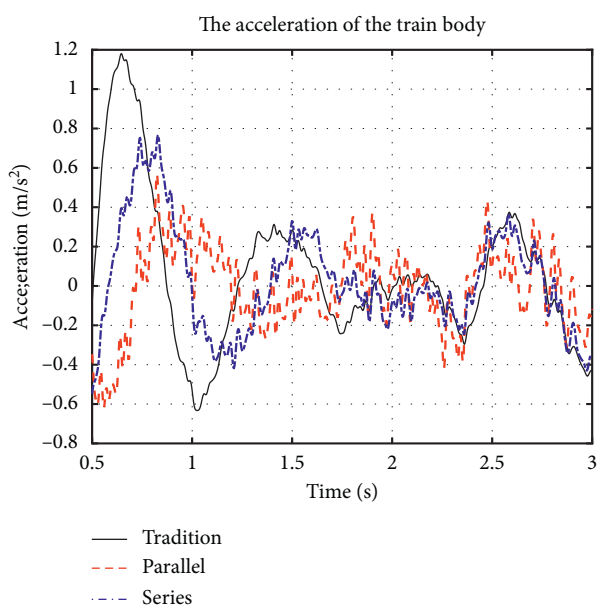

Figure 10: Acceleration of the train body.

Table 9: The performance of the rail-train coupling system.

Acceleration	Vehicle body (m/s^2)	Vehicle pitch (rad/s^2)	Rail (m/s^2)	Sleeper (m/s^2)	Ballast (m/s^2)
Tradition	0.3841	0.0196	0.6176	0.8573	0.5934
Parallel	0.2165	0.0215	0.6214	0.7469	0.5046
Improvement	43.64%	-9.73%	-0.6%	12.88%	14.96%
Series	0.2678	0.0165	0.5794	0.6839	0.4608
Improvement	30.29%	15.84%	6.19%	20.24%	22.35%

From the acceleration of the train body, we can see that either the train model only or the rail-train coupling system can be improved by the introduction of inerters. However, the pitch acceleration suffers more noise when the inerter is connected in parallel, so the combination of inerters matters and the optimization needs to be thorough.

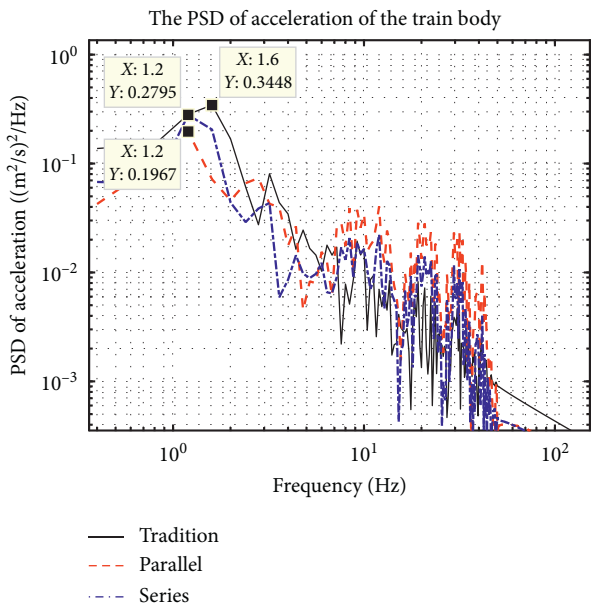

Figure 11: PSD of train body acceleration.

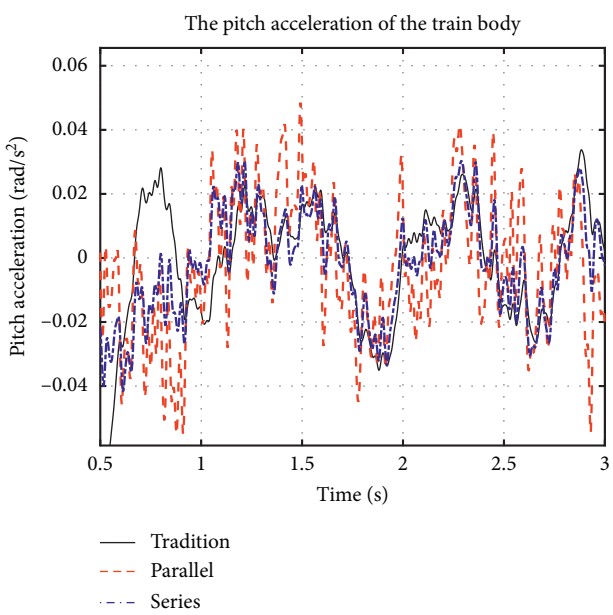

Figure 12: Pitch acceleration of train body.

4.2. Performance of the Rail System. In this section, performance of the rail system is analysed. The location 1/2L is selected in the middle of the whole distance, at which all the rail, sleeper, and ballast are discussed.

Figure 14 shows the acceleration of the rail at 1/2L in the time domain. In Figure 14(a), the time window is the same as train analysis when the whole train runs over the middle location of the rail. Two severe vibration periods happen in the time line which indicates that the front and rear bogies run over the location. The max acceleration of the rail in 1/2L is around 3-4 m/s^2. In Figure 14(b), a zoomed figure of Figure 14(a) is shown, which reflects the acceleration of the rail when the front bogie runs over, and it can be seen more

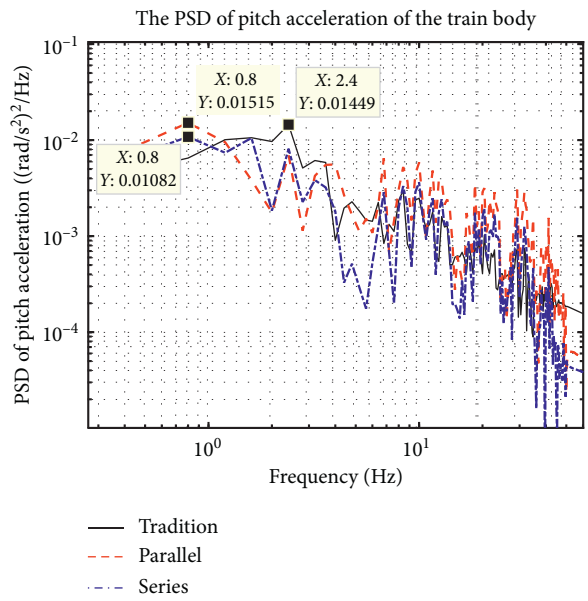

Figure 13: PSD of pitch acceleration.

in detail that both layouts with the inerter have a good agreement in tendency with the traditional one. However, the series one shows better vibration attenuation than the parallel one in some peaks. The RMS values prove the performances of the figure also shown in Table 9. For the parallel layout, 0.6% deterioration happens compared with the traditional one, which is so small that can be neglected. On the contrary, the series one gives a 6.19% improvement in the RMS value of the acceleration.

In the frequency domain, curves in Figure 15(a) are the PSD of all three layouts. The series one has a lower PSD curve during 0–10 Hz. The natural frequencies of the three curves are the same at 41.6 Hz in Figure 15(b). However, both inerter layouts show a lower amplitude of the PSD in natural frequency, and the series one gives much more attenuation about 22.2%.

Figure 16 shows the performance of the middle sleeper. From Figure 16(a), max acceleration is around 4 m/s^2. Figure 16(b) shows details that both layouts with the inerter attenuate the vibration of the sleeper, and the series one does better. RMS values of the sleeper acceleration in Table 9 show the improvement of 12.88% and 20.24%, respectively, compared with the traditional layout.

And, in the frequency domain in Figure 17, same as the PSD of the rail, all the layouts give the similar tendency of the curves. The natural frequency is 41.6 Hz as well, and inerter layouts lower the amplitude of the PSD. For the parallel layout, the attenuation is 21.45%, and for the series one, the number is 31.91%. However, around 20 Hz, both the layouts with inerters show the deterioration compared to the traditional layout.

The vibration of ballast is a very important index for the ballast track. The running safety and serve period of the track system are all affected by its performance. We can see from Figures 18(a) and 18(b) that the max amplitude of the ballast is less than 3 m/s^2, and the layouts with the inerter attenuate

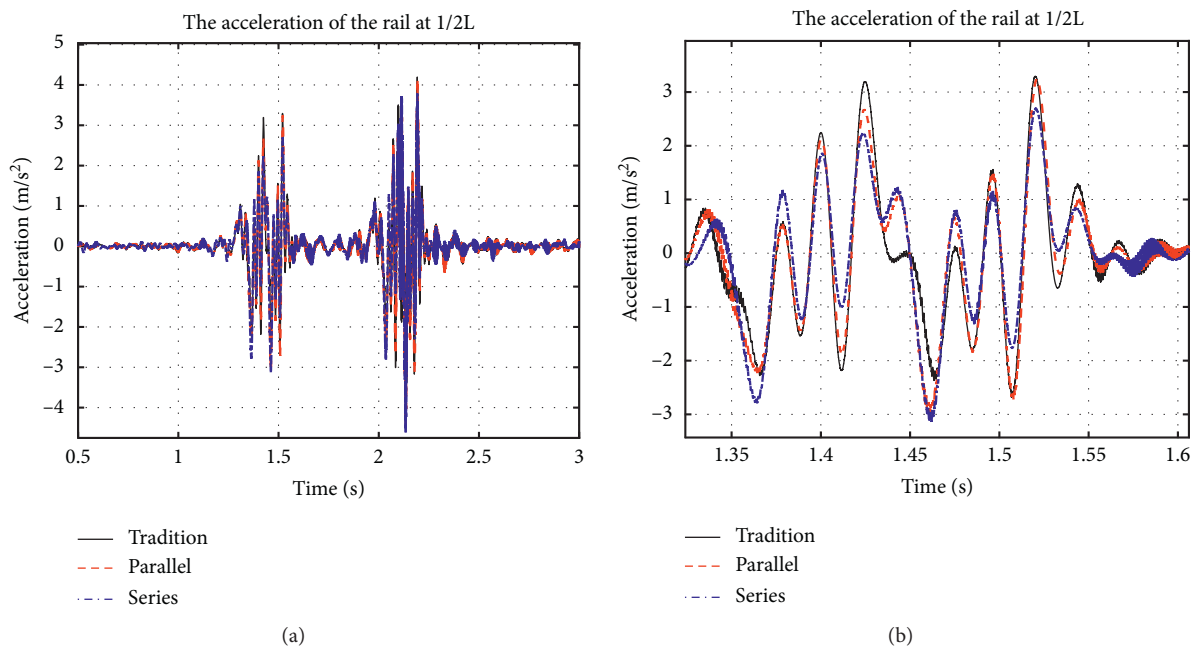

Figure 14: Acceleration of the rail at 1/2L. (a) The whole train runs over. (b) The front bogie runs over.

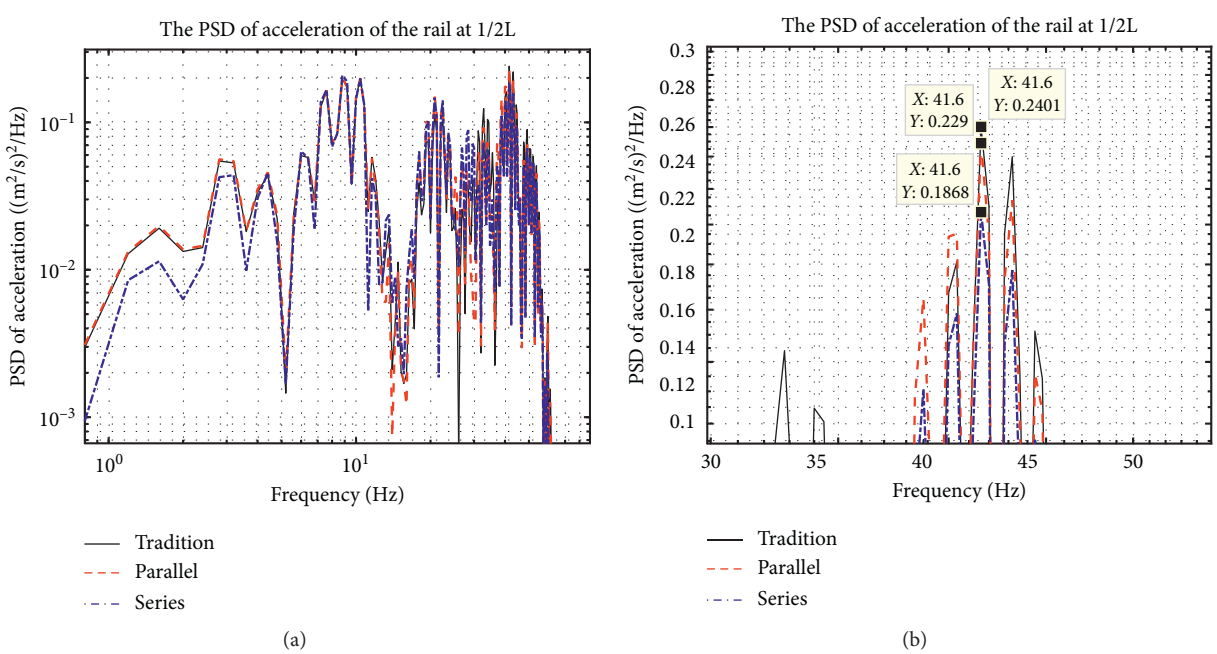

Figure 15: PSD of pitch acceleration. (a) Range of 0–100 Hz. (b) Peaks at natural frequency.

the vibration of the ballast. The improvement of the RMS value is 14.96% and 22.35% for parallel and series layouts, respectively. In the frequency domain in Figure 19, the natural frequencies are the same as the rail and sleeper, which is 41.6 Hz. And, the drop of the amplitude is 22.28% and 32.5% for parallel and series layouts. The deterioration exists around 20 Hz as well.

After evaluating both the performances of the train and rail system, both layouts with the inerter can benefit from the dynamic response in some level. And, we can find that the series layout is better than the parallel one. Inerters can attenuate vibration well when its natural frequency is under 10 Hz, while more vibration is introduced in a range of 10–40 Hz.

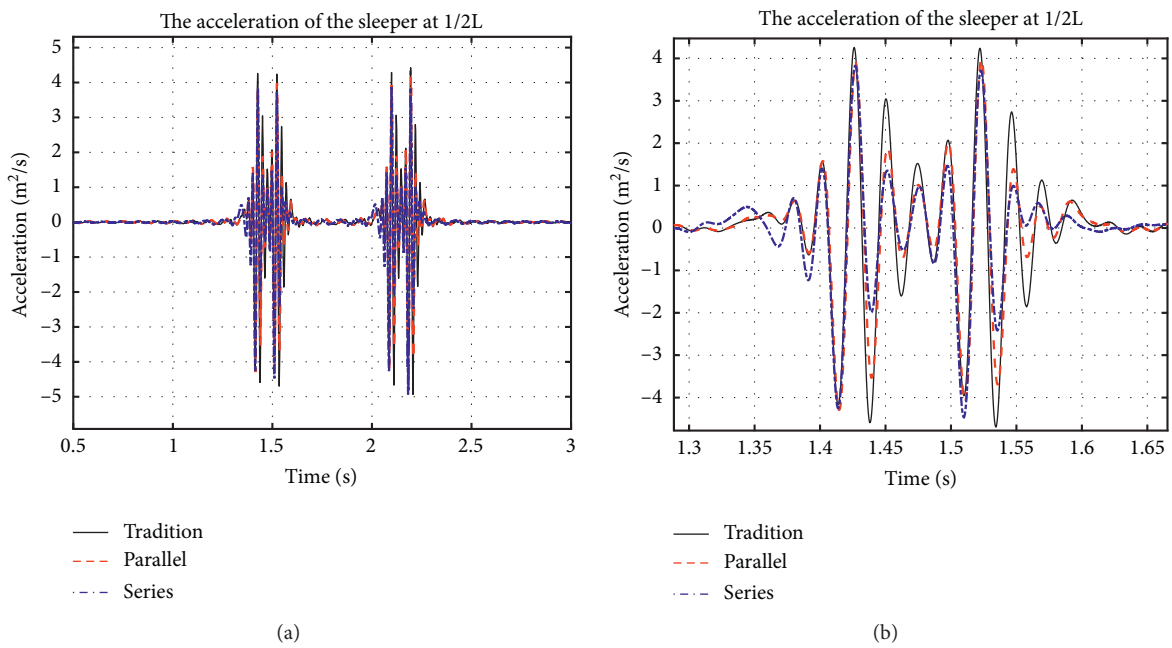

Figure 16: Acceleration of the sleeper at 1/2L. (a) The whole train runs over. (b) The front bogie runs over.

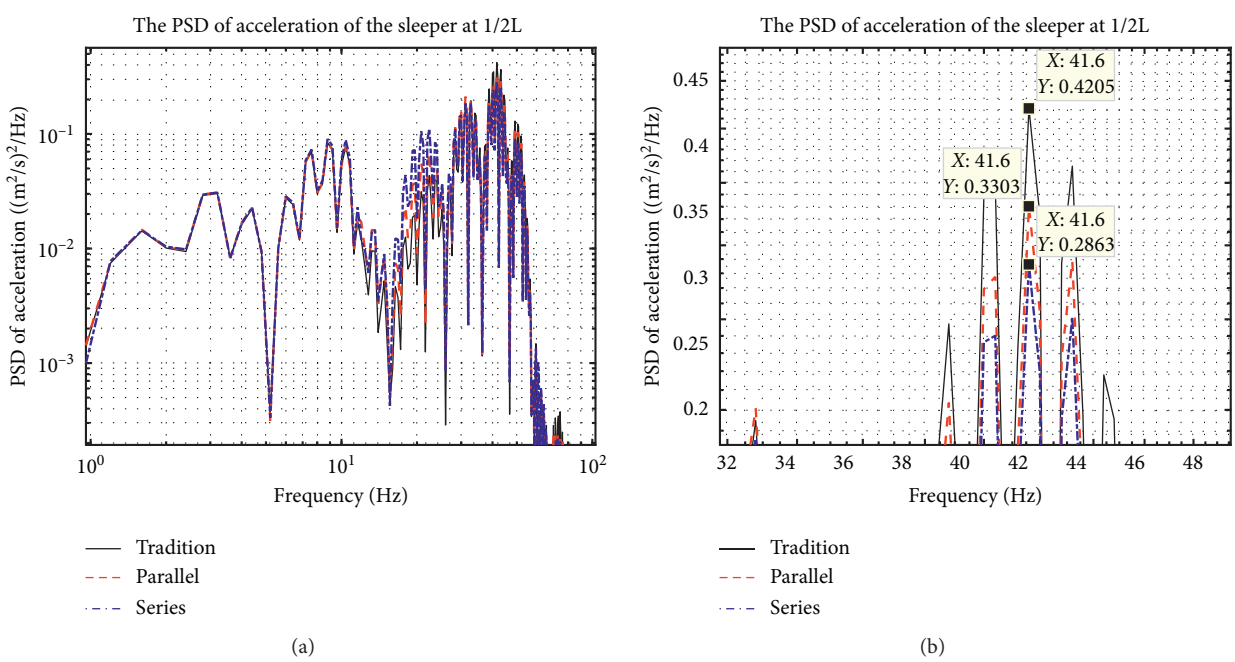

Figure 17: PSD of sleeper acceleration. (a) Range of 0–100 Hz. (b) Peaks at natural frequency.

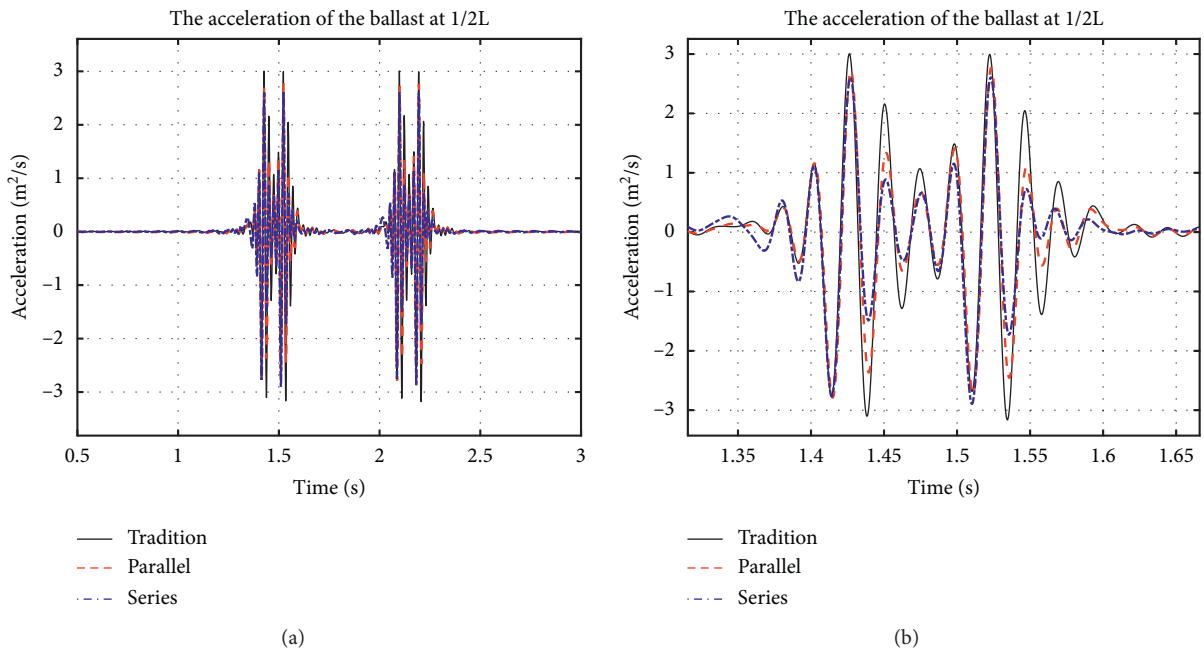

Figure 18: Acceleration of the ballast at 1/2L. (a) The whole train runs over. (b) The front bogie runs over.

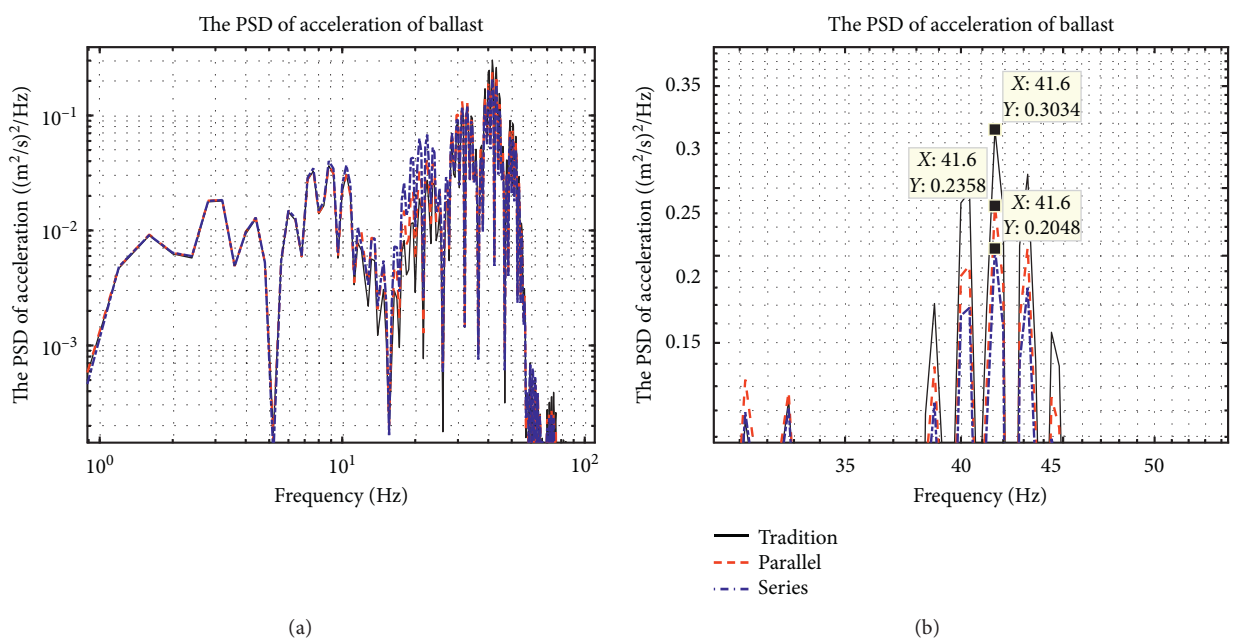

Figure 19: PSD of ballast acceleration. (a) Range of 0–100 Hz. (b) Peaks at natural frequency.

5. Conclusions

In this paper, vertical vibration performance of a rail-train coupling system is optimized and analysed with the introduction of inerters for both primary and secondary suspensions. The influence of the inerter for both the train and the rail system is discussed. The following conclusions can be drawn based on the obtained results.

(1) The inerter can be of benefit to both the typical Chinese passenger train and the traditional rail system with sleepers and ballast in their coupling system. 30.29% and 15.84% improvements are given in the train body acceleration and its pitch acceleration by the series layout. And, for the rail system, 6.19%, 20.24%, and 22.35% improvements are shown for the rail, sleeper, and ballast, respectively. This is of significant meaning for a ballast rail system. Serving period and maintaining consumption will be improved.

(2) The parallel and series connection layouts with the inerter are introduced and optimized by PSO. In the simulation of this study, the series layout shows a better performance in either amplitude attenuation or high frequency block aspects. The parallel layout gives a deterioration in the pitch acceleration of the train body.

(3) In this paper, inerters in both parallel and series layouts can attenuate vibration well in the range of 0–10 Hz, and the natural frequency of the train model lowered because of inerters. However, more noise is introduced in a range of 10–40 Hz for the train and around 20 Hz for the rail.

Two basic combinations of the inerters are discussed in this paper; for the future work, more complex but practical combination can be explored for better performance of the rail-train coupling system.

Appendix

Equations of the rail and train system with inerters:

Rail:

$$\begin{aligned}&\ddot{q}_k(t)+\sum_{i=1}^{N}C_{pi}Y_k(x_i)\sum_{h=1}^{MN}Y_h(x_i)\dot{q}_h(t)+\frac{EI}{m_r}\left(\frac{k\pi}{l}\right)^4 q_k(t)+\sum_{i=1}^{N}K_{pi}Y_k(x_i)\sum_{h=1}^{MN}Y_h(x_i)q_h(t)-\sum_{i=1}^{N}C_{pi}Y_k(x_i)\dot{Z}_{si}(t)\\&-\sum_{i=1}^{N}K_{pi}Y_k(x_i)Z_{si}(t)=\sum_{j=1}^{4}p_j(t)Y_k\left(x_{wj}\right),\quad (k=1\sim \mathrm{NM}).\end{aligned}\tag{A.1}$$

Sleeper:

$$\begin{aligned}&M_{si}\ddot{Z}_{si}(t)+\left(C_{pi}+C_{bi}\right)\dot{Z}_{si}(t)+\left(K_{pi}+K_{bi}\right)Z_{si}(t)-C_{bi}\dot{Z}_{bi}(t)-K_{bi}Z_{bi}(t)-C_{pi}\sum_{h=1}^{MN}Y_h(x_i)\dot{q}_h(t)\\&-K_{pi}\sum_{h=1}^{MN}Y_h(x_i)q_h(t)=0,\quad (i=1\sim N).\end{aligned}\tag{A.2}$$

Ballast:

$$\begin{aligned}&M_{bi}\ddot{Z}_{bi}(t)+\left(C_{bi}+C_{fi}+2C_{wi}\right)\dot{Z}_{bi}(t)+\left(K_{bi}+K_{fi}+2K_{wi}\right)Z_{bi}(t)-C_{bi}\dot{Z}_{si}(t)-K_{bi}Z_{si}(t)-C_{wi}\dot{Z}_{b(i+1)}(t)-K_{wi}Z_{b(i+1)}(t)\\&-C_{wi}\dot{Z}_{b(i-1)}(t)-K_{wi}Z_{b(i-1)}(t)=0,\quad (i=1\sim N).\end{aligned}\tag{A.3}$$

Train:

(1) 10 degrees of freedom with parallel connected inerters.

Body:

$$\begin{aligned} m_c\ddot{z}_c + 2B_{sz}\ddot{z}_c + 2C_{sz}\dot{z}_c + 2K_{sz}z_c - B_{sz}\ddot{z}_{t1} - B_{sz}\ddot{z}_{t2} - C_{sz}\dot{z}_{t1} - C_{sz}\dot{z}_{t2} - K_{sz}z_{t1} - K_{sz}z_{t2} = m_c g, \\ J_c\ddot{\beta}_c + 2B_{sz}l_c^2\ddot{\beta}_c + 2C_{sz}l_c^2\dot{\beta}_c + 2K_{sz}l_c^2\beta_c + B_{sz}l_c\ddot{z}_{t1} - B_{sz}l_c\ddot{z}_{t2} + C_{sz}l_c\dot{z}_{t1} - C_{sz}l_c\dot{z}_{t2} + K_{sz}l_cz_{t1} - K_{sz}l_cz_{t2} = 0. \end{aligned} \tag{A.4}$$

Bogies:

$$\begin{aligned} & m_t\ddot{z}_{t1} + \left(2B_{pz} + B_{sz}\right)\ddot{z}_{t1} + \left(2C_{pz} + C_{sz}\right)\dot{z}_{t1} + \left(2K_{pz} + K_{sz}\right)z_{t1} - B_{sz}\ddot{z}_c - B_{pz}\ddot{z}_{w1} - B_{pz}\ddot{z}_{w2} \\ & \quad - C_{sz}\dot{z}_c - C_{pz}\dot{z}_{w1} - C_{pz}\dot{z}_{w2} - K_{sz}z_c - K_{pz}z_{w1} - K_{pz}z_{w2} + B_{sz}l_c\ddot{\beta}_c + C_{sz}l_c\dot{\beta}_c + K_{sz}l_c\beta_c = m_t g, \\ & J_t\ddot{\beta}_{t1} + 2B_{pz}l_t^2\ddot{\beta}_{t1} + 2C_{pz}l_t^2\dot{\beta}_{t1} + 2K_{pz}l_t^2\beta_{t1} + B_{pz}l_t\ddot{z}_{w1} - B_{pz}l_t\ddot{z}_{w2} + C_{pz}l_t\dot{z}_{w1} - C_{pz}l_t\dot{z}_{w2} + K_{pz}l_tz_{w1} - K_{pz}l_tz_{w2} = 0, \\ & m_t\ddot{z}_{t2} + \left(2B_{pz} + B_{sz}\right)\ddot{z}_{t2} + \left(2C_{pz} + C_{sz}\right)\dot{z}_{t2} + \left(2K_{pz} + K_{sz}\right)z_{t2} - B_{sz}\ddot{z}_c - B_{pz}\ddot{z}_{w3} - B_{pz}\ddot{z}_{w4} \\ & \quad - C_{sz}\dot{z}_c - C_{pz}\dot{z}_{w3} - C_{pz}\dot{z}_{w4} - K_{sz}z_c - K_{pz}z_{w3} - K_{pz}z_{w4} - B_{sz}l_c\ddot{\beta}_c - C_{sz}l_c\dot{\beta}_c - K_{sz}l_c\beta_c = m_t g, \\ & J_t\ddot{\beta}_{t2} + 2B_zl_t^2\ddot{\beta}_{t2} + 2C_{pz}l_t^2\dot{\beta}_{t2} + 2K_{pz}l_t^2\beta_{t2} + B_{pz}l_t\ddot{z}_{w3} - B_{pz}l_t\ddot{z}_{w4} + C_{pz}l_t\dot{z}_{w3} - C_{pz}l_t\dot{z}_{w4} + K_{pz}l_tz_{w3} - K_{pz}l_tz_{w4} = 0. \end{aligned} \tag{A.5}$$

Wheelsets:

$$\begin{aligned} m_w\ddot{z}_{w1} + B_{pz}\ddot{z}_{w1} + C_{pz}\dot{z}_{w1} + K_{pz}z_{w1} - B_{pz}\ddot{z}_{t1} - C_{pz}\dot{z}_{t1} - K_{pz}z_{t1} + B_{pz}l_t\ddot{\beta}_{t1} + C_{pz}l_t\dot{\beta}_{t1} + K_{pz}l_t\beta_{t1} = m_w g - P_1, \\ m_w\ddot{z}_{w2} + B_{pz}\ddot{z}_{w2} + C_{pz}\dot{z}_{w2} + K_{pz}z_{w2} - B_{pz}\ddot{z}_{t1} - C_{pz}\dot{z}_{t1} - K_{pz}z_{t1} - B_{pz}l_t\ddot{\beta}_{t1} - C_{pz}l_t\dot{\beta}_{t1} - K_{pz}l_t\beta_{t1} = m_w g - P_2, \\ m_w\ddot{z}_{w3} + B_{pz}\ddot{z}_{w3} + C_{pz}\dot{z}_{w3} + K_{pz}z_{w3} - B_{pz}\ddot{z}_{t2} - C_{pz}\dot{z}_{t2} - K_{pz}z_{t2} + B_{pz}l_t\ddot{\beta}_{t2} + C_{pz}l_t\dot{\beta}_{t2} + K_{pz}l_t\beta_{t2} = m_w g - P_3, \\ m_w\ddot{z}_{w4} + B_z\ddot{z}_{w4} + C_{pz}\dot{z}_{w4} + K_{pz}z_{w4} - B_{pz}\ddot{z}_{t2} - C_{pz}\dot{z}_{t2} - K_{pz}z_{t2} - B_{pz}l_t\ddot{\beta}_{t2} - C_{pz}l_t\dot{\beta}_{t2} - K_{pz}l_t\beta_{t2} = m_w g - P_4. \end{aligned} \tag{A.6}$$

(2) 16 degrees of freedom with the inerter connected in series with the damper.

Body:

$$\begin{aligned} m_c\ddot{z}_c + 2B_{sz}\ddot{z}_c + 2K_{sz}z_c - B_{sz}\ddot{z}_{s1} - B_{sz}\ddot{z}_{s2} - K_{sz}z_{t1} - K_{sz}z_{t2} = m_c g, \\ J_c\ddot{\beta}_c + 2B_{sz}l_c^2\ddot{\beta}_c + 2K_{sz}l_c^2\beta_c + B_{sz}l_c\ddot{z}_{s1} - B_{sz}l_c\ddot{z}_{s2} + K_{sz}l_cz_{t1} - K_{sz}l_cz_{t2} = 0. \end{aligned} \tag{A.7}$$

Bogies:

$$\begin{aligned} m_t\ddot{z}_{t1} + 2B_{pz}\ddot{z}_{t1} + \left(2K_{pz} + K_{sz}\right)z_{t1} - B_{pz}\ddot{z}_{z1} - B_{pz}\ddot{z}_{z2} - C_{sz}\dot{z}_{s1} + C_{pz}\dot{z}_{t1} - K_{sz}z_c - K_{pz}z_{w1} - K_{pz}z_{w2} + K_{sz}l_c\beta_c = m_t g, \\ J_t\ddot{\beta}_{t1} + 2B_{pz}l_t^2\ddot{\beta}_{t1} + 2K_{pz}l_t^2\beta_{t1} + B_{pz}l_t\ddot{z}_{z1} - B_{pz}l_t\ddot{z}_{z2} + K_{pz}l_tz_{w1} - K_{pz}l_tz_{w2} = 0, \\ m_t\ddot{z}_{t2} + 2B_{pz}\ddot{z}_{t2} + \left(2K_{pz} + K_{sz}\right)z_{t2} - B_{pz}\ddot{z}_{z3} - B_{pz}\ddot{z}_{z4} - C_{sz}\dot{z}_{s2} + C_{pz}\dot{z}_{t2} - K_{sz}z_c - K_{pz}z_{w3} - K_{pz}z_{w4} - K_{sz}l_c\beta_c = m_t g, \\ J_t\ddot{\beta}_{t2} + 2B_{pz}l_t^2\ddot{\beta}_{t2} + 2K_{pz}l_t^2\beta_{t2} + B_{pz}l_t\ddot{z}_{z3} - B_{pz}l_t\ddot{z}_{z4} + K_{pz}l_tz_{w3} - K_{pz}l_tz_{w4} = 0. \end{aligned} \tag{A.8}$$

Wheelsets:

$$\begin{aligned}
m_w\ddot{z}_{w1} + C_{pz}\dot{z}_{w1} + K_{pz}z_{w1} - C_{pz}\dot{z}_{z1} - K_{pz}z_{t1} + K_{pz}l_t\beta_{t1} &= m_w g - P_1,\\
m_w\ddot{z}_{w2} + C_{pz}\dot{z}_{w2} + K_{pz}z_{w2} - C_{pz}\dot{z}_{z2} - K_{pz}z_{t1} - K_{pz}l_t\beta_{t1} &= m_w g - P_2,\\
m_w\ddot{z}_{w3} + C_{pz}\dot{z}_{w3} + K_{pz}z_{w3} - C_{pz}\dot{z}_{z3} - K_{pz}z_{t2} + K_{pz}l_t\beta_{t2} &= m_w g - P_3,\\
m_w\ddot{z}_{w4} + C_{pz}\dot{z}_{w4} + K_{pz}z_{w4} - C_{pz}\dot{z}_{z4} - K_{pz}z_{t2} - K_{pz}l_t\beta_{t2} &= m_w g - P_4.
\end{aligned} \tag{A.9}$$

Extra freedom between the damper and inerter in the suspension (Z_{si} represents the extra freedom between the damper and inerter in the ith secondary suspension; and, Z_{zi} represents the extra freedom between the damper and inerter in the jth primary suspension):

$$\begin{aligned}
B_{sz}\ddot{z}_{s1} - B_{sz}\ddot{z}_c + B_{sz}l_c\ddot{\beta}_c + C_{sz}\dot{z}_{s1} - C_{sz}\dot{z}_{t1} &= 0,\\
B_{sz}\ddot{z}_{s2} - B_{sz}\ddot{z}_c - B_{sz}l_c\ddot{\beta}_c + C_{sz}\dot{z}_{s2} - C_{sz}\dot{z}_{t2} &= 0,\\
B_{pz}\ddot{z}_{z1} - B_{pz}\ddot{z}_{t1} + B_{pz}l_t\ddot{\beta}_{t1} + C_{pz}\dot{z}_{z1} - C_{pz}\dot{z}_{w1} &= 0,\\
B_{pz}\ddot{z}_{z2} - B_{pz}\ddot{z}_{t1} - B_{pz}l_t\ddot{\beta}_{t1} + C_{pz}\dot{z}_{z2} - C_{pz}\dot{z}_{w2} &= 0,\\
B_{pz}\ddot{z}_{z3} - B_{pz}\ddot{z}_{t2} + B_{pz}l_t\ddot{\beta}_{t2} + C_{pz}\dot{z}_{z3} - C_{pz}\dot{z}_{w3} &= 0,\\
B_{pz}\ddot{z}_{z4} - B_{pz}\ddot{z}_{t2} - B_{pz}l_t\ddot{\beta}_{t2} + C_{pz}\dot{z}_{z4} - C_{pz}\dot{z}_{w4} &= 0.
\end{aligned} \tag{A.10}$$

Data Availability

The data used to support the findings of this study are available from the corresponding author upon request.

Conflicts of Interest

The authors declare that they have no conflicts of interest.

Acknowledgments

This work was supported by the National Nature Science Foundation under Grant 62063011, Science and Technology Program of Science and Technology Department of Yunnan Province under Grant 202001AU070032, Scientific Research Fund of Yunnan Education Department under Grant 2019J0046, and Scientific Research Initial Fund for Introduction of Talent of Kunming University of Science and Technology under Grant KKSY201801019.

References

[1] H. Magalhães, J. Pombo, J. Ambrósio, and J. F. A. Madeira, "Rail vehicle design optimization for operation in a mountainous railway track," *Innovative Infrastructure Solutions*, vol. 2, no. 1, pp. 2–7, 2017.

[2] P. P. Wang, Y. Yang, B. Yi, W. Zeng, and T. Wang, "Robust optimization of high-speed rail vehicle suspension parameters based on vertical running stability," *Journal of the Chinese Society of Mechanical Engineers*, vol. 40, no. 6, pp. 583–593, 2019.

[3] W. Liu, Y. Yang, P. Wang, X. Chen, and X. Wei, "Metamodel-based robust collaborative optimization for the suspension parameters of rail vehicles," *Journal of the Chinese Institute of Engineers*, vol. 42, no. 8, pp. 643–652, 2019.

[4] Y. He and J. McPhee, "Optimization of curving performance of rail vehicles," *Vehicle System Dynamics*, vol. 43, no. 12, pp. 895–923, 2005.

[5] P. Wang, X. Ma, J. Wang, J. Xu, and R. Chen, "Optimization of rail profiles to improve vehicle running stability in switch panel of high-speed railway turnouts," *Mathematical Problems in Engineering*, vol. 2017, Article ID 2856030, 13 pages, 2017.

[6] C. Dullinger, W. Struckl, and M. Kozek, "Simulation-based multi-objective system optimization of train traction systems," *Simulation Modelling Practice and Theory*, vol. 72, 2017.

[7] X. Sun, L. Chen, S. Wang, and X. Zhang, "Research on performance benefits in railway vehicle suspension employing inerter," *Journal of The China Railway Society*, vol. 39, no. 2, pp. 32–38, 2017.

[8] Y. He and J. McPhee, "Design optimization of rail vehicles with passive and active suspensions: a combined approach using genetic algorithms and multibody dynamics," *Vehicle System Dynamics*, vol. 37, no. 1, pp. 397–408, 2002.

[9] J. Huang, Y. Cao, and Y. W. Wang, "Adaptive proxy-based sliding mode control for a class of second-order nonlinear systems and its application to pneumatic muscle actuators," *ISA Transactions*, 2020.

[10] J. Huang, S. Ri, T. Fukuda, and Y. Wang, "A disturbance observer based sliding mode control for a class of underactuated robotic system with mismatched uncertainties,"

IEEE Transactions on Automatic Control, vol. 64, no. 6, pp. 2480–2487, 2019.

[11] J. Huang, M. Ri, D. Wu, and S. Ri, "Interval type-2 fuzzy logic modeling and control of a mobile two-wheeled inverted pendulum," *IEEE Transactions on Fuzzy Systems*, vol. 26, no. 4, pp. 2030–2038, 2018.

[12] D. Wu, C.-T. Lin, J. Huang, and Z. Zeng, "On the functional equivalence of TSK fuzzy systems to neural networks, mixture of experts, CART, and stacking ensemble regression," *IEEE Transactions on Fuzzy Systems*, vol. 28, no. 10, pp. 2570–2580, 2020.

[13] M. C. Smith, "Synthesis of mechanical networks: the inerter," *IEEE Transactions on Automatic Control*, vol. 47, no. 10, pp. 1648–1662, 2002.

[14] M. C. Smith and F. C. Wang, "Performance benefits in passive vehicle suspensions employing inerters," *Vehicle System Dynamics*, vol. 42, no. 3, pp. 235–257, 2004.

[15] A. Javidialesaadi and N. E. Wierschem, "An inerter-enhanced nonlinear energy sink," " *Mechanical Systems and Signal Processing*, vol. 129, pp. 449–454, 2019.

[16] W. M. Kuhnert, P. J. P. Gonçalves, D. F. Ledezma-Ramirez, and M. J. Brennan, "Inerter-like devices used for vibration isolation: a historical perspective," *Journal of the Franklin Institute*, vol. 358, no. 1, pp. 1070–1086, 2021.

[17] F. C. Wang, Y. C. Chen, and C. H. Lee, "Design and optimization of inerter layouts for a multi-layer building model," *SICE*, vol. 4, pp. 1076–1081, 2016.

[18] F.-C. Wang, M.-K. Liao, B.-H. Liao, W.-J. Su, and H.-A. Chan, "The performance improvements of train suspension systems with mechanical networks employing inerters," *Vehicle System Dynamics*, vol. 47, no. 7, pp. 805–830, 2009.

[19] F.-C. Wang and M.-K. Liao, "The lateral stability of train suspension systems employing inerters," *Vehicle System Dynamics*, vol. 48, no. 5, pp. 619–643, 2010.

[20] F.-C. Wang, M.-R. Hsieh, and H.-J. Chen, "Stability and performance analysis of a full-train system with inerters," *Vehicle System Dynamics*, vol. 50, no. 4, pp. 545–571, 2012.

[21] J. Z. Jiang, A. Z. Matamoros-Sanchez, A. Zolotas, R. M. Goodall, and M. C. Smith, "Passive suspensions for ride quality improvement of two-axle railway vehicles," *Proceedings of the Institution of Mechanical Engineers, Part F: Journal of Rail and Rapid Transit*, vol. 229, no. 3, pp. 315–329, 2015.

[22] J. Z. Jiang, A. Z. Matamoros-Sanchez, R. M. Goodall, and M. C. Smith, "Passive suspensions incorporating inerters for railway vehicles," *Vehicle System Dynamics*, vol. 50, pp. 263–276, 2012.

[23] W. M. Zhai, *Vehicle–Track Coupled Dynamics*, Science Press and Springer Nature Singapore Pte Ltd, Singapore, 2020.

[24] S. Timoshenko, D. H. Young, and W. Weaver Jr., *Vibration Problems in Engineering*, Wiley, Hoboken, NJ, USA, 4th ed edition, 1974.

[25] H. H. Jenkins, J. E. Stephenson, and G. A. Clayton, "The effect of track and vehicle parameters on wheel/rail vertical dynamic forces," *Railway Engineering Journal*, vol. 3, no. 1, pp. 2–16, 1974.

[26] H. Katsu, *Random Vibration Analysis*, Seismological Press, Beijing, China, 1977.

[27] W. M. Zhai, "Two simple fast integration methods for large-scale dynamic problems in engineering," *International Journal for Numerical Methods in Engineering*, vol. 39, no. 24, pp. 199–214, 1996.

Hindawi
Complexity
Volume 2021, Article ID 6660857, 14 pages
https://doi.org/10.1155/2021/6660857

Research Article

Robust H_∞ Feedback Compensator Design for Linear Parabolic DPSs with Pointwise/Piecewise Control and Pointwise/Piecewise Measurement

Liu Yaqiang,[1] **Ren Zhigang**,[2] **and Jin Zengwang**[3,4]

[1]*School of Automation and Guangdong-HongKong-Macao Joint Laboratory for Smart Discrete Manufacturing, Guangdong University of Technology, Guangzhou, Guangdong 510006, China*
[2]*School of Automation and Guangdong Discrete Manufacturing KnowledgeAutomation Engineering Technology Research Center, Guangdong University of Technology, Guangzhou, Guangdong 510006, China*
[3]*School of Cybersecurity, Northwestern Polytechnical University, Xi'an, Shanxi 710072, China*
[4]*National Engineering Laboratory for Integrated Aero-Space-Ground-Ocean Big Data Application Technology, Xi'an, Shanxi 710072, China*

Correspondence should be addressed to Jin Zengwang; jin_zengwang@nwpu.edu.cn

Received 19 November 2020; Revised 19 February 2021; Accepted 24 March 2021; Published 12 April 2021

Academic Editor: Xue-bo Jin

In this paper, a robust H_∞ control problem of a class of linear parabolic distributed parameter systems (DPSs) with pointwise/piecewise control and pointwise/piecewise measurement has been investigated via the robust H_∞ feedback compensator design approach. A unified Lyapunov direct approach is proposed in consideration of the pointwise/piecewise control and point/piecewise measurement based on the distributions of the actuators and sensors. A new type of Luenberger observer is developed on the continuous interval of space domain to track the state of the system, and an H_∞ performance constraint with prescribed H_∞ attenuation levels is proposed in this paper. By utilizing Lyapunov technique, mathematical inequalities, and integration theory, a sufficient condition based on LMI for the exponential stability of the corresponding closed-loop coupled system under an H_∞ performance constraint is presented. Finally, the effectiveness of the proposed design method is verified by numerical simulation results.

1. Introduction

Distributed parameter systems (DPSs) are infinite-dimensional in nature and are generally modeled by partial differential equations (PDEs). DPSs are widely used in engineering systems [1–4], such as thermodynamics, chemical engineering, missile, aerospace, aviation, and nuclear fission and fusion. Control problem of DPSs has attracted extensive attention due to the important applications in engineering systems, such as the vibration control of flexible structures that the vibration process can be described by Euler–Bernoulli equations, the diffusion control of oil spill that the diffusion phenomena can be described by diffusion equations, and the temperature control of heating furnace that the thermal conduction process can be described by heat equations. In recent decades, fruitful achievements in the design of DPSs control have been achieved from many scholars all over the world [5–17].

Generally, control forms of DPSs can be divided into boundary control and in-domain control based on the actuators' location. Fruitful achievements on boundary control of DPSs that the actuators are located at the boundary area have been published already. For example, the boundary control problem of flexible robot manipulators has been developed to solve the DPSs with flexible structures [18–20]. This technique has been extended to the boundary anti-disturbance control and boundary adaptive robust control for flexible DPSs [21–23]. Boundary control of $1D$ nonlinear

parabolic DPSs has been studied in [24], in which the continuum backstepping method is utilized. Boundary feedback control of DPSs has been addressed in [25], and a novel combination of feedback idea and backstepping approach is presented in [26]. Sampled-data boundary control and sliding mode boundary control of DPSs have been studied in [27, 28], where a sampled-data strategy for the boundary control problem is proposed. Fuzzy boundary control based on the T-S fuzzy DPS model is shown in [29, 30]. H_∞ boundary control has been proposed in [31] that a linear matrix inequality (LMI) approach has been utilized. Meanwhile, there are also some achievements on in-domain control of DPSs. For example, pointwise control of DPSs with T-S fuzzy DPS model has been developed in [32], where a fuzzy state feedback controller is designed. Furthermore, this technique has been extended to the [33, 34]. Robust sampled-data control has been proposed in [35, 36], where the sampled-data pointwise controller method is applied. Mobile piecewise control of $1D$ DPSs has been studied in [37] that a mobile actuator-plus-sensor network is developed, and this technique has been extended to solve the $2D$ DPSs in [38]. More recently, collocated control and noncollocated control of in-domain control in DPSs have been studied deeply. Static collocated feedback control has been presented in [39, 40] that the static collocated pointwise and piecewise feedback controller has been designed for parabolic DPSs. For the noncollocated control that the actuators and sensors can never be placed at the same location exactly, the static feedback control has been studied in [32, 36, 41, 42], and the observer-based dynamic feedback control has been designed in [43–47]. The estimation problems in controller design of DPSs have been studied in [48–53], and for some DPSs with unknown parameters, parameter estimation methods have been applied in [54–58].The design and analysis methods have also been extended to switched control systems and filtering technique in [59–62]. Although there have been many promising efforts, there are still many control problems of DPSs need to be studied in the future.

In general, disturbance problems of DPSs are unavoidable because of the errors from model calculations and equipments. Thus, an approach of robust H_∞ control is proposed to deal with the control problem of DPSs with external disturbances. The robust H_∞ control has attracted much attention from many scholars over the past few decades. For example, an H_∞ static output feedback boundary controller for semilinear parabolic and hyperbolic DPSs is proposed in [31]. This idea has extended to solve the sampled-data distributed H_∞ control problem for a class of parabolic DPSs in [35]. An H_∞ fuzzy observer-based controller is proposed for a class of nonlinear parabolic DPSs in [63], and this technique has developed to the observer-based H_∞ sampled-data fuzzy control design in [46, 64] and mixed H_2/H_∞ fuzzy observer-based feedback control design in [65]. In this paper, we will extend the works in [66, 67] to design the H_∞ output feedback compensator for linear parabolic DPSs with external disturbances by using a unified Lyapunov approach. A sufficient condition for the static H_∞ feedback compensator can stabilize the DPSs under an H_∞ performance constraint with the collocated observation case which is first proposed in terms of standard linear matrix inequalities (LMIs); then, another sufficient condition for the observer-based dynamic H_∞ feedback compensator can stabilize the DPSs under an H_∞ performance constraint with the noncollocated observation case which is developed by using the Lyapunov direct method, Poincaré–Wirtinger inequality's variants, Cauchy–Schwartz inequality, integration by parts, and first mean value theorem for definite integrals.

The main contributions and novelty of this paper compared with the existing works before are summarized as follows:

(i) Different from the results in [32–34, 43, 44] that the pointwise/piecewise control and collocated (or noncollocated) pointwise/piecewise measurement are discussed separately, all the forms of control and observation are considered in this paper by a unified Lyapunov direct approach.

(ii) In contrast to the works in [66] that a unified Lyapunov-based compensator design for linear parabolic DPSs with free disturbance, this paper presents the static and dynamic robust H_∞ output feedback compensator design for linear DPSs with external disturbances. Meanwhile, a new type of Luenberger observer is designed for noncollocated observation in space with continuous observation functions.

(iii) An H_∞ performance constraint in the sense of $|\cdot|_2$ is proposed to deal with the external disturbance of the model and measurement disturbance in the measurement output.

The organizational structure of the remaining parts of this paper is arranged as follows: first, the problem formulation of this paper and some preliminary knowledge are presented in Section 2. Then, the static output feedback compensator design and observer-based dynamic output feedback compensator design in terms of collocated and noncollocated observation in space satisfying the H_∞ performance constraint are shown in Section 3. Section 4 provides some numerical simulation results of the corresponding closed-loop systems to show the effectiveness of the proposed design method. Finally, brief conclusions are followed in Section 5.

Notation: $\mathfrak{R}$, $\mathfrak{R}^m$, and $\mathfrak{R}^{m\times n}$ denote the set of all real numbers, m-dimensional Euclidean space, and the set of all $m\times n$ matrices, respectively. $\mathscr{H}\triangleq\mathscr{L}^2([0,L])$ is a real Hilbert space of square integrable functions with the inner product induced norm $|\cdot|_2$. $\mathscr{L}^2([0,\infty];\mathscr{H})$ is a real Hilbert space of square integrable functions $\varpi(\cdot,t)$ with $\|\varpi\|_{\mathscr{L}_2}\triangleq\int_0^\infty|\varpi(\cdot,t)|_2\,\mathrm{d}t$. $\mathscr{L}^2([0,\infty];\mathfrak{R}^n)$ is a real Hilbert space of square integrable functions $\zeta(t)$ with $\|\zeta\|_{\mathscr{L}_2}\triangleq\int_0^\infty\|\zeta(t)\|\mathrm{d}t$. $u_t(z,t)$ stands for the partial derivative of $u(z,t)$ with respect to t, i.e., $u_t(z,t)=\partial u(z,t)/\partial t$, $u_z(z,t)$, and $u_{zz}(z,t)$ stands for the first-order and second-order partial derivative of $u(z,t)$ with respect to z, i.e., $u_z(z,t)=\partial u(z,t)/\partial z$, $u_{zz}(z,t)=\partial^2 u(z,t)/\partial z^2$, respectively. $\mathscr{M}$ and $\mathscr{N}$ denote two sets of natural numbers, i.e., $\mathscr{M}\triangleq\{1,2,\ldots,m\}$, $\mathscr{N}\triangleq\{1,2,\ldots,n\}$.

2. Problem Formulation and Preliminaries

In this paper, we consider a class of one-dimensional linear parabolic DPSs with external disturbances of the following form:

$$\begin{cases} u_t(z,t) = u_{zz}(z,t) + \eta u(z,t) + d(z,t) \\ +\mathbf{h}^T(z)\mathbf{U}(t), \quad z \in (0,L), \\ \mathbf{y}(t) = \int_0^L \mathbf{s}(z)u(z,t)\mathrm{d}z + \boldsymbol{\omega}(t), \end{cases} \tag{1}$$

subject to the Robin boundary conditions in one dimension,

$$\begin{aligned} u_z(z,t)|_{z=0} &= a_1 u(0,t), \\ u_z(z,t)|_{z=L} &= -a_2 u(L,t), \end{aligned} \tag{2}$$

and the initial condition,

$$u(z,0) = u_0(z), \quad z \in [0,L], \tag{3}$$

where $z \in [0,L] \subset \mathfrak{R}$ denotes the spatial position between $[0,L]$, and $t \geq 0$ denotes time, respectively. $u(\cdot,t) \triangleq \{u(z,t), z \in [0,L]\} \in \mathscr{H}$, denotes the state variable. $\eta > 0$ is a known constant. $d(\cdot,\cdot) \triangleq \{d(z,t), z \in [0,L]\} \in \mathscr{L}^2([0,\infty],\mathscr{H})$ is an unknown bounded external disturbance and satisfies $\int_0^\infty |d(\cdot,t)|_2^2 \mathrm{d}t < \infty$. $\mathbf{h}(z) \triangleq [\, h(z) \;\; h_2(z) \cdots h_m(z)]^T \in \mathfrak{R}^m$ is a known integrable vector function of z, and the element $h_i(z)$ describes the distribution of i-th actuator on the spatial domain $[0,L]$. $\mathbf{U}(t)$ is a set of control inputs from m actuators, expressed as $\mathbf{U}(t) \triangleq [\, u_1(t) \;\; u_2(t) \;\; \cdots \;\; u_m(t)\,]^T \in \mathfrak{R}^m$. $\mathbf{y}(t)$ is a set of measurement outputs from n sensors, expressed as $\mathbf{y}(t) \triangleq [\, y_1(t) \;\; y_2(t) \;\; \cdots \;\; y_n(t)\,]^T \in \mathfrak{R}^n$. $\mathbf{s}(z) \triangleq [\, s_1(z) \;\; s_2(z) \cdots s_n(z)]^T \in \mathfrak{R}^n$ is a known integrable vector function of z, and the element $s_j(z)$ describes the distribution of j-th sensor on the spatial domain $[0,L]$. $\omega(\cdot) \triangleq [\, \omega_1(t) \;\; \omega_2(t) \;\; \cdots \;\; \omega_n(t)\,]^T \in \mathscr{L}^2([0,\infty];\mathfrak{R}^n)$ is the n-dimensional bounded measurement disturbance vector. It should be pointed out that when $\eta > 0.25\pi^2 L^{-2}$, the one-dimensional linear parabolic DPSs is unstable.

Remark 1. It is worth noting that equation (1) is equivalent to the following general form [68]:

$$\begin{aligned} \overline{u}_t(z,t) = {} & \overline{u}_{zz}(z,t) + 2f_z(z,t)\overline{u}_z(z,t) \\ & + \left(\eta + f_z^2(z,t) + f_{zz}(z,t) - f_t(z,t)\right)\overline{u}(z,t) \\ & + d(z,t) + \overline{h}^T(z)\overline{U}(t), \quad z \in (0,L), \end{aligned} \tag{4}$$

through the conversion of the following state variables and control variables:

$$\begin{cases} f(z,t) = f_1(z) + f_2(t), \\ \overline{u}(z,t) = \exp(-f(z,t))u(z,t), \\ \overline{\mathbf{h}}^T(z) = \exp(-f_1(z))\mathbf{h}^T(z), \\ \overline{\mathbf{U}}(t) = \exp(-f_2(t))\mathbf{U}(t), \end{cases} \tag{5}$$

where $f(\cdot,t) \triangleq \{f(z,t)\} \in \mathscr{H}^2(0,L)$ is a known scalar function and continuously differentiable in time t.

In practical applications of DPSs, the number of actuators and sensors is usually limited and actives at specified point or part thereof in the spatial domain, respectively. Therefore, the in-domain control forms of DPSs are generally divided into pointwise control and local piecewise control according to the distribution of actuators. In this paper, two forms of in-domain control are both considered; the actuators' spatial distribution functions $h_i(z)$ are described as follows:

$$h_i(z) \triangleq \delta(z - \overline{z}_i), \quad i \in \mathscr{M} \text{ (pointwise control case)}, \tag{6}$$

$$h_i(z) \triangleq \begin{cases} 1 & z \in [\overline{z}_i^-, \overline{z}_i^+] \\ 0 & \text{elsewhere} \end{cases}, \quad i \in \mathscr{M} \text{ (local piecewise control case)}, \tag{7}$$

where $\delta(\cdot)$ is the Dirac delta function [69]. The points $\overline{z}_i, i \in \mathscr{M}$, and local subdomains $[\overline{z}_i^-, \overline{z}_i^+], i \in \mathscr{M}$, satisfy $0 < \overline{z}_1 < \overline{z}_2 < \cdots < \overline{z}_m < L$ and $0 < \overline{z}_1^- < \overline{z}_1^+ < \overline{z}_2^- < \overline{z}_2^+ < \cdots < \overline{z}_m^- < \overline{z}_m^+ < L$, which imply the chosen functions $g_i(z), i \in \mathscr{M}$, produce pointwise control at the points $\overline{z}_i$ and local piecewise uniform control over $[\overline{z}_i^-, \overline{z}_i^+]$, respectively. Meanwhile, the spatial domain $[0,L]$ can be divided into m parts by a spatial domain decomposition approach that $0 = z_1 < z_2 \cdots < z_{m+1} = L$. The locations of the actuators for pointwise control and local piecewise control satisfy the relationships $\overline{z}_i \in (z_i, z_{i+1}), i \in \mathscr{M}$, and $[\overline{z}_i^-, \overline{z}_i^+] \subset (z_i, z_{i+1})$, $i \in \mathscr{M}$.

Similar to the actuators' distribution, the in-domain observation forms are generally divided into pointwise measurement and local piecewise measurement; the sensors' spatial distribution functions $s_j(z), j \in \mathscr{N}$ are described in this paper as follows:

$$s_j(z) \triangleq \delta(z - \widetilde{z}_j), \quad j \in \mathscr{N} \text{ (pointwise measurement case)}, \tag{8}$$

$$s_j(z) \triangleq \begin{cases} 1 & z \in [\widetilde{z}_j^-, \widetilde{z}_j^+] \\ 0 & \text{elsewhere} \end{cases}, \quad j \in \mathscr{N} \text{ (local piecewise measurement case)}. \tag{9}$$

The points $\tilde{z}_j, j \in \mathcal{N}$, and local subdomains $[\tilde{z}_j^-, \tilde{z}_j^+], j \in \mathcal{N}$ satisfy $0 < \tilde{z}_1 < \tilde{z}_2 < \cdots < \tilde{z}_n < L$ and $0 < \tilde{z}_1^- < \tilde{z}_1^+ < \tilde{z}_2^- < \tilde{z}_2^+ < \cdots < \tilde{z}_n^- < \tilde{z}_n^+ < L$, which imply the chosen functions $c_j(z), j \in \mathcal{N}$ produce pointwise observation at the points $\tilde{z}_j$ and local piecewise uniform observation over $[\tilde{z}_j^-, \tilde{z}_j^+]$, respectively. At the same time, the spatial domain $[0, L]$ can be divided into n parts by a spatial domain decomposition approach that $0 = \hat{z}_1 < \hat{z}_2 \cdots < \hat{z}_{n+1} = L$. The locations of the sensors for pointwise measurement and local piecewise measurement satisfy the relationships $\tilde{z}_j \in (z_j, z_{j+1}), j \in \mathcal{N}$ and $[\tilde{z}_j^-, \tilde{z}_j^+] \subset (\hat{z}_j, \hat{z}_{j+1}), j \in \mathcal{N}$.

For the linear parabolic DPS (1)–(3), the following H_∞ performance constraint is proposed under the zero initial condition $u_0(\cdot) = 0$:

$$\int_0^\infty |u(\cdot,t)|_2^2 \mathrm{d}t \le \gamma_1^2 \int_0^\infty |d(\cdot,t)|_2^2 \mathrm{d}t + \gamma_2^2 \int_0^\infty \|\boldsymbol{\omega}(t)\|^2 \mathrm{d}t, \tag{10}$$

where $\gamma_1 > 0$ and $\gamma_2 > 0$ are the prescribed H_∞ attenuation levels.

For the development of stability analysis in this paper, two exponential stability definitions in the sense of $|\cdot|_2$ of the linear parabolic DPS (1)–(3) are defined.

Definition 1. The linear parabolic DPS (1)–(3) with $\mathbf{U}(t) = 0$ and $d(\cdot,t) = 0$ is exponentially stable in the sense of $|\cdot|_2$, when there exist two constants $\varepsilon_1 \ge 1$ and $\varepsilon_2 > 0$ satisfying the expression $|u(\cdot,t)|_2 \le \varepsilon_1 |u_0(\cdot)|_2 \exp(-\varepsilon_2 t)$ for any $t \ge 0$.

Definition 2. The linear parabolic DPS (1)–(3) with the designed output feedback compensator is exponentially stable in the sense of $|\cdot|_2$ under an H_∞ performance constraint, when the corresponding closed-loop DPS with $d(\cdot,t) = 0$ and $\omega(t) = 0$ is exponentially stable in the sense of $|\cdot|_2$; meanwhile, the H_∞ performance constraint in (10) is ensured when the initial value of $u(z,t)$ is zero ($u_0(z) = 0$) and all $d(\cdot,\cdot) \in \mathcal{L}_2(0,\infty;\mathcal{H}), \omega(\cdot) \in \mathcal{L}_2(0,\infty;\mathfrak{R}^n)$.

The following lemmas are very useful for the development of the robust H_∞ compensator design in this paper.

Lemma 1 (Poincaré–Wirtinger inequality's variants). *For a scalar function $u \in \mathcal{H}^1(0,L)$, we have*

$$\begin{aligned} &\int_0^L (u(s) - u(z))^2 \mathrm{d}s \le 4\tau_1 \pi^{-2} \int_0^L \left(\frac{\mathrm{d}u(s)}{\mathrm{d}s}\right)^2 \mathrm{d}s, \\ &\int_0^L (u(s) - u_l)^2 \mathrm{d}s \le 4\tau_2 \pi^{-2} \int_0^L \left(\frac{\mathrm{d}u(s)}{\mathrm{d}s}\right)^2 \mathrm{d}s, \end{aligned} \tag{11}$$

where $z \in [0,L]$, $\tau_1 \triangleq \max\{z^2, (L-z)^2\}$, $u_l \triangleq (z_2 - z_1)^{-1} \int_{z_1}^{z_2} u(z)\mathrm{d}z$, $[z_1, z_2] \subset [0,L]$, and $\tau_2 \triangleq \max\{z_2^2, (L-z_1)^2\}$. For more detailed details, please refer to the lemma in [66].

Lemma 2 *(Cauchy–Schwartz inequality [70]). For any two scalar functions $\vartheta_1 \in \mathcal{H}^1(0,L)$ and $\vartheta_2 \in \mathcal{H}^1(0,L)$, there exists constant $\tau_3 > 0$ which makes the following inequality hold:*

$$\begin{aligned} \int_0^L \vartheta_1(z)\vartheta_2(z)\mathrm{d}s &\le \|\vartheta_1(z)\|\|\vartheta_2(z)\| \\ &\le \frac{\tau_3}{2}\|\vartheta_1(z)\|^2 + \frac{1}{2\tau_3}\|\vartheta_2(z)\|^2. \end{aligned} \tag{12}$$

3. Robust H_∞ Feedback Compensator Design

Based on the distributions of actuators and sensors that $h_i(z), i \in \mathcal{M}$, in (6) (or (7)) and $s_j(z), j \in \mathcal{N}$, in (8) (or (9)), the observation obtained from sensors can be divided into collocated observation in space (i.e., $\mathbf{h}(z) = \mathbf{s}(z)$) and noncollocated observation in space (i.e., $\mathbf{h}(z) \ne \mathbf{s}(z)$). In other words, the collocated observation in space is a special case of noncollocated observation. Meanwhile, the noncollocated observation in space (i.e., $\mathbf{h}(z) \ne \mathbf{s}(z)$) consists of the following cases: pointwise control and noncollocated pointwise observation case, pointwise control and noncollocated piecewise observation case, piecewise control and noncollocated pointwise observation case, and piecewise control and noncollocated piecewise observation case. In this section, all the noncollocated observation cases will be considered to study the robust H_∞ dynamic output feedback compensator design for the DPS (1)–(3).

A new type of Luenberger-type observer for the DPS (1)–(3) is constructed as follows:

$$\begin{cases} \hat{u}_t(z,t) = \hat{u}_{zz}(z,t) + \eta\hat{u}(z,t) + \hat{\mathbf{h}}^T(z)\mathbf{U}(t) \\ +\hat{s}^T(z)\hat{\mathbf{L}}[\mathbf{y}(t) - \hat{y}(t)], \quad t > 0, z \in (0,L), \\ \hat{u}_z(z,t)|_{z=0} = a_1\hat{u}(0,t), \\ \hat{u}_z(z,t)|_{z=L} = -a_2\hat{u}(L,t), \\ \hat{u}(z,0) = \hat{u}_0(z), \quad z \in [0,L], \\ \hat{y}(t) = \displaystyle\int_0^L \mathbf{s}(z)\hat{u}(z,t)\mathrm{d}z, \quad t \ge 0, \end{cases} \tag{13}$$

where $\hat{u}(z,t)$ denotes the state of the observer; $0 < \hat{L} \triangleq \mathrm{diag}\{l_1, l_2, \ldots, l_n\} \in \mathfrak{R}^{n\times n}$ is the observer gain to be determined.

The observation functions $\hat{s}(z) \triangleq [\hat{s}_1(z)\ \hat{s}_2(z)\ \cdots\ \hat{s}_n(z)]^T$ are choosen as

$$\hat{s}_j(z) \triangleq \begin{cases} 1 & z \in [\hat{z}_j, \hat{z}_{j+1}] \\ 0 & \text{elsewhere} \end{cases}, \quad j \in \mathcal{N}, \tag{14}$$

such that $0 = \hat{z}_1 < \hat{z}_2 < \cdots < \hat{z}_n < \hat{z}_{n+1} = L$.

Then, we design an observer-based dynamic output feedback compensator of the following form:

$$\mathbf{U}(t) = -\hat{\mathbf{K}} \int_0^L \hat{\mathbf{h}}(z)\hat{u}(z,t)\mathrm{d}z, \quad t \ge 0, \tag{15}$$

where $0 < \hat{K} \triangleq \mathrm{diag}\{k_1, k_2, \ldots, k_m\} \in \mathfrak{R}^{m\times m}$ is the compensator gain in the form of $m \times m$ diagonal matrix, and the compensator functions $\hat{h}(z) \triangleq [\hat{h}_1(z)\ \hat{h}_2(z)\ \cdots\ \hat{h}_m(z)]^T \in \mathfrak{R}^m$ are choosen as

$$\widehat{h}_i(z) \triangleq \begin{cases} 1 & z \in [z_i, z_{i+1}] \\ 0 & \text{elsewhere} \end{cases}, \quad i \in \mathscr{M}, \tag{16}$$

such that $0 = z_1 < z_2 < \cdots < z_m < z_{m+1} = L$.

The estimation error state is defined as

$$e(z,t) \triangleq u(z,t) - \widehat{u}(z,t), \quad z \in [0, L]. \tag{17}$$

From formulas (1)–(3) and (13)–(17), the estimation error system is represented as

$$\begin{cases} e_t(z,t) = e_{zz}(z,t) + \eta e(z,t) + d(z,t) \\ -\widehat{s}^T(z)\widehat{\mathbf{L}}\int_0^L \mathbf{s}(z)e(z,t)\mathrm{d}z \\ -\widehat{s}^T(z)\widehat{\mathbf{L}}\omega(t), \quad z \in (0, L), \\ e_z(z,t)|_{z=0} = a_1 e(0,t), \\ e_z(z,t)|_{z=L} = -a_2 e(L,t), \\ e(z,0) = e_0(z), \quad z \in [0, L], \end{cases} \tag{18}$$

where the initial value $e_0(z) \triangleq u_0(z) - \widehat{u}_0(z)$.

Substituting the designed dynamic feedback compensator (15) and the estimation error state (17) into the DPS (1)–(3), the following closed-loop system is obtained as follows:

$$\begin{cases} u_t(z,t) = u_{zz}(z,t) + \eta u(z,t) + d(z,t) \\ -\mathbf{h}^T(z)\widehat{\mathbf{K}}\int_0^L \widehat{\mathbf{h}}(z)u(z,t)\mathrm{d}z \\ +\mathbf{h}^T(z)\widehat{\mathbf{K}}\int_0^L \widehat{\mathbf{h}}(z)e(z,t)\mathrm{d}z, \quad z \in (0, L), \\ u_z(z,t)|_{z=0} = a_1 u(0,t), \\ u_z(z,t)|_{z=L} = -a_2 u(L,t), \\ u(z,0) = u_0(z), \quad z \in [0, L]. \end{cases} \tag{19}$$

Hence, the closed-loop coupled DPS is represented by the estimation error system (18) and the closed-loop system (19) with expressions (6) (or (7)) and (8) (or (9)). The objective of this subsection is to seek an effective method to design an observer-based dynamic output feedback compensator such that the resulting closed-loop coupled DPS is exponentially stable under an H_∞ performance constraint in the sense of $|\cdot|_2$ with prescribed H_∞ attenuation levels γ_1 and γ_2.

The following theorem provides a sufficient condition for the exponential stability of the closed-loop coupled DPS (18), (19), (6) (or (7)), and (8) (or (9)) with $d(\cdot,t) = 0, \omega(t) = 0$ in the sense of $|\cdot|_2$.

Theorem 1. *Consider a class of linear parabolic DPSs (1)–(3) with $d(\cdot,t) = 0, \omega(t) = 0$ for noncollocated observation (i.e., $\mathbf{h}(z) \neq \mathbf{s}(z)$). If there exist compensator gains k_i, $i \in \mathscr{M}$, and scalars $\widehat{l}_j$, $j \in \mathscr{N}$,satisfying the following LMI constraints:*

$$\widehat{\Pi}_i \triangleq \begin{bmatrix} \eta - \dfrac{\pi^2}{4\phi_i} & \dfrac{\pi^2\sigma_i}{4\phi_i} - \dfrac{k_i}{2} & 0 \\ \dfrac{\pi^2\sigma_i}{4\phi_i} - \dfrac{k_i}{2} & -\dfrac{\pi^2\sigma_i^2}{4\phi_i} & k_i \\ 0 & k_i & -2\varepsilon \end{bmatrix} < 0, \quad i \in \mathscr{M}, \tag{20}$$

$$\widehat{\Psi}_j \triangleq \begin{bmatrix} q\eta - \dfrac{q\pi^2}{4\varphi_j} + \dfrac{\varepsilon}{2} & \dfrac{q\pi^2\widehat{\sigma}_j}{4\varphi_j} - \dfrac{\widehat{l}_j}{2} \\ \dfrac{q\pi^2\widehat{\sigma}_j}{4\varphi_j} - \dfrac{\widehat{l}_j}{2} & -\dfrac{q\pi^2\widehat{\sigma}_j^2}{4\varphi_j} \end{bmatrix} < 0, \quad j \in \mathscr{N}, \tag{21}$$

in which

$$\widehat{\sigma}_j \triangleq \begin{cases} 1, & j \in \mathscr{N} \text{ (pointwise observation case)}, \\ \dfrac{1}{\widetilde{z}_j^R - \widetilde{z}_j^L}, & j \in \mathscr{N} \text{ (local piecewise observation case)}, \end{cases}$$

$$\varphi_j \triangleq \begin{cases} \max\left\{\left(\widehat{z}_{j+1} - \widetilde{z}_j\right)^2, \left(\widetilde{z}_j - \widehat{z}_j\right)^2\right\}, & j \in \mathscr{N} \text{ (pointwise measurement case)}, \\ \max\left\{\left(\widehat{z}_{j+1} - \widetilde{z}_j^L\right)^2, \left(\widetilde{z}_j^R - \widehat{z}_j\right)^2\right\}, & j \in \mathscr{N} \text{ (piecewise measurement case)}, \end{cases} \tag{22}$$

and then there exists an observer-based dynamic output feedback compensator (15) ensuring the exponential stability of the closed-loop coupled DPS (18), (19), (6) (or (7)), and (8) (or (9)) with $d(\cdot,t) = 0, \omega(t) = 0$ in the sense of $|\cdot|_2$.

Proof. Assume the LMIs (20) and (21) are fulfilled. Consider the following Lyapunov function candidate:

$$V(t) = V_1(t) + V_2(t), \tag{23}$$

in which

$$V_2(t) = 0.5q\int_0^L e^2(z,t)\mathrm{d}z, \tag{24}$$

where $q > 0$ is a Lyapunov parameter to be determined.

The time derivative of $V_1(t)$ for the closed-loop system (19) is

$$\begin{aligned}\dot{V}_1(t) \le & -\int_0^L u_z^2(z,t)\mathrm{d}z + \eta\int_0^L u^2(z,t)\mathrm{d}z \\ & -\int_0^L u(z,t)\mathbf{h}^T(z)\mathrm{d}z\widehat{\mathbf{K}}\int_0^L \widehat{\mathbf{h}}(z)u(z,t)\mathrm{d}z + \int_0^L u(z,t)\mathbf{h}^T(z)\mathrm{d}z\widehat{\mathbf{K}}\int_0^L \widehat{\mathbf{h}}(z)e(z,t)\mathrm{d}z \\ = & -\int_0^L u_z^2(z,t)\mathrm{d}z + \eta\int_0^L u^2(z,t)\mathrm{d}z - \sum_{i=1}^m k_i u(z_c,t)\int_{z_i}^{z_{i+1}} u(z,t)\mathrm{d}z \\ & + \sum_{i=1}^m k_i u(z_c,t)\int_{z_i}^{z_{i+1}} e(z,t)\mathrm{d}z.\end{aligned} \tag{25}$$

Based on the Cauchy–Schwartz inequality, the following inequality is fulfilled for any scalar $\varepsilon > 0$:

$$\int_{z_i}^{z_{i+1}} k_i u(z_c,t)e(z,t)\mathrm{d}z \le \frac{1}{2}\left(\varepsilon^{-1}\int_{z_i}^{z_{i+1}} k_i^2 u^2(z_c,t)\mathrm{d}z + \varepsilon\int_{z_i}^{z_{i+1}} e^2(z,t)\mathrm{d}z\right). \tag{26}$$

Due to $\overline{z}_i \in (z_i, z_{i+1})$ and $[\overline{z}_i^-, \overline{z}_i^+] \subset (z_i, z_{i+1}), i \in \mathscr{M}$, by Poincaré–Wirtinger inequality's variants in Lemma 1, the following inequality is fulfilled for each $z \in [z_i, z_{i+1}], i \in \mathscr{M}$:

$$\int_{z_i}^{z_{i+1}} u_z^2(z,t)\mathrm{d}z \ge \frac{\pi^2}{4\phi_i}\int_{z_i}^{z_{i+1}} \left(u(z,t) - \sigma_i u(z_c,t)\right)^2\mathrm{d}z. \tag{27}$$

Substituting the inequalities (27) and (26) into (25), we get

$$\begin{aligned}\dot{V}_1(t) \le & -\sum_{i=1}^m \int_{z_i}^{z_{i+1}} \frac{\pi^2}{4\phi_i}\left(u(z,t) - \sigma_i u(z_c,t)\right)^2\mathrm{d}z + \eta\sum_{i=1}^m \int_{z_i}^{z_{i+1}} u^2(z,t)\mathrm{d}z \\ & -\sum_{i=1}^m \int_{z_i}^{z_{i+1}} k_i u(z_c,t)u(z,t)\mathrm{d}z + \frac{1}{2\varepsilon}\sum_{i=1}^m \int_{z_i}^{z_{i+1}} k_i^2 u^2(z_c,t)\mathrm{d}z + \frac{\varepsilon}{2}\sum_{i=1}^m \int_{z_i}^{z_{i+1}} e^2(z,t)\mathrm{d}z \\ = & \sum_{i=1}^m \int_{z_i}^{z_{i+1}} \mathbf{u}_i^T(z,t)\Pi_i\mathbf{u}_i(z,t)\mathrm{d}z + \frac{\varepsilon}{2}\int_0^L e^2(z,t)\mathrm{d}z,\end{aligned} \tag{28}$$

where

$$\Pi_i \triangleq \begin{bmatrix} \eta - \dfrac{\pi^2}{4\phi_i} & \dfrac{\pi^2\sigma_i}{4\phi_i} - \dfrac{k_i}{2} \\ \dfrac{\pi^2\sigma_i}{4\phi_i} - \dfrac{k_i}{2} & -\dfrac{\pi^2\sigma_i^2}{4\phi_i} + \dfrac{k_i^2}{2\varepsilon} \end{bmatrix} < 0, \quad i \in \mathscr{M}. \tag{29}$$

The time derivative of $V_2(t)$ is

$$\begin{aligned}\dot{V}_2(t) \le & -q\int_0^L e_z^2(z,t)\mathrm{d}z + q\eta\int_0^L e^2(z,t)\mathrm{d}z - q\int_0^L e(z,t)\widehat{s}^T(z)\widehat{\mathbf{L}}\int_0^L \mathbf{s}(z)e(z,t)\mathrm{d}z \\ = & -q\int_0^L e_z^2(z,t)\mathrm{d}z + q\eta\int_0^L e^2(z,t)\mathrm{d}z - \sum_{j=1}^n \widehat{l}_j e(\widehat{z}_s,t)\int_{\widehat{z}_j}^{\widehat{z}_{j+1}} e(z,t)\mathrm{d}z,\end{aligned} \tag{30}$$

where $\widehat{l}_j = ql_j, e(\widehat{z}_s, t) = \int_0^L s_j(z)e(z,t)\mathrm{d}z, j \in \mathcal{N}$. The following expression is utilized by applying integration by parts and considering the boundary conditions in (18):

$$\begin{aligned}\int_0^L e(z,t)e_{zz}(z,t)\mathrm{d}z &= e(z,t)e_z(z,t)|_{z=0}^{z=L} - \int_0^L e_z^2(z,t)\mathrm{d}z \\ &= -a_2e^2(L,t) - a_1e^2(0,t) - \int_0^L e_z^2(z,t)\mathrm{d}z \\ &\le -\int_0^L e_z^2(z,t)\mathrm{d}z.\end{aligned} \tag{31}$$

As $\widetilde{z}_j \in (\widehat{z}_j, \widehat{z}_{j+1}), [\widetilde{z}_j^-, \widetilde{z}_j^+] \subset (\widehat{z}_j, \widehat{z}_{j+1}), j \in \mathcal{N}$, and $0 = \widehat{z}_1 < \widehat{z}_2 < \cdots < \widehat{z}_n < \widehat{z}_{n+1} = L$. By Lemma 1, we get for each $z \in [\widehat{z}_j, \widehat{z}_{j+1}], j \in \mathcal{N}$,

$$\int_{\widehat{z}_j}^{\widehat{z}_{j+1}} e_z^2(z,t)\mathrm{d}z \ge \frac{\pi^2}{4\varphi_j}\int_{\widehat{z}_j}^{\widehat{z}_{j+1}} \left(e(z,t) - \widehat{\sigma}_j e(\widehat{z}_s,t)\right)^2\mathrm{d}z. \tag{32}$$

Thus, the expression (30) can be rewritten as

$$\begin{aligned}\dot{V}_2(t) &\le -\frac{q\pi^2}{4\varphi_j}\sum_{j=1}^n\int_{\widehat{z}_j}^{\widehat{z}_{j+1}} \left(e(z,t) - \widehat{\sigma}_j e(\widehat{z}_s,t)\right)^2\mathrm{d}z + q\eta\sum_{j=1}^n\int_{\widehat{z}_j}^{\widehat{z}_{j+1}} e^2(z,t)\mathrm{d}z \\ &\quad - \sum_{j=1}^n\int_{\widehat{z}_j}^{\widehat{z}_{j+1}} \widehat{l}_j e(\widehat{z}_s,t)e(z,t)\mathrm{d}z \\ &= \sum_{j=1}^n\int_{\widehat{z}_j}^{\widehat{z}_{j+1}} \mathbf{e}_j^T(z,t)\Psi_j\mathbf{e}_j(z,t)\mathrm{d}z,\end{aligned} \tag{33}$$

where $\mathbf{e}_j(z,t) \triangleq [\, e(z,t) \;\; e(\widehat{z}_s,t)\,]^T, j \in \mathcal{N}$, and

$$\Psi_j \triangleq \begin{bmatrix} q\eta - \dfrac{q\pi^2}{4\varphi_j} & \dfrac{q\pi^2\widehat{\sigma}_j}{4\varphi_j} - \dfrac{\widehat{l}_j}{2} \\ \dfrac{q\pi^2\widehat{\sigma}_j}{4\varphi_j} - \dfrac{\widehat{l}_j}{2} & -\dfrac{q\pi^2\widehat{\sigma}_j^2}{4\varphi_j} \end{bmatrix} < 0, \quad j \in \mathcal{N}. \tag{34}$$

From (28) and (33), the time derivative of $V(t)$ defined in (23) is given as

$$\begin{aligned}\dot{V}(t) &= \dot{V}_1(t) + \dot{V}_2(t) \\ &\le \sum_{i=1}^m\int_{z_i}^{z_{i+1}} \mathbf{u}_i^T(z,t)\Pi_i\mathbf{u}_i(z,t)\mathrm{d}z + \frac{\varepsilon}{2}\int_0^L e^2(z,t)\mathrm{d}z + \sum_{j=1}^n\int_{\widehat{z}_j}^{\widehat{z}_{j+1}} \mathbf{e}_j^T(z,t)\Psi_j\mathbf{e}_j(z,t)\mathrm{d}z \\ &\le \sum_{i=1}^m\int_{z_i}^{z_{i+1}} \mathbf{u}_i^T(z,t)\Pi_i\mathbf{u}_i(z,t)\mathrm{d}z + \sum_{j=1}^n\int_{\widehat{z}_j}^{\widehat{z}_{j+1}} \mathbf{e}_j^T(z,t)\widehat{\Psi}_j\mathbf{e}_j(z,t)\mathrm{d}z.\end{aligned} \tag{35}$$

By the Schur complement and the LMI constraint (20), we have

$$\Pi_i < 0, \quad i \in \mathcal{M}. \tag{36}$$

It can be deduced from the LMI (21) and the inequality (36) that there exists an appropriate constant $\alpha_2 > 0$, satisfying the following inequalities:

$$\begin{aligned}\Pi_i + 0.5\alpha_2\mathbf{I} \le 0, &\quad i \in \mathcal{M}, \\ \widehat{\Psi}_j + 0.5\alpha_2\mathbf{I} \le 0, &\quad j \in \mathcal{N}.\end{aligned} \tag{37}$$

Substituting the inequalities (37) to (35), we obtain

$$\begin{aligned}\dot{V}(t) &\le -0.5\alpha_2\sum_{i=1}^m\int_{z_i}^{z_{i+1}} \mathbf{u}_i^T(z,t)\mathbf{u}_i(z,t)\mathrm{d}z \\ &\quad - 0.5\alpha_2\sum_{j=1}^n\int_{\widehat{z}_j}^{\widehat{z}_{j+1}} \mathbf{e}_j^T(z,t)\mathbf{e}_j(z,t)\mathrm{d}z \\ &\le -\alpha_2\left(V_1(t) + q^{-1}V_2(t)\right) \le -\alpha_2\kappa V(t),\end{aligned} \tag{38}$$

where $\kappa \triangleq \min\{1, q^{-1}\}$. Integrating from 0 to t for the inequality (38), we can get $V_1(t) \le V_1(0)\exp(-\alpha_1 t)$, which

implies $|u(\cdot,t)|_2 \le |u_0(\cdot)|_2 \exp(-0.5\alpha_1 t)$, $t \ge 0$. Thus, we can obtain $\sqrt{|u(\cdot,t)|_2^2 + |e(\cdot,t)|_2^2} \le \sqrt{\max\{1,q\}/\min\{1,q\}}$ $\sqrt{|u_0(\cdot)|_2^2 + |e_0(\cdot)|_2^2} \exp(-0.5\alpha_2 \kappa t)$. In other words, the closed-loop coupled DPS (18), (19), (6) (or (7)), and (8) (or (9)) with $d(\cdot,t) = 0, \omega(t) = 0$ is exponentially stable in the sense of $|\cdot|_2$. The proof is complete. □

Next, the H_∞ performance analysis is developed for the closed-loop coupled DPS (18), (19), (6) (or (7)), and (8) (or (9)) with the initial value $u_0(\cdot) = 0$ and all $d \in \mathscr{L}_2(0,\infty;\mathscr{H}), \omega \in \mathscr{L}_2(0,\infty;\mathfrak{R}^n)$. The following theorem provides a sufficient condition for exponential stability in the sense of $|\cdot|_2$ of the closed-loop coupled DPS (18), (19), (6) (or (7)), and (8) (or (9)) under a prescribed H_∞ performance constraint (10) based on the LMI conditions.

Theorem 2. *Consider a class of linear parabolic DPSs (1)–(3), given H_∞ attenuation levels $\gamma_1 > 0, \gamma_2 > 0$ and constant $0 < r < 1$, if there exist compensator gains k_i, $i \in \mathscr{M}$ and scalars $\widehat{l}_j$, $j \in \mathscr{N}$, satisfying the following LMI constraints:*

$$\widehat{\Gamma}_i \triangleq \begin{bmatrix} \mathfrak{p}_i & \mathfrak{q}_i & 0 & 0.5 \\ \mathfrak{q}_i & -\dfrac{\pi^2\sigma_i^2}{4\phi_i} & k_i & 0 \\ 0 & k_i & -2\varepsilon & 0 \\ 0.5 & 0 & 0 & -\dfrac{r\gamma_1^2}{\Delta z_i} \end{bmatrix} < 0, \quad i \in \mathscr{M}, \tag{39}$$

$$\Theta_j \triangleq \begin{bmatrix} \mathfrak{h}_j & \mathfrak{v}_j & 0.5q & -\dfrac{\widehat{l}_j}{2} \\ \mathfrak{v}_j & -\dfrac{q\pi^2\widehat{\sigma}_j^2}{4\varphi_j} & 0 & 0 \\ 0.5q & 0 & -\dfrac{(1-r)\gamma_1^2}{\Delta\widehat{z}_j} & 0 \\ -\dfrac{\widehat{l}_j}{2} & 0 & 0 & -\dfrac{\gamma_2^2}{\Delta\widehat{z}_j} \end{bmatrix} < 0, \quad j \in \mathscr{N}, \tag{40}$$

in which

$$\begin{aligned} \mathfrak{p}_i &\triangleq \eta - \frac{\pi^2}{4\phi_i} + 1, \\ \mathfrak{q}_i &\triangleq \frac{\pi^2\sigma_i}{4\phi_i} - \frac{k_i}{2}, \\ \mathfrak{h}_j &\triangleq q\eta - \frac{q\pi^2}{4\varphi_j} + \frac{\varepsilon}{2}, \\ \mathfrak{v}_j &\triangleq \frac{q\pi^2\widehat{\sigma}_j}{4\varphi_j} - \frac{\widehat{l}_j}{2}, \\ \Delta\widehat{z}_j &\triangleq \widehat{z}_{j+1} - \widehat{z}_j, \quad j \in \mathscr{N}, \end{aligned} \tag{41}$$

and then there exists an observer-based dynamic output feedback compensator (15) ensuring the exponential stability of the closed-loop coupled DPS (18), (19), (6) (or (7)), and (8) (or (9)) under a prescribed H_∞ performance constraint (10).

Proof. From expressions (18), (19), and (35), the time derivative of $V(t)$ is rewritten as

$$\begin{aligned} \dot{V}(t) \le & \sum_{i=1}^{m} \int_{z_i}^{z_{i+1}} \mathbf{u}_i^T(z,t)\Pi_i\mathbf{u}_i(z,t)\mathrm{d}z \\ & + \sum_{j=1}^{n} \int_{\widehat{z}_j}^{\widehat{z}_{j+1}} \mathbf{e}_j^T(z,t)\widehat{\Psi}_j\mathbf{e}_j(z,t)\mathrm{d}z + \int_0^L u(z,t)d(z,t)\mathrm{d}z + q\int_0^L e(z,t)d(z,t)\mathrm{d}z \\ & - \sum_{j=1}^{n} \int_{\widehat{z}_j}^{\widehat{z}_{j+1}} \widehat{l}_j\omega_j(t)e(z,t)\mathrm{d}z. \end{aligned} \tag{42}$$

Considering the H_∞ performance constraint in (10) and constant $0 < r < 1$, we have

$$\begin{aligned}
&\dot{V}(t) + |u(\cdot,t)|_2^2 - \gamma_1^2 |d(\cdot,t)|_2^2 - \gamma_2^2 \|\boldsymbol{\omega}(t)\|^2 \\
&\le \sum_{i=1}^{m} \int_{z_i}^{z_{i+1}} \mathbf{u}_i^T(z,t)\Pi_i \mathbf{u}_i(z,t)\mathrm{d}z + \sum_{j=1}^{n} \int_{\widehat{z}_j}^{\widehat{z}_{j+1}} \mathbf{e}_j^T(z,t)\widehat{\Psi}_j \mathbf{e}_j(z,t)\mathrm{d}z \\
&\quad + \int_0^L u(z,t)d(z,t)\mathrm{d}z + q\int_0^L d(z,t)e(z,t)\mathrm{d}z - \sum_{j=1}^{n} \int_{\widehat{z}_j}^{\widehat{z}_{j+1}} \widehat{l}_j \omega_j(t) e(z,t)\mathrm{d}z \\
&\quad + \sum_{i=1}^{m} \int_{z_i}^{z_{i+1}} u^2(z,t)\mathrm{d}z - \sum_{i=1}^{m} \frac{r\gamma_1^2}{\Delta z_i} \int_{z_i}^{z_{i+1}} d^2(z,t)\mathrm{d}z \\
&\quad - \sum_{j=1}^{n} \frac{(1-r)\gamma_1^2}{\Delta \widehat{z}_j} \int_{\widehat{z}_j}^{\widehat{z}_{j+1}} d^2(z,t)\mathrm{d}z - \sum_{j=1}^{n} \frac{\gamma_2^2}{\Delta \widehat{z}_j} \int_{\widehat{z}_j}^{\widehat{z}_{j+1}} \omega_j^2(t)\mathrm{d}z \\
&\le \sum_{i=1}^{m} \int_{z_i}^{z_{i+1}} \widehat{\mathbf{u}}_i^T(z,t)\Gamma_i \widehat{\mathbf{u}}_i(z,t)\mathrm{d}z + \sum_{j=1}^{n} \int_{\widehat{z}_j}^{\widehat{z}_{j+1}} \widehat{e}_j^T(z,t)\Theta_j \widehat{e}_j(z,t)\mathrm{d}z,
\end{aligned} \tag{43}$$

where $\widehat{u}_i(z,t) \triangleq \left[\, u(z,t) \;\; u(z_c,t) \;\; d(z,t) \,\right]^T, i \in \mathscr{M}$, $\widehat{e}_j(z,t) \triangleq \left[\, e(z,t) \;\; e(\widehat{z}_s,t) \;\; d(z,t) \;\; \omega_j(t) \,\right]^T, j \in \mathscr{N}$, and

$$\Gamma_i \triangleq \begin{bmatrix} \eta - \dfrac{\pi^2}{4\phi_i} + 1 & \dfrac{\pi^2\sigma_i}{4\phi_i} - \dfrac{k_i}{2} & 0.5 \\ \dfrac{\pi^2\sigma_i}{4\phi_i} - \dfrac{k_i}{2} & -\dfrac{\pi^2\sigma_i^2}{4\phi_i} + \dfrac{k_i^2}{2\varepsilon} & 0 \\ 0.5 & 0 & -\dfrac{r\gamma_1^2}{\Delta z_i} \end{bmatrix}, \quad i \in \mathscr{M}. \tag{44}$$

By the Schur complement and the LMI constraint (40), we have

$$\Gamma_i < 0, \quad i \in \mathscr{M}. \tag{45}$$

It is easily obtained from (43) in consideration of the inequality (45) and the LMI (40) that

$$\dot{V}(t) + |u(\cdot,t)|_2^2 - \gamma_1^2 |d(\cdot,t)|_2^2 - \gamma_2^2 \|\boldsymbol{\omega}(t)\|^2 \le 0, \quad \forall t \ge 0. \tag{46}$$

Intergrating (46) from 0 to ∞ and considering the zero initial value $u_0(\cdot) = 0$, we get the expression (10). In other words, the H_∞ performance constraint (10) with the given prescribed H_∞ attenuation levels $\gamma_1 > 0$ and $\gamma_2 > 0$ is guaranteed for the closed-loop coupled DPSs (18), (19), (6) (or (7)), and (8) (or (9)) with the initial value $u_0(\cdot) = 0$ and all $d \in \mathscr{L}_2(0,\infty;\mathscr{H})), \omega \in \mathscr{L}_2(0,\infty;\mathfrak{R}^n)$. Meanwhile, the LMI constraints (20) and (21) in Theorem 1 can be derived from the LMI constraints (39) and (40) in Theorem 2. Therefore, the closed-loop coupled DPS (18), (19), (6) (or (7)), and (8) (or (9)) is exponential stable in the sense of $|\cdot|_2$ under a prescribed H_∞ performance constraint (10). The proof is complete. □

4. Numerical Simulation

In this section, we will provide some numerical simulations to demonstrate the effectiveness of the proposed design strategy. For the linear parabolic DPS (1)–(3), given the constants $\eta = 3, L = 1, a_1 = 0.5$, and $a_2 = 0$, set the initial value $u_0(z) = 0.5\sin(0.5L^{-1}\pi x) + 0.5\pi, z \in [0,L]$, $d(z,t) = \cos(\pi z)\exp(-t)$, the open-loop profile of evolution of $u(z,t)$, and the open-loop trajectory of $|u(\cdot,t)|_2$, as shown in Figure 1. It is easily seen from Figure 1 that the linear parabolic DPS (1)–(3) with $\mathbf{U}(t) = 0$ is unstable.

The numerical simulations of the corresponding closed-loop coupled DPS (18), (19), (7), and (9) for local piecewise control and noncollocated local piecewise measurement case in space are then shown. Assume three actuators and two sensors are applied for implementation of the proposed design method, that is, $m = 3, n = 2$, and $\mathscr{M} = \{1,2,3\}, \mathscr{N} = \{1,2\}$. Three actuators are respectively distributed over $[0.1L, 0.3L]$, $[0.4L, 0.6L]$, and $[0.7L, 0.9L]$ over the spatial domain $[0,L]$, and two sensors are respectively distributed over $[[0.2L, 0.4L], [0.6L, 0.8L]$ over the spatial domain $[0,L]$, i.e., $\overline{z}_1^- = 0.1L$, $\overline{z}_1^+ = 0.3L$, $\overline{z}_2^- = 0.4L$, $\overline{z}_2^+ = 0.6L$, $\overline{z}_3^- = 0.7L$, $\overline{z}_3^+ = 0.9L$ and $\widetilde{z}_1^- = 0.2L, \widetilde{z}_1^+ = 0.4L, \widetilde{z}_2^- = 0.6L, \widetilde{z}_2^+ = 0.8L$, respectively. Set $z_1 = 0$, $z_2 = (L/3)$, $z_3 = (2L/3)$, and $z_4 = L$ and $\widehat{z}_1 = 0, \widehat{z}_2 = 0.5L$, and $\widehat{z}_3 = L$. Through numerical calculations, we can get $\Delta z_1 = \Delta z_2 = \Delta z_3 = (L/3)$, $\Delta\widehat{z}_1 = \Delta\widehat{z}_2 = 0.5L, \sigma_1 = \sigma_2 = \sigma_2 = 5L^{-1}, \widehat{\sigma}_1 = \widehat{\sigma}_2 = 5L^{-1}, \phi_1 = 0.09L^2, \phi_2 = 0.0711L^2, \phi_3 = 0.09L^2$, and $\varphi_1 = 0.16L^2, \varphi_2 = 0.2178L^2$. Set

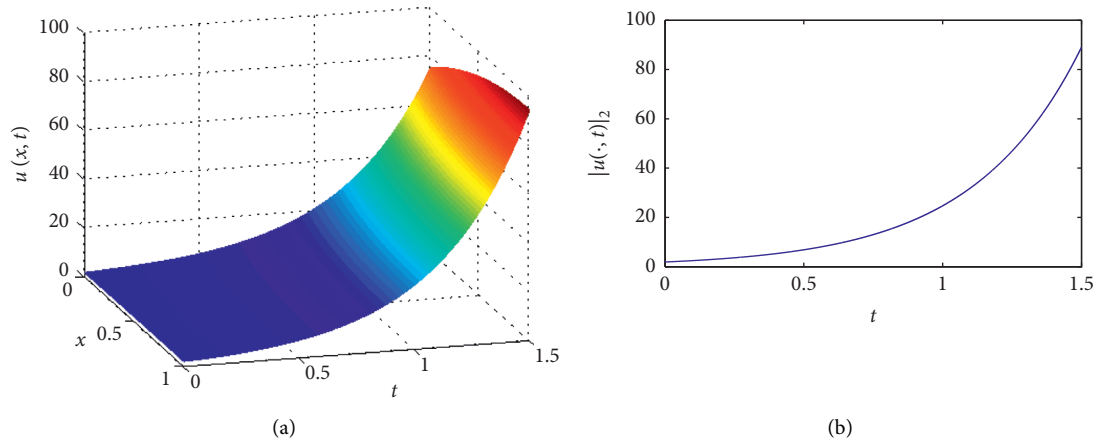

Figure 1: Simulation results for the open-loop linear parabolic DPS (1)–(3). (a) Open-loop profile of evolution of $u(z,t)$. (b) Open-loop trajectory of $|u(\cdot,t)|_2$.

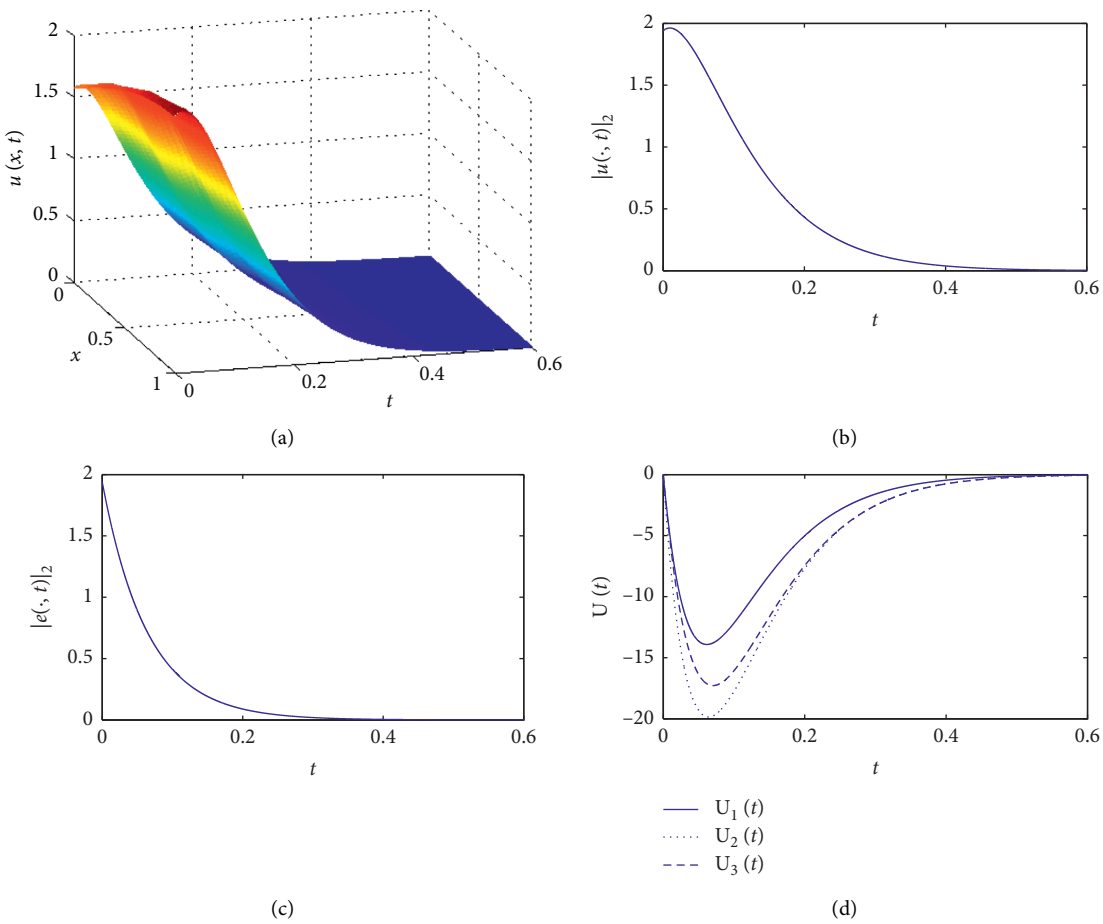

Figure 2: Closed-loop coupled DPS (18), (19), (7), and (9) with $d(z,t) = 0$ and $\omega(t) = 0$ for local piecewise control and noncollocated local piecewise measurement in space. (a) Closed-loop profile of evolution of $u(z,t)$. (b) Closed-loop trajectory of $|u(\cdot,t)|_2$. (c) Closed-loop trajectory of $|e(\cdot,t)|_2$. (d) Trajectory of dynamic output feedback compensator $\mathbf{U}(t)$.

$\varepsilon = 10, r = 0.5$; by solving the LMIs (39) and (40), we get the optimised H_∞ attenuation levels as $\gamma_1 = 20.6102, \gamma_2 = 18.6307$, compensator gains $k_1 = 52.1015$, $k_2 = 71.7887$, and $k_3 = 52.1015$, and observer gains $l_1 = 77.0853, l_2 = 69.8957$. Applying the designed observer-based dynamic output feedback compensator (15) with the calculated compensator gains and observer gains, the closed-loop profile of evolution of $u(z,t)$, the closed-loop trajectory of $|u(\cdot,t)|_2$, $|e(\cdot,t)|_2$,

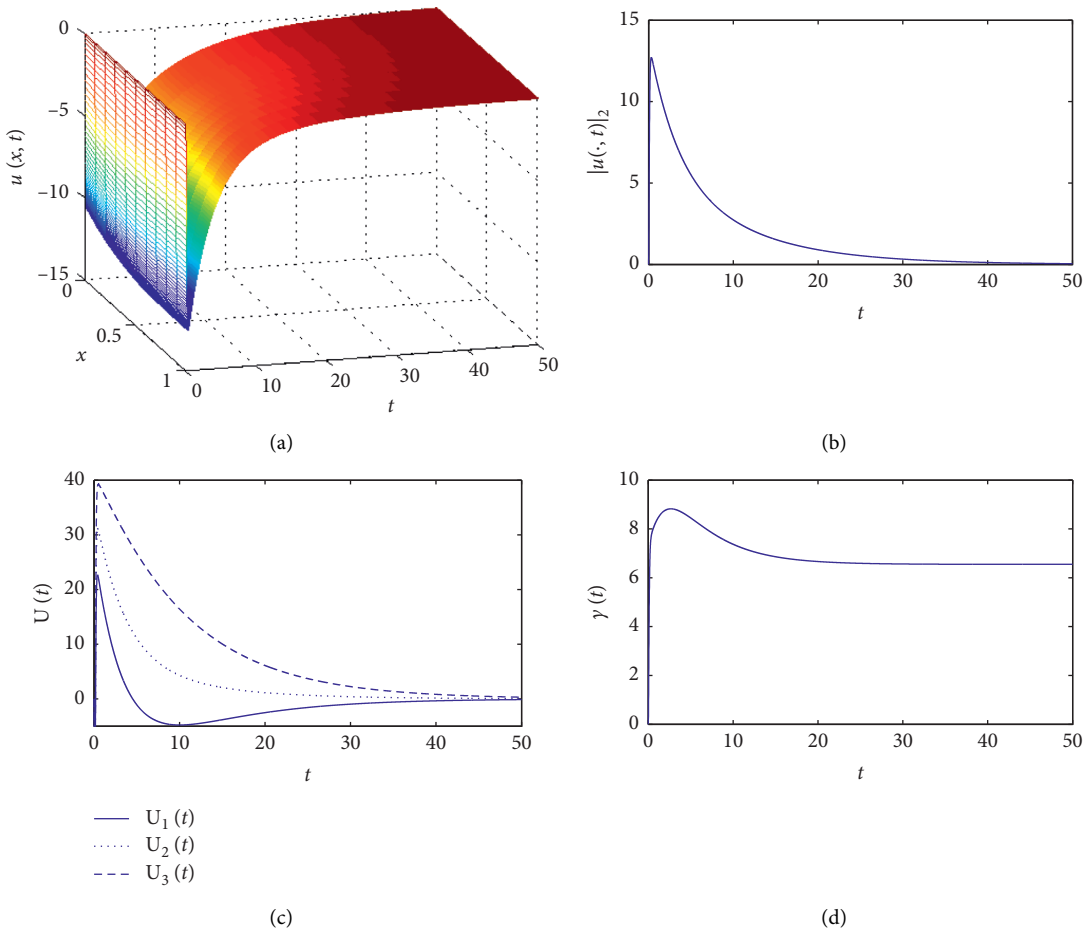

Figure 3: Closed-loop coupled DPS (18), (19), (7), and (9) with $u_0(\cdot) = 0$ and $d(z,t) = \cos(\pi x)\exp(-t)$, $\omega(t) \triangleq [\exp(-0.1t) \;\; \exp(-0.3t)]$, for local piecewise control and noncollocated local piecewise measurement in space. (a) Closed-loop profile of evolution of $u(z,t)$. (b) Closed-loop trajectory of $|u(\cdot,t)|_2$. (c) Trajectory of observer-based dynamic output feedback compensator $\mathbf{U}(t)$. (d) The trajectory of $\gamma(t)$.

and the trajectory of the observer-based dynamic output feedback compensator $\mathbf{U}(t)$ of the form (15) with $d(z,t) = 0$, $\omega(t) = 0$ are shown in Figure 2. The simulation results indicate that the designed observer-based dynamic output feedback compensator (15) can stabilize the MIMO PDE (1)–(3) with $d(\cdot,t) = 0, \omega(t) = 0$ in the sense of $|\cdot|_2$.

Figure 3 presents the closed-loop profile of evolution of $u(z,t)$, the closed-loop trajectory of $|u(\cdot,t)|_2$, the observer-based dynamic output feedback compensator $\mathbf{U}(t)$ in (14), and the trajectory of $\gamma(t)$ for the closed-loop coupled DPS (18), (19), (7), and (9) with $u_0(\cdot) = 0$ and $d(z,t) = \cos(\pi x)$ $\exp(-t)$, $\omega(t) \triangleq [\exp(-0.1t) \;\; \exp(-0.3t)]$. It is easily seen from Figure 3 that $\gamma(t) < \min\{\gamma_1, \gamma_2\}$, which implies $\int_0^\infty |u(\cdot,t)|_2^2 \mathrm{d}t \le \gamma_1^2 \int_0^\infty |d(\cdot,t)|_2^2 \mathrm{d}t + \gamma_2^2 \int_0^\infty \|\omega(t)\|^2 \mathrm{d}t$; the H_∞ performance constraint (10) is guaranteed. The simulation results indicate that the designed observer-based dynamic output feedback compensator (15) can stabilize the linear parabolic DPS (1)–(3) with $u_0(\cdot) = 0$ and $d(z,t) = \cos(\pi x)\exp(-t)$, $\omega(t) \triangleq [\exp(-0.1t) \;\; \exp(-0.3t)]$, in the sense of $|\cdot|_2$.

5. Conclusions

In this paper, the robust H_∞ feedback compensator for a class of linear parabolic DPSs with external disturbances has been investigated in consideration of the pointwise/piecewise control and pointwise/piecewise measurement based on the distributions of the actuators and sensors. A new type of Luenberger observer is designed to solve the difficulty caused by noncollocated observation and track the state of the PDEs. It is different from the previous observer design method that all the cases of the pointwise/piecewise control and pointwise/piecewise measurement are considered via a defined unified distribution function. An observer-based dynamic output feedback compensator is designed and an H_∞ performance constraint is proposed under the zero initial condition. By utilizing Poincaré–Wirtinger inequality's variants, Cauchy–Schwartz inequality, integration by parts, and first mean value theorem for definite integrals, sufficient conditions on the exponential stability of the corresponding closed-loop system under an H_∞

performance constraint in the sense of $|\cdot|_2$ are presented in terms of LMI constraints. Finally, numerical simulation results of the resulting closed-loop systems are provided to illustrate the effectiveness of the proposed design strategy.

Data Availability

The data of this paper come from the official website of sample enterprises, which can be obtained.

Conflicts of Interest

The authors declare that they have no conflicts of interest.

Acknowledgments

This work was supported in part by the Grants of National Key R&D Program of China (2020AAA0108304), National Natural Science Foundation of China (62003275, U1911401, 62073088, and U1701261), Fundamental Research Funds for the Central Universities of China with Grant (31020190QD039), Guangdong Basic and Applied Basic Research Foundation (2019A1515011606), and Guangdong Provincial Key Laboratory of Electronic Information Products Reliability Technology (2017B030314151).

References

[1] P. D. Christofides, *Nonlinear and Robust Control of PDE Systems: Methods and Applications to Transport-Reaction Processes*, Birkhauser, Boston, MA, USA, 2001.

[2] H.-X. Li and C. Qi, *Spatio-Temporal Modeling of Nonlinear Distributed Parameter Systems: A Time/Space Separation Based Approach*, Spinger-Verlag, Amsterdam, The Netherlands, 2011.

[3] K.-K. Xu, H.-X. Li, and H.-D. Yang, "Local-properties-embedding-based nonlinear spatiotemporal modeling for lithium-ion battery thermal process," *IEEE Transactions on Industrial Electronics*, vol. 65, no. 12, pp. 9767–9776, 2018.

[4] B. Roffel and B. H. Betlem, *Advanced Practical Process Control*, Springer, Berlin, Germany, 2004.

[5] R. Padhi and S. F. Ali, "An account of chronological developments in control of distributed parameter systems," *Annual Reviews in Control*, vol. 33, no. 1, pp. 59–68, 2009.

[6] B. Luo, H.-N. Wu, and H.-X. Li, "Adaptive optimal control of highly dissipative nonlinear spatially distributed processes with neuro-dynamic programming," *IEEE Transactions on Neural Networks and Learning Systems*, vol. 26, no. 4, pp. 684–696, 2014.

[7] Z.-P. Wang and H.-N. Wu, "Finite dimensional guaranteed cost sampled-data fuzzy control for a class of nonlinear distributed parameter systems," *Information Sciences*, vol. 327, pp. 21–39, 2016.

[8] W. He, T. Meng, X. He, and S. S. Ge, "Unified iterative learning control for flexible structures with input constraints," *Automatica*, vol. 96, pp. 326–336, 2018.

[9] W. He, T. Meng, X. He, and C. Sun, "Iterative learning control for a flapping wing micro aerial vehicle under distributed disturbances," *IEEE Transactions on Cybernetics*, vol. 49, no. 4, pp. 1524–1535, 2018.

[10] W. Kang and E. Fridman, "Distributed sampled-data control of Kuramoto-Sivashinsky equation," *Automatica*, vol. 95, pp. 514–524, 2018.

[11] Z.-P. Wang and H.-N. Wu, "Sampled-data fuzzy control with guaranteed cost for nonlinear parabolic PDE systems via static output feedback," *IEEE Transactions on Fuzzy Systems*, vol. 28, no. 10, pp. 2452–2465, 2019.

[12] R. Wang, C. Wang, H. Sun, Z. Chen, and Y. Sun, "Sensor fault signal reconstruction based on sliding mode observer for flight control systems," *International Journal of Modelling, Identification and Control*, vol. 32, no. 3-4, pp. 204–211, 2019.

[13] Z.-P. Wang, H.-N. Wu, and H.-X. Li, "Fuzzy control under spatially local averaged measurements for nonlinear distributed parameter systems with time-varying delay," *IEEE Transactions on Cybernetics*, vol. 51, no. 3, pp. 1359–1369, 2019.

[14] S.-H. Tsai, J.-W. Wang, E.-S. Song, and H.-K. Lam, "Robust H_∞ control for nonlinear hyperbolic PDE systems based on the polynomial fuzzy model," *IEEE Transactions on Cybernetics*, 2019.

[15] Z. Li, Q. Cai, Z. Ren, H. Zhang, M. Fu, and Z. Wu, "Optimal control of a class of semi-linear stochastic evolution equations with applications," *IET Control Theory & Applications*, vol. 13, no. 4, pp. 602–608, 2019.

[16] Y. Li, C.-Y. Chen, and C. Li, "Stochastic stability criteria for neutral distributed parameter systems with markovian jump," *Complexity*, vol. 2020, Article ID 9450786, , 2020.

[17] Z.-P. Wang, H.-N. Wu, and T. Huang, "Sampled-data fuzzy control for nonlinear delayed distributed parameter systems," *IEEE Transactions on Fuzzy Systems*, 2020.

[18] W. He, X. He, M. Zou, and H. Li, "Pde model-based boundary control design for a flexible robotic manipulator with input backlash," *IEEE Transactions on Control Systems Technology*, vol. 27, no. 2, pp. 790–797, 2018.

[19] W. He, H. Gao, C. Zhou, C. Yang, and Z. Li, "Reinforcement learning control of a flexible two-link manipulator: an experimental investigation," *IEEE Transactions on Systems, Man, and Cybernetics: Systems*, 2020.

[20] W. He, T. Wang, X. He, L.-J. Yang, and O. Kaynak, "Dynamical modeling and boundary vibration control of a rigid-flexible wing system," *IEEE/ASME Transactions on Mechatronics*, vol. 25, no. 6, pp. 2711–2721, 2020.

[21] Z. Zhao, C. K. Ahn, and H.-X. Li, "Boundary anti-disturbance control of a spatially nonlinear flexible string system," *IEEE Transactions on Industrial Electronics*, vol. 67, no. 6, pp. 4846–4856, 2019.

[22] Z. Zhao, X. He, Z. Ren, and G. Wen, "Boundary adaptive robust control of a flexible riser system with input nonlinearities," *IEEE Transactions on Systems, Man, and Cybernetics: Systems*, vol. 49, no. 10, 2018.

[23] J.-W. Wang, Y.-Q. Liu, and C.-Y. Sun, "Adaptive neural boundary control design for nonlinear flexible distributed parameter systems," *IEEE Transactions on Control Systems Technology*, vol. 27, no. 5, pp. 2085–2099, 2018.

[24] R. Vazquez and M. Krstic, "Control of 1-d parabolic PDEs with volterra nonlinearities, part i: design," *Automatica*, vol. 44, no. 11, pp. 2778–2790, 2008.

[25] B.-Z. Guo and W. Guo, "The strong stabilization of a one-dimensional wave equation by non-collocated dynamic boundary feedback control," *Automatica*, vol. 45, no. 3, pp. 790–797, 2009.

[26] M. Krstic, B.-Z. Guo, A. Balogh, and A. Smyshlyaev, "Control of a tip-force destabilized shear beam by observer-based boundary feedback," *SIAM Journal on Control and Optimization*, vol. 47, no. 2, pp. 553–574, 2008.

[27] M. Cheng, V. Radisavljevic, C. Chang, C. Lin, and W. Su, "A sampled-data singularly perturbed boundary control for a

heat conduction system with noncollocated observation," *IEEE Transactions on Automatic Control*, vol. 54, no. 6, pp. 1305–1310, 2009.

[28] M.-B. Cheng, V. Radisavljevic, and W.-C. Su, "Sliding mode boundary control of a parabolic PDE system with parameter variations and boundary uncertainties," *Automatica*, vol. 47, no. 2, pp. 381–387, 2011.

[29] H.-N. Wu, J.-W. Wang, and H.-X. Li, "Fuzzy boundary control design for a class of nonlinear parabolic distributed parameter systems," *IEEE Transactions on Fuzzy Systems*, vol. 22, no. 3, pp. 642–652, 2014.

[30] X. Song, M. Wang, S. Song, and J. Man, "Dissipativity-based controller design for time-delayed ts fuzzy switched distributed parameter systems," *Complexity*, vol. 2018, Article ID 6215945, , 2018.

[31] E. Fridman and Y. Orlov, "An lmi approach to H_∞ boundary control of semilinear parabolic and hyperbolic systems," *Automatica*, vol. 45, no. 9, pp. 2060–2066, 2009.

[32] J.-W. Wang, H.-X. Li, and H.-N. Wu, "A membership-function-dependent approach to design fuzzy pointwise state feedback controller for nonlinear parabolic distributed parameter systems with spatially discrete actuators," *IEEE Transactions on Systems, Man, and Cybernetics: Systems*, vol. 47, no. 7, pp. 1486–1499, 2017.

[33] J.-W. Wang and H.-N. Wu, "Exponential pointwise stabilization of semilinear parabolic distributed parameter systems via the takagi-sugeno fuzzy PDE model," *IEEE Transactions on Fuzzy Systems*, vol. 26, no. 1, pp. 155–173, 2018.

[34] J.-W. Wang and H.-N. Wu, "Design of suboptimal local piecewise fuzzy controller with multiple constraints for quasi-linear spatiotemporal dynamic systems," *IEEE Transactions on Cybernetics*, 2019.

[35] E. Fridman and N. B. Am, "Sampled-data distributed H_∞ control of transport reaction systems control of transport reaction systems," *SIAM Journal on Control and Optimization*, vol. 51, no. 2, pp. 1500–1527, 2013.

[36] E. Fridman and A. Blighovsky, "Robust sampled-data control of a class of semilinear parabolic systems," *Automatica*, vol. 48, no. 5, pp. 826–836, 2012.

[37] M. A. Demetriou, "Guidance of mobile actuator-plus-sensor networks for improved control and estimation of distributed parameter systems," *IEEE Transactions on Automatic Control*, vol. 55, no. 7, pp. 1570–1584, 2010.

[38] M. A. Demetriou, "Adaptive control of 2-d PDEs using mobile collocated actuator/sensor pairs with augmented vehicle dynamics," *IEEE Transactions on Automatic Control*, vol. 57, no. 12, pp. 2979–2993, 2012.

[39] J.-W. Wang and H.-N. Wu, "Lyapunov-based design of locally collocated controllers for semi-linear parabolic PDE systems," *Journal of the Franklin Institute*, vol. 351, no. 1, pp. 429–441, 2014.

[40] A. Selivanov and E. Fridman, "Sampled-data relay control of diffusion PDEs," *Automatica*, vol. 82, pp. 59–68, 2017.

[41] W.-H. Chen, S. Luo, and W. X. Zheng, "Sampled-data distributed H_∞ control of a class of 1-D parabolic systems under spatially point measurements control of a class of 1-d parabolic systems under spatially point measurements," *Journal of the Franklin Institute*, vol. 354, no. 1, pp. 197–214, 2017.

[42] J.-W. Wang, S.-H. Tsai, H.-X. Li, and H.-K. Lam, "Spatially piecewise fuzzy control design for sampled-data exponential stabilization of semilinear parabolic PDE systems," *IEEE Transactions on Fuzzy Systems*, vol. 26, no. 5, pp. 2967–2980, 2018.

[43] J. W. Wang, Y. Q. Liu, and C. Y. Sun, "Observer-based dynamic local piecewise control of a linear parabolic PDE using non-collocated local piecewise observation," *IET Control Theory & Applications*, vol. 12, no. 3, pp. 346–358, 2018.

[44] J.-W. Wang, Y.-Q. Liu, and C.-Y. Sun, "Pointwise exponential stabilization of a linear parabolic PDE system using non-collocated pointwise observation," *Automatica*, vol. 93, pp. 197–210, 2018.

[45] Y. Q. Liu, J. W. Wang, and C. Y. Sun, "Observer-based output feedback compensator design for linear parabolic PDEs with local piecewise control and pointwise observation in space," *IET Control Theory & Applications*, vol. 12, no. 13, pp. 1812–1821, 2018.

[46] H.-N. Wu and Z.-P. Wang, "Observer-based H_∞ sampled-data fuzzy control for a class of nonlinear parabolic PDE systems sampled-data fuzzy control for a class of nonlinear parabolic PDE systems," *IEEE Transactions on Fuzzy Systems*, vol. 26, no. 2, pp. 454–473, 2018.

[47] J.-W. Wang and J.-M. Wang, "Dynamic compensator design of linear parabolic mimo PDEs in n-dimensional spatial domain," *IEEE Transactions on Automatic Control*, vol. 66, no. 3, pp. 1399–1406, 2020.

[48] W. Youn and H. Myung, "Robust interacting multiple model with modeling uncertainties for maneuvering target tracking," *IEEE Access*, vol. 7, pp. 65427–65443, 2019.

[49] J. Xue-bo, L. Xiao-feng, S. Ting-li, S. Yan, and M. Bei-bei, "Closed-loop estimation for randomly sampled measurements in target tracking system," *Mathematical Problems in Engineering*, vol. 2014, Article ID 315908, , 2014.

[50] H. Zhang, X. Zhou, Z. Wang, and H. Yan, "Maneuvering target tracking with event-based mixture kalman filter in mobile sensor networks," *IEEE Transactions on Cybernetics*, vol. 50, no. 10, pp. 4346–4357, 2019.

[51] X. Zhang, F. Ding, and E. Yang, "State estimation for bilinear systems through minimizing the covariance matrix of the state estimation errors," *International Journal of Adaptive Control and Signal Processing*, vol. 33, no. 7, pp. 1157–1173, 2019.

[52] X. Zhang and F. Ding, "Hierarchical parameter and state estimation for bilinear systems," *International Journal of Systems Science*, vol. 51, no. 2, pp. 275–290, 2020.

[53] F. Ding, "State filtering and parameter estimation for state space systems with scarce measurements," *Signal Processing*, vol. 104, pp. 369–380, 2014.

[54] F. Ding, X. Zhang, and L. Xu, "The innovation algorithms for multivariable state-space models," *International Journal of Adaptive Control and Signal Processing*, vol. 33, no. 11, pp. 1601–1618, 2019.

[55] X. Zhang and F. Ding, "Adaptive parameter estimation for a general dynamical system with unknown states," *International Journal of Robust and Nonlinear Control*, vol. 30, no. 4, pp. 1351–1372, 2020.

[56] X. Zhang, F. Ding, and L. Xu, "Recursive parameter estimation methods and convergence analysis for a special class of nonlinear systems," *International Journal of Robust and Nonlinear Control*, vol. 30, no. 4, pp. 1373–1393, 2020.

[57] F. Ding, L. Xu, D. Meng, X.-B. Jin, A. Alsaedi, and T. Hayat, "Gradient estimation algorithms for the parameter identification of bilinear systems using the auxiliary model," *Journal of Computational and Applied Mathematics*, vol. 369, Article ID 112575, 2020.

[58] F. Ding, L. Lv, J. Pan, X. Wan, and X.-B. Jin, "Two-stage gradient-based iterative estimation methods for controlled autoregressive systems using the measurement data,"

International Journal of Control, Automation and Systems, vol. 88, pp. 886–896, 2019.

[59] R. Wang, Y. Li, H. Sun, Y. Zhang, and Y. Sun, "Performance analysis of switched control systems under common-source digital upsets modeled by MDHMM," *Complexity*, vol. 2018, Article ID 4329053, , 2018.

[60] R. Wang, P. Du, W. Zhong, H. Han, and H. Sun, "Analyses and encryption implementation of a new chaotic system based on semitensor product," *Complexity*, vol. 2020, Article ID 1230804, , 2020.

[61] X.-B. Jin, H.-X. Wang, X.-Y. Wang, Y.-T. Bai, T.-L. Su, and J.-L. Kong, "Deep-learning prediction model with serial two-level decomposition based on bayesian optimization," *Complexity*, vol. 2020, Article ID 4346893, , 2020.

[62] J. Pan, H. Ma, X. Jiang, W. Ding, and F. Ding, "Adaptive gradient-based iterative algorithm for multivariable controlled autoregressive moving average systems using the data filtering technique," *Complexity*, vol. 2018, Article ID 9598307, , 2018.

[63] H. Wu and H. Li, "H_∞ Fuzzy observer-based control for a class of nonlinear distributed parameter systems with control constraints," *IEEE Transactions on Fuzzy Systems*, vol. 16, no. 2, pp. 502–516, 2008.

[64] B. Luo, T. Huang, H.-N. Wu, and X. Yang, "Data-driven H_∞ control for nonlinear distributed parameter systems control for nonlinear distributed parameter systems," *IEEE Transactions on Neural Networks and Learning Systems*, vol. 26, no. 11, pp. 2949–2961, 2015.

[65] J.-W. Wang and J.-M. Wang, "Mixed H_2/H_∞ sampled-data output feedback control design for a semi-linear parabolic PDE in the sense of spatial L∞ norm h_2/H_∞ sampled-data output feedback control design for a semi-linear parabolic pde in the sense of spatial l_∞ norm," *Automatica*, vol. 103, pp. 282–293, 2019.

[66] J.-W. Wang, "A unified lyapunov-based design for a dynamic compensator of linear parabolic mimo PDEs," *International Journal of Control*, pp. 1–8, 2019.

[67] Y. Liu and C. Sun, "H_∞ piecewise control for linear parabolic distributed parameter systems with piecewise observation in space piecewise control for linear parabolic distributed parameter systems with piecewise observation in space," *IEEE Access*, vol. 7, pp. 62865–62874, 2019.

[68] J.-W. Wang, "Exponentially stabilizing observer-based feedback control of a sampled-data linear parabolic multiple-input-multiple-output pde," *IEEE Transactions on Systems, Man, and Cybernetics: Systems*, 2019.

[69] V. Balakrishnan, "All about the Dirac delta function (?)," *Resonance*, vol. 8, no. 8, pp. 48–58, 2003.

[70] M. Krstic and A. Smyshlyaev, *Boundary Control of PDEs: A Course on Backstepping Designs*, SIAM, Philadephia, PA, USA, 2008.

Hindawi
Complexity
Volume 2021, Article ID 5577675, 19 pages
https://doi.org/10.1155/2021/5577675

Research Article

Distributed Event-Triggered Output Synchronization of Complex-Valued Memristive Reaction-Diffusion Complex Networks with Spatial Sampled-Data

Tiane Chen and Zaihe Cheng

School of Internet of Things, Wuxi Institute of Technology, Wuxi 214121, China

Correspondence should be addressed to Tiane Chen; chente@wxit.edu.cn

Received 4 February 2021; Revised 24 February 2021; Accepted 13 March 2021; Published 26 March 2021

Academic Editor: Xue-bo Jin

This study addresses the problem of output quasisynchronization for coupled complex-valued memristive reaction-diffusion complex networks via the distributed event-triggered control scheme. First, by using the separate method, set value mapping, and intermediate value theorem, the complex-valued memristive reaction-diffusion complex networks can be transferred into two semi-uncertain real-valued reaction-diffusion complex networks. Second, a distributed output piecewise event-triggered control (OPETC) scheme with spatial sampled-data is first proposed including a spatial sampling event-triggered generator and spatiotemporal sampling state feedback controller. Furthermore, this scheme can effectively save the measurement resources and lower the update rate of controllers in spatial and time domain. Third, the synchronization analysis is considered by utilizing an appropriate Lyapunov function, the Halanay inequality, and the improved Wirtinger inequality. Subsequently, several output event-triggered quasisynchronization criteria are derived. The relations among event trigger conditions, spatial sampling interval, convergence rate, and control gain are given by rigorous mathematical derivation. Finally, multiple simulations are compared to substantiate the validation of the OPETC scheme.

1. Introduction

Complex networks have excited continuous interest for their nonlinear learning characteristics and have been extensively implemented in various domains such as deep learning [1–3], natural language analyzation, optimization computing, and image segments. When two or more networks interact, coupled complex networks, such as coupled neural networks (CNNs), can be formed and have attracted much considerable attentions for their significant collective dynamical behaviour. As an important collective dynamical behaviour, synchronization means that the states of complex networks are always consistent over time. Many crucial results about the synchronization of CNNs have been achieved in literatures [4–7]. For instance, Bai and Xu [4] studied the synchronization of CNNs with hybrid coupling, Luo and Yao [5] investigated the finite-time synchronization of uncertain complex dynamic networks, Wang et al. [6] researched the synchronization of coupled CNNs via the pinning method, and Ding et al. [7] considered the impulsive synchronization of complex networks.

It should be highlighted that most research studies suppose that the electromagnetic fields of complex networks are uniform, and the networks states vary only with time. In fact, inhomogeneous electromagnetic fields inevitably exist in cellular networks [8], genetic regulatory networks, and traffic networks. In nonuniform electromagnetic fields, the networks states in different spatial positions are distinct and change simultaneously. This phenomenon can be expressed as the reaction-diffusion (RD) term in mathematical models. Then, the CNNs model is transformed into coupled RD neural networks (CRDNNs) with infinite dimensional states. Up to now, plenty of impressive studies on the synchronization of CRDNNs have been achieved. The authors

investigated the impulsive synchronization [9], the adaptive synchronization [10], and the passivity [11] of CRDNNs. The abovementioned works assumed that the global spatial state information was known, and all these research studies aimed to synchronize all states. In some applications, it is costly and not necessary to measure the whole infinite dimensional state and to synchronize all states. Therefore, it is valuable to research partial state synchronization using incomplete measurements. Partial state synchronization named output synchronization (OS) has been investigated in literatures [12–15]. The authors [16] studied OS of CRDNNs with input constraints via continuous time control, and the authors [17] investigated OS of CRDNNs with spatial sampled-data via continuous time control. To our knowledge, few results about OS of CRDNNs have been investigated via noncontinuous time control. This is our first motivation for this study.

Abovementioned investigations of complex networks have intensively emerged with state-independent weights realized by resistors. As a special resistor, memristor has been proposed by Chua [18] and has been realized first by HP Labs. Memristor can retain its history state owing to its switch characteristic which makes the memristor an attractive candidate to emulate the biological brain to improve machine intelligence [19, 20]. Consequently, memristive reaction-diffusion neural networks (MRDNNs) can be constructed with richer properties than common CRDNNs. Accordingly, it is significant to study MRDNNs with state-dependent weight. Until now, many worthwhile results about MRDNNs have been achieved. Global synchronization [21, 22], exponential Lag synchronization [23], and fixed-time synchronization [24] of MRDNNs have been studied. Nonetheless, the mismatch of the master-slave system due to state-dependent parameters inevitably causes the synchronization error of the collective behaviour to change in a certain range. That is quasisynchronization [25]. Actually, the research results on quasisynchronization of MRDNNs have not yet been published. This is our second motivation for this study.

Different from real-valued neural networks, complex-valued neural networks own more complicated properties. Some scientific questions, such as the phase-sensitive detection [26] and exclusive or problem [27] in optical signal processing, can only be addressed by complex-valued neural networks. Complex-valued MRDNNs (CMRDNNs) have complex-valued states, state-dependent parameter, and complex-valued activation function which are more general than real-valued MRDNNs. Hence, it is necessary to investigate CMRDNNs. Besides, the existing difficulty is that complex-valued functions may not be bounded or analytic [28]. Many assumptions about real-valued functions cannot be utilized in the complexed-valued domain without any preprocessing. Thus, the general approach is to convert complex-valued functions into two parts: real and imaginary parts. Using this conversion method, intermittent control synchronization [28], exponential sampled-data synchronization, [29] and pinning control synchronization [30] of complex-valued memristive networks were investigated without considering RD term. Nevertheless, the synchronization problem of CMRDNNs has rarely been addressed. Song et al. [31] studied the finite-time synchronization of CMRDNNs with known full state information and activation function bounds. Therefore, it is meaningful to further research the synchronization problem of CMRDNNs with incomplete measurements.

To achieve the synchronization of complex networks, many control strategies have been studied, such as continuous time control [16], sampled-data estimation and control [29, 32], and intermittent control [28]. Among these control strategies, sampled-data control has received wider attention because this method can reduce communication bandwidth. Sampled-data control includes time-triggered control and event-triggered control [33–35]. Compared with the time-triggered control mechanism, the event-triggered control scheme updates information only when the measurement error satisfies the triggering threshold condition, which leads to a lower information exchange rate. Therefore, the event-triggered sampling control strategy performs better than the time-triggered method [36]. Event trigger's form can be considered as $\|e(x,t)\|^2 > \gamma\|z(x,t)\|^2 + \eta(t)$. The event trigger is considered static one when the function $\eta(t)$ is a constant, and the event trigger is considered dynamic one when the derivative of the function $\eta(t)$ is not zero [37]. Thus, the event-triggered control strategy can be classified into dynamical event triggers and static event triggers according to the function $\eta(t)$. Meanwhile, the event-triggered control can be classified into centralized control and distributed control according to the scope of the controller. In large-scale coupled networks, it is difficult to realize complete centralized control. Thus, further research on distributed event-triggered control is crucial, and one of the primary problems to be prevented by event-triggered control scheme is Zeno phenomenon. As far as we know, the distributed event-triggered control strategy for synchronization of CMRDNNs with incomplete spatial measurement has not been studied so far. This is our third motivation for this study.

Motivated by the abovementioned analysis, the main aim of this work is to establish the output quasisynchronization conditions of CMRDNNs via distributed event-triggered partial spatial control strategy. More specially, some questions should be solved: How to obtain the error model of the master-slave networks systems with state-dependent parameters? How to design an efficient distributed piecewise event-triggered control strategy using incomplete measurement to achieve output synchronization? What are the effects of dynamic event trigger and static event trigger on quasisynchronization? To achieve the control goal and answer the above three questions, there are three innovations in this study:

(1) A general CMRDNNs mathematical model with the output matrix is proposed. By using set-valued mappings, differential inclusions, and nonfragile techniques, the real-valued synchronization error model with uncertainty parameters is derived, and the assumption conditions about activation functions are more relaxed.

(2) We establish a distributed output piecewise event-triggered control (OPETC) strategy with spatial

sampled-data to ensure the convergent speed and to reduce the communication cost. By using some inequalities and an appropriate Lyapunov functional, several universal criteria guaranteeing the output quasisynchronization of the discussed networks are established, where the relations among diffusion coefficients, control gains, memristive complex-valued range, and time delays are clear.

(3) By comparing the simulation results of time trigger, dynamical event trigger, static event trigger, and piecewise event trigger, the high efficiency of the OPETC strategy is verified.

The structure of this study is as follows: the mathematical model is established and some assumptions are given. Then, the real-valued synchronization error models with uncertainty parameters are deduced in Section 2. A distributed piecewise event-triggered control strategy with spatial sampled-data is designed, and several universal criteria guaranteeing the output quasisynchronization of the discussed networks are deduced in Section 3. Simulation examples are given to compare the effect of different triggers and to corroborate the quasisynchronization conditions in Section 4. Section 5 draws the conclusion of this study and clarifies our future research.

2. Preliminaries

In this section, we provide some necessary lemmas and show the process of deriving the mathematical model of the master-slave networks system to two real-valued error models.

2.1. Notations. Let $\mathcal{N} = \{0, 1, 2, \ldots\}$ and $\mathcal{N}^+ = \{1, 2, \ldots\}$. For each $n \in \mathcal{N}^+$, $\mathcal{N}_n = \{0, 1, 2, \ldots, n\}$ and $\mathcal{N}_n^+ = \{1, 2, \ldots, n\}$. $\mathcal{R}$ and $\mathcal{C}$ denote the set of real-valued space and complex-valued space, respectively. Similarly, $\mathcal{R}^n$ and $\mathcal{C}^n$ represent the sets of n-dimensional real-valued and n-dimensional complex-valued vectors. $\mathcal{R}^{n\times N}$ and $\mathcal{C}^{n\times N}$ describe the sets of $n \times N$ real-valued matrices and complex-valued matrices. The Hilbert space of square integrable functions over Ω is denoted by $\mathcal{L}_n^2(\Omega)$ with norm $\|z(x,\cdot)\|^2 = \int_\Omega z^T(x,\cdot)z(x,\cdot)\mathrm{d}x$, $\Omega = (0, l)$, and $n \in \mathcal{N}^+$. $\mathcal{I}_n$ is a n-dimensional identity matrix. $\mathcal{H}_n^1(\Omega) = \{z \in \mathcal{L}_n^2(\Omega) | /\mathrm{d}z\mathrm{d}x \in \mathcal{L}_n^2(\Omega)\}$ is a Sobolev space which is also a subspace of $\mathcal{L}_n^2(\Omega)$. T denotes the matrix transposition, and $\otimes$ represents the Kronecker product. l denotes the imaginary part with $\iota = \sqrt{-1}$. $z(x,\cdot) = z^R(x,\cdot) + \iota z^I(x,\cdot)$, $z^R(x,\cdot) \in \mathcal{R}$, and $z^I(x,\cdot) \in \mathcal{R}$.

2.2. Model Transform. In a master-slave system scheme, there are two coupled networks with the same structure and diverse initial values. The master-coupled complex-valued memristive reaction-diffusion networks can be expressed as

$$\begin{cases} \dfrac{\partial \tilde{z}_i(x,t)}{\partial t} = -A\tilde{z}_i(x,t) + B\dfrac{\partial^2 \tilde{z}_i(x,t)}{\partial x^2} + c(\tilde{z}_i(x,t))f_i(\tilde{z}_i(x,t)) + \sum_{j=1}^{N} d_{ij}\Gamma g_j\big(\tilde{z}_j\big(x, t-\tau_j(t)\big)\big), \\ \tilde{y}_i(x,t) = \beta\tilde{z}_i(x,t), \end{cases} \tag{1}$$

where $\tilde{z}_i(x,t) = (\tilde{z}_{i1}(x,t), \cdots, \tilde{z}_{in}(x,t))^T \in \mathcal{H}_n^1(\Omega)$ denotes the state information of the ith networks with $i \in \mathcal{N}_N^+$, $t \in [t_0, +\infty)$ and $t_0 \geq 0$; $x \in \Omega$ corresponds to the space variable; $A \in \mathcal{R}^{n\times n}$ represents the self-inhibition coefficient; $B \in \mathcal{R}^{n\times n}$ denotes the diffusion coefficient; $\tau_j(t)$ represents the nonnegative time-varying transmission delay from the jth networks to the ith networks; $\overline{\tau} = \max(\tau_j(t))$; $c(\tilde{z}_{\mathrm{i}}(x,t))$ is the connection weights with memristive characteristic; $f_i(\cdot)$ corresponds to the neural activation vector function of the ith networks; $\Gamma \in \mathcal{R}^{n\times n}$ is the inner coupling matrix; $D = (d_{ij})_{N\times N} \in \mathcal{C}^{N\times N}$ denotes the coupling strength matrix where $d_{ii} = -\sum_{j=1, j\neq i}^{N} d_{ij}$; $g_j(\cdot)$ denotes the complex-valued state function; $\tilde{y}_i(x,t) \in \mathcal{C}^{\mathrm{r}\times 1}$ is the output vector; $\beta \in \mathcal{R}^{r\times n}$ represents the output matrix; and $\beta^{\mathrm{T}}\beta$ is the idempotent matrix.

The initial values and the Dirichlet boundary values of the master networks are given by

$$\begin{aligned} &\hat{z}_i(x,s) = \hat{v}_i(x,s),\ (x,t) \in \Omega \times [t_0 - \overline{\tau}, t_0], \\ &\hat{z}_i(0,t) = \hat{z}_i(l,t) = 0,\ (x,t) \in \partial\Omega \times [t_0 - \overline{\tau}, +\infty], \end{aligned} \tag{2}$$

,where $\tilde{v}_i(x,s)$ is a complex-valued function.

Similarly, the slave networks can be designed as

$$\begin{cases} \dfrac{\partial \hat{z}_i(x,t)}{\partial t} = -A\hat{z}_i(x,t) + B\dfrac{\partial^2 \hat{z}_i(x,t)}{\partial x^2} + c_i(\hat{z}_i(x,t))f_i(\hat{z}_i(x,t)) + \sum_{j=1}^{N} d_{ij}\Gamma g_j\big(\hat{z}_j\big(x, t-\tau_j(t)\big)\big) + \hat{u}_i(x,t), \\ \hat{y}_i(x,t) = \beta\hat{z}_i(x,t), \end{cases} \tag{3}$$

where $\hat{u}_i(x,t) \in \mathscr{H}_n^1(\Omega)$ is the control input of the ith networks to achieve output synchronization; the initial condition and the Dirichlet boundary condition of the slave networks are given by

$$\begin{aligned} &\hat{z}_i(x,s) = \hat{v}_i(x,s),\ (x,t) \in \Omega \times [t_0 - \overline{\tau}, t_0], \\ &\hat{z}_i(0,t) = \hat{z}_i(l,t) = 0,\ (x,t) \in \partial\Omega \times [t_0 - \overline{\tau}, +\infty], \end{aligned} \tag{4}$$

where $\hat{v}_i(x,s)$ is a complex-valued function.

Suppose that c_i^0 and c_i^1 are two complex-valued constants and $v_i(x,t) \in \mathscr{C}$. According to the switch property of memristor, the connection weight $c_i(v_i(x,t))$ can be defined as

$$c_i(v_i(x,t)) = \begin{cases} c_i^0, & v_i(\cdot,t)\uparrow, \\ c_i^1, & v_i(\cdot,t)\downarrow, \\ \lim\limits_{s \longrightarrow t^-} c_i(v_i(\cdot,t)), & v_i(\cdot,t)\ \text{unchange}, \end{cases} \tag{5}$$

where $c_i^0 = c_i^{0R} + \imath c_i^{0I}$, $c_i^1 = c_i^{1R} + \imath c_i^{1I}$, $\overline{c}_i^R = \max\{c_i^{0R}, c_i^{1R}\}$, $\underline{c}_i^R = \min\{c_i^{0R}, c_i^{1R}\}$, $\overline{c}_i^I = \max\{c_i^{0I}, c_i^{1I}\}$, and $\underline{c}_i^I = \min\{c_i^{0I}, c_i^{1I}\}$.

We can formulate equations (1) and (3) in a compact matrix form as

$$\begin{cases} \dfrac{\partial \tilde{z}(x,t)}{\partial t} = -(I_N \otimes A)\tilde{z}(x,t) + (I_N \otimes B)\dfrac{\partial^2 \tilde{z}(x,t)}{\partial x^2} + C(\tilde{z}(x,t))f(\tilde{z}(x,t)) + D \otimes \Gamma g(\tilde{z}(x,t-\tau(t))), \\ \tilde{y}(x,t) = (I_N \otimes \beta)\tilde{z}(x,t), \\ \dfrac{\partial \hat{z}(x,t)}{\partial t} = -(I_N \otimes A)\hat{z}(x,t) + (I_N \otimes B)\dfrac{\partial^2 \hat{z}(x,t)}{\partial x^2} + C(\hat{z}(x,t))f(\hat{z}(x,t)) + D \otimes \Gamma g(\hat{z}(x,t-\tau(t))) + u(x,t), \\ \hat{y}(x,t) = (I_N \otimes \beta)\hat{z}(x,t), \end{cases} \tag{6}$$

where $\tilde{z}(x,t) = (\tilde{z}_1^T(x,t), \ldots, \tilde{z}_N^T(x,t))^T$, $\hat{z}(x,t) = (\hat{z}_1^T(x,t), \ldots, \hat{z}_N^T(x,t))^T$, $u(x,t) = [u_1^T(x,t), u_2^T(x,t), \ldots, u_N^T(x,t)]^T$, $C(\tilde{z}(x,t)) = (c_1(\tilde{z}_1^T(x,t)), \ldots, c_N(\tilde{z}_N^T(x,t)))^T$, $C(\hat{z}(x,t)) = (c_1(\hat{z}_1^T(x,t)), \ldots, c_N(\hat{z}_N^T(x,t)))^T$, $f(\cdot) = (f_1^T(\cdot), \ldots, f_N^T(\cdot))^T$, $g(\cdot) = (g_1^T(\cdot), \ldots, g_N^T(\cdot))^T$, $\tilde{y}(x,t) = (\tilde{y}_1^T(x,t), \ldots, \tilde{y}_N^T(x,t))^T$, and $\hat{y}(x,t) = (\hat{y}_1^T(x,t) \ldots, \hat{y}_N^T(x,t))^T$.

Assume that the master-slave networks (equations (1) and (3)) with Dirichlet boundary conditions have unique continuous solutions $\tilde{z}_i(x,t)$ and $\hat{z}(x,t)$, respectively.

Remark 1. The authors [17] considered the reaction-diffusion term and output matrix. The mathematical model in [38] included memristive parameters and reaction-diffusion terms without complex-valued state and output matrix. The authors [31] investigated complex-valued states, memristive parameters, and reaction-diffusion term without considering output matrix. Different from literatures [17, 31, 38], this study introduces complex value states, memristive parameters, reaction-diffusion terms, and output matrices into the mathematical model, which are more general and practical in applications.

Our goal is to synchronize the master system (equation (1)) and the slave system (equation (3)). Then, we naturally need to derivate the error model of the master-slave system. However, many assumptions about real-valued functions cannot be utilized in the complexed-valued domain. Meanwhile, the existence of memristive parameters leads to parameter mismatch of the master networks system and the slave one. Obviously, there are some difficulties in deriving the error model directly. Thus, the model should be converted. First, the complex-valued model is converted into two real-valued models by using some assumptions. Second, the real-valued synchronization error model can be obtained by using different techniques.

Assumption 1. $z(x,t)$, $C(z(x,t))$, and $f(z(x,t))$ can be divided into real and imaginary parts, respectively.

$$\begin{cases} z(x,t) = z^R(x,t) + \imath z^I(x,t), \\ C(z(x,t)) = C^R(z(x,t)) + \imath C^I(z(x,t)), \\ f(z(x,t)) = f^R(z(x,t)) + \imath f^I(z(x,t)), \end{cases} \tag{7}$$

where $z^R(x,t), C^R(z(x,t))$, and $f^R(z(x,t))$ are the real parts; $z^I(x,t), C^I(z(x,t))$, and $f^I(z(x,t))$ are the imaginary parts.

Lemma 1 see ([39]). *For any function* $\{v(\xi) | \xi \in [a,b], v(\xi) \in \mathscr{H}_n^1(a,b)\}$. *If* $x(a) = 0$ *or* $x(b) = 0$, *then*

$$\int_a^b v^T(\xi)v(\xi)\mathrm{d}\xi \le \frac{4(b-a)^2}{\pi^2}\int_a^b \left(\frac{\partial v(\xi)}{\partial \xi}\right)^T \frac{\partial v(\xi)}{\partial \xi}\mathrm{d}\xi. \tag{8}$$

Corollary 1 see ([40, 41]). *For any function* $\{x(\xi) | \xi \in [a,b], x(\xi) \in \mathscr{H}_n^1(a,b)\}$, $c = a$ *or* b. *If* $r_0, r_1, r_2, r_3 > 0$, *then the following integral inequalities hold,*

$$-r_0\int_a^b\left(\frac{\partial x(\xi)}{\partial\xi}\right)^2 d\xi - r_1\int_a^b x^2(c)d\xi \le -r_2\int_a^b x^2(\xi)d\xi, \tag{9}$$

where $r_2 = \pi^2 r_0 r_1/(\pi^2 r_0 + 4(b-a)^2 r_1)$.

Similarly, we can get

$$-r_0\int_a^b\left(\frac{\partial x(\xi)}{\partial\xi}\right)^2 d\xi + r_1 x^2(c) \le r_3\int_a^b x^2(\xi)d\xi, \tag{10}$$

where $r_3 = \pi^2 r_0 r_1/(\pi^2 r_0 - 4(b-a)^2 r_1)$.

Lemma 2 see ([25, 42]). *Assume that the function* $W(t) \ge 0$ *for all* $t \in (-\infty, +\infty)$,

$$\begin{cases} \dfrac{dW(t)}{dt} \le \alpha(t)W(t) + \beta(t)\sup\limits_{t-\tau(t)\le s\le t} W(s) + \gamma(t), & t \ge t_0, \\ W(t) = |\psi(t)|, & t \le t_0, \end{cases} \tag{11}$$

where $\psi(t)$ *is bounded and continuous and three functions* $-\alpha(t)$, $\beta(t)$, *and* $\gamma(t)$ *are continuous and positive. If there exists* $\sigma > 0$ *and* $\alpha(t) + \beta(t) \le -\sigma$ *for* $t \ge t_0$, *then we have* $W(t) \le (\overline{\gamma}/\sigma) + \sup_{t-\tau(t)\le s\le t} W(s)\exp(-\underline{\eta}(t-t_0))$, *where* $\overline{\gamma} = \sup_{t_0\le t}\gamma(t)$ *and* $\underline{\eta} = \inf_{t_0\le t}\{\eta(t)\colon \overline{\eta}(t) + \alpha(t) + \beta(t)\exp(\eta(t)\tau(t)) = 0\}$.

Under Assumption *1*, equation *(6)* can be divided into two real-valued mathematical models as

$$\begin{cases} \dfrac{\partial \tilde{z}^R(x,t)}{\partial t} = -(I_N\otimes A)\tilde{z}^R(x,t) + (I_N\otimes B)\dfrac{\partial^2\tilde{z}^R(x,t)}{\partial x^2} + C^R(\tilde{z}(x,t))f^R(\tilde{z}(x,t)), \\ -C^I(\tilde{z}(x,t))f^I(\tilde{z}(x,t)) + D\otimes\Gamma g^R(\tilde{z}(x,t-\tau(t))), \\ \tilde{y}^R(x,t) = (I_N\otimes\beta)\tilde{z}^R(x,t), \\ \dfrac{\partial \tilde{z}^I(x,t)}{\partial t} = -(I_N\otimes A)\tilde{z}^I(x,t) + (I_N\otimes B)\dfrac{\partial^2\tilde{z}^I(x,t)}{\partial x^2} + C^R(\tilde{z}(x,t))f^I(\tilde{z}(x,t)), \\ +C^I(\tilde{z}(x,t))f^R(\tilde{z}(x,t)) + D\otimes\Gamma g^I(\tilde{z}(x,t-\tau(t))), \\ \tilde{y}^I(x,t) = (I_N\otimes\beta)\tilde{z}^I(x,t), \end{cases} \tag{12}$$

$$\begin{cases} \dfrac{\partial \hat{z}^R(x,t)}{\partial t} = -(I_N\otimes A)\hat{z}^R(x,t) + (I_N\otimes B)\dfrac{\partial^2\hat{z}^R(x,t)}{\partial x^2} + C^R(\hat{z}(x,t))f^R(\hat{z}(x,t)), \\ -C^I(\hat{z}(x,t))f^I(\hat{z}(x,t)) + D\otimes\Gamma g^R(\hat{z}(x,t-\tau(t))) + u^R(x,t), \\ \hat{y}^R(x,t) = (I_N\otimes\beta)\hat{z}^R(x,t), \\ \dfrac{\partial \hat{z}^I(x,t)}{\partial t} = -(I_N\otimes A)\hat{z}^I(x,t) + (I_N\otimes B)\dfrac{\partial^2\hat{z}^I(x,t)}{\partial x^2} + C^R(\hat{z}(x,t))f^I(\hat{z}(x,t)), \\ +C^I(\hat{z}(x,t))f^R(\hat{z}(x,t)) + D\otimes\Gamma g^I(\hat{z}(x,t-\tau(t))) + u^I(x,t), \\ \hat{y}^I(x,t) = (I_N\otimes\beta)\hat{z}^I(x,t). \end{cases} \tag{13}$$

Let $\underline{C}_i = diag\{\underline{c}_1, \ldots, \underline{c}_n\}$, $\overline{C}_i = diag\{\overline{c}_1, \ldots, \overline{c}_n\}$, $\underline{C} = diag\{\underline{C}_i\}_{N\times N} \in \mathscr{C}^{nN\times nN}$, $\overline{C} = diag\{\overline{C}_i\}_{N\times N} \in \mathscr{C}^{nN\times nN}$, and $C(v(x,t)) \in co\{\underline{C}, \overline{C}\}$. Using some properties of set-valued mapping [43], equations (12) and (13) can be expressed as the differential inclusions:

$$\begin{cases} \dfrac{\partial \tilde{z}^R(x,t)}{\partial t} \in -(I_N \otimes A)\tilde{z}^R(x,t) + (I_N \otimes B)\dfrac{\partial^2 \tilde{z}^R(x,t)}{\partial x^2} + co\left\{\overset{R}{\underline{C}}, \overline{C}^R\right\} f^R(\tilde{z}(x,t)) \\ -co\left\{\overset{I}{\underline{C}}, \overline{C}^I\right\} f^I(\tilde{z}(x,t)) + D \otimes \Gamma g^R(\tilde{z}(x,t-\tau(t))), \\ \dfrac{\partial \tilde{z}^I(x,t)}{\partial t} \in -(I_N \otimes A)\tilde{z}^I(x,t) + (I_N \otimes B)\dfrac{\partial^2 \tilde{z}^I(x,t)}{\partial x^2} + co\left\{\overset{R}{\underline{C}}, \overline{C}^R\right\} f^I(\tilde{z}(x,t)) \\ +co\left\{\overset{I}{\underline{C}}, \overline{C}^I\right\} f^R(\tilde{z}(x,t)) + D \otimes \Gamma g^I(\tilde{z}(x,t-\tau(t))), \\ \dfrac{\partial \hat{z}^R(x,t)}{\partial t} \in -(I_N \otimes A)\hat{z}^R(x,t) + (I_N \otimes B)\dfrac{\partial^2 \hat{z}^R(x,t)}{\partial x^2} + co\left\{\overset{R}{\underline{C}}, \overline{C}^R\right\} f^R(\hat{z}(x,t)) \\ -co\left\{\overset{I}{\underline{C}}, \overline{C}^I\right\} f^I(\hat{z}(x,t)) + D \otimes \Gamma g^R(\hat{z}(x,t-\tau(t))) + u^R(x,t), \\ \dfrac{\partial \hat{z}^I(x,t)}{\partial t} \in -(I_N \otimes A)\hat{z}^I(x,t) + (I_N \otimes B)\dfrac{\partial^2 \hat{z}^I(x,t)}{\partial x^2} + co\left\{\overset{R}{\underline{C}}, \overline{C}^R\right\} f^I(\hat{z}(x,t)) \\ +co\left\{\overset{I}{\underline{C}}, \overline{C}^I\right\} f^R(\hat{z}(x,t)) + D \otimes \Gamma g^I(\hat{z}(x,t-\tau(t))) + u^I(x,t), \end{cases} \tag{14}$$

where $\underline{C}_i^R = \mathrm{diag}\left\{\underline{c}_1^R, \ldots, \underline{c}_n^R\right\}, \overline{C}_i^R = \mathrm{diag}\{\overline{c}_1^R, \ldots, \overline{c}_n^R\}$, $\underline{C}_i^I = \mathrm{diag}\left\{\underline{c}_1^I, \ldots, \underline{c}_n^I\right\}, \overline{C}_i^I = \mathrm{diag}\{\overline{c}_1^I, \ldots, \overline{c}_n^I\}$, $\underline{C}^R = \mathrm{diag}\{\underline{C}_i^R\}_{N\times N}$, $\overline{C}^R = \mathrm{diag}\left\{\overline{C}_i^R\right\}_{N\times N}$, $\underline{C}^I = \mathrm{diag}\{\underline{C}_i^I\}_{N\times N}$, $\overline{C}^I = \mathrm{diag}\left\{\overline{C}_i^I\right\}_{N\times N}$, $\underline{C}^R, \overline{C}^R, \underline{C}^I, \overline{C}^I \in \mathscr{C}^{nN\times nN}$, $C^R(\tilde{z}(x,t)) \in co\left\{\underline{C}^R, \overline{C}^R\right\}$, and $C^I(\tilde{z}(x,t)) \in co\left\{\underline{C}^I, \overline{C}^I\right\}$.

Assumption 2. $f^R(\cdot)$, $f^I(\cdot)$, $g^R(\cdot)$, and $g^I(\cdot)$ are the bounded activation functions and are Lipschitz continuous. There exist positive values h_f^R,, h_f^I, h_g^R, h_g^I as

$$\begin{cases} \left\|f^R(\xi_1) - f^R(\xi_2)\right\|^2 \le h_f^R\left\|\xi_1 - \xi_2\right\|^2, \\ \left\|f^I(\xi_1) - f^I(\tilde{z}(x,t))\right\|^2 \le h_f^I\left\|\xi_1 - \xi_2\right\|^2, \\ \left\|g^R(\xi_1) - g^R(\xi_2)\right\|^2 \le h_g^R\left\|\xi_1 - \xi_2\right\|^2, \\ \left\|g^I(\xi_1) - g^I(\tilde{z}(x,t))\right\|^2 \le h_g^I\left\|\xi_1 - \xi_2\right\|^2, \end{cases} \tag{15}$$

that hold for any $\xi_1, \xi_2 \in \mathscr{H}_n^1(a,b)$.

Remark 2. Assumption 2 is more relaxed than the one in the literatures [36, 38] and does not need to know the bounds of the state.

Assumption 3. The activation function term in equation (14) satisfies the following conditions:

$$\begin{cases} co\left\{\overset{R}{\underline{C}},\overline{C}^R\right\} f^R(\tilde{z}(x,t)) - co\left\{\overset{R}{\underline{C}},\overline{C}^R\right\} f^R(\hat{z}(x,t)) \subseteq co\left\{\overset{R}{\underline{C}},\overline{C}^R\right\}\left(f^R(\tilde{z}(x,t)) - f^R(\hat{z}(x,t))\right), \\ co\left\{\overset{I}{\underline{C}},\overline{C}^I\right\} f^I(\tilde{z}(x,t)) - co\left\{\overset{I}{\underline{C}},\overline{C}^I\right\} f^I(\hat{z}(x,t)) \subseteq co\left\{\overset{I}{\underline{C}},\overline{C}^I\right\}\left(f^I(\tilde{z}(x,t)) - f^I(\hat{z}(x,t))\right), \\ co\left\{\overset{R}{\underline{C}},\overline{C}^R\right\} f^I(\tilde{z}(x,t)) - co\left\{\overset{R}{\underline{C}},\overline{C}^R\right\} f^I(\hat{z}(x,t)) \subseteq co\left\{\overset{R}{\underline{C}},\overline{C}^R\right\}\left(f^I(\tilde{z}(x,t)) - f^I(\hat{z}(x,t))\right), \\ co\left\{\overset{I}{\underline{C}},\overline{C}^I\right\} f^R(\tilde{z}(x,t)) - co\left\{\overset{I}{\underline{C}},\overline{C}^I\right\} f^R(\hat{z}(x,t)) \subseteq co\left\{\overset{I}{\underline{C}},\overline{C}^I\right\}\left(f^R(\tilde{z}(x,t)) - f^R(\hat{z}(x,t))\right), \end{cases} \tag{16}$$

where $\tilde{z}(x,t), \hat{z}(x,t)$ are the solutions of equation (6) with the Dirichlet boundary condition.

Denote the error state, the error output, and the error activation function as $z^R(x,t) = \hat{z}^R(x,t) - \tilde{z}^R(x,t), z^I(x,t) = \hat{z}^I(x,t) - \tilde{z}^I(x,t), y^R(x,t) = \hat{y}^R(x,t) - \tilde{y}^R(x,t), y^I(x,t) = \hat{y}^I(x,t) - \tilde{y}^I(x,t)$, $H_f^R(\hat{z}(x,t) - \tilde{z}(x,t)) = f^R(\hat{z}(x,t)) - f^R(\tilde{z}(x,t)), H_f^I(\hat{z}(x,t) - \tilde{z}(x,t)) = f^I(\hat{z}(x,t)) - f^I(\tilde{z}(x,t))$, and $H_g^R(\hat{z}(x,t) - \tilde{z}(x,t)) = g^R(\hat{z}(x,t)) - g^R(\tilde{z}(x,t)), H_g^I(\hat{z}(x,t) - \tilde{z}(x,t)) = g^I(\hat{z}(x,t)) - g^I(\tilde{z}(x,t))$.

Under Assumption 3, the error system of equation (14) can be rephrased as

$$\begin{cases} \dfrac{\partial z^R(x,t)}{\partial t} \in -(I_N \otimes A) z^R(x,t) + (I_N \otimes B)\dfrac{\partial^2 z^R(x,t)}{\partial x^2} + co\left\{\overset{R}{\underline{C}},\overline{C}^R\right\} H_f^R(z(x,t)) \\ -co\left\{\overset{I}{\underline{C}},\overline{C}^I\right\} H_f^I(z(x,t)) + D \otimes \Gamma H_g^R(z(x,t-\tau(t))) + u^R(x,t), \\ y^R(x,t) = (I_N \otimes \beta) z^R(x,t), \\ \dfrac{\partial z^I(x,t)}{\partial t} \in -(I_N \otimes A) z^I(x,t) + (I_N \otimes B)\dfrac{\partial^2 z^I(x,t)}{\partial x^2} + co\left\{\overset{R}{\underline{C}},\overline{C}^R\right\} H_f^I(z(x,t)) \\ +co\left\{\overset{I}{\underline{C}},\overline{C}^I\right\} H_f^R(z(x,t)) + D \otimes \Gamma H_g^R(z(x,t-\tau(t))) + u^I(x,t), \\ y^I(x,t) = (I_N \otimes \beta) z^I(x,t). \end{cases} \tag{17}$$

There exist measurable matrices $\widetilde{C}^R(x,t) \in co\left\{\underline{C}^R, \overline{C}^R\right\}, \widetilde{C}^I(x,t) \in co\left\{\underline{C}^I, \overline{C}^I\right\}$, and one has

$$\begin{cases} \dfrac{\partial z^R(x,t)}{\partial t} = -(I_N \otimes A)z^R(x,t) + (I_N \otimes B)\dfrac{\partial^2 z^R(x,t)}{\partial x^2} + \widetilde{C}^R(x,t)H_f^R(z(x,t)) \\ -\widetilde{C}^I(x,t)H_f^I(z(x,t)) + D \otimes \Gamma H_g^R(z(x,t-\tau(t))) + u^R(x,t), \\ y^R(x,t) = (I_N \otimes \beta)z^R(x,t), \\ \dfrac{\partial z^I(x,t)}{\partial t} = -(I_N \otimes A)z^I(x,t) + (I_N \otimes B)\dfrac{\partial^2 z^I(x,t)}{\partial x^2} + \widetilde{C}^R(x,t)H_f^I(z(x,t)) \\ +\widetilde{C}^I(x,t)H_f^R(z(x,t)) + D \otimes \Gamma H_g^R(z(x,t-\tau(t))) + u^I(x,t), \\ y^I(x,t) = (I_N \otimes \beta)z^I(x,t), \end{cases} \tag{18}$$

with the initial values and the boundary values of networks as

$$\begin{cases} z(0,t) = z(l,t) = 0, \quad t \in [t_0 - \overline{\tau}, +\infty], \\ z(x,t) = \nu(x,t), \\ \nu(x,t) = \widehat{\nu}(x,t) - \widetilde{\nu}(x,t), \\ (x,t) \in \Omega \times [t_0 - \overline{\tau}, t_0]. \end{cases} \tag{19}$$

Because the time-varying parameter is known, upper and lower bounds can be converted into a general semi-uncertain parameter by using the intermediate value theorem. There exists any $\varsigma_i(x,t)$ satisfied $0 \le \varsigma_i(x,t) \le 1$, and $\widetilde{c}_i^R(x,t) = \underline{c}_i^R + (\overline{c}_i^R - \underline{c}_i^R)\varsigma_i^R(x,t), \widetilde{c}_i^I(x,t) = \underline{c}_i^I + (\overline{c}_i^I - \underline{c}_i^I)\varsigma_i^I(x,t)$. Then, $\widetilde{C}(x,t)$ varies over time and can be expressed as semi-uncertain parameters:

$$\begin{cases} \widetilde{C}^R(x,t) = \underset{\underline{C}}{R} + \left(\overline{C}^R - \underset{\underline{C}}{R}\right)F^R(x,t), \\ \widetilde{C}^I(x,t) = \underset{\underline{C}}{I} + \left(\overline{C}^I - \underset{\underline{C}}{I}\right)F^I(x,t), \end{cases} \tag{20}$$

where $F^T(x,t)F(x,t) \le I_{nN}$, $F^R(x,t) = \mathrm{diag}(F_1^R(x,t), \ldots, F_N^R(x,t)), F_i^R(x,t) = \mathrm{diag}(\varsigma_1^R(x,t), \ldots, \varsigma_n^R(x,t))$, $F^I(x,t) = \mathrm{diag}(F_1^I(x,t), \ldots, F_N^I(x,t)), F_i^I(x,t) = \mathrm{diag}(\varsigma_1^I(x,t), \ldots, \varsigma_n^I(x,t))$, and $O^R = (\overline{C}^R - \underline{C}^R), O^I = (\overline{C}^I - \underline{C}^I)$.

Remark 3. Equations (18) and (20) can be seen as real-valued error models with semi-uncertainty parameters.

3. Output Event-Triggered Synchronization of CMRDNNs

3.1. Piecewise Event-Triggered Control Strategy. The state feedback input controller of the slave networks system can be designed as follows.

$$u_i(x,t) = -\sum_{q=1}^{Q} u_i(x_q,t) = -\sum_{q=1}^{Q} \alpha(x_q)L_i\beta^{\mathrm{T}}\beta z_i(x_q,t_k^i), \tag{21}$$

where $L_i = \mathrm{diag}\{L_{i1}, L_{i2}, \ldots, L_{in}\}$, $i \in \mathcal{N}_n$; $\alpha(x_q)$ denotes a spatial distributed operator with $\int_\Omega z(x,t)\alpha(x_q)\mathrm{d}x = z(x_q,t)$, and Q represents the number of the spatial sampled-data. For simplicity, $\alpha(x_q)$ can be replaced by α.

Remark 4. $u_i(x_q,t)$ only uses the output state in the partial spatial domain x_q and at some discrete time instantst_k. Thus, $u_i(x_q,t)$ can be seen as a distributed spatiotemporal sampled-data controller. Different from the spatial sampled-data controller designed in [17], this controller designed in equation (21) is a spatial and temporal sampling control.

Let $u(x,t) = [u_1^T(x,t), u_2^T(x,t), \ldots, u_N^T(x,t)]^T$, $L = \mathrm{diag}\{L_1, L_2, \ldots, L_N\}$, and $u(x,t)$ can be formulated into the real-valued compact matrix form:

$$\begin{cases} u^R(x,t) = -\sum_{q=1}^{Q} \alpha L^R(I_N \otimes \beta^T\beta)z^R(x_q,t_k), \\ u^I(x,t) = -\sum_{q=1}^{Q} \alpha L^I(I_N \otimes \beta^T\beta)z^I(x_q,t_k), \end{cases} \tag{22}$$

where $z^R(x_q,t_k) = (z_1^{RT}(x_q,t_k^1),\ldots,z_N^{RT}(x_q,t_k^N))^T$, and $z^I(x_q,t_k) = (z_1^{IT}(x_q,t_k^1),\ldots,z_N^{IT}(x_q,t_k^N))^T$.

The transmission time sequence of the input controller can be determined by event-triggered conditions.

The information flow diagram of the distributed event-triggered control mechanism corresponding to the ith slave system is shown in Figure 1, where the event trigger is used to determine whether the controller updates with the current spatial sampling signal. That is, an update event is determined by the event-triggered condition [44]:

The distributed output event-triggered condition is designed as

$$t_{k+1}^i = \inf\left\{t\colon t \geq t_k^i, \sum_{q=1}^{Q}\left(\beta e_i\left(x_q,t\right)\right)^T \beta e_i\left(x_q,t\right) - \sum_{q=1}^{Q}\gamma_i\left(\beta z_i\left(x_q,t\right)\right)^T \beta z_i\left(x_q,t\right) - \overline{\eta}_i(t) > 0\right\}, \tag{23}$$

where $e_i(x_q,t) = z_i(x_q,t_k^i) - z_i(x_q,t)$; t_{k+1}^i denotes the next event-triggered time instants of the ith networks; and $\gamma_i, \overline{\eta}_i(t) > 0$ represent parts of the event trigger which can be adaptive derived later.

The condition of equation (23) can generate a triggering time sequence $\{t_0^i,\cdots,t_k^i,t_{k+1}^i,\cdots\}$ for the ith networks control.

Let $e(x,t) = (e_1^T(x,t),\ldots,e_N^T(x,t))^T$, $\Upsilon = \text{diag}\{\gamma_1,\ldots\gamma_{,\text{N}}\}$, and the real-valued compact form of event-triggered condition can be expressed as

$$\begin{cases} \sum_{q=1}^{Q} e^{RT}\left(x_q,t\right)\left(I_N\otimes\beta^T\beta\right)e^R\left(x_q,t\right) > \sum_{q=1}^{Q} z^{RT}\left(x_q,t\right)\left(\Upsilon\otimes\beta^T\beta\right)z^R\left(x_q,t\right) + \overline{\eta}^R(t), \\ \sum_{q=1}^{Q} e^{IT}\left(x_q,t\right)\left(I_N\otimes\beta\right)e^I\left(x_q,t\right) > \sum_{q=1}^{Q} z^{IT}\left(x_q,t\right)\left(\Upsilon\otimes\beta\right)z^I\left(x_q,t\right) + \overline{\eta}^I(t), \end{cases} \tag{24}$$

where $\overline{\eta}(t) = \overline{\eta}^R(t) + \imath\overline{\eta}^I(t)$, $\overline{\eta}^R(t) = \sum_{i=1}^N \overline{\eta}_i^R(t)$, and $\overline{\eta}^I(t) = \sum_{i=1}^N \overline{\eta}_i^I(t)$.

Assume $\overline{\eta}_i(t)$ is a piecewise function as

$$\overline{\eta}_i(t) = \left(\overline{\eta}_{i0}^R + \imath\overline{\eta}_{i0}^I\right)ff(t),\ ff(t) = \begin{cases} \exp\left(-\kappa_1\left(t-t_0\right)\right),\ t_0 < t < t_f, \\ \exp\left(-\kappa_1\left(t_f-t_0\right)\right),\quad t \geq t_f, \end{cases} \tag{25}$$

where four parameters $\overline{\eta}_{i0}^R, \overline{\eta}_{i0}^I, \overline{\eta}_{i0}^R$, and $\overline{\eta}_{i0}^I$ are the positives, $\overline{\eta}_0^R = \sum_{i=1}^N \overline{\eta}_i^R(t_0)$, and $\overline{\eta}_0^I = \sum_{i=1}^N \overline{\eta}_i^I(t_0)$.

From equation (25), we find that $t_{k+1}^i > t_k^i$ is always satisfied. Therefore, the Zeno behaviour can be naturally excluded.

Remark 5. The distributed event-triggered method in [38] defined an event trigger for each neural network, and each event trigger required the entire state information of the corresponding neural networks. Different from the definition in [38], the distributed event trigger defined in equation (14) uses spatial sampled-data, which reduces the communication load and decreases the measurement cost.

Remark 6. Because the semi-uncertain error system always has a certain range of error [25], quasisynchronization is a more realistic goal. Meanwhile, to better solving the Zeno problem, the function $\overline{\eta}_i(t)$ in the event-triggered condition must be positive. Therefore, the piecewise function $\overline{\eta}_i(t)$ in equation (25) is a good selection which is different from the exponential function in literatures [45, 46].

Using the above distributed output piecewise event-triggered control strategy (equations (24) and (25)), the quasisynchronization conditions are obtained, and a theorem is constructed for the master-slave networks system in Section 3.2.

3.2. Synchronization Analysis

Theorem 1. *Under Assumptions 1, 2, and 3, using the distributed piecewise event-triggered mechanism (equation (23)) and the sampling controller (equation (21)), the master-slave networks systems (equations (1) and (3)) can be output quasisynchronized within the error Θ, and the error system (equation (18)) converges exponentially to the error level Θ with the convergence index $\underline{\kappa}_2 > 0$, if the criteria are satisfied:*

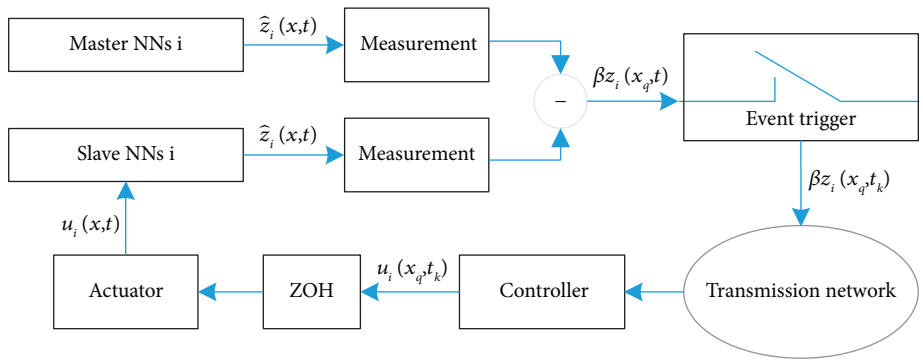

FIGURE 1: The ith event-triggered controller structure of the ith master-slave system.

$$\begin{cases} \dfrac{1}{\varepsilon^2}(2\varepsilon - 1) > \Upsilon, \\ \lambda_1 > \lambda_2 \exp(\kappa_2(t)\tau(t)) > 0, \end{cases} \tag{26}$$

where

$$\begin{aligned}
\Theta &= \frac{\varepsilon}{\lambda_1 - \lambda_2}\left(\lambda_{\max}(L^R)\overline{\eta}_0^R + \lambda_{\max}(L^I)\overline{\eta}_0^I\right)\sup_{t\geq t_0} ff(t), \\
ff(t) &= \begin{cases} \exp(-\kappa_1(t-t_0)), & t_0 < t < t_f, \\ \exp(-\kappa_1(t_f - t_0)), & t \geq t_f, \end{cases} \\
\underline{\kappa}_2 &= \inf_{t_0 \leq t}\{\kappa_2(t)\colon \kappa_2(t) - \lambda_1 + \lambda_2 \exp(\kappa_2(t)\tau(t)) = 0\}, \\
\lambda_1 &= \lambda_{\min}\left\{\left(2(I_N \otimes A) + \mathscr{R}_{1R} - \frac{3}{\varepsilon}I_{Nn} - \varepsilon h_f^R(\mathscr{P}_{1R} + \mathscr{P}_{1I})\right), 2(I_N \otimes A) + \mathscr{R}_{1I} - \frac{3}{\varepsilon}I_{Nn} - \varepsilon h_f^I(\mathscr{P}_{1R} + \mathscr{P}_{1I})\right\}, \\
\lambda_2 &= \lambda_{\max}\left\{(I_N \otimes \beta^T\beta)\varepsilon h_g^R \mathscr{P}_2, (I_N \otimes \beta^T\beta)\varepsilon h_g^I \mathscr{P}_2\right\} \\
\mathscr{R}_{1R} &= M_1 M_2 L^R\left(M_1 + 2\xi_1 M_2 L^R\right)^{-1}, \\
\mathscr{R}_{1I} &= M_1 M_2 L^I\left(M_1 + 2\xi_1 M_2 L^I\right)^{-1}, \\
\mathscr{P}_{1R} &= C^{RT}C^R + O^{RT}O^R, \\
\mathscr{P}_{1I} &= C^{IT}C^I + O^{IT}O^I, \\
\mathscr{P}_2 &= \left(D^T D \otimes \Gamma^T\Gamma\right) \\
M_1 &= 2(I_N \otimes B), \\
M_2 &= \left(\left(2 - \frac{1}{\varepsilon}\right)I_N - \varepsilon\Upsilon\right) \otimes I_n, \\
\xi_1 &= \frac{1}{\pi^2}\left(\max_{2\leq q\leq Q}\{x_q - x_{q-1}, x_1, (l - x_Q)\}\right)^2,
\end{aligned} \tag{27}$$

where $\lambda_{\min}$ and $\lambda_{\max}$ mean the minimum and maximum eigenvalues, respectively.

Proof. Construct the following Lyapunov functional for the system (equation (18)) as

$$\begin{aligned}
V(t) = &\int_\Omega z^{RT}(x,t)\left(I_N \otimes \beta^T\right)(I_N \otimes \beta)z^R(x,t)\mathrm{d}x \\
&+ \int_\Omega z^{IT}(x,t)\left(I_N \otimes \beta^T\right)(I_N \otimes \beta)z^I(x,t)\mathrm{d}x.
\end{aligned} \tag{28}$$

By using integral formula of division and equation (18), we can derive

$$\begin{aligned}\int_{\Omega} z^{RT}(x,t)2\left(I_N\otimes\beta^T\beta B\right)\frac{\partial^2 z^R(x,t)}{\partial x^2}\mathrm{d}x &\le -\int_{\Omega}\frac{\partial z^{RT}(x,t)}{\partial x}2\left(I_N\otimes\beta^T\beta B\right)\frac{\partial z^R(x,t)}{\partial x}\mathrm{d}x,\\ \int_{\Omega} z^{IT}(x,t)2\left(I_N\otimes\beta^T\beta B\right)\frac{\partial^2 z^I(x,t)}{\partial x^2}\mathrm{d}x &\le -\int_{\Omega}\frac{\partial z^{IT}(x,t)}{\partial x}2\left(I_N\otimes\beta^T\beta B\right)\frac{\partial z^I(x,t)}{\partial x}\mathrm{d}x.\end{aligned} \tag{29}$$

According to equation (24) and by using Cauchy inequality yields

$$\begin{aligned}&-2\int_{\Omega} z^{RT}(x,t)\left(I_N\otimes\beta^T\beta\right)\sum_{q=1}^{Q}\alpha\left(I_N\otimes\beta^T\beta\right)L^R z^R\left(x_q,t_k\right)\mathrm{d}x\\ &=-2\sum_{q=1}^{Q} z^{RT}\left(x_q,t\right)\left(I_N\otimes\beta^T\beta\right)L^R\left(e^R\left(x_q,t\right)+z^R\left(x_q,t\right)\right)\\ &\le\sum_{q=1}^{Q}\left(\left(\frac{1}{\varepsilon}-2\right)z^{RT}\left(x_q,t\right)\left(I_N\otimes\beta^T\beta\right)L^R z^R\left(x_q,t\right)+\varepsilon e^{RT}\left(x_q,t\right)\left(I_N\otimes\beta^T\beta\right)L^R e^R\left(x_q,t\right)\right)\\ &=-\sum_{q=1}^{Q} z^{RT}\left(x_q,t\right)\left(\left(2-\frac{1}{\varepsilon}\right)I_N-\varepsilon\Upsilon\right)\otimes\left(\beta^T\beta\right)L^R z^R\left(x_q,t\right)+\eta^R(t).\end{aligned} \tag{30}$$

Similarly,

$$\begin{aligned}&-2\sum_{q=1}^{Q} z^{IT}\left(x_q,t\right)\left(I_N\otimes\beta^T\beta\right)L^I z^I\left(x_q,t_k\right)\\ &\le-\sum_{q=1}^{Q} z^{IT}\left(x_q,t\right)\left(\left(2-\frac{1}{\varepsilon}\right)I_N-\varepsilon\Upsilon\right)\\ &\otimes\left(\beta^T\beta\right)L^I z^I\left(x_q,t\right)+\eta^I(t).\end{aligned} \tag{31}$$

where $\eta^R(t)=\varepsilon\lambda_m(L^R)\overline{\eta}^R(t)$ and $\eta^I(t)=\varepsilon\lambda_m(L^I)\overline{\eta}^I(t)$.

According to Lemma 1, Corollary 1, and the boundary condition of equation (18),

$$\begin{aligned}&-\int_{\Omega}\frac{\partial z^{RT}(x,t)}{\partial x}2\left(I_N\otimes\beta^T\beta B\right)\frac{\partial z^R(x,t)}{\partial x}\mathrm{d}x\\ &-\sum_{q=1}^{Q} z^{RT}\left(x_q,t\right)\left(\left(2-\frac{1}{\varepsilon}\right)I_N-\varepsilon\Upsilon\right)\otimes\left(\beta^T\beta\right)L^R z^R\left(x_q,t\right)\\ &\le-\int_{\Omega} z^{RT}(x,t)\left(I_N\otimes\beta^T\beta\right)\mathscr{R}_{1R}z^R(x,t)\mathrm{d}x.\end{aligned} \tag{32}$$

Similarly,

$$\begin{aligned}&-\int_{\Omega}\frac{\partial z^{IT}(x,t)}{\partial x}2\left(I_N\otimes\beta^T\beta B\right)\frac{\partial z^I(x,t)}{\partial x}\mathrm{d}x-\sum_{q=1}^{Q} z^{IT}\left(x_q,t\right)\left(\left(2-\frac{1}{\varepsilon}\right)I_N-\varepsilon\Upsilon\right)\otimes\left(\beta^T\beta\right)L^I z^I\left(x_q,t\right)\\ &\le-\int_{\Omega} z^{IT}(x,t)\left(I_N\otimes\beta^T\beta\right)\mathscr{R}_{1I}z^I(x,t)\mathrm{d}x,\end{aligned} \tag{33}$$

where $\mathscr{R}_{1R}=M_1M_2L^R(M_1+2\xi_1M_2L^R)^{-1}$, $\mathscr{R}_{1I}=M_1M_2L^I(M_1+2\xi_1M_2L^I)^{-1}$, $M_1=2(I_N\otimes B)$, $\Upsilon<(1/\varepsilon^2)(2\varepsilon-1)I_N$, $M_2=((2-(1/\varepsilon))I_N-\varepsilon\Upsilon)\otimes I_n$, and $\xi_1=(1/\pi^2)(\max_{2\le q\le Q}\{x_q-x_{q-1},x_1,(l-x_Q)\})^2$.

According to Assumption 2 and Cauchy inequality, the real part and imaginary part of the activation function can be derived:

$$\begin{cases} 2\int_{\Omega} z^{RT}(x,t)\left(I_N\otimes\beta^T\beta\right)\widetilde{C}^R(x,t)\mathrm{H}_f^R(z(x,t))\mathrm{d}x - 2\int_{\Omega} z^{RT}(x,t)\left(I_N\otimes\beta^T\beta\right)\widetilde{C}^I(x,t)\mathrm{H}_f^I(z(x,t))\mathrm{d}x \\ \le \int_{\Omega} z^{RT}(x,t)\left(I_N\otimes\beta^T\beta\right)\left(\frac{2}{\varepsilon}I_{Nn}+\varepsilon h_f^R\mathscr{P}_{1R}\right)z^R(x,t)\mathrm{d}x + \int_{\Omega} z^{IT}(x,t)\left(I_N\otimes\beta^T\beta\right)\left(\varepsilon h_f^I\mathscr{P}_{1I}\right)z^I(x,t)\mathrm{d}x, \\ 2\int_{\Omega} z^{IT}(x,t)\left(I_N\otimes\beta^T\beta\right)\left(\widetilde{C}^R(x,t)\mathrm{H}_f^I(z(x,t))+\widetilde{C}^I(x,t)\mathrm{H}_f^R(z(x,t))\right)\mathrm{d}x \\ \le \int_{\Omega} z^{IT}(x,t)\left(I_N\otimes\beta^T\beta\right)\left(\frac{2}{\varepsilon}I_{Nn}+\varepsilon h_f^I\mathscr{P}_{1R}\right)z^I(x,t)\mathrm{d}x + \int_{\Omega} z^{RT}(x,t)\left(I_N\otimes\beta^T\beta\right)\left(\varepsilon h_f^R\mathscr{P}_{1I}\right)z^R(x,t)\mathrm{d}x, \end{cases} \tag{34}$$

where $\mathscr{P}_{1R} = C^{RT}C^R + O^{RT}O^R$ and $\mathscr{P}_{1I} = C^{IT}C^I + O^{IT}O^I$.

Real part and imaginary part of the state-coupling part can be processed as follows:

$$\begin{cases} 2\int_{\Omega} z^{RT}(x,t)\left(I_N\otimes\beta^T\beta\right)(D\otimes\Gamma)\mathrm{H}_g^R(z(x,t-\tau(t)))\mathrm{d}x \\ \le \int_{\Omega} z^{RT}(x,t)\frac{1}{\varepsilon}\left(I_N\otimes\beta^T\beta\right)z^R(x,t)\mathrm{d}x + \int_{\Omega} z^{RT}(x,t-\tau(t))\left(I_N\otimes\beta^T\beta\right)\varepsilon h_g^R\mathscr{P}_2 z^R(x,t-\tau(t))\mathrm{d}x, \\ 2\int_{\Omega} z^{IT}(x,t)\left(I_N\otimes\beta^T\beta\right)(D\otimes\Gamma)\mathrm{H}_g^I(z(x,t-\tau(t)))\mathrm{d}x \\ \le \int_{\Omega} z^{IT}(x,t)\frac{1}{\varepsilon}\left(I_N\otimes\beta^T\beta\right)z^I(x,t)\mathrm{d}x + \int_{\Omega} z^{IT}(x,t-\tau(t))\left(I_N\otimes\beta^T\beta\right)\varepsilon h_g^I\mathscr{P}_2 z^I(x,t-\tau(t))\mathrm{d}x. \end{cases} \tag{35}$$

where $\mathscr{P}_2 = (D^TD\otimes\Gamma^T\Gamma)$.

According to equation (28) to equation (35),

$$\begin{aligned} \dot{V}(t) &= 2\int_{\Omega} z^{RT}(x,t)\left(\mathrm{I}_N\otimes\beta^{\mathrm{T}}\beta\right)\frac{\partial z^R(x,t)}{\partial t}\mathrm{d}x + 2\int_{\Omega} z^{IT}(x,t)\left(I_N\otimes\beta^{\mathrm{T}}\beta\right)\frac{\partial z^I(x,t)}{\partial t}\mathrm{d}x \\ &\le \int_{\Omega} z^{RT}(x,t)\left(I_N\otimes\beta^{\mathrm{T}}\beta\right)\left(-2\left(\mathrm{I}_N\otimes A\right)-\mathscr{R}_{1R}+\frac{3}{\varepsilon}I_{Nn}+\varepsilon\mathrm{h}_f^R\left(\mathscr{P}_{1R}+\mathscr{P}_{1I}\right)\right)z^R(x,t) \\ &\quad + \int_{\Omega} z^{IT}(x,t)\left(I_N\otimes\beta^{\mathrm{T}}\beta\right)\left(-2\left(I_N\otimes A\right)-\mathscr{R}_{1I}+\frac{3}{\varepsilon}I_{Nn}+\varepsilon\mathrm{h}_f^I\left(\mathscr{P}_{1R}+\mathscr{P}_{1I}\right)\right)z^I(x,t)\mathrm{d}x \\ &\quad + \int_{\Omega} z^{RT}(x,t-\tau(t))\left(I_N\otimes\beta^{\mathrm{T}}\beta\right)\varepsilon h_g^R\mathscr{P}_2 z^R(x,t-\tau(t))\mathrm{d}x \\ &\quad + \int_{\Omega} z^{IT}(x,t-\tau(t))\left(I_N\otimes\beta^{\mathrm{T}}\beta\right)\varepsilon h_g^I\mathscr{P}_2 z^I(x,t-\tau(t))\mathrm{d}x \\ &\quad + \varepsilon\left(\lambda_m\left(L^R\right)\overline{\eta}^R(t)+\lambda_m\left(L^I\right)\overline{\eta}^I(t)\right) \\ &\le -\lambda_1 V(t)+\lambda_2 V(t-\tau(t))+\varepsilon\left(\lambda_{\max}\left(L^R\right)\overline{\eta}^R(t)+\lambda_{\max}\left(L^I\right)\overline{\eta}^I(t)\right), \end{aligned} \tag{36}$$

with $\lambda_0, \lambda_1, \lambda_2$ defined in Theorem 1.

From Lemma 2, we can obtain

$$V(t) \le \Theta + \sup_{t-\tau(t)\le s\le t} V(s)\exp\left(-\underline{\kappa}_2(t-t_0)\right), \tag{37}$$

where $\Theta = (\varepsilon/(\lambda_1-\lambda_2))(\lambda_{\max}(L^R)\ \overline{\eta}_0^R + \lambda_{\max}(L^I)\overline{\eta}_0^I)\ \sup_{t\ge t_0} ff(t)$, $\underline{\kappa}_2 = \inf_{t_0\le t}\{\kappa_2(t)\colon \quad \kappa_2(t) - \lambda_1 + \lambda_2 \exp \quad (\kappa_2(t)\tau(t)) = 0\}$, and $\lambda_1 > \lambda_2 \exp(\kappa_2(t)\tau(t))$.

If $ff(t)$ is set as equation (25) and $\kappa_1 \ge \underline{\kappa}_2$, then the error system in equations (18) and (20) converges exponentially to Θ with the exponential index $\underline{\kappa}_2$. That is, the master-slave system (equations (1) and (3)) achieves quasisynchronization within the error levelΘ. □

4. Numerical Examples

This section mainly completes multiple numerical simulations to testify the theoretical results.

Consider the master-slave error networks system as

$$\begin{aligned}\frac{\partial z_i(x,t)}{\partial t} &= -Az_i(x,t) + B\frac{\partial^2 z_i(x,t)}{\partial x^2}\\ &\quad + c_i(z_i(x,t))f_i(z_i(x,t)) + \sum_{j=1}^{N} d_{ij}\Gamma g_j\\ &\quad \cdot\left(z_j\left(x, t-\tau_j(t)\right)\right) - \sum_{q=1}^{Q}\alpha\left(x_q\right)L_i\beta^T\beta z_i\left(x_q, t_k\right),\end{aligned} \tag{38}$$

where $i = 1, 2, N = 2, n = 3,\ g_i(\cdot) = f_i(\cdot) = \tan\ h(\cdot)$;

$$\begin{aligned}
c_1(v(\cdot,s)) &= \begin{cases} -0.5 - 1.2\iota, & v(\cdot,s)\downarrow,\\ -0.4 - 1.1\iota & v(\cdot,s)\uparrow,\\ \lim\limits_{s\longrightarrow t^-}(v(\cdot,s)) & v(\cdot,s)\text{ unchange},\end{cases}\\
c_2(v(\cdot,s)) &= \begin{cases} -1 - 1\iota, & v(\cdot,s)\downarrow,\\ -0.9 - 0.9\iota, & v(\cdot,s)\uparrow,\\ \lim\limits_{s\longrightarrow t^-}(v(\cdot,s)), & v(\cdot,s)\text{ unchange},\end{cases}\\
A &= \begin{bmatrix} 0.1 & 0 & 0\\ 0 & 0.1 & 0\\ 0 & 0 & 0.1\end{bmatrix},\\
B &= \begin{bmatrix} 0.5 & 0 & 0\\ 0 & 0.5 & 0\\ 0 & 0 & 0.5\end{bmatrix},\\
D &= \begin{bmatrix} -0.3 & 0.3\\ 0.3 & -0.3\end{bmatrix},\\
\Gamma &= \begin{bmatrix} 0.5 & 0 & 0\\ 0 & 0.5 & 0\\ 0 & 0 & 0.5\end{bmatrix}.
\end{aligned} \tag{39}$$

The positions of two spatial point measurements are $x_1 = 0.25l$, $x_2 = 0.75l$. The initial conditions of the master system are

$$\begin{aligned}\widetilde{z}_1(x,0) &= \begin{pmatrix} (2-2\cos(3\pi x)) + i(1-\cos(4\pi x))\\ (1-3\sin(5\pi x)) + i(2-3\sin(4\pi x))\\ (-1.5+0.5\sin(4\pi x)) + i(-0.5+\sin(3\pi x))\end{pmatrix},\\
\widetilde{z}_2(x,0) &= \begin{pmatrix} \cos(5\pi x) + i(1+2\cos(6\pi x))\\ (3-3\sin(3\pi x)) + i(4-\sin(2\pi x))\\ (1.5+2\sin(2\pi x)) + i(3+3\sin(2\pi x))\end{pmatrix}.\end{aligned} \tag{40}$$

The initial conditions of the slave system are

$$\begin{cases} \widehat{z}_1(x,0) = ((3\cos(2\pi x) - 2) + (4\cos(\pi x) - 3)\iota, 3 + 1.5\iota, 1 + 1\iota)^T,\\ \widehat{z}_2(x,0) = (5\cos(7\pi x) - 3 + (5\cos(7\pi x) - 3)\iota, 1 + 1\iota, 1 + 1\iota)^T.\end{cases} \tag{41}$$

4.1. Output Static Event-Triggered Control (OSETC) with $\beta = (100; 010)$. Event trigger's parameters satisfied with equation (26) are set as $\gamma_i = 0.02$,, $\overline{\eta}_i(t) = 0.01$, and $L_{ij} = 10$. And the simulation results are shown in Figures 2–4. Figure 2 represents the jth dimensional state norm evolution of the ith error networks over time. The real-valued state norm evolution and the imaginary-valued one can be formulated as

$$\begin{cases} \left\|z_{ij}^R(x,t)\right\|^2 = \int_\Omega z_{ij}^{RT}(x,t), z_{ij}^R(x,t)\mathrm{d}x,\\ \left\|z_{ij}^I(x,t)\right\|^2 = \int_\Omega z_{ij}^{IT}(x,t), z_{ij}^I(x,t)\mathrm{d}x, \quad i = 1,2,\ j = 1,2,3.\end{cases} \tag{42}$$

Figures 2–4 show that the first dimension and the second dimension of the error state converge over time, while the third dimension does not converge. That is, the output synchronization has been realized which matches the output matrix. Figure 5 shows that the four triggered time series are different which are consistent with their distribution characteristics of the four event triggers.

4.2. Output Piecewise Event-Triggered Control (OPETC) with $\beta = (100; 010; 001)$. The output matrix β is a unit matrix, and the output states are common full-dimensional states. Event trigger's parameters are set as $\gamma_i = 0.02$, $\overline{\eta}_i(t) = 0.01\ \exp(-0.5t)$ for $(t \le 7)$, $\overline{\eta}_i(t) = 0.01\ \exp(-3.5)$ for $(t > 7)$, and the input control gain is $L_{ij} = 10$. These parameters are satisfied with equation (26), and the simulation results are shown in Figures 6 and 7. Figure 6 indicates that the real part (Figure 6(a)) and the imaginary part (Figure 6(b)) of the error state converge over time. While, Figure 7 denotes that the four triggered time series that are independent of each other.

4.3. Multistrategy Comparison. The simulations of output static event-triggered control (OSETC), output dynamic event-triggered control (ODETC), and output time-

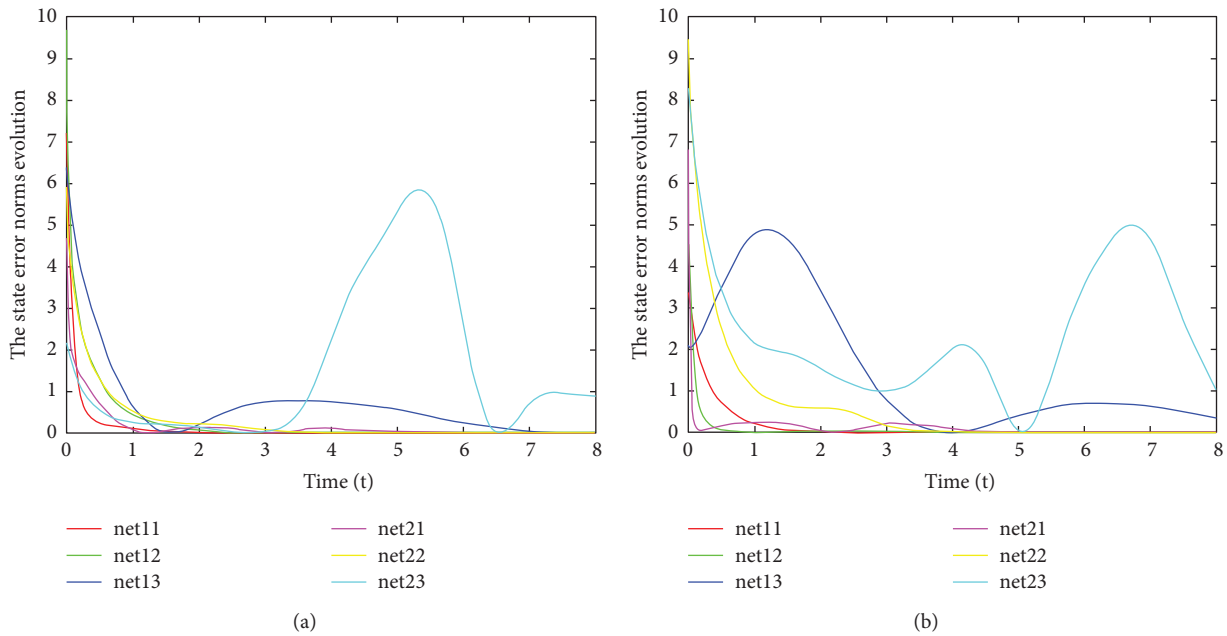

Figure 2: Real part and imaginary part of state error norm evolution under the output static event-triggered control. net11, net12, and net13 represent three-dimensional state norm evolution of the 1st error network. net21, net22, and net23 represent three-dimensional state norm evolution of the 2nd error network. (a) Real part of state error evolution. (b) Imaginary part of state error evolution.

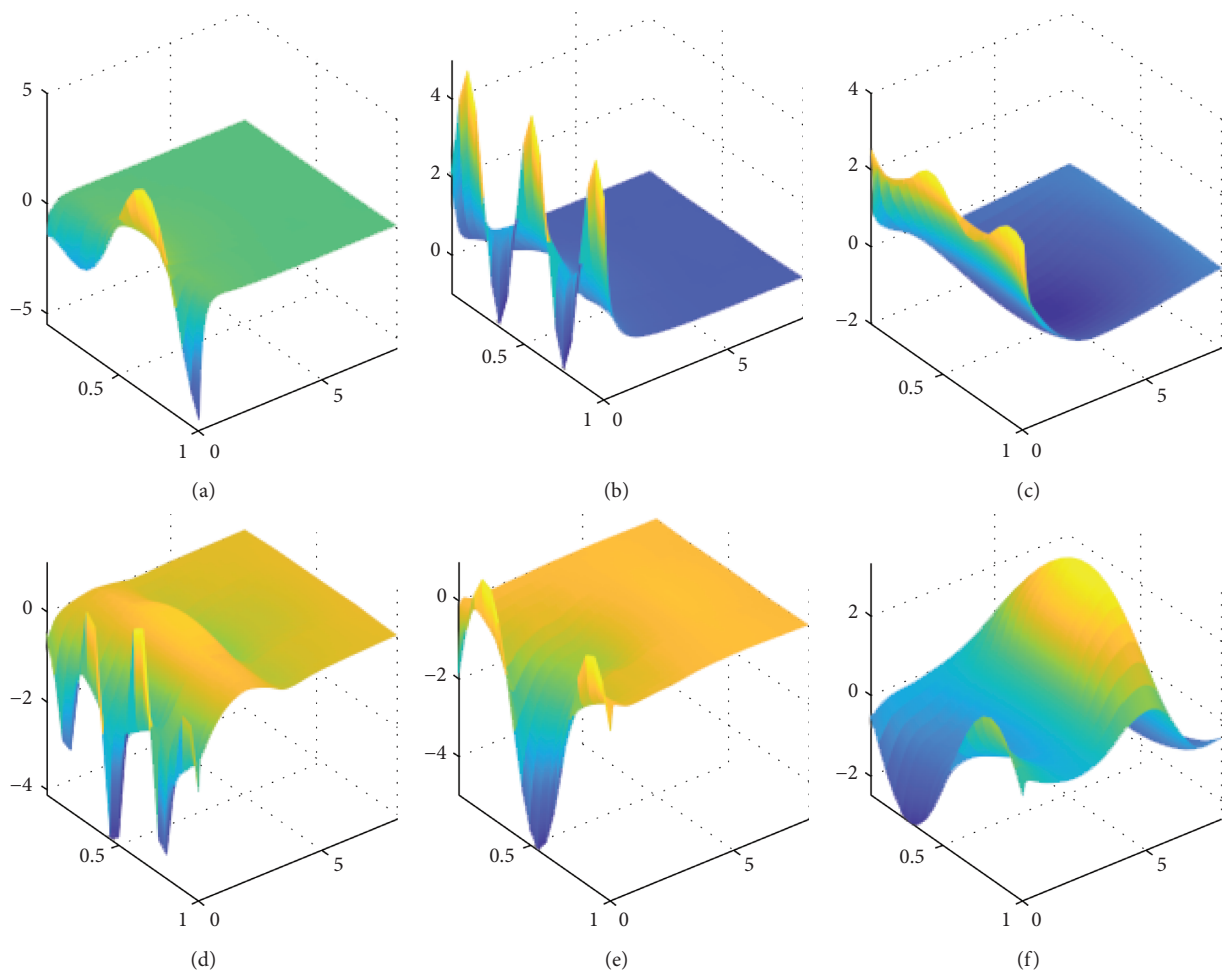

Figure 3: Real part of state error evolution under the output static event-triggered control. net11, net12, and net13 represent 3-dimensional real-valued state evolution of the 1sterror network. net21, net22, and net23 represent 3-dimensional real-valued state evolution of the 2nd error network. "real" denotes real part. (a) net11-real. (b) net12-real. (c) net13-real. (d) net21-real. (e) net22-real. (f) net23-real.

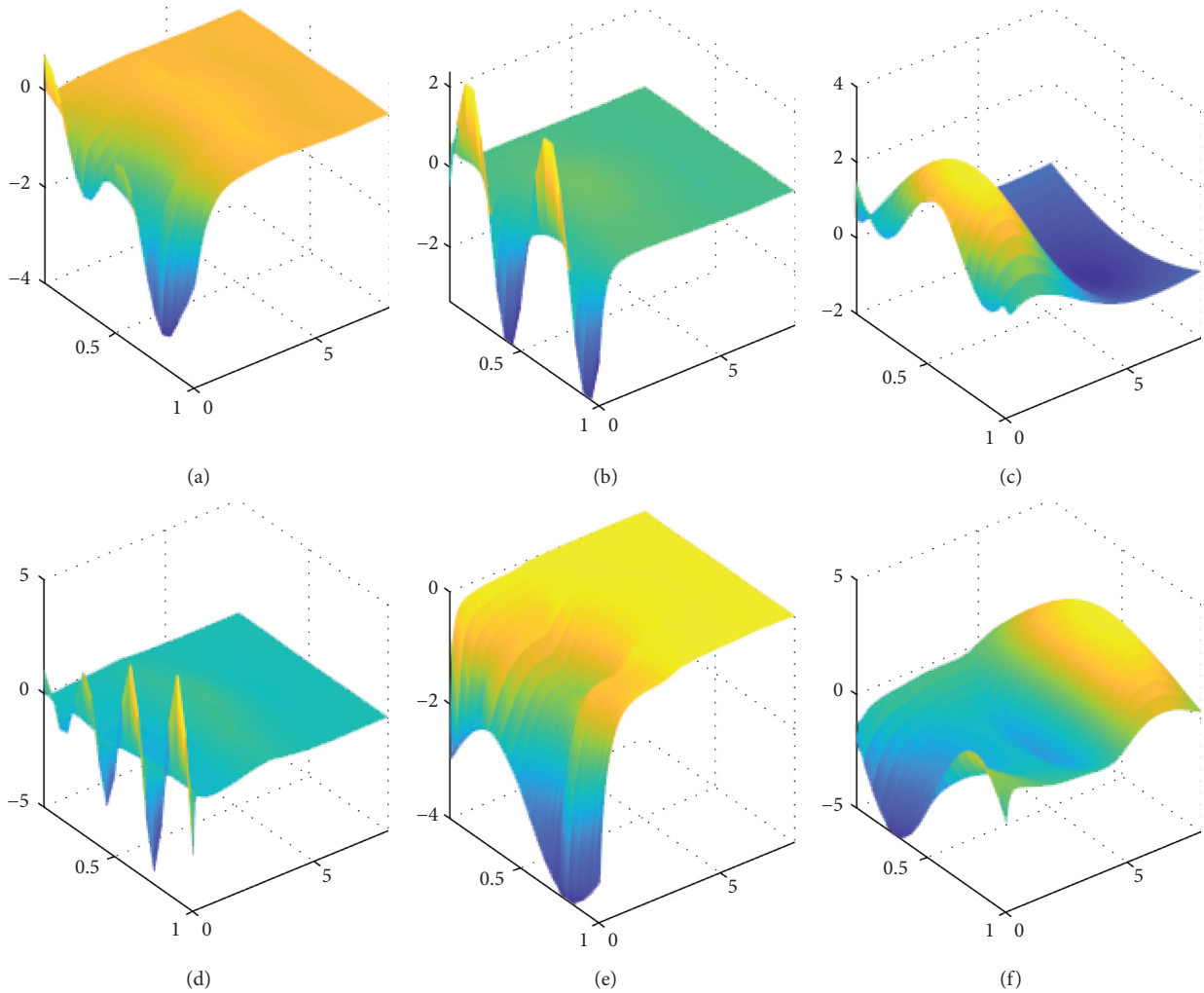

Figure 4: Imaginary part of state error evolution under the output static event-triggered control. net11, net12, and net13 represent 3-dimensional state evolution of the 1st error network. net21, net22, and net23 represent 3-dimensional state evolution of the 2nd error network. "im" denotes imaginary part. (a) net11-im. (b) net12-im. (c) net13-im. (d) net21-im. (e) net22-im. (f) net23-im.

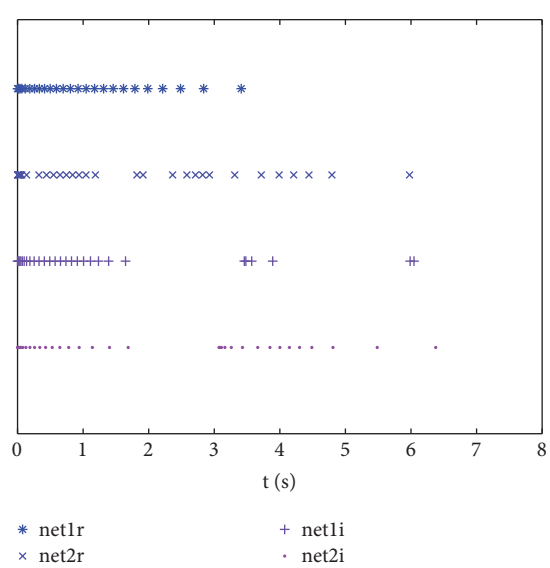

Figure 5: The event-triggered time instants t_k^i in the error networks (17) under the output static event-triggered control. net1r and net2r mean the real-valued parts of the slave networks 1 and 2. net1i and net2i represent the imaginary parts of the slave networks 1 and 2, respectively.

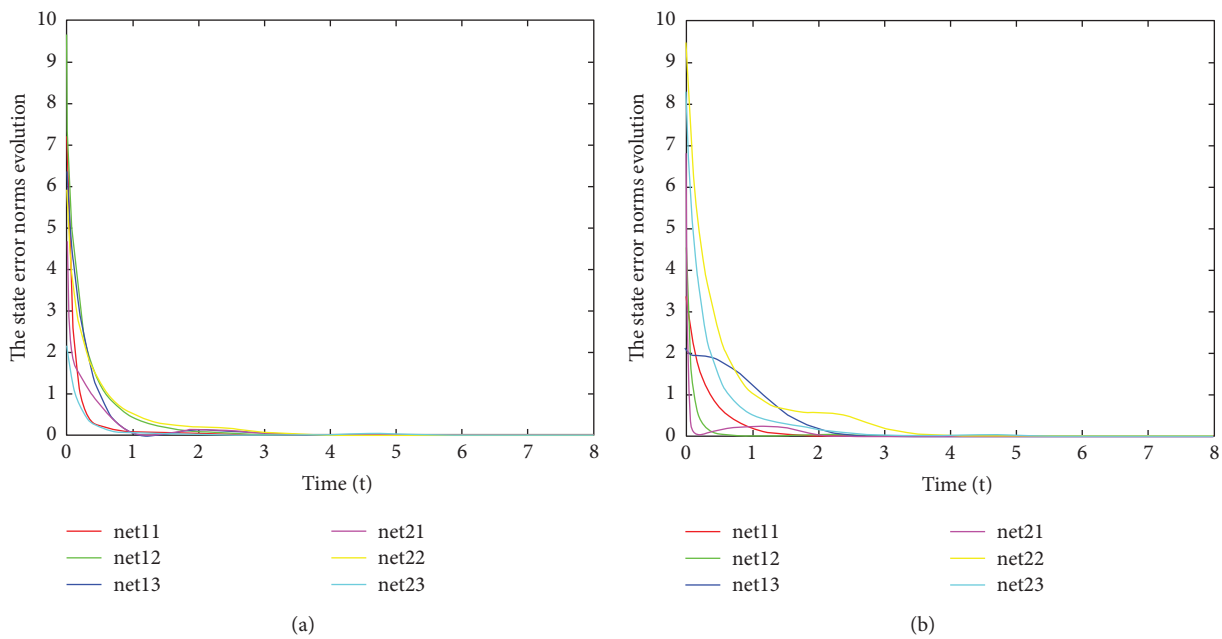

Figure 6: Real part and imaginary part of state error evolution under the piecewise event-triggered control. (a) Real part of state error evolution. (b) Imaginary part of state error evolution.

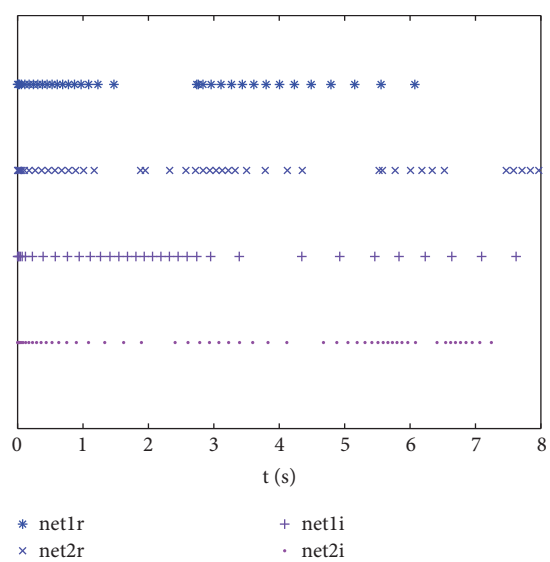

Figure 7: The event-triggered time instants t_k^i in the error networks (17) under the piecewise event-triggered control.

triggered control (OTTC) have been realized where the scale parameter of event trigger is $\gamma_i = 0.02$; the function parameter of the static event trigger is $\overline{\eta}_i(t) = 0.01$; the function parameter of the dynamic event trigger is $\overline{\eta}_i(t) = 0.01\exp(-0.5t)$; the output matrix is $\beta = (100; 010; 001)$; and the time trigger interval is 88 ms. Some results have been achieved and given in Table 1. To compare the update numbers of the controller with different control strategies, the data in Table 1 can be analysed. The data in column 2 and column 3 of Table 1 show that the update rate of OTTC is greater than that of OSETC and ODETC with similar error decreased. The simulation results in columns 4 and 5 imply that the number of controller update increases over time even if the error norm is small enough. Thus, the simulation results demonstrate the first hint; output event-triggered control (OETC) is more effective than output time-triggered control (OTTC), and the similar conclusion can be referred from [36].

The OSETC strategy and ODETC strategy can be further compared using the information in Table 1. The number of controller update in OSETC shown in column 2 is greater than that of ODETC when state norm is below 0.1. Moreover, the growth rate of controller update in OSETC shown in columns 2 and 4 is lower than that of ODETC. Then, the second hint can be drawn; ODETC is more effective than

Table 1: Six control strategies for synchronization of CMRDNNs.

Control strategy	Number of update, state norm ≤0.1	Time (s), state norm ≤0.1	Number of controller update, $T_f = 8$ s	State norms $*10^3$, $T_f = 8$ s
	Four values: real part of net1and net2 and imaginary part of net1 and net2			
OSETC	25, 30, 26, 33	3.5, 6.4, 4.4, 6.4	25, 30, 28, 33	56.4, 56.5, 6.9, 0.7.4
ODETC	18, 27, 20, 28	3.4, 6.4, 4.5, 4.9	23, 30, 25, 33	7.0, 28.8, 18.8, 57.4
OTTC	41, 45, 49, 63	3.6, 4.0, 4.3, 5.5	90, 90, 90, 90	0.1, 0.4, 0.2, 3.1

Table 2: Three control strategies for synchronization of CMRDNNs.

Control strategy	$T_f = 8$ s, controller update numbers	$T_f = 15$ s, controller update numbers
OSETC	29, 32, 29, 31	31, 37, 34, 40
ODETC	26, 30, 24, 31	36, 54, 34, 56
OPETC	26, 30, 24, 31	28, 31, 29, 36

OSETC at the first stage, and OSETC is better than ODETC at the following stage.

Based the above analysis, the distributed output piecewise event-triggered control (OPETC) which combines OSETC and ODETC has been realized, and the results are given in Table 2. Comparing the data in column 2 and column 3 of Table 2, we can find that OPETC has better performance than ODETC and OSETC. This simulation validates the similar theoretical analysis of Theorem 1.

5. Conclusions

The research model in this study is complex and general, including complex-valued states, memristive parameters, state coupling, reaction-diffusion term, and output matrix. First, by combining differential inclusion and nonfragile techniques, a general method is developed to overcome the difficulty of the master-slave system parameter mismatch caused by memristor. Second, an efficient distributed piecewise event-triggered control strategy using incomplete measurement has been designed to achieve output synchronization which not only reduces the update rate of the controller but also decreases the measurement cost. Finally, it is verified that the new distributed piecewise event trigger can achieve better quasisynchronous performance through theoretical analysis and experimental simulation. What is more, the distributed output piecewise event-triggered control strategy can be used for the synchronization control of general one-order reaction-diffusion neural networks without adding any other conditions. To verify wide effectiveness of this control strategy, the OPETC strategy will be extended to two-order or even higher-order neural networks, which is one of our future works.

Data Availability

The data used to support the findings of this study are available from the corresponding author upon request.

Conflicts of Interest

The authors declare that there are no conflicts of interest.

Acknowledgments

This work was supported by the Natural Foundations of China (61773182) and Wuxi Internet of Things Industry funding project.

References

[1] X. Jin, X. Yu, T. Su, D. Yang, and L. Wang, "Distributed deep fusion predictor for a multi-sensor system based on causality entropy," *Entropy*, vol. 23, no. 2, pp. 1–19, 2021.

[2] X. Jin, J. Zhang, T. Su, Y. Bai, J. Kong, and X. Wang, "Wavelet-deep optimized model for nonlinear multi-component data forecasting," *Computational Intelligence and Neuroscience*, 2021.

[3] X.-B. Jin, H.-X. Wang, X.-Y. Wang, Y.-T. au, T.-L. Su, and J.-L. Kong, "Deep-learning prediction model with serial two-level decomposition based on Bayesian optimization," *Complexity*, vol. 2020, Article ID 4346803, 14 pages, 2020.

[4] Y. K. Bai and R. Xu, "New synchronization criteria for an array of neural networks with hybrid coupling and time-varying delays," *Nonlinear Analysis: Modelling and Control*, vol. 21, no. 1, pp. 57–76, 2016.

[5] Y. Luo and Y. Yao, "Finite-time synchronization of uncertain complex dynamic networks with time-varying delay," *Advances in Difference Equations*, vol. 32, no. 1, pp. 1–22, 2020.

[6] Y. Wang, J. Lu, J. Liang, J. Cao, and M. Perc, "Pinning synchronization of nonlinear coupled Lur'e networks under hybrid impulses," *IEEE Transactions on Circuits and Systems II: Express Briefs*, vol. 66, no. 3, pp. 432–436, 2019.

[7] D. Ding, Z. Tang, Y. Wang, and Z. Ji, "Adaptive synchronization of complex dynamical networks via distributed pinning impulsive control," *Neural Processing Letters*, vol. 52, no. 3, pp. 2669–2686, 2020.

[8] L. O. Chua, M. Hasler, G. S. Moschytz, and J. Neirynck, "Autonomous cellular neural networks: a unified paradigm for pattern formation and active wave propagation," *IEEE Transactions on Circuits and Systems I: Fundamental Theory and Applications*, vol. 42, no. 10, pp. 559–577, 1995.

[9] P.-C. Wei, J.-L. Wang, Y.-L. Huang, B.-B. Xu, and S.-Y. Ren, "Impulsive control for the synchronization of coupled neural networks with reaction-diffusion terms," *Neurocomputing*, vol. 207, pp. 539–547, 2016.

[10] L. Shanmugam, P. Mani, R. Rajan, and Y. H. Joo, "Adaptive synchronization of reaction-diffusion neural networks and its

application to secure communication," *IEEE Transactions on Cybernetics*, vol. 50, no. 3, pp. 911–922, 2018.

[11] L. Wang and J.-L. Wang, "Adaptive passivity and synchronization of coupled reaction-diffusion neural networks with multiple state couplings or spatial diffusion couplings," *Neurocomputing*, vol. 377, pp. 168–181, 2020.

[12] L. Wang, Y. Jing, and Z. Kong, "Output synchronization of complex network," *Journal of Northeastern University. Natural Science*, vol. 29, no. 6, pp. 60041–60049, 2008.

[13] J.-L. Wang, H.-N. Wu, T. Huang, and M. Xu, "Output synchronization in coupled neural networks with and without external disturbances," *IEEE Transactions on Control of Network Systems*, vol. 5, no. 4, pp. 2049–2061, 2018.

[14] D.-Y. Wang, J.-L. Wang, S.-Y. Ren, and Y.-L. Huang, "Output synchronization and H∞ output synchronization of complex dynamical networks with multiple derivative couplings," *Journal of the Franklin Institute*, vol. 356, no. 1, pp. 407–440, 2019.

[15] Q. Wang and J.-L. Wang, "Finite-time output synchronization of undirected and directed coupled neural networks with output coupling," *IEEE Transactions on Neural Networks and Learning Systems*, vol. 99, pp. 1–12, 2020.

[16] C. Yang, X. Li, and J. Qiu, "Output synchronization control with input constraint of complex networks with reaction–diffusion terms," *Neural Computing and Applications*, vol. 30, no. 1, pp. 1–8, 2018.

[17] B. Lu, H. Jiang, C. Hu, and A. Abdurahman, "Spacial sampled-data control for H∞ output synchronization of directed coupled reaction-diffusion neural networks with mixed delays," *Neural Networks*, vol. 123, pp. 429–440, 2020.

[18] L. Chua, "Resistance switching memories are memristors," *Applied Physics A*, vol. 102, no. 4, pp. 765–783, 2011.

[19] W. Zhang, C. Li, T. Huang, and X. He, "Synchronization of memristor-based coupling recurrent neural networks with time-varying delays and impulses," *IEEE Transactions on Neural Networks and Learning Systems*, vol. 26, no. 12, pp. 3308–3313, 2015.

[20] L. Wang, H. He, and Z. Zeng, "Global synchronization of fuzzy memristive neural networks with discrete and distributed delays," *IEEE Transactions on Fuzzy Systems*, vol. 28, no. 9, pp. 2022–2034, 2020.

[21] Z. Tu, N. Ding, L. Li, Y. Feng, L. Zou, and W. Zhang, "Adaptive synchronization of memristive neural networks with time-varying delays and reaction-diffusion term," *Applied Mathematics and Computation*, vol. 311, pp. 118–128, 2017.

[22] S. Wang, Z. Guo, S. Wen, and T. Huang, "Global synchronization of coupled delayed memristive reaction-diffusion neural networks," *Neural Networks*, vol. 123, pp. 362–371, 2019.

[23] Y. Liu, X. Liao, and C. Li, "Exponential lag synchronization of memristive neural networks with reaction diffusion terms via neural activation function control and fuzzy model," *Asian Journal of Control*, vol. 22, no. 1, pp. 346–361, 2018.

[24] S. Wang, Z. Guo, S. Wen, T. Huang, and S. Gong, "Finite/fixed-time synchronization of delayed memristive reaction-diffusion neural networks," *Neurocomputing*, vol. 375, pp. 1–8, 2020.

[25] W. Li, X. Gao, and R. Li, "Stability and synchronization control of inertial neural networks with mixed delays," *Applied Mathematics and Computation*, vol. 367, pp. 1–14, 2020.

[26] H. Akira, "Applications of complex-valued neural networks to coherent optical computing using phase-sensitive detection scheme," *Information Sciences Applications*, vol. 2, no. 2, pp. 103–117, 1994.

[27] T. Titta, "Orthogonality of decision boundaries in complex-valued neural networks," *Neural Comput.*vol. 16, no. 1, pp. 73–97, 2004.

[28] S. Zhang, Y. Yang, and X. Sui, "The intermittent control synchronization of complex-valued memristive recurrent neural networks with time-delays," *Neural Processing Letters*, vol. 50, no. 3, pp. 2119–2139, 2019.

[29] H. Li, X. Gao, and R. Li, "Exponential stability and sampled-data synchronization of delayed complex-valued memristive neural networks," *Neural Processing Letters*, vol. 51, no. 1, pp. 193–209, 2019.

[30] S. Zhu, D. Liu, C. Yang, and J. Fu, "Synchronization of memristive complex-valued neural networks with time delays via pinning control method," *IEEE Transactions on Cybernetics*, vol. 50, no. 8, pp. 3806–3815, 2019.

[31] X. Song, J. Man, S. Song, Y. Zhang, and Z. Ning, "Finite/fixed-time synchronization for Markovian complex-valued memristive neural networks with reaction-diffusion terms and its application," *Neurocomputing*, vol. 414, pp. 131–142, 2020.

[32] X. Jin, X. Lian, T. Su, Y. Shi, and B. Miao, "Closed-loop estimation for randomly sampled measurements in target tracking system," *Mathematical Problems in Engineering*, vol. 2014, no. 2, pp. 1–12, Article ID 315908, 2014.

[33] T. Li, T. Wang, G. Zhang, and S. Fei, "Event-triggered output synchronization in master-slave Lur'e systems with heterogeneous dimensions," *Circuits, Systems, and Signal Processing*, vol. 36, no. 2, pp. 811–833, 2017.

[34] T. Li, Y. Yu, T. Wang, and S. Fei, "Decentralized adaptive event-triggered synchronization of neutral networks with time-varying delays," *Circuits Systems and Signal Processing*, vol. 38, pp. 1–17, 2018.

[35] X. Li, W. Zhang, J. Fang, and H. Li, "Event-triggered exponential synchronization for complex-valued memristive neural networks with time-varying delays," *IEEE Transactions on Neural Networks and Learning Systems*, vol. 99, pp. 2162–2388, 2019.

[36] S. Wang, Y. Cao, T. Huang, Y. Chen, and S. Wen, "Event-triggered distributed control for synchronization of multiple memristive neural networks under cyber-physical attacks," *Information Sciences*, vol. 518, pp. 361–375, 2020.

[37] W. Yao, C. Wang, Y. Sun, C. Zhou, and H. Lin, "Synchronization of inertial memristive neural networks with time-varying delays via static or dynamic event-triggered control," *Neurocomputing*, vol. 404, pp. 367–380, 2020.

[38] Y. Huang, S. Lin, and E. Yang, "Event-triggered passivity of multi-weighted coupled delayed reaction-diffusion memristive neural networks with fixed and switching topologies," *Communications in Nonlinear Science & Numerical Simulation*, vol. 89, pp. 1–28, 2020.

[39] C. A. Swanson, "Wirtinger's inequality," *SIAM Journal on Mathematical Analysis*, vol. 9, no. 3, pp. 484–491, 1978.

[40] A. Selivanov and E. Fridman, "Delayed point control of a reaction-diffusion PDE under discrete-time point measurements," *Automatica*, vol. 96, pp. 224–233, 2018.

[41] T. Chen and Z. Cheng, "Synchronization of inertial reaction-diffusion complex networks with mixed time delays via spatiotemporal sampling control," *International Journal of Modelling, Identification and Control*, 2021.

[42] L. Wen, Y. Yu, and W. Wang, "Generalized halanay inequalities for dissipativity of volterra functional differential equations," *Journal of Mathematical Analysis and Applications*, vol. 347, no. 1, pp. 169–178, 2008.

[43] A. D. Ioffe, "Single-valued representation of set-valued mappings II; application to differential inclusions," *SIAM Journal on Control and Optimization*, vol. 21, no. 4, pp. 641–651, 1983.

[44] R. Zhang, D. Zeng, S. Zhong, and Y. Yu, "Event-triggered sampling control for stability and stabilization of memristive neural networks with communication delays," *Applied Mathematics and Computation*, vol. 310, pp. 57–74, 2017.

[45] X. Hai, G. Ren, Y. Yu, C. Xu, and Y. Zeng, "Pinning synchronization of fractional and impulsive complex networks via event-triggered strategy," *Communications in Nonlinear Science & Numerical Simulation*, vol. 82, pp. 1–16, 2020.

[46] L. Baudouin, S. Marx, and S. Tarbouriech, "Event-triggered damping of a linear wave equation," *IFAC-PapersOnLine*, vol. 52, no. 2, pp. 58–63, 2019.

Hindawi
Complexity
Volume 2021, Article ID 5564184, 19 pages
https://doi.org/10.1155/2021/5564184

Research Article

Adaptive Integral Second-Order Sliding Mode Control Design for Load Frequency Control of Large-Scale Power System with Communication Delays

Anh-Tuan Tran,[1] Bui Le Ngoc Minh,[2,3] Phong Thanh Tran,[1] Van Van Huynh,[1] Van-Duc Phan,[4] Viet-Thanh Pham,[1] and Tam Minh Nguyen[2]

[1]*Modeling Evolutionary Algorithms Simulation and Artificial Intelligence, Faculty of Electrical & Electronics Engineering, Ton Duc Thang University, Ho Chi Minh City, Vietnam*
[2]*Faculty of Electrical and Electronics Engineering, Ho Chi Minh City University of Technology and Education, Ho Chi Minh City, Vietnam*
[3]*Faculty of Industrial Engineering, Tien Giang University, Mỹ Tho, Tien Giang Province 840000, Vietnam*
[4]*Faculty of Automobile Technology, Van Lang University, Ho Chi Minh City, Vietnam*

Correspondence should be addressed to Van Van Huynh; huynhvanvan@tdtu.edu.vn

Received 7 January 2021; Revised 12 February 2021; Accepted 10 March 2021; Published 22 March 2021

Academic Editor: Rui Wang

Nowadays, the power systems are getting more and more complicated because of the delays introduced by the communication networks. The existence of the delays usually leads to the degradation and/or instability of power system performance. On account of this point, the traditional load frequency control (LFC) approach for power system sketches a destabilizing impact and an unacceptable system performance. Therefore, this paper proposes a new LFC based on adaptive integral second-order sliding mode control (AISOSMC) approach for the large-scale power system with communication delays (LSPSwCD). First, a new linear matrix inequality is derived to ensure the stability of whole power systems using Lyapunov stability theory. Second, an AISOSMC law is designed to ensure the finite time reachability of the system states. To the best of our knowledge, this is the first time the AISOSMC is designed for LFC of the LSPSwCD. In addition, the report of testing results presents that the suggested LFC based on AISOSMC can not only decrease effectively the frequency variation but also make successfully less in mount of power oscillation/fluctuation in tie-line exchange.

1. Introduction

In modern power networks, the frequency stability is one of the significant problems related to the large-scale power system (LSPS) with communication delays. The system has been more and more complicated for LFC due to matched or mismatched uncertainties, load variations, and time-delays [1–4]. Communications time-delay is necessary in the LSPS; it cannot ignore and remove in the practical LSPS. So, the time-delay must consider in the area control error (ACE) signal. Normally, the time-delay can appear in the state variables or in the input channel of LSPS. The input control signal is transported to the power plants through communication networks with delay time. The state delay-time is the essential reason to effect on delaying the basic elements of communication or transportation in the LSPS. The deviation of tie-line exchange power and frequency are combined and known as an ACE to confirm the control frequency aim for the LSPS. The balance in both the tie-line and frequency exchange power is assured when an ACE is controlled and limited. In the LSPS model, the time-delay of ACE from regulation station to control area of the system is important [4–6]. Moreover, the time-delay is known as time lag in the power system model. That is, a big challenge to

design the control algorithm to deal with the time-delay in the LSPS. In ACE control signal, the time lag may occur and lead to oscillation and instability in the LSPS [6–9]. Therefore, it is absolutely necessary to consider and explore the LFC for the LSPSwCD. The main objectives of LFC for each control area are continuing to keep the nominal value of the system frequency in range of the standard value and to act in accordance with the scheduled active power interchange with neighboring control areas.

In general, the previous LFC scheme such as PID control has been used to maintain tie-line power and frequency at schedule value which is one of the simplest controllers [10–13]. A suitable design of PID controller which is constructed on the direct synthesis method in frequency domain is given in [10]. In [11], a fractional-order PID control approach is built for the single-area LFC model using the Kharitonov's theorem to eliminate steady state error. Robust PID controller-based stability boundary locus and Kharitonov's theorem were used for LFC of the LSPS [12]. In [13], an ant lion algorithm is combined with PID to optimize the LFC loop parameters for improving the frequency regulation. The above approaches are suitable for application to design LFC of power network with nominal parameter and no uncertainty. However, the practical power network is always influenced or touched by an external factor of the uncertainties such as different load disturbances, which effect on the stability of power network. In order to overcome drawbacks and resolve the LFC problem effectively, advanced control techniques are developed for LFC design consisting of neural network and fuzzy control [14–16]. In [14], the LFC scheme for the LSPS was established and constructed on the adaptive fuzzy control method. A novel fuzzy PID control strategy with the fractional-order integrator and filtered derivative action was suggested to resolve automatic generation control for the power network [15]. In [16], the optimized operation of LFC is proposed for the LSPS with hybrid energy storage system.

On the other hand, as a powerful robust control strategy, SMC has been successfully applied to a wide variety of practical systems [17–19]. The terminal SMC is designed for LFC with the renewable power networks [20]. In [21], the adaptive double integral SMC is proposed for LFC of the LSPS where the time-delay is not considered. The goal of Sarkar was to design an adaptive integral higher order SMC for LFC problems to guarantee the frequency variation [22]. In [23], this article indicated nonlinear SMC with parametric uncertainties for LFC utilization in the LSPS to vary the system damping characteristics under uncertainties and step load disturbances. The approach given in [24] developed the strategy of SMC by model order-reduction of the LFC approach of the microhydropower system. A new full order SMC scheme in the paper [25] is utilized to eliminate and avoid the singularity of derivative of terms with fractional power elements. A novel adaptive SMC method has been used and developed for the LFC of the LSPS [26]. The proportional and integral switching surface was established for LFC of LSPS where the chattering problem is existed due to first-order SMC used [27]. The SMC-based LFC of above approaches can reduce the tie-line power and frequency deviations to ensure the stability of power network. However, the performance of LSPS using control scheme given in [20–27] is achieved without considering the time-delay in the power grids. In addition, the existence of the delays usually leads to the degradation and/or instability of power network performance. In order to solve this problem, the control scheme given in [28–30] is proposed to regulate the frequency deviation of the LSPS in the presence of communication delays and sudden load change. In [31], the LFC of the LSPS with nonlinear perturbations and time-varying delays are proposed using SMC. In [32], the sliding mode LFC is designed for the LSPS with time-delay and load disturbance. The sliding mode LFC strategy is suggested for the LSPS with time-delay and significant wind power penetration [33]. However, these SMC approaches are developed based on first-order time derivative [31–33]. In addition, the first-order SMC provides low accuracies due to chattering phenomenon in the control input. Therefore, in this paper, the second-order SMC is proposed to solve this problem. Moreover, an adaptive control method is adopted to estimate the unknown upper bound of aggregated uncertainties. To the best of our knowledge, the adaptive integral second-order sliding mode control (AISOSMC) scheme has not been developed for LFC problem in the LSPSwCD so far. The major contributions of this paper are displayed as follows:

- The novel theory based on AISOSMC approach is offered for the LSPSwCD
- The continuous control law is developed to deal with the influence of time-delay related to ACE on the LFC problem of the LSPSwCD
- A state feedback controller containing both present and delayed state information is designed to improve tolerable delay margin of the LSPSwCD
- A new LMI is established for proving the stability of whole PSPS based on Lyapunov stability theory
- The proposed LFC based on AISOSMC can not only decrease effectively the frequency variation but also make successfully less in mount of power oscillation/fluctuation in tie-line exchange

2. Mathematical Model of a Large-Scale Power System with Communication Delays (LSPSwCD)

In this part, we model the LSPSwCD. Figure 1 is the block diagram of the ith area of the LSPS with communication delay [28–30]. The model of the ith area system is composed of a governor, a nonreheat turbine, and a generator. The output of the generator is the frequency error. The tie-line power error is linearly proportional to the integration of frequency error. The linear combination of frequency error and the tie-line power error is the area control error (ACE). In addition, the time-delay of ACE signal is considered in the power network.

Nevertheless, when the load variation with minor change occurs during its conventional process, then the

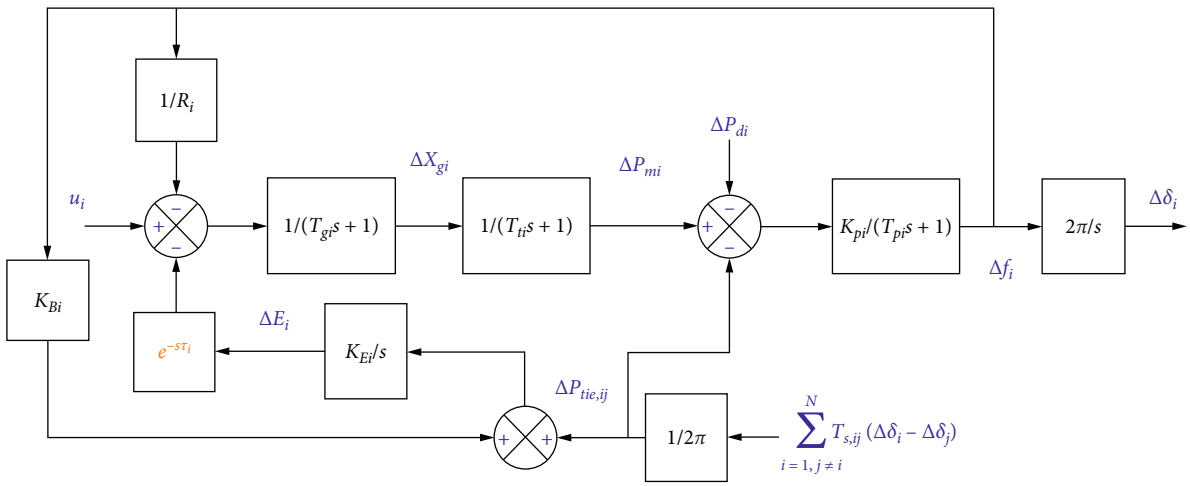

FIGURE 1: The structure of ith area of the LSPSwCD.

mathematical model of power network can be linearized near the stable operating point. Therefore, the dynamic equations of the above i^{th} area system are expressed as follows:

$$\begin{aligned}
\Delta\dot{f}_i(t) &= -\frac{1}{T_{pi}}\Delta f_i(t) + \frac{K_{Pi}}{T_{pi}}\Delta P_{mi}(t) - \frac{K_{Pi}}{T_{pi}}\Delta P_{di}(t) - \frac{K_{Pi}}{2\pi T_{pi}}\sum_{i=1,j\neq i}^{N} T_{s,ij}\left[\Delta\delta_i(t) - \Delta\delta_j(t)\right],\\
\Delta\dot{P}_{mi}(t) &= -\frac{1}{T_{ti}}\Delta P_{mi}(t) + \frac{1}{T_{ti}}\Delta X_{gi}(t),\\
\Delta\dot{X}_{gi}(t) &= -\frac{1}{T_{gi}R_i}\Delta f_i(t) - \frac{1}{T_{gi}}\Delta X_{gi}(t) - \frac{1}{T_{gi}}\Delta E_i(t-\tau_i) + \frac{1}{T_{gi}}u_i(t),\\
\Delta\dot{E}_i(t) &= K_{Bi}K_{Ei}\Delta f_i(t) + \frac{K_{Ei}}{2\pi}\sum_{i=1,j\neq i}^{N} T_{s,ij}\left[\Delta\delta_i(t) - \Delta\delta_j(t)\right],\\
\Delta\dot{\delta}_i(t) &= 2\pi\Delta f_i(t),
\end{aligned} \tag{1}$$

with $i = 1$ to N and N is denoted as the number of areas, where $\Delta f_i(t)$ and $\Delta f_j(t)$ are the frequency variation of the ith area and the jth area, $\Delta P_{mi}(t)$ is the variation in governor output command, $\Delta X_{gi}(t)$ is the governor valve position of each area, $\Delta\delta_i(t)$ and $\Delta\delta_j(t)$ are the changes of rotor angle deviations of the ith area and the jth area, $\Delta P_{di}(t)$ is the incremental change in local load of each area, $T_{s,ij}$ is the tie-line power coefficient between the ith area and the jth area, T_{gi} is the time constant of governor, T_{ti} is the turbine time constant, and T_{pi} is the time constant in power network, respectively. K_{pi}, R_i, K_{Ei}, and K_{Bi} are power network gain, droop coefficient of individual area, speed regulation coefficient, and frequency bias factor. $\Delta E_i(t-\tau_i)$ is the area control error with the time-delay and $u_i(t)$ is the control input.

In state-space form, the system state variables are used as

$$z_i(t) = \left[\Delta f_i(t)\ \ \Delta P_{mi}(t)\ \ \Delta X_{gi}(t)\ \ \Delta E_i(t)\ \ \Delta\delta_i(t)\right]^T. \tag{2}$$

So, the LSPSwCD described by Figure 1 can be written and expressed in state-space representation as follows:

$$\begin{aligned}
\dot{z}_i(t) &= A_i z_i(t) + D_i z_i(t-\tau_i) + B_i u_i(t)\\
&\quad + \sum_{j=1;j\neq i}^{N} H_{ij} z_j(t) + F_i \Delta P_{di}(t),
\end{aligned} \tag{3}$$

where $i = 1, 2, \ldots, N$ and N *is* denoted as the number of areas.

The state-space matrix $A_i, B_i, D_i, F_i, H_{ij}$ in mathematical model is given as follows:

$$A_i = \begin{bmatrix} \frac{-1}{T_{Pi}} & \frac{K_{Pi}}{T_{Pi}} & 0 & 0 & -\frac{K_{Pi}}{2\pi T_{Pi}} \sum_{i=1, j\neq i}^{N} T_{s,ij} \\ 0 & -\frac{1}{T_{Ti}} & \frac{1}{T_{Ti}} & 0 & 0 \\ -\frac{1}{R_i T_{Gi}} & 0 & -\frac{1}{T_{Gi}} & 0 & 0 \\ K_{Bi} K_{Ei} & 0 & 0 & 0 & \frac{K_{Ei}}{2\pi} \sum_{i=1, j\neq i}^{N} T_{s,ij} \\ 2\pi & 0 & 0 & 0 & 0 \end{bmatrix},$$

$$D_i = \begin{bmatrix} 0 & 0 & 0 & 0 & 0 \\ 0 & 0 & 0 & 0 & 0 \\ 0 & 0 & 0 & -\frac{1}{T_{Gi}} & 0 \\ 0 & 0 & 0 & 0 & 0 \\ 0 & 0 & 0 & 0 & 0 \end{bmatrix},$$

$$H_{ij} = \begin{bmatrix} 0 & 0 & 0 & 0 & -\frac{K_{Pi}}{2\pi T_{Pi}} \sum_{i=1, j\neq i}^{N} T_{s,ij} \\ 0 & 0 & 0 & 0 & 0 \\ 0 & 0 & 0 & 0 & 0 \\ 0 & 0 & 0 & 0 & \frac{K_{Ei}}{2\pi} \sum_{i=1, j\neq i}^{N} T_{s,ij} \\ 0 & 0 & 0 & 0 & 0 \end{bmatrix},$$

$$B_i = \begin{bmatrix} 0 \\ 0 \\ \frac{1}{T_{Gi}} \\ 0 \\ 0 \end{bmatrix};$$

$$F_i = \begin{bmatrix} -\frac{K_{Pi}}{T_{Pi}} \\ 0 \\ 0 \\ 0 \\ 0 \end{bmatrix}. \tag{4}$$

In applied LSPSwCD, the operating point fluctuates continually induced by the fluctuating resource and load disturbance. In addition, by considering CDs element, the dynamic model of LSPSwCD with the uncertainties and parameter variations in equation (3) are further redefined as

$$\begin{aligned}\dot{z}_i(t) &= [A_i + \Delta A_i(z_i,t)]z_i(t) + [D_i + \Delta D_i(z_i, t-\tau_i)]z_i(t-\tau_i) + B_i[u_i(t) + \xi_i(z_i,t)] \\ &\quad + \sum_{j=1;j\neq i}^{N} [H_{ij} + \Delta H_{ij}(z_j,t)]z_j(t) + F_i \Delta P_{di}(t) \\ &= A_i z_i(t) + D_i z_i(t-\tau_i) + B_i u_i(t) + \sum_{j=1;j\neq i}^{N} H_{ij} z_j(t) + w_i(z_i,t),\end{aligned} \tag{5}$$

where A_i, D_i, B_i, and H_{ij} are the system matrices with nominal value, $\Delta A_i(z_i,t)$, $\Delta H_{ij}(z_j,t)$, and $\Delta D_i(z_i, t-\tau_i)$ are the parameter uncertainties, and $B_i\xi_i(z_i,t)$ is the disturbance input signal. The lumped uncertainty $w_i(z_i,t)$ is defined as follows:

$$\begin{aligned}w_i(z_i,t) &= \Delta A_i(z_i,t)z_i(t) + \Delta D_i(z_i,t-\tau_i)z_i(t-\tau_i) \\ &\quad + B_i\xi_i(z_i,t) + \sum_{i=1;j\neq i}^{N} \Delta H_{ij} z_j(t) + F_i \Delta P_{di}(t).\end{aligned} \tag{6}$$

Assumption 1. The lumped uncertainties $w_i(z_i,t)$ and the differential of $\dot{w}_i(z_i,t)$ are bounded, i.e., there exist known scalars γ_i and ∂_i such that $\|w_i(z_i,t)\| \le \gamma_i$ and $\|\dot{w}_i(z_i,t)\| \le \partial_i$, where $\|.\|$ is the matrix norm.

Assumption 2. The time-delay state vector must satisfy the condition $\|z_i(t-\tau_i)\| \le z_{i\max}$, $z_{i\max} = \max\|z_{i\max}\|$, where $\|.\|$ is the matrix norm.

In order to prove the system stability, we recall some lemmas.

Lemma 1 (see [34]). *Let* $\mathbf{X}$ *and* $\mathbf{Y}$ *be actual matrices with appropriate dimension, then, for any scalar* $\mu > 0$*, the sequent matrix inequality obtains*

$$\mathbf{X^T Y} + \mathbf{Y^T X} \le \mu \mathbf{X^T X} + \mu^{-1}\mathbf{Y^T Y}. \tag{7}$$

Lemma 2 (see [35]). *ie following matrix inequality*

$$\begin{bmatrix} P(z) & \Gamma(z) \\ \Gamma^T(z) & Q(z) \end{bmatrix} > 0, \tag{8}$$

where $P(z) = P^T(z)$, $Q(z) = Q^T(z)$, $\Gamma(z)$ *depends affinely on* z, *is equivalent to* $Q(z) > 0$ *and* $P(z) - \Gamma(z)Q^{-1}(z)\Gamma^T(z) > 0$.

Lemma 3 (see [35]). *Assume that* $x \in R^n$, $y \in R^n$, $\mathbf{N} \in R^{n\times n}$, *and* $\mathbf{N}$ *is the positive definite matrix. Then, the inequality*

$$x^T\mathbf{N}y + y^T\mathbf{N}x \le \frac{1}{\varepsilon}x^T\mathbf{N}x + \varepsilon y^T\mathbf{N}y, \tag{9}$$

holds for all $\varepsilon > 0$.

3. Adaptive Integral Second-Order Sliding Mode Control (AISOSMC) Design for LFC of Large-Scale Power System with Communication Delays (LSPSwCD)

In this section, the AISOSMC method is developed for LFC of the LSPSwCD under mismatched parameter uncertainties and load disturbances. To solve this problem, we work step by step to design and implement the new controller approach. Firstly, the integral sliding surface (ISS) is represented for LSPSwCD to assure that the whole system is asymptotically stable. Secondly, the decentralized adaptive integral second-order sliding mode control law (DAISOSMCL) is designed to force the system trajectories to the sliding manifold and keep it there for after.

3.1. Stability Analysis of a LSPSwCD in Sliding Mode Dynamics. In detail, we first begin to propose and build an ISS for a LSPS:

$$\sigma_i[z_i(t)] = E_i z_i(t) - \int_0^t E_i(A_i - B_iT_i)z_i(\tau)\mathrm{d}\tau, \tag{10}$$

where E_i is the constant matrix and T_i is the design matrix, matrix E_i is designed to guarantee that matrix E_iB_i is nonsingular and matrix T_i is chosen via pole assignment such that the eigenvalues of matrix $(A_i - B_iT_i)$ are always less than zero.

If we recognize and differentiate $\sigma_i[z_i(t)]$ with respect to time combined with (3), then

$$\dot{\sigma}_i[z_i(t)] = E_i\left[A_i z_i(t) + D_i z_i(t-\tau_i) + B_i u_i(t) + \sum_{j=1;j\neq i}^{N} H_{ij} z_j(t) + w_i(z_i,t)\right] - E_i(A_i - B_iT_i)z_i(t). \tag{11}$$

So, the setting $\sigma_i[z_i(t)] = \dot{\sigma}_i[z_i(t)] = 0$; the equivalent control is rewritten by

$$u_i^{\mathrm{eq}}(t) = -(E_iB_i)^{-1}\left[E_iA_iz_i(t) + E_iD_iz_i(t-\tau_i) + \sum_{j=1;j\neq i}^{N} E_iH_{ij}z_j(t) + E_iw_i(z_i,t)\right] - [E_i(A_i - B_iT_i)z_i(t)]. \tag{12}$$

Substituting $u_i(t)$ with $u_i^{\mathrm{eq}}(t)$ into the LSPSwCD yields the sliding motion:

$$\dot{z}_i(t) = (A_i - B_iT_i)z_i(t) + \left[I - B_i(E_iB_i)^{-1}E_i\right]D_iz_i(t-\tau_i) + \sum_{j=1;j\neq i}^{N}\left[I - B_i(E_iB_i)^{-1}E_i\right]H_{ij}z_j(t) + \left[I - B_i(E_iB_i)^{-1}E_i\right]w_i(z_i,t). \tag{13}$$

The introduction of the following theorem makes a condition that the AISOSMC dynamic equation (11) is asymptotically stable.

Theorem 1. *The sliding motion (13) is asymptotically stable if and only if there includes symmetric positive definite matrix Q_i, P_i, $i = 1, 2, \ldots, N$, and positive scalars q, φ_i. and β_j such that the following LMIs hold:*

$$\begin{bmatrix} \Omega_i + \sum_{\substack{j=1\\ j\neq i}}^{N} \beta_j^{-1}H_{ji}^TH_{ji} & 0 & D_i^T\left[I - B_i(E_iB_i)^{-1}E_i\right]^T & Q_i\left[I - B_i(E_iB_i)^{-1}E_i\right] \\ 0 & -P_i & 0 & 0 \\ \left[I - B_i(E_iB_i)^{-1}E_i\right]D_i & 0 & -qQ_i^{-1} & 0 \\ \left[I - B_i(E_iB_i)^{-1}E_i\right]^TQ_i & 0 & 0 & -\varphi_i^{-1} \end{bmatrix} < 0, \tag{14}$$

where $\Omega_i = (A_i - B_iT_i)^TQ_i + Q_i(A_i - B_iT_i) + Q_i + P_i$.

Proof. To study and analyze stability of the sliding motion (13), we use the Lyapunov function as follows:

$$V = \sum_{i=1}^{N}\left[z_i^T(t)Q_iz_i(t) + \int_{t-\tau_i}^{t} z_i^T(s)P_iz_i(s)\mathrm{d}s\right], \tag{15}$$

where $Q_i, P_i > 0$ satisfies (14). Then, taking the time derivative of (15) and using equation (13), we obtain

$$\begin{aligned} \dot{V} = \sum_{i=1}^{N}\Big\{&\left[z_i^T(t)\left[(A_i - B_iT_i)^TQ_i + Q_i(A_i - B_iT_i)\right]z_i(t)\right. \\ &+ z_i^T(t-\tau_i)D_i^T\left[I - B_i(E_iB_i)^{-1}E_i\right]^TQ_iz_i(t) + z_i^T(t)Q_i\left[I - B_i(E_iB_i)^{-1}E_i\right]D_iz_i(t-\tau_i) \\ &+ \sum_{j=1;j\neq i}^{N} z_j^T(t)H_{ij}^T\left[I - B_i(E_iB_i)^{-1}E_i\right]^TQ_iz_i(t) + \sum_{j=1;j\neq i}^{N} z_i^T(t)Q_i\left[I - B_i(E_iB_i)^{-1}E_i\right]H_{ij}z_j(t) \\ &\left.+ w_i^T(z_i,t)\left[I - B_i(E_iB_i)^{-1}E_i\right]^TQ_iz_i(t) + z_i^T(t)Q_i\left[I - B_i(E_iB_i)^{-1}E_i\right]w_i(z_i,t)\right] \\ &+ z_i^T(t)P_iz_i(t) - z_i^T(t-\tau_i)P_iz_i(t-\tau_i)\Big\}. \end{aligned} \tag{16}$$

To apply Lemma 1 in equation (16), we obtain

$$\begin{aligned}\dot{V} \leq \sum_{i=1}^{N}\Big\{ & z_i^T(t)\big[(A_i - B_iT_i)^TQ_i + Q_i(A_i - B_iT_i)\big]z_i(t) \\ & + z_i^T(t-\tau_i)D_i^t\big[I - B_i(E_iB_i)^{-1}E_i\big]^TQ_iz_i(t) + z_i^T(t)Q_i\big[I - B_i(E_iB_i)^{-1}E_i\big]D_iz_i(t-\tau_i) \\ & + \sum_{j=1;j\neq i}^{N} z_i^T(t)\beta_i^{-1}Q_i\big[I - B_i(E_iB_i)^{-1}E_i\big]\big[I - B_i(E_iB_i)^{-1}E_i\big]^TQ_iz_i(t) \\ & + \sum_{j=1;j\neq i}^{N} z_j^T(t)\beta_iH_{ij}^TH_{ij}z_j(t) + z_i^T(t)P_iz_i(t) - z_i^T(t-\tau_i)P_iz_i(t-\tau_i) \\ & + \chi_i^{-1}z_i^T(t)Q_i\big[I - B_i(E_iB_i)^{-1}E_i\big]\big[I - B_i(E_iB_i)^{-1}E_i\big]^TQ_iz_i(t) + \chi_iw_i^T(z_i,t)w_i(z_i,t)\Big\}.\end{aligned} \tag{17}$$

Using Lemma 3 and equation (17), we get

$$\begin{aligned}\dot{V} \leq \sum_{i=1}^{N}\Big\{ & z_i^T(t)\big[(A_i - B_iT_i)^TQ_i + Q_i(A_i - B_iT_i)\big]z_i(t) \\ & + z_i^T(t-\tau_i)D_i^T\big[I - B_i(E_iB_i)^{-1}E_i\big]^TQ_i\big[I - B_i(E_iB_i)^{-1}E_i\big]D_iz_i(t-\tau_i) + z_i^T(t)Q_iz_i(t) \\ & + \sum_{j=1;j\neq i}^{N} z_i^T(t)\beta_i^{-1}Q_i\big[I - B_i(E_iB_i)^{-1}E_i\big]\big[I - B_i(E_iB_i)^{-1}E_i\big]^TQ_iz_i(t) \\ & + \sum_{j=1;j\neq i}^{N} z_j^T(t)\beta_iH_{ij}^TH_{ij}z_j(t) + z_i^T(t)P_iz_i(t) - z_i^T(t-\tau_i)P_iz_i(t-\tau_i) \\ & + \chi_i^{-1}z_i^T(t)Q_i\big[I - B_i(E_iB_i)^{-1}E_i\big]\big[I - B_i(E_iB_i)^{-1}E_i\big]^TQ_iz_i(t) + \chi_iw_i^T(z_i,t)w_i(z_i,t)\Big\}.\end{aligned} \tag{18}$$

Since $\sum_{i=1}^{N}\sum_{j=1,j\neq i}^{N} z_j^T(t)\beta_i^{-1}H_{ij}^TH_{ij}z_j(t) = \sum_{i=1}^{N}\sum_{j=1,j\neq i}^{N} z_i^T(t)\beta_j^{-1}H_{ji}^TH_{ji}z_i(t)$, we achieve that

$$\begin{aligned}\dot{V} \leq \sum_{i=1}^{N}\Big\{ & z_i^T(t)\Big[(A_i - B_iT_i)^TQ_i + Q_i(A_i - B_iT_i) + Q_i \\ & + \varphi_iQ_i\big[I - B_i(E_iB_i)^{-1}E_i\big]\big[I - B_i(E_iB_i)^{-1}E_i\big]^TQ_i\Big]z_i(t) \\ & + \sum_{j=1;j\neq i}^{N} z_i^T(t)\beta_jH_{ji}^TH_{ji}z_i(t) + \chi_iw_i^T(z_i,t)w_i(z_i,t) \\ & + z_i^T(t-\tau_i)D_i^T\big[I - B_i(E_iB_i)^{-1}E_i\big]^TQ_i\big[I - B_i(E_iB_i)^{-1}E_i\big]D_iz_i(t-\tau_i) \\ & + z_i^T(t)P_iz_i(t) - z_i^T(t-\tau_i)P_iz_i(t-\tau_i)\Big\},\end{aligned} \tag{19}$$

where $\varphi_i = \chi_i^{-1} + (N-1)\beta_i^{-1}$.

The matrix $D_i^T[I - B_i(E_iB_i)^{-1}E_i]^TQ_i[I - B_i(E_iB_i)^{-1}E_i]D_i$ is the semipositive definite. Since the $z_i(t)$ for $i = 1, 2, \ldots, N$ are independent of each other. Then, from equation (32) of paper [36], the following is true:

$$V(z_1(t-\tau_1), z_2(t-\tau_2), z_3(t-\tau_3), \ldots, z_N(t-\tau_N)) \le qV(z_1(t), z_2(t), z_3(t), \ldots, z_N(t)), \tag{20}$$

for $q > 1$ is equivalent to

$$\begin{aligned}&\sum_{i=1}^{N}\left\{z_i^T(t-\tau_i)D_i^T\left[I - B_i(E_iB_i)^{-1}E_i\right]^TQ_i\left[I - B_i(E_iB_i)^{-1}E_i\right]D_iz_i(t-\tau_i)\right\}\\ &\le q\sum_{i=1}^{N}\left\{z_i^T(t)D_i^T\left[I - B_i(E_iB_i)^{-1}E_i\right]^TQ_i\left[I - B_i(E_iB_i)^{-1}E_i\right]D_iz_i(t)\right\}.\end{aligned} \tag{21}$$

Then, we can get the following equation:

$$\begin{aligned}\dot{V} \le \sum_{i=1}^{N}\Big\{&z_i^T(t)\Big[(A_i - B_iT_i)^TQ_i + Q_i(A_i - B_iT_i) + Q_i + P_i\\ &+ \varphi_iQ_i\left[I - B_i(E_iB_i)^{-1}E_i\right]\left[I - B_i(E_iB_i)^{-1}E_i\right]^TQ_i\\ &+ qD_i^T\left[I - B_i(E_iB_i)^{-1}E_i\right]^TQ_i\left[I - B_i(E_iB_i)^{-1}E_i\right]D_i\Big]z_i(t)\\ &+ \sum_{j=1;j\neq i}^{N} z_i^T(t)\beta_jH_{ji}^TH_{ji}z_i(t) - z_i^T(t-\tau_i)P_iz_i(t-\tau_i)\\ &+ \chi_iw_i^T(z_i,t)w_i(z_i,t)\Big\}.\end{aligned} \tag{22}$$

Based on Assumption 1, the following equation can be achieved:

$$\begin{aligned}\dot{V} \le \sum_{i=1}^{N}\Big\{&z_i^T(t)\Big[(A_i - B_iT_i)^TQ_i + Q_i(A_i - B_iT_i) + Q_i + P_i\\ &+ \varphi_iQ_i\left[I - B_i(E_iB_i)^{-1}E_i\right]\left[I - B_i(E_iB_i)^{-1}E_i\right]^TQ_i\\ &+ qD_i^T\left[I - B_i(E_iB_i)^{-1}E_i\right]^TQ_i\left[I - B_i(E_iB_i)^{-1}E_i\right]D_i\Big]z_i(t)\\ &+ \sum_{j=1;j\neq i}^{N} z_i^T(t)\beta_jH_{ji}^TH_{ji}z_i(t) - z_i^T(t-\tau_i)P_iz_i(t-\tau_i) + \iota_i\Big\},\end{aligned} \tag{23}$$

where $\iota_i = \chi_i\gamma_i^2$.

Define the augmented vector

$$\begin{aligned}\Psi_i(t) &= \left[z_i^T(t)\ \ z_i^T(t-\tau_i)\right]^T,\\ \dot{V} &\le \Psi_i^T(t)\Theta_i\Psi_i(t) + \iota_i.\end{aligned} \tag{24}$$

From Lemma 2 and LMI (14), we get

$$\Theta_i = -\begin{bmatrix}\Xi_i & 0\\ 0 & -P_i\end{bmatrix} > 0, \tag{25}$$

where

$$\begin{aligned}\Xi_i = {}&(A_i - B_iT_i)^TQ_i + Q_i(A_i - B_iT_i) + Q_i + P_i + \varphi_iQ_i\left[I - B_i(E_iB_i)^{-1}E_i\right]\left[I - B_i(E_iB_i)^{-1}E_i\right]^TQ_i\\ &+ qD_i^T\left[I - B_i(E_iB_i)^{-1}E_i\right]^TQ_i\left[I - B_i(E_iB_i)^{-1}E_i\right]D_i + \sum_{j=1,j\neq i}^{N}\beta_j^{-1}H_{ji}^TH_{ji}.\end{aligned} \tag{26}$$

According to equations (23) and (25), we obtain

$$\dot{V} \leq \sum_{i=1}^{N}\left[-\lambda_{\min}(\Theta_i)\|\Psi_i(t)\|^2 + \iota_i\right], \tag{27}$$

where the constant value ι_i and the eigenvalue $\lambda_{\min}(\Theta_i) > 0$. Therefore, $\dot{V} < 0$ is achieved with $\|\Psi_i(t)\| > \sqrt{(\iota_i/\lambda_{\min}(\Theta_i))}$. Hence, the sliding motion of system (13) is asymptotically stable. □

Remark 1. The adaptive integral second-order sliding mode control design is composed of the hitting phase and the sliding phase. The proposed controller is used to force the system state trajectories to sliding phase and keep the system state trajectories on it thereafter. If the disturbance and uncertainty satisfy the matching condition $\text{rank}[B_i, w_i(z_i, t)] = \text{rank}[B_i]$, the system in the sliding mode is invariant to disturbance and uncertainty. The stability of system under matched condition is easier than mismatched condition. The proposed controller can compensate for disturbance and uncertainty directly under matched condition. Therefore, the stability of the system in the sliding mode under mismatched condition $\text{rank}[B_i, w_i(z_i, t)] \neq \text{rank}[B_i]$ has been considered and proved using LMI technique based on Lyapunov stability theory.

3.2. First-Order SMC Design. In order to guarantee the reachability of state variables to the ISS (10), the decentralized first-order integral SMC law is designed as follows [18]:

$$\begin{aligned} u_i^{\text{FOSMC}}(t) = -(E_iB_i)^{-1}\Big\{&\|E_i\|\|B_i\|\|T_i\|\|z_i(t)\| + \|E_i\|\|D_i\|\|z_i(t-\tau_i)\| \\ &+ \sum_{j=1;j\neq i}^{N}\|E_j\|\|H_{ji}\|\|z_i(t)\| + \|E_i\|\overline{\gamma}_i + \widetilde{\varepsilon}_i \text{sat}\{\sigma_i[z_i(t)]\}\Big\}, \end{aligned} \tag{28}$$

where $\widetilde{\varepsilon}_i > 0$ and

$$\text{sat}\{\sigma_i[z_i(t)]\} = \begin{cases} 1, & \sigma_i[z_i(t)] > 1, \\ \sigma_i[z_i(t)], & \text{When } -1 \leq \sigma_i[z_i(t)] \leq 1, \\ -1, & \sigma_i[z_i(t)] < -1. \end{cases} \tag{29}$$

Remark 2. The first-order SMC can be used to study LFC of power system under matched uncertainties. However, the parametric uncertainties not usually satisfy the matched condition in real power network. Consequently, some main constraints are necessary to design the first-order SMC to compensate the uncertainties, which can guarantee the convergence in nominal frequency and the system stability but the system trajectories cannot reach to origin point. Therefore, the second-order ISS has been used as the following part to force the system trajectory to equivalent point and to make better the transient performance.

3.3. Decentralized Adaptive Integral Second-Order Sliding Mode Control Law (DAISOSMCL) Design. In this step, the DAISOSMCL is developed for the LSPSwCD to reduce the frequency deviation. The main purpose of the proposed control scheme is to effect on the second-order derivative of the sliding variables $\sigma_i[z_i(t)]$. By using the discontinuous control signal $\dot{u}_i(t)$, it is simple to make $\sigma_i[z_i(t)]$ and $\dot{\sigma}_i[z_i(t)]$ converge to zero. So, the input control signal $u_i(t)$ of LSPSwCD can get by integrating the discontinuous signal $\dot{u}_i(t)$ to make continuous signal $u_i(t)$. Therefore, the DAISOSMCL approach removes some undesired frequency oscillations in the control signal of LSPSwCD.

We define and establish the sliding manifold (SMd) $G_i[z_i(t)]$ as

$$G_i[z_i(t)] = \dot{\sigma}_i[z_i(t)] + \varepsilon_i\sigma[z_i(t)], \tag{30}$$

$$\dot{G}_i[z_i(t)] = \ddot{\sigma}_i[z_i(t)] + \varepsilon_i\dot{\sigma}_i[z_i(t)], \tag{31}$$

where $\varepsilon_i > 0$ is a positive constant, according to equation (30); the equation (31) can be redefined as

$$\begin{aligned} \dot{G}_i[z_i(t)] = E_i\Big[&A_i\dot{z}_i(t) + D_i\dot{z}_i(t-\tau_i) + B_i\dot{u}_i(t) + \sum_{j=1;j\neq i}^{N} H_{ij}\dot{z}_j(t) + \dot{w}_i(z_i, t)\Big] \\ &- E_i(A_i - B_iT_i)\dot{z}_i(t) + \varepsilon_i\dot{\sigma}_i[z_i(t)]. \end{aligned} \tag{32}$$

Based on the definition of sliding surface and SMd, the continuous DAISOSMCL for LFC of a LSPSwCD is given as follows:

$$\dot{u}_i(t) = \dot{u}_i^{\mathrm{SOSMC}}(t) + \dot{u}_i^{\mathrm{adt}}(t), \tag{33}$$

where

$$\begin{aligned}\dot{u}_i^{\mathrm{SOSMC}}(t) = -(E_iB_i)^{-1}\Big[&\|E_i\|\|B_i\|\|T_i\|\|\dot{z}_i(t)\| + \|E_i\|\|D_i\|\|\dot{z}(t-\tau_i)\| + \sum_{j=1;j\neq i}^{N}\|E_j\|\|H_{ji}\|\|\dot{z}_i(t)\| \\ &+ \varepsilon_i\|\dot{\sigma}_i[z_i(t)]\| + \|E_i\|\partial_i + \bar{\varepsilon}_i\Big]\frac{G_i[z_i(t)]}{\|G_i[z_i(t)]\|},\end{aligned} \tag{34}$$

$$\dot{u}_i^{\mathrm{adt}}(t) = -(E_iB_i)^{-1}I\left[\hat{\partial}_i(t)\|E_i\| + \bar{p}_i\frac{\partial_i^2}{4}\right], \quad i = 1, 2, \ldots, N,$$

where

$$\dot{\hat{\partial}}_i(t) = p_i\left(-\bar{p}_i\hat{\partial}_i(t) + \|E_i\|\right), \quad i = 1, 2, \ldots, N, \tag{35}$$

in which p_i and $\bar{p}_i$ are the positive constants.

Then, we have the main result which is presented as follows.

Theorem 2. *Consider the closed loop of the power systems with the DAISOSMCL (33). Then, every solution trajectory of system state is directed towards the SMd $G_i[z_i(t)]$, and once the trajectory hits the SMd $G_i[z_i(t)]$, it remains on the sliding manifold thereafter.*

Proof. The Lyapunov function is introduced as follows:

$$\bar{V}(t) = \sum_{i=1}^{N}\left\{\|G_i[z_i(t)]\| + \frac{0.5}{p_i}\tilde{\partial}_i^2\right\}, \tag{36}$$

where $\tilde{\partial}_i(t) = \partial_i - \hat{\partial}_i(t)$.

So, taking the derivative of $\bar{V}(t)$, we have

$$\begin{aligned}\dot{\bar{V}} &= \sum_{i=1}^{N}\left[\frac{G_i^T[z_i(t)]}{\|G_i[z_i(t)]\|}\dot{G}_i[z_i(t)] - \tilde{\partial}_i(t)\frac{\dot{\hat{\partial}}_i(t)}{p_i}\right] \\ &= \sum_{i=1}^{N}\frac{G_i^T[z_i(t)]}{\|G_i[z_i(t)]\|}\left\{E_i\left[A_i\dot{z}_i(t) + D_i\dot{z}(t-\tau_i) + B_i\dot{u}_i(t) + \sum_{\substack{j=1\\ j\neq i}}^{N}H_{ij}\dot{z}_j(t) + \dot{w}_i(z_i,t)\right]\right. \\ &\quad \left. -E_i(A_i - B_iT_i)\dot{z}_i(t) + \varepsilon_i\dot{\sigma}_i[z_i(t)]\right\} - \sum_{i=1}^{N}\tilde{\partial}_i(t)\frac{\dot{\hat{\partial}}_i(t)}{p_i}.\end{aligned} \tag{37}$$

According to equation (37) and property $\|AB\| \leq \|A\|\|B\|$, we have

$$\begin{aligned}\dot{\overline{V}} &= \sum_{i=1}^{N}\left\{E_i\left[A_i\dot{z}_i(t) + D_i\dot{z}(t-\tau_i) + B_i\dot{u}_i(t) + \sum_{\substack{j=1\\ j\neq i}}^{N} H_{ij}\dot{z}_j(t) + \dot{w}_i(z_i,t)\right]\right\}\\ &\quad + \sum_{i=1}^{N}\frac{G_i^T[z_i(t)]}{\|G_i[z_i(t)]\|}E_iB_i\dot{u}_i(t) - \sum_{i=1}^{N}\tilde{\partial}_i(t)\frac{\dot{\hat{\partial}}_i(t)}{p_i}\\ &\le \sum_{i=1}^{N}\left\{\|E_i\|\|B_i\|\|T_i\|\|\dot{z}_i(t)\| + \|E_i\|\|D_i\|\|\dot{z}_i(t-\tau_i)\| + \delta_i\|\dot{\sigma}_i[z_i(t)]\|\right.\\ &\quad \left. + \sum_{\substack{j=1\\ j\neq i}}^{N}\|E_i\|\|H_{ij}\|\|\dot{z}_i(t)\| + \|E_i\|\|\dot{w}_i(z_i,t)\|\right\} + \sum_{i=1}^{N}\frac{G_i^T[z_i(t)]}{\|G_i[z_i(t)]\|}E_iB_i\dot{u}_i(t) - \sum_{i=1}^{N}\tilde{\partial}_i(t)\frac{\dot{\hat{\partial}}_i(t)}{p_i}.\end{aligned} \tag{38}$$

Using Assumption 1, we achieve

$$\begin{aligned}\dot{\overline{V}} &\le \sum_{i=1}^{N}\left\{\|E_i\|\|B_i\|\|T_i\|\|\dot{z}_i(t)\| + \|E_i\|\|D_i\|\|\dot{z}_i(t-\tau_i)\| + \|E_i\|\partial_i\right.\\ &\quad \left. + \sum_{\substack{j=1\\ j\neq i}}^{N}\|E_j\|\|H_{ji}\|\|\dot{z}_i(t)\| + \varepsilon_i\|\dot{\sigma}_i[z_i(t)]\|\right\}\\ &\quad + \sum_{i=1}^{N}\frac{G_i^T[z_i(t)]}{\|G_i[z_i(t)]\|}E_iB_i\dot{u}_i(t) - \sum_{i=1}^{N}\tilde{\partial}_i(t)\frac{\dot{\hat{\partial}}_i(t)}{p_i}.\end{aligned} \tag{39}$$

Using the DAISOSMCL (33) yields

$$\begin{aligned}\dot{\overline{V}} &\le \sum_{i=1}^{N}\left[-\overline{\varepsilon}_i - \hat{\partial}_i(t)\|E_i\| - \overline{p}_i\frac{\partial_i^2}{4} + \|E_i\|\partial_i\right] - \sum_{i=1}^{N}\left[\partial_i\|E_i\|\right] - \sum_{i=1}^{N}\left[\overline{p}_i\hat{\partial}_i^2(t) - \overline{p}_i\partial_i\hat{\partial}_i(t) - \hat{\partial}_i(t)\|E_i\|\right]\\ &= \sum_{i=1}^{N}\left(-\overline{\varepsilon}_i - \overline{p}_i\frac{\partial_i^2}{4}\right) - \sum_{i=1}^{N}\left[\overline{p}_i\hat{\partial}_i^2(t) - \overline{p}_i\partial_i\hat{\partial}_i(t)\right]\\ &= \sum_{i=1}^{N}\left[\left(-\overline{\varepsilon}_i - \overline{p}_i\frac{\partial_i^2}{4}\right) - \sum_{i=1}^{N}\left[\overline{p}_i\left(\hat{\partial}_I(t) - \partial_i\right)^2 - \overline{p}_i\frac{\partial_i^2}{4}\right]\right.\\ &= \sum_{i=1}^{N}-\overline{\varepsilon}_i - \sum_{i=1}^{N}\left[\overline{p}_i\left(\hat{\partial}_I(t) - \partial_i\right)^2\right].\end{aligned} \tag{40}$$

The above inequality implies that the system trajectories of the LSPSwCD (3) reach the SMd $G_i[z_i(t)]$ and keep it for later. □

Remark 3. The SMC is capable to reach the bounded system stability and is able to maintain within a range to converge zero, and then the power system is notably stable. Equation

(10) indicates that the integral term $\int_0^t E_i(A_i - B_iT_i)z_i(\tau)\mathrm{d}\tau$ is only reflected in the proposed DAISOSMCL (33). Therefore, the control law (33) is to improve the performance of steady state error in comparison with the traditional integral SMC.

4. Results and Discussion

Based on the interconnected time-delay power network, the four cases are offered to prove the strength of the suggested AISOSMC approach under the required conditions such as the different load disturbances and the parameter variations. A LSPSwCD is analyzed to explain the robustness and effectiveness of the suggested AISOSMC approach. The parameters of LSPSwCD were given in [22] as shown Table 1.

Case 1. The presented LFC based on AISOSMC is used to compare with the traditional LFC approach under the same condition in [22]. The proposed LFC based on AISOSMC has been examined with different step load disturbance effect on the thermal power plant with nominal parameter conditions. We have considered the system parameters of matched uncertainties. In this case, the load disturbances are $\Delta P_{d1} = 0.02, \Delta P_{d2} = 0.015$, and $\Delta P_{d3} = 0.01$ (p.u.MW) at $t_1 = 0$ in three areas of the LSPS. The frequency deviations of $\Delta f_1, \Delta f_2$, and Δf_3 for the LSPS with delay-time as $\tau_i = 0.1$ s $(i = 1, 2, 3)$ are displayed in Figures 2–4 which are the tie-line power deviation and control input signal for three-area power networks. It is easy to realize that the transient responses achieved in the proposed LFC based on AISOSMC is faster in the settling time, but it has less magnitude of overshoot percentage with the proposed recent controller in [22].

Remark 4. Due to Figures 2 to 4, the testing simulation results in this part are appointed in Table 2. In particular, the report of results can show in an effective comparison while the time-delay communication is considered for the large-scale power network. Therefore, the system performance of the suggested AISOSMC is well balanced, and frequency variation is zero after 1s.

Case 2. As the same matched parameter uncertainty of the three areas is used in [22], the cosine function around the nominal operation point is used to verify the usefulness and robustness of the suggested controller to load disturbance. The step load disturbances in LSPSwCD are chosen as $\Delta P_{d1} = 0.01$ p.u.MW at $t_1 = 0$ s and $\Delta P_{d2} = 0.015$ p.u.MW at $t_2 = 0$ and $\Delta P_{d3} = 0.02$ p.u.MW at $t_3 = 0$.

$$\Delta A_1 = \begin{bmatrix} 0 & 0 & 0 & 0 & 0 \\ 0 & 0 & 0 & 0 & 0 \\ -2.26\cos(t) & 2\cos(t) & -2.604\cos(t) & 3\cos(t) & 0 \\ 0 & 0 & 0 & 0 & 0 \\ 0 & 0 & 0 & 0 & 0 \end{bmatrix}$$

and the matched uncertainty among subsystems are assumed the same as [22] and $\Delta A_1 = \Delta A_2 = \Delta A_3$.

Table 1: The parameters of three-area power system.

Areas	T_{Pi}	K_{Pi}	T_{Ti}	T_{Gi}	R_i	K_{Ei}	K_{Bi}	K_{ij}
1	20	120.0	0.30	0.080	2.4	10.0	0.41	0.550
2	25	112.5	0.33	0.072	2.7	9.0	0.37	0.650
3	20	115.0	0.35	0.070	2.5	7.1	0.40	0.545

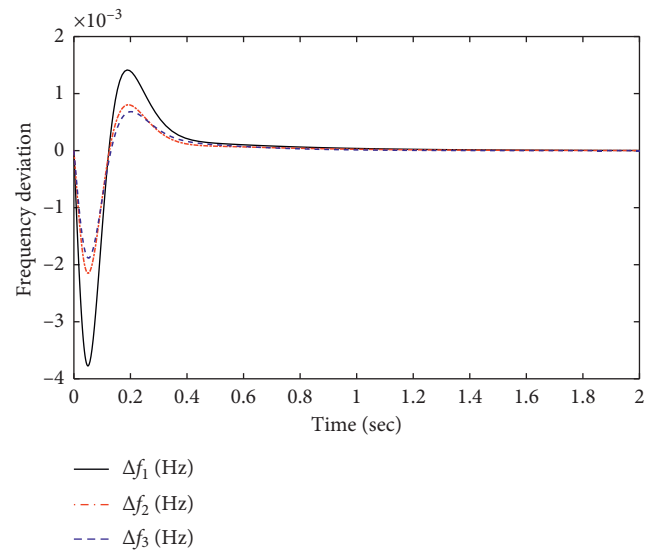

Figure 2: Frequency variation of the system.

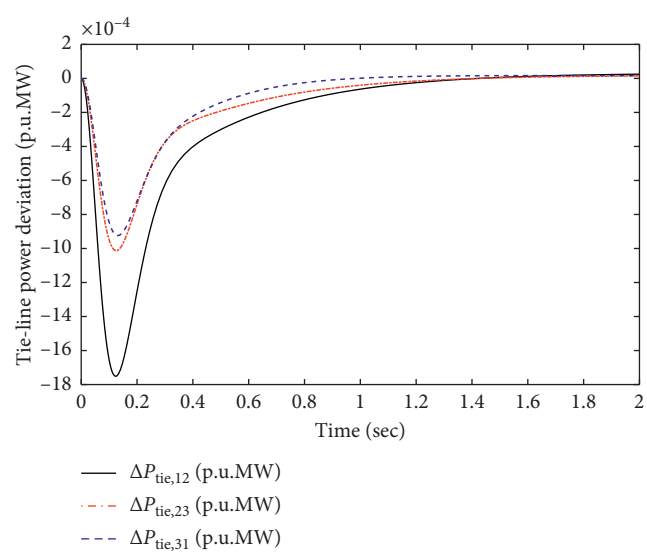

Figure 3: Tie-line variation of the system.

Figure 5 indicates that the proposed LFC based on AISOSMC to three areas with CDs, $\tau_i = 0.1$; the frequency deviation reaching to zero is about 2 s much smaller than the comparative LFC used in [22] within 10 s. Figure 6 plots the control signal of the system under matched uncertainty. The tie-line power variations of three areas with LFC based on

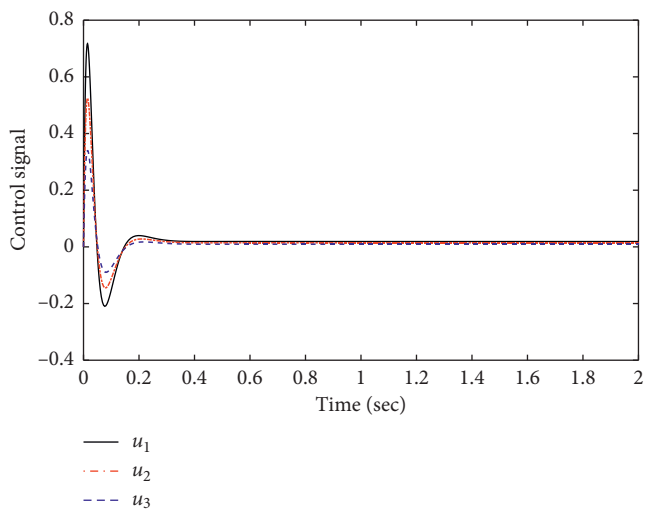

Figure 4: Control signal of the system.

Table 2: Comparison between the proposed AISOSMC method with the previous method in [22].

Kinds of controller	The AISOSMC approach		Previous load frequency controller in [22]	
Parameters	T_s (s)	Max. $O.\ S$ (pu)	T_s (s)	Max. $O.\ S$ (pu)
Δf_1	1	-3.8×10^{-3}	2	-3.8×10^{-3}
Δf_2	1	-2.1×10^{-3}	2	-2.1×10^{-3}
Δf_3	1	-1.9×10^{-3}	2	-2.0×10^{-3}

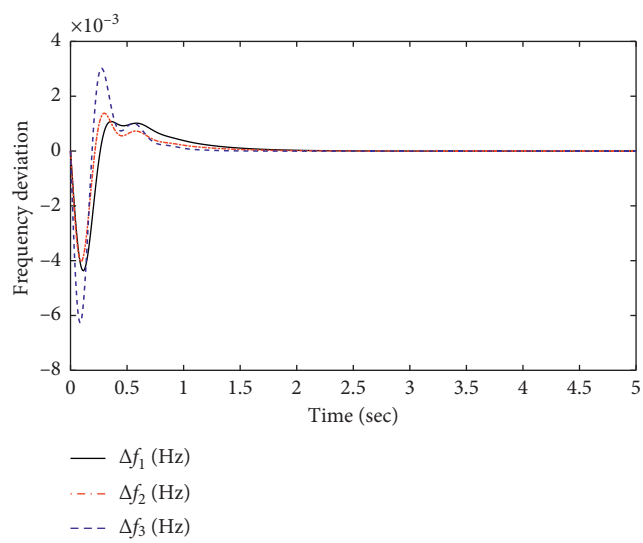

Figure 5: Frequency deviation of the system under matched uncertainty.

AISOSMC always are kept with maximum value as 4.7×10^{-3} p.u.MW in Figure 7.

Remark 5. In this configuration, the influents of time-delay signals are considered to compare with the simulation result in [22], the DAISOSMCL based on the offered switching surface can not only make better in the response speed but also upgrade the transient performance to decrease the overshoot percentage. So, the designed control method is powerful and strong enough to regulate and control the matched parameter uncertainties of multiarea interconnected time-delay grids.

Case 3. In this case, the load disturbances are $\Delta P_{d1} = 0.01$ p.u.MW at $t_1 = 0$ s, $\Delta P_{d2} = 0.02$ p.u.MW at $t_2 = 0$, and $\Delta P_{d3} = 0.03$ p.u.MW at $t_3 = 0$ in area 1, area 2, and area 3,

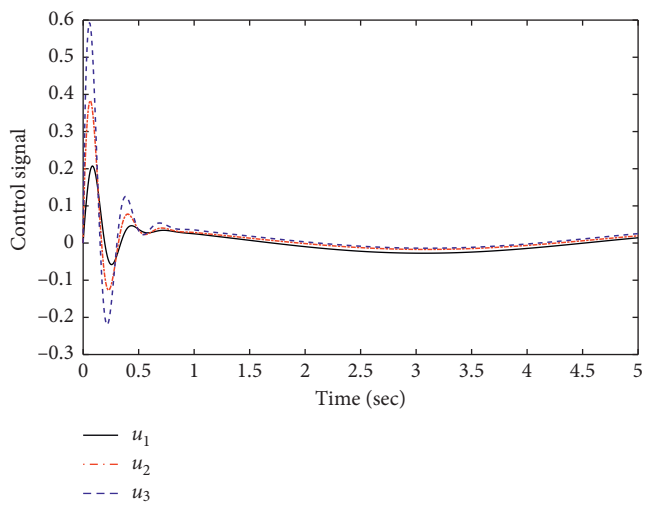

Figure 6: Control signal of the system under matched uncertainty.

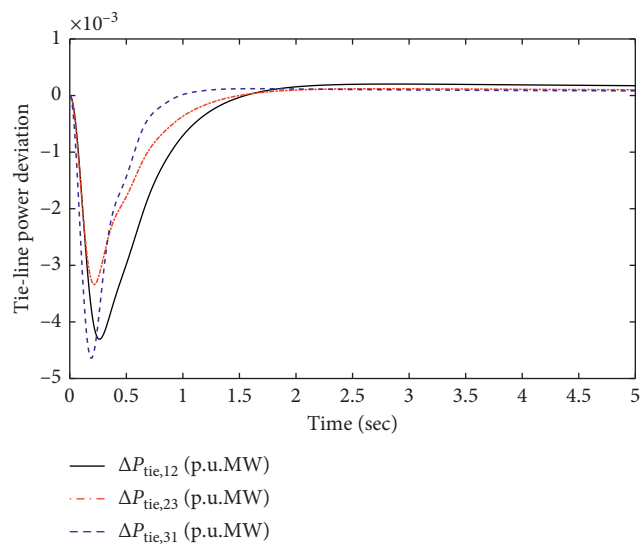

Figure 7: Tie-line deviation of the system under matched uncertainty.

respectively. We discuss about the impact of mismatch parameter uncertainty in the state matrix and values of the time-delay as $\tau_i = 0.2\,\text{s}$ $(i = 1, 2, 3)$ for all the subsystems of LSPSwCD which are designed as follows:

$$\Delta A_1 = \begin{bmatrix} 0 & \Delta f_1 & 0 & 0 & 0 \\ \sin(t) & 0 & 0 & 0 & 0 \\ 0 & 0 & \cos(t) & \cos(t) & 0 \\ 0 & 0 & 0 & 0 & \cos(t) \\ \cos(t) & 0 & 0 & 0 & 0 \end{bmatrix}, \quad \Delta A_2 = \Delta A_3 = \Delta A_1. \tag{41}$$

The mismatch interconnected between subsystems is designed as follows:

$$\Delta H_{12} = \begin{bmatrix} 0 & 0 & 0 & 0 & 0.178\cos(t) \\ 0 & 0 & 0 & 0 & 0 \\ 0 & 0 & 0 & 0 & 0 \\ 0 & 0 & 0 & 0 & -0.296\sin(t) \\ 0 & 0 & 0 & 0 & 0 \end{bmatrix}, \quad \Delta H_{12} = \Delta H_{23} = \Delta H_{31}. \tag{42}$$

The frequency variation in LSPSwCD is displayed in Figure 8, the control input signal is presented in Figure 9, and tie-line power variation is displayed in Figure 10. We observe the system performance, the transient response makes achievement by the proposed control scheme which reduces the amplitude of over/undershoot percentage. It is

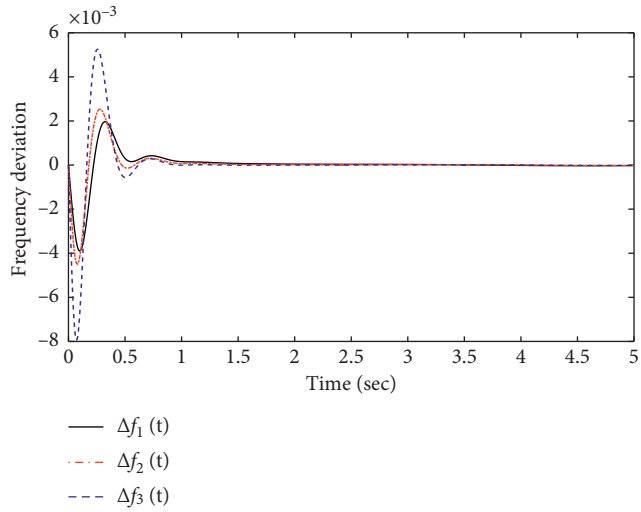

Figure 8: Frequency deviation of the system under mismatched uncertainty.

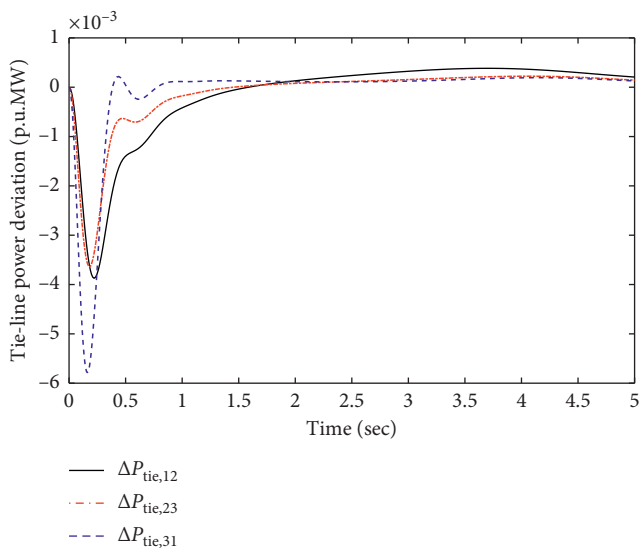

Figure 9: Tie-line deviation of the system under mismatched uncertainty.

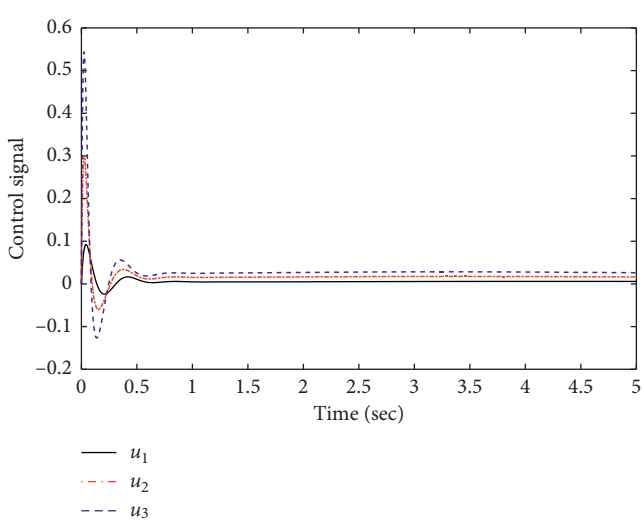

Figure 10: Control signal of the system under mismatched uncertainty.

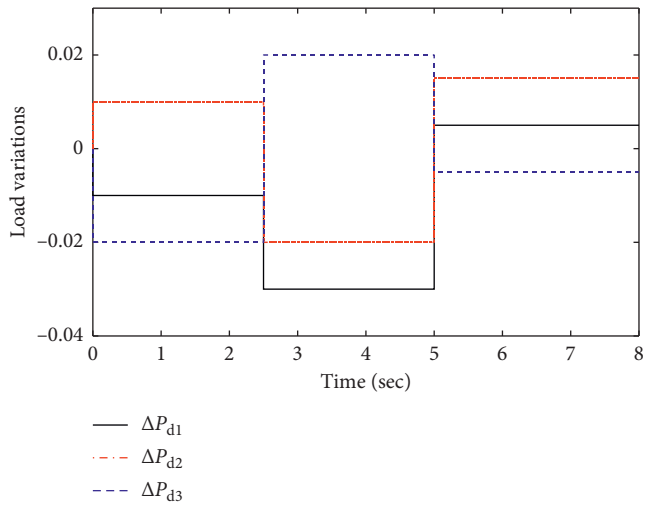

Figure 11: Load variations of three-area power network.

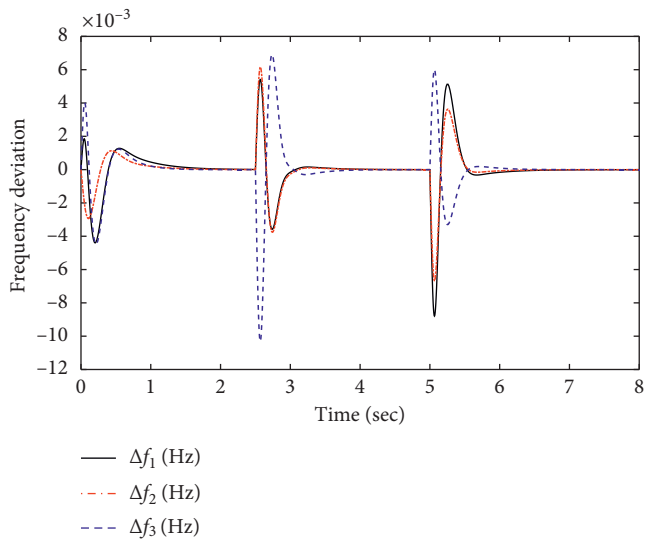

Figure 12: Frequency variation of the system under load variations and mismatched uncertainty.

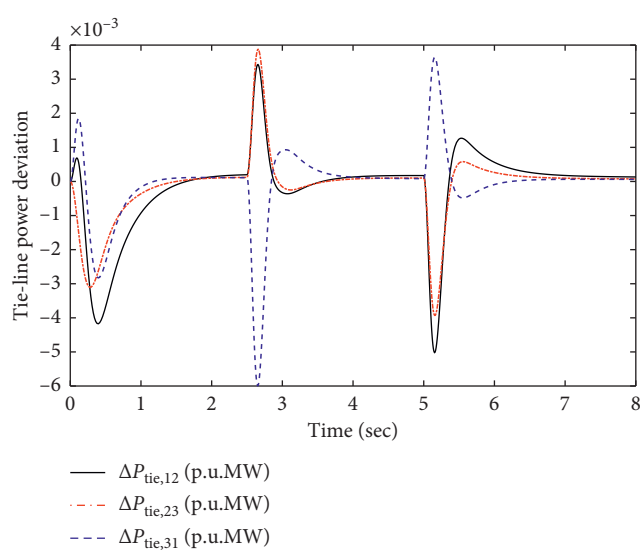

Figure 13: Tie-line power variation of the system under load variations and mismatched uncertainty.

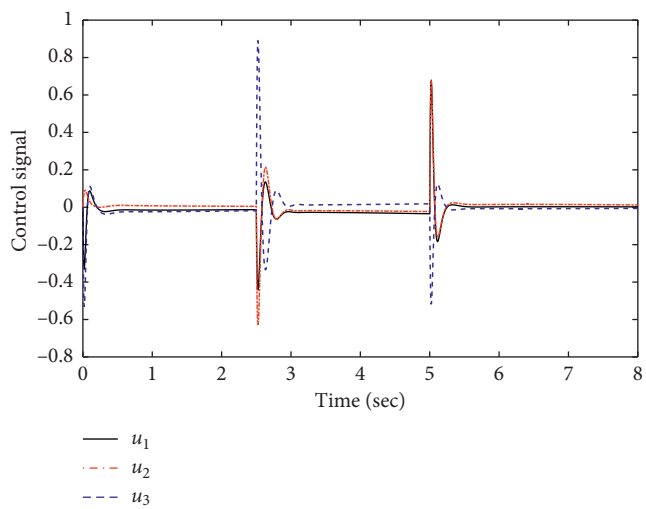

Figure 14: Control signal of the system under load variations and mismatched uncertainty.

to be clear that the input control signal is to converge quickly and drive the tie-line power variation and frequency variation to zero. Therefore, the suggested controller carried out with better design, both in terms of reducing the over/undershoots and minimizing the settling time in comparison to [21, 22].

Remark 6. In this case, though considering to the influence of the mismatched uncertainty of LSPSwCD, the performance of proposed controller still is kept powerful and stable. Therefore, the proposed ISOSMC is proved to be suitable for LSPSwCD. The approach given in [21, 22] cannot be applied for the LSPSwCD of this case.

Case 4. In this case, the nominal parameters of LSPSwCD are in Table 1 and the same parameters with previous cases. However, in the practical power system, the parameters of LSPSwCD are always varied due to different operation conditions. Therefore, the parameters of LSPSwCD are selected to vary by ±20% synchronously from their normal values. The delay time is 0.2 s and load variation is as shown in Figure 11. The tie-line power and frequency deviation decay quickly as observed in Figures 12 and 13. The control signal has been presented in Figure 14. It is to be clear that the proposed control scheme is able to handle with the time-delay and random load disturbances. It is proved that the proposed DAISOSMCL has the good quality and achievement to reject disturbance with small control signal.

Remark 7. In this approach, the structure of LSPSwCD is more general than the approach given in [28–33]. Also, the system responses in terms of convergence of frequency variation and power exchange error are improved by using the proposed DAISOSMCL. Therefore, the proposed design controller is suitable for LFC of LSPSwCD.

5. Conclusions

In this paper, the LFC based on decentralized adaptive integral second-order sliding mode control (DAISOSMC) has been developed for the large-scale power system with communication delays (LSPSwCD), load variations, and parameter uncertainties. It is shown that the proposed DAISOSMCL ensures the finite time reachability of the system states and moreover the dynamics of LSPSwCD in the sliding mode is asymptotically stable under certain conditions. To the best of our knowledge, this is the first time the DAISOSMC approach is designed for LFC of the LSPSwCD. The report of simulation results indicates that the proposed DAISOSMC approach can adequately make less the deviation of the tie-line power and frequency variation of LSPSwCD. The suggested control scheme is therefore proved to be more effective for the LSPSwCD implementation.

Data Availability

Data used to support the findings of this study are included within the article.

Conflicts of Interest

The authors declare no conflicts of interest.

Acknowledgments

This research was funded by the Foundation for Science and Technology Development of Ton Duc Thang University (FOSTECT), website: http://fostect.tdtu.edu.vn, under Grant FOSTECT.2017.BR.05.

References

[1] D. Guha, P. K. Roy, and S. Banerjee, "Load frequency control of interconnected power system using grey wolf

optimization," *Swarm and Evolutionary Computation*, vol. 27, pp. 97–115, 2016.

[2] M. Ma, C. Zhang, X. Liu, and H. Chen, "Distributed model predictive load frequency control of the multi-area power system after deregulation," *IEEE Transactions on Industrial Electronics*, vol. 27, pp. 5129–5139, 2016.

[3] K. Liao and Y. Xu, "A robust load frequency control scheme for power systems based on second-order sliding mode and extended disturbance observer," *IEEE Transactions on Industrial Informatics*, vol. 14, no. 7, pp. 3076–3086, 2017.

[4] K. P. S. Parmar, S. Majhi, and D. P. Kothari, "LFC of an interconnected power system with multi-source power generation in deregulated power environment," *International Journal of Electrical Power & Energy Systems*, vol. 57, pp. 277–286, 2014.

[5] V. Çelik, M. T. Özdemir, and K. Y. Lee, "Effects of fractional-order PI controller on delay margin in single-area delayed load frequency control systems," *Journal of Modern Power Systems and Clean Energy*, vol. 7, no. 2, pp. 380–389, 2019.

[6] R. Dey, S. Ghosh, G. Ray, and A. Rakshit, "H∞ load frequency control of interconnected power systems with communication delays," *International Journal of Electrical Power & Energy Systems*, vol. 42, no. 1, pp. 672–684, 2012.

[7] Y. Cui, G. Shi, L. Xu, X. Zhang, and X. Li, "Decentralized $H\infty$ load frequency control for multi-area power systems with communication uncertainties," *In Advanced Computational Methods in Energy, Power, Electric Vehicles, and Their Integration*, vol. 4, pp. 429–438, 2017.

[8] H. Zhang, J. Liu, and S. Xu, "H-infinity load frequency control of networked power systems via an event-triggered scheme," *IEEE Transactions on Industrial Electronics*, vol. 67, no. 8, pp. 7104–7113, 2019.

[9] S. Prasad, S. Purwar, and N. Kishor, "H -infinity based nonlinear sliding mode controller for frequency regulation in interconnected power systems with constant and time-varying delays," *IET Generation, Transmission & Distribution*, vol. 10, no. 11, pp. 2771–2784, 2016.

[10] M. N. Anwar and S. Pan, "A new PID load frequency controller design method in frequency domain through direct synthesis approach," *International Journal of Electrical Power & Energy Systems*, vol. 67, pp. 560–569, 2015.

[11] S. Sondhi and Y. V. Hote, "Fractional order PID controller for load frequency control," *Energy Conversion and Management*, vol. 85, pp. 343–353, 2014.

[12] S. Saxena and Y. V. Hote, "Decentralized PID load frequency control for perturbed multi-area power systems," *International Journal of Electrical Power & Energy Systems*, vol. 81, pp. 405–415, 2016.

[13] N. Kouba, M. Menaa, K. Tehrani, and M. Boudour, "Optimal tuning for load frequency control using ant lion algorithm in multi-area interconnected power system," *Intelligent Automation & Soft Computing*, vol. 25, no. 2, pp. 279–294, 2019.

[14] H. A. Yousef, K. AL-Kharusi, M. H. Albadi, and N. Hosseinzadeh, "Load frequency control of a multi-area power system: an adaptive fuzzy logic approach," *IEEE Transactions on Power Systems*, vol. 29, no. 4, pp. 1822–1830, 2014.

[15] M. Gheisarnejad and M. H. Khooban, "Design an optimal fuzzy fractional proportional integral derivative controller with derivative filter for load frequency control in power systems," *Transactions of the Institute of Measurement and Control*, vol. 41, no. 9, pp. 2563–2581, 2019.

[16] D. Xu, J. Liu, X. Yan, and W. Yan, "A novel adaptive neural network constrained control for multi-area interconnected power system with hybrid energy storage," *IEEE Transactions on Industrial Electronics*, vol. 65, no. 8, pp. 6625–6634, 2017.

[17] Z. Sun, F. Xing, S. Che, B. Hu, and D. Sun, "Designing and optimization of fuzzy sliding mode controller for nonlinear systems," *Computers, Materials & Continua*, vol. 61, no. 1, pp. 119–128, 2019.

[18] Q. Zhu and Z. Yang, "Intelligent power compensation system based on adaptive sliding mode control using soft computing and automation," *Computer Systems Science and Engineering*, vol. 34, no. 4, pp. 179–189, 2019.

[19] K. Khayati, "Multivariable adaptive sliding-mode observer-based control for mechanical systems," *Canadian Journal of Electrical and Computer Engineering*, vol. 38, no. 3, pp. 253–265, 2015.

[20] D. Qian and G. Fan, "Neural-network-based terminal sliding mode control for frequency stabilization of renewable power systems," *IEEE/CAA Journal of Automatica Sinica*, vol. 5, no. 3, pp. 706–717, 2018.

[21] B. Le Ngoc Minh, V. V. Huynh, T. M. Nguyen, and Y. W. Tsai, "Decentralized adaptive double integral sliding mode controller for multi-area power systems," *Mathematical Problems in Engineering*, vol. 2018, Article ID 2672436, 11 pages, 2018.

[22] M. K. Sarkar, A. Dev, P. Asthana, and D. Narzary, "Chattering free robust adaptive integral higher order sliding mode control for load frequency problems in multi-area power systems," *IET Control Theory & Applications*, vol. 12, no. 9, pp. 1216–1227, 2018.

[23] S. Prasad, S. Purwar, and N. Kishor, "Non-linear sliding mode load frequency control in multi-area power system," *Control Engineering Practice*, vol. 61, pp. 81–92, 2017.

[24] D. Qian, S. Tong, and X. Liu, "Load frequency control for micro hydro power plants by sliding mode and model order reduction," *Automatika*, vol. 56, no. 3, pp. 318–330, 2015.

[25] J. Guo, "Application of full order sliding mode control based on different areas power system with load frequency control," *ISA Transactions*, vol. 92, pp. 23–34, 2019.

[26] J. Guo, "Application of a novel adaptive sliding mode control method to the load frequency control," *European Journal of Control*, vol. 12, pp. 3050–3071, 2020.

[27] Y. Mi, Y. Fu, C. Wang, and P. Wang, "Decentralized sliding mode load frequency control for multi-area power systems," *IEEE Transactions on Power Systems*, vol. 28, no. 4, pp. 4301–4309, 2013.

[28] S. K. Pradhan and D. K. Das, "H∞ Load frequency control design based on delay discretization approach for interconnected power systems with time delay," *Journal of Modern Power Systems and Clean Energy*, vol. 2, pp. 1–10, 2020.

[29] C. Fu and W. Tan, "Decentralized load frequency control for power systems with communication delays via active disturbance rejection," *IET Generation, Transmission & Distribution*, vol. 12, no. 6, pp. 1397–1403, 2017.

[30] C. Fu, C. Wang, L. Y. Wang, and D. Shi, "An alternative method for mitigating impacts of communication delay on load frequency control," *International Journal of Electrical Power & Energy Systems*, vol. 119, Article ID 105924, 2020.

[31] A. E. Onyeka, Y. Xing-Gang, Z. Mao, B. Jiang, and Q. Zhang, "Robust decentralized load frequency control for interconnected time delay power systems using sliding mode techniques," *IET Control Theory and Applications*, vol. 14, no. 3, pp. 470–480, 2019.

[32] Y. Sun, Y. Wang, Z. Wei, G. Sun, and X. Wu, "Robust H∞ load frequency control of multi-area power system with time delay: a sliding mode control approach," *IEEE/CAA Journal of Automatica Sinica*, vol. 5, no. 2, pp. 610–617, 2017.

[33] Y. Mi, X. Hao, Y. Liu et al., "Sliding mode load frequency control for multi-area time-delay power system with wind power integration," *IET Generation, Transmission & Distribution, Transmission & Distribution*, vol. 11, no. 18, pp. 4644–4653, 2017.

[34] S. Boyd, E. L. Ghaoui, E. Feron, and V. Balakrishna, "Linear matrix inequalities in system and control theory," *Society for Industrial and Applied Mathematics*, vol. 15, 1994.

[35] V. V. Huynh, Y.-W. Tsai, and P. V. Duc, "Adaptive output feedback sliding mode control for complex interconnected time-delay systems," *Mathematical Problems in Engineering*, vol. 2015, Article ID 239584, 15 pages, 2015.

[36] X.-G. Yan, S. K. Spurgeon, and C. Edwards, "Global decentralised static output feedback sliding-mode control for interconnected time-delay systems," *IET Control Theory & Applications*, vol. 6, no. 2, pp. 192–202, 2012.

Hindawi
Complexity
Volume 2021, Article ID 6672812, 13 pages
https://doi.org/10.1155/2021/6672812

Research Article

A Robust Fault-Tolerant Control for Quadrotor Helicopters against Sensor Faults and External Disturbances

Ban Wang,[1] **Peng Huang**,[2] **and Wei Zhang**[1]

[1]*School of Aeronautics, Northwestern Polytechnical University, Xi'an, Shaanxi 710072, China*
[2]*Chinese Flight Test Establishment, Xi'an, Shaanxi 710089, China*

Correspondence should be addressed to Ban Wang; wangban@nwpu.edu.cn

Received 2 January 2021; Revised 2 February 2021; Accepted 6 March 2021; Published 20 March 2021

Academic Editor: Jing Na

This paper presents an active fault-tolerant control strategy for quadrotor helicopters to simultaneously accommodate sensor faults and external disturbances. Unlike most of the existing fault diagnosis and fault-tolerant control schemes for quadrotor helicopters, the proposed fault diagnosis scheme is able to estimate sensor faults while eliminating the effect of external disturbances. Moreover, the proposed fault-tolerant control scheme is capable to eliminate the adverse effect of external disturbances as well by designing a disturbance observer to effectively estimate the unknown external disturbances and integrating with the designed integral sliding-mode controller. In this case, the continuous operation of the quadrotor helicopter is ensured while avoiding the unexpected control chattering. In addition, the stability of the closed-loop system is theoretically proved. Finally, the effectiveness and advantages of the proposed scheme are validated and demonstrated through comparative numerical simulations of the quadrotor helicopter under different faulty and uncertain scenarios.

1. Introduction

Unmanned quadrotor helicopters have recently been widely used by commercial industries and academic communities due to their vertical take-off and landing capability, low cost, and great maneuverability. In order to allow the aircraft to track desired orientation commands, while preventing it from flipping over and crashing, the quadrotor attitude control system is becoming more and more sophisticated with increasing requirements for high performance and reliability. Many control approaches have been proposed for tracking control of quadrotor helicopters [1–3]. However, most of the aforementioned literatures did not take potential faults in the system into account. Sensors are identified as the weak link in aerospace engineering systems based on being more vulnerable to damage or being more sensitive in construction than other components [4, 5]. A fault in an attitude sensor can be regarded as an unexpected change of sensor operation affecting the sensor output [6, 7]. In the case of sensor faults, measurements of state variables and other quantities of interests may no longer be reliable which may degrade quadrotor flight performance or even cause a catastrophic accident. Thus, the faulty measurements cannot be used for output or state feedback control directly without any correction algorithms. To meet the stringent demands of system reliability, physical redundancy in the form of identical sensors or multiple types of sensors is often configured [8]. Nevertheless, redundant sensors are not always feasible due to the constraints of cost, weight, and complexity, especially for small-size unmanned aerial vehicles (UAVs). In this case, analytical redundancy constituted by the knowledge of the considered system becomes a viable supplement. In the study by Zhong et al. [9], a two-stage extended Kalman filter is developed for detecting, isolating, and identifying inertial measurement unit (IMU) sensor faults of an unmanned quadrotor helicopter, while mitigating the impact of model uncertainties. In the study by Matus-Vargas et al. [10], a fault-tolerant control scheme for a multirotor with altitude sensor faults caused by the ground effect is presented and validated by simulations and experiments. In the study by Zhang and Xiao [11], a sliding mode observer with the adaptive regulation law is proposed

for multiple sensor fault detection and reconstruction without knowing the upper bound of the unknown faults. In the study by Tan et al. [12], a sliding mode control combined with the RBF neural network is designed to deal with the failures of the sensor and actuator. Considerable research results have been reported on sensor fault diagnosis. A fault diagnosis system normally performs three major tasks: fault detection, fault isolation, and fault estimation. Among various types of fault diagnosis approaches that have been developed, sliding mode observer-based fault diagnosis has been proven to be an effective way to detect, isolate, and estimate faults for many systems due to the inherent robustness of sliding mode algorithms to unknown modeling uncertainties and disturbances [13–15]. In the study by Patton et al. [13], the derivative of the considered sensor fault is assumed to be zero, and the concept of equivalent output injection is employed to reconstruct the fault. Then, in the study by Tan and Edwards [14], the assumption of constant sensor fault is relaxed to a more general case but it assumes that the considered system needs to be open-loop stable. In the study by Alwi et al. [15], the proposed scheme overcomes the limitation that the open-loop system is required to be stable and is capable to estimate incipient sensor faults. Note that, the aforementioned research only deals with the diagnosis of sensor faults. From the control point of view, after fault occurrence, whether the fault can be compensated and the system can maintain its original tracking performance are of importance. In other words, the integrated design of the controller and fault diagnosis scheme needs to be further investigated. The stability of the closed-loop system with reconstructed measurements needs to be proved. Therefore, with application to quadrotor helicopters, the fault diagnosis and fault-tolerant control for quadrotor helicopters has been an important research topic in recent years with the growing demands for safety, reliability, and maintainability [16–18]. The timely diagnosis and correction of faults in a quadrotor system are critical in avoiding abnormal system performance and reducing the unexpected accidents significantly.

During the last decade, various fault diagnosis approaches have been proposed with the advances in control theory [19–23]. Most of the proposed diagnosis systems contain only fault detection and isolation (FDI), which cannot provide more comprehensive information of the corresponding fault, such as magnitude of the fault. Fault estimation, which is also referred to as fault identification, can provide the estimated magnitude of the fault. It plays an important role in active fault-tolerant control (AFTC) since it can provide the required fault information to reconfigure the controller. In [24, 25], nonlinear adaptive estimation methods are presented to detect, isolate, and estimate sensor bias faults in accelerometer and gyroscope measurements of a quadrotor helicopter. In the study by Zhong et al. [26], an adaptive two-stage extended Kalman filter is proposed for sensor fault detection and diagnosis of a quadrotor helicopter based on its kinematic model. Nonetheless, fault diagnosis is a very important procedure, and it is not sufficient to ensure safe operation of the quadrotor helicopter. For safety-critical systems, the diagnosis of a particular system fault is not the ultimate goal, whereas the continuity of operation is a key feature, and the closed-loop system should be capable of maintaining its prespecified performance in terms of quality, safety, and stability despite the presence of faults [27]. This calls for the appearance of FTC systems.

In the context of FTC for quadrotor helicopters, most of the research works in the literature focus on actuator faults [28–32]. Research on sensor FTC for quadrotor helicopters is very limited compared to the sensor fault diagnosis system and actuator FTC system [33, 34]. In the study by Zhang et al. [33], a tracking controller and a sensor fault detection and isolation scheme were separately developed for a quadrotor helicopter. The proposed fault diagnosis system can only detect and isolate sensor faults and is not integrated with the designed controller to accommodate faults in an active fashion. In the study by Qin et al. [34], a fault diagnosis unit is designed to estimate sensor faults and synthesized with a two-level PID controller to constitute an active FTC scheme for a quadrotor helicopter. However, the proposed scheme in [34] is based on a linear model of the quadrotor helicopter. In practical situations, the existence of system parameter variations, nonlinearity, and disturbances can make the model-based fault diagnosis and FTC system ineffective. Consequently, it is vital to take robustness into consideration, while designing model-based fault diagnosis and FTC systems.

In an attempt to solve the aforementioned difficulties for improving system robustness, this paper presents a novel observer-based fault diagnosis and FTC scheme for quadrotor helicopters against sensor faults and disturbances. The main contributions of this paper are summarized as follows:

(1) In the face of sensor faults and external disturbances, an active FTC scheme is proposed to simultaneously accommodate them in terms of both fault diagnosis and fault-tolerant control based on integral sliding-mode control, sliding mode observer, and disturbance observer.

(2) Unlike most of the existing fault diagnosis schemes for quadrotor helicopters, the proposed fault diagnosis scheme is able to estimate sensor faults, while eliminating the effect of external disturbances.

(3) A disturbance observer is constructed to estimate the lumped disturbances and integrated with the designed sliding-mode controller, which can help to avoid the unexpected control chattering. The stability of the closed-loop system is theoretically proved.

The rest of this paper is arranged as follows. The dynamic model of the studied quadrotor helicopter and problem statement are presented in Section 2. The detailed design procedures of the proposed fault diagnosis and FTC scheme are described in Section 3. Then, the numerical simulation results are demonstrated in Section 4 to validate the effectiveness of the proposed scheme. Finally, general conclusions of this paper are summarized in Section 5.

2. Quadrotor Model and Problem Statement

2.1. Quadrotor Model Description. The studied quadrotor helicopter is an underactuated system with six degrees of freedom driven by four motors mounted in a cross configuration, as shown in Figure 1. The voltage inputs imposed on the motors drive the corresponding propellers to generate forces and torques. Each pair of the opposite propellers turns the same way, i.e., the front and rear propellers rotate clockwise and the left and right ones spin counterclockwise. In order to facilitate the modeling of the quadrotor helicopter, two coordinate systems are employed: the earth-fixed frame $\{E\}$ and the body-fixed frame $\{B\}$. The origin of the earth-fixed frame is attached on the ground, while the origin of the body-fixed frame is coincident with the center of gravity of the studied quadrotor helicopter. The axes of the earth-fixed frame are denoted as (o_e, x_e, y_e, z_e), and the axes of the body-fixed frame are denoted as (o_b, x_b, y_b, z_b).

Considering the attitude control of the quadrotor helicopter, by employing the Newton–Euler formulation, the dynamic model of the quadrotor helicopter can be expressed as follows:

$$\tau^B = J\dot{\omega}^B + \omega^B \times J\omega^B, \tag{1}$$

where $\tau^B = [\tau_x, \tau_y, \tau_z]^T$ is the resultant torque vector and $\omega^B = [p, q, r]^T$ is the angular velocity vector with respect to the body-fixed frame, respectively, and $J = \mathrm{diag}([J_x, J_y, J_z]) = \mathrm{diag}([0.03, 0.03, 0.04])\,\mathrm{kg{\cdot}m^2}$ is a diagonal matrix that stands for the moments of inertia of three axes of the studied quadrotor helicopter with the assumption that the axes of the body-fixed frame are coincident with the principal axes of inertia of the studied quadrotor helicopter.

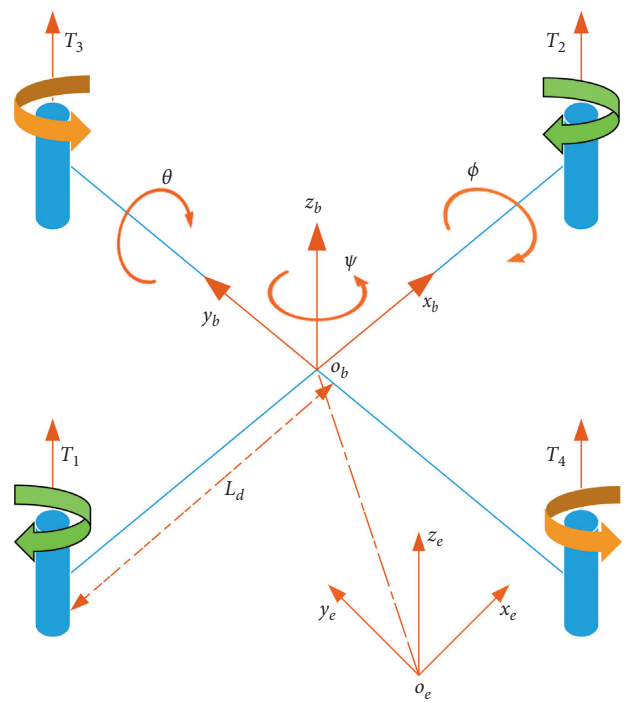

Figure 1: The configuration of the studied quadrotor helicopter.

The corresponding torques imposed on the quadrotor helicopter consist of the propeller-generated torque, the gyroscopic torque, and the rotational motion-induced torque, which can be described as

$$\tau^B = \begin{bmatrix} 0 & 0 & K_u L_d & -K_u L_d \\ K_u L_d & -K_u L_d & 0 & 0 \\ K_y & K_y & -K_y & -K_y \end{bmatrix} \begin{bmatrix} u_1 \\ u_2 \\ u_3 \\ u_4 \end{bmatrix} - \sum_{i=1}^{4} I_r \left(\omega^B \times \begin{bmatrix} 0 \\ 0 \\ 1 \end{bmatrix} \right) (-1)^{i+1} \Omega_i + \begin{bmatrix} -k_{d1}\dot{\phi} \\ -k_{d2}\dot{\theta} \\ -k_{d3}\dot{\psi} \end{bmatrix}, \tag{2}$$

where ϕ, θ, and ψ is the roll, pitch, and yaw angle of the quadrotor helicopter defined in the earth-fixed frame, respectively, I_r is the inertial moment of the propeller, Ω_i $(i = 1, 2, \ldots, 4)$ is the ith propeller's rotational speed, k_{di} $(i = 1, 2, \ldots, 4)$ is the drag coefficient, and u_i $(i = 1, 2, \ldots, 4)$ is the pulse width modulation (PWM) input of the ith motor, and the control input signals are within the range $[0.05, 0.1]$. A command of 0.05 corresponds to zero throttle, which will cause the motors to stop, and a command of 0.1 corresponds to full throttle. $K_u = 120\mathrm{N}$ is a positive gain related to propeller-generated force, $K_y = 4\mathrm{N\,m}$ is a positive gain related to propeller-generated torque, and $L_d = 0.2\,\mathrm{m}$ is the distance between the motor and the center of gravity of the quadrotor helicopter.

Then, by substituting (2) into (1), it leads to

$$\begin{cases} \dot{p} = \dfrac{J_y - J_z}{J_x} qr + \dfrac{u_\phi}{J_x} - I_r \dot{\theta}\Omega - k_{d1}\dot{\phi}, \\ \dot{q} = \dfrac{J_z - J_x}{J_y} pr + \dfrac{u_\theta}{J_y} + I_r \dot{\phi}\Omega - k_{d2}\dot{\theta}, \\ \dot{r} = \dfrac{J_x - J_y}{J_z} pq + \dfrac{u_\psi}{J_z} - k_{d3}\dot{\psi}, \end{cases} \tag{3}$$

where $u_\phi = K_u L_d (u_3 - u_4)$, $u_\theta = K_u\, L_d (u_1 - u_2)$, and $u_\psi = K_y (u_1 + u_2 - u_3 - u_4)$.

The kinematic differential equation of the quadrotor helicopter can be described as

$$\begin{bmatrix} \dot{\phi} \\ \dot{\theta} \\ \dot{\psi} \end{bmatrix} = \begin{bmatrix} 1 & \sin\phi\tan\theta & \cos\phi\tan\theta \\ 0 & \cos\phi & -\sin\phi \\ 0 & \sin\phi\sec\theta & \cos\phi\sec\theta \end{bmatrix} \begin{bmatrix} p \\ q \\ r \end{bmatrix}. \tag{4}$$

Assuming that the changes of roll and pitch angles are small, the transformation matrix between the angular velocities and the Euler angle rates is close to an identity matrix. Thus, the nonlinear system in (4) is linearized as

$$\begin{cases} \dot{\phi} = p, \\ \dot{\theta} = q, \\ \dot{\psi} = r. \end{cases} \tag{5}$$

To facilitate the subsequent design procedures, (3) and (5) are simplified as the following nonlinear affine system:

$$\begin{cases} \dot{x} = Ax + Df(x) + Bu + W\Delta_d, \\ y = Cx + Ff_s, \end{cases} \tag{6}$$

where $x \in \mathbb{R}^n = [\phi, \theta, \psi, p, q, r]^T$, $y \in \mathbb{R}^p = [\phi, \theta, \psi]^T$, $u \in \mathbb{R}^m = [u_\phi, u_\theta, u_\psi]^T$, $f(x) \in \mathbb{R}^s = [qr, pr, pq]^T$, $\Delta_d \in \mathbb{R}^r$, r represents the lumped model uncertainties and external disturbances, which are assumed to be unknown but bounded, and $f_s \in \mathbb{R}^q$ is an unknown vector which represents an additive bias resulting from sensor faults.

According to the above definitions, the known constant matrices in (6) can be described as

$$A = \begin{bmatrix} 0 & 0 & 0 & 1 & 0 & 0 \\ 0 & 0 & 0 & 0 & 1 & 0 \\ 0 & 0 & 0 & 0 & 0 & 1 \\ 0 & 0 & 0 & 0 & 0 & 0 \\ 0 & 0 & 0 & 0 & 0 & 0 \\ 0 & 0 & 0 & 0 & 0 & 0 \end{bmatrix},$$

$$B = \begin{bmatrix} 0 & 0 & 0 \\ 0 & 0 & 0 \\ 0 & 0 & 0 \\ J_x^{-1} & 0 & 0 \\ 0 & J_y^{-1} & 0 \\ 0 & 0 & J_z^{-1} \end{bmatrix},$$

$$D = \begin{bmatrix} 0 & 0 & 0 \\ 0 & 0 & 0 \\ 0 & 0 & 0 \\ \dfrac{J_y - J_z}{J_x} & 0 & 0 \\ 0 & \dfrac{J_z - J_x}{J_y} & 0 \\ 0 & 0 & \dfrac{J_x - J_y}{J_z} \end{bmatrix}, \tag{7}$$

$$C = \begin{bmatrix} 1 & 0 & 0 & 0 & 0 & 0 \\ 0 & 1 & 0 & 0 & 0 & 0 \\ 0 & 0 & 1 & 0 & 0 & 0 \end{bmatrix}.$$

3. Active Fault-Tolerant Control Strategy

3.1. Overview of the Proposed AFTC Scheme. A general structure of the developed AFTC scheme against sensor faults and disturbances is illustrated in Figure 2. The overall control system is constructed by a sensor fault diagnosis unit and a disturbance observer-based sliding-mode controller. The real-time information about sensor faults is provided by the fault diagnosis unit. Subsequently, the disturbance observer-based sliding-mode controller is proposed and integrated with the fault diagnosis unit to drive the quadrotor helicopter track the reference signals in the presence of sensor faults and disturbances.

3.2. Sensor Fault Diagnosis

Assumption 1. rank(CW) = rank(W).

Assumption 2. The nonlinear term $f(x)$ is assumed to be known and Lipschitz about x uniformly, i.e., $\forall x_1, x_2 \in \mathbb{R}^n$,

$$\|f(x_1) - f(x_2)\| \le \|\mathscr{L}_f x_1 - x_2\|, \tag{8}$$

where $\mathscr{L}_f$ is the Lipschitz constant and is assumed to be unknown.

Assumption 3. The considered sensor faults f_s and their derivatives $\dot{f}_s$ are bounded and defined by

$$\varepsilon_s = \sup_{t>0}\|f_s\|, \text{ and } \varepsilon_{ss} = \sup_{t>0}\|\dot{f}_s\|. \tag{9}$$

Lemma 1. *Under Assumption 1, there exist linear transformations of state and output:*

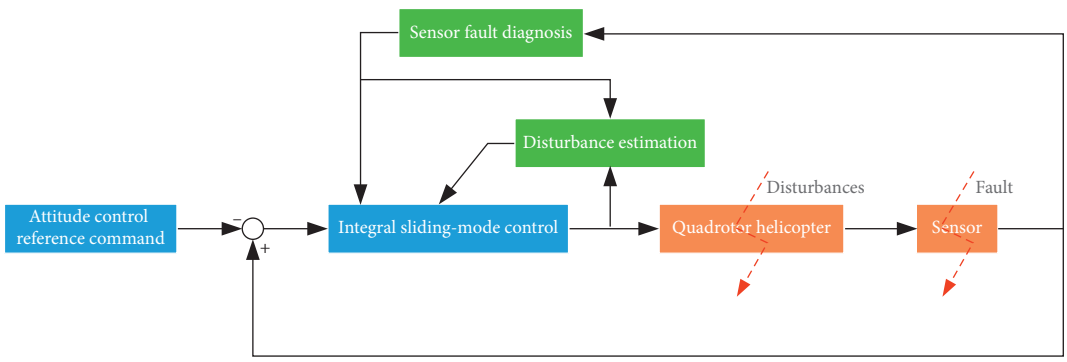

Figure 2: The schematic of the proposed AFTC strategy in the presence of sensor faults and external disturbances.

$$z = Tx = \begin{bmatrix} z_1 \\ z_2 \end{bmatrix}, \quad h = Sy = \begin{bmatrix} h_1 \\ h_2 \end{bmatrix}, \tag{10}$$

such that the system matrices become

$$\begin{aligned} \mathrm{TAT}^{-1} &= \begin{bmatrix} A_1 & A_2 \\ A_3 & A_4 \end{bmatrix}, \\ \mathrm{TB} &= \begin{bmatrix} B_1 \\ B_2 \end{bmatrix}, \\ \mathrm{TD} &= \begin{bmatrix} D_1 \\ D_2 \end{bmatrix}, \\ \mathrm{SCT}^{-1} &= \begin{bmatrix} C_1 & 0 \\ 0 & C_4 \end{bmatrix}, \\ \mathrm{SF} &= \begin{bmatrix} 0 \\ F_2 \end{bmatrix}, \\ \mathrm{TW} &= \begin{bmatrix} W_1 \\ 0 \end{bmatrix}, \end{aligned} \tag{11}$$

where $T \in \mathbb{R}^{n\times n}$, $S \in \mathbb{R}^{p\times p}$, $z_1 \in \mathbb{R}^r$, $z_2 \in \mathbb{R}^{n-r}$, $h_1 \in \mathbb{R}^r$, $h_2 \in \mathbb{R}^{p-r}$, $A_1 \in \mathbb{R}^{r\times r}$, $A_4 \in \mathbb{R}^{(n-r)\times(n-r)}$, $B_1 \in \mathbb{R}^{r\times m}$, $D_1 \in \mathbb{R}^{r\times s}$, $C_1 \in \mathbb{R}^{r\times r}$, $C_4 \in \mathbb{R}^{(p-r)\times(n-r)}$, $F_2 \in \mathbb{R}^{(p-r)\times q}$, *and* $W_1 \in \mathbb{R}^{r\times r}$.

By applying both transformation matrices T and S, original system (6) can be converted into the following two subsystems as

$$\begin{cases} \dot{z}_1 = A_1 z_1 + A_2 z_2 + D_1 f\left(T^{-1} z\right) + B_1 u + W_1 \Delta_d, \\ h_1 = C_1 z_1, \end{cases} \tag{12}$$

$$\begin{cases} \dot{z}_2 = A_3 z_1 + A_4 z_2 + D_2 f\left(T^{-1} z\right) + B_2 u, \\ h_2 = C_4 z_2 + F_2 f_s. \end{cases} \tag{13}$$

After coordinate transformations, one can observe that subsystem (12) is only sensitive to lumped disturbances, and subsystem (13) is free from lumped disturbances but subject to sensor faults. In order to estimate f_s, the sensor faults in (13) are treated as actuator faults by defining a new state $z_3 = \int_0^t h_2(\tau)\mathrm{d}\tau$. In this case, an augmented system with the state vector $\overline{z} = [z_2, z_3]^T$ can be given as

$$\begin{cases} \dot{\overline{z}} = \overline{A}\overline{z} + \overline{A}_3 z_1 + \overline{D}_2 f\left(T^{-1} z\right) + \overline{B} u + \overline{F} f_s, \\ h_3 = \overline{C}\overline{z}, \end{cases} \tag{14}$$

where $\overline{z} \in \mathbb{R}^{n+p-2r}$, $h_3 = z_3 \in \mathbb{R}^{p-r}$, $\overline{A} = \begin{bmatrix} A_4 & 0 \\ C_4 & 0 \end{bmatrix} \in \mathbb{R}^{(n+p-2r)\times(n+p-2r)}$, $\overline{A}_3 = \begin{bmatrix} A_3 \\ 0 \end{bmatrix} \in \mathbb{R}^{(n+p-2r)\times r}$, $\overline{D}_2 = \begin{bmatrix} D_2 \\ 0 \end{bmatrix} \in \mathbb{R}^{(n+p-2r)\times s}$, $\overline{B} = \begin{bmatrix} B_2 \\ 0 \end{bmatrix} \in \mathbb{R}^{(n+p-2r)\times m}$, $\overline{F} = \begin{bmatrix} 0 \\ F_2 \end{bmatrix} \in \mathbb{R}^{(n+p-2r)\times q}$, and $\overline{C} = \begin{bmatrix} 0 & I_{p-r} \end{bmatrix} \in \mathbb{R}^{(p-r)\times(n+p-2r)}$.

Moreover, since z_2 is used in subsystem (12), with the new state vector $\overline{z}$, subsystem (12) can be accordingly rewritten as

$$\begin{cases} \dot{z}_1 = A_1 z_1 + \overline{A}_2 \overline{z} + D_1 f\left(T^{-1} z\right) + B_1 u + W_1 \Delta_d, \\ h_1 = C_1 z_1, \end{cases} \tag{15}$$

where $\overline{A}_2 = \begin{bmatrix} A_2 & 0 \end{bmatrix} \in \mathbb{R}^{r\times(n+p-2r)}$.

Therefore, for subsystems (15) and (14), two sliding mode observers are designed as follows:

$$\begin{cases} \dot{\hat{z}}_1 = A_1 \hat{z}_1 + \overline{A}_2 \hat{\overline{z}} + B_1 u + \frac{1}{2}\hat{k}_1 P_1 C_1^{-1}\left(h_1 - \hat{h}_1\right) + D_1 f\left(T^{-1}\hat{z}\right) + \left(A_1 - A_1^s\right) C_1^{-1}\left(h_1 - \hat{h}_1\right) + v_1, \\ \hat{h}_1 = C_1 \hat{z}_1, \end{cases} \tag{16}$$

$$\begin{cases} \dot{\hat{z}} = \overline{A}\hat{z} + \overline{A}_3 C_1^{-1} h_1 + \overline{D}_2 f\left(T^{-1}\hat{z}\right) + \overline{B}u + \overline{L}\left(h_3 - \hat{h}_3\right) + \frac{1}{2}\hat{k}_2 \overline{D}_2 \overline{H}\left(h_3 - \hat{h}_3\right) + \overline{F}v_2, \\ \hat{h}_3 = \overline{C}\hat{z}, \end{cases} \tag{17}$$

where $\hat{z} = [(C_1^{-1}S_1 y)^T, ([I_{n-r}0]\hat{z})^T]^T$, $A_1^s \in \mathbb{R}^{r\times r}$ is a stable matrix that needs to be determined, P_1 is the Lyapunov matrix of A_1^s, $\overline{L} = [\overline{L}_1 \overline{L}_2]^T \in \mathbb{R}^{(n+p-2r)\times(p-r)}$ is the observer gain matrix with $\overline{L}_1 \in \mathbb{R}^{(n-r)\times(p-r)}$, and $\overline{H} \in \mathbb{R}^{j\times(p-r)}$.

The discontinuous output error injection term v_1, which is used to eliminate the effects of disturbances on state estimation, is designed as

$$v_1 = \begin{cases} \left(\|W_1\|\xi + \epsilon_1\right)\dfrac{P_1\left(C_1^{-1}h_1 - \hat{z}_1\right)}{\left\|P_1\left(C_1^{-1}h_1 - \hat{z}_1\right)\right\|}, & \text{if } C_1^{-1}h_1 \neq \hat{z}_1, \\ 0, & \text{otherwise}, \end{cases} \tag{18}$$

where ϵ_1 is a positive scalar to be determined.

Similarly, the discontinuous output error injection term v_2 can be designed as

$$v_2 = \begin{cases} \left(\epsilon_s + \epsilon_2\right)\dfrac{F_0\left(h_3 - \hat{h}_3\right)}{\left\|F_0\left(h_3 - \hat{h}_3\right)\right\|}, & \text{if } h_3 \neq \hat{h}_3, \\ 0, & \text{otherwise}, \end{cases} \tag{19}$$

where $F_0 \in \mathbb{R}^{q\times(p-r)}$ is a matrix and ϵ_2 is a positive scalar that needs to be determined.

In addition, $\hat{k}_1$ and $\hat{k}_2$ are determined by the following adaptation laws as

$$\dot{\hat{k}}_1 = l_{k_1} P_1\left(C_1^{-1}h_1 - \hat{z}_1\right)^2, \tag{20}$$

$$\dot{\hat{k}}_2 = l_{k_2} \overline{H}\left(h_3 - \hat{h}_3\right)^2, \tag{21}$$

where l_{k_1} and l_{k_2} are positive constants.

Then, by defining the state estimation errors as $\tilde{z}_1 = z_1 - \hat{z}_1$ and $\tilde{\overline{z}} = \overline{z} - \hat{\overline{z}}$, the corresponding sliding surface can be constructed as

$$\sigma = \left\{\left(\tilde{z}_1, \tilde{\overline{z}}\right): \tilde{z}_1 = 0, C\tilde{\overline{z}} = 0\right\}. \tag{22}$$

Accordingly, the state estimation error dynamics can be obtained as follows:

$$\dot{\tilde{z}}_1 = A_1^s \tilde{z}_1 + \overline{A}_2 \tilde{\overline{z}} + D_1\left(f\left(T^{-1}z\right) - f\left(T^{-1}\hat{z}\right)\right) - \frac{1}{2}\hat{k}_1 P_1 \tilde{z}_1 + W_1\Delta_d - v_1, \tag{23}$$

$$\dot{\tilde{\overline{z}}} = (\overline{A} - \overline{LC})\tilde{\overline{z}} + \overline{D}_2\left(f\left(T^{-1}z\right) - f\left(T^{-1}\hat{z}\right)'\right) - \frac{1}{2}\hat{k}_2 \overline{D}_2 \overline{HC}\tilde{\overline{z}} + \overline{F}\left(f_s - v_2\right). \tag{24}$$

Considering the fact that, after reaching the constructed sliding surface, the desired sliding motion needs to be maintained thereafter, namely, $\overline{C}\tilde{\overline{z}} = 0$, which results in that

$$\overline{C}(\overline{A} - \overline{LC})\tilde{\overline{z}} + \overline{CD}_2\left(f\left(T^{-1}z\right) - f\left(T^{-1}\hat{z}\right)\right) - \frac{1}{2}\hat{k}_2 \overline{CD}_2 \overline{HC}\tilde{\overline{z}} + \overline{CF}\left(f_s - v_{2eq}\right) = 0, \tag{25}$$

where v_{2eq} denotes the equivalent output error injection signal, which can be approximated as

$$v_{2eq} = \left(\epsilon_s + \epsilon_2\right)\frac{F_0\left(h_3 - \hat{h}_3\right)}{\left\|F_0\left(h_3 - \hat{h}_3\right)\right\| + \delta}, \tag{26}$$

with δ representing a small positive scalar for reducing the chattering effect.

In this sense, according to (25), the sensor fault can be approximated as

$$\hat{f}_s \approx \left(\epsilon_s + \epsilon_2\right)\frac{F_0\left(h_3 - \hat{h}_3\right)}{\left\|F_0\left(h_3 - \hat{h}_3\right)\right\| + \delta}. \tag{27}$$

Theorem 1. *Given a nonlinear affine system (6) with Assumptions 1–3 and the proposed observers (16) and (17), by employing adaptation schemes (20) and (21), state estimation error dynamics (23) and (24) can be driven to the defined sliding surface given by (22) if the gains ϵ_1 and ϵ_2 satisfy that*

$$\epsilon_1 \geq \|\overline{A}_2\|\|\tilde{\bar{z}}\| + \mathscr{L}_f\|T^{-1}\|D_1\|\tilde{z}\| + \eta_1, \tag{28}$$

$$\epsilon_2 \geq \mathscr{L}_f\|T^{-1}\|\overline{D}_2\frac{\|\tilde{z}\|}{\|\overline{F}\|} + \eta_2, \tag{29}$$

where η_1 and η_2 are positive scalars.

Proof of Theorem 1. Consider the following Lyapunov candidate functions:

$$\begin{aligned} V_1 &= \tilde{z}_1^T P_1 \tilde{z}_1, \\ V_2 &= \tilde{z}^T \overline{P}\tilde{z}. \end{aligned} \tag{30}$$

Then, by substituting equations (23) and (24), the time derivative of V_1 and V_2 can be, respectively, calculated as

$$\dot{V}_1 = \tilde{z}_1^T\left(A_1^{sT}P_1 + P_1A_1^s\right)\tilde{z}_1 + 2\tilde{z}_1^T P_1\overline{A}_2\tilde{\bar{z}} + 2\tilde{z}_1^T P_1 W_1\Delta_d - \hat{k}_1\|P_1\tilde{z}_1^2\| + 2\tilde{z}_1^T P_1 D_1\left(f\left(T^{-1}z\right) - f\left(T^{-1}\hat{z}\right)\right) - 2\tilde{z}_1^T P_1 v_1, \tag{31}$$

$$\dot{V}_2 = \tilde{z}^T\left((\overline{A} - \overline{LC})^T\overline{P} + \overline{P}(\overline{A} - \overline{LC})\right)^{\underline{L}} - \hat{k}_2\tilde{z}^T\overline{PD}_2\overline{HC\tilde{z}} + 2\tilde{z}^T\overline{PD}_2\left(f\left(T^{-1}z\right) - f\left(T^{-1}\hat{z}\right)\right) + 2\tilde{z}^T\overline{PF}\left(f_s - v_2\right). \tag{32}$$

Since $P_1 = P_1{}^T > 0$ and $A_1^s < 0$, (31) and (32) can be rewritten as follows:

$$\begin{aligned} \dot{V}_1 &\leq 2\tilde{z}_1^T P_1\overline{A}_2\tilde{\bar{z}} + 2\tilde{z}_1^T P_1 D_1\left(f\left(T^{-1}z\right) - f\left(T^{-1}\hat{z}\right)\right) + 2\tilde{z}_1^T P_1 W_1\Delta_d - 2\tilde{z}_1^T P_1 v_1 \\ &= 2\tilde{z}_1^T P_1\left(\overline{A}_2\tilde{\bar{z}} + D_1\left(f\left(T^{-1}z\right) - f\left(T^{-1}\hat{z}\right)\right) + W_1\Delta_d - v_1\right) \leq 2P_1\tilde{z}_1\left(\overline{A}_2\|\tilde{z}\| + \mathscr{L}_f T^{-1}D_1\|\tilde{z}\| - \epsilon_1\right), \end{aligned} \tag{33}$$

$$\begin{aligned} \dot{V}_2 &\leq 2\tilde{z}^T\overline{PD}_2\left(f\left(T^{-1}z\right) - f\left(T^{-1}\hat{z}\right)\right) - \hat{k}_2\tilde{\bar{z}}^T\overline{PD}_2\overline{HC\tilde{z}} + 2\tilde{z}^T\overline{PF}\left(f_s - v_2\right) \\ &\leq 2\|P\tilde{z}\|\left(\mathscr{L}_f T^{-1}D_2\|\tilde{z}\| - \|F\|\epsilon_2\right). \end{aligned} \tag{34}$$

Finally, substituting (28) and (29) into (33) and (34) leads to that

$$\begin{aligned} \dot{V}_1 &\leq -2\eta_1 P_1\tilde{z}_1, \\ \dot{V}_2 &\leq -2\eta_2\|\overline{P}\tilde{z}\|. \end{aligned} \tag{35}$$

Therefore, the desired sliding motion can be achieved and maintained.

3.3. Integral Sliding-Mode Control Design. The design of a sliding mode controller is typically composed of two steps. The first step features the construction of a sliding surface, on which the system performance can be maintained as expected. The second step is concerned with the selection of an appropriate control law to drive the sliding variable reach the designed sliding surface and thereafter keep the sliding motion within the close neighborhood of the sliding surface. However, during the reaching phase, the insensitivity of the sliding mode controller cannot be ensured. One way to solve this problem is to employ the integral sliding-mode control scheme, such that the robustness of the system can be guaranteed throughout the entire response of the system starting from the initial time instant [35].

In order to facilitate the integral sliding-mode control design, the nonlinear system described in (6) can be rewritten in the following integral chain format as

$$\begin{cases} \dot{x}_1 = x_2, \\ \dot{x}_2 = f(x_2) + B_u u + d, \end{cases} \tag{36}$$

where $x_1 = [\phi, \theta, \psi]^T$ and $x_2 = [p, q, r]^T$.

By denoting x_1^d as the desired trajectory of the quadrotor helicopter, the corresponding tracking error vector can be defined as

$$x_1^e = x_1 - x_1^d = \begin{bmatrix} \phi - \phi_d \\ \theta - \theta_d \\ \psi - \psi_d \end{bmatrix}. \tag{37}$$

Then, with this tracking error vector (37), the integral sliding surface for the controlled system is defined as follows:

$$S = \dot{x}_1^e + k_{c2}x_1^e + k_{c1}\int_{t_0}^{t} x_1^e(\tau)\mathrm{d}\tau - k_{c2}x_1^e(t_0) - \dot{x}_1^e(t_0), \tag{38}$$

where t_0 is the initial time instant and the diagonal matrices k_{c1} and k_{c2} represent the design parameters.

From this definition, one can observe that the integral term renders the sliding motion occur at the initial time instant t_0. Accordingly, the system trajectory under integral-sliding mode control starts from the designed sliding surface, and the reaching phase is eliminated compared to conventional sliding mode control.

The continuous sliding-mode control part is designed by equalizing $\dot{S} = 0$ as

$$u_0 = B_u^{-1}\left(\dot{x}_1^d - k_{c2}\dot{x}_1^e - k_{c1}x_1^e - f(x_2)\right). \tag{39}$$

The discontinuous control part to reject disturbances is designed as

$$u_1 = -B_u^{-1}k_{c3}\,\mathrm{sat}(S), \tag{40}$$

where k_{c3} is a diagonal matrix constructed with positive high gains that make the designed sliding surface attractive, and the sat function is defined as [36]:

$$\mathrm{sat}(S) = \begin{cases} \mathrm{sign}(S), & \text{if } \|S\| > \Phi, \\ \dfrac{S}{\Phi}, & \text{if } \|S\| \le \Phi, \end{cases} \tag{41}$$

with Φ representing the boundary layer thickness.

However, in order to account for the unknown disturbances, the discontinuous control gain k_{c3} needs to be chosen greater than the upper bound of the unknown disturbances, which may lead to unexpected control chattering. Therefore, a nonlinear disturbance observer needs to be designed and synthesized with the designed sliding-mode control to reduce the discontinuous control gain.

3.4. Nonlinear Disturbance Observer Design and Synthesis with Sliding Mode Control

Assumption 4. The disturbances in system (36) are bounded and defined by $D_d = \sup_{t>0}\|d\|$.

Assumption 5. The lumped disturbances can be represented by the following exogenous system [37, 38]:

$$\begin{cases} \dot{\zeta} = A_d\zeta, \\ d = C_d\zeta. \end{cases} \tag{42}$$

To estimate the unknown disturbances, a nonlinear disturbance observer is designed as

$$\begin{aligned} \dot{\hat{z}} &= [A_d - \lambda C_d]z + A_d\mu - \lambda[C\mu + f(x_2) + B_u u], \\ \hat{\zeta} &= z + \mu, \\ \hat{d} &= C_d\hat{\zeta}. \end{aligned} \tag{43}$$

With the estimated disturbances $\hat{d}$, the disturbance estimation error is defined as

$$d_e = d - \hat{d}. \tag{44}$$

Assumption 6. The disturbance estimation error is bounded by $D_e = \sup_{t>0}\|d_e\|$.

By recalling the sliding mode control derived in (39) and (40), with the estimated sensor faults and disturbances, the composite control law can be constructed as follows:

$$u = B_u^{-1}\left(\ddot{\hat{x}}_1^d - k_{c2}\dot{\hat{x}}_1^e - k_{c1}\hat{x}_1^e - f(x_2) - \hat{d}\right) - B_u^{-1}k_{c3}\,\mathrm{sat}(S). \tag{45}$$

Theorem 2. *Consider a nonlinear affine system (36) with exogenous disturbances (42). Given the designed integral sliding surface (38), by employing the disturbance estimation (43) and the feedback control law (45), the system tracking performance can be guaranteed as expected in the presence of unknown disturbances with the discontinuous control gain chosen as $k_{c3} \ge \eta + D_e$.*

Proof of Theorem 2. To prove Theorem 2, a nonnegative Lyapunov function is defined as

$$V_3 = \frac{1}{2}S^T S. \tag{46}$$

The time derivative of V_3 for $S \neq 0$ can be calculated as

$$\begin{aligned} \dot{V}_3 &= S^T\dot{S} = S^T\left(f(x_2) + B_u B_u^{-1}\left(\ddot{\hat{x}}_1^d - k_{c2}\dot{\hat{x}}_1^e - k_{c1}\hat{x}_1^e - f(x_2) - \hat{d} - k_{c3}\mathrm{sat}(S)\right) + d - \ddot{\hat{x}}_1^d + k_{c2}\dot{\hat{x}}_1^e + k_{c1}\hat{x}_1^e\right), \\ &= S^T\left(-k_{c3}\mathrm{sat}(S) + d - \hat{d}\right) \le S^T\left(-(\eta + D_e)\mathrm{sat}(S) + D_e\right) \le -\eta\|S\|. \end{aligned} \tag{47}$$

Therefore, the stability of the controller system can be guaranteed with the designed control law (45) in the presence of unknown exogenous disturbances.

Remark 1. Since the unknown disturbances have been precisely estimated by the disturbance observer, the magnitude of the estimation error can be kept much smaller than that of the disturbance. Thus, compared to conventional sliding-mode control, the value of the discontinuous control gain is significantly reduced, which can alleviate the control chattering problem to some extent.

4. Simulation Tests and Discussion

In this section, the proposed AFTC strategy against sensor faults and external disturbances will be validated. To achieve an effective evaluation of the proposed AFTC strategy, three different faulty patterns are considered for the attitude control system of the quadrotor helicopter. In addition, for comparison, the tracking performance of a conventional sliding-mode control is also investigated to demonstrate the advantages of the proposed control strategy.

It can be observed from Figures 3–5 that during $20 < t < 40$s and $50 < t < 70$s, all the attitude measurement systems fail simultaneously. By using the proposed sensor

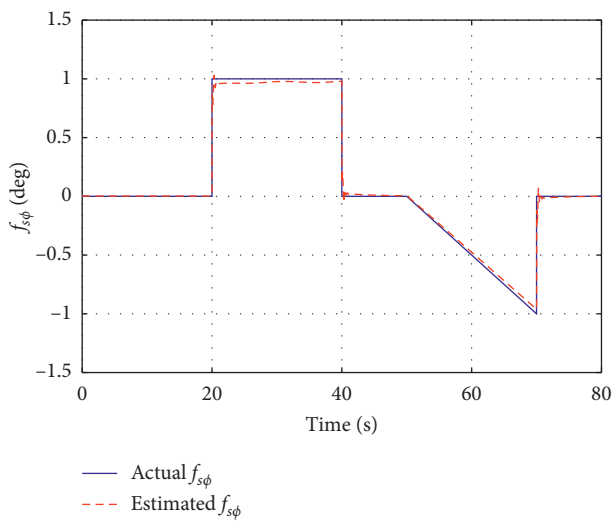

FIGURE 3: Performance of the $f_{s\phi}$ sensor fault estimation in the presence of external disturbances.

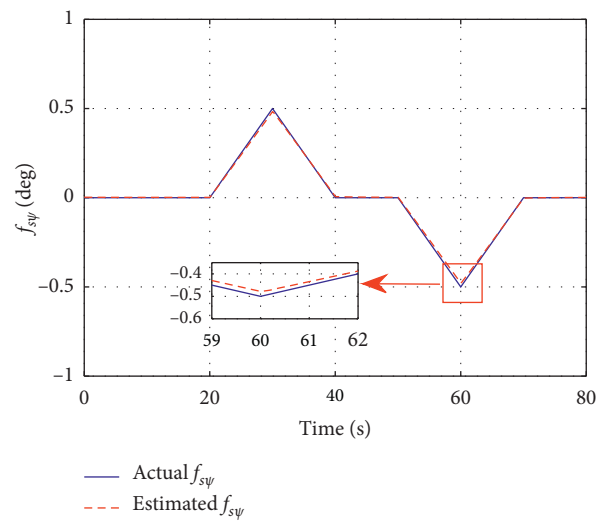

FIGURE 5: Performance of the $f_{s\psi}$ sensor fault estimation in the presence of external disturbances.

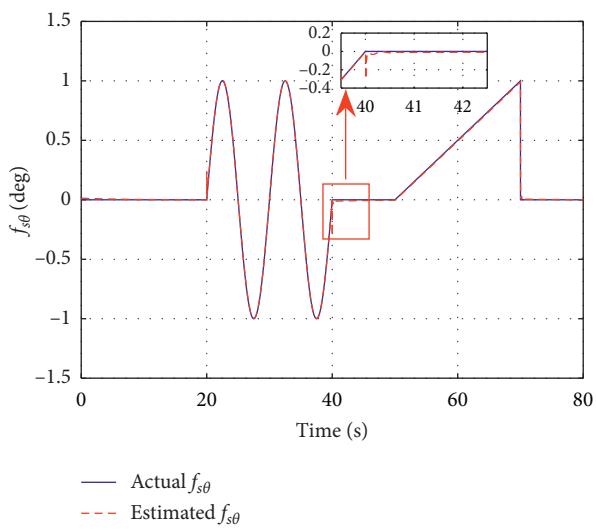

FIGURE 4: Performance of the $f_{s\theta}$ sensor fault estimation in the presence of external disturbances.

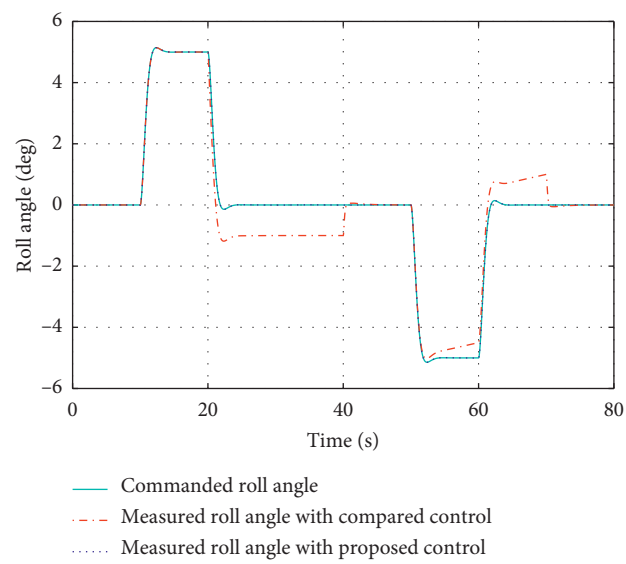

FIGURE 6: Comparison of roll tracking performance in the presence of sensor faults.

fault estimation scheme, the sensor faults can be accurately estimated, and the unbiased attitude estimation is provided for the feedback control. For comparison, the tracking performance of the compared conventional sliding-mode control without the sensor fault diagnosis system is studied, which is shown as the dash-dotted red line in Figures 6–8. In this case, the attitude measurements are directly utilized by the feedback controller. Therefore, the attitude of the quadrotor helicopter cannot follow the reference commands when there exist sensor faults, and the response of the quadrotor helicopter is obviously influenced by the wrong sensor measurements. For example, as shown in Figure 6, during $20 < t < 40$s, the reference command for the roll angle is zero, but the response is -1 deg due to the occurrence of sensor fault. In contrast, with the sensor diagnosis system, the sensor faults can be accurately estimated, and the quadrotor helicopter can still follow the reference commands very well even in the presence of sensor faults as can be observed from the dashed blue line of Figures 6–8.

In order to further test the capability of the proposed control strategy against both sensor faults and external disturbances, two different scenarios are tested. In scenario 1, in addition to the aforementioned sensor faults, at 5 s, a

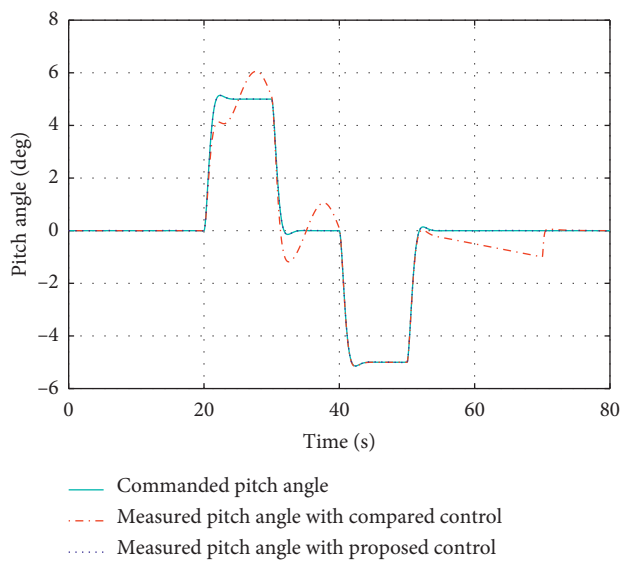

Figure 7: Comparison of pitch tracking performance in the presence of sensor faults.

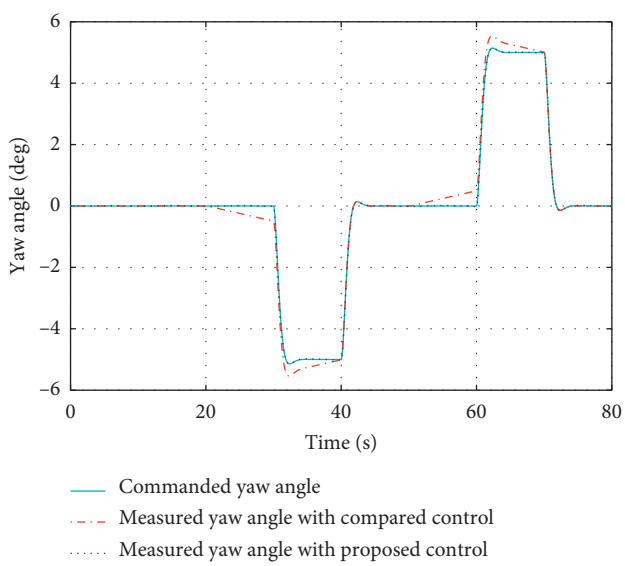

Figure 8: Comparison of yaw tracking performance in the presence of sensor faults.

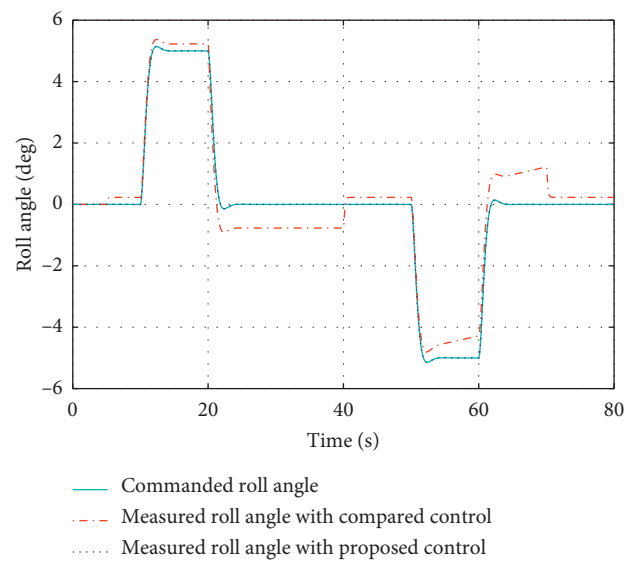

Figure 9: Comparison of roll tracking performance in the presence of both sensor faults and constant external disturbances.

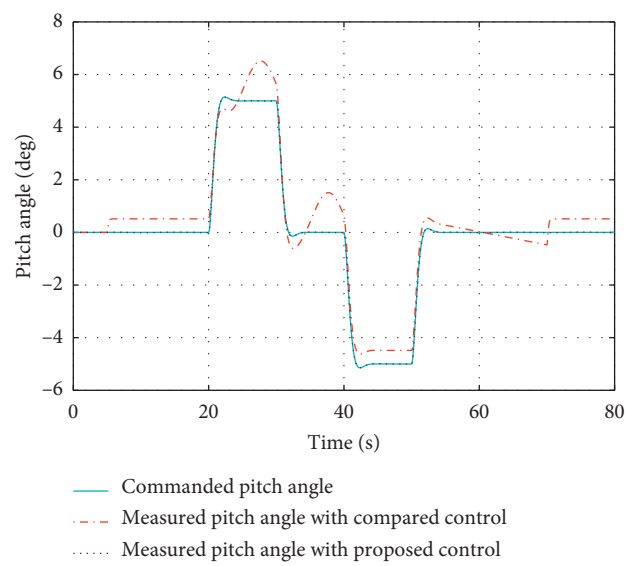

Figure 10: Comparison of pitch tracking performance in the presence of both sensor faults and constant external disturbances.

constant external disturbance with three different amplitudes is injected to roll, pitch, and yaw motions, respectively. The attitude tracking performances are demonstrated in Figures 9–11. It can be observed that, after the disturbance is injected to the roll, pitch, and yaw motion of the quadrotor helicopter at 5 s, even if there is no sensor fault at that time, there still exist attitude tracking errors with the compared control, as shown in the dash-dotted red line. However, with the proposed control, the injected external disturbances can be estimated and compensated accordingly. In this case, the desired attitude tracking performance can be maintained even in the presence of both sensor faults and constant external disturbances, as shown in the dashed blue line.

In scenario 2, a time-varying disturbance with three different amplitudes is injected to the quadrotor helicopter at 5 s to further validate the tracking performance of the

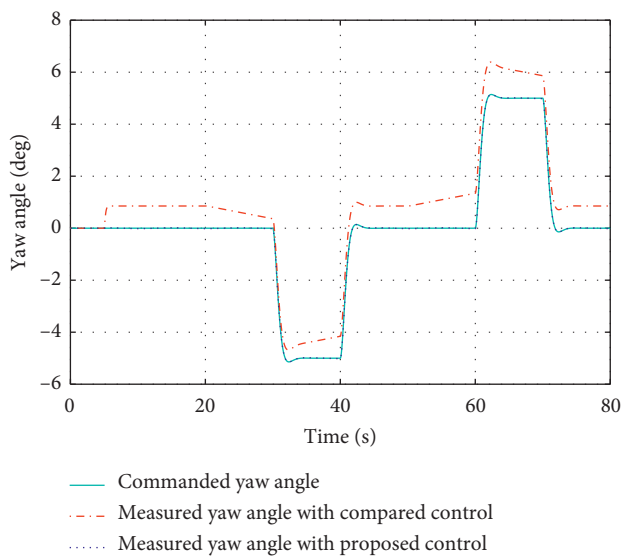

Figure 11: Comparison of yaw tracking performance in the presence of both sensor faults and constant external disturbances.

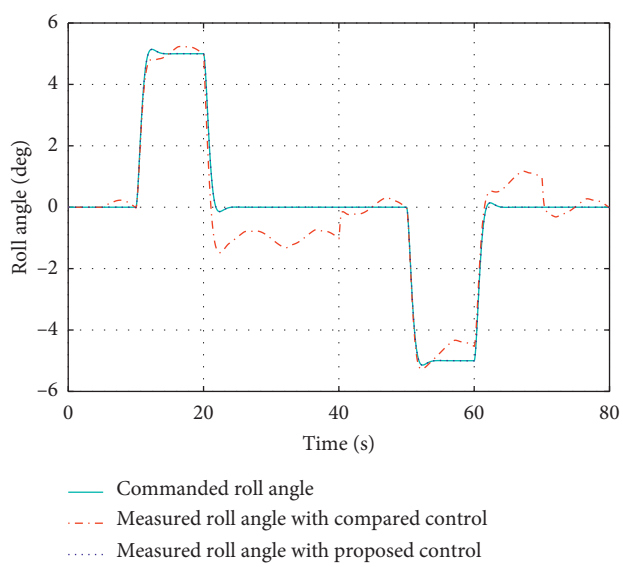

Figure 12: Comparison of roll tracking performance in the presence of both sensor faults and time-varying external disturbances.

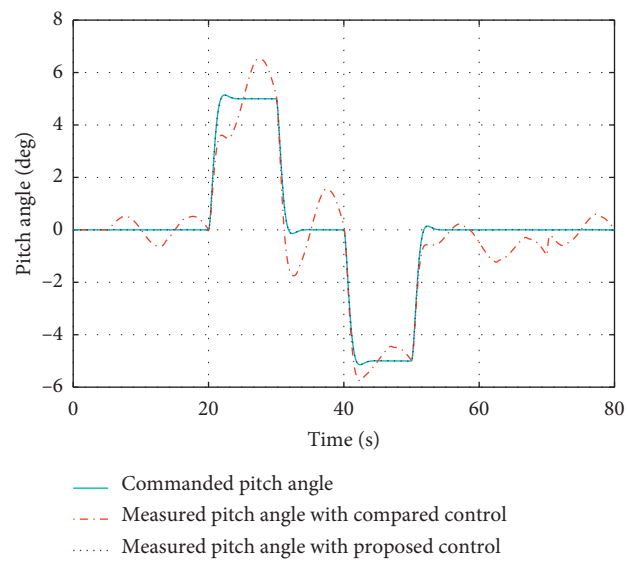

Figure 13: Comparison of pitch tracking performance in the presence of both sensor faults and time-varying external disturbances.

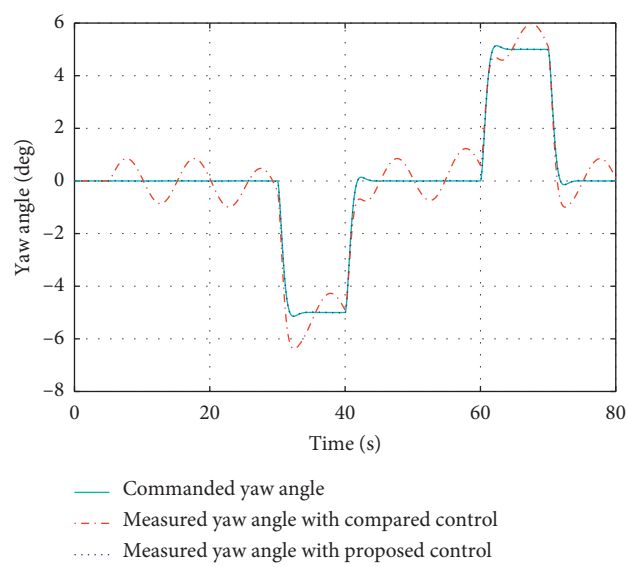

Figure 14: Comparison of yaw tracking performance in the presence of both sensor faults and time-varying external disturbances.

proposed control strategy in the presence of both sensor faults and time-varying external disturbances. The corresponding attitude tracking performances are shown in Figures 12–14. Compared to scenario 1, the system tracking performance with the compared control is more affected. On the contrary, even in this situation, the proposed control strategy can still maintain a satisfactory system tracking performance, which confirms the effectiveness and superiority of the proposed control strategy.

5. Conclusions

In this paper, an active fault-tolerant control strategy is proposed for a quadrotor helicopter against sensor faults and external disturbances. The proposed fault diagnosis scheme has the capability to accurately estimate the sensor faults and eliminate the effect of disturbances, which is then integrated with a robust controller in an active fashion to ensure the continuous operation of the quadrotor helicopter. For controlling the quadrotor helicopter, a disturbance observer

is designed to effectively estimate the external disturbances and synthesized with the designed integral sliding-mode controller, which can help the baseline controller to avoid control chattering. In addition, the stability of the closed-loop system is theoretically proved. In comparison with a conventional sliding-mode control, the demonstrated numerical simulation results show the effectiveness and advantages of the proposed active fault-tolerant control strategy under different faulty and uncertain scenarios.

Data Availability

The data used to support the findings of this study are included within this article.

Conflicts of Interest

The authors declare that there are no conflicts of interest.

Acknowledgments

This research work was partially supported by the Fundamental Research Funds for the Central Universities.

References

[1] T. Huang, D. Huang, Z. Wang, and A. Shah, "Robust tracking control of a quadrotor UAV based on adaptive sliding mode controller," *Complexity*, vol. 2019, Article ID 7931632, 15 pages, 2019.

[2] C. Li, Y. Zhang, and P. Li, "Full control of a quadrotor using parameter-scheduled backstepping method: implementation and experimental tests," *Nonlinear Dynamics*, vol. 89, no. 2, pp. 1259–1278, 2017.

[3] Y. Zhang, N. Xu, G. Zhu, L. Sun, S. Cao, and X. Zhang, "Adaptive robust dynamic surface integral sliding mode control for quadrotor UAVs under parametric uncertainties and external disturbances," *Complexity*, vol. 2020, Article ID 8879364, 20 pages, 2020.

[4] X. Yu, Y. Fu, and Y. Zhang, "Aircraft fault accommodation with consideration of actuator control authority and gyro availability," *IEEE Transactions on Control Systems Technology*, vol. 26, no. 4, pp. 1285–1299, 2018.

[5] R. Wang, Y. Li, H. Sun, Y. Zhang, and Y. Sun, "Performance analysis of switched control systems under common-source digital upsets modeled by MDHMM," *Complexity*, vol. 2018, Article ID 4329053, 12 pages, 2018.

[6] J. Zhang, A. K. Swain, and S. K. Nguang, "Robust sensor fault estimation scheme for satellite attitude control systems," *Journal of the Franklin Institute*, vol. 350, no. 9, pp. 2581–2604, 2013.

[7] R. Wang, C. Wang, H. Sun, Z. Chen, and Y. Sun, "Sensor fault signal reconstruction based on sliding mode observer for flight control systems," *International Journal of Modelling, Identification and Control*, vol. 32, no. 3-4, pp. 204–211, 2019.

[8] M. K. Jeerage, "Reliability analysis of fault-tolerant IMU architectures with redundant inertial sensors," *IEEE Aerospace and Electronic Systems Magazine*, vol. 5, no. 7, pp. 23–28, 1990.

[9] Y. Zhong, W. Zhang, Y. Zhang, J. Zuo, and H. Zhan, "Sensor fault detection and diagnosis for an unmanned quadrotor helicopter," *Journal of Intelligent & Robotic Systems*, vol. 96, no. 3-4, pp. 555–572, 2019.

[10] A. Matus-Vargas, G. Rodriguez-Gomez, and J. Martinez-Carranza, "A monocular SLAM-based controller for multirotors with sensor faults under ground effect," *Sensors*, vol. 19, no. 22, p. 4948, 2019.

[11] Z. Zhang and B. Xiao, "Sensor fault reconstruction based on adaptive sliding mode observer for forklift fault-tolerant control system," *Applied Sciences*, vol. 10, no. 4, p. 1278, 2020.

[12] J. Tan, Y. Fan, P. Yan, C. Wang, and H. Feng, "Sliding mode fault tolerant control for unmanned aerial vehicle with sensor and actuator faults," *Sensors*, vol. 19, no. 3, p. 643, 2019.

[13] C. Edwards, S. K. Spurgeon, and R. J. Patton, "Sliding mode observers for fault detection and isolation," *Automatica*, vol. 36, no. 4, pp. 541–553, 2000.

[14] C. P. Tan and C. Edwards, "Sliding mode observers for detection and reconstruction of sensor faults," *Automatica*, vol. 38, no. 10, pp. 1815–1821, 2002.

[15] H. Alwi, C. Edwards, and C. P. Tan, "Sliding mode estimation schemes for incipient sensor faults," *Automatica*, vol. 45, no. 7, pp. 1679–1685, 2009.

[16] Y. Zhang and J. Jiang, "Bibliographical review on reconfigurable fault-tolerant control systems," *Annual Reviews in Control*, vol. 32, no. 2, pp. 229–252, 2008.

[17] Y. M. Zhang, A. Chamseddine, C. A. Rabbath et al., "Development of advanced FDD and FTC techniques with application to an unmanned quadrotor helicopter testbed," *Journal of the Franklin Institute*, vol. 350, no. 9, pp. 2396–2422, 2013.

[18] X. Fang, H. Fan, and L. Liu, "Robust finite-time tracking for uncertain linear systems with actuator faults," *Complexity*, vol. 2020, Article ID 2463790, 13 pages, 2020.

[19] P. Lyu, J. Lai, J. Liu, H. H. T. Liu, and Q. Zhang, "A thrust model aided fault diagnosis method for the altitude estimation of a quadrotor," *IEEE Transactions on Aerospace and Electronic Systems*, vol. 54, no. 2, pp. 1008–1019, 2018.

[20] F. Xu, J. Tan, X. Wang, V. Puig, B. Liang, and B. Yuan, "Mixed active/passive robust fault detection and isolation using set-theoretic unknown input observers," *IEEE Transactions on Automation Science and Engineering*, vol. 15, no. 2, pp. 863–871, 2018.

[21] Y. Al Younes, H. Noura, A. Rabhi, A. El Hajjaji, and N. Al Hussien, "Sensor fault detection and isolation in the quadrotor vehicle using nonlinear identity observer approach," in *Proceedings of 2013 Conference on Control and Fault-Tolerant Systems*, Nice, France, October 2013.

[22] J. Gao, Q. Zhang, and J. Chen, "EKF-based actuator fault detection and diagnosis method for tilt-rotor unmanned aerial vehicles," *Mathematical Problems in Engineering*, vol. 2020, Article ID 8019017, 12 pages, 2020.

[23] B. Wang, Y. Shen, and Y. Zhang, "Active fault-tolerant control for a quadrotor helicopter against actuator faults and model uncertainties," *Aerospace Science and Technology*, vol. 99, Article ID 105745, 2020.

[24] R. C. Avram, X. Zhang, and J. Muse, "Quadrotor accelerometer and gyroscope sensor fault diagnosis using nonlinear adaptive estimation methods," *International Journal of Prognostics and Health Management*, vol. 7, no. 1, pp. 1–10, 2016.

[25] R. C. Avram, X. Zhang, and J. Muse, "Quadrotor sensor fault diagnosis with experimental results," *Journal of Intelligent & Robotic Systems*, vol. 86, no. 1, pp. 115–137, 2017.

[26] Y. Zhong, W. Zhang, and Y. M. Zhang, "Sensor fault diagnosis for unmanned quadrotor helicopter via adaptive two-stage extended Kalman filter," in *Proceedings of 2017 International*

Conference on Sensing, Diagnostics, Prognostics, and Control (SDPC), pp. 493–498, Shanghai, China, August 2017.

[27] C. Zhu, C. Li, X. Chen, K. Zhang, X. Xin, and H. Wei, "Event-triggered adaptive fault tolerant control for a class of uncertain nonlinear systems," *Entropy*, vol. 22, no. 6, p. 598, 2020.

[28] B. Wang and Y. Zhang, "An adaptive fault-tolerant sliding mode control allocation scheme for multirotor helicopter subject to simultaneous actuator faults," *IEEE Transactions on Industrial Electronics*, vol. 65, no. 5, pp. 4227–4236, 2018.

[29] F. Chen, W. Lei, K. Zhang, G. Tao, and B. Jiang, "A novel nonlinear resilient control for a quadrotor UAV via backstepping control and nonlinear disturbance observer," *Nonlinear Dynamics*, vol. 85, no. 2, pp. 1281–1295, 2016.

[30] N. P. Nguyen and S. K. Hong, "Active fault-tolerant control of a quadcopter against time-varying actuator faults and saturations using sliding mode backstepping approach," *Applied Sciences*, vol. 9, no. 19, p. 4010, 2019.

[31] B. Wang, X. Yu, L. Mu, and Y. Zhang, "A dual adaptive fault-tolerant control for a quadrotor helicopter against actuator faults and model uncertainties without overestimation," *Aerospace Science and Technology*, vol. 99, p. 105744, 2020.

[32] R. Wang, L. Gao, C. Bai, and H. Sun, "U-Model-Based sliding mode controller design for quadrotor UAV control systems," *Mathematical Problems in Engineering*, vol. 2020, Article ID 4343214, 11 pages, 2020.

[33] F. R. Lopez-Estrada, J.-C. Ponsart, D. Theilliol, Y. M. Zhang, and C.-M. Astorga-Zaragoza, "LPV model-based tracking control and robust sensor fault diagnosis for a quadrotor UAV," *Journal of Intelligent & Robotic Systems*, vol. 84, no. 1-4, pp. 163–177, 2016.

[34] L. Qin, X. He, R. Yan, and D. Zhou, "Active fault-tolerant control for a quadrotor with sensor faults," *Journal of Intelligent & Robotic Systems*, vol. 88, no. 2-4, p. 449X67, 2017.

[35] V. Utkin and J. Shi, "Integral sliding mode in systems operating under uncertainty conditions," in *Proceedings of 35th IEEE Conference on Decision and Control*, pp. 4591–4596, Kobe, Japan, December 1996.

[36] J. J. Slotine and S. S. Sastry, "Tracking control of non-linear systems using sliding surfaces, with application to robot manipulators†," *International Journal of Control*, vol. 38, no. 2, pp. 465–492, 1983.

[37] W.-H. Chen, "Disturbance observer based control for nonlinear systems," *IEEE/ASME Transactions on Mechatronics*, vol. 9, no. 4, pp. 706–710, 2004.

[38] W.-H. Chen, J. Yang, L. Guo, and S. H. Li, "Disturbance-observer-based control and related methods-An overview," *IEEE Transactions on Industrial Electronics*, vol. 63, no. 2, pp. 1083–1095, 2015.

Hindawi
Complexity
Volume 2021, Article ID 6673461, 10 pages
https://doi.org/10.1155/2021/6673461

Research Article

Person Reidentification Model Based on Multiattention Modules and Multiscale Residuals

Yongyi Li,[1] **Shiqi Wang**,[1] **Shuang Dong**,[1] **Xueling Lv**,[2] **Changzhi Lv**,[1] **and Di Fan**[1]

[1]*Shandong University of Science and Technology, Qingdao, Shandong 266590, China*
[2]*Department of Management and Economics, Tianjin University, Tianjin 300072, China*

Correspondence should be addressed to Di Fan; skd992372@sdust.edu.cn

Received 25 November 2020; Revised 27 January 2021; Accepted 27 February 2021; Published 19 March 2021

Academic Editor: Rui Wang

At present, person reidentification based on attention mechanism has attracted many scholars' interests. Although attention module can improve the representation ability and reidentification accuracy of Re-ID model to a certain extent, it depends on the coupling of attention module and original network. In this paper, a person reidentification model that combines multiple attentions and multiscale residuals is proposed. The model introduces combined attention fusion module and multiscale residual fusion module in the backbone network ResNet 50 to enhance the feature flow between residual blocks and better fuse multiscale features. Furthermore, a global branch and a local branch are designed and applied to enhance the channel aggregation and position perception ability of the network by utilizing the dual ensemble attention module, as along as the fine-grained feature expression is obtained by using multiproportion block and reorganization. Thus, the global and local features are enhanced. The experimental results on Market-1501 dataset and DukeMTMC-reID dataset show that the indexes of the presented model, especially Rank-1 accuracy, reach 96.20% and 89.59%, respectively, which can be considered as a progress in Re-ID.

1. Introduction

As an important video intelligent analysis technology, person reidentification (Re-ID) uses computer vision technology to realize the identification and matching of target pedestrians in a multicamera network with non-overlapping fields of view. That is, given a pedestrian test image (Probe), the pedestrian image is retrieved under cross-monitoring equipment from all gallery images (Gallery) [1]. Compared with the perspective scenes of fixed monitoring equipment, person reidentification technology solves the problem of its visual limitations and can be well matched with pedestrian detection and pedestrian tracking scenes. It is a key technology for target tracking, urban intelligent security, and prevention and control of public places such as supermarkets, airports, stations, exhibition halls, and exhibition centers.

In recent years, research in the field of person rerecognition has focused on representation learning [2], metric learning [3], local features [4], video sequences [5], and Generative Adversarial Networks (GAN) generated images [6]. The performance of the person reidentification system is getting better and better, and it has made great progress. However, in the real scene, the problems of different image scales, low resolution, occlusion, and illumination differences that seriously affect the recognition effect are still not well resolved. Therefore, in recent years, many scholars have begun to study the attention mechanism and local features in order to improve the performance of the recognition model. At present, there has been some progress in the basic network and local features.

In terms of basic networks, most of models used ResNet50 as the backbone network, but also improved lightweight convolution models as the backbone network were also selected, such as Omni-Scale Feature Learning Network (OSnet) [7] and Robust-Re-ID [8]. The improvement ideas of these networks to the basic network mainly focus on the research and application of the attention mechanism. For example, Hou et al. proposed Interaction-and-Aggregation Network (IA-Net) [9], which constructs an

IA block by combining channel attention and spatial attention and then embeds it in the residual network to aggregate channel and spatial information. Chen et al. proposed the Mixed High-Order Attention Network (MHN) [10], which uses the high-order attention distribution High-Order Attention (HOA) module to obtain more feature information. Chen and Ding et al. proposed Attentive But Diverse Network (ABD-net) [11], which combines channel attention and position attention in parallel and adds them to the local feature network for feature fusion. Xia et al. proposed Second-Order Nonlocal Attention (SONA) network [12], which adds covariance matrix to the first-order nonlocal attention structure to make it second-order structure. This method effectively enhances the information flow between residual convolution blocks.

In terms of local features, image horizontal block is a common step in local feature extraction [4]. However, the disadvantage is that the requirements for image alignment are relatively high. If the two images are not aligned up and down, it is likely that body parts will be misplaced and compared, such as head and background contrast, which will increase the probability of model judgment error. Therefore, Zhang et al. designed a dynamic alignment network AlignedReID [13], which can automatically align image blocks from top to bottom without additional information. Some literatures used some prior knowledge to align pedestrians. For example, Zhao et al.'s spindle net [14] first estimated the key points of travelers with the attitude estimation model and then used affine transformation to align the same key points. In addition, Sun et al. proposed a Part-based Convolutional Baseline (PCB) [15] method to divide the feature map into six blocks horizontally and used refined part pooling (RPP) method for local alignment. Later, some researchers found that the combination of global features and local features can improve the expression ability of the network, and the local features are divided more carefully. Wang et al. proposed Multiple Granularities Network (MGN) [16] based on discriminative features, which uses a more detailed combination of local features and global features and achieves quite good recognition results. In addition, Zheng et al. [17] proposed the pyramid block model, which integrates the local and global information and the progressive clues between them and solves the occlusion problem to a certain extent.

However, there are still some problems to be solved in the above-mentioned attention mechanism and local features research. For example, some attention mechanisms need multiple matrix calculations, and the coupling with the original network is not ideal when joining the basic network. In addition, in the segmentation of feature map, the more blocks, the better local feature expression, but it will increase the amount of model parameters. If there are few blocks, the recognition rate will not be improved. In this regard, we designed a person reidentification model based on attention fusion and multiscale residuals. The model mainly solves the problems of poor coupling between attention mechanism and original network and scientific expression of local features. The model uses an improved ResNet50 as the backbone network and is designed with global and local branch structures. The paper added Combined Attention Fusion Module (CAFM) and Multiscale Residual Fusion Module (MSFM) to the original ResNet50 [18] to effectively concatenate the feature information between residual blocks and better integrate multiscale features. The global branch uses a Dual Ensemble Attention Module (DEAM) to enhance the network's channel aggregation and location awareness capabilities. The local branch is divided into fine-grained features by multiproportion block method to further refine the local features. In the experiment, the network in this paper has achieved good results on the Market-1501 and DukeMTMC-reID datasets, and the indicators are better than other Re-ID networks.

2. Person Reidentification Model Based on Attention Fusion and Multiscale Residuals

The algorithm model framework of this paper is shown in Figure 1. Firstly, the improved ResNet50 network and local and global branches are used to extract pedestrian features of Probe and Gallery, respectively. Then the similarity between Probe and Gallery pedestrian features is calculated. Finally, the similarity scores are sorted to obtain the retrieval results of all the images of Probe in the Gallery. The model in this paper is based on the ResNet50 network with multiple improvements and model extensions to enhance feature extraction and expression capabilities and effectively improve the recognition rate.

The feature extraction network designed in this paper is shown in Figure 2. Its backbone network is an improved ResNet 50, and it is equipped with global attention branch and local fine-grained feature branch. For the improvement of the backbone network, Combined Attention Fusion Module (CAFM) is added after ResNet50 Stage1 to strengthen the flow of feature information between residual blocks. Multiscale Residual Fusion Module (MSFM) is added after Stage4, which can perform multiscale feature extraction and selective fusion of the original residual features. For the design of the branch structure, the Dual Ensemble Attention Module (DEAM) is introduced into the global branch to strengthen the fusion of channel attention and position attention. Multiproportion block method is used to optimize the expression of fine-grained features in local branches.

2.1. The Improved ResNet 50 Network. ResNet 50 contains a total of 50 convolutional layers, which are input layer, output layer, and 48 hidden convolutional layers. 48 hidden layers are divided into four stages in the form of $3+4+6+3$ convolution residual bottleneck. In this paper, CAFM and MSFM are introduced into the backbone network for improvement, and the step size of the downsampling convolutional layer in Stage4 is changed from 2 to 1.The following is a detailed description of CAFM and MSFM.

2.1.1. Combined Attention Fusion Module (CAFM). The attention mechanism is a very important and effective method in deep learning [19]. Its essence is to linearly weigh

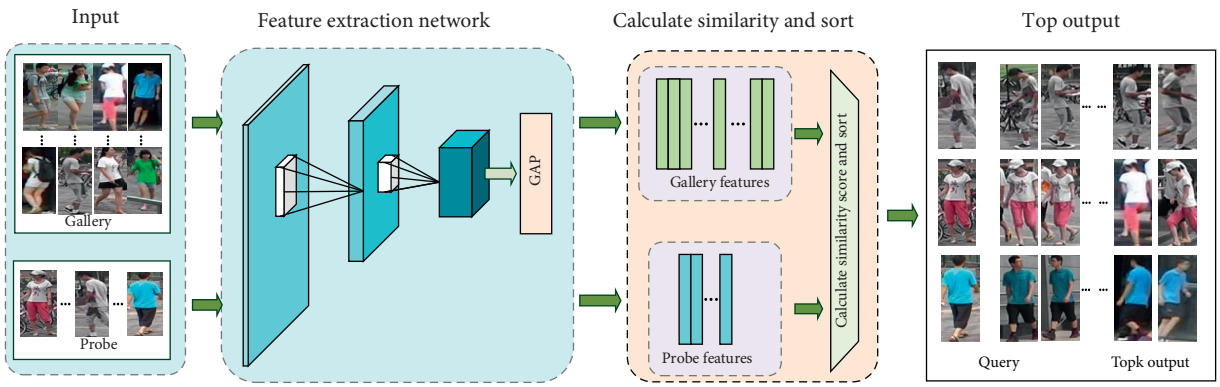

Figure 1: The overall framework of the algorithm model.

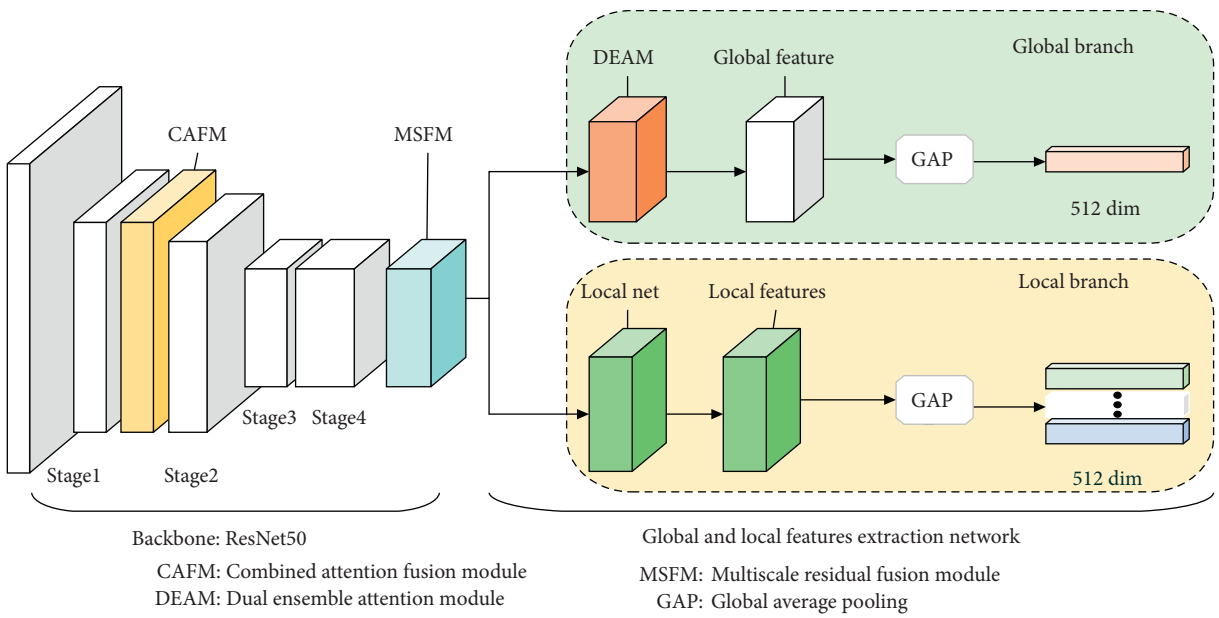

Figure 2: Schematic diagram of feature extraction network structure.

the relationship between things to obtain a new representation. In the field of person reidentification, the attention mechanism is often used to focus the attention of the network on the pedestrian's body, thereby eliminating the influence of factors such as background and occlusion. We designed the combined structure of Channel Attention Module (CAM) [11] and Nonlocal Attention Module (NAM) [20] and embedded it in the residual structure, which can fully concatenate the information between the residual blocks and increase the network's attention to the target feature. The specific structure of the module is shown in Figure 3.

In Figure 3, the input characteristics firstly fuse the channel information through the channel attention module (CAM), and the important location is perceived by the nonlocal attention module (NAM), and finally the attention information features integrated with the original input features. The Channel Attention Module is shown in Figure 3(b). It integrates all the relevant features in the channel map and selectively strengthens the correlated channel map. Nonlocal Attention Module (NAM) is shown in Figure 3(c). In theory, NAM is a position attention mechanism. Each position value of its output is a weighted average of other position values, which represents the dependence between pixels and other pixels. Among them, the function of softmax is to map the feature value between 0 and 1 to get the attention map.

2.1.2. Multiscale Residual Fusion Module (MSFM). Multiscale Residual Fusion Module is a dynamic selection mechanism that enables each neuron to select different receptive fields according to the size of the target feature [21].The Multiscale Residual Fusion Module structure designed in this paper is shown in Figure 4(b), which is mainly divided into two parts: multiscale feature extraction and feature selective fusion. The multiscale feature extraction part is mainly used for convolution extraction with different sizes of convolution kernels [22]. Taking into account the requirements of parameter weights and network performance, the module of this paper selects three sizes of convolution kernels of 3×3, 5×5, and 7×7

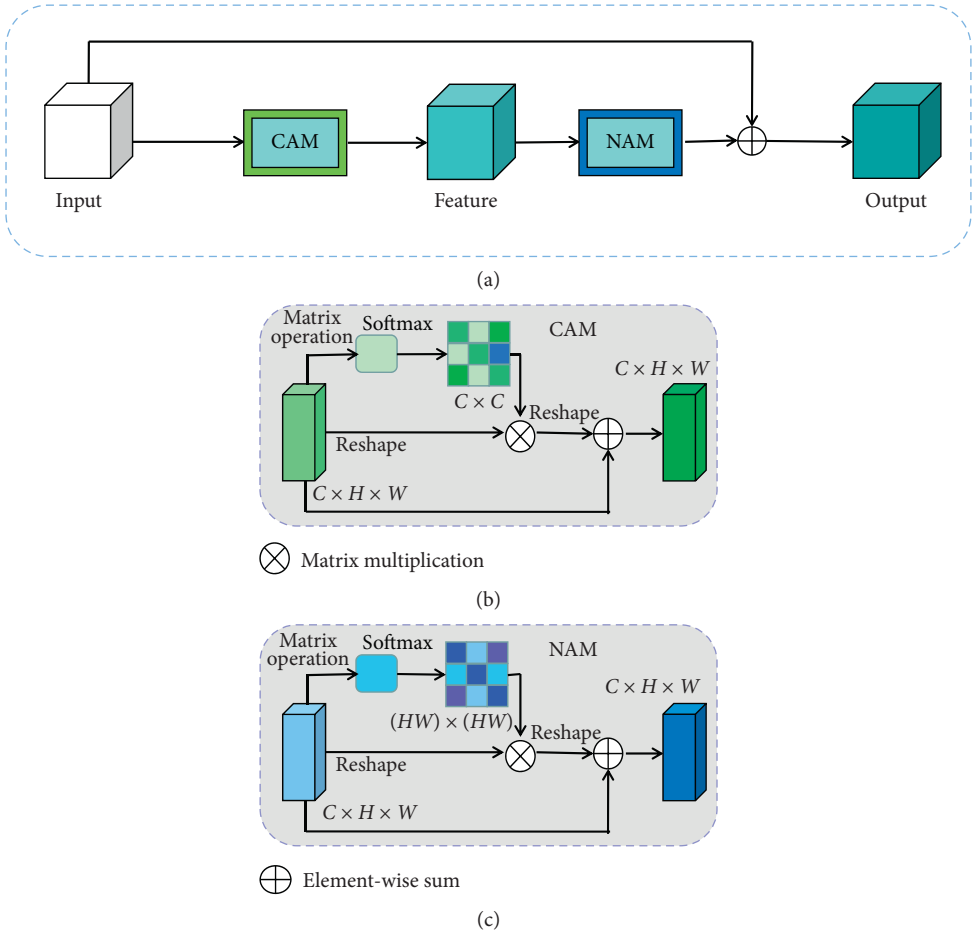

Figure 3: Structure of Combined Attention Fusion Module. (a) CAFM. (b) CAM. (c) NAM.

to extract features by group convolution. Feature selective fusion part is to fuse multichannel information for weight selection [20]. According to the selected weights, the feature images of convolution kernel with different sizes are fused.

The Multiscale Residual Fusion Module adopts a gate mechanism to control the information flow into the different branches of the next convolutional layer [23]. This mechanism fuses the information of all branches to realize the adaptive adjustment of the receptive fields of different sizes of neurons. This module first performs simple pixel-level addition and fusion of multibranch features to obtain feature $U \in R^{C\times H\times W}$, as shown in formula (1), where $U_r, U_f, U_s \in R^{CHW}$ are the output features of the three convolution channels.

$$U = U_t + U_f + U_s. \tag{1}$$

U uses global average pooling to encode global information to generate statistical information $S \in R^C$ on the channel. The c-th element S_c in S is obtained by compression calculation on the $H \times W$ dimension of U.

$$S_c = \frac{1}{H \times W} \sum_{i=1}^{H} U \sum_{j=1}^{W} (c, i, j). \tag{2}$$

Then normalize and nonlinearly operate on S to produce a compact feature $Z \in R^{C\times 1}$, which is obtained through a fully connected layer. Then softmax is operated on Z on the channel to get the soft attention information $\alpha, \beta, \gamma \in R^{C\times 1}$ between the three branch channels. Finally, α, β, γ are multiplied and fused together with U_t, U_f, U_s in the channel dimension to obtain a multiscale fusion feature. The calculation formula is as follows:

$$\begin{aligned} \alpha &= e^{AZ}/E, \\ \beta &= e^{BZ}/E, \\ \gamma &= e^{CZ}/E, \end{aligned} \tag{3}$$

$$U' = \alpha \cdot U_t + \beta \cdot U_f + \gamma \cdot U_s. \tag{4}$$

Among them, $E = e^{AZ} + e^{BZ} + e^{CZ}$; matrices $A, B, C \in R^{C\times C}$ represent the weight matrix of three branches, respectively, which are used to selectively fuse different scale features.

2.2. Global Feature Extraction Network Based on Dual Ensemble Attention Module. The combination of global features and local features is a common feature expression in pedestrian recognition network in recent years. The global branch of this paper uses the Dual Ensemble Attention

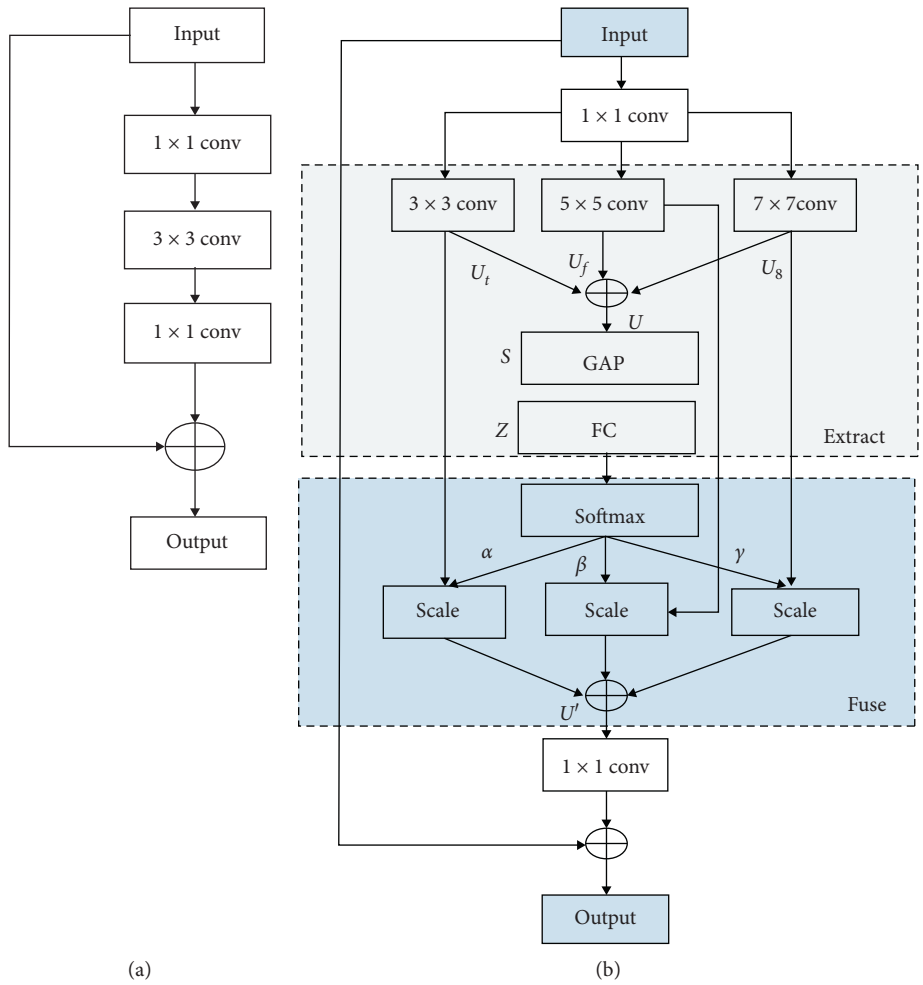

Figure 4: Structure diagram of Multiscale Residual Fusion Module. (a) Original residual structure. (b) Multiscale residual structure.

Module (DEAM) to further enhance the global features in space and channel dimensions on the basis of the output characteristics of the backbone network [24].

Based on the idea of ensemble learning [25], global branch designs two pairs of CAM and NAM into two-stage deep attention module [26]. As shown in Figure 5, this module models the semantic correlation information of spatial dimension and channel dimension, respectively. In the first stage, two basic CAM and NAM are integrated to realize the preliminary extraction of channel and position features. In the second stage, two improved CAM and NAM are integrated, and channel attention and position attention of the first stage are integrated, respectively. Through the weighted connection with the first stage, the second stage collects the information of attention block in the first stage, which further strengthens the learning ability of attention module. In the second stage, the information weighted fusion mode is shown in equation (5), where μ and τ are manually set parameters.

$$\begin{cases} M = \mu * M1 + \tau * M2, \\ N = \mu * N1 + \tau * N2. \end{cases} \tag{5}$$

2.3. Local Feature Based on Multiproportion Block and Reorganization. The design of local branch network is mainly to strengthen the expression of local features. This paper uses multiproportion block method to refine the fine-grained features and selects the part information with obvious features to enhance the network expression. What is different from the past is that we adopt a multiproportion block method to feature reorganization. In this method, the information of important parts is reused through block reorganization, and the information of secondary parts is weakened or discarded in varying degrees [27]. This design is derived from the observation of a large number of pedestrian pictures in reality and public datasets. It is found that the upper body features in the pictures are significantly stronger than the lower body. For example, the upper body has important fine-grained features such as human faces, hair, clothes logos, and hats, but the lower body has only monotonous legs and shoes, and there is no obvious distortion with the change of posture. In terms of occlusion, the lower body is the easiest to be occluded, such as people riding a bicycle, carrying a handbag to block their legs, and walking and being blocked by lawns and motor vehicles. If the

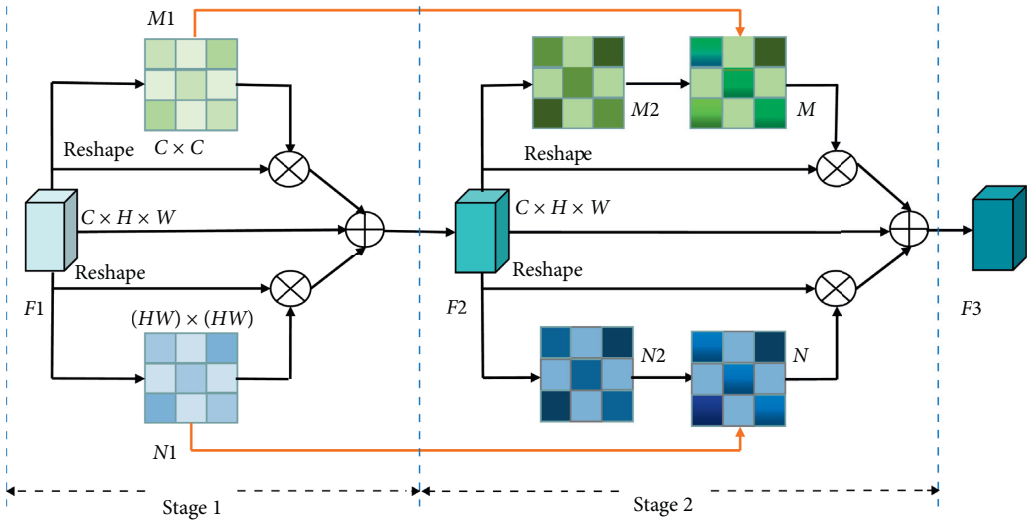

Figure 5: Structure diagram of Dual Ensemble Attention Module.

occluded parts or weak features receive more attention, the rerecognition effect will be reduced.

Some literatures have given more proportion of block patterns, but the more blocks, the heavier the network burden, and the improvement of identification index is not obvious. After experimental analysis, we designed a more optimized multiproportion block reorganization method, and the principle is shown in Figure 6. We first cut the H dimension of the feature map horizontally with different proportions of 1/2, 2/3, and 3/4 and then select the top 1/2, bottom 1/2, top 2/3, and top 3/4 of the feature map to be expressed as the local feature in cooperation with the global branch. This method not only reflects the importance of the top body characteristics but also covers the characteristics of the lower body. Through the upper 1/2, top 2/3, and top 3/4 blocks, characteristics such as head, torso, hands, and accessories are strengthened many several times. The bottom 1/2 block contains the characteristics of the lower body such as legs and shoes.

3. Experiments

The person reidentification network model experiment proposed in this paper uses NVIDIA V100 16G graphics card to accelerate calculations in the CUDA10 environment and is implemented based on the PyTorch open-source framework and Python language programming.

3.1. Experimental Datasets and Their Extension. The experimental data in this article come from the Market-1501 dataset and DukeMTMC-reID dataset. The Market-1501 dataset was collected on the campus of Tsinghua University. The images come from 6 different cameras, one of which is of low resolution. The dataset contains a total of 32,668 pictures of pedestrians with 1501 IDs. The training set has 751 IDs and a total of 12936 images. The test set has 750 IDs and a total of 19,732 images. In all training sets, there are on average 17.2 pieces of training data for each ID. The

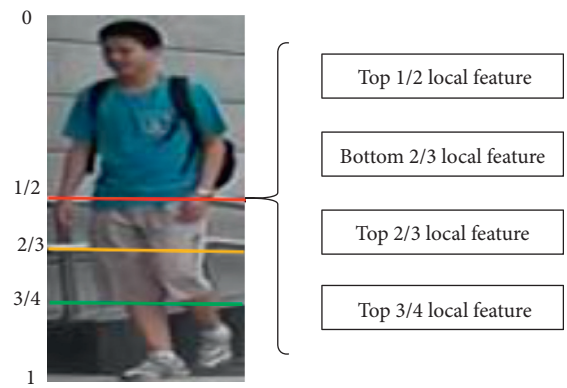

Figure 6: Schematic diagram of multiproportion block and reorganization.

DukeMTMC-reID dataset was collected at Duke University in the United States. The images came from 8 different cameras, and the borders of the pedestrian images were manually marked. The dataset provides training set and test set and has pedestrian attributes (gender, long and short sleeves, backpack, etc.) annotations. The training set contains 16522 images with a total of 702 IDs. On average, each ID has 23.5 training images, and the test set contains 17,661 images.

In order to improve the expression ability and generalization ability of the model, we expanded and preprocessed the dataset image, adopted random erasing, random horizontal flip, and data standardization [25], and adjusted the image size uniformly. The size is 384×128, and the RGB three-channel image is normalized with the mean value [0.485, 0.456, 0.406] and variance [0.229, 0.224, 0.225].

3.2. Experimental Parameters and Methods. In training, the ResNet50 model parameters pretrained on ImageNet dataset are used to initialize the model, and triplet hard loss with batch hard mining (TriHard loss) and cross entropy loss are used to accelerate convergence. The weight of triplet loss is

0.3, the margin is set to 1.2, and the weight of ID loss is 1, with label smoothing. In the model training, we first fix the initial weight of ResNet50 in the first 10 epochs and only train the weights of attention module and branch network and then continue training after releasing the last 90 epochs. The initial learning rate was 0.0003 when batch size was set to 32, and the learning rate decreased to 0.1 times at 30 and 60 epoch. In the experiment, Adam optimizer is selected to train the network. The momentum parameter is set to 0.9 and the weight attenuation coefficient is set to 0.0005. We also used label smoothing [28] and BNNeck [21] training methods.

In the test, the performance of the model was evaluated by two widely used indexes: Cumulative Match Characteristic (CMC) curve and mean average precision (mAP).

3.3. Experiment and Result Analysis. We use ResNet 50 as the baseline and then gradually add the designed modules for ablation experiments to observe the characteristics of the improvement measures of the model in this paper. The training and testing all adopt the aforementioned experimental parameters and methods. The added modules include Dual Ensemble Attention Module (DEAM), Combined Attention Fusion Module (CAFM), Multiscale Residual Fusion Module (MSFM), and local branch network (local-net). Among them, local-net $(n\text{-}1)/n$ means that the local branch is divided into n blocks with different proportions, and the upper $(n\text{-}1)/n$ part of the feature map is selected for local feature expression. We conducted experiments on the Market-1501 and DukeMTMC-reID datasets, respectively, and the comparison indicators were the mean average precision (mAP) and Rank-1 accuracy. The specific experimental results are shown in Table 1.

It can be seen from Table 1 that, on the Rank-1 accuracy of the Market-1501 dataset, the accuracy increased by 0.8% after adding DEAM based on the baseline (92.93%). On the basis of DEAM, we conducted more detailed experiments on local-net. It can be seen from the table that as the number of blocks increases, the accuracy rises. But when the number of blocks n is 5, the accuracy starts to decline, so our local-net selects the network structure when n is 4, and the Rank-1 accuracy reaches 95.57%. Then we added CAFM and MSFM to the comparative experiment based on the DEAM. It is found that the Rank-1 accuracy increases by about 0.5% after adding the two modules, but the mAP does not improve. After adding local-net, it is obvious that mAP and Rank-1 accuracies have increased significantly, which fully shows the importance of local branch. Finally, we combined all the improvement methods, and the mAP reaches 88.18% and Rank-1 accuracy reaches 96.20%. On the DukeMTMC-reID dataset, the Rank-1 accuracy increases with the addition of the above modules, reaching 89.59%.

From the overall ablation experiment, it is found that, in the Market-1501 dataset, the improvement method that has the greatest effect on the index improvement is the local-net design. This fully shows the effectiveness of multiproportion block scheme and the importance of local features. In terms of other modules, although the DEAM module is not as obvious as local-net, the accuracy is also greatly improved. For CAFM and MSFM modules, the improvement effect of single module may not be obvious. But, after using them together, especially with the local branch design, the experiment has achieved good results. To sum up, the modules we designed are effective.

In order to investigate the role of each module more comprehensively, we conducted a series of experiments on the Market-1501 dataset and obtained the CMC curve in the range of Ranks-1-40 of each module network, as shown in Figure 7. The abscissa of the CMC graph represents the number of hits, and the ordinate represents the hit probability of each rank. The five curves in Figure 7 are the performance of the ResNet50-based baseline after adding DEAM, local-net, CAFM, and MSFM. It can be seen from Table 1 and Figure 7 that the design modules and practices in this article have an improved identification index. The model in this paper incorporates the advantages of DEAM, local-net, CAFM, and MSFM, and the overall performance is greatly improved compared to the pure ResNet50. With the increase of each module, the performance also has a certain degree of improvement.

3.4. Comparison with Other Re-ID Models. We have compared the model with the person reidentification models based on Stripe, GAN, and Global Feature and Attention [7] in recent years. The experimental results are shown in Table 2. The scatter plot of several network indicators based on the Market-1501 dataset is shown in Figure 8.

As can be seen in Table 2, the Rank-1 (96.2%) accuracy of this model on the Market-1501 dataset is the same as Robust-ReID and is better than several other network models. mAP (88.2%) is better than other network models, except that it is slightly lower than Robust-Re-ID, SONA, and ABD-net. On the DukeMTMC-ReID dataset, the Rank-1 (89.6%) accuracy is higher than other network models except Robust-Re-ID, but the mAP (76.4%) is slightly lower than several models. This may be because the local part of the block combination has more features and there is greater redundancy. In the similarity comparison, although the first hit rate is high, the index on the n-th hit rate is not high, which leads to lower mAP. We will continue to pay attention and study this issue. In addition, we also performed a Re-ranking [36] experiment on the model in this paper, and the results are listed in the last row of Table 2. The results showed that mAP and Rank-1 accuracies reached 94.6% and 96.5% on the Market-1501 dataset, respectively, and mAP and Rank-1 accuracies reached 89.5% and 91.9% on the DukeMTMC-ReID dataset, respectively.

At the same time, the advantages of this model can be clearly seen in Figure 8. The overall index is better than the other 18 network models except Robust-Re-ID, especially in the Rank-1 accuracy.

3.5. Visualization Experiment and Results. We select four query sets on the Market-1501 dataset and perform Re-ID feature extraction [37] and similarity matching experiments [38] in the Gallery library. The matching results are shown in

Table 1: Ablation experiment results of each module.

Method	Market-1501		DukeMTMC-ReID	
	mAP	Rank-1	mAP	Rank-1
Baseline	84.14	92.93	72.75	85.95
Baseline + DEAM	85.28	93.73	75.21	87.52
Baseline + DEAM + CAFM	85.02	94.17	74.85	87.36
Baseline + DEAM + MSFM	84.87	94.29	75.46	87.43
Baseline + DEAM + local-net (1/2)	83.97	94.71	72.58	86.67
Baseline + DEAM + local-net (1/2 + 2/3)	84.76	94.95	73.75	86.40
Baseline + DEAM + local-net	87.54	95.57	77.10	87.75
Baseline + DEAM + local-net (+4/5)	87.13	95.15	74.56	87.84
Baseline + DEAM + local-net + CAFM	86.87	95.84	75.75	88.36
Baseline + DEAM + local-net + MSFM	87.44	95.90	76.12	88.30
Baseline + DEAM + local-net + CAFM + MSFM	**88.18**	**96.20**	**76.35**	**89.59**

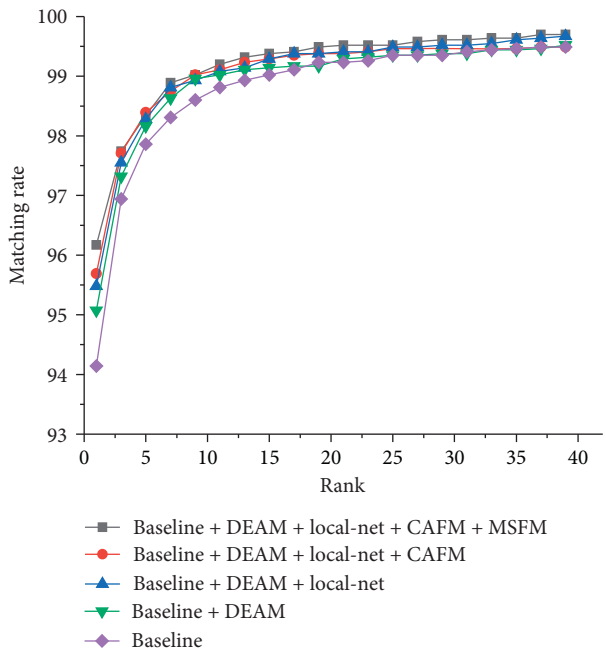

Figure 7: CMC curves of five networks on the Market-1501 dataset.

Table 2: Experimental results of this model compared with other Re-ID models.

Type	Method	Market-1501		DukeMTMC-reID	
		mAP	Rank-1	mAP	Rank-1
Stripe-based	AlignedReID [13]	77.7	90.6	67.4	81.2
	PCB + RPP [15]	81.6	93.8	69.2	83.3
	BFE [29]	85.0	94.5	75.8	88.7
	MGN [16]	86.9	95.7	78.4	88.7
	Pyramid [17]	88.2	95.7	79.0	89.0
	LocalCNN [30]	87.4	95.9	-	-
GAN-based	PN-GAN [31]	72.6	89.4	53.2	73.6
	DG-Net [32]	86.0	94.8	74.8	86.6
Global Feature	SVDNet [33]	62.1	82.3	56.8	76.7
	IA-Net [9]	83.1	94.4	73.4	87.1
	OS-Net [7]	84.9	94.8	73.5	88.6
	BagOfTricks [21]	85.9	94.5	76.4	86.4
	AGW [34]	87.8	95.1	79.6	89.0
Attention-based	MHN [10]	85.0	95.1	77.2	89.1
	ABD-Net [12]	88.3	95.6	78.6	89.0
	RGA-SC [35]	88.1	95.8	74.9	85.1
	SONA [12]	88.8	95.7	78.3	89.5
	Robust-ReID [8]	**89.7**	**96.2**	**80.3**	**89.8**
	Ours	88.2	**96.2**	76.4	89.6
	Ours(Re-rank)	**94.6**	**96.5**	**89.5**	**91.9**

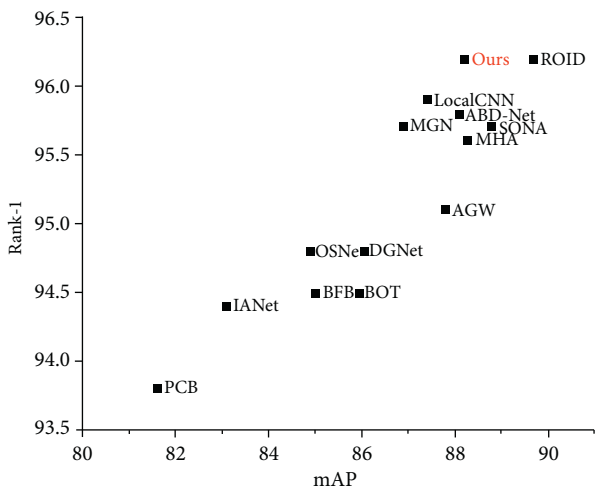

Figure 8: Comparison of indicators between this model and several other Re-ID network models.

Figure 9: Top-10 ranking list for some query images on Market-1501 datasets.

Figure 9. Figure 9 mainly shows the matching results of the images in Ranks-1–10. The green box indicates that the image matches the Gallery library image correctly, belonging to the same ID, and the red box indicates the matching error. It can be seen that, for most pedestrian images, although there are some factors such as background interference, low resolution, and misalignment, the model in this paper can match correctly and achieve high accuracy. It can also be seen from the matching errors of the two red boxes in Figure 9 that the reason for the matching error may be that the backpack covers the important information of the upper body of pedestrians or there are few positive samples, and the search is complete in Rank-8. Therefore, there are many reasons for model matching errors, such as less positive samples, less feature information, and more interference from occlusion and background.

4. Conclusions

Applying attention mechanism to improve the performance of person reidentification model has become a hot topic and has made some progress indeed. However, there are still some problems to be solved, such as matrix operation, coupling problem with original network, and optimizing attention. In this paper, person reidentification model, attention mechanism, and block scheme are studied, and a person reidentification model based on multiattention and multiscale residuals is proposed. Multiple attention models are added to the backbone network and global branches. The multiscale residuals and multiproportion block and reorganization are used to obtain better local and global features. The experimental results show that the model in this paper has some progress in indicators and has certain advantages.

Further, we also notice that although the indicators have improved to some extent, they are still not ideal, and there are still errors in Rank-n. We also analyze the reasons for them. In the next steps, we will continue to study Re-ID problems under occlusion and small samples conditions and try to give improvement or solutions. Another research direction is model lightweight. On the basis of ensuring the recognition rate, the lightweight model can reduce the requirement of system computing power and is better applied to the economic and efficient scene.

Data Availability

The data used to support the findings of this study are available from the corresponding author upon request.

Conflicts of Interest

The authors declare that there are no conflicts of interest regarding the publication of this paper.

References

[1] F. Wang, B. Zhao, C. Huang, and Y. Yan, "Person Re-identification based on multi-scale and attention fusion," *Journal of Electronics and Information Technology*, vol. 42, pp. 1–8, 2020.

[2] L. Zheng, Y. Yang, and A. G. Hauptmann, "Person Re-identification: past, present and future," in *Proceedings of the Computer Vision and Pattern Recognition*, Las Vegas, NV, USA, 2016.

[3] A. Hermans, L. Beyer, and B Leibe, "Defense of the triplet loss for person re-identificationencoding," in *Proceedings of the Computer Vision and Pattern Recognition*, pp. 1526–1535, Honolulu, HI, USA, 2017.

[4] H. Luo, W. Jiang, X. Fan, and S. Zhang, "A survey on deep learning based person Re-identification," *Acta Automatica Sinica*, vol. 45, no. 11, pp. 2032–2049, 2019.

[5] H. Liu, Z. Jie, K. Jayashree et al., "Video-based person Re-identification with accumulative motion context," *IEEE Transactions on Circuits and Systems for Video Technology*, vol. 28, no. 10, pp. 2788–2802, 2018.

[6] L. Wei, S. Zhang, W. Gao, and Q. Tian, "Person transfer GAN to bridge domain gap for person Re-identification," in

Proceedings of the Computer Vision and Pattern Recognition, pp. 79–88, Salt Lake City, UT, USA, 2018.

[7] K. Zhou, Y. Yang, A. Cavallaro, and T. Xiang, "Omni-scale feature learning for person Re-identification," in *Proceedings of the Computer Vision and Pattern Recognition*, pp. 3702–3712, Long Beach, CA, USA, 2019.

[8] H. Lawen, A. Bencohen, and M. Protter, "Attention network robustification for person ReID," in *Proceedings of the Computer Vision and Pattern Recognition*, Long Beach, CA, USA, 2019.

[9] R. Hou, B. Ma, H. Chang, X. GU, and S. Shan, "Interaction-and-aggregation network for person Re-identification," in *Proceedings of the Computer Vision and Pattern Recognition*, pp. 9317–9326, Long Beach, CA, USA, 2019.

[10] B. Chen, W. Deng, and J. Hu, "Mixed high-order attention network for person Re-identification," in *Proceedings of the Computer Vision and Pattern Recognition Proceedings of the Computer Vision*, pp. 371–381, Long Beach, CA, USA, 2019.

[11] T. Chen, S. Ding, J. Xie, Y. Yuan, and W. Chen, "ABD-net: attentive but Diverse person Re-identification," in *Proceedings of the Computer Vision and Pattern Recognition*, pp. 8351–8361, Long Beach, CA, USA, 2019.

[12] X. Bryan, Y. Gong, Y. Zhang, and P. Christian, "Second-order non-local attention networks for person Re-identification," in *Proceedings of the Computer Vision and Pattern Recognition*, pp. 3760–3769, Long Beach, CA, USA, 2019.

[13] X. Zhang, H. Luo, X. Fan et al., "Aligned-reID: surpassing human-level performance in person re-identification," 2018, https://arxiv.org/abs/1711.08184.

[14] H. Zhao, M. Tian, S. Sun, J. Shao, and J. Yan, "Spindle net: person re-identification with human body region guided feature decomposition and fusion," in *Proceedings of the Computer Vision and Pattern Recognition*, pp. 1077–1085, Honolulu, HI, USA, 2017.

[15] Y. Sun, L. Zheng, Y. Yang, Q. Yian, and S. Wang, "Beyond Part Models: person retrieval with refined Part Pooling (and A strong convolutional baseline)," in *Proceedings of the European conference on computer vision*, pp. 480–496, Munich, Germany, 2018.

[16] G. Wang, Y. Yuan, X. Chen, J. Li, and X. Zhou, *Learning Discriminative Features With Multiple Granularities For Person Re-Identification*, pp. 274–282, ACM multimedia, Chengdu, China, 2018.

[17] F. Zheng, C. Deng, X. Sun, X. Jiang, and R. Ji, "Pyramidal person Re-identification via multi-loss dynamic training," in *Proceedings of the Computer Vision and Pattern Recognition*, pp. 8514–8522, Long Beach, CA, USA, 2019.

[18] K. He, X. Zhang, S. Ren, and J. Sun, "Deep residual learning for image recognition," in *Proceedings of the Computer Vision and Pattern Recognition*, pp. 770–778, Las Vegas, NV, USA, 2016.

[19] J. Hu, L. Shen, S. Albanie, G. Sun, and E. Wu, "Squeeze-and-Excitation networks," *IEEE Transactions on Pattern Analysis and Machine Intelligence*, vol. 42, no. 8, pp. 2011–2023, 2019.

[20] X. Wang, R. Girshick, A. Gupta, and K. He, "Non-local neural networks," in *Proceedings of the Computer Vision and Pattern Recognition*, pp. 7794–7803, Salt Lake City, UT, USA, 2018.

[21] H. Luo, Y. Gu, X. Liao, S. Lai, and W. Jiang, "Bag of tricks and a strong baseline for deep person Re-identification," in *Proceedings of the Computer Vision and Pattern Recognition*, pp. 1487–1495, Long Beach, CA, USA, 2019.

[22] D. Fan, S. Fang, G. Wang, S. Gao, and X. Liu, "The visual human face super-resolution reconstruction algorithm based on improved deep residual network," *EURASIP Journal on Advances in Signal Processing*, vol. 1, pp. 1–10, 2019.

[23] X. Li, W. Wang, X. Hu, and J. Yang, "Selective kernel networks," in *Proceedings of the Computer Vision and Pattern Recognition*, pp. 510–519, Long Beach, CA, USA, 2019.

[24] X. Ma, J. Guo, S. Tang, Z. Qiao, and Q. Chen, "DCANet: learning connected attentions for convolutional neural networks," in *Proceedings of the Computer Vision and Pattern Recognition*, Washington, DC, 2020.

[25] X. Yu, Z. Zhang, L. Wu et al., "Deep ensemble learning for human action recognition in still images," *Complexity*, vol. 2020, no. 1, 23 pages, Article ID 9428612, 2020.

[26] J. Fu, J. Liu, H. Tian, Y. Li, and Y. Bao, "Dual attention network for scene segmentation," in *Proceedings of the Computer Vision and Pattern Recognition*, pp. 3146–3154, Long Beach, CA, USA, 2019.

[27] G. Wang, S. Gao, and D. Fan, "A G2G similarity guided pedestrian Re-identification algorithm," *Journal of Physics: Conference Series*, vol. 1453, Article ID 012035, 2020.

[28] Y. Lin, W. Chi, W. Sun, S. Liu, and D. Fan, "Human action recognition algorithm based on improved ResNet and skeletal keypoints in single image," *Mathematical Problems in Engineering*, vol. 2020, Article ID 6954174, 12 pages, 2020.

[29] Z. Dai, M. Chen, X. Gu, S. Zhu, and P. Tan, "Batch DropBlock network for person Re-identification and beyond," in *Proceedings of the Computer Vision and Pattern Recognition*, pp. 3690–3700, Long Beach, CA, USA, 2019.

[30] J. Yang, X. Shen, X. Tian, H. Li, and J. Huang, "Local convolutional neural networks for person reidentifification," in *Proceedings of the 2018 ACM Multimedia Conference on Multimedia Conference*, pp. 1074–1082, Seoul, Korea, 2018.

[31] X. Qian, Y. Fu, T. Xiang et al., "Pose-normalized image generation for person Re-identification," in *Proceedings of the European conference on computer vision*, pp. 661–678, Munich, Germany, 2018.

[32] Z. Zheng, X. Yang, Z. Yu, L. Zheng, and Y. Yang, "Joint discriminative and generative learning for person Re-identification," in *Proceedings of the Computer Vision and Pattern Recognition*, pp. 2138–2147, Long Beach, CA, USA, 2019.

[33] Y. Sun, L. Zheng, W. Deng, and S. Wang, "SVDNet for pedestrian retrieval," in *Proceedings of the Computer Vision and Pattern Recognition*, pp. 3820–3828, Washington, DC, 2020.

[34] M. Ye, J. Shen, G. Lin, T. Xiang, and C. Steven, "Deep learning for person re-identification: a survey and outlook," in *Proceedings of the Computer Vision and Pattern Recognition*, Washington, DC, 2020.

[35] Z. Zhang, C. Lan, W. Zeng, X. Jin, and Z. Chen, "Relation-aware global attention for person Re-identification," in *Proceedings of the Computer Vision and Pattern Recognition*, pp. 3186–3195, Washington, DC, 2020.

[36] Z. Zhong, L. Zheng, D. Cao, and S. Li, "Re-ranking person Re-identification with k-reciprocal encoding," in *Proceedings of the Computer Vision and Pattern Recognition*, pp. 3652–3661, Honolulu, HI, USA, 2017.

[37] Z. Yang, J. Liu, T. Liu, L. Wang, and S. Zhao, "Circle-based ratio loss for person reidentification," *Complexity*, vol. 2020, no. 12, 11 pages, Article ID 9860562, 2020.

[38] G. Wang, S. Wang, W. Chi, S. Liu, and D. Fan, "A person reidentification algorithm based on improved siamese network and hard sample," *Mathematical Problems in Engineering*, vol. 2020, Article ID 3731848, 11 pages, 2020.

Hindawi
Complexity
Volume 2021, Article ID 5519566, 11 pages
https://doi.org/10.1155/2021/5519566

Research Article

Modeling and Parameter Optimization of Dynamic Characteristic Variables of Ballast Bed during Operation for Dynamic Track Stabilizer

Bo Yan and Jingjing Yang

Kunming University of Science and Technology, Kunming 650500, China

Correspondence should be addressed to Jingjing Yang; 20170050@kust.edu.cn

Received 16 January 2021; Revised 8 February 2021; Accepted 2 March 2021; Published 11 March 2021

Academic Editor: Rui Wang

The high traffic density of railway line causes ballasted track to be extremely busy, and thus it is particularly important to improve the efficiency during railway maintenance. The changing law of dynamic characteristics of ballast bed during operation for the dynamic track stabilizer is conducive to optimize simulation analysis of the vehicle-track system, so as to provide an optimized choice of operating parameters for promoting the pertinence and efficiency of dynamic track stabilizer. This paper presents the acceleration response of vehicle-track-subgrade system during operation of a WD-320 dynamic track stabilizer and proposes the range of effective operating parameters. Then, the influence of operating parameters on the dynamic characteristics of the ballast bed is discussed for searching the optimal operating parameters under the single factor influence. Finally, the change laws including the support stiffness, damping, lateral resistance, and subsidence for the ballast bed are studied, and a parameterized model for dynamic characteristics of the ballast bed which can optimize the selection for operating parameters is constructed, rendering an effective reference variable for improving the simulation accuracy of the vehicle-track coupling system.

1. Introduction

At present, high speed and heavy loading are the development direction of the railway traffic system, which leads to the extremely busy status of railway transportation. In order to protect the railway system's security, stability, and high-speed operation, both academia and engineers have spent a lot of time and made great effort to study the rail and vehicle vibration problems, resulting in establishment of many analysis theories and methods [1, 2]. With the development of the study from an independent and simplified analysis to the coupling, complex, and large random system, the dynamics research of the vehicle-track system also gradually becomes mature [3–5]. At the same time, the quality of the railway line directly affects the safe and high-speed traffic of vehicles, so the maintenance of railway lines should be strengthened. Therefore, the large-scale railway maintenance equipment plays a significant role in railway traffic system. The common large-scale railway maintenance equipment includes screen cleaning vehicle, tamping vehicle, stabilizing vehicle, and ramming and stabilizing integrated vehicle. However, the simulation and experimental research on such equipment are limited. In this paper, in order to accelerate the development of modern railway construction, we provide some effective references for optimizing the large-scale railway maintenance equipment and improving the operation accuracy, operation efficiency, and track quality.

There are many particles in the ballast bed, which are discrete making the mechanisms of bearing and force transmission very complicated [6]. In general, after the railway maintenance operations such as bottom cleaning and tamping with the large mechanical equipment, the ballast of the ballast bed is not dense enough. After the operations of cleaning, tamping, and stabilizing, the lateral resistance of the sleeper can reach 80% of the level before railway maintenance; that is, the dynamic track stabilizer can

quickly improve the quality and the stability of the ballast bed [7]. When a dynamic track stabilizer operates on the complex vehicle-track-subgrade system, multiple factors including the operating parameters of the vehicle and the mechanical characteristics of the ballast bed will affect each other. It is essential to analyze and define the more important evaluation indicators for measuring the effect after the operations and confirming the influence on the quality state for track under different operating parameters, as well as establishing the optimal operating parameters model to maximize the values of the evaluation indicators. These efforts to improve the efficiency and effectiveness of stable operation definitely have significant practical value. In particular, it can provide theoretical references for the optimization and design of the stable device. The lateral resistance and the vertical resistance of the ballast bed are closely related to the stability of the track-subgrade system and track creep [8, 9]. The running vehicle directly applies dynamic load on the ballast bed through the track structure. Therefore, the dynamic characteristics of the ballast bed are the most critical factor for determining the passing speed of vehicles [10, 11]. In order to clearly discuss the contact force between the train wheels and the rail during the movement of the vehicle, a vehicle-track-subgrade system model has been constructed in the early work. Then the vibration response of the ballast bed and subgrade caused by the moving vehicle were simulated on the basis of the vehicle-track-subgrade interaction model [12–17]. Previous studies have found that there is a certain relationship between the geometric irregularity of the track and the settlement of the ballast bed. However, the discreteness and randomness of motion of the ballast make this relationship very complicated, and further in-depth and detailed research is very difficult [18]. The dynamic characteristics are an important index to evaluate the quality of the ballast bed, but they are difficult to obtain. It is a challenge to analyze and study the influence of unequal conditions of the quality for the ballast bed. Chou et al. [19] used the function method to achieve curve fitting and established a regression function model, which provides a good approach and reference for us. The adaptive repetitive learning control and the predefined time sliding mode control proposed by Wang et al. [20, 21] provide good research ideas for us. When the vehicle is passing, the overall state of the ballast bed is relatively no mutation, so the parameter values of the dynamic characteristics are relatively unchanged. After the dynamic track stabilizer passed the line in working, the ballasts are rearranged, and the density also is changed, resulting in a change in the overall state of the ballast bed. Therefore, the parameter values of the dynamic characteristics of the ballast bed will be changed also [22].

In this paper, we study the acceleration response of the vehicle-track-subgrade system during the operation of the WD-320 dynamic track stabilizer and propose the range for operation parameters of effective maintenance working. The structure and principle of dynamic track stabilizer are shown in Figures 1 and 2. Moreover, we also investigate the influence of operating parameters on the status of the ballast bed and put forward the optimal operating parameters under the single factor influence. Finally, the change laws of the support stiffness, damping, lateral resistance, and subsidence of the ballast bed are studied. A parameterized model of the dynamic characteristics of the ballast bed is constructed, which can optimize the selection of operating parameters to improve the efficiency during railway maintenance and effectively solve the problem of less maintenance time caused by high traffic density.

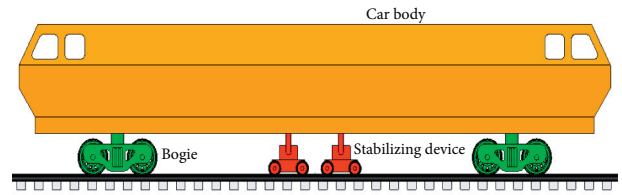

Figure 1: Structure diagram of the WD-320 dynamic track stabilizer.

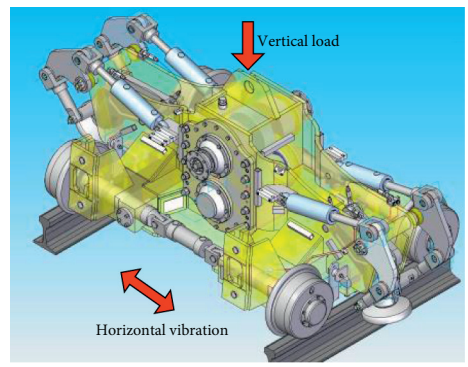

Figure 2: The principle of stabilizing device.

2. Field Test

The acceleration and displacement data of the body, bogie, stabilizer, rail, sleeper, and other components of the dynamic track stabilizer in different working parameters are very important dynamic responses. After obtaining the field test response of the dynamic track stabilizer, the measured data are compared with the simulation data to verify the practicality of the mathematical model established before, which is optimized to increase the simulation accuracy. Finally, the mathematical model is applied to the vehicle-track system's simulation, analysis, and optimization design. This paper conducts a more detailed field test. The main test's pieces of equipment are the WD-320 dynamic track stabilizer, two sets of Donghua DH-5922 dynamic signal test and analysis system (including sensors and computers), files, sandpaper, and so forth. The installation of the acceleration sensors is shown in Figures 3 and 4. Finally, the acceleration response data of each component were obtained.

We have gotten some effective opinions and demonstrations through field test and analysis, where the lateral resistance of sleepers is an important indicator and parameter in evaluating the quality state of the ballast bed. By

Figure 3: Sensor installation on the stabilizing device and bogie.

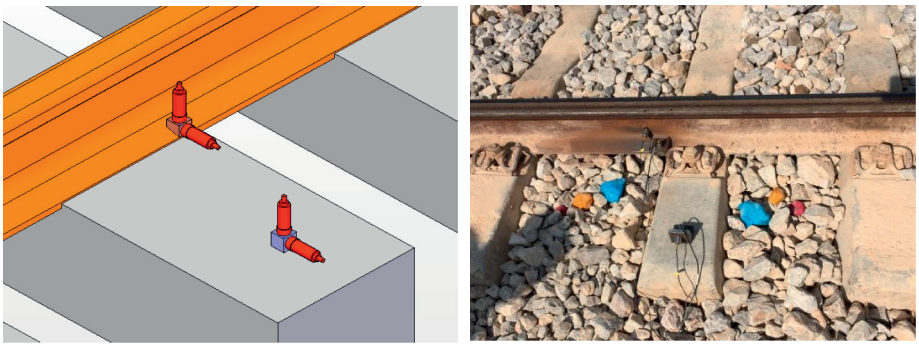

Figure 4: Schematic diagram of sensor installation on the rail and sleeper.

learning from some existing working principles and methods, we designed and manufactured a lateral resistance test device, which can easily get the lateral resistance value of sleepers to study the influence of different operating parameters. The schematic diagram and field test diagram are shown in Figures 5 and 6, respectively.

The test procedure is described as follows. We selected and marked three sleepers close to each other on a railroad and ensured that the ballasts under the sleepers are in similar state. Under a certain parameter, the tamping vehicle starts and passes through the marked sleepers. Then, remove the fasteners of the marked sleepers to separate the sleepers from the rail, and dig up part of the ballast on one side of the sleeper perpendicular to the rail. Subsequently, install the lateral resistance test device. Operate the test device to make the sleepers move 0.5, 1, 1.5, 2, 2.5, and 3 mm relative to the rail, and record the lateral resistance value of each marked sleeper at that time. After the test of each sleeper is completed, move the sleeper back to its original position. Furthermore, install the fasteners, and backfill the ballast to its original state. Subsequently, let the WD-320 dynamic track stabilizer work on the railway under given working parameters and pass the marked sleepers. Repeat the previous test process: remove the fasteners, install the device, measure and record the resistance value, move back the sleeper, install the fasteners, and backfill the ballast. So far, the different values of the lateral resistance when the sleeper moves at the same displacement in the two tests before and after can be obtained, that is, the change of the lateral resistance of the sleeper before and after the dynamic track stabilizer passes the railway line under a given working parameter [23]. Finally, after repeating experiments, the lateral resistance values of the sleeper under working with unequal operating parameters are successfully obtained.

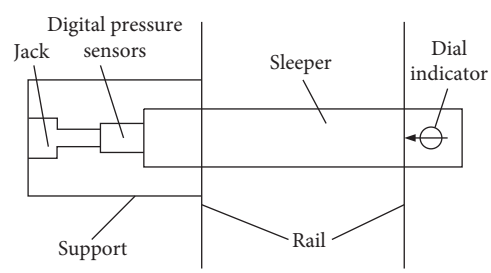

Figure 5: Schematic diagram of device for lateral resistance test.

Figure 6: Lateral resistance test of sleeper.

3. Acceleration Response Analysis

Through the dynamic signal test and analysis, the dynamic response signals of the vehicle-track system under different operating parameters, including vehicle speed, vibration frequency, and down pressure, are obtained. As shown in Figure 7, the lateral acceleration and vertical acceleration of sleepers versus time are given when vehicle-track system operated at a fixed speed of 1.5 km/h and a vibration frequency of 28 Hz under the pressure conditions of 50, 60, and 70 bar, respectively.

The signal envelope analysis method is utilized to analyze the time-domain signals of the acceleration of each component of the vehicle-track system, which are obtained by field tests for studying the influence of different operating parameters on each component of the system.

The corresponding envelope curves based on the relevant public announcement of envelope calculation have been calculated and drawn, as shown in Figures 8–11.

It has been observed from Figure 10 that when the operating pressure is less than or equal to 60 bar, as the operating pressure increases, the acceleration dynamic response of the rail does not change significantly. However, when the operating pressure reaches 70 bar, the acceleration dynamic response of the rail increases significantly and, in particular, has a sudden change. Therefore, for the steel rails, it is not recommended to select the value of pressure greater than or equal to 70 bar as the down pressure parameter during operation. Similarly, the operating vibration frequency should not exceed 30 Hz.

4. Ballast Bed Quality Status Analysis

The evaluation indicators and parameters of the quality state of the ballast bed are complex and are affected by many factors, including the particle index characteristics and fouling rate of ballast, the support stiffness and resistance of sleeper, elasticity and permeable performance of ballast bed, density, irregularity of the track, and physical geometry size of ballast bed [24, 25]. The track geometry and position refer to the geometry, relative positions, and basic dimensions of each part of the track. Under the premise of ensuring the track geometry and position, the ballast bed state can be roughly appraised by measuring the lateral resistance [26]. Based on the real-time measurement, feedback, and adjustment of the high-precision measurement system of the large railway maintenance vehicles, the railway line after the maintenance working will have better track geometry and position. In summary, the quality of the track bed can be roughly appraised by comparing the value of the lateral resistance of the sleeper after maintenance working [23].

When the WD-320 dynamic track stabilizer was tested in the field, the vehicle's working speed was set as 1.2 km/h, 1.5 km/h, and 1.8 km/h, the vibration frequency was set as 20 Hz, 22 Hz, 25 Hz, 28 Hz, 30 Hz, and 35 Hz, and the pressure was set as 50 bar, 60 bar, and 70 bar, respectively. The lateral resistance value in each working state was recorded, and then the changes in the lateral resistance of the sleeper before and after the operation were analyzed. The curves of the increase rate of the lateral resistance of the sleeper after the operation under different vibration parameters are fitted out, as shown in Figure 12.

It can be found from Figure 12 that the lateral resistance value of the sleeper increases a lot after the operation at the vibration frequencies of 18, 22, 25, 28, and 30 Hz. The lateral resistance value is not increased or the increase is not obvious after operation at frequencies less than 18 Hz or more than 30 Hz. When a certain value between 18 Hz and 30 Hz is selected as the vibration frequency parameter of operation, the quality state of the ballast bed will be improved effectively. It demonstrates that 18–30 Hz is the effective range of vibration frequency for the WD-320 dynamic track stabilizer. Moreover, when the value of the vibration frequency parameter is between 25 and 30, the quality state of the ballast bed is significantly improved. The analysis found that the optimal vibration frequency of operation for the dynamic track stabilizer is 28 Hz.

Using the same method for comparative analysis, it can be found that the effective range of pressure for the WD-320 dynamic track stabilizer is 50–70 bar, and the optimal operating parameter of pressure is 60 bar.

The influence of different working speeds on the lateral resistance value is not obvious, so that the difference in the vehicle speed does not affect the quality state of the ballast bed effectively.

5. Dynamic Analysis of Ballast Bed

5.1. EDEM Simulation. In recent years, the discrete element method has developed rapidly, and it has become an important method that is widely used in the study of solid particles. Using this method to simulate the working process of a dynamic track stabilizer, the dynamic response characteristics of the vehicle-track-subgrade system can be studied appropriately. In this paper, the software of extended distinct element method (EDEM) was used for simulation analysis. In order to avoid the huge computational workload caused by simulating the entire vehicle-track system, the movement of a sleeper was simply simulated. Five kinds of typical ballast particles were selected, for making the simulation closer to the reality of railway, as shown in Figure 13. We superimposed spheres of different radii to form a complex-shaped composite particle and thereby established an irregular-shaped ballast particle model. Then, the response during operation with different parameters was simulated, and the corresponding dynamic characteristic data of the ballast bed were extracted.

5.2. Lateral Resistance Analysis. According to the simulation data, the lateral resistances of the sleeper when the sleeper moves 0.5, 1, 1.5, 2, 2.5, and 3 mm were extracted, and then the curves of the lateral resistance under different working conditions were drawn, as shown in Figures 14 and 15.

Figures 14(a)–14(d) show the lateral resistances of sleeper under different conditions, in which the vibration frequencies were fixed at 20 Hz, 25 Hz, 28 Hz, and 30 Hz and the pressures were set up as 40 bar, 50 bar, and 60 bar,

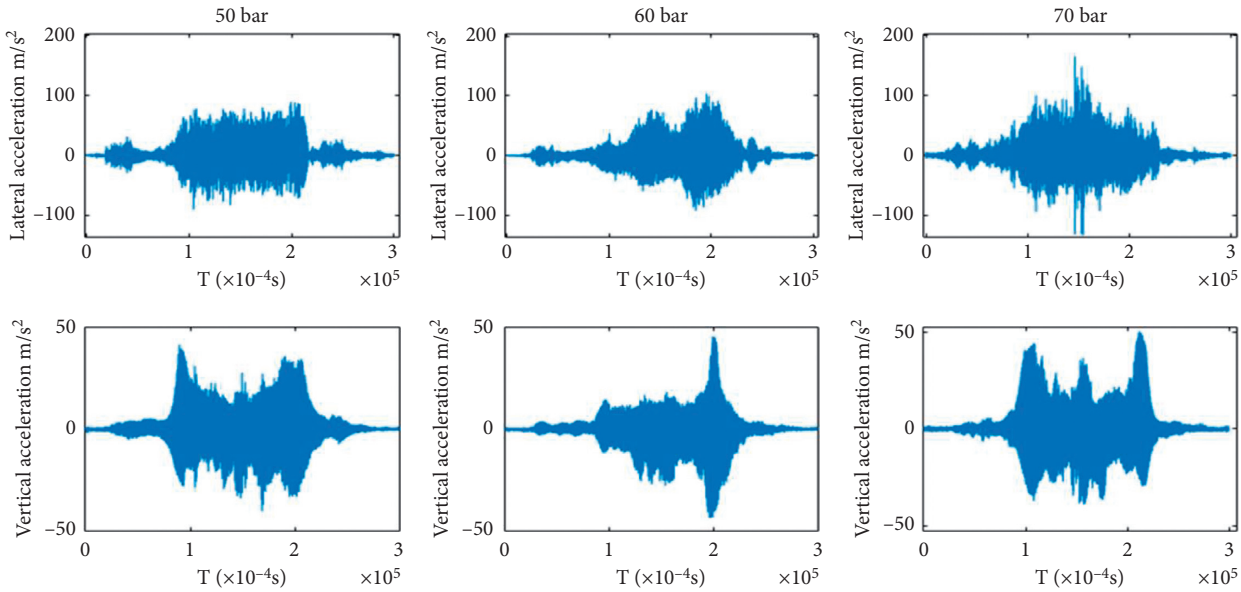

Figure 7: Comparison of acceleration of sleeper under different pressures.

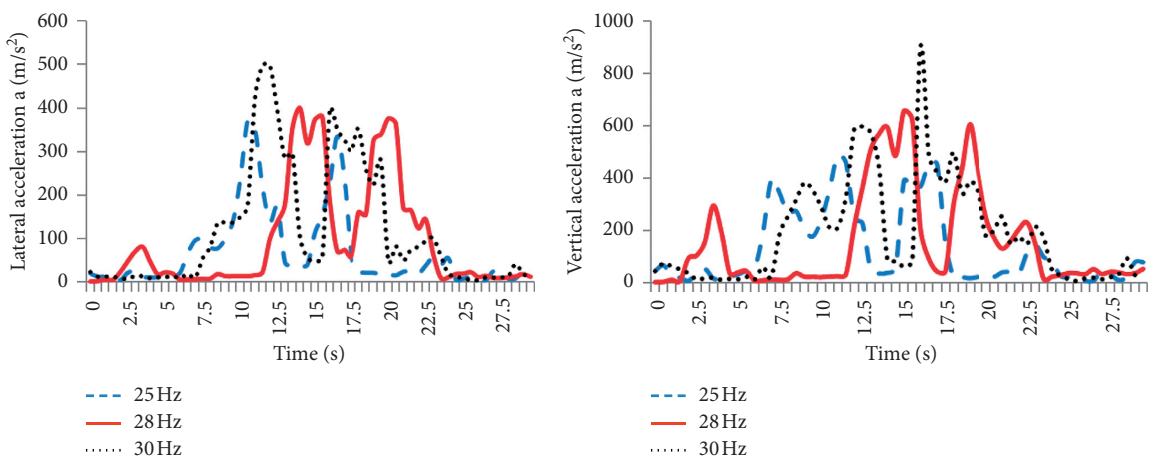

Figure 8: The envelope of acceleration of rail under different vibration frequencies.

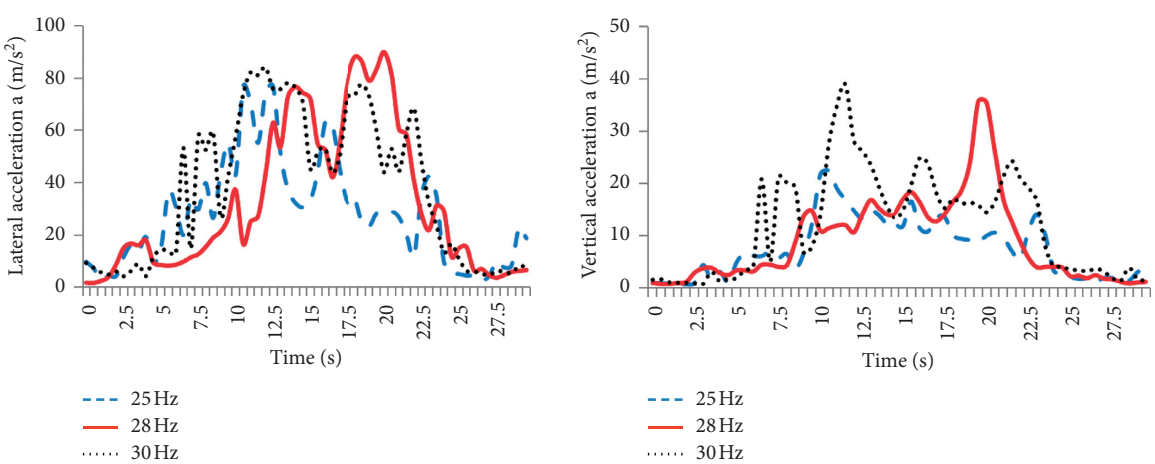

Figure 9: The envelope of acceleration of sleeper under different vibration frequencies.

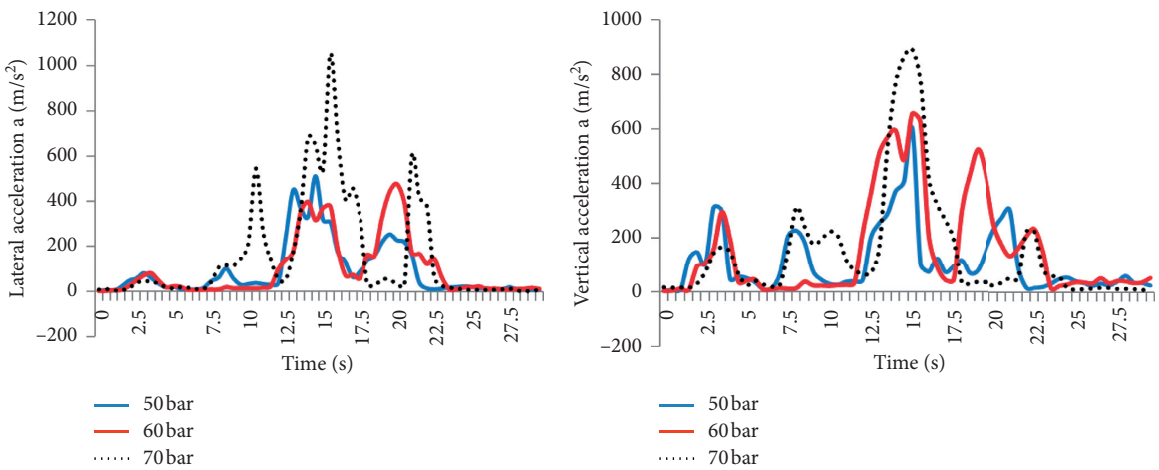

Figure 10: The envelope of acceleration of rail under different pressures.

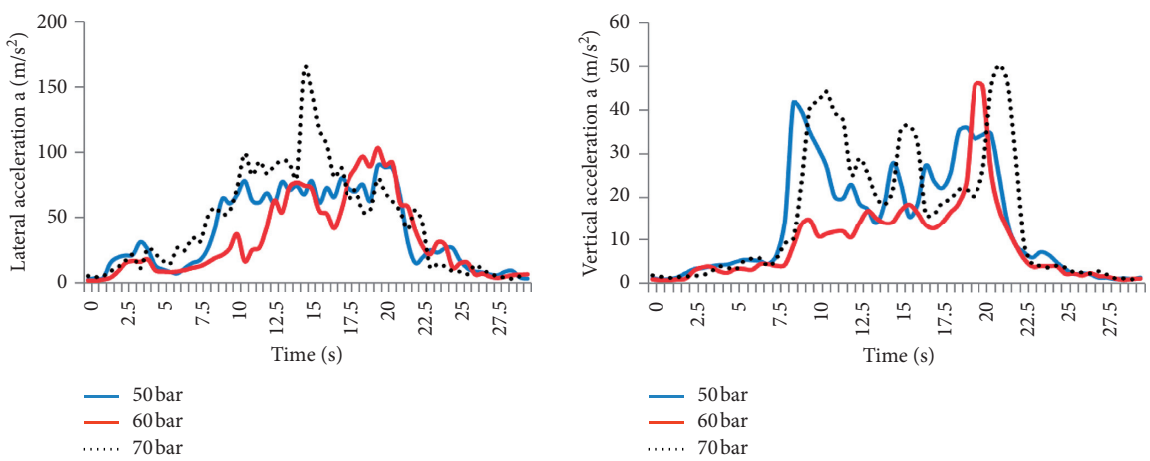

Figure 11: The envelope of acceleration of sleeper under different pressures.

respectively. It can be seen from Figure 14 that, after operation in different working conditions under the fixed vibration frequency and different pressures, as the sleeper moves laterally to the same displacement, the lateral resistance value of the sleeper under the 60 bar working condition was always the largest and increased steadily. Therefore, the 60 bar working condition is the optimal pressure for the ballast bed to quickly reach a better quality state. Figures 15(a) and 15(b) show the lateral resistances of sleeper under different conditions that the vibration frequencies were set up as 20 Hz, 25 Hz, 28 Hz, and 30 Hz, and the pressures were fixed at 50bar and 60bar, respectively. It can be seen that, after operating in different working conditions with the same pressure and different vibration frequencies, the lateral resistance value of the sleeper at 28 Hz was steadily increased without sudden changes.

In summary, under the operating conditions of 60 bar pressure and 28 Hz vibration frequency, the lateral resistance of the sleeper increased stably, so that the ballast bed can reach a better quality state quickly. This conclusion is consistent with the factory site.

5.3. Stiffness Influence Analysis. In the discrete element method, the plant model is divided into independent units, and the position of all cells is updated at each time step. By tracking and analyzing the microscopic motion of each element, the macroscopic motion of the entire object is obtained [27]. The damping of the ballast bed and the stiffness of the support sleeper are two important characteristic parameters for studying the dynamic characteristics of the ballast bed.

According to $K = F/\triangle Z$, a constant force is applied to the ballast bed at a certain moment of the simulation analysis, and then the compression amount of the ballast bed is obtained. Finally, the support stiffness of the sleeper at this time is calculated. For a single-degree-of-freedom damped vibration system similar to the entire track bed, the damping can be calculated from the free vibration attenuation curve, which is a common method. According to the differential equations of motion, Euler's formula, and shock experiment data, the damping vibration curve of a single-degree-of-freedom system can be obtained easily [22].

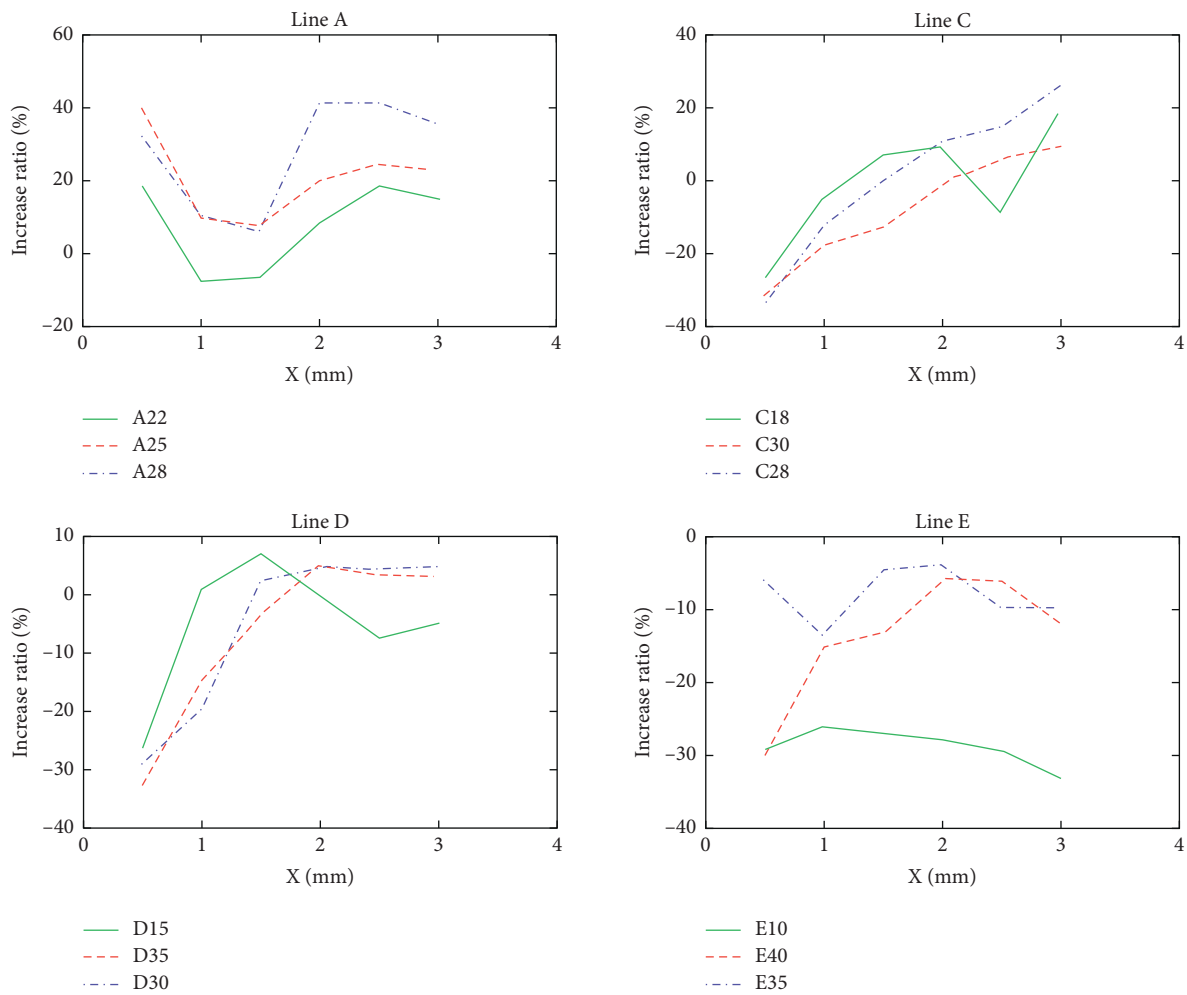

Figure 12: Comparison of the lateral resistance.

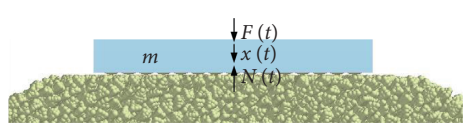

Figure 13: The analysis model of sleeper-track bed system.

Assuming that, in a vibration period, the peak values of vibration displacement were A1 and A2, the logarithmic decrement can be expressed as

$$\delta = \ln A_1 - \ln A_2 = \xi\omega_n T = \xi\omega_n \frac{2\pi}{\omega_d} = \frac{2\pi\xi}{\sqrt{1-\xi^2}}. \quad (1)$$

Then, according to the above formula, ξ can be calculated. Finally, the value of damping can be obtained as

$$\xi = \delta / \sqrt{4\pi^2 + \delta^2}, \quad (2)$$

$$c = 2\xi\sqrt{mk}. \quad (3)$$

The compression amount of the ballast bed at a moment can be found by analyzing the simulation data. Due to the fact that $F = K^* \triangle Z$, the supporting stiffness values of the sleeper at the moment can be calculated. Analyze the data and get the attenuation peak values of A1 and A2, and then calculate the damping value by formulas (1)–(3). The curve of the settlement of the integrated ballast with the time is shown in Figure 16. The curve of increase ratio of the sleeper support stiffness under different working conditions is shown in Figure 17.

5.4. Mechanical Characteristic Variable Model. In order to reduce the amount of calculation and shorten the calculation time, we simplified the details and conditions when using the EDEM software for simulation. For example, the details of the ballast particles were not refined, and the collision between particles and ballast slip damage was not considered. Therefore, there must be a certain difference between simulation and reality, but it will not affect the result. As

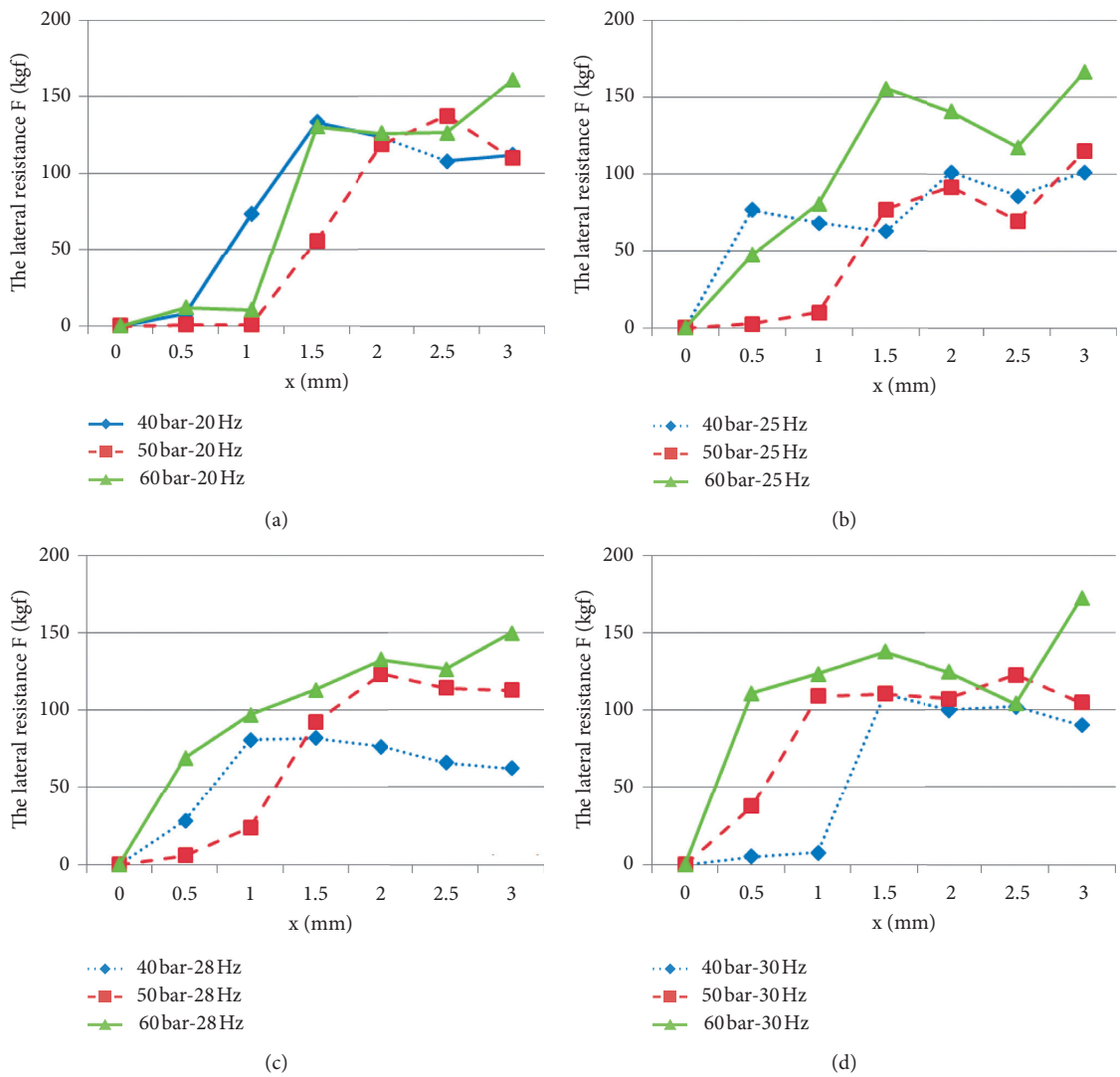

Figure 14: The curve of the lateral resistance under fixed frequencies and different pressures.

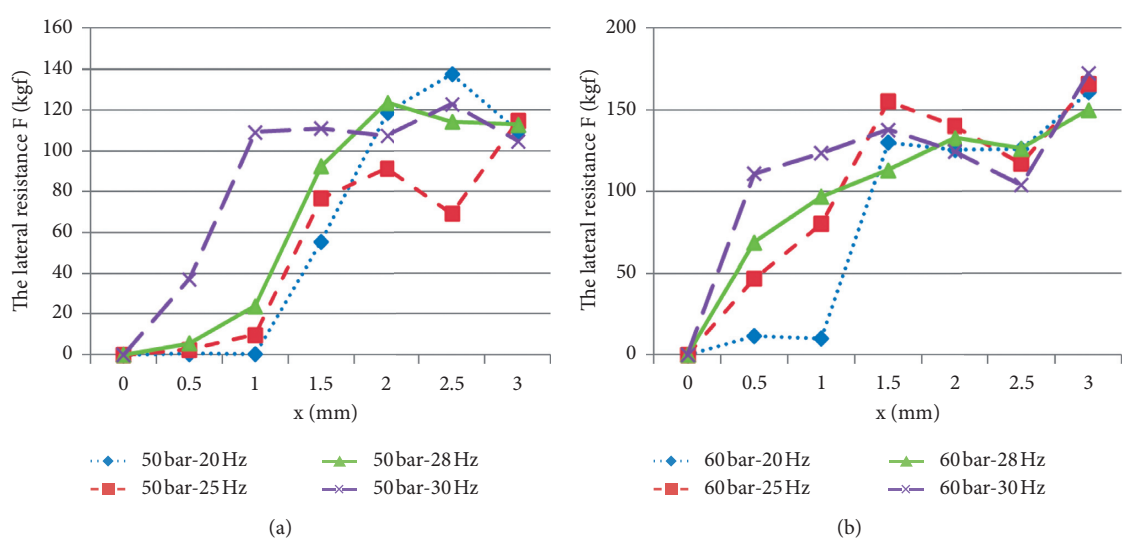

Figure 15: The curve of the lateral resistance under different frequencies and fixed pressures.

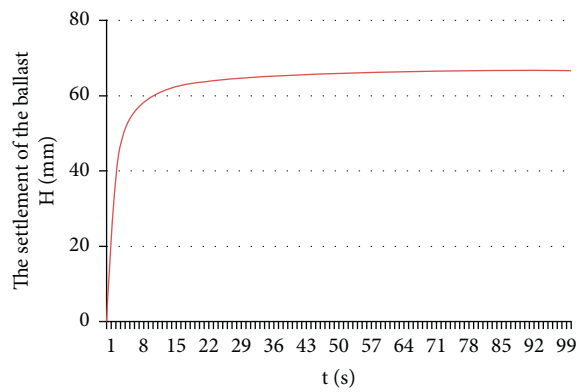

Figure 16: The curve of the settlement of the integrated ballast with the time.

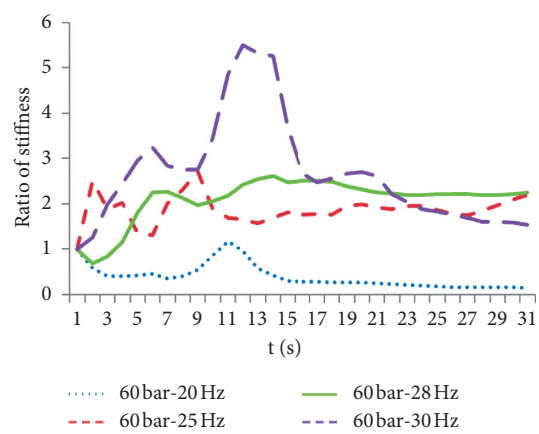

Figure 17: The curve of increase ratio of the sleeper support stiffness under different working conditions.

mentioned earlier, we have verified the consistency between the simulation results and the real situation, indicating that EDEM simulation has a good reference function and can be used to study the changes and development trends of the real situation. Therefore, it is feasible to use the EDEM software to simulate the operating process, as well as studying the influence on the stiffness of the sleeper support and the damping of the ballast bed under different working conditions of the dynamic track stabilizer.

In the simulations of previous scholars, the response of the running vehicle under the steady state of the ballast bed was studied. At this time, the dynamic characteristic parameters of the ballast bed are all equivalent parameters with fixed values. There is no research on the change of the dynamic characteristics of the ballast bed during the working process of the maintenance equipment. During the working process, the values of dynamic performance parameter for the ballast bed are constantly changing over time, but these parameter values cannot be easily measured. Therefore, it is necessary to study the change law of the dynamic characteristic parameters of the ballast bed during working process and propose a time function model of these parameters, which is very important to improve the accuracy of the simulation.

Through the above research, we have obtained the optimal operating parameters under a single factor influence. Therefore, we used simulation to study the change of the supporting stiffness with time under the pressure parameter that was fixed at 60 bar and the vibration frequency parameter that was fixed at 28 Hz. Assuming that K_0 is the value of sleeper supporting stiffness after operation of the tamping vehicle, K_t is the value of sleeper supporting stiffness after operation with the dynamic track stabilizer for t seconds. For $B = K_t/K_0$, B is the ratio of sleeper supporting stiffness before and after operation with the dynamic track stabilizer [22]. Based on the analysis data, the fitting curve of B with time was drawn under the working condition with the optimal operating parameters, as shown in Figure 18. The figure shows that the value of B increases rapidly with time in the initial stage. Moreover, the increase of B value gradually stabilizes after 3 seconds. From Figure 16, it can be found that, after the operation time exceeds 30 seconds, the ballast bed basically no longer settles, and it reaches a relatively stable state. After that, the supporting stiffness of the sleeper and the damping of the ballast bed basically no longer change with time. The regression analysis was carried out by MATLAB software, and the functional model of sleeper supporting stiffness changing with time under operation with the optimal parameters was obtained:

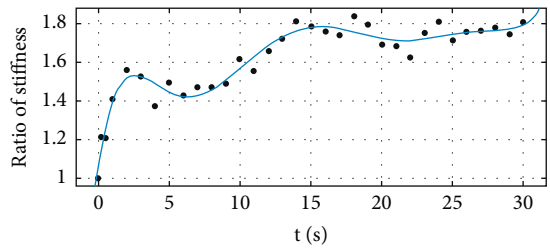

Figure 18: The ratio curve of the sleeper support stiffness.

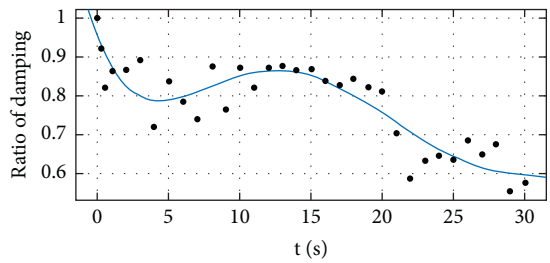

Figure 19: The ratio curve of ballast damping.

$$K_t = \left(\begin{array}{c} 1.579e^{-8}t^7 - 1.886e^{-6}t^6 + 9.007e^{-5}t^5 - 2.18e^{-3}t^4 + 2.786e^{-2}t^3 \\ -1.775e^{-1}t^2 + 4.928e^{-1}t + 1.049 \end{array} \right) K_0, \quad (0 \le t \le 30). \tag{4}$$

Similarly, assuming that C_0 is the value of ballast damping after operation of the tamping vehicle, C_t is the value of ballast damping after operation with the dynamic track stabilizer for t seconds. For $E = C_t/C_0$, E is the ratio for the value of ballast damping before and after operation with the dynamic track stabilizer. Based on the analysis data, the fitting curve of E with time was drawn under the working condition with the optimal operating parameters, as shown in Figure 19. The regression analysis was carried out by MATLAB software, and the functional model of the damping changing with time under working with the optimal operating parameters was constructed:

$$C_t = \left(-3.45e^{-7}t^5 + 3.401e^{-5}t^4 - 1.19e^{-3}t^3 + 1.709e^{-2}t^2 - 9.259e^{-2}t + 0.9515\right)C_0. \tag{5}$$

We constructed the parameterized models C_t and K_t for the dynamic characteristics of the ballast bed, which provides an effective reference variable for improving the accuracy of the simulation of the vehicle-track coupling system.

6. Conclusion

In the paper, we have taken the WD-320 dynamic track stabilizer as a research target to study the acceleration response of the ballast bed during the operation, the influence of operating parameters on the quality state of the ballast bed, and the changing law of the supporting stiffness, damping, and subsidence of the ballast bed. We have found that 18–30 Hz is the effective range of vibration frequency parameter for the dynamic track stabilizer, and when the value of the vibration frequency parameter is between 25 and 30, the quality state of the ballast bed is significantly improved. The optimal operating parameter of vibration frequency for the WD-320 dynamic track stabilizer is 28 Hz. Moreover, the effective range of pressure parameter for the WD-320 dynamic track stabilizer is 50–70 bar, and the optimal operating parameter of pressure is 60 bar. Finally, we have constructed the parameterized models C_t and K_t for the dynamic characteristics of the ballast bed which can optimize the selection of operating parameters, which provides an effective reference variable for improving the accuracy of the simulation of the vehicle-track-subgrade coupling system. The above results revealed that it can improve the efficiency during railway maintenance and effectively solve the problem of less maintenance time caused by high traffic density.

Data Availability

The data were curated by the authors and are available upon request.

Conflicts of Interest

The authors declare that there are no conflicts of interest regarding the publication of this paper.

Acknowledgments

This work was supported in part by KUST Talent Introduction Scientific Research Program (Grant nos. KKSY201855004 and KKSY201765024).

References

[1] S. Dietz, G. Hippmann, and G. Schupp, "Interaction of vehicles and flexible tracks by co-simulation of multibody vehicle systems and finite element track models," *Vehicle System Dynamics*, vol. 37, no. sup1, pp. 372–384, 2002.

[2] K. Popp, I. Kaiser, and H. Kruse, "System dynamics of railway vehicles and track," *Archive of Applied Mechanics*, vol. 72, no. 11, pp. 949–961, 2003.

[3] N. Chaar and M. Berg, "Simulation of vehicle-track interaction with flexible wheelsets, moving track models and field tests," *Vehicle System Dynamics*, vol. 44, no. sup1, pp. 921–931, 2006.

[4] W. M. Zhai, *Vehicle Track Coupling Dynamics*, Science Press, Beijing, China, Third edition, 2007.

[5] J. Oscarsson, "Dynamic train-track-ballast interaction with unevenly distributed track properties," *Vehicle System Dynamics*, vol. 37, no. sup1, pp. 385–396, 2002.

[6] J.-l. Xiao, H. Liu, J.-M. Xu, P. Wang, G.-Z. Liu, and R. Chen, "Longitudinal resistance performance of granular ballast beds under cyclic symmetric displacement loading," *Journal of Zhejiang University-Science A*, vol. 18, no. 8, pp. 648–659, 2017.

[7] F. D. Zhao, *Dynamic Track Stabilizer*, China Railway Press, Beijing, China, 2006.

[8] A. Kish and G. Samavedam, "Dynamic buckling of continuous welded rail track: theory, tests, and safety concepts," *Transportation Research Record*, vol. 29, no. 1289, pp. 23–38, 1991.

[9] M. Esmaeili, R. Nouri, and K. Yousefian, "Experimental comparison of the lateral resistance of tracks with steel slag ballast and limestone ballast materials," *Proceedings of the Institution of Mechanical Engineers, Part F: Journal of Rail and Rapid Transit*, vol. 231, no. 2, pp. 175–184, 2017.

[10] H. L. Yao, Z. Hu, Z. Lu, and H. Wang, "Analytical model to predict dynamic responses of railway subgrade due to highspeed trains considering wheel-track interaction," *International Journal of Geomechanics*, vol. 16, no. 2, p. 15, Article ID 0401506, 2016.

[11] L. A. Yang, W. Powrie, and J. A. Priest, "Dynamic stress analysis of a ballasted railway track bed during train passage," *Journal of Geotechnical and Geoenvironmental Engineering*, vol. 135, no. 5, pp. 680–689, 2009.

[12] G. Kouroussis and O. Verlinden, "Prediction of railway induced ground vibration through multibody and finite element modelling," *Mechanical Sciences*, vol. 4, no. 1, pp. 167–183, 2013.

[13] G. Kouroussis, D. Connolly, P. K. Vogiatzis, and O. Verlinden, "Modelling the environmental effects of railway vibrations from different types of rolling stock: a numerical study," *Shock and Vibration*, vol. 2015, p. 15, Article ID 142807, 2015.

[14] P. Alves Costa, R. Calçada, and A. Silva Cardoso, "Track-ground vibrations induced by railway traffic: in-situ measurements and validation of a 2.5 D FEM-BEM model," *Soil Dynamics and Earthquake Engineering*, vol. 32, no. 1, pp. 111–128, 2011.

[15] C. H. Chiang and P. H. Tsai, "A numerical study of the screening effectiveness of open trenches for high-speed train-induced vibration," *Shock and Vibration*, vol. 2014, p. 15, Article ID 489090, 2014.

[16] W. Zhai, Z. He, X. Song, and X. Li, "Prediction of high-speed train induced ground vibration based on train-track-ground system model," *Earthquake Engineering and Engineering Vibration*, vol. 9, no. 4, pp. 545–554, 2011.

[17] P. Galvín, A. Romero, and J. Domínguez, "Vibrations induced by HST passage on ballast and non-ballast tracks," *Soil Dynamics and Earthquake Engineering*, vol. 30, no. 9, pp. 862–873, 2010.

[18] W. M. Zhai, C. F. Zhao, H. Xia et al., "Basic scientific issues on dynamic performance evolution of the high-speed railway infrastructure and its service safety (in Chinese)," *Science in China Series E-Technological Sciences*, vol. 44, pp. 645–660, 2014.

[19] Y. X. Chou, Y. Gu, J. C. Liu et al., "Modelling arterial blood pressure waveforms for extreme bradycardia and tachycardia by curve fitting with Gaussian functions," *International Journal of Modelling, Identification and Control*, vol. 32, pp. 3-4, 2019.

[20] S. Wang, J. Na, and Q. Chen, "Adaptive predefined performance sliding mode control of motor driving systems with disturbances," *IEEE Transactions on Energy Conversion*, p. 1, 2020.

[21] Q. Chen, X. Yu, M. Sun, C. Wu, and Z. Fu, "Adaptive repetitive learning control of PMSM servo systems with bounded nonparametric uncertainties: theory and experiments," *IEEE Transactions on Industrial Electronics*, p. 1, 2020.

[22] B. Yan, Y. Y. Huang, B. Hu, and X. J. Wang, "Mechanical characteristics optimization of ballast bed variable on operating process for the dynamic track stabilizer," in *Proceedings of the 9th International Conference On Modelling, Identification and Control*, pp. 874–879, Kunming, China, July 2017.

[23] B. Yan, B. Hu, and Y. Y. Huang, "Prediction model with optimal matching parameters for a dynamic track stabilizer during railway maintenance," *International Journal Modelling, Identification and Control*, vol. 33, no. No. 4, pp. 369–377, 2019.

[24] Y. Hao, *Railway Engineering*, China Railway Press, Beijing, China, 2000.

[25] S. G. Zeng, *Railway Discrete Ballast Track*, China Railway Press Publishers, Beijing, China, 1997.

[26] F. Chen, *Research on Technical Measures to Improve the Speed of Railway Opening*, Doctoral Dissertation, Beijing Jiaotong University, Beijing, China, 2007.

[27] G. M. Hu, *Discrete Element Analysis and Simulation of Particle System*, Wuhan University of Technology press, Wuhan, China, 2010.

Hindawi
Complexity
Volume 2021, Article ID 6687146, 9 pages
https://doi.org/10.1155/2021/6687146

Research Article

Defect Detection of Pandrol Track Fastener Based on Local Depth Feature Fusion Network

Zhaomin Lv, Anqi Ma, Xingjie Chen, and Shubin Zheng

School of Urban Rail Transportation, Shanghai University of Engineering Science, Shanghai 201620, China

Correspondence should be addressed to Zhaomin Lv; zhaomin_lv@sues.edu.cn

Received 19 November 2020; Revised 3 February 2021; Accepted 24 February 2021; Published 4 March 2021

Academic Editor: Rui Wang

There are three main problems in track fastener defect detection based on image: (1) The number of abnormal fastener pictures is scarce, and supervised learning detection model is difficult to establish. (2) The potential data features obtained by different feature extraction methods are different. Some methods focus on edge features, and some methods focus on texture features. Different features have different detection capabilities, and these features are not effectively fused and utilized. (3) The detection of the track fastener clip will be interfered by the track fastener bolt subimage. Aiming at the above three problems, a method for track fastener defects detection based on Local Deep Feature Fusion Network (LDFFN) is proposed. Firstly, the track fastener image segmentation method is used to obtain the track fastener clip subimage, which can effectively reduce the interference of bolt subimage features on the track fastener clip detection. Secondly, the edge features and texture features of track fastener clip subimages are extracted by Autoencoder (AE) and Restricted Boltzmann Machine (RBM), and the features are fused. Finally, the similarity measurement method Mahalanobis Distance (MD) is used to detect defects in track fasteners. The effectiveness of the proposed method is verified by real Pandrol track fastener images.

1. Introduction

With the continuous growth of the world economy, railway transportation plays a more and more important role in the economic lifeline. In order to meet the growing demand for economic development, railway construction has also increased year by year. Railway track is composed of several key parts, such as sleeper, rail, and fastener. As the connecting part of fixed track and sleeper, track fastener is an important part to ensure the safety of railway operation. Huge safety risks and even major accidents were caused by the defective track fasteners, such as breaks or missing. Defective track fastener is caused by the contact friction and vibration impact between the hub and the track, as well as the impact of the natural environment [1, 2].

At present, the state of track fasteners is mainly detected by manual inspection. Manual inspection method is inefficient, and many uncontrollable risk factors may be caused by manual inspection, such as missed inspection and false inspection. With the rapid development of automation technology [3–6], manual inspection has been difficult to adapt to the rapid development of track transit. The inspection of track traffic needs to be automated. Automating the track fastener detection technology [7, 8] is significant to track operation and maintenance. However, the existing track fastener defect detection methods are limited, and the detection accuracy is low.

In recent years, with the rapid development of artificial intelligence technology [9, 10], image processing methods based on deep learning have become a research hotspot [11–13]. Deep learning networks have achieved important research results in image classification [14, 15]. The defect detection method of track fastener based on deep learning avoids complicated feature extraction. The manual design and selection of image features are replaced by automatic extraction of image features by computer. The deep learning network automatically learns the pattern recognition system of features from the data set, and the information in the image can be extracted more comprehensively [16]. Although the feature extraction of deep learning is shown to be

far superior to traditional "artificial design features," the existing track fastener defect detection network based on deep learning is a supervised network, and a large amount of labeled sample data is required for a supervised network. For example, when using convolutional neural networks to detect defects in track fasteners [17], a large number of labeled training sample images are required. However, the actual situation is that the number of abnormal samples of track fastener is rare, which is limited for the establishment of supervised learning model.

Because the supervised network is limited by the number of abnormal fastener images, it is difficult to establish, so the unsupervised network is adopted. However, different deep learning networks have different structure and depth. With different deep learning networks, the features of track fastener image are extracted differently, and the detection ability of different features is also different. The feature information of track fastener image extracted by single network is not comprehensive enough, and the feature information of track fastener image cannot be used well. For example, the edge feature of the track fastener image is extracted [18–20]. Edge feature is an important feature of image, and image edge is the discontinuity of image features such as pixel gray distribution. Image edge is the set of pixels whose characteristics around the image change step or ridge. The edge extraction is mainly to retain the sharply changed area of the image, and the contour edge of the track fastener can be obtained. The edge contour feature of the track fastener image is helpful to distinguish the state of track fastener loss and track fastener clip loosening. The texture feature of track fastener is extracted [21–23]. The image texture feature is a global feature, and the visual features of homogeneity in the image are reflected. The arrangement properties of the surface structure of the object surface with slow or periodic changes are reflected. The texture feature can effectively represent the clip detail feature of track fastener image, and the clip detail feature of track fastener image is helpful to identify the fracture state of track fastener clip. These features are not well integrated and utilized at the same time, and the feature information of track fastener image is not fully expressed, which leads to a high rate of missing alarm in track fastener defect detection [24–26].

Because, for Pandrol fasteners, the track fastener picture is composed of the track fastener clip subimage and the track fastener bolt subimage, the defect of the track fastener is mainly determined by the state of the track fastener clip subimage. When the deep learning network is used to extract the full image feature, the bolt subimage feature in the image will also be extracted into the discriminant feature, which will interfere with the detection of track fastener defects.

Therefore, in view of the above-mentioned problems in the detection of track fastener defects: the number of abnormal samples of track fastener images is sparse; image features are not fully utilized; and track fastener detection is interfered by the feature of track fastener bolt subimage. A method that is based on LDFFN to detect the Pandrol track fastener defects is proposed. Firstly, the Pandrol track fastener picture is segmented by the automatic segmentation algorithm of track fastener pictures. The bolt information in the picture is removed to obtain the track fastener clip subpicture, so as to avoid the interference of the bolt subgraph feature on the track fastener defect detection. Secondly, AE [27, 28] and RBM [29, 30] are used to extract clip subimage features of track fastener, because AE focuses on edge feature for extracting subimage features of track fastener clip [31], while RBM focuses on texture feature [32, 33]. Considering that the edge feature is advantageous for detecting the state of track fastener loss and track fastener clip loosening, the texture feature is advantageous for detecting the broken state of the track fastener clip. Therefore, the subimage features of the track fasteners extracted by AE and RBM are fused to obtain the locally deeply integrated track fastener features [34]. Finally, the similarity measurement method MD [35] is used to detect the status of track fasteners. The image features of track fastener can be fully extracted by unsupervised LDFFN, the interference of bolt diagram of track fastener on defect detection of track fastener can be avoided, and the problem that the number of abnormal images of track fastener is rare can be solved.

The second part of this article briefly introduces two deep learning networks, AE and RBM. The third part describes the proposed defect detection method of track fasteners based on LDFFN. The fourth part verifies the effectiveness of the LDFFN-based track fastener defect detection method through experimental comparative analysis. The fifth part summarizes and prospects the full text.

2. Neural Network

2.1. AE. AE is an unsupervised neural network model that can learn the hidden features of the input data, which is called encoding. At the same time, the original input data can be reconstructed with the learned new features, which is called decoding [36]. From an intuitive point of view, AE can be used for feature dimensionality reduction, similar to principal component analysis but more compared to the performance of principal component analysis, which is due to the fact that AE has stronger nonlinear feature extraction capabilities. The main structure of AE is shown in Figure 1.

X is represented as the input of AE encodes, H is represented as the new feature, and X' is represented as the output of AE decodes.

The encoding process is as follows:

$$H = f(WX + b). \tag{1}$$

The decoding process is as follows:

$$X' = g(W'H + d), \tag{2}$$

where f and g are represented as activation functions of the encoding network and the decoding network, respectively; $\{W, b\}$ and $\{W', d\}$ are represented as the connection weights and biases corresponding to the network. Usually, $W' = W^T$, and $\theta = \{W, b, d\}$ is represented as the parameter of AE. When $S = [X^{(j)}]_{i=1}^{N}$ is represented as the sample data set, the overall loss function of AE is

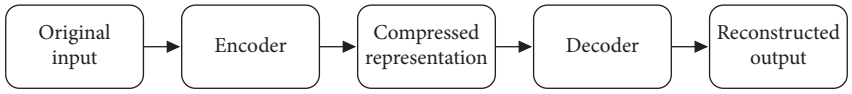

Figure 1: AE structure diagram.

$$J_{AE}(\theta) = \sum_{x \in S} L(X, g(f(X))), \tag{3}$$

where $L(X, g(f(X)))$ is represented as the reconstruction error function and $L(X, g(f(X)))$ is determined by functions f and g. By calculating the minimum value of $J_{AE}(\theta)$, the parameter θ of the AE neural network can be solved.

2.2. RBM. Boltzmann machines are a large class of neural network models, but the most used model in practical applications is RBM. The RBM model itself is very simple, just a two-layer neural network. The main structure of RBM is shown in Figure 2.

$(v_1, v_2, \ldots, v_m)$ is represented as the RBM network visible nodes. $(h_1, h_2, \ldots, h_n)$ is represented as the RBM network hidden nodes. Each visible node is only related to n hidden nodes and is independent of other visible nodes. That is, the state of this visible node is only affected by the influence of $n$hidden nodes. For each hidden node, it is only affected by m visible nodes. $a = (a_1, a_2, \ldots, a_m)$ is represented as the offset of the visible node. $b = (b_1, b_2, \ldots, b_n)$ is represented as the offset of the hidden node.

3. Defect Detection Method of Track Fasteners Based on LDFFN

3.1. Automatic Segmentation of Track Fastener Pictures. The Pandrol track fastener image is composed of the track fastener clip subgraph and the track fastener bolt subgraph. Normally, if the fastener bolt is damaged, it will not be reflected in the image, and the damage of the fastener clip will be reflected in the image. Track fastener defect detection will be disturbed by the track fastener bolt which is not damaged. In this paper, in order to reduce the interference of track fastener bolts, the image of track fastener will be automatically segmented.

In the first step, the input image is grayscale processed [37]. Because the color image data of track fasteners is relatively large, the calculation is time-consuming. The grading empirical formula is expressed as follows:

$$\begin{aligned}\mathrm{Gray}(x, y) = {} & 0.299 * \mathrm{Red}(x, y) + 0.587 * \mathrm{Green}(x, y) \\ & + 0.114 * \mathrm{Blue}(x, y),\end{aligned} \tag{4}$$

where $\mathrm{Red}(x, y)$ is represented as pixels in the red channel. $\mathrm{Green}(x, y)$ is represented as pixels in the green channel. $\mathrm{Blue}(x, y)$ is represented as pixels in the blue channel.

In the second step, histogram equalization is performed on the gray image [38]. The contrast and detail of the image are improved.

$$p_x(i) = p(x = i) = \frac{n_i}{n}, \quad (0 \le i \le L - 1), \tag{5}$$

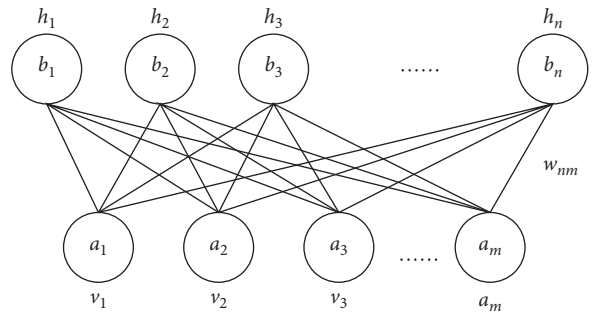

Figure 2: RBM structure diagram.

where n is represented as the number of pixels in the image, n_i is represented as the number of pixels in each gray level of the original image, L is represented as the number of gray levels of the original image, and $p_x(i)$ is the probability of occurrence of a pixel of gray i in the image. Equation (6) is cumulative normalization.

$$cdf_x(i) = \sum_{j=0}^{i} p_x(j), \quad (0 \le i \le L - 1), \tag{6}$$

$$g(i) = \mathrm{round}\left(255 \times \mathrm{cd}f_x(i)\right), \quad (0 \le i \le L - 1), \tag{7}$$

where $\mathrm{cd}f_x(i)$ is represented as the cumulative distribution probability, round indicates that the number is rounded, L is represented as the number of gray levels of the original image, 255 represents the maximum gray level after histogram equalization, and $g(i)$ represents the pixel value of the pixel histogram whose gray level is i in the original image after equalization.

In the third step, the gray image is denoised by Gaussian filtering [39]. Image noise can be removed by Gaussian filter. Gaussian filter denoising can keep the edge of the image well, and more of the overall gray distribution characteristics of the image can be preserved.

In the fourth step, a sample image is made for the subimage of track fastener clip. Thereafter, grayscale, grayscale histogram equalization, and Gaussian filtering are performed on the sample picture.

In the fifth step, find the location of the track fastener clip subimage in the track fastener image. The most similar place with the track fastener clip subgraph sample is the target area. The normalized correlation coefficient [40] is used to locate the best similar region, and the subimage of track fastener clip is segmented.

3.2. Track Fastener Defect Detection Based on LDFFN. Firstly, AE and RBM are used to extract the image features of the training set of track fastener clip subgraph. Then the AE

extracted features and RBM extracted features are combined in series, and MD is used to detect the track fastener defects.

MD is used to measure the distance between a sample point X and a set of data distribution D. X is represented as a sample point. D is represented as the set of data. u is represented as the mean value of D. v is represented as the covariance of D. Then the MD between the sample and the set is

$$D_M(X,u) = \sqrt{(X-u)^T v^{-1} (X-u)}. \tag{8}$$

The covariance matrix, inverse matrix, and mean vector of training set are calculated, and then MD is calculated. The maximum value of the training set MD is selected as the detection threshold, and the image to be tested is processed in the same way to calculate the MD. If MD is less than or equal to the threshold value, the test image is judged as normal fastener, and if MD is greater than the threshold value, the test image is judged as abnormal fastener.

Flow chart of detection of defects in Pandrol track fasteners based on LDFFN is shown in Figure 3. The first part is to import the training set of track fastener image. Firstly, the track fastener image is segmented by the automatic segmentation algorithm of track fastener image to obtain the track fastener clip subgraph. Secondly, AE and RBM are used to extract the subimage features of track fastener clip, and then the extracted subimage features of track fastener clip are fused. Finally, MD of fusion features is calculated, MD of training set is selected as threshold of detection image, and feature fusion network model is saved after training. The second part is the test part. Firstly, the test image of track fastener image is imported. Secondly, the training set image is segmented by the automatic segmentation algorithm of track fastener image, and the training set image of track fastener clip subimage is obtained. Finally, through the trained feature fusion network model, the MD of each image to be tested is calculated to determine the status of track fastener image. If the calculated MD is less than or equal to the threshold value, the tested track fastener image is judged as normal track fastener image. If the calculated MD is greater than the threshold value, the tested track fastener image is judged as abnormal track fastener image.

4. Experiments and Applications

4.1. Data Set. The picture of track fasteners in this article comes from the Shijiazhuang-Taiyuan high-speed rail line, called Pandrol fasteners. The state of common Pandrol track fasteners is shown in Figure 4, where (a) is the image of normal track fasteners; (b) is the image of broken track fastener; (c) is the image of loose track fastener.

A total of 1064 pictures and 84 pictures of normal and abnormal track fasteners, respectively, on Pandrol are presented. Among them, there are 542 left fasteners for the normal track, 42 left fasteners for the abnormal track, 522 right fasteners for the normal track, and 42 right fasteners for the abnormal track. In this paper, the detection indexes in reference are cited for comparison of detection efficiency.

(1) Segmentation rate (SR): N^O is represented as the number of original images, and N^S is represented as the number of pictures successfully segmented [41].

$$SR = \frac{N^S}{N^O} \times 100\%. \tag{9}$$

(2) False alarm rate (FAR), missed alarm rate (MAR), and error rate (ER): D_A^A indicates that the abnormal track fastener detection result is abnormal; D_A^N indicates that the abnormal track fastener test result is normal; D_N^N indicates that the normal track fastener test result is normal; D_N^A indicates that the normal track fastener test result is abnormal [41].

$$\begin{aligned} FAR &= \frac{D_N^A}{D_N^N + D_N^A} \times 100\%, \\ MAR &= \frac{D_A^N}{D_A^A + D_A^N} \times 100\%, \\ ER &= \frac{D_N^A + D_A^N}{D_N^N + D_N^A + D_A^A + D_A^N} \times 100\%. \end{aligned} \tag{10}$$

4.2. Experimental Process and Results

4.2.1. Reconstruction of Picture Features of Track Fasteners. Feature reconstruction images of track fastener are shown in Figure 5. (a) is the reconstruction image of track fastener image extracted by AE, and (b) is the image feature reconstruction map of track fastener extracted by RBM. The edge feature of track fastener contour can be better extracted by AE, and the internal texture feature of track fastener can be better extracted by RBM. Therefore, the image extracted by AE and RBM is fused in this paper. Edge features and texture features are included in the fusion features. The fusion features can fully express the information in the image, and track fastener defects are more conducive to be detected.

4.2.2. Defect Detection Results of Pandrol Track Fasteners Based on Deep Feature Fusion Network (DFFN). Based on the DFFN-based Pandrol track fastener defect detection method, the image features of the track fastener are extracted through AE and RBM, the extracted full-image features are feature-fused, and then the state of the track fastener is detected by MD.

There are 542 normal left track fasteners and 42 abnormal left track fasteners. Among them, 300 normal left track fastener pictures are randomly selected to train the network, and the remaining left track fastener pictures are used for detection. There are 522 normal right track fasteners and 42 abnormal right track fasteners. Among them, 300 normal right track fastener pictures are randomly selected to train the network, and the remaining right track fastener pictures are used for detection.

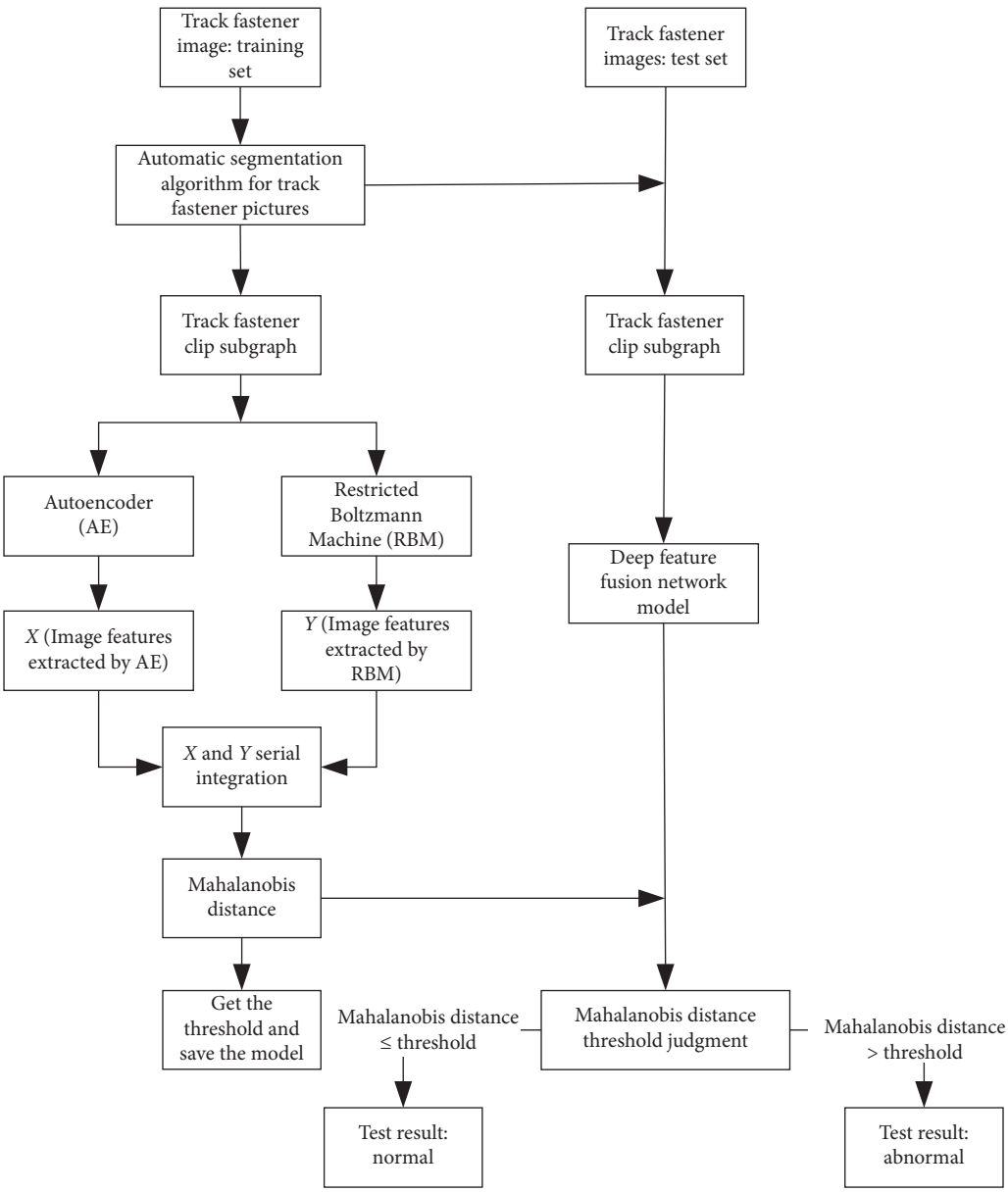

Figure 3: Flow chart of detection of defects in Pandrol track fasteners based on LDFFN.

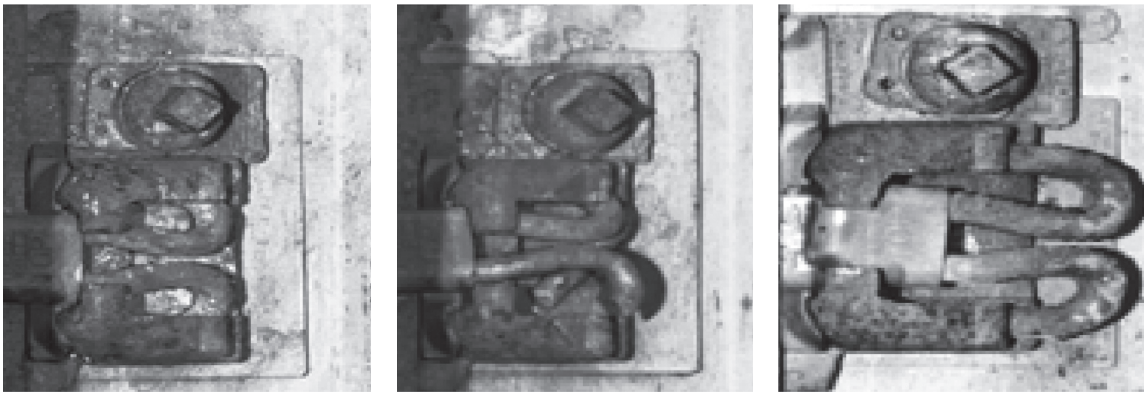

(a) (b) (c)

Figure 4: Common track fastener status. (a) The image of normal track fasteners. (b) The image of broken track fastener. (c) The image of loose track fastener.

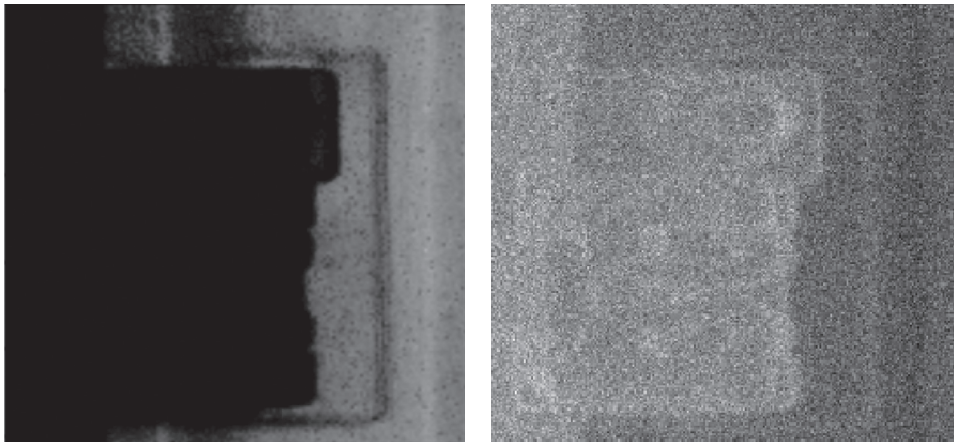

(a) (b)

Figure 5: Image feature reconstruction of track fasteners. (a) Image feature reconstruction extracted by AE. (b) Image feature reconstruction extracted by RBM.

For AE extraction of track fastener image features, two coding layers and two decoding layers are designed in AE network. When encoding, the image dimension is reduced to 256 dimensions. Through the first coding layer, the ReLU activation function is used to output 128 dimensions; through the second coding layer, the ReLU activation function is used to output 64 dimensions; and then the output of the second encoding is used as the input of decoding. The 256-dimensional image features are output by two decoding layers. Training AE model, set the training cycle to 100 and the bit size to 100 and save the model. When RBM is used to extract the image features of track fastener, RBM is called directly, and the training period is set to 100 and the bit size is 100. Then, the track fastener image features extracted by AE and the track fastener image features extracted by RBM are fused in serial, and the covariance matrix, inverse matrix of covariance matrix, and mean vector of training set are calculated, and then MD is calculated.

The defects detection results of Pandrol track fasteners based on DFFN are shown in Table 1. For Pandrol track fastener, the track fastener defect detection method based on AE or RBM extraction track fastener image features has high error rate and missing alarm rate. The false alarm rate and error rate of track fastener defect detection are effectively reduced by DFFN that combines AE and RBM. It shows that the image features of track fasteners extracted by AE and RBM are merged, and the image edge features and texture features are used at the same time, which is more conducive to the detection of track fastener defects. The performance of track fastener defect detection has been improved.

4.2.3. Verification of Feature Interference of Bolt Subgraph of Pandrol Track Fastener. The abnormal pictures detected in DFFN test pictures are displayed, and some pictures are normal. DFFN detects normal pictures as abnormal pictures. In order to find out the reason, the automatic segmentation algorithm of track fastener image is used to segment the image, and only the track fastener clip subimage is used for detection. The result shows that the same picture of track fasteners is an abnormal picture when the full picture is used for detection. The test result is a normal picture when only the track fasteners clip subimage is used for testing. In fact, the detected picture is a normal track fastener image. The results show that the defect detection of track fasteners is interfered by the features of the bolt subgraphs of track fasteners. The characteristic interference verification diagram of the bolt subgraph of the Pandrol track fastener is shown in Figure 6.

4.2.4. Experimental Results of Automatic Segmentation of Pandrol Track Fastener Pictures. The input image of track fastener is processed by gray processing, gray histogram equalization, and Gaussian filtering, and the normalized correlation coefficient is used to locate the clip area of the track fastener and segment it.

The segmentation results of the Pandrol track fastener pictures are shown in Table 2. The experiment was compared and analyzed. Experiments show that it is better to segment the picture after grayscale, histogram equalization, and Gaussian filtering. Pictures that are unsuccessfully segmented are defined as false alarm image in track fastener detection and counted in the detection false alarm rate.

4.2.5. Defect Detection Results of Pandrol Track Fasteners Based on LDFFN. For the left and right fasteners, 300 normal track fastener clip subimages were used for training, and the remaining clip subimages were used for detection. The data set is the same as DFFN.

The defect detection results of Pandrol track fasteners based on LDFFN are shown in Table 3. For the track fastener of Pandrol, the false alarm rate and error rate of track fastener defect detection method based on LDFFN are effectively reduced compared with the track fastener defect detection method based on DFFN. It is proved that the defect detection of track fasteners is interfered by the

Table 1: Defects detection results of Pandrol track fasteners based on DFFN.

Track fastener	Detection method	D_N^N (piece)	D_N^A (piece)	D_A^A (piece)	D_A^N (piece)	*FAR* (%)	*MAR* (%)	*ER* (%)
Left track fastener	AE	214	28	38	3	11.57	7.14	10.92
	RBM	212	30	37	5	12.40	11.90	12.32
	DFFN	212	30	42	0	12.40	0	10.56
Right track fastener	AE	197	26	39	4	11.26	9.52	11.36
	RBM	194	28	37	5	12.61	11.90	12.50
	DFFN	193	29	42	0	13.06	0	10.98

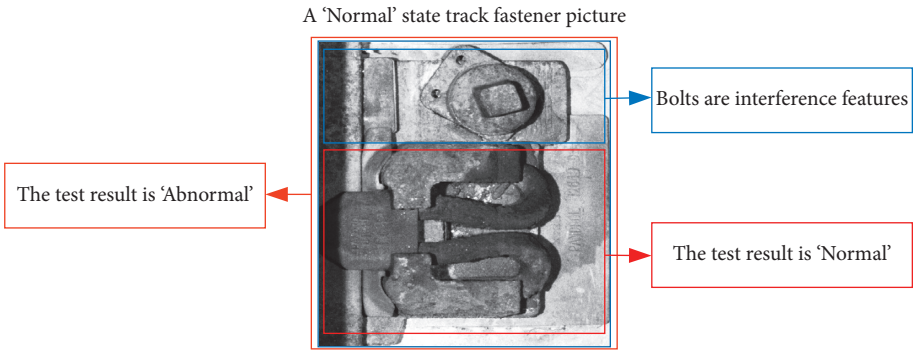

Figure 6: The characteristic interference verification diagram of the bolt subgraph of the Pandrol track fastener.

Table 2: Track fastener pictures automatic segmentation results.

Image processing method	N^O (piece)	N^S (piece)	*SR* (%)
Original	1064	1012	95.11
Grayscale	1064	1037	97.46
Grayscale + histogram equalization	1064	1052	98.87
Grayscale + histogram equalization + Gaussian filtering	1064	1062	99.81

Table 3: Defect detection results of Pandrol track fasteners based on LDFFN.

Track fastener	Detection method	D_N^N (piece)	D_N^A (piece)	D_A^A (piece)	D_A^N (piece)	*FAR* (%)	*MAR* (%)	*ER* (%)
Left track fastener	DFFN	212	30	42	0	12.40	0	10.56
	LDFFN	231	11	42	0	4.55	0	3.87
Right track fastener	DFFN	193	29	42	0	13.06	0	10.98
	LDFFN	213	9	42	0	4.05	0	3.41

features of the bolt subimages of track fasteners. The track fastener clip subimage obtained by the automatic segmentation algorithm of track fastener images is used for track fastener defect detection, which can effectively reduce the false alarm rate and error rate of detection. The performance of track fastener defect detection has been improved. The validity of Pandrol track fastener defects based on LDFFN is verified by experiments.

5. Conclusion

In this paper, a defect detection method for track fastener of Pandrol based on LDFFN is proposed. Firstly, the clip subgraph of track fasteners is obtained through the automatic segmentation algorithm of track fastener images. Secondly, through AE and RBM, the edge feature and texture feature of the track fastener clip subimage are extracted, respectively, and the extracted track fastener clip subimage features are fused. Finally, the similarity measurement method MD is used to detect the status of track fasteners. The problem that the feature of track fastener bolt subimage interferes with the detection of track fastener defects and the problem of the sparse number of abnormal image samples of track fasteners are solved by the Pandrol track fastener defect detection method based on LDFFN. Moreover, the deep fusion features include both the edge feature and texture feature of the image. The full expression of the image feature makes the track fastener defect more conducive to be detected. The experimental results verify the effectiveness of the proposed LDFFN-based method for detecting defects in Pandrol track fasteners.

When the defect detection of track fastener is carried out through the track fastener picture, the information of the bolt subpicture of track fastener is not effectively used, and whether the bolt is loose cannot be detected. In the future, the research will attempt to detect the track fastener bolts by other detection methods, so that the information of the track fastener bolts can be effectively used.

Data Availability

The data used to support the findings of this study are available from the corresponding author upon request.

Conflicts of Interest

The authors declare that there are no conflicts of interest regarding the publication of this paper.

Acknowledgments

This work was supported by the National Natural Science Foundation of China (Grant no. 51975347), Shanghai Science and Technology Committee (Grant no. 18030501300), Shanghai Sailing Program (18YF1409200), Talent Program of Shanghai University of Engineering Science, and the Opening Project of Shanghai Trusted Industrial Control Platform (TICPSH202003021-ZC).

References

[1] W. Xiukun, Y. Ziming, L. Yuxin et al., "Railway track fastener defect detection based on image processing and deep learning techniques: acomparative study," *Engineering Applications Of Artificial Intelligence*, vol. 80, pp. 66–81, 2019.

[2] X. Gibert, V. M. Patel, and R. Chellappa, "Deep multi-task learning for railway track inspection," *IEEE Transactions On Intelligent Transportation Systems*, vol. 18, no. 1, pp. 153–164, 2017.

[3] J. Zarei, M. A. Tajeddini, and H. R. Karimi, "Vibration analysis for bearing fault detection and classification using an intelligent filter," *Mechatronics*, vol. 24, no. 2, pp. 151–157, 2014.

[4] H. R. Karimi, M. Zapateiro, and N. Luo, "A linear matrix inequality approach to robust fault detection filter design of linear systems with mixed time-varying delays and nonlinear perturbations," *Journal of the Franklin Institute*, vol. 347, no. 6, pp. 957–973, 2010.

[5] H. R. Karimi, "Robust synchronization and fault detection of uncertain master-slave systems with mixed time-varying delays and nonlinear perturbations," *International Journal of Control, Automation and Systems*, vol. 9, no. 4, p. 671, 2011.

[6] Y. Li, H. R. Karimi, Q. Zhang, D. Zhao, and Y. Li, "Fault detection for linear discrete time-varying systems subject to random sensor delay: a Riccati equation approach," *IEEE Transactions on Circuits and Systems I: Regular Papers*, vol. 65, no. 5, pp. 1707–1716, 2018.

[7] H. Feng, Z. Jiang, F. Xie, P. Yang, J. Shi, and L. Chen, "Automatic fastener classification and defect detection in vision-based railway inspection systems," *IEEE Transactions on Instrumentation and Measurement*, vol. 63, no. 4, pp. 877–888, 2014.

[8] Y. J. Qiu, X. J. Chen, and Z. M. Lv, "Rail fastener positioning based on double template matching," *Complexity*, vol. 2020, Article ID 8316969, 10 pages, 2020.

[9] Z. Lv, X. Yan, and Q. Jiang, "Batch process monitoring based on self-adaptive subspace support vector data description," *Chemometrics and Intelligent Laboratory Systems*, vol. 170, pp. 25–31, 2017.

[10] Z. Lv, X. Yan, Q. Jiang et al., "Just-in-time learning–multiple subspace support vector data description used for non-Gaussian dynamic batch process monitoring," *Journal Of Chemometrics*, vol. 33, no. 6, 2019.

[11] T. Poggio and H. N. Mhaskar, "Deep vs. shallow networks: an approximation theory perspective," *Analysis And Applications*, vol. 14, 2016.

[12] Y. Lecun, Y. Bengio, and G. Hinton, "Deep learning," *Nature*, vol. 521, no. 7553, pp. 436–444, 2015.

[13] A. Krizhevsky, I. Sutskever, and G. E. Hinton, "ImageNet classification with deep convolutional neural networks," *Communications of the ACM*, vol. 60, no. 6, pp. 84–90, 2017.

[14] K. He, X. Zhang, S. Ren et al., "Deep residual learning for image recognition," in *Proceedings of the IEEE Conference on Computer Vision and Pattern Recognition (CVPR)*, Las Vegas, NV, USA, June 2016.

[15] C. Szegedy, W. Liu, Y. Jia et al., "Going deeper with convolutions," in *Proceedings of the IEEE Conference On Computer Vision And Pattern Recognition (CVPR)*, Boston, MA, USA, June 2015.

[16] Y. Chen, Z. Lin, X. Zhao, G. Wang, and Y. Gu, "Deep learning-based classification of hyperspectral data," *IEEE Journal of Selected Topics in Applied Earth Observations and Remote Sensing*, vol. 7, no. 6, pp. 2094–2107, 2014.

[17] J. Chen, Z. Liu, H. Wang, A. Nunez, and Z. Han, "Automatic defect detection of fasteners on the catenary support device using deep convolutional neural network," *IEEE Transactions on Instrumentation and Measurement*, vol. 67, no. 2, pp. 257–269, 2018.

[18] N. S. Vu and A. Caplie, "Enhanced patterns of oriented edge magnitudes for face recognition and image matching," *IEEE Transactions on Image Processing*, vol. 21, no. 3, pp. 1352–1365, 2012.

[19] X. Kang, X. Xiang, S. Li, and J. A. Benediktsson, "PCA-based edge-preserving features for hyperspectral image classification," *IEEE Transactions on Geoscience and Remote Sensing*, vol. 55, no. 12, pp. 7140–7151, 2017.

[20] D. Piotr and C. Lawrence, "Fast edge detection using structured forests," *IEEE Transactions on Pattern Analysis & Machine Intelligence*, vol. 37, 2015.

[21] H. Fan, P. C. Cosman, Y. Hou, and B. Li, "High-speed railway fastener detection based on a line local binary pattern," *IEEE Signal Processing Letters*, vol. 25, no. 6, pp. 788–792, 2018.

[22] X. Tan and B. Triggs, "Enhanced local texture feature sets for face recognition under difficult lighting conditions," *IEEE Transactions on Image Processing*, vol. 19, no. 6, pp. 1635–1650, 2010.

[23] A. Satpathy, X. Xudong Jiang, and H. L. How-Lung Eng, "LBP-based edge-texture features for object recognition," *IEEE Transactions on Image Processing*, vol. 23, no. 5, pp. 1953–1964, 2014.

[24] L. Liu, F. Zhou, and Y. He, "Automated status inspection of fastening bolts on freight trains using a machine vision approach," *Proceedings of the Institution of Mechanical Engineers, Part F: Journal of Rail and Rapid Transit*, vol. 230, no. 7, pp. 1629–1641, 2016.

[25] E. Resendiz, J. Hart, and N. Ahuja, "Automated visual inspection of railroad tracks," *Intelligent Transportation Systems, IEEE Transactions on*, vol. 14, no. 2, pp. 751–760, 2013.
[26] Y. Li, H. Trinh, N. Haas et al., "Rail component detection, optimization, and assessment for automatic rail track inspection," *IEEE Transactions On Intelligent Transportation Systems*, vol. 15, no. 2, pp. 760–770, 2014.
[27] M. Farahani and A. Mohammadzadeh, "Domain adaptation for unsupervised change detection of multisensor multitemporal remote-sensing images," *International Journal of Remote Sensing*, vol. 41, no. 10, pp. 3902–3923, 2020.
[28] Y. Bengio, A. Courville, and P. Vincent, "Representation learning: a review and new perspectives," *IEEE Transactions on Pattern Analysis and Machine Intelligence*, vol. 35, no. 8, pp. 1798–1828, 2013.
[29] P. Tamilselvan and P. Wang, "Failure diagnosis using deep belief learning based health state classification," *Reliability Engineering & System Safety*, vol. 115, pp. 124–135, 2013.
[30] Y. Chen, X. Zhao, and X. Jia, "Spectral–Spatial classification of hyperspectral data based on deep belief network," *IEEE Journal of Selected Topics in Applied Earth Observations and Remote Sensing*, vol. 8, no. 6, pp. 1–12, 2015.
[31] Z. Fan, D. Bi, L. He et al., "Low-level structure feature extraction for image processing via stacked sparse denoising autoencoder," *Neurocomputing*, vol. 243, pp. 12–20, 2017.
[32] D. Bibin, M. S. Nair, and P. Punitha, "Malaria parasite detection from peripheral blood smear images using deep belief networks," *IEEE Access*, vol. 5, 2017.
[33] N. Liu and J.-m. Kan, "Improved deep belief networks and multi-feature fusion for leaf identification," *Neurocomputing*, vol. 216, pp. 460–467, 2016.
[34] W. Xue, X. Dai, and L. Liu, "Remote sensing scene classification based on multi-structure deep features fusion," *IEEE Access*, vol. 8, pp. 28746–28755, 2020.
[35] M. Kstinger, M. Hirzer, P. Wohlhart et al., "Large scale metric learning from equivalence constraints," in *Proceedings of the IEEE Conference on Computer Vision and Pattern Recognition (CVPR)*, Providence, RI, USA, June 2012.
[36] W. Liu, Z. Wang, X. Liu et al., "A survey of deep neural network architectures and their applications," *Neurocomputing*, vol. 234, pp. 11–26, 2017.
[37] C. Kanan and G. W. Cottrell, "Color-to-Grayscale: does the method matter in image recognition," *PLoS One*, vol. 7, no. 1, pp. 133–139, 2012.
[38] T. Celik, "Two-dimensional histogram equalization and contrast enhancement," *Pattern Recognition*, vol. 45, no. 10, 2012.
[39] P. Bing, "Bias error reduction of digital image correlation using Gaussian pre-filtering," *Optics And Lasers In Engineering*, vol. 51, no. 10, pp. 1161–1167, 2013.
[40] M. Debella-Gilo and A. Kääb, "Sub-pixel precision image matching for measuring surface displacements on mass movements using normalized cross-correlation," *Remote Sensing of Environment*, vol. 115, no. 1, pp. 130–142, 2011.
[41] A. Q. Ma, Z. M. Lv, X. J. Chen et al., "Pandrol track fastener defect detection based on local convolutional neural networks," *Proceedings of institution of Mechanical Engineers Part I-Journal of Systems and Control Engineering*, 2020.

Hindawi
Complexity
Volume 2021, Article ID 6649629, 8 pages
https://doi.org/10.1155/2021/6649629

Research Article

Robust Stabilization of Stochastic Markovian Jump Systems with Distributed Delays

Guilei Chen,[1] Zhenwei Zhang,[2] Chao Li,[2] Dianju Qiao,[3] and Bo Sun[3]

[1]*Department of Fundamental Courses, Shandong University of Science and Technology, Tai'an 271000, Shandong, China*
[2]*College of Electronic and Information Engineering, Shandong University of Science and Technology, Qingdao 266590, Shandong, China*
[3]*College of Intelligent Equipment, Shandong University of Science and Technology, Tai'an 271000, Shandong, China*

Correspondence should be addressed to Chao Li; dalichaoxiao@163.com

Received 11 December 2020; Revised 4 February 2021; Accepted 18 February 2021; Published 27 February 2021

Academic Editor: Xue-bo Jin

This paper addresses the robust stabilization problem for a class of stochastic Markovian jump systems with distributed delays. The systems under consideration involve Brownian motion, Markov chains, distributed delays, and parameter uncertainties. By an appropriate Lyapunov–Krasovskii functional, the novel delay-dependent stabilization criterion for the stochastic Markovian jump systems is derived in terms of linear matrix inequalities. When given linear matrix inequalities are feasible, an explicit expression of the desired state feedback controller is given. The designed controller, based on the obtained criterion, ensures asymptotically stable in the mean square sense of the resulting closed-loop system. The convenience of the design is greatly enhanced due to the existence of an adjustable parameter in the controller. Finally, a numerical example is exploited to demonstrate the effectiveness of the developed theory.

1. Introduction

Stochastic Markovian jump systems (SMJSs) driven by continuous-time Markov chains have played an important role in many branches of science and industry. One can use the SMJSs to model many practical dynamical systems where they may experience abrupt changes in their structure and parameters, such as failure-prone manufacturing systems, power systems and economic systems. In the past decades, the stability and control problems of the SMJSs have received a great deal of attention and many results have been reported in [1–9]. Especially, it plays an important role in the field of control, such as in the field of adaptive tracking control, using feedback Markov jump nonlinear time-delay system to design a self-adaptive tracking controller can effectively improve the output tracking performance, which has very important practical application value and theoretical research significance in robot arm operating system and aircraft trajectory tracking system.

On the contrary, time delays are often encountered in many industrial and physical systems, and they are also a great source of systems instability, oscillation, and poor performance. We have seen an increasing interest in the stabilization of this class of systems [10–13]. Recently, distributed time-delay systems, a particular case of time-delay systems, have also drawn much research interest [14–18]. This is mainly because distributed delay systems are often used to model the time lag phenomenon in thermodynamics and in ecology, as well as epidemiology such as predator-prey systems. In [19], the state feedback control problem for a class of discrete-time stochastic with distributed delays has been considered by using linear matrix inequality approach. In [20], Zhu and Cao studied the adaptive synchronization problem for a class of stochastic neural networks with time-varying delays and distributed delays.

Recently, Yan et al. investigated the guaranteed cost stabilization problem for a class of stochastic Markovian jump systems with incomplete transition rates. The new state and output feedback finite-time guaranteed cost controllers

design methods are proposed, and a new N-mode optimization algorithm is given to minimize the upper bound of cost function [21]. In [22], the robust finite-time H_∞ control problem for a class of uncertain singular stochastic Markovian jump systems with partially unknown transition rates via proportional differential control law was solved. New sufficient conditions for the existence of mode-dependent desired controllers are derived in terms of linear matrix inequalities. The designed proportional differential controller ensures finite-time stability in the mean square sense and also satisfies a prescribed H_∞ performance level of the resulting closed-loop system for all admissible uncertainties. Zhu and Yang investigated the fault-tolerant control problems of stochastic Markovian jump systems with actuator faults including loss of effectiveness, stuck, and outage [23]. Le Van Hien and Hieu Trinh studied the stability analysis problems of two-dimensional Markovian jump state-delayed systems in the Roesser model with uncertain transition probabilities [24]. In addition to the above research on Markov stable systems with time delay, there are many literatures on the stability control of other systems, which can be used for reference in this paper. In [25], Na et al. proposed an adaptive fuzzy control scheme to control the input delay of a nonlinear suspension system. Jin et al. researched the problem of robot movement in a complex environment, using artificial intelligence to solve the problem of robot state control and tracking [26]. In [27], Zhu and Zheng studied the asymptotic stability analysis and PWA state feedback control design for a class of discrete nonlinear systems by using smooth approximation technique. Xue-Bo Jin et al. proposed a way to control both dynamic model update and states fusion estimation to achieve real-time indoor RFID tracking [28]. In [29], Liu et al. designed a constrained generalized predictive current controller to control the charging current to keep the internal temperature of the battery in an ideal range. In [30], Wang and Na proposed a new adaptive parameter estimation method to solve the nonlinear servo mechanism with friction compensation and combined with robust integral to solve the bounded interference, which improved the accuracy. Stochastic Markov jump systems are widely used in various fields, and a large number of applications and research examples have been reported. In [31], Zhang et al. designed filters for a class of linear Markov jump systems with time-varying delays, and the designed filter ensures the stochastic stability of the filtering error system. In [32], Wu et al. designed a full-order filter by studying the problem of H_∞ filtering for 2D discrete Markov jump systems, which guarantees the filtering error system to be mean square asymptotically stable. However, to the best of the author's knowledge, there are few works undertaken on the robust control for stochastic Markovian jump systems with time-varying delays and distributed delays. We find that the robust control problems of such systems have not been fully investigated and there is still room for further investigation.

This paper focuses on the robust control for stochastic Markovian jump systems with distributed delays. A new delay-dependent stabilization criterion for the stochastic Markovian jump systems with distributed delays is established in terms of linear matrix inequalities (LMIs). When these LMIs are feasible, an explicit expression of the desired state feedback controller with an adjustable positive parameter is given. The designed controller can guarantee the resulting closed-loop system to be mean square asymptotically stable for all admissible uncertainties and distributed delays.

Notation: the notation used throughout this paper is fairly standard. $\mathbb{R}^n$ denotes the n-dimensional Euclidean space and $\mathbb{R}^{n\times m}$ is the set of all $n\times m$ real matrices. The notation $X>0$ denotes that X is a symmetric positive definite matrix. The superscripts "T" and "−1" represent the transpose and the inverse of a matrix, respectively. Let the notation "I" denote an identity matrix, and let the notation "$*$" denote the transposed entries in the symmetric positions of a symmetric matrix. The notation diag(·) stands for a block-diagonal matrix.

2. Model Formulation and Preliminaries

Consider the following stochastic Markovian jump systems with time-varying delays and distributed delays:

$$\begin{aligned} dx(t) &= \begin{bmatrix} \left(A_1(r(t)) + \Delta A_1(r(t))\right)x(t) + \left(A_2(r(t)) + \Delta A_2(r(t))\right)x(t-h(t)) \\ + \left(A_3(r(t)) + \Delta A_3(r(t))\right)\int_{t-h(t)}^{t} x(s)\mathrm{d}s + B(r(t))u(t) \end{bmatrix} dt \\ &\quad + \left[\left(E_1(r(t)) + \Delta E_1(r(t))\right)x(t) + \left(E_2(r(t)) + \Delta E_2(r(t))\right)x(t-h(t))\right]dw(t) \\ x(t) &= \varphi(t), \forall t \in [-\tau, 0], \end{aligned} \tag{1}$$

where $x(t)\in\mathbb{R}^n$ is the state and $u(t)\in\mathbb{R}^m$ is the control input vector. $A_1(r(t))$, $A_2(r(t))$, $A_3(r(t))$, $B(r(t))$, $E_1(r(t))$, and $E_2(r(t))$ are known matrices with appropriate dimensions. $\Delta A_1(r(t))$, $\Delta A_2(r(t))$, $\Delta A_3(r(t))$, $\Delta E_1(r(t))$, and $\Delta E_2(r(t))$ denote norm-bounded real-valued matrix functions which satisfy the assumption:

$$\begin{aligned}&[\Delta A_1(r(t))\Delta A_2(r(t))\Delta A_2(r(t))\Delta E_1(r(t))\Delta E_2(r(t))]\\&\quad = M(r(t))F(r(t))[N_1(r(t))N_2(r(t))N_3(r(t))N_4(r(t))N_5(r(t))],\end{aligned} \tag{2}$$

where $M(r(t))$, $N_1(r(t))$, $N_2(r(t))$, $N_3(r(t))$, $N_4(r(t))$, and $N_5(r(t))$ are known matrices of appropriate dimensions, while $F(r(t))$ is an unknown matrix function satisfying $F^T(r(t))F(r(t)) \le I$. And, $r(t)$, $t \ge 0$, denotes a right-continuous Markov process on the probability space taking values in a finite set $S = \{1, 2, \ldots, N\}$ with generator $\Gamma = (\lambda_{ij})_{N\times N}$ given by

$$P\{r(t+\Delta) = j | r(t) = i\} = \begin{cases} \lambda_{ij}\Delta + o(\Delta), & i \ne j, \\ 1 + \lambda_{ii}\Delta + o(\Delta), & i = j, \end{cases} \tag{3}$$

where $\Delta > 0$. Here, $\lambda_{ij} \ge 0$ is the transition rate from state i to state j if $i \ne j$, and $\lambda_{ii} = -\sum_{j\ne i}\lambda_{ij}$. The delay $h(t)$ is a time-varying differentiable function that satisfies: $0 < h(t) \le \tau < \infty$, $\dot{h}(t) \le \lambda < 1$, where $\tau$and λ are constants. The initial condition $\varphi(t)$ is a continuous function from $[-\delta, 0]$ to $\mathbb{R}^n$.

The purpose of this paper is to design a state feedback controller, and the expression is shown as

$$u(t) = -\frac{\rho}{2}B^T(r(t))P(r(t))x(t), \tag{4}$$

such that system (1) is asymptotically stable in the mean square sense, where ρ is an adjustable positive parameter.

For the sake of simplicity, we write the matrix $D(r(t) = k)$, which is dependent on the Markov chain, as $D(k)$.

Let us introduce the following lemmas which are essential in establishing our main result.

Lemma 1 (see [33]). *For matrices $P \in \mathbb{R}^{n\times n}$, $M \in \mathbb{R}^{n\times k}$, $N \in \mathbb{R}^{\ell\times n}$, and $F \in \mathbb{R}^{k\times\ell}$ with $P > 0$, $F^TF \le I$ and the scalar $\varepsilon > 0$, we have the following inequalities:*

$$(\mathrm{MFN})^TP + P(\mathrm{MFN}) \le \varepsilon \mathrm{PMM}^TP + \varepsilon^{-1}N^TN. \tag{5}$$

Lemma 2 (see [34]). *For matrices $P \in \mathbb{R}^{n\times n}$, $M \in \mathbb{R}^{n\times k}$, $N \in \mathbb{R}^{\ell\times n}$, and $F \in \mathbb{R}^{k\times\ell}$ with $P > 0$, $F^TF \le I$ and the scalar $\varepsilon > 0$, if $P^{-1} - \varepsilon MM^T > 0$, then*

$$(A + \mathrm{MFN})^TP^{-1}(A + \mathrm{MFN}) \le A^T\left(P - \varepsilon \mathrm{MM}^T\right)^{-1}A + \varepsilon^{-1}N^TN. \tag{6}$$

Lemma 3 (see [35]). *For the given matrix $P > 0$, if there is a vector function $\omega(s)$: $[0, \gamma] \longrightarrow R^n$ such that the integrals $\int_0^\gamma \omega^T(s)P\omega(s)ds$ and $\int_0^\gamma \omega(s)ds$ are well defined, then the following inequality holds:*

$$\gamma\int_0^\gamma \omega^T(s)P\omega(s)\mathrm{d}s \ge \left(\int_0^\gamma \omega^T(s)\mathrm{d}s\right)P\left(\int_0^\gamma \omega(s)\mathrm{d}s\right). \tag{7}$$

3. Main Results

In this section, we aim at the robust stabilization problem for a class of stochastic Markovian jump systems with distributed delays.

Theorem 1. *Consider the stochastic Markovian jump system with distributed time delays (1). For a given positive scalar τ, if there exist matrices $X(k) > 0$ $(k = 1, 2, \ldots, N)$, $Q > 0$, $R > 0$, and $H > 0$ and the positive scalars ε_j $(j = 1, 2)$ such that the following LMI (8) holds:*

$$\begin{bmatrix} \Omega_{11} & \Omega_{12} & \Omega_{13} & X(k)E_1^T(k) & X(k)N_4^T(k) & X(k)N_1^T(k) & \Omega_{17} \\ * & \Omega_{22} & 0 & X(k)E_2^T(k) & X(k)N_5^T(k) & X(k)N_2^T(k) & 0 \\ * & * & \Omega_{33} & 0 & 0 & X(k)N_3^T(k) & 0 \\ * & * & * & \Omega_{44} & 0 & 0 & 0 \\ * & * & * & * & -\varepsilon_2 I & 0 & 0 \\ * & * & * & * & * & -\varepsilon_1 I & 0 \\ * & * & * & * & * & * & \Omega_{77} \end{bmatrix} < 0, \tag{8}$$

where

$$\begin{aligned}
\Omega_{11} &= A_1(k)X(k) + X(k)A_1^T(k) + Q(k) + \gamma_{kk}X(k) + 2\tau^2R + \tau H - \rho B(k)B^T(k),\\
\Omega_{12} &= A_2(k)X(k),\\
\Omega_{13} &= A_3(k)X(k),\\
\Omega_{22} &= -(1-\lambda)Q,\\
\Omega_{33} &= -R - \frac{1}{\tau}H,\\
\Omega_{44} &= -X + \varepsilon_2 MM^T,\\
\Omega_{17} &= \left[\sqrt{\gamma_{k1}}X(k), \ldots, \sqrt{\gamma_{k-1,1}}X(k), \sqrt{\gamma_{k+1,1}}X(k), \ldots, \sqrt{\gamma_{kN}}X(k)\right],\\
\Omega_{77} &= \mathrm{diag}(-X(1), \ldots, -X(k-1), -X(k+1), \ldots, -X(N)),
\end{aligned} \tag{9}$$

and the state feedback controller is chosen as (4), then the resulting closed-loop system is mean square asymptotically stable.

Proof. To prove this theorem, let us introduce the Lyapunov–Krasovskii functional candidate $V(x_t, r(t) = k)$ as follows:

$$\begin{aligned} LV(x_t, r(t) = k) = {} & x^T(t)P(r(t))x(t) + \int_{t-h(t)}^{t} x^T(s)Qx(s)\mathrm{d}s \\ & + \int_{t-\tau}^{t}\left[\int_{s}^{t}(u - t + 2\tau)x^T(u)Rx(u)\mathrm{d}u\right]\mathrm{d}s + \int_{-\tau}^{0}\int_{t+\theta}^{t} x^T(s)Hx(s)\mathrm{d}s\mathrm{d}\theta, \end{aligned} \tag{10}$$

where

$$\begin{aligned} P(r(t)) &= X^{-1}(r(t)), \\ Q &= X(r(t))\widetilde{Q}X(r(t)), \\ R &= X(r(t))\widetilde{R}X(r(t)), \\ H &= X(r(t))\widetilde{H}X(r(t)). \end{aligned} \tag{11}$$

Along the trajectory of system (1), it yields that

$$\begin{aligned} LV(x_t, k) = {} & 2x^T(t)P(k)\big[\big(A_1(k) + \Delta A_1(k)\big)x(t) + \big(A_2(k) + \Delta A_2(k)\big)x(t - h(t)) \\ & + \big(A_3(k) + \Delta A_3(k)\big)\int_{t-h(t)}^{t} x(s)\mathrm{d}s - \frac{\rho}{2}B(k)B^T(k)P(k)x(t)\Big] \\ & + \sum_{l=1}^{N}\gamma_k x^T(t)P(l)x(t) + x^T(t)Qx(t) \\ & - \int_{t-\tau}^{t}(u - t + 2\tau)x^T(u)Rx(u)\mathrm{d}u - \int_{t-\tau}^{t}\left[\int_{s}^{t}x^T(u)Rx(u)\mathrm{d}u\right]\mathrm{d}s \\ & + 2\tau^2 x^T(t)Rx(t) - (1 - \dot{h}(t))x^T(t - h(t))Qx(t - h(t)) \\ & + \frac{\tau x^T(t)}{Hx(t)} - \int_{t-\tau}^{t}x^T(s)Hx(s)\mathrm{d}s - \int_{t-\tau}^{t}\left[\int_{z}^{t}x^T(u)Rx(u)\mathrm{d}u\right]\mathrm{d}s \\ & + \left[x^T(t)\big(E_1(k) + \Delta E_1(k)\big)^T + x^T(t - h(t))\big(E_2(k) + \Delta E_2(k)\big)^T\right]P(k) \\ & \times\left[\big(E_1(k) + \Delta E_1(k)\big)x(t) + \big(E_2(k) + \Delta E_2(k)\big)x(t - h(t))\right] \\ \le {} & 2x^T(t)P(k)\big[\big(A_1(k) + \Delta A_1(k)\big)x(t) + \big(A_2(k) + \Delta A_2(k)\big)x(t - h(t)) \\ & + \big(A_3(k) + \Delta A_3(k)\big)\int_{t-h(t)}^{t} x(s)\mathrm{d}s - \frac{\rho}{2}B(k)B^T(k)P(k)x(t)\Big] \\ & + \sum_{l=1}^{N}\gamma_{kl}x^T(t)P(l)x(t) + x^T(t)Qx(t) - \tau\int_{t-h(t)}^{t}x^T(u)Rx(u)\mathrm{d}u \\ & + 2\tau^2 x^T(t)Rx(t) + \tau x^T(t)Hx(t) - \int_{t-h(t)}^{t}x^T(s)Hx(s)\mathrm{d}s \\ & - (1 - \lambda)x^T(t - h(t))Qx(t - h(t)) \\ & + \left[x^T(t)\big(E_1(k) + \Delta E_1(k)\big)^T + x^T(t - h(t))\big(E_2(k) + \Delta E_2(k)\big)^T\right]P(k) \\ & \times\left[\big(E_1(k) + \Delta E_1(k)\big)x(t) + \big(E_2(k) + \Delta E_2(k)\big)x(t - h(t))\right]. \end{aligned} \tag{12}$$

According to Lemma 2, we can obtain the inequalities as follows:

$$-\tau\int_{t-h(t)}^{t} x^T(u)\widetilde{R}x(u)\mathrm{d}u \le -\left(\int_{t-h(t)}^{t} x^T(u)\mathrm{d}u\right)\widetilde{R}\left(\int_{t-h(t)}^{t} x(u)\mathrm{d}u\right), \tag{13}$$

$$-\int_{t-h(t)}^{t} x^T(u)\widetilde{H}x(u)\mathrm{d}u \le -\frac{1}{\tau}\left(\int_{t-h(t)}^{t} x^T(u)\mathrm{d}u\right)\widetilde{H}\left(\int_{t-h(t)}^{t} x(u)\mathrm{d}u\right). \tag{14}$$

Combining inequalities (12)–(14), it follows that

$$\begin{aligned} LV(x_t,k) \le{}& 2\eta^T(t)\Omega\eta^T(t)\left[x^T(t)\left(E_1(k)+\Delta E_1(k)\right)^T + x^T(t-h(t))\left(E_2(k)+\Delta E_2(k)\right)^T\right] \\ &\times P(k)\left[\left(E_1(k)+\Delta E_1(k)\right)x(t) + \left(E_2(k)+\Delta E_2(k)\right)x(t-h(t))\right], \end{aligned} \tag{15}$$

where

$$\begin{aligned} \Theta &= \begin{bmatrix} \Theta_{11} & \Theta_{12} & \Theta_{13} \\ * & \Theta_{22} & 0 \\ * & * & \Theta_{33} \end{bmatrix}, \\ \Theta_{11} &= P(k)\left(A_1(k)+\Delta A_1(k)\right) + \left(A_1(k)+\Delta A_1(k)\right)^T P(k) - \rho P(k)B(k), \\ &\quad \cdot B^T(k)P(k) + \sum_{l=1}^{N}\gamma_{kl}P(l) + Q + 2\tau^2 R + \tau H, \\ \Theta_{12} &= P(k)\left(A_2(k)+\Delta A_2(k)\right), \\ \Theta_{13} &= P(k)\left(A_3(k)+\Delta A_3(k)\right), \\ \Theta_{22} &= -(1-\lambda)\widetilde{Q}, \\ \Theta_{33} &= -\widetilde{R} - \frac{1}{\tau}\widetilde{H}. \end{aligned} \tag{16}$$

From Lemmas 1 and 2, we arrive at the inequalities as follows:

$$\begin{aligned} &P(k)\begin{bmatrix} \Delta A_1(k) & \Delta A_2(k) & \Delta A_3(k) \\ * & 0 & 0 \\ * & * & 0 \end{bmatrix} + \begin{bmatrix} \Delta A_1(k) & \Delta A_2(k) & \Delta A_3(k) \\ * & 0 & 0 \\ * & * & 0 \end{bmatrix}^T P(k) \le \\ &\cdot \varepsilon_1 \begin{bmatrix} P(k)M(k) \\ 0 \\ 0 \end{bmatrix}\begin{bmatrix} M^T(k)P(k) & 0 & 0 \end{bmatrix} + \varepsilon_1^{-1}\begin{bmatrix} N_1^T(k) \\ N_2^T(k) \\ N_3^T(k) \end{bmatrix}\begin{bmatrix} N_1(k) & N_2(k) & N_3(k) \end{bmatrix}. \end{aligned} \tag{17}$$

Noting expressions (14), (15), and (17), we can obtain a sufficient condition of $\mathscr{L}V(x_t,k)<0$ as follows:

$$\begin{bmatrix} \widetilde{\Theta}_{11} & P(k)A_2(k) & P(k)A_3(k) & E_1^T & N_4^T(k) & N_1^T(k) \\ * & \Theta_{22} & 0 & E_2^T & N_5^T(k) & N_2^T(k) \\ * & * & \Theta_{33} & 0 & 0 & N_3^T(k) \\ * & * & * & \Theta_{44} & 0 & 0 \\ * & * & * & * & -\varepsilon_2 I & 0 \\ * & * & * & * & * & -\varepsilon_1 I \end{bmatrix} < 0, \tag{18}$$

where

$$\begin{aligned} \widetilde{\Theta}_{11} &= P(k)A_1(k) + A_1^T(k)P(k) - \rho P(k)B(k)B^T(k)P(k) \\ &\quad + \sum_{l=1}^{N} \gamma_{kl}P(l) + \widetilde{Q} + 2\tau^2\widetilde{R} + \tau\widetilde{H}, \\ \Theta_{44} &= -\left((P(k))^{-1} - \varepsilon_2 M(k)M^T(k)\right). \end{aligned} \tag{19}$$

□

Premultiplying and postmultiplying (18) by diag $(P^{-1}(k), P^{-1}(k), P^{-1}(k), I, I, I, I)$ and diag$(P^{-1}(k), P^{-1}(k), P^{-1}(k), I, I, I, I)$, respectively, and using Schur complement, one can obtain the desired result and the theorem is proved.

4. A Numerical Example

In this section, we will give a numerical example to illustrate the effectiveness of the proposed theory in this paper.

Consider the stochastic Markovian jump systems with distributed delays (1) with two modes and the following parameters:

$$\begin{aligned} &A_1(1) = \begin{bmatrix} 3 & 15 \\ 10 & 20 \end{bmatrix}, A_2(1) = \begin{bmatrix} 10 & 1 \\ 2 & 7 \end{bmatrix}, A_3(1) = \begin{bmatrix} 10 & 7 \\ 15 & 2 \end{bmatrix}, \\ &B(1) = \begin{bmatrix} 1.5 & 0 \\ 1 & 7 \end{bmatrix}, \\ &E_1(1) = \begin{bmatrix} 1 & 0 \\ 0 & 3 \end{bmatrix}, E_2(1) = \begin{bmatrix} -2 & 1 \\ 0 & 1 \end{bmatrix}, \\ &M(1) = \begin{bmatrix} 0.2 \\ 0.1 \end{bmatrix}, \\ &N_1(1) = \begin{bmatrix} -0.1 & 0.2 \end{bmatrix}, N_2(1) = \begin{bmatrix} 0.1 & 0 \end{bmatrix}, N_3(1) = \begin{bmatrix} 0.1 & -0.1 \end{bmatrix}, N_4(1) = \begin{bmatrix} 0.1 & -0.1 \end{bmatrix}, N_5(1) = \begin{bmatrix} 0.1 & -0.1 \end{bmatrix}, \\ &A_1(2) = \begin{bmatrix} 7 & 10 \\ 3 & 15 \end{bmatrix}, A_2(2) = \begin{bmatrix} 5 & 10 \\ 20 & 7 \end{bmatrix}, A_3(2) = \begin{bmatrix} 20 & 3 \\ 5 & 15 \end{bmatrix}, \\ &B(2) = \begin{bmatrix} 0.5 & 0.3 \\ -0.1 & 0.5 \end{bmatrix}, \\ &E_1(2) = \begin{bmatrix} 3 & 0 \\ 0 & 1 \end{bmatrix}, E_2(2) = \begin{bmatrix} 1 & -1 \\ 0 & 3 \end{bmatrix}, \\ &M(2) = \begin{bmatrix} 0.5 \\ 0.3 \end{bmatrix}, \\ &N_1(2) = \begin{bmatrix} -0.3 & 0.5 \end{bmatrix}, N_2(2) = \begin{bmatrix} 0.3 & 0 \end{bmatrix}, N_3(2) = \begin{bmatrix} 0.3 & -0.3 \end{bmatrix}, N_4(2) = \begin{bmatrix} 0.3 & -0.3 \end{bmatrix}, N_5(2) = \begin{bmatrix} 0.3 & -0.1 \end{bmatrix}, \\ &\tau = 1.6512, \\ &\lambda = 0.5, \\ &\gamma_{11} = -0.5, \gamma_{12} = 0.5, \gamma_{21} = 0.5, \gamma_{22} = -0.5. \end{aligned} \tag{20}$$

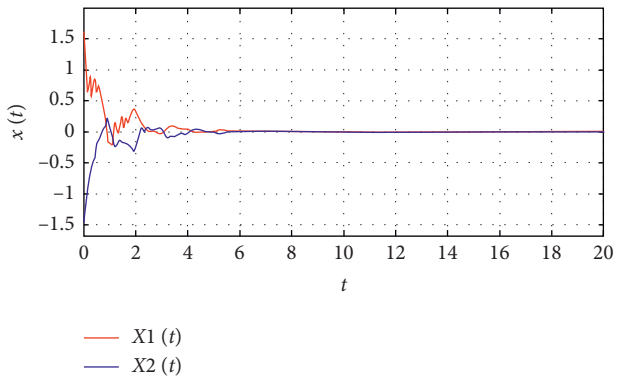

Figure 1: State 1 response curve.

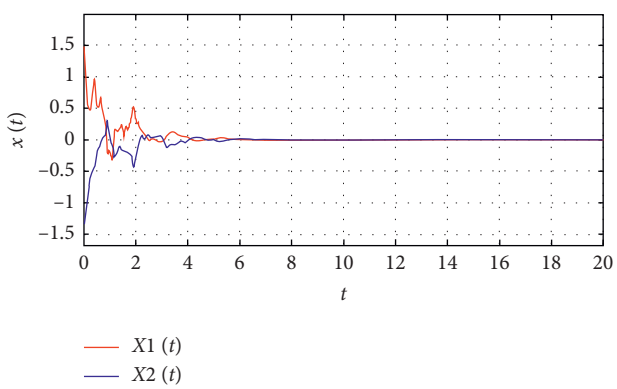

Figure 2: State 2 response curve.

Using the MATLAB toolbox to solve the linear matrix inequality (8), we can obtain the two-state feedback gain matrices as

$$K(1) = \begin{bmatrix} -2.1078 & -1.4312 \\ 0.0701 & -10.1233 \end{bmatrix}, \quad K(2) = \begin{bmatrix} -1.3563 & 0.0285 \\ -1.0616 & -1.3812 \end{bmatrix}. \tag{21}$$

The obtained state feedback gains $K(1)$ and $K(2)$ satisfy Lyapunov's second theorem (asymptotic stability theorem), so the designed state feedback controller satisfies the requirement of mean square asymptotic stability of the closed-loop system.

According to the results, the state trajectories of two different states are drawn by MATLAB, as shown in Figures 1 and 2, respectively.

The simulation diagram is shown in the above figures. From the two figures, it can be seen that, under the constraints of the controller, the two states become asymptotically stable over time, and finally, approach 0.

According to the above derivation results and state trajectory curves, we know that the resulting closed-loop system is mean square asymptotically stable, thus proving the validity of the theory.

5. Conclusions

In this paper, the robust control problem for a class of stochastic Markovian jump systems with distributed delays is investigated. A new delay-dependent stabilization sufficient condition is proposed. Designed state feedback controller can guarantee the resulting closed-loop system mean square asymptotically stable for all admissible uncertainties and distributed delays.

The research results of this paper can be widely used in power systems, chemical systems, networked intelligent systems, aircraft systems, etc., so it has a certain reference value and significance for other related fields.

Data Availability

The data used to support the findings of this study are available from the corresponding author upon request.

Conflicts of Interest

The authors declare that they have no conflicts of interest.

Acknowledgments

This study was supported by the Natural Science Foundation of Shandong Province (ZR2017MF048), National Natural Science Foundation of China (Grant no. 71801144), Key Research and Development Project of Shandong Province (Grant no. 2019GGX101008), and Science and Technology Plan for Colleges and Universities of Shandong Province (J17KA214 and J18KB159).

References

[1] O. L. V. Costa, J. B. R. do Val, and J. C. Geromel, "Continuous-time state-feedback H2-control of Markovian jump linear systems via convex analysis," *Automatica*, vol. 35, no. 2, pp. 259–268, 1999.

[2] J. Song, S. He, F. Liu, Y. Niu, and Z. Ding, "Data-driven policy iteration algorithm for optimal control of continuous-time Itô stochastic systems with Markovian jumps," *IET Control Theory & Applications*, vol. 10, no. 12, pp. 1431–1439, 2016.

[3] S. Long and S. Zhong, "Improved results for stochastic stabilization of a class of discrete-time singular Markovian jump systems with time-varying delay," *Nonlinear Analysis: Hybrid Systems*, vol. 23, pp. 11–26, 2017.

[4] H. G. Zhang and Y. C. Wang, "Stability analysis of Markovian jumping stochastic Cohen-Grossberg neural networks with mixed time delays," *IEEE Transactions on Neural Networks*, vol. 19, no. 2, pp. 366–370, 2008.

[5] R. Saravanakumar, M. Syed Ali, and H. R. Karimi, "Robust H_∞ control of uncertain stochastic Markovian jump systems with mixed time-varying delays," *International Journal of Systems Science*, vol. 48, no. 4, pp. 862–872, 2017.

[6] R. C. Hu, H. Dong, X. D. Gu, and Z. C. Deng, "Feedback stabilization of multi-DOF nonlinear stochastic Markovian jump systems," *International Journal of Robust and Nonlinear Control*, vol. 29, no. 16, pp. 5654–5667, 2019.

[7] C. D. Zheng and N. Sun, "Mode-dependent stochastic synchronization criteria for Markovian hybrid neural networks

with random coupling strengths," *Journal of the Franklin Institute*, vol. 354, no. 13, pp. 5559–5588, 2017.

[8] G. L. Chen, J. Sun, and J. W. Xia, "Robust sampled-data control for Itô stochastic Markovian jump systems with state delay," *International Journal of Robust and Nonlinear Control*, vol. 28, no. 15, pp. 4345–4366, 2018.

[9] Z. G. Yan, Y. X. Song, and X. P. Liu, "Finite-time stability and stabilization for Itô-type stochastic Markovian jump systems with generally uncertain transition rates," *Applied Mathematics and Computation*, vol. 321, pp. p12–525, 2018.

[10] H. Zhang, Z. Liu, G. B. Huang, and Z. Wang, "Novel weighting-delay-based stability criteria for recurrent neural networks with time-varying delay," *IEEE Transactions on Neural Networks*, vol. 21, no. 1, pp. 91–106, 2010.

[11] W. H. Zhang, L. R. Xue, and X. S. Jiang, "Global stabilization for a class of stochastic nonlinear systems with SISS-like conditions and time delay," *International Journal of Robust and Nonlinear Control*, vol. 28, no. 13, pp. 3909–3926, 2018.

[12] Y. Wang, H. Zhang, and X. Liu, "Robust H_∞ control based on fuzzy hyperbolic model with time-delay," *Progress in Natural Science*, vol. 18, no. 11, pp. 1429–1435, 2008.

[13] L. X. Chen, G. P. Cai, and W. D. Zhang, "Robust H_∞ control of building structures with time delay," *International Journal of Acoustics and Vibrations*, vol. 22, no. 1, pp. 14–26, 2017.

[14] K. Gu, "An improved stability criterion for systems with distributed delays," *International Journal of Robust and Nonlinear Control*, vol. 13, no. 9, pp. 819–831, 2003.

[15] J. Yoneyama, "Robust stability and stabilizing controller design of fuzzy systems with discrete and distributed delays," *Information Sciences*, vol. 178, no. 8, pp. 1935–1947, 2008.

[16] W.-H. Chen and W. X. Zheng, "Delay-dependent robust stabilization for uncertain neutral systems with distributed delays," *Automatica*, vol. 43, no. 1, pp. 95–104, 2007.

[17] H. R. Henríquez, C. Cuevas, M. Rabelo, and A. Caicedo, "Stabilization of distributed control systems with delay," *Systems & Control Letters*, vol. 60, no. 9, pp. 675–682, 2011.

[18] F. Gouaisbaut and Y. Ariba, "Delay range stability of a class of distributed time delay systems," *Systems & Control Letters*, vol. 60, no. 3, pp. 211–217, 2011.

[19] Z. Wang, Y. Liu, G. Wei, and X. Liu, "A note on control of a class of discrete-time stochastic systems with distributed delays and nonlinear disturbances," *Automatica*, vol. 46, no. 3, pp. 543–548, 2010.

[20] Q. Zhu and J. Cao, "Adaptive synchronization under almost every initial data for stochastic neural networks with time-varying delays and distributed delays," *Communications in Nonlinear Science and Numerical Simulation*, vol. 16, no. 4, pp. 2139–2159, 2011.

[21] Z. G. Yan, H. J. Park, and W. H. Zhang, "Finite-time guaranteed cost control for Itô Stochastic Markovian jump systems with incomplete transition rates," *International Journal of Robust and Nonlinear Control*, vol. 27, no. 1, pp. 66–83, 2017.

[22] L. Li, Q. Zhang, and G. Li, "Robust finite-time H_∞ control for uncertain singular stochastic Markovian jump systems via proportional differential control law," *IET Control Theory & Applications*, vol. 8, no. 16, pp. 1625–1638, 2014.

[23] J. W. Zhu and G. H. Yang, "Adaptive sliding-mode control for stochastic Markovian jumping systems with actuator faults," *IET Control Theory and Applications*, vol. 10, no. 6, pp. 664–673, 2016.

[24] L. V. Hien and H. Trinh, "Stability analysis of two-dimensional Markovian jump state-delayed systems in the Roesser model with uncertain transition probabilities," *Information Sciences*, vol. 368, pp. 403–417, 2016.

[25] J. Na, Y. Huang, X. Wu, S.-F. Su, and G. Li, "Adaptive finite-time fuzzy control of nonlinear active suspension systems with input delay," *IEEE Transactions on Cybernetics*, vol. 50, no. 6, pp. 2639–2650, 2020.

[26] X.-B. Jin, T.-L. Su, J.-L. Kong, Y.-T. Bai, B.-B. Miao, and C. Dou, "State-of-the-Art mobile intelligence: enabling robots to move like humans by estimating mobility with artificial intelligence," *Applied Sciences*, vol. 8, no. 3, p. 379, 2018.

[27] Y. Z. Zhu and W. X. Zheng, "Multiple Lyapunov functions analysis approach for discrete-time switched piecewise-affine systems under dwell-time constraints," *IEEE Transactions on Automatic Control*, vol. 99, p. 1, 2019.

[28] X. B. Jin, "Parallel irregular fusion estimation based on nonlinear filter for indoor RFID tracking system," *International Journal of Distributed Sensor Networks*, vol. 12, no. 5, pp. 377–379, 2016.

[29] K. Liu, K. Li, and C. Zhang, "Constrained generalized predictive control of battery charging process based on a coupled thermoelectric model," *Journal of Power Sources*, vol. 347, pp. 145–158, 2017.

[30] S. Wang and J. Na, "Parameter estimation and adaptive control for servo mechanisms with friction compensation," *IEEE Transactions on Industrial Informatics*, vol. 16, no. 11, pp. 6816–6825, 2020.

[31] B. Y. Zhang, W. X. Zheng, and S. Y. Xu, "Filtering of markovian jump delay systems based on a new performance index," *IEEE Transactions on Circuits and Systems I: Regular Papers*, vol. 60, no. 5, pp. 1250–1263, 2013.

[32] L. G. Wu, P. Shi, H. J. Gao, and C. H. Wang, "filtering for 2D markovian jump systems," *Automatica*, vol. 44, no. 7, pp. 1849–1858, 2008.

[33] L. Xie, M. Fu, and C. E. de Souza, "H/sub infinity/control and quadratic stabilization of systems with parameter uncertainty via output feedback," *IEEE Transactions on Automatic Control*, vol. 37, no. 8, pp. 1253–1256, 1992.

[34] H. Gao and C. Wang, "Delay-dependent robust $H_\infty$and $L_2 - L_\infty$ filtering for a class of uncertain nonlinear time-delay systems," *IEEE Transaction Automatic Control*, vol. 48, no. 9, pp. 1253–1256, 2003.

[35] K. Gu, "A integral inequality in the stability problem of time-delay systems," in *Proceeding of the 39th IEEE Conference on Decision and Control*, pp. 2805–2810, Sydney, Australia, December 2000.

Hindawi
Complexity
Volume 2021, Article ID 6663851, 11 pages
https://doi.org/10.1155/2021/6663851

Research Article

Multiscale Feature Filtering Network for Image Recognition System in Unmanned Aerial Vehicle

Xianghua Ma, Zhenkun Yang, and Shining Chen

School of Electrical and Electronic Engineering, Shanghai Institute of Technology, Shanghai 201418, China

Correspondence should be addressed to Xianghua Ma; xhuam@sit.edu.cn

Received 19 November 2020; Revised 28 December 2020; Accepted 3 February 2021; Published 19 February 2021

Academic Editor: Rui Wang

For unmanned aerial vehicle (UAV), object detection at different scales is an important component for the visual recognition. Recent advances in convolutional neural networks (CNNs) have demonstrated that attention mechanism remarkably enhances multiscale representation of CNNs. However, most existing multiscale feature representation methods simply employ several attention blocks in the attention mechanism to adaptively recalibrate the feature response, which overlooks the context information at a multiscale level. To solve this problem, a multiscale feature filtering network (MFFNet) is proposed in this paper for image recognition system in the UAV. A novel building block, namely, multiscale feature filtering (MFF) module, is proposed for ResNet-like backbones and it allows feature-selective learning for multiscale context information across multiparallel branches. These branches employ multiple atrous convolutions at different scales, respectively, and further adaptively generate channel-wise feature responses by emphasizing channel-wise dependencies. Experimental results on CIFAR100 and Tiny ImageNet datasets reflect that the MFFNet achieves very competitive results in comparison with previous baseline models. Further ablation experiments verify that the MFFNet can achieve consistent performance gains in image classification and object detection tasks.

1. Introduction

To understand the environment, unmanned aerial vehicles (UAVs) need to integrate information from various sensors such as cameras, lidar, radar, and GPS. The information from the camera provides a straightforward way of visual perception, which supports further advanced thinking and reasoning for UAV. One of the important tasks in the visual perception of UAV, image recognition [1, 2] has always been a research hotspot. Convolutional neural networks (CNNs) have been widely used in solving visual cognition tasks, such as image classification [3, 4], object detection [5], and salient object detection [6]. Unlike traditional hand-crafted features (e.g., HOG [7]), features learned by CNNs based on data require minimal human involvement during training. Thus, most of the recent research on visual recognition is based on network engineering. It is becoming increasingly important to design better CNN architectures for visual recognition tasks.

Generally, for the design criterion of convolution networks, there are three important issues: depth, width, and cardinality. In 2015, Simonyan and Zisserman [8] designed an effective and very deep network by stacking blocks of the same shape, which achieved the state-of-the-art performance. However, as CNNs become increasingly deeper, gradient propagation becomes more difficult. In order to alleviate the problem of gradient disappearance caused by the increase of network depth, He et al. [9] proposed a deep residual learning approach, which referred to the input of the layer to learn the residual function. Experiments showed that this residual learning method can be easily optimized and can obtain higher accuracy by increasing the depth. Szegedy et al. [10] showed that width was another important factor to improve the performance of CNNs. Compared with shallower and less extensive networks, the main advantage of this method was that it can significantly improve the accuracy with a moderate increase in computing demand. ResNeXt [11] employed the potential of grouped convolutions and empirically showed that increasing cardinality was more effective than going deeper or wider as capacity increases. In 2016, Zagoruyko and Komodakis [12]

demonstrated that using more channels and a wider convolution can improve detection accuracy. Then, Huang et al. [13] proposed a dense convolutional network, which utilized direct connections between any two layers with the same feature map size to strengthen feature propagation. Ding et al. [14] designed a novel convolutional network, which used asymmetric convolutions to strengthen the square convolution filters.

Other network studies [15–18] exploited the potential of network from attention mechanism. For example, Hu et al. [15] designed a novel squeeze and excitation (SE) block that adaptively recalibrates channel-wise feature responses by emphasizing the interdependent channel maps. After that, Woo et al. [16] introduced a simple attention module called CBAM, which exploited both spatial and channel-wise attention to emphasize meaningful features along channel and spatial axes. Li et al. [17] proposed selective kernel networks (SKNets), which realized the adaptive receptive field sizes of neurons in a nonlinear approach. Furthermore, previous work [18] captured multiscale features through the additive effects of feature-selective and spatial attention. Targets appear at different scales in the image frame and are often occluded by clutter, which is a major challenge for image recognition algorithms in UAV applications. Therefore, multiscale feature representation is particularly critical for image recognition system in the UAV. However, most existing multiscale feature representation methods using attention mechanism simply employ several attention blocks to adaptively recalibrate the feature response, which overlooks the context information at a multiscale level.

Based on this analysis, in this paper, a multiscale feature filtering network (MFFNet) is proposed for image recognition system in the UAV. In MFFNet, we propose a novel building block, called multiscale feature filtering (MFF) module. Our key idea is to retain important information about smaller and insignificant objects by allowing feature-selective learning for multiscale context information across multiparallel branches. These branches employ multiple atrous convolutions at different scales, respectively, and further adaptively generate channel-wise feature responses by emphasizing channel-wise dependencies.

It is possible to construct an MFF network (MFFNet) by simply replacing the standard 3×3 filters in ResNet-like backbones with MFF modules. Besides, while the template for the MFF module is generic, the role it performs varies at different depths throughout the MFFNet. To compare the difference between the MFF module and standard 3×3 filter, we visualize the class activation mapping using Grad-CAM [19] and observe that the MFFNet-based CAM results tend to focus on the whole object more than other baseline networks. Experimental results on CIFAR [20], Tiny ImageNet [21], PASCAL VOC 2007 [22], MS COCO [23], and UAV123 [24] datasets show that our proposed method can achieve consistent performance gains in image recognition tasks.

The rest of the paper is organized as follows: Section 2 introduces our proposed MFFNet and presents the details of multiscale feature filtering (MFF) module. Section 3 shows experimental settings and analyses experimental results. Section 4 concludes this study and describes future work of this paper.

2. Method

In this section, the MFFNet, a novel backbone network for image recognition system in the UAV, is introduced. An overview of MFFNet is depicted in Figure 1. A MARNet contains four stages, and each stage contains multiple MFF units. Each MFF unit consists of a sequence of a 1×1 convolution, an MFF module, a 1×1 convolution, and a further skip layer. Figure 2 shows the schema of an MFF unit.

Furthermore, we present the details of multiscale feature filtering (MFF) module. The MFF module consists of three submodules: split module (SM), multiscale branch module (MBM), and fusion module (FM).

2.1. MFFNet Architecture. MFF modules can be integrated into a standard architecture, such as ResNet [9], by replacing every 3×3 layer with MFF modules. Here, MFF modules are used with MFF units. By making this change to each such module in the MFF unit, an MFFNet network can be constructed. Further variants that integrate MFF modules with ResNeXt [11], DenseNet [13], ShuffleNetV2 [25], and MobileNetV2 [26] can be constructed by following similar schemes. Like ResNet-50 and ResNeXt-50, MFFNet-50 and MFFNeXt-50 can be constructed by simply stacking a set of MFF units. MFFNet-50 can be obtained by changing the number of MFF units per stage. MFFNeXt-50 can be obtained from MFFNet-50 by changing the bottleneck width [12] and cardinality [11] of the MFF units. The cardinality, c, is the number of groups within a filter, whereas the bottleneck width, d, is the number of channels in a layer.

Table 1 shows the MFFNet-50 and MFFNeXt-50 architectures with four phases, using $\{3, 4, 6, 3\}$ MFF units. The filter sizes and feature dimensionalities of a residual block are shown inside the brackets. The number of stacked blocks for each stage is shown outside the brackets. "$B = 3$" denotes an MFF module with three branches, and "$c = 32$" suggests grouped convolutions with 32 groups.

2.2. Multiscale Feature Filtering Module. The structure of the MFF module is illustrated in Figure 3. First, in MFF module, given an input feature map, to obtain fine-grained multiscale information, the SM divides the input feature map into multiple feature map subsets. Second, to capture the objects at different scales, the MBM employs multiple atrous convolutions with different rates. Meanwhile, these branches use atrous convolutions instead of standard convolutions to reduce the model's parameters. Besides, the MBM further selectively generates channel-wise feature responses by emphasizing channel-wise dependencies. Once channel-wise feature responses with different scales are captured, the transformed features are connected by skip structures to enhance feature propagation. Third, a channel concatenation operator is applied to fuse previously captured information from different branches.

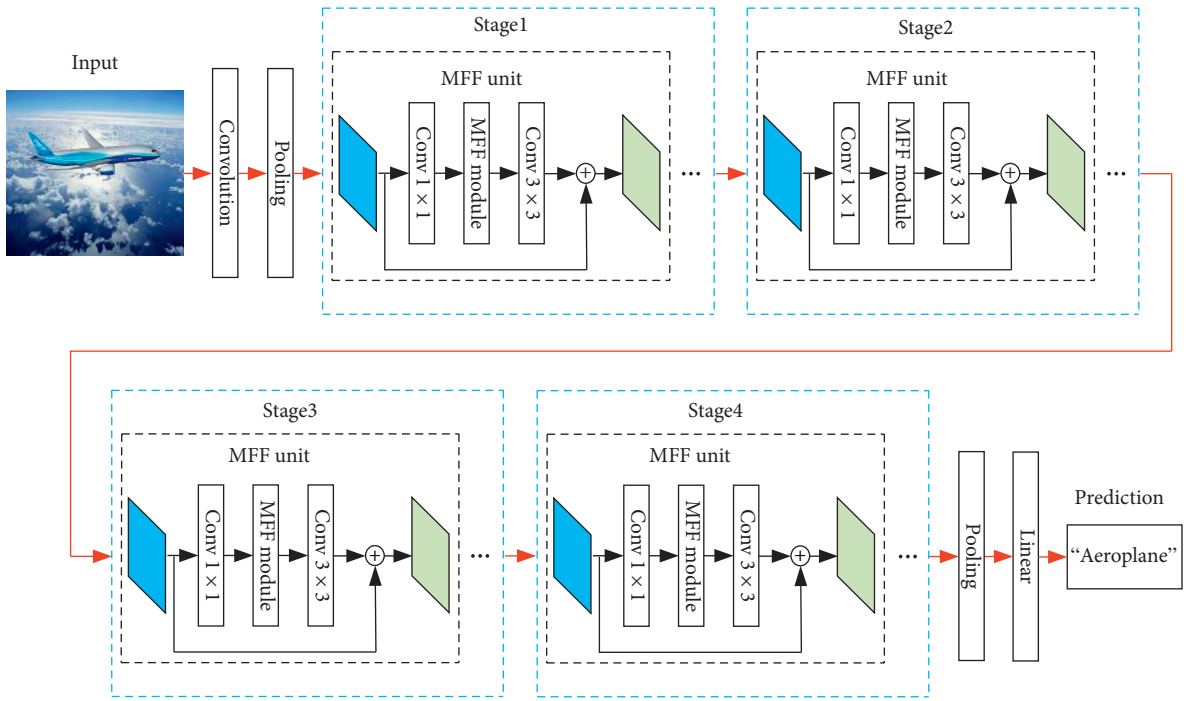

Figure 1: An MFFNet with four stages.

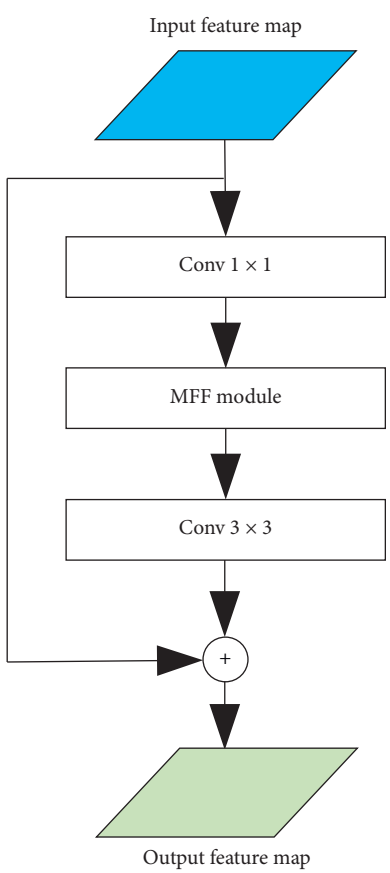

Figure 2: An MFF unit.

2.2.1. Split Module. As shown in Figure 1, in split module (SM), for any given input feature map $X \in \mathbb{R}^{H\times W\times C'}$, where $X = [X^1, X^2, \ldots, X^{C'}]$, to obtain fine-grained multiscale information, the SM first equally splits X into n feature map subsets, such as the three feature map subsets shown in Figure 1, namely, $X_1 \in \mathbb{R}^{H\times W\times C}$, $X_2 \in \mathbb{R}^{H\times W\times C}$, and $X_3 \in \mathbb{R}^{H\times W\times C}$, where $C = (C'/3)$. H, W, and C denote the height, width, and number of channels of the feature map, respectively.

2.2.2. Multiscale Branch Module. The multiscale branch module (MBM) consists of three branches, namely, A-branch, B-branch, and C-branch. Moreover, each branch contains a feature filtering module (FFM). The structure of the feature filtering module (FFM) is depicted in Figure 4.

$$m^c = F_{gm}(U^c) = \max\left[\sum_{i=1}^{H}\sum_{j=1}^{W} U^c(i,j)\right], \tag{1}$$

In FFM, we selectively generate channel-wise feature responses by emphasizing channel-wise dependencies. Specifically, for the preprocessed feature map $U \in \mathbb{R}^{H\times W\times C}$, firstly an FFM uses global average pooling and global max pooling to generate two different channel-wise statistics as $n \in \mathbb{R}^C$ and $m \in \mathbb{R}^C$. The global average pooling and global max pooling operations are denoted as F_{ga} and F_{gm}. Specifically, the c-th element of n and m is calculated as

$$n^c = F_{ga}(U^c) = \frac{1}{H\times W}\sum_{i=1}^{H}\sum_{j=1}^{W} U^c(i,j), \tag{2}$$

Table 1: The third and fourth columns show the architecture of MFFNet-50 and MFFNeXt-50, respectively.

Layers	Output size	MFFNet-50	MFFNeXt-50 (32 × 4d)
Convolution	112 × 112	Conv 7 × 7, 64, stride 2	
Pooling	56 × 56	Max pool 3 × 3, stride 2	
Stage 1	56 × 56	$\begin{bmatrix} 1\times 1, & 64 \\ \mathrm{MFF}[b=3], & 64 \\ 1\times 1, & 512 \end{bmatrix} \times 3$	$\begin{bmatrix} 1\times 1, & 128 \\ \mathrm{MFF}[b=3, c=32], & 128 \\ 1\times 1, & 256 \end{bmatrix} \times 3$
Stage 2	28 × 28	$\begin{bmatrix} 1\times 1, & 128 \\ \mathrm{MFF}[b=3], & 128 \\ 1\times 1, & 512 \end{bmatrix} \times 4$	$\begin{bmatrix} 1\times 1, & 256 \\ \mathrm{MFF}[b=3, c=32], & 256 \\ 1\times 1, & 512 \end{bmatrix} \times 4$
Stage 3	14 × 14	$\begin{bmatrix} 1\times 1, & 256 \\ \mathrm{MFF}[b=3], & 256 \\ 1\times 1, & 1024 \end{bmatrix} \times 6$	$\begin{bmatrix} 1\times 1, & 512 \\ \mathrm{MFF}[b=3, c=32], & 512 \\ 1\times 1, & 1024 \end{bmatrix} \times 6$
Stage 4	7 × 7	$\begin{bmatrix} 1\times 1, & 512 \\ \mathrm{MFF}[b=3], & 512 \\ 1\times 1, & 2048 \end{bmatrix} \times 3$	$\begin{bmatrix} 1\times 1, & 1024 \\ \mathrm{MFF}[b=3, c=32], & 1024 \\ 1\times 1, & 2048 \end{bmatrix} \times 3$
Classification layer	1 × 1	Global average pool 1000 d fully connected, softmax	

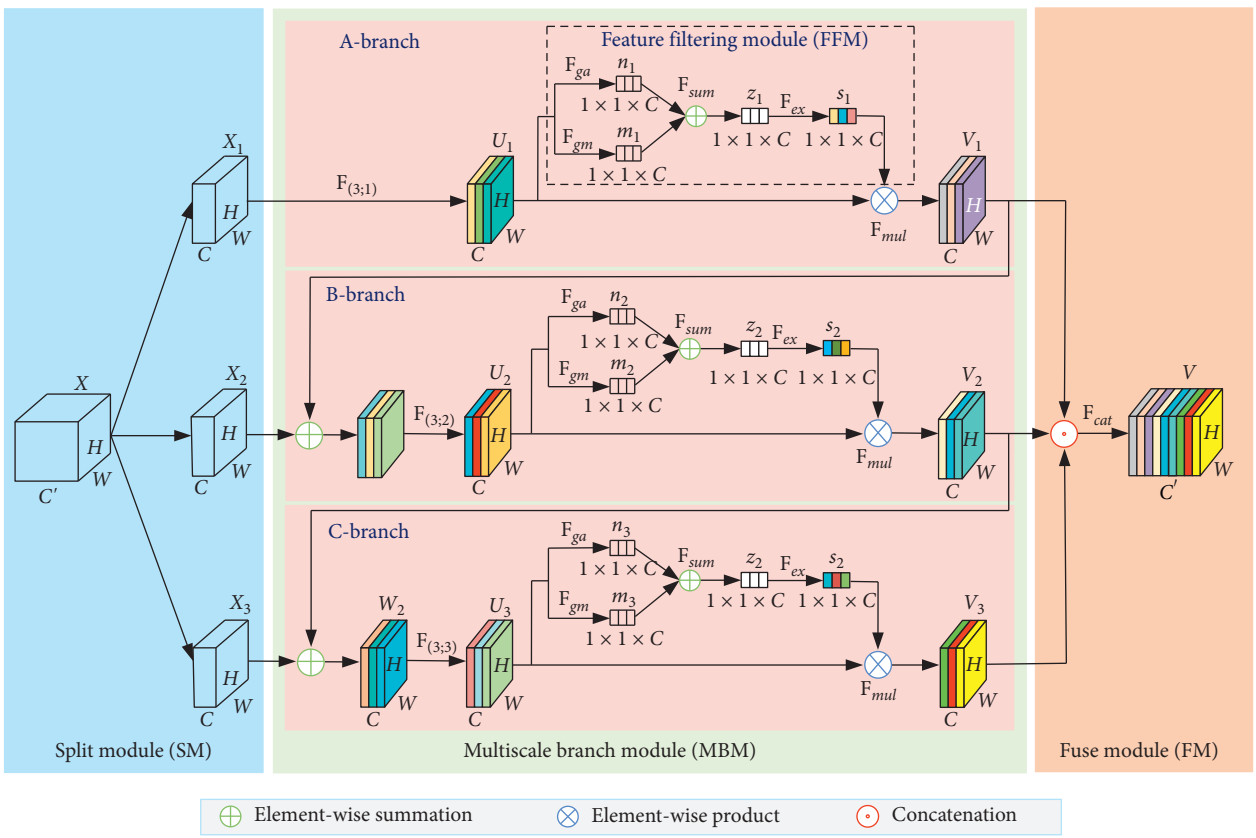

Figure 3: The structure of the multiscale feature filtering (MFF) module.

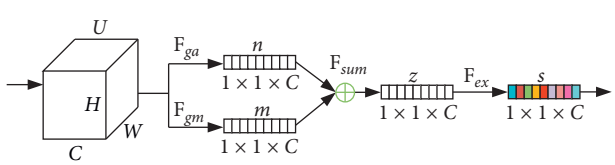

Figure 4: The structure of the feature filtering module (FFM).

where $U = [U^1, U^2, \ldots, U^c]$. U^c denotes the c-th feature map channel in the feature map U. In addition, $U^c(i, j)$ refers to (i, j) – th pixel in U^c.

Then, to fuse the transformed feature information from global average pooling and global max pooling, an element-wise summation is used to obtain finer global channel-wise statistics as $z \in \mathbb{R}^C$.

$$z = F_{\text{sum}}(n, m) = n \oplus m, \tag{3}$$

where F_{sum} indicates the element-wise summation operation between channel-wise statistics n and m. Furthermore, in order to make use of the previously fused feature information, the previously global channel-wise statistics z is forwarded to a F_{ex} function, which is composed of one dimensionality-reduction layer with parameters M_1 and reduction ratio l, dimensionality-increasing layer with parameters M_2, sigmoid activation function, and ReLU activation function. The final output of the FFM is computed as

$$s = F_{ex}(z) = \sigma\left(M_2 \delta\left(M_1 z\right)\right), \tag{4}$$

where σ and δ are the sigmoid and ReLU activation function, respectively. $M_1 \in \mathbb{R}^{(C/l)\times C}$ and $M_2 \in \mathbb{R}^{C\times(C/l)}$, where $l = 16$.

Employing large atrous rate enlarges the model's receptive field, so that object coding can be performed at multiple scales. As shown in Figure 5, A-branch, B-branch, and C-branch employ three atrous convolutions with different atrous rates r, where $r = \{1, 2, 3\}$. In addition, these branches use atrous convolutions with different rates instead of standard convolutions to reduce the model's parameters.

For any atrous convolution layer, the learned set of convolution filters $G = [G^1, G^2, \ldots, G^c]$, where $G^c \in \mathbb{R}^{K\times K\times C}$ refers to the parameters of the corresponding c-th convolution filter. Let $I \in \mathbb{R}^{H\times W\times C}$ denote the input of the atrous convolution layer. $U = [U^1, U^2, \ldots, U^c]$ are the output of the atrous convolution layer. For the c-th filter at such a layer, the corresponding output feature map channel is

$$U^c = F_{(K;r)}\left(G^c, I\right), \tag{5}$$

where $F_{(K;r)}$ denotes an atrous convolution layer with filter size $K \times K$ and atrous rate r.

In A-branch, for the input feature map subset X_1 obtained from the split module, an atrous convolution layer with filter size 3×3 and atrous rate $r = 1$ is conducted to generate the output feature map U_1 of a specific scale. For the c-th filter at such a layer, $K = 3$ and $r = 1$ are put into equation (5) to obtain the c-th output feature map channel.

$$U_1^c = F_{3\times 1}\left(G(1)^c, X_1\right), \tag{6}$$

where $F_{(3;1)}$ denotes an atrous convolution layer with filter size 3×3 and atrous rate $r = 1$. $G(1)$ denotes the learned set of $F_{(3;1)}$. $G(1) = [G(1)^1, G(1)^2, \ldots, G(1)^c]$ and $X_1 = [X_1^1, X_1^2, \ldots, X_1^c]$.

Further, in order to take advantage of the information aggregated in the feature filtering module (FFM), the feature map U_1 is sent to the FFM. The output of the FFM in A-branch is denoted as s_1. The final output V_1 of the A-branch is obtained by rescaling the feature map U_1 with an element-wise multiplication operation.

$$V_1 = F_{\text{mul}}\left(U_1, s_1\right) = U_1 \otimes s_1, \tag{7}$$

where F_{mul} indicates the element-wise multiplication operation.

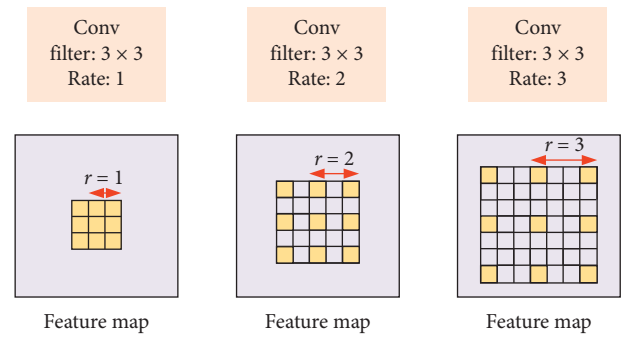

Figure 5: Atrous convolution with filter size 3×3 and different rates. A-branch: atrous convolution with filter size 3×3 and rate $(r) = 1$. B-branch: atrous convolution with filter size 3×3 and rate $(r) = 2$. C-branch: atrous convolution with filter size 3×3 and rate $(r) = 3$.

In B-branch, to enhance feature propagation, firstly we fuse the output V_1 of the A-branch and the feature map subset X_2 obtained from the split module by using an element-wise summation operation. Thus, the fusion output feature map W_1 of V_1 and X_2 is computed as

$$W_1 = F_{\text{sum}}\left(V_1, X_2\right) = V_1 \oplus X_2. \tag{8}$$

Then, an atrous convolution layer with filter size 3×3 and atrous rate $r = 2$ is conducted to generate the output feature map U_2. For the c-th filter at such a layer, $K = 3$ and $r = 2$ are put into equation (1) to obtain the c-th output feature map channel.

$$U_2^c = F_{(3;2)}\left(G(2)^c, W_1\right), \tag{9}$$

where $F_{(3;2)}$ denotes an atrous convolution layer with filter size 3×3 and atrous rate $r = 2$. $G(2)$ denotes the learned set of $F_{(3;2)}$. $G(2) = [G(2)^1, G(2)^2, \ldots, G(2)^c]$ and $W_1 = [W_1^1, W_1^2, \ldots, W_1^c]$.

Similar to the A-branch, in order to take advantage of the information aggregated in the feature filtering module (FFM), the feature map U_2 is sent to the FFM. The output of the FFM in B-branch is denoted as s_2. The final output V_2 of the B-branch is obtained by rescaling the feature map U_2 with an element-wise multiplication operation.

$$V_2 = F_{\text{mul}}\left(U_2, s_2\right) = U_2 \otimes s_2. \tag{10}$$

For the C-branch, similar to the B-branch, firstly we fuse the output V_2 of the C-branch and the feature map subset X_3 obtained from the split module by using an element-wise summation operation. Thus, the fusion output feature map W_2 of V_2 and X_3 is computed as

$$W_2 = F_{\text{sum}}\left(V_2, X_3\right) = V_2 \oplus X_3. \tag{11}$$

Then, an atrous convolution layer with filter size 3×3 and atrous rate $r = 3$ is conducted to generate the output feature map U_3. For the c-th filter at such a layer, $K = 3$ and $r = 3$ are put into equation (1) to obtain the c-th output feature map channel.

$$U_3^c = F_{(3;3)}\left(G(3)^c, W_2\right), \tag{12}$$

where $F_{(3;3)}$ denotes an atrous convolution layer with filter size 3×3 and atrous rate $r = 3$. $G(3)$ denotes the learned set of $F_{(3;3)}$. $G(3) = [G(3)^1, G(3)^2, \ldots, G(3)^c]$ and $W_2 = [W_2^1, W_2^2, \ldots, W_2^c]$.

The final output V_3 of the C-branch is obtained by rescaling the feature map U_3 with an element-wise multiplication operation.

$$V_3 = F_{\text{mul}}\left(U_3, s_3\right) = U_3 \otimes s_3, \tag{13}$$

where s_3 is the output of the FFM in the C-branch.

2.3. Fusion Module. As shown in Figure 1, in order to take advantage of the feature information aggregated in the multiscale branch module (MBM), the outputs of A-branch, B-branch, and C-branch are forwarded to the fusion module (FM), which is implemented by a concatenation function. The output of FM is V, which can be calculated by

$$V = F_{\text{cat}}\left(V_1, V_2, V_3\right) = V_1 \odot V_2 \odot V_3, \tag{14}$$

where F_{cat} denotes the concatenation operation between feature maps.

3. Experimental Results and Analysis

In this section, we describe experiments that study the effectiveness of MFF modules for a range of tasks, datasets, and model architectures. Besides, all models are implemented by using the PyTorch framework.

For image classification tasks, we evaluate all models on the CIFAR-100 and Tiny ImageNet datasets. The objects in the CIFAR-100 and Tiny ImageNet datasets have features of different scales, which can effectively verify the effectiveness of our proposed MFFNet in the UAV. For benchmarking, we evaluate the single-crop top-1 error rate and adopt the same data augmentation scheme used in [9, 27]. Moreover, we train the network using stochastic gradient descent with momentum 0.9, weight decay 0.0001, and a mini-batch size of 32 on 1 RTX 2080Ti GPU. For the CIFAR-100 and Tiny ImageNet datasets, every model is trained for 200 epochs. We start with a learning rate of 0.1, which is divided by 10 at 60, 120, and 160 epochs, respectively.

For object detection tasks, all models are trained in the PASCAL VOC 2007 and MS COCO datasets with 1 RTX 2080Ti GPU and the mini-batch size is 2 images. We use a weight decay of 0.0001 and a momentum of 0.9. In addition, all models are trained for 80k iterations with a learning rate of 0.002 and then for 30k iterations with 0.0001. Other implementation details are as in [28]. Besides, in order to verify the effectiveness of our proposed method, we further test the MFFNet on the UAV123 dataset, which is captured from a low-altitude aerial perspective.

3.1. Experiments on Tiny ImageNet. We evaluate our method on the Tiny ImageNet dataset, which contains 100k training images, 10k validation images, and 10k test images in 200 classes. Each class has 500 training images, 50 validation images, and 50 test images. An input image is 224×224 pixels randomly cropped from a resized image. We use ResNet-50, ResNet-101, and ResNeXt-50 as the representatives for the residual model architecture. In addition, we compare the results with those from the SENet and SKNet model architectures, which are based on attention mechanisms. We compare the single-crop top-1 error rate of each baseline and its MFFNet counterpart on the Tiny ImageNet dataset. As shown in Table 2, MFFNeXt-50 achieves significant performance gains over ResNeXt-50, with a reduction of 3.82% in the error rate. Compared with ResNet-50, MFFNet-50 is better by 1.04%. Meanwhile SENet-29 ($16c \times 32d$) achieves 33.67% error and MFFNeXt-50 ($32c \times 4d$) achieves 32.76% error. MFFNeXt-50 is better than SKNet-29 ($16c \times 32d$) by 2.27%. Besides, MFFNeXt-50 ($32c \times 4d$) achieves a top-1 error rate of 32.59%, although SENet-29 ($16c \times 32d$) needs 26.88% more parameters.

Table 2: Single 224×224 cropped top-1 error rate (%) and complexity comparisons on the Tiny ImageNet validation set. #P is the number of parameters. Atrous rate $r = \{1, 2, 3\}$.

Models	#P	Top-1 error rate (%)
ResNet-50	24.59	35.97
ResNet-101	43.24	35.15
ResNeXt-50 ($32c \times 4d$)	24.21	34.91
SENet-29 ($16c \times 32d$)	34.78	33.87
SKNet-29 ($16c \times 32d$)	27.45	33.55
MFFNet-50	25.82	35.03
MFFNet-101	44.86	33.84
MFFNeXt-50 ($32c \times 4d$)	25.43	32.59

The top-1 testing error rate versus number of epochs for the different architectures is shown in Figure 6. SKNet-29 ($16c \times 32d$) needs 27.45 M parameters, whereas MFFNeXt-50 ($32c \times 4d$) needs only 25.43 M trainable parameters and achieves a higher accuracy. The results show that MFF modules consistently improve the performance of state-of-the-art CNNs.

3.2. Experiments on CIFAR-100. To further evaluate the performance of the MFFNet, we conduct experiments on CIFAR-100. This dataset consists of 60k 32×32 color images drawn from 100 classes. There are 50k training images and 10k testing images. The 100 classes in CIFAR-100 are grouped into 20 superclasses. Each image has a fine label and a coarse label. We use implementations of ShuffleNetV2 $1\times$, MobileNetV2 $1\times$, ResNet-50, ResNeXt-50, ResNet-101, and DenseNet-BC-121 ($k = 12$) as the representative models. Similar to ShuffleNet [3], ShuffleNetV2 $1\times$ and MobileNetV2 $1\times$ mean scaling the number of filters by 1 time.

Table 3 shows more results of single-crop testing on CIFAR-100. Note that while ResNet-50 achieves a 21.55% error rate, MFFNet-50 achieves a 21.06% error rate. Moreover, MFFNeXt-50 ($32c \times 4d$) outperforms ResNeXt-50 ($32c \times 4d$) by achieving 20.03% top-1 error. For lightweight models, we compare ShuffleNetV2 $1\times$ with MFF and MobileNetV2 $1\times$ with MFF to the original ShuffleNetV2 $1\times$ and MobileNetV2 $1\times$, ShuffleNetV2 $1\times$ with MFF and

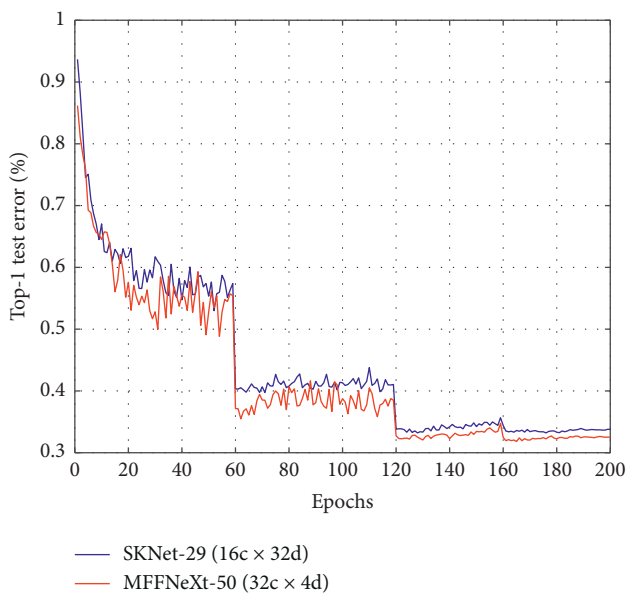

Figure 6: Top-1 testing error rate versus number of epochs for Tiny ImageNet. The numbers of parameters for SKNet-29 (16c × 32d) and MFFNeXt-50 (32c × 4d) are 27.45 M and 25.43 M, respectively.

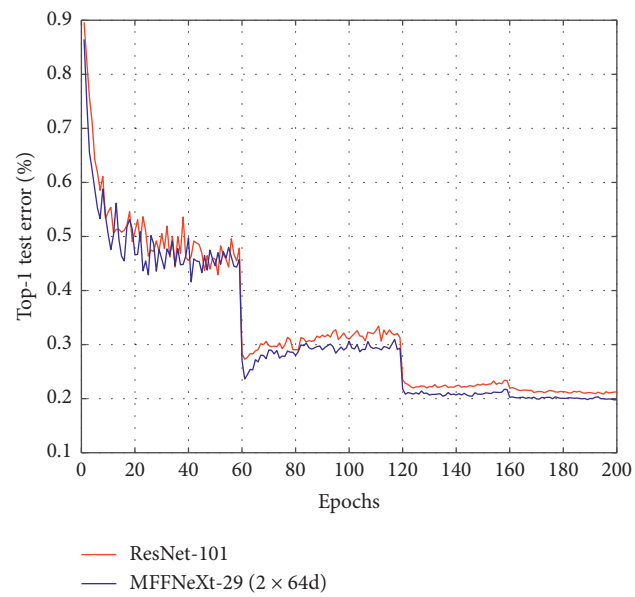

Figure 7: Top-1 testing error rate versus number of epochs for CIFAR-100. The numbers of parameters for ResNet-101 and MFFNeXt-29 (2c × 64) are 42.70 M and 9.37 M, respectively.

Table 3: Single 224 × 224 cropped top-1 error (%) and complexity comparisons on CIFAR-100. Atrous rate $r = \{1, 2, 3\}$.

Models	#P	Top-1 error rate (%)
ShuffleNetV2 1 ×	1.36	30.58
MobileNetV2 1 ×	2.37	30.21
ResNet-50	23.68	21.55
ResNet-101	42.70	21.25
ResNeXt-50 (32c × 4d)	23.14	20.59
ResNeXt-29 (2c × 64d)	9.22	22.63
ResNeXt-29 (4c × 64)	36.58	21.29
DenseNet-BC-121 ($k = 12$)	7.05	22.93
ShuffleNetV2 1 × + MFF	1.41	29.62
MobileNetV2 1 × + MFF	2.53	29.27
MFFNet-50	24.86	21.06
MFFNet-101	44.23	20.31
MFFNeXt-50 (32c × 4d)	24.61	20.03
MFFNeXt-29 (2c × 64d)	9.37	19.78
MFFNeXt-29 (4c × 64d)	37.85	17.36
DenseNet-BC-121 ($k = 12$) + MFF	7.59	21.54

MobileNetV2 1 × with MFF outperform original ShuffleNetV2 1 × and MobileNetV2 1 × by 0.96% and 0.94%, respectively.

In addition, for densely connected models, we choose a DenseNet-BC network with 121 layers. DenseNet-BC-121 ($k = 12$) with MFF achieves a performance gain of 1.29% over DenseNet-BC-121 ($k = 12$). The top-1 testing error rate versus number of epochs for the different architectures is shown in Figure 7. We can clearly see that MFFNeXt-29 (2c × 64d) outperforms ResNet-101 by achieving 19.78% top-1 error, although ResNet-101 needs more parameters.

3.3. Ablation Studies on CIFAR-100. To further validate the effectiveness of the MFFNet, we undertake ablation studies on the CIFAR-100 dataset. We first evaluate the trade-off between cardinality c and bottleneck width d. Next, in MFF module, we investigate the impact of changes in the complexity on performance by combining different atrous rates r.

3.3.1. Cardinality versus Width. To study the effects of the cardinality c and the width of the bottleneck d, we start from the three-branch case and fix the setting atrous rates $r = \{1, 2, 3\}$. We first evaluate the trade-off between cardinality c and bottleneck width d. Table 4 shows the results. MFFNeXt-29 (2c × 64d) has a top-1 error of 19.78%, which is 2.78% lower than that for MFFNeXt-29 (1c × 64d). We can see that as the cardinality c increases from 1 to 4 for constant bottleneck width, the error rate falls. In addition, as the bottleneck width d increases from 24 to 64 for constant cardinality c, the error rate again decreases.

We also note that increasing cardinality c can achieve much better results than going wider. For instance, MFFNeXt-29 (2c × 40d) performs better than MFFNeXt-29 (1c × 64d), even though it has 66.33% fewer parameters. MFFNeXt-29 (2c × 64d) needs 9.37 M parameters, whereas MFFNeXt-29 (4c × 40d) needs only 9.21 M trainable parameters and achieves a higher accuracy.

3.3.2. Combinations of Different Atrous Rates. Next, we investigate combinations of different atrous rates. The atrous rate r is used to control the receptive field size. MFFNet uses 3 × 3 filters with different atrous rates r. To limit the search

Table 4: Single 224×224 cropped top-1 error (%) and complexity comparisons on CIFAR-100. Atrous rate $r = \{1, 2, 3\}$.

Models	#P	Top-1 error rate (%)
MFFNeXt-29 (1c × 24d)	0.43	27.61
MFFNeXt-29 (1c × 40d)	1.05	24.73
MFFNeXt-29 (1c × 64d)	3.98	22.56
MFFNeXt-29 (2c × 24d)	0.76	24.03
MFFNeXt-29 (2c × 40d)	1.34	20.62
MFFNeXt-29 (2c × 64d)	9.37	19.78
MFFNeXt-29 (4c × 24d)	3.67	20.45
MFFNeXt-29 (4c × 40d)	9.21	19.01

Table 5: Results for MFFNeXt-29 (2c × 64d) for combinations of different atrous rates.

Models	$r = 1$	$r = 2$	$r = 3$	$r = 4$	#P	Top-1 error rate (%)
MFFNeXt-29 (2c × 64d)	Y	Y	N	N	6.63	20.77
MFFNeXt-29 (2c × 64d)	Y	N	Y	N	6.63	20.24
MFFNeXt-29 (2c × 64d)	Y	N	N	Y	6.63	20.01
MFFNeXt-29 (2c × 64d)	Y	Y	Y	N	9.37	19.78
MFFNeXt-29 (2c × 64d)	Y	Y	N	Y	9.37	19.49
MFFNeXt-29 (2c × 64d)	Y	N	Y	Y	9.37	19.75
MFFNeXt-29 (2c × 64d)	Y	Y	Y	Y	12.11	19.83

Table 6: Results for MobileNetV2 1 × with MFF for combinations of different atrous rates.

Models	$r = 1$	$r = 2$	$r = 3$	$r = 4$	#P (M)	Top-1 error rate (%)
MobileNetV2 1 × + MFF	Y	Y	N	N	2.44	29.65
MobileNetV2 1 × + MFF	Y	N	Y	N	2.44	29.59
MobileNetV2 1 × + MFF	Y	N	N	Y	2.44	30.25
MobileNetV2 1 × + MFF	Y	Y	Y	N	2.53	29.27
MobileNetV2 1 × + MFF	Y	Y	N	Y	2.53	29.79
MobileNetV2 1 × + MFF	Y	N	Y	Y	2.53	30.21
MobileNetV2 1 × + MFF	Y	Y	Y	Y	2.61	30.18

space, we use only four different atrous rates, $r = 1$, 2, 3, and 4. To study their effects, we change the other three branches for the 3×3 filter with $r = 1$ in the first filter branch of the MFF modules. Tables 5 and 6 show the top-1 error rate for MFFNeXt-29 (2c × 64d) and MobileNetV2 1 × with MFF. We can make three major observations as follows:

(1)First, when the number of branches in an MFF module $b = 2$, the top-1 error rate for MFFNeXt-29 (2c × 64d) gradually decreases as the atrous rate in the second branch increases. Moreover, MFFNeXt-29 (2c × 64d) achieves the lowest top-1 error for $r = \{1, 4\}$. In contrast, the top-1 error rate of MobileNetV2 1 × with MFF gradually increased as the atrous rate in the second branch increased.

(2) Second, when the number of branches in an MFF module $b = 3$, MFFNeXt-29 (2c × 64d) achieves the lowest top-1 error rate for $r = \{1, 2, 4\}$. However, MobileNetV2 1 × with MFF has the lowest top-1 error rate for $r = \{1, 2, 3\}$.

(3) Third, when the number of branches in an MFF module $b = 4$, MFFNeXt-29 (2c × 64d) and MobileNetV2 1 × with MFF do not achieve the lowest top-1 error rate. For example, MFFNeXt-29 (2c × 64d) with $b = 3$ achieves higher accuracy, although MFFNeXt-29 (2c × 64d) with $b = 4$ needs 22.63% more parameters. MobileNetV2 1 × with MFF for $r = \{1, 2, 3\}$ outperforms MobileNetV2 1 × with MFF for $r = \{1, 2, 3, 4\}$ by above 0.91% accuracy.

3.3.3. Class Activation Mapping. To intuitively understand the multiscale representation ability of MFFNet, we visualize the class activation mapping (CAM) using Grad-CAM for different networks. Grad-CAM uses gradients to calculate the importance of the spatial locations in convolutional layers.

Figure 8 compares the CAM for representative backbone networks. The areas that have a larger impact on the classification are covered with lighter colors. We can clearly see that the MFFNet-based CAM results tend to focus on the whole object more than ResNet.

3.3.4. Object Detection. The PASCAL VOC 2007 and MS COCO datasets are in 20 and 80 object categories, respectively. The PASCAL VOC 2007 dataset has about 5k trainval images and 5k test images. We use the 5k trainval images and 5k test images for training and 5k test images for validation. The MS COCO dataset has 80k images for training, 40k for validation, and 20k for testing. We used the 80k training set plus a 35k validation subset for training and a 5k validation subset for validation. We adopt Faster-RCNN [28] as our detection method and evaluate the average precision (AP)

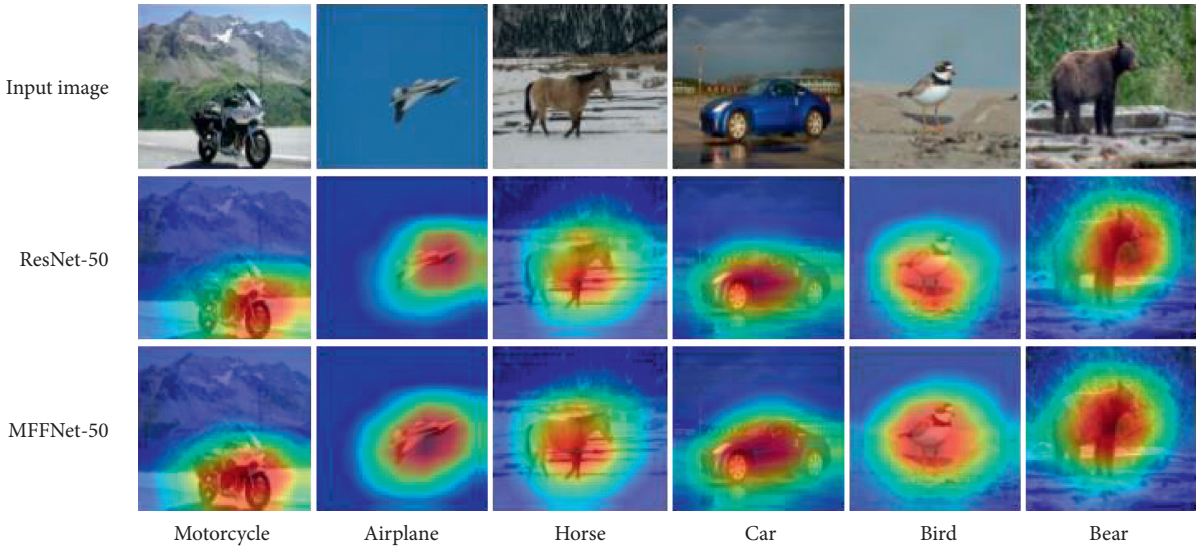

Figure 8: Grad-CAM visualization results, using ResNet-50 and our proposed MFFNet-50 with atrous rates $r = \{1, 2, 4\}$ as the backbone networks.

Table 7: Object detection. The detector is Faster-RCNN. Atrous rates $r = \{1, 2, 4\}$.

Backbone	Dataset	AP (%)	Inference (ms)
ResNet-101	VOC 2007	71.4	73.9
MFFNet-101 (ours)	VOC 2007	72.8	75.5
ResNet-101	COCO	25.6	135.3
MFFNet-101 (ours)	COCO	26.9	138.5

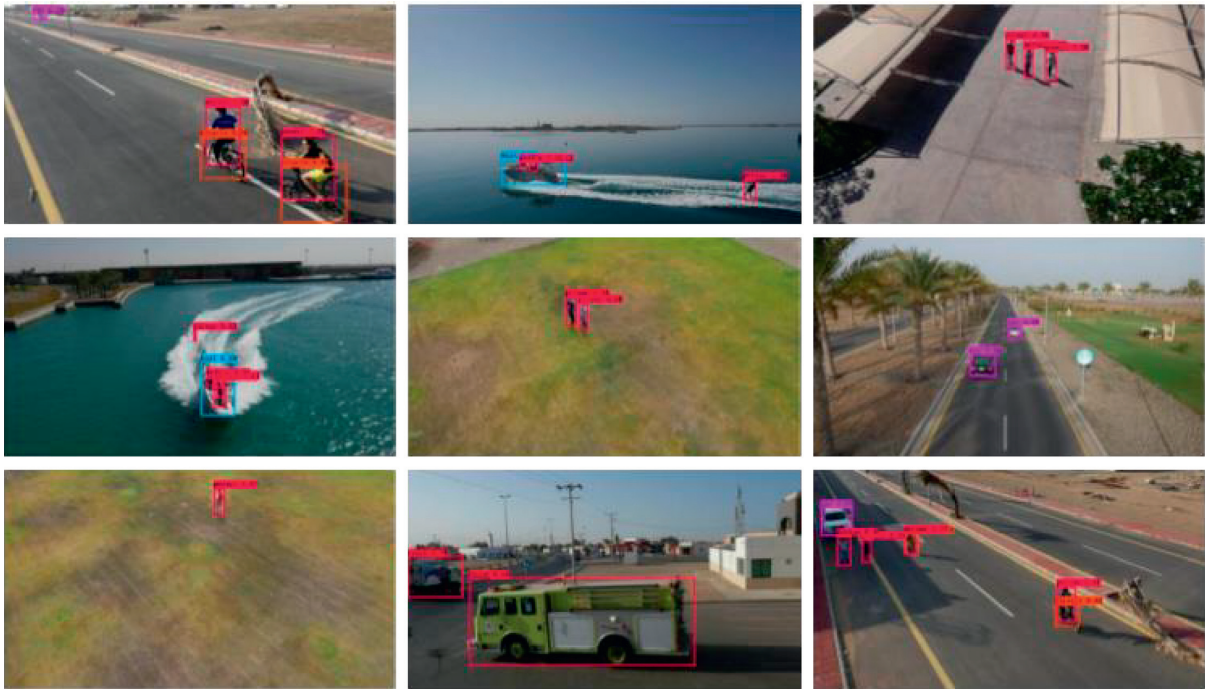

Figure 9: Detection examples generated by MFFNet-101 as backbone networks on UAV123 dataset. MARNet-101 is trained on the VOC 2007 trainval + test.

for PASCAL VOC 2007 and MS COCO. Moreover, ResNet-101 and MFFNet-101 are used as our backbone networks.

On the PASCAL VOC 2007 dataset, MFFNet-101 outperforms ResNet-101 by 1.4% on AP. On the MS COCO dataset, we improve ResNet-101 by 1.3%. Table 7 shows that MFFNet-101 has a little longer inference latency than ResNet-101 but is more accurate. For instance, on the PASCAL VOC 2007 dataset, we improve the ResNet-101 baseline by 1.4% for AP for only 1.6 ms of additional inference latency. On the MS COCO dataset, MFFNet-101 has an AP of 26.9%, which is 1.3% higher than the ResNet-101 baseline of 25.6% for only 3.2 ms of additional inference latency. These results demonstrate the general performance improvement of using MFF modules in object detection. Figure 9 shows detection examples generated by our proposed MFFNet-100 as backbone networks on UAV123 dataset. It can be seen that our method is able to detect target objects successfully regardless of their shapes, sizes, orientations, and appearances.

4. Conclusions

To address the multiscale recognition problem in the UAV visual perception, this paper establishes a new convolutional network architecture (MFFNet). In MFFNet, the MFF module is designed by employing multiple atrous convolutions at different rates with feature-selective learning ability. The MFF module is implemented via three operations: split module (SM), multiscale branch module (MBM), and fusion module (FM). In addition, MFF module can selectively generate channel-wise feature responses by emphasizing channel-wise dependencies. We further explore the effect of atrous rate on the multiscale representation ability of CNNs. Image classification results on CIFAR-100 and Tiny ImageNet datasets demonstrate that our proposed method achieves very competitive results on various benchmarks. Grad-CAM visualization results demonstrate that the MFFNet-based CAM results tend to focus on the whole object more than other baseline networks. That is, the MFFNet has a stronger multiscale representation ability, which can achieve better recognition accuracy in the UAV. Experimental results on PASCAL VOC 2007, MS COCO, and UAV123 datasets show that our proposed method achieves consistent performance gains in object detection, which is beneficial to expanding the application of UAV. We will further explore the effect of multiscale representation on image recognition results in future work.

Data Availability

The detailed mechanism model and model parameters of MFFNet are given in the article. The results are computed on the PyCharm software with the model and given parameters, while the relevant results are also given in the article.

Conflicts of Interest

The authors declare no conflicts of interest.

Acknowledgments

This work was supported by the National Major Science and Technology Projects of China (Grant no. 2019ZX04026001).

References

[1] A. Zeggada, S. Benbraika, F. Melgani, and Z. Mokhtari, "Multilabel conditional random field classification for UAV images," *IEEE Geoscience and Remote Sensing Letters*, vol. 15, no. 3, pp. 399–403, 2018.

[2] A. Zeggada, F. Melgani, and Y. Bazi, "A deep learning approach to UAV image multilabeling," *IEEE Geoscience and Remote Sensing Letters*, vol. 14, no. 5, pp. 694–698, 2017.

[3] A. Krizhevsky, I. Sutskever, N. V. Lake Tahoe, and G. E. Hinton, "ImageNet classification with deep convolutional neural networks," in *Processing Advances in Neural Information Processing Systems*, pp. 1097–1105, MIT press, London, UK, 2012.

[4] X. Zhang, X. Zhou, M. Lin, and J. Sun, "Shufflenet: An extremely efficient convolutional neural network for mobile devices," in *Proceedings of the 2018 IEEE/CVF Conference on Computer Vision and Pattern Recognition*, pp. 6848–6856, Salt Lake City, UT, USA, 2018.

[5] J. Redmon and A. Farhadi, "Yolo9000: better, faster, stronger," in *Proceedings of the 2017 IEEE Conference on Computer Vision and Pattern Recognition (CVPR)*, pp. 6517–6525, Honolulu, HI, USA, July 2017.

[6] G. Li and Y. Yu, "Contrast-oriented deep neural networks for salient object detection," *IEEE Transactions on Neural Networks and Learning Systems*, vol. 29, no. 12, pp. 6038–6051, 2018.

[7] N. Dalal and B. Triggs, "Histograms of oriented gradients for human detection," in *Proceedings of the 2005 IEEE Conference on Computer Vision and Pattern Recognition (CVPR)*, pp. 886–893, San Diego, CA, USA, June 2005.

[8] K. Simonyan and A. Zisserman, "Very deep convolutional networks for large-scale image recognition," in *Proceedings of the 3rd International Conference on Learning Representations, ICLR 2015*, pp. 1409–1556, San Diego, CA, USA, May 2015.

[9] K. He, X. Zhang, S. Ren, and J. Sun, "Deep residual learning for image recognition," in *Proceedings of the 2016 IEEE Conference on Computer Vision and Pattern Recognition (CVPR)*, pp. 770–778, Las Vegas, NV, USA, June 2016.

[10] C. Szegedy, W. Liu, Y. Jia et al., "Going deeper with convolutions," in *Proceedings of the 2015 IEEE Conference on Computer Vision and Pattern Recognition (CVPR)*, pp. 1–9, Boston, MA, USA, June 2015.

[11] S. Xie, R. Girshick, P. Dollár, Z. Tu, and K. He, "Aggregated residual transformations for deep neural networks," in *Proceedings of the 2017 IEEE Conference on Computer Vision and Pattern Recognition (CVPR)*, pp. 5987–5995, Honolulu, HI, USA, July 2017.

[12] S. Zagoruyko and N. Komodakis, "Wide residual networks," 2016, https://arxiv.org/abs/1605.07146.

[13] G. Huang, Z. Liu, L. v. d. Maaten, and K. Q. Weinberger, "Densely connected convolutional networks," in *Proceedings of the IEEE Conference on Computer Vision and Pattern Recognition (CVPR)*, pp. 2261–2269, Honolulu, HI, USA, July 2017.

[14] X. Ding, Y. Guo, G. Ding, and J. Han, "ACNet: strengthening the kernel skeletons for powerful CNN via asymmetric convolution blocks," in *Proceedings of the 2019 IEEE/CVF*

International Conference on Computer Vision (ICCV), pp. 1911–1920, Seoul, South Korea, October 2019.

[15] J. Hu, L. Shen, and G. Sun, "Squeeze-and-excitation networks," in *Proceedings of the 2018 IEEE/CVF Conference on Computer Vision and Pattern Recognition*, pp. 7132–7141, Salt Lake City, UT, USA, June 2018.

[16] S. Woo, J. Park, J.-Y. Lee, and I. S. Kweon, "CBAM: convolutional block attention module," https://arxiv.org/abs/1807.06521.

[17] X. Li, W. Wang, X. Hu, and J. Yang, "Selective kernel networks," in *Proceedings of the IEEE conference on computer vision and pattern Recognition (CVPR)*, pp. 510–519, Seattle, WA, USA, July 2019.

[18] X. Ma, Z. Yang, and Z. Yu, "FSRFNet: feature-selective and spatial receptive fields networks," *Applied Sciences*, vol. 9, no. 19, p. 3954, 2019.

[19] R. R. Selvaraju, M. Cogswell, A. Das et al., "Grad-CAM: visual explanations from deep networks via gradient-based localization," in *Proceedings of the 2017 IEEE International Conference on Computer Vision (ICCV)*, pp. 618–626, Venice, Italy, October 2017.

[20] A. Krizhevsky and G. Hinton, "Learning multiple layers of features from tiny images," Technical Report, University of Toronto, Toronto, Canada, 2009.

[21] L. Yao and J. Miller, "Tiny ImageNet classification with convolutional neural networks," *CS 231N*, vol. 2, p. 8, 2015.

[22] M. Everingham, L. Van Gool, C. K. I. Williams, J. Winn, and A. Zisserman, "The Pascal visual object classes (VOC) challenge," *International Journal of Computer Vision*, vol. 88, no. 2, pp. 303–338, 2010.

[23] T.-Y. Lin, M. Maire, S. Belongie et al., "Microsoft COCO: common objects in context," in *Proceedings of the European Conference on Computer Vision*, pp. 740–755, Springer, Zurich, Switzerland, September 2014.

[24] M. Mueller, N. Smith, and B. Ghanem, "A benchmark and simulator for UAV tracking," in *Proceedings of the European Conference on Computer Vision*, pp. 445–461, Amsterdam, Netherlands, October 2016.

[25] N. Ma, X. Zhang, H.-T. Zheng, and J. Sun, "ShuffleNet v2: practical guidelines for efficient CNN architecture design," in *Proceedings of the IEEE Conference on Computer Vision and Pattern Recognition (CVPR)*, pp. 116–131, Munich, Germany, September 2018.

[26] M. Sandler, A. Howard, M. Zhu, A. Zhmoginov, and L. C. Chen, "MobileNet v2: inverted residuals and linear bottlenecks," in *Proceedings of the 2018 IEEE/CVF Conference on Computer Vision and Pattern Recognition*, pp. 4510–4520, Salt Lake City, UT, USA, June 2018.

[27] C. Szegedy, V. Vanhoucke, S. Ioffe, J. Shlens, and Z. Wojna, "Rethinking the inception architecture for computer vision," in *Proceedings of the 2016 IEEE Conference on Computer Vision and Pattern Recognition (CVPR)*, pp. 2818–2826, Las Vegas, NV, USA, June 2016.

[28] S. Ren, K. He, R. Girshick, and J. Sun, "Faster R-CNN: towards real-time object detection with region proposal networks," *IEEE Transactions on Pattern Analysis and Machine Intelligence*, vol. 39, no. 6, pp. 1137–1149, 2017.

Hindawi
Complexity
Volume 2021, Article ID 6655488, 10 pages
https://doi.org/10.1155/2021/6655488

Research Article

A Novel Routing Control Technique for the Energy Hole in the Underwater Acoustic Distributed Network

Dong Xiao,[1] Min Zhao,[2] Ning Jia,[1] Tong-Rui Peng,[3] Yan Chen,[1] and Li Ma[1]

[1]*Institute of Acoustics, Chinese Academy of Sciences, Beijing 100190, China*
[2]*Economic Research Institute, State Grid Jibei Electric Power Company Limited, Beijing 100038, China*
[3]*College of Science, Shanghai Institute of Technology, Shanghai 201418, China*

Correspondence should be addressed to Dong Xiao; xiaodong@mail.ioa.ac.cn and Tong-Rui Peng; tongrui2.peng@sit.edu.cn

Received 18 November 2020; Revised 11 January 2021; Accepted 27 January 2021; Published 18 February 2021

Academic Editor: Rui Wang

The energy hole is a severe problem for underwater acoustic distributed networks in that it affects the normal operations of the network and shortens the network's life span. To deal with this problem, a loop-free routing control technique is proposed in this paper. The classical shortest-path routing control method is used to generate multiple disjointed routing tables. The residual energy of the nodes and the changing information of the uplink/downlink matrix are added to the data frames for distribution. The source node specifies the routing path to transmit the data frames based on the changing information, and the relay nodes route the data frames strictly according to the routing path designated by the source node. Besides, the energy consumption of the relay node is saved by replying to the pseudo-ACK frame. Simulation experiments are implemented in four typical scenarios, and the results reflect that the proposed technique could extend the network's life span by approximately 10% when compared to other mature techniques. Besides, it has no other negative effects on the normal operations of the network.

1. Introduction

1.1. Background and Literature Review. The underwater acoustic distributed network which consisted of fixed sensor nodes is widely used for collecting data and exchanging information in the environment of underwater [1]. However, the energy holes are severely affecting the normal operations of the system and shortening the network's life span [2]. To avoid energy holes, a variety of excellent engineering methods are proposed, e.g., reducing hardware power consumption [3], decreasing software calculations, sleep-awaken strategies [4], optimizing and configuring battery power, adjusting node-deployment density [5], configuring topology [6], and other methods through balancing the energy consumption of nodes. The main design ideas are based on four assumptions, which are specified as follows:

(1) No auxiliary information or equipment is needed, and the cost function is designed to adjust the transmission power or routing path based on factors, such as residual energy of nodes, channel characteristics, and link quality [2, 7–9]

(2) The auxiliary information, such as the geographic location, the deployment depth, the azimuth of arrival, and distances between nodes, is used to adjust the transmission power or routing path [10–17]

(3) Machine learning methods (e.g., Q-learning and ant colony algorithm) are used [18–20]

(4) Mobile nodes are used as auxiliary equipment for data collection, and their movement trajectories and collection strategies are planned [21–26]

An arc-shaped hierarchical network composed of 1 central node and 50 static nodes is constructed in [7]. It selects the routing paths based on the efficiency of the path energy and the path lifetime. Besides, prior knowledge of the network topology is required. A congestion control and load balancing technique for cluster-based underwater acoustic sensor networks is proposed in [8], but the route hops or paths are not mentioned. A routing strategy that leads to an

even energy depletion among all sensors in the network and consequently an improved network life span is proposed in [2], but the network is assumed to be arranged as a star topology. A dynamic routing control method is presented in [9], but the route paths are controlled and distributed only by the sink node, which consumes considerable energy. A routing algorithm based on link quality is proposed in [10], which reduces retransmission times, but requires the geographic location information of the node as support. Nodes' one-hop neighbour is redefined based on signal attenuation, and a distributed energy-efficient routing protocol for UASNs is designed in [11], but it assumes each node knows its neighbours' positions. An energy-balancing and delay-restricted routing protocol is proposed in [12], but the location, residual energy, and load of its neighbours must be aware of by every node. A new clustering algorithm based on the low-energy adaptive clustering hierarchy (LEACH) protocol is proposed in [13], but the cluster head's position is needed. An improved protocol called energy-balanced pressure routing (EBPR) is proposed in [14], but the depth information of each node and periodical broadcast are needed. An improved reliability and energy-balanced routing algorithm (REBAR) is proposed in [15], but distances between source nodes and sink nodes are needed. A detailed description of the ad hoc underwater acoustic network protocol is presented in [16], which is an improved ad hoc on-demand distance vector (AODV) routing control method, and distance information is needed. An energy-efficient routing scheme is presented for underwater acoustic sensor networks (UW-ASN) in [17], which is based on the directed diffusion routing scheme. An adaptive, energy-efficient, and lifetime-aware routing protocol based on reinforcement learning, QELAR, is proposed and simulated in [18, 19], but considerable energy is consumed by periodical broadcast. A fair energy usage routing algorithm, which uses the ant colony optimization algorithm (ACO) to balance the network energy, is proposed in [20], but it is designed for wireless sensor networks only.

In this study, the nodes are deployed randomly so that some essential information, e.g., neighbour information, depth information of other nodes, and geographical location information, is difficult to obtain, and no mobile node is deployed. Therefore, only the first and the third types of assumptions are considered. The first and third types of assumptions require routing control for transmitting data, and table-driven routing [5, 27] and on-demanding routing [28, 29] are two main routing control methods. Currently, the on-demand routing control method has been reported in most published reports. On the one hand, considering that the fixed underwater acoustic distributed network nodes carry limited energy and are difficult to move after deployment, the routing changes are relatively rare, and there is no need to search for routing paths repeatedly. On the other hand, most load balancing methods do not focus on routing loops that are prone to occur when routing paths change.

1.2. The Motivation of This Paper. It is found that when geographic location and topology information is lacking, routing loops are likely to occur when searching for the routing path to achieve load balancing. Repeated route searching and routing loops both lead to rapid node energy consumption, shortened network life, large channel resource occupation, and increased end-to-end delays of data packets. A few methods use loop detection to break routing loops, but they cannot fundamentally eliminate routing loops. This paper concentrates on how to delay the appearing time of the energy hole in the underwater acoustic distributed network as late as possible, and that is to save the energy of the nodes on critical routing paths and eliminate routing loops while searching for the routing path to balance the load.

1.3. Contributions of This Paper. There are four contributions of this paper.

A novel loop-free routing control technique for the energy hole in the underwater acoustic distributed network is proposed to delay the appearance time of the energy hole (the first failed node) without negative effects on the normal operations.

To avoid the routing loop problem, the routing path of the data frame is designated by its source node, and the relay nodes will route the data frame strictly according to the routing path designated by the source node.

The link quality and the residual energy of the nodes are used by the source node to select the routing path, and the data load and the energy consumption are balanced.

The energy consumption is saved by replying pseudo-ACK frames by relay nodes.

1.4. Paper Organization. The rest of the paper is organized as follows: Section 2 describes the problem formulation of the energy hole in underwater acoustic distributed networks. Section 3 presents a detailed introduction of the proposed technique. Section 4 provides a detailed description of the simulation experiments and analyses the results to demonstrate the advantages of the proposed technique. Section 5 concludes the paper.

2. Problem Formulation

For underwater acoustic distributed networks, extended propagation delays, severe attenuations, narrow available communication bandwidth, low communication rates, and complicated underwater acoustic environments will increase the consumption of the transmission energy. Owing to premature energy exhaustion, the energy holes, which refer to failure nodes located on critical routing paths, become challenging problems, and they affect the network's normal operation and shorten the life span.

To solve the energy hole problems, the load-balanced methods, which extend the life of the network by balancing the energy consumption of each node, are widely used. However, once a routing loop is formed, the data frames will be transmitted within the network repeatedly and cannot reach the destination node. Consequently, the energy of the node is consumed quicker and the limited channel resource is occupied a lot, which damage the performance of the load-balanced methods.

In this study, a novel loop-free route control technique is proposed for solving the routing loop problem. The classical shortest-path routing control method is used to generate multiple disjointed routing tables. The residual energy of the nodes and the changing information of the uplink/downlink matrix are added to the data frames for distribution. The source node specifies the routing path to transmit the data frame based on the changing information, while relay nodes route the data frame strictly according to the routing path designated by the source node. Besides, the energy consumption of the relay node is saved by replying the pseudo-ACK frame.

3. Routing Control Technique for the Energy Hole

3.1. Generation of the Routing Table. The procedures of generating the routing table can be explained as follows:

(1) Assume there are totally T nodes in the network and at least two other nodes in the communication range of each node, which means that each node has at least one backup routing table.

(2) A unique address t, where $t \in [0, T)$, is initialized for each node.

(3) A link matrix, Q, and a residual energy table, E, must be built through the self-organization process (see Appendix) for each node, wherein link matrix, Q, has T rows and T columns, with the element, q_{ij}, in row i and column j, representing the link quality from node i to node j, and $q_{ij} \in [0, Q]$, $i, j \in [0, T)$. The residual energy table, E, has T rows and one column, with the element, e_i, of the i-th term being the residual energy of node i, where $e_i \in [0, E]$.

(4) Routing tables are created according to Q and E.

(5) A routing index table, S, is created after all routing tables have been calculated. S contains T rows and one column, where the i-th element, s_i, indicates that the i-th routing path in group t, recorded in the s_i-th routing table, is selected as the routing path from the local node to node i.

3.2. Data Transmission. Figure 1 presents the format of the data frame. The change information of the link matrix includes row/column number, uplink/downlink, and change results, which are used to communicate the uplink/downlink changes between the local node and others. If the destination node address of the data frame is dst, it is transmitted according to the dst-th routing path of group t in the s_{dst}-th routing table. After transmission, the information and transmission time of the data frame are recorded and enter the ACK waiting state. If ACK waiting timer expires, the data frame will be retransmitted, and the transmission record will be updated. If the retransmission limit is exceeded, the data frame will be put into the tail of transmitting queue. The flowchart of the node-transmitting terminal is shown in Figure 2.

3.3. Data Reception. Figure 3 presents the flowchart of the node-receiving terminal, and data processing can only be performed when the CRC checksum is correct. Each node follows this flowchart to process the received data frame and update the transmitting information table.

3.3.1. Selection of the Routing Table. Update the link matrix, Q, and the residual energy table, E, according to the received data frame, and note the node address with the smallest residual energy in the residual energy table as em. Then, according to equation (1), the routing cost, tmp_b, from local node t in the entire routing table to any other node, j, is calculated:

$$tmp_b = \begin{cases} 0, & j = t, \\ \infty, & j \neq t \text{ 且 } rh_{btj} = 0, \\ \sum_{k=1}^{rh_{btj}} \dfrac{\Delta ch_{bk} + \Delta en_{bk}}{rh_{btj}}, & j \neq t \text{ 且 } rh_{btj} \neq 0, \end{cases} \tag{1}$$

wherein

$$\begin{aligned} \Delta en_{bk} &= \begin{cases} 0, & rr_{btjk} = G, \\ WE^2 \times (E - e_{jk}), & rr_{btjk} = em, \\ WE \times (E - e_{jk}), & \text{else}, \end{cases} \\ \Delta ch_{bk} &= \begin{cases} 0, & rr_{btjk} = G, \\ WQ^2 \times (Q - q_{jk}), & rr_{btjk} \neq G\, q_{jk} = 0, \\ WQ \times (Q - q_{jk}), & rr_{btjk} \neq G\, q_{jk} \neq 0. \end{cases} \end{aligned} \tag{2}$$

G means broadcast. When $j = t$, the local loop path of the local node is given, and no calculation is needed. rh_{btj} is the hop count required by the local node to reach node j in the b-th routing table. The hop count is used as the denominator to allow some routing paths having a large number of hop counts to be selected. Δen_{bk} is the residual energy cost, and Δch_{bk} is the link quality cost. rr_{btjk} is the address of the k-th hop node in the b-th routing table from the local node to node j, $b \in [0, B]$, and B is the routing table having lowest selection cost, and the sequence number of this routing table is assigned to s_j, as shown in the following:

$$s_j = \arg\min_{b \in [0,B)} \{tmp_b\}. \tag{3}$$

When the data frame sent by the source node does not receive the ACK frame returned by the destination node within a limited time, the routing index table, S, is updated according to the above process and retransmitted.

3.3.2. Update of the Link Matrix. When the data frame transmitted or relayed by this node is correctly responded to by the correct next hop node within the limited time, the uplink/downlink matrix of the node is updated according to equations (4) and (5):

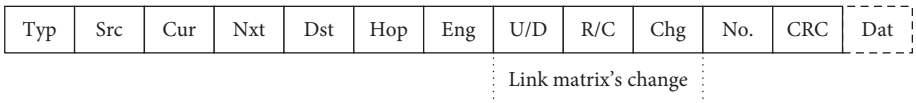

Figure 1: Format of the data frame. ACK frame does not include the Dat segment.

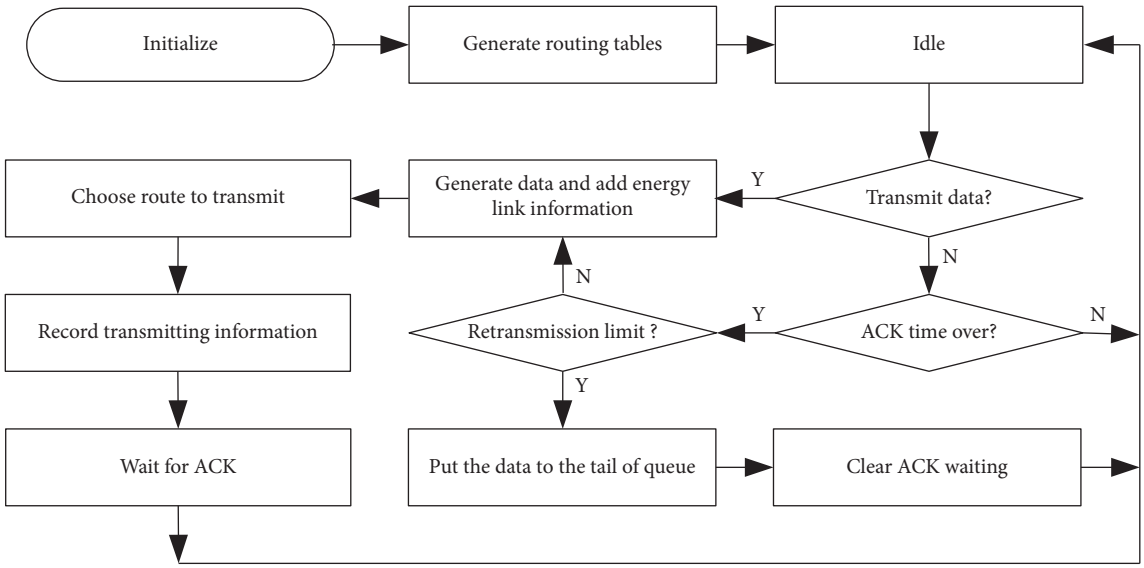

Figure 2: Flowchart of the transmitting terminal.

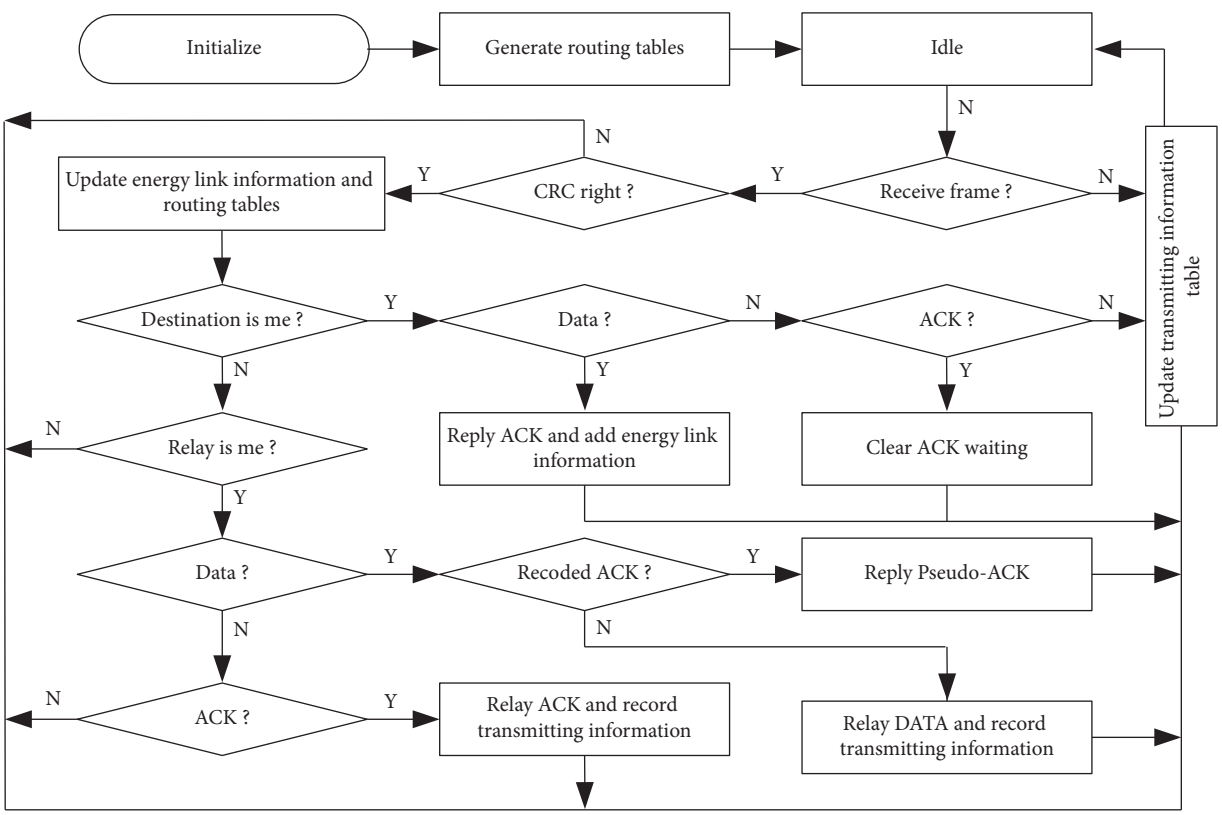

Figure 3: Flowchart of the receiving terminal.

$$q_{t\,cur} = \begin{cases} Q, & q_{t\,cur} = Q, \\ q_{t\,cur} + 1, & \text{else}, \end{cases} \tag{4}$$

$$q_{cur\,t} = \begin{cases} Q, & q_{cur\,t} = Q, \\ q_{cur\,t} + 1, & \text{else}. \end{cases} \tag{5}$$

If the correct response is not received within the limited time, the uplink/downlink matrix of the node is updated according to equations (6) and (7), respectively:

$$q_{t\,cur} = \begin{cases} 0, & q_{t\,cur} = 0, \\ q_{t\,cur} - 1, & \text{else}, \end{cases} \tag{6}$$

$$q_{cur\,t} = \begin{cases} 0, & q_{cur\,t} = 0, \\ q_{cur\,t} - 1, & \text{else}. \end{cases} \tag{7}$$

In equations (4)–(7), *cur* represents the next hop address. The correct response includes two cases. When the next hop address of the frame is the relay node, the frame should be relayed. When the next hop node is the destination node of the data frame, the ACK frame should be replied. After the update is completed, when the change of an element in the link matrix exceeds a certain threshold, the change is assigned to the next data frame sent by the node. When the data frame sent by the source node does not receive the ACK frame replied by the destination node within a limited time, the corresponding elements in the uplink/downlink matrix are valued according to equations (6) and (7), respectively.

3.3.3. Data Relay. When a node receives a frame from another node, if the next hop address in the frame is the address of itself, it must relay the frame. Before relaying a data frame, the node must check its own transmission record. If it is found that an ACK frame corresponding to the data frame has been transmitted, it pretends that it is the destination node of the data frame and replies a pseudo-ACK frame to the source node. If there is no transmission record corresponding to the data frame that needs to be relayed before relaying a DATA frame, the routing path from the source node of the data frame to its destination node in all routing tables must be found. Then, according to the path, the current address in the required relay data frame is changed to its own node number, and the next hop address is changed to the next-hop node number on the path. After the hop count is increased by one, the content redundancy check is recalculated and transmitted.

4. Results and Discussion

A half-duplex underwater acoustic communication method is designed using OPNET software, a tool used to simulate the behaviour and performance of different types of networks, and the underwater acoustic channel is modelled. Four typical node-deployment scenarios are simulated, and simulation results are compared with those using a traditional shortest-path route control method.

4.1. Modelling and Design of Half-Duplex Underwater Acoustic Communication. The wireless link is divided into 14 pipeline model stages for modelling in OPNET. In the node model, the centre frequency, the bandwidth, the modulation method, the transmission rate, and the error-correction coding of both transmitter and receiver are set. In OPNET, the wireless link adopts the full-duplex mode by default. However, at present, most underwater acoustic communications can only use half-duplex.

During the simulation, the underwater acoustic communication parameters are set to BPSK (binary phase-shift keying) modulation in the half-duplex mode. The centre frequency is 8 kHz, the bandwidth is 4 kHz, the communication rate is 1 kbps, the effective distance is 5 km, the transmission power is 20 W, the standby (including receiving) power is 0.1 W, and the battery capacity of each node is 16,000 J. Additionally, the master node is powered by shore-based power, excluding energy consumption. In the underwater acoustic communication process, the following pipeline model stages need attention.

In stage 6, the underwater wave propagation speed (1,500 m/s) differs from the default electromagnetic-wave propagation speed and must be modified.

In stage 8, the code must be rewritten based on the underwater acoustic propagation attenuation model to calculate the received power. The mesoscale empirical formula in the classic Marsh–Schulkin model is used in the simulation process, and the formula is

$$TL = 15\log_{10} R + \alpha R + \alpha_t\left(\frac{R}{H} - 1\right) + 5\log_{10} H + 60 - k_L, \tag{8}$$

where $H = [(L + D)/3]^{0.5}$ is the span (km), L is the depth of the mixed layer (m), D is the depth of the ocean (m), R is the horizontal distance (km), α is the absorption coefficient (dB/km), α_t is the effective attenuation coefficient in shallow water (dB, reflection loss per sea surface-bottom reflection, which is related to frequency, sea conditions, and bottom quality), and k_L is the near-field anomaly correction (dB, related to frequency and bottom quality).

$$\alpha_t = 2.0 + 0.25 \times (f - 2.0),$$

$$\alpha = 8.686 \times 10^3 \times \left[\frac{SAf_T f^2}{f_T^2 + f^2} + \frac{Bf^2}{f_T}\right]\left(1 - 6.54 \times 10^{-4} P\right). \tag{9}$$

The unit of α is dB/km, S is thousandth of salinity (usually, 35‰), $A = 2.34 \times 10^{-6}$, $B = 3.38 \times 10^{-6}$, f is the acoustic frequency (kHz), P is the static pressure (atmospheric pressure), and f_T is the relaxation frequency (kHz).

$$f_T = 21.9 \times 10^{(6-(1520/(T+273)))}. \tag{10}$$

In actual underwater acoustic communications, when collisions occur between multiple received signals, they cannot be received correctly. Therefore, the influence of noise crosstalk between signals is amplified during the noise crosstalk of stage 9.

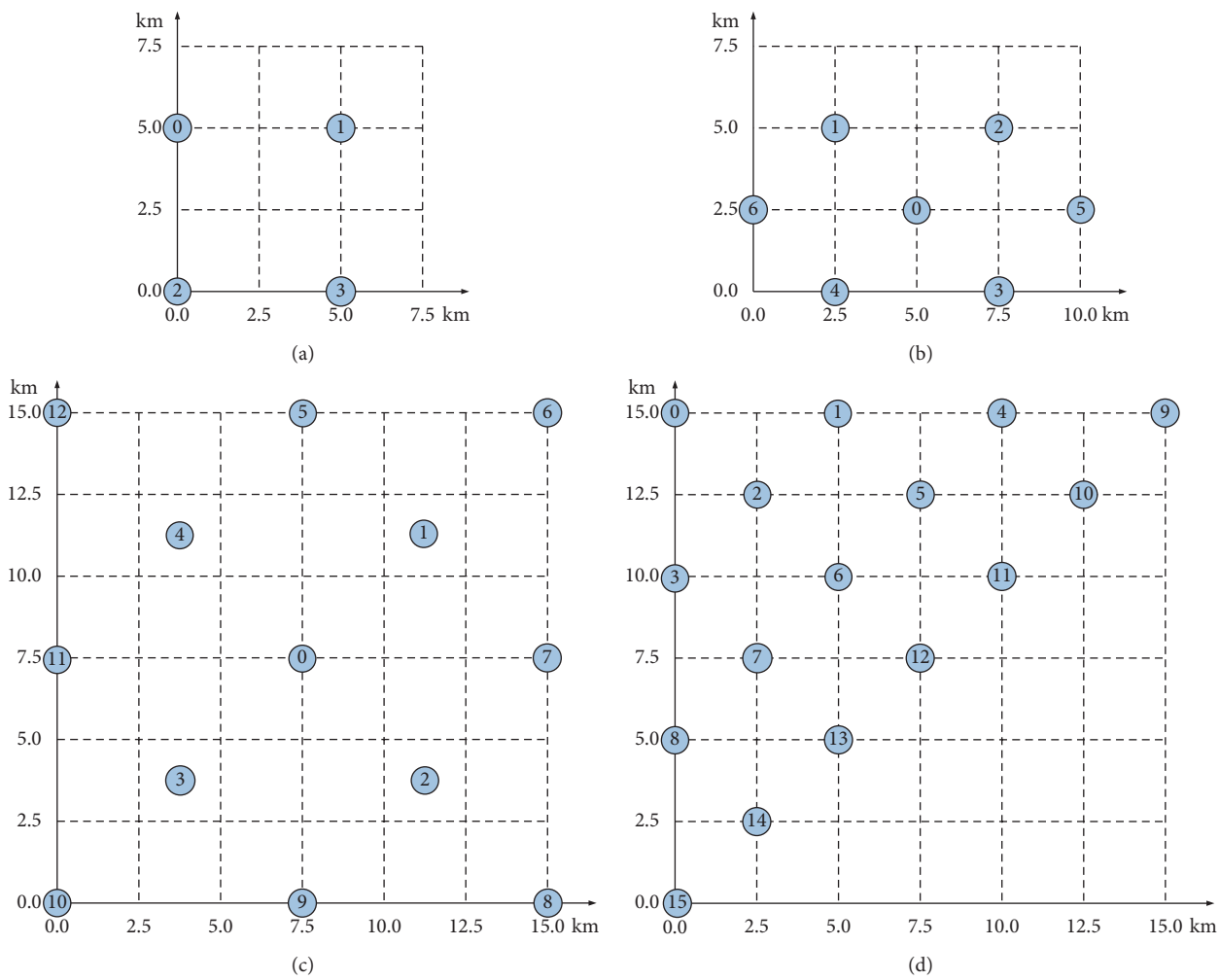

Figure 4: Simulation cases. (a) Case of 4 nodes. (b) Case of 7 nodes. (c) Case of 13 nodes. (d) Case of 16 nodes.

In stage 10, the ocean background noise level should be calculated, and a classic empirical formula should be adopted in the simulation [30]. It is divided into four categories for calculation, as shown in the following:

$$NL_B = NL + 10\log_{10} B, \tag{11}$$

where

$$\begin{aligned} NL &= 10\log_{10}\left(\sum_{i=1}^{4} 10^{NL_i/10}\right), \\ NL_1 &= 17 - 30\log_{10} f, \\ NL_2 &= 40 + 20(VD - 0.5) + 26\log_{10} f - 60\log_{10}(f + 0.03), \\ NL_3 &= 50 + 7.5w^{0.5} + 20\log_{10} f - 40\log_{10}(f + 0.4), \\ NL_4 &= -15 + 20\log_{10} f. \end{aligned} \tag{12}$$

In the formula, VD represents the vessel density, and $VD \in [0, 1]$. B is the signal bandwidth. f is the centre frequency of the signal, and the unit is HZ. w is the wind speed, and the unit is m/s.

By adjusting parameters, such as transmission power, in the 11th stage, the bit error rates without collision are about 10^{-3}, and the bit error rates with collision are in the order of 10^{-1}.

4.2. Results' Analysis. Figure 4 presents the simulation results for the four typical node-deployment situations using the traditional shortest-path routing control method.

Considering the case of node 4, the lengths of each segment of the data frame are data type (4 bits), source address (4 bits), current address (4 bits), next hop address (4 bits), destination address (4 bits), hop count (4 bits), residual energy of the source (4 bits), change information of the link matrix (4 bits), frame number (8 bits), data segment (256 bits), and checking (8 bits). The ratio of useful information (data segment) is 84.2%. A link matrix, Q, and a residual energy table, E, are established for each node through a network self-organization method, wherein $Q = 3$, $E = 15$, and

Table 1: Route table of each node.

	Source	Destination	Hop 0	Hop 1	Hop 2	Hop 3	Hop count
Route table 0	Node 0	Node 0	0	G	G	G	0
		Node 1	0	1	G	G	1
		Node 2	0	2	G	G	1
		Node 3	0	2	3	G	2
	Node 1	Node 0	1	0	G	G	1
		Node 1	1	G	G	G	0
		Node 2	1	3	2	G	2
		Node 3	1	3	G	G	1
	Node 2	Node 0	2	0	G	G	1
		Node 1	2	3	1	G	2
		Node 2	2	G	G	G	0
		Node 3	2	3	G	G	1
	Node 3	Node 0	3	2	0	G	2
		Node 1	3	1	G	G	1
		Node 2	3	2	G	G	1
		Node 3	3	G	G	G	0
Route table 1	Node 0	Node 0	0	G	G	G	0
		Node 1	0	1	G	G	1
		Node 2	0	2	G	G	1
		Node 3	0	2	3	G	2
	Node 1	Node 0	1	0	G	G	1
		Node 1	1	G	G	G	0
		Node 2	1	3	2	G	2
		Node 3	1	3	G	G	1
	Node 2	Node 0	2	0	G	G	1
		Node 1	2	3	1	G	2
		Node 2	2	G	G	G	0
		Node 3	2	3	G	G	1
	Node 3	Node 0	3	2	0	G	2
		Node 1	3	1	G	G	1
		Node 2	3	2	G	G	1
		Node 3	3	G	G	G	0

Table 2: Comparison results of different techniques (in terms of network lifetime).

		1 min	2 min	3 min	4 min	5 min	6 min	7 min	8 min	9 min	10 min
4 nodes	Traditional	451.8	703.4	909.6	1080.6	1215.6	1326.7	1428.5	1488.6	1584.5	1630.6
	Greedy	518.6	830.5	1050.6	1232.6	1395.5	1470.6	1575.5	1680.6	1755.6	1810.6
	Proposed	558.5	878.6	1101.8	1264.5	1380.6	1506.8	1617.7	1688.6	1755.7	1800.6
7 nodes	Traditional	693.6	1030.6	1302.6	1468.6	1595.6	1686.6	1778.8	1872.6	1926.5	1930.8
	Greedy	441.7	670.6	876.5	1016.5	1170.5	1248.7	1400.5	1464.5	1557.7	1580.7
	Proposed	841.5	1222.6	1479.8	1628.6	1760.6	1836.8	1911.7	1976.7	2034.6	2060.6
13 nodes	Traditional	580.8	962.6	1185.5	1336.6	1480.6	1596.6	1652.8	1712.5	1809.6	1860.6
	Greedy	451.8	844.6	1132.5	1238.6	1396.7	1435.0	1561.8	1672.6	1737.6	1810.6
	Proposed	694.6	1080.8	1326.6	1484.7	1615.6	1723.9	1778.7	1856.8	1872.6	1960.7
16 nodes	Traditional	687.6	1080.6	1338.6	1488.6	1640.6	1698.6	1806.6	1840.8	1908.8	1950.6
	Greedy	792.0	1083.7	13447	1456.7	1590.9	1740.6	1778.5	1752.6	1881.6	1951.5
	Proposed	958.6	1382.6	1608.6	1784.6	1880.6	1950.7	2030.6	2088.6	2016.6	2100.6

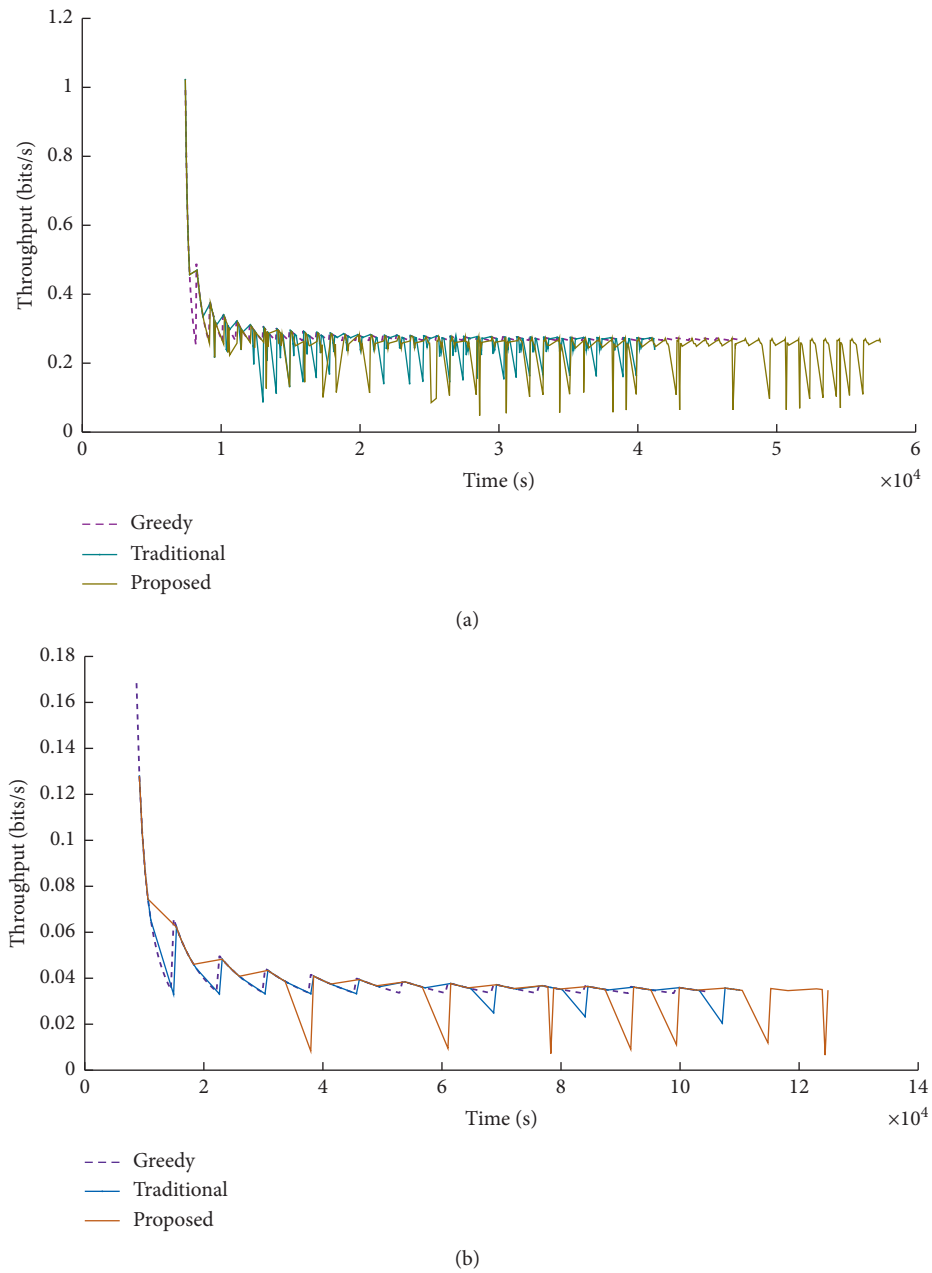

Figure 5: Comparison of the network throughput among the traditional technique, greedy technique, and proposed technique. (a) Transmission interval 1 minute. (b) Transmission interval 8 minutes. Traditional technique does not use load-balancing algorithms, and its lifetime is short than the proposed technique.

$$Q = \begin{bmatrix} 0 & 3 & 3 & 0 \\ 3 & 0 & 0 & 3 \\ 3 & 0 & 0 & 3 \\ 0 & 3 & 3 & 0 \end{bmatrix}, \tag{13}$$

$$E = \begin{bmatrix} 15 & 15 & 15 & 15 \end{bmatrix}.$$

The routing table of each node is shown in Table 1, and G stands for "broadcast."

The transmission interval of the data frame in each case can be divided into 10 levels: 1, 2, 3, 4, 5, 6, 7, 8, 9, and 10 minutes. Network lifetime in this paper is defined as the lifetime of the first exhausted node for the traditional technique, greedy technique, and proposed technique under different node-deployment conditions and different data frame intervals.

In Table 2, the comparisons of the network lifetime of the traditional technique, greedy technique, and proposed technique under different node-deployment conditions and different data frame intervals are listed, and the time unit is minute. Overall, compared with the traditional technique

which does not use load-balancing route control, the proposed technique can extend the network life by about 10% on average. And the greedy technique which uses the greedy algorithm for load-balancing route control performs better than the traditional technique when no route loop is shaped during the simulation. If any route loop is shaped, the performance of the technique related becomes the worst.

The proposed technique extends the network life. Moreover, its network throughput is basically the same as the traditional technique. Take the case of 16 nodes in Figure 4(d) with data frame intervals of 1 minute and 8 minutes as an example. The network throughput comparisons between the traditional technique, greedy technique, and proposed technique are shown in Figure 5. The network throughput shown in the figures is the net throughput. Thus, only the number of bits contained in the data segment in the data frame is calculated. It can be seen from both figures that the throughput of the proposed technique is basically the same as that of the traditional technique and greedy technique.

5. Conclusions

In this study, a loop-free routing control technique is proposed to solve the problem of energy holes in underwater acoustic distributed networks. Both link qualities and residual energies of the nodes are used for balancing the data load. All nodes are learned through the same routing tables during the period of self-organization, and the source node specifies the routing path, and then the relay nodes follow it to route the data frames strictly. Besides, the pseudo-ACK frame is replied by the relay node to save energy consumption. Simulation experiments are implemented in four typical scenarios, and the results show that the proposed technique extends the network life by approximately 10% while ensuring the network throughput.

Appendix

The self-organization process is explained in the authors' previously published papers [31, 32]. Here, the authors provide a brief summary as follows:

(1) It is supposed that the network contains T nodes. Each node has an empty link matrix, Q, and residual energy table, E, before deployment.

(2) After deployment of all nodes, each node sends neighbour-finding frames one by one for several turns. When other nodes receive the neighbour-finding frames, update their link matrix, Q, according to equation 5, and set the corresponding element e_{cur} in the energy table, E, to E. After several turns of neighbour finding, each node gets its own column of link matrix, Q, filled with some nonzero elements.

(3) Each node broadcasts the fusing frame just once, which contains its own column of link matrix, Q. When other nodes receive the fusing frame, fill the corresponding column of their own link matrices, Q, and broadcast the fusing frame again.

(4) Each node checks its link matrix, Q. If there is any empty column, send an inquiring frame to its neighbours to ask for the empty column. When the neighbours receive the inquiring frame, every neighbour checks its corresponding column of the link matrix, Q. If the corresponding column is not empty, the neighbour node will send the replying frame to answer the node who sends the inquiring frame. Each node takes the inquiring-replying for several turns until all nodes have the same link matrix, Q, and the same residual energy table, E, after completing self-organization.

(5) According to equation A1, each node calculates the elements of the routing matrix, R:

$$r_{ij} = \begin{cases} \infty, & q_{ij} \times e_i = 0, \\ WQ \times \left(Q - q_{ij}\right) + WE \times \left(E - e_i\right), & q_{ij} \times e_i \neq 0. \end{cases} \tag{A.1}$$

WQ and WE are the weights of link quality and residual energy, respectively. According to the routing matrix, R, the related routing algorithm (e.g., Dijkstra) is used to calculate the routing table and the backup routing tables. When the backup routing table is being calculated, it is necessary to bypass the nodes that the previous route has passed in order to ensure that there are no overlapping nodes between the routing tables. Each routing table contains T groups, and each group contains T entries. Each entry in the routing table should contain information, such as the destination address, the next hop address to which the destination node should be delivered, and the hop count required to reach the destination node. For the unreachable node, the next hop address is assigned to "broadcast," and the hop count is assigned to "0."

Data Availability

Almost all the data are presented in the tables of this paper. If there is a need for any other information, the corresponding author may be contacted by e-mail.

Conflicts of Interest

The authors declare that there are no conflicts of interest regarding the publication of this paper.

Acknowledgments

This work was supported in part by the Youth Innovation Promotion Association, Chinese Academy of Sciences (no. 2020024) and the Institute of Acoustics Chinese Academy of Sciences Young Elite Researcher Project (no. QNYC201702).

References

[1] R. Thangarajan, T. Siva, and R. Boopalachakaravarthy, "Adaptive energy efficient routing protocol with extended lifetime in underwater sensor networks," in *Proceedings of the ICCSNT*, pp. 322–326, Dalian, China, October 2013.

[2] F. Bouabdallah, C. Zidi, and R. Boutaba, "Joint routing and energy management in underwater acoustic sensor networks," *IEEE Transactions on Network and Service Management*, vol. 14, no. 2, pp. 456–471, 2017.

[3] W. Elmannai, K. Elleithy, A. Shrestha et al., "A new algorithm based on discrete fourier transform to improve the lifetime of underwater wireless sensor networks communications," in *Proceedings of the ASEE Zone*, vol. 1, pp. 1–5, Bridgeport, CT, USA, February 2014.

[4] C.-C. Lin, D.-J. Deng, and S.-B. Wang, "Extending the lifetime of dynamic underwater acoustic sensor networks using multi-population harmony search algorithm," *IEEE Sensors Journal*, vol. 16, no. 11, pp. 4034–4042, 2016.

[5] S. Cheema, N. Javaid, S. A. Sheikh et al., "A balanced energy adaptive routing protocol with sector based node selection in underwater WSNs," in *Proceedings of the NBIS*, pp. 84–90, Ostrava, Czech Republic, September 2016.

[6] W. Y. Fu, D. S. Li, J. Chen et al., "Topology optimization based on balanced network energy and load in underwater acoustic sensor network," in *Proceedings of the 6th WiCOM*, pp. 1–5, Chengdu, China, December 2011.

[7] Z. Liao, D. Li, and J. Chen, "A network access mechanism for multihop underwater acoustic local area networks," *IEEE Sensors Journal*, vol. 16, no. 10, pp. 3914–3926, 2016.

[8] N. Goyal, M. Dave, and A. K. Verma, "Congestion control and load balancing for cluster based underwater wireless sensor networks," in *Proceedings of the PDGC*, pp. 462–467, Solan, India, March 2016.

[9] H. T. Zhang, W. D. Jiang, F. Tong et al., "Dynamic routing control based on energy balancing in underwater acoustic networks," *Journal of Applied Sciences*, vol. 23, no. 4, pp. 336–340, 2005.

[10] G. Z. Sun, C. J. Zhang, Z. Z. Lyu et al., "Routing protocols based on link-quality for underwater acoustic sensor networks," *Mechatronics*, vol. 15, no. 8, pp. 45–49, 2009.

[11] P. Wang, "Transmission loss threshold based routing design for underwater acoustic sensor networks," *Electronic Science & Technology*, vol. 2, no. 1, pp. 108–113, 2015.

[12] X. Liu, Y. Li, C. H. Zhang et al., "Energy-balancing and delay-restricted routing protocol for underwater acoustic networks," *Journal of Network New Media*, vol. 2, no. 6, pp. 12–16, 2013.

[13] X. Li, Y. Q. Wang, and J. J. Zhou, "An energy-efficient clustering algorithm for underwater acoustic sensor networks," in *Proceedings of the ICCECT*, pp. 711–714, Liaoning, China, September 2012.

[14] K. Wang, Y. Z. Tian, and Y. H. Shi, "Energy balanced pressure routing protocol for underwater sensor networks," in *Proceedings of the ICS*, pp. 216–220, Chiayi, China, December 2016.

[15] P. Handa, Dr.B. S. Sohi, and N. Kumar, "Energy efficient hybrid routing protocol for underwater acoustic sensor network," in *Proceedings of the ICEEOT*, pp. 2573–2578, Chennai, India, March 2016.

[16] H. J. Shi and F. W. Liu, "Research of EBAP algorithm for ad Hoc underwater acoustic network," in *Proceedings of the 3rd ICCC*, pp. 464–468, Chengdu, China, December 2017.

[17] G. S. Yang, M. B. Xiao, E. Cheng et al., "Energy saving route finding mechanism in underwater acoustic sensor networks," *Journal of Beijing University of Posts and Telecommunications*, vol. 32, no. Sup, pp. 88–92, 2009.

[18] T. S. Hu and Y. S. Fei, "QELAR: a Q-learning-based energy-efficient and lifetime-aware routing protocol for underwater sensor networks," in *Proceedings of the IEEE IPCCC*, pp. 247–255, Austin, TX, USA, December 2008.

[19] W. B. Zhang, "Design of virtual-path based energy efficiency routing for underwater acoustic sensor networks," M. S. thesis, Tsinghua University, Beijing, China, 2012.

[20] H. W. Liang, W. M. Chen, S. Li et al., "An ACO-based fair energy usage routing algorithm for wireless sensor networks," *Pattern Recognition and Artificial Intelligence*, vol. 20, no. 2, pp. 275–280, 2007.

[21] J. S. Abbasi, N. Javaid, S. Gull et al., "Balanced energy efficient rectangular routing protocol for underwater wireless sensor networks," in *Proceedings of the IWCMC*, pp. 1634–1640, Valencia, Spain, June 2017.

[22] M. F. Huang, K. Zhang, Z. W. Zeng et al., "An AUV-assisted data gathering scheme based on clustering and matrix completion for smart ocean," *IEEE Internet of Things Journal*, vol. 7, no. 10, 2020.

[23] G. J. Han, J. X. Du, C. Lin et al., "An energy-balanced trust cloud migration scheme for underwater acoustic sensor networks," *IEEE Transcation Wireless Communications*, vol. 19, no. 3, pp. 1636–1649, 2019.

[24] A. Majid, I. Azam, A. Waheed et al., "An energy efficient and balanced energy consumption cluster based routing protocol for underwater wireless sensor networks," in *Proceedings of the 30th AINA*, pp. 324–333, Crans-Montana, Switzerland, March 2016.

[25] S. Shen, A. D. Zhan, P. L. Yang et al., "Exploiting sink mobility to maximize lifetime in 3d underwater sensor networks," in *Proceedings of the IEEE ICC*, pp. 1–7, Cape Town, South Africa, May 2010.

[26] J. M. J. Kartha and L. Jacob, "Lifetime enhancement in sparse underwater acoustic sensor networks using mobile elements," in *Proceedings of the SPCOM*, pp. 1–6, Bangalore, India, July 2012.

[27] W. Hyder, J. Poncela, and P. Otero, "Self-organized routing for radial underwater networks," in *Proceedings of the INDIACom*, pp. 918–922, New Delhi, India, March 2016.

[28] T. Liu, Q. L. Zhao, and L. B. Zhang, "Modified AODV routing protocol in underwater acoustic networks," in *Proceedings of the ICEICT*, pp. 191–194, Harbin, China, August 2016.

[29] N. Rajpoot and R. S. Kushwah, "An improved prophet routing protocol for underwater communication," in *Proceedings of the ICCN*, pp. 27–32, Gwalior, India, November 2015.

[30] R. F. W. Coates, *Underwater Acoustic Systems*, pp. 92-93, Macmillan, Basingstoke, UK, 1990.

[31] D. Xiao, L. P. Wei, G. Chen et al., "Inquiring flooding broadcast algorithm for underwater acoustic sensor self-organization networks," *Journal of Applied Acoustics*, vol. 34, no. 1, pp. 58–64, 2015.

[32] Y. X. Feng, D. Xiao, Y. Chen et al., "Relative self-positioning method for small-scale underwater acoustic network nodes without precise synchronization," *Acta Acustica*, vol. 45, no. 4, pp. 486–496, 2020.

Hindawi
Complexity
Volume 2021, Article ID 8812187, 17 pages
https://doi.org/10.1155/2021/8812187

Research Article

Nonsingular Integral Sliding Mode Attitude Control for Rigid-Flexible Coupled Spacecraft with High-Inertia Rotating Appendages

Gaowang Zhang, Xueqin Chen, Ruichen Xi, and Huayi Li

Research Center of the Satellite Technology, Harbin Institute of Technology, Harbin 150080, China

Correspondence should be addressed to Xueqin Chen; cxqhit@163.com

Received 21 September 2020; Revised 2 January 2021; Accepted 18 January 2021; Published 16 February 2021

Academic Editor: Rui Wang

This study addresses the challenge of attitude tracking control for a rigid-flexible spacecraft with high-inertia rotating appendages. The Lagrange method was used to establish the kinematic and dynamic models of the spacecraft. The translation and rotation of the spacecraft, vibrations of solar panels, and imbalance caused by the rotating appendages, which cause a complex control problem, were considered. To address the complex control problem, a novel, fast nonsingular integral sliding mode control method is proposed to perform the attitude tracking function of spacecraft. A sliding mode control law was established for the high-inertia appendages to maintain an appropriate angular velocity during rotation. Finally, the effectiveness of the proposed attitude control law was verified by numerical simulations for a spacecraft with high-inertia rotating appendages and symmetrical flexible solar panels.

1. Introduction

With the increased complexity of modern space missions, modern spacecraft carry many rigid and flexible components, such as manipulators, solar panels, antennas, and cameras. Additionally, many modern spacecraft components possess highly nonlinear characteristics. Owing to the strong nonlinearity of spacecraft systems and the improvements in the spacecraft attitude control and tracking accuracy, attitude control and tracking for spacecraft with multiple appendages have become a very complex problem.

Modern spacecraft are predominantly powered by large, lightweight solar panels. To absorb as much solar energy as possible, it is necessary that the solar panels rotate while the spacecraft moves to ensure the panels are oriented perpendicular to the incident light. Notably, during rapid maneuvering, the rotation and vibration of flexible components reduce the stiffness and increase the nonlinearity of the spacecraft system. These components are always coupled with the attitude and orbital motion of the rigid body of spacecraft, thus increasing the complexity of spacecraft attitude control and tracking problem [1, 2]. Li et al. [3] used cooperative tracking protocols to address unknown nonlinear dynamics problems with an adaptive learning law, which solved the leader-following tracking problem of fractional-order multiagent systems. For multiagent systems with unknown disturbances and input saturation, Zhou et al. [4] proposed an event-triggered control method based on disturbance observer to solve the following consistency problem. Li et al. [5] proposed a finite-time fuzzy adaptive control (AC) scheme to address the finite-time adaptive fuzzy control problem for a class of multiinput multioutput (MIMO) nonlinear nonstrict feedback systems. Tong et al. [6] proposed a novel observer-based adaptive fuzzy output-feedback control method to solve the output-feedback backstepping control design problem in uncertain strict-feedback nonlinear systems. To solve the fault observer design problem of Markovian jumped systems, Chen et al. [7] proposed two types of adaptive observer methods that could avoid the sliding

surface switching problem. Zhao et al. [8] proposed a control strategy combined with filtered backstepping and adaptive technique to solve the problem of adaptive finite-time attitude control for multiple spacecraft with unknown external disturbances. The solar panel of the Feng Yun-3 (FY-3) spacecraft rotates relative to the spacecraft body to ensure the solar panel generates sufficient energy for the system [9]. In addition, external disturbances, inertial variability, and nonlinearity pose difficulties for the design of fast and accurate attitude control schemes, such as proportional integral derivative (PID) control, active disturbance rejection control (ADRC) [10], AC [11, 12], sliding mode control (SMC) [13], and finite-time control (FTC) [14]. SMC exhibits excellent performance in uncertain nonlinear systems. Thus, various sliding mode variable structure control methods have been proposed for spacecraft attitude tracking, such as integral SMC [15], second-order SMC [16], and terminal SMC [17].

As a form of finite-time control, terminal SMC has attracted increasing attention owing to its robustness and anti-interference properties. Terminal SMC has been applied to spacecraft attitude control but with limitations because of singularity and slow convergence. Zhao [18] proposed a finite-time command filter backstepping approach based on a finite-time adaptive fuzzy tracking control scheme for a class of unknown nonlinear systems. In recent years, nonsingular terminal SMC has attracted increasing attention for applications in complex spacecraft attitude control owing to its advantageous characteristics. Lu et al. [19] proposed an effective SMC strategy for a nonlinear spacecraft model with external disturbances and inertial uncertainty that could effectively solve the problem of spacecraft attitude tracking control. Yousefpour et al. [20] proposed an integral terminal SMC method based on a disturbance observer for the tracking control of a hyperchaotic memory resistance oscillator. To solve the precise trajectory tracking control problem of unmanned vehicles, Lv et al. [21] proposed a nonsingular integral SMC law based on a finite-time disturbance observer. In [19–21], effective disturbance observers were designed for controlled systems to achieve high performance in the presence of inertia uncertainties and external disturbances. Na [22] proposed an alternative AC with prescribed performance to solve the output tracking problem of nonlinear systems with unknown dead zones. Chen et al. [23] designed an adaptive finite-time controller based on the fast TSM control principle to overcome the singularity problem of nonlinear systems. Na [22] and Chen et al. [23] designed effective attitude control schemes for systems with problems such as uncertain inertia terms, unknown disturbances, and sudden actuator failure. To solve the attitude tracking problem for a rigid platform spacecraft with rotating flexible appendages, Shi et al. [24] proposed the nonsingular terminal SMC algorithm for the finite-time tracking control of n-order nonlinear dynamical systems. To achieve underactuated attitude stabilization, Yue et al. [25] designed a higher-level SMC part to stabilize the angular velocity combined with a tracking control part to track desired angular velocities. Furthermore, [24, 25] demonstrated effective control laws for nonlinear dynamical systems to achieve finite-time convergence and strong robustness. Alshamali et al. [26] designed an observer-based backstepping controller to solve attitude tracking problems with the angles of satellite dynamics under external disturbances. Wang et al. [27] proposed an adaptive SMC scheme to control the chaotic oscillation of a complex seven-dimensional power system. The proposed scheme avoided the singularity problem and improved the accuracy of attitude control as well. Finally, Peng et al. [28] proposed a fast, nonsingular integral terminal SMC scheme for a class of nonlinear systems by introducing a power integral term. This type of scheme can be used to avoid the singularity problem without constraints and to achieve finite-time convergence of the system state. These control methods exhibit good performance and robustness in many systems but are unsuitable for rigid-flexible coupled spacecraft with high-inertia rotating appendages.

In recent years, the number of high-inertia rotating appendages in spacecraft has increased. "high inertia" is mainly in the relative sense, and high-inertia components generally refer to appendages with similar mass as spacecraft or high-inertia matrixes. However, no unified and quantifiable standard is available in the academic field. These components often contain both static and dynamic imbalances, thus producing an unbalanced disturbance torque. Therefore, higher accuracy is required for the attitude control of spacecraft. Miao et al. [29] designed a fast, nonsingular SMC method integrated with an adaptive method, which has been proven to have a higher convergence speed and increased robustness than previous terminal SMC methods. However, high-inertia components and flexible solar panels were not considered in their study. Gui et al. [30] proposed a novel integral TSM controller integrated with an adaptive fault-tolerant control law to solve the attitude tracking problem for a rigid spacecraft; however, a rigid-flexible coupled spacecraft was not considered. This TSM controller exhibited better control performance, including higher convergence speed and estimation accuracy, than the conventional controllers reported in [29, 30]. Xie [31] designed a composite compensation controller to account for the control torques and reduce the impulse characteristics of the disturbance torque during the acceleration of rotating components. Further, the effectiveness of the controller was proven using a semi-physical simulation system; additionally, the coupling effect between the high-inertia components and platform and the characteristics of unbalanced disturbance torque were analyzed. In addition, a PD control algorithm combined with repetitive control was designed. Regarding the unbalanced characteristics of high-inertia rotating appendages, Chai [32, 33] used the Kalman filter method to effectively and accurately estimate unbalanced interference torques caused by appendage rotation.

Among the broad array of studies conducted to date, only a few studies address the problem of attitude tracking control of rigid-flexible coupled platforms with high-inertia components. To bridge this divide, this study proposes a novel, fast integral SMC strategy for spacecraft with high-inertia components and flexible solar panels and demonstrates the applicability of this approach to facilitate the attitude tracking of

spacecraft systems. The primary contributions of this work are listed below:

(1) A rigid-flexible coupling spacecraft with rotating components is considered, and the mathematical and dynamic models are established

(2) An attitude control law for the high-inertia components of a spacecraft system, integrated with a novel, fast nonsingular integral SMC law for symmetrical solar panels, and a spacecraft platform to enable accurate spacecraft attitude tracking are demonstrated

The remainder of this paper is organized as follows. Section 2 introduces the dynamic and kinematic models for spacecraft attitude tracking with high-inertia rotating appendages and symmetrical solar panels. Section 3 introduces the proposed fast nonsingular integral SMC law. Section 4 presents the numerical simulation results to demonstrate the effectiveness of the control algorithm. Finally, Section 5 concludes the study.

2. Preliminary Modeling

A rigid spacecraft model with large, rigid rotating inertial components and symmetrical flexible solar panels was considered in this study. The coordinate system included the inertial reference frame $OXYZ$, orbital reference frame $OX_oY_oZ_o$, spacecraft platform reference frame $ox_sy_sz_s$, large rigid rotating component body-fixed frame $ox_py_pz_p$, and flexible solar panels body-fixed frame $ox_ay_az_a$ (Figure 1)—these were defined as R, R_o, R_s, R_p, andR_a, respectively. The y-axes of R_s, R_p, and R_a were parallel. The flexible solar panels were installed on the $\pm y$-axis, and the large rigid rotating components were installed on the x-axis of the platform coordinate system R.

The rigid-flexible coupling spacecraft model consisted of kinematic and dynamic equations, which are described in the following sections.

2.1. Kinematic Model of the Spacecraft System. Because the Euler angle has a singularity, the Euler equation is not suitable for spacecraft with a wide range of attitude motion. To avoid the singularity and complex calculations, the unit quaternions are often used to describe the kinematics of a spacecraft. A unit quaternion is expressed as $Q_s = \left[q_0 \;\; \mathbf{q}_s^T \right]^T = \left[q_0 \;\; q_1 \;\; q_2 \;\; q_3 \right]^T$, where q_0 and $\mathbf{q}_s = \left[q_1 \;\; q_2 \;\; q_3 \right]^T$are the scalar and vector parts of the quaternion, respectively, and q_0 and $\boldsymbol{q}_s$ satisfy the condition $q_0^2 + \mathbf{q}_s^T\mathbf{q}_s = 1$.

The kinematic equation with the quaternion of spacecraft can be given as

$$\dot{\mathbf{Q}} = \frac{1}{2}E(\mathbf{q}_s) * \omega_b = \frac{1}{2}\begin{bmatrix} -\mathbf{q}_s^T \\ \tilde{\mathbf{q}}_s + q_0 I_3 \end{bmatrix} * \omega_s, \tag{1}$$

where ω_s denotes the angular attitude velocity of the spacecraft relative to the inertial system and $\tilde{\mathbf{q}}_s$ represents the skew symmetric matrix of $\mathbf{q}_s$such that

$$\tilde{q}_s = \begin{bmatrix} 0 & -q_3 & q_2 \\ q_3 & 0 & -q_1 \\ -q_2 & q_1 & 0 \end{bmatrix}. \tag{2}$$

The desired orbital coordinate system for the spacecraft tracking system is denoted asR_o, and Q_d is the expected attitude quaternion. Thus, $\mathbf{Q}_d = \left[q_{d0} \;\; \mathbf{q}_d^T \right]^T$, and the kinematic equation is defined as

$$\dot{\mathbf{Q}}_d = \frac{1}{2}E(\mathbf{q}_d) * \omega_d, \tag{3}$$

where ω_d is the desired angular velocity from R_o relative to R. In addition, the attitude tracking error quaternion is defined as $\mathbf{Q}_e = \left[q_{e0} \;\; \mathbf{q}_e^T \right]^T$ such that

$$\mathbf{Q}_e = \begin{bmatrix} q_{e0} \\ \mathbf{q}_e \end{bmatrix} = \begin{bmatrix} q_{s0}q_{d0} + \mathbf{q}_d^T\mathbf{q}_s \\ q_{d0}\mathbf{q}_s + \tilde{\mathbf{q}}_s\mathbf{q}_d - q_{s0}\mathbf{q}_d \end{bmatrix}, \tag{4}$$

which describes the error R_s relative to R_o.

The principle of two vector attitude determinations was used to determine the desired quaternion of the spacecraft. The desired quaternion could then be used to obtain the attitude transformation matrix of the spacecraft orbit R_o relative to the inertial orbit R. According to the known position vector $\mathbf{X}$ and velocity vector $\mathbf{V}$ of the spacecraft, matrix B is the projection of $\mathbf{X}$ and $\mathbf{V}$ of the spacecraft in R, and matrix A is the projection of $\mathbf{X}$ and $\mathbf{V}$ of the spacecraft in R_o. The unique transformation matrix is then defined as

$$C_{BA} = B^{-1}A, \tag{5}$$

where the matrixes B and A can be defined as

$$B = \left[\frac{\mathbf{X}}{|\mathbf{X}|}, \frac{\mathbf{X}\times\mathbf{V}}{|\mathbf{X}\times\mathbf{V}|}, \frac{\mathbf{X}\times(\mathbf{X}\times\mathbf{V})}{|\mathbf{X}\times(\mathbf{X}\times\mathbf{V})|} \right],$$

$$A = \begin{bmatrix} 0 & 0 & -1 \\ 0 & -1 & 0 \\ -1 & 0 & 0 \end{bmatrix}. \tag{6}$$

Thus, the desired quaternion can be obtained as follows:

$$\begin{aligned} q_0 &= \frac{1}{2}\sqrt{1 + C_{BA}(1,1) + C_{BA}(2,2) + C_{BA}(3,3)}, \\ q_1 &= \frac{1}{4q_0}\left(C_{BA}(2,3) - C_{BA}(3,2)\right), \\ q_2 &= \frac{1}{4q_0}\left(C_{BA}(3,1) - C_{BA}(1,3)\right), \\ q_3 &= \frac{1}{4q_0}\left(C_{BA}(1,2) - C_{BA}(2,1)\right), \end{aligned} \tag{7}$$

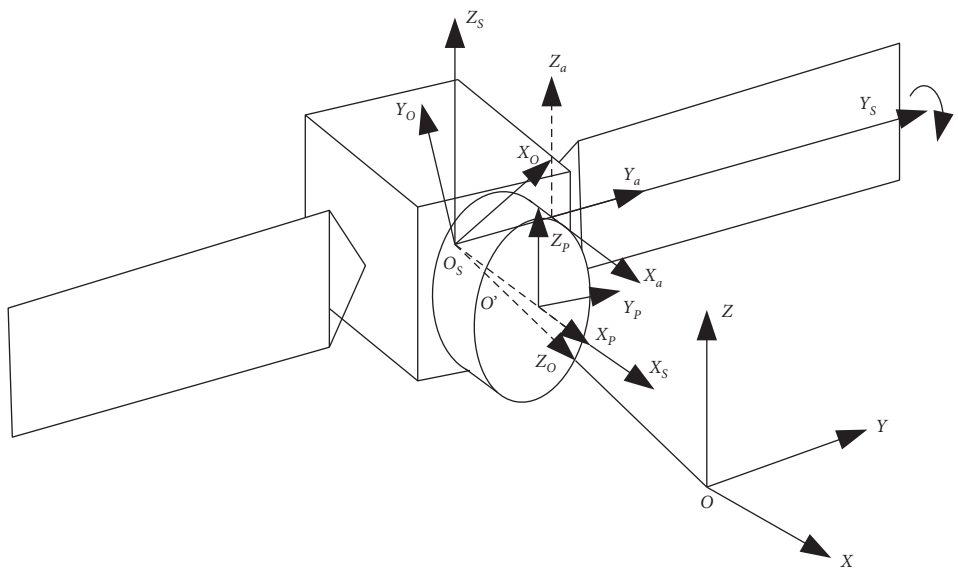

Figure 1: Coordinate system of spacecraft with appendages.

where C_{sd} is the coordinate transformation matrix from R_o to R_s, which can be calculated as

$$C_{sd} = \left(q_{e0}^2 - \mathbf{q}_e^T \mathbf{q}_e\right) I_3 + 2\mathbf{q}_e \mathbf{q}_e^T - 2q_{e0}\tilde{\mathbf{q}}_e. \tag{8}$$

The angular attitude velocity tracking error of the spacecraft is defined as

$$\omega_e = \omega_s - C_{sd}\omega_d. \tag{9}$$

The high-inertia component is the rotation around the $\mathbf{x}_s$-axis of the spacecraft platform with the desired attitude angular velocity $\omega_{pd} = [\omega_{pd}, 0, 0]^T$. Similarly, the flexible solar panels rotate around the $\mathbf{y}_s$-axis of the spacecraft platform with the desired attitude angular velocity $\omega_{ad} = [0, \omega_{ad}, 0]^T$. The kinematic equation for the desired attitude of the high-inertia components is $\dot{Q}_{pd} = (1/2)E(\mathbf{q}_{pd})\omega_{pd}$ and that for the flexible solar panels is $\dot{Q}_{ad} = (1/2)E(\mathbf{q}_{ad})\omega_{ad}$. Thus, the real kinematic equations are $\dot{Q}_p = (1/2)E(\mathbf{q}_p)\omega_p$ and $\dot{Q}_a = (1/2)E(\mathbf{q}_a)\omega_a$. The quaternion for the attitude tracking error can be obtained using (4), such that the attitude tracking error of the flexible solar panels is

$$\mathbf{Q}_{ae} = \begin{bmatrix} q_{ae0} \\ \mathbf{q}_{ae} \end{bmatrix} = \begin{bmatrix} q_{a0}q_{ad0} + \mathbf{q}_{ad}^T \mathbf{q}_a \\ q_{ad0}\mathbf{q}_a + \tilde{\mathbf{q}}_a \mathbf{q}_{ad} - q_{a0}\mathbf{q}_{ad} \end{bmatrix}. \tag{10}$$

The angular attitude velocity tracking error of the high-inertia components and flexible solar panels can be, respectively, expressed as

$$\begin{aligned} \boldsymbol{\omega}_{pe} &= \boldsymbol{\omega}_p - \boldsymbol{\omega}_{pd}, \\ \boldsymbol{\omega}_{ae} &= \boldsymbol{\omega}_a - \boldsymbol{\omega}_{ad}. \end{aligned} \tag{11}$$

When the high-inertia components and the flexible solar panels rotate only around the $\mathbf{x}_s$-axis and $\mathbf{y}_s$-axis, respectively, of the spacecraft platform, the rotational angle of the former is set as $\theta_p \in [0, 2\pi]$ and that of the latter is set as $\theta_a \in [0, 2\pi]$. The rotational angles can be calculated by

$$\begin{aligned} \boldsymbol{\theta}_p &= \int \boldsymbol{\omega}_p \mathrm{d}t, \\ \boldsymbol{\theta}_{ai} &= \int \boldsymbol{\omega}_{ai} \mathrm{d}t. \end{aligned} \tag{12}$$

The transformation matrixes from R_p and R_a to R_s are then defined as

$$\begin{aligned} C_{ps} &= \begin{bmatrix} 1 & 0 & 0 \\ 0 & \cos(\theta_{px}) & \sin(\theta_{px}) \\ 0 & -\sin(\theta_{px}) & \cos(\theta_{px}) \end{bmatrix}, \\ C_{abi} &= \begin{bmatrix} \cos(\theta_{ayi}) & 0 & -\sin(\theta_{ayi}) \\ 0 & 1 & 0 \\ \sin(\theta_{ayi}) & 0 & \cos(\theta_{ayi}) \end{bmatrix}. \end{aligned} \tag{13}$$

2.2. Dynamics of the Spacecraft System. We considered the rotation of the rigid high-inertia components and flexible solar panels on the rigid-flexible coupling spacecraft, as well as the translation and rotation of the spacecraft platform and the modal vibration of the solar panels. The Lagrange method was used to deduce the complex equations and the dynamic model equations of the spacecraft system attitude, as follows:

$$\left(M + m_p + 2m_a\right)\ddot{X} = \mathbf{P}_s, \tag{14a}$$

$$\begin{aligned} &\mathbf{J}_s\dot{\omega}_s + \tilde{\boldsymbol{\omega}}_s\left(\mathbf{J}_s\boldsymbol{\omega}_s + \mathbf{R}_{sp}\boldsymbol{\omega}_p + \mathbf{R}_{sa}\boldsymbol{\omega}_a\right) + \mathbf{F}_{sa}\ddot{\eta}_{ai} \\ &\quad + \mathbf{R}_{sa}\dot{\omega}_{ai} + \mathbf{R}_{sp}\dot{\omega}_p = \mathbf{T}_s + \mathbf{T}_{sdp} + \mathbf{d}, \end{aligned} \tag{14b}$$

$$\mathbf{J}_{ai}\dot{\omega}_{ai} + \mathbf{F}_{ai}\ddot{\eta}_{ai} + \mathbf{R}_{sai}^T\dot{\omega}_s = \mathbf{T}_{ai}\,(i = -y, y), \tag{14c}$$

$$\ddot{\eta}_{ai} + 2\zeta_{ai}\boldsymbol{\Omega}_{ai}\dot{\eta}_{ai} + \boldsymbol{\Lambda}_{ai}\boldsymbol{\eta}_{ai} + \mathbf{R}_{sa}^T\dot{\omega}_s + \mathbf{F}_{ai}^T\dot{\omega}_{ai} = 0\,(i = -y, +y), \tag{14d}$$

where M is the mass of the spacecraft platform; m_p is the mass of the high-inertia component; $m_a$is the mass of a single flexible solar panel; P_s denotes the combined external forces on the spacecraft system; the inertia matrix with respect to R_s of the spacecraft is defined as J_s and satisfies the equation $J_s = J_{s0} + C_{sa}J_{a0}C_{sa}^T + C_{sp}J_pC_{sp}^T$; J_{a0} is the inertia matrix of the flexible solar panel relative to the platform when it is not rotating; J_p is the inertia matrix of the high-inertia rotating component with respect to the platform; T_s and T_a denote the torque of the spacecraft platform and the solar panels, respectively; T_d is the unknown external disturbance torque; T_{sdp} is the sum of the dynamic and static unbalanced torques and the bearing torque of high-inertia components under the influence of coupling; η_a denotes the modal coordinates of the solar panel; Ω_a is the diagonal matrix of the modal frequency of the solar panel; Λ_a is the stiffness matrix of the solar panel such that $\Lambda_a = \Omega_a^2$; ξ_a is the damping ratio of the solar panel. Notably, all these parameters are diagonal matrixes. From (14a)–(14b), $\mathbf{F}_{sa} = \mathbf{F}_{sa\_\text{right}} + \mathbf{F}_{sa\_\text{left}}$ and $\mathbf{R}_{sa} = \mathbf{R}_{sa\_\text{right}} + \mathbf{R}_{sa\_\text{left}}$.

The connection point between the high-inertia rotation component and the platform was modeled as shown in Figure 1. In this paper, $\mathbf{r}_s$ denotes the vector from the connection point to the origin of the high-inertia rotation component's $R_s$coordinate system; $\mathbf{r}_p$ denotes the vector from the origin of the R_p coordinate system to the connection point; and $\mathbf{r}$ denotes the vector from the connection point to the mass element dm on the high-inertia rotation component. When the high-inertia rotation component rotates around the x-axis at the angular velocityω_p, the unbalanced torque $\mathbf{T}_{sd}$ can be generated on the satellite platform. The dynamic equations for a high-inertia appendage are as follows:

$$\begin{aligned}\mathbf{T}_{sd} &= -\mathbf{r}_p \times \int_p \left[\boldsymbol{\omega}_p \times \left(\boldsymbol{\omega}_p \times \mathbf{r}\right)\right] \mathrm{d}m - \mathbf{r} \\ &\quad \times \int_p \left[\boldsymbol{\omega}_p \times \left(\boldsymbol{\omega}_p \times \mathbf{r}\right)\right] \mathrm{d}m \\ &= -\boldsymbol{\omega}_p \times \left(\mathbf{J}_p \boldsymbol{\omega}_p\right) + \mathbf{m}_p \boldsymbol{\omega}_p^T \boldsymbol{\omega}_p \left(\mathbf{r}_s \times \mathbf{r}_p\right),\end{aligned} \tag{15}$$

$$\mathbf{J}_p \dot{\omega}_p + \mathbf{R}_{sp}^T \dot{\omega}_s = \mathbf{T}_p, \tag{16}$$

$$\mathbf{T}_{sdp} = \mathbf{T}_{sd} - \mathbf{T}_p, \tag{17}$$

where T_p is the control torque of the high-inertia component. Because the solar panels only rotate about the y-axis relative to the spacecraft platform, $\mathbf{F}_{sa}$denotes the coupling coefficient matrix of the rotation of the spacecraft platform with the vibration of the solar panels such that

$$F_{sa} = \left[f_{sa1} \begin{bmatrix} \sin(\theta_{ay}) \\ 1 \\ \cos(\theta_{ay}) \end{bmatrix}, f_{sa2} \begin{bmatrix} \sin(\theta_{ay}) \\ 1 \\ \cos(\theta_{ay}) \end{bmatrix}, \ldots, f_{sa6} \begin{bmatrix} \sin(\theta_{ay}) \\ 1 \\ \cos(\theta_{ay}) \end{bmatrix} \right], \tag{18}$$

where f_{sa} is the coefficient matrix of the platform rotation to the solar panel vibration, which is related to the rotating angle θ_{ay}, $\mathbf{F}_a$ is the coupling coefficient matrix between the vibration and rotation of solar panels, $\mathbf{R}_{sa}$ is the coupling coefficient matrix of rotation between the solar panels and the platform and is calculated in a similar manner as equation (18), with r_{sa} as the angle-independent coefficient, and $\mathbf{R}_{sp}$ is the matrix of vibration of the high-inertia component with the rotation of the spacecraft platform. The high-inertia component rotates only around the x-axis relative to the spacecraft platform; thus, $\mathbf{R}_{sp}$ can be described by a variation of (16).

Equation (13) shows the dynamic equations of the spacecraft system, including the translation of the platform, as well as the rotation of the high-inertia components and solar panels. Upon substituting (5) and (11) into (14a)-(14d), we obtain

$$\boldsymbol{\Theta}\dot{\omega} + \boldsymbol{\Gamma} + \boldsymbol{\Delta} = \mathbf{T}, \tag{19}$$

where

$$\begin{aligned}
\boldsymbol{\omega} &= \left[\, \boldsymbol{\omega}_e \;\; \boldsymbol{\omega}_{ae} \,\right]^T, \\
\boldsymbol{\Theta} &= \begin{bmatrix} \mathbf{J}_{s0} - \mathbf{F}_{sa}\mathbf{F}_{sa}^T & \mathbf{R}_{sa} - \mathbf{F}_{sa}\mathbf{F}_a^T \\ \mathbf{R}_{sa}^T - \mathbf{F}_a\mathbf{F}_{sa}^T & \mathbf{J}_a - \mathbf{F}_a\mathbf{F}_a^T \end{bmatrix} \\
\boldsymbol{\Gamma} &= \begin{bmatrix} \mathbf{R}_{sP}\dot{\omega}_P + \boldsymbol{\omega}_s \times \left(\mathbf{J}_{s0}\boldsymbol{\omega}_s + \mathbf{R}_{sp}\boldsymbol{\omega}_p + \mathbf{R}_{sa}\boldsymbol{\omega}_a\right) + \left(\mathbf{J}_{s0} - \mathbf{F}_{sa}\mathbf{F}_{sa}^T\right)\left(-\tilde{\boldsymbol{\omega}}_e\mathbf{C}_{sd}\boldsymbol{\omega}_d + \mathbf{C}_{sd}\dot{\omega}_d\right) - \mathbf{T}_{sdp} \\ \mathbf{R}_{sa}^T - \mathbf{F}_a\mathbf{F}_{sa}^T\left(-\tilde{\boldsymbol{\omega}}_e\mathbf{C}_{sd}\boldsymbol{\omega}_d + \mathbf{C}_{sd}\dot{\omega}_d\right) \end{bmatrix}, \\
\boldsymbol{\Delta} &= \begin{bmatrix} \Delta_1 \\ \Delta_2 \end{bmatrix} = \begin{bmatrix} \mathbf{F}_{sa}\left(2\boldsymbol{\zeta}_{ai}\boldsymbol{\Omega}_{ai}\dot{\eta}_{ai} + \boldsymbol{\Lambda}_{ai}\boldsymbol{\eta}_{ai}\right) + \left(C_{sa}\mathbf{J}_{a0}C_{sa}^T + C_{sp}\mathbf{J}_pC_{sp}^T\right)\left(\dot{\omega}_e - \tilde{\boldsymbol{\omega}}_eC_{sd}\boldsymbol{\omega}_d + C_{sd}\dot{\omega}_d\right) - \mathbf{d} + \Delta\left(\mathbf{F}_{sa}, \mathbf{R}_{sa}\right) \\ \Delta\left(\mathbf{F}_{sa}, \mathbf{R}_{sa}\right) \end{bmatrix}, \\
\mathbf{T} &= \begin{bmatrix} \mathbf{T}_s \\ \mathbf{T}_a \end{bmatrix}.
\end{aligned} \tag{20}$$

Remark 1. The moment of inertia of the spacecraft system has the specific form $J = J_0 + \Delta J$, where J_0 is the nonsingular nominal constant matrix, and ΔJ is the uncertainty of moment of inertia and is a bounded constant.

Remark 2. $(\Delta F_{sa}, \Delta R_{sa}, \Delta R_{sp})$ represent the combined uncertainties on parameters F_{sa}, R_{sa}, and R_{sp}; these uncertainties exist because, although the high-inertia components and solar panels rotate predominantly around one axis of the spacecraft, they exhibit small rotations around the other axes. Thus, the combined uncertainties are bounded.

Remark 3. The disturbance Δ is bounded, and satisfies $\Delta \le \Delta_d$, where d is a constant.

3. Sliding Mode Control Law Design

Lemma 1. *The extended Lyapunov of finite-time stability can be expressed in the form of a fast TSM as follows [34, 35]:*

$$\dot{V}(x) + \lambda_1 V(x) + \lambda_2 V^{\gamma}(x) \ge 0. \tag{21}$$

If (18) satisfies the conditions $\lambda_1 > 0, \lambda_2 > 0$ and $0 < \gamma < 1$, the convergence time can be given by

$$T \le \frac{1}{\lambda_1 (1-\gamma)} \ln \frac{\lambda_1 V^{1-\gamma}(x_0) + \lambda_2}{\lambda_2}. \tag{22}$$

Lemma 2. *For any $x_i \in R$ $(i = 1, 2, \ldots, n)$ and a positive real number $\gamma \in (0, 1)$, the following inequality holds [36]:*

$$\left(\sum_{i=1}^{n} |x_i|^2\right)^{(1+\gamma/2)} \le \sum_{i=1}^{n} |x_i|^{1+\gamma}. \tag{23}$$

Lemma 3. *We consider the system $\dot{x} = f(x, u)$, where f is a continuous function that satisfies $f(0) = 0$, and a Lyapunov function $V(x)$ that satisfies [37]*

$$\dot{V}(x) + \lambda V^{\alpha}(x) \le 0, \tag{24}$$

where $\lambda > 0$, $0 < \alpha < 1$. Then, the origin is a finite-time stable equilibrium of the system $\dot{x} = f(x, u)$. Let T represent the time required for the system to reach $V(x) \equiv 0$. If $\mathbf{x}_0$ is the initial system state, the convergence time satisfies

$$T \le \frac{V^{1-\alpha}(\mathbf{x}_0)}{\lambda (1-\alpha)}. \tag{25}$$

Using the quaternion for the attitude tracking error of the spacecraft platform and solar panel to describe the attitude system state, we can write $\mathbf{x} = [\,\mathbf{q}_e \;\; \mathbf{q}_{ae}\,]^T$ and define

$$\dot{x} = [\dot{q}_e \;\; \dot{q}_{ae}]^T = \frac{1}{2}\mathbf{E}\boldsymbol{\omega}. \tag{26}$$

Thus, $\ddot{x}$ can be given as

$$\ddot{x} = \frac{1}{4}\mathbf{L} + \frac{1}{2}(\mathbf{E}\Theta)(\mathbf{T} - \boldsymbol{\Gamma} - \boldsymbol{\Delta}). \tag{27}$$

Finally, the augmented matrix $\mathbf{E}$ can be written as $\mathbf{E} = \begin{bmatrix} \mathbf{E}(\mathbf{q}_e) & 0 \\ 0 & \mathbf{E}(\mathbf{q}_{ae}) \end{bmatrix}$ and $\mathbf{L} = \begin{bmatrix} \mathbf{q}_e \omega_e^T \omega_e \\ \mathbf{q}_{ae} \omega_{ae}^T \omega_{ae} \end{bmatrix}$.

3.1. Controller Design of the Spacecraft Platform and Solar Panel

3.1.1. Integral Sliding Mode Surface Design. The integral sliding mode surface can be defined by

$$\mathbf{S} = \mathbf{k}_x \dot{\mathbf{x}} + \int_0^t \mathbf{C}_1 \mathbf{S}_1 (\boldsymbol{\lambda}_1, \boldsymbol{\rho}_1, \mathbf{x}, \boldsymbol{\varepsilon}_1) + \mathbf{C}_2 \mathbf{S}_2 (\boldsymbol{\lambda}_2, \boldsymbol{\rho}_2, \dot{\mathbf{x}}, \boldsymbol{\varepsilon}_2) \mathrm{d}t, \tag{28}$$

where $\mathbf{C}_1 = \mathrm{diag}(c_{11}, c_{12}, c_{13}, c_{14}, c_{15}, c_{16})$ and $\mathbf{C}_2 = \mathrm{diag}(c_{21}, c_{22}, c_{23}, c_{24}, c_{25}, c_{26})$, and

$$\begin{aligned} \boldsymbol{\gamma}_1 &= [\gamma_{11}, \gamma_{12}, \gamma_{13}, \gamma_{14}, \gamma_{15}, \gamma_{16}]^T, \\ \boldsymbol{\gamma}_2 &= [\gamma_{21}, \gamma_{22}, \gamma_{23}, \gamma_{24}, \gamma_{25}, \gamma_{26}]^T, \\ \boldsymbol{\varepsilon}_1 &= [\varepsilon_{11}, \varepsilon_{12}, \varepsilon_{13}, \varepsilon_{14}, \varepsilon_{15}, \varepsilon_{16}]^T, \\ \boldsymbol{\varepsilon}_2 &= [\varepsilon_{21}, \varepsilon_{22}, \varepsilon_{23}, \varepsilon_{24}, \varepsilon_{25}, \varepsilon_{26}]^T, \end{aligned} \tag{29}$$

where $c_{1i} > 0$ and $c_{2i} > 0$ are the sliding surface design matrixes for $i = 1, 2, \ldots, 6$. Furthermore, the vectors $\mathbf{S}_1$ and $\mathbf{S}_2$ can be defined as

$$\begin{aligned} \mathbf{S}_1 &= [S_{11}, S_{12}, S_{13}, S_{14}, S_{15}, S_{16}]^T, \\ \mathbf{S}_2 &= [S_{21}, S_{22}, S_{23}, S_{24}, S_{25}, S_{26}]^T. \end{aligned} \tag{30}$$

In (30), S_{1i} and S_{2i} are defined as

$$\begin{aligned} S_{1i}(\gamma_{1i}, \rho_{1i}, x_{1i}, \varepsilon_{1i}) &= \begin{cases} |x_{1i}|^{\gamma_{1i}}, & \text{if } |x_{1i}| \le \varepsilon_{1i}, \\ \varepsilon_{1i}^{\gamma_{1i}-\rho_{1i}} |x_{1i}|^{\rho_{1i}} \mathrm{sign}(x_{1i}), & \text{if } |x_{1i}| > \varepsilon_{1i}, \end{cases} \\ S_{2i}(\gamma_{2i}, \rho_{2i}, \dot{x}_{2i}, \varepsilon_{2i}) &= \begin{cases} |\dot{x}_{2i}|^{\gamma_{2i}}, & \text{if } |\dot{x}_{2i}| \le \varepsilon_{2i}, \\ \varepsilon_{2i}^{\gamma_{2i}-\rho_{2i}} |\dot{x}_{2i}|^{\rho_{2i}} \mathrm{sign}(\dot{x}_{2i}), & \text{if } |\dot{x}_{2i}| > \varepsilon_{2i}, \end{cases} \end{aligned} \tag{31}$$

where γ_{1i} and γ_{2i} are the positive constant gains, which satisfy $0 < \gamma_{2i} < 1$ and $\gamma_{1i} = (\gamma_{2i}/2 - \gamma_{2i})$. In the same way, ρ_{1i}, ρ_{2i}, ε_{1i}, and ε_{2i} are the positive constant gains, which satisfy $\rho_{1i} \ge 1$, $\rho_{2i} \ge 1$, $\varepsilon_{1i} > 0$, and $\varepsilon_{2i} > 0$, respectively.

The control torque $\mathbf{T}$ can be expressed as follows:

$$\begin{aligned} \mathbf{T} = {} & 2(\mathbf{K}_x \mathbf{E}\Theta)^{-1} (-\boldsymbol{\tau}\mathbf{S} - \mathbf{K}_s \mathrm{sgn}(\mathbf{S}) - \mathbf{C}_1 \mathbf{S}_1 (\boldsymbol{\gamma}_1, \boldsymbol{\rho}_1, \mathbf{x}, \boldsymbol{\varepsilon}_1) \\ & - \mathbf{C}_2 \mathbf{S}_2 (\boldsymbol{\gamma}_2, \boldsymbol{\rho}_2, \dot{x}, \boldsymbol{\varepsilon}_2)) + \frac{1}{2}(\mathbf{E}\Theta)^{-1} \mathbf{L} + \boldsymbol{\Gamma} + \boldsymbol{\Delta}. \end{aligned} \tag{32}$$

Remark 4. From (28), it is observed that the controller parameters γ_{1i}, γ_{2i}, k_{xi}, C_{1i}, and C_{2i} affect the convergences performances of the closed-loop systems. Smaller γ_{1i} and γ_{2i} and larger k_{xi}, C_{1i}, and C_{2i} will yield a more quick convergence of the attitude tracking error $\mathbf{x}(t)$; $\mathbf{x}$ can be further reduced by increasing the control parameters τ and k_S.

3.1.2. Proof. With the spacecraft attitude dynamics model described in (14a)-(14d), the integral sliding mode (see (28)) and the control law (see (32)) were designed. The system state will slide to the equilibrium point in a finite time after reaching the sliding mode surface. Based on Lyapunov theory, it can be proved that

$$V = \frac{1}{2}\mathbf{S}^T\mathbf{S}, \tag{33}$$

because

$$\begin{aligned}\dot{\mathbf{S}} &= \mathbf{k}_x\ddot{x} + \mathbf{C}_1\mathbf{S}_1\left(\boldsymbol{\gamma}_1, \boldsymbol{\rho}_1, \mathbf{x}, \boldsymbol{\varepsilon}_1\right) + \mathbf{C}_2\mathbf{S}_2\left(\boldsymbol{\gamma}_2, \boldsymbol{\rho}_2, \dot{x}, \boldsymbol{\varepsilon}_2\right)\\ &= \mathbf{k}_x\left[\frac{1}{4}\mathbf{L} + \frac{1}{2}\left(\mathbf{E}\Theta\right)\left(\mathbf{T} - \boldsymbol{\Gamma} - \boldsymbol{\Delta}\right)\right] + \mathbf{C}_1\mathbf{S}_1\left(\boldsymbol{\gamma}_1, \boldsymbol{\rho}_1, \mathbf{x}, \boldsymbol{\varepsilon}_1\right)\\ &\quad + \mathbf{C}_2\mathbf{S}_2\left(\boldsymbol{\gamma}_2, \boldsymbol{\rho}_2, \dot{x}, \boldsymbol{\varepsilon}_2\right).\end{aligned} \tag{34}$$

Differentiating V with respect to time yields (30); from (32), it can be determined that

$$\begin{aligned}\dot{V} &= \mathbf{S}^T\dot{\mathbf{S}} = \mathbf{S}^T\left\{\mathbf{k}_x\left[\frac{1}{4}\mathbf{L} + \frac{1}{2}\left(\mathbf{E}\Theta\right)\left(\mathbf{T} - \boldsymbol{\Gamma} - \boldsymbol{\Delta}\right)\right]\right.\\ &\quad \left. + \mathbf{C}_1\mathbf{S}_1\left(\boldsymbol{\gamma}_1, \boldsymbol{\rho}_1, \mathbf{x}, \boldsymbol{\varepsilon}_1\right) + \mathbf{C}_2\mathbf{S}_2\left(\boldsymbol{\gamma}_2, \boldsymbol{\rho}_2, \dot{x}, \boldsymbol{\varepsilon}_2\right)\right\}\\ &= \mathbf{S}^T\left[-\boldsymbol{\tau}\mathbf{S} - \mathbf{K}_s\operatorname{sgn}\left(\mathbf{S}\right)\right] = -\tau V - k_s V^{(1/2)}.\end{aligned} \tag{35}$$

According to Lemma 1, the convergence time can be determined as

$$T \le \frac{2}{\tau}\ln\frac{\tau V^{(1/2)}\left(x_0\right) + k_s}{k_s}. \tag{36}$$

3.2. Controller Design for High-Inertia Components. The high-inertia components rotate around the x-axis at a certain attitude angular velocity relative to the spacecraft platform. Thus, a control law can be designed for these components.

3.2.1. Sliding Mode Surface Design. The sliding mode function is defined as

$$S_p = K_P\omega_{Pe} + K_d\operatorname{sig}^{\gamma}\left(\dot{\omega}_{Pe}\right), \tag{37}$$

where $K_P = \operatorname{diag}\left(k_{p1}, k_{p2}, k_{p3}\right)$, $K_d = \operatorname{diag}\left(k_{d1}, k_{d2}, k_{d3}\right)$, and $\gamma > 1$ is a positive odd number. When the sliding mode function $S_p = 0$, the attitude angular velocity tracking error of the high-inertia component is equal to 0 ($\omega_{Pe} = 0$) because

$$\dot{\omega}_{Pe} = \left|\frac{k_{pi}}{k_{di}}\omega_{Pe}\right|^{(1/\gamma)}\operatorname{sign}\left(\frac{k_{pi}}{k_{di}}\omega_{Pe}\right) = \frac{k_{pi}}{k_{di}}\left|\omega_{Pe}\right|^{(1/\gamma)}\operatorname{sign}\left(\omega_{Pe}\right). \tag{38}$$

The control torque $\mathbf{T}_p$ can be expressed as

$$\mathbf{T}_p = \mathbf{J}_p\left(\mathbf{k}_p\right)^{-1}\left(-\tau\mathbf{S}_p - k_d\operatorname{sig}^{\gamma}\left(\ddot{\omega}_{pe}\right)\right) + R_{sp}^T\dot{\omega}_s. \tag{39}$$

3.2.2. Proof. As the high-inertia component dynamics model described in (16), the sliding mode (see (37)) was designed. The system state slides to the equilibrium point in a finite time after reaching the sliding mode surface. Based on Lyapunov theory, it can be proved that

$$V_2 = \frac{1}{2}\omega_{Pe}^T J\omega_{Pe}. \tag{40}$$

Differentiation of V_2 with respect to time yields

$$\begin{aligned}V_2 &= \omega_{Pe}^T J\omega_{Pe}\sum_1^3\frac{k_{pi}}{k_{di}}\omega_{Pe}^T J\left|\omega_{Pei}\right|^{(1/\gamma)}\operatorname{sign}\left(\omega_{Pei}\right)\\ &= -\sum_1^3\frac{k_{pi}}{k_{di}}J\left|\omega_{Pei}^2\right|^{(\gamma+1/2\gamma)}\\ &\le -\min\left\{\frac{k_{pi}}{k_{di}}\right\}\left(2\cdot\frac{1}{2}J\sum_1^3\omega_{Pei}\right)^{(\gamma+1/2\gamma)}\\ &= -\min\left\{\frac{k_{pi}}{k_{di}}\right\}\cdot 2^{(\gamma+1/2\gamma)}V^{(\gamma+1/2\gamma)}.\end{aligned} \tag{41}$$

Furthermore, letting $\xi = -\min\left\{k_{pi}/k_{di}\right\}\cdot 2^{(\gamma+1/2\gamma)}$, $\dot{V}_2$ satisfies

$$\dot{V}_2 + \xi V_2^{(\gamma+1/2\gamma)} \le 0. \tag{42}$$

Finally, the convergence time can be determined according to Lemma 3, as follows:

$$T_p \le \frac{2\gamma V_2^{(\gamma+1/2\gamma)}(0)}{\xi(\gamma - 1)}. \tag{43}$$

4. Numerical Simulation Results

This section presents numerical simulations to demonstrate the performance of the proposed nonsingular integral sliding mode controller (NISMC). The results of the proposed method are compared with those of the fast TSM finite-time controller (FSMC) designed by Yang and Yang in [38] and the PD controller. The simulation results of the spacecraft with high-inertia components and flexible solar panels are presented, and the proposed control laws are demonstrated to have superior performance. The fast-sliding mode finite-time controller exhibits higher convergence speed and an accurate attitude tracking and control of the component angle. In this analysis, the desired angular velocity of the flexible solar panels about the y-axis of the spacecraft was set as $\omega_{ad} = 0.1$ rad/s and that of the large rigid inertial component about the x-axis of the spacecraft as $\omega_{pd} = 0.2$ rad/s. The expected attitude of the spacecraft platform is the coordinate system R_s that coincides with R_o.

Figures 2 and 3 present the results of the vector component of the error quaternion and the error of the attitude angular velocity of the platform, respectively. Figure 4 presents the results of the vector component of the error quaternion of the flexible solar panels. Figures 5 and 6 present the results of the error of the attitude angular

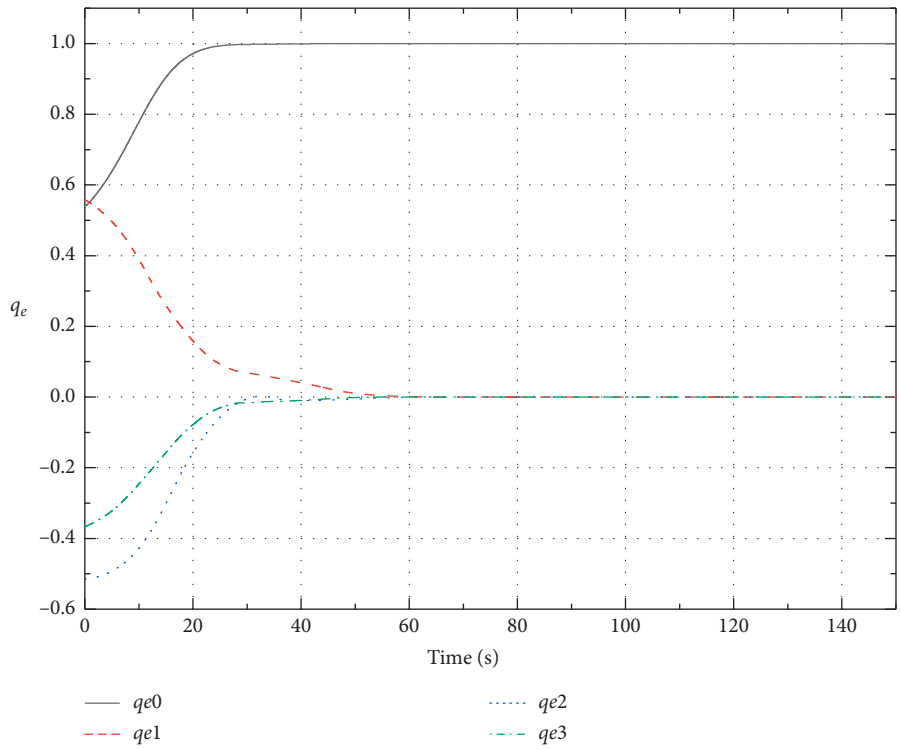

Figure 2: Trajectories of the vector component of the platform error quaternion.

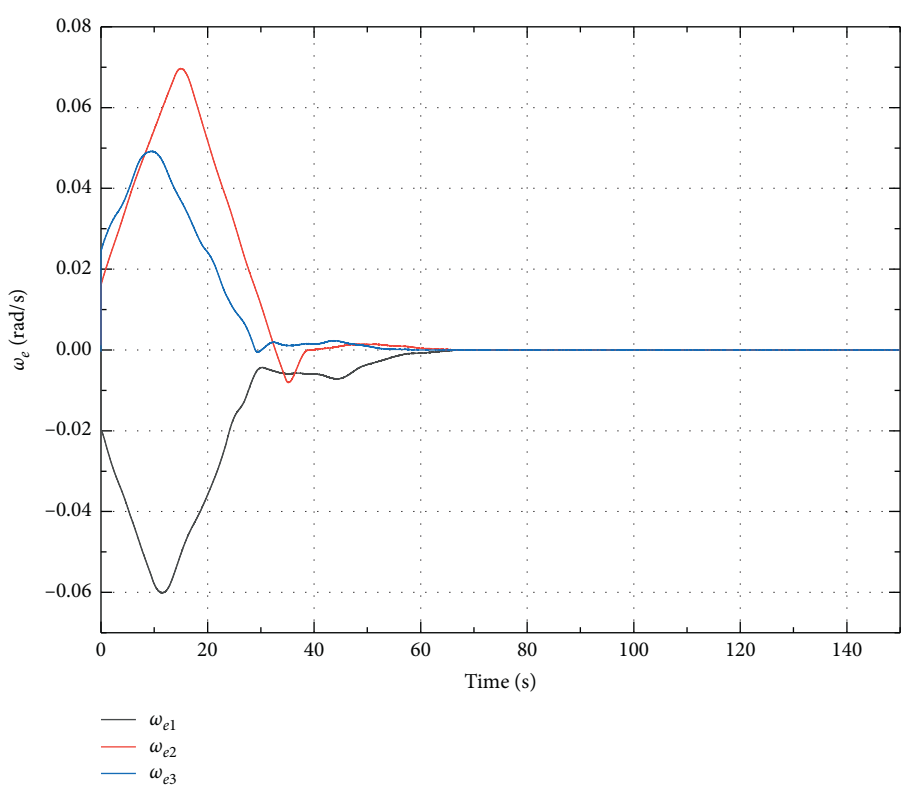

Figure 3: Trajectories of the error of attitude angular velocity of platform.

velocity and the attitude angular velocity of the flexible solar panels relative to the spacecraft platform. Figure 7 shows the attitude angular velocity and error of the angular velocity of the large rigid inertial component that rotates around the x-axis of the spacecraft platform. Figures 3, 5, and 7 indicate that the error of the attitude angular velocity

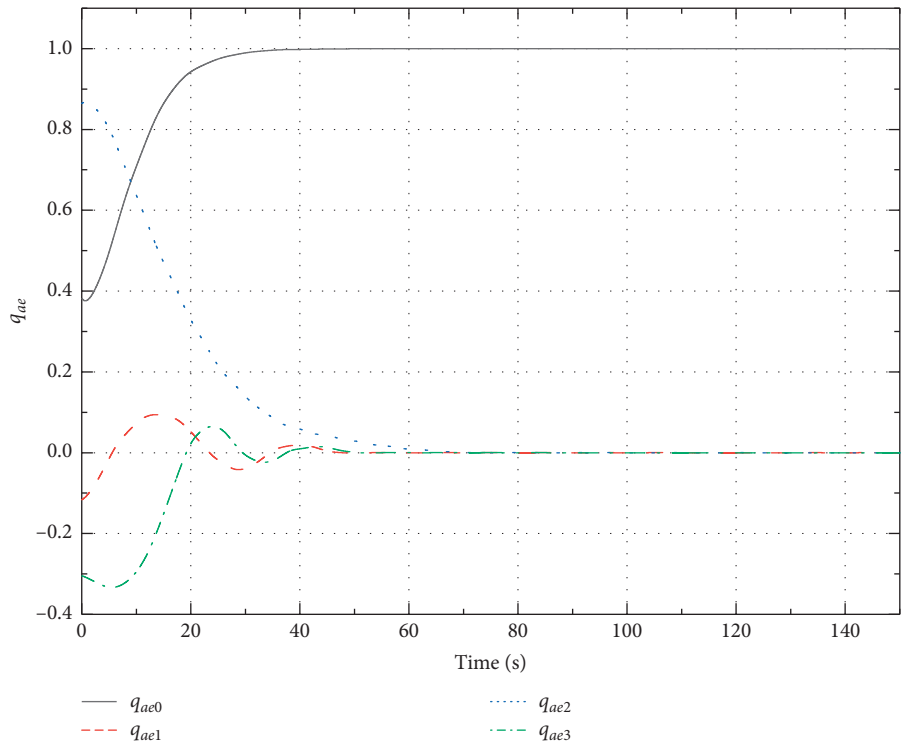

Figure 4: Trajectories of vector component of the error quaternion of flexible solar panel.

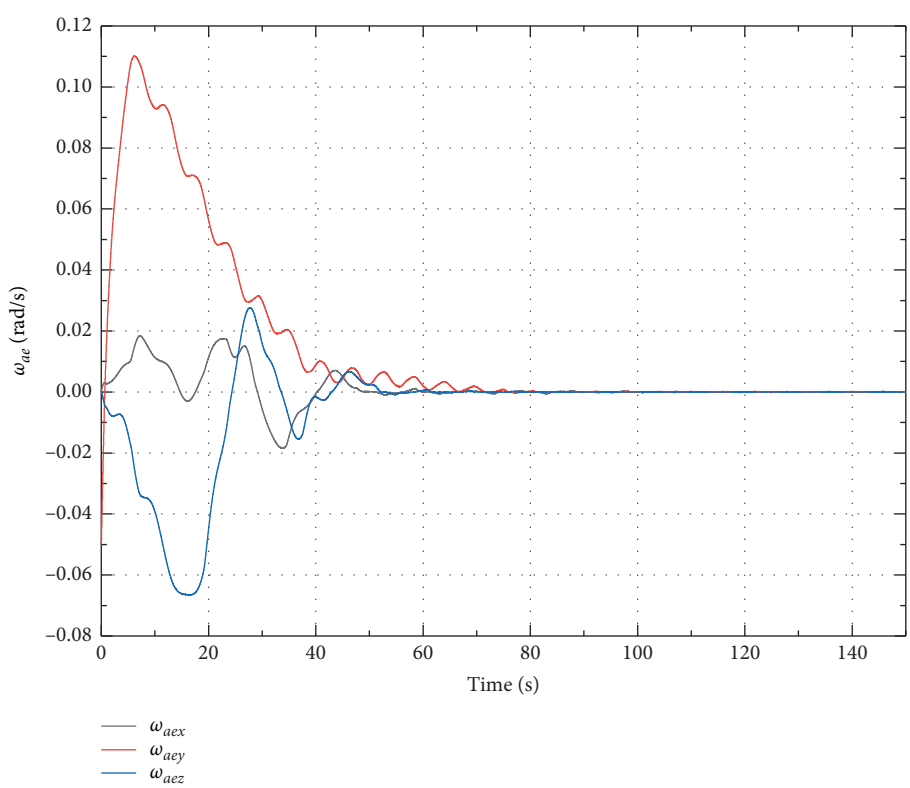

Figure 5: Trajectories of the error of attitude angular velocity of flexible solar panel.

of the spacecraft satisfies the constraint. Therefore, the system can reach the sliding surface in a finite time, and when the system enters the sliding surface, it can maintain sliding mode motion. Therefore, the designed controller can ensure that the system tracks the desired attitude angle and angular velocity.

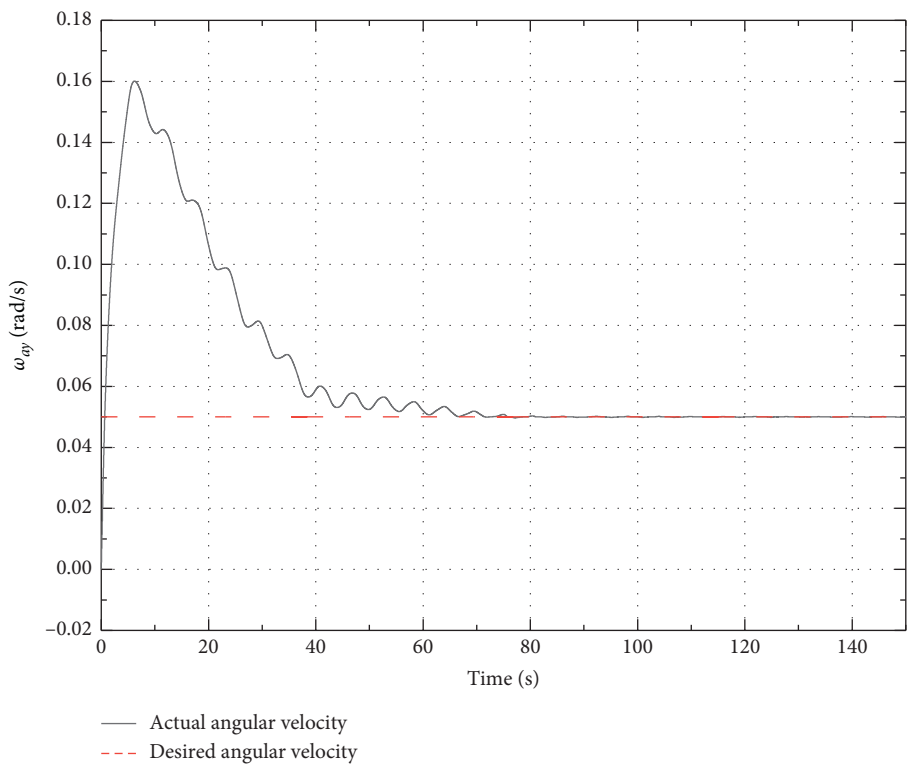

Figure 6: Trajectories of the y-axis flexible solar panel's attitude angular velocity.

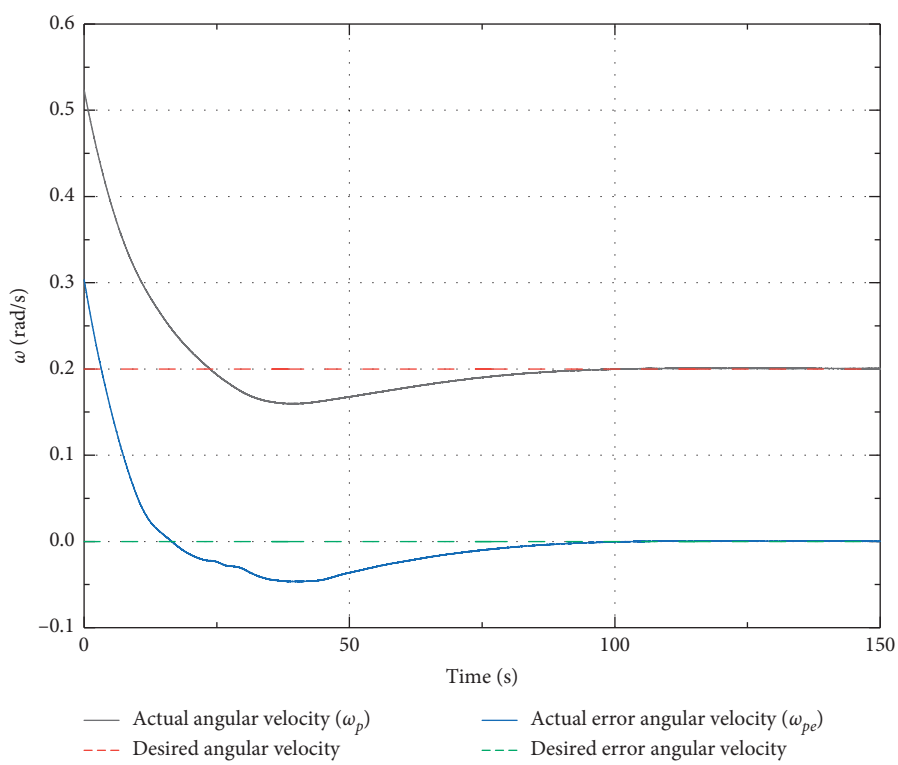

Figure 7: Trajectories of angular velocity and error of angular velocity of the large rigid inertial component.

Figures 8–11 present the results of the error quaternion and the error of angular velocity of the flexible solar panels and platform. These figures indicate that the proposed method converges faster than the existing methods (FSMC and PD). Table 1 presents the results of the stable error of attitude angular velocity and the stable error quaternion of

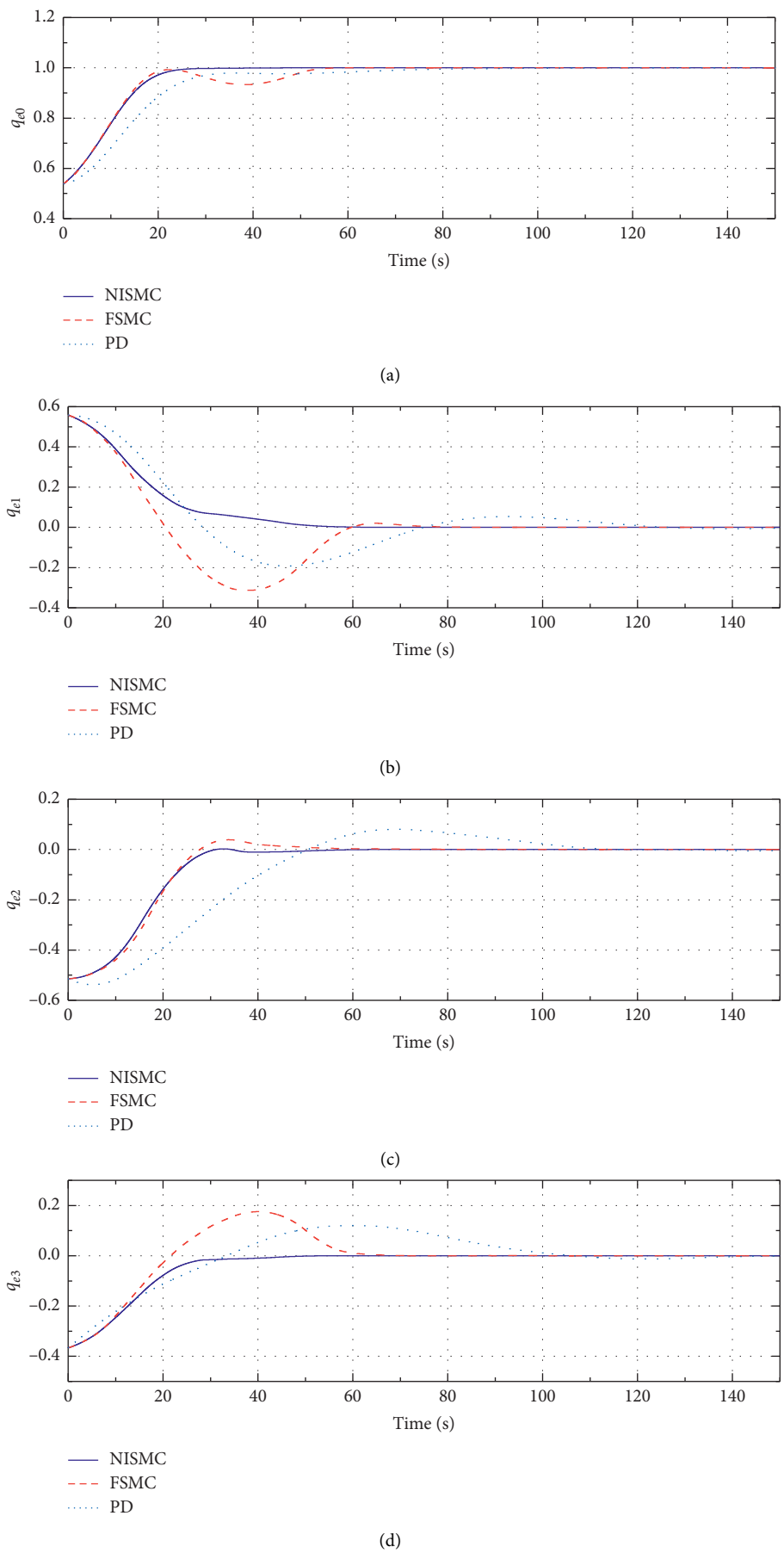

Figure 8: Comparison of platform error quaternions.

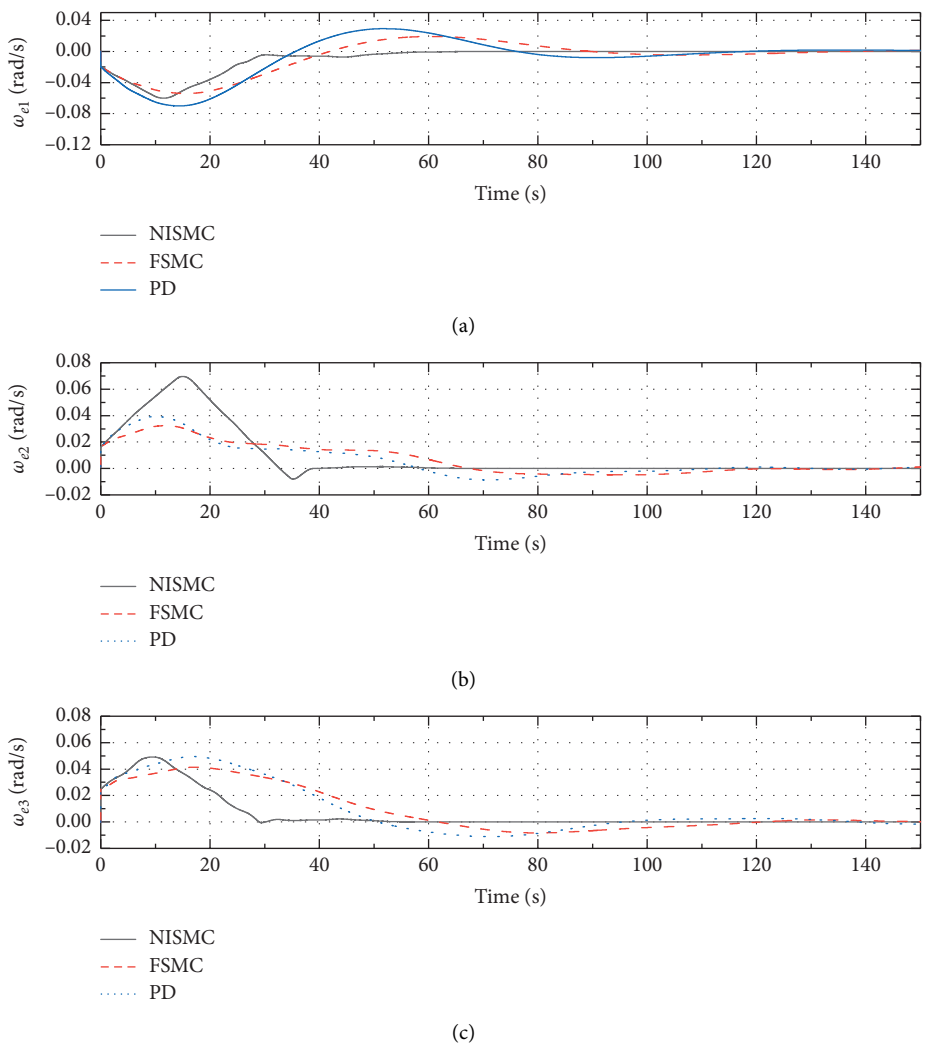

Figure 9: Comparison of errors of attitude angular velocity of platform.

the flexible solar panels and platform. The table indicates that the stable error of attitude angular velocity of the large rigid inertial component is 3.622×10^{-4}.

Figures 8 and 9 show that NISMC drives the attitude tracking errors to the origin faster than the existing FSMC and PD algorithms. In specific, NISMC takes ~60 s for the error quaternion to converge to the equilibrium position, whereas the FSMC and PD require ~80 s and ~110 s, respectively. Furthermore, NISMC takes ~55 s for the error angular velocity to converge to the equilibrium position, whereas the FSMC and PD algorithms require ~120 s. In the steady-state response region, the final stable error quaternion and the final error of attitude angular velocity of the platform are 3.560×10^{-7} and 1.798×10^{-5}, respectively, under the NISMC algorithm.

Figures 10 and 11 indicate that the NISMC takes ~70 s for the error quaternion of the flexible solar panels to converge to the equilibrium position, whereas the FSMC and PD require ~100 s and ~110 s, respectively. Furthermore, NISMC takes ~75 s for the error of angular velocity to converge to the equilibrium position, whereas the FSMC and PD algorithms require ~105 s. The final stable error quaternion of the flexible solar panels is 1.704×10^{-5} and the final error of attitude angular velocity of the platform is 1.114×10^{-5}, under the NISMC algorithm.

Table 1 presents the final stable error quaternion and the final error of attitude angular velocity of the platform under the FSMC and PD algorithms. Clearly, the magnitude of the error of angular velocity and error quaternion is smaller under the NISMC algorithm than under other control laws, indicating that the system has high steady-state accuracy.

These results demonstrate the superiority of the proposed NISMC algorithm in terms of faster convergence and higher stable accuracy over other control algorithms.

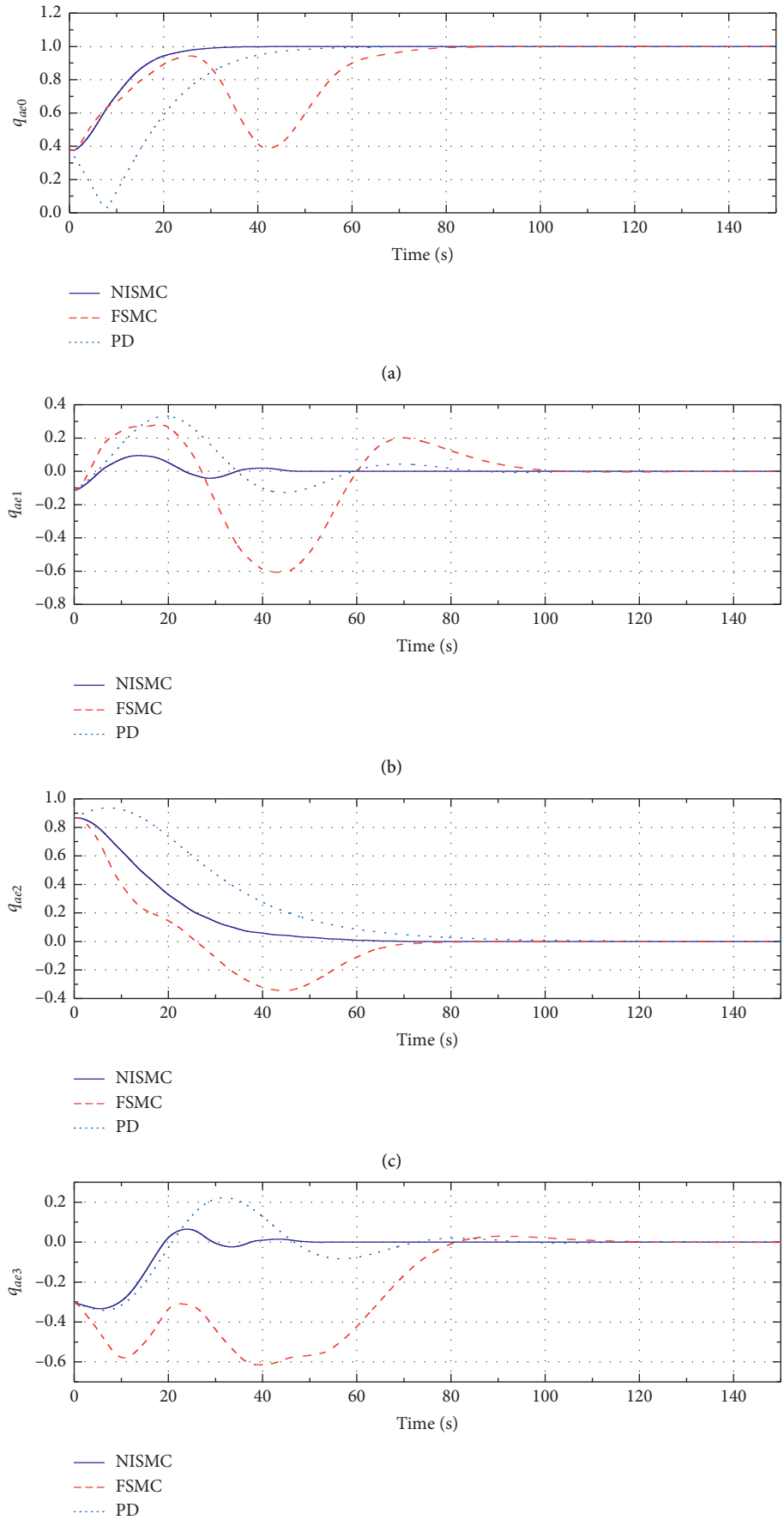

Figure 10: Comparison of error quaternions of flexible solar panels.

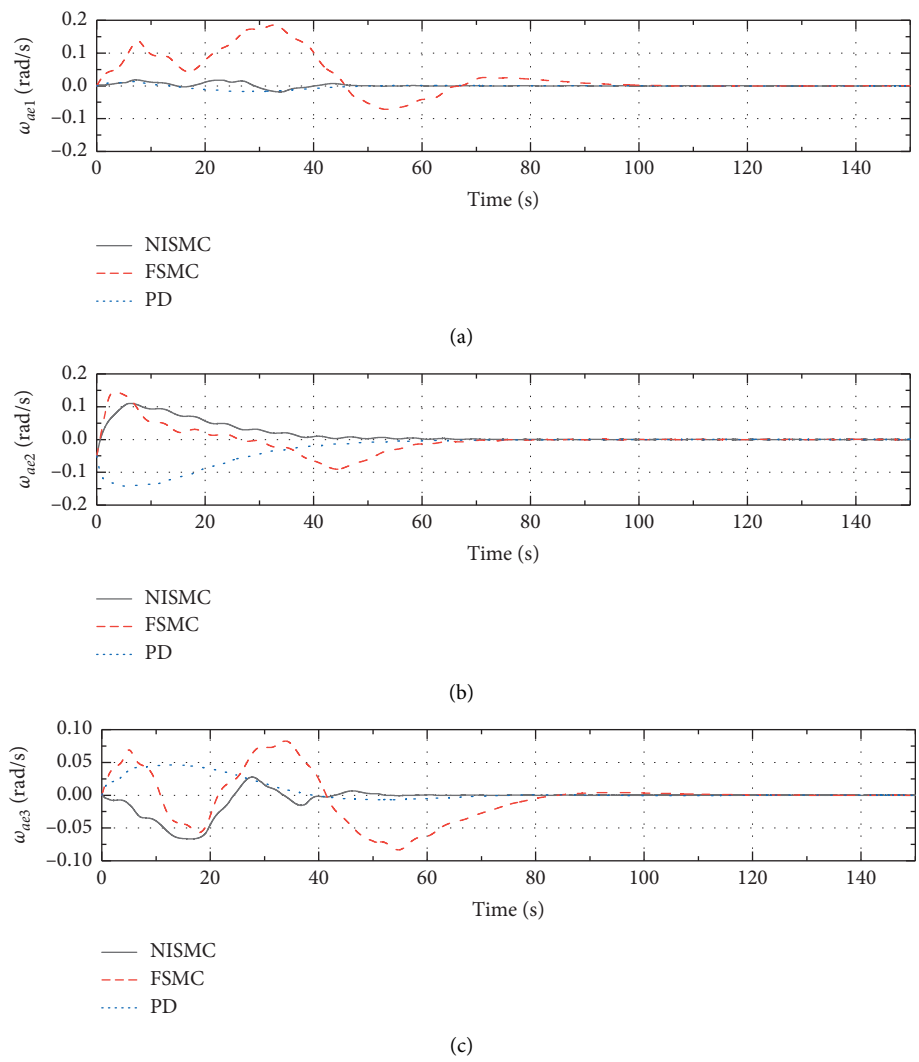

Figure 11: Comparison of errors of attitude angular velocity of flexible solar panels.

Table 1: Parameter control performance.

Control strategy	NISMC	FSMC	PD
Stable error of attitude angular velocity of platform	1.798×10^{-5}	5.074×10^{-4}	0.0012
Stable error of attitude angular velocity of flexible solar panels	1.114×10^{-5}	1.243×10^{-4}	0.0018
Stable error quaternion of platform	3.560×10^{-7}	2.574×10^{-4}	0.00391
Stable error quaternion of flexible solar panels	1.704×10^{-5}	6.819×10^{-4}	0.00115

5. Conclusions

A novel integral sliding mode control law was proposed for spacecraft systems with high-inertia components and flexible solar panels. The proposed control scheme exhibited faster convergence and provided precise attitude tracking in terms of external imbalances caused by appendages, rotation and vibration of flexible solar panels, and parametric uncertainties. Using numerical simulations, the control method was shown to allow an accurate tracking of the desired spacecraft attitude and the rotation of the flexible solar panels and high-inertia components around the special axis with a stable angular speed. Therefore, the control scheme offers a valuable contribution to the design of future space missions in both theoretical and practical respects. As future work, high-flexibility appendages, such as flexible antennas and connecting adapters as magnetic bearings, would be considered. Problems such as parameter uncertainty and actuator saturation demand advanced control methods to realize special state-constrained attitude maneuvering without any intrusion into the forbidden zones. Given the increasing complexity of space missions and the resulting changes to spacecraft design, I believe that this study will be of interest to those who work in aerospace engineering and similar fields.

Appendix

The initial parameters of numerical simulation are as follows. The initial position of the spacecraft is $\mathbf{X}_0 = \left[\, 1097.540456 \;\; 6040.616206 \;\; -12.924317 \,\right]^T$ km, and its initial velocity is $\mathbf{V}_0 = \left[\, -7.450822 \;\; 0.308646 \;\; 1.538879 \,\right]^T$ km/s in the coordinate system R. The initial quaternion of the platform is $\mathbf{Q}_s = \left[\, -0.3696 \;\; -0.5301 \;\; 0.6621 \;\; -0.4372 \,\right]^T$, and its initial angular velocity is $\omega_{s0} = \left[\, -0.02 \;\; 0.015 \;\; 0.025 \,\right]^T$. The initial angular velocity of the flexible solar panels is $\omega_{a0} = \left[\, 0 \;\; 0 \;\; 0 \,\right]^T$, and that of the high-inertia component is $\omega_{p0} = \left[\, 0 \;\; 0 \;\; 0 \,\right]^T$. The mass of the spacecraft platform is 1850 kg. J_{s0} represents the inertia matrix of the spacecraft platform and is defined as

$$J_{s0} = \begin{bmatrix} 4938.75 & 0 & 0 \\ 0 & 4642.63 & 0 \\ 0 & 0 & 6607.31 \end{bmatrix}. \tag{A.1}$$

The mass of a single flexible solar panel is 65 kg. J_{sa} represents the inertia matrix relative to a single flexible solar panel and is defined as

$$J_{sa} = \begin{bmatrix} 251.385 & 35.56 & 1.417 \\ 35.56 & 44.17 & -1.834 \\ 1.417 & -1.834 & 875.97 \end{bmatrix}. \tag{A.2}$$

The mass of the high-inertia component is 800 kg. J_{sp} represents the inertia matrix relative to the high-inertia component and is defined as

$$J_{sp} = \begin{bmatrix} 764.385 & 76.201 & 1.417 \\ 76.201 & 652.17 & -2.17 \\ 1.417 & -2.17 & 875.97 \end{bmatrix}. \tag{A.3}$$

The constant coefficient matrix of the vibration of solar panels relative to its rotation is

$$F_a = \begin{bmatrix} -1.989e1 & -3.141e-10 & -1.578e-2 & 2.984 & -1.0287 & 3.945e-3 \\ 1.398e-2 & 8.598e-8 & -3.214 & 5.028e-2 & 5.982e-2 & 1.174 \\ 2.791e-8 & -1.913 & -5.027e-8 & 3.13e-10 & 2.016e-9 & -5.279e-9 \end{bmatrix}. \tag{A.4}$$

The damping coefficient of the solar panel is 0.004, and the modal frequency of the flexible solar panel is $\Omega_a = \mathrm{diag}\,[0.7033, 0.8021, 1.102, 1.3006, 2.755, 3.044]$. Furthermore, $\Lambda_a = \Omega_a^2$. The coupling coefficient matrix that relates to the angle of the $+y$-axis between solar panels' vibration and platform's rotation is f_{sa_right}, given by

$$f_{sa\_\mathrm{right}\_1} = \begin{bmatrix} 1.996e-10 & -1.425e1 & 8.016e-13 \\ -2.451e-2 & -2.016 & 5.946e-3 \\ 14.5 & 1.916e-9 & 6.824e-11 \end{bmatrix},$$

$$f_{sa\_\mathrm{right}\_2} = \begin{bmatrix} -15.0146 & -2.125e-9 & 2.616e-9 \\ -2.451 & 2.516e-2 & 4.346e-9 \\ 2.143e-9 & 16.16 & 2.124e-6 \end{bmatrix},$$

$$f_{sa\_\mathrm{right}\_3} = \begin{bmatrix} -2.842e-8 & 8.164e-3 & -1.921e-10 \\ 1.274e-4 & 9.524e-3 & -2.014 \\ -8.302e-3 & -2.840e-8 & -1.56e-8 \end{bmatrix},$$

$$f_{sa\_\mathrm{right}\_4} = \begin{bmatrix} -1.519e-9 & 3.441 & 2.502e-11 \\ 1.376e-2 & -0.546 & -3.014e-2 \\ -3.412 & -5.840e-9 & 2.021e-8 \end{bmatrix},$$

$$f_{sa\_\mathrm{right}\_5} = \begin{bmatrix} 5.842e-9 & -1.245 & -1.721e-10 \\ -1.204e-3 & -0.629 & 2.514e-2 \\ 1.425 & -6.840e-10 & -1.462e-8 \end{bmatrix},$$

$$f_{sa\_\mathrm{right}\_6} = \begin{bmatrix} -1.627e-9 & -5.314e-2 & -2.701e-10 \\ 2.204e-5 & 2.429e-2 & 1.017 \\ -0.7253 & -1.747e-8 & -1.629e-10 \end{bmatrix}. \tag{A.5}$$

The constant matrix of the $-y$-axis solar panels' vibration to the platform's rotation is f_{sa_left} and is defined as

$$f_{sa\_\mathrm{left}\_1} = \begin{bmatrix} 1.923e-10 & -1.464e1 & 1.107e-12 \\ -2.397e-2 & -2.111 & 5.589e-3 \\ 14.745 & 1.867e-9 & 6.977e-11 \end{bmatrix},$$

$$f_{sa\_\mathrm{left}\_2} = \begin{bmatrix} -15.7046 & -2.1074e-9 & 2.819e-9 \\ -2.5415 & 2.624e-2 & 4.402e-9 \\ 2.271e-9 & 1.5963e1 & 9.924e-5 \end{bmatrix},$$

$$f_{sa\_\mathrm{left}\_3} = \begin{bmatrix} -2.822e-8 & 8.132e-3 & -1.893e-10 \\ 1.24e-4 & 9.245e-3 & -1.9184 \\ -8.295e-3 & -2.789e-8 & -1.506e-8 \end{bmatrix},$$

$$f_{sa\_\mathrm{left}\_4} = \begin{bmatrix} -1.589e-9 & 3.941 & 2.752e-11 \\ 1.731e-2 & -0.740 & -3.214e-2 \\ -3.410 & -5.836e-9 & 2.122e-8 \end{bmatrix},$$

$$f_{sa\_\mathrm{left}\_5} = \begin{bmatrix} 5.857e-9 & -1.347 & -1.691e-10 \\ -1.344e-3 & -0.867 & 2.474e-2 \\ 1.476 & -6.753e-10 & -1.512e-8 \end{bmatrix},$$

$$f_{sa\_\mathrm{left}\_6} = \begin{bmatrix} -1.616e-9 & -5.324e-2 & -2.671e-10 \\ 2.134e-5 & 2.527e-2 & 1.457 \\ -0.923 & -1.547e-8 & -1.591e-10 \end{bmatrix}. \tag{A.6}$$

Here, r_{sa_right} represents the coupling rotation coefficient matrix of the $+y$-axis between the solar panels and the platform; similarly, r_{sa_left} is given as

$$r_{sa\_\text{right}\_1} = \begin{bmatrix} 5.996e-11 & 0 & 6.213e-3 \\ 0 & 4.88e1 & 1.613e-12 \\ -3.75e2 & 0 & 1.216e-6 \end{bmatrix},$$

$$r_{sa\_\text{right}\_2} = \begin{bmatrix} -1.329e-7 & 0 & -1.717e-1 \\ 0 & -8.964e-5 & 0 \\ 1.826e-3 & 1.023e-13 & 1.071e-10 \end{bmatrix},$$

$$r_{sa\_\text{right}\_3} = \begin{bmatrix} 3.462e2 & 0 & -1.213e-6 \\ 0 & 1.0121 & 0 \\ -4.956e-9 & 0 & 9.016e-3 \end{bmatrix},$$

$$f_{sa\_\text{left}\_1} = \begin{bmatrix} 6.106e-11 & 0 & 6.115e-3 \\ 0 & 4.69e1 & 1.718e-12 \\ -3.68e2 & 0 & -1.203e-6 \end{bmatrix},$$

$$f_{sa\_\text{left}\_2} = \begin{bmatrix} -1.006e-7 & 0 & -1.998e-1 \\ 0 & -8.964e-5 & 0 \\ 1.904e-3 & -1.021e-13 & 1.176e-10 \end{bmatrix},$$

$$f_{sa\_\text{left}\_3} = \begin{bmatrix} 3.501e2 & 0 & -1.116e-6 \\ 0 & 1.0121 & 0 \\ -4.755e-9 & 0 & 9.314e-3 \end{bmatrix}. \tag{A.7}$$

Furthermore, r_{sp} represents the constant rotating coupling coefficient matrix between the high-inertia component and the platform and is given as

$$r_{sp\_1} = \begin{bmatrix} 2.206e-6 & -1.128e-6 & 6.213e-3 \\ 0 & 4.88e-8 & 0 \\ -3.75e-12 & 0 & 1.216e-8 \end{bmatrix},$$

$$r_{sp\_2} = \begin{bmatrix} 3.173e-5 & 0 & -1.213e-7 \\ 0 & 1.012e-7 & 1.038e-9 \\ -1.097e-12 & 0 & 9.016e-11 \end{bmatrix}, \tag{A.8}$$

$$r_{sp\_3} = \begin{bmatrix} 3.462e-5 & 0 & -1.213e-6 \\ 2.277e-7 & 5.02e-8 & 0 \\ -4.956e-10 & 0 & 4.414e-13 \end{bmatrix}.$$

Data Availability

The data used to support the findings of this study are included within the article.

Conflicts of Interest

The authors declare that there are no conflicts of interest regarding the publication of this paper.

Acknowledgments

This work was supported by the National Natural Science Foundation of China (nos. 61833009, 61690212, and 91438202) and the National Key Research and Development Plan (no. 2016YFB0500901).

References

[1] C. Sendi and M. A. Ayoubi, "Robust fuzzy tracking control of flexible spacecraft via a T-S fuzzy model," *IEEE Transactions on Aerospace and Electronic Systems*, vol. 54, no. 1, pp. 170–179, 2017.

[2] Z. Liu, J. Liu, and L. Wang, "Disturbance observer based attitude control for flexible spacecraft with input magnitude and rate constraints," *Aerospace Science and Technology*, vol. 72, pp. 486–492, 2018.

[3] Z. Li, L. Gao, W. Chen, and Y. Xu, "Distributed adaptive cooperative tracking of uncertain nonlinear fractional-order multi-agent systems," *IEEE/CAA Journal of Automatica Sinica*, vol. 7, no. 1, pp. 292–300, 2020.

[4] Q. Zhou, G. Chen, R. Lu, and W. Bai, "Disturbance-observer-based event-triggered control for multi-agent systems with input saturation," *Scientia Sinica Informationis*, vol. 49, no. 11, pp. 1502–1516, 2019.

[5] Y. Li, K. Li, and S. Tong, "Finite-time adaptive fuzzy output feedback dynamic surface control for MIMO nonstrict feedback systems," *IEEE Transactions on Fuzzy Systems*, vol. 27, no. 1, pp. 96–110, 2019.

[6] S. Tong, X. Min, and Y. Li, "Observer-based adaptive fuzzy tracking control for strict-feedback nonlinear systems with unknown control gain functions," *IEEE Transactions on Cybernetics*, vol. 50, no. 9, pp. 3903–3913, 2020.

[7] L. Chen, P. Shi, and M. Liu, "Fault reconstruction for Markovian jump systems with iterative adaptive observer," *Automatica*, vol. 105, pp. 254–263, 2019.

[8] L. Zhao, J. Yu, and P. Shi, "Command filtered backstepping-based attitude containment control for spacecraft formation," *IEEE Transactions on Systems, Man, and Cybernetics: Systems*, vol. 51, no. 2, p. 1278, 2021.

[9] Z. Yang, N. Lu, J. Shi, P. Zhang, C. Dong, and J. Yang, "Overview of FY-3 payload and ground application system," *IEEE Transactions on Geoscience and Remote Sensing*, vol. 50, no. 12, pp. 4846–4853, 2012.

[10] J. Han, *The Technique for Estimating and Compensating the Uncertainties: Active Disturbance Rejection Control Technique*, National Defense Industry Press, Beijing, China, 2008.

[11] X. Cao, P. Shi, Z. Li, and M. Liu, "Neural-network-based adaptive backstepping control with application to spacecraft attitude regulation," *IEEE Transactions on Neural Networks and Learning Systems*, vol. 29, no. 9, pp. 4303–4313, 2018.

[12] Q. Liu, M. Liu, and J. Yu, "Adaptive fault-tolerant control for attitude tracking of flexible spacecraft with limited data transmission," *IEEE Transactions on Systems, Man, and Cybernetics: Systems*, p. 1, 2019.

[13] M. Liu, L. Zhang, P. Shi, and Y. Zhao, "Fault estimation sliding-mode observer with digital communication constraints," *IEEE Transactions on Automatic Control*, vol. 63, no. 10, pp. 3434–3441, 2018.

[14] S. Yu, X. Yu, B. Shirinzadeh, and Z. Man, "Continuous finite-time control for robotic manipulators with terminal sliding mode," *Automatica*, vol. 41, no. 11, pp. 1957–1964, 2005.

[15] A. Sofyalı and E. Jafarov, "Robust stabilization of spacecraft attitude motion under magnetic control through time varying

integral sliding mode," *International Journal of Robust and Nonlinear Control*, vol. 29, no. 11, pp. 3446–3468, 2019.

[16] Q. Li, L. Liu, Y. Deng, S. Tang, and Y. Zhao, "Twistor-based synchronous sliding mode control of spacecraft attitude and position," *Chinese Journal of Aeronautics*, vol. 31, no. 5, pp. 1153–1164, 2018.

[17] W. Liu, Z. Feng, and A. Bi, "A novel nonsingular terminal sliding mode control combined with global sliding surface for uncertain nonlinear second-order systems," *Transactions of the Institute of Measurement and Control*, vol. 42, no. 7, pp. 1294–1300, 2020.

[18] L. Zhao, G. Liu, and J. Yu, "Finite-time adaptive fuzzy tracking control for a class of nonlinear systems with full-state constraints," *IEEE Transactions on Fuzzy Systems*, p. 1, 2020.

[19] K. Lu, Y. Xia, Z. Zhu, and M. V. Basin, "Sliding mode attitude tracking of rigid spacecraft with disturbances," *Journal of the Franklin Institute*, vol. 349, no. 2, pp. 413–440, 2012.

[20] A. Yousefpour and H. Jahanshahi, "Fast disturbance-observer-based robust integral terminal sliding mode control of a hyperchaotic memristor oscillator," *The European Physical Journal Special Topics*, vol. 228, no. 10, pp. 2247–2268, 2019.

[21] S. Lv, N. Wang, X. Liang, and M. Er, "Finite-time disturbance observer based nonsingular integral terminal sliding mode trajectory tracking control of unmanned surface vehicles," in *Proceedings of the 2016 IEEE Chinese Guidance, Navigation and Control Conference (CGNCC)*, pp. 1109–1113, Nanjing, China, 2016.

[22] J. Na, "Adaptive prescribed performance control of nonlinear systems with unknown dead zone," *International Journal of Adaptive Control and Signal Processing*, vol. 27, no. 5, pp. 426–446, 2013.

[23] Q. Chen, X. Ren, J. Na, and D. Zheng, "Adaptive robust finite-time neural control of uncertain PMSM servo system with nonlinear dead zone," *Neural Computing and Applications*, vol. 28, no. 12, pp. 3725–3736, 2016.

[24] N. Shi, Z. Kang, Z. Zhao, and Q. Meng, "Adaptive vector nonsingular terminal sliding mode control for a class of n-order nonlinear dynamical systems with uncertainty," *Mathematical Problems in Engineering*, vol. 2020, Article ID 7309417, 12 pages, 2020.

[25] C. Yue, K. D. Kumar, Q. Shen, C. H. Goh, and T. H. Lee, "Attitude stabilization using two parallel single-gimbal control moment gyroscopes," *Journal of Guidance, Control, and Dynamics*, vol. 42, no. 2, pp. 1353–1364, 2019.

[26] S. Alshamali and E. Aljuwaiser, "Design of robust observer-based backstepping control for a satellite control system," *Mathematical Problems in Engineering*, vol. 2019, Article ID 7412194, 9 pages, 2019.

[27] J. Wang, L. Liu, C. Liu, and X. Li, "Adaptive sliding mode control based on equivalence principle and its application to chaos control in a seven-dimensional power system," *Mathematical Problems in Engineering*, vol. 2020, Article ID 1565460, 13 pages, 2020.

[28] P. Li, J. Ma, Z. Zheng, and L. Geng, "Fast nonsingular integral terminal sliding mode control for nonlinear dynamical systems," in *Proceedings of the 2014 IEEE 53rd Annual Conference On Decision And Control (CDC)*, pp. 4739–4746, IEEE, Los Angeles, CA, USA, 2015.

[29] Y. Miao, I. Hwang, M. Liu, and F. Wang, "Adaptive fast nonsingular terminal sliding mode control for attitude tracking of flexible spacecraft with rotating appendage," *Aerospace Science and Technology*, vol. 93, Article ID 105312, 2019.

[30] H. Gui and G. Vukovich, "Adaptive fault-tolerant spacecraft attitude control using a novel integral terminal sliding mode," *International Journal of Robust and Nonlinear Control*, vol. 27, no. 16, pp. 3174–3196, 2017.

[31] Y. Xie, *Research on Dynamic Balance Technique of Satellite with Large Rotating Components*, Harbin Institute of Technology, Harbin, China, 2019.

[32] L. Chai, *On-orbit Estimation of Unbalanced Torques Acting on Satellite Platform with Large Inertia Rotating Payloads [D]*, " Harbin Institute of Technology, Harbin, China, 2019.

[33] Z. Zhu, Y. Xia, and M. Fu, "Attitude stabilization of rigid spacecraft with finite-time convergence," *International Journal of Robust and Nonlinear Control*, vol. 21, no. 6, pp. 686–702, 2011.

[34] Q. Hu, X. Huo, and B. Xiao, "Reaction wheel fault tolerant control for spacecraft attitude stabilization with finite-time convergence," *International Journal of Robust Nonlinear Control*, vol. 23, no. 8, pp. 1737–1752, 2012.

[35] G. Hardy, J. Littlewood, and G. Pólya, *Inequalities*, Cambridge University Press, Cambridge, UK, 1952.

[36] S. P. Bhat and D. S. Bernstein, "Finite-time stability of continuous autonomous systems," *SIAM Journal on Control and Optimization*, vol. 38, no. 3, pp. 751–766, 2000.

[37] C. Zhong, L. Wu, J. Guo, Y. Guo, and Z. Chen, "Robust adaptive attitude manoeuvre control with finite-time convergence for a flexible spacecraft," *Transactions of the Institute of Measurement and Control*, vol. 40, no. 2, p. 425, 2016.

[38] L. Yang and J. Yang, "Nonsingular fast terminal sliding-mode control for nonlinear dynamical systems," *International Journal of Robust and Nonlinear Control*, vol. 21, pp. 1865–1879, 2011.

Hindawi
Complexity
Volume 2021, Article ID 6673568, 12 pages
https://doi.org/10.1155/2021/6673568

Research Article

Command Filtering and Barrier Lyapunov Function-Based Adaptive Control for PMSMs with Core Losses and All-State Restrictions

Xiaoling Wang and Jinpeng Yu

College of Automation, Qingdao University, Qingdao 266071, Shandong, China

Correspondence should be addressed to Jinpeng Yu; yjp1109@126.com

Received 26 October 2020; Revised 18 January 2021; Accepted 28 January 2021; Published 10 February 2021

Academic Editor: Xue-bo Jin

With the troubles of core losses and all-state confined to certain limitations which are the innate traits of permanent magnet synchronous motors (PMSMs), this article develops a command filtered adaptive backstepping approach to follow the track of PMSM's desired rotor position. To begin with, the RBF neural network technique is utilized to get close to the uncharted nonlinear terms which existed in PMSM's mathematical model. Meanwhile, an advanced adaptive command filter control methodology is constructed to avoid the computing explosion during the process of backstepping design. Furthermore, to make sure that all the state variables are confined into certain ranges, we employed the barrier Lyapunov function (BLF) at every step of the controllers construction. In addition, an error compensating mechanism is proposed to neutralize filtering errors and only one adaptive law is required. At last, simulation results bear out the superiority of the aforementioned control scheme.

1. Introduction

Lately, permanent magnet synchronous motors (PMSMs) are employed broadly in real-world utilization. This proverbial usage is due to the advantageous PMSMs features like straightforward mechanism, petit size, great productiveness, and dependable manipulation. Nevertheless, the PMSM's real-time mathematic model set contains tremendous nonlinearity and multivariables issues which may lead to a challenging mission to acquire optimum control results. So, in order to enhance the PMSM's control effectiveness, many advanced control techniques have been proposed, for instance, PI control [1, 2], sliding mode control [3–5], adaptive backstepping control [6], and other control schemes [7, 8]. Among these methodologies, the backstepping control technique is now becoming a basic foundation to construct controllers for high complexity models since it was designed to obtain asymptotic tracking and global stability. Besides, the load turbulence and time-variant parameters issues can be ripped out of the operation of PMSMs by making use of the adaptive control technique.

However, "certain functions must be linear" and "explosion of complexity" issues which are rooted in the traditional backstepping control methods are very tricky to be dealt with. For one thing, along with the development of radial basis function (RBF) neural networks (NNs) [9–11], the nonlinear systems' unknown functions can be approximated by this algorithm based on the adaptive control method and this proposal can rule out the dependency of the accurate mathematical model. For another, in [12–14], a command filtered-based backstepping method was developed to tackle the "explosion of complexity" problem and the error compensation technique is employed to make the filtering outcomes more accurate. To be specific, the command filters' input signals are designed as virtual control functions and the filters' outputs can eliminate explosive terms. Moreover, the error compensation mechanism will neutralize the filtering deviations to some extent. But these

published methodologies have not considered the state constraints problem of PMSM drive systems.

In fact, according to the PMSM's inherent features, its state variables should be confined to reasonable boundaries. For instance, if the rotor angular velocity, stator current, or other state variables of PMSM are out of the state constraints, the motor's performance will be influenced and may even result in severe security issues. Take stator current as an example, exorbitant current value will lead to serious overheating problems to the rotators which would speed up the aging of insulation materials and decrease the equipment's service lifespan. Accordingly, state limitations are indispensable during the PMSM's controllers construct process. Fortunately, many significant achievements have been obtained in the all-state constrained nonlinear control field, such as [15, 16] and from these approaches, the barrier Lyapunov functions (BLFs) are normally utilized to hold off the limitation transgressions.

Apart from state variables restrictions, in order to get perfect control performance of PMSMs, the core loss impact also should be taken into consideration when the driving frequency spikes, which is correlated with the high-speed operation. The control accuracy will drop sharply with tremendous core losses, and thus the solution of PMSMs with iron losses problem is crucial to actual applications. As far as we know, the core losses and all-state restrictions issues which are rooted in nonlinear high-ordered PMSM drive systems have not been studied by using command filtered adaptive backstepping approach.

So, with these previous observations, we took core losses and all-state restrictions which are the inherent properties of PMSM drive systems into considerations, and then we developed a BLFs-based adaptive command filtered neural control method. Disparate from the conventional control schemes, this method's main novelties are concluded as follows:

(1) Unlike [17], the command filters are used to tackle the "explosion of complexity" issue which cannot be neglected in adaptive backstepping control for nonlinear systems.

(2) Distinct from [17, 18], this paper considers the core losses issue in PMSM's mathematical model and thus makes this method be more applicable in actual usages.

(3) Different from [12, 19], the errors that arose from command filters are neutralized by compensating signals to diminish their negative influence upon control performance.

(4) This article just requires one single adaptive law during the controllers construction process, which can facilitate the calculation compared to [20], so that the control scheme's effectiveness will be improved.

In the posterior section of this paper, simulation figures and a comparison table are displayed to substantiate the effectiveness and robustness of the submitted control approach.

2. Related Works

2.1. Nonlinear Control Methods. Many approaches are proposed to enhance the control effectiveness of nonlinear systems. In [21], Zheng et al. utilized a stable adaptive PI control strategy in the discrete-time domain for the PMSM drive system. The PI controller is capable of automatic online tuning of the control gains based on the gradient descent method and the experimental results illustrated the tracking performance is favorable. Li et al. [22] put forward the sliding-mode control method to deal with nonlinear active suspension systems. They designed an adaptive sliding-mode controller to guarantee the reachability of the specified switching surface. Yin et al. designed a backstepping controller for the switch complex nonlinear system in [23]. During the construction process, they developed a state backstepping controller to realize the exponential stability of the observer-backstepping feedback control system. Zhang et al. presented a linear quadratic regulator-based proportion integral differential equivalent controller for PMSM in [24]. The method was implemented through the dSPACE digital signal processor system and the experimental result confirmed its effectiveness.

2.2. Approximation Techniques. To enlarge the practical field of the backstepping method, the nonlinear terms in the nonlinear systems' mathematical model need to be dealt with. The literature [25–28] has utilized the fuzzy logic systems (FLS) to approximate unknown nonlinearities in different kinds of scenarios. And the approximation results verified that this technique can well serve its original purpose. In [29–31], the authors employed the LSTM and the GRU techniques to predict traffic speed, power load, and traffic flow, respectively. And the experimental results indicate these two kinds of deep recurrent networks are skilled in modeling abilities, which make them more suitable for sequence-based long-term tasks. In [32], Bai et al. utilized a compound autoregressive network to predict multivariate time series. Jin et al. proposed two nonlinear estimation methods to achieve real-time indoor RFID tracking in [33]. In [9], Fu et al. utilized the RBF neural networks to cope with the unknown nonlinear functions. The finite-time adaptive neural controller was proposed via the new command filter backstepping technique, and the tracking error converges to a small neighborhood of the origin in finite time.

2.3. Filtering Algorithms. Some scholars put forward a variety of filtering methods in recent years. In [34], Bai et al. proposed a neuron-based Kalman filter to enhance the control effect of various intelligent terminals and promote the sensing level. They introduced the neuronunits into the conventional Kalman filter framework and thus the filtering process could be optimized to reduce the effect of the unpractical system model and hypothetical parameters. In [35, 36], the authors employed the dynamic surface control (DSC) technique to resolve the "explosion of complexity" problem, and it is a first-ordered filtering method for every step's virtual input during the traditional backstepping

controllers design. But the DSC technique does not take the deviations ascribed to the first-order filters into account, which may induce unwanted influence on the control result. In [37], the adaptive filtering technique was proposed to filter the complex noise and obtain the true measurements' value and thus the MEMS gyroscope performance can be improved. In [38], the authors proposed a state filtering-based least squares parameter estimation for bilinear systems. Zhang et al. developed a novel state estimation algorithm to enhance the computational efficiency based on delta operator in [39].

2.4. PMSM Innate Features and Identification Methods. In [40, 41], the authors take full-state constraints of nonlinear systems into consideration and constructed the barrier Lyapunov functions to ensure the state constraints are not transgressed. In [42], Zhao et al. proposed a health performance evaluation method to detect anomaly occurrences and evaluate the multirotor system's real-time health condition. Ding et al. in [43, 44] derived gradient-based and two-stage gradient-based iterative algorithms to generate more accurate parameter estimation to overcome the difficulty of state and input identifications. In [45], Zhang et al. developed joint estimation algorithms for states and parameters of nonlinear systems to make the parameter estimates converge to their true values. With the identification methods in [43–45], the parameters of the mathematical models can be obtained accordingly.

3. Dynamic Model and Preparations

In the $d-q$ frame of axes, the PMSM's dynamic model with core losses from [46] can be described as

$$\begin{cases} \dfrac{\mathrm{d}\theta}{\mathrm{d}t} = \omega, \\ \dfrac{\mathrm{d}\omega}{\mathrm{d}t} = \dfrac{n_p\lambda_{PM}}{J} i_{oq} + \dfrac{n_p\left(L_{m\,d} - L_{mq}\right) i_{oq} i_{od}}{J} - \dfrac{T_L}{J}, \\ \dfrac{\mathrm{d}i_{oq}}{\mathrm{d}t} = \dfrac{R_c}{L_{mq}} i_q - \dfrac{R_c}{L_{mq}} i_{oq} - \dfrac{n_p L_d}{L_{mq}} \omega i_{o\,d} - \dfrac{n_p\lambda_{PM}}{L_{mq}}\omega, \\ \dfrac{\mathrm{d}i_q}{\mathrm{d}t} = -\dfrac{R_s}{L_{lq}} i_q + \dfrac{R_c}{L_{lq}} i_{oq} + \dfrac{1}{L_{lq}} u_q, \\ \dfrac{\mathrm{d}i_{o\,d}}{\mathrm{d}t} = \dfrac{R_c}{L_{md}} i_d - \dfrac{R_c}{L_{md}} i_{o\,d} + \dfrac{n_p L_q}{L_{md}} \omega i_{oq}, \\ \dfrac{\mathrm{d}i_d}{\mathrm{d}t} = -\dfrac{R_s}{L_{ld}} i_d + \dfrac{R_c}{L_{ld}} i_{o\,d} + \dfrac{1}{L_{ld}} u_d, \end{cases} \tag{1}$$

where θ, ω, n_p, J, T_L, R_s, and R_c represent rotor position, rotor angular speed, quantity of pole pairs, rotor momental inertia, load torque, stator resistance, and core loss resistance, sequentially. u_d stands for the d-axis voltage and u_q represents the q-axis voltage. i_d is the d-axis current while i_q is the q-axis current. L_d and L_q present as stator inductors. L_{ld} and L_{lq} represent leakage inductances, while L_{md} and L_{mq} are the notations of magnetic inductances. Finally, λ_{PM} stands for the excitation flux. To simplify the above mathematical equations, we employ the following symbolizations:

$$\begin{aligned} x_1 &= \theta, \\ x_2 &= \omega, \\ x_3 &= i_{oq}, \\ x_4 &= i_q, \\ x_5 &= i_{od}, \\ x_6 &= i_d, \\ a_1 &= n_p\lambda_{PM}, \\ a_2 &= n_p\left(L_{md} - L_{mq}\right), \\ b_1 &= \frac{R_c}{L_{mq}}, \\ b_2 &= -\frac{n_p L_d}{L_{mq}}, \\ b_3 &= -\frac{n_p\lambda_{PM}}{L_{mq}}, \\ b_4 &= -\frac{R_s}{L_{lq}}, \\ b_5 &= \frac{R_c}{L_{lq}}, \\ c_1 &= \frac{R_c}{L_{md}}, \\ c_2 &= -\frac{n_p L_q}{L_{md}}, \\ c_3 &= -\frac{R_s}{L_{ld}}, \\ c_4 &= \frac{R_c}{L_{ld}}, \\ d_1 &= \frac{1}{L_{lq}}, \\ d_2 &= \frac{1}{L_{ld}}. \end{aligned} \tag{2}$$

With the aforementioned symbolizations, the mathematical model set will be converted into

$$\begin{aligned}
\dot{x}_1 &= x_2,\\
\dot{x}_2 &= \frac{a_1}{J}x_3 + \frac{a_2}{J}x_3x_5 - \frac{T_L}{J},\\
\dot{x}_3 &= b_1x_4 - b_1x_3 + b_2x_2x_5 + b_3x_2,\\
\dot{x}_4 &= b_4x_4 + b_5x_3 + d_1u_q,\\
\dot{x}_5 &= c_1x_6 - c_1x_5 - c_2x_2x_3,\\
\dot{x}_6 &= c_3x_6 + c_4x_5 + d_2u_d.
\end{aligned} \tag{3}$$

The ultimate goal of this paper is to develop the controllers u_q along with u_d to make the rotor position x_1 track the desired signal x_d as perfect as possible while the state variables x_i are demanded to meet the premises that $|x_i| < k_{c_i}$ $(i = 1, 2, 3, 4, 5, 6)$, in which $k_{c_i} > 0$.

The RBF neural network is a feedforward network with three layers of neurons called the input layer, the hidden layer, and the output layer. Figure 1 is the graphic illustration of the structure of the RBF neural network. Additionally, the input layer contains an equal number of nodes to the dimension of the input vector. The hidden layer's nodes number depends on the complexity of the problem. The output layer's nodes number equals the dimension of the output vector. The weight parameter W stands for the link between nodes and it only exists between the hidden and output layers. The self-training law will be given later. The k-means clustering algorithm which is a kind of unsupervised algorithm of RBF neural network will be used in this paper. With the neural network's theory and its parameters' definitions which can be found in [47], we know that any time-consecutive function $\varphi(z)$ can be estimated by RBF NNs. The estimate functions $\hat{\varphi}(z) = W^{*T}S(Z)$ satisfy the premise of $R^q \longrightarrow R$, in which q stands for input dimensions. Moreover, the NNs' input variable Z needs to be within the domain of $Z \in \Omega_Z \subset R^q$ and the weight vector W^* is formed as $W^* = [\Phi_1^*, \ldots, \Phi_l^*]^T$, where l represents the quantity of NNs nodes. We choose the Gaussian basis function $S(Z) = ([p_1(Z), p_2(Z), \ldots, p_n(Z)]^T / \sum_{i=1}^{n} p_i(Z))$ and $p_i(Z) = \exp[(-(Z-\eta_i)^T(Z-\eta_i))/\gamma_i^2]$ for $i = 1, 2, \ldots, n$, where $\eta_i = [\eta_{i1}, \eta_{i2}, \ldots, \eta_{in}]^T$ is the center vector and γ_i is the Gaussian function's width. So, with the above definitions, the inequality $\|W_i(S_i(k))\|^2 \le l_i$ $(i = 1, \ldots, n)$ holds.

Lemma 1 *From* [12], we have the definition of command filters listed as

$$\begin{aligned}
\dot{e}_1 &= \omega_n e_2,\\
\dot{e}_2 &= -2\xi\omega_n e_2 - \omega_n(e_1 - \alpha_1).
\end{aligned} \tag{4}$$

From the above equations, we know that the output variables e_1 and e_2 can be obtained by the input variable α_1. In order to do so, there are some rules that should be satisfied. Firstly, for all $t \ge 0$, the first and second ordered time derivative forms of α_1 should meet the demands of $|\dot{\alpha}_1| < \rho_1$ and $|\ddot{\alpha}_1| < \rho_2$ while ρ_1, ρ_2 are positive constants. Secondly, the initial conditions of these variables should satisfy that $e_1(0) = \alpha_1(0)$, $e_2(0) = 0$. Consequently, $|\dot{e}_1|$, $|\ddot{e}_1|$, and $|\dddot{e}_1|$ will be bounded into certain ranges. Additionally, with $\xi \in (0, 1]$ and $\omega_n > 0$, the deviation between the input and output signals will satisfy that $|e_1 - \alpha_1| \le \mu$.

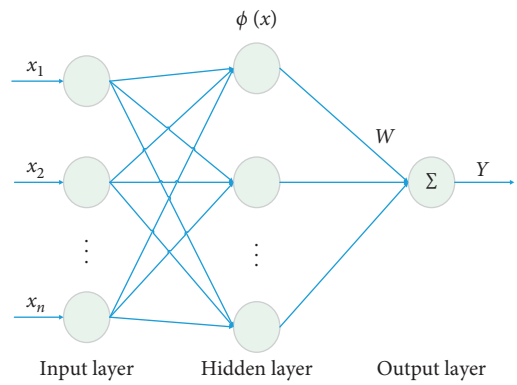

Figure 1: The structure of RBF neural network.

Assumption 1 (see [41]). The desired signal x_d and its first-ordered time derivative form $\dot{x}_d$ should both be smooth, limited, and known. Thus, they can meet the demands of $|x_d| \le Y_0 < k_{c_1}$ and $|\dot{x}_d| \le Y_1$, in which Y_0 and Y_1 are positive constants.

4. Command Filtered Self-Adaptive Neural Network Controllers Construction

During this process, we constructed the self-adaptive command filtered neural network controllers for PMSMs with core losses and all-state restrictions based on the BLFs. To begin with, we define the error variables as

$$\begin{aligned}
z_1 &= x_1 - x_d,\\
z_2 &= x_2 - x_{1,c},\\
z_3 &= x_3 - x_{2,c},\\
z_4 &= x_4 - x_{3,c},\\
z_5 &= x_5,\\
z_6 &= x_6 - x_{4,c},\\
v_1 &= z_1 - \zeta_1,\\
v_2 &= z_2 - \zeta_2,\\
v_3 &= z_3 - \zeta_3,\\
v_4 &= z_4 - \zeta_4,\\
v_5 &= z_5 - \zeta_5,\\
v_6 &= z_6 - \zeta_6,
\end{aligned} \tag{5}$$

where x_d is the desired rotor position trajectory and α_i are the input variables of the filters while $x_{i,c}$ represent the filters' output variables, in which $i = 1, 2, 3, 4$. To neutralize the filtering errors which are the values of $x_{i,c} - \alpha_i$, at every filtering step, we use the error compensation technique and ζ_i represent the compensation signals, where $i = 1, 2, 3, 4, 5, 6$. Additionally, we introduce a tight set

$\Omega_v = \{|v_i| < k_{b_i}, i = 1, 2, \ldots, 6\}$, in which the constants k_{b_i} should be positive. During the next construction process, the error renumeration variables ζ_i, the virtual controllers α_i, and the real controllers u_d and u_q will be given.

Step 1. In [15], the barrier Lyapunov function was proposed. So, with the description, we select the first BLF V_1 as

$$V_1 = \frac{1}{2}\log\left(\frac{k_{b_1}^2}{k_{b_1}^2 - v_1^2}\right). \tag{6}$$

Within the compact set Ω_v, the first-ordered time derivative form of V_1 should be

$$\dot{V}_1 = K_{v_1}\dot{v}_1 = K_{v_1}\left(z_2 + x_{1,c} - \dot{x}_d - \dot{\zeta}_1\right), \tag{7}$$

in which $K_{v_i} = (v_i/(k_{b_i}^2 - v_i^2))$, $i = 1, 2, \ldots, 6$. Next, we conceive the virtual controller α_1 and the remunerate variable ζ_1 as

$$\begin{aligned} \alpha_1 &= -k_1 z_1 + \dot{x}_d, \\ \dot{\zeta}_1 &= -k_1\zeta_1 + \zeta_2 + \left(x_{1,c} - \alpha_1\right), \end{aligned} \tag{8}$$

where $k_1 > 0$ is designed to be the control gain and the terms $k_i > 0$ $(i = 1, 2, \ldots, 6)$ will be applied in constructing other virtual control laws and compensation signals later on. By using (8), (7) can be converted into the following equation:

$$\dot{V}_1 = -k_1 K_{v_1} v_1 + K_{v_1} v_2. \tag{9}$$

Step 2. Similarly, we set up the second BLF as

$$V_2 = V_1 + \frac{J}{2}\log\left(\frac{k_{b_2}^2}{k_{b_2}^2 - v_2^2}\right), \tag{10}$$

where V_2 should be time-consecutive within the compact set Ω_v, so we compute its first-ordered time derivative form and apply $\dot{V}_1$ into it to get the following equation:

$$\begin{aligned} \dot{V}_2 &= \dot{V}_1 + JK_{v_2}\dot{v}_2 \\ &= -k_1 K_{v_1} v_1 + K_{v_1} v_2 + K_{v_2}\left(a_1 x_3 + a_2 x_3 x_5 - T_L - J\dot{x}_{1,c} - J\dot{\zeta}_2\right). \end{aligned} \tag{11}$$

When it comes to actual applications, T_L is presumed to be unknown but should be limited to a certain range. Therefore, we assume $|T_L| \le d$, in which the constant d should be positive. With Young's inequality theorem, we have $-K_{v_2}T_L \le (1/2\varepsilon_1^2)K_{v_2}^2 + (1/2)\varepsilon_1^2 d^2$ with $\varepsilon_1 > 0$.

So, rewritten $\dot{V}_2$ as

$$\dot{V}_2 \le -k_1 K_{v_1} v_1 + K_{v_1} v_2 + K_{v_2}\left(a_1 x_3 - J\dot{\zeta}_2 + f_2(Z)\right) + \frac{1}{2}\varepsilon_1^2 d^2, \tag{12}$$

in which $f_2(Z) = a_2 x_3 x_5 - J\dot{x}_{1,c} + (1/2\varepsilon_1^2)K_{v_2}$, $Z = [x_1, x_2, x_3, x_4, x_5, x_6, x_d, \dot{x}_d]^T$. With the aforementioned description of RBF NNs, we know that it always has a RBF NN $W_2^T S_2(Z)$ to make $f_2(Z) = W_2^T S_2(Z) + \delta_2(Z)$ holds, where $\delta_2(Z)$ is the estimate error. Then, for any $\varepsilon_2 > 0$, $\delta_2(Z)$ will satisfy that $|\delta_2(Z)| \le \varepsilon_2$. So, under the premise of $l_2 > 0$, we have

$$\begin{aligned} K_{v_2} f_2(Z) &= K_{v_2}\left(W_2^T S_2(Z) + \delta_2(Z)\right) \\ &\le \frac{\|W_2\|^2 K_{v_2}^2 S_2^T S_2}{2l_2^2} + \frac{l_2^2}{2} + \frac{K_{v_2}^2}{2} + \frac{\varepsilon_2^2}{2}. \end{aligned} \tag{13}$$

Design the second virtual control signal α_2 along with the remuneration variable ζ_2 as

$$\begin{aligned} \alpha_2 &= -\frac{1}{a_1}\left(k_2 z_2 + \frac{K_{v_2}}{2} + \frac{K_{v_2}\widehat{\theta} S_2^T S_2}{2l_2^2} + K_{v_1}\left(k_{b_2}^2 - v_2^2\right)\right), \\ \dot{\zeta}_2 &= -\frac{1}{J}\left(k_2\zeta_2 - a_1\zeta_3 - a_1\left(x_{2,c} - \alpha_2\right)\right), \end{aligned} \tag{14}$$

with $\widehat{\theta}$ being the approximation of θ, which will be constructed later on. Applying (13) and (14) into (12), we have

$$\begin{aligned} \dot{V}_2 \le &-k_1 K_{v_1} v_1 - k_2 K_{v_2} v_2 + K_{v_2} a_1 v_3 + \frac{1}{2}\varepsilon_1^2 d^2 \\ &+ \frac{\left(\|W_2\|^2 - \widehat{\theta}\right)K_{v_2}^2 S_2^T S_2}{2l_2^2} + \frac{l_2^2}{2} + \frac{\varepsilon_2^2}{2}. \end{aligned} \tag{15}$$

Step 3. Construct the third BLF as

$$V_3 = V_2 + \frac{1}{2}\log\left(\frac{k_{b_3}^2}{k_{b_3}^2 - v_3^2}\right), \tag{16}$$

V_3 is continuous within the compact set Ω_v, so we compute its first-ordered time derivative form and apply $\dot{V}_2$ into it, then we get

$$\begin{aligned} \dot{V}_3 \le &-\sum_{i=1}^{2} k_i K_{v_i} v_i + K_{v_2} a_1 v_3 + K_{v_3}\left(b_1 x_4 - \dot{x}_{2,c} - \dot{\zeta}_3 + f_3(Z)\right) \\ &+ \frac{\left(\|W_2\|^2 - \widehat{\theta}\right)K_{v_2}^2 S_2^T S_2}{2l_2^2} + \frac{l_2^2}{2} + \frac{\varepsilon_2^2}{2} + \frac{1}{2}\varepsilon_1^2 d^2, \end{aligned} \tag{17}$$

in which $f_3(Z) = -b_1 x_3 + b_2 x_2 x_5 + b_3 x_2$. Akin to Step 2, it always has a RBF NN $W_3^T S_3(Z)$ to make $f_3(Z) = W_3^T S_3(Z) + \delta_3(Z)$ holds, where $\delta_3(Z)$ is the estimate error. Then, for any $\varepsilon_3 > 0$, $\delta_3(Z)$ will satisfy that $|\delta_3(Z)| \le \varepsilon_3$. With the premise of $l_3 > 0$, we deduce that

$$\begin{aligned} K_{v_3} f_3(Z) &= K_{v_3}\left(W_3^T S_3(Z) + \delta_3(Z)\right) \\ &\le \frac{\|W_3\|^2 K_{v_3}^2 S_3^T S_3}{2l_3^2} + \frac{l_3^2}{2} + \frac{K_{v_3}^2}{2} + \frac{\varepsilon_3^2}{2}. \end{aligned} \tag{18}$$

Set the third virtual control law α_3 along with the remuneration variable ζ_3 as

$$\alpha_3 = -\frac{1}{b_1}\left(k_3 z_3 + \frac{K_{v_3}}{2} + \frac{K_{v_3}\widehat{\theta} S_3^T S_3}{2l_3^2} + a_1 K_{v_2}\left(k_{b_3}^2 - v_3^2\right) - \dot{x}_{2,c}\right),$$
$$\dot{\zeta}_3 = -k_3\zeta_3 + b_1\zeta_4 + b_1\left(x_{3,c} - \alpha_3\right). \tag{19}$$

Applying (18) and (19) into (17), we have

$$\dot{V}_3 \le -\sum_{i=1}^{3} k_i K_{v_i} v_i + b_1 K_{v_3} v_4 + \sum_{i=2}^{3}\frac{\left(\|W_i\|^2 - \widehat{\theta}\right)K_{v_i}^2 S_i^T S_i}{2l_i^2} + \sum_{i=2}^{3}\frac{l_i^2}{2} + \sum_{i=2}^{3}\frac{\varepsilon_i^2}{2} + \frac{1}{2}\varepsilon_1^2 d^2. \tag{20}$$

Step 4. Design the next BLF V_4 as

$$V_4 = V_3 + \frac{1}{2}\log\left(\frac{k_{b_4}^2}{k_{b_4}^2 - v_4^2}\right). \tag{21}$$

Akin to $\dot{V}_3$, $\dot{V}_4$ will be listed as

$$\dot{V}_4 \le -\sum_{i=1}^{3} k_i K_{v_i} v_i + b_1 K_{v_3} v_4 + K_{v_4}\left(d_1 u_q - \dot{x}_{3,c} - \dot{\zeta}_4 + f_4(Z)\right) + \sum_{i=2}^{3}\frac{\left(\|W_i\|^2 - \widehat{\theta}\right)K_{v_i}^2 S_i^T S_i}{2l_i^2} + \sum_{i=2}^{3}\frac{l_i^2}{2} + \sum_{i=2}^{3}\frac{\varepsilon_i^2}{2} + \frac{1}{2}\varepsilon_1^2 d^2, \tag{22}$$

in which $f_4(Z) = b_4 x_4 + b_5 x_3$. Akin to the last step, it always has a neural network $W_4^T S_4(Z)$ to make that $f_4(Z) = W_4^T S_4(Z) + \delta_4(Z)$ holds, where $\delta_4(Z)$ stands for the estimate error. Then, for any $\varepsilon_4 > 0$, $\delta_4(Z)$ will satisfy that $|\delta_4(Z)| \le \varepsilon_4$. So, with the premise of $l_4 > 0$, we can obtain that

$$K_{v_4} f_4(Z) = K_{v_4}\left(W_4^T S_4(Z) + \delta_4(Z)\right) \le \frac{\|W_4\|^2 K_{v_4}^2 S_4^T S_4}{2l_4^2} + \frac{l_4^2}{2} + \frac{K_{v_4}^2}{2} + \frac{\varepsilon_4^2}{2}. \tag{23}$$

Now, we set the actual control signal u_q and the remunerate variable ζ_4 as

$$u_q = -\frac{1}{d_1}\left(k_4 z_4 + \frac{1}{2}K_{v_4} + \frac{K_{v_4}\widehat{\theta} S_4^T S_4}{2l_4^2} + b_1 K_{v_3}\left(k_{b_4}^2 - v_4^2\right) - \dot{x}_{3,c}\right),$$
$$\dot{\zeta}_4 = -k_4\zeta_4. \tag{24}$$

Then, with the terms of (23) and (24), the inequality (22) will result in

$$\dot{V}_4 \le -\sum_{i=1}^{4} k_i K_{v_i} v_i + \sum_{i=2}^{4}\frac{\left(\|W_i\|^2 - \widehat{\theta}\right)K_{v_i}^2 S_i^T S_i}{2l_i^2} + \sum_{i=2}^{4}\frac{l_i^2}{2} + \sum_{i=2}^{4}\frac{\varepsilon_i^2}{2} + \frac{1}{2}\varepsilon_1^2 d^2. \tag{25}$$

Step 5. Set the next BLF V_5 as

$$V_5 = V_4 + \frac{1}{2}\log\left(\frac{k_{b_5}^2}{k_{b_5}^2 - v_5^2}\right), \tag{26}$$

where V_5 is continuous within the compact set Ω_v, so we compute its first-ordered time derivative form and apply $\dot{V}_4$ into it; then, we have

$$\dot{V}_5 \le -\sum_{i=1}^{4} k_i K_{v_i} v_i + K_{v_5}\left(c_1 x_6 - \dot{\zeta}_5 + f_5(Z)\right) + \sum_{i=2}^{4}\frac{\left(\|W_i\|^2 - \widehat{\theta}\right)K_{v_i}^2 S_i^T S_i}{2l_i^2} + \sum_{i=2}^{4}\frac{l_i^2}{2} + \sum_{i=2}^{4}\frac{\varepsilon_i^2}{2} + \frac{1}{2}\varepsilon_1^2 d^2, \tag{27}$$

in which $f_5(Z) = -c_1 x_5 - c_2 x_2 x_3 = W_5^T S_5(Z) + \delta_5(Z)$, $|\delta_5(Z)| \le \varepsilon_5$. With the premise of $l_5 > 0$, we can deduce that

$$K_{v_5} f_5(Z) = K_{v_5}\left(W_5^T S_5(Z) + \delta_5(Z)\right) \le \frac{\|W_5\|^2 K_{v_5}^2 S_5^T S_5}{2l_5^2} + \frac{l_5^2}{2} + \frac{K_{v_5}^2}{2} + \frac{\varepsilon_5^2}{2}. \tag{28}$$

Design the fourth virtual control signal α_4 along with the remunerate variable ζ_5 as

$$\alpha_4 = -\frac{1}{c_1}\left(k_5 z_5 + \frac{K_{v_5}}{2} + \frac{K_{v_5}\widehat{\theta} S_5^T S_5}{2l_5^2}\right),$$
$$\dot{\zeta}_5 = -k_5\zeta_5 + c_1\zeta_6 + c_1\left(x_{4,c} - \alpha_4\right). \tag{29}$$

By using (28) and (29), inequality (27) can be transformed as

$$\dot{V}_5 \le -\sum_{i=1}^{5} k_i K_{v_i} v_i + c_1 K_{v_5} v_6 + \sum_{i=2}^{5}\frac{\left(\|W_i\|^2 - \widehat{\theta}\right)K_{v_i}^2 S_i^T S_i}{2l_i^2} + \sum_{i=2}^{5}\frac{l_i^2}{2} + \sum_{i=2}^{5}\frac{\varepsilon_i^2}{2} + \frac{1}{2}\varepsilon_1^2 d^2. \tag{30}$$

Step 6. Design the sixth BLF V_6 as follows:

$$V_6 = V_5 + \frac{1}{2}\log\left(\frac{k_{b_6}^2}{k_{b_6}^2 - v_6^2}\right). \tag{31}$$

Similarly,

$$\dot{V}_6 \le -\sum_{i=1}^{5} k_i K_{v_i} v_i + c_1 K_{v_5} v_6 + K_{v_6}\left(d_2 u_d - \dot{x}_{4,c} - \dot{\zeta}_6 + f_6(Z)\right) + \sum_{i=2}^{5} \frac{\left(\|W_i\|^2 - \widehat{\theta}\right) K_{v_i}^2 S_i^T S_i}{2l_i^2} + \sum_{i=2}^{5} \frac{l_i^2}{2} + \sum_{i=2}^{5} \frac{\varepsilon_i^2}{2} + \frac{1}{2}\varepsilon_1^2 d^2. \tag{32}$$

in which $f_6(Z) = c_3 x_6 + c_4 x_5 = W_6^T S_6(Z) + \delta_6(Z)$, $|\delta_6\ (Z)| \le \varepsilon_6$. With the premise of $l_6 > 0$, we have

$$K_{v_6} f_6(Z) = K_{v_6}\left(W_6^T S_6(Z) + \delta_6(Z)\right) \le \frac{\|W_6\|^2 K_{v_6}^2 S_6^T S_6}{2l_6^2} + \frac{l_6^2}{2} + \frac{K_{v_6}^2}{2} + \frac{\varepsilon_6^2}{2}. \tag{33}$$

Another actual control law u_d along with the remunerate variable ζ_6 will be constructed as

$$u_d = -\frac{1}{d_2}\left(k_6 z_6 + \frac{1}{2}K_{v_6} + \frac{K_{v_6}\widehat{\theta} S_6^T S_6}{2l_6^2} + c_1 K_{v_5}\left(k_{b_6}^2 - v_6^2\right) - \dot{x}_{4,c}\right),$$
$$\dot{\zeta}_6 = -k_6 \zeta_6. \tag{34}$$

Substituting (33) and (34) into (32), we get

$$\dot{V}_6 \le -\sum_{i=1}^{6} k_i K_{v_i} v_i + \sum_{i=2}^{6} \frac{(\theta - \widehat{\theta}) K_{v_i}^2 S_i^T S_i}{2l_i^2} + \sum_{i=2}^{6}\left(\frac{l_i^2}{2} + \frac{\varepsilon_i^2}{2}\right) + \frac{1}{2}\varepsilon_1^2 d^2, \tag{35}$$

where $\theta = \max\left\{\|W_2\|^2, \|W_3\|^2, \|W_4\|^2, \|W_5\|^2, \|W_6\|^2\right\}$ and $\widetilde{\theta} = \widehat{\theta} - \theta$. Define the final BLF as

$$V = V_6 + \frac{1}{2r}\widetilde{\theta}^2. \tag{36}$$

Then, we compute the V's first-ordered time derivative form as

$$\dot{V} \le -\sum_{i=1}^{6} k_i K_{v_i} v_i + \sum_{i=2}^{6}\left(\frac{l_i^2}{2} + \frac{\varepsilon_i^2}{2}\right) + \frac{1}{r}\widetilde{\theta}\left(-\sum_{i=2}^{6} \frac{r K_{v_i}^2 S_i^T S_i}{2l_i^2} + \dot{\widehat{\theta}}\right) + \frac{1}{2}\varepsilon_1^2 d^2. \tag{37}$$

From (37), we choose the self-adaptive signal (also serve as self-training law) $\widehat{\theta}$ as

$$\dot{\widehat{\theta}} = \sum_{i=2}^{6} \frac{r K_{v_i}^2 S_i^T S_i}{2l_i^2} - m\widehat{\theta}, \tag{38}$$

in which the constants m and r should be positive.

Theorem 1. *From this aforementioned design process, we have proposed the real controllers (u_q and u_d), the self-adaptive signal $\widehat{\theta}$, and the remunerate variables ($\zeta_i, i = 1, 2, 3, 4, 5, 6$), and thus, with the PMSM driving systems satisfying Assumption 1 in set Ω_v, by selecting reasonable system parameters and by guaranteeing all-state variables within limitations, we can verify that the tracking errors would be bounded into a small range of origin.*

Proof. The detailed proof will be elaborated in the next section. □

5. Stability Analysis

To illustrate the system's constancy, replacing (38) into (37),

$$\dot{V} \le -\sum_{i=1}^{6} k_i K_{v_i} v_i + \sum_{i=2}^{6}\left(\frac{l_i^2}{2} + \frac{\varepsilon_i^2}{2}\right) + \frac{1}{2}\varepsilon_1^2 d^2 - \frac{m\widetilde{\theta}\widehat{\theta}}{r}. \tag{39}$$

It has been verified that $\log k_{b_i}^2/(k_{b_i}^2 - v_i^2) < (v_i^2/(k_{b_i}^2 - v_i^2))$ in the set $|v_i| < k_{b_i}$ in [48]. Plus, by using $-\widetilde{\theta}\widehat{\theta} \le -(\widetilde{\theta}^2/2) + (\theta^2/2)$, the inequality (39) will be converted into

$$\dot{V} \le -\sum_{i=1}^{6} k_i \log\left(\frac{k_{b_i}^2}{k_{b_i}^2 - v_i^2}\right) - \frac{m\widetilde{\theta}^2}{2r} + \sum_{i=2}^{6}\left(\frac{l_i^2}{2} + \frac{\varepsilon_i^2}{2}\right) + \frac{1}{2}\varepsilon_1^2 d^2 + \frac{m\theta^2}{2r} \le -aV + b, \tag{40}$$

in which $a = \min\{2k_1, (2k_2/J), 2k_3, 2k_4, 2k_5, 2k_6, m\}$ and $b = \sum_{i=2}^{6}((l_i^2/2) + \varepsilon_i^2/2) + (1/2)\varepsilon_1^2 d^2 + (m\theta^2/2r)$. With (40), we can infer that $(\log k_{b_i}^2/(k_{b_i}^2 - v_i^2))$ and $\widetilde{\theta}$ will be all inside of the confined bounds. For inequality (40), multiplying e^{at} at both sides, we have $(\mathrm{d}(V(t)e^{at})/(\mathrm{d}t) \le be^{at})$. Next, at the time range of $[0, t]$, we integrate this inequality and then it can be transformed into

$$V(t) \le \left(V(0) - \frac{b}{a}\right)e^{-at} + \frac{b}{a} \le V(0) + \frac{b}{a}. \tag{41}$$

From inequality (41), we have $|v_i| < k_{b_i}$ and $\widetilde{\theta}$ will be all limited to certain bounds. Moreover, we can infer that $\lim_{t\longrightarrow\infty}(\log(k_{b_i}^2/(k_{b_i}^2 - v_i^2))) \le (2b/a)$ and $\lim_{t\longrightarrow\ \infty}|v_1| \le k_{b_1}\sqrt{1 - e^{-(2b/a)}}$.

Remark 1. For compensating signals, we set the Lyapunov function as

$$V_0 = \frac{1}{2}\zeta_1^2 + \frac{J}{2}\zeta_2^2 + \frac{1}{2}\zeta_3^2 + \frac{1}{2}\zeta_4^2 + \frac{1}{2}\zeta_5^2 + \frac{1}{2}\zeta_6^2. \tag{42}$$

By employing Lemma 1, we can obtain

$$\begin{aligned}\dot{V}_0 &= \zeta_1\dot{\zeta}_1 + J\zeta_2\dot{\zeta}_2 + \zeta_3\dot{\zeta}_3 + \zeta_4\dot{\zeta}_4 + \zeta_5\dot{\zeta}_5 + \zeta_6\dot{\zeta}_6 \\ &\le -k_1\zeta_1^2 + \zeta_1\zeta_2 + |\zeta_1|\mu - k_2\zeta_2^2 + a_1\zeta_2\zeta_3 + a_1|\zeta_2|\mu - k_3\zeta_3^2 \\ &\quad + b_1\zeta_3\zeta_4 + b_1|\zeta_3|\mu - k_4\zeta_4^2 - k_5\zeta_5^2 + c_1\zeta_5\zeta_6 \\ &\quad + c_1|\zeta_5|\mu - k_6\zeta_6^2 \\ &\le -(k_1-1)\zeta_1^2 - \left(k_2 - \frac{1}{2} - a_1\right)\zeta_2^2 - \left(k_3 - \frac{a_1}{2} - b_1\right)\zeta_3^2 \\ &\quad - \left(k_4 - \frac{b_1}{2}\right)\zeta_4^2 - (k_5 - c_1)\zeta_5^2 - \left(k_6 - \frac{c_1}{2}\right)\zeta_6^2 \\ &\quad + \frac{1 + a_1 + b_1 + c_1}{2}\mu^2 \\ &\le -a_0V_0 + b_0.\end{aligned} \tag{43}$$

in which $a_0 = \min\{2(k_1 - 1), (2/J)(k_2 - (1/2) - a_1), 2(k_3 - (a_1/2) - b_1), 2(k_4 - (b_1/2)), 2(k_5 - c_1), 2(k_6 - (c_1/2))\}$, and $b_0 = ((1 + a_1 + b_1 + c_1)/2)\mu^2$. Therefore, with these two equations, we have

$$\lim_{t\longrightarrow\infty}|\zeta_i| \le \sqrt{\frac{1 + a_1 + b_1 + c_1}{a_0}}\mu, \tag{44}$$

where $i = 1, 2, \ldots, 6$. Since $\nu_1 = z_1 - \zeta_1$, we can infer that $|z_1| \le |\nu_1| + |\zeta_1| < k_{b_1}\sqrt{1 - e^{-(2b/a)}} + \sqrt{((1 + a_1 + b_1 + c_1)/a_0)}\mu$.

Remark 2. Ensue from the definition of a and b, along with the proper control variables m and $k_i\,(i = 1, 2, \ldots, 6)$, small variables $\varepsilon_j\,(j = 2, 3, \ldots, 6)$, $l_n\,(n = 2, 3, \ldots, 6)$, and large parameter r, the rotor position tracking error $|z_1|$ will be small enough to meet the control requirement. On account of $z_1 = x_1 - x_d$ as well as $x_d \le Y_0$, we have $|x_1| < k_{b_1} + \sqrt{((1 + a_1 + b_1 + c_1)/a_0)}\mu + Y_0 \le k_{c_1}$. With the definition of α_1 in equation (8), we know that α_1 contains the terms of z_1 as well as $\dot{x}_d$. Therefore, the upper limitation of α_1 which is noted as ι_1 holds. From $|x_{1,c} - \alpha_1| \le \mu$, we have $|x_{1,c}| \le \mu + \iota_1 \le \lambda_1$. Additionally, with $\nu_2 = z_2 - \zeta_2$, we get $|z_2| \le |\nu_2| + |\zeta_2| < k_{b_2} + \sqrt{((1 + a_1 + b_1 + c_1)/a_0)}\mu$. So, with $z_2 = x_2 - x_{1,c}$, it is obvious that $|x_2| \le |z_2| + |x_{1,c}| < k_{c_2}$. Parallelly, it can be verified that $|x_3| < k_{c_3}$, $|x_4| < k_{c_4}$, $|x_5| < k_{c_5}$, and $|x_6| < k_{c_6}$. At this point, the proof is accomplished.

6. Simulation Results

To substantiate the control scheme's validity, a simulation has been conducted in this part. The PMSM's parameters with core losses are chosen as Table 1.

We set all-state variables' original conditions to zero and choose $x_d = 0.5\sin(t) + 0.5\sin(0.5t)$ as the desired signal. So, $\theta = \max\left\{\|W_2\|^2, \|W_3\|^2, \|W_4\|^2, \|W_5\|^2, \|W_6\|^2\right\} = 0$. Moreover, the limitations of PMSM's state variables are $|x_1| \le 2$, $|x_2| \le 15$, $|x_3| \le 30$, $|x_4| \le 30$, $|x_5| \le 15$, $|x_6| \le 20$.

Table 1: Parameters of PMSM with core losses.

$L_d = 0.00977$ H	$L_{md} = 0.007$ H	$\lambda_{PM} = 0.0844$ Wb
$L_q = 0.00977$ H	$L_{mq} = 0.008$ H	$J = 0.002\,\mathrm{Kg}\cdot\mathrm{m}^2$
$L_{ld} = 0.00177$ H	$R_s = 2.21\,\Omega$	$n_p = 3$
$L_{lq} = 0.00177$ H	$R_c = 200\,\Omega$	

Additionally, we selected the load toque as $T_L = \begin{cases} 1, 0 \le t < 15 \\ 1.5, t \ge 15 \end{cases}$. All these parameters of PMSM are obtained based on former experiences in [17, 20, 24]. Certainly, they can be obtained by some identification methods, such as gradient estimation algorithms [43], two-stage gradient-based iterative estimation method [44], or recursive parameter estimation methods [45].

As to the RBF neural network, the neurons' quantity is 11 and we choose the activate functions as $S(x) = ([p_2(x), p_3(x), \ldots, p_6(x)]^T / \sum_{i=2}^{6} p_i(x))$ and $p_i(x) = \exp[((-(x - \eta_i)^T (Z - \eta_i))/\gamma_i^2)]$ for $i = 2, 3, 4, 5, 6$. The activate functions' centers are scattered evenly in scale $[-5, 5]$, and their widths are all defined as 1.

(a) To control the PMSM driving system with core losses and all-state restrictions, we developed the BLFs-based adaptive command filtered neural network controllers. So, during this simulation, we employed control coefficients as $k_1 = 10$, $k_2 = 7$, $k_3 = 100$, $k_4 = 50$, $k_5 = 20$, $k_6 = 30$, $r = 0.05$, $m = 0.02$, $l_2 = l_3 = l_4 = l_5 = l_6 = 0.25$, $k_{b_1} = 1$, $k_{b_2} = 10$, $k_{b_3} = 20$, $k_{b_4} = 20$, $k_{b_5} = 10$, $k_{b_6} = 15$, $\xi = 0.9$, and $\omega_n = 2000$.

(b) To show the superiority of the introduced methodology in this article, we also established the dynamic surface adaptive neural network controllers to control this system. To be comparable, we utilized identically the same parameters which are displayed in (a).

Next, Figures 2–7 illustrate these two simulations outcomes, in which Figures 2(a)–7(a) display the BLFs-based command filtered control (CFC) approach which was introduced in the frontal part of this article, while Figures 2(b)–7(b) demonstrate the dynamic surface control (DSC) scheme under the same circumstance. Figure 2 simulate the curves of x_1 and x_d. Figure 3 display the tracking error z_1. Figures 4 and 5 are the curves of u_q and u_d, respectively. Figures 6 and 7 are the performances of state variables x_2, x_3, x_4, x_5, and x_6.

From these simulation outcomes, we can observe that even under load torque uncertainty, these two approaches can both follow the given trajectory nicely. But it cannot be ignored that the tracking error which is showed in Figure 3(a) is much smaller than the error that was displayed in Figure 3(b). Moreover, the state variables in Figures 6(a) and 7(a) are controlled in the confined ranges, but i_{oq} of Figure 6(b) is varying from −20 to 60, which overstepped the presupposed current's constraint (Table 2).

Remark 3. Disparate from the DSC control method without taking filtering errors into consideration, in this paper, we

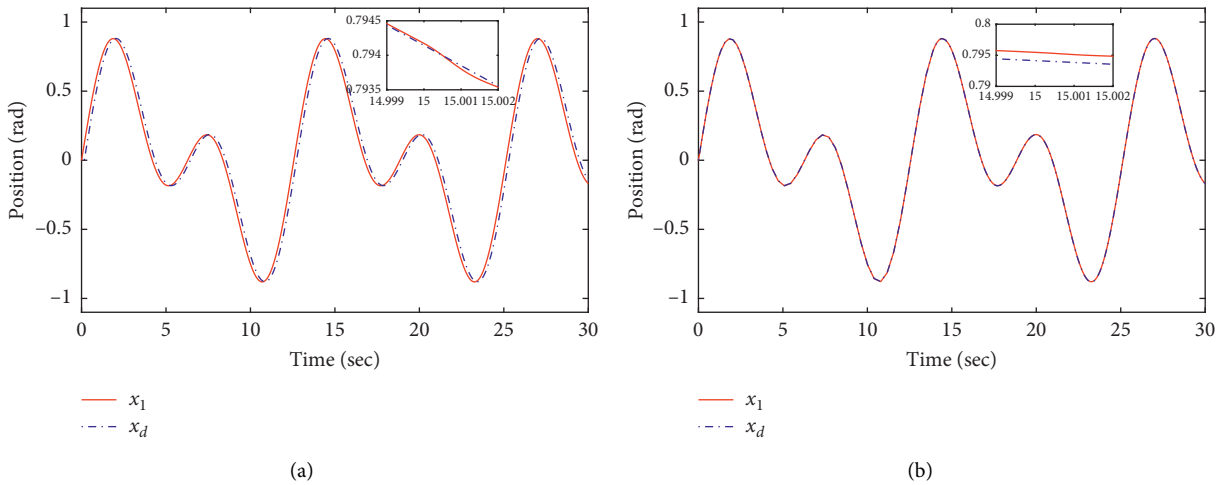

Figure 2: (a) x_1 and x_d for BLFs-based CFC. (b) x_1 and x_d for DSC.

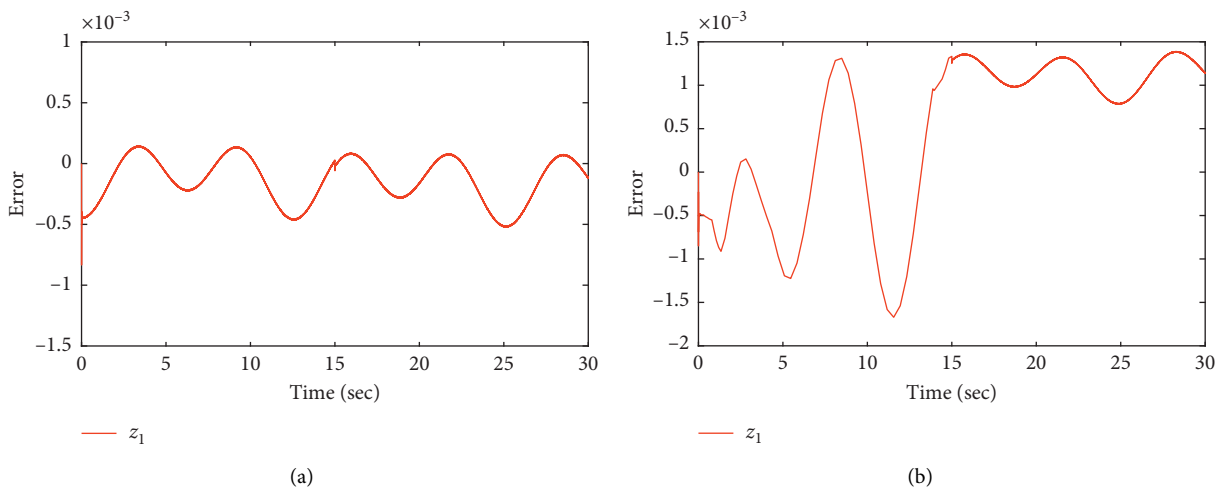

Figure 3: (a) Tracking error for BLFs-based CFC. (b) Tracking error for DSC.

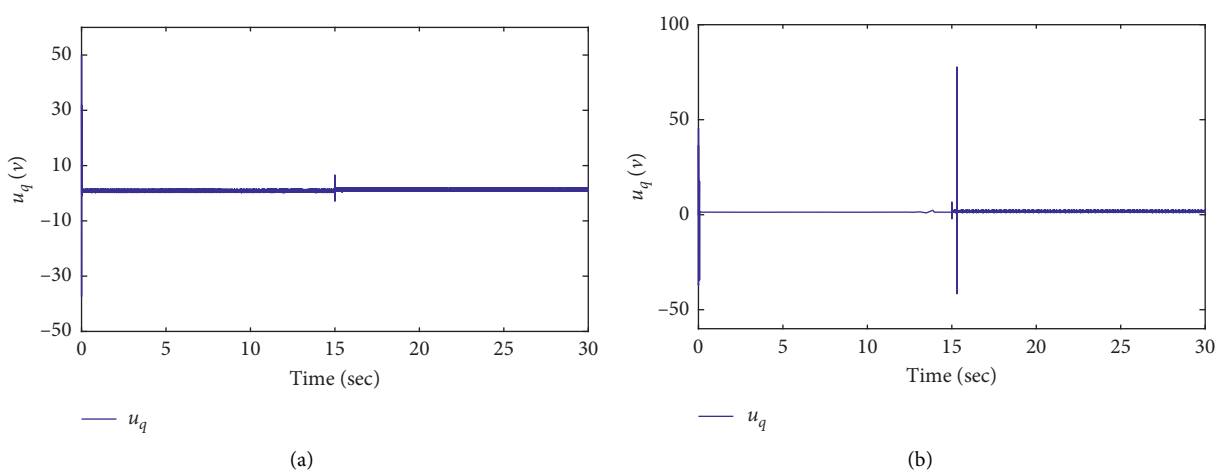

Figure 4: (a) u_q for BLFs-based CFC. (b) u_q for DSC.

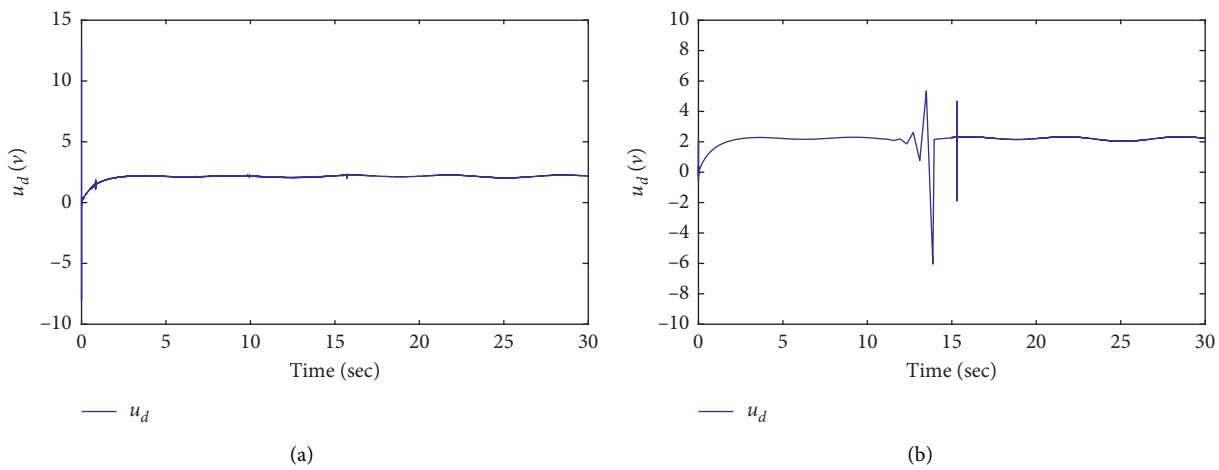

Figure 5: (a) u_d for BLFs-based CFC. (b) u_d for DSC.

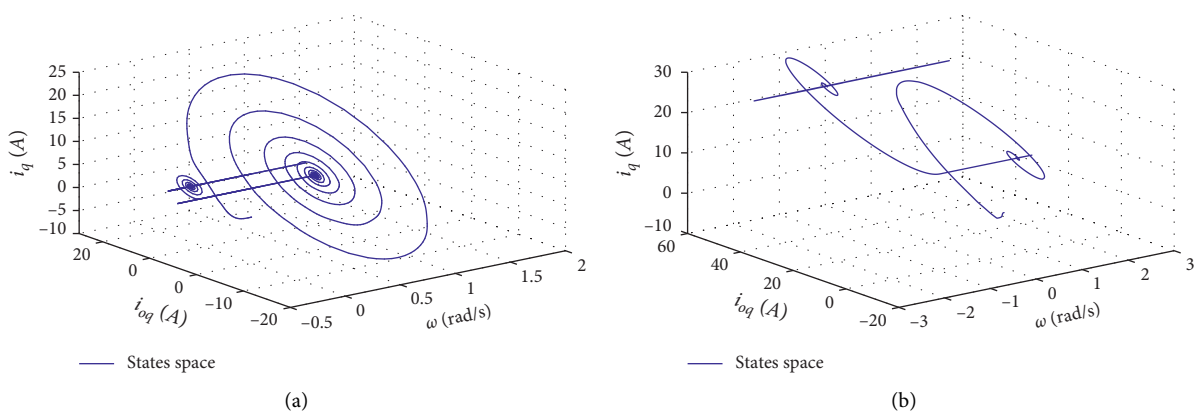

Figure 6: (a) ω, i_{oq}, i_q for BLFs-based CFC. (b) ω, i_{oq}, i_q for DSC.

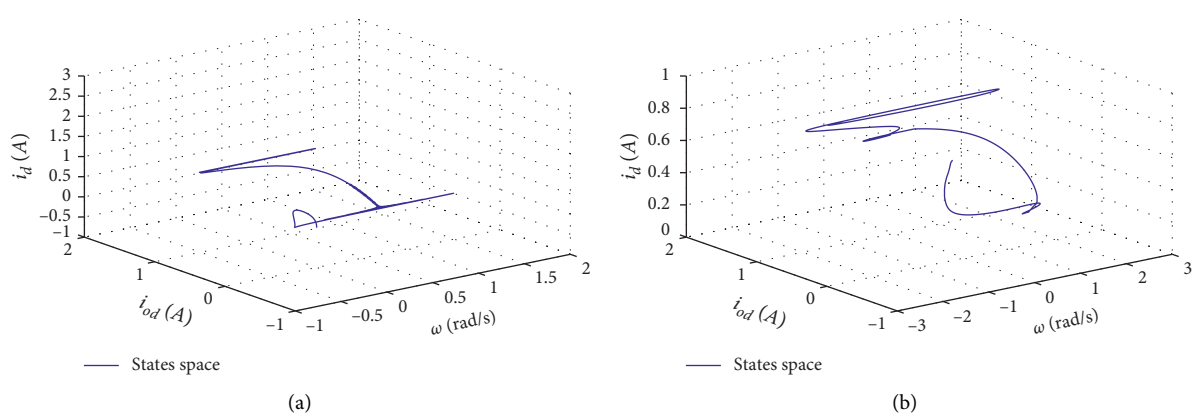

Figure 7: (a) ω, i_{od}, i_d for BLFs-based CFC. (b) ω, i_{od}, i_d for DSC.

developed the BLFs-based adaptive command filtered neural control approach. This approach can not only guarantee that the state variables would confine into reasonable bounds but also ensure that the tracing deviation would congest into a smaller range of zero, which will be much more functional and robust in real-world applications.

Table 2: The comparison performances between CFC and DSC.

Item	CFC	DSC
Absolute percentage of tracking error (%)	0.05	0.2
Variation range of ω	[−0.5, 2]	[−3, 3]
Variation range of i_q	[−10, 25]	[−10, 30]
Variation range of i_{oq}	[−20, 20]	[−20, 60]
Variation range of i_d	[−1, 3]	[0, 1]
Variation range of i_{od}	[−1, 2]	[−1, 2]

7. Conclusion

This paper developed a BLFs-based self-adaptive command filtered neural network control approach to work out the position tracking problem of the PMSM driving system with core losses and all-state restrictions. By merging BLFs into CFC techniques, the issues of "explosion of complexity" and all-state restrictions can be well resolved. Additionally, virtual control laws were constructed to ensure the position tracking error would be limited to a minute range of zero. In the end, simulation performances illustrated the system's adaptability and antidisturbance ability.

Data Availability

The data used to support the findings of this study are partially included within the article. Further information is available from the corresponding author upon request.

Conflicts of Interest

The authors declare that there are no conflicts of interest regarding the publication of this paper.

Acknowledgments

This article was partially supported by the National Key Research and Development Plan (2017YFB1303503), the NSFC (61973179), and the Taishan Scholar Special Project Fund (TSQN20161026).

References

[1] J. K. Seok, J. K. Lee, and D. C. Lee, "Sensorless speed control of nonsalient permanent-magnet synchronous motor using rotor-position-tracking PI controller," *IEEE Transactions on Industrial Electronics*, vol. 53, no. 2, pp. 399–405, 2006.

[2] M. Tursini, F. Parasiliti, and D. Q. Zhang, "Real-time gain tuning of PI controllers for high-performance PMSM drives," *IEEE Transactions on Industry Applications*, vol. 38, no. 4, pp. 1018–1026, 2002.

[3] V. Q. Leu, H. H. Choi, and J.-W. Jung, "Fuzzy sliding mode speed controller for PM synchronous motors with a load torque observer," *IEEE Transactions on Power Electronics*, vol. 27, no. 3, pp. 1530–1539, 2012.

[4] H. Li, P. Shi, D. Yao, and L. Wu, "Observer-based adaptive sliding mode control for nonlinear Markovian jump systems," *Automatica*, vol. 64, pp. 133–142, 2016.

[5] H. L. Liu, X. P. Shi, X. T. Bi, and J. Zhang, "Backstepping based terminal sliding mode control for rendezvous and docking with a tumbling spacecraft," *International Journal of Innovative Computing, Information and Control*, vol. 12, no. 3, pp. 929–940, 2016.

[6] J. Yu, P. Shi, C. Lin, and H. Yu, "Adaptive neural command filtering control for nonlinear MIMO systems with saturation input and unknown control direction," *IEEE Transactions on Cybernetics*, vol. 50, no. 6, pp. 2536–2545, 2020.

[7] Z. Wu, B. Jiang, and Y. Kao, "Finite-time H_∞ filtering for Itô stochastic Markovian jump systems with distributed time-varying delays based on optimisation algorithm," *IET Control Theory & Applications*, vol. 13, no. 5, pp. 702–710, 2019.

[8] H. S. Yu, J. P. Yu, J. Liu, and Q. Song, "Nonlinear control of induction motors based on state error PCH and energy-shaping principle," *Nonlinear Dynamics*, vol. 72, no. 1-2, pp. 49–59, 2013.

[9] C. Fu, Q.-G. Wang, J. Yu, and C. Lin, "Neural network-based finite-time command filtering control for switched nonlinear systems with backlash-like hysteresis," *IEEE Transactions on Neural Networks and Learning Systems*, pp. 1–6, 2020.

[10] W. He, Y. Chen, and Z. Yin, "Adaptive neural network control of an uncertain robot with full-state constraints," *IEEE Transactions on Cybernetics*, vol. 46, no. 3, pp. 620–629, 2016.

[11] J. Yu, P. Shi, J. Liu, and C. Lin, "Neuroadaptive finite-time control for nonlinear MIMO systems with input constraint," *IEEE Transactions on Cybernetics*, pp. 1–8, 2020.

[12] W. J. Dong, J. A. Farrell, M. Polycarpou, V. Djapic, and M. Sharma, "Command filtered adaptive backstepping," *IEEE Transactions on Control Systems Technology*, vol. 20, no. 3, pp. 566–580, 2012.

[13] J. A. Farrell, M. Polycarpou, M. Sharma, and W. Wenjie Dong, "Command filtered backstepping," *IEEE Transactions on Automatic Control*, vol. 54, no. 6, pp. 1391–1395, 2009.

[14] J. P. Yu, P. Shi, X. K. Chen, and G. Z. Cui, "Finite-time command filtered adaptive control for nonlinear systems via immersion and invariance," *SCIENCE CHINA Information Sciences*, 2009.

[15] K. P. Tee, S. S. Ge, and E. H. Tay, "Barrier Lyapunov functions for the control of output-constrained nonlinear systems," *Automatica*, vol. 45, no. 4, pp. 918–927, 2009.

[16] C. Fu, J. Yu, L. Zhao, H. Yu, C. Lin, and Y. Ma, "Barrier Lyapunov function-based adaptive fuzzy control for induction motors with iron losses and full state constraints," *Neurocomputing*, vol. 287, pp. 208–220, 2018.

[17] Y. Liu, J. Yu, H. Yu, C. Lin, and L. Zhao, "Barrier Lyapunov functions-based adaptive neural control for permanent magnet synchronous motors with full-state constraints," *IEEE Access*, vol. 5, pp. 10382–10389, 2017.

[18] X. Yang, J. Yu, Q.-G. Wang, L. Zhao, H. Yu, and C. Lin, "Adaptive fuzzy finite-time command filtered tracking control for permanent magnet synchronous motors," *Neurocomputing*, vol. 337, no. 14, pp. 110–119, 2019.

[19] H. Luo, J. Yu, C. Lin, Z. Liu, L. Zhao, and Y. Ma, "Finite-time dynamic surface control for induction motors with input saturation in electric vehicle drive systems," *Neurocomputing*, vol. 369, no. 5, pp. 166–175, 2019.

[20] J. P. Yu, B. Chen, H. S. Yu, and J. W. Gao, "Adaptive fuzzy backstepping position tracking control for permanent magnet synchronous motor," *Control and Decision*, vol. 25, no. 10, pp. 1547–1551, 2010.

[21] S. Zheng, X. Tang, B. Song, S. Lu, and B. Ye, "Stable adaptive PI control for permanent magnet synchronous motor drive based on improved JITL technique," *ISA Transactions*, vol. 52, no. 4, pp. 539–549, 2013.

[22] H. Li, J. Yu, C. Hilton, and H. Liu, "Adaptive sliding-mode control for nonlinear active suspension vehicle systems using

T-S fuzzy approach," *IEEE Transactions on Industrial Electronics*, vol. 60, no. 8, pp. 3328–3338, 2013.

[23] Q. Yin, M. Wang, and H. Jing, "Stabilizing backstepping controller design for arbitrarily switched complex nonlinear system," *Applied Mathematics and Computation*, vol. 369, Article ID 124789, 2020.

[24] Y. Zhang, C. M. Akujuobi, W. H. Ali, C. L. Tolliver, and L.-S. Shieh, "Load disturbance resistance speed controller design for PMSM," *IEEE Transactions on Industrial Electronics*, vol. 53, no. 4, pp. 1198–1208, 2006.

[25] W. Chang and S. Tong, "Adaptive fuzzy tracking control design for permanent magnet synchronous motors with output constraint," *Nonlinear Dynamics*, vol. 87, no. 1, pp. 291–302, 2017.

[26] G. Cui, J. Yu, and P. Shi, "Observer-based finite-time adaptive fuzzy control with prescribed performance for nonstrict-feedback nonlinear systems," *IEEE Transactions on Fuzzy Systems*, p. 1, 2021.

[27] Y. Wei, J. Qiu, P. Shi, and L. Wu, "A piecewise-Markovian Lyapunov approach to reliable output feedback control for fuzzy-affine systems with time-delays and actuator faults," *IEEE Transactions on Cybernetics*, vol. 48, no. 9, pp. 2723–2735, 2018.

[28] Z. Zhao, J. Yu, L. Zhao, H. Yu, and C. Lin, "Adaptive fuzzy control for induction motors stochastic nonlinear systems with input saturation based on command filtering," *Information Sciences*, vol. 463-464, pp. 186–195, 2018.

[29] Z. Y. Cui, R. M. Ke, and Y. H. Wang, "Deep bidirectional and unidirectional LSTM recurrent neural network for network-wide traffic speed prediction," 2018, https://arxiv.org/abs/1801.02143.

[30] X.-B. Jin, H.-X. Wang, X.-Y. Wang, Y.-T. Bai, T.-L. Su, and J.-L. Kong, "Deep-Learning prediction model with serial two-level decomposition based on bayesian optimization," *Complexity*, vol. 2020, Article ID 4346803, 14 pages, 2020.

[31] R. Fu, Z. Zhang, and L. Li, "Using LSTM and GRU neural network methods for traffic flow prediction," in *Proceedings of the 2016 31st Youth Academic Annual Conference of Chinese Association of Automation (YAC)*, pp. 324–328, Wuhan, China, November 2016.

[32] Y. T. Bai, X. B. Jin, X. Y. Wang, T. L. Su, J. L. Kong, and Y. T. Lu, "Compound autoregressive network for prediction of multivariate time series," *Complexity*, vol. 2019, Article ID 9107167, 11 pages, 2019.

[33] X. B. Jin, C. Dou, T. L. Su, X. F. Lian, and Y. Shi, "Parallel irregular fusion estimation based on nonlinear filter for indoor RFID tracking system," *International Journal of Distributed Sensor Networks*, vol. 2016, no. 8, Article ID 1472930, 11 pages, 2016.

[34] Y.-T. Bai, X.-Y. Wang, X.-B. Jin, Z.-Y. Zhao, and B.-H. Zhang, "A neuron-based Kalman filter with nonlinear autoregressive model," *Sensors*, vol. 20, no. 1, p. 299, 2020.

[35] M. Chen, G. Tao, and B. Jiang, "Dynamic surface control using neural networks for a class of uncertain nonlinear systems with input saturation," *IEEE Transactions on Neural Networks and Learning Systems*, vol. 26, no. 9, pp. 2086–2097, 2015.

[36] J. Ma, Z. Zheng, and P. Li, "Adaptive dynamic surface control of a class of nonlinear systems with unknown direction control gains and input saturation," *IEEE Transactions on Cybernetics*, vol. 45, no. 4, pp. 728–741, 2015.

[37] Y. Bai, X. Wang, X. Jin, T. Su, J. Kong, and B. Zhang, "Adaptive filtering for MEMS gyroscope with dynamic noise model," *ISA Transactions*, vol. 101, pp. 430–441, 2020.

[38] X. Zhang, F. Ding, L. Xu, and E. Yang, "State filtering-based least squares parameter estimation for bilinear systems using the hierarchical identification principle," *IET Control Theory & Applications*, vol. 12, no. 12, pp. 1704–1713, 2018.

[39] X. Zhang, F. Ding, L. Xu, and E. Yang, "Highly computationally efficient state filter based on the delta operator," *International Journal of Adaptive Control and Signal Processing*, vol. 33, no. 6, pp. 875–889, 2019.

[40] Y.-J. Liu, J. Li, S. Tong, and C. L. P. Chen, "Neural network control-based adaptive learning design for nonlinear systems with full-state constraints," *IEEE Transactions on Neural Networks and Learning Systems*, vol. 27, no. 7, pp. 1562–1571, 2016.

[41] J. Yu, L. Zhao, H. Yu, and C. Lin, "Barrier Lyapunov functions-based command filtered output feedback control for full-state constrained nonlinear systems," *Automatica*, vol. 105, pp. 71–79, 2019.

[42] Z. Zhao, X. Wang, P. Yao, and Y. Bai, "A health performance evaluation method of multirotors under wind turbulence," *Nonlinear Dynamics*, vol. 102, no. 3, pp. 1701–1715, 2020.

[43] F. Ding, L. Xu, D. D. Meng, X. B. Jin, A. Alsaedi, and T. Hayate, "Gradient estimation algorithms for the parameter identification of bilinear systems using the auxiliary model," *Journal of Computational and Applied Mathematics*, vol. 369, Article ID 112575, 2019.

[44] F. Ding, L. Lv, J. Pan, X. Wan, and X.-B. Jin, "Two-stage gradient-based iterative estimation methods for controlled autoregressive systems using the measurement data," *International Journal of Control, Automation and Systems*, vol. 18, no. 4, pp. 886–896, 2020.

[45] X. Zhang, F. Ding, and L. Xu, "Recursive parameter estimation methods and convergence analysis for a special class of nonlinear systems," *International Journal of Robust and Nonlinear Control*, vol. 30, no. 4, pp. 1373–1393, 2020.

[46] J. Yu, P. Shi, W. Dong, B. Chen, and C. Lin, "Neural network-based adaptive dynamic surface control for permanent magnet synchronous motors," *IEEE Transactions on Neural Networks and Learning Systems*, vol. 26, no. 3, pp. 640–645, 2015.

[47] Y.-J. Liu and S. Tong, "Adaptive NN tracking control of uncertain nonlinear discrete-time systems with nonaffine dead-zone input," *IEEE Transactions on Cybernetics*, vol. 45, no. 3, pp. 497–505, 2015.

[48] B. B. Ren, S. Z. Ge, and K. P. Tee, "Adaptive neural control for output feedback nonlinear systems using a Barrier Lyapunov function," *IEEE Transactions on Neural Networks and Learning Systems*, vol. 21, no. 8, pp. 1339–1345, 2010.

Hindawi
Complexity
Volume 2021, Article ID 8839391, 7 pages
https://doi.org/10.1155/2021/8839391

Research Article

Online Optimal Control of Robotic Systems with Single Critic NN-Based Reinforcement Learning

Xiaoyi Long, Zheng He, and Zhongyuan Wang

School of Computer Science, Wuhan University, Wuhan 430072, China

Correspondence should be addressed to Zheng He; hezheng@whu.edu.cn

Received 29 August 2020; Revised 21 October 2020; Accepted 11 January 2021; Published 9 February 2021

Academic Editor: Jing Na

This paper suggests an online solution for the optimal tracking control of robotic systems based on a single critic neural network (NN)-based reinforcement learning (RL) method. To this end, we rewrite the robotic system model as a state-space form, which will facilitate the realization of optimal tracking control synthesis. To maintain the tracking response, a steady-state control is designed, and then an adaptive optimal tracking control is used to ensure that the tracking error can achieve convergence in an optimal sense. To solve the obtained optimal control via the framework of adaptive dynamic programming (ADP), the command trajectory to be tracked and the modified tracking Hamilton-Jacobi-Bellman (HJB) are all formulated. An online RL algorithm is the developed to address the HJB equation using a critic NN with online learning algorithm. Simulation results are given to verify the effectiveness of the proposed method.

1. Introduction

In the control field and practical applications, reinforcement learning (RL) [1, 2] and adaptive dynamic programming (ADP) [3, 4] play a critical role to address the optimal control problems. The purpose of optimal control is to design a stabilizing control law by minimizing a predefined performance function. A lot of work focusing on the regulation problem for optimal control using the RL/ADP algorithms has been reported [5, 6] in the past years. The objective is to solve an optimal control that can maximize or minimize the system output energy and control actions, where the associated optimal control equations can be numerically solved via neural networks (NNs). From the perspective of both the theoretical study and practical application, these results pave a new way to solve the optimal control problems. Relevant surveys about the recent developments on the RL and ADP can be referred to [7, 8].

RL was first developed in the intelligent control field, which was used to address the discrete-time Markov decision problems. Then, it has been extended to solve the continuous-time (CT) systems. With respect to optimal control designs, Abu-Khalaf et al. [9] suggested a policy iteration (PI) for the optimal regulation of CT nonlinear systems with actuator saturation. To overcome the problem of using the time derivatives of CT dynamics, Lewis et al. [10] developed an integral RL (IRL) technique for systems with partially known dynamics, where the full system information is avoided. In [11], the authors have employed an actor-critic structure and developed a synchronous PI algorithm for CT systems. In this framework, both the optimal cost function and control policy are estimated using NNs, whose weights are updated online simultaneously. For completely unknown system dynamics, the results in [12] showed that a model-free PI approach can be developed for CT linear systems, which can online calculate the optimal solutions using the input/output measurements. This principle was subsequently extended to nonlinear systems in [13, 14]. Another intelligent learning method used in the RL, experience replay (ER), was recently incorporated into the synthesis of ADP for optimal control in [15], where the past system observations are utilized together with the current information to enhance the convergence speed of the online learning.

Moreover, most existing results on the ADP-based optimal control designs focus on the optimal regulation

problems only. However, in the practical application, optimal tracking control problem (OTCP) is more widely used than the optimal regulation problem [16–18], in particular for robotic applications. However, the OTCP is more challenging to address than the regulation problem, since its solution is usually composed of a feedforward action to guarantee the perfect tracking and a feedback action to stabilize the closed-loop system dynamics [19]. For linear systems, the solution of OTCP is calculated by addressing the Riccati equations [20], while for nonlinear systems, the existing solution for the OTCP can be derived with a feedforward term by employing the dynamics inversion and a feedback term by calculating a complex HJB equation [16, 21]. However, it is well known that deriving the solution of OTCP is typically intractable, especially for the online tracking control. Hence, only few results have been reported to address the OTCP in the literature, in particular for robotic systems.

According to the above facts, we propose a new RL algorithm to realize the optimal tracking control of robotic systems. To this end, the system model is rewritten as a state-space form, which will contribute to the realization of optimal tracking control. Then, a steady-state control is designed, and then an adaptive optimal tracking control is used to retain that the tracking error converges in an optimal manner. To derive this optimal control, the command trajectory to be tracked and the modified tracking Hamilton–Jacobi–Bellman (HJB) can be formulated. Finally, an online RL method is used to address the derived HJB equation using a single critic NN approximation. Numerical simulations are also given to show the validity of the proposed approach. The contributions can be summarized as follows:

(1) To achieve the optimal tracking control, the robotic system model is transformed into a canonical form, which will contribute to the realization of optimal tracking control.

(2) A critic NN is applied to reconstruct the cost function with guaranteed convergence, such that the actor NN used in the existing ADP structures is avoided and the computational costs can be reduced.

(3) A RL algorithm is proposed to obtain the solution of the derived HJB equation, which can guarantee the convergence of critic NN weights to ensure the optimal tracking error convergence.

The paper is structured as follows: in Section 2, the system model is transformed into a canonical form, and a tracking performance function is constructed. In Section 3, an adaptive steady-state control is designed and an optimal control is developed with RL to make the tracking error dynamics convergent. For this purpose, a single critic NN is applied to estimate the solution of the HJB equation and update the optimal control action. Section 4 gives some simulation results to show the validity of the developed control and learning techniques. Conclusions are summarized in Section 5.

Notations: $\mathfrak{R}$ denotes the real number set. $\mathfrak{R}^n$ is the n-dimensional real vector. $\mathfrak{R}^{n\times m}$is the real matrices. $\|\cdot\|$ denotes the Euclidean norm of a vector in $\mathfrak{R}^n$ or a matrix in $\mathfrak{R}^{n\times m}$. I is the identity matrix, and 0×0 means the zero matrix. $\lambda_{\max}$ and $\lambda_{\min}$ are the maximal and minimum eigenvalues of a matrix, respectively. $\mathrm{diag}\{[a_1, a_2, a_3, \ldots, a_n]\}$ is a diagonal matrix with component $a_1, \ldots, a_n$. $(\cdot)_x = \partial(\cdot)/\partial(x)$ defines the partial differential operation.

2. Preliminaries and Problem Statement

In this paper, we consider the general rigid body dynamics for a nonlinear robotic manipulator. On the basis of the Lagrangian formulation, the manipulator dynamics can be formulated as [22, 23]

$$M(q)\ddot{q} + C(q,\dot{q})\dot{q} + G(q) = \tau, \tag{1}$$

where $q = q(t) \in \mathfrak{R}^n$ denotes the generalized coordinates representing the joint position and $\dot{q}$, $\ddot{q}$ denote the derivatives of joint position (e.g., velocity and acceleration) with respect to time t. Let n denote the number of degrees of freedom and $M(q)$ denote a positive definite $n\times n$ inertia matrix which is invertible, $C(q,\dot{q}) \in \mathfrak{R}^n$ are the Coriolis/centripetal dynamics, and $G(q)$ represents the gravitational dynamics.

For the brevity of notation, we set $x_1 = q$, $x_2 = \dot{q}$, and $u = \tau$; then,

$$\begin{cases} \dot{x}_1 = x_2, \\ \dot{x}_2 = -M^{-1}Cx_2 - M^{-1}G + M^{-1}u. \end{cases} \tag{2}$$

Hence, we write system (1) as a state-space form as

$$\dot{x}(t) = f(x) + gu(t), \tag{3}$$

where $x(t) = \begin{bmatrix} q & \dot{q} \end{bmatrix}^T \in \mathfrak{R}^n$ is the system state, $f(x) = \begin{bmatrix} x_2 & -M^{-1}(Cx_2 + G) \end{bmatrix}^T$ is the known system dynamics, which is a continuous function with $f(0) = 0$, $g = \begin{bmatrix} 0 & M^{-1} \end{bmatrix}^T$is the control gain matrix, and $u(t) \in \mathfrak{R}^m$ denotes the control torque.

Assumption 1. The system dynamics $f(x)$ with $f(0) = 0$ are Lipschitz. Hence, system (3) is stable, i.e., a continuous control $u(t) \in \Omega$ can be found to stabilize the system, where Ω is an admissible set.

This paper aims to find an optimal control $u(t)$ to ensure that the system state $x(t)$ tracks a desired trajectory $x_d(t)$ by minimizing the following cost function:

$$V(u(t), e(t)) = \int_t^{\infty} \left[e^T(t)Qe(t) + u^T(t)Ru(t)\right]\mathrm{d}t, \tag{4}$$

where Q and R are positive definite symmetric matrices [2]. $\Psi(\Omega)$ is the set of admissible policies [9], $e^T(t)Qe(t) + u^T(t)Ru(t)$ is a positive utility function, and $e(t)$ is the tracking error defined as

$$e(t) = x(t) - x_d(t), \tag{5}$$

where $x_d(t) \in \mathfrak{R}^n$ is the reference trajectory. In this paper, the reference trajectory $x_d(t)$ and its derivative $\dot{x}_d(t)$ are assumed to be continuous and bounded.

Remark 1. There have been several methods developed to solve the tracking control problem of robotic systems, e.g., [24, 25]. However, most existing robotic controllers are not designed in the optimal manner, i.e., the required control actions may be large. Differing from these results, a novel RL algorithm is proposed in the following sections to design an optimal control for robotic systems to achieve trajectory tracking and reduce the required control energy.

Remark 2. For linear OTCP scheme, the derivation of optimal solution is shown in [18], i.e., $u = -R^{-1}B_0^T Sx + R^{-1}B_0^T v_{ss}$ with B_0 being the input matrix, and S can be solved by addressing a Riccati equation and v_{ss} is the feedforward action. Different from linear systems, the tracking control problem for nonlinear systems is not trivial since we cannot obtain a uniform formulation as the linear cases. This fact stimulated the current study.

3. Online Dynamic Tracking Control

To realize the optimal tracking control design, we decompose the control input u into two parts [18, 21] as

$$u = u_s + u_e, \tag{6}$$

where u_s and $u_e$are the steady-state control and optimal control, which are applied to make the steady-state trajectory tracking and stabilize the tracking error dynamics optimally, respectively. Figure 1 shows the proposed control system structure.

3.1. Steady-State Tracking Control. Since u_s can be adopted to ensure that the control error converges to zero in the steady-state, then we have from (3) that

$$u_s = g^+\left[\dot{x}_d - f(x) - Ke\right], \tag{7}$$

where $K > 0$ is the feedback gain set by the desingers and $g^+ = [(g^T g)^{-1} g^T]$ is defined as the generalized inverse of g.

Then, based on (3) and (7), we have the tracking error e as

$$\dot{e} = f(x) + g(u_s + u_e) - \dot{x}_d = -Ke + gu_e. \tag{8}$$

From equations (7) and (8), we know that the tracking control of system (3) can be considered the regulation problem of (8). Hence, an optimal control u_e will be designed to stabilize tracking error dynamics (8) in an optimal manner.

3.2. Approximate Optimal Tracking Control. The controller u_e can be used to make (8) converge in an optimal sense. For this purpose, we can rewrite the infinite horizon cost function (4) as follows:

$$V(e(t)) = \int_t^\infty \left[e^T(t)Qe(t) + u_e^T(t)Ru_e(t)\right]\mathrm{d}t. \tag{9}$$

Then, an admissible control policy u_e should be found so that cost function (9) of system (8) can be minimized. To this end, the Lyapunov equation of (7) is given by

$$0 = V_e^T\left[-Ke + gu_e\right] + e^T Qe + u_e^T Ru_e, \tag{10}$$

with $V_e = (\partial V/\partial e)$ being the partial differential.

Then, the optimal cost function $V^*(e)$ is given as

$$V^*(e) = \min_{u_e}\left(\int_t^\infty \left[e^T(t)Qe(t) + u_e^{*T}(t)Ru_e^*(t)\right]\mathrm{d}t\right), \tag{11}$$

and the derived HJB equation is shown as

$$0 = \min_{u_e} H(e, u_e^*, V^*). \tag{12}$$

The optimal control u_e can be derived by solving $(\partial H(e, u_e^*, V^*)/\partial u_e^*) = 0$ from (10) as

$$u_e^* = -\frac{1}{2}R^{-1}g^T\frac{\partial V^*(e)}{\partial e}. \tag{13}$$

The problem to be finally addressed is to solve HJB equation (12) to obtain the optimal cost function $V^*(e)$ required in control (13).

3.2.1. Online Reinforcement Learning Algorithm. To calculate the above optimal control, we can recall the policy iteration (PI) method. Inspired by [1, 26], a policy iteration algorithm can be given as follows:

(1) Select a small positive constant κ. Let $i = 0$ and $V^{(0)} = 0$, then set an initial admissible control policy $u_e^{(0)}$.

(2) Solve the nonlinear Lyapunov equation using the control policy $u_e^{(i)}$

$$0 = e^T Qe + u_e^{T(i)}Ru_e^{(i)} + \left(\nabla V^{(i+1)}(e)\right)^T\left(-Ke + gu_e^i\right), \tag{14}$$

with $V^{(i+1)}(0) = 0$.

(3) Improve the control policy by

$$u_e^{(i+1)} = -\frac{1}{2}R^{-1}g^T\nabla V^{(i+1)}. \tag{15}$$

(4) If $|V^{(i+1)}(e) - V^{(i)}(e)| \le \kappa$, stop the iteration and take the approximate optimal control; else, let $i = i + 1$and go back to Step 2.

The above PI scheme can guarantee the convergence to the optimal cost function and control action, i.e., $V^{(i)} \longrightarrow V^*$ and $u_e^{(i)} \longrightarrow u^*$ as $i \longrightarrow \infty$. The convergence proof of the PI algorithm was detailed in [9].

3.2.2. Neural Network Approximation. The above policy iteration method is run *offline*. To implement online optimal control, we will introduce an online learning method in this section.

From HJB equation (12), it is generally difficult to derive its solution. As shown in [27, 28], we will use a critic NN to estimate the ideal cost function $V^*(e)$. In this paper, the cost

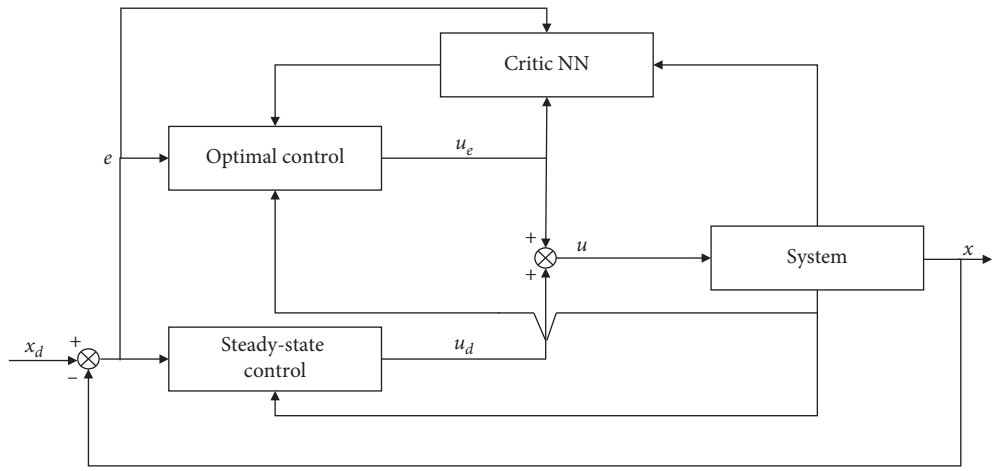

Figure 1: Schematic of the proposed control system.

function can be considered as smooth, then a critic NN [26, 28] is applied to approximate $V^*(e)$ as

$$V^*(e) = W^T\sigma(e) + \varepsilon(e), \tag{16}$$

where $W \in \mathfrak{R}^l$ is the ideal NN weight, $\sigma(e) \in \mathfrak{R}^l$ is the activation function, l is the number of neurons, and $\varepsilon(e)$ is the approximation error. Then, we have its derivative with respect to e as

$$\nabla V(e) = (\nabla\sigma(e))^T W + \nabla\varepsilon(e), \tag{17}$$

where $\nabla\sigma(e) = (\partial\sigma(e)/\partial e) \in \mathfrak{R}^{l\times n}$ and $\nabla\varepsilon(e) = (\partial\varepsilon(e)/\partial e) \in \mathfrak{R}^n$are the partial derivatives. Then, based on (17), equation (10) is represented as

$$0 = e^T Qe + u_e^{*T} Ru_e^* + \left(W^T\nabla\sigma(e) + (\nabla\varepsilon(e))^T\right)\dot{e}. \tag{18}$$

Assumption 2 (see [9, 26]). Consider the critic NN weight W with the regressor $\nabla\sigma(e)$, and then the error $\varepsilon(e)$ and its gradient $\nabla\varepsilon(e)$ are all bounded. Moreover, we have $\varepsilon(e) \longrightarrow 0$ and $\nabla\varepsilon(e) \longrightarrow 0$ as $l \longrightarrow \infty$.

According to ideal cost function (16), the actual cost function can be given as

$$\widehat{V}(e) = \widehat{W}^T\sigma(e), \tag{19}$$

which can be used to estimate the practical cost function. For critic NN (19), we can select $\sigma(e)$ such that $\widehat{V}(e) > 0$ for $e \neq 0$ and $\widehat{V}(e) = 0$ for $e = 0$. Then, we have

$$\nabla\widehat{V}(e) = (\nabla\sigma(e))^T\widehat{W}, \tag{20}$$

where $\nabla\widehat{V}(e) = (\partial\widehat{V}(e)/\partial e)$.

Then, the approximated Hamiltonian function can be derived as

$$0 \triangleq H(x, u, \widehat{W}) = e^T Qe + u_e^T Ru_e + \widehat{W}^T\nabla\sigma(e)\dot{e} = e_c. \tag{21}$$

For training the critic NN to obtain the control action, it is expected to estimate $\widehat{W}$ to minimize the objective function $E = (1/2)e_c^T e_c$. Hence, the gradient descent algorithm can be used to update the critic NN weights $\widehat{W}$ by

$$\dot{\widehat{W}} = -\Gamma\left[\frac{\partial E}{\partial\widehat{W}}\right] = -\Gamma e_c\left[\frac{\partial e_c}{\partial\widehat{W}}\right], \tag{22}$$

where $\Gamma > 0$ is the learning gain.

Based on (18), the Hamiltonian function is

$$0 = e^T Qe + u_e^{*T} Ru_e^* + W^T\nabla\sigma(e)\dot{e} = e_{c2}, \tag{23}$$

where $e_{c2} = -(\nabla\varepsilon(e))^T\dot{e}$ is the residual error.

Define $\vartheta = \nabla\sigma(e)\dot{e}$ and $\widetilde{W} = W - \widehat{W}$ as the estimation error of the critic NN weights, and a positive constant ϑ_M with $\|\vartheta\| \le \vartheta_M$. Then, from (21) and (23), we have $e_{c2} - e_c = \widetilde{W}^T\vartheta$. Hence, the estimation error dynamics are given by

$$\dot{\widetilde{W}} = -\dot{\widehat{W}} = \Gamma\left(e_{c2} - \widetilde{W}^T\vartheta\right)\vartheta. \tag{24}$$

The persistent excitation (PE) condition is required to retain the critic NN weights convergence and the condition $\|\vartheta\| \ge \vartheta_m$ with a positive constant ϑ_m. This condition can be satisfied in this paper since we consider the tracking control problem, and thus, the probing noise used in many existing ADP literature studies may be not necessary.

When implementing the online optimal control algorithm with critic NN (16), we have from (13) and (17) the optimal control as

$$u_e^* = -\frac{1}{2}R^{-1}g^T\left((\nabla\sigma(e))^T W + \nabla\varepsilon(e)\right). \tag{25}$$

Then, the approximated control action with critic NN (19) is formulated as

$$u_e^* = -\frac{1}{2}R^{-1}g^T(\nabla\sigma(e))^T\widehat{W}. \tag{26}$$

Equation (26) implies that with the updated critic NN weights $\widehat{W}$, the approximated control action can be calculated directly. Consequently, the widely used actor-critic structure can be simplified, and only the critic NN is adopted in this paper to reduce the computational cost.

Next, the stability of the proposed algorithm is given.

Lemma 1. *For error system (8) with control (26) and learning law (22), then the estimation error dynamics (24) are uniformly ultimately bounded (UUB).*

Proof. We select the Lyapunov function candidate as $J(t) = tr(\widetilde{W}^T\Gamma^{-1}\widetilde{W})$. Then, the time derivative of the Lyapunov function along the trajectory of error dynamics (24) is

$$\dot{J}(t) = 2tr\left(\widetilde{W}^T\Gamma^{-1}\dot{\widetilde{W}}\right) = 2tr\left(\widetilde{W}^T\left(e_{c2} - \widetilde{W}^T\vartheta\right)\vartheta\right). \quad (27)$$

After some mathematical manipulations, we have

$$\dot{J}(t) \leq -(2-\Gamma)\left\|\widetilde{W}^T\vartheta\right\|^2 + \frac{1}{\Gamma}e_{c2}^2. \quad (28)$$

Considering the Cauchy–Schwarz inequality and noticing the assumption $\|\vartheta\| \leq \vartheta_M$, we can conclude that $\dot{J}(t) < 0$ as long as $0 < \Gamma < 2$ and

$$\|\widetilde{W}\| > \sqrt{\frac{e_{c2}^2}{\Gamma(2-\Gamma)\vartheta_M^2}}. \quad (29)$$

According to the Lyapunov theory, we obtain that the estimation error is UUB.

4. Simulation

To demonstrate the validity of the developed method, a numerical simulation based on a SCARA robot plant is given. Consider the dynamics of a two degree-of-freedom SCARA robot system as

$$\dot{x} = \begin{bmatrix} \dot{x}_1 \\ \dot{x}_2 \end{bmatrix} = \begin{bmatrix} x_2 \\ -M^{-1}Cx_2 - M^{-1}G + M^{-1}u \end{bmatrix}, \quad (30)$$

where $x_1 = [\,q_1 \;\; q_2\,]$ and $x_2 = [\,\dot{q}_1 \;\; \dot{q}_2\,]$ are the SCARA robot's joint position and velocity vectors. The inverse of inertia matrix M^{-1}, Coriolis dynamics C, and gravity dynamics G is shown as

$$M^{-1} = \frac{\begin{bmatrix} b & -b-c \\ -b-c & a+b+2c \end{bmatrix}}{\left(ab-c^2\right)},$$
$$C = \begin{bmatrix} -2d\dot{q}_2 & -d\dot{q}_2 \\ d\dot{q}_1 & 0 \end{bmatrix}, \text{and } G = \begin{bmatrix} 0 \\ 0 \end{bmatrix}, \quad (31)$$

with $a = 0.613$, $b = 0.1173$, $c = 0.1584 \quad \cos(q_2)$, and $d = 0.1584\sin(q_2)$, and the detail modelling process can be found in [29].

Then, system (30) can be formulated as

$$\dot{x}(t) = f(x) + gu(t), \quad (32)$$

where $f(x) = [\,x_2 \;\; -M^{-1}(Cx_2 + G)\,]^T$ denote the drift dynamics and $g = [\,0 \;\; M^{-1}\,]^T$ denotes the control gain. To complete the optimal tracking control, equation (7) for system (30) can be given as $u_d = g^+[\dot{x}_d - f(x) - Ke]$ with $K = 0.8$. The initial critic NN weights are selected as

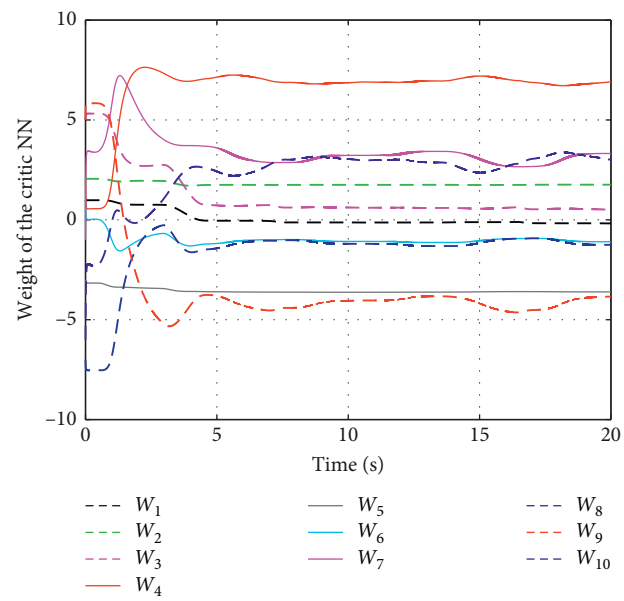

Figure 2: Convergence of the critic NN weights.

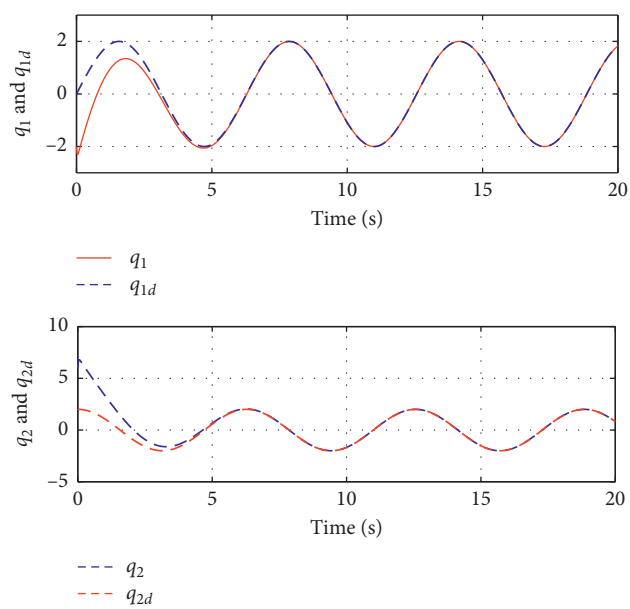

Figure 3: Position tracking of joint 1 and joint 2 of SCARA.

$\widehat{W} = [\,1 \;\; 2 \;\; 5 \;\; 2 \;\; -3 \;\; 1 \;\; -1 \;\; -7 \;\; 5 \;\; -6\,]^T$, and the initial system states are $x_1 = [-2, 6]^T$ and $x_2 = [-2.4, 1]^T$. In the learning process, we set the learning gain as $\Gamma = 0.02$. The activation function of the critic NN is chosen as $\sigma = [e_1^2, e_1e_2, e_1e_3, e_1e_4, e_2^2, e_2e_3, e_2e_4, e_3^2, e_3e_4, e_4^2]$, and the weighting matrices Q and R are selected as identity matrices as [29]. The desired trajectory x_d are given as $x_d = [q_{1d}, q_{2d}, dq_{1d}, dq_{2d}]$, where $q_{1d} = 2\sin(t)$, $q_{2d} = 2\cos(t)$, $dq_{1d} = q_{2d}$, and $dq_{2d} = -q_{1d}$. During the implementation of the policy iteration algorithm, we take the sinusoidal signals as the reference and thus the persistence excitation condition

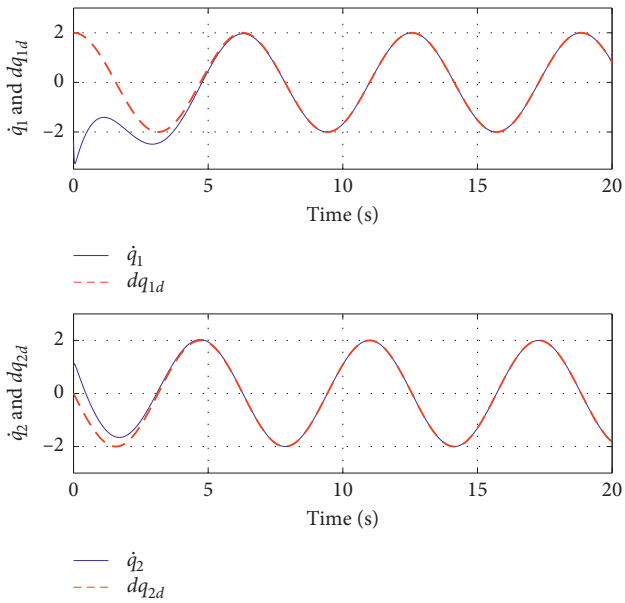

Figure 4: Velocity tracking of joint 1 and joint 2 of SCARA.

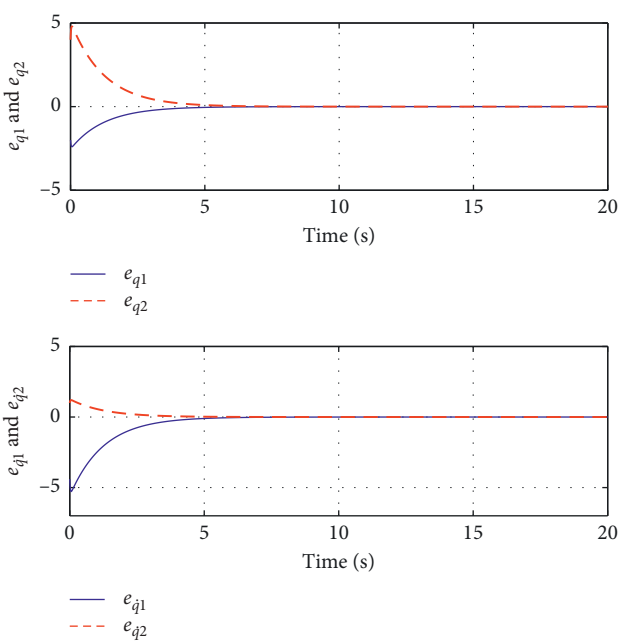

Figure 5: Tracking error convergence.

has been fulfilled. In this case, the probing noise introduced into the system can be avoided.

With these parameter configurations, numerical simulations are conducted and simulation results are given in Figures 2–5. The online profile of the approximated critic NN weights $\widehat{W}$ with proposed adaptive law (22) are displayed in Figure 2, which converge to the vector $[-0.4847, 1.6323, -0.4100, 6.0223, -3.8430, -1.3071, 1.9629, -2.2160, -3.7896, 2.9225]^T$ after a short transient stage. Clearly, we can find that the weights are convergent when

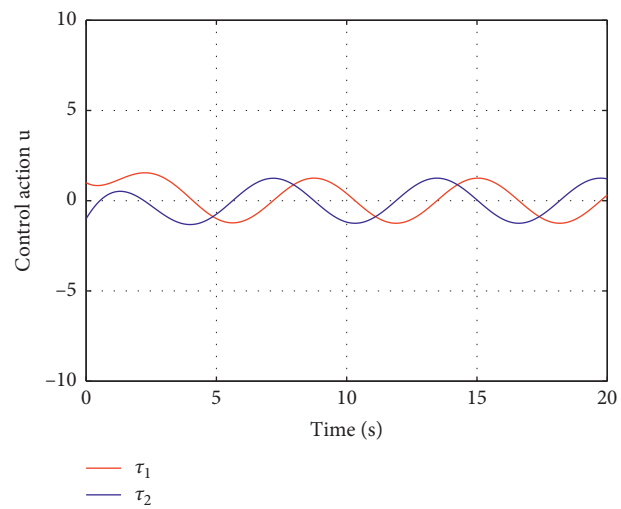

Figure 6: Control action (u).

performing the proposed online learning. With these online updated critic NN weights, the estimated control can converge to the ideal solution. As a consequence, the system tracking performances are given in Figures 3 and 4, which indicate that the system states can track the desired trajectories with the proposed optimal control. To better show the motion tracking results, the tracking errors are given in Figure 5, which converge to zero with very smooth profiles. Moreover, the control input is given as Figure 6, which is also bounded. It can be found from above simulations that the proposed optimal control can realize perfect tracking control. Specifically, the proposed RL algorithm can retain convergent response for the critic NN.

5. Conclusion

The optimal tracking control design for robotic systems using the RL algorithm is presented in this paper. The system model is first transformed into a canonical form, which can facilitate the realization of optimal tracking control design. To maintain the tracking response, a steady-state control is designed, and then an optimal tracking control is used to ensure the tracking error dynamics to be optimal. The online RL algorithm is dedicated to solving the HJB equation using a critic NN. Numerical simulations are given to show the effectiveness of the proposed technique. We will study the nonlinear optimal tracking problem with fully unknown system dynamics in the future work.

Data Availability

The data used to support the findings of this study were curated by the authors and are available upon request.

Conflicts of Interest

The authors declare that there are no conflicts of interest regarding the publication of this paper.

Acknowledgments

This work was supported by the National Key R&D Project (2016YFE0202300), National Natural Science Foundation of China (U1903214, 62071339, 61671332, and U1736206), and Hubei Province Technological Innovation Major Project (2019AAA049).

References

[1] R. S. Sutton and A. G. Barto, *Reinforcement Learning: An Introduction*, MIT press, Cambridge, MA, USA, 1998.

[2] F. L. Lewis and D. Liu, *Reinforcement Learning and Approximate Dynamic Programming for Feedback Control*, Vol. 17, John Wiley and Sons, Hoboken, NJ, USA, 2013.

[3] W. B. Powell, *Approximate Dynamic Programming: Solving the Curses of Dimensionality*, Vol. 703, John Wiley & Sons, Hoboken, NJ, USA, 2007.

[4] H. Zhang, D. Liu, Y. Luo, and D. Wang, *Adaptive Dynamic Programming for Control: Algorithms and Stability*, Springer Science and Business Media, Berlin, Germany, 2012.

[5] S. Bhasin, R. Kamalapurkar, M. Johnson, K. G. Vamvoudakis, F. L. Lewis, and W. E. Dixon, "A novel actor-critic-identifier architecture for approximate optimal control of uncertain nonlinear systems," *Automatica*, vol. 49, no. 1, pp. 82–92, 2013.

[6] Y. Lv, J. Na, Q. Yang, X. Wu, and Y. Guo, "Online adaptive optimal control for continuous-time nonlinear systems with completely unknown dynamics," *International Journal of Control*, vol. 89, no. 1, pp. 99–112, 2016.

[7] S. Chen Anthony and H. Guido, "Adaptive optimal control via continuous-time Q-learning for unknown nonlinear affine systems," in *Proceedings of the 2019 IEEE 58th Conference on Decision and Control (CDC)*, pp. 1007–1012, IEEE, Nice, France, December 2019.

[8] J. Y. Lee, J. B. Park, and Y. H. Choi, "Integral Q-learning and explorized policy iteration for adaptive optimal control of continuous-time linear systems," *Automatica*, vol. 48, no. 11, pp. 2850–2859, 2012.

[9] M. Abu-Khalaf and F. L. Lewis, "Nearly optimal control laws for nonlinear systems with saturating actuators using a neural network HJB approach," *Automatica*, vol. 41, no. 5, pp. 779–791, 2005.

[10] D. Vrabie and F. Lewis, "Neural network approach to continuous-time direct adaptive optimal control for partially unknown nonlinear systems," *Neural Networks*, vol. 22, no. 3, pp. 237–246, 2009.

[11] K. G. Vamvoudakis, D. Vrabie, and F. L. Lewis, "Online adaptive algorithm for optimal control with integral reinforcement learning," *International Journal of Robust and Nonlinear Control*, vol. 24, no. 17, pp. 2686–2710, 2014.

[12] Y. Jiang and Z.-P. Jiang, "Computational adaptive optimal control for continuous-time linear systems with completely unknown dynamics," *Automatica*, vol. 48, no. 10, pp. 2699–2704, 2012.

[13] R. Song, F. L. Lewis, and Q. Wei, "Off-policy integral reinforcement learning method to solve nonlinear continuous-time multiplayer nonzero-sum games," *IEEE Transactions on Neural Networks and Learning Systems*, vol. 28, pp. 704–713, 2016.

[14] R. Song, Q. Wei, and Q. Li, "Off-policy integral reinforcement learning method for multi-player non-zero-sum games," in *Adaptive Dynamic Programming: Single and Multiple Controllers*, pp. 227–249, Springer, Berlin, Germany, 2019.

[15] H. Modares, F. L. Lewis, and M.-B. Naghibi-Sistani, "Integral reinforcement learning and experience replay for adaptive optimal control of partially-unknown constrained-input continuous-time systems," *Automatica*, vol. 50, no. 1, pp. 193–202, 2014.

[16] H. Modares and F. L. Lewis, "Optimal tracking control of nonlinear partially-unknown constrained-input systems using integral reinforcement learning," *Automatica*, vol. 50, no. 7, pp. 1780–1792, 2014.

[17] Y. Lv, X. Ren, and J. Na, "Online Nash-optimization tracking control of multi-motor driven load system with simplified RL scheme," *ISA Transactions*, vol. 98, pp. 251–262, 2020.

[18] J. Na and G. Herrmann, "Online adaptive approximate optimal tracking control with simplified dual approximation structure for continuous-time unknown nonlinear systems," *IEEE/CAA Journal of Automatica Sinica*, vol. 1, pp. 412–422, 2014.

[19] G. Xiao, Y. Luo, H. Zhang, and H. Jiang, "Data-driven optimal tracking control for a class of affine non-linear continuous-time systems with completely unknown dynamics," *IET Control Theory and Applications*, vol. 10, no. 6, pp. 700–710, 2016.

[20] H. Modares and F. L. Lewis, "Linear quadratic tracking control of partially-unknown continuous-time systems using reinforcement learning," *IEEE Transactions on Automatic Control*, vol. 59, no. 11, pp. 3051–3056, 2014.

[21] Y. Lv, X. Ren, and J. Na, "Adaptive optimal tracking controls of unknown multi-input systems based on nonzero-sum game theory," *Journal of the Franklin Institute*, vol. 356, no. 15, pp. 8255–8277, 2019.

[22] F. Piltan, N. Sulaiman, H. Nasiri, S. Allahdadi, and M. A. Bairami, "Novel robot manipulator adaptive artificial control: design a novel siso adaptive fuzzy sliding algorithm inverse dynamic like method," *International Journal of Engineering*, vol. 5, pp. 399–418, 2011.

[23] L. Peng and P.-Y. Woo, "Neural-fuzzy control system for robotic manipulators," *IEEE Control Systems Magazine*, vol. 22, pp. 53–63, 2002.

[24] Y.-C. Chang and B.-S. Chen, "A nonlinear adaptive H/sup/spl infin//tracking control design in robotic systems via neural networks," *IEEE Transactions on Control Systems Technology*, vol. 5, pp. 13–29, 1997.

[25] D. Zhao, S. Li, and Q. Zhu, "Adaptive synchronised tracking control for multiple robotic manipulators with uncertain kinematics and dynamics," *International Journal of Systems Science*, vol. 47, no. 4, pp. 791–804, 2016.

[26] D. Wang, D. Liu, and H. Li, "Policy iteration algorithm for online design of robust control for a class of continuous-time nonlinear systems," *IEEE Transactions on Automation Science and Engineering*, vol. 11, no. 2, pp. 627–632, 2014.

[27] Y. Lv and X. Ren, "Approximate Nash solutions for multi-player mixed-zero-sum game with reinforcement learning," *IEEE Transactions on Systems, Man, and Cybernetics: Systems*, vol. 49, pp. 2739–2750, 2018.

[28] J. Zhao, J. Na, and G. Gao, "Adaptive dynamic programming based robust control of nonlinear systems with unmatched uncertainties," *Neurocomputing*, vol. 395, pp. 56–65, 2020.

[29] J. Na, M. N. Mahyuddin, G. Herrmann, X. Ren, and P. Barber, "Robust adaptive finite-time parameter estimation and control for robotic systems," *International Journal of Robust and Nonlinear Control*, vol. 25, no. 16, pp. 3045–3071, 2015.

Hindawi
Complexity
Volume 2021, Article ID 8704924, 10 pages
https://doi.org/10.1155/2021/8704924

Research Article

Multisensor-Weighted Fusion Algorithm Based on Improved AHP for Aircraft Fire Detection

Rui Wang,[1] **Yahui Li**,[1] **Hui Sun**,[1] **and Kaixin Yang**[2]

[1]*College of Information Engineering and Automation, Civil Aviation University of China South Campus, Tianjin 300300, China*
[2]*Tianjin College, University of Science & Technology Beijing, Tianjin 301830, China*

Correspondence should be addressed to Hui Sun; shhappy1@hotmail.com

Received 18 July 2020; Revised 10 August 2020; Accepted 11 January 2021; Published 28 January 2021

Academic Editor: Mojtaba Ahmadieh Khanesar

Aiming at the high false alarm rate when using single sensor to detect fire in aircraft cabin, a multisensor data fusion method is proposed to detect fire. First, the weights of multiple factors, that is, temperature, smoke concentration, CO concentration, and infrared ray intensity in the event of fire, were calculated by using the improved analytic hierarchy process (AHP) method on each sensor node of wireless sensor network, and the probability of fire event in the cabin was evaluated by multivariable-weighted fusion method. Second, based on the mutual support among the evaluation data of fire probabilities of each node, the adaptive weight coefficient is assigned to each evaluation value, and the weighted fusion of all evaluation values of each node is conducted to obtain the fire probability. In the end, compared to the threshold of probability, the fire alarm is determined. Comparing the proposed algorithm to the grey fuzzy neural network fusion algorithm and fuzzy logic fusion algorithm in terms of the time consumption for fire detection and sending alarm and the accuracy of fire alarm perspectives, the experiments demonstrate that the proposed fire detection algorithm can detect the fire within 10*s* and reduce the false alarm rate to less than 0.5%, which verifies the superiority of the algorithm in promptness and accuracy. In the meanwhile, the fault tolerance of the algorithm is proved as well.

1. Introduction

It is well known that safety is always the priority for aircrafts flights; furthermore, fire is a big threat for flight safety. Therefore, fire detection issues for aircrafts have become the focus for aircraft environmental monitoring. It is necessary to develop an effective method to realize the real-time and effective monitoring of cabin environments and provide the timely and accurate alarm for emergencies. Tracking and estimating the target system can effectively monitor the system condition [1–3]. At present, fire alarm method can only make alarm decision based on specific parameters (such as temperature, smoke, fire, and gas), which is vulnerable to external interferences and often gives false alarm [4]. For example, when the dust particles in the cabin reach a certain concentration, the sensor will mistakenly consider them as flame smokes and then send an alarm signal. There are multiple false fire alarms for the aircraft industrial applications. For example, on March 4, 2019, a Boeing 777 flying from Beijing to Los Angeles made an emergency landing at Russia's Anadyr Airport because a fire alarm broke out in the rear cargo compartment during flight. Unfortunately, after inspections, the cargo hold was normal and there was no sign of fire. At the end, it was concluded that the aircraft fire information was out of order. Once the fire alarm signal is sent, an emergency landing is required. Therefore, false fire alarms definitely affect the safety, increase the burden of crew works, and bring about more economy loss for civil aviation industry. In the future, aircraft manufacturing will develop towards flying wirelessly instead of flying by wire; therefore, it will become a trend to use WSN technology for aircraft cabin or cargo environment monitoring. For example, Wang et al. utilized the distributed wireless sensor monitoring network to monitor and estimate multiple contaminants and overcome the hypersensitivity of the single sensor in

aircraft cabins [5, 6]. Currently, WSN-based multisensor indoor fire detection technology usually uses the data detected by multiple sensors to fuse and obtain the probability of fire event, which greatly improves the accuracy of fire alarms. General methods of multisensor data fusion include fuzzy logic fusion based on neural network [7], fuzzy logic fusion [8], and D-S evidence inference [9]. The above method fuses the environmental information collected by temperature sensor, smoke sensor, CO gas sensor, and flame infrared ray sensor, effectively improving the accuracy of fire detection.

The above commonly used fusion algorithms mainly rely on the establishment of fuzzy reasoning rules and the construction of neural networks. Although the detection accuracy is greatly improved to some extent when the input variables are increased, the detection and decision time becomes longer. However, China civil aviation regulations article 25.858 states that the fire alarm should be notified to the flight crew by visual indication in less than one minute. Therefore, it is necessary to design a method to more accurately and timely determine the fire alarm when fusing multiple variables. Some existing literatures demonstrate that the fuzzy logic fusion algorithm based on neural network can make the fusion result close to the real result by means of connecting weights between training networks [10, 11]. However, when the input variable increases, the number of network layers increases, the data set to be trained increases, and the detection time increases. In order to shorten the fusion time to some extent, the weight of each fusion variable in the probability assessment of fire event can be considered; then, the sensor data can be estimated. Among them, analytic hierarchy process (AHP) is widely used in multivariable weight calculation and system state evaluation [12–15]. For example, Yang et al. used fuzzy AHP and deviation maximization method to determine the subjective and objective weight of each index and evaluated the risk degree of voltage sag of each observation point by weighting the comprehensive weight and its pressure drop, so as to take corresponding measures timely [12].

Various fusion methods introduced above are all under the assumption that the sensors work normally under the ideal conditions for fire alarm system; however, environmental complexity and uncertainty often cause sensor malfunctions, further cause the large deviation, and seriously affect the fusion result. In order to avoid the above problem, relevant works have been conducted partly in the following researches. Yu et al. defined the relationship between data as conditional function dependence and microfunction dependence, so as to avoid inaccuracy caused by inconsistency of data to a certain extent [16]. Yang et al. proposed a multisensor weighted fusion method based on augmented support matrix to avoid the low fusion accuracy [17].

The main contributions of this paper are conducted from the promptness and accuracy requirement for the aircraft environment, respectively. First, this paper designs a new "multivariable-weighted fusion" fire assessment algorithm based on the improved AHP. Therefore, the algorithm can quickly detect the fire situation when fusing variables simultaneously and greatly reduce the false alarm rate. Second, this paper develops an adaptive-weighted fusion method to fuse the multiple variables for each sensor node when some sensors malfunction. By constructing the support degree matrix as the adaptive distribution weight coefficient of each node, to a certain extent, the proposed method avoids the low fusion accuracy due to the measurement deviation coming from the faulty sensors.

The structure of this paper is arranged as follows. The first section is the introduction. In Section 2, an improved AHP and multivariable-weighted fusion algorithm are introduced to evaluate the probability of fire event for each sensor node. Section 3 proposes an adaptive-weighted fusion method to evaluate the probability of fire event of all nodes when some sensors malfunction. Section 4 presents the simulation experiments verifying the accuracy, fast response, and fault tolerance of the proposed algorithm. The conclusion of this paper is drawn in Section 5.

2. A Fire Assessment Algorithm Based on a Multivariable-Weighted Fusion

In this section, an improved AHP method is studied and a multivariable weight calculation method is proposed to determine the weight of temperature, smoke concentration, CO concentration, and infrared ray intensity for fire event. A new "multivariable-weighted fusion" algorithm is proposed at each sensor node of WSN to obtain the evaluation value of each node on the probability of fire event in the cabin.

2.1. Multivariable Weight Calculation Based on Improved AHP Method. To evaluate and judge the fire events in aircrafts, it is necessary to determine weight of the relevant variables scientifically and reasonably for the fire evaluation process. This paper mainly adopts the improved AHP method to determine the weight of variables [18]. In traditional AHP, the weight of influencing factors in event decision-making is obtained by selecting a reasonable judgment matrix. However, due to the randomness of judgment matrix selection, the calculated weight may be deviated from the actual weight. In order to ensure that the obtained weights can reflect the influence degree of variables more accurately, the improved AHP calculates the optimal weight of variables in the weight interval by selecting several reasonable judgment matrices. The optimal weight is closer to the actual influence degree of variables.

The basic process of the improved AHP method for evaluating fire events is introduced as follows:

Step 1: suppose that the variables determining the fire event probability are temperature, smoke concentration, CO concentration, and infrared ray intensity. The variables are expressed as $x_i\,(i = 1, 2, 3, 4)$ and i is the subscript of the variable. denote x_1 as the temperature, x_2 as the smoke concentration, x_3 as the CO concentration, and x_4 as the infrared light intensity.

Step 2: establish the judgment matrix.

The influence degree relation between variables is expressed quantitatively by the judgment matrix. Let the judgment matrix be $C\varepsilon R^{n\times n}$, where n represents the number of variables [19].

The form of the judgment matrix C is

$$C = \begin{bmatrix} c_{11} & c_{12} & \cdots & c_{1n} \\ c_{21} & c_{22} & \cdots & c_{2n} \\ \vdots & \cdots & \cdots & \vdots \\ c_{n1} & c_{n2} & \cdots & c_{nn} \end{bmatrix}. \quad (1)$$

The matrix element, $c_{ij} = x_i/x_j$ (i and j are the variable indexes), represents the importance degree for variables determining the probability of fire event.

The rule for determining element c_{ij} is shown below:

If x_i and x_j are equally important, then $c_{ij} = 1$ and $c_{ji} = 1$
If x_i is slightly more important than x_j, then $c_{ij} = 3$ and $c_{ji} = 1/3$
If x_i is obviously more important than x_j, then $c_{ij} = 5$ and $c_{ji} = 1/5$
If x_i is much more important than x_j, then $c_{ij} = 7$ and $c_{ji} = 1/7$
If x_i is absolutely more important than x_j, then $c_{ij} = 9$ and $c_{ji} = 1/9$

If the importance relationship for x_i and x_j is located between the relationships illustrated above, c_{ij} can also select 2, 4, 6, and 8. In fact, the element c_{ij} can be any integer between 1 and 9 [20].

Step 3: check the consistency of the judgment matrix.

In this paper, the improved AHP can calculate the optimal weight of each variable by selecting multiple judgment matrices. In order to avoid a large error between the weights obtained, the consistency of C should be tested. When the judgment matrix C is completely consistent, $c_{ij} = 1$, $\sum_{i=1}^{n} \lambda_i = \sum_{i=1}^{n} c_{ij} = n$ (λ is the eigenvalue of matrix C), a unique nonzero $\lambda = \lambda_{\max} = n$ exists. When the judgment matrix is inconsistent, $\lambda_{\max} \geq n$.

At this moment,

$$\lambda_{\max} + \sum_{i\neq \max}^{n} \lambda_i = \sum_{i=1}^{n} n. \quad (2)$$

Then,

$$\lambda_{\max} - n = -\sum_{i\neq \max}^{n} \lambda_i. \quad (3)$$

The average value is used as the index to test the consistency of judgment matrix:

$$\text{C.I.} = \frac{\lambda_{\max} - n}{n-1} = \frac{-\sum_{i=\max}\lambda_{\max}}{n-1}. \quad (4)$$

When $\lambda_{\max} = n$ and $C.I. = 0$, C can be judged to be exactly consensus. The larger the $C.I.$ is, the worse the consistency of the judgment matrix will be. Generally, it is only required that the consistency of the matrix be reasonable if C.I. ≤ 0.1.

The consistency of the judgment matrix is related to its dimension. The greater the dimension n of the judgment matrix is, the worse the consistency of the judgment matrix is. Therefore, the consistency requirement of high-dimensional judgment matrix should be relaxed. In this case, the modified RI (RI values are listed in Table 1 [21]) can be introduced and the more reasonable value, $C.R.$, can be taken as the index to measure the consistency of the judgment matrix. When $C.R. < 0.1$, it is generally considered that the consistency of the judgment matrix is acceptable.

Step 4: calculate the weight intervals of variables by using the eigenvector method.

Based on the judgment matrix constructed above, the weight of each variable was calculated by the eigenvector method, and the calculated weight was written into the form of interval, denoted as the weight interval of the variable (the interval is composed of independent weight points).

After arbitrarily selecting a reasonable judgment matrix, a weight of variable can be calculated according to the eigenvector method. The calculation formulas are listed as follows [22]:

$$M_{i,k} = \prod_{j=1}^{n} c_{ij,k}, \quad (5)$$

$$W_{i,k} = \sqrt[n]{M_{i,k}}, \quad (6)$$

$$\overrightarrow{W}_{i,k} = \frac{W_{i,k}}{\sum_{i=1}^{n} W_{i,k}}, \quad (7)$$

where i is the variable index ($i = 1, 2, 3, 4$) and k is the number of reasonably selected judgment matrices ($k \in N^+$). $\overrightarrow{W}_{i,k}$ is a weight value for the ith variable under the kth judgment matrix. So, there are k weights for each variable i.

The k weights of each variable obtained above are written in the form of interval, which is the weight interval of the variable. For any variable i, selecting k judgment matrices, a weight interval of variable i can be obtained by using formulas (5)–(7), and the interval contains k weights.

Step 5: obtain the optimal weight.

The optimal weight fully considers all weights during the weight interval so as to ensure that the final evaluation result can better reflect the actual situations. At the same time, the optimal weight fusion can effectively avoid the tedious calculation process in fusion and improve the response speed of fire event evaluation. Suppose that W_i represents a

Table 1: *RI* values under different orders of judgment matrices.

The order of the matrix	RI
1	0
2	0
3	0.52
4	0.89
5	1.12
6	1.26
7	1.36
8	1.41

weight of the variable i, and the reasonable judgment matrix is $m(m \in N^+)$; the objective function is constructed as

$$\min \sum_{i=1}^{4} \sum_{k=1}^{m} \left(\overrightarrow{W}_{i,k} - w_i \right)^2. \quad (8)$$

The constraint condition of the objective function is

$$\sum_{i=1}^{4} w_i = 1. \quad (9)$$

Based on formulas (8) and (9), the optimal weight of the ith variable is denoted as w_i^*.

2.2. Fire Probability Assessment Algorithm Based on Variable-Weighted Fusion. According to the actual value of each variable in different environments, the interval of temperature (°C) is set in the range of [0, 100], smoke concentration (ppm) is located in the range of [100, 1000], CO concentration (ppm) lies in the range of [10, 100], and infrared ray intensity (lux) is placed in the range of [100, 1000]. Each variable range is normalized in the range of [0-] by using the following formula [23]:

$$x_i^* = \frac{x_i - \min(x_i)}{\max(x_i) - \min(x_i)}, \quad (10)$$

where $\max(x_i)$ is the maximum value for variable i and $\min(x_i)$ is the minimum value for variable i.

Suppose N sensor nodes are deployed in the aircraft, the normalized variable value is denoted as x_i^* $(i = 1, 2, 3, 4)$, the optimal weight of the variable is w_i^* $(i = 1, 2, 3, 4)$, the weighted result of variables is the fire probability, and the calculation formula is

$$p_{i^*} = \sum_{i=1}^{4} x_i^* w_i^*, \quad i^* \varepsilon 1, 2, \ldots, N, \quad (11)$$

where p_{i*} is the assessment result of the probability of fire for node i^*.

3. An Adaptive-Weighted Fusion Algorithm Based on Support Degree Matrix

In order to ensure the accuracy of fire alarm, it is necessary to adaptively fuse the fire probability values coming from each node. At the same time, in order to avoid the impact resulting from sensor failures on the accuracy of fusion results, this section proposes an adaptive-weighted fusion algorithm based on support degree matrix. This algorithm can objectively demonstrate the support degree among each node data and even the unknown assessment ability of the fire event probability for each node. By constructing the augmented matrix, the weight coefficients of fire probability assessment for each node are adaptively adjusted in order to achieve the best fusion. The characteristics of this algorithm include online data fusion for a large amount of data as well as better fault tolerant capability by adaptively allocating the weight coefficients according to the reliability.

3.1. Support Degree Matrix Construction. Assume that there are N sensor nodes (each node is composed of temperature, smoke concentration, CO concentration, and intensity of the infrared light sensors) to measure the environment variables and calculate the fire event probability. Let $p_i * (k)$ and $p_j * (k)$ represent the fire event probability evaluation values of sensor nodes i^* and j^* $(i^*, j^* \epsilon (1, 2, \ldots, N))$ at the moment k, respectively. When the difference between $p_i * (k)$ and $p_j * (k)$ is too large, these two sensor nodes do not support each other at time k. If the difference is small, it means that these two nodes support each other. If a node is supported by many nodes at the same time, it can be considered as a valid fire probability assessment value. Otherwise, the node will be assigned a lower weight during the fusion process.

Define a support degree function, $r_{i^* j^*}(k)$, which employs the exponential function in the fuzzy set to express the mutual support degree between $p_i * (k)$ and $p_j * (k)$:

$$r_{i^* j^*}(k) = \exp\left(-\alpha \cdot \left(p_{i^*}(k) - p_{j^*}(k) \right)^2 \right). \quad (12)$$

The parameter α can be adjusted in order to alter the fusion accuracy conveniently, generally set to 0.8 [17].

At the moment k, the mutual support degree of sensors i^* and j^* can be described in a matrix according to the support degree function $r_i * {}_j * (k)$:

$$R_N^{(k)} = \begin{bmatrix} 1 & r_{12}(k) & \cdots & r_{1N}(k) \\ r_{21}(k) & 1 & \cdots & r_{2N}(k) \\ \cdots & \cdots & \cdots & \cdots \\ r_{N1}(k) & r_{N2}(k) & \cdots & 1 \end{bmatrix}. \quad (13)$$

As for the elements in the $i^{*\text{th}}$ column of $R_N^{(k)}$, the bigger $\sum_{j^*=1}^{N} r_{i^* j^*}(k)$ is, the more reliable node i^* is, and vice versa.

3.2. Augmented Support Degree Matrix Construction. At each sampling time, the proposed method adds a new row and a new column in the original support degree matrix to integrate all the assessments and forms a new augmented support degree matrix. The newly inserted dimension aims at measuring the mutual support degree between all current assessments and previous assessments.

Augmented dimension can be obtained by the following steps:

(1) When $k = 1$, define the average of the first N assessment values $\overline{p}$ (1) as the initial estimate $\widehat{p}_0$.

(2) The augmented row and column at time k are

$$\begin{cases} r_{i^*(N+1)}(k) = \exp\left(-\alpha \cdot \left(p_{i^*} - \widehat{p}_{k-1}\right)^2\right), \\ r_{(N+1)j^*}(k) = \exp\left(-\alpha \cdot \left(\widehat{p}_{k-1} - p_{j^*}\right)^2\right), \\ r_{(N+1)(N+1)}(k) = 1, \end{cases} \tag{14}$$

where $\widehat{p}_{k-1}$ represents the fused result at time $(k-1)$.

(3) The following formula can be used to obtain the augmented support degree matrix at time k:

$$R_{N+1}^{(k)} = \begin{bmatrix} 1 & \cdots & r_{1N}(k) & r_{1(N+1)}(k) \\ \cdots & 1 & \cdots & \cdots \\ r_{N1}(k) & \cdots & 1 & r_{N(N+1)}(k) \\ r_{(N+1)1}(k) & \cdots & r_{(N+1)N}(k) & 1 \end{bmatrix}, \tag{15}$$

where $R_{N+1}^{(k)}$ is the integrated support degree of all the nodes at each sampling time.

3.3. Adaptive-Weighted Fusion Based on the Assessment Values of Each Node. Let $w_i * (k)$ denote the fusion weight coefficient of $p_i * (k)$ ($w_{N+1}(k)$ is the weight coefficient of the fusion result $\widehat{p}_{k-1}$ at the time of $(k-1)$); $w_i * (k)$ satisfies

$$\sum_{i^*=1}^{N+1} w_{i^*}(k) = 1, \quad 0 \le w_{i^*}(k) \le 1. \tag{16}$$

In the augmented support degree matrix, $R_{N+1}^{(k)}$, the weight coefficient of $p_i * (k)$ can be obtained by integrating the $i^{*\text{th}}$ column of $R_{N+1}^{(k)}$. Assume that there is a set of vectors, $b_{j^*}(k)$ ($j^* = 1, \ldots, N+1$), and each element is the result of integration with respect to $r_j * {}_i * (k)$ for i^*, and $w_i * (k)$ is

$$w_{i^*}(k) = b_1(k) r_{1i^*}(k) + \cdots + b_{N+1}(k) r_{(N+1)i^*}(k), \tag{17}$$

where $i^*, j^* = 1, 2, \ldots, N+1$.

According to (15), we rewrite (17) as

$$W = R_{N+1}^{(k)} B, \tag{18}$$

where $W = [w_1(k), w_2(k), \cdots, w_{N+1}(k)]^T$ and $B = [b_1(k), b_2(k), \cdots, b_{N+1}(k)]^T$.

Since $r_{i^*j^*}(k) \ge 0$, $R_{N+1}^{(k)}$ is a nonnegative symmetrical matrix and is based on Perron–Frobenius theorem, the maximum modulus eigenvalue λ^* can be calculated ($\lambda^* > 0$) [24].

Then,

$$\lambda^* B = R_{N+1}^{(k)} B. \tag{19}$$

Calculate the positive eigenvector B corresponding to λ^*:

$$W = \lambda^* B. \tag{20}$$

The weight coefficient is proportional to that of eigenvectors, and the relationship is shown in the following equation:

$$\frac{w_{i^*}(k)}{w_{j^*}(k)} = \frac{b_{i^*}(k)}{b_{j^*}(k)}. \tag{21}$$

According to (16), the weight coefficient of each node is

$$w_{i^*}(k) = \frac{b_{i^*}(k)}{b_1(k) + \cdots + b_{N+1}(k)} = \frac{b_{i^*}(k)}{\sum_{j^*=1}^{N+1} b_{j^*}(k)}, \tag{22}$$

where $i^*, j^* = 1, 2, \ldots N+1$.

Then, the final fusion expression is obtained by

$$\widehat{p}_k = \sum_{i^*=1}^{N+1} w_{i^*}(k) p_{i^*}(k) = \sum_{i^*=1}^{N+1} \frac{b_{i^*}(k)}{\sum_{j^*=1}^{N+1} b_{j^*}(k)} p_{i^*}(k), \tag{23}$$

where $\widehat{p}_k$ represents the fire event probability in the aircraft environment after data fusion. Comparing it to the fire threshold probability, if the probability is greater than the threshold, the system will send out a fire alarm signal.

According to [25, 26], the critical value of fire event is set as follows: temperature is 55°C, smoke concentration is 700 ppm, CO concentration is 20 ppm, and infrared light intensity is 760 lux. The above variables are normalized, and the result of the fire threshold probability is obtained by (11).

Two portions, online and offline fire event detection processes, are included in the proposed algorithm for aircraft cabins in the paper. The specific steps are listed in Figure 1. Steps 1 to 5 in the second section are used for the offline weight calculation, aiming at obtaining the weight of variable x_i ($i = 1, 2, 3, 4$). Furthermore, the online detection process includes three steps. First, the measured environmental variables are normalized by formula (10). Second, the fire probability is evaluated by formula (11) for each node. Third, use the adaptive-weighted fusion algorithm to calculate the actual fire probability $\widehat{p}_k$ in the aircraft and compare it with the threshold probability to determine whether a fire alarm is released or not (Figure 1).

4. Simulation Experiments Analysis

In this section, suppose that 50 sensor nodes are placed in aircraft cabin and cargo. Each node is composed of temperature, smoke concentration, CO concentration, and infrared ray intensity sensors. The deployment schematic diagram of nodes is shown in Figure 2. The environmental parameters collected at each node are $X^{i^*} = [x_1, x_2, x_3, x_4]$ ($i^* = 1, 2, \ldots, 50$), and the units for each variable are °C for temperature, ppm for smoke concentration and CO concentration, and lux for infrared ray intensity, respectively. Under the same experimental conditions, the proposed online fire detection algorithm is compared to the grey fuzzy neural network fusion algorithm in [7] and the fuzzy logic fusion algorithm in [8] to verify the superiority of online fire detection algorithm in terms of promptness, accuracy, and fault tolerance.

4.1. The Optimal Weight Calculation for Each Variable. As illustration about variable weights calculation in the second section, the assumptions about the influence degree ranking for each variable x_i ($i = 1, 2, 3, 4$) are placed as follows:

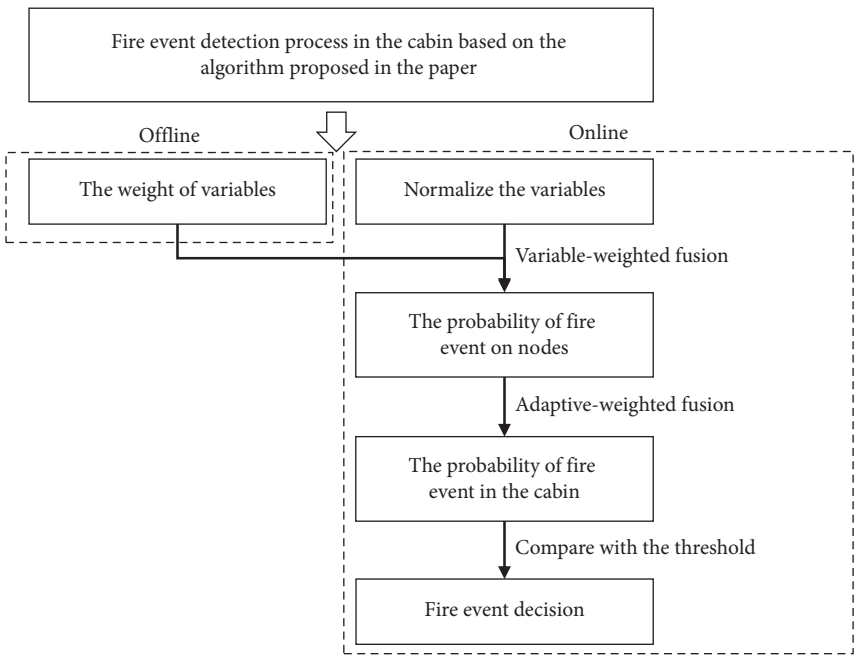

Figure 1: Fire detection flowchart.

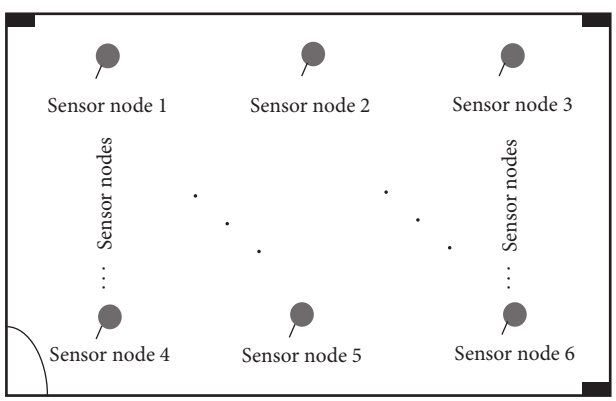

Figure 2: Schematic diagram of sensor node deployment for fire detection.

$$\begin{aligned}
&\text{Assumption 1: } x_1 > x_2 > x_3 > x_4,\\
&\text{Assumption 2: } x_1 > x_2 > x_4 > x_3,\\
&\text{Assumption 3: } x_1 > x_3 > x_2 > x_4,\\
&\text{Assumption 4: } x_1 > x_3 > x_4 > x_2,\\
&\text{Assumption 5: } x_1 > x_4 > x_2 > x_3,\\
&\text{Assumption 6: } x_1 > x_4 > x_3 > x_2,\\
&\qquad\vdots\\
&\text{Assumtpion 24: } x_4 > x_3 > x_2 > x_1.
\end{aligned} \tag{24}$$

There are 24 assumptions in total named as A1, A2, ... A24.

According to the assumptions given above, calculate the weight interval of each variable when k was 5 (B_1~B_5 are judgment matrices) and the optimal weight of each variable within the weight interval based on formulas (8) and (9). Table 2 describes the process of weight interval calculation (take the weight interval obtained under assumption 13 as an example). Table 3 lists the optimal weight of each variable under all the assumptions.

Five groups of environmental parameters were selected in this experiment, that is, $X^1 = [38, 500, 18, 188]$, $X^2 = [89, 580, 30, 200]$, $X^3 = [39, 450, 70, 229]$, $X^4 = [51, 750, 38, 199]$, and $X^5 = [39, 480, 19, 705]$. Using the online detection algorithm under five groups of parameters, the fire event probabilities under A1, A2, ..., A24 are obtained, respectively. Under the same input condition, calculate the fire event probability under the assumptions of A1, A2, ..., A24 and compare it with the fire probability calculated by the fuzzy fusion algorithm based on the "IF THEN" rule shown in [8]. The curves shown in Figure 3 illustrate the error of the fire probabilities between the online algorithm under A1, A2, ..., A24 and the fuzzy fusion algorithm shown in [8], and Figure 3 demonstrates that the probability under A13 is close to that obtained by fuzzy fusion algorithm under the same condition.

4.2. Promptness and Accuracy Analysis of Online Detection Algorithm. From the perspective of the time requirement for fire detection and alarm signal issuance, this paper analyzes the promptness of the proposed online detection algorithm, the grey fuzzy neural network fusion algorithm in [7], and the fuzzy logic fusion algorithm in [8] about fire detection. The paper conducts 100 trials, and the parameters are randomly selected among the corresponding intervals, x_1 located in the interval (55, 100), x_2 placed in the interval (700, 1000), x_3 located in the interval (20, 100), and x_4 set in the interval (760, 1000). As can be seen in Figure 4, under the same input parameters, the proposed online detection algorithm can realize the fire alarm within 10s and 23s for the

Table 2: Calculation results of variable weight interval under A13.

Judgment matrices	$B_1 = \begin{bmatrix} 1 & 3 & 1/5 & 3 \\ 1/3 & 1 & 1/7 & 3 \\ 5 & 7 & 1 & 7 \\ 1/3 & 1/3 & 1/7 & 1 \end{bmatrix}$	$B_2 = \begin{bmatrix} 1 & 2 & 1/5 & 4 \\ 1/2 & 1 & 1/7 & 4 \\ 5 & 7 & 1 & 7 \\ 1/4 & 1/4 & 1/7 & 1 \end{bmatrix}$	$B_3 = \begin{bmatrix} 1 & 1 & 1/5 & 2 \\ 1 & 1 & 1/6 & 4 \\ 5 & 6 & 1 & 8 \\ 1/2 & 1/4 & 1/8 & 1 \end{bmatrix}$	$B_4 = \begin{bmatrix} 1 & 1 & 1/5 & 2 \\ 1 & 1 & 1/6 & 4 \\ 5 & 6 & 1 & 7 \\ 1/2 & 1/4 & 1/7 & 1 \end{bmatrix}$	$B_5 = \begin{bmatrix} 1 & 2 & 1/7 & 2 \\ 1/2 & 1 & 1/5 & 3 \\ 7 & 5 & 1 & 6 \\ 1/2 & 1/3 & 1/6 & 1 \end{bmatrix}$
The weight of x_1	0.1908	0.1587	0.1298	0.1314	0.1486
The weight of x_2	0.1032	0.1356	0.1533	0.1566	0.1301
The weight of x_3	0.6471	0.6493	0.6572	0.6490	0.6515
The weight of x_4	0.0589	0.0564	0.0597	0.0630	0.0698
Weight interval of x_1	[0.1298, 0.1314, 0.1486, 0.1587, 0.1908]				
Weight interval of x_2	[0.1032, 0.1301, 0.1356, 0.1533, 0.1566]				
Weight interval of x_3	[0.6471, 0.6490, 0.6493, 0.6515, 0.6572]				
Weight interval of x_4	[0.0564, 0.0589, 0.0597, 0.0630, 0.0698]				

Table 3: The output result of the optimal weight of each variable under all assumptions.

	Variable weights (in x_1, x_2, x_3, x_4 order)		
A1	[0.6492, 0.1474, 0.1439, 0.0595]	A2	[0.6492, 0.1474, 0.0595, 0.1439]
A3	[0.6492, 0.1439, 0.1474, 0.0595]	A4	[0.6492, 0.0595, 0.1474, 0.1439]
A5	[0.6492, 0.1439, 0.0595, 0.1474]	A6	[0.1474, 0.6492, 0.1439, 0.0595]
A7	[0.1474, 0.6492, 0.1439, 0.0595]	A8	[0.1474, 0.6492, 0.0595, 0.1439]
A9	[0.1439, 0.6492, 0.1474, 0.0595]	A10	[0.0595, 0.6492, 0.1474, 0.1439]
A11	[0.1439, 0.6492, 0.0595, 0.1474]	A12	[0.0595, 0.6492, 0.1439, 0.1474]
A13	[0.1474, 0.1439, 0.6492, 0.0595]	A14	[0.1474, 0.0595, 0.6492, 0.1439]
A15	[0.1439, 0.1474, 0.6492, 0.0595]	A16	[0.0595, 0.1474, 0.6492, 0.1439]
A17	[0.1439, 0.0595, 0.6492, 0.1474]	A18	[0.0595, 0.1439, 0.6492, 0.1474]
A19	[0.1474, 0.1439, 0.0595, 0.6492]	A20	[0.1474, 0.0595, 0.1439, 0.6492]
A21	[0.1439, 0.1474, 0.0595, 0.6492]	A22	[0.0595, 0.1474, 0.1439, 0.6492]
A23	[0.1439, 0.0595, 0.1474, 0.6492]	A24	[0.0595, 0.1439, 0.1474, 0.6492]

grey fuzzy neural network fusion algorithm and within 20*s* for the fuzzy logic fusion algorithm. It is obvious that the online detection algorithm is superior to the other algorithms in the promptness of fire alarm under the same input parameters.

The core of the online detection algorithm is to calculate the weight of each variable. Take A13 as an example. A set of weights [0.6492, 0.1474, 0.1439, 0.0595] is selected when the number of judgment matrices, k, is 5. Figure 5 illustrates the relationship between the selected number of judgment matrices k and the false alarm rate of fire detection, where it is assumed that when k is 5, the false alarm rate of fire is 3% as the initial condition. It is easy to observe that the more reasonable number of judgment matrices is selected, the more accurate the fire event probability is. When k is greater than 20, the online detection algorithm reduces the false alarm rate to less than 0.5% and effectively improves the accuracy of fire alarm.

4.3. Fault Tolerance of Online Detection Algorithm Analysis. This subsection discusses the deviation of fire event probability when sensor faults occur by using the proposed method under the 50 sensor nodes' network. Assume that the parameters of the experimental conditions are as follows: ambient temperature is 38°C, the smoke concentration is 650 ppm, the CO concentration is 14 ppm, and the infrared ray intensity is 700 lux. When all nodes are working normally, the fire event probability is estimated by three methods as shown in Table 4. Correspondingly, these values are regarded as the reference true values for the fault tolerance analysis.

The error square (SE) is adopted as the standard to evaluate the detection accuracy of the above three algorithms defined as

$$\mathrm{SE}^j = \left(p^j - \hat{p}^j\right)^2, \tag{25}$$

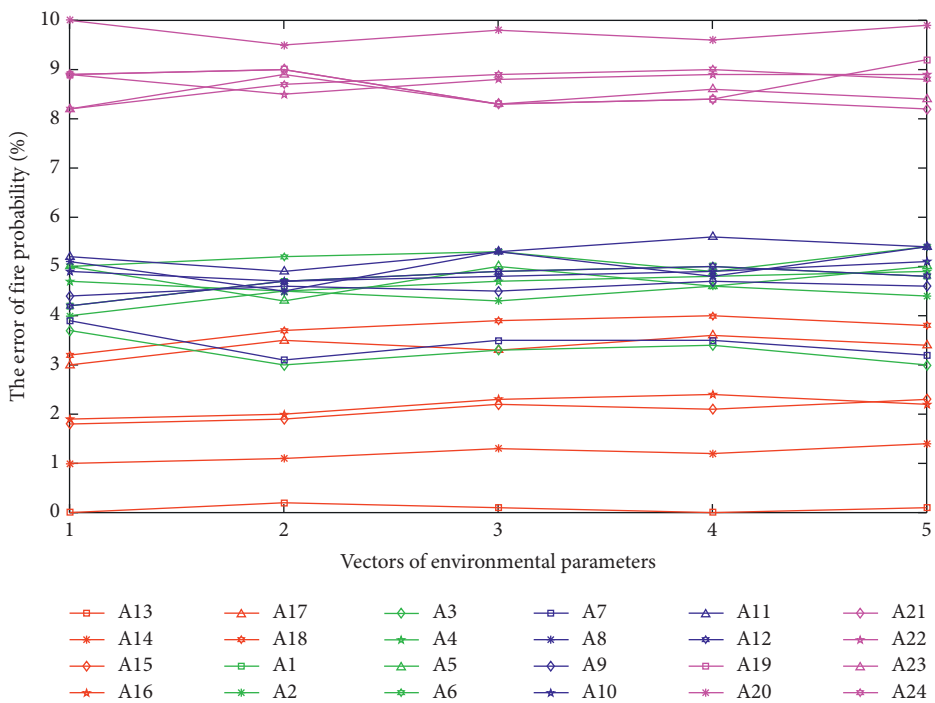

Figure 3: The error curve of fire probability.

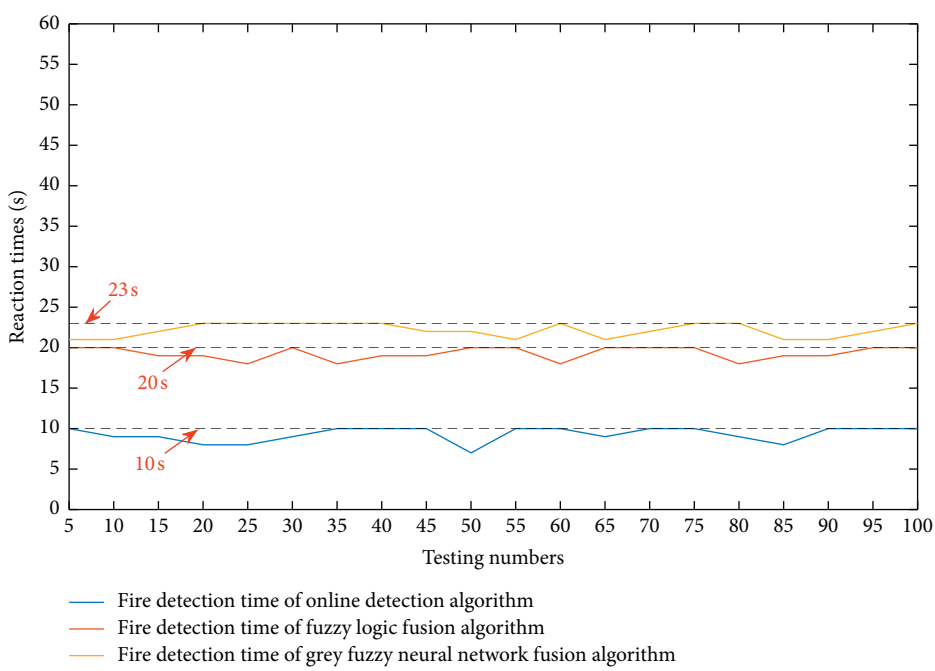

Figure 4: Comparison diagram of detection time of three fire detection algorithms.

where j is the subscript of detection algorithm ($j = 1, 2, 3$), p^j represents the reference value of fire probability under j algorithm, and $\widehat{p}^j$ represents the estimated fire event probability after fusion of 50 nodes under j^{th} algorithm.

Generally, when SE reaches 2, it is considered that a large deviation occurs, and the corresponding fire detection results become invalid. As seen from Figure 6, when the number of fault nodes reaches 10, the detection algorithms proposed by [7, 8] will become invalid and the detection accuracy of the algorithm will decrease sharply, which cannot meet the requirements of the practical application system. On the contrary, SE value calculated by the proposed method increases gently and a large deviation occurs only after the fault nodes reach 30 due to the adaptive-weighted fusion algorithm based on the mutual support degree matrix. Therefore, in the actual fire detection system, the fault

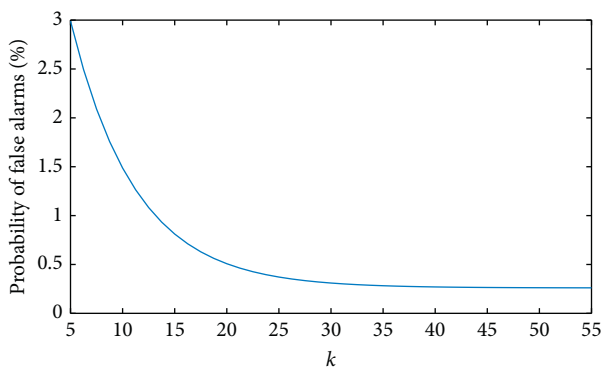

Figure 5: The relationship curve between the number of judgment matrices k and the false alarm rate of fire detection.

Table 4: The real value of fire probability corresponding to the three detection algorithms.

Fire detection algorithm	Fire probability (%)
Grey fuzzy neural network fusion method	30.56
Fuzzy logic fusion method	29.48
Online detection method	28.62

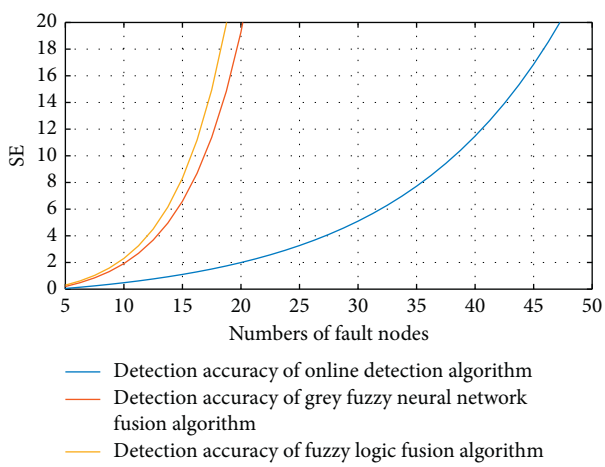

Figure 6: Comparison diagram of detection accuracy of three algorithms.

tolerance of the proposed online detection algorithm is much better.

5. Conclusions

In this paper, on the one hand, the online fire detection algorithm uses improved AHP and multivariable-weighted fusion algorithm to evaluate the fire event probability in cabin at each node. On the other hand, the fire probability evaluation values of all nodes are fused by adaptive-weighted fusion algorithm based on the augmented support matrix during online detection. Experiments show that the algorithm can complete fire detection and alarm within 10 s. Comparing the proposed method to other fire detection algorithms, it greatly reduces the time required for fire detection and alarm, effectively avoids the spread of fire, and makes subsequent fire-suppression work smoother to a certain extent. In the meanwhile, the false alarm rate of fire has been reduced to less than 0.5%, which plays an important role in promoting the development of civil aviation in the future in terms of safety and economy. At the same time, the simulation results show that the online detection algorithm has better fault tolerance than other fire detection algorithms in the WSN with faulty sensors.

Data Availability

The data used to support the findings of this study are available from the corresponding author upon request.

Conflicts of Interest

The authors declare that there are no conflicts of interest regarding the publication of this paper.

Acknowledgments

This work was supported by the Scientific Research Foundation for the Returned Overseas Chinese Scholars, State Education Ministry, Tianjin Natural Science Foundation (18JCYBJC42300), and Scientific Research Project of Tianjin Education Commission (2019KJ143). The authors would like to extend their sincere gratitude to Professor Youmin Zhang from Concordia University, Canada, for his instructive advices and suggestions on this paper.

References

[1] X. Jin, J. Du, and J. Bao, "Target tracking of a linear time invariant system under irregular sampling," *International Journal of Advanced Robotic Systems*, vol. 9, no. 5, p. 219, 2012.

[2] X. Jin, X. Lian, T. Su, Y. Shi, and B. Miao, "Closed-Loop estimation for randomly sampled measurements in target tracking system," *Mathematical Problems in Engineering*, vol. 2014, pp. 1–12, 2014.

[3] X. Jin, C. Dou, T. Su, X. Lian, and Y. Shi, "Parallel irregular fusion estimation based on nonlinear filter for indoor RFID tracking system," *International Journal of Distributed Sensor Networks*, vol. 2016, no. 8, pp. 1–11, 2016.

[4] Y. Liang and W. Tian, "Multi-sensor fusion approach for fire alarm using bp neural network," 2016.

[5] R. Wang, Y. Li, H. Sun, and Z. Chen, "Analyses of integrated aircraft cabin contaminant monitoring network based on Kalman consensus filter," *ISA Transactions*, vol. 71, pp. 112–120, 2017.

[6] R. Wang, X. Wang, H. Sun, Y. Huang, and Z. Chen, "Analysis of estimator and energy consumption with multiple faults over the distributed integrated WSN," *International Journal of Modelling, Identification and Control*, vol. 32, no. 2, pp. 154–168, 2019.

[7] S. Liu, X. Luo, W. Yao et al., "Aspirating fire detection system with high sensitivity and multi-parameter," 2014.

[8] R. Sowah, K. O. Ampadu, A. R. Ofoli, K. Koumadi, G. A. Mills, and J. Nortey, "A fire-detection and control system in automobiles: implementing a design that uses fuzzy logic to anticipate and respond," *IEEE Industry Applications Magazine*, vol. 25, no. 2, pp. 57–67, 2019.

[9] S. Duan, K. Yang, D. Mao, and J. Ren, "Fuzzy evidence theory-based algorithm in application of fire detection," *Computer Engineering and Applications*, vol. 53, no. 5, pp. 231–235, 2017.
[10] M. Yang, Y. Geng, K. Yu, X. Li, and S. Zhang, "BP neural network data fusion algorithm optimized based on adaptive fuzzy particle swarm optimization," 2018.
[11] K. Lamamra, A. Allam, and H. Afiane, "Artificial neural networks for acquisition and processing of sensors data in a radiotherapy application," *International Journal of Simulation and Process Modelling*, vol. 13, no. 1, pp. 15–23, 2018.
[12] F. Yang, Y. Shen, X. Cui et al., "Voltage sag severity assessment based on multi-objective decision analytic hierarchy process," 2018.
[13] H. Sun, F. Qiao, Z. Wang, and L. Guo, "A two-level identification model for selecting the coordination strategy for the urban arterial road based on fuzzy logic," *International Journal of Simulation and Process Modelling*, vol. 14, no. 6, pp. 478–487, 2019.
[14] W. Gao and K. Hong, "The portfolio balanced risk index model and analysis of examples of large-scale infrastructure project," *Complexity*, vol. 2017, pp. 1–13, 2017.
[15] W. Li, Y. Ye, N. Hu, X. Wang, and Q. Wang, "Real-time warning and risk assessment of tailings dam disaster status based on dynamic hierarchy-grey relation analysis," *Complexity*, vol. 2019, no. 9, pp. 1–14, 2019.
[16] M. Yu, X. Zhao, and Z. Xu, "Survey on using dependencies to improve data consistency," *Journal of Computer Applications*, vol. 38, no. 2, pp. 72–76, 2018.
[17] J. Yang, F. Gong, and Y. Ma, "A multi-sensors data fusion method based on the augmented support degree," 2010.
[18] S. Hu and J. Liu, "Application of fuzzy comprehensive evaluation method in product design scheme decision," *Journal of Machine Design*, vol. 37, no. 1, pp. 135–139, 2020.
[19] C. Ai and F. Feng, "A supplement to saaty's consistency theory of judgment matrix in the analytic hierarchy process," 2017.
[20] Q. Tian, C. Huang, H. Yu, Y. Du, and X. Zhou, "Approach for determining weight of resource allocation in coupled task set based on AHP," *Computer Engineering and Applications*, vol. 54, no. 21, pp. 25–30, 2018.
[21] H. Xu, P. He, W. Hsu, Y. Lee, and C. Ho, "Establishment of assessment indexes for intelligent elderly residential space by analytic hierarchy process," *Healthcare and Sustainability (ECBIOS)*, vol. 2019, pp. 69–72, 2019.
[22] W. Dong, J. Fu, Z. Jie, and J. Wang, "Study on operation evaluation of charging and discharging network based on improved analytic hierarchy process and fuzzy synthetic evaluation," 2018.
[23] Y. Liu, X. Yan, C.-A. Zhang, and W. Liu, "An ensemble convolutional neural networks for bearing fault diagnosis using multi-sensor data," *Sensors*, vol. 19, no. 23, p. 5300, 2019.
[24] L. Zheng, D. W. H. Cai, and C. W. Tan, "Max-min fairness rate control in wireless networks: optimality and algorithms by perron-frobenius theory," *IEEE Transactions on Mobile Computing*, vol. 17, no. 1, pp. 127–140, 2018.
[25] S. Zeng, X. Tong, and P. Shen, "Design of fire detection system based on wireless multi-sensor information fusion," *Journal of Hubei Polytechnic University*, vol. 35, no. 6, pp. 23–27, 2019.
[26] O. Giandi and R. Sarno, "Prototype of fire symptom detection system," 2018.

Hindawi
Complexity
Volume 2021, Article ID 6695221, 12 pages
https://doi.org/10.1155/2021/6695221

Research Article

A Staged Finite-Time Control Strategy for Formation of Underactuated Unmanned Surface Vehicles

Hui Ye, Xiaofei Yang, Chunxiao Ge, and Zhaoping Du

School of Electronics and Information, Jiangsu University of Science and Technology, Zhenjiang 212003, China

Correspondence should be addressed to Hui Ye; yehuicc@just.edu.cn

Received 1 December 2020; Revised 16 December 2020; Accepted 30 December 2020; Published 13 January 2021

Academic Editor: Rui Wang

The formation control issue for a group of underactuated unmanned surface vehicles (USVs) is discussed in the paper, and a staged finite-time control strategy for the USVs is proposed. Firstly, we try to steer each USV to its own starting point in the formation for a limited time, under the initial condition that each of these vehicles is parked at random. To deal with the nonholonomic behavior of the system, the dynamics of the USV is transformed into cascade systems. Then, the finite-time controller is designed for each vehicle based on homogeneity theory. After each USV reaches its own starting point with desired orientation, the model of the vehicle is decomposed into two subsystems under the Serret-Frenet frame. In order to maintain the formation pattern, two finite-time distributed controllers are developed for the surge subsystem and the yaw subsystem, respectively. The settling time for the staged control strategy is limited. Numerical simulations are carried out to illustrate the effectiveness of the proposed formation control strategy.

1. Introduction

Over the last decade, a great attention has been paid by scholars on unmanned surface vehicles (USVs), which can be used to perform various tasks, such as marine surveillance, oil spill collection, environmental monitoring, bathymetric mapping, and marine floor investigation [1]. These tasks are usually complexity and onerous, which are difficult to do by a single vehicle. Multivehicle cooperation is the inevitable choice, which can not only accomplish the tasks efficiently but also ensure personnel safety, reduce system cost, and provide redundancy against individual failure. Typical cooperative control issues of multiagent systems include consensus, distributed tracking, formation control, containment control, swarming, and aggregation. In this paper, the formation control of multiple USVs is considered.

There are two main difficulties in the formation control problem of underactuated USVs, one of which exists in the motion control of each single vehicle. Most existing USVs are typical underactuated systems, whose number of actuators is fewer than their degrees of freedom (DOF). The trajectory tracking control of the underactuated USV is studied in [2, 3], and the virtual target is adopted to generate the reference trajectory. The path following of the underactuated USV is usually addressed by introducing the Serret-Frenet frame and global coordinate transformation [4, 5]. Then, the underactuated problem is converted to a virtual fully actuated problem by designing the virtual control law. For the stabilization of the underactuated USVs, nonsmooth or time-varying cascaded design is usually proposed due to the nonholonomic constraints [6]. Moreover, finite-time controllers are developed in [7, 8] via adding one power integrator technique and terminal sliding mode method, respectively.

Another difficulty is to maintain formation pattern of multiple USVs, which will encounter issues of communication and coordination. From a review of the literature, there are mainly four methods used for the formation control of multiple vehicles, including virtual structure method [9], graph theory method [10], behavioral based approach [11], and leader-follower strategy [12, 13]. Among these methods, the leader-follower strategy is most preferred in practice for the formation of USVs because of its high

reliability and easily implementation [14]. A robust adaptive formation controller is proposed in [15] for the formation of USVs with uncertainties and ocean disturbances, where neural networks and dynamic surface control technique are used to capture them. In [16], a parameter estimation- and upper bound estimation-based sliding mode control scheme is presented to deal with the model uncertainties and environmental disturbances. The control constraint issues in the formation of underactuated USVs are also considered by many scholars. In [17], a formation tracking controller is developed by using generalized saturation functions to reduce the risk of actuator saturation. The receding horizon control algorithm is adopted in [18] for the formation tracking of a feet of underactuated autonomous underwater vehicles (AUVs) with constrained inputs. In [19], auxiliary dynamic systems and disturbance observers are designed to deal with input saturations and disturbances respectively, and a robust controller is developed for time-varying formation control of underactuated AUVs. The fault tolerant control problem in the leader-follower formation of USVs is considered in [20], while both parametric and nonparametric system uncertainties are discussed.

Another popular method for USV formation control is based on the graph theory, which is proposed to settle the consensus problem of multiagents. The literature [21] considers the cooperative control of a group of underactuated USVs using the relative information between neighbor's information with the aid of results from graph theory and Lyapunov techniques. In [22], a distributed maneuvering controller of multiple USVs is designed in the presence of unknown state constraints. An RNN-based command governor is provided between the kinematic controller and the kinetics controller. A cooperative path maneuvering controller is designed based on a line of sight guidance scheme in [23], where the modular adaptive control method is employed to identify uncertain kinematics and unknown kinetics of each vehicle.

Currently, finite-time formation control of multiple USVs become an active research area, since a lot of works have been carried out in both the finite-time control of single USV [24–26] and the finite-time consensus of multiagents [27–29]. In [30], the finite-time formation control of underactuated USVs is investigated with consideration of model uncertainty and environmental disturbance. The reference trajectory of each USV is given first according to the desired geometric pattern. Then, a nonlinear controller with fractional power feedback is designed for each USV, to make sure each vehicle follows its own trajectory in finite time. In [31], the terminal sliding mode approach is used to deal with the finite-time formation of underactuated ships. Specifically, a generalized error which contains topology information of communication is defined so that the method based on graph theory can be used for the nonlinear system.

Motivated by the aforementioned works, the finite-time control for single USV and the finite-time cooperative control for multiple USVs are integrated is this paper. A staged finite-time control scheme is proposed for the formation of multiple underactuated USVs. Our major contributions are listed as follows:

(1) To deal with the underactuated nature and achieve the goal of finite-time convergence, we mainly separate the formation control process into two stages. In the first stage, we try to steer each USV to its own starting point in the formation configuration for a limited time. In the second stage, the formation pattern is maintained by using two finite-time cooperative controllers. As a consequence, the resulting control scheme can guarantee finite-time convergence.

(2) In the first stage, the positioning problem of every single underactuated USV is regard as a finite-time stability problem of the homogeneous system. Homogeneous theory is applied in the control design, to make each vehicle get to its own position in the formation pattern.

(3) In the second stage, the model of each USV can be decoupled into two subsystems with a series of integrators: the surge subsystem and the yaw subsystem. Taking communication link topology into account, two finite-time cooperative controllers are designed based on graph theory to maintain the formation pattern.

The remainders of the paper are organized as follows. In Section 2, preliminaries and problem formulation are introduced. Section 3 presents the main results on the staged control algorithm design, where finite-time control for single USV is designed in Section 3.1 and finite-time cooperative control for formation maintenance is given in Section 3.2. In order to illustrate the effectiveness of the proposed control laws, numerical simulation results are presented in Section 4. Finally, some conclusion remarks are drawn in Section 5.

2. Preliminary

In this section, theories of finite-time stability, homogeneity, and algebraic graph are introduced briefly, and some lemmas are given. Then, the kinematics and dynamics of the underactuated USV are provided, and the task of formation control for multiple USVs is summarized.

2.1. Finite-Time Stability and Homogeneity. Both asymptotic stability and finite-time convergence of the closed-loop system are required in our design, which leads to the conception of the finite-time stability.

Definition 1. Consider the system

$$\begin{aligned} \dot{x} &= \mathbf{f}(\mathbf{x}), \\ \mathbf{f}(0) &= 0, \quad \mathbf{x} \in \mathbb{R}^n, \end{aligned} \tag{1}$$

where $\mathbf{f}\colon \mathbb{R}^n \longrightarrow \mathbb{R}^n$ is continuous. Assume that, for every initial condition $\mathbf{x}(0) = \mathbf{x}_0 \in \mathbb{R}^n$, system (1) possesses a unique solution $\mathbf{x}(t) = \xi(t, \mathbf{x}_0)$ in forward time which is defined on $[0, \infty)$. The origin is said to be a finite-time stable equilibrium of (1) if there exists an open neighborhood $\mathcal{U}$ of

the origin and a function $t_f: \mathcal{U} \longrightarrow [0, \infty)$ called the settling time function such that the following statements hold:

(1) For every $\mathbf{x}_0 \in \mathcal{U}/\{0\}$,
$$\begin{cases} \xi(t, \mathbf{x}_0) \in U/\{0\}, & \text{for } 0 \le t < t_f(x_0), \\ \xi(t, \mathbf{x}_0) = 0, & \text{for } t \ge t_f(x_0). \end{cases}$$

(2) $\lim_{t \longrightarrow t_f(\mathbf{x}_0)} \xi(t, \mathbf{x}_0) = 0$.

The origin is said to be a globally finite-time stable equilibrium if it is a finite-time stable equilibrium and $\mathcal{U} = \mathbb{R}^n$.

In general, there are three techniques which can be used to achieve finite-time stability for the feedback stabilization, including homogeneous theory, terminal sliding mode method, and adding one power integrator approach [32]. In this paper, nonsmooth feedback finite-time controllers are designed with the help of the homogeneous system.

Definition 2 (see [32]). Consider the dilation of the form $\delta_\varepsilon^{(\gamma_1, \ldots, \gamma_n)}(x_1, \ldots, x_n) = (\varepsilon^{\gamma_1} x_1, \ldots, \varepsilon^{\gamma_n} x_n)$, where $x_1, \ldots, x_n$ are suitable coordinates on $\mathbb{R}^n$ and $\gamma_1, \ldots, \gamma_n$ are positive real numbers. A vector field is homogeneous of degree k if and only if the ith component f_i is homogeneous of degree $k + \gamma_i$. System (1) is said to be a homogeneous system if its vector field $\mathbf{f}$ is homogeneous.

The connection between the finite-time stability and the homogeneous system is concluded in the following two lemmas.

Lemma 1 (see [32]). *For system (1), suppose there exists an open neighborhood $\mathcal{U}$ of the origin, a $\mathcal{C}^1$ positive definite function $V(\mathbf{x})$, and real number $\varepsilon > 0$ and $0 < \alpha < 1$, such that $\dot{V}(\mathbf{x}) + \varepsilon V^\alpha(\mathbf{x})$ is negative semidefinite on $\mathcal{U}$. Then, the origin is a finite-time stable equilibrium of the system.*

Lemma 2 (see [32]). *Suppose that system (1) is homogeneous of degree k with respect to $(\gamma_1, \ldots, \gamma_n)$, the origin is a finite-time stable equilibrium of (1) if and only if the origin is an asymptotically stable equilibrium of (1) and $k < 0$.*

Consider the following chain of integrators:
$$\begin{aligned} \dot{x}_1 &= x_2, \quad x_1(t_0) = x_{10}, \\ \dot{x}_2 &= x_3, \quad x_2(t_0) = x_{20}, \\ &\vdots \quad \vdots \\ \dot{x}_n &= u, \quad x_n(t_0) = x_{n0}. \end{aligned} \tag{2}$$

System (2) is finite-time convergent to the origin if the control input is designed as
$$u = -k_1 x_1^{\alpha_1} - k_2 x_2^{\alpha_2} - \cdots - k_n x_n^{\alpha_n}, \tag{3}$$
where the exponents $\alpha_i \in (0, 1)$, $i = 1, \ldots, n-1$, are selected satisfying
$$\begin{aligned} \alpha_i &= \frac{\alpha_{i+1}\alpha_{i+2}}{(2\alpha_{i+2} - \alpha_{i+1})}, \\ \alpha_{n+1} &= 1, \\ \alpha_n &= \alpha, \quad 0 < \alpha < 1. \end{aligned} \tag{4}$$

The item $x_i^{\alpha_i}$ is defined as $|x_i|^{\alpha_i} \operatorname{sgn}(x_i)$, where $\operatorname{sgn}(\cdot)$ is the sign function. The gains k_i, $i = 1, \ldots, n$, are selected such that the following matrix is Huiwitz:
$$\mathbf{A}_x = \begin{pmatrix} 0 & 1 & 0 & \ldots & 0 \\ 0 & 0 & 1 & \ldots & 0 \\ \vdots & \vdots & \vdots & \ddots & \vdots \\ 0 & 0 & 0 & \ldots & 1 \\ -k_1 & -k_2 & -k_3 & \ldots & -k_n \end{pmatrix}. \tag{5}$$

Define the Lyapunov function candidate $V(\zeta) = \zeta^T \mathbf{P} \zeta$ with $\zeta = (x_1^{\alpha_1}, x_2^{\alpha_2}, \ldots, x_n^{\alpha_n})^T$. $\mathbf{P}$ and $\mathbf{Q}$ are symmetric positive definite matrices satisfying
$$\mathbf{P}\mathbf{A}_\mathbf{x} + \mathbf{A}_x^T \mathbf{P} = -\mathbf{Q}. \tag{6}$$

Lemma 3 (see [33]). *Consider system (2) together with (3). The state $\mathbf{x} = (x_1, x_2, \ldots, x_n)^T$ converges to the origin for a finite time. Moreover, the upper bound of the settling time can be estimated as*
$$t_f(\mathbf{x}_0) \le \frac{\alpha V(\boldsymbol{\zeta}_0)^{(1-\alpha/\alpha)}}{(1-\alpha)\rho}, \tag{7}$$
for all $\mathbf{x}_0 = (x_{10}, x_{20}, \ldots, x_{n0})^T$ in some open neighborhood $\mathcal{U}$ of the origin, where $\rho = \lambda_{min}(\mathbf{Q})/\lambda_{max}(\mathbf{P})$. $\lambda_{min}(\mathbf{Q}) > 0$ is the minimum eigenvalue of the matrix $\mathbf{Q}$, and $\lambda_{max}(\mathbf{P}) > 0$ is the maximum eigenvalue of the matrix $\mathbf{P}$.

2.2. Graph Theory. The communication links topology among the group of NSVs can be represented by a graph $\mathcal{G} = \{\mathcal{V}, \mathcal{E}, \mathcal{A}\}$, where $\mathcal{V} = \{v_1, v_2, \ldots, v_m\}$ is the set of vehicles, $\mathcal{E}$ represents the set of links between the vehicles (also called edge set), and $\mathcal{A}$ is the weighted coefficients of edge set $\mathcal{E}$. In the directed graph, $(i, j) \in \mathcal{E}$ represents the jth vehicle can communicate with i^{th} vehicle, but not conversely. The ith vehicle is called the parent node, and the jth vehicle is also called the child node of the ith vehicle, and they are neighbors. In the undirected graph, $(i, j) \in \mathcal{E}$ denotes the information can be exchanged between the two vehicles. All vehicles are connected with a single undirected path. However, in the directed graph, each vehicle has only one parent node, except for one vehicle, which is called the root. If m vehicles are in the scenario, then the associated adjacency matrix of $\mathcal{G}$ can be defined as $\mathbf{A} = \{a_{ij}\}_{m \times m} \in \mathbb{R}^{m \times m}$. $a_{ij} > 0$ if and only if there is a link from j^{th} vehicle to i^{th} vehicle; otherwise, $a_{ij} = 0$. The Laplacian matrix $\mathbf{L} = \{l_{ij}\}_{m \times m} \in \mathbb{R}^{m \times m}$ associated with the matrix $\mathbf{A}$ is defined by $l_{ii} = \sum_{j=1}^m a_{ij}$ and $l_{ij} = -a_{ij}$, when $i \ne j$. The Laplacian matrix can be written as $\mathbf{L} = \mathbf{D} - \mathbf{A}$, where $\mathbf{D}$ is the degree matrix [34].

Consider a virtual leader v_0 moving with the group centroid. Define the augmented graph as $\overline{\mathcal{G}} = \{\overline{\mathcal{V}}, \overline{\mathcal{E}}, \overline{\mathcal{A}}\}$, where $\overline{\mathcal{V}} = \{v_0, v_1, \ldots, v_m\}$ and $\overline{\mathcal{E}} = \subseteq \mathcal{V} \times \mathcal{V}$ are the new node set and edge set, respectively. Diagonal matrix $\mathbf{B} = \operatorname{diag}\{a_{10}, a_{20}, \ldots, a_{m0}\}$ is called the leader adjacency matrix,

where $a_{i0} > 0$ if follower i is connected to the leader; otherwise, $a_{i0} = 0$. In this work, the communication topology verifies the following assumption.

Assumption 1. The graph $\mathcal{G}$ associated with the follower is undirected, and in the graph $\overline{\mathcal{G}}$ the leader has directed path to all followers.

Lemma 4 (see [35]). *Under Assumption 1,* $\mathbf{L} + \mathbf{B}$ *is a symmetric positive definite matrix.*

2.3. Mathematical Model of Underactuated USV. Two reference coordinate systems are defined to describe the model of the USV, where $X_E O_E Y_E$ is the earth-fixed inertial frame and $X_b O_b Y_b$ is the body-fixed frame, as shown in Figure 1. The model state of the USV in horizontal plane is given by (x, y, ψ, u, v, r), where x, y, and ψ denote the position and orientation of the vehicle in the earth-fixed frame, u, v, and r denote the surge, sway, and yaw velocity of the vehicle in the body-fixed frame, respectively.

Based on the above definition, the kinematic model of the USV can be described as

$$\begin{aligned} \dot{x} &= u\cos\psi - v\sin\psi, \\ \dot{y} &= u\sin\psi + v\cos\psi, \\ \dot{\psi} &= r. \end{aligned} \tag{8}$$

And the dynamic model of the USV can be given by

$$\begin{aligned} m_u\dot{u} - m_v vr + d_u u &= \tau_u, \\ m_v\dot{v} + m_u ur + d_v v &= 0, \\ m_r\dot{r} - m_{uv}uv + d_r r &= \tau_r, \end{aligned} \tag{9}$$

where d_u, d_v, and d_r are the hydrodynamic damping of the vehicle and m_u, m_v, and m_r are the inertia of the vehicle including added masses in surge, sway, and yaw. Besides, m_{uv} is the hydrodynamic added mass and τ_u and τ_r are the surge force and yaw moment, respectively.

It can be seen from (9) that the USV can only get the surge force and yaw moment from the thrusters and the rudder in the stern, and there is no sway force from the vessel thruster, so the vehicle is a typical underactuated system.

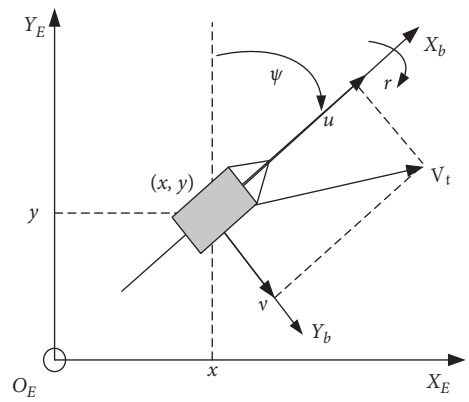

Figure 1: The earth-fixed inertial and the body-fixed frame.

2.4. Formation of Multiple USVs. Consider a group of m USVs, whose mathematical models are expressed as (8) and (9). For clarity, the subscript "i" $(i = 1, \ldots, m)$ is used to distinguish one from another. Such as, the state of the USV i is denoted by $(x_i, y_i, \psi_i, u_i, v_i, r_i)$. Assume that all the USVs are scattered randomly in the water at any initial states. The goal of this work is to steer these vehicles to achieve the prescribed formation pattern along a given straight line or arc path with a desired speed. Moreover, the settling time is required to be finite. Without loss of generality, the earth-fixed frame is defined with its origin located on the center of the formation at starting point. The X_E-axis coincides with the tangent of path with the positive axis pointing to the motion direction of the group, as shown in Figure 2.

A feasible desired trajectory can be described by the states $(x_0, y_0, \psi_0, u_0, v_0, r_0)$ of the group centroid which is moving along the path. The object of the control system can be expressed as follows.

In the first stage:

$$\begin{cases} \lim\limits_{t\longrightarrow t_{f1}} x_i(t) - x_0(t_{f1}) = \Delta x_i, \\ \lim\limits_{t\longrightarrow t_{f1}} y_i(t) - y_0(t_{f1}) = \Delta y_i, \\ \lim\limits_{t\longrightarrow t_{f1}} \psi_i(t) - \psi_0(t_{f1}) = \Delta\psi_i, \end{cases} \begin{cases} \lim\limits_{t\longrightarrow t_{f1}} u_i(t) = 0, \\ \lim\limits_{t\longrightarrow t_{f1}} v_i(t) = 0, \quad \text{for } i = 1, \ldots, m, \\ \lim\limits_{t\longrightarrow t_{f1}} r_i(t) = 0. \end{cases} \tag{10}$$

In the second stage:

$$\begin{cases} \lim\limits_{t\longrightarrow t_{f2}} (s_i(t) - s_0(t)) = \Delta s_i, \\ \lim\limits_{t\longrightarrow t_{f2}} (d_i(t) - d_0(t)) = \Delta d_i, \end{cases} \quad \text{for } i = 1, \ldots, m, \tag{11}$$

where $(\Delta x_i, \Delta y_i, \Delta\psi_i)$ are the relative position and orientation of USV i to the group centroid, (s_i, d_i) are longitudinal and transversal displacements of USV i with respect to the path, and $(\Delta s_i, \Delta d_i)$ are the longitudinal and transversal distances between USV i and the group centroid.

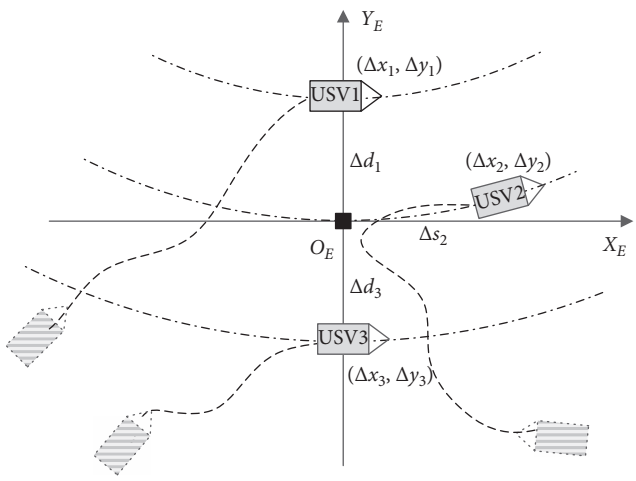

Figure 2: The reference frame and the formation pattern of the NSVs.

3. Staged Control Design for the Formation of USVs

For formation control of the USVs, vehicles should be forced to achieve the desired formation firstly and then maintain the geometric configuration. Consequently, the proposed control strategy includes two stages. In the first stage, each vehicle is steered to its own position in the formation pattern within a finite time. After that, the dynamics of the underactuated USV can be transformed into two integrator systems. In the second stage, two finite-time cooperative controllers are employed to maintain the formation shape and guarantee the stabilities of the systems.

3.1. Finite-Time Control for Single USV. In this stage, each vehicle is controlled separately to reach its initial position in the formation. We hope that this process could be completed in a limited time. For the underactuated USV i, its desired pose vector to the group centroid is $(\Delta x_i, \Delta y_i, \Delta\psi_i)$. We can transform the set point tracking problem of USV i to the stabilization problem by defining the following new state variables:

$$\begin{cases} \overline{x}_i = x_i - \Delta x_i, \\ \overline{y}_i = y_i - \Delta y_i, \\ \overline{\psi}_i = \psi_i - \Delta\psi_i. \end{cases} \tag{12}$$

Then, the kinematic equation of USV i can be rewritten as

$$\begin{cases} \dot{\overline{x}}_i = u_i\cos\overline{\psi}_i - v_i\sin\overline{\psi}_i, \\ \dot{\overline{y}}_i = u_i\sin\overline{\psi}_i + v_i\cos\overline{\psi}_i, \\ \dot{\overline{\psi}}_i = r_i. \end{cases} \tag{13}$$

Since the mathematical model of the underactuated USV is a typical nonholonomic system, the following global coordinate transformation is employed before control design [36]:

$$\begin{cases} z_{1i} = \overline{x}_i\cos\overline{\psi}_i + \overline{y}_i\sin\overline{\psi}_i, \\ z_{2i} = -\overline{x}_i\sin\overline{\psi}_i + \overline{y}_i\cos\overline{\psi}_i + \dfrac{m_v}{d_v}v_i, \\ z_{3i} = \overline{\psi}_i, \\ z_{4i} = -\dfrac{m_u}{d_v}u_i - z_{1i}, \\ z_{5i} = v_i, \\ z_{6i} = r_i, \end{cases} \tag{14}$$

$$\begin{cases} \tau_{1i} = \left(\dfrac{d_u}{d_v} - 1\right)u_i - z_{2i}z_{6i} - \dfrac{\tau_{ui}}{d_v}, \\ \tau_{2i} = \dfrac{m_{uv}}{m_r}u_iv_i - \dfrac{d_r}{m_r}r_i + \dfrac{\tau_{ri}}{m_r}, \end{cases}$$

where (τ_{1i}, τ_{2i}) represents the new input transformation pattern. Thus, system (13) together with (9) can be transformed into

$$\begin{cases} \dot{z}_{2i} = z_{4i}z_{6i}, \\ \dot{z}_{3i} = z_{6i}, \\ \dot{z}_{4i} = \tau_{1i}, \\ \dot{z}_{6i} = \tau_{2i}, \end{cases} \tag{15}$$

$$\begin{cases} \dot{z}_{1i} = -\dfrac{d_v}{m_u}z_{1i} - \dfrac{d_v}{m_u}z_{4i} + z_{2i}z_{6i} - \dfrac{m_v}{d_v}z_{5i}z_{6i}, \\ \dot{z}_{5i} = -\dfrac{d_v}{m_v}z_{5i} + \dfrac{d_v}{m_v}z_{6i}\left(z_{1i} + z_{4i}\right). \end{cases} \tag{16}$$

Remark 1 (see [36]). The system stabilization problem in (13) and (9) is equal to systems (15) and (16). If system (16) is global asymptotic convergent within finite time, the overall system of (15) and (16) is global asymptotic convergent.

Remark 2. As (τ_{ui}, τ_{ri}) and (τ_{1i}, τ_{2i}) can be converted to each other, just (τ_{1i}, τ_{2i}) need to be designed to make variables $z_{1i}, z_{2i}, z_{3i}, z_{4i}, z_{5i}$, and z_{6i} asymptotically converge to zero, which means that the tuple $(x_i, y_i, \psi_i, u_i, v_i, r_i)$ converges to $(\Delta x_i, \Delta y_i, \Delta\psi_i, 0, 0, 0)$. That is to say, the USV has arrived to its initial place in the formation pattern with desired orientation.

In view of the above remarks, our objective has shifted from set point tracking for each USV to simply stabilizing system (15). Note that this system does not satisfy Brockett's necessary condition. Hence, we divide system (15) into two cascade subsystems and try to provide a discontinuous

control law. Suppose z_{6i} is not zero at the initial time, such as $z_{6i}(0) \neq 0$. The first cascade subsystem is given as the follows:

$$\begin{cases} \dot{z}_{2i} = z'_{4i}, \\ \dot{z}'_{4i} = \tau'_{1i}, \end{cases} \tag{17}$$

where $z'_{4i} = z_{6i}(0)z_{4i}$ and $\tau'_{1i} = z_{6i}(0)\tau_{1i}$. The finite-time control law is designed as

$$\begin{aligned} &\tau'_{1i} = -k_{1i}z_{2i}^{\alpha_1} - k_{2i}z_{4i}^{\alpha_2}, \\ &\tau_{2i} = 0, \quad \text{for } t \in [0, t_{1i}], \end{aligned} \tag{18}$$

where the exponents α_1, α_2 are selected as $\alpha_1 = \alpha_2/(2-\alpha_2)$, $0 < \alpha_2 < 1$. The gains k_{1i} and k_{2i} are selected to satisfy

$$\mathbf{P}_{1i}\begin{pmatrix} 0 & 1 \\ -k_{1i} & -k_{2i} \end{pmatrix} + \begin{pmatrix} 0 & 1 \\ -k_{1i} & -k_{2i} \end{pmatrix}^T \mathbf{P}_{1i} = -\mathbf{Q}_{1i}. \tag{19}$$

Thus, t_{1i} is the settling time which can be calculated by

$$t_{1i} = \frac{\alpha_2\left(\boldsymbol{\zeta}_{1i}^T(0)\mathbf{P}_{1i}\boldsymbol{\zeta}_{1i}(0)\right)^{(1-\alpha_2)/\alpha_2}}{(1-\alpha_2)\rho_{1i}}, \tag{20}$$

where $\zeta_{1i}(0) = (z_{2i}(0), z_{4i}(0))^T$ and $\rho_{1i} = \lambda_{\min}(\mathbf{Q}_{1i})/\lambda_{\max}(\mathbf{P}_{1i})$. According to Lemma 3, the feedback control law (18) presents a homogeneous closed-loop system with negative degree of homogeneity. Thus, the states z_{2i} and z_{4i} of system (17) reach to zero in finite time; then, τ_{2i} would not affect system (17) any more. Moreover, τ_{2i} can be designed independently for the second cascade system:

$$\begin{cases} \dot{z}_{3i} = z_{6i}, \\ \dot{z}_{6i} = \tau_{2i}. \end{cases} \tag{21}$$

After time t_{1i}, we have

$$\begin{aligned} &\tau'_{1i} = 0, \\ &\tau_{2i} = -k_{3i}z_{3i}^{\alpha_3} - k_{4i}z_{6i}^{\alpha_4}, \quad \text{for } t \in (t_{1i}, t_{1i} + t_{2i}], \end{aligned} \tag{22}$$

where the exponents α_3 and α_4 are selected as $\alpha_3 = \alpha_4/(2-\alpha_4)$, $0 < \alpha_4 < 1$. The gains k_{3i} and k_{4i} are selected to satisfy

$$\mathbf{P}_{2i}\begin{pmatrix} 0 & 1 \\ -k_{3i} & -k_{4i} \end{pmatrix} + \begin{pmatrix} 0 & 1 \\ -k_{3i} & -k_{4i} \end{pmatrix}^T \mathbf{P}_{2i} = -\mathbf{Q}_{2i}. \tag{23}$$

Thus, t_{2i} is the settling time which can be calculated by

$$t_{2i} = \frac{\alpha_4\left(\boldsymbol{\zeta}_{2i}^T(t_{1i})\mathbf{P}_{2i}\boldsymbol{\zeta}_{2i}(t_{1i})\right)^{(1-\alpha_4)/\alpha_4}}{(1-\alpha_4)\rho_{2i}}, \tag{24}$$

where $\zeta_{1i}(t_{1i}) = (z_{3i}(t_{1i}), z_{6i}(t_{1i}))^T$ and $\rho_{2i} = \lambda_{\min}(\mathbf{Q}_{2i})/\lambda_{\max}(\mathbf{P}_{2i})$. By using Lemma 3 again, the control law (22) makes the states z_{3i} and z_{6i} of system (21) converge to zero in finite time.

After that the states of (15) converge to zero, system (16) is also asymptotically stabilized according to Remark 1. Actually, system (16) is simplified to first-order systems, whose settling time periods are $3m_u/d_v$ and $3m_v/d_v$. We let

$$t_{3i} = \max\left\{\frac{3m_u}{d_v}, \frac{3m_v}{d_v}\right\}. \tag{25}$$

So, the final convergence time of all USVs is calculated as

$$t_{f1} = \max_i\{t_{1i} + t_{2i} + t_{3i}\}. \tag{26}$$

That is to say, all USVs can arrive to their positions in the formation pattern after time t_{f1}.

3.2. Cooperative Control for Formation Maintenance. The goal of the second stage is to maintain the formation pattern by means of finite-time distributed control. It is assumed that only local distributed state information would be utilized by each vehicle to make its own surge velocity and yaw angular consistent with others. Consider a virtual leader moving with the group centroid, labeled 0. The communication graph $\overline{\mathcal{G}}$ among the n vehicles and the virtual leader satisfies Assumption 1.

After the first stage, the group of USVs has come into a prespecified geometric pattern with desired yaw angular. A reference path Γ_0 is previously specified for the centroid of the group which must be followed by the group of the USVs, as shown in Figure 3. The kinematic model of each vehicle can be rewritten according to the Serret–Frenet frame. Suppose that there is a virtual S-F frame $X_tO_0X_n$ moving along the path Γ_0 for the virtual vehicle 0. The kinematics of vehicle i expressed in new state coordinates is [37]

$$\begin{aligned} &\dot{d}_i = u_i\sin\varphi_i + v_i\cos\varphi_i, \\ &\dot{\varphi}_i = r_i - c\dot{s}_i, \\ &\dot{s}_i = \frac{1}{1-cd_i}(u_i\cos\varphi_i - v_i\sin\varphi_i), \end{aligned} \tag{27}$$

where $\varphi_i = \psi_i - \Delta\psi_i - \psi_0$ and c is the curvature of the path which is constant for the straight line or arc. Since each vehicle is on its own path and tangent to it at the initial moment, we assume that $d_i \approx \Delta d_i, v_i \approx 0$ and $\sin\varphi_i \approx \varphi_i$, $\cos\varphi_i \approx 1$. We define

$$\begin{aligned} &\overline{r}_i = r_i - c\dot{s}_i, \\ &h_i = \frac{1}{1-cd_i}, \\ &\tau_{3i} = \frac{1}{m_u}(\tau_{ui} - d_u u_i), \\ &\tau_{4i} = \frac{1}{m_r}(\tau_{ri} - d_r r_i) - ch_i\tau_{3i}. \end{aligned} \tag{28}$$

Then, the dynamics of vehicle i can be decoupled into two subsystems: the surge subsystem

$$\begin{aligned} &\dot{s}_i = h_i u_i, \\ &\dot{u}_i = \tau_{3i}, \end{aligned} \tag{29}$$

and the yaw subsystem

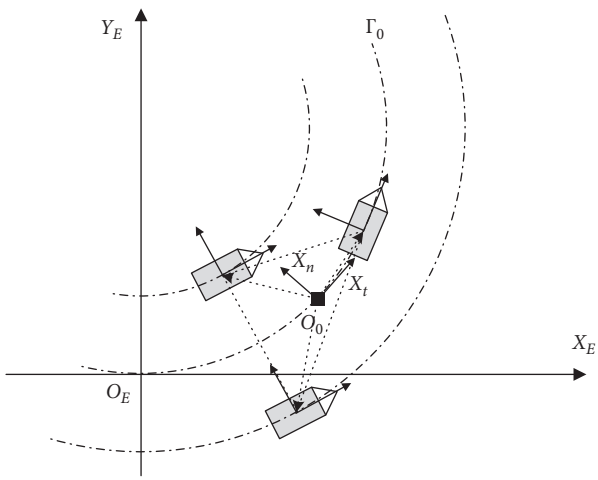

Figure 3: The virtual leader and the Serret–Frenet frame.

$$\begin{aligned}\dot{d}_i &= u_i\varphi_i,\\ \dot{\varphi}_i &= \bar{r}_i,\\ \dot{\bar{r}}_i &= \tau_{4i}.\end{aligned} \tag{30}$$

Suppose that $h_i, i = 1, \ldots m$ are not zero. The cascade subsystem (29) can be written as

$$\begin{aligned}\dot{s}_i &= u_{1i}',\\ \dot{u}_{1i}' &= \tau_{3i}',\end{aligned} \tag{31}$$

where $u_i' = h_i u_i$ and $\tau_{3i}' = h_i\tau_{3i}$. The finite-time distributed protocols based on the relative position and relative velocity are designed as

$$\begin{aligned}\tau_{3i}' = &-k_{5i}\left(\sum_{j=1}^{m} a_{ij}\left(s_i - s_j - \left(\Delta s_i - \Delta s_j\right)\right) + a_{i0}\left(\left(s_i - \Delta s_i\right) - s_0\right)\right)^{\alpha_5}\\ &- k_{6i}\left(\sum_{j=0}^{m} a_{ij}\left(u_i' - u_j'\right) + a_{i0}\left(u_i' - u_0'\right)\right)^{\alpha_6}, \quad \text{for } t \in \left(t_{f1}, \infty\right),\end{aligned} \tag{32}$$

where the exponents α_5 and α_6 are selected as $\alpha_5 = \alpha_6/(2-\alpha_6)$, $0 < \alpha_6 < 1$. The gains k_{5i} and k_{6i} are selected such that $s^2 + k_{6i}s + k_{5i}$ are Hurwitz polynomials.

Similarly, $u_i, i = 1, \ldots m$ are assumed to change slowly and not zero. The cascade system (30) can be written as

$$\begin{aligned}\dot{d}_i &= \varphi_i',\\ \dot{\varphi}_i' &= \bar{r}_i',\\ \dot{\bar{r}}_i' &= \tau_{4i}',\end{aligned} \tag{33}$$

where $\varphi_i' = u_i\varphi'$, $\bar{r}_i' = u_i\bar{r}_i$, and $\tau_{4i}' = u_i\tau_{4i}$. The finite-time distributed protocols based on the relative position and relative velocity are designed as

$$\begin{aligned}\tau_{4i}' = &-k_{7i}\left(\sum_{j=1}^{m} a_{ij}\left(d_i - d_j - \left(\Delta d_i - \Delta d_j\right)\right) + a_{i0}\left(\left(d_i - \Delta d_i\right) - d_0\right)\right)^{\alpha_7}\\ &- k_{8i}\left(\sum_{j=1}^{m} a_{ij}\left(\varphi_i' - \varphi_j'\right) + a_{i0}\left(\varphi_i' - \varphi_0'\right)\right)^{\alpha_8}\\ &- k_{9i}\left(\sum_{j=1}^{m} a_{ij}\left(\bar{r}_i' - \bar{r}_j'\right) + a_{i0}\left(\bar{r}_i' - \bar{r}_0'\right)\right)^{\alpha_9}, \quad \text{for } t \in \left(t_{f1}, \infty\right),\end{aligned} \tag{34}$$

where α_7, α_8, and α_9 are selected as $\alpha_7 = \alpha_8\alpha_9/(2\alpha_9 - \alpha_8)$ and $\alpha_8 = \alpha_9/(2-\alpha_9)$, $0 < \alpha_9 < 1$. The gains k_{7i}, k_{8i}, and k_{9i} are selected such that $s^3 + k_{9i}s^2 + k_{8i}s + k_{7i}$ are Hurwitz polynomials.

The main result is given by the following theorem.

Theorem 1. *Under Assumption 1, protocols (32) and (34) can guide system (31) and (33) to realize finite-time consensus, respectively.*

Proof. For systems (33) and (34), define the error states as

$$\begin{aligned}e_{i,1} &= \sum_{j=1}^{m} a_{ij}\left(d_i - d_j - \left(\Delta d_i - \Delta d_j\right)\right) + a_{i0}\left(\left(d_i - \Delta d_i\right) - d_0\right),\\ e_{i,2} &= \sum_{j=1}^{m} a_{ij}\left(\varphi_i' - \varphi_j'\right) + a_{i0}\left(\varphi_i' - \varphi_0'\right),\\ e_{i,3} &= \sum_{j=1}^{m} a_{ij}\left(\bar{r}_i' - \bar{r}_j'\right) + a_{i0}\left(\bar{r}_i' - \bar{r}_0'\right).\end{aligned} \tag{35}$$

Denoting $\mathbf{e}_1 = (e_{1,1}, e_{2,1}, \ldots e_{m,1})^T$, $\mathbf{e}_2 = (e_{1,2}, e_{2,2}, \ldots e_{m,2})^T$, and $\mathbf{e}_3 = (e_{1,3}, e_{2,3}, \ldots e_{m,3})^T$, it is straightforward to express the error dynamics as

$$\begin{aligned}\dot{e}_1 &= \mathbf{e}_2,\\ \dot{e}_2 &= \mathbf{e}_3,\\ \dot{e}_3 &= (\mathbf{L} + \mathbf{B})\left(-\mathbf{K}_7\mathbf{e}_1^{a_7} - \mathbf{K}_8\mathbf{e}_2^{a_8} - \mathbf{K}_9\mathbf{e}_3^{a_9}\right),\end{aligned} \tag{36}$$

where $\mathbf{K}_7 = \mathrm{diag}\{k_{71}, k_{72}, \ldots, k_{7m}\}$, $\mathbf{K}_8 = \mathrm{diag}\{k_{81}, k_{82}, \ldots, k_{8m}\}$, $\mathbf{K}_9 = \mathrm{diag}\{k_{91}, k_{92}, \ldots, k_{9m}\}$, and $\mathbf{e}_j^{\alpha}$, $j = 1, 2, 3$, denotes $(e_{1,j}^{\alpha}, e_{2,j}^{\alpha}, \ldots, e_{m,j}^{\alpha})^T$.

Let

$$\begin{aligned}\mathbf{A}_e &= \begin{pmatrix} 0 & \mathbf{I} & 0\\ 0 & 0 & \mathbf{I}\\ -\mathbf{K}_7 & -\mathbf{K}_8 & -\mathbf{K}_9\end{pmatrix},\\ \mathbf{M} &= \begin{pmatrix} \mathbf{I} & & \\ & \mathbf{I} & \\ & & \mathbf{L}+\mathbf{B}\end{pmatrix},\\ \overline{\mathbf{A}}_e &= \mathbf{M}\mathbf{A}_e = \begin{pmatrix} 0 & \mathbf{I} & 0\\ 0 & 0 & \mathbf{I}\\ -(\mathbf{L}+\mathbf{B})\mathbf{K}_7 & -(\mathbf{L}+\mathbf{B})\mathbf{K}_8 & -(\mathbf{L}+\mathbf{B})\mathbf{K}_9\end{pmatrix}.\end{aligned} \tag{37}$$

Consider a Lyapunov function candidate $\mathbf{V}(\mathbf{e}) = \mathbf{e}^T\mathbf{P}_e\mathbf{e}$, where $\mathbf{e} = (\mathbf{e}_1^T, \mathbf{e}_2^T, \mathbf{e}_3^T)^T$ and $\mathbf{P}_e = \mathbf{P}_e^T > 0$. It is obviously that $\mathbf{A}_e$ is a Hurwitz satisfying the Lyapunov equation $\mathbf{P}_e\mathbf{A}_e + \mathbf{A}_e^T\mathbf{P}_e = -\mathbf{Q}_e$, where $\mathbf{Q}_e = \mathbf{Q}_e^T > 0$. Since $\mathbf{M}$ is a symmetric positive definite matrix, the Lyapunov equation $\overline{\mathbf{P}}_e\overline{\mathbf{A}}_e + \overline{\mathbf{A}}_e^T\overline{\mathbf{P}}_e = -\mathbf{Q}_e$ holds with $\overline{\mathbf{P}}_e = \mathbf{P}_e\mathbf{M}^{-1} > 0$, which means that $\overline{V}(\mathbf{e}) = \mathbf{e}^T\overline{\mathbf{P}}_e\mathbf{e}$ is a Lyapunov function for the linear system $\dot{e} = \overline{A}_e\mathbf{e}$.

From the proof of Theorem 1 in [33], we can see that $V(\zeta_e) = \zeta_e^T\overline{\mathbf{P}}_e\zeta_e$ is a Lyapunov function for system (36), where $\zeta_e = ((\mathbf{e}_1^{\alpha_7})^T, (\mathbf{e}_2^{\alpha_8})^T, (\mathbf{e}_3^{\alpha_9})^T)^T$. So, system (36) is asymptotically stable. Moreover, it can be verified that system (36) is a homogeneous system of degree $\alpha_9 - 1/\alpha_9 < 0$. Hence, by Lemma 2, system (36) is finite-time convergent to the origin. It follows that the finite-time consensus problem of system (33) with protocol (34) is solved.

The finite-time consensus of system (31) with protocol (32) can be proved similarly. Theorem 1 is proven.

4. Numerical Simulation and Results

To illustrate the effectiveness of the proposed control law, a simulation study based on the model is presented in [15]. The same model parameters are chosen as in [38] and given as follows: $m_u = 25.8$, $m_v = 33.8$, $m_r = 2.76$, $m_{uv} = 6.2$, $d_u = 12 + 2.5|u|$, $d_v = 17 + 4.5|v|$, and $d_r = 0.5 + 0.1|r|$.

Without loss of generality, in our simulation scene, we assume that there are only 3 USVs in the formation. Consider the fact that not all the follower vehicles can receive information from each other, but all of them can directly communicate with the "virtual leader," as depicted in Figure 4. In addition, their initial conditions and the desired positions and orientations of each USV in the first stage are listed in Table 1.

According to the setting of aforementioned scenario, the adjacent matrix $\mathbf{A}$, the degree matrix $\mathbf{D}$, the Laplace matrix $\mathbf{L}$, and the leader adjacency matrix $\mathbf{B}$ can be deduced as follows:

$$\mathbf{A} = \begin{bmatrix} 0 & 1 & 0 \\ 1 & 0 & 1 \\ 0 & 1 & 0 \end{bmatrix},$$
$$\mathbf{D} = \begin{bmatrix} 1 & 0 & 0 \\ 0 & 2 & 0 \\ 0 & 0 & 1 \end{bmatrix},$$
$$\mathbf{L} = \begin{bmatrix} 1 & -1 & 0 \\ -1 & 2 & -1 \\ 0 & -1 & 1 \end{bmatrix}, \tag{38}$$
$$\mathbf{B} = \begin{bmatrix} 1 & 0 & 0 \\ 0 & 1 & 0 \\ 0 & 0 & 1 \end{bmatrix}.$$

The expected path of the group centroid is given as a circle with radius 100 m. Thus, the expected paths for USV1, USV2, and USV3 are concentric circles with radius 90 m, 100 m, and 110 m, respectively. According to the design guideline, the control parameters are chosen as listed in Tables 2 and 3.

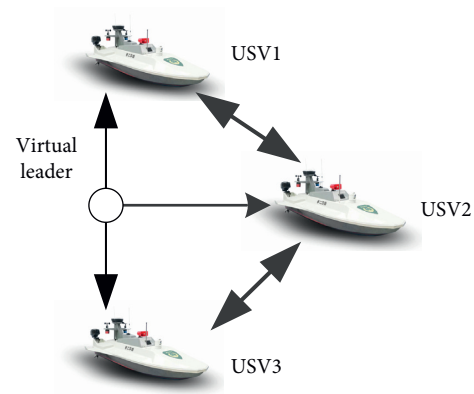

Figure 4: The communication links relationship in the formation.

Table 1: Initial and desired states of the USVs.

Initial states	USV1: [−30, 60, π/3, 0, 0,−π/18] USV2: [-20,-30, π/2, 0, 0,−π/18] USV3: [50,-50,−π/4, 0, 0, π/18]
Desired states in formation	USV1: [0, 10, 0, 0, 0, 0] USV2: [6.3, 0.2, π/50, 0, 0, 0] USV3: [0, −10, 0, 0, 0, 0]

Table 2: The gains of the controllers.

Gains	k_1	k_2	k_3	k_4	k_5	k_6	k_7	k_8	k_9
USV1	5	0.5	0.1	1	0.5	0.5	5	5	5
USV2	5	0.5	0.1	1	0.5	0.5	5	5	5
USV3	5	0.5	0.1	1	0.5	0.5	5	5	5

Table 3: The exponents of the controllers.

Exponents	α_1	α_2	α_3	α_4	α_5	α_6	α_7	α_8	α_9
USV	1.81	0.90	1.81	0.90	0.20	0.33	0.25	0.33	0.50

The final convergence time t_{f1} of the first stage for all USVs is selected as 150s, which is more than the sum of t_{1i}, t_{2i}, and t_{3i}. In the second stage, we assume that there is a virtual leader moving along the path with a fixed velocity $u_t = 2m/s$.

The simulation results are shown in Figures 5–8. Figure 5 shows the formation trajectory of the USVs under the proposed control scheme. It can be seen that each of the USVs could arrive at their own starting points in formation first and then could track the desired paths and maintain the triangular pattern well.

Figure 6 shows the curves of the states and control inputs of the USVs. It can be observed that, in the first stage, the positions of the USVs converge to the expected values within about 40 seconds, before the first switch of the control algorithm. And then the orientations of the USV converge to the expected values within about 140 seconds, which is also before the second switching time of the

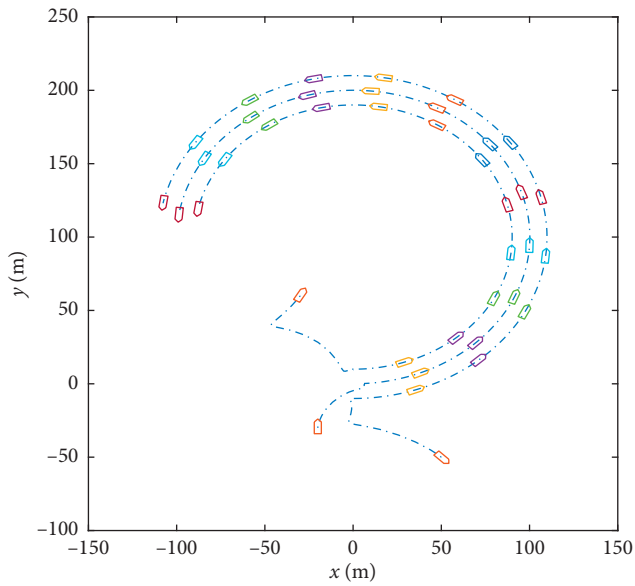

Figure 5: Trajectory of the USVs.

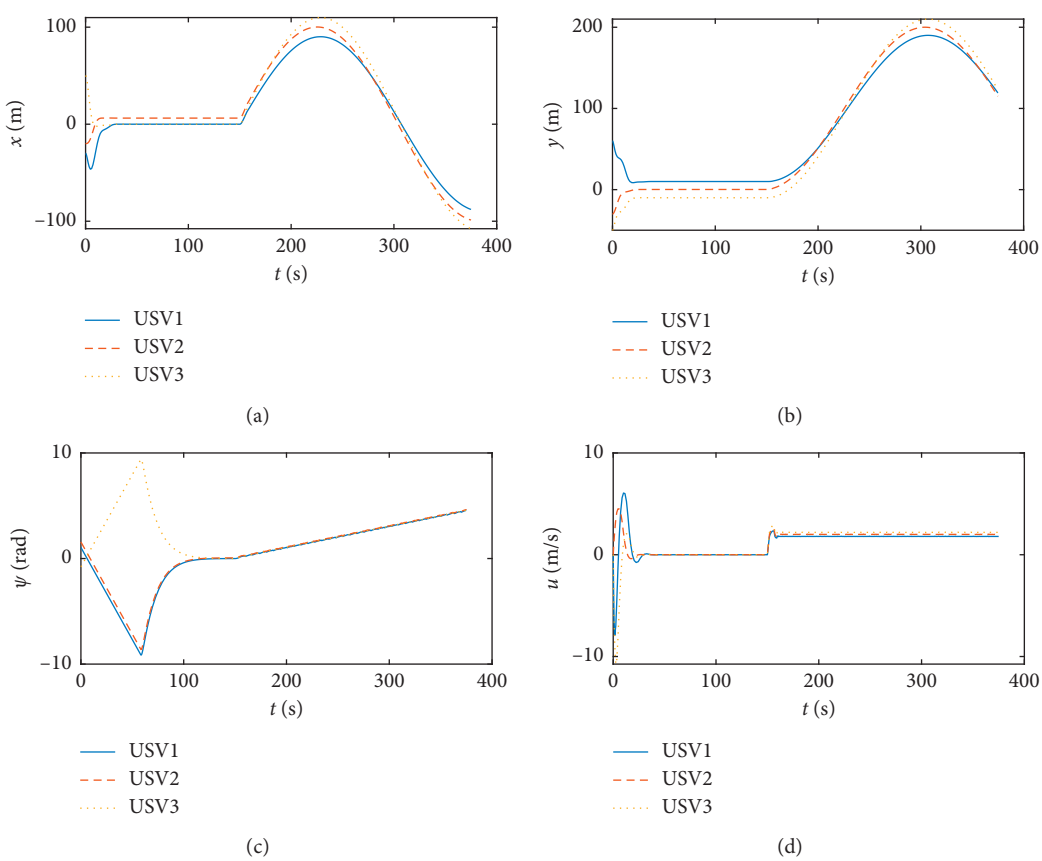

Figure 6: Continued.

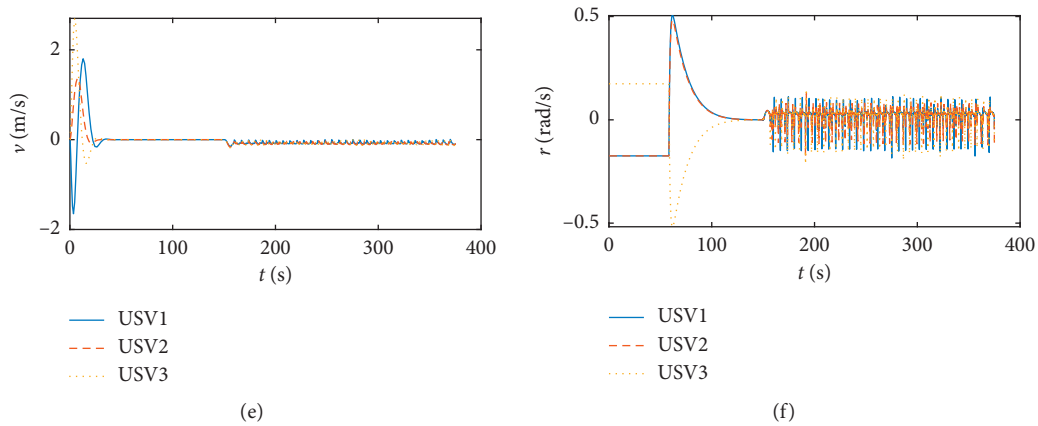

Figure 6: Curves of states with respect to time.

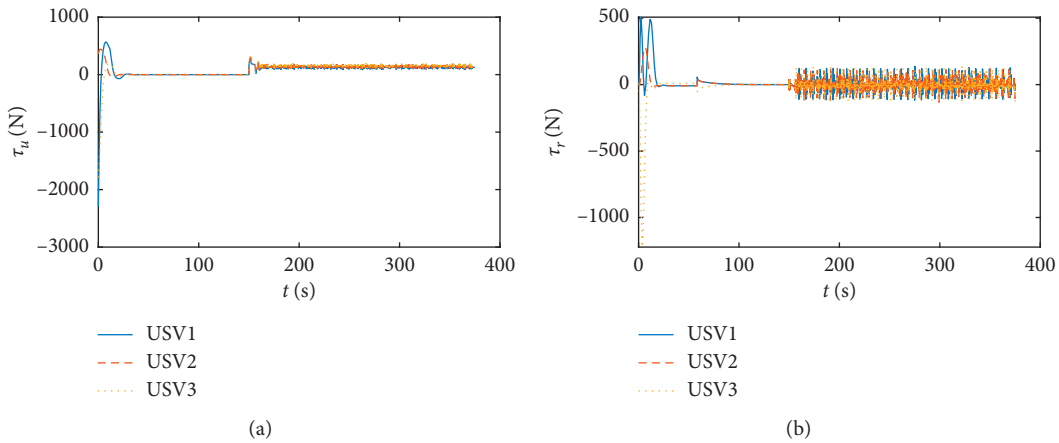

Figure 7: Curves of control efforts with respect to time.

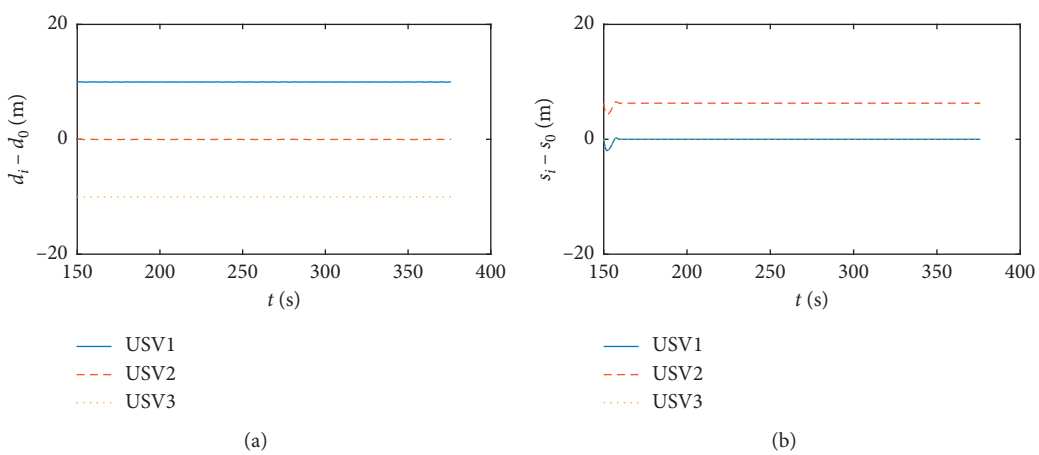

Figure 8: Curves of state errors $d_i - d_0$ and $s_i - s_0$ with respect to time.

control algorithm. The control inputs of the USVs are depicted in Figure 7. In the first stage, the exponents α_2 and α_4 have great influences on the convergence time. A good choice of them can greatly reduce the settling time of stage one. In the second stage, the feedback gains of the yaw subsystem k_{7i}, k_{8i}, and k_{9i} are usually selected to more than the gains of the surge subsystem k_{5i} and k_{6i}, to make the USVs on their paths.

Figure 8 shows the errors of the longitudinal displacement and the transversal displacement between the follower vehicles and the leader vehicle. The cooperative control starts working after which every USV gets to its own start points. Therefore, the time starts at 150 seconds and the errors of the displacements are constant, which means that the formation of the USV is kept well.

5. Conclusion

A formation control strategy based on finite-time control and leader-follower theory is proposed in the paper to achieve formation maneuver control for USVs. The formation control process is divided into two stages. In the first stage, all the USVs would be steered to their starting points in the formation pattern in finite time. Then, in the second stage, all the vehicles would be controlled to maintain the formation pattern based on finite-time distributed cooperative control. By using tools from homogeneous theory, it is theoretically shown that the proposed protocol can guarantee finite-time converge and consensus, respectively. Numerical simulation is made to illustrate effectiveness of our strategy.

Data Availability

The data used to support the findings of this study are available from the corresponding author upon request.

Conflicts of Interest

The authors declare no conflicts of interest.

Authors' Contributions

X. Y. and H. Y. conceptualized the study; H. Y. and X. Y. developed methodology; C. G. and H. Y. developed software; C. G. and Z. D. carried out formal analysis; C. G. investigated the study; H. Y, C. G., and X. Y. wrote the original draft.

Acknowledgments

This work was supported in part by the National Natural Science Foundation of China under Grant 61903163, Natural Science Foundation of the Jiangsu Higher Education Institutions of China under Grants 18KJB520010 and 19KJB510023, Jiangsu Province Postgraduate Innovation Plan under Grant 1032161916, and Zhenjiang Key Research and Design Project under Grant GY2018026.

References

[1] Z. Liu, Y. Zhang, X. Yu, and C. Yuan, "Unmanned surface vehicles: an overview of developments and challenges," *Annual Reviews in Control*, vol. 41, pp. 71–93, 2016.

[2] Z. Dong, L. Wan, Y. Li, T. Liu, and G. Zhang, "Trajectory tracking control of underactuated USV based on modified backstepping approach," *International Journal of Naval Architecture and Ocean Engineering*, vol. 7, no. 5, pp. 817–832, 2015.

[3] Y.-L. Liao, M.-J. Zhang, L. Wan, and Y. Li, "Trajectory tracking control for underactuated unmanned surface vehicles with dynamic uncertainties," *Journal of Central South University*, vol. 23, no. 2, pp. 370–378, 2016.

[4] Y.-L. Liao, M.-J. Zhang, and L. Wan, "Serret-frenet frame based on path following control for underactuated unmanned surface vehicles with dynamic uncertainties," *Journal of Central South University*, vol. 22, no. 1, pp. 214–223, 2015.

[5] T. Liu, Z. Dong, H. Du, L. Song, and Y. Mao, "Path following control of the underactuated USV based on the improved line-of-sight guidance algorithm," *Polish Maritime Research*, vol. 24, no. 1, pp. 3–11, 2017.

[6] K.-C. Cao and Y.-P. Tian, "A time-varying cascaded design for trajectory tracking control of non-holonomic systems," *International Journal of Control*, vol. 80, no. 3, pp. 416–429, 2007.

[7] Z. C. Zhang, *Stabilization and Tracking Control for Nonholonomic and Underactuated System*, Ph.D. thesis, Southeast University of China, Nanjing, China, 2016.

[8] B. W. Zeng, *Research on Nonlinear Control of Waterjet Propulsion Surface Unmanned Naval Vessel*, Ph.D. thesis, Harbin Engineering University, Harbin, China, 2012.

[9] R. W. Beard, J. Lawton, and F. Y. Hadaegh, "A coordination architecture for spacecraft formation control," *IEEE Transactions on Control Systems Technology*, vol. 9, no. 6, pp. 777–790, 2001.

[10] X. Cai and M. D. Queiroz, "Adaptive rigidity-based formation control for multirobotic vehicles with dynamics," *IEEE Transactions on Control Systems Technology*, vol. 23, no. 1, pp. 389–396, 2015.

[11] T. Balch and R. C. Arkin, "Behavior-based formation control for multirobot teams," *IEEE Transactions on Robotics and Automation*, vol. 14, no. 6, pp. 926–939, 1998.

[12] L. Consolini, F. Morbidi, D. Prattichizzo, and M. Tosques, "Leader-follower formation control of nonholonomic mobile robots with input constraints," *Automatica*, vol. 44, no. 5, pp. 1343–1349, 2008.

[13] K. D. Godard, K. Dev Kumar, and A. Zou, "Robust stationkeeping and reconfiguration of underactuated spacecraft formations," *Acta Astronautica*, vol. 105, no. 2, pp. 495–510, 2014.

[14] J. Wang, J. Y. Liu, and H. Yi, "Formation control of unmanned surface vehicles with vision sensor constraints," 2015.

[15] Z. H. Peng and D. Wang, "Adaptive dynamic surface control for formations of autonomous surface vehicles with uncertain dynamics," *IEEE Transactions on Control Systems Technology*, vol. 21, no. 2, pp. 513–520.

[16] Z. Sun, G. Zhang, Y. Lu, and W. Zhang, "Leader-follower formation control of underactuated surface vehicles based on sliding mode control and parameter estimation," *ISA Transactions*, vol. 72, pp. 15–24, 2018.

[17] K. Shojaei, "Leader-follower formation control of underactuated autonomous marine surface vehicles with limited torque," *Ocean Engineering*, vol. 105, pp. 196–205, 2015.

[18] H. Li, P. Xie, and W. Yan, "Receding horizon formation tracking control of constrained underactuated autonomous underwater vehicles," *IEEE Transactions on Industrial Electronics*, vol. 64, no. 6, pp. 5004–5013, 2017.

[19] J. Li, J. Du, and W.-J. Chang, "Robust time-varying formation control for underactuated autonomous underwater vehicles with disturbances under input saturation," *Ocean Engineering*, vol. 179, pp. 180–188, 2019.

[20] X. Jin, "Fault tolerant finite-time leader-follower formation control for autonomous surface vessels with LOS range and angle constraints," *Automatica*, vol. 68, pp. 228–236, 2016.

[21] W. Dong, "Cooperative control of underactuated surface vessels," *IET Control Theory & Applications*, vol. 4, no. 9, pp. 1569–1580, 2010.

[22] Z. H. Peng and J. Wang, "Distributed maneuvering of autonomous surface vehicles based on neurodynamic optimization and fuzzy approximation," *IEEE Trans. on Control Systems Technology*, vol. 26, no. 3, pp. 1083–1090, 2017.

[23] L. Liu, D. Wang, Z. Peng, and T. Li, "Modular adaptive control for LOS-based cooperative path maneuvering of multiple underactuated autonomous surface vehicles," *IEEE Transactions on Systems, Man, and Cybernetics: Systems*, vol. 47, no. 7, pp. 1613–1624, 2017.

[24] N. Wang and C. J. Qian, "Adaptive robust finite-time trajectory tracking control of fully actuated marine surface vehicles," *IEEE Transactions on Control Systems Technology*, vol. 24, no. 4, pp. 1454–1462, 2015.

[25] N. Wang and Z. Sun, "Finite-time observer based guidance and control of underactuated surface vehicles with unknown sideslip angles and disturbances," *IEEE Access*, vol. 6, no. 6, pp. 14060–14070, 2018.

[26] Q. Hou, L. Ma, S. Ding, X. Yang, and X. Chen, "Composite finite-time straight-line path-following control of an underactuated surface vessel," *Journal of the Franklin Institute*, vol. 357, no. 16, Article ID 11496, 2020.

[27] M. Ghasemi and S. G. Nersesov, "Finite-time coordination in multiagent systems using sliding mode control approach," *Automatica*, vol. 50, no. 4, pp. 1209–1216, 2014.

[28] Y. Liu and Z. Geng, "Finite-time formation control for linear multi-agent systems: a motion planning approach," *Systems & Control Letters*, vol. 85, pp. 54–60, 2015.

[29] Y. Zhao, Z. Duan, and G. Wen, "Finite-time consensus for second-order multi-agent systems with saturated control protocols," *IET Control Theory & Applications*, vol. 9, no. 3, pp. 312–319, 2014.

[30] C. Huang, X. Zhang, and G. Zhang, "Improved decentralized finite-time formation control of underactuated USVs via a novel disturbance observer," *Ocean Engineering*, vol. 174, pp. 117–124, 2019.

[31] T. Li, R. Zhao, C. L. P. Chen, L. Fang, and C. Liu, "Finite-time formation control of under-actuated ships using nonlinear sliding mode control," *IEEE Transactions on Cybernetics*, vol. 48, no. 11, pp. 3243–3253, 2018.

[32] S. H. Ding and S. H. Li, "A survey for finite-time control problems," *Control and Decision*, vol. 26, no. 2, pp. 161–169, 2011.

[33] M. Basin, Y. Shtessel, and F. Aldukali, "Continuous finite- and fixed-time high-order regulators," *Journal of the Franklin Institute*, vol. 353, no. 18, pp. 5001–5012, 2016.

[34] C. Godsil and G. F. Royle, *Algebraic Graph Theory*, Springer Science & Business Media, New York, NY, USA, 2013.

[35] F. L. Lewis, H. Zhang, K. Hengster-Movric et al., *Cooperative Control of Multi-Agent Systems: Optimal and Adaptive Design Approaches*, Springer Science & Business Media, New York City, NY, USA, 2013.

[36] J. Cheng, J. Yi, and D. Zhao, "Stabilization of an underactuated surface vessel via discontinuous control," in *Proceedings of the American Control Conference*, pp. 206–211, Denver, CO, USA, 2007.

[37] K. D. Do and J. Pan, "State-and output-feedback robust path-following controllers for underactuated ships using serret-frenet frame," *Ocean Engineering*, vol. 31, no. 5, pp. 587–613, 2004.

[38] K. D. Do and J. Pan, "Global robust adaptive path following of underactuated ships," *Automatica*, vol. 42, no. 10, pp. 1713–1722, Oct. 2006.

Hindawi
Complexity
Volume 2021, Article ID 6686977, 8 pages
https://doi.org/10.1155/2021/6686977

Research Article

A Novel Dynamic Routing Approach to Distributed Wireless Sensor Network in Aircraft Environment

Hui Sun,[1,2] **Chengrui Bai**,[1,3] **Yahui Li**,[1] **and Kaixin Yang**[4]

[1]*College of Information Engineering and Automation, Civil Aviation University of China, South Campus, Tianjin 300300, China*
[2]*Department of Engineering Design and Mathematics, University of the West of England, Frenchy Campus, Coldharbour Lane, Bristol, BS16 1QY, UK*
[3]*Freescale Semiconductor (China) Limited, Tianjin 300385, China*
[4]*Tianjin College, University of Science & Technology Beijing, Tianjin 301830, China*

Correspondence should be addressed to Hui Sun; shhappy1@hotmail.com

Received 14 October 2020; Revised 23 November 2020; Accepted 30 December 2020; Published 13 January 2021

Academic Editor: Jing Na

The trend to implement the monitoring system with a wireless sensor network has been becoming urgent due to guaranteed flight safety and the passengers comfortability in travel. In this paper, a new dynamic routing algorithm is proposed to prolong the lifetime of the monitoring system with a distributed network based on the *K*-coverage method, and filter algorithm to be used for data fusion. Finally, the simulation results validate the effectiveness of the proposed approach.

1. Introduction

In recent years, the civil aviation industry has developed rapidly in China. Passenger and cargo transitions have maintained fast growth from 2014 to 2018. In this case, air travel is considered to be the priority option [1]. The flight safety, environmental quality, and comfort in cabin are focused by passengers. [2]. To meet the extremely high requirements of flight safety and avoid the miss alarms, the sensors used in the monitoring system are always with strict sensitivities. However, this kind of system will lead to false alarms. For examples, on November 13, 2017, the flight CZ6406 of China Southern Airlines was diverted to Changsha Airport due to a fire false alarm in cargo during flight. On March 19, 2019, a Boeing 777 aircraft of British Airways was made a forced landing in St. John's, Canada, after takeoff because of the same issue [3]. The frequent occurrence of false alarm events will cause a lot of economic losses and give passengers uncomfortable travel experience. Therefore, it is very important to reduce the fire false alarm rate in airplanes. At present, wired single-point sensors in airplanes can no longer meet the practical demands. A wireless sensor network including a large number of nodes with a specific algorithm can be used to play an important role than that of single-point wired sensors [4]. Furthermore, this kind of network can be applied in different areas such as UAV systems and environment monitoring. [5–8]. Wang et al. designed a WSN for pollutant monitoring in the cabin [7] and analyzed network failures cases [8]. They also proposed to use WSN for monitoring fire in the cargo compartment of commercial aircraft and deployed sensors based on the *K*-coverage index redundantly. However, they did not discuss the energy consumption and lifetime of WSN for aircraft applications [9]. In this article, a dynamic deployment method of WSN is discussed. This method is mainly focused on the dynamic balance of coverage and energy consumption in WSN aircraft environment application.

The coverage of the monitoring area and the available service time of the network are two important indicators needed to be considered for a WSN operation. So an energy-saving approach applied in cabin WSN based on the low-energy adaptive clustering hierarchy (LEACH) protocol is taken into consideration [10]. However, due to the strong randomness of the LEACH protocol in the cluster establishment phase, it will lead to creating unreasonable topology [11]. Many articles combined LEACH with other algorithm to improve overall performance. Kaddi et al. proposed a kangaroo method-based LEACH protocol, which has a good

energy consumption performance and can prolong WSN lifetime [12]. Mohapatra et al. proposed a partitioned-based energy-efficient-LEACH (PE-LEACH) protocol which tends to the energy-based fault-tolerant technique, and it performs better than the LEACH protocol [13].

Therefore, in this article, a novel coverage index, K-coverage, with a certain probability is proposed to be a criterion of network lifetime. Then an improved binary artificial bee colony-LEACH (LEACH, LEACH-IBABC) algorithm is proposed with the index mentioned above. This approach makes active nodes and cluster head nodes to the global optimization in order to reduce the energy consumption and extend the lifetime of WSN. The structure of this article is arranged as follows: First, a probabilistic sensing model with a dynamic K-coverage deployment index with a certain probability is proposed. Second, a new LEACH-IBABC algorithm is proposed for the dynamic K-coverage deployment of WSN applied in aircraft cabins. Third, simulation verification and analysis are discussed. Finally, conclusions are drawn. The main contribution of this article is to combine the classical LEACH protocol with a new IBABC algorithm to reduce WSN energy consumptions and prolong network lifetime based on the constraint of the new coverage index, dynamic K-coverage.

2. Sensing Model and Coverage Rate Index of Wireless Sensor Network

2.1. Probabilistic Sensing Model of Wireless Sensor Nodes. In practical applications, the sensing probability of the monitoring grid points does not simply follow a Boolean model. It is determined by the distance, d_{ml}, between the sensor node (SN) and the monitored target, the physical parameters of the node, and the interference of the surrounding environment. The sensing probability can more accurately reflect the coverage capability of wireless sensor nodes for the real environment [14]. The probability mentioned above varying with distance d_{ml} is noted as the probabilistic sensing model (PSM).

Definition 1. Effective sensing radius: in terms of the probabilistic sensing model, when d_{ml} is smaller than the effective sensing radius $R_{s,\max}$ of the wireless sensor node, the target point to be monitored (TPM) can be effectively monitored and covered, so the sensing probability p_{ml} is 1. Otherwise, the probability p_{ml} is less than 1. $R_{s,\max}$ is a threshold value of d_{ml}. Furthermore, that probability exponentially decreases as the Euclidean distance between SN and TPM increases.

Suppose that the deployed sensor nodes are homogeneous in this article, the sensing model is optimized and obtained in (1) by deriving from the model proposed in [15]:

$$p_{\mathrm{ml}} = \begin{cases} 1, & d_{\mathrm{ml}} \le R_{s,\max}, \\ e^{-\alpha d_{\mathrm{ml}}}, & d_{\mathrm{ml}} > R_{s,\max} \text{ and } p_{\mathrm{ml}} \ge p_{\mathrm{thr}}, \\ 0, & p_{\mathrm{ml}} < p_{\mathrm{thr}}, \end{cases} \tag{1}$$

where m is the index of SN. l is the index of TPM. And the parameter α ($\alpha > 0$) describes the decreasing rate of the sensing (monitoring) probability p_{ml} when distance d_{ml} increases. As d_{ml} is continuously increasing till p_{ml} is less than a predefined threshold p_{thr}, the possibility of TMP successfully monitored is too small to make error monitoring results. Therefore, p_{ml} is zero in this condition. p_{thr} ($0 < p_{\mathrm{thr}} < 1$) is a relatively small value close to 0.

To calculate the threshold value of d_{ml}, let $e^{-\alpha d_{\mathrm{ml}}} = p_{\mathrm{thr}}$, then the threshold value of d_{ml} can be obtained as shown in the following equation:

$$d_{\mathrm{ml}} = \frac{1}{\alpha} \ln \frac{1}{p_{\mathrm{thr}}}. \tag{2}$$

Substituting (2) into (1), we can obtain the following equation:

$$p_{\mathrm{ml}} = \begin{cases} 1, & d_{\mathrm{ml}} \le R_{s,\max}, \\ e^{-\alpha d_{\mathrm{ml}}}, & R_{s,\max} < d_{\mathrm{ml}} < \frac{1}{\alpha} \ln \frac{1}{p_{\mathrm{thr}}}, \\ 0, & d_{\mathrm{ml}} \ge \frac{1}{\alpha} \ln \frac{1}{p_{\mathrm{thr}}}. \end{cases} \tag{3}$$

Equation (3) shows a complete piecewise function of p_{ml} according to variable d_{ml}.

Taking an effective sensing radius $R_{s,\max} = 1.5$ m as an example, Figure 1 shows the change of the monitoring probability p_{ml} as the distance d_{ml} varies.

As shown in Figure 1 ($\alpha = 0.3$), if the distance between SN and TPM is 0, the monitored probability of TPM is 1. If the distance between SN and TPM is larger than $R_{s,\max}$, the probability value p_{ml} decreases smoothly. And the probability decreases sharply at the beginning, and the decreasing speed is faster in the early stage than that in the latter stage. When the distance is larger than $(1/\alpha)\ln(1/p_{\mathrm{thr}})$, p_{ml} is 0.

2.2. Probabilistic Sensing Model-Based Dynamic K-Coverage Deployment with a Certain Probability of WSN in Aircraft Cabin. In general, the coverage rate of wireless sensor networks is defined as shown below:

$$\mathrm{COV}(S) = \frac{\bigcup_{i=1}^{N_s} \mathrm{Area}(s_i)}{L \times W \times H}, \tag{4}$$

where the length of the area to be monitored is L. The width is W. The height is H. And the set of all sensor nodes $S = \{s_1, s_2, \ldots, s_{Ns}\}$. Area ($s_i$) represents the coverage area of SN, which is the center of a sphere with the sensing radius. Due to the complexity of the calculation, a regional three-dimensional meshing method is used to find a deployment solution to WSN in aircraft cabin. In Figure 2, the solid dots are wireless sensor nodes. The hollow dots are grid points. In this article, consider each grid point as a TPM in the aircraft environment.

As mentioned before, the monitoring probability matrix $P = [p_{\mathrm{ml}}]_{NS \times NGP}$ where $m = 1, 2, \ldots, N_s$, N_s is the number of

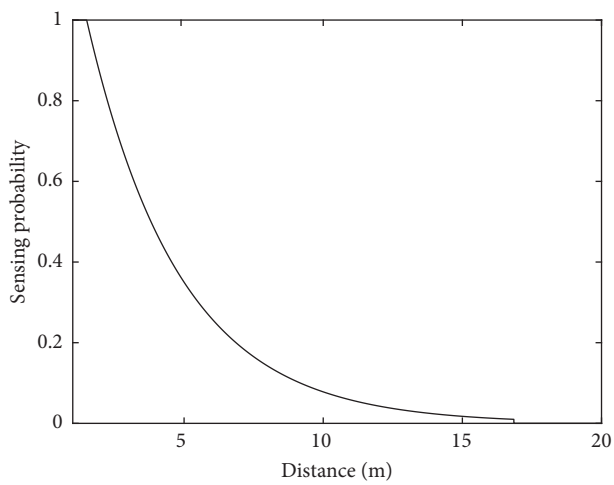

Figure 1: The relationship between sensing probability and distance when $\alpha = 0.3$.

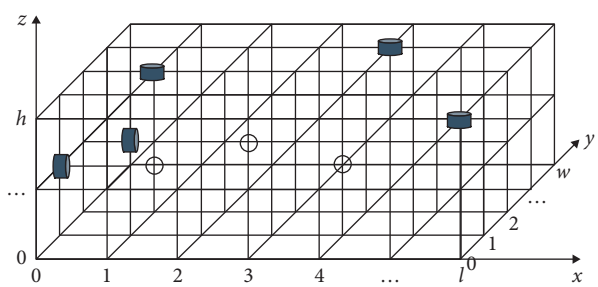

Figure 2: Schematic diagram of the three-dimensional area meshing.

sensor nodes, $l = 1, 2, \ldots, N_{GP}$, and N_{GP} is the total number of grid points (equivalent to TPM). The set of all sensor nodes is expressed as $S = \{s_q \mid q \in [1, N_s]\}$.

For any grid point l, the covering probability is the joint probability shown below:

$$p_l = 1 - (1 - p_{1l})(1 - p_{2l}) \cdots (1 - p_{N_s l}) = 1 - \prod_{m=1}^{N_s} (1 - p_{ml}). \tag{5}$$

In this article, a constant value, p_A, is defined as monitoring accuracy. And the joint probability of all monitored TPMs should not be smaller than p_A. The parameter p_A should be larger for the higher requirements of environments.

When $K = 1$ and $\forall p_l \geq p_A$, the wireless sensor network has achieved the coverage for grid point l with joint probability p_A.

When $K > 1$, assume that the subset of the sensor nodes $\mathrm{SEN}_q \subseteq S$ contains n_s sensor nodes ($1 \leq n_s \leq N_s$), and each sensor node in the subset is different from others. Each subset SEN_q is independent of others:

$$\begin{gathered} \cup_{q=1}^{K} \mathrm{SEN}_q \subseteq S, \\ \forall 1 \leq q_1, q_2 \leq k, \\ \mathrm{SEN}_{q_1} \cap \mathrm{SEN}_{q2} = \varnothing. \end{gathered} \tag{6}$$

If there are at least K SEN_q subsets and all the sensor nodes of each subset cover the grid point l with the joint probability p_A, all the nodes of set S achieve K-coverage at grid point l with the probability p_A. Moreover, if each grid point in the area to be monitored is K-coverage with probability p_A, the wireless sensor network can achieve K-coverage with probability p_A in that area. By changing the values of the monitoring accuracy p_A and the coverage degree K, the coverage index of the network can be adjusted.

In this article, when plenty of sensor nodes have been deployed in the aircraft cabin, the dynamic K-coverage and deployment algorithm is used to decide which sensor nodes are activated in each cycle, so that the active nodes of the wireless sensor network should ensure that each grid point in the cabin is covered by at least K groups of sensor nodes with probability p_A.

Parameters K and p_A are two important coverage indicators of WSN. The larger the values of K and p_A are, the more the nodes are required, the more accurate the fire monitor is, however, the higher the energy consumption is. On the contrary, it is impossible to meet the coverage and accuracy requirements if these two parameters are too small. In the next section, a new routing protocol is proposed to save energy.

3. Intelligent-Based Dynamic Routing Approach to Energy saving

A routing protocol is one of the key technologies in wireless sensor network-related technologies. In recent years, four types of protocols have been developed for wireless sensor networks. They are geographic-based routing protocols, data center-based routing protocols, cluster-based routing protocols, and hybrid routing protocols. And each type of protocol has produced many branches.

The cluster-based routing protocol separates the sensor nodes into different groups. And each group of sensor nodes is organized by a cluster head (CH). All cluster heads are controlled by a base station (BS) or sink node. The LEACH protocol is the most basic and popular cluster-based routing protocol. The clustering method of the LEACH protocol is shown in Figure 3.

3.1. Energy Consumption Model of Sensor Node. To prolong the lifetime of WSN applied in aircraft, it is necessary to develop an energy-saving algorithm.

The energy consumption of nodes in wireless sensor networks is mainly divided into the following categories:

(1) The inherent operating energy consumption

It is created from SN hardware themselves without sensing and communicating with other nodes.

(2) The energy consumption on collecting and sensing

It occurs in collecting information and detecting the environment. The time interval of collecting environmental information, T_{sense}, will affect the energy consumption speed.

(3) The energy consumption of data transmission

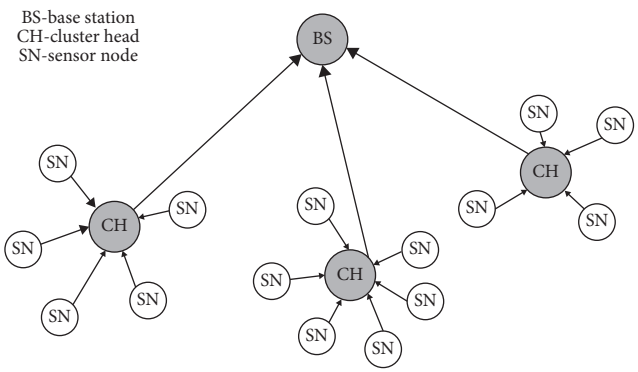

Figure 3: Schematic diagram of LEACH protocol topology.

It occurs in transmitting the sensing data amplified by the power amplifiers.

Figure 4 is a block diagram of a conventional wireless sensor network node module.

A wireless sensor network node is composed of four hardware modules: sensing module, processing module, wireless communication module, and energy supply module.

According to the energy consumption model in [16], the energy consumption of data transmitting and receiving from sensor node m_1 to m_2 can be visually shown in Figure 5.

As shown in Figure 5, the energy consumed by the transmitter can be calculated by using the following equation:

$$E_{\mathrm{Tx}}(L,d) = E_{\mathrm{Tx-elec}}(L) + E_{\mathrm{Tx-amp}}(L,d) = \begin{cases} E_{\mathrm{elec}} \cdot L + \varepsilon_{\mathrm{fs}} \cdot L \cdot d^2, & d < d_0, \\ E_{\mathrm{elec}} \cdot L + \varepsilon_{\mathrm{mp}} \cdot L \cdot d^4, & d \geq d_0, \end{cases} \quad (7)$$

where L is the number of bits of data transmitted between two nodes. Parameter d is the distance between any two communication nodes. E_{elec} represents the energy consumption of the circuit. Parameters $\varepsilon_{\mathrm{fs}}$ and $\varepsilon_{\mathrm{mp}}$ represent the energy consumption of the transmitter amplifier per square meter per bit. d_0 is the threshold distance and is defined in equation (8). If d is less than d_0, the free space channel model is adopted, and the power amplifier coefficient is $\varepsilon_{\mathrm{fs}}$. Otherwise, the multipath attenuation model is used, and the power amplifier coefficient is $\varepsilon_{\mathrm{mp}}$:

$$d_0 = \sqrt{\frac{\varepsilon_{\mathrm{mp}}}{\varepsilon_{fs}}}. \quad (8)$$

The energy consumption of the receiver is shown in the following equation:

$$E_{\mathrm{Rx}}(L) = E_{\mathrm{Rx-elec}}(L). \quad (9)$$

The energy consumption on data fusion of the cluster head can be calculated by the following equation:

$$E_A = L \cdot E_{\mathrm{DA}}, \quad (10)$$

where E_{DA} represents the required energy for data fusion per bit assuming that there is no energy consumption in the collecting process.

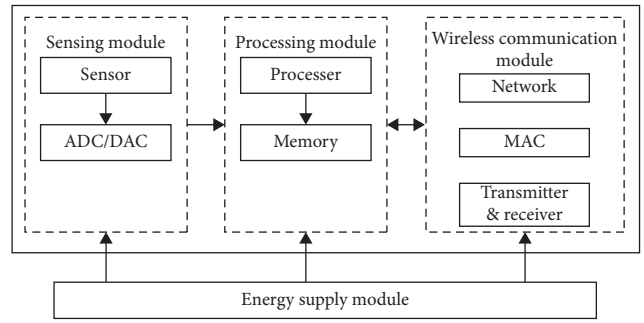

Figure 4: Block diagram of the sensor node model.

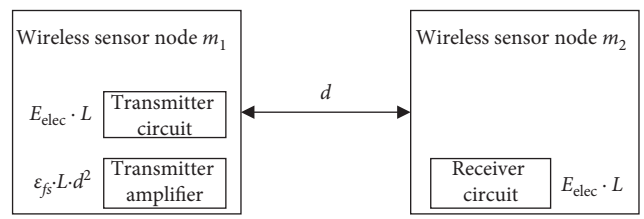

Figure 5: Schematic diagram of energy consumption for SN data transmission.

3.2. LEACH-IBABC Algorithm. This section proposes a new protocol algorithm-LEACH-IBABC based on the basic LEACH protocol and energy consumption model mentioned above.

Normally, "round" is a basic unit in the LEACH protocol. Each node of the wireless sensor network has a specific probability to be a cluster head in one round. Based on this idea, the load of the network can be distributed to each node uniformly to prolong the lifetime of the network [17].

A wireless sensor network organized by the LEACH protocol includes at least one base station or sink node. The base station or sink node collects data from all cluster heads without considering the energy consumption. In this article, all nodes are assumed to own the same initial energy, and the transmission energy consumption is symmetrical between the communication pair. A node can adjust the transmission power automatically to minimize energy consumption by calculating the distance between the transmitter and receiver ends based on the strength of the received signal.

All sensor nodes participate in coverage and sensing for the basic LEACH protocol. Therefore, the network coverage is high in the early operation stage. However, when some nodes' energy is exhausted, the network coverage ratio might not be guaranteed and may decrease rapidly. Then the wireless sensor network with a low coverage ratio is not suitable for aircraft cabin scenarios. However, as mentioned above, WSN should ensure that the coverage ratio meets the K-coverage index with probability p_A to decrease false alarms and missed alarms.

Inspired by the LEACH-C algorithm, the base station can be used as a center to manage the status of each node (working or sleeping) and cluster working mode (cluster head or cluster member) [18]. This algorithm operates in the cluster establishment phase of each round. In the operation

process, an optimal node subset S_D selected from the K-covered node set S is set to work mode and participates in the dynamic coverage of WSN in this round. And other nodes are in sleep mode to save energy. It is an NP hard problem to select the optimal node subset. To solve this problem, the artificial bee colony algorithm-based LEACH protocol is proposed. In this article, since each node has only two states: working and sleeping, a binary artificial bee colony (BABC) algorithm is used. Compared to the classic ABC algorithm, the improved BABC algorithm uses different search formulas at each stage.

The objective of the optimal operating node subset is selected to satisfy K-coverage with probability p_A with most $E_{\text{rest\_sum}}$ and least n_s. $E_{\text{rest\_sum}}$ is the total residual energy of the operating nodes at the end of this round, and n_s is the total number of operating nodes. In this case, it will not only balance the network load energy consumption and allow nodes with the highest energy to work first, but also ensure coverage ratio and avoid triggering too many nodes simultaneously. Therefore, the total energy consumption of the wireless sensor network is reduced.

In the initialization stage, the food source corresponds to a feasible solution to the practical problem. At this stage, each dimension of each feasible solution generates a random number r_{ij} $(0 < r_{ij} < 1)$, and the value of the dimension is determined according to equation (11). Then each feasible solution is assigned to an employed bee:

$$v_{ij} = \begin{cases} 0, & 0 \le r_{ij} \le 0.5, \\ 1, & 0.5 < r_{ij} \le 1, \end{cases} \tag{11}$$

where $i = 1, 2, \ldots, \text{NP}$, $j = 1, 2, \ldots, N_s$, and v_{ij} is the jth dimension of the ith feasible solution. NP is the number of feasible solutions, also represents the number of employed bees. N_s is the number of sensor nodes, also represents the dimension of the feasible solution in this article. The initial feasible solution of the IBABC algorithm is shown in Figure 6.

After allocating the employed bee to each feasible solution in the initialization stage, the fitness value of each solution is calculated by equation (12). The fitness value of the solution corresponds to the quality of the feasible solution:

$$\text{fit}_i(k) = E_{\text{rest\_sum}}(k) \times \text{COV}(k, S) - \alpha \cdot n_s(k), \tag{12}$$

where $\text{fit}_i(k)$ represents the fitness value of the ith solution in the kth iteration. $E_{\text{rest\_sum}}(k)$ represents the total predicted residual energy at the end of the current round according to the current topology. COV (k, S) means the network coverage ratio in the kth iteration. $n_s(k)$ is the number of operating nodes in the kth iteration. The impact factor of the node numbers, α, is a constant equal to 0.1 in this article. In general, at the end of the current round, the more the residual energy is, the larger the network coverage ratio is, the fewer the number of awakened nodes are, the larger the fitness value and the better the quality of the solution are. The steps for the coverage ratio COV (S) based on the probability sensing model are shown in Table 1.

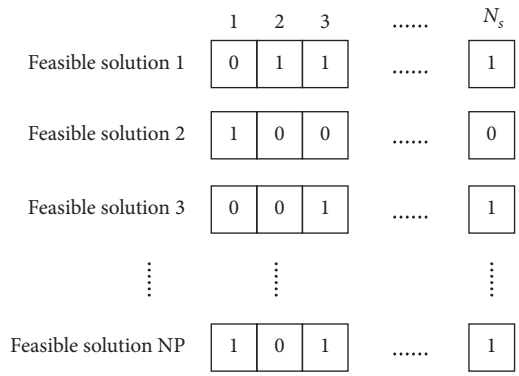

Figure 6: Schematic diagram of the feasible solution of the IBABC algorithm.

Table 1: Pseudocode for calculating COV(S) of K-covered network coverage rate based on probability p_A.

Function PSM_K-coverage_Calculate_Coverage_Rate()(PSMKCCR)
BEGIN
01. *for* each grid point T_j (x_{Tj}, y_{Tj}, z_{Tj})
02. Calculate the total probability p_j that all sensors cover grid point T_j
03. $p_j = 1 - (1 - P_{1j})(1 - P_{2j}) \cdots (1 - P_{N_s j}) = 1 - \prod_{i=1}^{N_s}(1 - P_{ij})$
04. Define node set UNUSED = S, USED = ϕ, SS $\subseteq$ UNUSED
05. *for* $q = 1 : K$
06. *if* $\exists$SS $\subseteq$ UNESED, $p_j \ge p_A$
07. TEMP++
08. Put the sensor nodes in SS into *USED*
09. *end*
10. *if* TEMP = = K
11. T_j is covered with probability p_A, covpoint++
12. TEMP is set zero
13. *end*
14. *end*
15. *end*
16. covrate = covpoint/$[(l+1)(w+1)(h+1)]$
END

In the employed bee stage, each employed bee i selects a neighbor u randomly and generates a random number φ_{ij} $(0 < \varphi_{ij} < 1)$. Then the candidate feasible solution is generated according to the following equation:

$$v_{ij}(k, t+1) = \begin{cases} v_{ij}(k, t), & \varphi_{ij} > \dfrac{\text{fit}_i(k)}{\text{fit}_i(k) + \text{fit}_u(k)}, \\ v_{uj}(k, t), & \text{otherwise}, \end{cases} \tag{13}$$

where k represents the current iteration. $i \ne u$. That means the selected neighbor cannot be the same as the current feasible solution. $v_{ij}(k, t)$ is the jth dimension of the ith solution. $v_{uj}(k, t)$ is the jth dimension of the feasible solution of a selected neighbor, u. $v_{ij}(k, t+1)$ is derived from $v_{ij}(k, t)$ and $v_{uj}(k, t)$. The employed bee uses a greedy selection method to judge whether to select the candidate feasible

solution. If the candidate feasible solution is better than the original feasible solution, the original feasible solution will be replaced. Otherwise, the original state is unchanged, and the cumulative times of inactivity for a feasible solution increases by 1.

In the follower bee stage, the probability of each feasible solution selected by the follower bee can be calculated by the following equation:

$$p_i(k) = \frac{\mathrm{fit}_i(k)}{\sum_1^{\mathrm{NP}} \mathrm{fit}_n(k)} + 0.1, \tag{14}$$

where k represents the current iteration. $p_i(k)$ is the probability that the ith feasible solution is selected by a follower bee in the kth iteration. If a follower bee selects a feasible solution, a candidate feasible solution is calculated using equation (13) to improve the quality of the current feasible solution. If the quality of the candidate feasible solution is better than that of the current feasible solution, the current feasible solution is replaced. Then the employed bee uses this new candidate feasible solution. Otherwise, the original state remains unchanged, and the cumulative times of inactivity for a feasible solution increases by 1. This is similar to that in the employed bee stage.

In the scout bee stage, the cumulative times of inactivity for a feasible solution is checked with the threshold *Limit*. If the variable value is larger than *Limit*, the employed bee for exploring the current feasible solution changes into a scouter. And a new feasible solution is generated by equation (11), and the cumulative times of inactivity for a feasible solution is reset. Then the scouter changes into an employed bee. In the process, only one scouter exists. If the scouter stage is over, the optimal solution of all feasible solutions is recorded.

After selecting the optimal operating node subset S_D, it is necessary to find a group of cluster head node subset S_{DH} from S_D to act as the cluster heads in this round. Since the dimension of S_D is not too large, the fitness value of all feasible solutions can be obtained by the ergodic method. The steps are listed as follows:

(1) To predict the energy consumption of each node in the current round according to the energy consumption model and calculate the residual energy of each node.

(2) To ensure that the total energy consumption of the operating nodes is the lowest under the S_{DH} network topology, and make sure that the standard deviation of the node energy consumption is the smallest. The fitness value is calculated by using the following equation:

$$\mathrm{fit}_{i\_\mathrm{DH}} = E_{\mathrm{sum}} \cdot \mathrm{SD}\left(E_{m\_\mathrm{sum}}\right). \tag{15}$$

In equation (15), fitness value $\mathrm{fit}_{i\_\mathrm{DH}}$ is used to evaluate the topology quality of the ith feasible solution. If the consumption of energy of the whole WSN and the standard deviation of the node energy consumption are smaller simultaneously, the fitness value is smaller, and the quality of this topology organized by LEACH-IBABC is better, which brings a more balanced energy consumption.

In the aircraft environment, it is necessary to ensure that the operating nodes can meet the coverage index. In this article, the network is considered to get the maximum lifetime when the coverage index cannot be reached due to the exhaustion of some nodes. Figure 7 shows the flow chart of the LEACH-IBABC algorithm.

4. Simulation and Analysis of the Proposed Method

This section presents the simulation validation and compares the lifetime of WSN between the LEACH and LEACH-IBABC algorithms. This article considers a WSN with the K-coverage ($K = 3$) index deployed in an aircraft cargo model with 80 sensor nodes in total. Each node has the same initial energy. The simulation parameters are set as follows:

(1) Cluster head selection probability $p = 0.1$

(2) The initial energy of each sensor node $E_0 = 0.02$ J

(3) Transmitting and receiving circuit energy consumption $E_{\mathrm{elec}} = 50$ pJ/(bit m^{-2})

(4) Transmitter amplifier energy consumption parameters $\varepsilon_{\mathrm{fs}} = 10$ pJ/(bit m^{-2}) and $\varepsilon_{\mathrm{mp}} = 0.0013$ pJ/(bit m^{-4})

(5) Data fusion energy consumption $E_{\mathrm{DA}} = 5$ pJ/bit

(6) The data packet length $L_d = 4000$ bit, and the control packet length $L_c = 32$ bit

(7) PSM is used as the sensing model of sensor nodes, and the monitoring accuracy $p_A = 0.99$

(8) Coverage degree $K = 1$

The corresponding simulation results are shown in Figures 8 and 9. As illustrated in Figure 8, the network using the LEACH algorithm cannot meet 2-coverage with probability 0.99 after the 106th round and cannot meet the 2-coverage with probability 0.9 after the 131st round. However, the network with the LEACH-IBABC algorithm cannot meet 2-coverage with probability 0.99 after the 154th round and cannot meet 2-coverage with probability 0.9 after the 189th round. As curves shown in Figure 8, the LEACH-IBABC algorithm prolongs the network lifetime. When the monitoring coverage index is 2-coverage with probability 0.99, the WSN runs 48 more rounds, so the network lifetime is increased by 45.3%. When the monitoring coverage index is 2-coverage with probability 0.9, the WSN runs 58 more rounds, so the network lifetime is increased by 44.3%.

The residual energy comparisons between two algorithms as the number of active rounds change are shown in Figure 9. When it goes to the 106th round, the residual energy of WSN using LEACH-IBABC is 2.43 J more than the WSN using LEACH. This helps the WSN using LEACH-IBABC runs 48 more rounds. When it goes to the 131th round, the residual energy of WSN using LEACH-IBABC is 3.18 J more than the WSN using LEACH. This helps the WSN using LEACH-IBABC runs 58 more rounds. The total residual energy by using the LEACH-IBABC algorithm

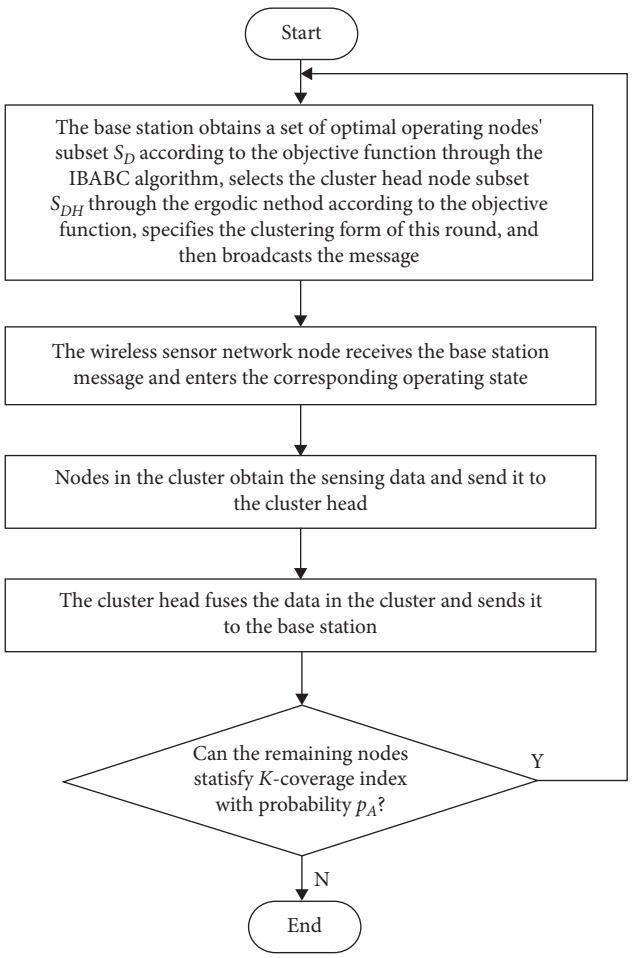

Figure 7: Flow chart of LEACH-IBABC algorithm.

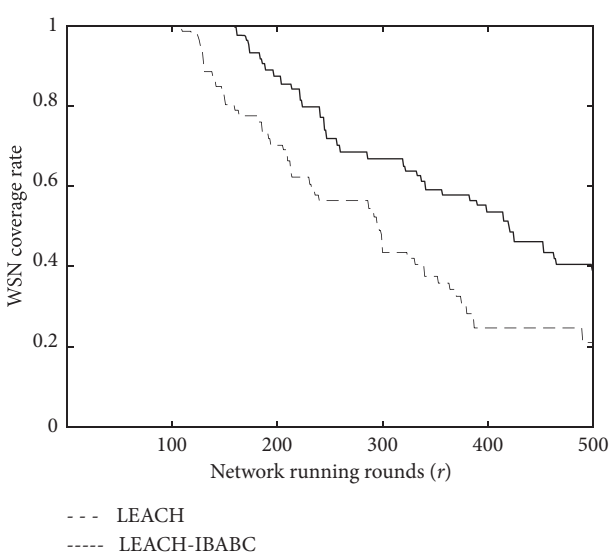

Figure 8: Coverage rate comparison of LEACH and LEACH-IBABC *vs* the number of running rounds.

reduces slower than that of the LEACH algorithm in the early stage.

Therefore, the LEACH-IBABC approach can be used to organize the global optimal topology and reduce the overall energy consumption of the network. On one hand, the base station handles the task of topology allocation of WSN, so the calculation burden of the nodes is reduced greatly. On the other hand, each node only needs to select the different states according to the base station information and send the collected sensing information to the cluster head directly. Therefore, the energy consumption of nodes is reduced, and the lifetime of the network is prolonged.

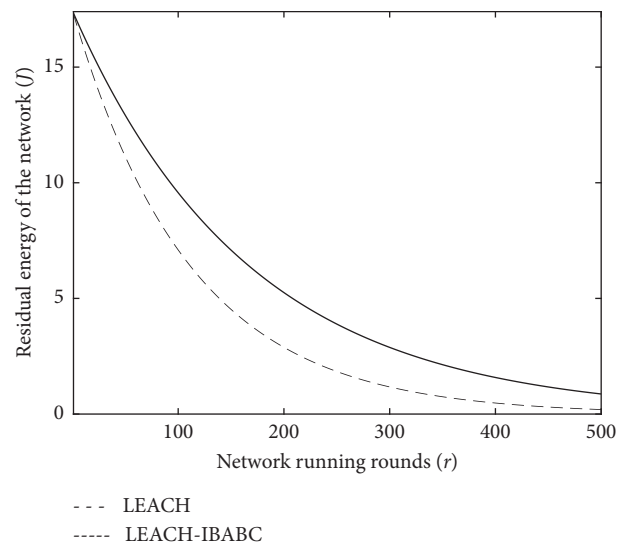

Figure 9: Residual energy comparison of LEACH and LEACH-IBABC *vs* the number of running rounds.

5. Conclusions

In this article, a dynamic routing approach to WSN, the LEACH-IBABC algorithm, is proposed for the aircraft environment. In this method, the IBABC algorithm is designed to select the operating node subset S_D which is a global optimization by using the artificial bee colony algorithm. In this case, the nodes with more residual energy have the priority to participate in the current round and meet the requirements of the K-coverage index with a probability p_A. The others are in sleep mode. Then the optimal cluster head node subset S_{DH} is selected with the proposed algorithm to decrease energy consumption and make a better load balance. Therefore, the information selected from the nodes is estimated by using the Kalman filter. Finally, the simulation results prove that the proposed algorithm can reduce energy consumptions and prolong network lifetime based on the constraint of the coverage index.

Data Availability

The figures.zip data used to support the findings of this study are available from the corresponding author upon request.

Conflicts of Interest

The authors declare that there are no conflicts of interest regarding the publication of this paper.

Acknowledgments

The authors would like to extend our sincere gratitude to Prof. Youmin Zhang from Concordia University, Canada, for his instructive advice and suggestions on this paper. This work was supported by Tianjin Natural Science Foundation, 18JCYBJC42300, and Scientific Research Project of Tianjin Education Commission, 2019KJ143.

References

[1] CAAC, "Civil aviation industry development statistical bulletin," 2018, http://www.caac.gov.cn/XXGK/XXGK/TJSJ/201905/t20190508_196033.html.

[2] B. Qiu, G. Y. Bai, D. S. Zhu, L. L. Li, J. H. Fan, and T. B. Liu, "Analysis on quality of air in aircraft cabins," *Journal of Environmental Hygiene*, vol. 4, no. 2, pp. 143–146, 2014.

[3] CCTV, "A british airways boeing airliner made an emergency landing at st. johns airport in canada with no casualties," 2018, http://m.news.cctv.com/2019/03/19/ARTI4BzdoIQcrNR9JZX7dGE6190319.shtml.

[4] W. J. Yu, X. B. Li, X. Li, and Z. Zeng, "Constrained relay node deployment using an improved multi-objective artificial bee colony in wireless sensor networks," *Ksii T Internet Inf*, vol. 11, no. 6, pp. 2889–2909, 2017.

[5] Z. Yu, Y. Zhang, B. Jiang, J. Fu, Y. Jin, and T. Chai, "Composite adaptive disturbance observer-based decentralized fractional-order fault-tolerant control of networked UAVs," *IEEE Transactions on Systems, Man, and Cybernetics: Systems*, pp. 1–15, 2020.

[6] Z. Yu, Z. Liu, Y. Zhang, Y. Qu, and C.-Y. Su, "Distributed finite-time fault-tolerant containment control for multiple unmanned aerial vehicles," *IEEE Transactions on Neural Networks and Learning Systems*, vol. 31, no. 6, pp. 2077–2091, 2020.

[7] R. Wang, Y. Li, H. Sun, and Z. Chen, "Analyses of integrated aircraft cabin contaminant monitoring network based on Kalman consensus filter," *ISA Transactions*, vol. 71, no. 1, pp. 112–120, 2017.

[8] R. Wang, X. Wang, H. Sun, Y. Huang, and Z. Chen, "Analysis of estimator and energy consumption with multiple faults over the distributed integrated WSN," *International Journal of Modelling, Identification and Control*, vol. 32, no. 2, pp. 154–168, 2019.

[9] R. Wang, C. Bai, L. Gao, and H. Sun, "A 3-D deployment and coverage algorithm for aircraft cargo,"vol. 582, pp. 1335–1343, in *Proceedings of the 11th International Conference on Modelling, Identification and Control*, vol. 582, pp. 1335–1343, Springer, Tianjin, China, July 2019.

[10] A. Al-Baz and A. El-Sayed, "A new algorithm for cluster head selection in LEACH protocol for wireless sensor networks," *International Journal of Communication Systems*, vol. 31, pp. 1–13, 2018.

[11] C. Liu, G. F. Chen, and W. F. Ma, "Research and improvement on the LEACH protocol of wireless sensor network," *Journal of Changchun University of Science and Technology(Natural Science Edition)*, vol. 41, no. 2, pp. 129–133, 2018.

[12] M. Kaddi, K. Benahmed, and M. Omari, "LEACH-KANG: A new routing protocol for WSN based on leach protocol and Kangaroo method," in *Proceedings of the 2017 International Conference on Mathematics and Information Technology (ICMIT)*, pp. 273–278, Adrar, Algeria, 2017.

[13] H. Mohapatra and A. K. Rath, "Fault tolerance in WSN through PE-LEACH protocol," *IET Wireless Sensor Systems*, vol. 9, no. 6, pp. 358–365, 2019.

[14] W. J. Yu, *Research On Artificial Bee Colony Based Deployment Problem In Wireless Sensor Network*, University of Electronic Science and Technology of China, Chengdu, China, 2018.

[15] H. Li, T. H. Dai, and L. N. Gao, "Research of WSN's routing protocol based on improved ant colony algorithm," *Control Engineering of China*, vol. 24, no. 11, pp. 2201–2205, 2017.

[16] W. B. Heinzelman, A. P. Chandrakasan, and H. Balakrishnan, "An application-specific protocol architecture for wireless microsensor networks," *IEEE Transactions on Wireless Communications*, vol. 1, no. 4, pp. 660–670, 2002.

[17] W. H. Zhang, L. Y. Li, L. M. Zhang, and X. Z. Wang, "Energy consumption balance improvement of LEACH of WSN," *Chinese Journal of Sensors and Actuators*, vol. 21, no. 11, pp. 1918–1922, 2008.

[18] X. Wang and S. Wu, "Performance comparison of LEACH and LEACH-C protocols by NS2," in *Proceedings of the 2010 Ninth International Symposium on Distributed Computing and Applications to Business, Engineering and Science*, pp. 254–258, Los Alamitos, CA, USA, August 2010.

Hindawi
Complexity
Volume 2021, Article ID 6627043, 17 pages
https://doi.org/10.1155/2021/6627043

Research Article

Single-Leg Structural Design and Foot Trajectory Planning for a Novel Bioinspired Quadruped Robot

Mingfang Chen, Qi Li, Sen Wang, Kaixiang Zhang, Hao Chen, and Yongxia Zhang

Faculty of Mechanical and Electrical Engineering, Kunming University of Science and Technology, Kunming 650500, China

Correspondence should be addressed to Sen Wang; wangsen0401@126.com

Received 13 November 2020; Revised 9 December 2020; Accepted 23 December 2020; Published 12 January 2021

Academic Editor: Xue-bo Jin

To meet the stability requirements for moving quadruped robots, it is important to design a rational structure for a single leg and plan the trajectory of the foot. First, a novel electrically driven leg mechanism for a quadruped robot is designed in this paper to reduce the inertia of the leg swing. Second, a modified foot trajectory based on a compound cycloid is proposed, which has swing-back and retraction motion and continuous velocity in the x-axis direction. Third, a Simulink platform is built to verify the correctness of the proposed foot trajectory. The simulation result shows that when the flight phase and the stand phase switch, the impact of torque is smaller than the foot trajectory before modification. Finally, an experimental platform is constructed, and a control algorithm is written into the controller to realize the foot proposed trajectory. The results of the experiment prove the feasibility of the leg mechanism and the rationality of the proposed foot trajectory.

1. Introduction

Robotics have become an active research area in recent years. Bioinspired foot robots have become a topic of interest in the field of robot research, because of their unique motion form, control method, and adaptability in complex environments [1, 2]. The stability and load capacity of a quadruped robot are much better than those of the biped robot. The complexity of the mechanism and control strategy are simpler than those of hexapod and multilegged robots [3, 4]. Thus, quadruped robots have a wide range of applications in military transportation, forest detection, and emergency rescue scenarios [5].

The main driving methods for bioinspired quadruped robots are electric drive and hydraulic drive [6]. For example, the BigDog and LS3 robots developed by Boston Dynamics [7, 8], the HyQ robot designed by the Italian Institute of Technology [9, 10], and the bioinspired quadruped robot developed by Shandong University [11] all use the hydraulic driving method. Hydraulic systems have the advantages of large output power [12], small inertia, and sensitive action. Therefore, a hydraulically driven quadruped robot can achieve high load capacity and high control accuracy, but its ratio of self-weight and rated load is generally large, making it difficult to miniaturize the robot. Due to the presence of hydraulic components such as hydraulic cylinders, the inertia of the leg is large, so it is difficult to achieve high-speed running actions. In contrast, electrically powered quadruped robots, such as the LittleDog and SpotMini robots developed by Boston Dynamics [13, 14], the Laikago robot designed by Unitree [15], and the MiniCheetah robot developed by MIT [16], have the advantages of low noise, convenient speed regulation, strong anti-interference ability, and stable speed. The leg structures of these robots often use joint motors to directly drive the leg motion or a synchronous belt to transmit the motion. However, electrical components such as joint motors increase the inertia of the leg, and the synchronous belt transmission method cannot sustain a large load. With the rapid development of high-torque motors and high-performance magnetic bearing [17], high-load and high-speed electrically driven quadruped robots have become an important research direction in recent years. Therefore, it is meaningful to study the low-inertia and high-strength electrically driven leg structure.

Whatever the driving method of the robot is, the goal is to obtain better load capacity, adaptability, and stability in a complex environment. The factors that affect the stability of bioinspired quadruped robots are complex, and the control strategy is critical. In existing reports on advanced quadruped robots, the control algorithms are not open source. Therefore, research on the control strategy of quadruped robots remains a topic of interest in current research. Single-leg trajectory planning is an important part of the quadruped robot's motion control and a key factor of the bioinspired quadruped robot's motion ability. Therefore, an electrically driven leg mechanism for a quadruped robot is designed in this paper, and a compound cycloid foot trajectory with swing-back and retraction motion is proposed. Then, a single-leg simulation platform is built, and a kinematic and dynamic simulation of the proposed modified trajectory is carried out on the simulation platform. Finally, the experiment is carried out, and the feasibility of the leg mechanism and the rationality of this foot trajectory is verified by the simulation and experiment. This work lays a foundation for the development of the whole machine.

2. Brief Description of Mechanism

The driving mode of quadruped robots generally adopts hydraulic or electric drives. Electric drives have the advantages of high control accuracy and precise motion tracks compared with hydraulic drive modes, and the electric driving mode is suitable for light- and medium-load bioinspired quadruped robots. Thus, the leg mechanism designed in this paper adopts an electric drive.

To improve the stability and movement ability of the quadruped robot [18], the leg of the quadruped robot designed in this paper adopts a knee and elbow face-to-face structure. The quadruped robot model is shown in Figure 1 and includes the machine body, waist structure, leg structure, and electrical components. The leg mechanism includes three degrees of freedom (DOF): hip joint side swing, hip joint front swing, and knee joint front swing.

Common leg structural models of quadruped robots include zoom structures and linkage structures. The zoom structure leg is highly efficient, and the control strategy is relatively simple, but it is often bulky and does not have bionic characteristics; therefore, it is inconvenient to install and is not conducive to robot miniaturization. For example, the ASV [19] robot developed by the Ohio State University adopts the zoom structure; its ratio of self-weight to bearing weight is only 0.08, and the performance of the whole machine is poor.

Linkage structure legs can be categorized as series types, parallel types, and parallel-series types. A series leg is simple in structure, easy to control, and has a large working space, but its load carrying capacity is relatively small, and installing the drive unit or transmission element at the joint increases the inertia of the leg, such as the ANYmal robot developed by ANYbotics [20].

Inspired by a cat's leg structure, Park et al. [21] designed a single-DOF parallel leg mechanism composed of 9 connecting rods and 1 spring. The experimental results showed

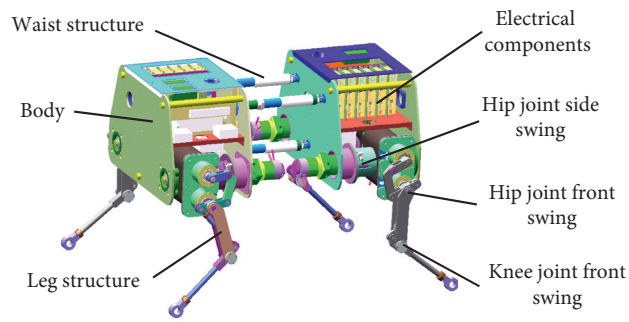

Figure 1: Quadruped robot model.

that the robot of this leg mechanism can run on flat ground at a speed of 0.75 m/s. However, because the leg mechanism has only one active DOF, it is difficult to achieve a rich foot trajectory, and the foot trajectory formed during the movement is affected by the robot's weight and the terrain. For heavy loads and irregular terrain, the adaptability of this kind of leg structure needs to be further verified.

The parallel-series leg has the advantages of a larger working space and high load capacity. For example, the Baby-Elephant robot designed by Shanghai Jiao Tong University [22] uses a parallel-series leg structure, but this leg structure does not have bionic characteristics. There are often more DOFs, which complicates the control strategy, and more driving elements and transmission elements will also increase the inertia of the leg movement, which is not conducive to improving the maneuverability of the whole machine.

Although the leg structure of the quadruped robot has been studied by many scholars, designing a leg mechanism with both high mobility and high load capacity remains a research challenge. In this paper, a parallel leg structure of a quadruped robot is designed. The proposed leg mechanism can achieve a rich foot trajectory and has a large workspace and good rigidity and strength. This kind of structure is compact and easy to install.

In this paper, the leg adopts rod mechanism whose force transmission is simple. To reduce the mass and inertia of the leg, the motor that drives the knee joint is integrated into the hip joint, as shown in Figure 2.

The front swing joints of the hip and knee include the motor flange plate, shank drive rod, intermediate connecting rod 1, intermediate connecting rod 2, joint bearing rod, thigh connecting rod, and shank connecting rod. Among these, the shank drive rod, intermediate connecting rod 1, intermediate connecting rod 2, and motor flange plate are simplified to form a parallelogram mechanism. The intermediate connecting rod 2, joint bearing rod, leg connecting rod, and leg connecting rod are simplified to form an antiparallelogram mechanism. The motor drives the shank drive rod to rotate through the output shaft of the reducer, and then the parallelogram and antiparallelogram mechanisms drive the shank connecting rod to realize forward swing.

The design of the parallelogram mechanism and the antiparallelogram mechanism integrates the drive motor of the knee joint and the hip joint into the body part. Therefore,

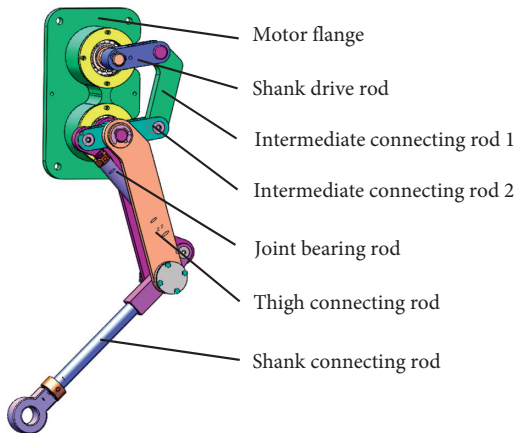

Figure 2: Single-leg model.

it avoids the motor following the swing of the leg when the leg moves forward and reduces the inertia when the leg swings.

3. Kinematic Modeling of Single-Leg Mechanism

To facilitate research, most scholars tend to simplify their models when planning the foot trajectory of quadruped robots; thus, the simplified model is shown in Figure 3. According to the simplified model, there are three DOFs on a single leg. The DOF of hip joint lateral swing can realize the lateral swing of the leg. The DOF of hip joint front swing can achieve the back-and-forth swing of the thigh; and the DOF of the knee joint enables the back-and-forth swing of the shank. Among them, the DOF of hip joint lateral swing and the DOF of hip joint front swing can achieve rich foot trajectory in a 2D plane, and the DOF of the knee joint can adjust the stability of the whole machine so that the quadruped robot can adapt to complex terrain.

To achieve a kinematic analysis of a single leg, the D-H coordinated system is established on the left hind leg model, as shown in Figure 4. The initial position of the coordinate system 0 coincides with coordinate system 1. The z-axis of frames 1, 2, and 3 coincides with the axis of each joint, the x-axis coincides with the connecting rod, and the y-axis is derived from the right-hand rule. The z-axis of frame 4 is perpendicular to the paper, and other axis directions are shown in Figure 4. According to the D-H method and the established coordinate system, the D-H parameters are obtained, as shown in Table 1 [23].

Figure 3 shows that each leg can be simplified into four parts, namely, the body, hip, thigh, and shank. They are represented by i, corresponding to $i = 1$, 2, 3, and 4, respectively. Then, the transformation matrix of the coordinate system on linkage i relative to the coordinate system on $i = -1$ is obtained, as shown in the following equation:

$$ {}^{i-1}_{i}T = \begin{bmatrix} \cos\theta_i & -\sin\theta_i & 0 & a_{i-1} \\ \sin\theta_i\cos\alpha_{i-1} & \cos\theta_i\cos\alpha_{i-1} & -\sin\alpha_{i-1} & -\sin\alpha_{i-1}d_i \\ \sin\theta_i\sin\alpha_{i-1} & \cos\theta_i\sin\alpha_{i-1} & \cos\alpha_{i-1} & \cos\alpha_{i-1}d_i \\ 0 & 0 & 0 & 1 \end{bmatrix}. \tag{1} $$

We substitute the data in Table 1 into equation (1) and then the transformation matrix can be obtained as ${}^{0}_{1}T$, ${}^{1}_{2}T$, ${}^{2}_{3}T$, and ${}^{3}_{4}T$. According to the formula ${}^{0}_{4}T = {}^{0}_{1}T{}^{1}_{2}T{}^{2}_{3}T{}^{3}_{4}T$, ${}^{0}_{4}T$ is obtained, as shown in the following equation:

$$ {}^{0}_{4}T = {}^{0}_{1}T{}^{1}_{2}T{}^{2}_{3}T{}^{3}_{4}T = \begin{bmatrix} C_1C_{23} & -C_1S_{23} & S_1 & L_3C_1C_{23} + L_2C_1C_2 + L_1C_1 \\ S_1C_{23} & -S_1S_{23} & -C_1 & L_3S_1C_{23} + L_2S_1C_2 + L_1S_1 \\ S_{23} & C_{23} & 0 & L_3S_{23} + L_2S_3 \\ 0 & 0 & 0 & 1 \end{bmatrix}, \tag{2} $$

where $C_1 = \cos\theta_1, S_1 = \sin\theta_1, C_{23} = \cos(\theta_2 + \theta_3)$, and

$$ S_{23} = \sin(\theta_2 + \theta_3). \tag{3} $$

Let the coordinates of the foot end be (p_x, p_y, p_z); then the forward kinematics model of the simplified single-leg model is

$$ \begin{bmatrix} p_x \\ p_y \\ p_z \\ 0 \end{bmatrix} = {}^{0}_{4}T \begin{bmatrix} 0 \\ 0 \\ 0 \\ 1 \end{bmatrix} = \begin{bmatrix} l_3\cos(\theta_1)\cos(\theta_2 + \theta_3) + l_2\cos(\theta_1)\cos(\theta_2) + l_1\cos(\theta_1) \\ l_3\sin(\theta_1)\cos(\theta_2 + \theta_3) + l_2\sin(\theta_1)\cos(\theta_2) + l_1\sin(\theta_1) \\ l_3\sin(\theta_2 + \theta_3) + l_2\sin(\theta_3) \\ 1 \end{bmatrix}. \tag{4} $$

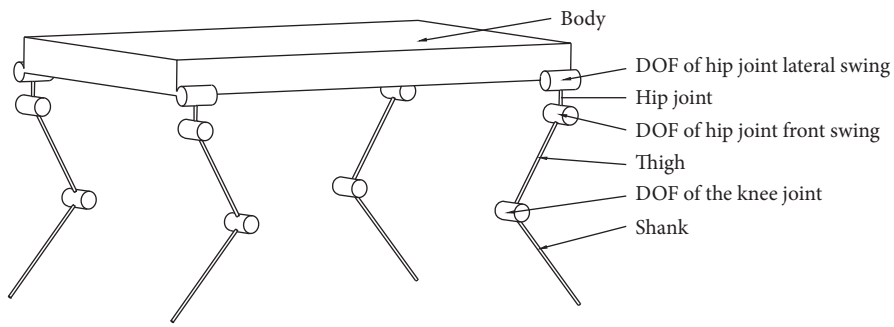

Figure 3: Simplified quadruped robot model.

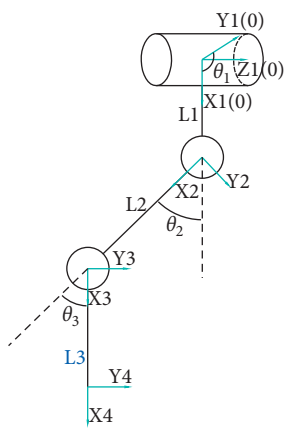

Figure 4: Simplified single-leg model.

Table 1: D-H parameters.

i	α_{i-1}	a_{i-1}	d_i	θ_i
1	0	0	0	θ_1
2	90°	l_1	0	θ_2
3	0	l_2	0	θ_3
4	0	l_3	0	0

With formulas $[{}^1_2T]^{-1}[{}^0_1T]^{-1}{}^0_4T = {}^2_3T{}^3_4T$ and $[{}^2_3T]^{-1}[{}^1_2T]^{-1}[{}^0_1T]^{-1}{}^0_4T = {}^3_4T$, equation (5) can be obtained, which is the inverse kinematics model of the single leg of the quadruped robot.

$$\begin{cases} \theta_1 = \arctan\left(\dfrac{P_y}{P_x}\right), \\ \theta_2 = 2\arctan\left(\dfrac{L_3C_3 + L_2 \pm \sqrt{(L_3C_3 + L_2)^2 + (L_3C_3)^2 - P_z^2}}{L_3S_3 + P_z}\right), \\ \theta_3 = \arccos\left(\dfrac{(P_x - (L_1C_1/C_1))^2 + P_z^2 - L_3^2 - L_2^2}{2L_2L_3}\right), \quad C_1 \neq 0. \end{cases} \tag{5}$$

The meaning of each symbol in the formula is the same as the previous formula.

According to the designed leg mechanism, its mechanism diagram is built as shown in Figure 5.

The solid line in the figure is the leg linkage, and the dotted line is the auxiliary line. The parameters of each link are shown in Table 2.

As the diagram of leg mechanism shows, quadrilateral ABCD is a parallelogram and quadrilateral DEFG is an antiparallelogram; ΔDEG and ΔEDF are congruent triangles, the same as ΔFEG and ΔGDF. According to the geometric relations in Figure 5 and cosine theorem, the value of β_1 can be calculated under the condition of knowing θ_2 and θ_3 as follows:

$$\beta_1 = 280 + \theta_2 - \theta_3 - 2\arccos\frac{l_{EF} - l_{DF}\cos(\theta_3 - 10)}{\sqrt{l_{EF}^2 + l_{DF}^2 - 2l_{EF}l_{DF}\cos(\theta_3 - 10)}}. \tag{6}$$

According to the mapping relationship between β_1 with θ_2 and θ_3, the driving joint angle of the designed single-leg mechanism can be solved, and then a simulation and experiment can be carried out to verify the modified trajectory's rationality.

4. Workspace Analysis of the Leg Mechanism

The workspace of the leg mechanism of the quadruped robot refers to the set of spatial position points that can be reached by the reference point of the foot end, which is a key parameter used to evaluate the feasibility and efficiency of the leg mechanism of the quadruped robot. In this paper, the Monte Carlo method is used to calculate the robot's foot workspace in a 2D plane. The specific steps are as follows:

(1) Calculate the positive kinematics model of the single-leg mechanism

(2) Determine the range of motion angle of each joint and determine the constraint relationship between each angle

(3) Program in MATLAB and draw the workspace of the single-leg mechanism

The workspace obtained by MATLAB is shown in Figure 6.

Figure 6 shows that the leg mechanism proposed in this article has a large workspace, can achieve a step height of more than 200 mm, and has a large step length.

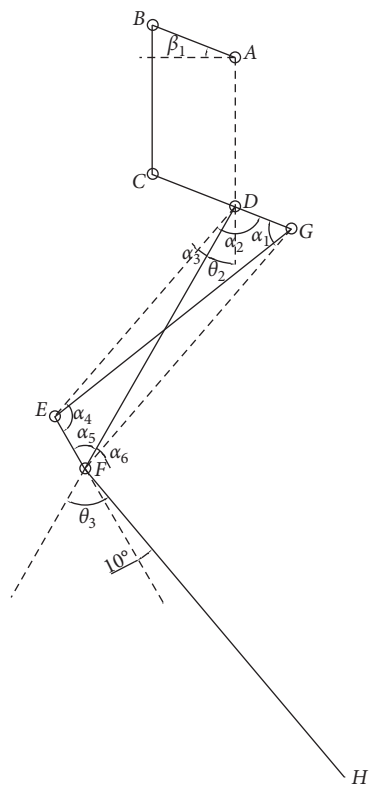

Figure 5: Schematic diagram of leg mechanism.

Table 2: Parameters of each link.

Linkage	Size (mm)
Thigh connecting rod L_{DF}	170
Shank connecting rod L_{FH}	227
Parallelogram mechanism L_{AB}/L_{BC}	50/84
Antiparallelogram mechanism L_{DG}/L_{GE}	34/170

5. Trajectory Planning of Foot

The quadruped robot's leg alternates between the flight phase and stand phase while walking. The stand phase is the process from the foot end of one leg touching the ground to leaving the ground, bearing the weight of the whole body and adjusting the robot's stability. The flight phase is the process of the foot end from leaving the ground to touching the ground. The main parameters of the flight phase include step height and the step length, among which the step height determines the ability of the quadruped robot to overcome obstacles, and the step length determines the size of the stride length of the quadruped robot. Therefore, gait planning mainly refers to the planning of the flight phase, and the track of the stand phase usually adopts a simple linear track.

Flight phase trajectory planning is a key step to achieve dynamic walking for a quadruped robot. To realize good stability during fast movement, foot trajectory planning should satisfy the following as much as possible: the trajectory of the foot should be a circular curve to ensure that the speed and acceleration of the foot are continuous without abrupt change and that the angular velocity and acceleration of the joint are smooth and continuous; there is no impact between the foot and the ground; that is, the velocity and acceleration are 0 when landing and leaving the ground; unnecessary motion should be avoided [6]; and the foot end and the ground should be prevented from producing relative slide as much as possible.

For the flight phase trajectory, a trajectory planning method based on a compound cycloid was proposed in [24], which was verified in [25]. To solve the problems of sliding and dragging when the robot's foot contacts the ground, [26] proposed a modification to the compound cycloid planning method. To solve the problem of a sudden change in acceleration when $t = 0$ and $t = T_m$ in the modified trajectory equation, [1, 10] improved the displacement equation in the y-direction vertical to the ground and proposed a zero-impact trajectory. The improved trajectory equation is

$$x = S\left[\frac{t}{T_m} - \frac{1}{2\pi}\sin\left(2\pi\frac{t}{T_m}\right)\right] - \frac{S}{2},$$

$$y = \begin{cases} 2H\left[\dfrac{t}{T_m} - \dfrac{1}{4\pi}\sin\left(4\pi\dfrac{t}{T_m}\right)\right], & 0 \le t < \dfrac{T_m}{2}, \\ 2H\left[1 - \dfrac{t}{T_m} + \dfrac{1}{4\pi}\sin\left(4\pi\dfrac{t}{T_m}\right)\right], & \dfrac{T_m}{2} \le t < T_m, \end{cases} \tag{7}$$

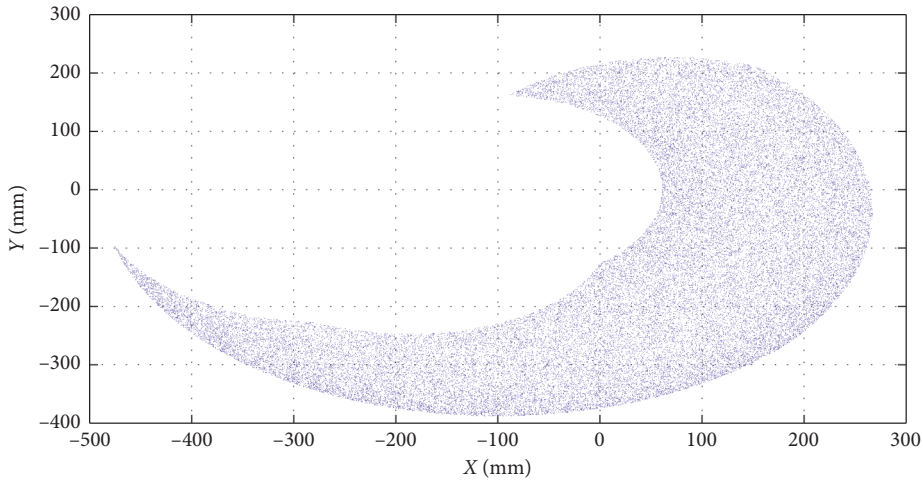

Figure 6: Workspace of leg mechanism.

where S is the stride length of the flight phase; H is the step height of the flight phase; and T_m is the period time of the flight phase.

However, the above trajectory only considers the motion of the flight phase; that is, the speed and acceleration of the forward direction are 0 at the moment when the foot touches and leaves the ground, but the motion of the support phase is ignored. Considering that the robot is extremely fast in its running motion, the motion of the stand phase can be equivalent to the linear motion of uniform speed. Therefore, at the moment of the transition between the flight phase and the stand phase, the x-direction that the robot forwards will generate a great acceleration, which will impact the motor at the joints and cause the vibration of the whole machine. Hildebrand studied the foot track of a fast-moving cheetah [27] and found that, during fast movement, the foot track of the cheetah was a closed curve, and the end of the foot retreated and swung back when landing and leaving the ground. The foot track is shown in Figure 7. Karssen et al. also found that swing-back and retraction of the leg could improve the stability and anti-interference ability of the robot during walking and running [28–31]. In addition, according to videos such as "Big-Dog" and "Spot-Mini" published by Boston Dynamics, it was also found that the robot adopts the foot trajectory with retraction motion and swing-back motion when moving forward.

From the above analysis, it can be seen that the speed and acceleration of the x-axis have a buffer when there is swing-back and retraction movement. To reduce the impact phenomenon of the x-axis during the transition between the flight phase and the stand phase, the movement in the x-axis direction of equation (7) is modified, and the movement of retraction and swing-back is added on the basis of the original x-axis movement. Assuming that the period time T_m of the flight phase remains unchanged, the original motion time of the x-axis changes to T_n, and the motion time of both the retraction and the swing-back is T_e; then $T_m = T_n + 2T_e$. With reference to sinusoidal motion, for the swing-back motion, let the curve equation of acceleration be

$$\ddot{x} = A_e \sin\pi \frac{t}{T_e}. \tag{8}$$

The velocity equation obtained by integration is

$$\dot{x} = -A_e \frac{T_e}{\pi} \cos\pi \frac{t}{T_e} + C_1. \tag{9}$$

We know from the two endpoints of the velocities that $\dot{x} = v = -(S/T_m)$ when $t = 0$. When $t = T_e$, $\dot{x} = 0$. Therefore, it can be determined that $A_e = ((S\pi)/(2T_m T_e))$ and $C_1 = -(S/(2T_m))$. Thus,

$$\dot{x} = -\frac{S}{2T_m} \cos\pi \frac{t}{T_e} - \frac{S}{2T_m}. \tag{10}$$

The equation of the swing-back motion curve can be obtained by integration:

$$x = -\frac{\mathrm{ST}_e}{2T_m \pi} \sin\pi \frac{t}{T_e} - \frac{S}{2T_m} t + C_2, \tag{11}$$

$x = C_2$ when $t = 0$, and when $t = T_e$, $x = (\mathrm{ST}_e/2T_m) + C_2$. Therefore, C_2 is the coordinate value of x-axis from the location, and the value of the swing-back is $(\mathrm{ST}_e/2T_m)$ which is related to the ratio of T_e to T_m.

Similarly, the curve equation of the retraction motion is

$$x = \frac{\mathrm{ST}_e}{2T_m \pi} \sin\pi \frac{(t - T_e - T_n)}{T_e} - \frac{S}{2T_m} (t - T_e - T_n) + C_3, \tag{12}$$

where C_3 is the coordinate value of the initial point of the retraction on the x-axis, namely, the maximum point of movement in the x-axis direction.

Therefore, the modified trajectory curve equation can be obtained as follows:

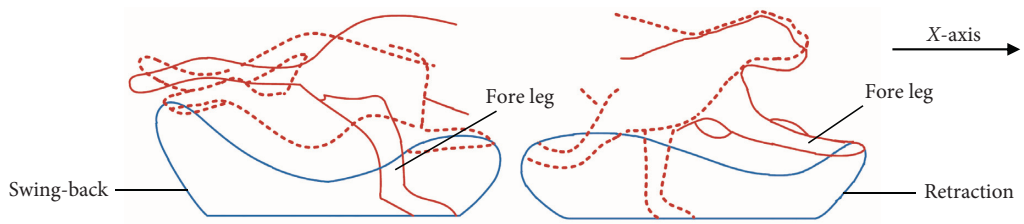

Figure 7: Track curve of cheetah foot.

$$x = \begin{cases} -\dfrac{ST_e}{2T_m\pi}\sin\pi\dfrac{t}{T_e} - \dfrac{S}{2T_m}t + C_2, & 0 \le t \le T_e, \\ S\left[\dfrac{t-T_e}{T_n} - \dfrac{1}{2\pi}\sin\left(2\pi\dfrac{t-T_e}{T_n}\right)\right] - \dfrac{S}{2}, & T_e \le t \le T_e + T_n, \\ \dfrac{ST_e}{2T_m\pi}\sin\pi\dfrac{(t-T_e-T_n)}{T_e} - \dfrac{S}{2T_m}(t-T_e-T_n) + C_3, & T_e + T_n \le t \le T_m, \end{cases}$$
$$y = \begin{cases} 2H\left[\dfrac{t}{T_m} - \dfrac{1}{4\pi}\sin\left(4\pi\dfrac{t}{T_m}\right)\right], & 0 \le t < \dfrac{T_m}{2}, \\ 2H\left[1 - \dfrac{t}{T_m} + \dfrac{1}{4\pi}\sin\left(4\pi\dfrac{t}{T_m}\right)\right], & \dfrac{T_m}{2} \le t < T_m, \end{cases} \tag{13}$$

where S is the step length, H is the step height, T_m is the period of the flight phase and the stand phase, T_e is the period of the swing-back movement and retraction movement of the flight phase, and T_n is the main motion period of the removal of the swing-back and retraction of the flight phase.

According to equation (13), the value of the swing-back and retraction is $(ST_e/2T_m)$; we can change it by choosing different ratio between T_e and T_m. The value is obtained by test method in this paper.

The trajectory for the stance phase adopts a simple linear trajectory, and its expression is shown in the following formula:

$$\begin{cases} x = \dfrac{S}{T_m}, \\ y = 0. \end{cases} \tag{14}$$

6. Construction and Simulation of the Single-Leg Model

6.1. Simulation System. SimMechanics is a MATLAB simulation toolbox that combines the functions of Simulink and MATLAB. It is convenient to use the block diagram of the SimMechanics module or directly import the 3D model from the 3D modeling software to conduct modeling and simulation of the mechanism. Moreover, the movement process of the mechanism can be visually displayed through the SimMechanics visualization tool [32], which provides a very simple and visual verification method for the foot track planning of the bioinspired quadruped robot.

SolidWorks-MATLAB cosimulation was used to build the simulation system. This is a convenient way to import models from SolidWorks to SimMechanics, and the simulation system and model for SimMechanics are shown in Figure 8. Then, the control module in SimMechanics is added to facilitate the writing of the control program. In the model, the length of the connecting rod is $\mathbf{l}_1 = 0, \mathbf{l}_2 = 170$, and $\mathbf{l}_3 = 227$. There are two rotational DOFs in the hip joint and one rotational DOF in the knee joint. Each joint can be controlled by the driving joint angle of the control subsystem output, and then we can obtain the designed trajectory of the foot.

To obtain the trajectory curve of the foot simulation, it is necessary to add a corresponding coordinate system to the foot, set the relative position of the coordinate system, and add components such as an oscilloscope, as shown in Figure 9.

Let the period time of the flight phase and the stand phase be $T_m = 2$ s and the period time of the swing-back and the retraction motion be $T_e = 0.4$ s; the step length is $S = 80$ cm, and the step height is $H = 50$ cm. Add trajectory equation (7) into the control subsystem, and run the simulation. The trajectory curve obtained is shown in Figure 10, which verifies the correctness of the simulation system and the kinematic model.

Once the modified trajectory curve expression (13) is written into the control subsystem, the simulation is run,

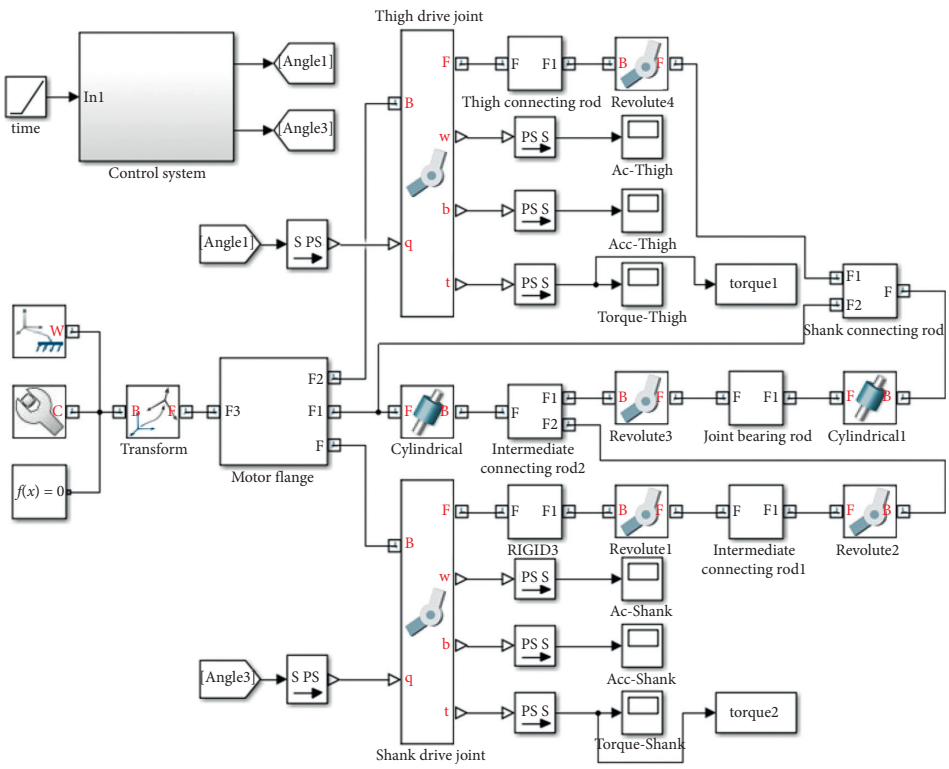

(a)

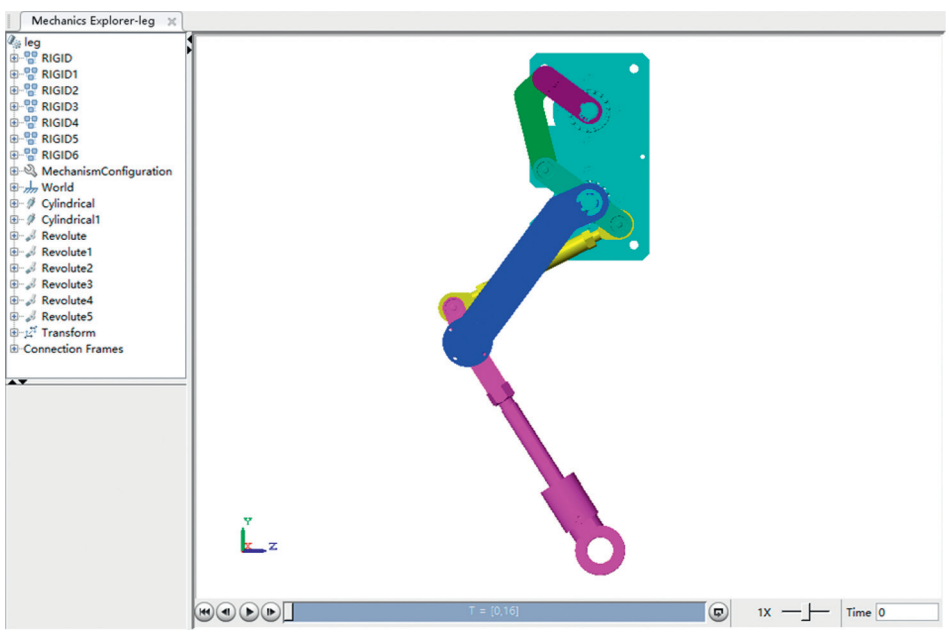

(b)

Figure 8: Simulation system and model of SimMechanics. (a) Simulation system. (b) Simulation model.

and we obtain the foot trajectory curve and motion cloud map, as shown in Figure 11. The modified foot track has obvious swing-back and retraction. According to $(ST_e/2T_m)$, the amount of swing-back and retraction can be calculated as 8 mm.

6.2. Analysis of Simulation Results. Through simulation, the velocity and acceleration curves of the foot in the x-direction can be obtained, as shown in Figures 12 and 13.

Figure 12 shows that the velocity of the trajectory curve before modification is discontinuous in the x-axis direction.

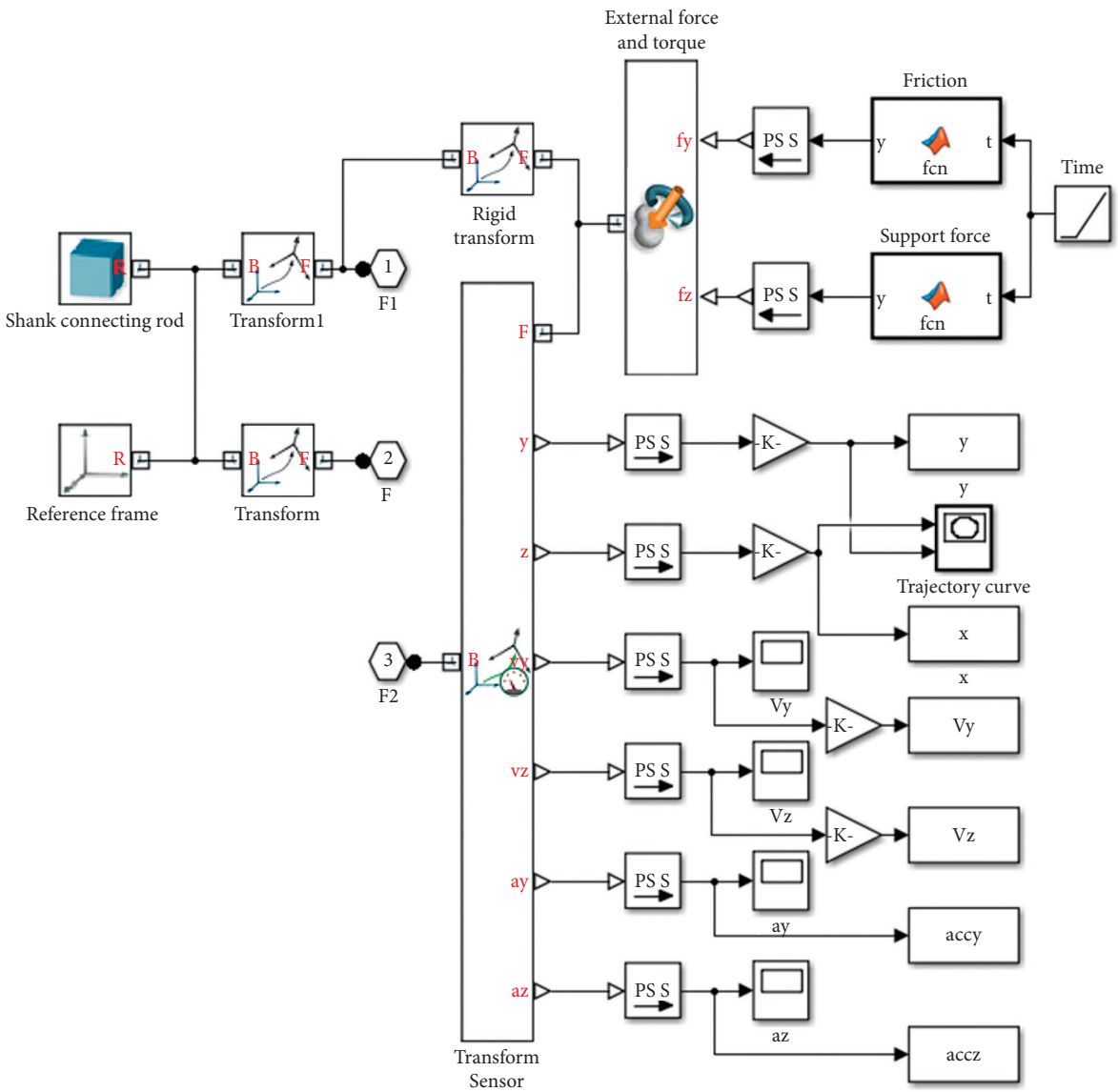

Figure 9: Display system of foot track.

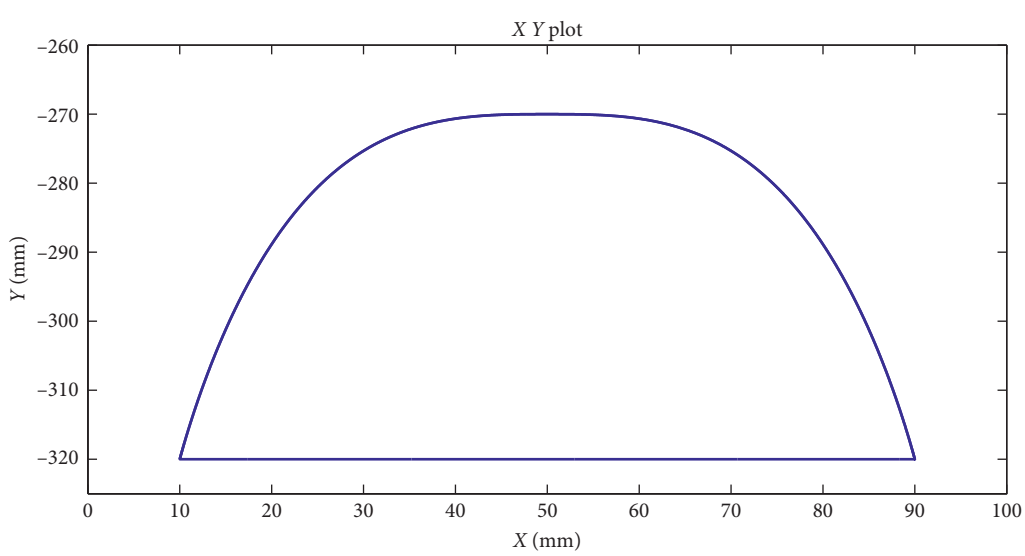

Figure 10: Trajectory curve of foot.

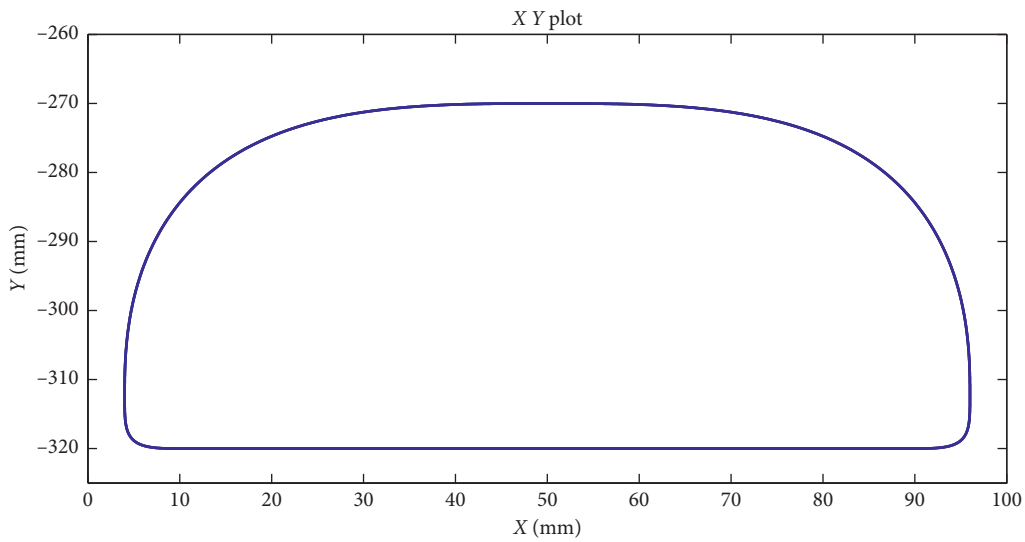

(a)

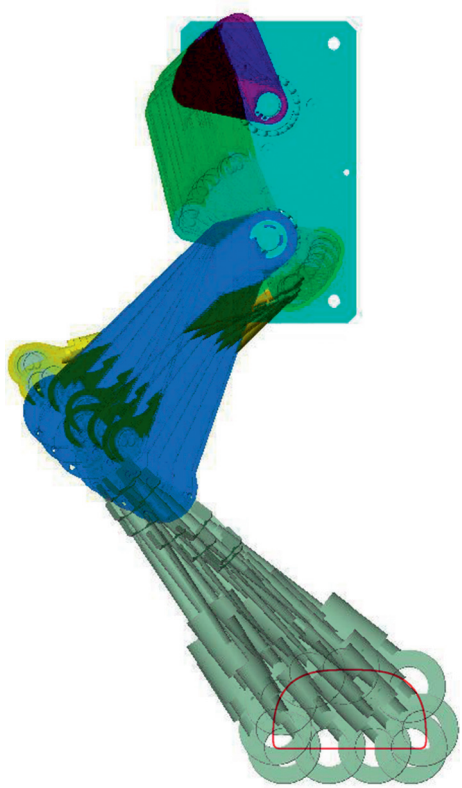

(b)

Figure 11: Modified trajectory: (a) curve and (b) cloud map.

Whenever the flight phase and the stand phase switch, there are always sudden changes in velocity, which will lead to a sudden change in acceleration and cause an impact in the x-axis direction. In the modified trajectory curve, the velocity in the x-axis direction transits smoothly when the flight phase and the stand phase switch.

The acceleration curve is shown in Figure 13. It can be seen from the acceleration curve that there is a sudden change in acceleration when the flight phase and the stand phase switch, and the acceleration in the x-axis direction changes dramatically before modification. The acceleration mutation is diminished somewhat after modifying the trajectory.

The driving torque of the shank motor and the thigh motor can be obtained through simulation, as shown in Figures 14 and 15. Compared with the trajectory in equation (7), it can be seen that the trajectory modified in this paper reduces the sudden change of the driving torque greatly

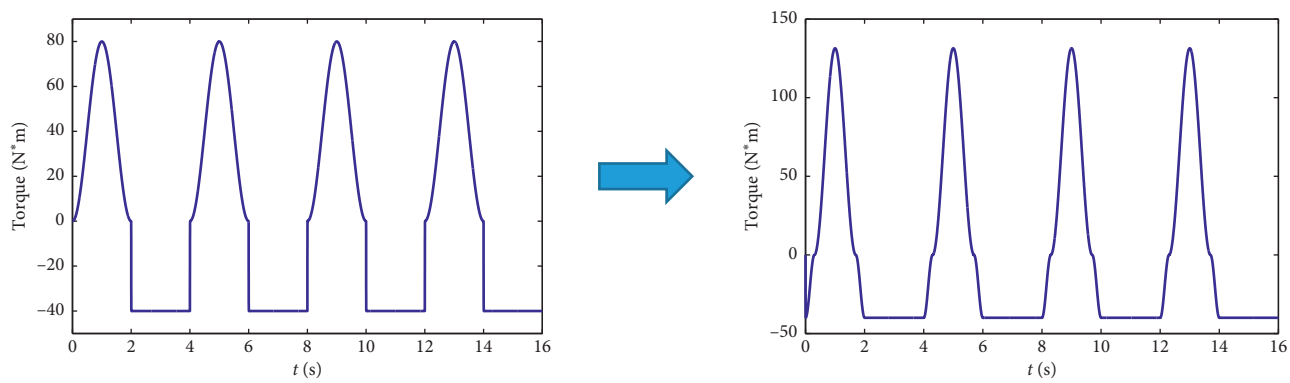

Figure 12: The velocity curve in the x-direction. (a) Unmodified curve. (b) Modified curve.

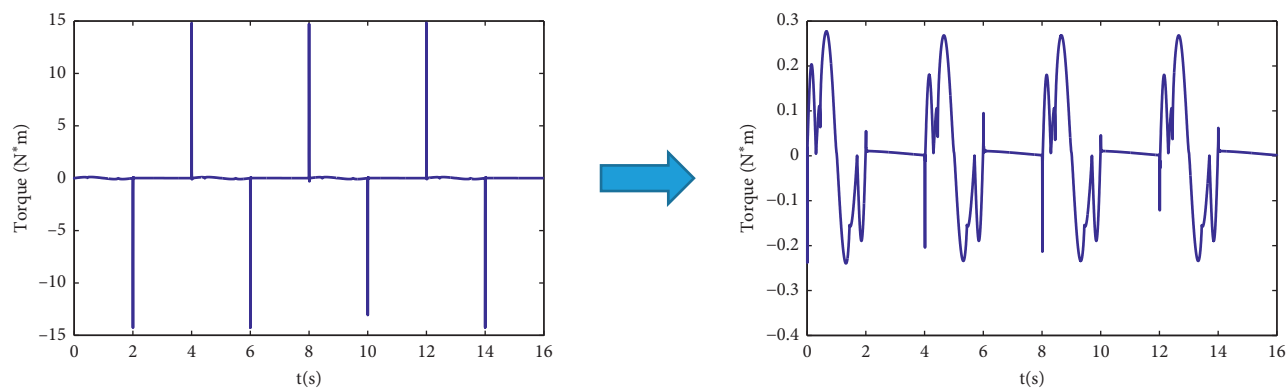

Figure 13: The acceleration curve in the x-direction. (a) Unmodified curve. (b) Modified curve.

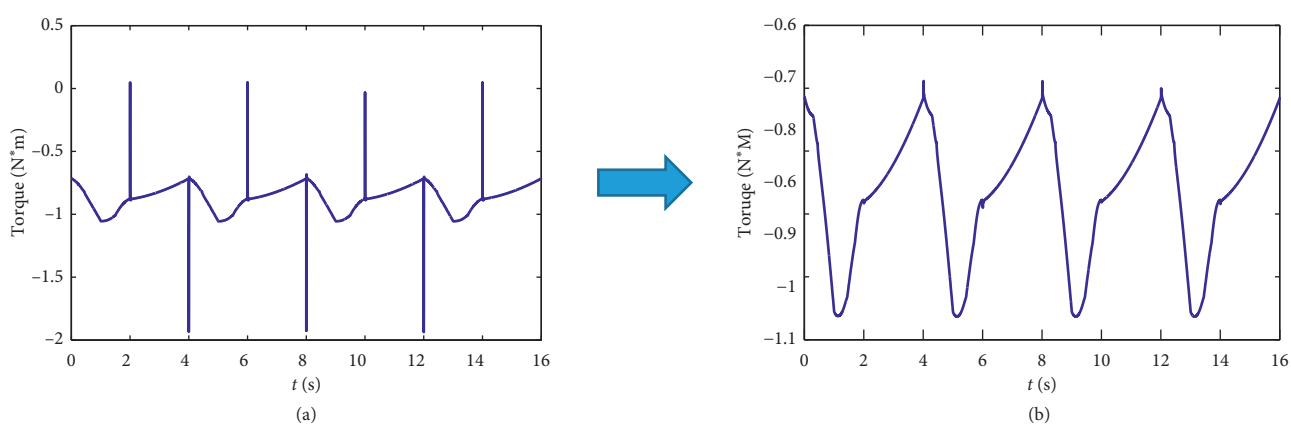

Figure 14: Driving torque curve of the shank motor. (a) Unmodified curve. (b) Modified curve.

when the flight phase and stand phase switch, which can reduce the vibration of the whole machine to a certain extent and improve the stability of the machine's walking gait.

The above simulation results are obtained under the condition of no reaction forces with the ground. To simulate the worst stress situation under real conditions, the maximum reaction forces that change with time should be added to each contact point of the single leg. We can conduct inverse dynamics to properly calculate ground reaction forces on single leg. The mass of the bionic quadruped robot designed in this paper is expected to be 60 kg, and we assume that the robot is walking in a laboratory environment that has relatively flat ground; the coefficient of friction between the foot end and the ground is 0.3. Then the reaction forces can be calculated based on these parameters. When the robot walks forward, the side swing joint is fixed, the weight of the

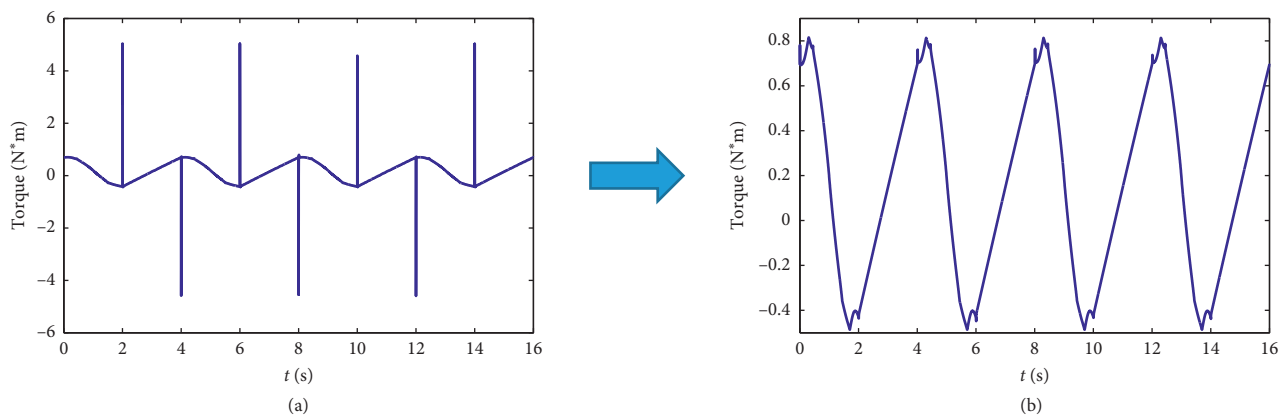

Figure 15: Driving torque curve of the thigh motor. (a) Unmodified curve. (b) Modified curve.

body is cast vertically on the support legs, and there is a vertically upward reaction force on the foot of the ground. In addition, there is friction between the foot and the ground. The stress on one leg is shown in Figure 16. The above-mentioned reaction forces change with time; for example, the friction force and the reaction force of the ground to the foot only exist when they are in contact with the ground. When these reaction forces are added, the simulated joint torque curves after and before modification are shown in Figure 17.

We use the percentage reduction of torque mutation to measure the optimization degree of the modified trajectory, so the formula is

$$P_{\text{to}} = \frac{\nabla To_1 - \nabla To_2}{\nabla To_1} \times 100\%, \tag{15}$$

where P_{to} is the percentage reduction of torque mutation, ∇To_1 is the torque mutation value corresponding to the trajectory before modification, and ∇To_2 is the torque mutation value corresponding to the trajectory modification.

Then, the value in Figure 17 is substituted into formula (15).

$$P_{\text{to1}} = \frac{(30.99 + 0.4202) - (25.52 + 0.4308)}{30.99 + 0.4202} \times 100\% = 17.38\%,$$

$$P_{\text{to2}} = \frac{(16.55 + 1.926) - (16.52 + 0.7151)}{16.55 + 1.926} \times 100\% = 6.71\%. \tag{16}$$

The maximum torque mutation of the thigh motor decreased by approximately 17%, and the maximum torque mutation of the shank motor decreased by approximately 7%.

In order to further verify the feasibility of the trajectory proposed in this paper, the MATLAB–ADAMS joint simulation of the whole robot is carried out. The simulation process is shown in Figure 18.

In the simulation, we set the motion period of both the flight phase and the stand phase as 1 s; step length is 80 mm and step height is 50 mm. The robot adopts a short gait in the simulation. Then, Figure 18 shows the motion during a specified period.

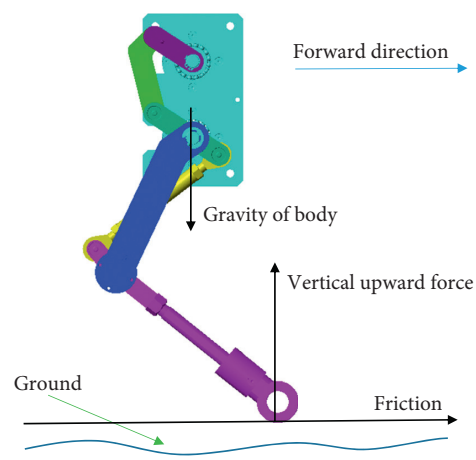

Figure 16: Reaction forces of the leg mechanism.

The simulation time is set to 38.5 s. Figure 19 shows the position of the robot at the start and end of the simulation.

The simulation of the robot shows that the quadruped robot can walk stably on flat ground with a tort gait. Therefore, the simulation proves the feasibility of the proposed trajectory.

7. Construction of Experimental Platform

It is very difficult and complex to carry out a dynamic robot walking experiment on a single-leg experimental platform. To verify the feasibility of the proposed single-leg mechanism and the rationality of the modified trajectory, we can track the foot trajectory during the experiment and compare it with the trajectory obtained from the simulation. Then, we can derive the properties of the proposed trajectory based on the consistency of the two trajectories.

To realize the proposed trajectory and track it, a single-leg experimental platform is constructed, as shown in Figure 20. The platform includes a single-leg motion system and a measurement system. The mechanical part of the single-leg motion system uses a rigid link structure, with two DOFs of the hip joint front swing and the knee joint front swing, and its total mass is 6 kg.

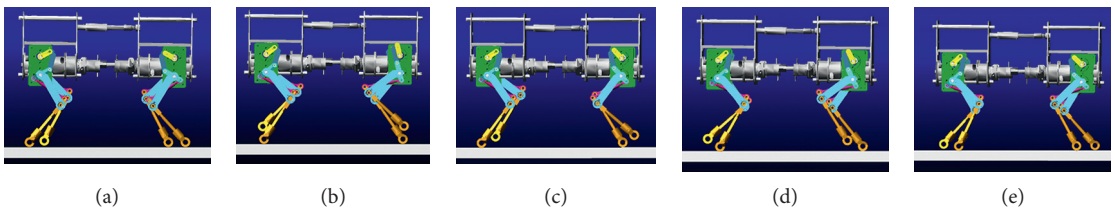

Figure 17: The motion of a period of flight phase. (a) $t = 0$ s. (b) $t = 0.25$ s. (c) $t = 0.5$ s. (d) $t = 0.75$ s. (e) $t = 1$ s.

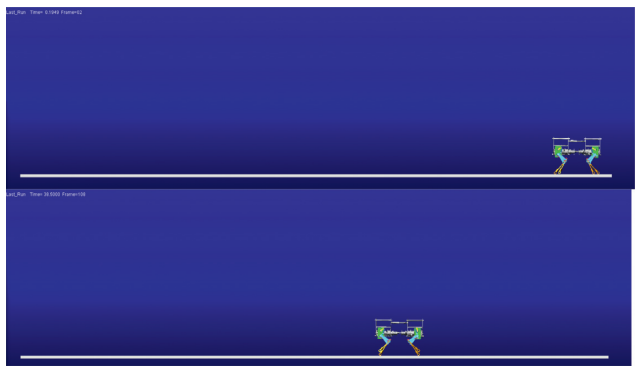

Figure 18: Starting and ending point of the robot simulation.

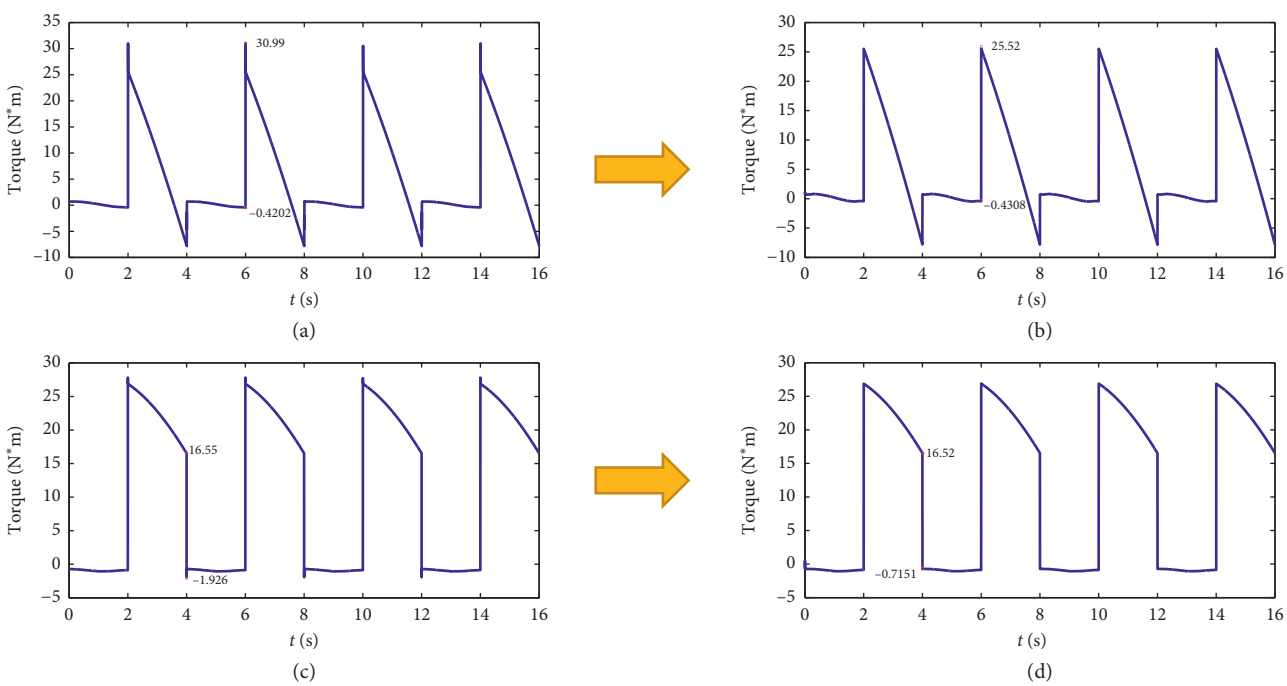

Figure 19: The torque curve of the motor after adding the simulated force. (a) Unmodified curve of thigh motor. (b) Modified curve of the thigh motor. (c) Unmodified curve of shank motor. (d) Modified curve of shank motor.

The Ethernet for Control Automation Technology (EtherCAT) fieldbus system is used to control the movement of the single leg. The system uses Ethernet as the basic framework, which has the advantages of fast transmission speed and large data packet capacity. All the interfaces of the bus topology structure are located on the coupler, no additional switches are needed, and space can be effectively used. The main electrical components are shown in Table 3.

The measurement system adopts a standard laser tracker designed by Automated Precision Inc. (API), and the model is an R-20Radian. To track the movement trajectory of the foot, the reflector of the laser tracker is magnetically

(a) (b) (c)

Figure 20: Experimental platform. (a) Single-leg system. (b) Main electrical components. (c) Measurement system.

Table 3: Main electrical components.

Name	Model	Main parameter	Function
Controller	PMAC CK3E-1310	16 axes	Bus control
Drive	Nanotec C5-E-2-21		
DC servo motor	DB59M024035-KYAN	3000 r/min	Actuator
Slave station	NX-ECC203		EtherCAT bus controller
	NX-ID5342	16 ports	Zero-position signal and power supply under voltage signal input
	NX-ID4342	8 ports	Digital input standby module
	NX-OD4121	8 ports	Digital output standby module
	NX-AD4603	8 ports	Analog input standby module

attracted to the foot, and the spatial position of the foot relative to the measurement coordinate system is calculated by the principle of laser interference.

To realize the foot trajectory we designed, the Position, Velocity, and Time (PVT) interpolation algorithm is used to interpolate the motion curve of the joint. Then, PMAC (Power PMAC IDE) is used for programming on a PC. The PC is connected to the controller with a network cable to complete the debugging and downloading of the control program. The control schematic is shown in Figure 21. The PMAC software's own drawing simulation tool was used to draw the foot trajectory in a single cycle, as shown in Figure 22. According to Figure 22, the step length is 80 mm, and the step height is 50 mm. The trajectory simulated by PMAC is consistent with the proposed trajectory, so the correctness of the proposed equation is preliminarily verified.

The movement process of the leg mechanism during the experiment is shown in Figure 23. It can be seen that the leg mechanism can move correctly according to the planned trajectory, which proves the feasibility of the leg mechanism proposed in this article. Figure 24 is the foot trajectory recorded by the laser tracker during the moment of the experiment, which shows that the trajectory of the experiment is approximately the same as the trajectory obtained by the simulation. And according to the experimental data, the step height and step length of the experimental running track are about 50 mm and 80 mm, respectively, it is consistent with the simulation data. Figure 24 shows that the trajectory has obvious retraction and back-swing movement. The obtained retraction and back-swing movement can reduce the impact of speed in the x-axis direction, so the joint torque will also be reduced. In addition, it should be noted that the shaking phenomenon in Figure 24 is caused by the low machining accuracy and assembly clearance of the leg mechanism. The realization of the trajectory in the experiment indirectly proves the rationality of the trajectory proposed in this paper.

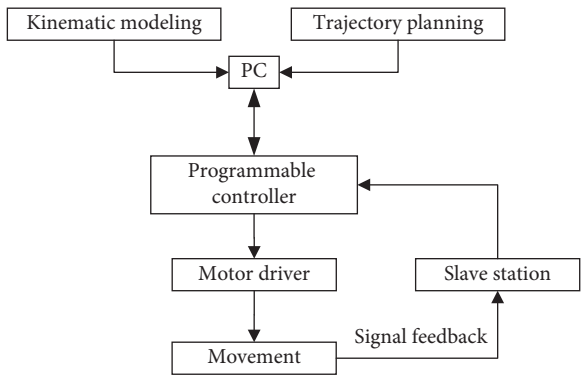

Figure 21: Control schematic diagram of the single-leg system.

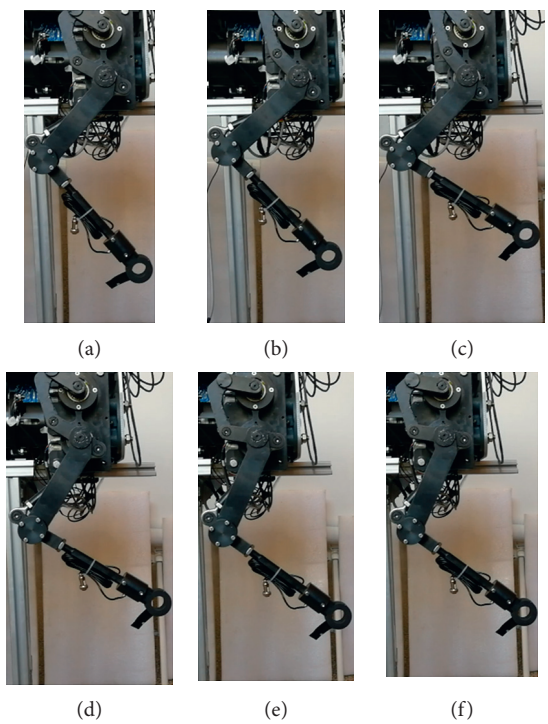

Figure 22: Process of the leg movement.

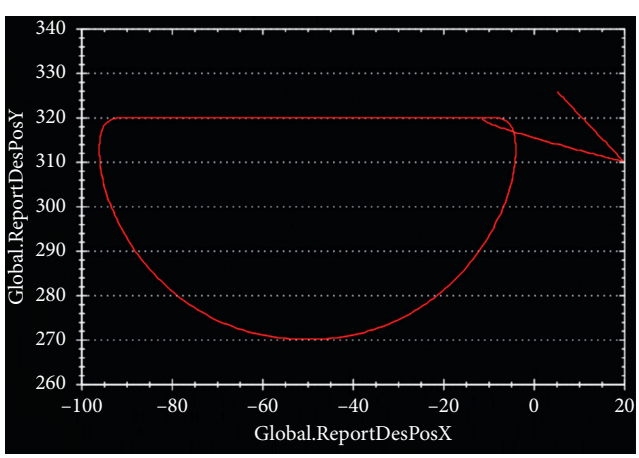

Figure 23: Movement trajectory of the foot (mm).

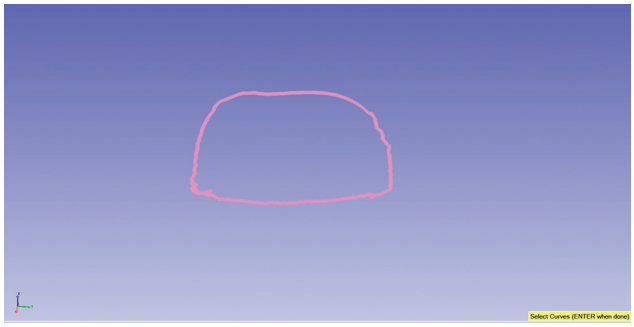

Figure 24: Foot track of the experiment.

8. Conclusions

(1) In this paper, a novel electrically driven leg mechanism of a quadruped robot is designed, which reduces the inertia of the leg swing.

(2) To reduce the torque mutation when the flight phase and stand phase switch, a foot trajectory based on the compound cycloid is proposed. The proposed foot trajectory has swing-back and retraction motion.

(3) A Simulink simulation platform is built to realize the foot trajectory of the single-leg mechanism. The results of the simulation show that the mechanism can achieve the foot trajectory proposed and that the impact of joint motor torque is reduced to some extent.

(4) A single-leg experimental platform was built, and the foot trajectory proposed in this paper was realized on the experimental platform. The realization of the trajectory proves the feasibility of the leg mechanism and the rationality of the proposed foot trajectory.

Subsequent research will focus on the following aspects: the experiment of the trajectory proposed in this article is applied to the whole machine to verify its practicability; the leg mechanism has a smaller workspace than the series-type linkage structure leg, so we will further optimize the length of each rod to increase its workspace; through comparison with the trajectory before correction, it is not difficult to find that the trajectory proposed in this article is at the same step height. With the step length, the trajectory is longer, so there may be increased energy consumption. The trajectory is constantly optimized and improved to address these potential problems.

Data Availability

The data used to support the findings of this study are available from the corresponding author upon request.

Conflicts of Interest

The authors declare that there are no conflicts of interest regarding the publication of this paper.

Acknowledgments

This study was supported by the National Natural Science Foundation of China (nos. 51965029, 61873115, and 51565021) and the National Key Research and Development Plan Project (no. 2017YFC1702503).

References

[1] L. Wang, J. Wang, S. Wang, and Y. He, "Strategy of foot trajectory generation for hydraulic quadruped robots gait planning," *Journal of Mechanical Engineering*, vol. 49, no. 1, pp. 39–44, 2013.

[2] M. Li, Z. Jiang, W. Guo, and L. Sun, "Leg prototype of a bio-inspired quadruped robot," *Robot*, vol. 36, no. 1, pp. 21–28, 2014.

[3] Y. Li, B. Li, J. Ruan, and X. Rong, "Research of mammal bionic quadruped robots: a review," in *Proceedings of the 2011 IEEE 5th International Conference on Robotics, Automation and Mechatronics (RAM)*, pp. 166–171, Qingdao, China, September 2011.

[4] J. Chen, H. San, and X. Wu, "Gait regulation of a bionic quadruped robot with antiparallelogram leg based on CPG oscillator," *Complexity*, vol. 2019, Article ID 5491298, 11 pages, 2019.

[5] P. Yin, P. Wang, M. Li et al., "A novel control strategy for quadruped robot walking over irregular terrain," in *Proceedings of the 2011 IEEE 5th International Conference on Robotics, Automation and Mechatronics (RAM)*, pp. 184–189, Qingdao, China, September 2011.

[6] L. Bai, Z. Long, X. Chen et al., "Design and analysis of a leg mechanism for a continuous electrically-driven quadruped robot," *Robot*, vol. 40, no. 2, pp. 136–145, 2018.

[7] D. Wooden, M. Malchano, K. Blankespoor et al., "Autonomous navigation for BigDog," in *Proceedings of the 2010 IEEE International Conference on Robotics and Automation*, pp. 4736–4741, Anchorage, Alaska, May 2010.

[8] K. Michael, *Meet Boston Dynamics' Ls3—the Latest Robotic War Machine*, University of Wollongong, Wollongong, Australia, 2012, https://theconversation.com/meet-boston-dynamics-ls3-the-latest-robotic-war-machine-9754.

[9] C. Semini, N. G. Tsagarakis, E. Guglielmino, M. Focchi, F. Cannella, and D. G. Caldwell, "Design of HyQ—a hydraulically and electrically actuated quadruped robot," *Proceedings of the Institution of Mechanical Engineers, Part I: Journal of Systems and Control Engineering*, vol. 225, no. 6, pp. 831–849, 2011, doi: 10.1109/TIE.2020.3020034.

[10] T. Boaventura, C. Semini, J. Buchli et al., "Dynamic torque control of a hydraulic quadruped robot," in *Proceedings of the 2012 IEEE International Conference on Robotics and Automation*, pp. 1889–1894, St Paul, MN, USA, May 2012.

[11] H. Chai, J. Meng, X. W. Rong, and Y. Li, "Design and implementation of scalf, an advanced hydraulic quadruped robot," *Robot*, vol. 36, no. 4, pp. 385–391, 2014.

[12] J. Na, Y. Li, Y. Huang, G. Gao, and Q. Chen, "Output feedback control of uncertain hydraulic servo systems," *IEEE Transactions on Industrial Electronics*, vol. 67, no. 1, pp. 490–500, 2019.

[13] M. P. Murphy, A. Saunders, C. Moreira, A. A. Rizzi, and M. Raibert, "The LittleDog robot," *The International Journal of Robotics Research*, vol. 30, no. 2, pp. 145–149, 2011.

[14] E. Ackerman, *Boston Dynamics' SpotMini is all Electric, Agile, and has a Capable Face-Arm*, IEEE Spectrum, New York, NY, USA, 2016, http://spectrum.ieee.org/automaton/robotics/home-robots/boston-dynamicsspotmini.

[15] Unitree-Laikago, *Unitree*, http://www.unitree.cc/e/action/ShowInfo.php?classid=6&id=1#.

[16] S. Seok, A. Wang, M. Y. Chuah et al., "Design principles for energy-efficient legged locomotion and implementation on the MIT cheetah robot," *IEEE/ASME Transactions on Mechatronics*, vol. 20, no. 3, pp. 1117–1129, 2015.

[17] D. Yang, X. Gao, E. Cui, and Z. Ma, "State-constraints adaptive backstepping control for active magnetic bearings with parameters nonstationarities and uncertainties," *IEEE Transactions on Industrial Electronics*, 2020.

[18] S. Meek, J. Kim, and M. Anderson, "Stability of a trotting quadruped robot with passive, underactuated legs," in *Proceedings of the 2008 IEEE International Conference on Robotics and Automation*, pp. 347–351, Pasadena, CA, USA, May 2008.

[19] R McGhee, "The adaptive suspension vehicle," *IEEE Control Systems Magazine*, vol. 6, no. 6, pp. 7–12, 1986.

[20] M. Hutter, C. Gehring, D. Jud et al., "Anymal-a highly mobile and dynamic quadrupedal robot," in *Proceedings of the 2016 IEEE/RSJ International Conference on Intelligent Robots and Systems (IROS)*, pp. 38–44, Daejeon, Korea, October 2016.

[21] J. Park, K.-S. Kim, and S. Kim, "Design of a cat-inspired robotic leg for fast running," *Advanced Robotics*, vol. 28, no. 23, pp. 1587–1598, 2014.

[22] X. Tian, F. Gao, X. Chen, and C. Qi, "Mechanism design and comparison for quadruped robot with parallel-serial leg," *Journal of Mechanical Engineering*, vol. 49, no. 6, pp. 81–88, 2013.

[23] J. C. John, "Manipulator kinematics," in *Introduction to Robotics*, pp. 14–105, Mechanical Engineering Press, Beijing, China, 3rd edition, 2006.

[24] Y. Sakakibara, K. Kan, Y. Hosoda, M. Hattori, and M. Fujie, "Foot trajectory for a quadruped walking machine," in *Proceedings of the IEEE International Workshop on Intelligent Robots and Systems, towards a New Frontier of Applications*, pp. 315–322, Tsuchiura, Japan, July 1990.

[25] D. He and P. S. Ma, "Simulation of dynamic walking of quadruped robot and analysis of walking stability," *Computer Simulation*, vol. 22, no. 2, pp. 146–149, 2005, in Chinese.

[26] Y. B. Li, B. Li, X. W. Rong, and J. Meng, "Mechanical design and gait planning of a hydraulically actuated quadruped bionic robot," *Journal of Shandong University*, vol. 41, no. 5, pp. 32–36, 2011.

[27] M. Hildebrand, "Further studies on locomotion of the cheetah," *Journal of Mammalogy*, vol. 42, no. 1, pp. 84–91, 1961.

[28] J. G. D. Karssen, M. Haberland, M. Wisse, and S. Kim, "The optimal swing-leg retraction rate for running," in *Proceedings of the 2011 IEEE International Conference on Robotics and Automation*, San Francisco, CA, USA, September 2011.

[29] M. Wisse, C. G. Atkeson, and D. K. Kloimwieder, "Swing leg retraction helps biped walking stability," in *Proceedings of the 5th IEEE-RAS International Conference on Humanoid Robots*, pp. 295–300, Tsukuba, Japan, December 2005.

[30] A. Seyfarth, H. Geyer, and H. Herr, "Swing-leg retraction: a simple control model for stable running," *Journal of Experimental Biology*, vol. 206, no. 15, pp. 2547–2555, 2003.

[31] D. G. E. Hobbelen and M. Wisse, "Swing-leg retraction for limit cycle walkers improves disturbance rejection," *IEEE Transactions on Robotics*, vol. 24, no. 2, pp. 377–389, 2008.

[32] K. Serbest, M. Berisha, and M. Cilli, "Dynamic analysis of three different high bar dismounts in the simmechanics environment," *Journal of Mechanics in Medicine and Biology*, vol. 18, no. 3, Article ID 1850030, 2018.

Hindawi
Complexity
Volume 2020, Article ID 6672709, 16 pages
https://doi.org/10.1155/2020/6672709

Research Article

Adaptive Fixed-Time 6-DOF Coordinated Control of Multiple Spacecraft Formation Flying with Input Quantization

Shiyu Wang,[1] Ruixia Liu ,[2,3] and Lihua Wen[1]

[1]*School of Astronautics, Northwestern Polytechnical University, Xian 710072, China*
[2]*School of Automation, Xi'an University of Posts and Telecommunications, Xian 710072, China*
[3]*Xi'an Key Laboratory of Advanced Control and Intelligent Process, Xi'an University of Posts and Telecommunications, Xian 710072, China*

Correspondence should be addressed to Ruixia Liu; ruixialiu@xupt.edu.cn

Received 10 October 2020; Revised 23 November 2020; Accepted 9 December 2020; Published 30 December 2020

Academic Editor: Jing Na

This paper investigates the fixed-time coordinated control problem of six-degree-of-freedom (6-DOF) dynamic model for multiple spacecraft formation flying (SFF) with input quantization, where the communication topology is assumed directed. Firstly, a new multispacecraft nonsingular fixed-time terminal sliding mode vector is derived by using neighborhood state information. Secondly, a hysteretic quantizer is utilized to quantify control force and torque. Utilizing such a quantizer not only can reduce the required communication rate but also can eliminate the control chattering phenomenon induced by the logarithmic quantizer. Thirdly, a 6-DOF fixed-time coordinated control strategy with adaptive tuning laws is proposed, such that the practical fixed-time stability of the controlled system is ensured in the presence of both upper bounds of unknown external disturbances. It theoretically proves that the relative tracking errors of attitude and position can converge into the regions in a fixed time. Finally, a numerical example is exploited to show the usefulness of the theoretical results.

1. Introduction

The recent decades have seen an ever increasing research interest in the coordinated control problem of spacecraft formation flying (SFF) due to its successful applications in the space industry such as atmosphere monitoring of the Earth, deep space exploration, and spacecraft on-orbit maintenance [1–5]. As is well known, the coordinated control of attitude and orbit are two equally important technologies. It is essential to achieve the desired attitude and position simultaneously for SFF mission [6, 7]. Owning to the dynamical coupling between orbit motion and attitude motion, these two motions can be considered as a whole six-degree-of-freedom (6-DOF) motion. Recently, the 6-DOF coordinated control of SFF has attracted considerable research attention [8, 9]. However, the control strategies proposed in the aforementioned literature can only guarantee asymptotic stability of the controlled systems [10–13].

For coordinated control problems of SFF, fast convergence performance is an important requirement [14–18]. In contrast to asymptotic stabilization controllers, the finite-time stabilization controllers can provide a faster response and better disturbance-rejection ability [19–22]. Therefore, the finite-time controllers have been developed in spacecraft formation control [23–25]. Even though the finite-time control methods can ensure the controlled systems finite-time stabilization, the convergence time relies on the information of initial system states, which gives rise to difficulties in practical applications [26]. To cope with this constraint, the fixed-time stable concept was applied to study finite-time controller design, in that the convergence time is upper bounded regardless of initial system states [27–29]. To date, fixed-time control strategies have been used for various control systems [30, 31] but less attention has been paid to fixed-time 6-DOF coordinated control problem for SFF, especially for external disturbances with unknown upper

bounds. Another significant issue in multiple SFF task is that the interspacecraft communication links are not always bidirectional, such as in the unidirectional spacecraft laser communication system. However, in some of the existing results, the coordinated control issue is investigated based on an assumption that the communication topology is undirected.

On another research frontier, networked control systems (NCSs) as an active field of research have been applied successfully in various modern complicated engineering processes [13, 32–35] such as unmanned vehicles, nuclear power stations, and aerospace engineering systems. In modern low-cost plug-and-play small spacecraft formation systems, the functional components connected by wireless networked media [36–39]. It is quite common that when the signal is transmitted between the control and actuator module via wireless networks, the SFF systems unavoidably suffer from quantization errors caused by quantization behavior which will degrade the control performance or even lead to instability [40–43]. Thus, it is needed to propose new controllers for SFF where the signal quantization is taken into consideration. Although some research attention has been centered on the quantized control problem of SFF, there is still no result available that considers 6-DOF coordinated control of multiple spacecraft formation in the presence of quantized input control signal. The complexity of the multiple spacecraft formation coordinated control task makes the quantized fixed-time coordinated control a serious challenge.

In this paper, we are motivated to deal with the problem of fixed-time 6-DOF adaptive coordinated control for multiple SFF with input quantization under directed communication topology. The main contributions of this paper are highlighted as follows: (1) the communication topology among follower spacecraft is described by a directed graph, which will bring more challenges than the case that the communication topology among follower spacecraft is described by an undirected graph. (2) A novel multi-spacecraft nonsingular FTTSM based on a 6-DOF dynamic model is designed, on which each spacecraft converges to its desired states while keeping synchronization with other formation spacecraft. (3) A fixed-time adaptive coordinate control strategy is derived to compensate for the effects of hysteretic quantizer and external disturbances on the control performance and guarantee the practical fixed-time stability of the controlled system.

The rest of this paper is organized as follows: in section 2, the modelling and preliminaries are presented. In section 3, a multispacecraft nonsingular fixed-time terminal sliding mode vector is designed. In section 4, a fixed-time adaptive coordinated control scheme is proposed. An illustrative example and a conclusion are given in Sections 5 and 6, respectively.

2. Modelling and Preliminaries

2.1. 6-DOF Dynamic Model. The 6-DOF dynamic model of spacecraft formation is represented as follows [8]:

$$\begin{cases} \dot{\mathrm{x}}_{1i} = \mathbf{\Lambda}(\dot{\mathrm{x}}_{1i})\mathbf{x}_{2i}, \\ \mathbf{G}_{fi}\dot{\mathrm{x}}_{2i} + \mathbf{C}(\mathbf{x}_{2i}) + \mathbf{N}(\mathbf{x}_{1i}) + \boldsymbol{\tau}_i = \mathbf{u}_i, \quad i = 1, 2, \ldots, n, \end{cases} \tag{1}$$

where

$$\begin{gathered} \mathbf{x}_{1i} = \begin{bmatrix} \boldsymbol{\rho}_i \\ \mathbf{q}_i \end{bmatrix}, \mathbf{x}_{2i} = \begin{bmatrix} \dot{\rho}_i \\ \boldsymbol{\omega}_i \end{bmatrix}, \mathbf{\Lambda}(\dot{\mathrm{x}}_{1i}) = \begin{bmatrix} \mathbf{I}_{3\times3} & 0_{3\times3} \\ 0_{3\times3} & \dfrac{\mathbf{T}(\mathbf{q}_i)}{2} \end{bmatrix}, \mathbf{G}_{fi} = \begin{bmatrix} m_{fi}\mathbf{I}_{3\times3} & 0_{3\times3} \\ 0_{3\times3} & \mathbf{J}_{fi} \end{bmatrix}, \\ \mathbf{C}(\mathbf{x}_{2i}) = \begin{bmatrix} \mathbf{C}(n_0)\dot{\rho}_i \\ \boldsymbol{\omega}_i^{\times}\mathbf{J}_{fi}\boldsymbol{\omega}_i \end{bmatrix}, \mathbf{N}(\mathbf{x}_{1i}) = \begin{bmatrix} N(\boldsymbol{\rho}_i, n_0, R) \\ 0_{3\times1} \end{bmatrix}, \boldsymbol{\tau}_i = \begin{bmatrix} \mathbf{F}_{di} \\ \mathbf{z}_i \end{bmatrix}, \mathbf{u}_i = \begin{bmatrix} \mathbf{u}_{fi} \\ \mathbf{u}_{ti} \end{bmatrix}, \\ \mathbf{T}(\mathbf{q}_i) = \begin{bmatrix} -\mathbf{q}_{vi}^T \\ q_{0i}\mathbf{I}_{3\times3} + \mathbf{q}_{vi}^{\times} \end{bmatrix}, C(n_0) = 2n_0\begin{bmatrix} 0 & -1 & 0 \\ 1 & 0 & 0 \\ 0 & 0 & 0 \end{bmatrix}, N(\boldsymbol{\rho}_i, n_0, R) = \begin{bmatrix} -\dot{n}_0 y_i - n_0^2 x_i - 2\dfrac{\mu}{R^3}x_i \\ \dot{n}_0 x_i - n_0^2 y_i + \dfrac{\mu}{R^3}y_i \\ \dfrac{\mu}{R^3}z_i \end{bmatrix}, \end{gathered} \tag{2}$$

where superscript i stands for the ith follower spacecraft; $\rho_i = [x_i\ y_i\ z_i]^T$ represents the relative position vector from the ith follower spacecraft to the leader spacecraft; $\omega_i \in \mathbb{R}^3$ denotes the angular velocity; $\mathbf{q}_i \in \mathbb{R}^4$ is the quaternion defined as $\mathbf{q}_i = [\,q_{0i}\ \ \mathbf{q}_{vi}\,]^T$, where $n_0 \in \mathbb{R}$ represents angular velocity of the virtual leader spacecraft; q_{0i} is the scalar part and $\mathbf{q}_{vi}$ is the vector part; $m_{fi} \in \mathbb{R}$ denotes the mass; $\mathbf{J}_{fi} \in \mathbb{R}^{3\times3}$ is the inertia matrix; $\mathbf{u}_{fi} \in \mathbb{R}^3$ represents the control force; $\mathbf{u}_{it} \in \mathbb{R}^3$ is the control torque; $\mathbf{F}_{di} \in \mathbb{R}^3$ is disturbance force; and $\mathbf{z}_i = \ell_i - \mathbf{T}_{iGT}$, where $\ell_i \in \mathbb{R}^3$ is

disturbance torque and $\mathbf{T}_{iGT} \in \mathbb{R}^3$ is the gravity gradient torque. The notation $\imath^{\times}$ for the vector $\imath = \begin{bmatrix} \imath_1 & \imath_2 & \imath_3 \end{bmatrix}^T$ represents the skew-symmetric matrix as follows:

$$l^{\times} = \begin{bmatrix} 0 & -l_3 & l_2 \\ l_3 & 0 & -l_1 \\ -l_2 & l_1 & 0 \end{bmatrix}. \tag{3}$$

It is worth to mention that the attitude and orbit are mutually coupled by $\mathbf{T}_{iGT} \in \mathbb{R}^3$, which is given as

$$\mathbf{T}_{iGT} = 3\mu \frac{\widehat{\mathbf{R}}_{fi}^{\times} \mathbf{J}_{fi} \widehat{\mathbf{R}}_{fi}}{\left(x_i^2 + (R + y_i)^2 + z_i^2\right)^{(3/2)}}, \tag{4}$$

where $\widehat{\mathbf{R}}_{fi} \in \mathbb{R}^3$ is the position unit vector. Since $\mathbf{T}_{iGT}$ is much smaller compared with control torque, $\mathbf{T}_{iGT}$ is always treated as a disturbance.

We define the following error states:

$$\mathbf{e}_{1i} = \begin{bmatrix} \boldsymbol{\rho}_i - \boldsymbol{\rho}_{di} \\ \mathbf{q}_{ei} \end{bmatrix}, \mathbf{e}_{2i} = \begin{bmatrix} \dot{\boldsymbol{\rho}}_{ei} \\ \boldsymbol{\omega}_{ei} \end{bmatrix} = \begin{bmatrix} \dot{\rho}_i - \dot{\rho}i_{di} \\ \boldsymbol{\omega}_i - R(\mathbf{q}_{ei})\boldsymbol{\omega}_{di} \end{bmatrix}, \tag{5}$$

where $\mathbf{q}_{ei}$ is error quaternion defined as $\mathbf{q}_{ei} = \begin{bmatrix} q_{0ei} & \mathbf{q}_{vei}^T \end{bmatrix}^T = \mathbf{q}_{ei} \otimes \overline{\mathbf{q}}_{di}$; $R(\mathbf{q}_{ei})$ is the rotation matrix from the ith follower spacecraft's reference frame to its body-fixed frame; and ρ_{di}, $\dot{\rho}_{di}$, ω_{di}, and $\mathbf{q}_{di}$ are the desired position, desired velocity, desired angular velocity, and desired attitude, respectively.

Then the 6-DOF relative error dynamic model of SFF can be expressed by

$$\begin{cases} \dot{\mathbf{e}}_{1i} = \boldsymbol{\Lambda}(\dot{\mathbf{e}}_{1i})\mathbf{e}_{2i}, \\ \mathbf{G}_{fi}\dot{\mathbf{e}}_{2i} + \mathbf{C}(\mathbf{e}_{2i}) + \mathbf{N}(\mathbf{e}_{1i}) + \boldsymbol{\tau}_i = \mathbf{u}_i, \end{cases} \tag{6}$$

where

$$\boldsymbol{\Lambda}(\dot{\mathbf{e}}_{1i}) = \begin{bmatrix} \mathbf{I}_{3\times3} & 0_{3\times3} \\ 0_{3\times3} & \dfrac{\mathbf{T}(\mathbf{q}_{ei})}{2} \end{bmatrix}, \mathbf{N}(\mathbf{e}_{1i}) = \begin{bmatrix} N(\boldsymbol{\rho}_i, n_0, R) - \ddot{\rho}_{di} \\ 0_{3\times1} \end{bmatrix},$$

$$\mathbf{C}(\mathbf{e}_{2i}) = \begin{bmatrix} C(n_0)\dot{\rho}_i \\ -\boldsymbol{\omega}_i^{\times}\mathbf{J}_{fi}\boldsymbol{\omega}_i + \mathbf{J}_{fi}(\boldsymbol{\omega}_{ei}^{\times}\boldsymbol{\omega}_{di} - R(\mathbf{q}_{ei})\dot{\omega}_{di}) \end{bmatrix}. \tag{7}$$

2.2. Graph Theory. It is supposed that the information flow among n follower spacecraft is described by a directed graph $\mathrm{G} = (\mathrm{V}, \chi, \mathrm{A})$, where $\mathrm{V} = \{\mathrm{V}_1, \mathrm{V}_2, \ldots, \mathrm{V}_n\}$ represents the set of nodes, $\chi \subseteq \mathrm{V} \times \mathrm{V}$ represents the set of edges, and $(\mathrm{V}_i, \mathrm{V}_j) \in \chi$ represents if and only if node V_i can receive the information of node V_j. In spacecraft 6-DOD coordinated control application, $(\mathrm{V}_i, \mathrm{V}_j) \in \chi$ represents only the jth spacecraft can obtain the ith spacecraft's states information. $\mathrm{A} = [a_{ij}] \in \mathbb{R}^{n\times n}$ denotes the weighted adjacency matrix of the graph G with entries

$$\begin{cases} a_{ij} > 0, & \text{if } ((\mathrm{V}_i, \mathrm{V}_j) \in \chi), \\ a_{ij} = 0, & \text{otherwise}, \end{cases} \tag{8}$$

where a_{ij} is the nonnegative element of A, which denotes communication quality between the ith spacecraft and jth spacecraft. It is noticeable that self-edges are not allowed, meaning that $a_{ii} = 0$.

The in-degree matrix of the graph G is $\mathbf{D}$ with entries

$$\mathbf{D} = \mathrm{diag}\{d_1, d_2, \ldots, d_n\}, \tag{9}$$

where

$$d_i = \sum_{j=1}^{n} a_{ij} = \sum_{j\in\chi_i} a_{ij}, \quad (i = 1, 2, \ldots, n). \tag{10}$$

The Laplacian matrix $\mathbf{L} \in \mathbb{R}^{n\times n}$ of the graph G is [44]

$$\mathbf{L} = \mathbf{D} - A. \tag{11}$$

2.3. Hysteretic Quantizer. To eliminate the control chattering phenomenon induced by logarithmic quantizer, a hysteretic quantizer is used to quantify control torque and force in this paper, which is similar to [45]. It can be expressed by

$$q(u(t)) \triangleq \begin{cases} u_J \mathrm{sgn}(u), & \begin{array}{l} \text{if } \dfrac{u_J}{1+\delta} < |u| \le \dfrac{u_J}{1-\delta}, \dot{u}_J < 0, \text{or}, \\ u_J < |u| \le \dfrac{u_J}{1-\delta}, \dot{u}_J > 0, \end{array} \\ u_J(1+\delta)\mathrm{sgn}(u), & \begin{array}{l} \text{if } u_j < |u| \le \dfrac{u_J}{1-\delta}, \dot{u}_J < 0, \text{or}, \\ \dfrac{u_J}{1-\delta} \le |u| \le \dfrac{u_J(1+\delta)}{1-\delta}, \dot{u}_J > 0, \end{array} \\ 0, & \begin{array}{l} \text{if } 0 \le |u| < \dfrac{u_{\min}}{1+\delta}, \dot{u}_J < 0, \text{or}, \\ \dfrac{u_{\min}}{1+\delta} \le |u| \le u_{\min}, \dot{u}_J > 0, \end{array} \\ q(u(t^-)), & \text{othercase}, \end{cases} \tag{12}$$

where $u_J = \rho^{(1-i)}u_{\min}$, $J = 1, 2, \ldots, n$ with $0 < \rho < 1$, $u_{\min} > 0$, and $\delta = (1 - \rho/1 + \rho)$. $q(u(t))$ is in the set $U = \{0, \pm u_i, \pm u_i(1+\delta)\}$. The map of the hysteresis quantizer $q(u(t))$ for $u > 0$ is illustrated in Figure 1.

Remark 1. The parameter ρ can be termed as a measure of quantization density. From the definition of ρ, we can see that the smaller parameter ρ is, the coarser the hysteretic quantizer becomes [45]. Therefore, the design of parameter ρ

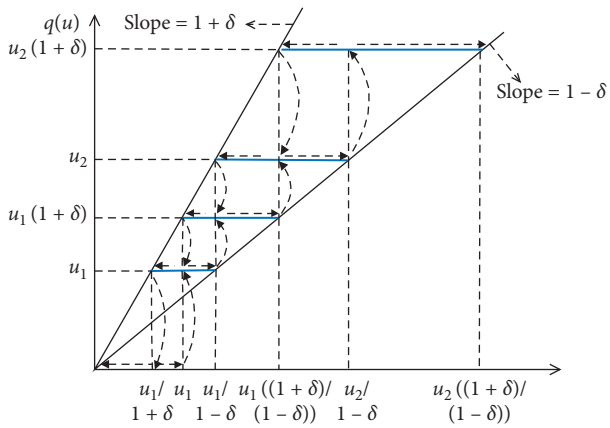

Figure 1: Map of $q(u(t))$ for $u > 0$.

should be based on a criterion to guarantee the control performance with a smaller quantization density. In addition, compared with a traditional logarithmic quantizer, the hysteretic quantizer (10) can avoid oscillations by adding additional quantization levels.

2.4. Preliminaries. For deriving the 6-DOF fixed-time coordinated controller, the lemmas are made as follows.

Lemma 1. *The hysteretic quantizer $q(u(t))$ is decomposed into two parts as*

$$q(u(t)) = D(u)u(t) + Q(t), \tag{13}$$

where $D(u)$ and $Q(t)$ satisfy

$$1 - \delta \le D(u) \le 1 + \delta,\ |Q(t)| \le u_{\min}. \tag{14}$$

The proof of Lemma 1 is similar to Theorem 1 in [45].

Lemma 2 (see [44]). *If G is a directed graph with N nodes, then all the eigenvalues of the weighted Laplace matrix* **L** *have nonnegative real part.*

Lemma 3 (see [46]). *For any matrix $M \in \mathbb{R}^{m\times m}$, $N \in \mathbb{R}^{n\times n}$, $X \in \mathbb{R}^{m\times m}$, and $Y \in \mathbb{R}^{n\times n}$, then the following equalities hold:*

(1) $(M \otimes N)(X \otimes Y) = MX \otimes NY$

(2) If the matrices M and N are invertible, then $(M \otimes N)^{-1} = M^{-1} \otimes N^{-1}$

(3) If the eigenvalues of M are $\lambda_1, \ldots, \lambda_m$ and the eigenvalues of N are $\mu_1, \ldots, \mu_n$, then the eigenvalues of $M \otimes N$ can be expressed by $\lambda_i \mu_j$ $(i = 1, \ldots, m;\ j = 1, \ldots, n)$

Lemma 4 (see [47]). *For any $x, y \in \mathbb{R}$, if $\nu \in \mathbb{R}^+$ and $\nu > 1$, then*

$$|x + y|^{\nu} \le 2^{\nu-1}\left|x^{\nu} + y^{\nu}\right|. \tag{15}$$

Lemma 5 (see [48]). *If $x_i \in \mathbb{R}, i = 1, 2, \ldots, n$, and $0 < p \le 1$, then*

$$\left(\sum_{i=1}^{n}|x_i|\right)^{p} \le \sum_{i=1}^{n}|x_i|^{p} \le n^{1-p}\left(\sum_{i=1}^{n}|x_i|\right)^{p}. \tag{16}$$

Lemma 6 (see [47]). *Consider the nonlinear system given by*

$$\dot{x} = f(x, t),\ f(0, t) = 0, \qquad x \in \mathbb{R}^{n}. \tag{17}$$

Suppose that there exists a Lyapunov function $V(x)$ that satisfies the following condition:

$$\dot{V}(x) \le -\left(\alpha V(x)^{p} + \beta V(x)^{g}\right)^{k} + \upsilon, \quad x \in U_o, \tag{18}$$

where α, β, p, $g \in \mathbb{R}^+$, $pk < 1$, $gk > 1$, and $0 < \upsilon < \infty$. Then, the origin of system (17) is practical fixed-time stable and the residual set of the solution satisfies

$$\left\{\lim_{t\longrightarrow T} x | V(x) \le \min\left\{\alpha^{-(1/p)}\left(\frac{\upsilon}{1-\theta k}\right)^{(1/kp)}, \beta^{-(1/g)}\left(\frac{\upsilon}{1-\theta k}\right)^{(1/kg)}\right\}\right\}, \tag{19}$$

where θ is a scalar satisfying $0 < \theta \le 1$. The setting time is bounded by

$$T \le \frac{1}{\alpha^{k}\theta^{k}(1-pk)} + \frac{1}{\beta^{k}\theta^{k}(gk-1)}. \tag{20}$$

3. Multispacecraft Nonsingular Fixed-Time Terminal Sliding Mode

In this section, a multispacecraft nonsingular fixed-time terminal sliding mode (FTTSM) vector is proposed to realize the orbit and attitude coordinated control for SFF. The following assumptions are presented regarding the 6-DOF dynamic model.

Assumption 1. The total disturbance τ_i is assumed to be bounded due to the fact that magnetic forces, J_2 perturbations, gravitation, and solar radiation pressure are bounded.

Assumption 2. The desired angular velocity ω_{di} and its time derivative $\dot{\omega}_{di}$ are assumed to be bounded. The desired trajectory ρ_{di} and its time derivative $\dot{\rho}_{di}$ are assumed to be bounded.

In order to achieve coordinated control for multiple spacecraft formation, the sliding mode based on (6) is defined as

$$\mathbf{S} = [\mathbf{s}_1, \ldots, \mathbf{s}_i]^T, \tag{21}$$

where $\mathbf{s}_i = [s_{i,1}, s_{i,2}, \ldots, s_{i,k}]^T \in \mathbb{R}^{6\times 1}$, $i = 1, 2, \ldots, n$ and $k = 1, 2, \ldots, 6$, given by

$$\mathbf{s}_i = b_i \mathbf{G}_{fi}[\mathbf{e}_{2i} + \alpha_i(\mathbf{e}_{1i})] + \sum_{j=1}^{n} a_{ij}\left[\left(\mathbf{G}_{fi}\mathbf{e}_{2i} - \mathbf{G}_{fj}\mathbf{e}_{2j}\right) + \left(\mathbf{G}_{fi}\alpha_i(\mathbf{e}_{1i}) - \mathbf{G}_{fj}\alpha_j(\mathbf{e}_{1j})\right)\right], \tag{22}$$

with $\alpha_i(\mathbf{e}_{1i}) = [\alpha_{i,1}(e_{1i1}), \alpha_{i,2}(e_{1i2}), \ldots, \alpha_{i,k}(e_{1ik})]^T \in \mathbb{R}^{6\times 1}$, and

$$\alpha_{i,k}(e_{1ik}) = \begin{cases} \operatorname{sgn}\left(\sigma_{1i}\operatorname{sgn}(e_{1ik})^{p_1} + \sigma_{2i}\operatorname{sgn}(e_{1ik})^{p_2}\right)^{k_1}, & \text{if } \bar{s}_{i,k} = 0 \text{ or } \bar{s}_{i,k} \neq 0, |e_{1ik}| > \varepsilon, \\ l_{1i}e_{1ik} + l_{2i}\operatorname{sgn}(e_{1ik})^2, & \text{if } \bar{s}_{i,k} \neq 0, |e_{1ik}| \leq \varepsilon, \end{cases} \tag{23}$$

where $i = 1, \ldots, n$, $k = 1, 2, \ldots, 6$, $\bar{s}_i = [\bar{s}_{i,1}, \bar{s}_{i,2}, \ldots, \bar{s}_{i,6}]^T$, $\bar{s}_i = \mathbf{e}_{2i} + \operatorname{sgn}(\sigma_{1i}\operatorname{sgn}(\mathbf{e}_{1i})^{p_1} + \sigma_{2i}\operatorname{sgn}(\mathbf{e}_{1i})^{p_2})^{k_1}$, $l_{1i} = (2 - k_1)(\sigma_{1i}\varepsilon^{p_1-(1/k_1)} + \sigma_{2i}\varepsilon^{p_2-(1/k_1)})^{k_1}$, $l_{2i} = (k_1 - 1)(\sigma_{1i}\varepsilon^{p_1-(1/k_1)} + \sigma_{2i}\varepsilon^{p_2-(1/k_1)})^{k_1}$, $b_i > 0$ is control scheme gain to realize tracking control, $a_{ij} \geq 0$ is control scheme gain to realize coordinated control between ith and jth formation spacecraft, $\operatorname{sgn}(e_{1ik})^{p_1} = |e_{1ik}|^{p_1}\operatorname{sgn}(e_{1ik})$ and $\operatorname{sgn}(e_{1ik})^{p_2} = |e_{1ik}|^{p_2}\operatorname{sgn}(e_{1ik})$, $\sigma_{1i} > 0$, $\sigma_{1i} > 0$, $p_1 > 0$, $p_2 > 0\, k_1 > 0$ are designed parameters, $\operatorname{sgn}(\sigma_{1i}\operatorname{sgn}(e_{1ik})^{p_1} + \sigma_{2i}\operatorname{sgn}(e_{1ik})^{p_2})^{k_1} = |(\sigma_{1i}\operatorname{sgn}(e_{1ik})^{p_1} + \sigma_{2i}\operatorname{sgn}(e_{1ik})^{p_2})|^{k_1}\operatorname{sgn}(\sigma_{1i}\operatorname{sgn}(e_{1ik})^{p_1} + \sigma_{2i}\operatorname{sgn}(e_{1ik})^{p_2})$, $\varepsilon > 0$ is small constant, $0 < p_1k_1 < 1$, $p_2k_1 > 1$, and $\operatorname{sgn}(\cdot)$ is sign function.

Remark 2. It is supposed that the communication topology of SFF is undirected; we can obtain $a_{ij} = a_{ji}$, which simplifies the design and analysis of the controller. However, for the directed communication topology, $a_{ij} = a_{ji}$ does not hold. Therefore, compared with bidirectional communication topology, the coordinated control of formation spacecraft under directed communication topology is more challenging.

Remark 3. Note that the multispacecraft FTTSM (21) can be simplified as a modified terminal sliding mode (TSM) designed in [47] if $k_1 = 1$ and $p_2 = 0$; moreover, (21) coincides with the modified fast TSM designed in [49] for $k_1 = 1$. It is worth mentioning that when e_{1ik} converges to the region $|e_{1ik}| \leq \varepsilon$, the multispacecraft FTTSM is converted to the general sliding mode for $\bar{s}_{i,1} \neq 0$. Thus, the singularity problem of (21) can be effectively avoided. Moreover, by the choice of l_1 and l_2, the continuity of $\alpha_{i,k}$ and its first-order time derivative is guaranteed.

By Kronecker product, the sliding mode function (21) can be described by

$$\mathbf{S} = [(\mathbf{L} + \mathbf{B}) \otimes \mathbf{I}_6]\overline{\mathbf{G}}(\mathbf{e}_2 + \alpha(\mathbf{e}_1)), \tag{24}$$

where $\mathbf{L}$ is the weighted Laplace matrix, which is determined by directed topology, $\mathbf{B} = \operatorname{diag}[b_1, b_2, \ldots, b_n]$, $\mathbf{e}_2 = [\mathbf{e}_{21}^T, \mathbf{e}_{22}^T, \ldots, \mathbf{e}_{2n}^T]^T$, $\alpha(\mathbf{e}_1) = [\alpha_1^T(\mathbf{e}_{11}), \alpha_2^T(\mathbf{e}_{12}), \ldots, \alpha_n^T(\mathbf{e}_{1n})]^T$, $\overline{\mathbf{G}} = \operatorname{diag}[\mathbf{G}_{f1}, \mathbf{G}_{f2}, \ldots, \mathbf{G}_{fn}]$.

4. Design of Fixed-Time Adaptive Coordinated Control Scheme

In this section, a fixed-time adaptive 6-DOF coordinated control scheme is presented for multiple SFF with input quantization and external disturbances.

To design the control scheme, (6) can be derived as

$$\mathbf{G}_{fi}(\dot{e}_{2i} + \dot{\alpha}_i(\mathbf{e}_{1i})) = \mathbf{h}_i + D(u_i)\mathbf{u}_i + Q_i(t) + \boldsymbol{\tau}_i, \tag{25}$$

with

$$\dot{\alpha}_i(\mathbf{e}_{1i}) = \begin{cases} \sigma_{1i}p_1k_1\operatorname{diag}(|\sigma_{1i}\operatorname{sgn}(\mathbf{e}_{1i})^{p_1} + \sigma_{2i}\operatorname{sgn}(\mathbf{e}_{1i})^{p_2}|^{k_1-1}), \\ \cdot\operatorname{diag}(|\mathbf{e}_{1i}|^{p_1-1})\boldsymbol{\Lambda}(\dot{e}_{1i})\mathbf{e}_{2i} + \sigma_{2i}p_2k_1\operatorname{diag}(|\sigma_{1i}\operatorname{sgn}(\mathbf{e}_{1i})^{p_1}, \\ +\sigma_{2i}\operatorname{sgn}(\mathbf{e}_{1i})^{p_2}|^{k_1-1})\operatorname{diag}(|\mathbf{e}_{1i}|^{p_2-1})\boldsymbol{\Lambda}(\dot{e}_{1i})\mathbf{e}_{2i}, \\ \text{if } \bar{s}_{ik} = 0 \text{ or } \bar{s}_{ik} \neq 0, |e_{1ik}| > \varepsilon, \\ l_{1i}\boldsymbol{\Lambda}(\dot{x}_{1i})\mathbf{e}_{2i} + 2l_{2i}\operatorname{diag}(|e_{1i}|)\boldsymbol{\Lambda}(\dot{e}_{1i})(\mathbf{e}_{2i}), \\ \text{if } \bar{s}_{ik} \neq 0, |e_{1ik}| \leq \varepsilon, \end{cases}$$
$$\mathbf{h}_i = -\mathbf{C}(\mathbf{e}_{2i}) - \mathbf{N}(\mathbf{e}_{1i}) - \mathbf{G}_{fi} - \dot{e}_{2id} + \mathbf{G}_{fi}\dot{\alpha}_i(\mathbf{e}_{1i}). \tag{26}$$

Under Assumption 1, it can be seen that

$$\left(\left\|(\mathbf{L}+\mathbf{B})\otimes\mathbf{I}_6\right\|_1\left\|\boldsymbol{\tau}_i+Q_i(t)\right\|_1\right)^2\le c_i,\quad i=1,\ldots,n,\tag{27}$$

where c_i are nonnegative constant numbers.

The fixed-time adaptive controller is designed as

$$\mathbf{u}_i=-\frac{1}{1-\delta}\mathbf{h}_i+\frac{1}{1-\delta}\left(\sum_{j=1,j\neq i}^{n}a_{ij}+b_i\right)^{-1}\left[\sum_{j=1,j\neq i}^{n}a_{ij}\left((1-\delta)\mathbf{u}_j+\mathbf{h}_j\right)-\alpha_i\operatorname{sgn}(\mathbf{s}_i)^{\gamma1},-\beta_i\operatorname{sgn}(\mathbf{s}_i)^{\gamma2}-\frac{\widehat{c}_i}{2\mathfrak{J}_i^2}\mathbf{s}_i\right],\quad i=1,\ldots,n,\tag{28}$$

$$\dot{\widehat{c}}_i=-2\kappa_i\varrho_i\widehat{c}_i+\frac{\kappa_i}{2\mathfrak{J}_i^2}\left\|s_i\right\|,\quad i=1,\ldots,n,\tag{29}$$

where $0<\gamma1<1$, $\gamma2>1$, $\mathfrak{J}_i>0$, $\kappa_i>0$, and $\varrho_i>0$ are the controller parameters.

Theorem 1. *Consider the 6-DOF control system (6) with the fixed-time coordinated control law (28). If the parameter uncertainty and external disturbance satisfy Assumptions 1-2, then the sliding mode vector $\mathbf{s}_i$ will converge into*

$$\left\|s_i\right\|\le\Delta_s=\min\left\{\upsilon_1^{-(2/1+\gamma1)}\left(\frac{\upsilon}{1-\theta_o}\right)^{(2/1+\gamma1)},\left(\upsilon_2\left(\frac{1}{2^{\upsilon+12-1}}\right)^{n+k-1}\right)^{-(2/1+\gamma1)}\left(\frac{\upsilon}{1-\theta_o}\right)^{(2/1+\gamma2)}\right\},\tag{30}$$

in fixed time, where $\beta_{\min}=\min\{\beta_i\}$, $\alpha_{\min}=\min\{\alpha_i\}$, $\iota_{\min}=\min\{\iota_i\}$, $\upsilon_1=\min\{\alpha_{\min}2^{(\gamma1+1/2)},\iota_{\min^{(\gamma1+1/2)}}2^{(\gamma1+1/2)}\}$, $\upsilon_2=\min\{\beta_{\min}2^{(\gamma2+1/2)},\iota_{\min^{(\gamma2+1/2)}}2^{(\gamma2+1/2)}\}$, $\upsilon=\sum_{i=1}^{n}\varrho_i o_i c_i^2+1+\sum_{i=1}^{n}/\mathfrak{J}^2 2+\sum_{i=1}^{n}[((\iota_i/\kappa_i)\Delta_i^2)^{(\gamma2+1/2)}-(\iota_i/\kappa_i)\Delta_i^2]$, $\iota_i=\kappa_i(\varrho_i(2o_i-1)/2o_i)$, $\Delta_i>0$, $0<\theta_0\le1$, $o_i>(1/2)$.

Proof. We construct the following Lyapunov function candidate:

$$V_1=V_2+V_3,\tag{31}$$

with

$$V_2=\frac{1}{2}\mathbf{S}^T\mathbf{S},V_3=\frac{1}{2}\sum_{i=1}^{n}\kappa_i^{-1}\widetilde{c}_i^2,\tag{32}$$

where $\widetilde{c}_i=c_i-\widehat{c}_i$.

By the Kronecker product, the controller (28) can be rewritten as

$$\begin{aligned}\mathbf{U}=&-\frac{1}{1-\delta}\mathbf{H}+\frac{1}{1-\delta}\left[(\mathbf{D}+\mathbf{B})^{-1}\otimes\mathbf{I}_6\right]\\&[(\mathbf{A}\otimes\mathbf{I}_6)((1-\delta)\mathbf{U}+\mathbf{H})-\boldsymbol{\alpha}\operatorname{sgn}(\mathbf{S})^{\gamma1},\\&-\boldsymbol{\beta}\operatorname{sgn}(\mathbf{S})^{\gamma2}-\widehat{c}\mathbf{S}.\end{aligned}\tag{33}$$

where $\mathbf{U}=[\mathbf{u}_1,\ldots,\mathbf{u}_n]^T$, $\mathbf{H}=[h_1,\ldots,h_n]^T$, $\alpha=\operatorname{diag}[\alpha_1\mathbf{I}_6,\ldots,\alpha_n\mathbf{I}_6]$, $\alpha=\operatorname{diag}[\alpha_1\mathbf{I}_6,\ldots,\alpha_n\mathbf{I}_6]$, $\widehat{c}=\operatorname{diag}[(\widehat{c}_1/2\mathfrak{J}_1^2)\mathbf{I}_6,\ldots,(\widehat{c}_n/2\mathfrak{J}_n^2)\mathbf{I}_6]$.

Since $\mathbf{I}_{6n}-[(\mathbf{D}+\mathbf{B})^{-1}\otimes\mathbf{I}_6](\mathbf{A}\otimes\mathbf{I}_6)$ can be equivalently expressed as

$$\begin{aligned}&\mathbf{I}_{6n}-\left[(\mathbf{D}+\mathbf{B})^{-1}\otimes\mathbf{I}_6\right](\mathbf{A}\otimes\mathbf{I}_6),\\&=[(\mathbf{D}+\mathbf{B})^{-1}\otimes\mathbf{I}_6]\{(\mathbf{D}+\mathbf{B})\otimes\mathbf{I}_6]-\mathbf{A}\otimes\mathbf{I}_3\},\\&=\left[(\mathbf{D}+\mathbf{B})^{-1}\otimes\mathbf{I}_6\right][(\mathbf{L}+\mathbf{B})\otimes\mathbf{I}_6].\end{aligned}\tag{34}$$

It follows from (34) that

$$\begin{aligned}\mathbf{U}=&-\frac{1}{1-\delta}\mathbf{H}-\frac{1}{1-\delta}\left\{\mathbf{I}_{6n}-\left[(\mathbf{D}+\mathbf{B})^{-1}\otimes\mathbf{I}_6\right](\mathbf{A}\otimes\mathbf{I}_6)\right\}^{-1}\\&\left[(\mathbf{D}+\mathbf{B})^{-1}\otimes\mathbf{I}_6\right],\\&\times\left(\boldsymbol{\alpha}\operatorname{sgn}(\mathbf{S})^{\gamma1}+\boldsymbol{\beta}\operatorname{sgn}(\mathbf{S})^{\gamma2}+\widehat{c}\mathbf{S}\right),\\=&-\frac{1}{1-\delta}\mathbf{H}-\frac{1}{1-\delta}\left\{\left[(\mathbf{D}+\mathbf{B})^{-1}\otimes\mathbf{I}_6\right][(\mathbf{L}+\mathbf{B})\otimes\mathbf{I}_6]\right\}^{-1}\\&\left[(\mathbf{D}+\mathbf{B})^{-1}\otimes\mathbf{I}_6\right],\\&\times\left(\boldsymbol{\alpha}\operatorname{sgn}(\mathbf{S})^{\gamma1}+\boldsymbol{\beta}\operatorname{sgn}(\mathbf{S})^{\gamma2}+\widehat{c}\mathbf{S}\right),\\=&-\frac{1}{1-\delta}\mathbf{H}-\frac{1}{1-\delta}[(\mathbf{L}+\mathbf{B})\otimes\mathbf{I}_6]^{-1}\\&\left(\boldsymbol{\alpha}\operatorname{sgn}(\mathbf{S})^{\gamma1}+\boldsymbol{\beta}\operatorname{sgn}(\mathbf{S})^{\gamma2}+\widehat{c}\mathbf{S}\right).\end{aligned}\tag{35}$$

Considering (24) and (25), it can be shown that

$$\begin{aligned}\dot{V}_2 &= \mathbf{S}^T\dot{S},\\ &= \mathbf{S}^T\left[(\mathbf{L}+\mathbf{B})\otimes\mathbf{I}_6\right]\left(\mathbf{G}_{fi}\dot{\mathbf{e}}_{2i}+\mathbf{G}_{fi}\dot{\alpha}_i\left(\mathbf{e}_{1i}\right)\right),\\ &= \mathbf{S}^T\left[(\mathbf{L}+\mathbf{B})\otimes\mathbf{I}_6\right](\mathbf{H}+\mathbf{D}(U)\mathbf{U}+\mathbf{Q}(t)+\boldsymbol{\tau}),\end{aligned} \tag{36}$$

where $\tau=[\tau_1,\ldots,\tau_n]^T$, $\mathbf{D}(U)=\mathrm{diag}[\mathbf{D}(u_1),\ldots,\mathbf{D}(u_n)]$, $\mathbf{Q}(t)=[Q_1(t),\ldots,Q_n(t)]^T$.

Next, it can be derived that

$$\begin{aligned}\dot{V}_2 &= \mathbf{S}^T[\,(\mathbf{L}+\mathbf{B})\otimes\mathbf{I}_6\,](\,[(\mathbf{L}+\mathbf{B})\otimes\mathbf{I}_6]^{-1}\left(-\boldsymbol{\alpha}\mathrm{sgn}(\mathbf{S})^{\gamma 1}-\boldsymbol{\beta}\mathrm{sgn}(\mathbf{S})^{\gamma 2}-\mathbf{c}\mathbf{S}\right)+Q(t)+\boldsymbol{\tau}),\\ &= \mathbf{S}^T[\,(\mathbf{L}+\mathbf{B})\otimes\mathbf{I}_6\,](\boldsymbol{\tau}+Q(t))-\mathbf{S}^T\boldsymbol{\alpha}\mathrm{sgn}(S^{\gamma 1}-\mathbf{S}^T\boldsymbol{\beta}\mathrm{sgn}(\mathbf{S}^{\gamma 2}-\mathbf{S}^T\widehat{\mathbf{c}}\mathbf{S},\\ &\le \sum_{i=1}^{n}\left\|(\mathbf{L}+\mathbf{B})\otimes\mathbf{I}_6\right\|\left\|\boldsymbol{\tau}_i+Q_i(t)\right\|\left\|\mathbf{s}_i\right\|-\sum_{i=1}^{n}\frac{\widehat{c}_i}{2\mathfrak{J}_i^2}\left\|\mathbf{s}_i\right\|^2-\sum_{i=1}^{n}\sum_{k=1}^{p}\beta_i\left|s_{ik}\right|^{\gamma 2+1},\\ &\quad -\sum_{i=1}^{n}\sum_{k=1}^{p}\alpha_i\left|s_{ik}\right|^{\gamma 1+1},\\ &\le \sum_{i=1}^{n}\frac{\left\|((\mathbf{L}+\mathbf{B})\otimes\mathbf{I}_6\right\|_1\left\|\boldsymbol{\tau}_i+Q_i(t)\right\|_1)^2\left\|\mathbf{s}_i\right\|^2}{2\mathfrak{J}^2}+\sum_{i=1}^{n}\frac{\mathfrak{J}^2}{2}-\sum_{i=1}^{n}\frac{\widehat{c}_i}{2\mathfrak{J}_i^2}\left\|\mathbf{s}_i\right\|^2,\\ &\quad -\sum_{i=1}^{n}\sum_{k=1}^{p}\alpha_i\left(s_{ik}^2\right)^{(\gamma 1+1/2)}-\sum_{i=1}^{n}\sum_{k=1}^{p}\beta_i\left(s_{ik}^2\right)^{(\gamma 1+1/2)},\\ &\le \sum_{i=1}^{n}\frac{\widetilde{c}_i}{2\mathfrak{J}_i^2}\left\|\mathbf{s}_i\right\|^2+\sum_{i=1}^{n}\frac{\mathfrak{J}^2}{2}-\sum_{i=1}^{n}\sum_{k=1}^{p}\alpha_i\left(s_{ik}^2\right)^{(\gamma 1+1/2)}-\sum_{i=1}^{n}\sum_{k=1}^{p}\beta_i\left(s_{ik}^2\right)^{(\gamma 2+1/2)}.\end{aligned} \tag{37}$$

In addition, taking the derivative of V_3 yields

$$\begin{aligned}\dot{V}_3 &= \sum_{i=1}^{n}\kappa_i^{-1}\widetilde{c}_i\dot{\widetilde{c}}_i,\\ &= -\sum_{i=1}^{n}\frac{\widetilde{c}_i}{2\mathfrak{J}_i^2}\left\|\mathbf{s}_i\right\|^2+\sum_{i=1}^{n}2\varrho_i\widetilde{c}_i\widehat{c}_i.\end{aligned} \tag{38}$$

It is noticed from (37) and (38) that

$$\begin{aligned}\dot{V}_1 &\le -\sum_{i=1}^{n}\sum_{k=1}^{p}\alpha_i\left|s_{ik}\right|^{\gamma 1+1}-\sum_{i=1}^{n}\sum_{k=1}^{p}\beta_i\left|s_{ik}\right|^{\gamma 2+1}\\ &\quad +2\sum_{i=1}^{n}\varrho_i\widetilde{c}_i\widehat{c}_i+\sum_{i=1}^{n}\frac{\mathfrak{J}^2}{2}\end{aligned}. \tag{39}$$

From

$$\varrho_i\widetilde{c}_i\widehat{c}_i\le -\frac{\varrho_i(2o_i-1)}{2o_i}\widetilde{c}_i^2+\frac{\varrho_i o_i}{2}c_i^2 \tag{40}$$

and by substituting (40) into (39), we have

$$\begin{aligned}\dot{V}_1 &\le -\sum_{i=1}^{n}\sum_{k=1}^{p}\alpha_i\left|s_{ik}\right|^{\gamma 1+1}-\sum_{i=1}^{n}\sum_{k=1}^{p}\beta_i\left|s_{ik}\right|^{\gamma 2+1}-\sum_{i=1}^{n}\frac{\iota_i}{\kappa_i}\widetilde{c}_i^2+\sum_{i=1}^{n}\varrho_i o_i c_i^2,\\ &\quad -\sum_{i=1}^{n}\frac{\iota_i}{\kappa_i}\widetilde{c}_i^2-\sum_{i=1}^{n}\left(\frac{\iota_i}{\kappa_i}\widetilde{c}_i^2\right)^{(1+\gamma_1/2)}+\sum_{i=1}^{n}\left(\frac{\iota_i}{\kappa_i}\widetilde{c}_i^2\right)^{(1+\gamma_1/2)}+\sum_{i=1}^{n}\frac{\mathfrak{J}^2}{2}.\end{aligned} \tag{41}$$

where $(\iota_i/\kappa_i)=(\varrho_i(2o_i-1)/2o_i)$. □

Case 1. If $(\iota_i/\kappa_i)\widetilde{c}_i^2\ge 1$, we have

$$\left(\frac{\iota_i}{\kappa_i}\widetilde{c}_i^2\right)^{(1+\gamma_1/2)}\le\frac{\iota_i}{\kappa_i}\widetilde{c}_i^2. \tag{42}$$

Substituting (42) into (41) yields

$$\begin{aligned}\dot{V}_1 &\le -\sum_{i=1}^{n}\sum_{k=1}^{p}\alpha_i\left(s_{ik}^2\right)^{(\gamma 1+1/2)}-\sum_{i=1}^{n}\sum_{k=1}^{p}\beta_i\left(s_{ik}^2\right)^{(\gamma 2+1/2)}\sum_{i=1}^{n}\frac{\iota_i}{\kappa_i}\widetilde{c}_i^2\\ &\quad +\sum_{i=1}^{n}\varrho_i o_i c_i^2-\sum_{i=1}^{n}\left(\frac{\iota_i}{\kappa_i}\widetilde{c}_i^2\right)^{(\gamma 1+1/2)}+\sum_{i=1}^{n}\frac{\mathfrak{J}^2}{2}.\end{aligned} \tag{43}$$

According to Lemma 5, it is easy to prove that

$$\sum_{i=1}^{n}\sum_{k=1}^{p}\alpha_i\left(s_{ik}^2\right)^{(\gamma 1+1/2)}+\sum_{i=1}^{n}\left(\frac{\iota_i}{\kappa_i}\widetilde{c}_i^2\right)^{(1+\gamma 1/2)}\geq \upsilon_1 V_8^{(1+\gamma 1/2)}, \tag{44}$$

where $\upsilon_1=\min\{\alpha_{\min}2^{(\gamma 1+1/2)},\iota_{\min^{(\gamma 1+1/2)}}2^{(\gamma 1+1/2)}\}$, $\alpha_{\min}=\min\{\alpha_i\}$, $\iota_{\min}=\min\{\iota_i\}$.

By applying (44), (43) can be rewritten as

$$\begin{aligned}\dot{V}_1 \quad &\leq -\upsilon_1 V_1^{(1+\gamma 1/2)}-\sum_{i=1}^{n}\sum_{k=1}^{p}\beta_i\left(s_{ik}^2\right)^{(\gamma 2+1/2)}-\sum_{i=1}^{n}\frac{\iota_i}{\kappa_i}\widetilde{c}_i^2\\ &+\sum_{i=1}^{n}\varrho_i o_i c_i^2+\sum_{i=1}^{n}\frac{\mathfrak{I}^2}{2}\end{aligned}. \tag{45}$$

Case 2. If $(\iota_i/\kappa_i)\widetilde{c}_i^2<1$, one can obtain

$$\left(\frac{\iota_i}{\kappa_i}\widetilde{c}_i^2\right)^{(1+\gamma_1/2)}-\frac{\iota_i}{\kappa_i}\widetilde{c}_i^2\leq 1-\frac{\iota_i}{\kappa_i}\widetilde{c}_i^2<1. \tag{46}$$

Substituting (46) into (41) yields

$$\begin{aligned}\dot{V}_1 \leq &-\upsilon_1 V_1^{(1+\gamma 1/2)}-\sum_{i=1}^{n}\sum_{k=1}^{p}\beta_i\left(s_{ik}^2\right)^{(\gamma 2+1/2)}-\sum_{i=1}^{n}\frac{\iota_i}{\kappa_i}\widetilde{c}_i^2\\ &+\sum_{i=1}^{n}\varrho_i o_i c_i^2+1+\sum_{i=1}^{n}\frac{\mathfrak{I}^2}{2}.\end{aligned} \tag{47}$$

Furthermore, (47) can be rewritten as

$$\begin{aligned}\dot{V}_1 \leq &-\upsilon_1 V_1^{(1+\gamma 1/2)}-\sum_{i=1}^{n}\sum_{k=1}^{p}\beta_i\left(s_{ik}^2\right)^{(\gamma 2+1/2)}\\ &-\sum_{i=1}^{n}\frac{\iota_i}{\kappa_i}\widetilde{c}_i^2-\sum_{i=1}^{n}\left(\frac{\iota_i}{\kappa_i}\widetilde{c}_i^2\right)^{(\gamma 2+1/2)},\\ &+\sum_{i=1}^{n}\left(\frac{\iota_i}{\kappa_i}\widetilde{c}_i^2\right)^{(\gamma 2+1/2)}+\sum_{i=1}^{n}\varrho_i o_i c_i^2+1+\sum_{i=1}^{n}\frac{\mathfrak{I}^2}{2}.\end{aligned} \tag{48}$$

According to Lemma 5, we obtain

$$\sum_{i=1}^{n}\sum_{k=1}^{p}\beta_i\left(s_{ik}^2\right)^{(\gamma 2+1/2)}+\sum_{i=1}^{n}\left(\frac{\iota_i}{\kappa_i}\widetilde{c}_i^2\right)^{(1+\gamma 2/2)}\geq \upsilon_2\left(\frac{1}{2^{\gamma 2+12-1}}\right)V_5^{(1+\gamma 2/2)}, \tag{49}$$

where $\upsilon_2=\min\{\beta_{\min}2^{(\gamma 2+1/2)},\iota_{\min^{(\gamma 2+1/2)}}2^{(\gamma 2+1/2)}\}$, $\beta_{\min}=\min\{\beta_i\}$, $\iota_{\min}=\min\{\iota_i\}$.

From (49), we have

$$\begin{aligned}\dot{V}_1 \leq &-\upsilon_1 V_1^{(1+\gamma 1/2)}-\upsilon_2\left(\frac{1}{2^{\gamma 2+12-1}}\right)V_1^{(1+\gamma 2/2)}-\sum_{i=1}^{n}\frac{\iota_i}{\kappa_i}\widetilde{c}_i^2\\ &+\sum_{i=1}^{n}\left(\frac{\iota_i}{\kappa_i}\widetilde{c}_i^2\right)^{(\gamma 2+1/2)}+\sum_{i=1}^{n}\varrho_i o_i c_i^2+\sum_{i=1}^{n}\frac{\mathfrak{I}^2}{2}+1.\end{aligned} \tag{50}$$

Assume that there exists a compact set Π_i satisfying

$$\Pi_i=\left\{(\widetilde{c}_i|\left|\widetilde{c}_i\right|\leq\Delta_i\right\}, \tag{51}$$

where Δ_i is an unknown constant.

If $\Delta_i<\sqrt{(\zeta_i/\iota_i)}$, we can obtain

$$\frac{\iota_i}{\kappa_i}\widetilde{c}_i^2<1,\ \left(\frac{\iota_i}{\kappa_i}\widetilde{c}_i^2\right)^{(\gamma 2+1/2)}<\frac{\iota_i}{\kappa_i}\widetilde{c}_i^2. \tag{52}$$

If $\Delta_i\geq\sqrt{(\zeta_i/\iota_i)}$, we can obtain

$$\left(\frac{\iota_i}{\kappa_i}\widetilde{c}_i^2\right)^{(\gamma 2+1/2)}-\frac{\iota_i}{\kappa_i}\widetilde{c}_i^2\leq\left(\frac{\iota_i}{\kappa_i}\Delta_i^2\right)^{(\gamma 2+1/2)}-\frac{\iota_i}{\kappa_i}\Delta_i^2. \tag{53}$$

Denote

$$\upsilon=\sum_{i=1}^{n}\varrho_i o_i c_i^2+1+\sum_{i=1}^{n}\left[\left(\frac{\iota_i}{\kappa_i}\Delta_i^2\right)^{(\gamma 2+1/2)}-\frac{\iota_i}{\kappa_i}\Delta_i^2\right]. \tag{54}$$

Then, from the above analyses, we can further conclude that

$$\dot{V}_1\leq-\upsilon_1 V_1^{(1+\gamma 1/2)}-\upsilon_2\left(\frac{1}{2^{\gamma 2+12-1}}\right)^{n+k-1}V_1^{(1+\gamma 2/2)}+\upsilon. \tag{55}$$

With Lemma 6, system (6) is practical fixed-time stable. Furthermore, $\mathbf{s}_i$ will converge into the region

$$\Phi=\left\{\lim_{t\longrightarrow T_s}s_i|V_1\leq\min\left\{\upsilon_1^{-(2/1+\gamma 1)}\left(\frac{\upsilon}{1-\theta_o}\right)^{(2/1+\gamma 1)},\left(\upsilon_2\left(\frac{1}{2^{\upsilon+12-1}}\right)^{n+k-1}\right)^{-(2/1+\gamma 1)}\left(\frac{\upsilon}{1-\theta_o}\right)^{(2/1+\gamma 2)}\right\}\right\}, \tag{56}$$

in a fixed-time $T_s \leq (1/\vartheta_1\theta_o(1-\gamma 1+12)) + (1/\vartheta_2 (12^{\gamma 2+1}2-1)^n\theta_o(\gamma 2+12-1))$; that is, $\mathbf{s}_i$ will converge into the region$\| \mathbf{s}_i \| \leq \Delta_s$ in a fixed-time T_s.

Theorem 2. *When $\mathbf{s}_i$ reach the boundary Δ_s in fixed-time, the tracking error $\mathbf{e}_{1i}$ and $\mathbf{e}_{2i}$ will converge to*

$$\begin{aligned}
&\left|\mathbf{e}_{1i}\right| < \Delta_{e1i} = \max\left\{\varepsilon, \left(\frac{\Delta^1 k_s}{\sigma_{1i}}\right)^{(1/p_1)}, \left(\frac{\Delta^1 k_s}{\sigma_{2i}}\right)^{(1/p_2)}\right\},\\
&\left|\mathbf{e}_{2i}\right| < \Delta_{e2i} = \max\left\{\Delta_s + l_1\Delta_{e1ik} + l_2\Delta_{e1ik}^2,\right.\\
&\qquad \left.\Delta_s + \left(\sigma_{1i}\Delta_{e1i}^{p_1} + \sigma_{2i}\Delta_{e1i}^{p_2}\right)^{k_1}\right\},
\end{aligned} \tag{57}$$

in a fixed time, where $i = 1, \ldots, n$, $k = 1, 2, \ldots, 6$.

Proof. If $\bar{\mathbf{s}}_i = 0$, we can obtain

$$\bar{s}_i = \mathbf{e}_{2i} + \operatorname{sgn}\left(\sigma_{1i}\operatorname{sgn}(\mathbf{e}_{1i})^{p_1} + \sigma_{2i}\operatorname{sgn}(\mathbf{e}_{1i})^{p_2}\right)^{k_1} = 0, \quad i = 1, \ldots, n. \tag{58}$$

Furthermore, one can obtain

$$\begin{aligned}
&\dot{\rho}_{ei} + \operatorname{sgn}\left(\sigma_{1i}\operatorname{sgn}(\boldsymbol{\rho}_{ei})^{p_1} + \sigma_{2i}\operatorname{sgn}(\boldsymbol{\rho}_{ei})^{p_2}\right)^{k_1} = 0, \quad i = 1, \ldots, n,\\
&\boldsymbol{\omega}_{ei} + \operatorname{sgn}\left(\sigma_{1i}\operatorname{sgn}(\mathbf{q}_{ei})^{p_1} + \sigma_{2i}\operatorname{sgn}(\mathbf{q}_{ei})^{p_2}\right)^{k_1} = 0, \quad i = 1, \ldots, n.
\end{aligned} \tag{59}$$

Construct the following Lyapunov function candidate:

$$\begin{aligned}
V_4 &= \frac{1}{2}\boldsymbol{\rho}_{ei}^T\boldsymbol{\rho}_{ei} + \mathbf{q}_{ei}^T\mathbf{q}_{ei} + (1-q_{0ei})^2,\\
&= \frac{1}{2}\boldsymbol{\rho}_{ei}^T\boldsymbol{\rho}_{ei} + 2(1-q_{0ei}).
\end{aligned} \tag{60}$$

Denote

$$V_5 = \boldsymbol{\rho}_{ei}^T\boldsymbol{\rho}_{ei},\ V_6 = 2(1-q_{0ei}). \tag{61}$$

Taking the derivative of V_5 and V_6 yields

$$\begin{aligned}
\dot{V}_5 &= \boldsymbol{\rho}_{ei}^T\dot{\rho}_{ei},\\
&= \boldsymbol{\rho}_{ei}^T\left(-\operatorname{sgn}\left(\sigma_{1i}\operatorname{sgn}(\boldsymbol{\rho}_{ei})^{p_1} + \sigma_{2i}\operatorname{sgn}(\boldsymbol{\rho}_{ei})^{p_2}\right)^{k_1}\right),\\
&-\left|\sigma_{1i}\left(\rho_{ei}^T\rho_{ei}\right)^{((1/k_1)+p_1/2)} + \sigma_{2i}\left(\rho_{ei}^T\rho_{ei}\right)^{((1/k_1)+p_{21}/2)}\right|^{k_1},\\
&\leq -\left(\sigma_{1i}2^{((1/k_1)+p_1/2)}V_5^{((1/k_1)+p_1/2)} + \sigma_{2i}2^{((1/k_1)+p_2/2)}V_5^{((1/k_1)+p_2/2)}\right)^{k_1}.
\end{aligned} \tag{62}$$

Similarly, taking the derivative of V_6 yields

$$\begin{aligned}
\dot{V}_6 &= -2\dot{q}_{0ei},\\
&= \mathbf{q}_{iev}^T\boldsymbol{\omega}_{ei},\\
&= -\mathbf{q}_{iev}^T\left(\operatorname{sgn}\left(\sigma_{1i}\operatorname{sgn}(\mathbf{q}_{ei})^{p_1} + \sigma_{2i}\operatorname{sgn}(\mathbf{q}_{ei})^{p_2}\right)^{k_1}\right),\\
&= -\left|\sigma_{1i}\left(\mathbf{q}_{iev}^T\mathbf{q}_{iev}\right)^{((1/k_1)+p_1/2)} + \sigma_{2i}\left(\mathbf{q}_{iev}^T\mathbf{q}_{iev}\right)^{((1/k_1)+p_2/2)}\right|^{k_1},\\
&\leq -\left(\sigma_{1i}0.5^{((1/k_1)+p_1/2)}V_6^{((1/k_1)+p_1/2)} + \sigma_{2i}0.5^{((1/k_1)+p_2/2)}V_6^{((1/k_1)+p_2/2)}\right)^{k_1}.
\end{aligned} \tag{63}$$

Then, from (62) and (63), we can obtain that system error states $(\rho_{ei}, \mathbf{q}_{ei})$ converge into regions $(0, 0)$, at the same time $\dot{q}_{0ei} \in (-1, 1]$ converges to 1 in fixed-time by using Lemma 6. □

If $\bar{\mathbf{s}}_i \neq 0$ and $|e_{1ik}| < \varepsilon$, which implies that $|e_{1ik}|$ has converged to the region $|e_{1ik}| < \Delta_{e1ik} = \varepsilon$ in a fixed time. Then, from (23), we have

$$e_{2ik} + l_{1i}e_{1ik} + l_{2i}\mathrm{sgn}\left(e_{1ik}\right)^2 = \varpi_{ik}, \left|\varpi_{ik}\right| \le \Delta_s. \tag{64}$$

Moreover, it is easy to see that

$$\left|e_{2ik}\right| < \Delta_s + l_{1i}\Delta_{e1ik} + l_{2i}\Delta_{e1ik}^2, \tag{65}$$

which means that $|e_{2ik}|$ converges to the region $|e_{1ik}| < \Delta_{e1ik} = \varepsilon$ in a fixed time.

If $\bar{s}_i \neq 0$ and $|e_{1ik}| > \varepsilon$, we can obtain

$$\bar{s}_i = \mathbf{e}_{2i} + \mathrm{sgn}\left(\sigma_{1i}\mathrm{sgn}\left(\mathbf{e}_{1i}\right)^{p_1} + \sigma_{2i}\mathrm{sgn}\left(\mathbf{e}_{1i}\right)^{p_2}\right)^{k_1} \neq 0, \quad i = 1, \ldots, n, \tag{66}$$

which means

$$\bar{s}_i = \mathbf{e}_{2i} + \mathrm{sgn}\left(\sigma_{1i}\mathrm{sgn}\left(\mathbf{e}_{1i}\right)^{p_1} + \sigma_{2i}\mathrm{sgn}\left(\mathbf{e}_{1i}\right)^{p_2}\right)^{k_1} = \varpi_{ik}, \left|\varpi_{ik}\right| \le \Delta_s. \tag{67}$$

After a simple transformation, (67) can be rewritten as

$$\mathbf{e}_{2i} + \left(1 - \frac{\varpi_{ik}}{\mathrm{sgn}\left(\sigma_{1i}\mathrm{sgn}\left(\mathbf{e}_{1i}\right)^{\gamma 1} + \sigma_{2i}\mathrm{sgn}\left(\mathbf{e}_{1i}\right)^{\gamma 2}\right)^{k_1}}\right)\mathrm{sgn}\left(\sigma_{1i}\mathrm{sgn}\left(\mathbf{e}_{1i}\right)^{\gamma 1} + \sigma_{2i}\mathrm{sgn}\left(\mathbf{e}_{1i}\right)^{\gamma 2}\right)^{k_1} = 0. \tag{68}$$

When $1 - (\varpi_{ik}/\mathrm{sgn}(\sigma_{1i}\mathrm{sgn}(\mathbf{e}_{1i})^{p_1} + \sigma_{2i}\mathrm{sgn}(\mathbf{e}_{1i})^{p_2})^{k_1}) > 0$, (66) is still kept in the form of the FTTSM as in Case 1, which implies that

$$\left|\mathbf{e}_{1i}\right| < \left(\frac{\Delta^1 k_s}{\sigma_{1i}}\right)^{(1/p_1)}, \left|\mathbf{e}_{1i}\right| < \left(\frac{\Delta^1 k_s}{\sigma_{2i}}\right)^{(1/p_2)}. \tag{69}$$

Thus, system state $\mathbf{e}_{1i}$ will converge into the region

$$\left|\mathbf{e}_{1i}\right| < \Delta_{e1i} = \max\left\{\left(\frac{\Delta^1 k_s}{\sigma_{1i}}\right)^{(1/p_1)}, \left(\frac{\Delta^1 k_s}{\sigma_{2i}}\right)^{(1/p_2)}\right\}, \tag{70}$$

in a fixed time.

On the other hand, from (67), we can obtain that system state $\mathbf{e}_{2i}$ will converge to the region

$$\left|e_{2i}\right| < \Delta_{e2i} = \Delta_s + \left(\sigma_{1i}\Delta_{e1i}^{p_1} + \sigma_{2i}\Delta_{e1i}^{p_2}\right)^{k_1}, \tag{71}$$

in a fixed time.

Furthermore, we can conclude that

$$\begin{aligned} \left|e_{1i}\right| &< \Delta_{e1i} = \max\left\{\varepsilon, \left(\frac{\Delta^1 k_s}{\sigma_{1i}}\right)^{(1/p_1)}, \left(\frac{\Delta^1 k_s}{\sigma_{2i}}\right)^{(1/p_2)}\right\}, \\ \left|e_{2i}\right| &< \Delta_{e2i} = \max\left\{\Delta_s + l_1\Delta_{e1ik} + l_2\Delta_{e1ik}^2, \right. \\ &\quad \left. \Delta_s + \left(\sigma_{1i}\Delta_{e1i}^{p_1} + \sigma_{2i}\Delta_{e1i}^{p_2}\right)^{k_1}\right\}. \end{aligned} \tag{72}$$

Thus, $\mathbf{e}_{1i}$ and $\mathbf{e}_{2i}$, $i = 1, 2, 3$, will converge to the regions Δ_{e1i} and Δ_{e2i} in a fixed time, respectively.

Remark 4. Based on the multispacecraft FTTSM results, the property of graph theory and adaptive technique, a fixed-time 6-DOF coordinated control strategy is designed under directed communication topology. Subsequently, the system tracking error states can be guaranteed to converge their desired trajectories in a fixed time even with external disturbances and quantized control input. Note that this small region is determined by the controller parameters $\alpha_i > 0$, $\beta_i > 0$, and $\kappa_i > 0$. Thus, this small region is adjustable and can be reduced as needed.

Remark 5. By employing the adaptive method, the precise information of the external disturbance and parameters uncertain is not needed for the controller (28) design. Moreover, it is no required to make an additional assumption about interspacecraft communication topology in the designed fixed-time coordinated controller. Hence, the designed controller is suitable for any communication topology. Even if there is no communication link between the formation spacecraft, this proposed controller can still guarantee the practical fixed-time stability of each formation spacecraft.

5. Illustrative Example

To validate the proposed coordinated controller, we give an illustrative example in this section. The communicate topology of three follower spacecraft is described in Figure 2, in which "Sat $i\,(i = 1, 2, 3)$" denotes the ith formation spacecraft. The leader spacecraft is specified to a circular orbit with a radius of 6878 km and orbit angel velocity is $n_0 = 1.11 \times 10^{-3}$ rad/s.

The weighted Laplace matrix $\mathbf{L}$ is designed as

$$\mathbf{L} = \begin{bmatrix} 1 & 0 & -1 \\ -1 & 1 & 0 \\ 0 & -1 & 1 \end{bmatrix}. \tag{73}$$

The inertia matrix and mass are

$$\begin{aligned} \mathbf{J}_1 &= \begin{bmatrix} 10 & 1 & 0.4 \\ 1 & 8 & 0.2 \\ 0.4 & 0.2 & 7 \end{bmatrix}\mathrm{kg.m}^2, \mathbf{J}_2 = \begin{bmatrix} 11 & 0.5 & 0.4 \\ 0.5 & 9 & 0.2 \\ 0.4 & 0.2 & 7 \end{bmatrix}\mathrm{kg.m}^2, \\ \mathbf{J}_3 &= \begin{bmatrix} 9 & 0.5 & 0.7 \\ 0.5 & 3.5 & 0.3 \\ 0.7 & 0.2 & 8 \end{bmatrix}\mathrm{kg.m}^2, \; m_{fi} = 50\,\mathrm{kg}, \quad \forall i = 1, 2, 3. \end{aligned} \tag{74}$$

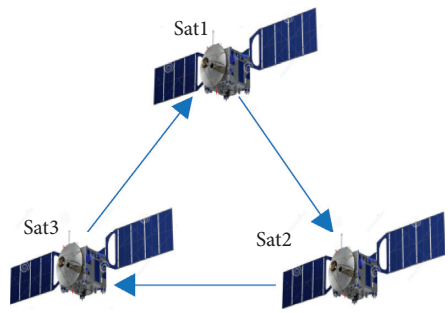

Figure 2: The directed communication topology of three follower spacecraft.

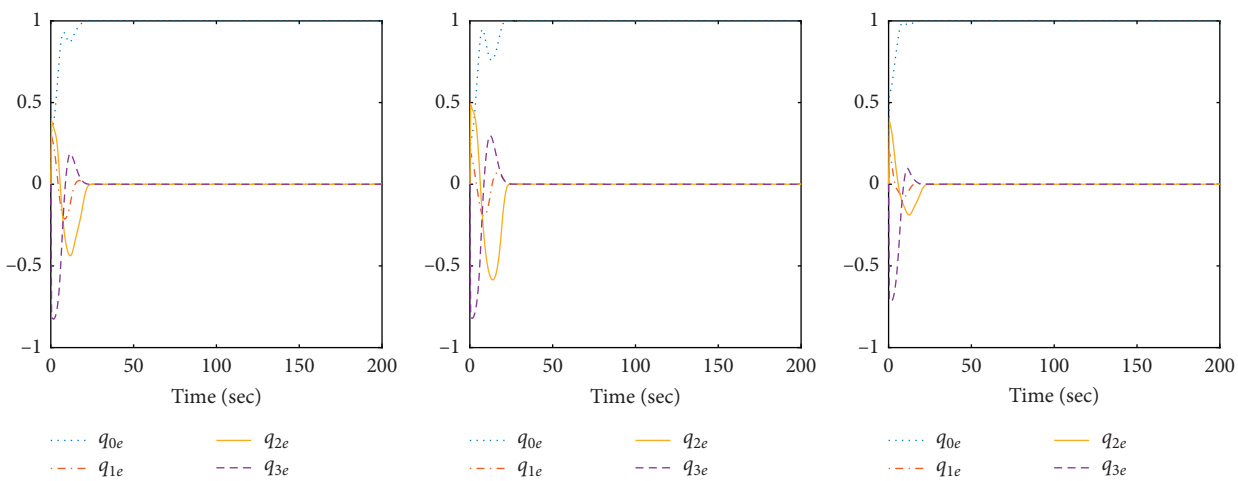

Figure 3: The curves of the relative attitude error. (a) Sat1. (b) Sat2. (c) Sat3.

The desired attitude quaternion and attitude angular velocity are

$$\mathbf{q}_{di} = [\,1\ \ 0\ \ 0\ \ 0\,]^T,\ \boldsymbol{\omega}_{di} = [\,0\ \ 0\ \ 0\,]^T \text{rad/s}, \quad \forall i = 1, 2, 3. \tag{75}$$

The initial attitude quaternion and attitude angular velocity are

$$\begin{aligned}
\mathbf{q}_1(0) &= [\,0.3317\ \ 0.3\ \ 0.4\ \ -0.8\,]^T, \boldsymbol{\omega}_1(0) = [\,0.07\ \ -0.05\ \ -0.04\,]^T \text{rad/s},\\
\mathbf{q}_2(0) &= [\,0.2646\ \ 0.2\ \ 0.5\ \ -0.8\,]^T, \boldsymbol{\omega}_2(0) = [\,0.07\ \ -0.05\ \ -0.04\,]^T \text{rad/s},\\
\mathbf{q}_3(0) &= [\,0.5568\ \ 0.2\ \ 0.4\ \ -0.7\,]^T, \boldsymbol{\omega}_3(0) = [\,0.06\ \ -0.05\ \ -0.05\,]^T \text{rad/s}.
\end{aligned} \tag{76}$$

The relative position and velocity are initialized:

$$\boldsymbol{\rho}_i(0) = [\,-10\ \ 160\ \ 50\,]^T \text{m},\ v_i(0) = [\,0\ \ 0\ \ 0\,]^T \text{m/s}, \quad \forall i = 1, 2, 3. \tag{77}$$

In order to form a triangle of three follower spacecraft, the desired relative position and velocity are specified as

$$\begin{aligned}
&\boldsymbol{\rho}_{1d} = [\,0\ \ 100\ \ 0\,]^T \text{m}, \boldsymbol{\rho}_{2d} = [\,0\ \ 200\ \ 0\,]^T \text{m},\\
&\boldsymbol{\rho}_{3d} = [\,0\ \ 150\ \ 50\sqrt{3}\,]^T \text{m}, \mathbf{v}_{di}(0) = [\,0\ \ 0\ \ 0\,]^T \text{m/s}, \quad \forall i = 1, 2, 3.
\end{aligned} \tag{78}$$

The external disturbance of torque and force are specified as

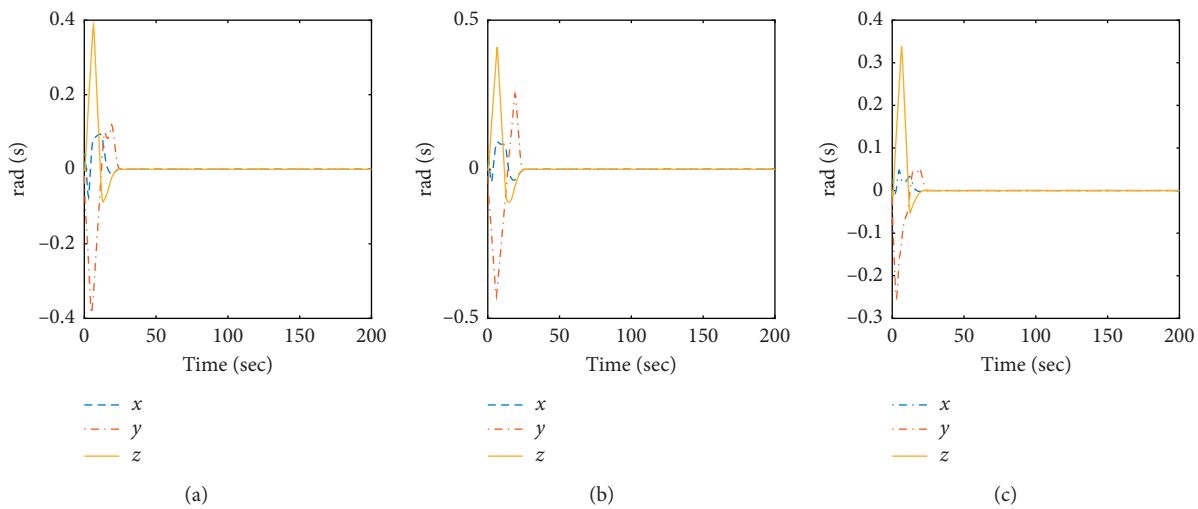

Figure 4: The curves of the relative angular velocity error. (a) Sat1. (b) Sat2. (c) Sat3.

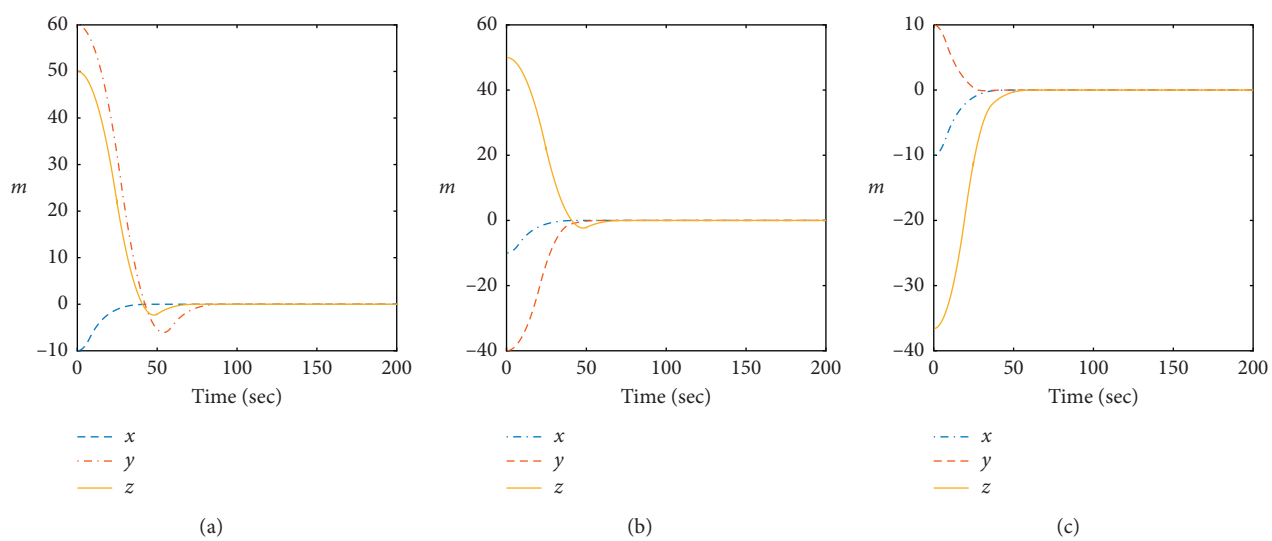

Figure 5: The curves of the relative position error. (a) Sat1. (b) Sat2. (c) Sat3.

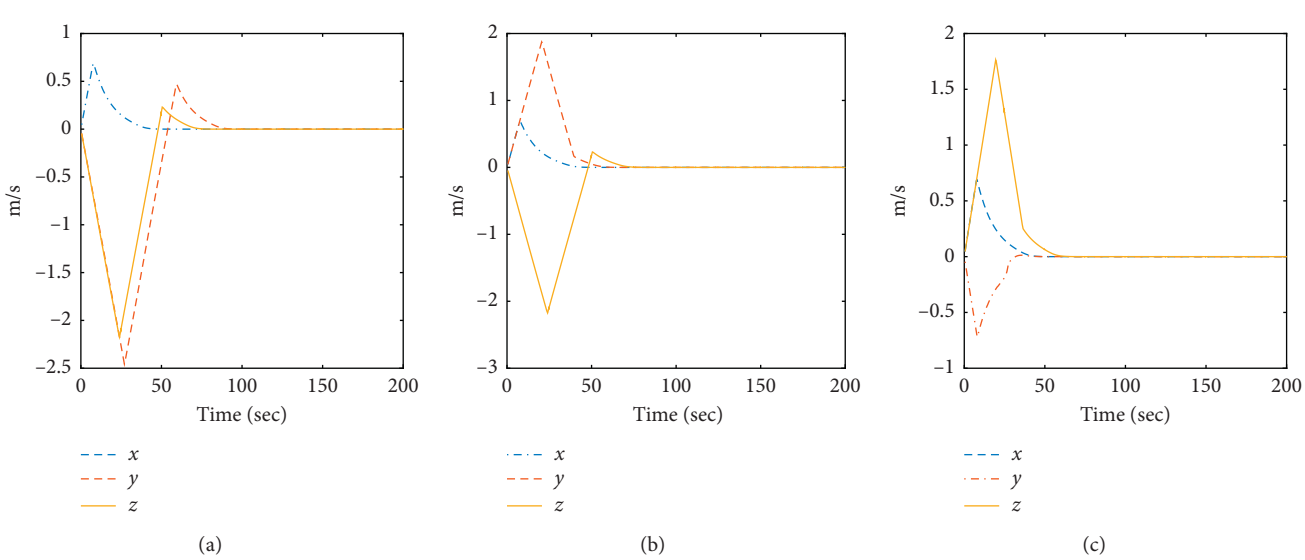

Figure 6: The curves of the relative velocity error. (a) Sat1. (b) Sat2. (c) Sat3.

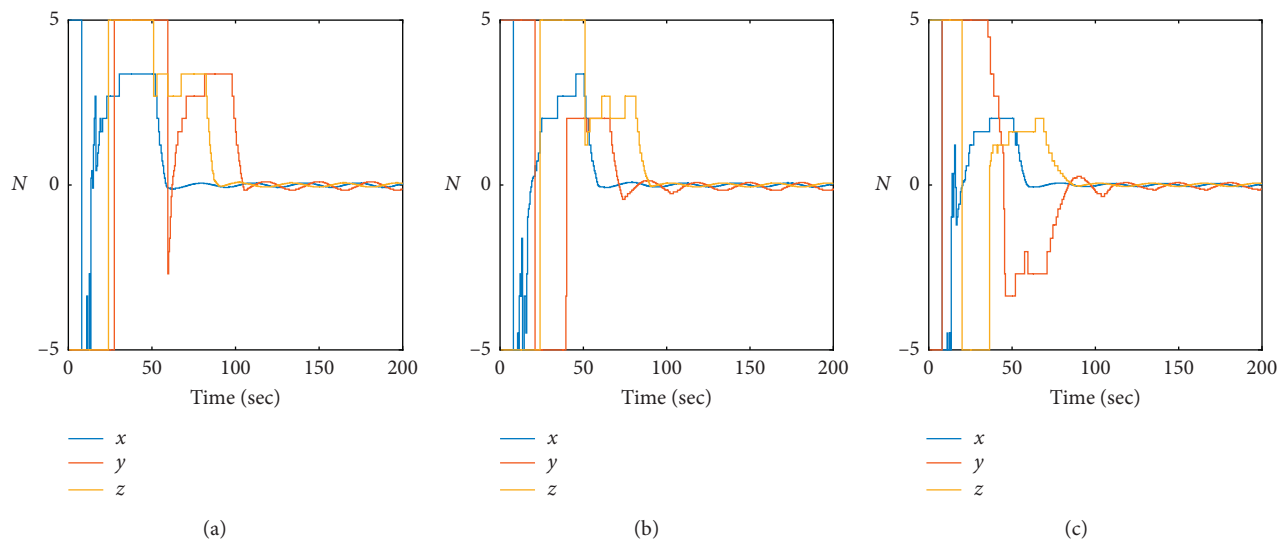

Figure 7: The curves of the quantized control force. (a) Sat1. (b) Sat2. (c) Sat3.

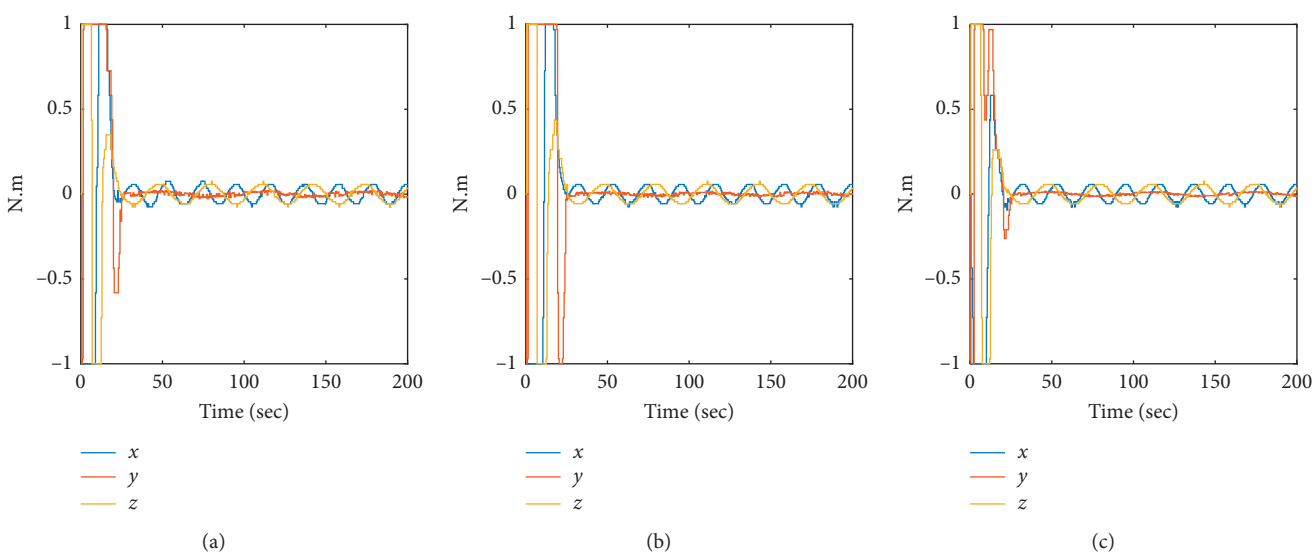

Figure 8: The curves of the quantized control torque. (a) Sat1. (b) Sat2. (c) Sat3.

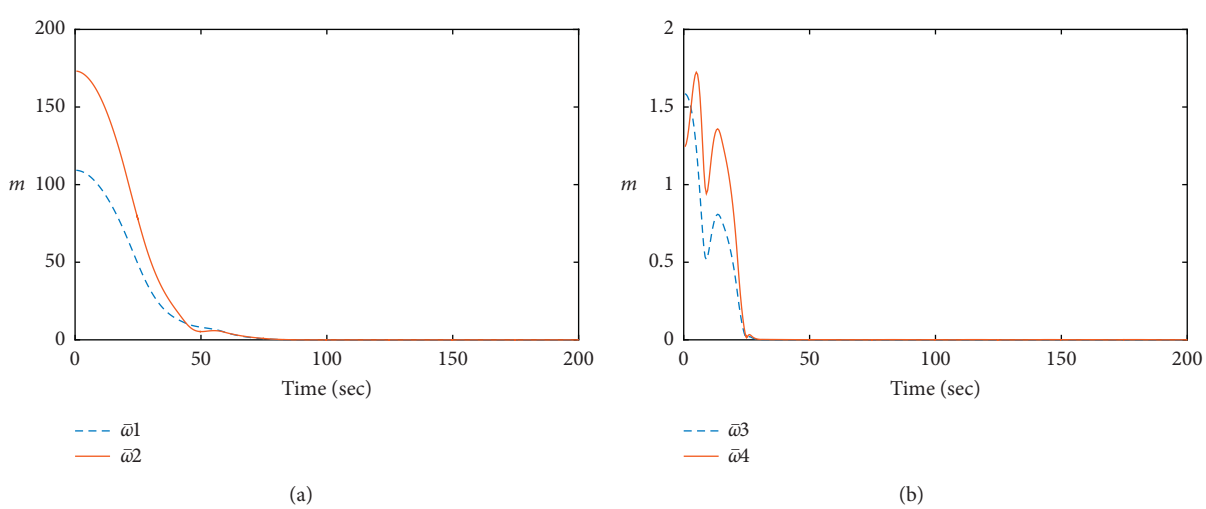

Figure 9: The curves of the performance indexes ϖ1 to ϖ4.

$$\begin{aligned}\mathbf{z}_i &= \left[\,0.06\cos(0.3t)\quad 0.01\sin(0.1t)\quad 0.06\cos(0.2t)\,\right]^T \mathrm{Nm},\\ \mathbf{F}_{it} &= \left[\,0.001\cos(0.02t) 0.002\sin(0.02t) -0.001\sin(0.02t)\,\right]^T \mathrm{N},\quad \forall i = 1,2,3.\end{aligned} \tag{79}$$

The maximum of input control force and torques are limited to 5 N and 1 Nm, respectively.

The following performance indexes are defined to describe the synchronization accuracy and tracking accuracy of the proposed control law (28):

$$\begin{aligned}&\varpi 1 = \sqrt{\sum_{i=1}^{3}\left\|\tilde{\rho}_i\right\|^2},\ \varpi 2 = \sqrt{\sum_{i=1}^{3}\sum_{j\in N_i}\left\|\tilde{\rho}_{i,j}\right\|^2},\\ &\varpi 3 = \sqrt{\sum_{i=1}^{3}\mathbf{q}_{vei}^T\mathbf{q}_{vei}},\ \varpi 4 = \sqrt{\sum_{i=1}^{3}\sum_{j\in N_i}\mathbf{q}_{i,jve}^T\mathbf{q}_{i,jve}}\ ,\end{aligned} \tag{80}$$

where $\tilde{\rho}_i = \rho_i - \rho_{di}$, $\tilde{\rho}_j = \rho_j - \rho_{jd}$, $\tilde{\rho}_{i,j} = \tilde{\rho}_i - \tilde{\rho}_j$, and $\mathbf{q}_{i,jve}$ is the vector part of $\mathbf{q}_{i,je} = \left[\,q_{i,j0e}\quad \mathbf{q}_{i,jve}^T\,\right]^T = \mathbf{q}_{ei}\otimes\mathbf{q}_{ej}$. From the definition of $\varpi 1$, $\varpi 2$, $\varpi 3$, and $\varpi 4$, it can be shown that smaller $\varpi 1$ and $\varpi 3$ can guarantee the better formation and attitude tracking performance, respectively; smaller $\varpi 2$ and $\varpi 4$ can ensure the better formation and attitude synchronization performance, respectively.

The control scheme (28), adaptive updating law (29), and hysteretic quantizer (12) parameters are chosen as $\gamma 1 = 0.9$, $\gamma 2 = 1.1$, $a_{12} = 0.5$, $a_{23} = 0.5$, $a_{31} = 0.5$, $\alpha_i = 0.1$, $\beta_i = 1$, $p_1 = 0.4$, $p_2 = 1.5$, $k_1 = 2$, $c_i = 0.1$, $b_i = 0.04$, $\kappa_i = 0.000002$, $\mathfrak{I}_i = 0.5$, $\varrho_i = 0.000002$, $\forall i = 1,2,3$, $\delta = 0.25$, and $u_{\min} = 0.00001$.

The simulation results of the controller (28) are shown in Figures 3 to 9, where Figure 3 depicts the relative attitude error and Figure 4 plots the relative angular velocity error. It can be observed that the relative attitude errors converge to near zero within 50 s, which has a fast convergence rate. The relative position error and relative velocity error are shown in Figures 5 and 6, respectively. It can be seen that the relative position errors converge to near zero about 85 s, which has a fast convergence rate. The quantized control force and torque are shown in Figures 7 and 8, respectively. The curves of the performance indexes $\varpi 1$ to $\varpi 4$ are depicted in Figure 9. As seen from the simulation results, the proposed fixed-time control strategy provides a good performance of tracking and synchronization.

6. Conclusion

In this paper, the fixed-time 6-DOF coordinated control problem has been studied for multiple spacecraft formation with input quantization under directed communication graph. A fixed-time adaptive coordinated control strategy is designed by using multispacecraft FTTSM vector such that, in the presence of the upper bounds of unknown external disturbances, the controlled system is practical fixed-time stable and, at the same time, the tracking errors converge to their desired trajectories in a fixed time. Compared with the existing finite-time stabilization controllers, the designed adaptive fixed-time coordinated controller in this paper is more suitable for practical engineering application due to its convergent time regardless of initial system states. An illustrative example is given to illustrate the performance of the presented fixed-time coordinated controller. It was shown that the presented controller not only can ensure each spacecraft's convergence to its desired states but also can provide the desired synchronization and tacking performance. Future study will focus on the extension of the presented controller under time-varying communication topology and communication time delay.

Data Availability

The data used to support the findings of this study are included within the article.

Conflicts of Interest

The authors declare that they have no conflicts of interest.

Acknowledgments

The authors of this paper acknowledge the financial support of the National Natural Science Foundation of China (nos. 11902255, U1837601, and U1233202).

References

[1] X. Cao, P. Shi, Z. Li, and M. Liu, "Neural-network-based adaptive backstepping control with application to spacecraft attitude regulation," *IEEE Transactions on Neural Networks and Learning Systems*, vol. 29, no. 9, pp. 4303–4313, 2018.

[2] D. Lee, A. K. Sanyal, and E. A. Butcher, "Asymptotic tracking control for spacecraft formation flying with decentralized collision avoidance," *Journal of Guidance, Control, and Dynamics*, vol. 38, no. 4, pp. 587–600, 2015.

[3] Q. Liu, M. Liu, and J. Yu, "Adaptive fault-tolerant control for attitude tracking of flexible spacecraft with limited data transmission," *IEEE Transactions on Systems, Man, and Cybernetics: Systems*, p. 1, 2019.

[4] D. Ye, M. Shi, and Z. Sun, "Satellite proximate interception vector guidance based on differential games," *Chinese Journal of Aeronautics*, vol. 31, no. 6, pp. 1352–1361, 2018.

[5] D. Ye, M. Shi, and Z. Sun, "Satellite proximate pursuit-evasion game with different thrust configurations," *Aerospace Science and Technology*, vol. 99, Article ID 105715, 2020.

[6] G. Dong, L. Cao, D. Yao, H. Li, and R. Lu, "Adaptive attitude control for multi-MUAVs with output dead-zone and actuator fault," *IEEE/CAA Journal of Automatica Sinica*, 2020.

[7] C. Yue, K. D. Kumar, Q. Shen, C. H. Goh, and T. H. Lee, "Attitude stabilization using two parallel single-gimbal control moment gyroscopes," *Journal of Guidance, Control, and Dynamics*, vol. 42, no. 2, pp. 1353–1364, 2019.

[8] Y. Lv, Q. Hu, G. Ma, and J. Zhou, "6 DOF synchronized control for spacecraft formation flying with input constraint and parameter uncertainties," *ISA Transactions*, vol. 50, no. 4, pp. 573–580, 2011.

[9] L. Sun and W. Huo, "6-DOF integrated adaptive backstepping control for spacecraft proximity operations," *IEEE Transactions on Aerospace and Electronic Systems*, vol. 51, no. 3, pp. 2433–2443, 2015.

[10] C. Liu, K. Shi, X. Yue, and Z. Sun, "Inertia-free saturated output feedback attitude stabilization for uncertain spacecraft," *International Journal of Robust and Nonlinear Control*, vol. 30, no. 13, pp. 5101–5121, 2020.

[11] C. Liu, X. Yue, K. Shi, and Z. Sun, "Inertia-free attitude stabilization for flexible spacecraft with active vibration suppression," *International Journal of Robust and Nonlinear Control*, vol. 29, no. 18, pp. 6311–6336, 2019.

[12] J. Na, Y. Huang, X. Wu, G. Gao, G. Herrmann, and J. Z. Jiang, "Active adaptive estimation and control for vehicle suspensions with prescribed performance," *IEEE Transactions on Control Systems Technology*, vol. 26, no. 6, pp. 2063–2077, 2018.

[13] Z. Zhu, Y. Pan, Q. Zhou, and C. Lu, "Event-triggered adaptive fuzzy control for stochastic nonlinear systems with unmeasured states and unknown backlash-like hysteresis," *IEEE Transactions on Fuzzy Systems*, p. 1, 2020.

[14] T. Chen, J. Shan, and H. Wen, "Distributed passivity-based control for multiple flexible spacecraft with attitude-only measurements," *Aerospace Science and Technology*, vol. 94, Article ID 105408, 2019.

[15] P. Li, X. Yu, and Y. Zhang, "The design of quasi-optimal higher order sliding mode control via disturbance observer and switching-gain adaptation," *IEEE Transactions on Systems, Man, and Cybernetics: Systems*, vol. 50, no. 11, pp. 4817–4827, 2020.

[16] Q. Li and Z. Deng, "Coordinated orbit-attitude-vibration control of a sun-facing solar power satellite," *Journal of Guidance, Control, and Dynamics*, vol. 42, no. 8, pp. 1863–1869, 2019.

[17] Z. Ning, Y. Xia, K. Lu, and Y. Li, "Decentralised finite-time attitude synchronisation and tracking control for rigid spacecraft," *International Journal of Systems Science*, vol. 46, no. 14, pp. 2493–2509, 2015.

[18] Q. Zhou, S. Zhao, H. Li, R. Lu, and C. Wu, "Adaptive neural network tracking control for robotic manipulators with dead zone," *IEEE Transactions on Neural Networks and Learning Systems*, vol. 30, no. 12, pp. 3611–3620, 2019.

[19] P. Du, Y. Pan, H. Li, and H.-K. Lam, "Nonsingular finite-time event-triggered fuzzy control for large-scale nonlinear systems," *IEEE Transactions on Fuzzy Systems*, p. 1, 2020.

[20] G. Lin, H. Li, H. Ma, D. Yao, and R. Lu, "Human-in-the-loop consensus control for nonlinear multi-agent systems with actuator faults," *IEEE/CAA Journal of Automatica Sinica*, 2020.

[21] M. Liu, L. Zhang, and W. X. Zheng, "Fault reconstruction for stochastic hybrid systems with adaptive discontinuous observer and non-homogeneous differentiator," *Automatica*, vol. 85, pp. 339–348, 2017.

[22] J. Na, Y. Huang, X. Wu, S.-F. Su, and G. Li, "Adaptive finite-time fuzzy control of nonlinear active suspension systems with input delay," *IEEE Transactions on Cybernetics*, vol. 50, no. 6, pp. 2639–2650, 2020.

[23] B. Huang, A.-J. Li, Y. Guo, and C.-Q. Wang, "Rotation matrix based finite-time attitude synchronization control for spacecraft with external disturbances," *ISA Transactions*, vol. 85, pp. 141–150, 2019.

[24] J. Na, S. Wang, Y. Liu, Y. Huang, and X. Ren, "Finite-time convergence adaptive neural network control for nonlinear servo systems," *IEEE Transactions on Cybernetics*, vol. 50, no. 6, pp. 2568–2579, 2019.

[25] H. Zhang, D. Yue, X. Yin, S. Hu, and C. X. Dou, "Finite-time distributed event-triggered consensus control for multi-agent systems," *Information Sciences*, vol. 339, pp. 132–142, 2016.

[26] Y. Xia, J. Zhang, K. Lu, and N. Zhou, *Finite Time and Cooperative Control of Flight Vehicles*, Springer, Singapore, 2019.

[27] A. Polyakov, "Nonlinear feedback design for fixed-time stabilization of linear control systems," *IEEE Transactions on Automatic Control*, vol. 57, no. 8, pp. 2106–2110, 2012.

[28] Y. Wu and Z. Wang, "Fuzzy adaptive practical fixed-time consensus for second-order nonlinear multiagent systems under actuator faults," *IEEE Transactions on Cybernetics*, p. 1, 2020.

[29] X. Yu, P. Li, and Y. Zhang, "Fixed-time actuator fault accommodation applied to hypersonic gliding vehicles," *IEEE Transactions on Automation Science and Engineering*, p. 1, 2020.

[30] A. Polyakov, "Distributed fixed-time attitude coordination control for multiple rigid spacecraft," *International Journal of Robust and Nonlinear Control*, vol. 2019, pp. 1–16, 2019.

[31] Z. Zuo, "Nonsingular fixed-time consensus tracking for second-order multi-agent networks," *Automatica*, vol. 54, pp. 305–309, 2015.

[32] H. Liang, X. Guo, Y. Pan, and T. Huang, "Event-Triggered fuzzy bipartite tracking control for network systems based on distributed reduced-order observers (revised manuscript of TFS-2019-1049)," *IEEE Transactions on Fuzzy Systems*, p. 1, 2020.

[33] M. Liu, L. Zhang, P. Shi, and Y. Zhao, "Fault estimation sliding-mode observer with digital communication constraints," *IEEE Transactions on Automatic Control*, vol. 63, no. 10, pp. 3434–3441, 2018.

[34] Z. Zuo, X. Cao, and Y. Wang, "Security control of multi-agent systems under false data injection attacks," *Neurocomputing*, vol. 404, pp. 240–246, 2020.

[35] Z. Zuo, P. Xie, and Y. Wang, "Output-based dynamic event-triggering control for sensor saturated systems with external disturbance," *Applied Mathematics and Computation*, vol. 374, Article ID 125043, 2020.

[36] A. Liu, W.-A. Zhang, L. Yu, H. Yan, and R. Zhang, "Formation control of multiple mobile robots incorporating an extended state observer and distributed model predictive approach," *IEEE Transactions on Systems, Man, and Cybernetics: Systems*, vol. 50, no. 11, pp. 4587–4597, 2020.

[37] C. Liu, G. Vukovich, Z. Sun, and K. Shi, "Observer-based fault-tolerant attitude control for spacecraft with input delay," *Journal of Guidance, Control, and Dynamics*, vol. 41, no. 9, pp. 2041–2053, 2018.

[38] M. Liu, L. Zhang, P. Shi, and Y. Zhao, "Sliding mode control of continuous-time Markovian jump systems with digital data transmission," *Automatica*, vol. 80, pp. 200–209, 2017.

[39] D. Wang, X. Mei, R. Weng, Z. Qu, and L. Zhang, "Hybrid filter design of fault detection for networked linear systems with variable packet dropout rate," *IET Control Theory and Applications*, vol. 13, no. 9, pp. 1239–1245, 2019.

[40] H. Li, P. Shi, D. Yao, and L. Wu, "Observer-based adaptive sliding mode control for nonlinear Markovian jump systems," *Automatica*, vol. 64, pp. 133–142, 2016.

[41] A. Liu, W.-A. Zhang, M. Z. Q. Chen, and L. Yu, "Moving horizon estimation for mobile robots with multirate sampling," *IEEE Transactions on Industrial Electronics*, vol. 64, no. 2, pp. 1457–1467, 2017.

[42] R. Liu, X. Cao, M. Liu, and Y. Zhu, "6-DOF fixed-time adaptive tracking control for spacecraft formation flying with input quantization," *Information Sciences*, vol. 475, pp. 82–99, 2019.

[43] H. Ma, H. Li, R. Lu, and T. Huang, "Adaptive event-triggered control for a class of nonlinear systems with periodic disturbances," *Science China Information Sciences*, vol. 63, no. 5, Article ID 150212, 2020.

[44] R. Merris, "Laplacian matrices of graphs: a survey," *Linear Algebra and Its Applications*, vol. 197, no. 198, pp. 143–176, 1994.

[45] F. Wang, Z. Liu, Y. Zhang, and C. L. P. Chen, "Adaptive quantized controller design via backstepping and stochastic small-gain approach," *IEEE Transactions on Fuzzy Systems*, vol. 24, no. 2, pp. 330–343, 2016.

[46] B. Wu, D. Wang, and E. K. Poh, "Decentralized robust adaptive control for attitude synchronization under directed communication topology," *Journal of Guidance, Control, and Dynamics*, vol. 34, no. 4, pp. 1276–1282, 2011.

[47] L. Zhao, J. Yu, C. Lin, and H. Yu, "Distributed adaptive fixed-time consensus tracking for second-order multi-agent systems using modified terminal sliding mode," *Applied Mathematics and Computation*, vol. 312, pp. 23–35, 2017.

[48] C. Qian and W. Lin, "A continuous feedback approach to global strong stabilization of nonlinear systems," *IEEE Transactions on Automatic Control*, vol. 46, no. 7, pp. 1061–1079, 2001.

[49] L. Yang and J. Yang, "Nonsingular fast terminal sliding-mode control for nonlinear dynamical systems," *International Journal of Robust and Nonlinear Control*, vol. 21, no. 16, pp. 1865–1879, 2011.

Hindawi
Complexity
Volume 2020, Article ID 8823674, 10 pages
https://doi.org/10.1155/2020/8823674

Research Article

Fuzzy Sliding Mode Control of a VAV Air-Conditioning Terminal Temperature System

Fuzhou Niu,[1] Ziyang Li,[2,3] Lijian Yang,[2,3] Zhengtian Wu,[2,3] Qixin Zhu,[1] and Baoping Jiang[2,3]

[1]*School of Mechanical Engineering, Suzhou University of Science and Technology, Suzhou, China*
[2]*School of Electronic and Information Engineering, Suzhou University of Science and Technology, Suzhou, China*
[3]*Suzhou Institute of Smart City, Suzhou University of Science and Technology, Suzhou, China*

Correspondence should be addressed to Zhengtian Wu; wzht8@mail.usts.edu.cn and Qixin Zhu; bob21cn@163.com

Received 1 September 2020; Revised 24 October 2020; Accepted 12 December 2020; Published 22 December 2020

Academic Editor: Xue-bo Jin

A varied air volume (VAV) air-conditioning system comprises diverse input and/or output disturbances, which are commonly nonlinear, with large lag and uncertainty. Based on the traditional control methods, testing the controlling parameters of a VAV air-conditioning system is challenging. Sliding mode control could improve the robustness of the system due to the adaptive capacity of disturbance rejection. Moreover, the fuzzy algorithm could be employed to determine the stability of a sliding control system by adjusting the parameters in the approach rate, reducing the switching frequency, and weakening chatter. Fuzzy sliding mode control is investigated in this paper to improve the performance of a VAV air-conditioning system. Simulation results verify that the sliding mode control is suitable for a VAV air-conditioning system to achieve good adaptability and robustness considering the influence of multiple external variable disturbances. In addition, the chattering of the system is improved after the introduction of fuzzy control.

1. Introduction

A variable air volume air-conditioning system belongs to an all-air air-conditioning system, which can automatically adjust the air supply volume of air conditioning according to the change in air-conditioning load and indoor air parameters. However, appropriate control strategies should be developed to solve the problems caused by the complexity of the control system because of the intricate VAV air-conditioning system terminal equipment and the high requirements for the overall control of the system.

Many scholars have proposed VAV air-conditioning control methods. For example, hysteresis relay feedback control was introduced into the model parameter identification of indoor temperature hysteresis characteristics, thereby providing a new method for the identification of the characteristics of indoor temperature hysteresis in [1]. For indoor fresh air demand, the total fresh air flow is dynamically corrected on the basis of the detected occupancy rate of each area and relevant measurement values using fresh air from the overventilated area [2]. A fault-tolerant control method was proposed in [3] to control the outdoor air circulation and AHU supply air temperature, which are, respectively, related to indoor air quality and humidity, to meet the ASHRAE standard in a VAV system. A neural fuzzy structure of a parameter self-tuning decoupled fuzzy neural PID controller was proposed in [4]. An adaptive neural network-based supply air temperature controller was introduced in [5] for the air handling unit in heating, ventilation, and air-conditioning systems.

The classical PID control equation with a decoupled coefficient was used as the Sugeno function to introduce the following part of the fuzzy rule, which improves the anti-interference capability of the system. However, some problems occur when only fuzzy control in air-conditioning systems is used. The two steps do not have a systematic design method and mainly rely on expert experience and repeated experiments of designers because of the two

important steps of fuzzy control design: the quantization range of parameters and the design of fuzzy rules. In addition, the design of fuzzy control is not systematic. Therefore, fuzzy control should be combined with some other control strategies in most cases to achieve the desired control effect. Since its emergence in the 1950s, sliding mode control (SMC) has been proven to be an effective control strategy for many nonlinear complex physical systems. SMC has witnessed considerable efforts undertaken in the field of theoretical analysis and SMC application. The following examples are provided. The issue of SMC for stochastic semi-Markovian jump systems was studied in [6, 7] with application to space robot manipulators. A sliding mode controller of active magnetic bearing was proposed in [8] to achieve rotor 3*D* trajectory control. A constraint design with a sliding mode strategy was proposed in [9] to improve the stability of aircraft engine control. A terminal sliding mode controller was designed in [10] to track the planned speed signal, which can timely suppress the adverse dynamic behavior of an electric vehicle after a tire blows out on a highway. A high-speed nonsingular terminal switch SMCl strategy for robots was proposed in [11]. This strategy enhanced the performance of the control system by switching between the sliding mode controllers according to different control requirements in different regions of the state space. A nonsingular terminal SMC algorithm was introduced in [12] to track the body position of a hexapod walking robot stably and accurately. This algorithm provided a reliable method to improve the walking and operating capability of a multilegged walking robot in a special environment. For the real-time tracking and stability of the control system, [13, 14] provide a good solution. Considering SMC combined with the fuzzy method, the research results were also rich. For instance, a fuzzy SMC strategy was proposed in [15] to solve the problem of independent control of temperature and humidity in air conditioners. In [16, 17], the prediction and dynamic analysis of the data model of the environment detected by the sensor is helpful to the accuracy of air-conditioning control. In view of the influence of data noise obtained by air-conditioning sensors on intelligent control, the filter designed in [18, 19] can be used to improve the control accuracy of the indoor environment. A novel integral fuzzy SMC for T-S fuzzy systems was also proposed in [20, 21] to address the issues of stabilization and dissipation (additional details are provided in [22–24] and references therein).

This study addresses the issue of SMC design for a VAV air-conditioning system. A VAV air-conditioning system with multiinput and multioutput, nonlinearity, large lag, uncertainty, and other characteristics is suitable because of the strong robustness of the SMC to the external disturbance and modeling dynamics of the system and the advantages of order reduction, decoupling, fast response, and easy implementation. However, some problems emerge in the design of SMC, and the most prominent one is chattering. Therefore, this study selects the improved power index approach rate and the parameters of the sliding mode approach rate through fuzzy control to minimize chattering.

2. VAV Air-Conditioning System Overview and Mathematical Model

2.1. VAV Air-Conditioning System Structure. The schematic of a VAV air-conditioning system is illustrated in Figure 1. A VAV air-conditioning system mainly comprises five components: air handling unit, air supply pipeline module, indoor air supply terminal, electric control unit, and a common all-air module.

Figure 1 shows the primary VAV return air system. After the indoor return air and outdoor fresh air are mixed, the mixed air is cooled and dehumidified and sent to each room. The air supply volume of the air conditioner is controlled by the air supply sensor and the blower at the end of the air conditioner to achieve the desired indoor temperature.

2.2. Air Supply Volume Controlling of a VAV Air Conditioner. As shown in Figure 2, the total air supply is adjusted by the fan speed and the guide vane valve, which is generally referred to as the fan control. An appropriate coordinated control algorithm should be designed and adopted to balance the fan speed and the room temperature by controlling the total air supply volume. Three common parameters are used to control the fan speed, namely, constant static pressure, variable static pressure, and total air volume control. In a prior study [25], a static pressure reset algorithm was proposed to minimize the static pressure in the air supply duct while maintaining regional comfort. This method is proven to be economical in practice and can reduce fan power consumption in VAV.

As shown in Figure 3, in a VAV air-conditioning system, the set value of the air supply temperature could directly influence the control of indoor temperature. The energy of an air-conditioning system is inefficiently used when the air supply temperature is substantially high. Meanwhile, uniform indoor air supply and minimum fresh air volume are required when the air supply temperature is substantially low. The methods of the set value determination of air supply temperature mainly include trial, error, and voting methods.

2.3. Room Temperature Control of a VAV Air-Conditioning System. Room temperature controls physical processes in a VAV terminal device, which changes the air supply volume by adjusting the deviation of indoor and desired room temperatures. The terminal of a VAV air-conditioning system can be divided into pressure-dependent and pressure-independent terminals according to different control modes. The pressure-independent terminal is adopted in this study because of the poor stability of the pressure-dependent type and serious system coupling. The control strategy is shown in Figure 4. A sliding mode controller is adopted to the room temperature control in this paper.

2.4. Mathematical Model of Air-Conditioning Room Temperature. The investigated area is an air-conditioned room, which is located in an office building. The temperature of the building is considerably higher in summer and/or

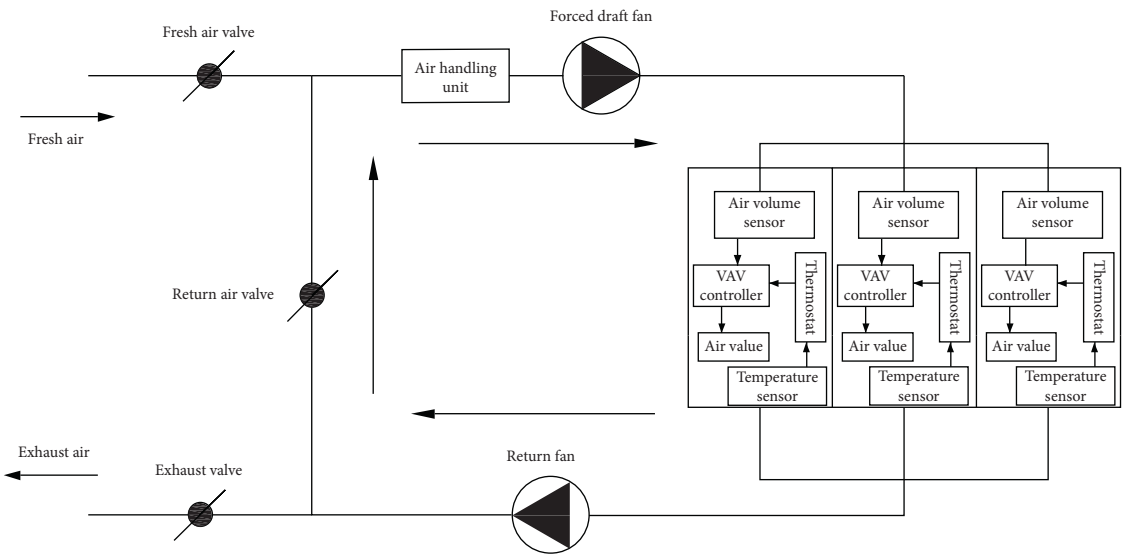

Figure 1: Structure diagram of the VAV air-conditioning system.

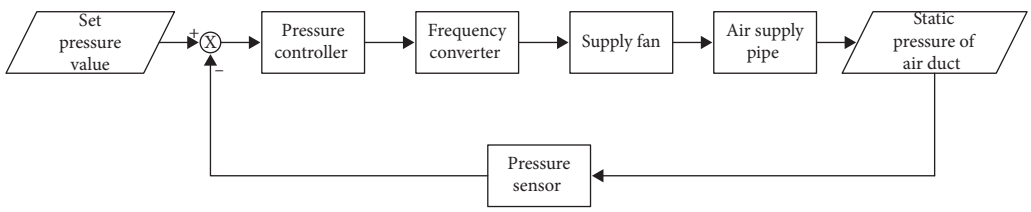

Figure 2: Diagram of the total air volume of a VAV air conditioner control system.

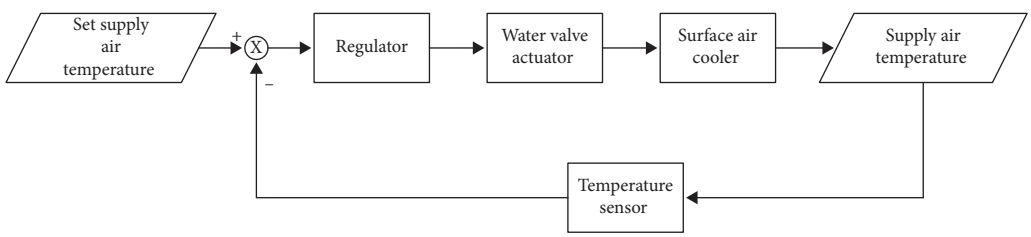

Figure 3: Diagram of the air temperature control of a VAV air-conditioning supply.

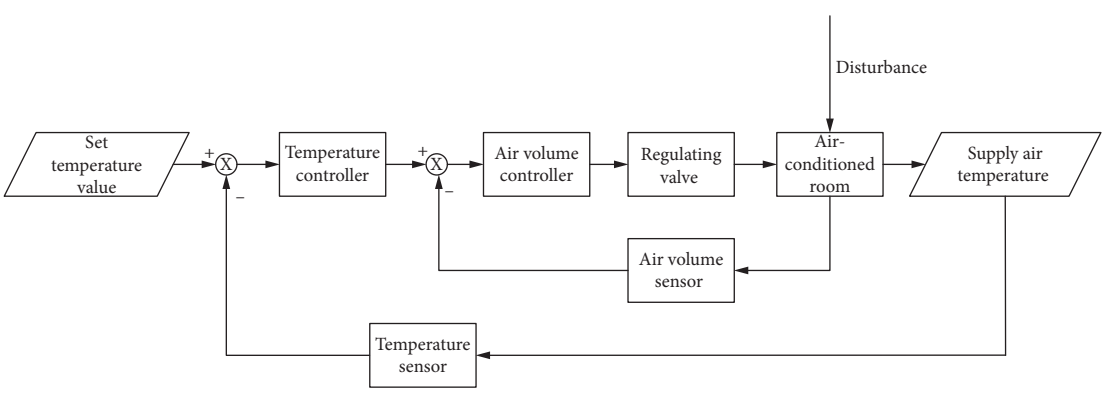

Figure 4: Diagram of the room temperature control of a VAV air-conditioning system.

daytime. The boundary conditions of air-conditioning rooms are affected by many factors, including solar radiation, internal heat dissipation, lighting energy, and radiation of walls and equipment. An accurate mathematical model of such a complex system is unavailable. The following assumptions are assigned to simplify the mathematical model of room temperature.

(1) Temperature is in a uniform distribution status in the air-conditioned room
(2) The air input and output in the air-conditioned room is in a balanced state
(3) The heat storage of enclosures is neglected
(4) Default adjacent rooms have a similar influence on the air-conditioned room
(5) Other parameters, including heat load of indoor equipment and individuals, are defined as indoor heat load interference

Considering these assumptions, the differential equation of the heat balance of the room based on the law of thermodynamics can be obtained as follows:

$$\rho_{\text{air}} V c_{\text{air}} \frac{\mathrm{d}T}{\mathrm{d}t} = Q_r(t) + Q_w(t) + Q_{\text{in}}, \tag{1}$$

where V is the volume of the air-conditioned room, m^3; ρ_{air} is the air density, kg/m^3; c_{air} is the specific heat capacity of air, kJ/(kg·°C); T is the temperature of the air-conditioned room, °C; $Q_r(t)$ is the heat provided by the air conditioner; $Q_w(t)$ is the indoor sensible heat; and Q_{in} is the indoor thermal load interference.

Because the air input and output of the air-conditioned room are in balance. So, $Q_r(t)$ is, respectively, expressed as follows:

$$Q_r(t) = G_s c_{\text{air}} (T_s - T). \tag{2}$$

The heat storage of enclosures is neglected. So, $Q_w(t)$ is, respectively, expressed as follows:

$$Q_w(t) = k_1 F_1 (T_i - T) + k_{\text{out}} F_{\text{out}} (T_{\text{out}} - T), \tag{3}$$

where G_s is the air supply volume, kg/s; T_s is the air supply temperature, °C; k_1 is the heat transfer coefficient of the adjacent room inner wall, $\text{kW/(m}^2\cdot{}^\circ\text{C)}$; F_1 is the heat transfer area of the adjacent room inner wall, m^2; k_{out} is the heat transfer coefficient of the external wall, $\text{kW/(m}^2\cdot{}^\circ\text{C)}$; F_{out} is the heat transfer area of the external wall, m^2; T_{out} is the outdoor ambient temperature, °C; and Q_{in} is the indoor heat load, kW.

3. Design of the Fuzzy Sliding Mode Controller

3.1. Design of the Sliding Mode Controller

3.1.1. Selection and Design of the Sliding Surface and Approach Rate. An integral sliding surface can smoothen the torque, reduce the steady-state error of a system, weaken the chattering, and enhance the stability of a controller. The integral sliding surface can be expressed as follows:

$$s = e + k_s \int_0^t e \mathrm{d}t, \tag{4}$$

where e is the deviation of actual and desired room temperatures; $e = T - T_d$, where T and T_d are the actual and desired temperatures of the air-conditioned room, respectively.

The exponential approach rate $\dot{s} = -\varepsilon \operatorname{sgn}(s) - ks$ is a typical approach rate, which can gradually reduce the approach speed from a large value to zero through the exponential approach term and help the moving point reach the switching surface at a low speed. However, if the constant k is increased, then the convergence rate is accelerated, but the chattering in the sliding mode stage is strengthened; if the constant ε is reduced, then the chattering in the sliding mode stage is weakened, but the convergence rate in the motion stage is slow. The general index approach rate is usually a compromise method to determine the constant but does not efficiently solves this problem [26].

The improved power exponential approach rate is selected to overcome the shortcomings of the exponential approach rate [27]:

$$\dot{s} = -\varepsilon |s|^{\alpha} \operatorname{sgn}(s) - ks^{\beta}, \tag{5}$$

where $\varepsilon > 0$, $0 \le \alpha <$, $k \ge 0$, and β is a positive odd number.

Given that $\lim_{s \longrightarrow 0^+} \dot{s} = \lim_{s \longrightarrow 0^+} -\varepsilon |s|^{a} \operatorname{sgn}(\mathrm{s}) - ks^{\beta} < 0$ and $\lim_{s \longrightarrow 0^-} \dot{s} = \lim_{s \longrightarrow 0^-} -\varepsilon |s|^{a} \operatorname{sgn}(\mathrm{s}) - ks^{\beta} > 0$, the power reaching law guarantees the existence of the sliding mode and the global arrival condition. In particular, when $\alpha = 0$ and $\beta = 1$, the above formula is the exponential approach rate; when $k = 0$, the above formula is the power approach rate.

When the moving point is far from the sliding mode switching surface, that is, when $|s| \ge 1$, $\varepsilon |s|^{\alpha} \ge \varepsilon$, and $ks^{\beta} \ge k$, the improved power index approach rate has a faster approach speed than the general index approach rate. When the moving point is close to the sliding mode surface, that is, when $|s| < 1$, $\varepsilon |s|^{\alpha} \le \varepsilon$, and $ks^{\beta} \le ks$, the approach speed slows down, and the chattering weakens.

3.1.2. Calculation of Control Rate. Through simultaneous formulas (1)–(3) and setting $Q_r(t)$ to u, the differential equation of the temperature of an air-conditioned room can be obtained as follows:

$$\rho_{\text{air}} V c_{\text{air}} \frac{\mathrm{d}T}{\mathrm{d}t} = u + k_1 F_1 (T_i - T) + k_{\text{out}} F_{\text{out}} (T_{\text{out}} - T) + Q_{\text{in}}. \tag{6}$$

The derivation of formula (4) can then be organized as follows:

$$\begin{aligned} \dot{s} = \dot{e} + k_s e = \frac{1}{\rho_{\text{air}} V c_{\text{air}}} \big(& u + k_1 F_1 (T_i - T) \\ & + k_{\text{out}} F_{\text{out}} (T_{\text{out}} - T) + Q_{\text{in}} \big) + k_s e. \end{aligned} \tag{7}$$

The convergence rate of the improved power index shown in simultaneous formula (5) can be further expressed as follows:

$$\frac{1}{\rho_{\text{air}} V c_{\text{air}}} * \left(u + k_1 F_1 \left(T_i - T\right) + k_{\text{out}} F_{\text{out}} \left(T_{\text{out}} - T\right) + Q_{\text{in}}\right) + k_s e = -\varepsilon |s|^{\alpha} \operatorname{sgn}(s) - k s^{\beta}. \tag{8}$$

In order to solve the problem of sensor measurement noise in sliding mode control, the noise of temperature measured by an air-conditioning sensor is generally unknown but bounded, and compared with the measured temperature, the noise is small, so the stability of the system can be guaranteed in the case of ignoring the noise. Therefore, the SMC law based on the improved power exponential approach law can be calculated as follows:

$$u = \rho_{\text{air}} V c_{\text{air}} \left(-\varepsilon |s|^{\alpha} \operatorname{sgn}(s) - k s^{\beta} - k_s e\right) - k_1 F_1 \left(T_i - T\right) - k_{\text{out}} F_{\text{out}} \left(T_{\text{out}} - T\right) - Q_{\text{in}}. \tag{9}$$

A defined Lyapunov function is provided as follows to prove the stability of the system:

$$\begin{aligned} v &= \frac{1}{2} s^2, \\ \dot{V}(s) &= \dot{s} s = (\dot{e} + k_s e) s \\ &= \left(\frac{1}{\rho_{\text{air}} V c_{\text{air}}} \times \left(u + k_1 F_1 \left(T_i - T\right) + k_{\text{out}} F_{\text{out}} \left(T_{\text{out}} - T\right) + Q_{\text{in}}\right) + k_s e\right) s. \end{aligned} \tag{10}$$

$\dot{V}(s) = -\varepsilon s |s|^{\alpha} \operatorname{sgn}(s) - k s^{\beta+1}$ can be obtained by integrating equation (9) into the above equation. The limitation of the approach rate parameters indicates that the value range of each parameter is $\varepsilon > 0$, $0 \le \alpha < 1$, $k \ge 0$, and β is the positive odd. Therefore, $\dot{V}(s) < 0$, and the system is asymptotically stable.

3.2. Design of the Fuzzy Switching Surface

3.2.1. Fuzziness of Approach Rate Parameters. An improved power index approach rate, which can reduce the chattering to a certain extent, is selected in this study. A one-dimensional fuzzy controller is proposed in this paper to improve the air-conditioning system and enhances its robustness in the operation process and ensures that the system can quickly access the sliding mode state while suppressing chattering. The comparison between sliding mode controllers without/with the fuzzy controller is investigated through simulation using the Matlab interface.

The input signal of the fuzzy adaptive sliding mode controller is the temperature error e, and the output signal is the approach law parameters ε and k. The fuzzy subsets of input variables are {negative big, negative middle, negative small, invariant, positive small, positive middle, positive big}, which can be shorted as {NB, NM, NS, Z, PS, PM, PB}, respectively. The fuzzy subsets of output variables are {NB, NS, Z, PS, PB}. The input quantization is in the (−1, 15) region, the output ε quantization is in the (0.003, 0.03) region, and the k quantization is in the (5, 40) region.

The entire fuzzy SMC process is shown in Figure 5.

3.2.2. Membership Function and Fuzzy Rules. The membership function is selected as a triangle membership function. Equal values are assigned to the fuzzy subset. The membership functions of the input and output signals are shown in Figures 6–8.

According to the actual control effect, the fuzzy control rules of the approach rate parameters ε and k are shown in Table 1.

According to the above fuzzy rules, when the deviation signal e is large, the fuzzy control system selects large ε and k to ensure that the system can approach the sliding surface at a fast speed. When e is small, the fuzzy control system selects small ε and k to reduce the approach speed and weaken system chattering [28].

3.2.3. Fuzzy Reasoning. The fuzzy controller in this study is built with the fuzzy module of MATLAB, and the center of gravity method is used to solve the fuzzy problem:

$$\begin{aligned} \varepsilon &= \frac{\int \varepsilon u_{\varepsilon}(\varepsilon) \mathrm{d}\varepsilon}{\int u_{\varepsilon}(\varepsilon) \mathrm{d}\varepsilon}, \\ k &= \frac{\int k u_k(k) \mathrm{d}k}{\int u_k(k) \mathrm{d}k}, \end{aligned} \tag{11}$$

where $u_{\varepsilon}(\varepsilon)$ and $u_k(k)$ are the corresponding membership functions.

4. Simulation Analysis

4.1. Design of a Simulation Model. The air-conditioned room is 5 m long, 4 m wide, and 3 m high. The initial temperature in the room is 30°C, and the air supply temperature is 16°C. The temperature change curve is assumed to between 7 : 00 and 19 : 00 in the building area [29], and the temperature change curves of the next room in the air-conditioned room are as shown in Figure 9.

Considering that the air-conditioned room belongs to the office building [14], the following assumptions for the heat load caused by the change in indoor personnel and the operation of computers and other equipment are presented as shown in Figure 10.

4.2. Influence of Approach Rate Parameters on the Control Effect. When ε and k are, respectively, set to 0.1 and 5, chattering is evident after the system reaches stability despite the fast response speed. When ε and k are, respectively, set to 0.001 and 5, the transition time increases despite the reduction in chattering as shown in Figure 11.

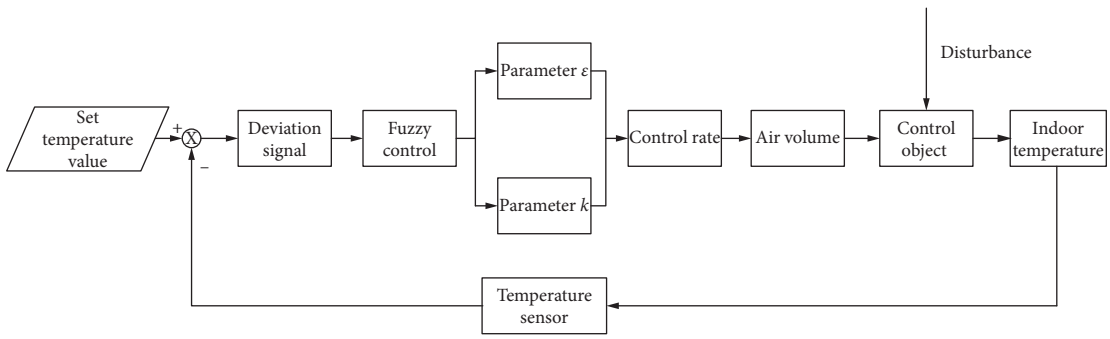

Figure 5: Flow chart of fuzzy SMC.

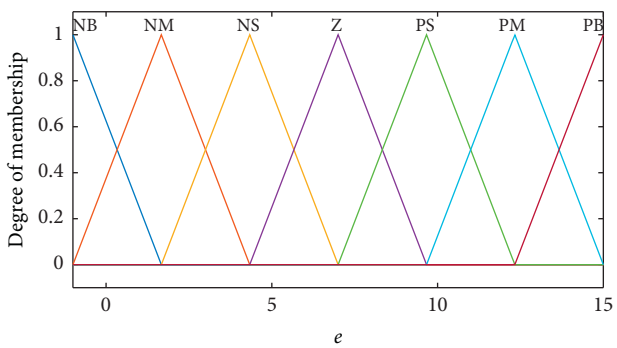

Figure 6: Membership function of temperature error e.

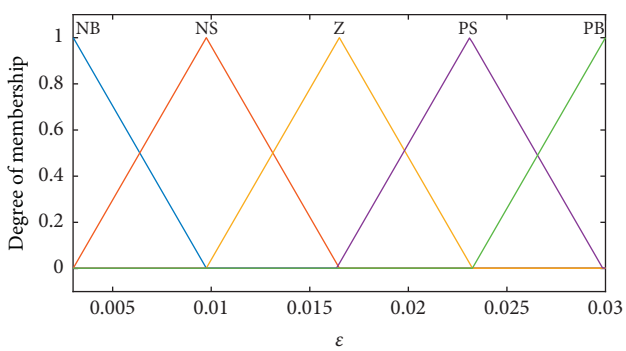

Figure 7: Membership function of approach law parameter ε.

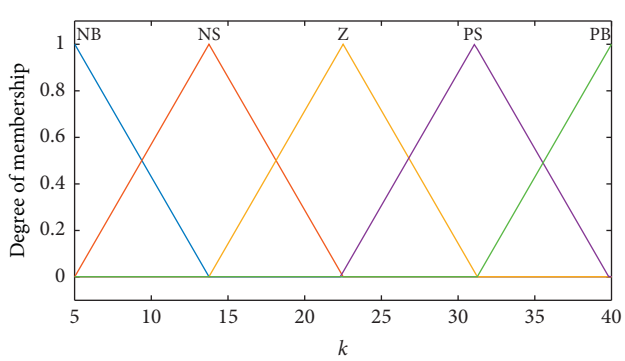

Figure 8: Membership function of approach law parameter k.

Table 1: Fuzzy control rule table of parameters ε and k.

e	NB	NM	NS	Z	PS	PM	PB
ε	NB	NS	PS	PB	PB	PB	PB
k	NB	Z	PS	PB	PB	PB	PB

4.3. Simulation Model and Results of the Fuzzy Sliding Mode Controller. When the fuzzy controller designed in Section 4.2 is used, the temperature response curve from 7 : 00 to 19 : 00 is presented as Figure 12. The system is robust when the external variables are substantially disturbed.

The temperature response curve of the fuzzy SMC is compared with the curve under the conditions of $\varepsilon = 0.1$ and $k = 5$. After the introduction of the fuzzy control, the system not only has a shorter transition time than the case of $\varepsilon = 0.1$ and $k = 5$ but also has a small steady-state static difference. Moreover, fuzzy control can suppress chattering and improve the dynamic and steady performance of the system. According to the response characteristics of room temperature under variable air volume regulation, the delayed response curves of room temperature under three methods are obtained through simulation experiments. And the experiments show that in the process of variable air volume adjustment, the delay caused by the delay of the end air volume to the fan speed and the air valve opening adjustment response is much smaller than the response delay of the room temperature to the room air volume change as shown in Figure 13.

The air supply volume of air-conditioned rooms changes with indoor and outdoor heat loads. The air supply volume of the system at 7 : 00–19 : 00 is presented in Figure 14.

Considering the running speed of the air conditioner fan, a servo system, in which the air temperature supply changes with the temperature deviation signal e, is designed to reduce the energy consumption of the fan. The input signal of the fuzzy controller is the temperature error e, and the output signal is supply air temperature Ts. The fuzzy subsets of input and output variables are {NB, NM, NS, Z, PS, PM, PB}. The input quantization is in the (0, 10) region, and the output Ts quantization is in the (10, 16) region. The fuzzy control rules are shown in Table 2.

The simulation results are shown in Figure 15. When the fan speed drops, the power consumption of the fan and the noise generated during its operation can be reduced, thereby providing a comfortable and quiet office environment for users.

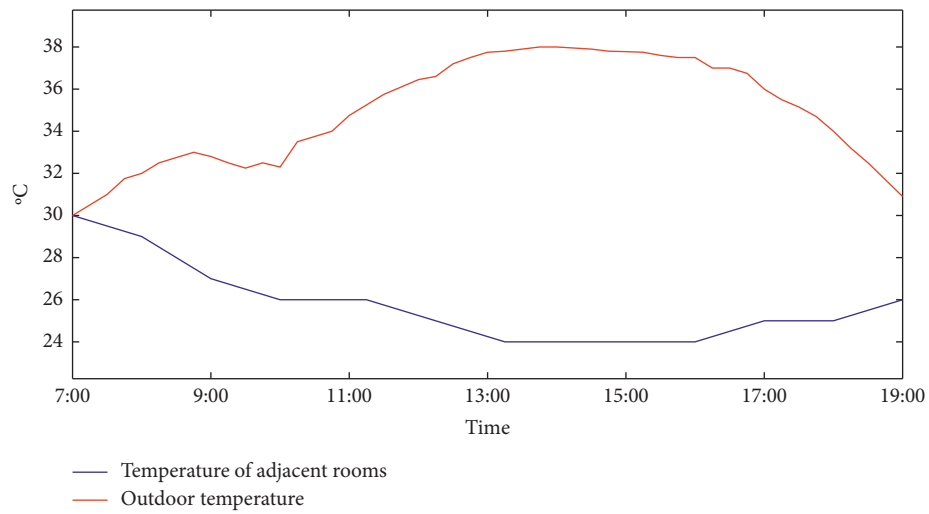

Figure 9: Outdoor temperature and temperature change of the next room.

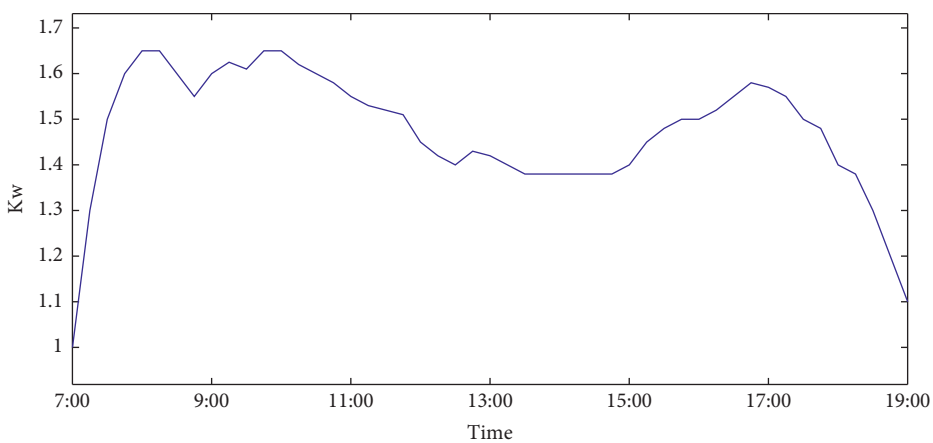

Figure 10: Indoor thermal load interference.

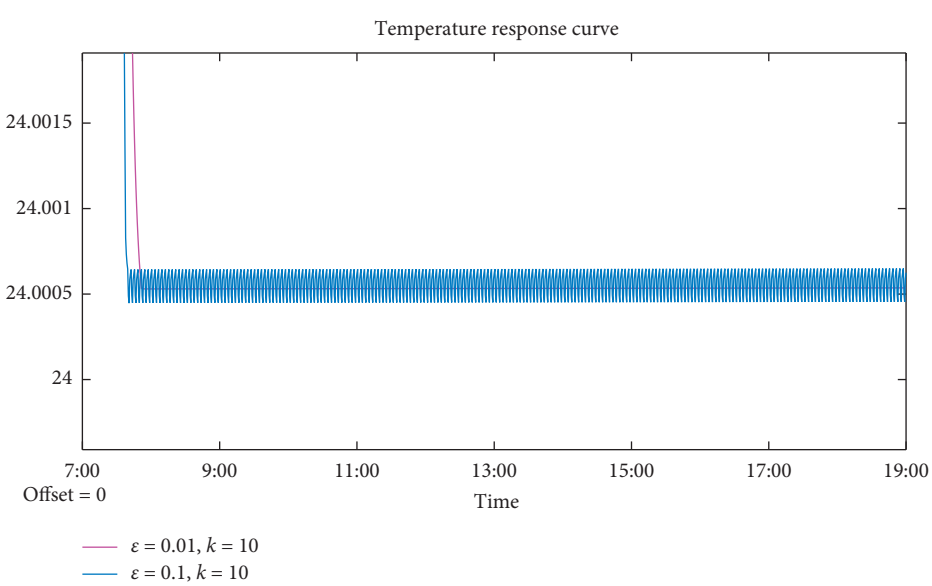

Figure 11: Temperature response curve with $\varepsilon = 0.1$, $k = 10$ and $\varepsilon = 0.001$, $k = 10$.

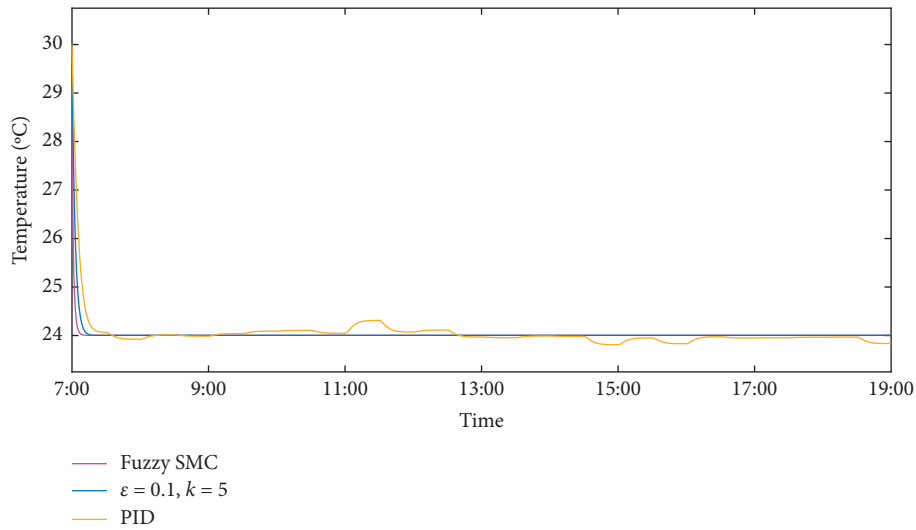

Figure 12: Temperature response curve comparison.

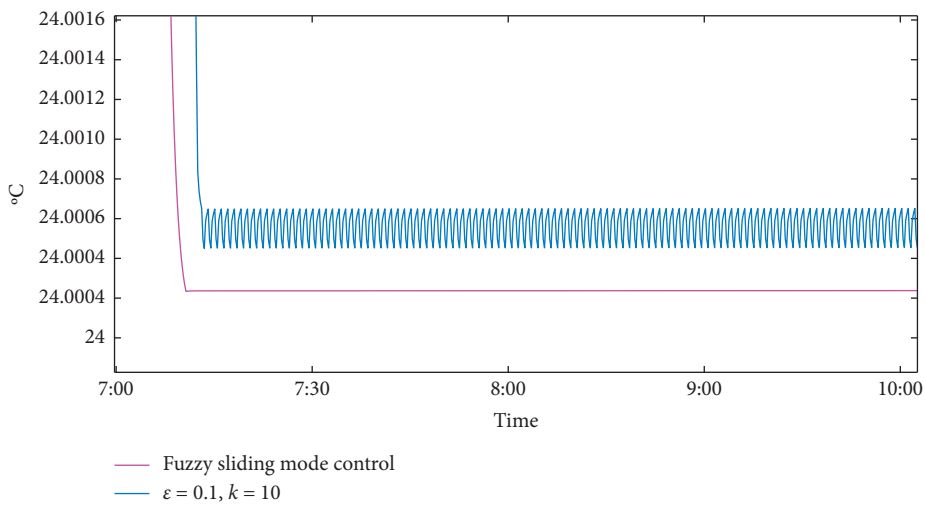

Figure 13: Local temperature response curve after fuzzy control.

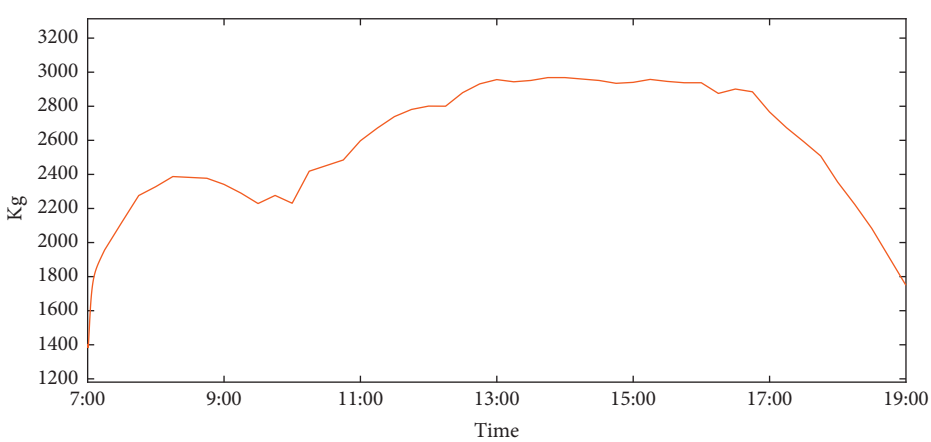

Figure 14: Change in the air supply volume of the system.

Table 2: Fuzzy control rule table of supply air temperature Ts.

e	NB	NM	NS	Z	PS	PM	PB
Ts	PB	PS	Z	NS	PB	NB	NB

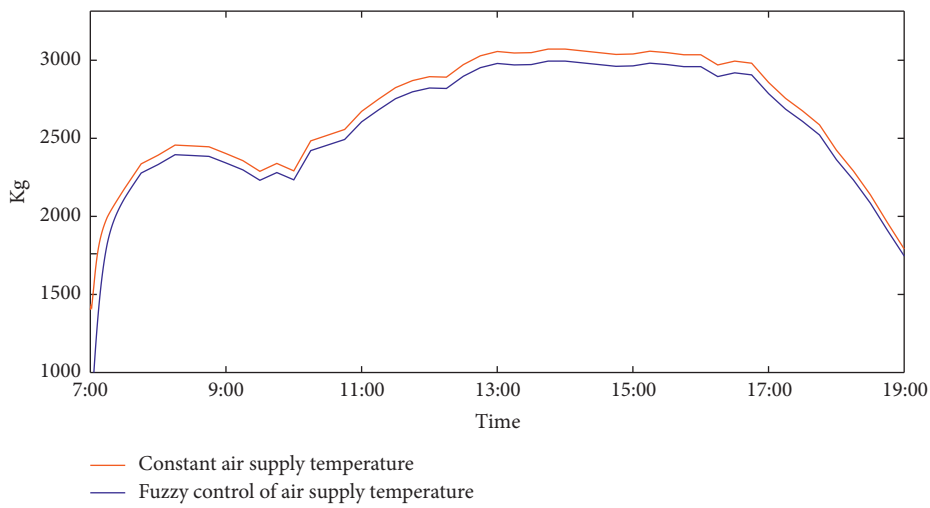

Figure 15: Comparison of air supply volume of the system.

5. Conclusion

Fuzzy SMC has a strong adaptive ability to the disturbance of systems and parameters. As such, applying it to an air-conditioning system with a high uncertainty can overcome the limitations of some traditional control methods and improve the overall stability of the system. In this study, the temperature model of an air-conditioned room is established on the basis of the characteristics of VAV air-conditioning, an SMC is used to regulate air volume, and the temperature is successfully controlled. Moreover, a fuzzy controller is designed in accordance with fuzzy theory to soften the SMC rate, effectively suppress the chattering of the system, and improve its dynamic performance.

Data Availability

The data in this study are measured by the author. The data used to support the findings of this study are available from the corresponding author upon request.

Conflicts of Interest

The authors declare that they have no conflicts of interest.

Authors' Contributions

Fuzhou Niu and Ziyang Li contributed equally to this work.

Acknowledgments

The authors confirm that all contributors to this research are listed. This work was partly supported by the NSFC (Grant nos. 61803279, 62003231, 11871366, and 61672371), the Qing Lan Project of Jiangsu, the High-Level Innovation and Entrepreneurship Talents Introduction Program of Jiangsu Province, the Open Project Funding from Anhui Province Key Laboratory of Intelligent Building and Building Energy Saving, Anhui Jianzhu University (Grant no. IBBE2018KX02ZD), the Natural Science Foundation of the Jiangsu Higher Education Institutions of China (Grant no. 18KJB460026), the Suzhou Science and Technology Foundation (Grant no. SYG201813), the Natural Science Foundation of Jiangsu Province (Grant nos. BK20170342 and BK20200989), and Jiangsu Province Graduate Practice Innovation Program (Grant no. SJCX19_0844).

References

[1] X. Li, S. Lin, J. Zhang, and T. Zhao, "Model parameter identification of indoor temperature lag characteristic based on hysteresis relay feedback control in VAV systems," *Journal of Building Engineering*, vol. 25, Article ID 100839, 2019.

[2] X. Xu, S. Wang, Z. Sun, and X. Fu, "A model-based optimal ventilation control strategy of multi-zone VAV air-conditioning systems," *Applied Thermal Engineering*, vol. 29, no. 1, pp. 91–104, 2008.

[3] X. Jin and Z. Du, "Fault tolerant control of outdoor air and AHU supply air temperature in VAV air-conditioning systems using PCA method," *Applied Thermal Engineering*, vol. 26, no. 11-12, pp. 1226–1237, 2005.

[4] I. Ganchev, A. Taneva, K. Kutryanski, and M. Petrov, "Decoupling fuzzy-neural temperature and humidity control in HVAC systems," *IFAC PapersOnLine*, vol. 52, no. 25, pp. 299–304, 2019.

[5] J. Zhu, Q. Yang, J. Lu, B. Zheng, and C. Yan, "An adaptive artificial neural network-based supply air temperature controller for air handling unit," *Transactions of the Institute of Measurement and Control*, vol. 37, no. 9, pp. 1118–1126, 2015.

[6] W. Qi, G. Zong, and H. Karimi, "Sliding mode control for nonlinear stochastic singular semi-Markov jump systems,"

IEEE Transactions on Automatic Control, vol. 65, no. 1, pp. 361–368, 2019.

[7] W. Qi, G. Zong, and H. Karimi, "Sliding mode control for nonlinear stochastic semi-Markov switching systems with application to SRMM," *IEEE Transactions on Industrial Electronics*, vol. 67, no. 5, pp. 3955–3966, 2019.

[8] X. Yao and Z. Chen, "Sliding mode control with deep learning method for rotor trajectory control of active magnetic bearing system," *Transactions of the Institute of Measurement and Control*, vol. 41, no. 5, pp. 1383–1394, 2019.

[9] S.-B. Yang, X. Wang, H.-N. Wang, and Y.-G. Li, "Sliding mode control with system constraints for aircraft engines," *ISA Transactions*, vol. 98, pp. 1–10, 2020.

[10] Y. Lu, M. Yue, Y. Liu, and L. Guo, "RBFNN based terminal sliding mode adaptive control for electric ground vehicles after tire blowout on expressway," *Applied Soft Computing Journal*, vol. 92, Article ID 106304, 2020.

[11] F. Zhang, "High-speed nonsingular terminal switched sliding mode control of robot manipulators," *IEEE/CAA Journal of Automatica Sinica*, vol. 4, no. 4, pp. 775–781, 2017.

[12] G. Chen, B. Jin, and Y. Chen, "Accurate and robust body position trajectory tracking of six-legged walking robots with nonsingular terminal sliding mode control method," *Applied Mathematical Modelling*, vol. 77, no. 2, pp. 1348–1372, 2020.

[13] X. Jin, X. Lian, T. Su, Y. Shi, and B. Miao, "Closed-loop estimation for randomly sampled measurements in target tracking system," *Mathematical Problems in Engineering*, vol. 2014, Article ID 315908, 12 pages, 2014.

[14] R. Wang, Y. Li, H. Sun, Y. Zhang, and Y. Sun, "Performance analysis of switched control systems under common-source digital upsets modeled by MDHMM," *Complexity*, vol. 2018, Article ID 4329053, 12 pages, 2018.

[15] L. Yang, Z. Li, Z. Wu, M. Xie, B. Jiang, and B. Fu, "Independent control of temperature and humidity in air conditioners by using fuzzy sliding mode approach," *Complexity*, vol. 2020, Article ID 1976584, 12 pages, 2020.

[16] B. Knüsel, C. Baumberger, M. Zumwald, D. N. Bresch, and R. Knutti, "Argument-based assessment of predictive uncertainty of data-driven environmental models," *Environmental Modelling & Software*, vol. 134, Article ID 104754, 2020.

[17] Y.-T. Bai, X.-B. Jin, X.-Y. Wang, X.-K. Wang, and J.-P. Xu, "Dynamic correlation analysis method of air pollutants in spatio-temporal analysis," *International Journal of Environmental Research and Public Health*, vol. 17, no. 1, p. 360, 2020.

[18] B. P. Epps and E. M. Krivitzky, "Singular value decomposition of noisy data: noise filtering," *Experiments in Fluids*, vol. 60, no. 8, 2019.

[19] L. Liu, H. Liu, F. Ding, A. Alsaedi, and T. Hayat, "Data filtering based maximum likelihood gradient estimation algorithms for a multivariate equation-error system with ARMA noise," *Journal of the Franklin Institute*, vol. 357, no. 9, pp. 5640–5662, 2020.

[20] B. Jiang, H. R. Karimi, Y. Kao, and C. Gao, "A novel robust fuzzy integral sliding mode control for nonlinear semi-Markovian jump T-S fuzzy systems," *IEEE Transactions on Fuzzy Systems*, vol. 26, no. 6, pp. 3594–3604, 2018.

[21] Y. Wang, H. Shen, H. Reza Karimi, and D. Duan, "Dissipativity-based fuzzy integral sliding mode control of continuous-time TS fuzzy systems," *IEEE Transactions on Fuzzy Systems*, vol. 26, no. 3, pp. 1164–1176, 2017.

[22] B. Jiang, H. Reza Karimi, Y. Kao, and C. Gao, "Takagi–Sugeno model based event-triggered fuzzy sliding-mode control of networked control systems with semi-markovian switchings," *IEEE Transactions on Fuzzy Systems*, vol. 28, no. 4, pp. 673–683, 2019.

[23] B. Jiang, H. Reza Karimi, S. Yang, Y. Kao, and C. Gao, "Takagi-Sugeno model-based reliable sliding mode control of descriptor systems with semi-Markov parameters: average dwell time approach," *IEEE Transactions on Systems, Man, and Cybernetics: Systems*, 2019.

[24] A. Rebai and K. Guesmi, "Robust adaptive fuzzy sliding mode controller for nonlinear uncertain hysteretic systems," *Transactions of the Institute of Measurement and Control*, vol. 42, no. 13, Article ID 014233122092102, 2020.

[25] T. Ahmed and P. Kevin Hallinan, "Statistically informed static pressure control in multiple-zone VAV systems," *Energy & Buildings*, vol. 135, pp. 244–252, 2017.

[26] B. Taran and A. Pirmohammadi, "Designing an optimal fuzzy sliding mode control for a two-link robot," *Journal of the Brazilian Society of Mechanical Sciences and Engineering*, vol. 42, no. 1, pp. 1–12, 2020.

[27] H. Tian, S. Xie, Z. Miao, L. Wang, and L. Ren, "Fuzzy sliding mode controller for aeroengine based on an improved power exponential reaching law," *Fire Control & Command Control*, vol. 41, no. 2, pp. 108–112, 2016.

[28] A.-H. Attia, S. F. Rezeka, and A. M. Saleh, "Fuzzy logic control of air-conditioning system in residential buildings," *Alexandria Engineering Journal*, vol. 54, no. 3, pp. 395–403, 2015.

[29] C. Liang, X. Li, X. Shao, and B. Li, "Direct relationship between the system cooling load and indoor heat gain in a non-uniform indoor environment," *Energy*, vol. 191, Article ID 116490, 2020.

Hindawi
Complexity
Volume 2020, Article ID 8863941, 9 pages
https://doi.org/10.1155/2020/8863941

Research Article

Life Cycle Assessment of Environmental Impact of Steelmaking Process

Huimin Liu,[1] **Qiqiang Li**,[1] **Guanguan Li**,[2] **and Ran Ding**[1]

[1]*The School of Control Science and Engineering, Shandong University, Jinan 250061, China*
[2]*Institute of Marine Science and Technology, Shandong University, Qingdao 266237, China3011*

Correspondence should be addressed to Qiqiang Li; qqli@sdu.edu.cn

Received 23 September 2020; Revised 13 November 2020; Accepted 25 November 2020; Published 3 December 2020

Academic Editor: Rui Wang

The steel industry is facing problems such as serious environmental pollution and high resource consumption. At the same time, it lacks effective methods to quantify potential environmental impacts. The purpose of this work is to conduct a specific environmental analysis of steelmaking production in steel plants. The ultimate goal is to discover the main pollution of steelmaking and identify potential options for improving the environment. This paper uses life cycle assessment method to carry out inventory and quantitative analysis on the environmental impact of steelmaking system. Through analysis, the hazards are divided into four major categories, which are human health, climate change, ecosystem quality, and resources. The results show that molten iron has the greatest impact on human health, followed by the greatest impact on resources. The impact of scrap steel on human health ranks third. Molten iron is a key process that affects human health, climate change, ecosystems quality, and resources. In addition, processes such as fuels, working fluids, and auxiliary materials also cause certain environmental damage, accounting for a relatively small proportion. Optimizing the utilization of scrap steel and molten iron resources and improving the utilization efficiency of resources and energy are helpful to reduce the environmental hazards of steelmaking system.

1. Introduction

The iron and steel industry is a pillar industry of the national economy and an energy-intensive industry. Energy consumption accounts for an increasing proportion, accounting for about 15% of the country's total industrial consumption. In the past three decades, crude steel production has more than doubled, reaching 84.26 million tons in 2019. This productivity inevitably imposes an environmental burden on the steelmaking sector. For example, in a country like China, the industry accounts for 12% of the national CO_2 emissions [1].Therefore, the steelmaking process must be analysed in order to have a clear understanding of the main environmental impacts and may involve the implementation of circular economy solution.

At present, there are many researches on the environmental impact assessment of China's steel industry, such as greenhouse gas emission reduction, air pollutant emission reduction, steel wastewater footprint and production capacity, resource and energy emissions, etc. However, the studies mentioned above fail to elucidate the upstream and downstream impacts, whereas life cycle assessment (LCA) is a method of summarizing and evaluating the potential environmental impacts of all inputs and outputs of a system of products (or services) throughout its life cycle. LCA is evaluated based on the contribution of the production process to the environment, including categories such as global warming potential (GWP), land acidification, land occupation, respirable organic, and human toxicity. Therefore, LCA can identify the unit processes with the greatest impact on the environment for targeted improvements [2].

Some studies have also been conducted on life cycle assessment of the steel industry worldwide. Reference [3] also carried out an LCA analysis of the production, selected 1 kg of metal as a functional unit, and evaluated the environmental impact of steel and stainless steel based on global warming potential, solid waste burden, and total energy

demand. In a comprehensive study, [4] compared the effects of different steels (slabs, hot-rolled, cold-rolled, hot-dip galvanized, and electrogalvanized steel) on fossil fuels, global warming potential, ecotoxicity, minerals, carcinogens, and respiratory inorganics; the results show that the hot-dip galvanized steel sheet has the greatest impact. In a recent study, [5] has developed a water footprint calculation model and calculated the water footprint of steel from the perspective of life cycle assessment. These data show that the steel plant poses a serious hazard to the water environment. Bieda conducted an inventory analysis on the blast furnace of an integrated steel plant in Krakow, Poland, and collected and sorted out the input and output list of the blast furnace [6]. Including sinter, limestone, etc., energy consumption and fuel include pulverized coal, natural gas, and blast furnace gas. The operating parameters, air pollutant discharge, and heavy metal discharge are given. Bieda performed an analysis of the continuous casting process at the Krakow comprehensive steel plant in Poland, which included not only energy consumption, fuel, materials, and waste but also operational data such as dust, iron, PM_{10}, and waste [7]. This is the basis of life cycle assessment analysis. Korol [8] conducted a life cycle assessment of Polish steel production by integrating steel production. The study pointed out that in the integrated steel production routes the production of pig iron in blast furnaces has the greatest impact on greenhouse gas emissions and fossil fuel consumption, and the sintering process of iron ore is the biggest cause of dust. The substitution of raw materials in the iron making process can effectively reduce the impact of the steel industry on the environment. Manfred comprehensively studies the current evaluation methods impact on resources and points out that it needs to be improved [9]. The three key issues in resource sustainability assessment are renewability, recyclability, and criticality. The model in this study has different representations of the impact on resource depletion and points out the differences in different resource types and scales. Liu used the life cycle assessment method to analyse 12 major iron ore mines and major steel producers, calculated the production intensity per unit of GDP, and finally proposed the problem of pollution distribution among international trade participants [10]. He pointed out that ecotoxicity is the most serious consequence in the steel production chain, which is not negligible compared with the impact of carbon emissions; he also pointed out that importing countries benefiting from pollution-free materials should share the environmental pollution caused by steel processing by trading partners.

In the above studies, the idea of life cycle assessment method is used, but due to different basis, the results are still not comparable. In addition, the impact categories considered in these studies cannot be compared with each other. Therefore, this study aims to make an accurate environmental analysis of a steel production in Shandong, China, and find out the improvement process. It uses specific scene data on-site to conduct LCA assessment of steel production in steel plants. The organization of this article is as follows: the next section explains the main LCA methods and inventories. Section 3 explains the results of the environmental impact assessment. In the last part, the results are discussed and some conclusions are drawn.

2. Materials and Methods

2.1. System Boundaries. The complete life cycle of a product is usually divided into the following stages [11]: (1) cradle to entry (raw material extraction and refining); (2) factory door to factory door (product manufacturing); and (3) factory door to grave (product use, recycling, and disposal). Due to the many uncertain factors caused by the LCA evaluation of product use, recycling, and disposal, in order to reduce the complexity of LCA evaluation and improve its operability, the selected boundary definition is "from cradle to factory door." According to the ingredients requirements, first put scrap steel into the furnace, then pour molten iron, and add appropriate slagging materials (such as quicklime, etc.). After feeding, insert the oxygen spray gun into the furnace from the top of the furnace and blow in oxygen to make it directly oxidize with the hot molten iron to remove impurities. When the composition and temperature of the molten steel meet the requirements, the steel can be tapped. All the materials and energy consumed by the production equipment involved in the process of steelmaking from the molten iron entering the steelmaking station, smelting into molten steel through the converter, and leaving the converter are taken into account. A ton of crude steel is used as the functional unit of the present study, in order to provide life cycle inventory (LCI) and all the results of quantitative standards [11]. The boundary definition of the steelmaking system in this study is shown in Figure 1. Scrap steel, molten iron, and waste treatment are involved (i.e., wastewater treatment, solid waste treatment in landfills, hazardous waste incineration, and air emission control). Each process considers the input of raw materials, transportation, energy generation, and consumption (for example, coal-based electricity, coal, and coke), direct waste emissions (for example, dust, nickel, SO_2, and NO_x), and land occupation.

2.2. Data Source and Life Cycle Inventory. Inventory analysis uses a survey model to collect and classify the raw materials, transportation, energy, infrastructure, direct discharge, and waste disposal in different steps of each process. In this study, most of the analysis data of energy resource consumption and pollutant emission inventory of the steelmaking system (obtained 1t molten steel products) was collected from a group company in Shandong Province, and part of the data was derived from literature [12] and the cleaner production (HJ/T294-2006, HJ/T426-2008, HJ/T 1262003, HJ/T 427-2008, HJ/T 428-2008, and HJ/T 318-2006) secondary indicators [13]. The life cycle list of molten steel products is shown in Table 1.

2.3. Life Cycle Impact Assessment Methodology. The steps of life cycle impact assessment are characterization, damage assessment, normalization, and single scoring. In the impact method, damage is divided into fifteen midpoint categories

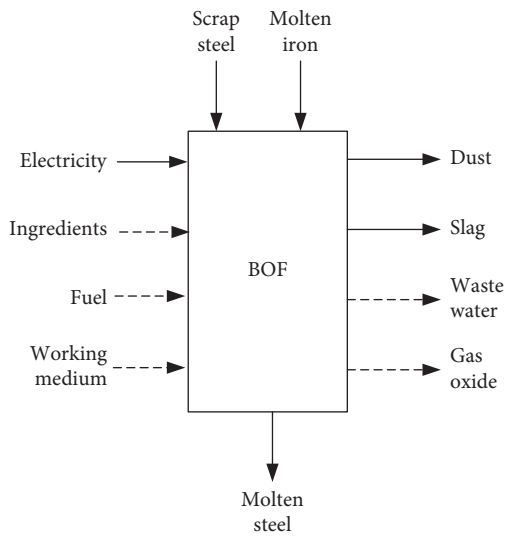

Figure 1: Simplified scheme of iron and steel production routes and processes.

Table 1: Life cycle inventories of molten steel. Value are presented per ton.

Inputs and outputs	Categories	Normal production	Clean production	Unit
Molten iron		1008	947	kg
Scrap steel		70.43	78	kg
Electricity		26.65	25s	kWh
Ingredients	Quicklime	50	50	kg
	Fe	20	20	kg
	Dolomite	20	20	kg
Fuel	Coke oven gas	0.16	0.16	m^3
	BOF gas	12.15	12.15	m^3
Working medium	Oxygen	37.28	37.28	m^3
	Nitrogen	45.12	45.12	m^3
	Argon	75.2	75.2	m^3
	Air	15.38	15.38	m^3
	Pure water	2.7	2.7	m^3
Emission	CO_2	28.28	28.28	kg
	SO_2	5.75	5.75	g
	NO_2	3.84	3.84	g
	CO	4.6	4.6	kg
	Waste water	1.07	1.07	m^3
	Dust	135	135	kg
	Cd	50	50	mg
	Cr	120	120	mg
	Cu	3090	3090	mg
	Ni	280	280	mg
	Pb	930	930	mg
	Zn	7500	7500	mg

[14] (carcinogens, noncarcinogens, respiratory inorganics, ionizing radiation, ozone layer depletion, respiratory organics, aquatic ecotoxicity, terrestrial ecotoxicity, terrestrial acid/nutrition, land occupation, aquatic acidification, aquatic eutrophication, global warming, nonrenewable energy, and mineral extraction), and for the convenience of explanation, the 15 midpoints are classified into four endpoint categories (human health, ecosystem quality, climate change, and resources). In this way, you can not only see the impact value of the midpoint category, but also intuitively see the final impact on the environment [15]. In this paper, the software SimaPro is used for calculation and the Impact 2002+ method is adopted.

3. Results and Discussion

Table 2 lists the life cycle inventory assessment (LCIA) midpoint results based on functional units. According to climate change, the midpoint of LCIA for the production of 1 ton of molten steel is 358.84 kg CO_2 equivalent, for aquatic acidification is 1.96 kg

Table 2: Life cycle assessment midpoint results of molten steel.

Categories	Unit	Total	Electricity	Scrap steel	Ingredients	Fuel	Molten iron	Working medium
Carcinogens	kg C_2H_3Cl eq	16.93	0.05	7.22	3.43	0.70	5.01	0.52
Noncarcinogens	kg C_2H_3Cl eq	158.18	0.75	73.35	16.97	0.03	66.43	0.65
Respiratory inorganics	kg $PM_{2.5}$ eq	0.42	0.01	0.04	0.05	0.01	0.27	0.05
Ionizing radiation	Bq C-14 eq	11990.73	77.76	0.00	425.30	19.96	5479.27	5988.44
Ozone layer depletion	kg CFC-11 eq	0.00	0.00	0.00	0.00	0.00	0.00	0.00
Respiratory organics	kg C_2H_4 eq	0.21	0.00	0.03	0.01	0.02	0.14	0.01
Aquatic ecotoxicity	kg TEG water	8102543.87	84954.23	38796.06	55164.71	244.41	7865355.15	58029.32
Terrestrial ecotoxicity	kg TEG soil	21450.23	68.07	16273.15	555.35	60.84	4089.03	403.79
Terrestrial acid/nitrification	kg SO_2 eq	7.12	0.23	0.58	1.28	0.09	4.07	0.87
Land occupation	m^2a	10.68	0.13	0.98	1.51	0.04	6.98	1.05
Aquatic acidification	kg SO_2 eq	1.96	0.08	0.16	0.38	0.02	0.95	0.37
Aquatic eutrophication	kg PO_4^{3-} eq	0.13	0.00	0.00	0.00	0.00	0.13	0.00
Global warming	kg CO_2 eq	358.54	25.68	56.22	91.71	5.30	120.63	59.01
Nonrenewable energy	MJ primary	27914.93	293.34	543.59	794.31	96.03	24870.01	1317.65
Mineral extraction	MJ surplus	3.25	0.02	0.24	2.09	0.01	0.58	0.30

SO_2, and for respiratory inorganics 0.42 kg $PM_{2.5}$ equivalent; the detailed values of 15 midpoints are shown in Table 2.

In order to compare the different impact categories of each midpoint and analyse the impact of each midpoint type on the overall situation, this study conducted a normalized analysis. The normalized midpoint results of each functional unit are shown in Figure 2. Two situations are considered: normal production and clean production. The difference is the ratio of scrap steel and molten iron in the production process. The cleaner production scene uses more steel scrap and less molten iron. It is worth noting that in both cases, the waste disposal method is assumed to be the same. In the environmental impact category, especially nonrenewable resources, respiratory inorganics, toxicity of aquatic organisms, and terrestrial ecotoxicity, the scene of normal production is significantly higher than the scene of cleaner production. These findings may be attributed to the fact that normal production requires more molten iron, which requires more fuel and ore, which will inevitably produce more waste water, waste gas, and slag during the treatment process. It also shows that recycling of scrap steel is a more scientific production method.

Table 3 and Figure 3 show the life cycle evaluation endpoint of the steelmaking system, which is obtained by classifying and weighing all intermediate damage types. It can be seen from Figure 3 that molten iron, scrap steel, and auxiliary materials have a greater impact on the environment. Among them, molten iron has a greater damage value to natural resources, human health, and the ecological environment. The damage value of scrap steel to human health is greater. It can be seen from Figure 3 that steel scrap and molten iron still have the greatest impact, which is basically consistent with the results [16]. In Figure 3, molten iron is the most harmful to natural resources, accounting for about 60%. Scrap steel is the most harmful to human health, which is about 60%. The impact of auxiliary materials and working fluids on the environment is second, and the impact of electricity and fuel is negligible.

3.1. Main Process. According to the results of normalization evaluation, the most important potential environmental impacts during the entire life cycle of molten steel products are noncarcinogens, nonrenewable energy, terrestrial ecotoxicity, global warming, respiratory organics, carcinogens, and aquatic ecotoxicity. Therefore, it is necessary to identify and analyse the key processes that cause the above environmental impacts, so as to put forward relevant recommendations. On the basis of the evaluation results of the midpoint in the life cycle, the key processes are identified, and the results are shown in Figure 4. It can be seen from Figure 4 that for the abovementioned impact categories, scrap steel and electricity are the most important environmental contributing factors, and their impact on most environmental categories accounts for more than 50%. Scrap steel has a particularly significant impact on noncarcinogens, terrestrial ecotoxicity, and carcinogens, and its contribution can reach more than 85% of its total environmental impact. It also has a significant impact on global warming and breathing organic matter. At the same time, the contribution of electricity to nonrenewable energy and aquatic ecotoxicity cannot be ignored.

3.2. Main Contributors. Based on the identification of main processes, this study also identifies the main substances in each main influence category, so as to put forward relevant opinions on the consumption of certain substance or pollutant discharge. This study identified the four key substances of environmental impact types in the endpoint evaluation, and the results are shown in Figure 5. Figure 5 shows the specific substances that contribute significantly to each major environmental category and their contribution rates. For the environmental impact of human health, coke accounts for 23%, iron ore for 22%, and residue for 17%, which is consistent with the serious pollution impact of molten iron. Coke and coal are the two substances that have the greatest impact on the ecosystem. It can be seen that the two are not clean production methods, and the proportion of clean energy should be increased. The key material in the potential environmental impact of climate change is scrap steel, which accounted for 28%, followed by coke and ore. Coke ore produces a large amount of carbon oxides, sulfur oxides, and nitrogen oxides during the smelting process,

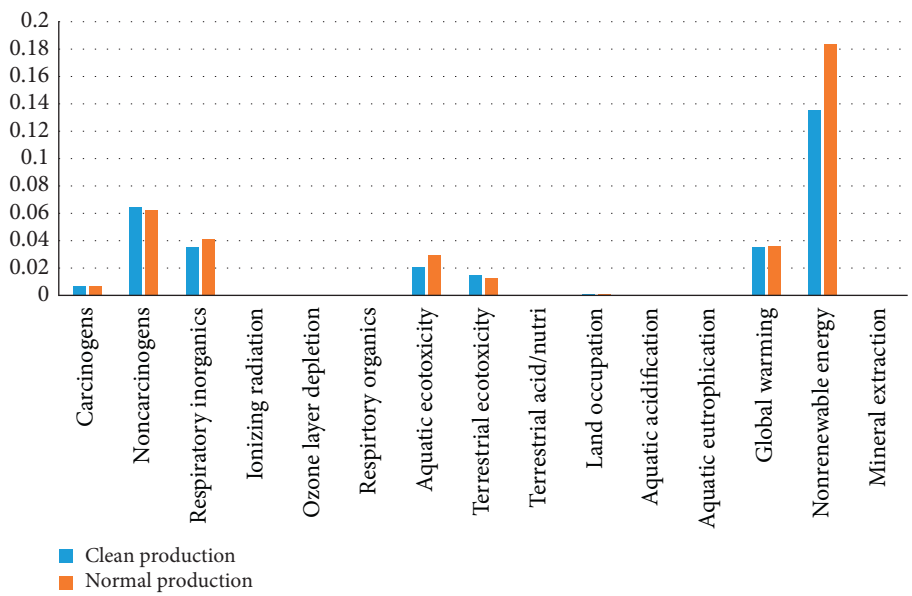

Figure 2: Normalized midpoint results.

Table 3: Life cycle assessment endpoint results of molten steel.

Categories	Unit	Total	Electricity	Scrap steel	Ingredients	Fuel	Molten iron	Working medium
Total	Pt	$3.74E-01$	$6.25E-03$	$5.48E-02$	$2.78E-02$	$2.40E-03$	$2.63E-01$	$2.04E-02$
Human health	Pt	$1.11E-01$	$1.35E-03$	$3.59E-02$	$1.25E-02$	$1.18E-03$	$5.48E-02$	$5.22E-03$
Ecosystem quality	Pt	$4.35E-02$	$3.79E-04$	$9.66E-03$	$7.40E-04$	$4.57E-05$	$3.20E-02$	$5.95E-04$
Climate change	Pt	$3.62E-02$	$2.59E-03$	$5.68E-03$	$9.26E-03$	$5.35E-04$	$1.22E-02$	$5.96E-03$
Resources	Pt	$1.84E-01$	$1.93E-03$	$3.58E-03$	$5.24E-03$	$6.32E-04$	$1.64E-01$	$8.67E-03$

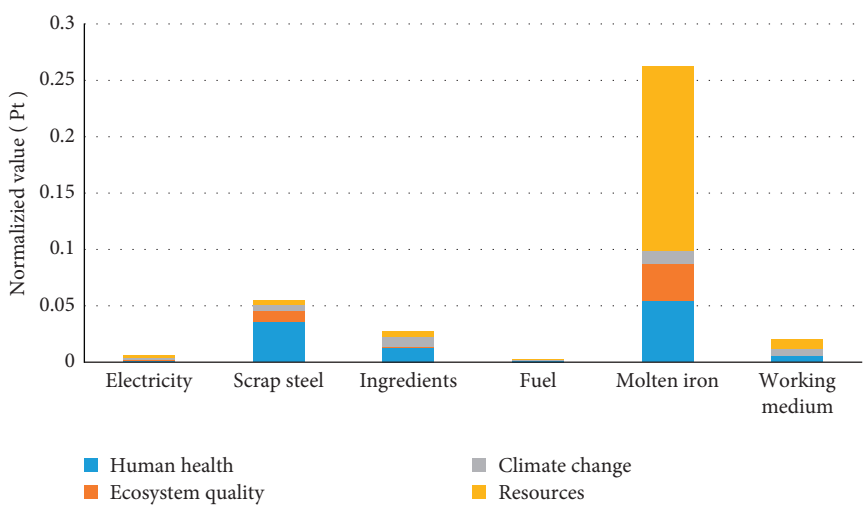

Figure 3: Single score result for 1t molten steel.

which has a greater adverse impact on the climate. Among the potential environmental impacts of natural resource damage, coke accounts for 52% and coal accounts for 37%, indicating that they not only have a greater impact on the above mentioned types, but also have a greater impact on natural resources. The development of clean energy is of great significance for the reduction of environmental impact in the steelmaking process.

3.3. Sensitivity and Uncertainty Analysis. Sensitivity analysis is a key part of LCA testing the sensitivity of LCI input data, which can be calculated [17] based on the percentage adjustment rule of input and output parameters (ISO 14044, 2006; ISO 14040, 2006). A sensitivity analysis was performed by changing 5% of the material input at a time [18].

Table 4 lists the results of the sensitivity analysis of the main contributors, aiming to determine the main impact on

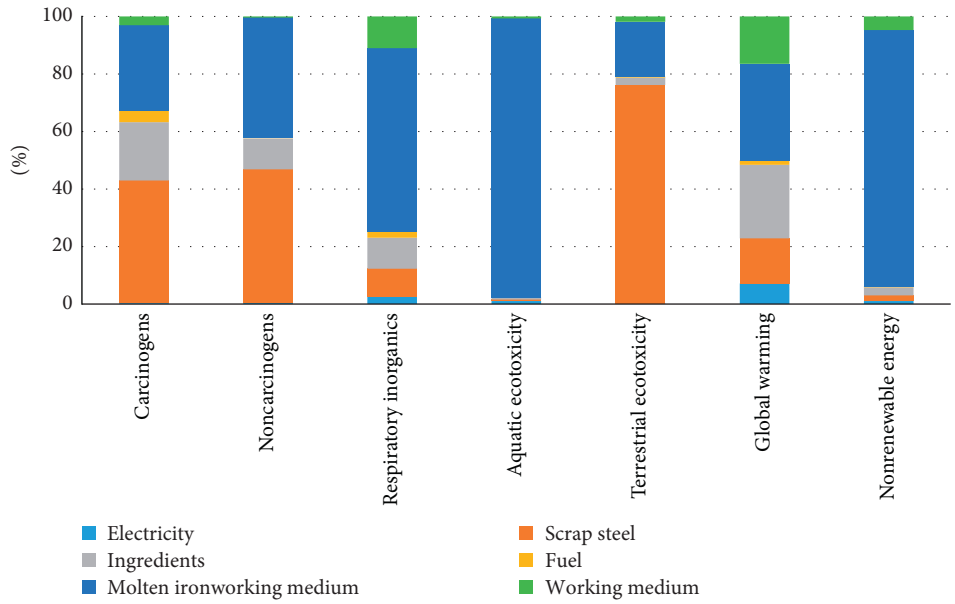

Figure 4: Main process that contribute to significantly affected categories.

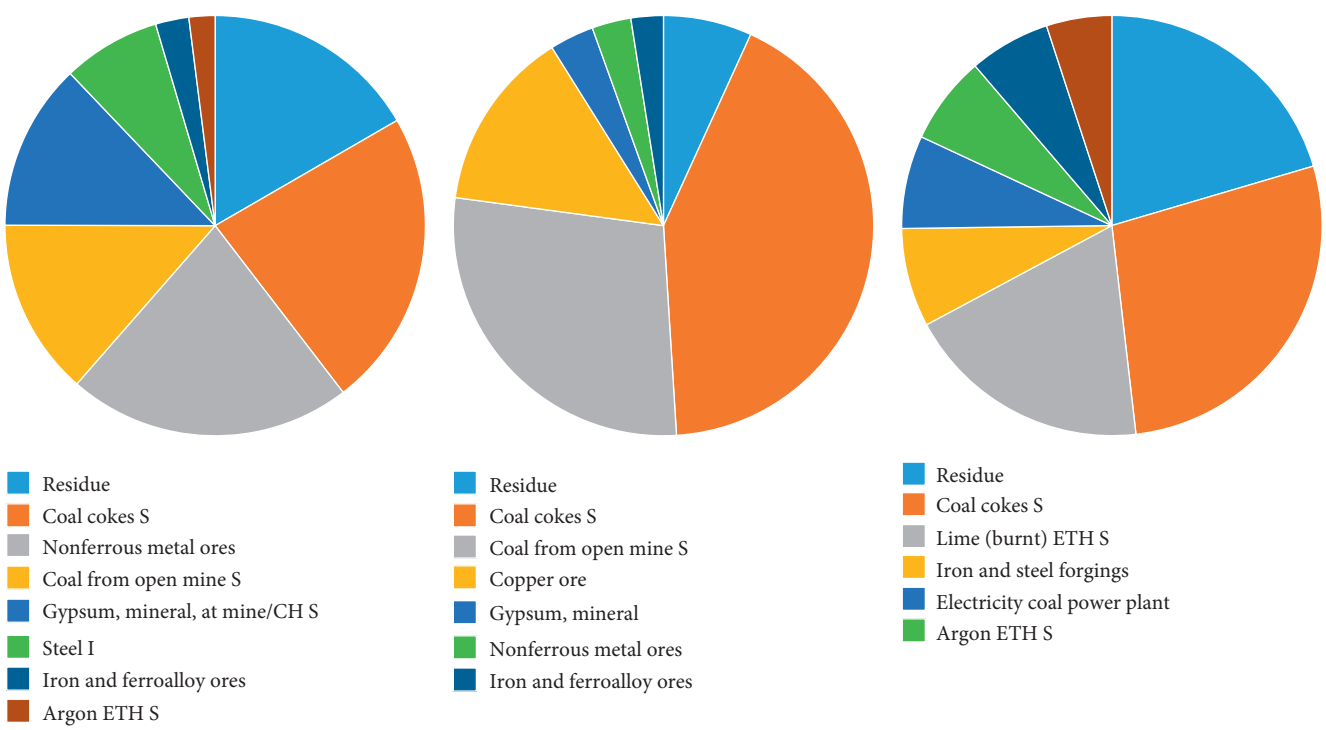

Figure 5: Continued.

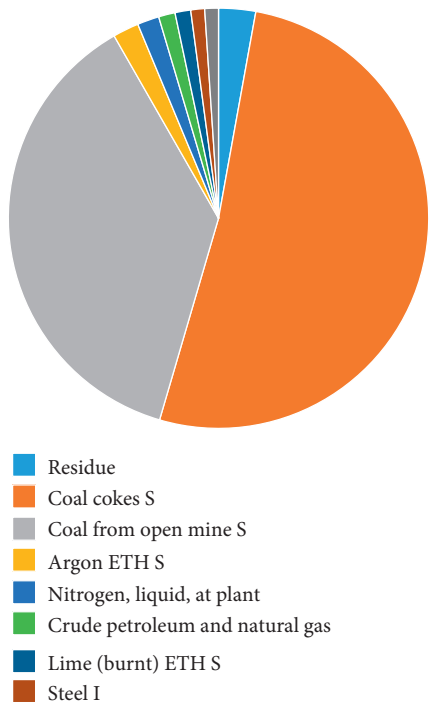

(d)

Figure 5: Contributions of the most significant substances to key categories. (a) Human health, (b) ecosystem quality, (c) climate change, and (d) resource.

Table 4: Sensitivity analysis.

Categories	Unit	Molten iron 5%	Scrap steel 5%	Electricity 5%
Carcinogens	kg C_2H_3Cl eq	$2.51E-01$	$3.61E-01$	$2.67E-03$
Noncarcinogens	kg C_2H_3Cl eq	$3.32E+00$	$3.67E+00$	$3.75E-02$
Respiratory inorganics	kg $PM_{2.5}$ eq	$1.34E-02$	$2.05E-03$	$5.26E-04$
Ionizing radiation	Bq C-14 eq	$2.74E+02$	$0.00E+00$	$3.91E+00$
Ozone layer depletion	kg CFC-11 eq	$2.03E-06$	$2.06E-06$	$1.21E-07$
Respiratory organics	kg C_2H_4 eq	$6.90E-03$	$1.52E-03$	$1.85E-04$
Aquatic ecotoxicity	kg TEG water	$3.93E+05$	$1.94E+03$	$4.27E+03$
Terrestrial ecotoxicity	kg TEG soil	$2.05E+02$	$8.14E+02$	$3.42E+00$
Terrestrial acid/nutrition	kg SO_2 eq	$2.04E-01$	$2.91E-02$	$1.18E-02$
Land occupation	m^2a	$3.49E-01$	$4.90E-02$	$6.77E-03$
Aquatic acidification	kg SO_2 eq	$4.74E-02$	$8.06E-03$	$3.81E-03$
Aquatic eutrophication	kg PO_4^{3}- eq	$6.38E-03$	$4.79E-05$	$6.92E-05$
Global warming	kg CO_2 eq	$6.03E+00$	$2.81E+00$	$1.29E+00$
Nonrenewable energy	MJ primary	$1.24E+03$	$2.72E+01$	$1.47E+01$
Mineral extraction	MJ surplus	$2.89E-02$	$1.22E-02$	$1.13E-03$

the LCIA results obtained in this study. The comparison of LCIA results in the steelmaking process shows that a 5% reduction in power consumption will result in a reduction of carbon dioxide emissions by about 1.29 kg CO_2 equivalent, and the nonrenewable energy is 1.47 MJ equivalent. For other scenarios and categories, similar analysis can be made using the sensitivity results shown in Table 4. The three main processes have the greatest impact on nonrenewable energy, global warming effect, and soil acidification. Among them, changes in molten iron have the greatest overall impact on the environment, followed by scrap steel and electricity. It can be seen that reducing the use of molten iron and developing cleaner steel production can effectively reduce environmental pollution.

Table 5 shows the probability comparison of different scenes performed using Monte Carlo simulation. The probability that cleaner production scenario has a higher global warming effect score than normal production is 43%, which means that the impact of cleaner production on global warming is lower than normal production. A similar situation can be observed from the uncertainty analysis results shown in Table 5. In general, except for carcinogens and land

Table 5: Uncertainty analysis.

Categories	Clean production ≥ normal production (%)
Aquatic acidification	20
Aquatic ecotoxicity	2
Aquatic eutrophication	2
Carcinogens	65
Global warming	43
Ionizing radiation	29
Land occupation	13
Mineral extraction	53
Noncarcinogens	54
Nonrenewable energy	3
Ozone layer depletion	44
Respiratory inorganics	12
Respiratory organics	9
Terrestrial acid/ nutrition	15
Terrestrial ecotoxicity	98

eutrophication, in most categories, cleaner production scenarios have the lowest environmental burden. Among the 15 impact categories, eleven categories are less than 50%, which means that the environmental impact of cleaner production is much lower than that of normal production.

4. Conclusions

According to the analysis and comparison of the above-mentioned molten steel production process, it can be found that molten iron has the most significant impact on the environment, accounting for 70% of the overall impact, of which the harm to resources can reach 89%, and its environmental load mainly comes from noncarcinogenic substances, terrestrial ecotoxicity, and global warming. Secondly, the impact of scrap steel on the environment accounts for 15%, and the damage to human health is about 32%. Its environmental load mainly comes from nonrenewable energy, respirable inorganic substances, and aquatic ecotoxicity. In contrast, the impact of auxiliary materials and working fluids is small, and the environmental impact of electricity and fuel is the smallest.

In the entire life cycle of molten steel products, the most important categories are as follows: nonrenewable energy, accounting for 49%, and 17% are noncarcinogens, 11% are respiratory organics, then terrestrial ecotoxicity, global warming, carcinogens, and aquatic ecotoxicity.

The IMPACT 2002+ method classifies the complex environmental impacts into four types of damage and applies the assessment results to the development and utilization of iron ore resources and ecological environment planning, which is conducive to the decision makers to make correct judgments. Comparing the environmental loads of different processes can also provide a scientific basis for decision makers and lay a foundation for product ecological design and cleaner production.

Of course, since the current research history of life cycle environmental impact assessment is not long, its methodology system is not perfect, there are many differences in the research of scholars in various countries, and there are few application fields in China, so there must be some limitations, such as the variability of the source of the life cycle inventory (different production processes of the same product); the uncertainty of the model used (such as the migration and transformation of pollutants in the environment is simplified through the multimedia model); the uncertainty of the selection in the life cycle analysis (for example, which allocation method and system boundary are used), etc. However, the life cycle environmental impact assessment (LCEA) provides a preliminary analysis of the energy and environmental problems in steel production and provides a good scientific basis for optimizing the development of the industry. Therefore, it is necessary to learn from the experience of international application of life cycle assessment method, accelerate its promotion and application, and truly realize the service for sustainable development.

Data Availability

The data used to support the findings of this study are available from the corresponding author upon request.

Conflicts of Interest

The authors declare that there are no conflicts of interest regarding the publication of this paper.

Acknowledgments

This work was supported by the National Science Foundation of China (61803174) and Shandong Provincial Natural Science Foundation (ZR2019BF024).

References

[1] W. Chen, X. Yin, and D. Ma, "A bottom-up analysis of China's iron and steel industrial energy consumption and CO_2 emissions," *Applied Energy*, vol. 136, pp. 1174–1183, 2014.

[2] C. Li, H. Bai, Y. Lu, J. Bian, Y. Dong, and H. Xu, "Life-cycle assessment for coal-based methanol production in China," *Journal of Cleaner Production*, vol. 188, pp. 1004–1017, 2018.

[3] T. E. Norgate, S. Jahanshahi, and W. J. Rankin, "Assessing the environmental impact of metal production processes," *Journal of Cleaner Production*, vol. 15, no. 8-9, pp. 838–848, 2007.

[4] R. Tongpool, A. Jirajariyavech, C. Yuvaniyama, and T. Mungcharoen, "Analysis of steel production in Thailand: environmental impacts and solutions," *Energy*, vol. 35, no. 10, pp. 4192–4200, 2010.

[5] Y. Gu, J. Xu, A. A. Keller et al., "Calculation of water footprint of the iron and steel industry: a case study in eastern China," *Journal of Cleaner Production*, vol. 92, pp. 274–281, 2015.

[6] B. Bieda, "Life cycle inventory processes of the mittal steel Poland (msp) S.A. In Krakow, Poland—blast furnace pig iron production—a case study," *International Journal of Life Cycle Assessment*, vol. 17, no. 6, pp. 787–794, 2012.

[7] B. Bieda, I. Skalna, B. Gawel, K. Grzesik, A. Henclik, and D. Sala, "Life cycle inventory processes of the integrated steel plant (ISP) in Krakow, Poland-continuous casting of steel (Ccs): a case study," *The International Journal of Life Cycle Assessment*, vol. 23, pp. 1274–1285, 2018.

[8] D. Burchart-Korol, "Life cycle assessment of steel production in Poland: a case study," *Journal of Cleaner Production*, vol. 54, pp. 235–243, 2013.

[9] R. A. F. Alvarenga, K.-H. Erb, H. Haberl, S. R. Soares, R. Van Zelm, and J. Dewulf, "Global land use impacts on biomass production-a spatial-differentiated resource-related life cycle impact assessment method," *International Journal of Life Cycle Assessment*, vol. 20, no. 4, pp. 440–450, 2015.

[10] Y. Liu, H. Li, S. Huang, H. An, R. Santagata, and S. Ulgiati, "Environmental and economic-related impact assessment of iron and steel production. A Call for shared responsibility in global trade," *Journal of Cleaner Production*, vol. 269, Article ID 122239, 2020.

[11] M. Finkbeiner, A. Inaba, R. B. H. Tan, K. Christiansen, and H. J. Klueppel, "The new international standards for life cycle assessment: Iso 14040 and Iso 14044," *The International Journal of Life Cycle Assessment*, vol. 11, no. 2, pp. 80–85, 2006.

[12] X. Li, W. Sun, L. Zhao, and J. Cai, "Material metabolism and environmental emissions of BF-BOF and EAF steel production routes," *Mineral Processing and Extractive Metallurgy Review*, vol. 39, pp. 50–58, 2018.

[13] China Nonferrous Metals Industry Yearbook, *China Nonferrous Metals Industry Yearbook Editorial Board 2014*, China Nonferrous Metals Industry, Beijing, China, 2014.

[14] M. Margni, R. Charles, S. Humbert, J. Payet, and O. Jolliet, "Impact 2002+: a new life cycle impact assessment methodology," *Int.j.life Cycle Assess*, vol. 8, no. 6, pp. 324–330, 2003.

[15] M. Owsianiak, A. Laurent, A. Bjorn, and M. Z. Hauschild, "Impact 2002+, recipe 2008 and Ilcd's recommended practice for characterization modelling in life cycle impact assessment: a case study-based comparison," *International Journal of Life Cycle Assessment*, vol. 19, no. 5, pp. 1007–1021, 2014.

[16] G. M. Olmez, F. B. Dilek, T. Karanfil, and U. Yetis, "The environmental impacts of iron and steel industry: a life cycle assessment study," *Journal of Cleaner Production*, vol. 130, pp. 195–201, 2016.

[17] J. Hong, Z. Yu, W. Shi, J. Hong, C. Qi, and L. Ye, "Life cycle environmental and economic assessment of lead refining in China," *The International Journal of Life Cycle Assessment*, vol. 22, pp. 909–918, 2016.

[18] Q. Wang, W. Liu, X. Yuan et al., "Environmental impact analysis and process optimization of batteries based on life cycle assessment," *Journal of Cleaner Production*, vol. 174, pp. 1262–1273, 2018.

Hindawi
Complexity
Volume 2020, Article ID 8882528, 8 pages
https://doi.org/10.1155/2020/8882528

Research Article

Research on the Multiobjective Optimization of Microwave Wireless Power Receiving in an Unmanned Aerial Vehicle Network

Yuanming Song,[1,2] **Yajie Liu**,[1,2] **Wanli Xu**,[3] **Xu Yang**,[1,2] **and Rui Wang**[1,2]

[1]*College of Systems Engineering, National University of Defense Technology, Changsha, Hunan 410073, China*
[2]*Hunan Key Laboratory of Multi-Energy System Intelligent Interconnection Technology (HKL-MSI2T), Changsha, Hunan 410073, China*
[3]*Institute of Systems Engineering, Academy of Military Sciences, Beijing 100091, China*

Correspondence should be addressed to Rui Wang; ruiwangnudt@gmail.com

Received 10 September 2020; Revised 23 September 2020; Accepted 26 September 2020; Published 9 October 2020

Academic Editor: Jing Na

With the wide application of various wireless energy transmission technologies and unmanned aerial vehicle clusters in both production and life, the use of microwave wireless energy transmission to provide a real-time energy supply for an unmanned aerial vehicle network in flight has become an effective way to extend its working time. This paper focuses on the optimization of the energy transmission efficiency and cost in the microwave wireless power receiving process of an unmanned aerial vehicle network. Considering the overall energy transmission efficiency from the power supply terminal to the power receiving network and the cost of the wireless power transmission equipment of the network, we have established a multiobjective wireless power receiving optimization model including a microwave energy emission source and an unmanned aerial vehicle network that receives energy. The model is optimized to select the best wireless power access point and the number of wireless power receiving modules in a network node. In the case study, the optimization model is solved using an evolutionary algorithm, and the solution results verify the effectiveness and correctness of the model.

1. Introduction

To date, near-field wireless power transmission technology, represented by electric field coupling and magnetic field coupling wireless energy transmission technology, has been widely used to conveniently charge consumer electronic products, provide uninterrupted power supplies to sensor networks, and charge electric vehicles [1–5]. In terms of far-field wireless power transmission, the effective wireless power transmission distance currently reaches the kilometer level [6, 7], and wirelessly transmitting power to unmanned aerial vehicles (UAVs) has also been verified in practice [8]. Among the various applications, microwave wireless power transmission, as a far-field wireless energy transmission technology with relatively mature technology and high long-distance transmission efficiency [9, 10], can well meet the needs of providing electrical energy for working UAVs. Therefore, this paper researches the background of microwave wireless power transmission technology.

In the current research on microwave wireless power transmission technology applications, point-to-point energy transmission is often considered [6, 11]. In this context, a higher point-to-point wireless power transmission efficiency is pursued by optimizing the transmission process and improving the efficiency of every energy conversion step [11]. Since UAV clustering research has been widely used, it is necessary to research wireless power transmission efficiency optimization for the power receiving terminals in an actual UAV network.

A microwave beam attenuates exponentially in a uniform atmosphere [12], and, at the same time, geometric attenuation is caused by beam divergence during transmission [13]. Atmospheric attenuation is only related to the transmission distance. Due to the nature of exponential

attenuation, the atmospheric attenuation rate is the same when microwaves are transmitted over the same distance in the same medium, regardless of whether they are forwarded through intermediate nodes. Geometric attenuation can be effectively avoided by adding an appropriate number of intermediate nodes during the energy transmission process or increasing the effective area (antenna aperture) of the receiving antenna at the receiving terminal. In the optimization of this paper, this characteristic of microwave wireless power transmission needs to be considered. Figure 1 compares the geometric attenuation of microwave wireless power transmission through the intermediate node and without the intermediate node at the same transmission distance when the antenna aperture of the intermediate node and the power receiving terminal is constant.

In a UAV network, each node is equipped with the same wireless power transmission equipment, and each node can receive and transmit wireless power. When using microwave wireless power transmission technology to power a UAV network, the power supply terminal can only provide point-to-point microwave power transmission. Affected by the size and weight of its equipment, it takes a long time for the power supply terminal to switch the power supply object, retrack, and start wireless power transmission. Therefore, it is necessary to select a node in the network as a wireless power access point (WPAP), which relays microwave power to other network nodes.

The selection of the WPAP needs to consider the power transmission efficiency from the microwave energy source (power supply terminal) to the access point and the transmission efficiency from the access point to the entire UAV network. UAV networks often need to work far away from the energy supply. In this case, if the power transmission efficiency from the power supply terminal to the WPAP is maximized, it is often necessary to select a node at the edge of the UAV network as the WPAP. However, it is known that choosing a point close to the center of the UAV network as the access point can maximize the power transmission efficiency from the WPAP to the entire UAV network. Besides, the choice of the WPAP will affect the performance requirements of the wireless power transmission equipment on the UAV network node and further affect the cost of the wireless power transmission equipment of the entire network. Therefore, optimization needs to be performed to select the best wireless power access point and the number of wireless power receiving modules in a network node considering the relative position of the power supply terminal and the energy receiving UAV network, the environmental conditions in the power transmission process, and the atmospheric attenuation and geometric attenuation during the wireless transmission of microwave energy. In the optimization, the requirement of minimizing the network power transmission equipment cost and the requirement of maximizing the network power receiving efficiency restrict each other, which constitutes a typical multiobjective optimization problem.

This paper establishes a power receiving optimization model that includes the microwave energy transmission source and an energy receiving UAV network, which is designed to maximize the overall power transmission efficiency and minimize the cost of the wireless power transmission equipment in the network. The model is optimized to select the best WPAP in the UAV network and the number of wireless power receiving modules in a network node. The main contributions of this paper are as follows:

(1) Corresponding unit models have been established for the wireless power supply terminal, UAV network nodes, and wireless power transmission equipment. On this basis, the UAV network power receiving optimization model is further constructed, and the atmospheric attenuation and geometric attenuation of the microwave beam are considered in the model.

(2) According to the nature of the problem and the characteristics of the model constraints, a solution method based on the coevolutionary constrained multiobjective optimization (CCMO) [14] framework is provided.

(3) Through the in-depth analysis of the solution results, the effectiveness and correctness of the viewpoints, the proposed model, and the solution method in this paper are verified.

2. Literature Review

Currently, there have been many studies on optimizing the wireless power receiving efficiency for a power receiving network [15–22]. Literature [15] is based on the near-field broadcast radio frequency signal energy transfer method with the objective of maximizing the amount of transferred energy at all receivers during the charging period and optimizing the energy receiving process of the sensor network. Literature [16] also uses near-field broadcast wireless power transfer technology to optimize the balance of energy collected by the sensor nodes in the network. Literatures [17–19] are based on simultaneous wireless information and power transfer technology, and the objective is to extend the survival time of sensor networks through different optimization methods.

Literature [20] is based on using magnetic field coupling wireless energy transmission technology to power a wireless power transmission network composed of multiple nodes. This kind of wireless power transmission network uses the strong coupling generated between the resonant bodies to form a "high-efficiency power transmission channel." Based on this principle, literature [21] used magnetic field coupling power transmission technology to transmit electrical energy to the receiving end 2 meters away, thus increasing the effective wireless power transmission distance. Literature [22] studies the network survival time optimization problem of this wireless power transmission network under active injection and passive injection. It is verified through experiments that the path optimization of the wireless power transmission network with active injection and passive injection can be effectively solved using the cellular genetic algorithm.

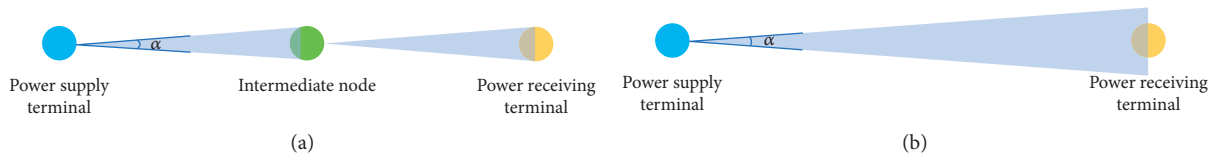

Figure 1: Comparison of the geometric attenuation of microwave wireless energy transmission.

In summary, the existing research studies on wireless power supply optimization for the energy receiving network are all based on near-field wireless power transmission technology. In terms of the applied research and related optimal design of far-field wireless power transmission, the receiving terminal is always a single node [6]. Due to the difference in the power transmission principle, far-field wireless energy transmission technology cannot use broadcasting or establish energy transmission channels to supply energy to the power receiving node in the form of a network; therefore, the problem of network wireless power receiving optimization using far-field wireless energy transmission technology urgently needs to be studied.

In this case, using microwave wireless energy transmission technology, this paper constructs a multiobjective optimization model with a UAV network as the energy receiving terminal to fill in the research gap on far-field wireless power supply optimization for the power receiving terminal in the form of a network.

3. Optimization Problem Modeling

3.1. Unit Models. The UAV network power receiving optimization model in this paper involves the wireless power supply terminal, the UAV network node, and the wireless power receiving module that can be mounted on the UAV network node. Since the wireless power transmission performance of the UAV network node is determined by the equipment it carries, the unit model is only constructed for the wireless power supply terminal, the wireless power supply module, and the wireless power receiving module. To simplify the calculation, this paper assumes that the microwave beam used in wireless power transmission is a plane wave, and the energy density on the beam section obeys a uniform distribution [23, 24].

3.1.1. Model of the Microwave Wireless Power Supply Terminal. The main parameters of the power supply terminal (fixed microwave energy-emitting source) include the microwave beam excitation angle ($\alpha_{\text{wav}}^{\text{ps}}$), the conversion efficiency ($\eta_{\text{wes}}^{\text{ps}}$) of converting electrical energy into microwave energy, and the three-dimensional coordinates (POS_{ps}) of the microwave source. When the microwave emitter at the power supply node emits microwaves in a certain direction in space, the energy distributed on the beam cross section ($P_{\text{mwsec}}(L_{\text{wet}})$) with a distance of L_{wet} from the power supply node can be calculated by the following formula:

$$P_{\text{mwsec}}(L_{\text{wet}}) = \eta_{\text{wes}}^{\text{ps}} \cdot \kappa \cdot e^{-\gamma \cdot L_{\text{wet}}} \cdot P_{\text{wes}}^{\text{ps}}, \tag{1}$$

where $P_{\text{wes}}^{\text{ps}}$ is the actual power of the microwave emitter at the power supply terminal; γ is the atmospheric attenuation coefficient, which is related to the atmospheric conditions along the beam transmission path; and κ is the tracking loss coefficient. The values of γ and κ are determined based on actual weather conditions and equipment conditions during transmission.

3.1.2. Model of the Microwave Wireless Power Supply Module. The microwave wireless power supply module is a modularized microwave energy emission source, and its main parameter types include the microwave beam excitation angle ($\alpha_{\text{wav}}^{\text{smod}}$), the conversion efficiency ($\eta_{\text{wes}}^{\text{smod}}$), and the module weight (m_{smod}). When the wireless power supply module emits microwaves in a certain direction in space, the energy distributed on the beam cross section ($P_{\text{mwsec}}(L_{\text{wet}})$) with a distance of L_{wet} from the wireless power supply module can be calculated by the following formula:

$$P_{\text{mwsec}}(L_{\text{wet}}) = \eta_{\text{wes}}^{\text{smod}} \cdot \kappa \cdot e^{-\gamma \cdot L_{\text{wet}}} \cdot P_{\text{wes}}^{\text{smod}}, \tag{2}$$

where $P_{\text{wes}}^{\text{smod}}$ is the actual working power of the wireless power supply module.

3.1.3. Model of the Microwave Wireless Power Receiving Module. The main parameters of the microwave wireless power receiving module are the receiving antenna aperture ($S_{\text{wer}}^{\text{rmod}}$), the efficiency ($\eta_{\text{wer}}^{\text{rmod}}$) of converting the microwave energy distributed on the effective area of the antenna into electric energy, and the module weight (m_{rmod}). When the distance between the receiving antenna and the microwave emitting source is L_{wet}, the beam excitation angle of the emitting source is α_{wav}, and the electric power P_{wer} converted from microwave energy by the receiving module is calculated by the following formula:

$$P_{\text{wer}} = \eta_{\text{wer}}^{\text{rmod}} \cdot \min\left(\frac{S_{\text{wer}}^{\text{rmod}}}{S_{\text{wav}}(\alpha_{\text{wav}}, L_{\text{wet}})}, 1\right) \cdot P_{\text{mwsec}}(L_{\text{wet}}). \tag{3}$$

Under the plane wave assumption, for the beam cross-sectional area in the equation, $S_{\text{wav}}(\alpha_{\text{wav}}, L_{\text{wet}})$, there is

$$S_{\text{wav}}(\alpha_{\text{wav}}, L_{\text{wet}}) = \pi\left(\tan\left(\frac{\alpha_{\text{wav}}}{2}\right) \cdot L_{\text{wet}}\right)^2, \quad \alpha_{\text{wav}} \in (0, \pi). \tag{4}$$

3.2. Microwave Wireless Power Receiving Model of the UAV Network. The UAV network microwave wireless power receiving model is mainly composed of a wireless power supply terminal and UAV network nodes equipped with

wireless power transmission modules. The power receiving process of the UAV network is as follows:

(a) Electric energy is first converted into microwave form at the wireless power supply terminal and transmitted to a WPAP node in the network in a point-to-point manner.

(b) When the WPAP receives microwave energy, it reserves the power needed to maintain its normal operation and transmits the remaining power to the node in the network with the least remaining power at that time via wireless power transmission. When the node that is receiving energy is no longer the node with the least remaining power in the network, the WPAP will switch the power transfer object to the node with the least remaining power in the network.

Based on the aforementioned energy receiving process, the UAV network can extend its working time as much as possible through the WPAP. The power transmission efficiency $\eta_{\text{PS-AP}}$ from the power supply terminal to the WPAP is calculated by the following formula:

$$\eta_{\text{PS-AP}} = \kappa \cdot \gamma^{L_{\text{PS-AP}}} \cdot \eta_{\text{wes}}^{\text{PS}} \cdot \eta_{\text{wer}}^{\text{rmod}} \cdot \min\left(\frac{S_{\text{wer}}^{N}}{S_{\text{wav}}\left(\alpha_{\text{wav}}^{\text{ps}}, L_{\text{PS-AP}}\right)}, 1\right), \tag{5}$$

where $L_{\text{PS-AP}}$ is the distance from the power supply terminal to the WPAP and S_{wer}^{N} is the energy receiving antenna aperture of a single UAV network node. Its calculation method is

$$S_{\text{wer}}^{N} = N_{\text{rmod}} \cdot S_{\text{wer}}^{\text{rmod}}, \tag{6}$$

where N_{rmod} is the number of wireless power receiving modules carried by a single UAV network node. The energy transfer efficiency $\eta_{\text{AP-}N}^{i}$ from the WPAP to the ith node in the network except the WPAP is calculated by the following formula:

$$\eta_{\text{AP-}N}^{i} = \kappa \cdot \gamma^{L_{\text{AP-}N}^{i}} \cdot \eta_{\text{wes}}^{\text{PS}} \cdot \eta_{\text{wer}}^{\text{rmod}} \cdot \min\left(\frac{S_{\text{wer}}^{N}}{S_{\text{wav}}\left(\alpha_{\text{wav}}^{\text{smod}}, L_{\text{AP-}N}^{i}\right)}, 1\right), \quad i \in \{1, 2, \ldots, N_{\text{node}} - 1\}, \tag{7}$$

where $L_{\text{AP-}N}^{i}$ is the distance from the WPAP to the ith node in the network except the WPAP and N_{node} is the total number of nodes in the UAV network.

3.3. Optimization Objectives. The primary goal of UAV network power receiving optimization is to maximize the overall power transmission efficiency from the power supply terminal to the power receiving network. In addition, the cost of the wireless power transmission equipment of the network needs to be considered. Therefore, the optimization objectives are to maximize the overall power transmission efficiency and minimize the cost of the wireless power transmission equipment of the network.

(a) *Overall Power Transmission Efficiency*. The overall power transfer efficiency ($\eta_{\text{PS-UN}}$) from the power supply terminal to the power receiving UAV network is calculated by the following formula:

$$\eta_{\text{PS-UN}} = \eta_{\text{PS-AP}} \cdot \frac{1 + \sum_{i=1}^{N_{\text{node}}-1} \eta_{\text{AP-}N}^{i}}{N_{\text{node}}}. \tag{8}$$

(b) *Cost of the Network Wireless Power Transmission Equipment*. The cost of the network wireless power transmission equipment (C_{mod}) is calculated by the following formula:

$$C_{\text{mod}} = N_{\text{node}} \cdot N_{\text{rmod}} \cdot C_{\text{rmod}}, \tag{9}$$

where C_{rmod} is the price of a single microwave wireless power receiving module. Since the number of microwave power supply modules is not involved in the optimization of this paper, their related costs are not reflected in C_{mod}.

4. Solving the Model

In the power receiving optimization of the UAV network in this paper, two mutually restrictive goals, maximizing the overall energy transmission efficiency ($\eta_{\text{PS-UN}}$) and minimizing the cost of the wireless power transmission equipment of the network (C_{mod}), need to be considered, which forms a typical multiobjective optimization problem. To solve this problem, it is necessary to optimize the overall energy transmission efficiency from the power supply terminal to the power receiving network and the cost of the wireless power transmission equipment of the network considering the atmospheric attenuation and geometric attenuation during the wireless transmission of microwave energy based on the relative position of the power supply terminal, the energy receiving UAV network, and the environmental conditions in the energy transmission process. In recent years, many new evolutionary algorithms with excellent performance have been continuously proposed [25, 26], and various coevolutionary algorithms have been applied to solve optimization problems in many fields [27, 28]. CCMO, as a newly proposed framework of multiobjective coevolutionary algorithms, has shown excellent performance on multiple benchmark problems [14], and its characteristics are also suitable for the experiments in this paper. Therefore, the optimization model in this paper is solved via CCMO.

In the solution, the decision variables are the serial number (SN_{WPAP}) of the UAV network node selected as the

WPAP and the number of wireless power receiving modules (N_{rmod}) in the UAV network node. Since the number of power supply modules carried by the UAV network node does not affect the efficiency of network power receiving, the number of power supply modules is not involved in the optimization. By default, all nodes of the UAV network are equipped with a set of wireless power supply modules. Besides, because the objective function in the optimization needs to be in a minimized form, the aforementioned optimization objective is converted to minimize the overall power loss rate ($1 - \eta_{\text{PS-UN}}$) and the wireless power transmission (WPT) equipment cost of the UAV network (C_{mod}) when solving the model.

Figure 2 shows the solution process of the UAV network power receiving optimization model based on CCMO. First, enter the parameters required for optimization: the model constraints, the range of decision variables, the number of population individuals, and the maximum number of iterations. Next, produce the initial main population and initial archive population and calculate the fitness of the individuals in the two populations. Then, enter the main loop of the algorithm through the coevolution of the archive population that only calculates the fitness of the individual and the main population that calculates the fitness of the individual and the degree of constraint violation simultaneously to quickly and effectively solve the constraint optimization problem in this paper. Finally, after reaching the maximum number of iterations, the resulting solution is output.

Based on the optimization objectives, decision variables, and constraints that have been determined above, the power receiving optimization problem of the UAV network can be described as follows:

Objective function:

$$\min F_{\text{obj}} = \left(1 - \eta_{\text{PS-UN}}, C_{\text{mod}}\right). \tag{10}$$

Restrictions:

$$\begin{aligned} \text{SN}_{\text{WPAP}} &\in \{1, 2, \ldots, N_{\text{node}}\}; \\ N_{\text{rmod}} &\geq 0,\ N_{\text{rmod}} \in Z; \\ N_{\text{rmod}} \cdot m_{\text{rmod}} + N_{\text{smod}} \cdot m_{\text{smod}} &\leq \text{ML}_{\text{node}}. \end{aligned} \tag{11}$$

In the previous formula, F_{obj} represents the objective function including two objectives; Z is the integer set; N_{smod} represents the number of wireless power supply modules carried by the UAV network node, which takes the value 1 in the solution of this paper; and ML_{node} represents the maximum load capacity of the UAV network node.

5. Case Study

5.1. Data Preparation. To verify the effectiveness of the optimization model, this paper conducts UAV network microwave wireless power receiving optimization based on the equipment technical parameters and cost data required for optimization, which are compiled from related literature and public data on commercial UAV platforms [6, 7, 12, 13]. The optimization process does not consider the occlusion caused by terrain changes or other reasons and assumes that the atmospheric environment in the experiment remains uniform and undisturbed.

The X-Y plane coordinates of the power supply terminal and the energy receiving UAV network node in the experiment are shown in Figure 3. The Z-axis coordinate of the power supply terminal is 0, and the Z-axis coordinates of the UAV network nodes are all 500. In the experiment, the UAV network nodes are numbered in the order from left to right and bottom to top (on the X-Y plane); the node number in the lower-left corner of the network in the figure is 1, and the node number in the upper right corner is 16. The experimental parameter settings in the solution are shown in Table 1.

5.2. Results and Analysis. When using CCMO to solve the UAV network power receiving optimization problem, the initial main population and the initial archive population containing 25 individuals are first generated, and then 100 evolutions are performed. The result of the last generation of the solution, the optimal Pareto frontier, is shown in Figure 4.

From the trend of the Pareto frontier in Figure 4, it can be seen that the overall power loss rate ($1 - \eta_{\text{PS-UN}}$) and the cost (C_{mod}) of network wireless power transmission equipment have an obvious negative correlation. An energy receiving UAV network with a low overall power loss rate needs to be at the expense of high network wireless power transmission equipment costs. Several sudden changes occurred on the slope of the Pareto frontier in Figure 4. This is because the schemes on the left and right of the slope change the point by selecting different nodes as the WPAP.

After 100 iterations, 25 nondominated UAV network microwave wireless power receiving schemes are finally obtained. These schemes are all theoretically optimal schemes, and decision makers can choose the most suitable planning scheme according to their preferences. For example, decision makers can prioritize the efficiency index of the UAV network power receiving, that is, they can select the optimal solution according to the value of $\eta_{\text{PS-UN}}$. In the Pareto frontier shown in Figure 4, eight representative solutions are selected for further analysis. The selected solutions are shown in Table 2.

It can be seen that in the optimal scheme, when the UAV network node closest to the power supply terminal is selected as the WPAP, the network node carrying fewer power receiving modules can optimize the power receiving efficiency of the network. When choosing the node closer to the center of the network as a WPAP, the network nodes need to carry more power receiving modules to achieve the optimal energy receiving efficiency of the network. Only by choosing a node closer to the center of the network as a WPAP can higher network power receiving efficiency be achieved. At

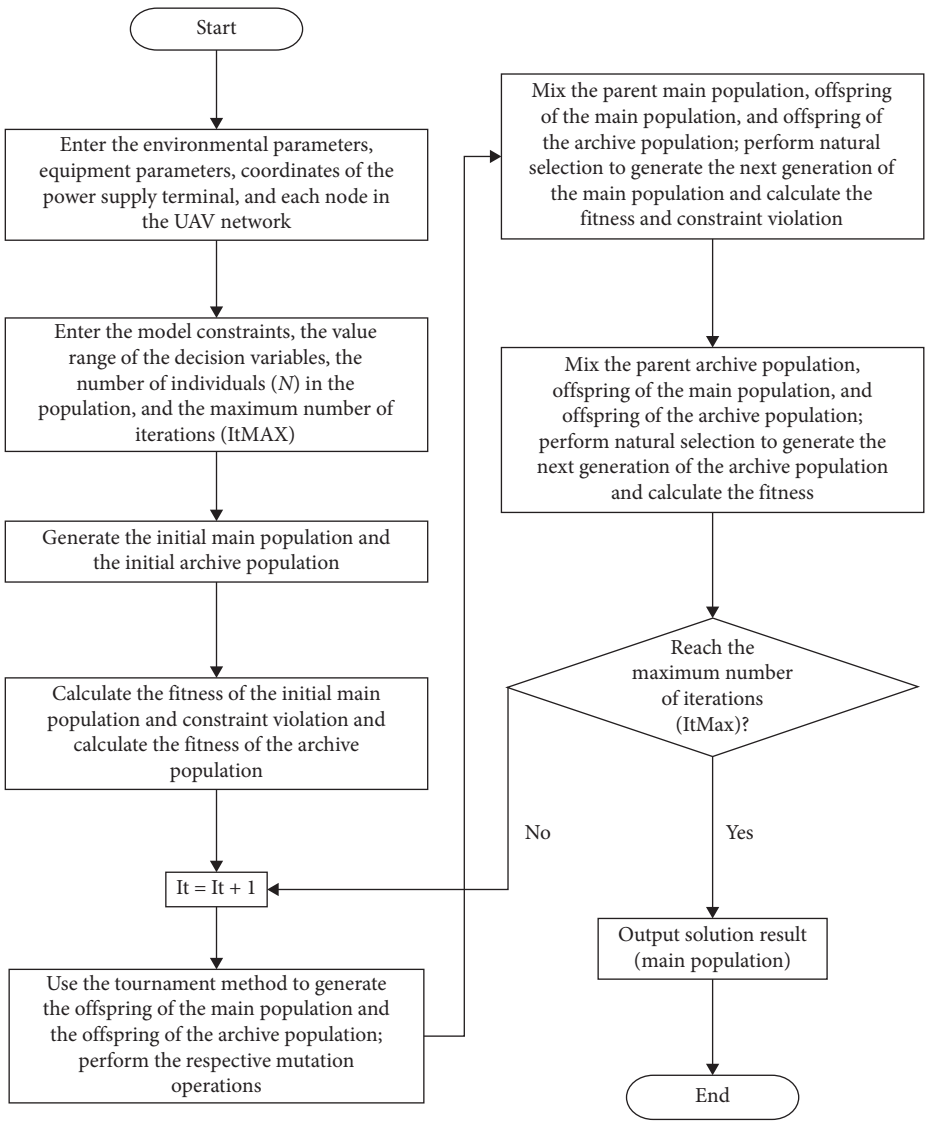

Figure 2: Flowchart of the solution based on CCMO.

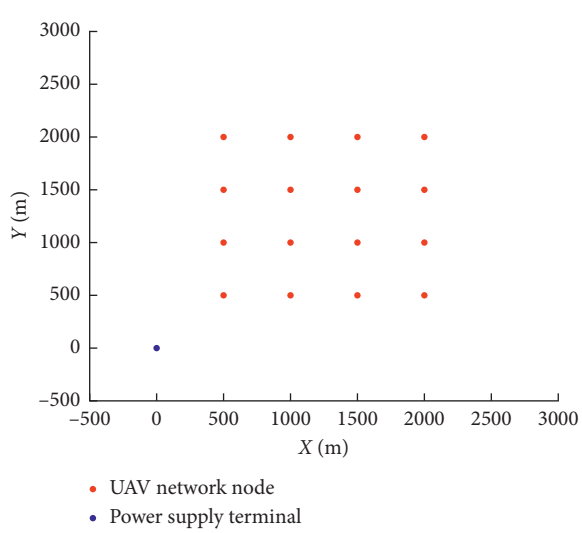

Figure 3: X-Y plane coordinates of UAV network nodes and the power supply terminal.

Table 1: Experimental parameters.

Symbol	Value
η_{wes}^{ps}	0.85
η_{wes}^{smod}	0.90
η_{wer}^{rmod}	0.70
γ	1.01×10^{-3}
κ	0.95
N_{node}	16
α_{wav}^{ps} (rad)	9.81×10^{-4}
α_{wav}^{smod} (rad)	9.81×10^{-4}
m_{smod} (kg)	0.55
m_{rmod} (kg)	0.30
ML_{node} (kg)	6
S_{wer}^{rmod} (m^2)	0.1
C_{rmod} (CNY)	1040

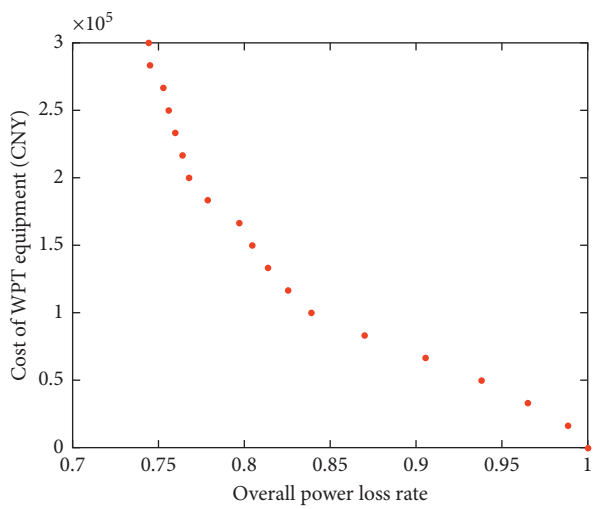

Figure 4: Last generation of the solution.

Table 2: The selected solutions.

Scheme number	Decision variable		Objective	
	SN_{WPAP}	N_{rmod}	η_{PS-UN} (%)	C_{mod} (CNY)
1	1	3	6.20	49920
2	1	6	16.10	99840
3	5	11	22.11	183040
4	2	12	23.22	199680
5	2	14	24.00	232960
6	5	15	24.39	249600
7	6	17	25.48	282880
8	6	18	25.53	299520

this time, the cost of network power receiving equipment is also higher.

In summary, the optimal Pareto front can be obtained by solving the model. The frontier shape conforms to theoretical expectations, and the correctness and effectiveness of the model have been verified. From the solution results, the closer the WPAP is to the energy supply end, the lower the cost of the network power receiving equipment required to achieve the optimal network power receiving efficiency. However, to achieve high network power receiving efficiency, it is necessary to select a node closer to the center of the UAV network as the WPAP, and this will result in higher network power receiving equipment costs.

6. Conclusions

To address the optimization problem of applying microwave wireless power transmission to supply electricity to the UAV network, this paper establishes a corresponding optimization model and performs optimization focused on the selection of the wireless power receiving point and the capacity of the wireless power receiving equipment on the UAV network node. In the practical application of various wireless power transmission technologies, the power transmission efficiency is always one of the key indicators. Besides, the impact of cost must be considered in practice. Therefore, the overall power transmission efficiency and the cost of network wireless power transmission equipment are adopted as objectives in the optimization. Considering that there is a strong coupling between the selection of the WPAP and the capacity optimization of the network power transmission equipment, the sequence number of the WPAP and the number of power receiving modules are coded on an individual in the model solving process based on CCMO. The solution results verify the effectiveness and correctness of the model and solution method in this paper. To achieve higher network power receiving efficiency, it is necessary to select a WPAP closer to the center of the UAV network, but this will cause higher network wireless power receiving equipment costs.

The follow-up research will modify and improve the model and solution method in this paper according to actual needs. The research results of this paper can provide theoretical support for the follow-up research on the construction and optimization of microwave wireless power supply networks composed of multiple links.

Data Availability

Almost all the data are presented in the tables of this paper. If there is a need for any other information, the corresponding author may be contacted by email.

Conflicts of Interest

The authors declare that there are no conflicts of interest regarding the publication of this paper.

Acknowledgments

This study was supported by the National Natural Science Foundation of China (grant nos. 71901210 and 61973310), the Hunan Youth Elite Program (2018RS3081), and the Key Project of National University of Defense Technology (ZK18-02-09).

References

[1] S. A. Mirbozorgi, H. Bahrami, M. Sawan, and B. Gosselin, "A smart multicoil inductively coupled array for wireless power

transmission," *IEEE Transactions on Industrial Electronics*, vol. 61, no. 11, pp. 6061–6070, 2014.

[2] J. Chen, C. W. Yu, and W. Ouyang, "Efficient wireless charging pad deployment in wireless rechargeable sensor networks," *IEEE Access*, vol. 8, pp. 39056–39077, 2020.

[3] J. Baek, S. I. Han, and Y. Han, "Optimal UAV route in wireless charging sensor networks," *IEEE Internet of Things Journal*, vol. 7, no. 2, pp. 1327–1335, 2020.

[4] Y. Gao, X. Zhang, Q. X. Yang, B. Wei, and L. Wang, "Bio-electromagnetic safety assessment of wireless charging environment for electric vehicles," *Journal of Electrotechnical Technology*, vol. 34, no. 17, pp. 3581–3589, 2019, in Chinese.

[5] F. Y. Lin, G. A. Covic, and J. T. Boys, "Evaluation of magnetic pad sizes and topologies for electric vehicle charging," *IEEE Transactions on Power Electronics*, vol. 30, no. 11, pp. 6391–6407, 2015.

[6] S. G. Li, Z. L. Chen, L. Song et al., "Research on Ku-band microwave wireless energy transmission system technology," *Journal of Microwaves*, vol. 35, no. 4, pp. 56–61, 2019, in Chinese.

[7] H. H. Ma, H. Xu, X. Li et al., "A highly efficient microwave wireless power transmission system," *Space Electronic Technology*, no. 1, pp. 1–5, 2016, in Chinese.

[8] AUVSI: LaserMotive, Lockheed Demonstrate Real-World Laser Power, 2012, https://www.flightglobal.com/news/articles/auvsi-lasermotive-lockheed-demonstrate-real-world-laser-375166/.

[9] W. Ni, F. Ding, J. Zong, W. W. Ji, and X. J. Liu, "Research progress of electric energy wireless transmission and energy interconnection technology," *Power Technology*, vol. 43, no. 2, pp. 357–360, 2019.

[10] R. M. Dickinson, "Performance of a high-power, 2.388 GHz receiving array in wireless power transmission over 1.54 km," in *Proceedings of the 1976 IEEE-MTT-S International Microwave Symposium*, pp. 139–141, Cherry Hill, NJ, USA, June 1976.

[11] R. C. Zhang and Y. H. Li, "C-band microwave wireless power transmission transmitter design," *Modern Electronic Technology*, vol. 40, no. 9, pp. 6–13, 2017, in Chinese.

[12] A. Prokes, "Atmospheric effects on availability of free space optics system," *Optical Engineering*, vol. 48, no. 6, pp. 066001-1–066001-9, 2009.

[13] M. Liu, X. G. Liu, J. Y. Mou, and X. J. Wu, "Analysis of optical power attenuation model for wireless optical communication," *Infrared and Laser Engineering*, vol. 41, no. 8, pp. 2136–2140, 2012, in Chinese.

[14] Y. Tian, T. Zhang, J. Xiao, X. Zhang, and Y. Jin, "A coevolutionary framework for constrained multi-objective optimization problems," *IEEE Transactions on Evolutionary Computation*, 2020.

[15] J. Xu, Y. Zeng, and R. Zhang, "UAV-enabled wireless power transfer: trajectory design and energy optimization," *IEEE Transactions on Wireless Communications*, vol. 17, no. 8, pp. 5092–5106, 2018.

[16] F. Huang, J. Chen, and H. Wang, "UAV-assisted SWIPT in internet of things with power splitting: trajectory design and power allocation," *IEEE Access*, vol. 7, pp. 68260–68270, 2019.

[17] M. Jiang, Y. Li, Q. Zhang, and J. Qin, "Joint position and time allocation optimization of UAV enabled wireless powered communication networks," *IEEE Transactions on Communications*, vol. 67, no. 5, pp. 3806–3816, 2019.

[18] L. Xie, J. Xu, and R. Zhang, "Throughput maximization for UAV-enabled wireless powered communication networks," *IEEE Internet of Things Journal*, vol. 6, no. 2, pp. 1690–1703, 2019.

[19] S. Cho, K. Lee, B. Kang, K. Koo, and I. Joe, "Weighted harvest-then-transmit: UAV-enabled wireless powered communication networks," *IEEE Access*, vol. 6, pp. 72212–72224, 2018.

[20] Y. Sun, X. Dai, and C. Tang, "Distributed wireless power transmission network," *Power Electronics*, no. 3, pp. 59–61, 2010, in Chinese.

[21] K. Leec, W. X. Zhong, and Y. R. Huis, "Effects of magnetic coupling of nonadjacent resonators on wireless power domino-resonator systems," *IEEE Transactions on Power Electronics*, vol. 27, no. 4, pp. 1905–1916, 2012.

[22] Y. Sun, J. Xia, C. Tang, and L. Xiang, "Optimization of wireless power transmission network path using cellular genetic algorithm," *Journal of Xi'an Jiaotong University*, vol. 51, no. 4, pp. 30–36, 2017.

[23] Links with focus on Malaysia, Proceeding of the International Conference in Computer and Communication Engineering, 2008.

[24] M. S. Sheikh, P. Kohldorfer, and E. Leitgeb, "Channel modeling for terrestrial free space optical links," in *Proceedings of the 2005 7th International Conference Transparent Optical Networks*, pp. 407–410, Barcelona, Spain, July 2005.

[25] R. Wang, Q. Zhang, and T. Zhang, "Decomposition-based algorithms using Pareto adaptive scalarizing methods," *IEEE Transactions on Evolutionary Computation*, vol. 20, no. 6, pp. 821–837, 2016.

[26] R. Wang, Z. Zhou, H. Ishibuchi, T. Liao, and T. Zhang, "Localized weighted sum method for many-objective optimization," *IEEE Transactions on Evolutionary Computation*, vol. 22, no. 1, pp. 3–18, 2018.

[27] R. Wang, R. C. Purshouse, and P. J. Fleming, "Preference-inspired coevolutionary algorithms for many-objective optimization," *IEEE Transactions on Evolutionary Computation*, vol. 17, no. 4, pp. 474–494, 2013.

[28] Y. Song, Y. Liu, R. Wang, and M. Ming, "Multi-objective configuration optimization for isolated microgrid with shiftable loads and mobile energy storage," *IEEE Access*, vol. 7, pp. 95248–95263, 2019.